

DataBookIII	2
Chapter_1	8
Chapter_2	36
Chapter_3	46
Chapter_4	66
Chapter_5	93
Chapter_7	120
Chapter_8	172
Chapter_9	199
Chapter_10	237
Chapter_11	266
Chapter_12	288
Chapter_13	322
Chapter_14	356
Chapter_15	395
Chapter_16	412
Chapter_17	437
Chapter_18	501
appA	532
appC	548
ref	549



# *Engineering Data Book III*

Written by Professor John R. Thome  
Director, Laboratory of Heat and Mass Transfer (LTCM)  
Faculty of Engineering Science and Technology  
Swiss Federal Institute of Technology Lausanne (EPFL)  
CH-1015 Lausanne, Switzerland

# Preface

Welcome to the new edition of Wolverine Tube Inc.'s *Wolverine Engineering Data Book III*. This book has been written primarily with heat transfer engineers in mind but also for research engineers who want to get caught up on the latest advances in heat transfer design methods for tubular heat exchangers. The objectives of the book are to present a limited review of the basic principles of heat transfer and then describe what I currently consider to be the best thermal design methods available. Hence, each chapter presents a detailed state-of-the-art review of heat transfer and fluid flow research of practical interest to heat exchanger designers, manufacturers and end users; however, for more exhaustive treatments the reader is recommended to go to the many references and other reviews cited.

The idea to make this a web-based book available on Wolverine Tube Inc.'s website is to make this information more readily available to the reader. New chapters will be added as they become ready and also the existing chapters will be updated with new methods as they appear in the literature every few years to keep this whole reference book up to date. Also, Chapter 1 presents a video gallery of heat transfer and flow phenomena that I think will be quite useful to heat transfer engineers who have never had the chance to see what is in fact happening inside their heat exchangers!

I, myself, have pulled *Wolverine Engineering Data Book II* down from the shelf many times over the years to look for design information to use my own engineering work. *Data Book II* is also available on the same website as *Data Book III* and contains much valuable information that has not been repeated in *Data Book III*.

Finally, I would like to thank Wolverine Tube Inc. for inviting me to write this new edition of *Data Book III*, in particular Massoud Neshan and Petur Thors of the Research and Development group.

John R. Thome, Author

## About the Author



**John R. Thome** is Professor of Heat and Mass Transfer at the Swiss Federal Institute of Technology in Lausanne (EPFL), Switzerland since 1998, where he is director of the Laboratory of Heat and Mass Transfer (LTCM) in the Faculty of Engineering Science and Technology (STI). His primary interests of research are two-phase flow and heat transfer, covering boiling and condensation of internal flows, external flows, enhanced surfaces and microchannels. He received his Ph.D. at Oxford University, England in 1978 and was formerly a professor at Michigan State University. From 1984 to 1998, he set up and operated his own international engineering consulting company specializing in enhanced heat transfer surfaces and enhanced heat exchanger design methods. He is the author of several books: *Enhanced Boiling Heat Transfer* (1990) and *Convective Boiling and Condensation* (1994). He received the ASME

Heat Transfer Division's Best Paper Award in 1998 for a 3-part paper on flow boiling heat transfer published in the *Journal of Heat Transfer*. The website of his laboratory is <http://lstm.epfl.ch> and his e-mail address is [john.thome@epfl.ch](mailto:john.thome@epfl.ch).

# Table of Contents

## **Chapter 1: Video Gallery of Flow Phenomena**

[Chapter 1](#) provides a video gallery of flow and heat transfer phenomena and their descriptions, along with links to other chapters that pertained to it.

## **Chapter 2: Design Considerations for Enhanced Heat Exchangers**

[Chapter 2](#) covers the thermal design considerations, mechanical design considerations, cost considerations, parametric studies on thermal designs, case studies of actual interventions and other practical information.

## **Chapter 3: Single-Phase Shell-Side Flows and Heat Transfer**

[Chapter 3](#) presents the most recent open literature version of the stream analysis method for shell-side flows in addition to the older graphical presentation of the Delaware method in *Wolverine Engineering Data Book II*.

## **Chapter 4: Enhanced Single-Phase Laminar Tube-Side Flows and Heat Transfer**

[Chapter 4](#) provides a treatment of correlations for predicting heat transfer and pressure drop for intube flows in corrugated tubes, ribbed tubes, finned tubes and with twisted tape inserts. It covers laminar flow and laminar flow augmentation.

## **Chapter 5: Enhanced Single-Phase Turbulent Tube-Side Flows and Heat Transfer**

[Chapter 5](#) provides a treatment of correlations for predicting heat transfer and pressure drop for intube flows in corrugated tubes, ribbed tubes, finned tubes and with twisted tape inserts. It covers turbulent flow and turbulent flow augmentation.

## **Chapter 6: Heat Transfer to Air-Cooled Heat Exchangers**

[Chapter 6](#) provides design methods for heat transfer and pressure drop to plain, wavy, corrugated, etc. plate-fin geometries typical of air-conditioning coils.

## **Chapter 7: Condensation on External Surfaces**

[Chapter 7](#) provides detail on condensation outside low finned tubes and enhanced condensing tubes, condensation of mixtures, tube row effects and intertube flow patterns, etc. It also includes more fundamentals that designers are interested in on effects of vapor shear, interfacial waves, condensate retention, etc.

## **Chapter 8: Condensation Inside Tubes**

[Chapter 8](#) provides design methods for condensation inside plain and microfin tubes.

## **Chapter 9: Boiling Heat Transfer on External Surfaces**

[Chapter 9](#) provides design methods for boiling outside plain, low-finned and enhanced tubes, evaporation of mixtures, etc. as single tubes and tube bundles. It includes the most widely used plain tube correlations and presents methods available for enhanced tubes and describes the fundamentals of pool boiling (nucleation, bubble dynamics, peak heat flux, etc.).

## **Chapter 10: Boiling Heat Transfer Inside Plain Tubes**

[Chapter 10](#) provides details on vertical and horizontal plain tube design methods.

## Chapter 11: Boiling Heat Transfer Inside Enhanced Tubes

[Chapter 11](#) provides details on microfin tubes, twisted tape inserts, corrugated tubes and porous coatings. It also presents the concepts of vertical and horizontal boiling and design methods.

## Chapter 12: Two-Phase Flow Patterns

[Chapter 12](#) provides flow pattern maps for vertical and horizontal intube flows (including Thome's flow pattern map which is becoming increasingly popular for adiabatic and evaporating flows). It also presents a shell-side flow pattern map and some background theory on transition from one regime to another.

## Chapter 13: Two-Phase Pressure Drop

[Chapter 13](#) provides a complete treatment of prediction of two-phase pressure drops for intube flows and shell-side flows. It also addresses oil effects on two-phase pressure drops.

## Chapter 14: Falling Film Evaporation

[Chapter 14](#) presents a summary of the status of falling film evaporation on the outside of horizontal tubes and tube bundles for plain and enhanced tubes.

## Chapter 15: Thermodynamics of Refrigerant Mixtures and Refrigerant-Oil Mixtures

[Chapter 15](#) presents an introduction to phase equilibria of mixtures that is useful to mechanical engineers. It shows the use and preparation of enthalpy curves for designing evaporators and condensers with mixtures. It also covers Thome's Thermodynamic Approach for modeling refrigerant-oil mixtures to show oil effects on the bubble point and enthalpy change of evaporating refrigerants that are important to include in the calculation of LMTD and energy balances.

## Chapter 16: Effects of Oil on Thermal Performance of Heat Exchangers

[Chapter 16](#) covers the effects on heat transfer and pressure drops of oil on intube evaporation in plain and microfin tubes. It also covers the effects of oil on pool boiling and bundle boiling on plain and enhanced tubes.

## Chapter 17: Void Fractions in Two-Phase Flows

[Chapter 17](#) presents the basic theory and predictions methods for the two-phase flows in vertical and horizontal channels and over tube bundles.

## Chapter 18: Post Dryout Heat Transfer

[Chapter 18](#) covers the heat transfer process and prediction method for describing heat transfer in the post dryout regime.

## Chapter 19: Flow Boiling and Two-Phase Flow of CO<sub>2</sub>

[Chapter 19](#) addresses experimental studies and prediction methods for CO<sub>2</sub>, together with some comparisons of these methods to experimental databases.

## Chapter 20: Two-Phase Flow and Flow Boiling in Microchannels

[Chapter 20](#) addresses both experimental studies and predication methods for microchannels, together with some comparisons of these methods to experimental databases and to one another.

## Chapter 21: Condensation in Microchannels

[Chapter 21](#) addresses experimental studies and predication methods for condensation inside small channels, together with some comparisons of these methods to experimental data and to one another.

### Appendix A:

[Appendix A](#) provides a list of all nomenclatures and their definitions.

### Appendix B:

[Appendix B](#) provides tables with properties of commonly used refrigerants (e.g. R-123, R-134a, etc.).

### Appendix C:

[Appendix C](#) provides web links to related websites, programs, and enhanced tube descriptions of Wolverine Tube, Inc.

### References:

[References](#) provide a list of resources that were used to write Wolverine Engineering Data Book III.

# Chapter 1

## Video Gallery of Flow Phenomena

(This chapter was updated in 2007. Note: the new videos require use of an updated video player.)

**Summary:** Numerous videos have been assembled here for two-phase flows and heat transfer phenomena (and still more will be added in the future) and are available here for the reader to view. Presently, only two-phase videos are shown but videos of single-phase enhancement phenomena will be included in the future.

### 1.1 INTRODUCTION TO THE VIDEO GALLERY

The motive behind the preparation of this video gallery is to make videos of single-phase and two-phase flow and heat transfer phenomena available for general viewing. For thermal designers normally performing computer calculations on heat exchangers, this is an opportunity for them to actually see what some of the processes really look like, albeit in idealized test conditions. The idea is also to make this chapter a forum to display interesting videos of such phenomena for others to see.

**Note:** Since the original video files are typically too large (5-40 Megabits) to view directly via the internet, the videos shown have had to cut to short time sequences (typically 2 seconds or less) that are looped to give the sensation of a continuous process and also processing of the images has been applied to achieve smaller file sizes, but at a small lose of quality. Some patience may be required on behalf of the reader to view these video files via the Internet.

**To use this chapter:** The chapter is organized by type of flow. Within each section, videos are listed by the flow process they show; the reader needs only to click on the video of his choice on the list to see the video and also obtain a brief description of the test setup and experimental conditions.

### 1.2 TWO-PHASE FLOW PATTERNS IN HORIZONTAL TUBES

Figure 1.1 depicts a two-phase flow pattern map for flow in a horizontal tube, illustrating the types of two-phase flow patterns typical of these flows and the range of conditions where particular flow regimes occur. Within a horizontal evaporator tube, Figure 1.2 depicts a composite diagram of the flow patterns that may be encountered when going from a subcooled liquid to complete evaporation. Similarly, Figure 1.3 shows composite diagrams of flow patterns confronted in condensation at high and low flow rates. The videos in this section, listed below, show numerous examples of these flows.

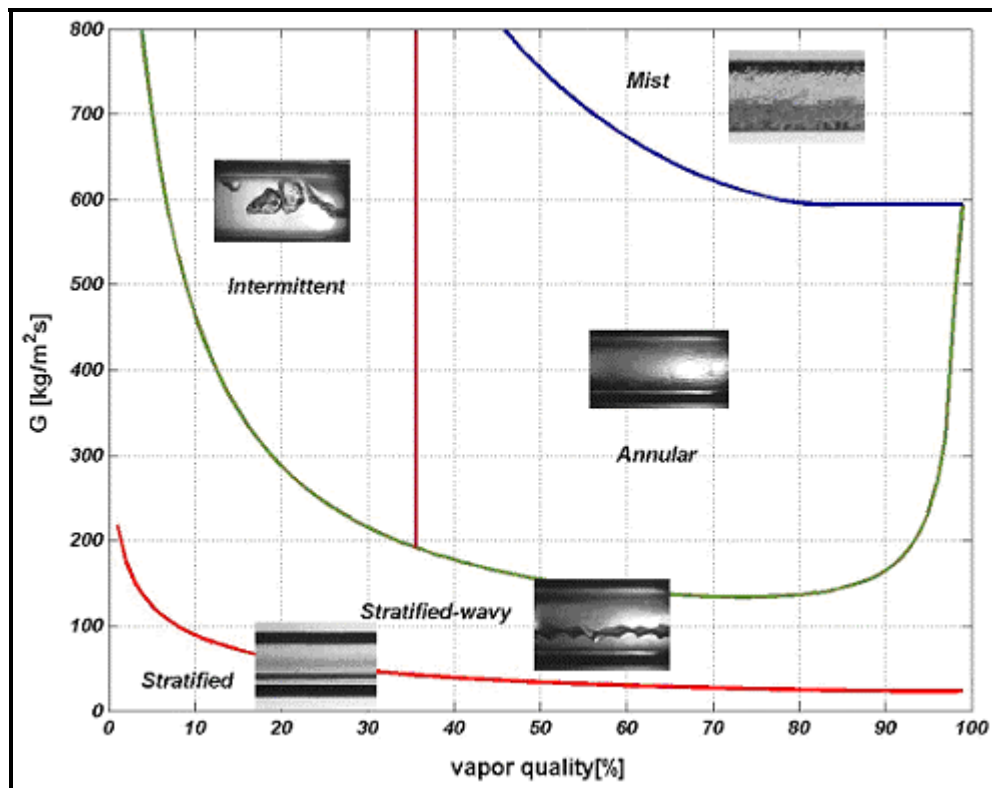


**Figure 1.1.** Flow pattern map for R-22 at a saturation temperature of 5°C (41°F) showing transition boundaries between two-phase flow regimes [where  $G$  is the mass velocity of the liquid + vapor inside the cross-section of the tube of internal diameter  $d = 13.82 \text{ mm}$  (0.544 in.)].

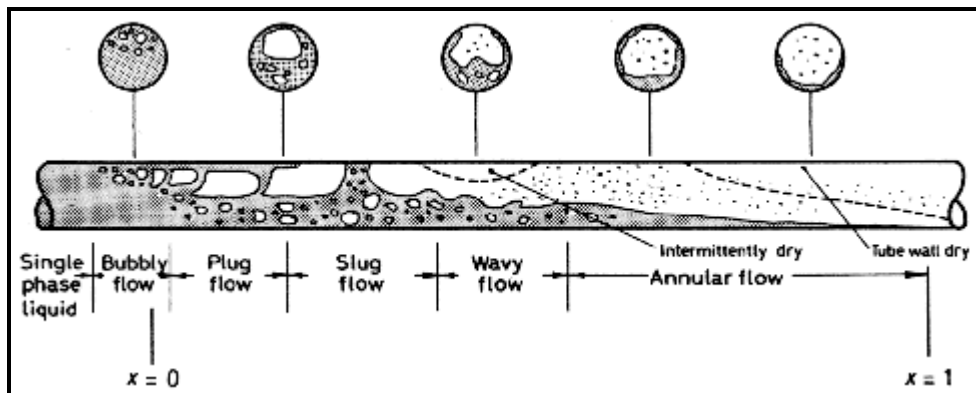


**Figure 1.2.** Illustration of two-phase flow patterns occurring in horizontal evaporator tube.

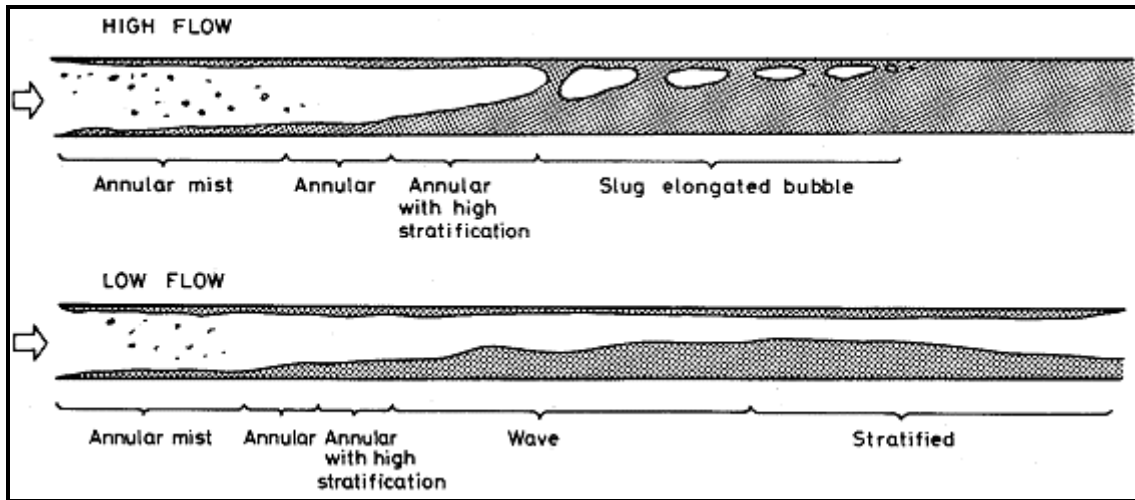


Figure 1.3. Illustration of two-phase flow patterns occurring in horizontal condenser tubes.

List of videos: (click on the one you wish to see)

**Video 1.2.1: Bubble flow.** The video displays flow of isolated bubbles inside a horizontal sightglass of 14.0 mm (0.551 in.) internal diameter. This flow is at a moderate mass velocity at a very low vapor quality and the bubble is essentially the initial step towards arriving at a plug flow. The fluid is ammonia at 5°C (41°F). The video was taken by Dr. O. Zürcher in collaboration with Profs. J.R. Thome and D. Favrat at the Swiss Federal Institute of Technology Lausanne (EPFL). For a description of the test facility, refer to: Zürcher, Favrat and Thome (2002).

**Video 1.2.2: Stratified-wavy flow.** The video displays a stratified-wavy flow (liquid in bottom and vapor in top of tube) inside a horizontal sightglass of 14.0 mm (0.551 in.) internal diameter. The fluid is ammonia at 5°C (41°F), a vapor quality of 0.20 and mass velocity of 26 kg/m<sup>2</sup>s (19126 lb/hr ft<sup>2</sup>). The video was taken by Dr. O. Zürcher in collaboration with Profs. J.R. Thome and D. Favrat at the Swiss Federal Institute of Technology Lausanne (EPFL). For a description of the test facility, refer to: Zürcher, Favrat and Thome (2002).

**Video 1.2.3: Plug/slug to intermittent flow transition.** The video displays a plug/slug flow at relatively low vapor quality inside a horizontal sightglass of 14.0 mm (0.551 in.) internal diameter. The fluid is ammonia at 5°C (41°F), a vapor quality of 0.06 and mass velocity of 180 kg/m<sup>2</sup>s (132408 lb/hr ft<sup>2</sup>). The video was taken by Dr. O. Zürcher in collaboration with Profs. J.R. Thome and D. Favrat at the Swiss Federal Institute of Technology Lausanne (EPFL). For a description of the test facility, refer to: Zürcher, Favrat and Thome (2002).

**Video 1.2.4: Annular flow.** The video displays an annular flow (liquid in an annular film on tube perimeter and vapor in center of tube) at relatively high vapor quality inside a horizontal sightglass of 14.0 mm (0.551 in.) internal diameter. The fluid is ammonia at 5°C (41°F), a vapor quality of 0.80 and mass velocity of 122 kg/m<sup>2</sup>s (89743 lb/hr ft<sup>2</sup>). The video was taken by Dr. O. Zürcher in collaboration with Profs. J.R. Thome and D. Favrat at the Swiss Federal Institute of Technology Lausanne (EPFL). For a description of the test facility, refer to: Zürcher, Favrat and Thome (2002).

**Video 1.2.5: Annular flow with partial dryout.** The video displays an annular flow with partial dryout around the upper perimeter (liquid in bottom and vapor in top of tube) at relatively high vapor quality (*essentially a stratified-wavy flow created by the partial dryout around upper perimeter of the tube*)

inside a horizontal sightglass of 14.0 mm (0.551 in.) internal diameter. The fluid is ammonia at 5°C (41°F), a vapor quality of 0.80 and mass velocity of 41 kg/m<sup>2</sup>s (30160 lb/hr ft<sup>2</sup>). The video was taken by Dr. O. Zürcher in collaboration with Profs. J.R. Thome and D. Favrat at the Swiss Federal Institute of Technology Lausanne (EPFL). For a description of the test facility, refer to: Zürcher, Favrat and Thome (2002).

**Video 1.2.6: Condensation flow regimes in plain tube.** The video displays the exit of a horizontal condenser tube cut at a 45° degree angle and situated inside a viewing chamber. The view is from the side. First, a flow pattern map is shown illustrating two superficial vapor velocities,  $J_G$ , that were studied, plotted versus the Martinelli parameter,  $X_{tt}$ . The inside diameter of the tube is 8.0 mm (0.315 in.). The fluid is R-134a at 40°C (104°F), vapor qualities ( $x$ ) of 0.49 and 0.26, and mass velocities ( $G$ ) of 200 and 400 kg/m<sup>2</sup>s (147120 and 294240 lb/hr ft<sup>2</sup>). The video was taken under the direction of Prof. Alberto Cavallini at the University of Padova, Padova, Italy. For a description of their test facility and related investigation, refer to: Censi et al. (2003). For a description of their flow pattern map, refer to: Cavallini et al. (2002).

**Video 1.2.7: Condensation flow regimes in microfin tube.** The video displays the exit of a horizontal condenser tube cut at a 45° degree angle and situated inside a viewing chamber. The view is from the side. First, a flow pattern map is shown illustrating two superficial vapor velocities,  $J_G$ , that were tested plotted versus the Martinelli parameter,  $X_{tt}$ . The inside diameter at the fin tip is 7.69 mm (0.303 in.). The fluid is R-134a at 40°C (104°F), vapor qualities ( $x$ ) of 0.51 and 0.25, and mass velocities ( $G$ ) of 200 and 400 kg/m<sup>2</sup>s (147120 and 294240 lb/hr ft<sup>2</sup>). This video can be compared to the plain tube video 1.2.6 and it is seen that the microfins imposed a more uniform distribution of liquid around the tube perimeter, especially at the lower mass velocity. The video was taken under the direction of Prof. Alberto Cavallini at the University of Padova, Padova, Italy. For a description of their test facility and related investigation, refer to: Censi et al. (2003). For a description of their flow pattern map, refer to: Cavallini et al. (2002).

**Video 1.2.8: Annular flow with entrainment of liquid droplets.** The video displays a side view of annular flow with a large number of small liquid droplets in a high velocity vapor core of the flow, inside a horizontal sightglass of 13.6 mm (0.535 in.) internal diameter. The fluid is R-22 at 5°C (41°F), a vapor quality of 0.65 and mass velocity of 600 kg/m<sup>2</sup>s (441000 lb/hr ft<sup>2</sup>). The video was taken by L. Wojtan in collaboration with Prof. J.R. Thome at the Swiss Federal Institute of Technology Lausanne (EPFL). For a description of the test facility, refer to: Ursenbacher, Wojtan and Thome (2004) and Wojtan, Ursenbacher and Thome (2004).

**Video 1.2.9: Transition from annular to mist flow.** The video displays a side view of a flow in the transition regime between annular flow with liquid entrainment (lower portion of tube) and mist flow (upper portion of tube), inside a horizontal sightglass of 13.6 mm (0.535 in.) internal diameter. The fluid is R-22 at 5°C (41°F), a vapor quality of 0.79 and mass velocity of 500 kg/m<sup>2</sup>s (367500 lb/hr ft<sup>2</sup>). The video was taken by L. Wojtan in collaboration with Prof. J.R. Thome at the Swiss Federal Institute of Technology Lausanne (EPFL). For a description of the test facility, refer to: Ursenbacher, Wojtan and Thome (2004) and Wojtan, Ursenbacher and Thome (2004).

**Video 1.2.10: Mist flow.** The video displays a cross-sectional view of mist flow (small liquid droplets in a high velocity vapor flow) inside a horizontal sightglass of 13.6 mm (0.535 in.) internal diameter. The fluid is R-22 at 5°C (41°F), a vapor quality of 0.90 and mass velocity of 400 kg/m<sup>2</sup>s (294000 lb/hr ft<sup>2</sup>). The cross-section of the tube is illuminated by a laser sheet and the liquid is highlighted by a trace of fluorescent powder. The video was taken by L. Wojtan in collaboration with Prof. J.R. Thome and Dr. T. Ursenbacher at the Swiss Federal Institute of Technology Lausanne (EPFL). For a description of the test facility, refer to: Ursenbacher, Wojtan and Thome (2004) and Wojtan, Ursenbacher and Thome (2004).

**Video 1.2.11: Annular flow with twisted tape insert at low mass velocity.** The video displays an annular flow with swirl from a twisted tape for flow inside a horizontal sight glass of 8.0 mm (0.315 in.) internal diameter. The fluid is R-507A at 5°C (41°F), a vapor quality of 0.33 and mass velocity of 100 kg/m<sup>2</sup>s (73500 lb/hr ft<sup>2</sup>). In a plain tube without twisted tape, the flow would be stratified-wavy and it is clear that the tape converts the flow to annular flow, including some liquid entrainment. The video was taken by J. Moreno Quiben in collaboration with Prof. J.R. Thome at the Swiss Federal Institute of Technology Lausanne (EPFL). For a description of the test facility (*without the twisted tape*), refer to: Moreno Quibén and Thome (2003).

**Video 1.2.12: Annular flow with twisted tape insert at medium mass velocity.** The video displays an annular flow with swirl from a twisted tape for flow inside a horizontal sight glass of 8.0 mm (0.315 in.) internal diameter. The fluid is R-507A at 5°C (41°F), a vapor quality of 0.18 and mass velocity of 150 kg/m<sup>2</sup>s (147100 lb/hr ft<sup>2</sup>). The flow is annular with a swirl effect from the tape and some liquid entrainment. The video was taken by J. Moreno Quiben in collaboration with Prof. J.R. Thome at the Swiss Federal Institute of Technology Lausanne (EPFL). For a description of the test facility (*without the twisted tape*), refer to: Moreno Quibén and Thome (2003).

**Video 1.2.13: Annular flow with twisted tape insert at high mass velocity.** The video displays an annular flow with swirl from a twisted tape for flow inside a horizontal sight glass of 8.0 mm (0.315 in.) internal diameter. The fluid is R-507A at 5°C (41°F), a vapor quality of 0.20 and mass velocity of 300 kg/m<sup>2</sup>s (220500 lb/hr ft<sup>2</sup>). The flow is annular with a swirl effect from the tape and some liquid entrainment. The video was taken by J. Moreno Quiben in collaboration with Prof. J.R. Thome at the Swiss Federal Institute of Technology Lausanne (EPFL). For a description of the test facility (*without the twisted tape*), refer to: Moreno Quibén and Thome (2003).

A study on air-water flow patterns inside a horizontal clear polycarbonate tube of 25.4 mm (1.0 in.) internal diameter was undertaken with water and air at about 15°C (60°F). The videos were taken by Jaeyong Kim in collaboration with Prof. Afshin Ghajar at the School of Mechanical and Aerospace Engineering, Oklahoma State University. For a description of their test facility, refer to Ghajar and Tang (2007).

**Video 1.2.14: Flow patterns in a horizontal tube as a function of gas superficial Reynolds number.** The tests were done for a fixed value of  $Re_{SL} = 5000$  (the liquid superficial Reynolds number) and a range of  $Re_{SG} = 1500$  to  $47600$  (the gas superficial Reynolds number). The superficial Reynolds number is that for a particular phase (its fraction of the total flow) as if it was flowing alone in the entire cross-section of the channel. Notice in particular the wide transition range between the different flow patterns. Initially the flow is in the slug flow pattern ( $Re_{SL} = 1500$  to  $6000$ ), whereas for  $Re_{SL} > 6000$  the flow is considered slug-wavy while for  $Re_{SL} > 16000$  turns into wavy-annular and finally becomes purely annular flow for  $Re_{SL} > 32000$ .

**Video 1.2.15: Annular flow in horizontal and slightly inclined tubes.** The tests were done for inclination angles of 0°, 2°, 5° and 7° with respect to the horizontal. In the video, the liquid superficial Reynolds number ( $Re_{SL}$ ) is fixed at 5000 and the gas superficial Reynolds number ( $Re_{SG}$ ) is kept at 47600. Notice in particular that there is no distinct effect on the flow movement due to inclination observable for the annular flow (this is in sharp contrast to what is observed for slug flow – refer to Video 1.2.16). The reason being, the inertia force carried by the flow of air in an annular flow is much larger than the buoyancy force difference between the air and water, such that there is almost no change in the shape of the annular flow pattern due to small angles of inclination.

**Video 1.2.16: Slug flow in horizontal and slightly inclined tubes.** The tests were done for inclination angles of 0°, 2°, 5° and 7° from the horizontal. In the video, the liquid superficial Reynolds number

$(Re_{SL})$  is fixed at 5000 and the gas superficial Reynolds number ( $Re_{SG}$ ) is kept at 1500. Notice in particular that at the  $2^\circ$  inclination angle not all the bubbles in the flow stay stationary in comparison to the bubbles in the horizontal flow. For the  $5^\circ$  and  $7^\circ$  inclination angles, the slugs start moving backward (back flow). The reason being, as the tube is inclined, the balance between the inertia force and buoyancy force is changed and rebalanced, such that the increase of the buoyancy force of the air affects the turbulence and the speed of the slug's traverse. In contrast to the annular flow video (see Video 1.2.15), inclination does show a significant influence on the slug flow movement.

A new, novel technique to highlight two-phase flow patterns in horizontal tubes has been proposed by Jassim, Newell and Chato (2007), from the Jassim (2006) thesis, for image enhancement and as an image recognition aid for determining flow regimes to develop probabilistic two-phase flow regime maps. The tests were for R-134a and R-410A with adiabatic horizontal flow at a saturation temperature of  $25^\circ\text{C}$  ( $77^\circ\text{F}$ ). In their videos, back lighting of the tube through a paper with black lines was used to highlight the liquid-vapor interface and the liquid phase as shown in Figure 1.4.

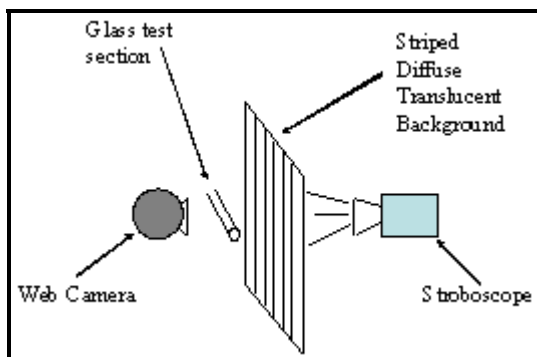


**Figure 1.4. Back lighting set up of Jassim (2006) to apply black lines onto the video images.**

The videos were taken for four glass tube internal diameters: 8.00 mm (0.315 in.), 5.43 mm (0.214 in.), 3.90 mm (0.154 in.) and 1.74 mm (0.068 in.). The videos were taken by E.W. Jassim during his Ph.D. in the laboratory of Profs. T.A. Newell and J.C. Chato at the Air Conditioning and Refrigeration Center at the Department of Mechanical Science and Engineering at the University of Illinois at Urbana-Champaign. The test setup and results are described in Jassim's (2006) thesis and in Jassim, Newell and Chato (2007). For detailed descriptions of the plates and their dimensions, refer to the thesis or paper.

**Video 1.2.17: Two-phase flow of R-134a in a 1.7 mm tube (1<sup>st</sup> run).** This run is for a mass velocity of  $400 \text{ kg/m}^2\text{s}$  ( $294000 \text{ lb/hft}^2$ ) at a vapor quality of 2% showing a slug flow.

**Video 1.2.18: Two-phase flow of R-134a in a 1.7 mm tube (2<sup>nd</sup> run).** This run is for a mass velocity of  $400 \text{ kg/m}^2\text{s}$  ( $294000 \text{ lb/hft}^2$ ) at a vapor quality of 8% showing a slug flow.

**Video 1.2.19: Two-phase flow of R-134a in a 1.7 mm tube (3<sup>rd</sup> run).** This run is for a mass velocity of  $400 \text{ kg/m}^2\text{s}$  ( $294000 \text{ lb/hft}^2$ ) at a vapor quality of 99% showing an annular flow.

**Video 1.2.20: Two-phase flow of R-134a in a 3.9 mm tube (1<sup>st</sup> run).** This run is for a mass velocity of  $100 \text{ kg/m}^2\text{s}$  ( $73600 \text{ lb/hft}^2$ ) at a vapor quality of 4% showing a slug flow.

**Video 1.2.21: Two-phase flow of R-134a in a 3.9 mm tube (2<sup>nd</sup> run).** This run is for a mass velocity of  $200 \text{ kg/m}^2\text{s}$  ( $147000 \text{ lb/hft}^2$ ) at a vapor quality of 12% showing an intermittent flow.

**Video 1.2.22:** *Two-phase flow of R-134a in a 5.4 mm tube (1<sup>st</sup> run).* This run is for a mass velocity of 100 kg/m<sup>2</sup>s (73600 lb/hft<sup>2</sup>) at a vapor quality of 12% showing a slug/stratified-wavy flow regime.

**Video 1.2.23:** *Two-phase flow of R-134a in a 5.4 mm tube (2<sup>nd</sup> run).* This run is for a mass velocity of 200 kg/m<sup>2</sup>s (147000 lb/hft<sup>2</sup>) at a vapor quality of 3% showing a slug flow regime.

**Video 1.2.24:** *Two-phase flow of R-134a in a 5.4 mm tube (3<sup>rd</sup> run).* This run is for a mass velocity of 200 kg/m<sup>2</sup>s (147000 lb/hft<sup>2</sup>) at a vapor quality of 39% showing an annular flow regime.

**Video 1.2.25:** *Two-phase flow of R-410A in a 1.7 mm tube (1<sup>st</sup> run).* This run is for a mass velocity of 400 kg/m<sup>2</sup>s (294000 lb/hft<sup>2</sup>) at a vapor quality of 44% showing an annular flow.

**Video 1.2.26:** *Two-phase flow of R-410A in a 3.9 mm tube (1<sup>st</sup> run).* This run is for a mass velocity of 300 kg/m<sup>2</sup>s (221000 lb/hft<sup>2</sup>) at a vapor quality of 55% showing an annular flow.

**Video 1.2.27:** *Two-phase flow of R-410A in a 3.9 mm tube (2<sup>nd</sup> run).* This run is for a mass velocity of 400 kg/m<sup>2</sup>s (294000 lb/hft<sup>2</sup>) at a vapor quality of 6% showing a slug flow.

**Video 1.2.28:** *Two-phase flow of R-410A in a 5.4 mm tube (1<sup>st</sup> run).* This run is for a mass velocity of 100 kg/m<sup>2</sup>s (73600 lb/hft<sup>2</sup>) at a vapor quality of 7% showing a slug flow.

**Video 1.2.29:** *Two-phase flow of R-410A in a 5.4 mm tube (2<sup>nd</sup> run).* This run is for a mass velocity of 400 kg/m<sup>2</sup>s (294000 lb/hft<sup>2</sup>) at a vapor quality of 18% showing an intermittent/annular flow.

**Video 1.2.30:** *Two-phase flow of R-410A in a 5.4 mm tube (3<sup>rd</sup> run).* This run is for a mass velocity of 400 kg/m<sup>2</sup>s (294000 lb/hft<sup>2</sup>) at a vapor quality of 87% showing an annular flow.

Numerous horizontal two-phase flow visualization studies have been undertaken at the UKAEA Harwell Laboratory under the direction of Prof. G. Hewitt of Imperial College, London. A selection of videos provided by Prof. Hewitt is shown below. For a description of his earlier work on two-phase flow visualization, refer to Arnold and Hewitt (1967) and Hewitt and Whalley (1980).

**Video 1.2.31:** *Axial view of annular flow in a horizontal tube.* The video shows an axial view taken of annular flow in a horizontal tube. The tests were done with water and air with the camera mounted at the end of the test section looking upstream in the tube with a flash tube synchronized with the camera for illumination of the flow from the side of the tube. The large fraction of the liquid phase entrained in the central vapor core is clearly visible. The video was taken at UKAEA Harwell Laboratory under direction of Prof. G. Hewitt of Imperial College London.

**Video 1.2.32:** *Axial view of annular air-water flow in a large horizontal tube.* The video shows an axial view taken of annular flow in a 78 mm (3.07 in.) horizontal tube. The tests were done with water and air with the camera mounted as shown in Figure 1.5. At the location of the “eye” looking upstream in the tube with a view of the flow at the illuminated plane. The air velocity was 20 m/s (65.6 ft/s) and the water velocity was 0.002 m/s (0.066 ft/s).

The large amount of the liquid phase entrained in the central vapor core is clearly visible, erupting from the thicker layer at the bottom of the tube. For a description of the test facility, see Badie, Lawrence and Hewitt (2001).

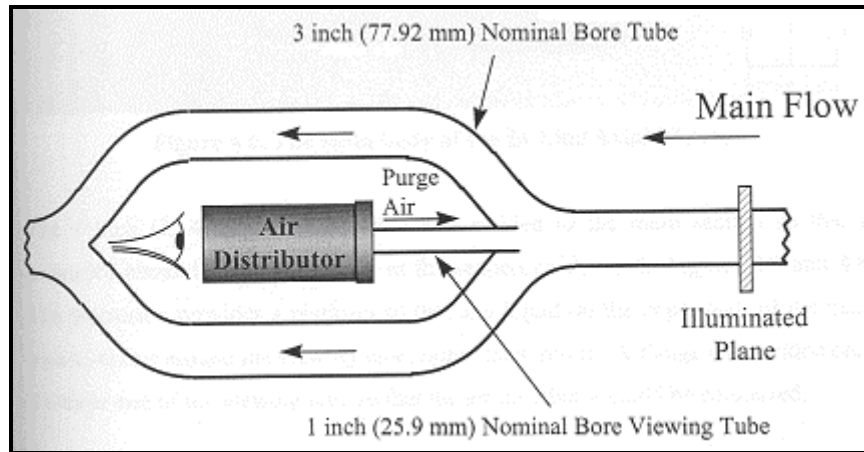


**Figure 1.5. Diagram of visualization test section of Badie, Lawrence and Hewitt (2001).**

**Video 1.2.33:** *Axial view of annular air-oil flow in a large horizontal tube.* The video shows an axial view taken of annular flow in the 78 mm (3.07 in.) horizontal tube described above. The tests were done with oil and air. The air velocity was 20 m/s (65.6 ft/s) and the oil velocity was 0.02 m/s (0.066 ft/s). The large fraction of the liquid phase entrained in the central vapor core is clearly visible, erupting from the thicker layer at the bottom of the tube and then draining back to the bottom. The video was taken by Mr. Sharikh Badie under the direction of Prof. G. Hewitt. For a description of the test facility, refer to: Badie, Lawrence and Hewitt (2001).

**Video 1.2.34 and video 1.2.35:** *Axial views of flow in a horizontal coiled tube.* The videos show axial views taken of flow in a horizontal coiled tube. The tests were done with water and air. The top video shows the flow traveling mostly on the inside of the curved surface and the lower video shows the flow after inversion with more liquid on the outside of the curved surface of the coil. The videos were taken by Prof. G. Hewitt at the Harwell Laboratory in the 1960's. The inversion effect was analyzed by Hewitt and Jayanti (1992) who explained it in terms of a balance of centrifugal, pressure and circumferential shear stress forces.

## 1.3 VOID FRACTION MEASUREMENTS IN HORIZONTAL TUBES

Dynamic cross-sectional void fractions have been measured at the Laboratory of Heat and Mass Transfer (LTCM) at the Swiss Federal Institute of Technology Lausanne (EPFL). In Figure 1.6 the simplified diagram of the experimental visualization setup is shown where the two-phase refrigerant flows inside the horizontal tube and is viewed from an oblique angle through the glass tube wall by the camera. The effects refraction through the glass tube wall and oblique view of the flow cross-section by the camera objective are taken into account in reconstruction of the true image, such that the flow structure can be analyzed as described in Figure 1.7 For a complete description, refer to: Ursenbacher, Wojtan and Thome (2004) and Wojtan, Ursenbacher and Thome (2004).

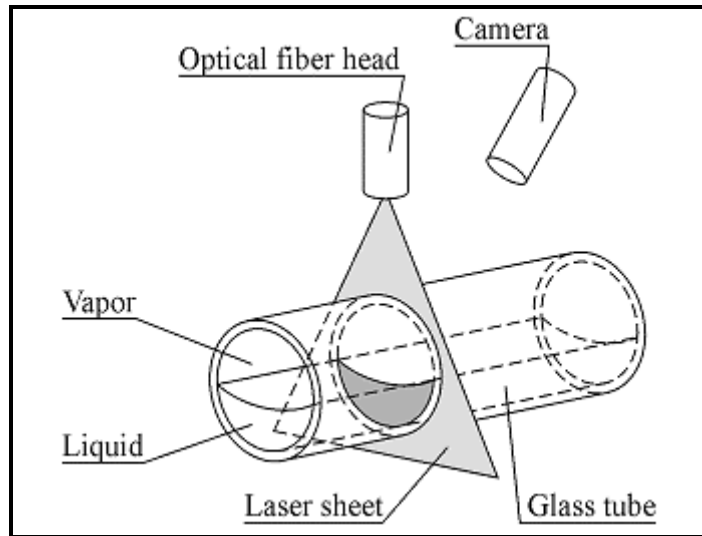


**Figure 1.6.** Cross-sectional void fraction visualization setup for a stratified flow in a horizontal tube.

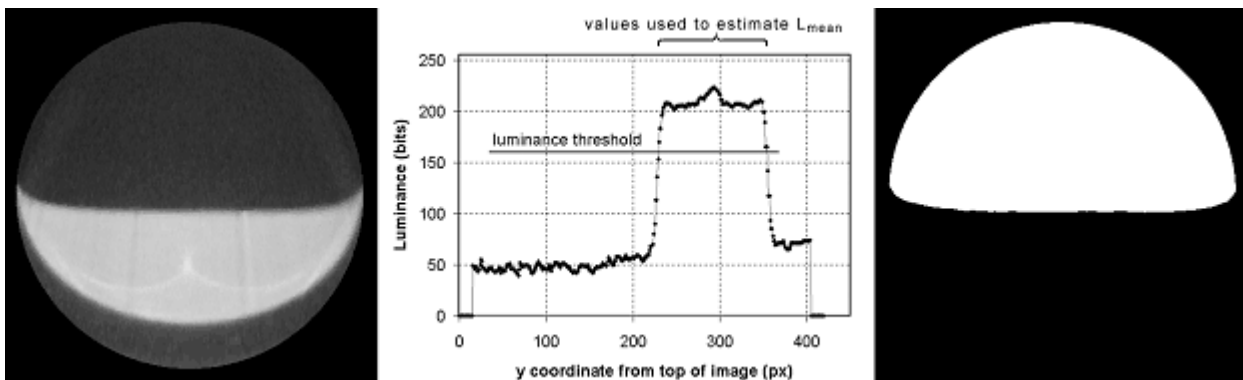


**Figure 1.7.** Left: Transformed cross-sectional image from actual video image of flow; Middle: variation in luminance intensity along the center vertical line of image; Right: Detected vapor (white) and liquid (black) zones in the tube, depicting shape of interface, dry angle around upper perimeter of tube and dynamic void fraction, i.e. number of white pixels divided by number of all white and black pixels.

List of videos: (click on the one you wish to see)

**Video 1.3.1:** *Overall view of air-water test facility with a slug flow.* The video shows the LTCM air-water test facility for observing two-phase flows and measuring void fractions inside a horizontal sight glass of 13.8 mm (0.543 in.) internal diameter. The liquid is water and the gas is air at room temperature. The video was taken in Laboratory of Heat and Mass Transfer under the direction of Prof. J.R. Thome at the Swiss Federal Institute of Technology Lausanne (EPFL).

**Video 1.3.2:** *Close up of air-water loop showing the video camera with a slug flow.* The video shows LTCM test facility for observing two-phase flows and measuring void fractions inside a horizontal sight glass of 13.8 mm (0.543 in.) internal diameter. The video shows the placement of the video camera above the glass tube for taking void fraction videos. The liquid is water and the gas is air at room temperature. The video was taken in Laboratory of Heat and Mass Transfer under the direction of Prof. J.R. Thome at the Swiss Federal Institute of Technology Lausanne (EPFL).

**Video 1.3.3: Air-water test loop with laser sheet cutting across tube just below camera.** The video shows a vertical laser sheet cutting across a horizontal tube for a slug flow inside a horizontal sightglass of 13.8 mm (0.543 in.) internal diameter. The video camera for recording the cross-section of the flow at the laser sheet is located just above and to the right of the images to be recorded. The second tube is only there for some other preliminary tests. The liquid is water and the gas is air at room temperature. The video was taken in Laboratory of Heat and Mass Transfer (LTCM) under the direction of Prof. J.R. Thome at the Swiss Federal Institute of Technology Lausanne (EPFL).

**Video 1.3.4: Original video of slug flow with effects of refractions of light.** The video shows the original view image (in slow motion) of the cross-section of the two-phase flow inside a horizontal sightglass of 13.8 mm (0.543 in.) internal diameter with the cross-sectional image compressed and distorted by the angle of the camera and the refraction of light through the glass tube wall. The liquid is water and the gas is air at room temperature. The video was taken in Laboratory of Heat and Mass Transfer by L. Wojtan under the direction of Prof. J.R. Thome at the Swiss Federal Institute of Technology Lausanne (EPFL). The video is not at actual speed.

**Video 1.3.5: Transformed video of same slug flow video.** The video shows the corrected video image (slow motion) of Video 1.3.4 in black and white inside a horizontal sightglass of 13.8 mm (0.543 in.) internal diameter, showing the cross-sectional view of the flow. The liquid is water (white) and the gas (black) is air at room temperature. The black areas *below* the liquid interface are caused by reflections and do not represent gas. The video was processed in Laboratory of Heat and Mass Transfer (LTCM) by Dr. T. Ursenbacher under the direction of Prof. J.R. Thome at the Swiss Federal Institute of Technology Lausanne (EPFL). The video is not at actual speed.

**Video 1.3.6: Black-and-white version of transformed image of same slug flow video.** The video shows the digitized image (slow motion) of a slug flow inside a horizontal sightglass of 13.8 mm internal diameter. The liquid occupies the lower portion of the tube (black) and the vapor the upper portion of the tube (white). The number of white pixels divided by the total pixels of the tube cross-section gives the instantaneous void fraction for each video image. The dry angle around the upper perimeter of the tube changes during the flow. The liquid is water and the gas is air at room temperature. The video was processed in the Laboratory of Heat and Mass Transfer (LTCM) by Dr. T. Ursenbacher under the direction of Prof. J.R. Thome at the Swiss Federal Institute of Technology Lausanne (EPFL). The video is not at actual speed.

**Video 1.3.7: R-410A slug flow video showing measured interfacial contour.** The video shows the digitized image of a slug flow inside a horizontal sightglass of 13.6 mm (0.535 in.) internal diameter. The liquid occupies the lower portion of the tube (white) and the vapor the upper portion of the tube (gray). The interface contour detected by the image processing program is superimposed on each image. The number of pixels above the interfacial contour divided by the total pixels of the tube cross-section gives the instantaneous void fraction for each video image. The dry angle around the upper perimeter of the tube is evident and changes during the flow. When liquid slugs pass by, the total cross-section is occupied by liquid. The fluid is R-410A at 5°C (41°F), a vapor quality of 0.103 and a mass velocity of 150 kg/m<sup>2</sup>s (110340 lb/hr ft<sup>2</sup>). The video was obtained and processed in the Laboratory of Heat and Mass Transfer (LTCM) by L. Wojtan and Dr. T. Ursenbacher under the direction of Prof. J.R. Thome at the Swiss Federal Institute of Technology Lausanne (EPFL). The video is at actual speed. The work is described in Ursenbacher, Wojtan and Thome (2004).

**Video 1.3.8: R-410A stratified-wavy flow video showing measured interfacial contour.** The video shows the digitized image of a stratified-wavy flow inside a horizontal sightglass of 13.6 mm (0.535 in.) internal diameter. The liquid occupies the lower portion of the tube (white) and the vapor the upper portion of the

tube (gray). The interface contour detected by the image processing program is superimposed on each image. The number of pixels above the interfacial contour divided by the total pixels of the tube cross-section gives the instantaneous void fraction for each video image. The dry angle around the upper perimeter of the tube is evident and changes during the flow. The movement of the contour with time is the result of the interfacial waves created by the vapour shear of the vapor on the liquid. The fluid is R-410A at 5°C (41°F), a vapour quality of 0.20 and a mass velocity of 70 kg/m<sup>2</sup>s (51492 lb/hr ft<sup>2</sup>). The video was obtained and processed in the Laboratory of Heat and Mass Transfer (LTCM) by L. Wojtan and Dr. T. Ursenbacher under the direction of Prof. J.R. Thome at the Swiss Federal Institute of Technology Lausanne (EPFL). The video is at actual speed. The work is described in Ursenbacher, Wojtan and Thome (2004).

## 1.4 TWO-PHASE FLOW PATTERNS IN VERTICAL TUBES

Example sketches of some of the typical two-phase flow patterns (mist flow is not shown) occurring in a vertical tube are shown in Figure 1.8. The first five videos below show the transition from a bubbly flow to a slug flow via bubble clustering.

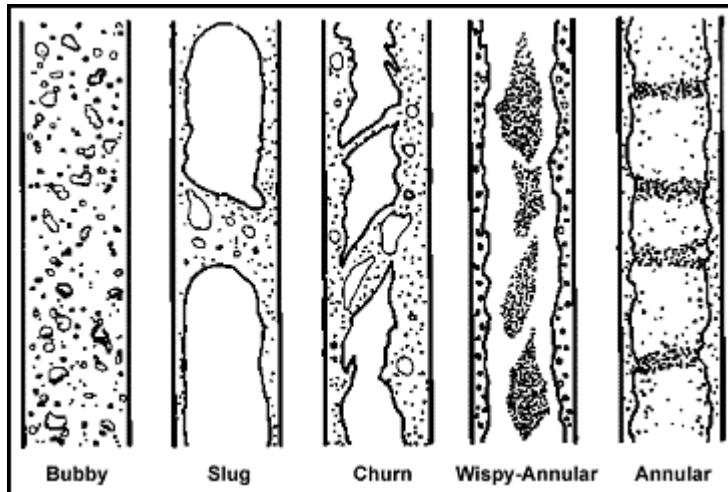


**Figure 1.8. Illustration of two-phase flow patterns occurring in vertical evaporator tube.**

**List of videos:** (click on the one you wish to see)

**Video 1.4.1: Dispersed bubble flow of air-water at void fraction of 5.1%.** The video shows a bubbly flow inside a vertical glass tube of 30 mm (1.181 in.) internal diameter. The liquid is water and the gas is air at ambient temperature. The flow is at a gas phase superficial velocity of 0.021 m/s and a liquid superficial velocity of 0.21 m/s. The flow depicts dispersed bubbles that have not yet begun to form into clusters. The video is at actual speed. The void fraction was measured using a microresistivity probe at the centerline of the channel. The videos were provided by the Laboratory for Fluid Dynamics and Thermodynamics (LFDT), Faculty of Mechanical Engineering, University of Ljubljana, Slovenia under the direction of Prof. Iztok Zun and were presented at the following international meeting: Zun and Polutnik (2001).

**Video 1.4.2: Bubbly flow of air-water at void fraction of 10.3% at start of clustering.** The video shows a bubbly flow inside a vertical glass tube of 30 mm (1.181 in.) internal diameter. The liquid is water and the gas is air at ambient temperature. The flow is at a gas phase superficial velocity of 0.029 m/s and a liquid

superficial velocity remains the same at 0.21 m/s. The flow depicts dispersed bubbles that have begun to form into clusters. The video is at actual speed. The void fraction was measured using a microresistivity probe at the centerline of the channel. The videos were provided by the Laboratory for Fluid Dynamics and Thermodynamics (LFDT), Faculty of Mechanical Engineering, University of Ljubljana, Slovenia under the direction of Prof. Iztok Zun and were presented at the following international meeting: Zun and Polutnik (2001).

**Video 1.4.3: Bubbly flow of air-water at void fraction of 13.9% with bubble clusters.** The video shows a bubbly flow with evident bubble clusters inside a vertical glass tube of 30 mm (1.181 in.) internal diameter. The liquid is water and the gas is air at ambient temperature. The flow is at a gas phase superficial velocity of 0.034 m/s and a liquid superficial velocity remains the same at 0.21 m/s. The flow depicts dispersed bubbles that have migrated together to form bubble clusters. The video is at actual speed. The void fraction was measured using a microresistivity probe at the centerline of the channel. The videos were provided by the Laboratory for Fluid Dynamics and Thermodynamics (LFDT), Faculty of Mechanical Engineering, University of Ljubljana, Slovenia under the direction of Prof. Iztok Zun and were presented at the following international meeting: Zun and Polutnik (2001).

**Video 1.4.4: Bubbly flow of air-water at void fraction of 15.4% with first slugs.** The video shows a bubbly flow with the first formation of slugs inside a vertical glass tube of 30 mm (1.181 in.) internal diameter. The liquid is water and the gas is air at ambient temperature. The flow is at a gas phase superficial velocity of 0.045 m/s and a liquid superficial velocity remains the same at 0.21 m/s. The flow depicts the point of transition of bubble clusters into vapor slugs with a high density of bubbles in the wake. The video is at actual speed. The void fraction was measured using a microresistivity probe at the centerline of the channel. The videos were provided by the Laboratory for Fluid Dynamics and Thermodynamics (LFDT), Faculty of Mechanical Engineering, University of Ljubljana, Slovenia under the direction of Prof. Iztok Zun and were presented at the following international meeting: Zun and Polutnik (2001).

**Video 1.4.5: Slug flow of air-water at void fraction of 17.0% with remaining bubbles.** The video shows a slug flow with numerous dispersed bubbles in the liquid phase inside a vertical glass tube of 30 mm (1.181 in.) internal diameter. The liquid is water and the gas is air at ambient temperature. The flow is at a gas phase superficial velocity of 0.058 m/s and a liquid superficial velocity remains the same at 0.21 m/s. The flow depicts well-established vapor slugs at these conditions. The video is at actual speed. The void fraction was measured using a microresistivity probe at the centerline of the channel. The videos were provided by the Laboratory for Fluid Dynamics and Thermodynamics (LFDT), Faculty of Mechanical Engineering, University of Ljubljana, Slovenia under the direction of Prof. Iztok Zun and were presented at the following international meeting: Zun and Polutnik (2001).

A study on the coalescence of two consecutive Taylor bubbles in a vertical tube has been investigated at the University of Tel Aviv by Profs. Shemer and Barnea. The videos were done for up flow of air and water in a very long vertical tube with an internal diameter of 25.0 mm (0.984 in.). The videos were taken at the University of Tel Aviv by C.A. Talvy under their direction. For a description of the test facility and their results, refer to: Talvy, Shemer and Barnea (2000) and Shemer, Gulitski and Barnea (2007).

**Video 1.4.6: Coalescence of two Taylor bubbles in a vertical tube.** The video shows a side view taken of a slug flow in a vertical tube (the tube itself is not visible in the video). The tests were done to study the influence of the separation distance between two consecutive bubbles upon the behavior of the trailing bubble. The higher speed of the trailing bubble and its collision with the upstream bubble is shown together with the deformation of the nose of the trailing bubble before the collision, all caused by the recirculating flow in the liquid slug between the bubbles (liquid currents are not visible in the video but can be inferred from the movement of small bubbles in the liquid slug).

**Video 1.4.7: Coalescence of Taylor bubbles in a vertical tube.** The video shows the side view of another slug flow in a vertical tube (the tube itself is not visible in the video). The trailing bubble collides with the upstream bubble but first the nose of the trailing bubble is severely disturbed before coalescence takes place. Also, the rear of the last bubble becomes highly unstable as this bubble accelerates to collide with the upstream bubble and is seen to break up into numerous small bubbles.

Numerous two-phase flow visualization studies in vertical tubes have been undertaken at the UKAEA Harwell Laboratory under the direction of Prof. G. Hewitt of Imperial College London. A selection of videos provided by Prof. Hewitt is shown below.

**Video 1.4.8: Axial view of annular flow in a vertical tube.** The video shows an axial view taken of annular flow in a vertical tube. The tests were done with up flow of water and air with the camera mounted at the top of the test section looking down the tube with laser light provided from the bottom of the test section for illumination. A large liquid entrainment in the central vapor core is clearly visible. The video was taken at UKAEA Harwell Laboratory by Dr. P. Whalley and Mr. Terry under direction of Prof. G. Hewitt. For a description of the test facility, refer to: Hewitt, Whalley and Terry (1979).

**Video 1.4.9: Side view of slug flow in a vertical tube with photochromatic dye tracing.** The video shows a side view taken of slug flow in a vertical tube with a photochromatic dye trace entering through the wall of the tube to indicate the direction of the local liquid flow. The direction of the flow is clearly visible, especially the flow reversal to down flow of the liquid film between the Taylor bubble and the wall. Also, the mixing in the liquid slug is clearly visible. The video was taken at UKAEA Harwell Laboratory under the direction of Prof. G. Hewitt. For a description of the test facility, refer to Walklate and Martin (1983).

**Video 1.4.10: Side view of churn flow in a vertical tube with photochromatic dye tracing.** The video shows a side view taken of churn flow in a vertical tube with a photochromatic dye trace entering through the wall of the tube to indicate the direction of the local liquid flow. The continuous gas flow through the core is clearly visible with waves carrying liquid upwards and falling liquid films between the waves. The video was taken at UKAEA Harwell Laboratory under the direction of Prof. G. Hewitt. For a description of the test facility, refer to Hewitt, Martin and Wilkes (1985).

## 1.5 ADIABATIC FALLING FILMS ON HORIZONTAL TUBE ARRAYS

Liquid films falling on horizontal tubes aligned as a vertical array (horizontal tubes one above the other) fall from tube to tube in distinct flow modes under the influence of gravity. As shown in Figure 1.9, the three principal intertube falling film flow modes are droplet, column and sheet, joined together by two transition regimes in which both droplets and columns coexist or columns and short sheets coexist. The videos illustrate these flows.

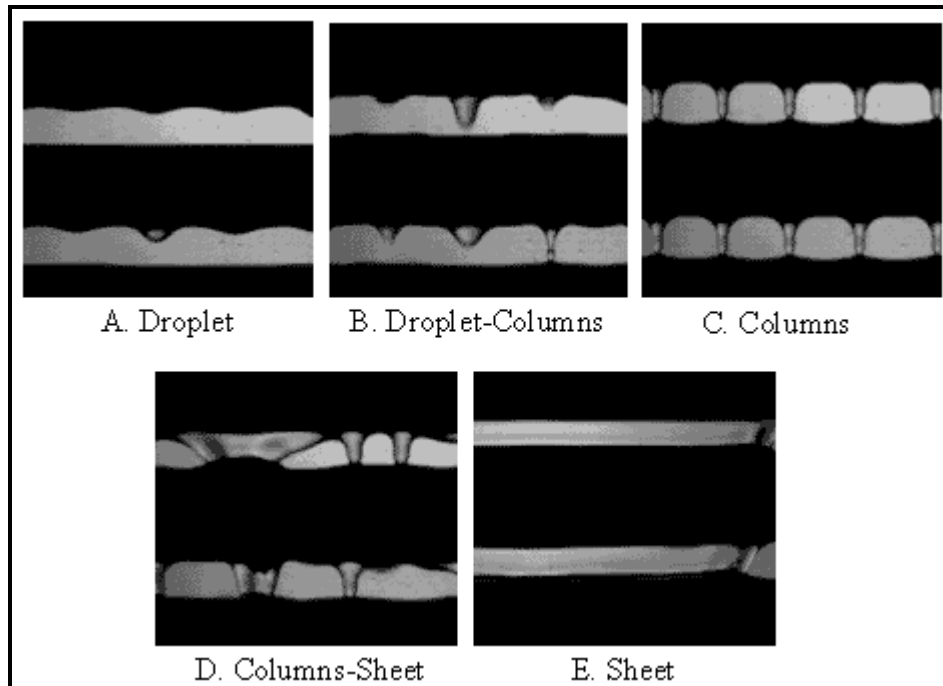


**Figure 1.9. Diagram illustrating three principal intertube falling film flow modes on an array of horizontal tubes one below another (A, C and E) and the two transition regimes (B and D).**

**List of videos:** (click on the one you wish to see)

**Video 1.5.1: Droplet flow mode.** The video shows the droplet flow mode from the bottom of the upper tube to the top of the lower tube. The tubes are plain with diameters of 19.05 mm (0.75 in.). The liquid is ethylene glycol falling in ambient air. The flow is near the transition to column flow mode as evidenced by the elongation of some of the liquid droplets into columns nearly reaching the lower tube. The video was obtained by J.F. Roques and V. Dupont in the Laboratory of Heat and Mass Transfer (LTCM) under the direction of Prof. J.R. Thome at the Swiss Federal Institute of Technology Lausanne (EPFL). The experimental test setup and work is described in: Roques, Dupont and Thome (2002).

**Video 1.5.2: Transition from droplet to column flow mode.** The video shows the transition in the flow regime from droplet flow mode to the column flow mode. The tubes are plain with diameters of 19.05 mm (0.75 in.). The liquid is ethylene glycol falling in ambient air. Both droplets and columns coexist along the tube, indicating the transition regime. The video was obtained by J.F. Roques and V. Dupont in the Laboratory of Heat and Mass Transfer (LTCM) under the direction of Prof. J.R. Thome at the Swiss Federal Institute of Technology Lausanne (EPFL). The experimental test setup and work is described in: Roques, Dupont and Thome (2002).

**Video 1.5.3: Inline column flow mode.** The video shows the inline column flow regime from the bottom of the upper tube onto the top of the lower tube. The tubes are plain with diameters of 19.05 mm (0.75 in.). The liquid is ethylene glycol falling in ambient air. The columns are very stable (difficult to see any movement) and nearly equally spaced. The video was obtained by J.F. Roques and V. Dupont in the Laboratory of Heat and Mass Transfer (LTCM) under the direction of Prof. J.R. Thome at the Swiss Federal Institute of Technology Lausanne (EPFL). The experimental test setup and work is described in: Roques, Dupont and Thome (2002).

**Video 1.5.4: Staggered column flow mode.** The video shows the staggered column flow regime from the bottom of the upper tube onto the top of the lower tube. The tubes are plain with diameters of 19.05 mm (0.75 in.). The liquid is ethylene glycol falling in ambient air. The columns are quite stable and nearly equally spaced and equally staggered. The staggered regime is achieved by increasing the film flow rate, which creates a crest of liquid at the top of the tube between impinging liquid jets. The thick liquid layer at a crest then flows around the tube to form the staggered column on the bottom. The video was obtained by J.F. Roques and V. Dupont in the Laboratory of Heat and Mass Transfer (LTCM) under the direction of Prof. J.R. Thome at the Swiss Federal Institute of Technology Lausanne (EPFL). The experimental test setup and work is described in: Roques, Dupont and Thome (2002).

**Video 1.5.5: Transition from column to sheet flow mode.** The video shows the transition from the staggered column flow regime to the sheet flow regime at intervals along the tube. The tubes are plain with diameters of 19.05 mm (0.75 in.). The liquid is ethylene glycol falling in ambient air. The short width of the sheets renders them unstable and surface tension pulls them into a wedge shape. Columns and small sheets tend to coalesce. The video was obtained by J.F. Roques and V. Dupont in the Laboratory of Heat and Mass Transfer (LTCM) under the direction of Prof. J.R. Thome at the Swiss Federal Institute of Technology Lausanne (EPFL). The experimental test setup and work is described in: Roques, Dupont and Thome (2002).

**Video 1.5.6: Sheet flow mode.** The video shows the sheet flow regime from the bottom of the upper tube to the top of the lower tube, i.e. the classic flow regime assumed for falling film condensation on tube rows by Nusselt (1916). The tubes are plain with diameters of 19.05 mm (0.75 in.). The liquid is ethylene glycol falling in ambient air. The surface tension forces on the ends of the sheet tend to pull them in. The video was obtained by J.F. Roques and V. Dupont in the Laboratory of Heat and Mass Transfer (LTCM) under the direction of Prof. J.R. Thome at the Swiss Federal Institute of Technology Lausanne (EPFL). The experimental test setup and work is described in: Roques, Dupont and Thome (2002).

**Video 1.5.7: Slow motion of transition from droplet to column mode.** The video shows a slow motion of a video of the transition of droplets to columns. The tubes are plain with diameters of 19.05 mm (0.75 in.). The liquid is water falling in ambient air. The original digital video was taken at 1000 images per second and has been slowed down for viewing. The video was obtained by J.F. Roques and V. Dupont in the Laboratory of Heat and Mass Transfer (LTCM) under the direction of Prof. J.R. Thome at the Swiss Federal Institute of Technology Lausanne (EPFL). The experimental test setup and work is described in: Roques, Dupont and Thome (2002).

**Video 1.5.8: Falling film of R-134a on plain tube at low flow rate.** The video shows flow of liquid R-134a film on plain tubes of 19.05 mm (0.75 in.) with intertube spacing of 9.5 mm (0.374 in.). The R-134a is at a saturation temperature of 20°C (68°F) with a flow rate per unit length of tube equal to 0.07 kg/m s (0.047 lb/ft s). The flow mode is near the transition from droplet to column mode (predominately droplet flow is observed) but the droplet flow is rather unstable. The video was obtained by D. Gstöhl and J.F. Roques in the Laboratory of Heat and Mass Transfer (LTCM) under the direction of Prof. J.R. Thome at the Swiss Federal Institute of Technology Lausanne (EPFL).

**Video 1.5.9: Falling film of R-134a on plain tube at medium flow rate.** The video shows flow of liquid R-134a film on plain tubes of 19.05 mm (0.75 in.) with intertube spacing of 9.5 mm (0.374 in.). The R-134a is at a saturation temperature of 20°C (68°F) with a flow rate per unit length of tube equal to 0.11 kg/m s (0.074 lb/ft s). The flow mode is column but they are rather unstable and cause some liquid to sling laterally off the bottom of the tube, typically observed in numerous other occasions. The video was obtained by D. Gstöhl and J.F. Roques in the Laboratory of Heat and Mass Transfer (LTCM) under the direction of Prof. J.R. Thome at the Swiss Federal Institute of Technology Lausanne (EPFL).

**Video 1.5.10: Falling film of R-134a on plain tube at high flow rate.** The video shows flow of liquid R-134a film on plain tubes of 19.05 mm (0.75 in.) with intertube spacing of 9.5 mm (0.374 in.). The R-134a is at a saturation temperature of 20°C (68°F) with a flow rate per unit length of tube equal to 0.36 kg/m s (0.241 lb/ft s). The flow mode is near the transition from column to sheet but the liquid columns are unstable and cause some liquid to sling laterally off the bottom of the tube, typically observed in numerous other occasions. The video was obtained by D. Gstöhl and J.F. Roques in the Laboratory of Heat and Mass Transfer (LTCM) under the direction of Prof. J.R. Thome at the Swiss Federal Institute of Technology Lausanne (EPFL).

## 1.6 FALLING FILM CONDENSATION ON HORIZONTAL TUBES

Condensation on horizontal tube bundles is a common process with the condensate from above tubes inundating the lower tubes. Hence, the condensate flowing from an upper tube to a lower tube characterizes the two-phase flow regime, called the intertube flow mode here.

**List of videos:** (click on the one you wish to see)

**Video 1.6.1: R-134a condensing on tube array in droplet mode flow.** The video shows R-134a condensing at 30°C (86°F) on the second tube of an array of tubes. The tubes are plain with diameters of 19.05 mm (0.75 in.) and the intertube spacing is 6.4 mm (0.25 in.). The heat flux on the second tube is 6400 W/m<sup>2</sup> (2030 Btu/h ft<sup>2</sup>). The flow is in the droplet mode. Elongation of the droplets during their departure is clearly visible and the spreading of the condensate upon impact on the lower tube. The video was taken by D. Gstöhl in the Laboratory of Heat and Mass Transfer (LTCM) under the direction of Prof. J.R. Thome at the Swiss Federal Institute of Technology Lausanne (EPFL). The experimental test setup is described in Gstöhl and Thome (2006c).

**Video 1.6.2: R-134a condensing on tube array in droplet mode near transition to column flow.** The video shows R-134a condensing at 30°C (86°F) on the sixth tube of an array of tubes. The tubes are plain with diameters of 19.05 mm (0.75 in.) and the intertube spacing is 6.4 mm (0.25 in.). The heat flux on the sixth tube is 8100 W/m<sup>2</sup> (2670 Btu/h ft<sup>2</sup>). The flow is in the droplet mode near the transition to column flow. The elongating droplets are unstable and perhaps this prevents the formation of stable columns at this condition. The video was taken by D. Gstöhl in the Laboratory of Heat and Mass Transfer (LTCM) under the direction of Prof. J.R. Thome at the Swiss Federal Institute of Technology Lausanne (EPFL). The experimental test setup is described in Gstöhl and Thome (2006c).

**Video 1.6.3: R-134a condensing on tube array in column mode.** The video shows R-134a condensing at 30°C (86°F) on the sixth tube of an array of tubes. The tubes are plain with diameters of 19.05 mm (0.75 in.) and the intertube spacing is 6.4 mm (0.25 in.). The heat flux on the sixth tube is 20000 W/m<sup>2</sup> (6340 Btu/h ft<sup>2</sup>). The flow is in the column mode and the columns are unstable. The video was taken by D. Gstöhl in the Laboratory of Heat and Mass Transfer (LTCM) under the direction of Prof. J.R. Thome at the Swiss Federal Institute of Technology Lausanne (EPFL). The experimental test setup is described in Gstöhl and Thome (2006c).

**Video 1.6.4: R-134a condensing on 6-tube array at low heat flux in droplet mode.** The video shows R-134a condensing at 30°C (86°F) on a six-tube array. The tubes are plain with diameters of 19.05 mm (0.75 in.) and the intertube spacing is 6.4 mm (0.25 in.). The heat flux on the top tube is 9500 W/m<sup>2</sup> (3010 Btu/h ft<sup>2</sup>) and on the bottom tube is 6700 W/m<sup>2</sup> (2120 Btu/h ft<sup>2</sup>). The flow is in the droplet mode from all tubes. The video was taken by D. Gstöhl in the Laboratory of Heat and Mass Transfer (LTCM) under the direction of Prof. J.R. Thome at the Swiss Federal Institute of Technology Lausanne (EPFL). The experimental test setup is described in Gstöhl and Thome (2006c).

**Video 1.6.5: R-134a condensing on 6-tube array at medium heat flux going from droplet to column mode.** The video shows R-134a condensing at 30°C (86°F) on a six-tube array. The tubes are plain with diameters of 19.05 mm (0.75 in.) and the intertube spacing is 6.4 mm (0.25 in.). The heat flux on the top tube is 26000 W/m<sup>2</sup> (8240 Btu/h ft<sup>2</sup>) and on the bottom tube is 20000 W/m<sup>2</sup> (6340 Btu/h ft<sup>2</sup>). The flow is in the droplet mode at the top and progresses to column mode at the bottom. The video was taken by D. Gstöhl in the Laboratory of Heat and Mass Transfer (LTCM) under the direction of Prof. J.R. Thome at the Swiss Federal Institute of Technology Lausanne (EPFL). The experimental test setup is described in Gstöhl and Thome (2006c).

## 1.7 FALLING FILM EVAPORATION ON HORIZONTAL TUBES

Falling film evaporation on horizontal tube bundles is becoming an important process in refrigeration systems, in which liquid is overfeed onto the top tube of an array of horizontal tubes and evaporates as the liquid falls under the influence of gravity. The liquid flow rate thus decreases progressively from tube to tube as it evaporates. The flow of the liquid film from tube to tube is characterized by the two-phase flow regime, called the intertube flow mode here. As can be seen in some of the videos below, heat transfer is not only by conduction or convection across the film but also by nucleate boiling on the tube wall within the film. This tends to create a mist of minute droplets of liquid and in some videos the “fog” created is visible.

**List of videos:** (click on the one you wish to see)

**Video 1.7.1: R-134a evaporating on array of plain tubes with partial dryout.** The video shows R-134a evaporating at 5°C (41°F) on an array of seven tubes. The tubes are plain with diameters of 19.05 mm (0.75 in.) and the intertube spacing is 6.4 mm (0.25 in.). The heat flux on the top tube is 55000 W/m<sup>2</sup> (17440 Btu/h ft<sup>2</sup>) and 30000 W/m<sup>2</sup> (9510 Btu/h ft<sup>2</sup>) on the bottom tube. The flow is mostly column mode with large instabilities. The video was taken by J.F. Roques in the Laboratory of Heat and Mass Transfer (LTCM) under the direction of Prof. J.R. Thome at the Swiss Federal Institute of Technology Lausanne (EPFL). For a description of the falling film heat transfer test facility, refer to: Roques (2004).

**Video 1.7.2: R-134a evaporating on array of plain tubes with nearly complete dryout.** The video shows R-134a evaporating at 5°C (41°F) on an array of seven tubes. The tubes are plain with diameters of 19.05 mm (0.75 in.) and the intertube spacing is 6.4 mm (0.25 in.). The heat flux on the top tube is 96000 W/m<sup>2</sup> (30440 Btu/h ft<sup>2</sup>) and 3000 W/m<sup>2</sup> (950 Btu/h ft<sup>2</sup>) on the bottom tube. The flow is mostly column mode with large instabilities and then droplet flow at the bottom. The film is nearly completely dried out on the lowest tube. The video was taken by J.F. Roques in the Laboratory of Heat and Mass Transfer (LTCM) under the direction of Prof. J.R. Thome at the Swiss Federal Institute of Technology Lausanne (EPFL). For a description of the falling film heat transfer test facility, refer to: Roques (2004).

**Video 1.7.3: Close up of nucleate boiling on top of tube with falling liquid film (droplet mode).** The video shows R-134a evaporating at 5°C (41°F) on an array of tubes. The tubes are plain with diameters of 19.05 mm (0.75 in.) and the intertube spacing is 6.4 mm (0.25 in.). The film flow is in droplet mode and nucleate boiling with bubbles erupting in the spreading film on the lower tube is clearly visible. The video was taken by J.F. Roques in the Laboratory of Heat and Mass Transfer (LTCM) under the direction of Prof. J.R. Thome at the Swiss Federal Institute of Technology Lausanne (EPFL). For a description of the falling film heat transfer test facility, refer to: Roques (2004).

**Video 1.7.4: Nucleate boiling and dryout on top of tube in droplet mode.** The video shows R-134a evaporating at 5°C (41°F) on an array of tubes. The tubes are plain with diameters of 19.05 mm (0.75 in.)

and the intertube spacing is 6.4 mm (0.25 in.). The film flow is in droplet mode and nucleate boiling occurs in the liquid film on the tube. Note the bubbles inside the droplets leaving the lower tube. Small liquid droplets created by the nucleate boiling process are also notable. The video was taken by J.F. Roques in the Laboratory of Heat and Mass Transfer (LTCM) under the direction of Prof. J.R. Thome at the Swiss Federal Institute of Technology Lausanne (EPFL). For a description of the falling film heat transfer test facility, refer to: Roques (2004).

**Video 1.7.5: Film condensation on upper tube with nucleate boiling in film on lower tube.** The video shows R-134a condensing on the upper tube (with cooling water inside tube) and evaporating on lower tube (hot water inside tube). The tubes are plain with diameters of 19.05 mm (0.75 in.) and the intertube spacing is 6.4 mm (0.25 in.). The film flow is in droplet mode and nucleate boiling is quite evident in the liquid film on the tube. The video was taken by J.F. Roques in the Laboratory of Heat and Mass Transfer (LTCM) under the direction of Prof. J.R. Thome at the Swiss Federal Institute of Technology Lausanne (EPFL). For a description of the falling film heat transfer test facility, refer to: Roques (2004).

**Video 1.7.6: Close up of nucleate boiling in film on lower tube (reverse shading).** The video shows R-134a evaporating on lower tube with nucleate boiling in the liquid film, inverting the black and white images. The tubes are plain with diameters of 19.05 mm (0.75 in.) and the intertube spacing is 6.4 mm (0.25 in.). The video was taken by J.F. Roques in the Laboratory of Heat and Mass Transfer (LTCM) under the direction of Prof. J.R. Thome at the Swiss Federal Institute of Technology Lausanne (EPFL). For a description of the falling film heat transfer test facility, refer to: Roques (2004).

## 1.8 POOL BOILING

Pool boiling is a fundamental process in two-phase heat transfer. Pool boiling is a two-phase natural convection process created by the buoyancy of the vapor bubbles, creating very dynamic and complex phenomena.

**List of videos:** (click on the one you wish to see)

The videos shown below document the pool boiling process on a flat, circular heated plate over all regimes of the pool boiling curve obtained in the same tests. The videos were taken for boiling on a heated copper test surface facing upwards with a 35 mm (1.4 in.) diameter situated at the bottom of a large boiling vessel. At the top of the videos, a 3D-movable micro-thermocouple probe and a micro-optical probe, respectively, are visible. The tests were carried out with saturated isopropanol at a pressure of 0.106 MPa (15.4 psia) and a saturation temperature of 83.3°C (182°F). All experiments are carried out under steady-state conditions. The surface temperature of the temperature-controlled test heater was fixed at five different temperatures as indicated on their pool boiling curve obtained for this test surface in Figure 1.10. Their five videos show all the important boiling regimes: low heat flux nucleate boiling (1<sup>st</sup> Video), developed nucleate boiling at higher heat flux (2<sup>nd</sup> Video), departure from nucleate boiling DNB (3<sup>rd</sup> Video), transition boiling (4<sup>th</sup> Video) and film boiling (5<sup>th</sup> Video). The videos were taken by Prof. H. Auracher, Prof. F. Ziegler and O. Koeppen at the Institut für Energietechnik, Technische Universität Berlin. More details about the test facility and visualizations are available in Buchholz (2005) and Buchholz et al. (2004).

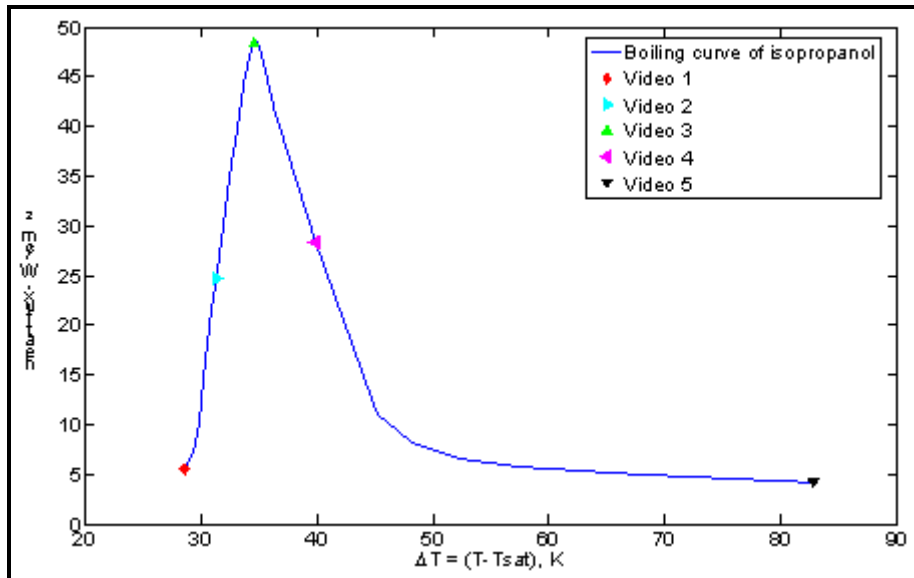


**Figure 1.10.** Pool boiling curve of Buchholz et al. (2004) for isopropanol showing the test conditions of their five videos.

[\*\*Video 1.8.1:\*\* Low heat flux nucleate pool boiling on a horizontal surface.](#)

[\*\*Video 1.8.2:\*\* Developed nucleate pool boiling on a horizontal surface.](#)

[\*\*Video 1.8.3:\*\* Departure from nucleate boiling \(DNB\) on a horizontal surface.](#)

[\*\*Video 1.8.4:\*\* Transition boiling on a horizontal surface.](#)

[\*\*Video 1.8.5:\*\* Film boiling on a horizontal surface.](#)

## 1.9 MICROCHANNEL TWO-PHASE FLOW PHENOMENA

Two-phase flow in microchannels is a process of growing industrial importance in compact heat exchangers and electronic cooling modules. The criterion to define the threshold from macro-scale to micro-scale two-phase flow and heat transfer is still not resolved but typically at normal operating pressures is taken to be at about 1-2 mm for the internal diameter of the channel. New flow pattern maps have been proposed and others are under development to describe and identify these flow regimes. Here some representative videos are shown.

**List of videos:** (click on the one you wish to see)

A large number of videos for two-phase flows in glass microchannels located at the exit of a microchannel evaporator of the same internal diameter have been taken by R. Revellin during his Ph.D. thesis in the Laboratory of Heat and Mass Transfer (LTCM) under the direction of Prof. J.R. Thome at the Swiss Federal Institute of Technology Lausanne (EPFL). Three sizes of microchannels were tested: 2.0, 0.8 and 0.5 mm internal diameters (0.0787, 0.0315 and 0.0197 in.) and also two refrigerants: R-134a and R-245fa. The experimental setup and observations are described in Revellin (2005), Revellin et al. (2006) and Revellin and Thome (2007). For the elongated bubble regimes in the two smaller microchannels, the bubble velocities and bubble lengths were determined by image processing of the videos shown here (plus

others), where the results are available in Agostini, Revellin and Thome (2007). A large selection of these videos is shown below. Only one video for the largest channel is shown. For the smaller two test sections, the test conditions are cited in each individual video itself.

**2.0 mm channel with R-134a:** One video at one mass velocity is shown.

**Video 1.9.1: Elongated bubble (slug) flow in a 2.0 mm microchannel tube.** The video shows R-134a in a 2.0 mm (0.079 in.) internal diameter glass tube located at the exit of a microchannel evaporation test section at room temperature. The length to diameter ratio of the elongated bubbles is larger than in macroscale channels. Note also the effect of buoyancy on the bubble that produces a much thinner liquid film at the top of the elongated bubble than at the bottom.

**0.5 mm channel with R-134a at 360 kg/m<sup>2</sup>s:** Seven videos over a range of vapor qualities at this nominal mass velocity are shown below (actual mass velocity is cited in the individual video).

[Video 1.9.2:](#) 2.9% vapor quality

[Video 1.9.3:](#) 3.7% vapor quality

[Video 1.9.4:](#) 5.0% vapor quality

[Video 1.9.5:](#) 6.8% vapor quality

[Video 1.9.6:](#) 9.0% vapor quality

[Video 1.9.7:](#) 13.7% vapor quality

[Video 1.9.8:](#) 19.4% vapor quality

**0.5 mm channel with R-134a at 520 kg/m<sup>2</sup>s:** Nine videos over a range of vapor qualities at this nominal mass velocity are shown below (actual mass velocity is cited in the individual video).

[Video 1.9.9:](#) 2.6% vapor quality

[Video 1.9.10:](#) 3.2% vapor quality

[Video 1.9.11:](#) 5.7% vapor quality

[Video 1.9.12:](#) 10.4% vapor quality

[Video 1.9.13:](#) 16.5% vapor quality

[Video 1.9.14:](#) 24.0% vapor quality

[Video 1.9.15:](#) 39.0% vapor quality

[Video 1.9.16:](#) 60.9% vapor quality

[Video 1.9.17:](#) 80.3% vapor quality

**0.5 mm channel with R-134a at 1500 kg/m<sup>2</sup>s:** Five videos over a range of vapor qualities at this nominal mass velocity are shown below (actual mass velocity is cited in the individual video).

[Video 1.9.18:](#) 1.3% vapor quality

[Video 1.9.19:](#) 1.9% vapor quality

[Video 1.9.20:](#) 2.6% vapor quality

[Video 1.9.21:](#) 3.9% vapor quality

[Video 1.9.22:](#) 5.3% vapor quality

**0.5 mm channel with R-245fa at 520 kg/m<sup>2</sup>s:** Ten videos over a range of vapor qualities at this nominal mass velocity are shown below (actual mass velocity is cited in the individual video).

[Video 1.9.23:](#) 3.8% vapor quality

[Video 1.9.24:](#) 4.0% vapor quality

[Video 1.9.25:](#) 4.7% vapor quality

[Video 1.9.26](#): 6.0% vapor quality

[Video 1.9.27](#): 7.9% vapor quality

[Video 1.9.28](#): 9.7% vapor quality

[Video 1.9.29](#): 11.9% vapor quality

[Video 1.9.30](#): 14.9% vapor quality

[Video 1.9.31](#): 22.9% vapor quality

[Video 1.9.32](#): 40.4% vapor quality

**0.5 mm channel with R-245fa at 1010 kg/m<sup>2</sup>s:** Six videos over a range of vapor qualities at this nominal mass velocity are shown below (actual mass velocity is cited in the individual video).

[Video 1.9.33](#): 3.9% vapor quality

[Video 1.9.34](#): 4.2% vapor quality

[Video 1.9.35](#): 4.7% vapor quality

[Video 1.9.36](#): 6.1% vapor quality

[Video 1.9.37](#): 7.7% vapor quality

[Video 1.9.38](#): 13.4% vapor quality

**0.5 mm channel with R-245fa at 1520 kg/m<sup>2</sup>s:** Three videos over a range of vapor qualities at this nominal mass velocity are shown below (actual mass velocity is cited in the individual video).

[Video 1.9.39](#): 4.8% vapor quality

[Video 1.9.40](#): 5.4% vapor quality

[Video 1.9.41](#): 6.5% vapor quality

**0.8 mm channel with R-134a at 200 kg/m<sup>2</sup>s:** Eleven videos over a range of vapor qualities at this nominal mass velocity are shown below (actual mass velocity is cited in the individual video).

[Video 1.9.42](#): 2.9% vapor quality

[Video 1.9.43](#): 3.9% vapor quality

[Video 1.9.44](#): 5.7% vapor quality

[Video 1.9.45](#): 7.6% vapor quality

[Video 1.9.46](#): 11.7% vapor quality

[Video 1.9.47](#): 16.1% vapor quality

[Video 1.9.48](#): 22.2% vapor quality

[Video 1.9.49](#): 30.5% vapor quality

[Video 1.9.50](#): 40.7% vapor quality

[Video 1.9.51](#): 52.3% vapor quality

[Video 1.9.52](#): 65.2% vapor quality

**0.8 mm channel with R-134a at 510 kg/m<sup>2</sup>s:** Nine videos over a range of vapor qualities at this nominal mass velocity are shown below (actual mass velocity is cited in the individual video).

[Video 1.9.53](#): 2.9% vapor quality

[Video 1.9.54](#): 3.7% vapor quality

[Video 1.9.55](#): 5.2% vapor quality

[Video 1.9.56](#): 7.8% vapor quality

[Video 1.9.57](#): 9.6% vapor quality

[Video 1.9.58](#): 23.6% vapor quality

[Video 1.9.59](#): 29.3% vapor quality

[Video 1.9.60](#): 37.4% vapor quality

**Video 1.9.61:** 72.5% vapor quality

**0.8 mm channel with R-134a at 1010 kg/m<sup>2</sup>s:** Nine videos over a range of vapor qualities at this nominal mass velocity are shown below (actual mass velocity is cited in the individual video).

**Video 1.9.62:** 0.7% vapor quality

**Video 1.9.63:** 1.1% vapor quality

**Video 1.9.64:** 1.6% vapor quality

**Video 1.9.65:** 2.4% vapor quality

**Video 1.9.66:** 3.3% vapor quality

**Video 1.9.67:** 5.1% vapor quality

**Video 1.9.68:** 7.4% vapor quality

**Video 1.9.69:** 13.3% vapor quality

**Video 1.9.70:** 28.5% vapor quality

**0.8 mm channel with R-134a at 1500 kg/m<sup>2</sup>s:** Six videos over a range of vapor qualities at this nominal mass velocity are shown below (actual mass velocity is cited in the individual video).

**Video 1.9.71:** 0.5% vapor quality

**Video 1.9.72:** 0.7% vapor quality

**Video 1.9.73:** 1.3% vapor quality

**Video 1.9.74:** 2.0% vapor quality

**Video 1.9.75:** 3.2% vapor quality

**Video 1.9.76:** 4.2% vapor quality

A series of five videos of evaporating flows at high heat fluxes in triangular cross-sectional microchannels with a transparent top plate have been taken at the Technion University under the direction of Prof. G. Hetsroni in Israel. The test fluid is water. The parallel microchannels are made in a silicon plate and have a hydraulic diameter of 0.130 mm (0.005 in.). The experimental setup and observations are described in Hetsroni (2005) and Hetsroni et al. (2002, 2003).

**Video 1.9.77:** *Overall view of the multi-microchannel test section.* The video shows several views of the test section used to obtain the high speed videos of the boiling process in the microchannels.

**Video 1.9.78:** *View of boiling in a multi-microchannel test section.* The video shows a large view of the boiling process in the microchannels for a fluid velocity of 0.095 m/s (0.31 ft/s) at a heat flux of 124 kW/m<sup>2</sup> (39300 Btu/h ft<sup>2</sup>).

**Video 1.9.79:** *Bubble burst in a channel of the multi-microchannel test section.* The video shows the burst of a large bubble during boiling in their microchannel test section with quasi-periodic dryout for a superficial liquid velocity of 0.075 m/s (0.246 ft/s) and a heat flux of 240 kW/m<sup>2</sup> (76100 Btu/h ft<sup>2</sup>).

**Video 1.9.80:** *Dryout in several channels of the multi-microchannel test section.* The video shows the dryout process in neighboring channels during boiling in their microchannel test section (this one with a hydraulic diameter of 0.160 mm rather than 0.130 mm) with a superficial liquid velocity of 0.075 m/s (0.246 ft/s) and a heat flux of 140 kW/m<sup>2</sup> (44400 Btu/h ft<sup>2</sup>).

**Video 1.9.81:** *Intermittent dryout with rewetting of a channel.* The video shows “explosive boiling” in a microchannel for a superficial liquid velocity of 0.095 m/s (0.31 ft/s) and a heat flux of 124 kW/m<sup>2</sup> (39300 Btu/h ft<sup>2</sup>). The field of view is 0.6 mm by 1.0 mm.

A series of videos of evaporating flows in horizontal, transparent glass microchannels have been taken at the Department of Mechanical Engineering, The University of Tokyo under the direction of Prof. N. Kasagi by Tzu-Hsiang Yen using R-123 as the test fluid. The two videos below were taken at a speed of 24,000 images per second and are shown in slow motion here. The videos show boiling nucleation at the channel wall, bubble growth, backflow and rewetting of the channel. The experimental setup and descriptions of their observations are presented in Yen et al. (2005) and Yen et al. (2006).

**Video 1.9.82:** *Flow pattern variation in a horizontal circular microchannel (1<sup>st</sup> Video)*. The video displays the variation in the flow patterns of convective boiling inside a horizontal, circular microchannel of 0.21 mm (0.0083 in.) diameter at a mass flux of  $400 \text{ kg/m}^2\text{s}$  ( $294000 \text{ lb/h ft}^2$ ), a heat flux of  $37.53 \text{ kW/m}^2$  ( $11900 \text{ Btu/h ft}^2$ ) and vapor quality of 0.074. The test fluid is R-123 and the tests were at a saturation temperature of  $27^\circ\text{C}$  ( $81^\circ\text{F}$ ) at 1.01 bar. Compared to the square channel below, fewer nucleation bubbles are generated and the period of flow pattern variation is shorter, while the variation of flow patterns is more complex. The video was taken by Tzu-Hsiang Yen in collaboration with Profs. N. Kasagi and M. Shoji. For a description of the test facility and detailed discussion of the phenomena, refer to: Yen et al. (2006).

**Video 1.9.83:** *Flow pattern variation in a horizontal square microchannel (2<sup>nd</sup> Video)*. The video displays the variation in the flow patterns of convective boiling inside a horizontal, square cross-sectional microchannel of 0.214 mm (0.0084 in.) hydraulic diameter at a mass flux of  $400 \text{ kg/m}^2\text{s}$  ( $294000 \text{ lb/h ft}^2$ ), a heat flux of  $39.25 \text{ kW/m}^2$  ( $12400 \text{ Btu/h ft}^2$ ) and a vapor quality of 0.069. The fluid is R-123 and the experimental conditions for this square channel are very similar to those of the circular channel above. Bubbles grow in both the downstream and upstream directions of the tube due to the very limited space in the microchannel, leading to a quasi-periodic flow pattern variation from bubbly to annular flow patterns at the same observation point. The video was taken by Tzu-Hsiang Yen in collaboration with Prof. N. Kasagi at The University of Tokyo and Prof. M. Shoji at the Energy Technology Institute, National Institute of Advanced Industrial Science and Technology (AIST). For a description of the test facility and detailed discussion of the phenomena, refer to: Yen et al. (2006).

A series of videos of capillary condensing flows in a horizontal, transparent glass microchannel have been taken at the Laboratoire d'Énergétique at the Université Paul Sabatier in Toulouse, France by B. Médéric, P. Lavieille and M. Miscevic. The test fluid is n-pentane at atmospheric pressure. Using a syringe pump, the mass velocities in the videos ranged from 9 to  $14 \text{ kg/m}^2\text{s}$  ( $6600$  to  $10300 \text{ lb/h ft}^2$ ). The glass channel has a diameter of 0.56 mm (0.022 in.). The vapor enters slightly superheated and partially condenses at a saturation temperature of  $36^\circ\text{C}$  ( $97^\circ\text{F}$ ). The five videos below were taken at a speed of 25 images per second and show elongated vapor bubbles with condensation at their interface with subsequent break off and flow downstream. The experimental setup, descriptions of their observations and void fraction measurements using their image processing technique are described in Médéric, Lavieille and Miscevic (2005).

**Video 1.9.84:** *Capillary condensation in a glass microchannel (1<sup>st</sup> Video)*. This video shows an oscillating elongated bubble at a mass velocity of  $9 \text{ kg/m}^2\text{s}$  ( $6600 \text{ lb/h ft}^2$ ).

**Video 1.9.85:** *Capillary condensation in a glass microchannel (2<sup>nd</sup> Video)*. This video shows an oscillating elongated bubble with rapid detachment of bubbles at a mass velocity of  $11 \text{ kg/m}^2\text{s}$  ( $8100 \text{ lb/h ft}^2$ ).

**Video 1.9.86:** *Capillary condensation in a glass microchannel (3<sup>rd</sup> Video)*. This video shows an oscillating elongated bubble at a mass velocity of  $14 \text{ kg/m}^2\text{s}$  ( $10300 \text{ lb/h ft}^2$ ).

**Video 1.9.87:** *Capillary condensation in a glass microchannel (4<sup>th</sup> Video)*. This video shows an oscillating elongated bubble splitting into small bubbles at a mass velocity of  $14 \text{ kg/m}^2\text{s}$  ( $10300 \text{ lb/h ft}^2$ ).

**Video 1.9.88:** *Capillary condensation in a glass microchannel (5<sup>th</sup> Video)*. This video shows a flow of condensing bubbles at a mass velocity of  $14 \text{ kg/m}^2\text{s}$  ( $10300 \text{ lb/h ft}^2$ ).

Videos of evaporating flows in a square matrix of silicon microchannels with a glass cover plate have been taken at the Heat Transfer Laboratory at the University of Houston by T. Cognata under the direction of Prof. K. Hollingsworth and Prof. L. Witte. The test fluid is R-11. The micro-heat exchanger is made from a DNA micro-array adapted for use as an evaporator. The channels are 0.050 mm (0.002 in.) wide separated by 0.150 mm (0.006 in.) silicon posts in a 45° alignment to the direction of flow. Using a syringe pump, the liquid enters at the right and partially evaporates as it flows to the left. The four videos were taken at a speed of 5000 images per second and show nucleation, short and elongated vapor bubbles and annular flow. The experimental setup, descriptions of their observations and heat transfer measurements are described in Cognata, Hollingsworth and Witte (2006).

**Video 1.9.89:** *Two-phase flow in a microscale heat exchanger (1<sup>st</sup> Video)*. This video shows evaporation at a heat flux of  $50 \text{ kW/m}^2$  ( $15850 \text{ Btu/h ft}^2$ ) at a mass velocity of  $141 \text{ kg/m}^2\text{s}$  ( $104000 \text{ lb/h ft}^2$ ) at the central zone of the test section.

**Video 1.9.90:** *Two-phase flow in a microscale heat exchanger (2<sup>nd</sup> Video)*. This video shows evaporation at a heat flux of  $50 \text{ kW/m}^2$  ( $15850 \text{ Btu/h ft}^2$ ) at a mass velocity of  $141 \text{ kg/m}^2\text{s}$  ( $104000 \text{ lb/h ft}^2$ ) at the inlet zone of the test section.

**Video 1.9.91:** *Magnified view of bubble flow in a microscale heat exchanger (3<sup>rd</sup> Video)*. This video shows the evaporation process at a heat flux of  $50 \text{ kW/m}^2$  ( $15850 \text{ Btu/h ft}^2$ ) at a mass velocity of  $141 \text{ kg/m}^2\text{s}$  ( $104000 \text{ lb/h ft}^2$ ) at the exit zone of the test section.

**Video 1.9.92:** *Magnified view of bubble flow in a microscale heat exchanger (3<sup>rd</sup> Video)*. This video shows a highly magnified view of the evaporation process for elongated bubbles at the intersection of several microchannels.

A video of evaporation at high heat flux was taken in a joint project between Profs. Xu, Gan, Zhang and Li of the Guagnzhou Institute of Energy Conversion of the Chinese Academy of Science, the Department of Thermal and Energy Engineering at the University of Science and Technology of China in Hefei and the Institute of Microelectronics at Peking University, Beijing, respectively. The test fluid was acetone. The ten parallel microchannels were made in a silicon plate with a hydraulic diameter of 0.1554 mm (0.006 in.). They are triangular in cross-section with a width of 0.300 mm (0.012 in.) at the top with the viewing plate and 0.212 mm deep (0.008 in.). The experimental setup, descriptions of their observations and analysis are presented in detail in Xu et al. (2005).

**Video 1.9.93:** *Nucleation and rapid dryout in a multi-microchannel element*. The video shows a slow motion view of the activation of multiple nucleation sites followed by very rapid vaporization at a heat flux of  $142 \text{ kW/m}^2$  ( $45000 \text{ Btu/h ft}^2$ ) and a liquid Reynolds number of 65.2. When the channels become “black” this means that they have dried out. The process is cyclical and the video shows one cycle of the process.

## 1.10 SINGLE-PHASE FLOW PHENOMENA

List of videos: (click on the one you wish to see)

No videos currently available.

## 1.11 CRITICAL HEAT FLUX IN AN ANNULUS

Critical heat flux (CHF) is an important diabatic two-phase phenomenon in saturated and subcooled flow boiling. It designates the departure from wet wall cooling of the heated channel by the liquid at high heat flux and is associated with a rapid rise in the wall temperature that may result in burnout of the test section if the applied heating is not cut off in time. For a description of a mechanistic model of CHF in subcooled boiling, refer to Celata et al. (1999) while the empirical CHF correlation of Katto and Ohno (1984) for saturated and subcooled CHF is presented elsewhere in this book.

Celata, Cumo and Mariani (1999) and Celata et al. (2000) have taken digital videos of the CHF process occurring in an annulus. Their test section is described in Figure 1.11. Two of the four walls of the square flow channel are made of Plexiglas so that the laser light is able to pass through these two transparent plates and thus illuminates the surface of the heater on which the boiling phenomena occurs. The other two walls are stainless steel. The heated surface is a solid cylindrical rod placed at the center of the square duct. The inside dimension of the square duct is 7.2 mm (0.28 in.). The cylindrical heater is 2 mm (0.079 in.) in diameter and 100 mm (3.94 in.) in length. The heater, one for each run, is made of stainless steel 316L and is uniformly heated over its length by Joule effect up to 90 kW.

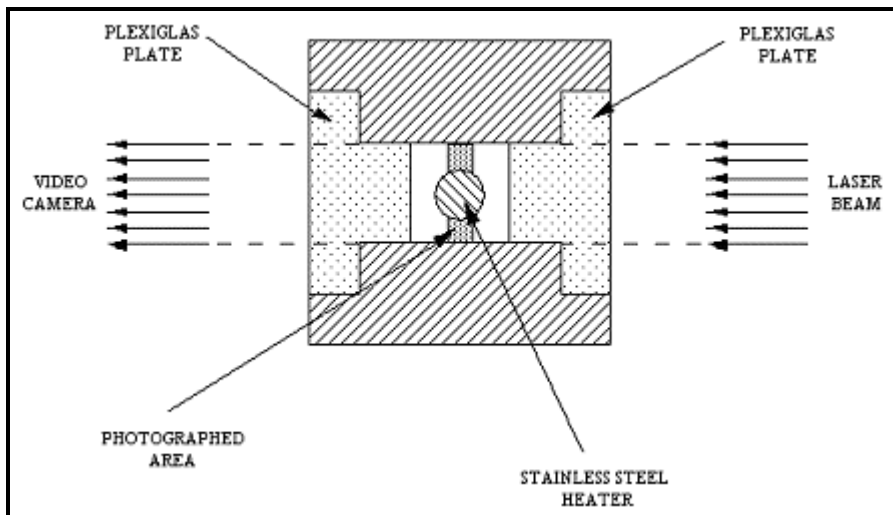


**Figure 1.11. Schematic diagram of the CHF test section of Celata and coworkers.**

Six videos from the above studies are shown below (one at normal speed and the second at slow motion for each of the three conditions). They were taken at ENEA Casaccia by A. Marianni and G. Zummo at the Institute of Thermal-Fluid Dynamics in Rome, Italy under the direction of Dr. G.P. Celata. The test fluid is demineralized water.

List of videos: (click on the one you wish to see)

**Video 1.11.1 and video 1.11.2 (slow motion): CHF in an Annulus (1<sup>st</sup> run).** The videos display CHF occurring at the following test conditions: inlet temperature is 20°C (68°F), outlet temperature is 32°C (89.6°F), outlet pressure is 2 bar (29.0 psia), inlet subcooling is 100 K (180°F), mass velocity is 2160 kg/m<sup>2</sup>s (1590000 lb/hft<sup>2</sup>) and liquid velocity is 2.2 m/s (7.2 ft/s). The heat flux of CHF in this video was 3900 kW/m<sup>2</sup> (1237000 Btu/h ft<sup>2</sup>).

**Video 1.11.3 and video 1.11.4 (slow motion): CHF in an Annulus (2<sup>nd</sup> run).** The videos display CHF occurring at the following test conditions: inlet temperature is 25°C (77°F), outlet temperature is 29°C (84.2°F), outlet pressure is 3 bar (43.5 psia), inlet subcooling is 110 K (198°F), mass velocity is 3250 kg/m<sup>2</sup>s (2390000 lb/hft<sup>2</sup>) and liquid velocity is 3.3 m/s (10.8 ft/s). The heat flux of CHF in this video was 9400 kW/m<sup>2</sup> (2980000 Btu/h ft<sup>2</sup>).

**Video 1.11.5 and video 1.11.6 (slow motion): CHF in an Annulus (3<sup>rd</sup> run).** The videos display CHF occurring at the following test conditions: inlet temperature is 22°C (71.6°F), outlet temperature is 27°C (80.6°F), outlet pressure is 1.1 bar (16 psia), inlet subcooling is 165 K (297°F), mass velocity is 7550 kg/m<sup>2</sup>s (5550000 lb/hft<sup>2</sup>) and liquid velocity is 7.5 m/s (24.6 ft/s). The heat flux of CHF in this video was 12700 kW/m<sup>2</sup> (4027000 Btu/h ft<sup>2</sup>).

## 1.12 FLASHING IN TUBES

Flashing is an important two-phase flow phenomenon. Flashing for example can occur when a liquid is suddenly reduced far below its saturation pressure without the immediate occurrence of boiling. For instance, flashing of a saturated or near saturated liquid may occur when passing through a nozzle, an expansion device or from a small to a larger channel. As a result, the liquid becomes superheated and thus unstable. The phenomenon is characterized by very rapid evaporation, which occurs in the videos below as a wave-like evaporation process, which in some cases may even have an adverse effect on the integrity of the system and safety.

The videos below display flashing of dodecane inside a vertical glass tube of 15 mm (0.59 in.) internal diameter. The tests were done with the glass tube filled with liquid dodecane separated from the low pressure reservoir by its own saturated vapor and a diaphragm. The experiments were done in an upright position so that the top of the tube corresponds to the right side of the images (initially the liquid is below its own high pressure vapor and the diaphragm that separates it from the low pressure reservoir). Each experiment started by piercing the diaphragm exposing the liquid and vapor to the low-pressure environment. In the video, the interface between the saturated liquid and its high pressure vapor is seen at the beginning before the thin diaphragm (which is not visible in the video) is burst. The evaporation wave moves from top to bottom. The videos were taken at 3000 images per second and are shown here in slow motion. The videos were taken by José Simões-Moreira during his Ph.D. in the laboratory of Prof. J.E. Shepherd at CalTech. The test setup and results are described in Simões-Moreira and Shepherd (1999) and in the Ph.D. thesis at RPI of Simões-Moreira (1994). José Simões-Moreira is presently a professor at the University of San Paolo in San Paolo, Brazil.

**List of videos:** (click on the one you wish to see)

**Video 1.12.1: Flashing in a vertical tube (1<sup>st</sup> run).** The 1<sup>st</sup> run is for an initial saturation temperature of the dodecane at 200°C (392°F) while the low pressure reservoir is at an initial pressure of 1 mbar absolute (0.015 psia), i.e. nearly at vacuum.

**Video 1.12.2: Flashing in a vertical tube (2<sup>nd</sup> run).** The 2<sup>nd</sup> run is for an initial temperature of the dodecane of 250°C (482°F) while the low pressure reservoir is at an initial pressure of 1 mbar absolute (0.015 psia).

**Video 1.12.3: Flashing in a vertical tube (3<sup>rd</sup> run).** The 3<sup>rd</sup> run is for an initial temperature of the dodecane of 250°C (482°F) while the low pressure reservoir is at a higher initial pressure of 0.75 bar absolute (10.9 psia).

## 1.13 TWO-PHASE FLOWS IN PLATE HEAT EXCHANGERS

Plate heat exchangers are an important type of two-phase heat exchanger used for both evaporation and condensation, especially in small to medium size refrigeration applications. Very few two-phase flow videos are available for flow between the plates. Presently, three distinct types of plates are illustrated in the videos. All tests were for R-134a with adiabatic upward flow at a saturation temperature of 10°C (50°F). In their videos, the vapor quality is denoted as “X” in %, the mass velocity is denoted as “G” in kg/m<sup>2</sup>s, “C” refers to Chevron plates, “LB” refers to long bump plates and “RB” refers to round bump plates. The nine videos below were taken by E.W. Jassim during his M.S. in the laboratory of Profs. T.A. Newell and J.C. Chato at the Air Conditioning and Refrigeration Center at the Department of Mechanical and Industrial Engineering at the University of Illinois at Urbana-Champaign. Only their videos at low vapor qualities are shown here. The test setup and results are described in Jassim, Newell and Chato (2006) and Jassim (2000). For detailed descriptions of the plates and their dimensions, refer to their publications.

**List of videos:** (click on the one you wish to see)

**Video 1.13.1: Two-phase flow in a chevron plate heat exchanger (1<sup>st</sup> run).** The 1<sup>st</sup> run is for a mass velocity of 60 kg/m<sup>2</sup>s (44100 lb/hft<sup>2</sup>) over the vapor quality range from 5 to 7%.

**Video 1.13.2: Two-phase flow in a chevron plate heat exchanger (2<sup>nd</sup> run).** The 2<sup>nd</sup> run is for a mass velocity of 90 kg/m<sup>2</sup>s (66200 lb/hft<sup>2</sup>) over the vapor quality range from 5 to 7%.

**Video 1.13.3: Two-phase flow in a chevron plate heat exchanger (3<sup>rd</sup> run).** The 3<sup>rd</sup> run is for a mass velocity of 125 kg/m<sup>2</sup>s (92000 lb/hft<sup>2</sup>) over the vapor quality range from 5 to 7%.

**Video 1.13.4: Two-phase flow in a long bump plate heat exchanger (1<sup>st</sup> run).** The 1<sup>st</sup> run is for a mass velocity of 60 kg/m<sup>2</sup>s (44100 lb/hft<sup>2</sup>) over the vapor quality range from 5 to 7%.

**Video 1.13.5: Two-phase flow in a long bump plate heat exchanger (2<sup>nd</sup> run).** The 2<sup>nd</sup> run is for a mass velocity of 90 kg/m<sup>2</sup>s (66200 lb/hft<sup>2</sup>) over the vapor quality range from 5 to 7%.

**Video 1.13.6: Two-phase flow in a long bump plate heat exchanger (3<sup>rd</sup> run).** The 3<sup>rd</sup> run is for a mass velocity of 125 kg/m<sup>2</sup>s (92000 lb/hft<sup>2</sup>) over the vapor quality range from 5 to 7%.

**Video 1.13.7: Two-phase flow in a round bump plate heat exchanger (1<sup>st</sup> run).** The 1<sup>st</sup> run is for a mass velocity of 60 kg/m<sup>2</sup>s (44100 lb/hft<sup>2</sup>) over the vapor quality range from 5 to 7%.

**Video 1.13.8: Two-phase flow in a round bump plate heat exchanger (2<sup>nd</sup> run).** The 2<sup>nd</sup> run is for a mass velocity of 90 kg/m<sup>2</sup>s (66200 lb/hft<sup>2</sup>) over the vapor quality range from 5 to 10%.

**Video 1.13.9:** *Two-phase flow in a round bump plate heat exchanger (3<sup>rd</sup> run).* The 3<sup>rd</sup> run is for a mass velocity of 125 kg/m<sup>2</sup>s (92000 lb/hft<sup>2</sup>) over the vapor quality range from 5 to 7%.

## Chapter 2

# DESIGN CONSIDERATIONS FOR ENHANCED HEAT EXCHANGERS

**SUMMARY:** This chapter focuses on heat transfer augmentation of tubular heat exchangers and describes existing and prospective applications of tubular heat transfer augmentations to a wide range of industries. Thermal, mechanical and economical considerations of particular importance are also presented.

### 2.1 Introduction

Enhanced tubes are used extensively in the refrigeration, air-conditioning and commercial heat pump industries while, in contrast, their consideration for use in the chemical, petroleum and numerous other industries is still not standard practice, although increasing. Designing *enhanced* tubular heat exchangers results in a much more compact design than conventional *plain* tube units, obtaining not only thermal, mechanical and economical advantages for the heat exchanger, but also for the associated support structure, piping and/or skid package unit, and also notably reduced cost for shipping and installation of all these components (which often bring the installed cost to a factor of 2 to 3 times that of the exchanger itself in petrochemical applications). The compact enhanced designs also greatly reduce the quantities of the two fluids resident within the exchanger, sometimes an important safety consideration. This chapter describes some of the practical considerations and advantages regarding the use of enhanced tubes and tube inserts in tubular heat exchangers and provides some guidelines for identifying their applications.

### 2.2 Thermal and Economic Advantages of Heat Transfer Augmentations

There are many thermal advantages of utilizing augmentations that must be weighed against their higher cost relative to plain tubing and their economic benefit on plant operation. For many small increases to production capacity (10 to 30%), the purchase and installation of completely new exchangers cannot be justified economically. However, when the heat exchangers are the "bottleneck" of a unit operation, then augmentations may be the right solution.

The principal advantage of introducing an augmentation is the possibility of substantially increasing thermal duty to meet the needs of new process conditions or production goals. This can be achieved either by:

1. Installing removable inserts inside the tubes,
2. Replacing a removable tube bundle with a new enhanced tube bundle,
3. Replacing the heat exchanger with a new enhanced tube heat exchanger of the same size or smaller.

The first two of these interventions can be completed without any modifications to the heat exchanger itself while all three can be implemented without changes to the original piping connections and to its supports. Hence, these interventions have the benefit of a minimum effect on the operating schedule of the production plant.

*What about replacements of existing installed units?* As a prime example of this latter point, a removable tube bundle is easily replaced during shutdown by a new enhanced tube bundle. Or, a fixed tubesheet unit can be partially replaced by using the same heads, piping and supports. Tube inserts, on the other hand, can be installed inside the tubes of an existing exchanger during a normally scheduled shutdown, resulting in no lost production. The installation may require that some (or all) of the pass partition plates in the heads be removed to reduce the number of tube passes and thus meet pressure drop limitations when installing twisted tapes, especially for laminar flows. These types of interventions have very high payback ratios and plant operating reliability because of their simplicity and avoid the necessity of purchasing a new larger plain tube unit, which would require costly engineering services and expensive changes to the heat exchanger supports, its foundation and piping and also loss of production during these modifications.

*What about new units in new plants?* For new heat exchangers, a well-optimized plain tube unit is normally the easy way out for heat exchanger designers, even though they unwittingly are often paying a premium of 20-50% in the cost of the unit compared to an enhanced unit for the same service. Another consideration regards difficult applications where space is not available for two or more exchangers in parallel or where weight/bundle removal restrictions on units mounted on structures is a problem, and these are situations where heat transfer augmentations have been used to advantage by well informed heat exchanger designers.

*What about cost savings?* The cost savings for appropriate applications of enhanced tubes to shell-and-tube heat exchangers in the petrochemical industries typically range from \$10,000 to \$200,000 per unit or more. Hence, several of these interventions a year easily justifies the engineering cost for evaluating otherwise conventional designs for appropriate use of an enhanced tube, such as a Wolverine Tube Trufin or Turbo-Chil tube with internal and external enhancements (internal helical ribs and external low fins).

*What about alloy tubes?* When utilizing high alloy tubes in heat exchangers (stainless steel, titanium, nickel alloys, duplex stainless steels, etc.), applying the appropriate augmentation can very significantly reduce their first cost. The augmentation may not only reduce the cost of the tubing, but also those of the heads and tubesheets (smaller diameters, smaller wall thicknesses, fewer tube holes to drill, less alloy cladding material, etc.). Even for conventional carbon steel heat exchangers, if the entire cost of the heat exchanger is included as it should be its total cost to the plant, a more compact, lighter weight enhanced shell-and-tube unit can greatly reduce the cost of shipping and installation. It is often estimated that the installed cost is 2 to 3 times the cost of the heat exchanger itself and hence a smaller enhanced unit will achieve a significant first cost savings when the true total cost is considered.

*What are typical prices per foot or meter of enhanced tubing?* These are difficult to describe in a simple set of tabular values since their prices are very dependent on the particular tube material involved (primarily related to its hardness and hence resistance to deformation during the enhancement production process) and the wall thickness specified and the base cost of the bare tube. In general, the enhanced tube cost multiplying factor falls as the base tube material cost increases. Price information is readily available by contacting the enhancement's manufacturer (Wolverine Tube Inc.) for an offer. A doubly-enhanced tube version is also often available for the application (enhanced on the tube-side as well as on the shell-side) and it typically is the best thermal and economic choice.

*What about heat exchanger cost savings?* As a quick measure, a thermal designer is tempted to compare an enhanced tube on a cost per foot basis versus its equivalent plain tube in the same material and wall gauge, which however is equivalent to purchasing a portable PC on its sticker price per kilogram of weight irrespective of performance. For low finned tubes, sometimes it is suggested to compare them on a  $(\$/m^2)/m$  basis, i.e. unit cost per meter of surface area per unit length. Since a low finned tube often has about 3 times the external surface area of a plain tube, if it costs 1.5 more per meter than a plain tube (a

typical rule-of-thumb value), then the real cost is about one-half that of a plain tube on this surface area basis. A more realistic comparison would be to look at the respective cost per meter of tubing divided by the overall heat transfer coefficient for the optimized units, which gives a cost to performance ratio. This approach includes the entire thermal effect of internal and external heat transfer augmentation and fouling factors in the evaluation. Yet another basis is to compare the total cost of the tubing for each type of unit, since that is what the fabricator actually pays for the tubing. Even so, this is still not a realistic evaluation since a large savings in the exchanger's shell, heads, tubesheets, and fabrication costs are gained by going to a more compact unit. Overall, the best choice is to get competitive bids from the heat exchanger fabricator on the conventional plain tube unit and on the enhanced tube unit, both optimized for the application. Typical savings will be from 15-40% even when the total tubing costs are identical. If we assume that (i) tubing, (ii) all other materials plus fixed costs and (iii) manpower each contribute equally (1/3 each) of the total cost of the heat exchanger, it is easy to see that very significant savings are gained from the second and third category as the heat exchanger gets smaller in size. Thus, the best *simple* economical yardstick to apply to the comparison is that of size reduction, i.e. if an enhanced unit uses 1/3 less tubes it will cost 1/3 less than the conventional unit, including the higher price per meter of the enhanced tubing. This is typically quite close to reality and easy for the thermal designer to evaluate himself.

## 2.3 Thermal Design and Optimization Considerations

One of the first questions about enhanced tubes to be asked is *When can I use them?* Continuing the discussion above, an *old* rule of thumb says that an augmentation should be considered when that fluid's thermal resistance is *three* times that of the other fluid. However, because doubly-enhanced tubes are readily available, i.e. those augmenting both the tube-side and the shell-side processes, almost any application can benefit thermally, and this old rule of thumb is really now only old technology. Hence, it is important to determine which augmentation(s) are applicable to the situation and then to run some simulated heat exchanger designs to determine the magnitude of the benefit in reduced size (and cost if possible) of the heat exchanger.

An important point to remember is that using an enhancement on one side of the tube will have a *positive* effect on the other side. For instance, in boiling processes an augmentation applied to the heating fluid tube surface will increase the heat flux in the smaller enhanced unit and thus the boiling heat transfer coefficient on the other side of the tube wall (which is positively effected by the larger heat flux) while also reducing the number of tubes that increases the mass velocity (and convective heat transfer) too. In single-phase applications, an augmentation will reduce the size of a new heat exchanger and thus increase the fluid velocity on the other side of the tube. This "free" enhancement is often overlooked unless a thermal design is performed for the enhanced tube unit. This *secondary augmentation* often contributes to a notable fraction of the reduction in unit size.

Another important point to remember...do *not* impose unnecessary or unwitting design restrictions on an enhanced tube heat exchanger. Compared to an optimized plain tube unit for the same application, the enhanced tube exchanger will almost always optimize to a different bundle configuration, such as shorter tube length, fewer tubes, perhaps choice of a different tube diameter, fewer tube passes, fewer bundles in parallel, etc. Thus, do not self-impose unnecessary restrictions on an enhanced unit's design.

On the other hand, many plain tube units, especially *horizontal condensers*, are poorly optimized and end up with small tube length to shell diameter ratios (sure sign of costly designs) because of the maximum tube length limit imposed during construction of most petrochemical processing plants. In these plants, nearly always a maximum length of 20 ft (6.1 m) tube length is imposed, which often has a very negative effect on achieving the real potential thermal performance of large plain tube tube-side and shell-side

condensers. On the contrary, enhanced tube units in these cases often optimize out to a shorter length than plain tube units and hence sometimes in these cases the enhanced tube unit is less than *one-half* the size of the plain tube unit or *two* units in parallel are now easily handled by *one* smaller enhanced unit. In these situations, often cost savings exceed 50% by applying an externally low finned tube, an internally microfinned tube or a doubly-enhanced tube.

The positive effect of the increased surface area of the enhancement should not be overlooked. The fouling factor is applied to the *entire* wetted surface area of an augmentation, not its nominal projection. This has the effect of reducing the thermal *resistance* due to the fouling factor; if the enhanced to plain surface area ratio is 3.0 such as for a low finned tube, the thermal resistance using the same fouling factor will be reduced to 1/3 the plain tube value. Even so, the *percent overdesign* for the fouled design compared to the clean design typically increases in an enhanced heat exchanger because the fouling factors remain the same in value while the tube-side and shell-side heat transfer coefficients are greatly increased, thus providing more *fouling insurance*.

The fouling factor also effects fin efficiency. The fouling resistance must be added to that of the heat transfer coefficient on the fin; hence the "effective" heat transfer coefficient on the fin is reduced, which increases the fin efficiency. Thus, the effective surface area of a finned surface increases as fouling increases, which partially compensates for the increase in fouling with time.

Most conventional heat exchanger design programs allow the user to input heat transfer data in one or more of the following manners, providing various possibilities to input information about enhancements to make an enhanced heat transfer design:

1. A fixed value of the heat transfer coefficient;
2. A fixed value to multiply the heat transfer coefficient relative to the internally calculated plain tube value;
3. A pressure drop multiplier term;
4. A single-tube nucleate pool boiling curve;
5. Constants for j-factor and f-factor curves;
6. A design safety factor that can be used as a multiplier for an enhanced heat transfer coefficient.

For intube single-phase processes, it is convenient to input a *fixed value* of the heat transfer coefficient or the *enhancement multiplier* in most cases. Instead, if the option is available, j- and f- factor curves can be entered. When using a multiplier, your program will multiply *its* plain tube coefficient's value, not necessary using the same correlation that was used to find the enhancement multiplier relative to the plain tube value.

Since tube-side and shell-side fouling factors are applied to their respective total wetted surface areas when calculating the overall heat transfer coefficient, for enhanced surfaces a conventional plain tube design software will normally incorrectly apply the fouling factors to the nominal internal and external surface areas of the tube. To properly determine the fouling resistances, the fouling factors must be applied to the actual respective surface areas. One way of doing this in a conventional plain tube design software is to divide the fouling factors by their respective surface area ratios first before inputting them into the program, which results in the same final effect. For example, if an internal helically ribbed tube has an internal area ratio of 1.8 with respect to the nominal area at the base of the ribs, then the tube-side fouling factor should be divided by 1.8 in order to respect the correct application of the fouling factor in calculating the overall heat transfer coefficient.

## 2.4 Mechanical Design and Construction Considerations

**Mechanical Stress Calculations.** Burst tests with internal pressure on integral low finned tubes have shown that the plain ends of the tube are the weakest point along the tube because the external helical fins act as reinforcement rings. One can also imagine that the same holds true for internal helical fins or ribs. Choice of the minimum wall thickness under the augmentation has a direct impact on the amount of metal per meter of tubing. Thus, this choice is economically important, especially for expensive alloy materials.

For most applications, the base wall thickness under the augmentation must be used for the mechanical stress calculations defined by various pressure vessel codes, such as that of ASME. For some applications, the ASME code will allow the original plain tube wall thickness before finning/deformation to be used in the minimum wall thickness calculation, rather than the wall thickness under the fins which would be more restrictive and lead to heavier tube walls. One such situation is for vacuum applications in surface condensers. Consult the applicable pressure vessel code for guidance.

**Heat Exchanger Fabrication.** Enhanced tubes normally have plain lengths at each end that are a little longer than the tubesheet thickness. This allows these tubes to be rolled and/or welded into the tubesheet. The outside diameter over the augmentation (such as a low finned tube) is equal to or slightly less than that of the plain ends. Thus, these tubes can be drawn into the tube bundle during assembly without any problems. Tube inserts normally have pull rings or attachments to install them, fix them in place and to remove them for cleaning.

**U-Tubes.** Nearly all integral heat transfer augmentations (i.e. those augmentations that are an integral part of the tube wall) can be bent into U's for U-tube heat exchangers. For the minimum-bending radius of a particular type of tube, one should refer to the manufacturer's recommendations (refer to Wolverine Tube Inc. recommendations).

**Mean Metal Temperature Differences.** Some fixed tubesheet plain tube designs result in very large mean metal temperature differences between the tubes and the heat exchanger shell. This large temperature difference causes unequal thermal expansion (or contraction) and large stresses. Since augmenting one fluid stream of an exchanger almost always shifts the controlling thermal resistance to the other fluid stream, an enhancement can be used to reduce the mean metal temperature difference and avoid using an expansion joint where they are undesirable. For instance, in a feed effluent heater with a single-phase hot gas on the shell-side being cooled by a tube-side fluid, the mean metal temperature difference will be reduced by about 1/3 by use of integral low finned tubes. In addition, the tube length will also usually optimize out to a shorter exchanger and thus further reduce the thermal differential stresses between the shell and tubes.

In any case, for a fixed tubesheet heat exchanger, it is good practice to check the effect of an augmentation on the mean metal temperature difference. When installing inserts in existing fixed tube units, it is good practice to compare the new mean metal temperature difference value against that used for the mechanical design of the exchanger.

## 2.5 Refrigeration and Air-Conditioning System Applications

The benefits of heat transfer augmentations in these systems are well-known to the industry and their use is the norm rather than the exception. Still, their selection, optimization and proper implementation are critical factors in order to realize the maximum benefit.

For intube boiling (or condensation), the aluminum star inserts that were once widely used have nearly been completely abandoned in favor of internally microfinned tubes. These microfinned tubes provide heat transfer augmentation similar to that of the star inserts but at a fraction of their increase in two-phase pressure drop. Wolverine Tube Inc. is a leading manufacturer of microfin tubes.

With air passing over air-conditioning coils, the newest louvered plate designs for "compact" heat exchangers provide a substantial increase in heat transfer compared to older designs. Thus, the inside coefficient is now often augmented with microfins. Use of an internal augmentation in turn reduces the length and weight of the unit, which reduces the number of louvered external plates required, increases air velocity and thus the air-side coefficient too. For a direct-expansion evaporator operating with the refrigerant in a stratified flow mode inside the tube, the top perimeter of the tube is not wetted by a plain tube while instead the helical microfins lift the liquid film around the top of the tube, making not only better use of the internal surface area of the tube but also the aluminum fins outside around the top of the tube as well.

For evaporation in flooded evaporators, many external augmentations are available commercially, most of which are normally produced in doubly-enhanced versions (i.e. with tube-side enhancement for the chilled water/cooling water/brine). Comparison of these augmentations should be made *not* on their single-tube performances but on their *bundle* performances, including tube-side augmentation for the water and the positive effect of the ID surface area ratio on reducing the fouling resistance.

For chilled water flowing inside tubes, highly efficient internal rib and fin designs provide a good tradeoff between heat transfer and pressure drop. For chilled water on the shell-side, i.e. dx-evaporator water chillers, the best tube selection may be a low finned tube with internal microfins where one pays for more tube metal per meter but will use only about one-half the meters of tubing.

## 2.6 Refinery and Petrochemical Plant Applications

Several examples of heat transfer augmentation interventions in chemical plants and refineries to look for are:

### Single-Phase Exchangers:

1. Use of integral low finned tubes in heat exchangers when the limiting thermal resistance is on the shell-side;
2. Use of tube inserts (wire mesh or twisted tape types) are highly effective in laminar flows inside tubes;
3. Installation of inserts on the tube-side of heat recovery units to increase energy recovery via a larger overall heat transfer coefficient and smaller temperature approaches;
4. Utilization of inserts in oil coolers of compressors and turbines to solve an overheating problem or realize smaller exchangers that are more convenient in package units.

To overcome the fact that laminar flow heat transfer coefficients are almost independent of fluid velocity and performance is difficult to improve using plain tubes even resorting to large pressure drops, either inserts or external low fins may be the simple solution. Properly designed units with tube inserts normally are much smaller in size and have smaller or equal pressure drops as conventional plain tube units.

**Reboilers:**

1. Substitution of a plain U-tube bundle with a *low finned tube* bundle or a *high performance boiling* tube bundle (such as one of the Turbo-B versions) to increase thermal capacity;
2. Installation of an insert in the heating fluid stream (tube-side) to increase horizontal reboiler heat duties, especially for hot effluent gases in feed effluent heaters;
3. Replacement of a plain tube bundle with an *enhanced tube bundle* that allows a cheaper, lower temperature heating stream to be used if available (such as low pressure steam instead of medium or high pressure steam);
4. For highly fouling, difficult to clean plain tube horizontal thermosyphon and kettle reboilers, substitution with a *low finned tube bundle* with a larger tube pitch and the same external surface area can reduce labor costs for heat exchanger cleaning substantially;
5. For reboiler-condensers in refrigerated process units, boiling and condensing augmentations can be used to decrease the log-mean-temperature-difference of these units and reduce the compression power required, saving as much as 5-10% of the power costs for these units.
6. *Internal microfins* are very effective for horizontal tube-side evaporators over the entire range of vapor qualities and particularly at low mass velocities.

**Condensers:**

1. Substitution of a plain U-tube bundle of an overhead condenser with a *low finned tube bundle* (or installation of inserts in an existing tube bundle) to increase the overall heat transfer coefficient, which reduces the distillation tower operating pressure and temperature, and saves energy in heating the tower's feed to a lower operating temperature;
2. Using *low finned tubes* as opposed to plain tubes can often reduce the number of shells in multiple shell condensers by a factor of two, especially for condensing multi-component vapors on the shell-side.
3. *Internal microfins* are very effective for horizontal tube-side condensers over the entire range of vapor qualities and particularly at low mass velocities.

**Air Coolers:**

1. For cooling viscous fluids in air-cooled heat exchangers, tube inserts inside high finned tubes can significantly reduce the number of parallel units and the plot size required (some air cooler manufacturers have already been building units with wire mesh type inserts, for instance);
2. Installing tube inserts can increase the cooling capacity of some existing air coolers during hot summer periods and also may alleviate the need for installation of additional cooling tower capacity in marginal cases.

In the hydrocarbon processing industries, some actual applications include:

1. Coolers (gas oil, glycols, atmospheric resids, phenol, refinery light ends, sulfinol, air-cooled lubricating oil, heavy wax distillates, CO gas, citric acid, fatty acids, Therminol-66 and many other fluids);
2. Heaters/pre-heaters (crude bottoms, acetylene, exhaust gases, polymers, naphthalene, post-critical ethylene, butyl rubber, solvents, styrene, cumene, heavy tar oil and crude oil);
3. Chillers and vaporizers (liquefied gases, refrigerants, light hydrocarbons, xylenes, MDEA, alcohols, ethylene glycol, glycerine);
4. Condensers (alcohols, tower overheads, multi-component vapor mixtures, refrigerants).

Other important applications include adhesives (heating and cooling of various process streams in their production) and plastics (heating and cooling of polymer melts such as PVC, acetate and polystyrene). Other applications are found in vacuum distillation units, lube oil plants and heavy oil production facilities, where many viscous fluids are present and laminar flows persist.

## 2.7 Air-Separation and Liquified Natural Gas Plant Applications

Plate-fin heat exchangers are widely used in these facilities. While plate-fin exchangers allow very close temperature approaches, their long and tortuous flow paths can have larger pressure drops than shell-and-tube units. Thus, the real gain in overall system efficiency must be looked at. *Enhanced boiling tubes* and *enhanced condensing tubes* are used to advantage in these facilities in their refrigeration system reboiler-condensers, with the heating fluid-side also augmented with fins.

## 2.8 Applications to Lubricating Oil Coolers

Intube heat transfer augmentations are particularly suited to increasing heat transfer coefficients in lubricating oil coolers. These coolers normally come as part of package or skid mounted units for compressors, turbines, motors, engines, etc. or are mounted on large construction equipment. Hence, a lighter weight, more compact cooler has many economical advantages. Normally an increase in tube-side heat transfer performance is obtained with an insert while meeting the same pressure drop limitations as for the plain tube unit. This is achieved by using fewer tube passes.

## 2.9 Power Plant Operations

Integral low finned tubes are becoming widely used in power plant main condensers. The external fins for condensing steam must be optimized for the right fin density and height. Use of external fins shifts the controlling thermal resistance to the cooling waterside. Thus, low finned tubes with internal ribs are particularly suitable for this application, especially when utilizing alloys. Corrugated tubes are also beneficial in these applications.

Installation of inserts on the tube-side (i.e. water-side) of an existing steam condenser (plain or low finned tube) increases the overall heat transfer coefficient and the vacuum in the steam chest; thus the steam turbine's power output can sometimes be increased by 0.5-2%, which represents very significant savings in fuel or additional capacity to a power utility at a minimum cost.

Fossil fuel power boilers are designed with internally ribbed tubes by some steam generator manufacturers. The swirl flow created by the ribs keeps the tube wall better wetted in this asymmetrical heat flux environment, which increases the critical heat flux before passing into the film boiling regime. Twisted tape inserts can be installed in tube sections prone to this problem in existing plain I.D. units.

## 2.10 Geothermal and Ocean-Thermal Power Plant Applications

The viability of geothermal and ocean-thermal power plants depends in part on the use of small temperature approaches in the heat exchangers in order to increase the cycle efficiency. Low temperature approaches result in low log-mean-temperature-differences and thus large heat exchanger surface areas. To minimize the size and cost of these units, typically built with expensive alloys such as titanium or 316-grade stainless steel, heat transfer augmentations are used in both the evaporator and the condenser.

For boiling on the outside of the tube bundle in the evaporator, low finned tubes or high performance boiling geometry tubes (such as Turbo-B) should be used. Since the shell-side is only in contact with the non-corrosive working fluid (a refrigerant or propane), the external enhancement does not have to be a high alloy.

For shell-side condensing, a low finned tube or an enhanced condensing tube such as Turbo-CSL is an appropriate choice. For the former, the fin density (fins/m), fin height and thickness should be optimized, choosing among the geometries commercially available in that particular material (refer to Wolverine Tube product tables).

Enhanced evaporators and condensers enjoy much larger tube-side water velocities, which increases the internal heat transfer coefficient and reduces fouling and scale formation. Table 2.1 shows the results for an actual geothermal condenser optimized using ENHANCED HEAT TRANSFER, a software program written by J.R. Thome and licensed throughout the world from HTI. The tube length was fixed by the application (portable truck transported unit) to 9.9 m (32.5 ft). The number of tubes (and shell) was significantly reduced in size. The design has a higher factor of reliability because the ratio of the clean overall heat transfer coefficient to the fouled value is much larger, 1.62 compared to 1.34, respectively.

**Table 2.1. Geothermal Condenser Design Case Study with 316L Stainless Tubing.**

Tube Type	Plain	19 fpi Low Fin	28 fpi Low Fin
<b>Heat Duty (MW)</b>	12.1	12.1	12.1
<b>LMTD (°C)</b>	10.0	10.0	10.0
<b>Tube-Side Water Flow Rate (kg/s)</b>	489	489	489
<b>R-11 Flow Rate in Shell (kg/s)</b>	68	68	68
<b>Condensing Pressure (bar)</b>	1.65	1.65	1.65
<b>Tube Nominal O.D. (mm)</b>	19.05	19.05	19.05
<b>Tube I.D. (mm)</b>	17.45	14.63	15.75
<b>Tube Length (mm)</b>	9900	9900	9900
<b>Water Fouling Factor (m<sup>2</sup>K/W)</b>	0.000176	0.000176	0.000176
<b>Fin Height/Thickness (mm)</b>	No fins	1.5/0.3	0.94/0.3
<b>Water Velocity in Tubes (m/s)</b>	1.19	2.14	1.97
<b>Number of Tubes Required</b>	1720	1363	1280
<b>Tube-Side Heat Transfer Coeff. (W/m<sup>2</sup>K)</b>	5790	9713	9034
<b>Shell-Side Heat Transfer Coeff. (W/m<sup>2</sup>K)</b>	3178	5831	6393
<b>Overall Heat Transfer Coeff. (W/m<sup>2</sup>K)</b>	1333	1691	1799
<b>Ratio of U<sub>o,finned</sub>/U<sub>o,plain</sub></b>	1.0	1.29	1.35
<b>Decrease in Required Length</b>	0%	-22%	-26%
<b>Ratio of U<sub>o,clean</sub>/U<sub>o,dirty</sub></b>	1.34	1.63	1.62

## 2.11 Applications in the Food Processing Industries

In the food processing industries, heat transfer augmentations are of particular benefit to pasteurizing temperature-sensitive foodstuffs and for heating or cooling viscous fluids, such as vegetable oils. Non-Newtonian fluids, such as power law fluids, can be augmented using tube inserts for laminar flows or integral tube enhancements, such as ribbed tubes, for turbulent flows.

## Chapter 3

# Single-Phase Shell-Side Flows and Heat Transfer

**SUMMARY:** The design method of Taborek (1983) for single-phase shell-side flows of shell-and-tube heat exchangers with *single segmental baffles* is presented here. The Taborek version of the Delaware method is thought to be the most accurate, reliable and complete method available in the open literature. The basic theory of single-phase shell-side flow in baffled heat exchangers is presented and then a complete treatment of the Taborek method for application to plain tubes and integral low finned tubes, such as the Wolverine Tube S/T Trufin tubes. The method predicts both heat transfer coefficients and pressure drops as a function of the tube bundle geometry and its dimensional description.

### 3.1 Introduction

Single-phase flow of liquids and gases over tube bundles is an important heat transfer process confronted in numerous types of heat exchanger applications. In contrast to single-phase heat transfer inside tubes, shell-side flows (i.e. those across the outside of the tubes in a baffled tube bundle confined by a heat exchanger shell) are particularly complex because of the many geometrical factors involved and the many possible fluid flow paths. Tinker (1951) was the first to give a physical description of this process, which was used in the development of what is often referred to as the *Delaware method*, proposed by Bell (1960, 1963) and republished in Bell (1986). Taborek (1983) proposed a new version of this design method for single-phase shell-side flows of shell-and-tube heat exchangers with single segmental baffles (essentially for what is called a TEMA E-shell) and described how to extend it to TEMA J-shells and F-shells and to E-shells with no-tubes-in-the-window. The basic theory of single-phase shell-side flow in baffled E-shell heat exchangers is presented here and then a more complete treatment of the Taborek method. This method is for flow over tube bundles with *single-segmental baffles*. Other types of baffles used in special applications include double-segmental baffles, triple-segmental baffles, disk-and-donut baffles, rod baffles and helical baffles; these alternative, less used geometries are not addressed here. In this chapter, first the method for *plain tubes* is described and then its extension to *integral low finned tubes*.

### 3.2 Stream Analysis of Flow Distribution in a Baffled Heat Exchanger

In a baffled shell-and-tube heat exchanger, only a fraction of the fluid flow through the shell-side of a heat exchanger actually flows across the tube bundle in the idealized path normal to the axis of the tubes. The remaining fraction of the fluid flows through "bypass" areas. As can be expected, the fluid seeks the flow path of less resistance from the inlet to the outlet of the exchanger. In a typical design, the *non-ideal* flows represent up to 40% of the total flow and hence it is imperative to account for their effects on heat transfer and pressure drop.

These flow paths in an actual heat exchanger with single-segmental baffles were first intuitively described by Tinker (1951) as depicted in his schematic diagram shown in Figure 3.1. The total flow is divided into individual streams designated by the letters shown in the diagram as follows:

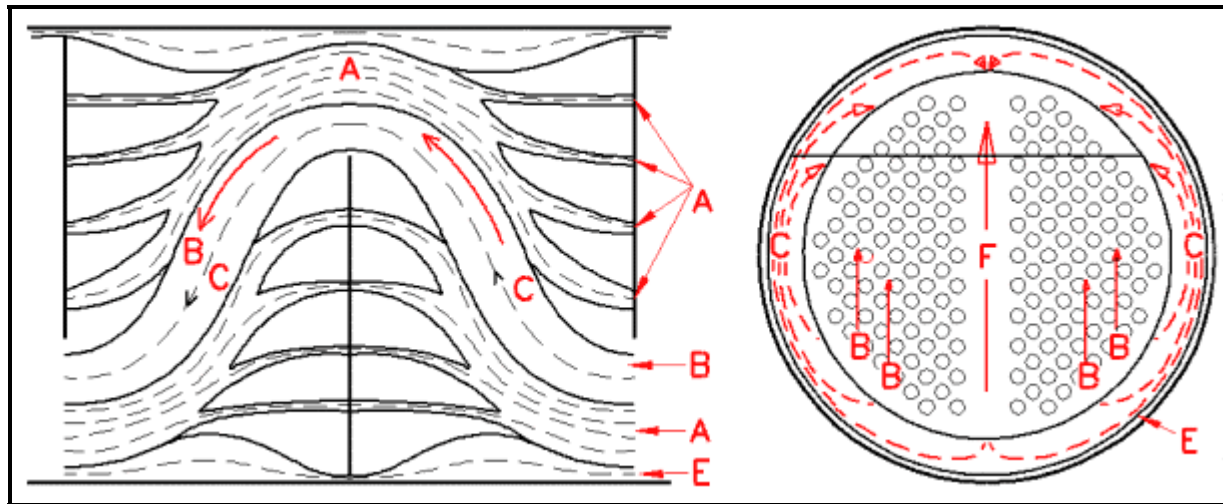


**Figure 3.1. Shell-side flow paths in a baffled heat exchanger according to Tinker (1951).**

The total flow is divided into individual streams designated by the letters shown in the diagram as follows:

- **Stream A:** The *tube hole leakage stream* represents the flow from one baffle compartment to the next that passes through the annular openings between the oversized holes for the tubes in the baffles and the outside of the tubes, as illustrated in Figure 3.2. The flow is driven by the pressure drop from one baffle compartment to the next. The leakage occurs through the diametral clearance between the diameter of the baffle hole minus the outside diameter of the tube. If the tubes are expanded into the baffles, then the diametral clearance is zero. This bypass stream is minimized by reducing the diametral clearance and completely eliminated if the clearance becomes zero.

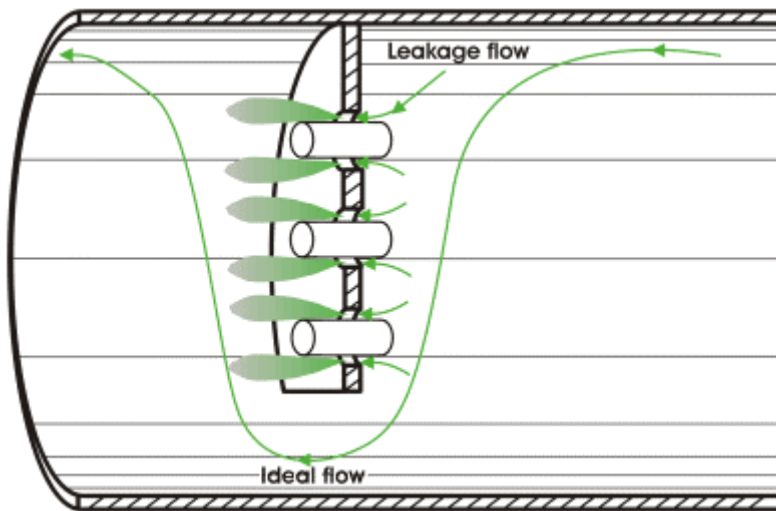


**Figure 3.2. Diagram of tube hole leakage stream A.**

- **Stream B:** The *crossflow stream* is the idealized cross flow over the tube bundle normal to the axis of the tubes. This is the preferred flow in a baffled shell-and-tube heat exchanger and is illustrated in Figure 3.1.

- **Stream C:** The *bundle bypass stream* flows through the annular opening between the outside of the tube bundle and the inner shell wall as illustrated in Figure 3.3. The diametral clearance for this flow to pass through is equal to the shell internal diameter minus the outer tube limit diameter of the tube bundle. The bundle bypass stream is reduced by minimizing the diametral clearance between the shell internal diameter and the outer tube limit diameter of the tube bundle and by installing pairs of sealing strips around the perimeter of the tube bundle to block this flow path and thereby force the fluid back into the tube bundle.

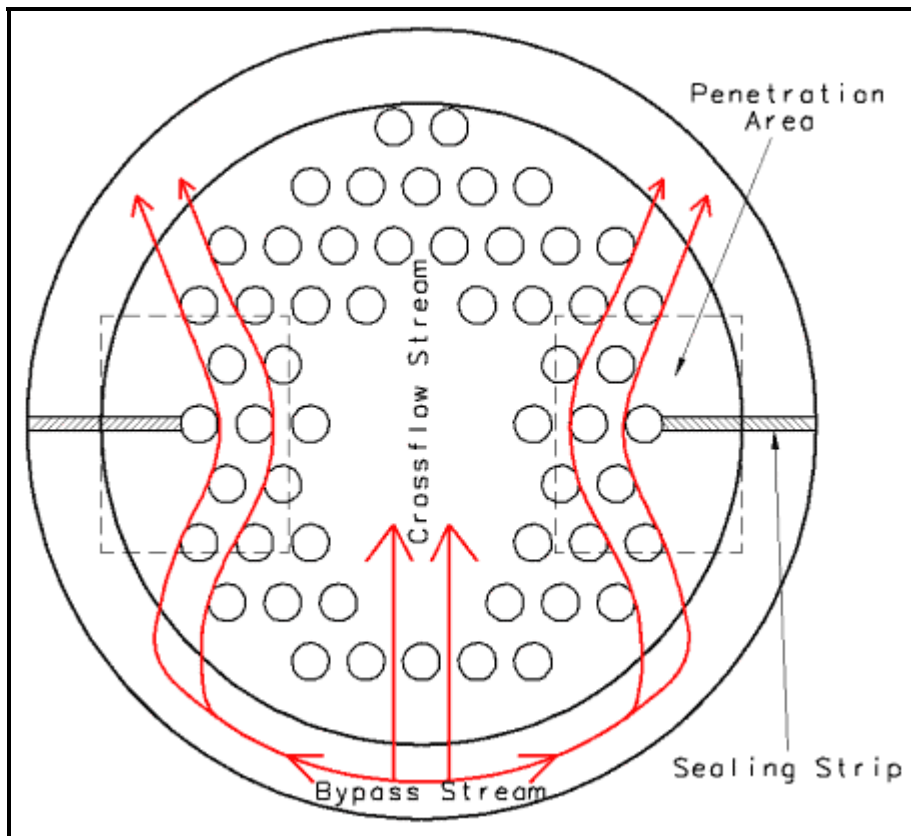


Figure 3.3. Schematic of bundle bypass stream C.

- **Stream E:** The *shell-to-baffle bypass stream* refers to the flow through the gap between the outer edge of the baffle and the inner shell wall as depicted in Figure 3.4. The diametral clearance is equal to the shell internal diameter minus the diameter of the baffle and is minimized by decreasing the construction clearance between the shell and the baffle to its feasible minimum.
- **Stream F:** The *pass partition bypass stream* refers to the flow through the open lanes in a tube bundle formed by omission of tubes in the bundle and tubesheet for placement of tubepass partition plates in the heads of multi-pass heat exchangers. It is illustrated in Figure 3.1. This stream only refers to those openings oriented in the *direction* of the fluid flow. Pass partition openings oriented *normal* to the flow path do *not* cause a bypass. This bypass stream thus only occurs in some multi-pass tube layouts and they can be eliminated by placement of several dummy tubes in each bypass lane to drive the fluid back into the tube bundle.

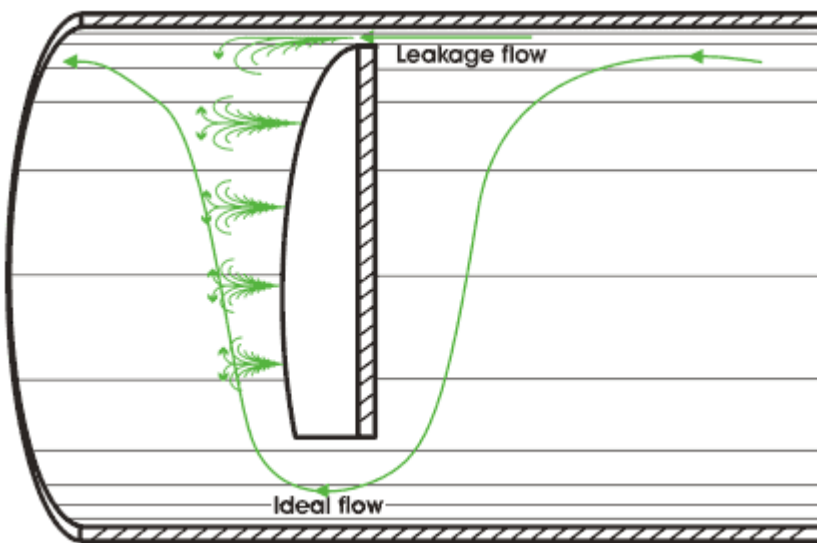


Figure 3.4. Schematic of shell-to-baffle bypass stream E.

### 3.3 Definition of Bundle and Shell Geometries

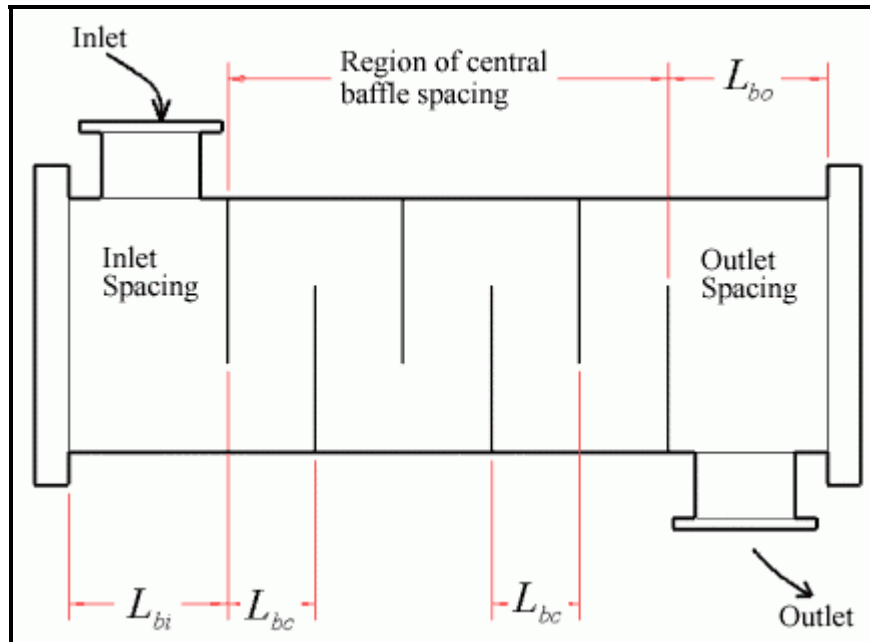


Figure 3.5. Single-segmental shell-and-tube heat exchanger showing baffle spacings.

Figure 3.5 depicts a single-segmental shell-and-tube bundle geometry with fixed tubesheets at both heads in which the shell-side flow makes one shell pass from one end of the tube bundle to the other with the flow directed across the tube bundle by the baffles. This is a common configuration used in refrigeration and petrochemical heat exchangers. The inlet, central and outlet baffle spacings are shown and are identified as  $L_{bi}$ ,  $L_{bc}$  and  $L_{bo}$ , respectively.  $L_{bi}$  and  $L_{bo}$ , are often equal in length to  $L_{bc}$ , except when the first and last baffle compartments must be enlarged to allow for the placement of the respective shell-side

nozzles. The baffle layout is determined from the inlet, central, and outlet baffle spacings and the effective tube length. The effective tube length  $L_{ta}$  is equal to the total tube length less the combined thickness of the two tubesheets. The number of baffles (an integer) and baffle spacings can be determined from these values. The effective length for determining the baffle spacing for a U-tube exchanger includes the straight length of the tube plus  $D_s/2$ , where  $D_s$  is the shell internal diameter. Thus the baffle spacing at the U-bend should include the tube straight length in this compartment plus  $(D_s/2)$ .

Figures 3.5, 3.6 and 3.7 reproduced from Taborek (1983) define the principal heat exchanger dimensions.  $D_{otl}$  is the *outer tube limit diameter* and  $D_{ctl}$  is the *centerline tube limit diameter* (note:  $D_{ctl} = D_{otl} - D_t$  where  $D_t$  is the outside diameter of the tubes). The *baffle cut height* is shown as a height  $L_{bch}$ ; the value of the baffle cut  $B_c$  is  $(L_{bch}/D_s) \times 100\%$ , i.e. given in terms of the *percent* of the shell internal diameter. The diametral clearance between the shell internal diameter  $D_s$  and outer tube limit diameter  $D_{otl}$  is  $L_{bb}$ . One-half of  $L_{bb}$  is the width of this bypass channel. A pass partition lane is shown with a width of  $L_p$ . The diametral clearance between the shell internal diameter  $D_s$  and the diameter of the baffle  $D_b$  is  $L_{sb}$ , where the gap is equal to  $L_{sb}/2$ .

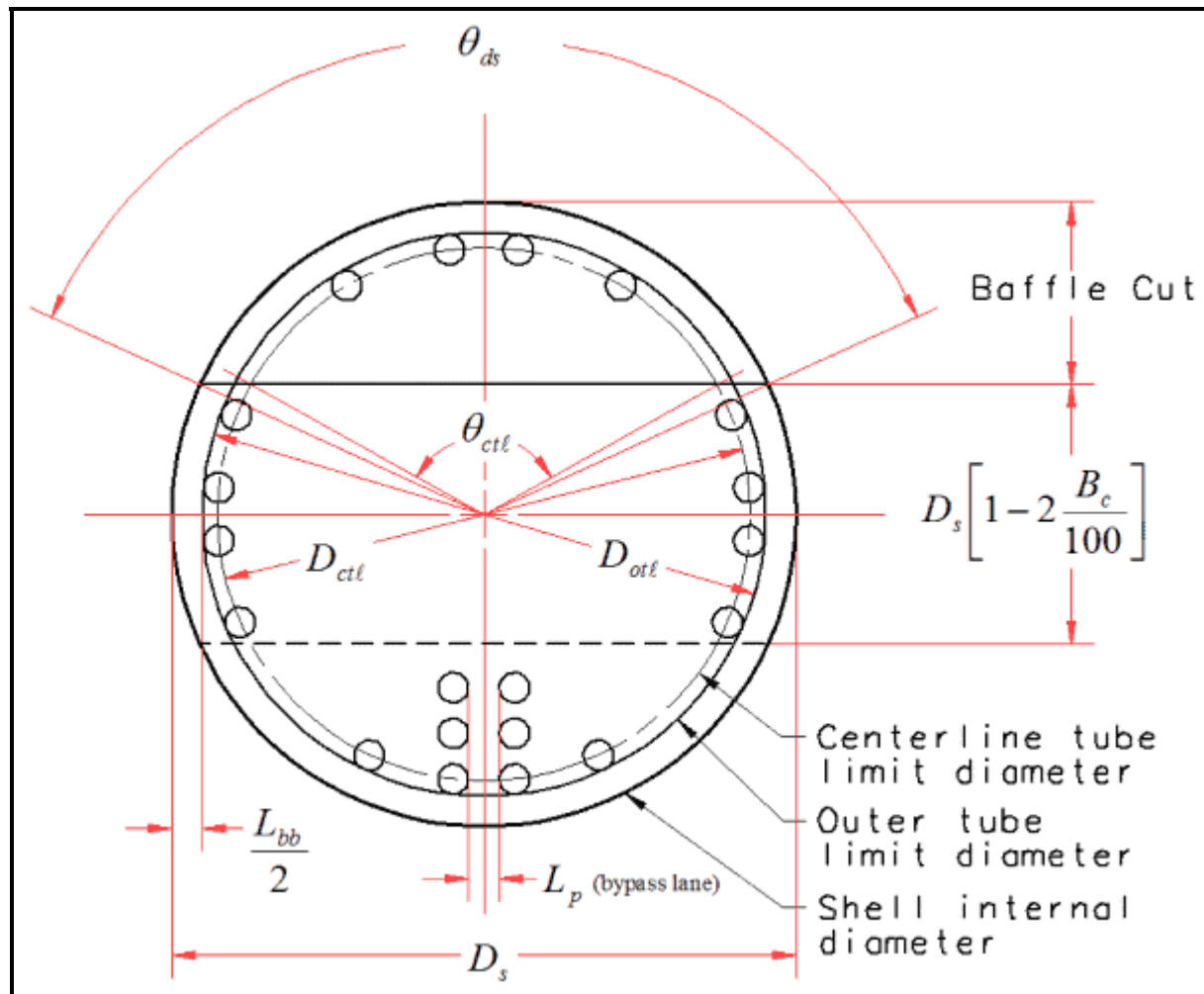
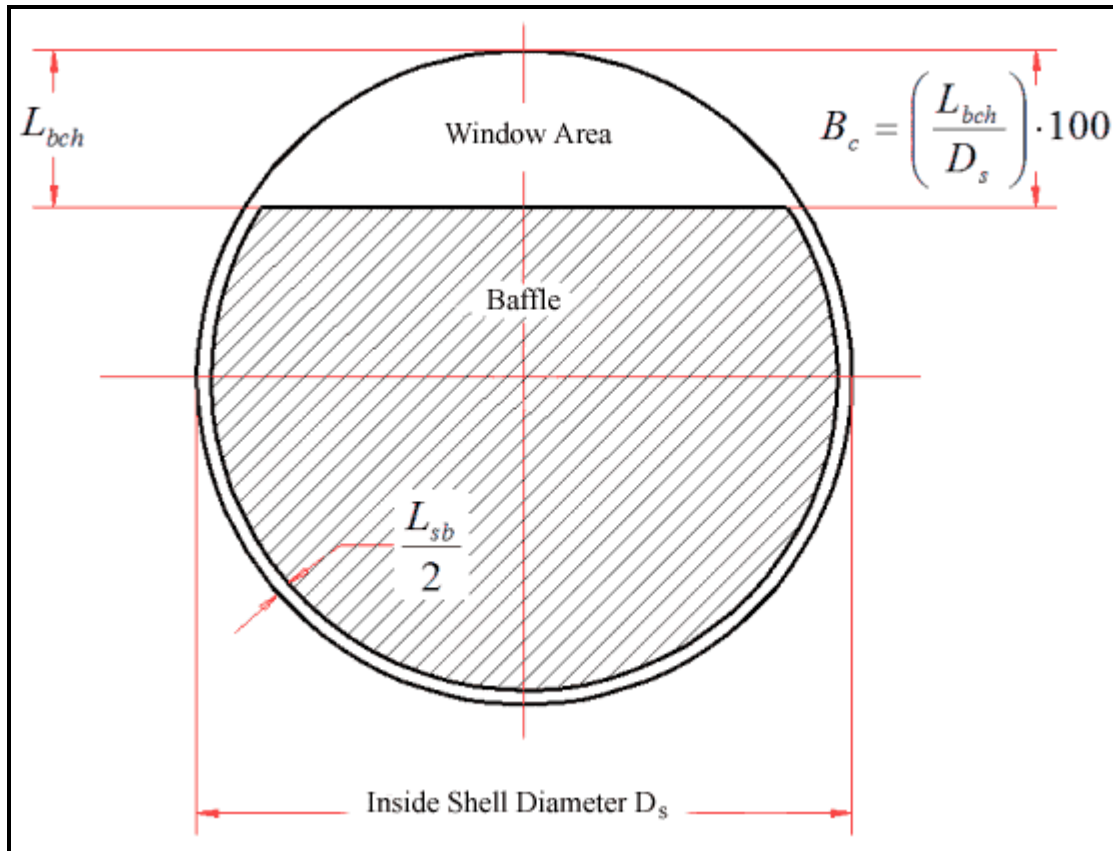


Figure 3.6. Baffle and tube bundle geometry.



**Figure 3.7. Baffle cut and clearance.**

The above dimensions  $D_s$ ,  $D_{otl}$ , baffle cut (% of  $D_s$ ),  $L_{bb}$  and  $L_{sb}$  can be obtained from a tube layout drawing of the heat exchanger. If the value of  $D_{otl}$  is not known,  $L_{bb}$  can be assumed to be equal to 9.525 mm (3/8 in.) for  $D_s < 300$  mm (11.81 in.) and  $L_{bb}$  can be assumed to be 15.875 mm (5/8 in.) for  $D_s > 1000$  mm (39.37 in.). For  $D_s$  from 300 to 1000 mm inclusive,  $L_{bb}$  can be assumed to be 12.7 mm (1/2 in.). These values are typical of TEMA heat exchanger specifications but are often smaller for direct-expansion evaporators. If  $L_{sb}$  is not known, it can be assumed that  $L_{sb} = 2.0$  mm for  $D_s < 400$  mm (15.75 in.) while for larger shells  $L_{sb} = 1.6 + 0.004D_s$  (mm). If the diametral clearance between the baffle holes and the outside of the tube is not known, the maximum TEMA value can be assumed 0.794 mm (1/32 in.) or a smaller value in the range from 0.397 mm (1/64 in.) to 0.794 mm. This clearance is equal to the baffle hole diameter minus  $D_t$ . Thermal performance is significantly improved by minimizing this clearance.

The three tube layouts addressed by the Taborek design method are shown in Figure 3.8: 30°, 45° and 90°. The 60° layout is not included. The *tube pitch* is  $L_{tp}$  and is defined as the distance center-to-center between tubes in the bundle. The *pitch parallel to the direction of flow* is  $L_{pp}$  while that *pitch normal to the direction of the flow* is  $L_{pn}$ .

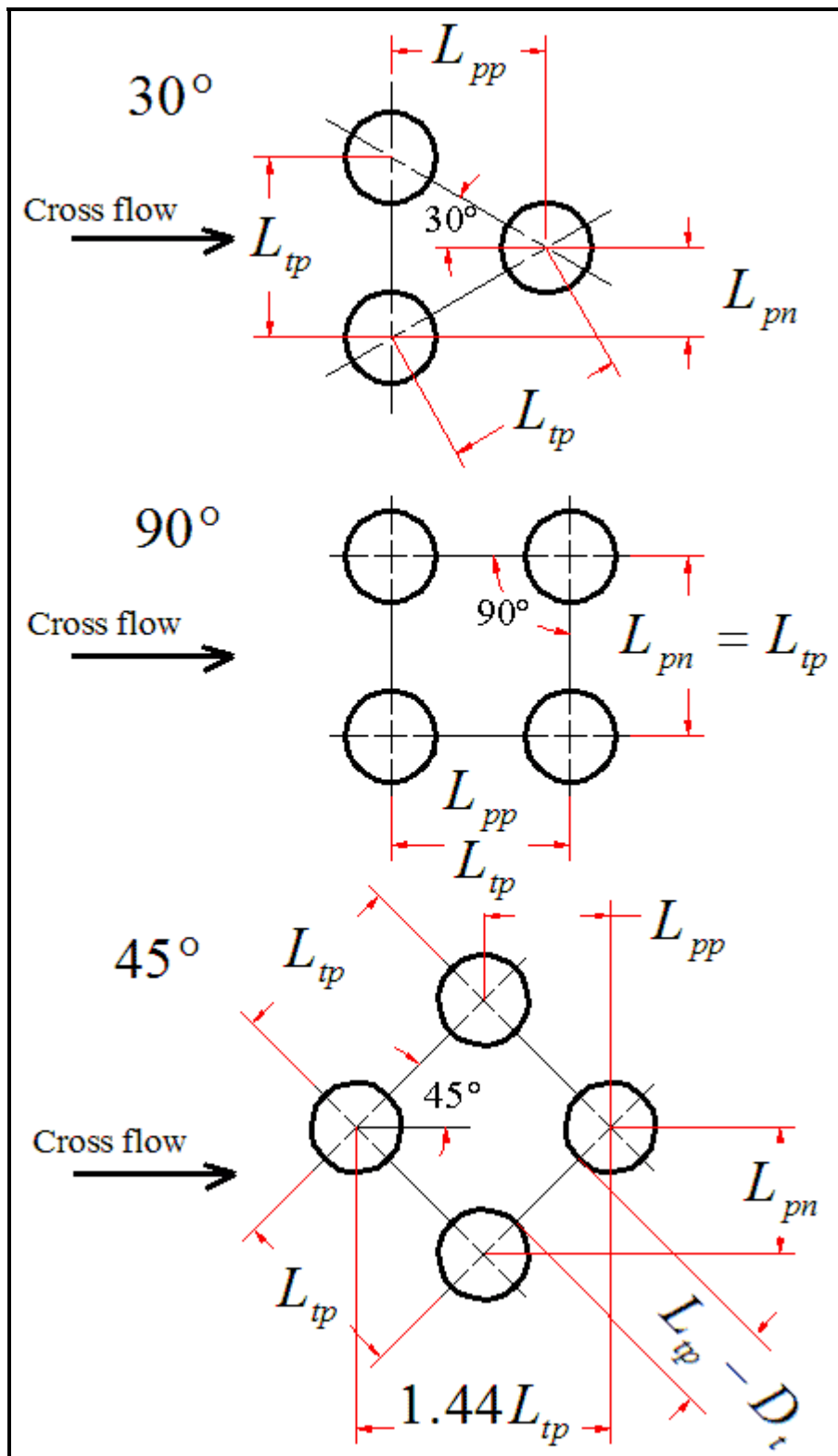


**Figure 3.8. Tube layouts.**

The number of tubes that fit within a shell depends on a number of geometrical factors, dimensions and clearances, principally the type of tube layout (triangular, square or rotated square) and the tube pitch.

The simple estimation method presented by Taborek (1983) for fixed tubesheets for single tubepass units without any tubes removed in the nozzle entrance and exit areas is:

$$N_{tt} = \frac{0.7854 D_{ct}^2}{C_1 L_{tp}^2} \quad [3.3.1]$$

where  $N_{tt}$  is the number of tubes,  $D_{ct}$  is the centerline tube limit diameter and  $L_{tp}$  is the tube pitch. The constant  $C_1 = 1.0$  for square ( $90^\circ$ ) and rotated square tube ( $45^\circ$ ) layouts and  $C_1 = 0.866$  for triangular ( $30^\circ$ ) tube layouts. Designs with multiple tubepasses (2, 4, ...) are commonly used and they will have fewer tubes than given by the above expression. Use of a tube count software program is highly recommended for an accurate estimate since tubes are often removed at the inlet nozzle to permit placement of an impingement plate and the number removed depends on the nozzle diameter. An accurate tube count improves the accuracy of the heat transfer and pressure drop calculations.

### 3.4 Stream Analysis of Heat Transfer in a Baffled Heat Exchanger

The stream analysis shell-side heat transfer coefficient for single-phase flow  $\alpha_{ss}$  is

$$\alpha_{ss} = (J_C J_L J_B J_R J_S J_\mu) \alpha_I \quad [3.4.1]$$

where  $\alpha_I$  is the ideal tube bank heat transfer coefficient calculated for all the flow across the tube bundle (that is all flow assumed to be in stream B).  $J_C$ ,  $J_L$ ,  $J_B$ ,  $J_R$  and  $J_S$  are the correction factors for the leakage and bypass flow effects and  $J_\mu$  is the wall viscosity correction factor. The corrections factors and ideal tube bank heat transfer correlations are described in the sections below. The value of  $\alpha_{ss}$  is the mean value for the whole tube bundle applied to the outside heat transfer surface area of the tubes. Mean bulk physical properties are used for evaluating the correlations.

#### 3.4.1 Baffle Cut Correction Factor ( $J_C$ )

The baffle cut correction factor  $J_C$  accounts for the non-ideal flow effects of window flow on heat transfer since the velocity through the window (that of the baffle cut) is not the same as that for cross-flow over the bundle. The window flow velocity can be larger or smaller than for cross-flow depending on the size of the cut and the baffle spacing. In addition, the window flow is partially longitudinal to the tubes, which is less effective than cross-flow. Therefore,  $J_C$  is a function of the baffle cut, the outer tube limit diameter and the window flow area and is calculated as follows:

$$J_C = 0.55 + 0.72 F_C \quad [3.4.2]$$

where  $F_C$  is

$$F_C = 1 - 2F_w \quad [3.4.3]$$

$F_w$  is the fraction of the cross-sectional area occupied by the window:

$$F_w = \frac{\theta_{ctl}}{360} - \frac{\sin \theta_{ctl}}{2\pi} \quad [3.4.4]$$

The angle of the baffle cut relative to the *centerline* of the heat exchanger is  $\theta_{ctl}$  (in degrees):

$$\theta_{ctl} = 2 \cos^{-1} \left\{ \frac{D_s}{D_{ctl}} \left[ 1 - 2 \left( \frac{B_c}{100} \right) \right] \right\} \quad [3.4.5]$$

The above expression is valid for baffle cuts from 15% to 45% of the shell diameter. Use of baffle cuts outside this range is not normally recommended because of the ensuing maldistribution of the flow.  $J_C$  typically ranges in value from 0.65 to 1.175 in a well-designed unit.

### 3.4.2 Baffle Leakage Correction Factor ( $J_L$ )

The pressure difference between neighboring baffle compartments forces a fraction of the flow through the baffle-to-tubehole gaps in the baffles (Stream A) and through the annular gap between the shell and the baffle edge (Stream E). These streams reduce the part of the flow that passes over the tube bundle as cross-flow (Stream B), reducing both the heat transfer coefficient *and* the pressure drop. Stream E is very detrimental to thermal design because it is not effective for heat transfer. The baffle leakage correction factor is calculated from the following expression:

$$J_L = 0.44(1 - r_s) + [1 - 0.44(1 - r_s)] \exp(-2.2r_{lm}) \quad [3.4.6]$$

where  $r_s$  is

$$r_s = \frac{S_{sb}}{S_{sb} + S_{tb}} \quad [3.4.7]$$

and  $r_{lm}$  is

$$r_{lm} = \frac{S_{sb} + S_{tb}}{S_m} \quad [3.4.8]$$

The *shell-to-baffle* leakage area  $S_{sb}$ , the *tube-to-baffle* hole leakage area  $S_{tb}$  for  $N_{tt}(1-F_w)$  tube holes and the cross-flow area at the bundle centerline  $S_m$  are determined as follows:

$$S_{sb} = 0.00436 D_s L_{sb} (360 - \theta_{ds}) \quad [3.4.9]$$

$$S_{tb} = \left\{ \frac{\pi}{4} \left[ (D_t + L_{tb})^2 - D_t^2 \right] \right\} N_{tt} (1 - F_w) \quad [3.4.10]$$

$$S_m = L_{bc} \left[ L_{bb} + \frac{D_{ctl}}{L_{tp,eff}} (L_{tp} - D_t) \right] \quad [3.4.11]$$

In the above expressions,  $L_{sb}$  is the diametral shell to baffle clearance and the baffle cut angle  $\theta_{ds}$  in degrees is

$$\theta_{ds} = 2 \cos^{-1} \left[ 1 - 2 \left( \frac{B_c}{100} \right) \right] \quad [3.4.12]$$

where  $L_{bc}$  is the central baffle spacing and  $L_{bb}$  is the bypass channel diametral gap, both described earlier. The effective tube pitch is  $L_{tp,eff}$ , which is equal to  $L_{tp}$  for  $30^\circ$  and  $90^\circ$  tube layouts while for  $45^\circ$  staggered layouts  $L_{tp,eff}$  is equal to  $0.707L_{tp}$ . For a well-proportioned heat exchanger,  $J_L > 0.7-0.9$  while values of  $J_L < 0.6$  should be avoided. The maximum value of  $J_L$  is 1.0. For refrigeration chillers and water-cooled condensers, a value of 0.85 to 0.90 is achievable because of their tighter construction tolerances and smaller clearances than TEMA standards.

### 3.4.3 Bundle Bypass Correction Factor ( $J_B$ )

The bundle bypass correction factor  $J_B$  accounts for the adverse effect of the flow between the inner shell wall and the tube bundle (Stream C) and the bypass lane created by any pass partition lanes (Stream F) in the direction of flow. Stream F is not always present and it can be eliminated completely by placing dummy tubes in the pass partition lanes. Stream C is reduced by a tighter fit of the tube bundle into the shell and also by placing sealing strips (in pairs) around the bundle perimeter, up to a maximum of one pair of strips for every two tube rows passed by the flow between the two baffle cuts. The bundle bypass correction factor  $J_B$  is

$$J_B = \exp \left[ -C_{bh} F_{sbp} \left( 1 - \sqrt[3]{2r_{ss}} \right) \right] \quad [3.4.13]$$

The empirical factor  $C_{bh} = 1.35$  for laminar flow ( $100 \geq Re$ ) and  $C_{bh} = 1.25$  for transition and turbulent flows ( $Re > 100$ ). To evaluate this expression, one requires the ratio of the bypass to the crossflow area  $F_{sbp}$ , and the ratio  $r_{ss}$  of the number of sealing strips  $N_{ss}$  (number of pairs if any) passed by the flow to the number of tube rows crossed between baffle tips in one baffle section  $N_{tcc}$ . First of all,  $F_{sbp}$  is given by

$$F_{sbp} = \frac{S_b}{S_m} \quad [3.4.14]$$

where  $S_m$  was given above and  $S_b$  is the bypass area:

$$S_b = L_{bc} [(D_s - D_{otl}) + L_{pl}] \quad [3.4.15]$$

where  $L_{pl}$  represents the width of the bypass lane between tubes. For situations without a pass partition lane or for such a lane normal to the flow direction, set  $L_{pl} = 0$  while for a pass partition lane parallel to the flow direction  $L_{pl}$  is equal to  $\frac{1}{2}$  the actual dimension of the lane or can be assumed to be equal to the tube diameter  $D_t$ . The ratio  $r_{ss}$  is

$$r_{ss} = \frac{N_{ss}}{N_{tcc}} \quad [3.4.16]$$

The value of  $N_{tcc}$  is obtained from

$$N_{tcc} = \frac{D_s}{L_{pp}} \left[ 1 - 2 \left( \frac{B_c}{100} \right) \right] \quad [3.4.17]$$

where  $L_{pp} = 0.866L_{tp}$  for a  $30^\circ$  layout,  $L_{pp} = L_{tp}$  for a  $90^\circ$  layout and  $L_{pp} = 0.707L_{tp}$  for a  $45^\circ$  layout. This expression has a maximum limit of  $J_B = 1$  at  $r_{ss} \geq \frac{1}{2}$ .

### 3.4.4 Unequal Baffle Spacing Correction Factor ( $J_S$ )

The unequal baffle spacing correction factor  $J_S$  accounts for the adverse effect of an inlet baffle spacing  $L_{bi}$  and/or outlet baffle spacing  $L_{bo}$  larger than the central baffle spacing  $L_{bc}$ . Some exchangers have a larger baffle spacing in the inlet and outlet nozzle compartments compared to the central baffle spacing, allowing placement of the shell-side nozzles without interference with the body flanges and without overlapping the first baffle. The flow velocity in these compartments is thus lowered and has an adverse influence on heat transfer. For larger inlet and outlet spacings than the central baffle spacing, the correction factor  $J_S < 1.0$ . For inlet and outlet baffle spacings equal to the central baffle spacing, no correction is required and  $J_S = 1.0$ . The value for  $J_S$  is determined directly from the effect on the flow velocity and is given by the following expression:

$$J_S = \frac{(N_b - 1) + (L_{bi}/L_{bc})^{1-n} + (L_{bo}/L_{bc})^{1-n}}{(N_b - 1) + (L_{bi}/L_{bc}) + (L_{bo}/L_{bc})} \quad [3.4.18]$$

where  $n = 0.6$  for turbulent flow and  $n = 1/3$  for laminar flow. The number of baffle compartments  $N_b$  is determined from the effective tube length and the baffle spacings.

### 3.4.5 Laminar Flow Correction Factor ( $J_R$ )

In laminar flows, heat transfer is reduced by the adverse temperature gradient formed in the boundary layer as the flow thermally develops along the flow channel. The laminar flow correction factor  $J_R$  accounts for this effect. For laminar shell-side flow  $J_R < 1.0$  (i.e. for  $100 \geq Re$ ) while for  $Re > 100$ , no correction is needed and  $J_R = 1.0$ . For  $20 \geq Re$ , the value of  $J_R$  is given by

$$J_R = (J_R)_{20} = \left( \frac{10}{N_c} \right)^{0.18} \quad [3.4.19]$$

where  $N_c$  is the total number of tube rows crossed by the flow in the entire heat exchanger:

$$N_c = (N_{tcc} + N_{tcw})(N_b + 1) \quad [3.4.20]$$

The number of tuberows crossed  $N_{tcc}$  between baffle tips has been noted above while the number of tube rows crossed in the window area  $N_{tcw}$  is

$$N_{tcw} = \frac{0.8}{L_{pp}} \left[ D_s \left( \frac{B_c}{100} \right) - \frac{D_s - D_{ctl}}{2} \right] \quad [3.4.21]$$

For  $Re > 20$  but  $Re < 100$ , the value is prorated as

$$J_R = (J_R)_{20} + \left( \frac{20 - Re}{80} \right) [(J_R)_{20} - 1] \quad [3.4.22]$$

The minimum value of  $J_R$  in all cases is 0.4.

### 3.4.6 Wall Viscosity Correction Factor ( $J_\mu$ )

Heat transfer and pressure drop correlations are normally evaluated using bulk physical properties obtained at the mean of the inlet and outlet temperatures. For heating and cooling of liquids, the effect of variation in properties between the bulk fluid temperature and the wall temperature is corrected by the viscosity ratio  $J_\mu$ , which is the ratio of the bulk viscosity  $\mu$  to the wall viscosity  $\mu_{wall}$ :

$$J_\mu = \left( \frac{\mu}{\mu_{wall}} \right)^m \quad [3.4.23]$$

The correction factor is greater than 1.0 for heating the shell-side fluid and vice-versa for cooling the shell-side fluid. The exponent for heating and cooling of liquids is usually set to  $m = 0.14$ . For gases, no correction is required for a gas being cooled while a correction based on temperature rather than viscosity is used for gases being heated as follows:

$$J_\mu = \left( \frac{T + 273}{T_{wall} + 273} \right)^{0.25} \quad [3.4.24]$$

where  $T$  is the bulk temperature and  $T_{wall}$  is the wall temperature. The wall temperature must be calculated from a preliminary heat transfer calculation to determine the viscosity at the wall.

### 3.4.7 Ideal Tube Bank Heat Transfer Coefficient ( $\alpha_I$ )

The ideal tube bank heat transfer coefficient  $\alpha_I$  is calculated for all the flow across the tube bundle (that is as if all the flow in the exchanger were in Stream B without any bypass flows) as:

$$\alpha_I = j_I c_p \dot{m} Pr^{-2/3} \quad [3.4.25]$$

The mass velocity of the fluid  $\dot{m}$  is based on the total flow  $M$  through the minimum flow area normal to the flow and is in units of  $\text{kg}/\text{m}^2\text{s}$ .  $Pr$  is the Prandtl number. The heat transfer factor  $j_I$  is obtained as follows:

$$j_I = a_1 \left( \frac{1.33}{L_{tp}/D_t} \right)^a Re^{a_2} \quad [3.4.26]$$

$$a = \frac{a_3}{1 + 0.14 Re^{a_4}} \quad [3.4.27]$$

The values of  $a_1$ ,  $a_2$ ,  $a_3$  and  $a_4$  are listed in Table 3.1 given by Taborek (1983). For the above methods, the shell-side cross-flow mass velocity at the maximum cross-section of the tube bundle is

$$\dot{m} = \frac{M}{S_m} \quad [3.4.28]$$

where M is the shell-side flow rate in kg/s and S<sub>m</sub> was defined earlier. The shell-side Reynolds number is then

$$Re = \frac{D_t \dot{m}}{\mu} \quad [3.4.29]$$

The Prandtl number is defined as

$$Pr = \frac{c_p \mu}{k} \quad [3.4.30]$$

The physical properties (viscosity  $\mu$ , specific heat  $c_p$  and thermal conductivity  $k$ ) are evaluated at the mean bulk fluid temperature. The effective tube length L<sub>ta</sub> is used to calculate the actual heat transfer surface area A<sub>o</sub> as

$$A_o = \pi D_t L_{ta} N_{tt} \quad [3.4.31]$$

for the number of tubes in the bundle N<sub>tt</sub>.

**Table 3.1. Empirical coefficients for calculation of j<sub>I</sub> and f<sub>I</sub>.**

Layout	Re	a <sub>1</sub>	a <sub>2</sub>	a <sub>3</sub>	a <sub>4</sub>	b <sub>1</sub>	b <sub>2</sub>	b <sub>3</sub>	b <sub>4</sub>
30°	10 <sup>5</sup> -10 <sup>4</sup>	0.321	-0.388	1.450	0.519	0.372	-0.123	7.00	0.500
	10 <sup>4</sup> -10 <sup>3</sup>	0.321	-0.388			0.486	-0.152		
	10 <sup>3</sup> -10 <sup>2</sup>	0.593	-0.477			4.570	-0.476		
	10 <sup>2</sup> -10	1.360	-0.657			45.10	-0.973		
	<10	1.400	-0.667			48.00	-1.000		
45°	10 <sup>5</sup> -10 <sup>4</sup>	0.370	-0.396	1.930	0.500	0.303	-0.126	6.59	0.520
	10 <sup>4</sup> -10 <sup>3</sup>	0.370	-0.396			0.333	-0.136		
	10 <sup>3</sup> -10 <sup>2</sup>	0.730	-0.500			3.500	-0.476		
	10 <sup>2</sup> -10	0.498	-0.656			26.20	-0.913		
	<10	1.550	-0.667			32.00	-1.000		
90°	10 <sup>5</sup> -10 <sup>4</sup>	0.370	-0.395	1.187	0.370	0.391	-0.148	6.30	0.378
	10 <sup>4</sup> -10 <sup>3</sup>	0.107	-0.266			0.0815	+0.022		
	10 <sup>3</sup> -10 <sup>2</sup>	0.408	-0.460			6.0900	-0.602		
	10 <sup>2</sup> -10	0.900	-0.631			32.100	-0.963		
	<10	0.970	-0.667			35.000	-1.000		

### 3.5 Stream Analysis of Shell-Side Pressure Drop in a Baffled Heat Exchanger

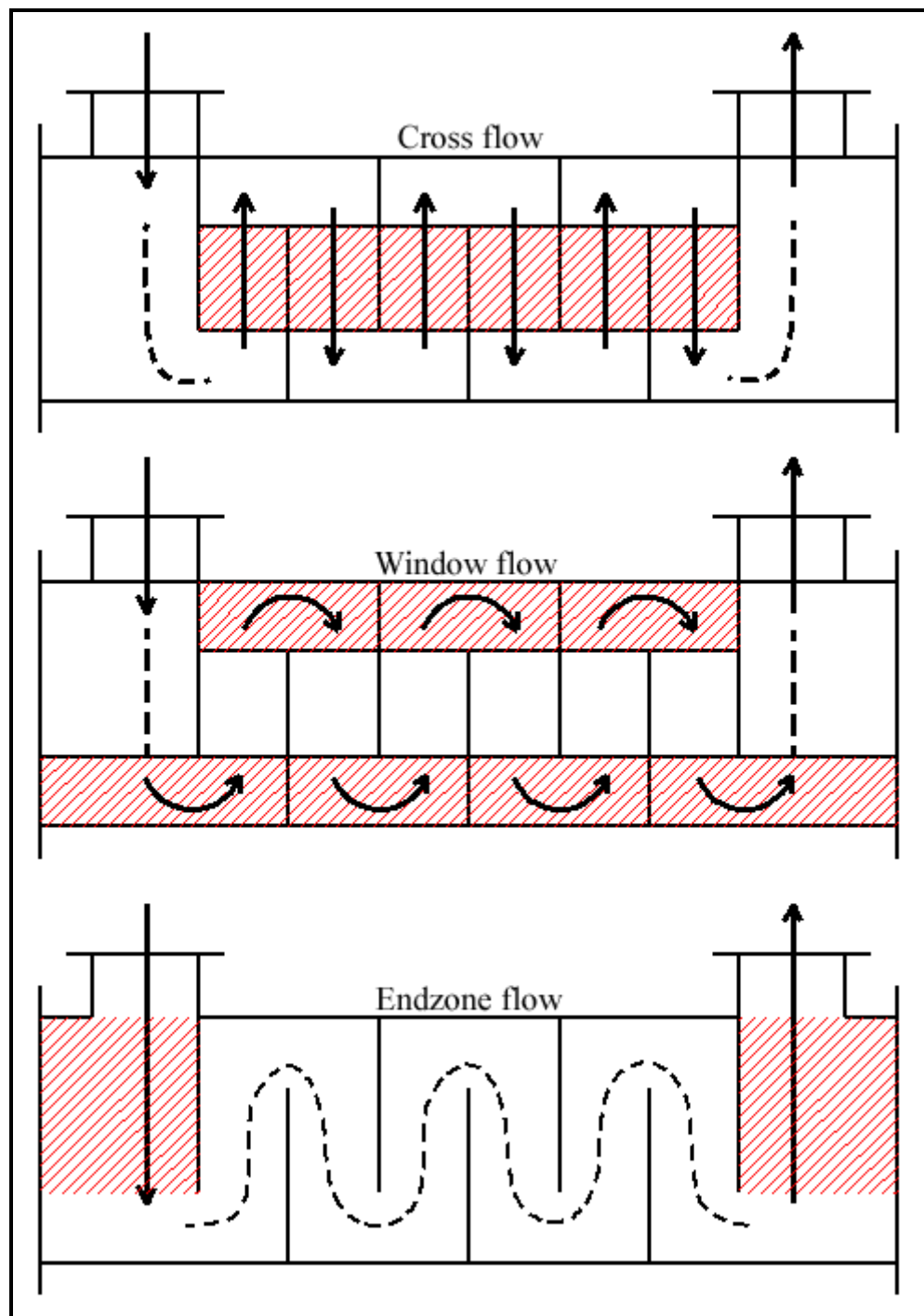


**Figure 3.9. Pressure drop regions in shell-side flow.**

The pressure drop for shell-side flow is equal to the sum of the inlet nozzle pressure drop, the bundle pressure drop and the outlet nozzle pressure drop. The inlet and outlet nozzle pressure drops can be

approximated as being equal to 2 velocity heads each. The bundle pressure drop is equal to the sum of the cross-flow pressure drops  $\Delta p_c$ , the window pressure drops  $\Delta p_w$ , and the two end zone pressure drops (first and last baffle compartments)  $\Delta p_e$  as illustrated in Figure 3.9. The bundle pressure drop  $\Delta p_{total}$ , excluding nozzles or impingement plates, is

$$\Delta p_{total} = \Delta p_c + \Delta p_w + \Delta p_e \quad [3.5.1]$$

The pressure drop  $\Delta p_c$  across tube bundle between the baffle tips is based on the ideal tube bank pressure drop  $\Delta p_{bl}$  for one baffle compartment with the central baffle spacing  $L_{bc}$ . The zones covered by this pressure drop are the central baffle compartments for flow between the baffle cuts. The pressure drop in all the central baffle compartments ( $N_b - 1$ ) is

$$\Delta p_c = \Delta p_{bl} (N_b - 1) R_B R_L \quad [3.5.2]$$

where  $\Delta p_{bl}$  is the ideal bundle pressure drop for one baffle compartment of the  $N_b$  compartments and is based on the mass velocity defined earlier. The expression for  $\Delta p_{bl}$  is:

$$\Delta p_{bl} = 0.002 f_I N_{tcc} \frac{\dot{m}^2}{\rho} R_\mu \quad [3.5.3]$$

The friction factor  $f_I$  is obtained from

$$f_I = b_1 \left( \frac{1.33}{L_{tp}/D_t} \right)^{b_2} Re^{b_3} \quad [3.5.4]$$

where

$$b = \frac{b_3}{1 + 0.14 Re^{b_4}} \quad [3.5.5]$$

The empirical constants for  $b$ ,  $b_1$ ,  $b_2$ ,  $b_3$  and  $b_4$  are taken from Table 3.1. The viscosity correction factor  $R_\mu$  on pressure drop is

$$R_\mu = \left( \frac{\mu}{\mu_w} \right)^{-m} \quad [3.5.6]$$

The values of  $m$  were cited earlier. The bypass correction factor  $R_B$  is

$$R_B = \exp \left[ -C_{bp} F_{sbp} \left( 1 - \sqrt[3]{2r_{ss}} \right) \right] \quad [3.5.7]$$

with the limit of  $R_B = 1$  for  $r_{ss} \geq 1/2$  while  $F_{sbp}$  was defined earlier. For the empirical factor  $C_{bp}$ , use  $C_{bp} = 4.5$  for laminar flow ( $100 \geq Re$ ) and  $C_{bp} = 3.7$  for transition and turbulent flows ( $Re > 100$ ). The leakage correction factor  $R_L$  is

$$R_L = \exp \left[ -1.33 (1 + r_s) r_{lm}^p \right] \quad [3.5.8]$$

where  $r_s$  and  $r_{lm}$  were defined earlier and the exponent  $p$  is

$$p = -0.15(1 + r_s) + 0.8 \quad [3.5.9]$$

The pressure drop and mass velocity in all  $N_b$  window zones for turbulent flow ( $Re > 100$ ) are

$$\Delta p_w = N_b \left[ (2 + 0.6N_{tw}) \frac{0.001\dot{m}_w^2}{2\rho} \right] R_L R_\mu \quad [3.5.10]$$

$$\dot{m}_w = \frac{M}{\sqrt{S_m S_w}} \quad [3.5.11]$$

where  $M$  is the shell-side flow rate in kg/s. The areas  $S_m$  and  $S_w$  are found from their appropriate expressions presented earlier. The 0.6 in the above expression accounts for the frictional effects and the factor 2 accounts for the velocity heads for the flow turnaround in the window. For laminar flow ( $100 \geq Re$ ), the equivalent expression is

$$\Delta p_w = N_b \left\{ 26 \left( \frac{\dot{m}_w \mu}{\rho} \right) \left[ \frac{N_{tw}}{L_{tp} - D_t} + \frac{L_{bc}}{D_w^2} \right] + \left[ \frac{0.002\dot{m}_w^2}{2\rho} \right] \right\} R_L R_\mu \quad [3.5.12]$$

The first term in brackets refers to the cross flow and the second term refers to the longitudinal flow. The hydraulic diameter of the baffle window is

$$D_w = \frac{4S_w}{\pi D_t N_{tw} + (\pi D_s \theta_{ds}/360)} \quad [3.5.13]$$

$\theta_{ds}$  was defined earlier.  $N_{tw}$  is the number of tubes in the window and is determined from the total number of tubes  $N_{tt}$  as

$$N_{tw} = N_{tt} F_w \quad [3.5.14]$$

where  $F_w$  was defined earlier.  $S_w$  is the net flow area in the window, given as

$$S_w = S_{wg} - S_{wt} \quad [3.5.15]$$

The area occupied by the  $N_{tw}$  tubes in the window is  $S_{wt}$  and is calculated as

$$S_{wt} = N_{tw} \left( \frac{\pi}{4} D_t^2 \right) \quad [3.5.16]$$

The gross window flow area without tubes in the window is  $S_{wg}$ , given as

$$S_{wg} = \frac{\pi D_s^2}{4} \left( \frac{\theta_{ds}}{360} - \frac{\sin \theta_{ds}}{2\pi} \right) \quad [3.5.17]$$

The pressure drop  $\Delta p_e$  in the two end zones of the tube bundle is

$$\Delta p_e = \Delta p_{bl} \left( 1 + \frac{N_{tcw}}{N_{tcc}} \right) R_B R_S \quad [3.5.18]$$

The pressure drop correction for unequal baffle spacings at the inlet and/or outlet with respect to the central baffle spacing is  $R_S$ , calculated as follows:

$$R_S = \left( \frac{L_{bc}}{L_{bo}} \right)^{2-n} + \left( \frac{L_{bc}}{L_{bi}} \right)^{2-n} \quad [3.5.19]$$

The tube numbers  $N_{tcw}$  and  $N_{tcc}$  were defined earlier as were methods for calculating  $\Delta p_{bl}$ ,  $R_B$  and  $R_\mu$ . For all baffle spacings of equal length,  $R_S = 2$ . In the above expression,  $N = 1$  for laminar flow ( $Re < 100$ ) and  $n = 0.2$  for turbulent flow.

## 3.6 Stream Analysis Applied to Low Finned Tube Bundles

In this section, the above plain tube method is applied to integral low finned tube bundles using the modifications proposed by Taborek (1983).

### 3.6.1 Low Finned Tubes and Applications

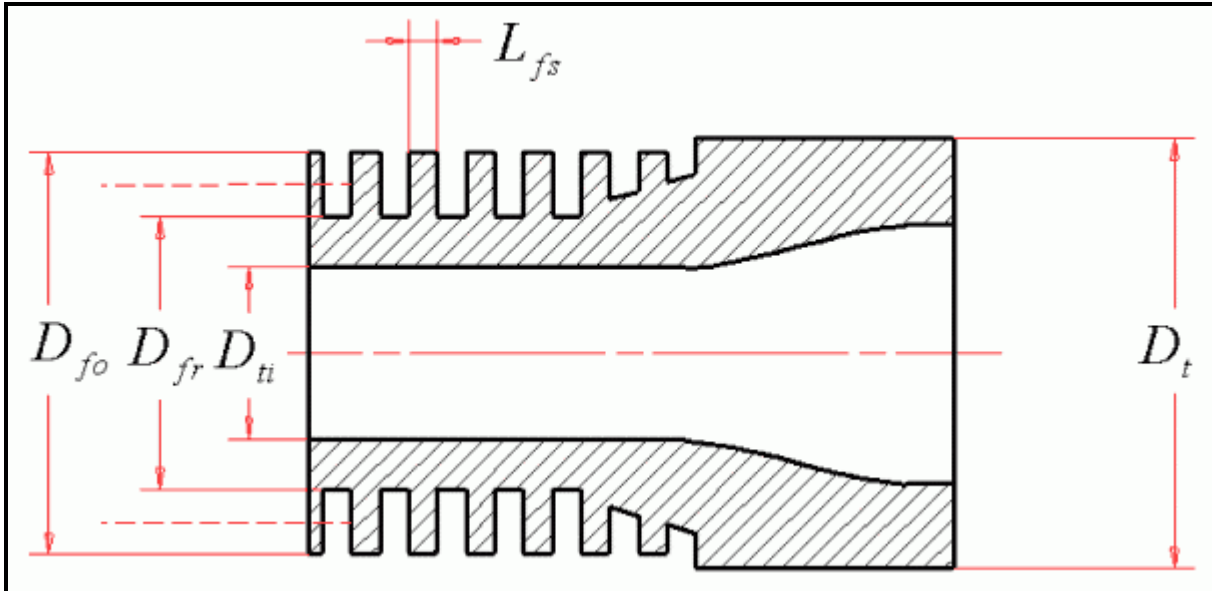


Figure 3.10. Geometric description of integral low finned tube.

Low finned tubes are an excellent heat transfer enhancement to apply to single-phase shell-side flows, for both liquid flows and even more so for gas flows. Figure 3.10 shows a geometric sketch of an integral low

finned tube that is defined by its following dimensions. The characteristic dimensions are: tube diameter at the plain unfinned end  $D_t$ , the tube diameter of the fin tips  $D_{fo}$  (typically equal to  $D_t$ ), the root diameter at the base of the fins  $D_{fr}$ , the tube internal diameter in the finned zone  $D_{ti}$ , the fin thickness  $L_{fs}$ , the number of fins per meter  $N_f$  and finally the actual wetted surface area per unit length  $A_{of}$ . Figure 3.11 shows a photograph of a selection of Wolverine Tube low finned tubes. Integral low finned tubes are available in nearly every common heat exchanger tube material. Common fin densities range from 630 to over 1000 fins per meter (commonly defined as their number of fins per inch, such as 19 fpi, 26 fpi, 28 and 30 fpi tubes). Typically fin heights are up to about a maximum of 1.5 mm (0.059 in.) while fin thickness is commonly about 0.3 mm (0.012 in.). Tables of integral low finned tubes with their dimensions are available from the [Wolverine Tube Inc.](#) website.

For many single-phase flows, it is advantageous to use integral low finned tubes rather than plain tubes. Low finned tubes are appropriate for applications where the shell-side (outside) heat transfer coefficient is small compared to the tube-side coefficient and/or when the shell-side fouling factor is controlling the design. The first situation most often occurs (a) when the shell-side flow is at the low end of the turbulent flow regime, in the transition regime or in the laminar flow regime, (b) when the allowable pressure drop is small, requiring use of large baffle cuts and baffle spacings, or (c) when a heat transfer augmentation is used on the inside of the tube, such as helical fins or ribs inside Wolverine Tube low finned tubes.

Another very important benefit of low finned tubes is their positive effect on the shell-side *fouling resistance*. Since the shell-side *fouling factor* is applied to the total wetted surface area (which is about 3 to 4 times that of a plain tube), the effective fouling resistance is reduced by a factor of 3 to 4 using the same fouling factor value as for the plain tube design. For large fouling factors or where the fouling resistance is significant (quite typical situation even for modest fouling factor values), the effect of the large surface area ratio of a low finned tube can dramatically increase the overall heat transfer coefficient. Hence, one uses a low finned tube to increase the shell-side heat transfer coefficient, to decrease the shell-side fouling resistance and to increase the tube-side velocity and heat transfer coefficient (also  $D_{ti}$  is less than that of the plain ends of the tube).

It is important to remember that when an external low finned tube is used, the internal diameter of the finned section of the tube  $D_{ti}$  should be used for determining the tube-side heat transfer coefficient and pressure drop. The most effective low finned tube geometry can be determined by trying several different fin densities. If corrosion allowances are important, thick fins should be used. For large corrosion allowances, fins may not be appropriate since they may be worn away.

### 3.6.2 Heat Transfer and Pressure Drops with Low Finned Tubes

The stream analysis method of Taborek (1983) for *plain tubes* was extended by Taborek in the same publication to application to *integral low finned tube bundles*. The changes to the above design equations are presented below. The heat transfer coefficient for the shell-side of a low finned tube bundle is used to



**Figure 3.11. A selection of low finned tubes of Wolverine Tube Inc.**

then calculate the overall heat transfer coefficient, at which point the fin efficiency of the low fins must be taken into account.

**Input data.** The following additional information is required for calculating the shell-side thermal performance of a low finned tube bundle:

Diameter over the fins:	$D_{fo}$
Fin root diameter:	$D_{fr}$
Number of fins per unit of tube length:	$N_f$
Average fin thickness (assuming rectangular profile):	$L_{fs}$
Wetted surface area of finned tube per unit of tube length:	$A_{of}$
Tube-to-baffle hole clearance:	$L_{tb}$

To determine  $L_{tb}$ , use  $D_{fo}$  in place of  $D_t$ . Normally,  $D_{fo}$  is equal to or slightly less than  $D_t$ .

### **Heat transfer and flow geometries.**

The total heat transfer surface area upon which to apply the shell-side heat transfer coefficient of the finned tube bundle  $\alpha_{ss}$  is  $A_o$ , which for the finned tube is obtained from the following expression:

$$A_o = A_{of} L_{ta} N_{tt} \quad [3.6.1]$$

The equivalent projected area of an integral low finned tube is less than that of a plain tube of the same diameter because of the openings between adjacent fins in the direction of flow. Hence, the “melt down” or equivalent projected diameter  $D_{req}$  is a function of the tube geometry and density as:

$$D_{req} = D_{fr} + 2L_{fh} N_f L_{fs} \quad [3.6.2]$$

and the fin height  $L_{fh}$  is

$$L_{fh} = \frac{D_{fo} - D_{fr}}{2} \quad [3.6.3]$$

Thus, wherever the plain tube diameter  $D_t$  appeared in the correlations and geometrical equations for the plain tube bank, it is replaced by  $D_{req}$  or as noted below:

$S_m$  calculations: use  $D_{req}$  in place of  $D_t$ .

$Re$  calculation: use  $D_{req}$  in place of  $D_t$ .

$S_{wt}$  calculation: use  $D_{fo}$  in place of  $D_t$ .

### **Ideal tube bank values of $j_I$ .**

The method for plain tubes is applicable to low finned tubes without modification with  $Re$  determined using  $D_{req}$  rather than  $D_t$  for  $Re > 1000$ . When  $Re < 1000$ , a laminar boundary layer overlap on the fins begins to adversely affect the heat transfer. This is accounted for by the following expression, applicable only when  $Re < 1000$ :

$$j_I = J_f j_{I,plain} \quad [3.6.4]$$

In Taborek (1983), a graph is given for the variation in  $J_f$  versus  $\log Re$  from  $Re = 20$  to  $Re = 1000$ , where  $J_f = 1.0$  at  $Re = 1000$ . This curve has been fitted here as follows:

$$J_f = 0.58 + 0.42 \left( \frac{\log(Re/20)}{\log(1000/20)} \right) \quad [3.6.5]$$

### Ideal tube bank values of $f_I$ .

The equivalent cross-flow area is larger for a finned tube bundle relative to an identical plain tube bundle because of the additional flow area between the fins. For finned tubes the friction factor is about 1.4 times larger than for a plain tube; however, the lower velocity due to the larger flow area from the open area between fins in the direction of flow is also taken into account in the Reynolds number  $Re$ . To calculate the friction factor for the low finned tube bank, first calculate  $f_{I,plain}$  using the finned tube values of  $Re$  and  $D_{req}$  from the plain tube correlation and then multiply this value by 1.4 as follows:

$$f_I = 1.4 f_{I,plain} \quad [3.6.6]$$

---

**Example calculation:** a detailed six-page example calculation is available in Taborek (1983) that is recommended to the reader.

## Chapter 4

# Enhanced Single-Phase Laminar Tube-side Flows and Heat Transfer

**SUMMARY:** This section presents methods for predicting heat transfer and pressure drop for laminar flows inside circular tubes, rectangular channels, spirally fluted tubes, internally ribbed or finned tubes, and in tubes with twisted tape inserts. First of all, an overview of prediction methods for laminar flow and heat transfer in plain tubes and in rectangular channels with high aspect ratios is presented for the reader's convenience. This is followed with a discussion of special effects on laminar flow heat transfer in microchannels, such as axial conduction, viscous heating, etc. Experimental results and prediction methods for laminar flow enhancements are then presented and discussed.

### 4.1 Introduction

This chapter covers laminar flow and heat transfer inside plain tubes, rectangular channels, microchannels, enhanced tubes and tubes with inserts. The commonly used prediction methods for heat transfer and pressure drop for plain tubes are first presented, followed by methods for rectangular channels (of particular interest to micro-scale heat transfer applications). Then, special effects on laminar flow heat transfer are addressed (axial conduction, viscous dissipation, etc.) and some guidelines are presented to note when these become important. Next, design methods for internally finned and spirally fluted tubes and tubes with twisted tape inserts are presented. The reader is referred to other sources for more detailed reviews of the literature and experimental results, such as the book of Webb (1994), the reviews by Bergles and Joshi (1983) on enhanced heat transfer, and Morini (2008) on special effects on laminar flows.

Tubular enhancements made by Wolverine Tube Inc. include corrugated tubes and tubes with integral internal fins or ribs. In particular, it must be pointed out that such tubes may provide enhancement relative to a plain tube when the fluid in the tube is being heated. Instead, when the fluid is being cooled, such geometries are not as effective because the more viscous cold fluid near the wall tends to hold up between the fins or corrugations and hence negate their effect on the flow. Furthermore, laminar flow enhancement is quite different than turbulent flow in that the fluid in a laminar flow does not "move" or "mix" unless it is forced to flow to the center of the channel or vice-versa. Hence, small ribs, corrugations and fins on internal tube walls that provide an excellent enhancement in a turbulent tubular flow may have little effect on a laminar flow.

Figure 4.1 shows a diagram of a single-start corrugated tube and Figure 4.2 depicts a photograph of a Wolverine Korodense corrugated tube. A corrugated tube is defined geometrically by the corrugation pitch,  $p$ , and the corrugation depth,  $e$ . The axial corrugation pitch is related to the internal diameter  $d_i$ , helix angle  $\beta$  relative to the axis of the tube and the number of starts  $n_s$  by the following geometrical equation:

$$p = \frac{\pi d_i}{n_s \tan \beta} \quad [4.1.1]$$

The external diameter over the corrugations on the outside of the tube is equal to that of the plain ends of the tube. The internal diameter is taken as the external diameter less twice the tube wall thickness. The internal area ratio of a corrugated tube relative to a plain tube of the same diameter  $d_i$  is slightly larger than one.

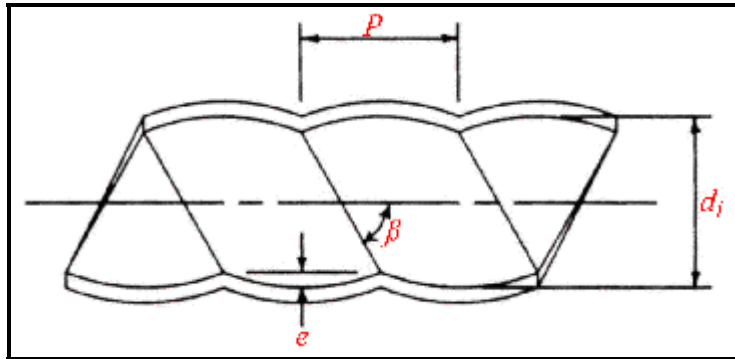


**Figure 4.1. Diagram of corrugated tube.**



**Figure 4.2. Photograph of Wolverine Korodense tube.**

Figure 4.3 depicts a schematic diagram for an internally finned or ribbed tube. These two names will be assumed to refer to the same geometry here. Helical internal *fins* or *ribs* (or also referred to as *ridges* in Wolverine Tube literature) are applied to the inside of low finned tubes such as Turbo-Chil and S/T Trufin and to enhanced boiling and condensing tubes, such as the various versions of Turbo-B and Turbo-C. The internal geometry is defined by the fin height, the mean fin thickness, the apex angle of the fin, the helix angle of the fin and the axial pitch of one fin to the next. The helix angle is related to the axial fin pitch by applying the expression above using the number of fins in place of the number of starts. The internal area ratio relative to a plain tube of the same diameter  $d_i$  ranges from about 1.3 to 2.0. The internal fins can be of various cross-sectional shapes. Most industrial tubes have fins (or ribs or ridges) with a trapezoidal cross-sectional profile (wider at the base than at the tip of the fin and with rounded corners). Figure 4.4 shows a photograph of a Wolverine Turbo-Chil low finned tube with internal helical fins.

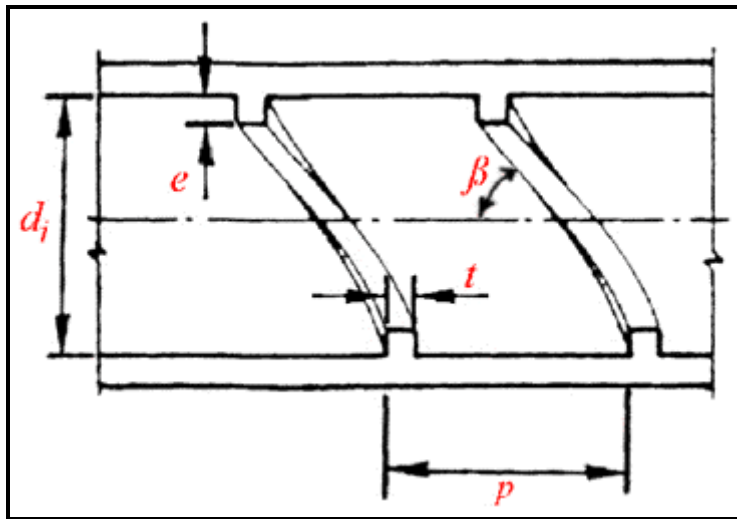


Figure 4.3. Diagram of internally finned or ribbed tube.



Figure 4.4. Photograph of Wolverine Turbo-Chil tube.

## 4.2 Transition of Flow and Entrance Shape Effects on Heat Transfer in Plain Tubes

Before discussing heat transfer enhancement of laminar, single-phase flows inside tubes, the effects of the tube inlet configuration on heat transfer and flow regime transition thresholds need to be addressed. For a summary of this topic, the reader is referred to Section 5.2 elsewhere in this book. In generally, laminar flow is normally assumed to occur at Reynolds numbers below 2300 (some also cite 2100); however, this threshold value is a function of the inlet shape among other things and methods for its calculation are given in Section 5.2. This topic has also been addressed by Gnielinski (1995) with propositions for the flow transition regimes and heat transfer methods.

## 4.3 Laminar Flow and Heat Transfer in Plain Circular Tubes

The most commonly used methods for predicting fully developed laminar flow heat transfer coefficients inside smooth, round tubes can be derived from first principles, which can be found in most textbooks and hence this theory is not reproduced here. For a uniform heat flux wall boundary condition (H) for fully developed laminar flow (both thermally and hydrodynamically), the Nusselt number is given by:

$$Nu_H = \frac{\alpha_{pt} d_i}{k} = 4.364 \quad [4.3.1]$$

The Nusselt number  $Nu_H$  is based on the tube diameter  $d_i$  and  $\alpha_{pt}$  is the convective heat transfer coefficient for a plain tube. As can be seen, the heat transfer coefficient is not a function of the Reynolds number or the Prandtl number. Similarly, for a uniform wall temperature wall boundary condition (T) for fully developed laminar flow, the Nusselt number is given by:

$$Nu_T = \frac{\alpha_{pt} d_i}{k} = 3.657 \quad [4.3.2]$$

Again, the heat transfer coefficient is not a function of the Reynolds or Prandtl numbers. The tubular Reynolds number  $Re$  is defined as:

$$Re = \frac{\dot{m} d_i}{\mu} \quad [4.3.3]$$

The mass velocity  $\dot{m}$  is in  $\text{kg/m}^2\text{s}$  and is obtained by dividing the mass flow rate in  $\text{kg/s}$  by the cross-sectional area of the tube in  $\text{m}^2$ . The Prandtl number  $Pr$  is obtained from the physical properties of the fluid and is defined as:

$$Pr = \frac{c_p \mu}{k} \quad [4.3.4]$$

The hydrodynamic entrance length  $z_{eh}$  to arrive at fully developed hydrodynamic flow can be estimated by the following expression:

$$\frac{z_{eh}}{d_i} = 0.03 Re \quad [4.3.5]$$

The value of 0.03 is used to arrive within 5% of the fully developed laminar friction factor while a value of 0.05 is used to arrive within 1.4% of that value, as is cited in Lienhard and Lienhard (2006). For the thermal developing length when the velocity profile is already fully developed before the heat transfer zone begins, the thermal entrance length  $z_{et}$  starting from that location is given by the expression:

$$\frac{z_{et}}{d_i} = 0.034 Re Pr \quad [4.3.6]$$

Thus, highly viscous flows, such as oils, practically never become fully developed. The value of 0.034 is used to arrive within 5% of the fully developed laminar heat transfer for a constant wall temperature condition while a value of 0.043 is used for a constant heat flux condition. When the velocity and temperature profiles develop simultaneously, the value tends to range between 0.028 and 0.053 depending on the wall condition and the Prandtl number. All of these values are those recommended in Lienhard and Lienhard (2006).

Shah and London (1978) give the analytical solutions to many laminar flow situations for hydrodynamically developing flows, thermally developing flows, simultaneously developing flows, etc. The most comprehensive work in the literature is for circular ducts for thermally developing flow. For practical design, Shah and London (1978) recommend the use of the following expressions for the local value of  $Nu_{T,z}$  for a constant wall temperature boundary ( $T$ ):

$$For z^* \leq 0.01: \quad Nu_{T,z} = \frac{\alpha_{pt} d_i}{k} = 1.077(z^*)^{-1/3} - 0.1 \quad [4.3.7a]$$

$$For z^* > 0.01: \quad Nu_{T,z} = \frac{\alpha_{pt} d_i}{k} = 3.657 + 6.874(1000z^*)^{-0.488} e^{-57.2z^*} \quad [4.3.7b]$$

The term  $z^*$  is a form of the Graetz number based on the length from the entrance of the channel  $z$ , given as:

$$z^* = \frac{\pi}{4Gz} \quad [4.3.8]$$

This expression includes the Graetz number, which is defined as:

$$Gz = \frac{Re Pr d_i}{z} \quad [4.3.9]$$

For a uniform wall heat flux boundary condition (H), Shah and London (1978) recommend using the following expressions for the local Nusselt number  $Nu_{H,z}$ :

$$For z^* \leq 0.00005: \quad Nu_{H,z} = \frac{\alpha_{pt} d_i}{k} = 1.302(z^*)^{-1/3} - 1 \quad [4.3.10a]$$

$$For 0.00005 < z^* \leq 0.0015: \quad Nu_{H,z} = \frac{\alpha_{pt} d_i}{k} = 1.302(z^*)^{-1/3} - 0.5 \quad [4.3.10b]$$

$$For z^* > 0.0015: \quad Nu_{H,z} = \frac{\alpha_{pt} d_i}{k} = 4.364 + 8.68(1000z^*)^{-0.506} e^{-41z^*} \quad [4.3.10c]$$

For simultaneously thermally and hydrodynamically developing flow, Shah and London (1978) recommend the use of the following equation for a constant wall temperature boundary condition ( $T$ ) for the local Nusselt number  $Nu_{T,z}$ :

$$\frac{\text{Nu}_{T,z} + 1.7}{5.357 \left\{ 1 + [388z^*/\pi]^{-8/9} \right\}^{3/8}} = \left[ 1 + \left( \frac{\pi/(284z^*)}{\left\{ 1 + (\text{Pr}/0.0468)^{2/3} \right\}^{1/2} \left\{ 1 + (388z^*/\pi)^{-8/9} \right\}^{3/4}} \right)^{4/3} \right]^{3/8}$$

[4.3.11]

Similarly for a uniform heat flux boundary condition (H) for simultaneously developing flow, they recommended:

$$\frac{\text{Nu}_{H,z} + 1}{5.364 \left\{ 1 + [220z^*/\pi]^{-10/9} \right\}^{3/10}} = \left[ 1 + \left( \frac{\pi/(115.2z^*)}{\left\{ 1 + (\text{Pr}/0.0207)^{2/3} \right\}^{1/2} \left\{ 1 + (220z^*/\pi)^{-10/9} \right\}^{3/5}} \right)^{5/3} \right]^{3/10}$$

[4.3.12]

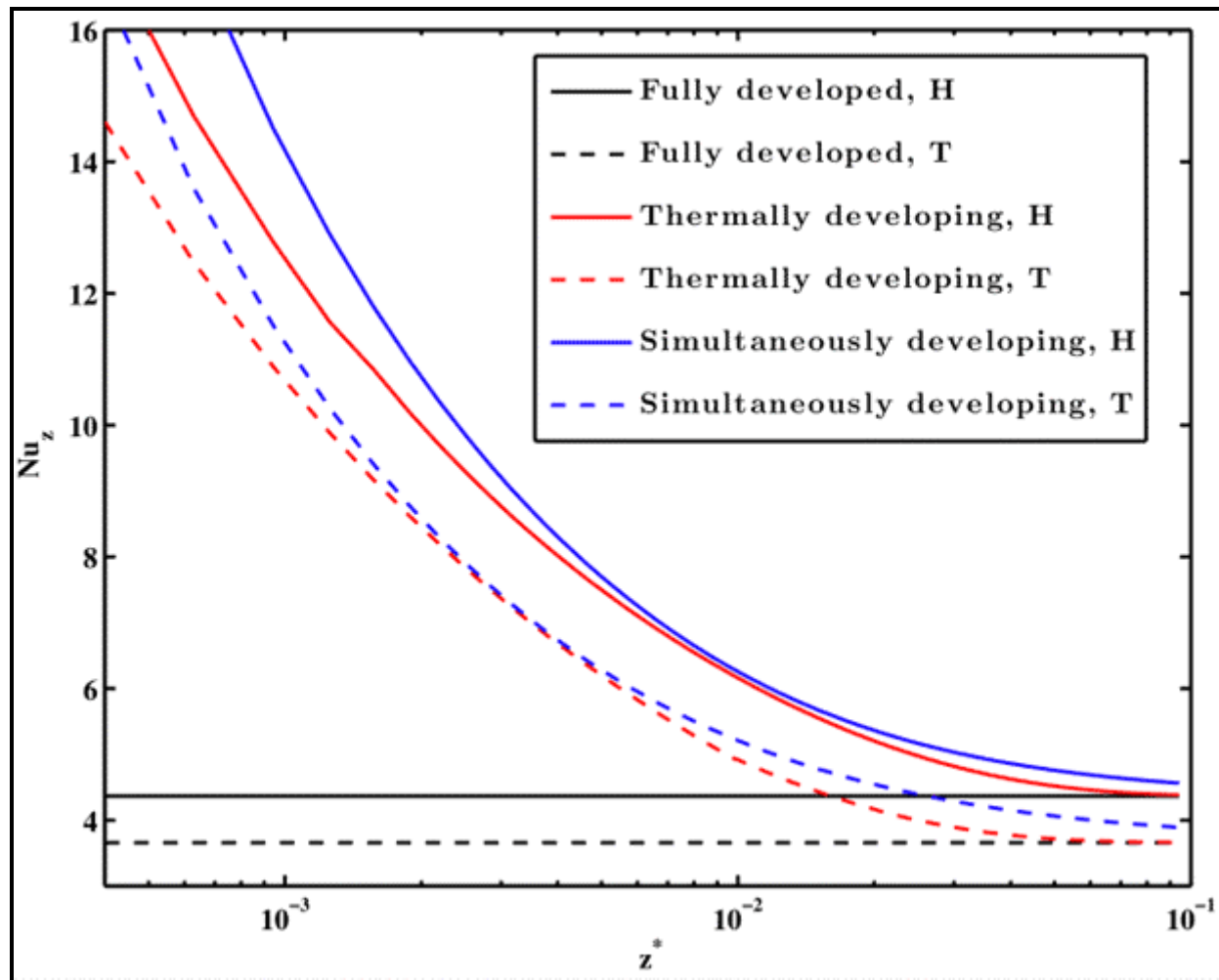


**Figure 4.5.** Local Nusselt numbers as a function of the dimensionless axial distance  $z^*$  inside a smooth circular channel for different boundary conditions and flow developments for uniform heat flux (H) and constant wall temperature (T) conditions.

Figure 4.5 shows the heat transfer simulations for single phase flow inside a circular tube for the different boundary conditions and flow developments. The Nusselt numbers in this graph are plotted versus the dimensionless length  $z^*$  used above, where  $z^*$  written in terms of the Reynolds and Prandtl numbers is:

$$z^* = \frac{\pi}{4} \left( \frac{z}{Re \Pr d_i} \right) \quad [4.3.13]$$

This diagram illustrates several important aspects of thermal entry regions. First of all, as the distance from the channel entrance is shortened (while keeping the Reynolds number, Prandtl number and tube diameter constant), the influence of the thermal boundary layer becomes more significant. Secondly, this is also true if the Reynolds number, Prandtl number or channel diameter is increased.

The Hausen (1943) equation is also often cited for the uniform wall temperature boundary condition (T) in a developing laminar flow:

$$Nu_T = \frac{\alpha_{pt} d_i}{k} = 3.657 + \frac{0.668 Re \Pr(d_i/z)}{1 + 0.04[\Pr(d_i/z)]^{2/3}} \quad [4.3.14]$$

In this expression,  $z$  is the length from the entrance of the tube and it gives the mean Nusselt number up to length  $z$ ,  $Nu_T$ . The older and simpler expression of Seider and Tate (1936) is also often quoted, for a combined entry length for a uniform wall temperature condition (T), that which gives the mean Nusselt number as:

$$Nu_T = \frac{\alpha_{pt} d_i}{k} = 1.86 Gz^{1/3} (\mu_{bulk}/\mu_{wall})^{0.14} \quad [4.3.15]$$

This expression can be used for both heating and cooling conditions and includes the fluid property effects through the bulk to wall viscosity ratio. It is applicable when  $0.48 < \Pr < 16700$  and  $0.0044 < (\mu_{bulk}/\mu_{wall})^{0.14} < 9.75$ . Bulk physical properties in the above expressions should be taken at the mean fluid temperature between inlet and outlet.

Gnielinski (1995) proposed a complete set of equations for the mean Nusselt number for laminar, transition and turbulent flows based on a large experimental database. In the laminar regime ( $Re < 2300$ ), the mean value of the Nusselt number up to length  $z$  was correlated with the Graetz number for the uniform temperature and uniform heat flux boundary conditions. For the uniform wall temperature condition (T), using the definition of  $Gz$  above, Gnielinski (1995) proposed the following asymptotic correlation for the mean Nusselt number  $Nu_T$ :

$$Nu_T = \frac{\alpha_{pt} d_i}{k} = \left\{ Nu_{T,1}^3 + [Nu_{T,2} - 0.7]^3 + Nu_{T,3}^3 \right\}^{1/3} \quad [4.3.16]$$

The individual values of  $Nu_{T,1}$ ,  $Nu_{T,2}$  and  $Nu_{T,3}$  are obtained as follows:

$$Nu_{T,1} = 3.66 \quad [4.3.17a]$$

$$Nu_{T,2} = 1.615 Gz^{1/3} \quad [4.3.17b]$$

$$Nu_{T,3} = \left( \frac{2}{1 + 22 Pr} \right)^{1/6} Gz^{1/2} \quad [4.3.17c]$$

For the uniform heat flux boundary condition (H), Gnielinski (1995) proposed two expressions for the mean Nusselt number  $Nu_H$ , where the larger of the two values of  $Nu_H$  from these expressions is used:

$$Nu_H = \frac{\alpha_{pt} d_i}{k} = \left\{ Nu_{H,1}^3 + 0.6^3 + [Nu_{H,2} - 0.6]^3 \right\}^{1/3} \quad [4.3.18a]$$

$$Nu_H = \frac{\alpha_{pt} d_i}{k} = 0.924 Gz^{1/3} \left( Re \frac{d_i}{Z} \right)^{1/6} \quad [4.3.18b]$$

The values of  $Nu_{H,1}$  and  $Nu_{H,2}$  are obtained as follows:

$$Nu_{H,1} = 4.364 \quad [4.3.19a]$$

$$Nu_{H,2} = 1.953 Gz^{1/3} \quad [4.3.19b]$$

In these expressions at very low Reynolds numbers, each tends to the Nusselt number corresponding to the respective theoretical value for fully developed flow.

For fluid property effects for the other methods, using the recommendations of Lienhard and Lienhard (2006), it is most common to correct these expressions by multiplying the heat transfer coefficient by the ratio of  $(\mu_{bulk}/\mu_{wall})^{0.11}$  for heating liquids ( $T_{wall} > T_{bulk}$ ) but  $(\mu_{bulk}/\mu_{wall})^{0.25}$  for cooling liquids ( $T_{wall} < T_{bulk}$ ). A single exponent of 0.14 is also found in many textbooks. Instead, for heating of gases the ratio  $(T_{bulk}/T_{wall})^{0.47}$  is used while no correction is used when cooling of a gas ( $T_{wall} < T_{bulk}$ ). These terms correct the heat transfer coefficient for the effect of the variation in viscosity between the bulk fluid temperature and that at the tube wall.

The pressure drop in a tube of length  $L$  is given by the expression:

$$\Delta p = \frac{2f \dot{m}^2 L}{\rho d_i} \quad [4.3.20]$$

For laminar fully developed flow, the following expression can be derived from first principles for the friction factor, adding then the viscosity ratio effect added:

$$f = \left( \frac{16}{Re} \right) \left( \frac{\mu_{bulk}}{\mu_{wall}} \right)^m \quad [4.3.21]$$

In the study by Marner and Bergles (1985), they recommended a value of  $m = -0.12$  for cooling of a fluid and  $m = -0.25$  when heating a fluid for: circular tubes, internally finned tubes and tubes with twisted tape inserts. For heat transfer in a plain tube, an internally finned tube and a tube with a twisted tape insert, they found the term  $(\mu_{bulk}/\mu_{wall})^{0.14}$  worked well for their data for both heating and cooling of liquids, finding however significantly different correlating expressions for the Nusselt number for heating and cooling that are described later in this chapter. These above expressions for heat transfer and pressure

drop, however, do not take into account any effects of natural convection on the flow, which can increase these values by two to three times.

The above expression can also be written for isothermal flows in terms of the Poiseuille number  $Po$  as:

$$f \text{Re} = Po = 16 \quad [4.3.22]$$

This is valid for a circular channel but varies for different channel cross-sectional geometries. For example, the value for a rectangular channel varies from 14.2 to 24, depending on the aspect ratio of the channel, while for an equilateral triangle the value is 13.33 and for an ellipse the value varies from 16 to 19.7, depending on the aspect ratio.

For a developing hydrodynamic boundary layer, the friction factors are higher. From a physical viewpoint, because of the reduction in the fluid velocity near the wall in the developing boundary layer, continuity requires that the fluid in the centre core must accelerate, which in turn thins the boundary layer. Once the opposing boundary layers meet at some distance down the length of the channel, the flow is fully developed. In the entrance region, however, the thinning of the boundary layer and the acceleration of the fluid in the core region give rise to an increase in shear. For a more detailed description, see for example White (1991). This increase in shear is reflected in an increase in pressure drop, which in turn is reflected in an increase in friction factor. This increase is termed the *apparent* friction factor, with Shah and London (1978) giving an interpolation formula for many duct shapes. This is given by

$$f_{\text{app}} \text{Re} = \frac{3.44}{\sqrt{\chi}} + \frac{Po + (K/4\chi) - (3.44/\sqrt{\chi})}{1 + (0.000212/\chi^2)} \quad [4.3.23]$$

where  $\chi = (z/d_i)/\text{Re}$  and  $K$  is the excess pressure drop in the hydrodynamic developed region given by Shah and London (1978) as  $K = 1.2 + 38/\text{Re}$ . The values of  $Po$  in the Poiseuille relation are those mentioned earlier for the various shaped channels. The value of the apparent friction factor is used in place of the usual value to calculate the pressure gradient.

## 4.4 Laminar Flow and Heat Transfer in Non-Circular Channels

Rectangular channels are an important non-circular shape channel and are characterized by their aspect ratio of  $2b/2a$ , where  $2a$  is the long side and  $2b$  is the short side of the rectangular cross-section. Table 4.1 gives tabular values for a selection of channel shapes and aspect ratios from Shah and London (1978) and Shah and Sekulić (2003) for fully developed laminar flow for the boundary conditions of uniform temperature ( $T$ ) and two uniform heat flux boundary conditions, where both represent a constant heat flux boundary condition along the channel axis but ( $H$ ) has a *constant wall temperature* around the perimeter of the channel while the other less known boundary condition ( $HA$ ) has a *constant heat flux* around the perimeter of the channel. Both boundary conditions yield the same Nusselt number for circular channels and parallel plates but they are significantly different for non-circular ducts since the local heat transfer coefficients around the perimeter are not uniform (the perimeter averaged values are reported in Table 4.1). The uniform temperature boundary condition ( $T$ ) is for when the boundary is everywhere at the same temperature, both axially and around the perimeter of the channel. In the literature, the condition ( $H$ ) is also referred to as ( $H1$ ) and ( $HA$ ) as ( $H2$ ).

**Table 4.1. Heat Transfer and Friction Factors for Fully Developed Laminar Flow in Various Shaped Channels.**

Geometry (z/d <sub>h</sub> )>100)	Aspect Ratio (2b/2a)	Nu <sub>H</sub>	Nu <sub>HA</sub>	Nu <sub>T</sub>	Po = f Re
Circle	-	4.364	-	3.657	16
Hexagon	-	4.002	3.862	3.340	15.054
Equilateral Triangle	-	3.11	1.892	2.47	13.25
Square	1	3.608	3.091	2.976	14.227
Rectangle	1/2	4.123	3.017	3.391	15.548
	1/4	5.331	2.940	4.439	18.233
	1/6	6.049	2.930	5.137	19.702
	1/8	6.490	2.940	5.597	20.585
Parallel Plates	0	8.235	5.3855	7.541	24

The exact boundary condition around the perimeter of the channel should be considered with care for small channels, viz. the heat transfer coefficient will be large and if the conduction resistance of the tube wall is comparable to the convective resistance within the duct, then temperature or wall heat flux variations around the channel perimeter become significant and thus non-uniform. This will significantly affect the value of the Nusselt number in a laminar flow. As pointed out by Lienhard and Lienhard (2006), rectangular duct values for a uniform wall heat flux, for example, tend to assume a uniform temperature condition around the perimeter of the tube, if the wall has no conduction resistance around its perimeter.

When applying methods to non-circular channels, the Reynolds number is based on the actual mean fluid velocity in the channel's cross-section of area A and the hydraulic diameter is  $d_h = 4A/P$ , where A is the cross-sectional area of the channel and P is the perimeter of the channel. Note that the mean velocity is *not* calculated with the area that could be determined with the hydraulic diameter.

For laminar fully developed flows in smooth rectangular channels (where an aspect ratio of  $2b/2a = 1$  for square channels and  $2b/2a = 0$  for two parallel plates), Shah and Sekulić (2003) give the follow equations for the Nusselt number for the boundary conditions (T), (H) and (HA):

$$Nu_T = \frac{\alpha_{pt} d_h}{k} = 7.541 \left[ 1 - 2.610 \left( \frac{2b}{2a} \right) + 4.790 \left( \frac{2b}{2a} \right)^2 - 5.119 \left( \frac{2b}{2a} \right)^3 + 2.702 \left( \frac{2b}{2a} \right)^4 - 0.548 \left( \frac{2b}{2a} \right)^5 \right] \quad [4.4.1]$$

$$Nu_H = \frac{\alpha_{pt} d_h}{k} = 8.235 \left[ \begin{array}{l} 1 - 2.041 \left( \frac{2b}{2a} \right) + 3.0853 \left( \frac{2b}{2a} \right)^2 \\ - 2.4765 \left( \frac{2b}{2a} \right)^3 + 1.0578 \left( \frac{2b}{2a} \right)^4 \\ - 0.1861 \left( \frac{2b}{2a} \right)^5 \end{array} \right] \quad [4.4.2]$$

$$Nu_{HA} = \frac{\alpha_{pt} d_h}{k} = 8.235 \left[ \begin{array}{l} 1 - 10.6044 \left( \frac{2b}{2a} \right) + 61.1755 \left( \frac{2b}{2a} \right)^2 \\ - 155.1803 \left( \frac{2b}{2a} \right)^3 + 176.9203 \left( \frac{2b}{2a} \right)^4 \\ - 72.9236 \left( \frac{2b}{2a} \right)^5 \end{array} \right] \quad [4.4.3]$$

Note that for  $(2b/2a) = 0$ , the above expressions give the fully developed flow values corresponding to two parallel plates. They apply when the heat is transferred from all sides of the rectangular channel. When one or more sides is/are adiabatic, the special rules apply...see there publication for details.

Shah and London (1978) tabulated the numerical results from Wibulswas (1966) as a function of the Graetz number in terms of  $z^*$  and the aspect ratio for handling of entrance region effects. For design purposes, the local perimeter averaged Nusselt values were put in terms of a Taylor series expansion for the uniform heat flux boundary condition (H), given by:

$$Nu_{H,z} = \frac{\alpha_{pt} d_h}{k} = 3.04 + \frac{0.0244}{z^*} + \frac{0.448}{(2b/2a)} - \frac{0.0000269}{(z^*)^2} + \frac{0.02}{(2b/2a)^2} - \frac{0.000678}{z^*(2b/2a)} \quad [4.4.4]$$

$$z^* = \frac{\pi}{4} \left( \frac{z}{Re Pr d_h} \right) \quad [4.4.5]$$

The ratio  $(2b/2a)$  is the aspect ratio of the channel ( $2a$  = width and  $2b$  = height) and is valid when  $0.05 \leq z^* \leq 0.2$  and  $0.25 \leq (2b/2a) \leq 1.0$ . In this expression, the hydraulic diameter is  $d_h$ . This expression is shown graphically in Figure 4.6. It predicts tabular values for rectangular channels with deviations of less than 2%. The method is based on the assumption that axial heat conduction, viscous dissipation and thermal energy sources within the fluid are negligible. A similar relationship was developed for a (T) boundary condition obtained from tabulated data of Wibulswas (1966), given as

$$\text{Nu}_{T,z} = \frac{\alpha_{pt} d_h}{k} = 2.117 + \frac{0.01667}{z^*} + \frac{0.6713}{(2b/2a)} - \frac{0.00001136}{(z^*)^2} + \frac{0.02835}{(2b/2a)^2} - \frac{0.000886}{z^*(2b/2a)} \quad [4.4.6]$$

This is valid when  $0.05 \leq z^* \leq 0.2$  and  $1/6 \leq (2b/2a) \leq 1.0$ .

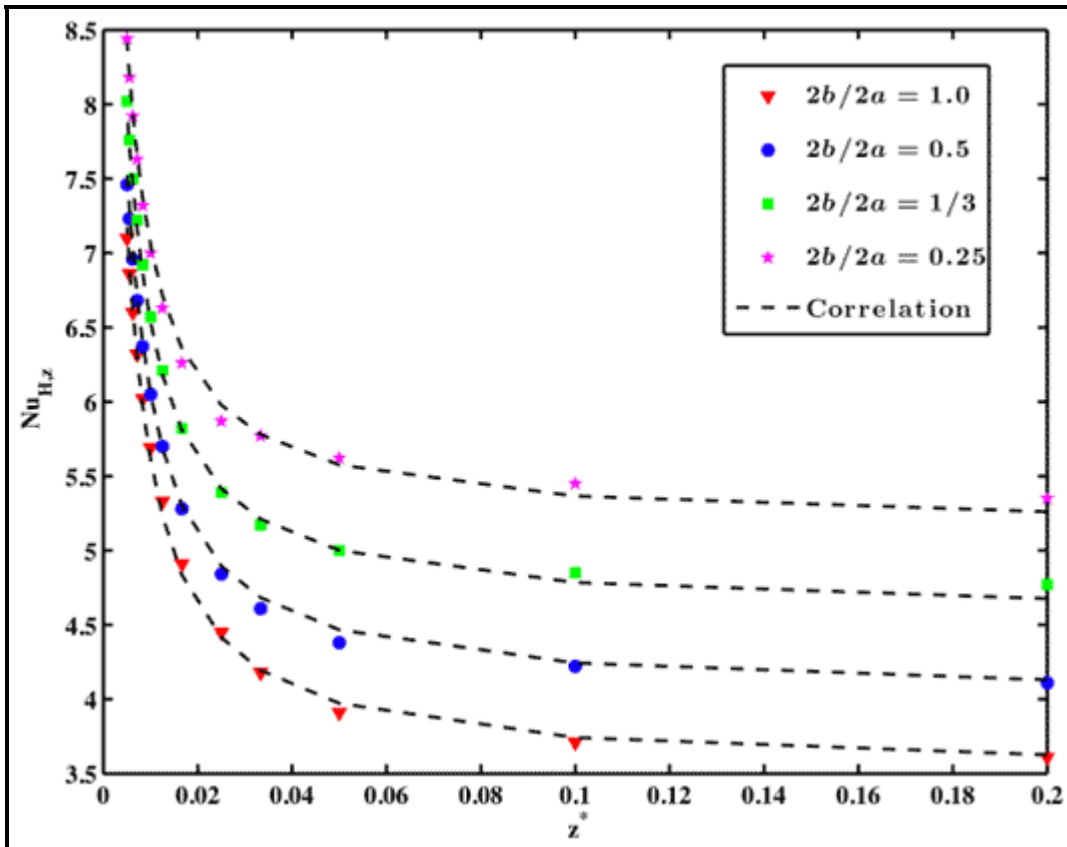


**Figure 4.6. Local Nusselt number expression for the (H) boundary condition compared to tabulated data plotted versus non-dimensional length from entrance for rectangular channels of various aspect ratios.**

For friction factors in rectangular channels, Wei and Joshi (2004) proposed the following expression for the apparent friction factor for laminar developing flows where  $\chi = (z/d_h)/\text{Re}$ :

$$f_{app} \text{Re} = \left[ \frac{3.44}{\sqrt{\chi}} + \frac{24 + (0.674/\chi) - (3.44/\sqrt{\chi})}{1 + (0.000029/\chi^2)} \right] F_{\text{aspect}} \quad [4.4.7]$$

$F_{\text{aspect}}$  is the aspect ratio correction factor, calculated from their polynomial expression:

$$F_{\text{aspect}} = 1 - 1.3553 \left( \frac{2b}{2a} \right) + 1.9467 \left( \frac{2b}{2a} \right)^2 - 1.7012 \left( \frac{2b}{2a} \right)^3 \\ + 0.9564 \left( \frac{2b}{2a} \right)^4 - 0.2537 \left( \frac{2b}{2a} \right)^5 \quad [4.4.8]$$

Another important method for predicting the friction factors and Nusselt numbers in the combined entrance region of non-circular ducts and channels (providing both local and average Nusselt numbers) is proposed by Muzychka and Yovanovich (2004). Their method is applicable to both isothermal (T) and iso-heat flux (H) boundary conditions and for a wide range of channel shapes. The reader is referred to their publication for details.

Various prediction methods are available for special microscale flow geometries. For example, Colgan et al. (2007) have tested water for interrupted microfin channel arrays and correlated the heat transfer and pressure drop results. For micro-pin-fin geometries, one is referred to the work of Brunschwiler et al. (2008) for tests with water and propositions for predicting pressure drops and heat transfer.

## 4.5 Special Effects on Laminar Flow and Heat Transfer in Microchannels

No new governing equations are required for laminar flow heat transfer in microchannels (channels less than ~1 mm) as noted by Morini (2008) in his detailed review on this subject, but the relative weight of the different terms in the momentum and energy equations can be very different when going from macroscale to microscale. Furthermore, he states that no natural or mixed convection are evidenced in the laminar regime in microchannels, even for large temperature differences between the fluid and the heated walls. According to Morini (2008), the first study on microscale flow was that of Poiseuille (1840), who tested channels having an internal diameter down to 15 microns in order to analyse the law of the mass flow rate in capillary tubes using water. These experimental data obtained by Poiseuille in 1840 were used to state the famous “Poiseuille law” for laminar flows through circular tubes, according to which the product of the friction factor times the Reynolds number is a constant ( $fRe = 16 = Po$  for circular tubes).

For the most part, laminar flow and heat transfer in microchannels is well described by the classical laminar flow theory above. However, special aspects can become significant in microchannels that were only of minor influence in larger channels. The smaller the diameter becomes, the more the behavior tends to deviate from the theoretical values derived for macro-channels. These behaviors have been observed by Tiselj et al. (2004), Celata et al. (2006a), Celata et al. (2006b), to name but a few. However, these deviations tend to only become evident as the channel size becomes very small.

As mentioned above, some effects neglected in macroscale flow become important in microscale flow. The reduction in the size of channels to the microscale can introduce some *scaling effects* and *micro-effects*, using the classification proposed by Herwig and Hausner (2003), who noted that it is important to distinguish between these two concepts. First of all, according to their analysis, *scaling effects* are those which may be neglected at the referenced geometrical scale, but which become important when the scale changes, e.g. the reduction of the channel diameter implies a larger reduction in its volume than in its internal surface area, so that the area-to-volume ratio tends to be very high as the channel size is reduced. This implies a prevalence of surface forces over body forces, such that the advection terms in the conservation equations prevail over those related to volume forces. Owing to this, microscale flow behavior can differ remarkably from macroscale channel flow. Secondly, *micro-effects* are those which

require a reformulation of the conservation equations and/or their associated boundary conditions as the characteristic scale of the system is reduced, e.g. this is confronted when the molecular mean free path of a gas flow becomes the same order of magnitude as the diameter of the channel, so that the fluid cannot be treated as a continuous phase and the Navier-Stokes equations are no longer appropriate for modeling the flow.

According to Morini (2006, 2008), the most important scaling effects are as follows in order of importance:

- Viscous dissipation (causes heating of the fluid);
- Conjugate effects (such as axial conduction along the channel walls);
- Thermal entrance effects (although this can be important in macrochannel flows as well).

Initially, neglecting these effects, numerous experimental papers concluded that the classical laminar flow theory did not work well for microchannels. However, this was shown by the above mentioned studies not to be true. For example, all the experimental runs of Celata et al. (2008) are in agreement with the classical methods for pure forced convection within the experimental uncertainty. This indicates that it is possible to use conventional methods for convective heat transfer coefficients in microchannels as long as the role of the main scaling effects (like viscous dissipation, conjugate heat transfer and so on) can be considered negligible (this should be verified on a case-by-case basis and not loosely assumed to be the situation in engineering applications). In fact, the classical methods do work but have to be supplemented by additional attention to details, such as the accurate measurement of the internal diameter of the channel, the “roundness” and uniformity of the cross-sectional profile of a circular channel, the internal roughness, including viscous heating in the energy balance, etc.

With particular respect to surface roughness of the interior of microchannels, Celata et al. (2008) observed no effect of the relative roughness (the ratio of the roughness to diameter), when it was below 4%, on the average Nusselt number in their laminar experimental tests. On the contrary, the tests of Kandlikar, Joshi and Tian (2001) demonstrated evidence of a strong effect of relative roughness on the Nusselt number in the laminar regime, even for relative roughnesses less than 2%. Therefore, the threshold of the effect of relative roughness seems to require more study and confirmation of when it becomes influential, besides any effect of the topology of the roughness.

The principal scaling effects noted above plus physical property effects are discussed in the subsections below. For readers interested in a more detailed discussion on single-phase microscale flows, they are referred to the book of Kandlikar and Garimella (2005) and the review of Morini (2008).

#### **4.5.1 Viscous Heat Dissipation**

It is common in macroscale theoretical developments to ignore the viscous heating term in the energy equation. In the microscale, this term can become important. According to Morini (2006), the bulk temperature difference between the inlet and outlet of a microchannel can be viewed as the sum of the temperature rise of the fluid due to the heat flux at the walls  $\Delta T_q$  and the temperature rise of the fluid due to viscous heat dissipation  $\Delta T_{visc}$ . This is mathematically given by

$$\Delta T_{bulk} = \Delta T_q + \Delta T_{visc} \quad [4.5.1]$$

It was shown that the temperature rise due to viscous heat dissipation  $\Delta T_{visc}$  is a function of the Reynolds number  $Re$ , the channel diameter  $d_i$  (or the hydraulic diameter  $d_h$ ), length of the microchannel  $L$  (or the distance from the entrance  $z$ ), and the Poiseuille number  $Po = f Re$ . This is given by

$$\Delta T_{visc} = 2 \text{Re} \left( \frac{v^2}{c_p} \right) \left( \frac{\text{Po L}}{d_i^3} \right) \quad [4.5.2]$$

The temperature rise increases with the square of the kinematic viscosity  $v$  and inversely to the cube of the channel diameter  $d_i$ . For an adiabatic channel wall condition, the temperature rise due to viscous heat dissipation can be put into a dimensionless form as

$$\frac{\Delta T_{visc}}{\Delta T_{ref}} = 4 \left( \frac{\text{Ec}}{\text{Re}} \right) \left( \frac{\text{Po L}}{d_i} \right) \quad [4.5.3]$$

Here, Ec is the Eckert number, which is given as

$$\text{Ec} = \frac{(\dot{m}/\rho)^2}{2c_p \Delta T_{ref}} \quad [4.5.4]$$

The top term on the right gives the mean velocity of the fluid. Po is the Poiseuille number, which is also given as  $(f \text{Re})$ . For laminar flow, this value is normally constant, depending on the shape of channel and its aspect ratio, as discussed earlier. The reference temperature rise  $\Delta T_{ref}$  can, as suggested by Morini (2006), be chosen as the value for which the dynamic viscosity of the fluid decreases by approximately 2-3%. Thus, for an adiabatic channel, the limit to which viscous heat dissipation can be neglected is when the temperature rise is less than the reference temperature difference  $\Delta T_{ref}$  in the above expression. This limit is given as:

$$4 \left( \frac{\text{Ec}}{\text{Re}} \right) \left( \frac{\text{Po L}}{d_i} \right) < 1 \quad [4.5.5]$$

Thus, the limiting Reynolds number where viscous dissipation cannot be neglected is when

$$\text{Re} > \frac{1}{2} \left( \frac{c_p}{v^2} \right) \frac{d_i^3}{L \text{Po}} \Delta T_{ref} \quad [4.5.6]$$

The above expression highlights the fact that when the internal diameter decreases, the limiting Reynolds number for which the viscous dissipation cannot be ignored tends to decrease.

For a heated channel, Morini (2006) showed that  $\kappa$ , the ratio of the temperature rise due to viscous heating to the temperature rise related to the heat flux at the walls, can be given by:

$$\kappa = \frac{\Delta T_{visc}}{\Delta T_q} = \frac{2Br \text{Po A}}{d_i} \quad [4.5.7]$$

In this expression A is the channel cross-sectional area, i.e. for a circular channel  $A/d_i^2 = \pi/4$ .

The Brinkman number Br is given in terms of the dynamic viscosity, the heat flux at the wall q and the mean fluid velocity calculated from the mass flux and density as:

$$Br = \frac{\mu(\dot{m}/\rho)^2}{q} \quad [4.5.8]$$

Setting a limit on the temperature ratio  $\kappa_{lim}$  gives the upper bound of when viscous heat dissipation can be neglected. Thus, this is when

$$Br < \frac{\kappa_{lim}}{2 A / (d_i^2 Po)} \quad [4.5.9]$$

This can be put in terms of the Reynolds number for a circular channel as follows:

$$Re < \frac{2 \kappa_{lim} q}{\pi Po} \frac{d_i \rho}{\mu^2 (\dot{m}/\rho)} \quad [4.5.10]$$

The limit set on the temperature ratio is suggested to be around 5% or  $\kappa_{lim} = 0.05$ . Therefore, an easy to implement criterion has been proposed by Morini (2006) for identifying those occasions when viscous heat effects are expected to be notable.

The effect of viscous dissipation may influence the fully developed Nusselt number due to the increase in the Reynolds number, implying an increase in the Brinkman number. Morini (2006) recommends the use of the following equation to obtain the fully developed Nusselt number that includes the effect of viscous heat dissipation  $Nu_{H,visc}$  for the uniform heat flux boundary condition (H):

$$Nu_{H,visc} = \frac{Nu_H}{1 + \sigma Br} \quad [4.5.11]$$

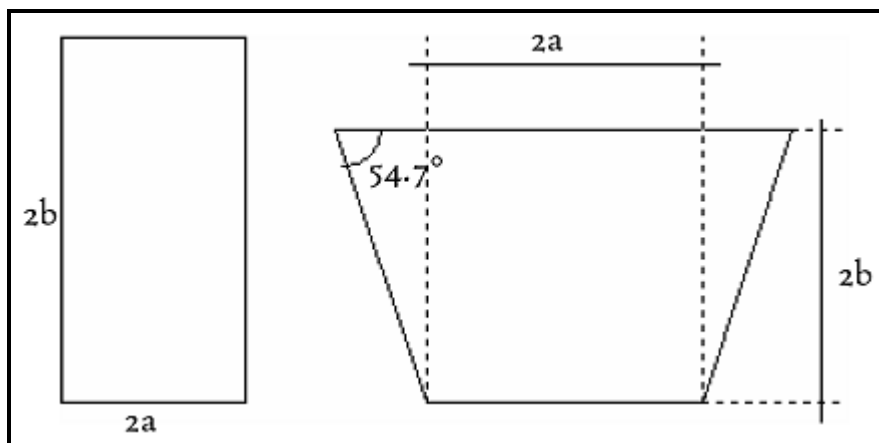


**Figure 4.7. Typical microchannel cross-sections obtained by chemical etching on <110> and <100> silicon wafers.**

Morini (2006) provided a list of values for  $Nu_H$  and  $\sigma$  for different aspect ratios of rectangular microchannels, reproduced here in Table 4.2. As a reference, for a circular microchannel  $Nu_H = 48/11$  and  $\sigma = 48\pi/11$ . Other papers by Morini (2005) and Morini and Spiga (2007) can be consulted on this topic of viscous heating. In Table 4.2, the values of  $Nu_H$  and  $\sigma$  are given for rectangular and trapezoidal cross-

sections. The trapezoidal cross section is very common in microfluidics when the microchannels are made from silicon wafers with a photolithographic based process. In this case one can obtain microchannels having a cross-section fixed by the orientation of the wafer crystal planes; for example, the microchannels etched in  $<110>$  or  $<100>$  silicon wafers have respectively a rectangular or trapezoidal cross-section with an apex angle of  $54.7^\circ$  imposed by the crystallographic morphology of the silicon, as illustrated in Figure 4.7 where the values of  $2b$  and  $2a$  are defined for these two shapes.

**Table 4.2.  $\text{Nu}_H$  and  $\sigma$  for various aspect ratios for rectangular and trapezoidal channels of Morini (2006).**

Aspect Ratio $2b/2a$	Rectangle		Trapezoid	
	$\text{Nu}_H$	$\sigma$	$\text{Nu}_H$	$\sigma$
0	8.235	-	8.235	-
0.05	7.451	131.35	7.302	136.51
0.1	6.785	67.98	6.575	73.17
0.2	5.738	36.57	5.536	41.79
0.3	4.990	26.39	4.852	31.58
0.4	4.472	21.57	4.391	26.68
0.5	4.123	18.91	4.073	23.88
0.6	3.895	17.36	3.850	22.14
0.7	3.750	16.42	3.691	20.98
0.8	3.664	15.89	3.577	20.19
0.9	3.620	15.62	3.493	19.62
1.0	3.608	15.54	3.431	19.22
1.25	3.664	15.89	3.338	18.63
1.67	3.895	17.36	3.277	18.28
2.0	4.123	18.91	3.261	18.22
3.33	4.990	26.39	5.251	18.44
5.0	5.738	36.57	3.236	18.70
10	6.789	67.98	3.188	18.99
$\infty$	8.235	-	3.093	19.15

#### 4.5.2. Wall-to-Fluid Conjugate Effects

Conjugate effects become important when the heat transfer due to axial conduction along the channel wall starts to compete with the convective heat transfer from the wall to the fluid. This happens when the laminar heat transfer coefficient is small and the thermal conductivity of the channel wall is high relative to that of the fluid. The result is a deviation in the axial boundary condition from that expected, which in turn influences the laminar convection heat transfer coefficient. This interaction between the convective heat transfer process, the axial conduction process and the boundary condition is referred to as a conjugate effect.

Mori, Sakakibara and Tanimoto (1974) performed a study on circular tubes with respect to the effect of the wall-to-fluid thermal conductivity ratio and the wall thickness on conduction along the tube wall. It was found that for a relatively high thermal conductivity ratio,  $(k_{\text{wall}}/k_{\text{fluid}})$ , if a uniform wall heat flux boundary is imposed, then the temperature distribution at the wall-fluid interface along the channel tends towards a constant value. The same result was found when increasing the ratio of the thickness of the wall to the length of the tube. The greater this ratio becomes, the more uniform the temperature along the tube at the wall-fluid interface tends to become, i.e. the high rate of axial conduction along the tube wall levels

out the axial temperature distribution. Thus, laminar flow solutions for an imposed uniform heat flux boundary condition, such as the solutions presented earlier in this chapter, will approach instead the solution for a constant wall temperature boundary.

The opposite is true for an imposed constant wall temperature boundary. In this case, the thicker the walls the more the solution approaches the uniform heat flux solution. This is because a thick wall has a higher radial thermal resistance, which allows the temperature gradient to develop on the inside wall in the axial direction, as pointed out by Shah and London (1978).

These axial conduction results may have serious implications with regard to determining local heat transfer coefficients of an experimental test section or on the thermal design of a micro-cooling system. In particular, for a channel with a uniform heat flux boundary condition, it is assumed that the bulk fluid temperature distribution from inlet to outlet is linear. However, if the tube wall is thick enough and the ratio of the wall to fluid thermal conductivity is high, then the imposed boundary is in fact closer to that of a constant wall temperature, for which the bulk temperature variation changes exponentially from inlet to outlet, not linearly. Thus, one must be careful when calculating the heat duty using a log mean temperature difference, for example, or even when using local calculations since the temperature profile of the bulk liquid is not that which would otherwise be expected.

These above observations by Mori, Sakakibara and Tanimoto (1974) were made for Graetz numbers equal to 50. From their study, it was shown that for an imposed uniform heat flux boundary, as the Graetz number increases, the conjugate problem approaches the uniform heat flux solution, while as it decreases it approaches the constant wall temperature solution. Based on analysis, for an imposed uniform heat flux boundary condition, the wall may be considered thin if  $t_{\text{wall}}/L < 0.0001$  for  $R_{\text{wall}} \approx 2 \times 10^{-7}$  and when  $t_{\text{wall}}/L < 0.001$  for  $R_{\text{wall}} > 10^{-5}$  in Shah and London (1978), where  $t_{\text{wall}}/L$  is the ratio of the wall thickness to the channel length and  $R_{\text{wall}}$  is the wall thermal resistance in (K/W). For an imposed constant temperature boundary, the wall may be considered thin if  $R_{\text{wall}} < 0.01$ .

Morini (2008) gives a criterion for when conjugate effects become important, in particular one must pay attention when  $\text{Re} < 200$ . This was based on his theoretical work and that performed by Peterson (1999) and Maranzana, Perry and Maillet (2004). His criterion for circular channels is given as

$$\left( \frac{k_{\text{wall}}}{k_{\text{fluid}}} \right) \left( \frac{D - d_i}{d_i z} \right) \frac{1}{\text{Re Pr}} > 0.01 \quad [4.5.12]$$

In this expression,  $D$  is the outside diameter of the channel of internal diameter  $d_i$  and  $k_{\text{wall}}$  is the thermal conductivity of the channel material. Then the term on the left is larger than 0.01, then conjugate effects become important and one must go to appropriate solution methods (beyond the scope of the present review here). For rectangular channels, his expression becomes:

$$\left( \frac{k_{\text{wall}}}{k_{\text{fluid}}} \right) \left( \frac{d_h}{L} \right) \left( \frac{(L_y)(L_x)}{(2a)(2b)} - 1 \right) \frac{1}{\text{Re Pr}} > 0.01 \quad [4.5.13]$$

In this expression,  $L_x$  and  $L_y$  are the width and height of the outside of the rectangular microchannel whose internal channel dimensions are  $2a$  and  $2b$ , respectively, as illustrated in Figure 4.8. Thus, the upper bound of Reynolds numbers, that is Reynolds numbers up to where conjugated effects are important, can be determined from the above expression, or from its rearrangement:

$$Re < \left( \frac{k_{wall}}{k_{fluid}} \right) \left( \frac{d_h}{L} \right) \left( \frac{(L_y)(L_x)}{(2a)(2b)} - 1 \right) \frac{100}{Pr} \quad [4.5.14]$$

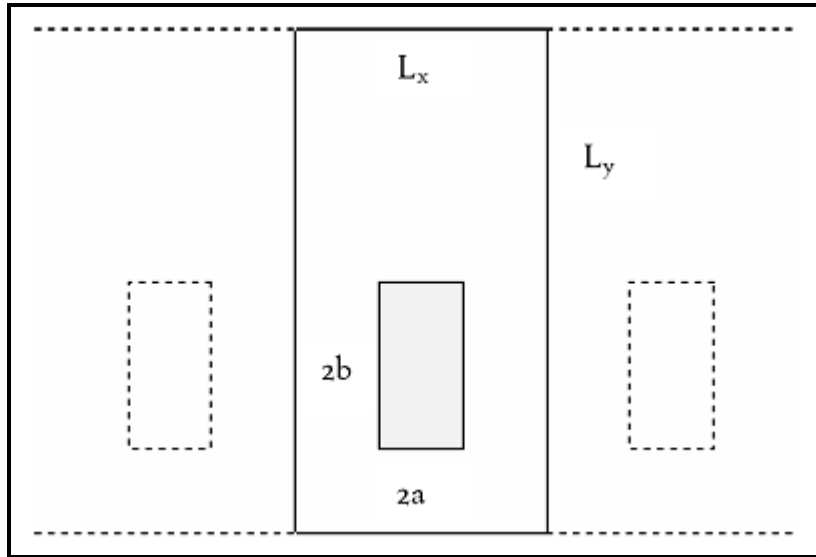


Figure 4.8. Diagram of rectangular microchannel.

#### 4.5.3. Entrance Region Effects

Thermal entrance effects may play an important role inside micro-channels. For a fluid entering a channel at a uniform temperature, the temperature profile starts to develop as it moves along the axial length of the channel. The Nusselt numbers in this thermally developing region are much higher than for fully developed flow, due to the thin thermal boundary layer in this region. Thermal entrance effects also become more pronounced as the Reynolds number increases. For thermally developing flow inside a circular tube with a uniform heat flux boundary, the method proposed earlier in this chapter can be used for local values of the Nusselt number. For length-averaged values of heat transfer coefficient, Morini (2006) suggests the use of the Hausen (1943) correlation format:

$$Nu = Nu_H + K_1 \frac{Gz}{1 + K_2 Gz^b} \quad [4.5.15]$$

where  $Nu_H$  is the fully developed value for the particular channel shape using the (T) and (H) boundary conditions. The values of the constants,  $K_1$ ,  $K_2$  and  $b$  for a circular channel are given in Table 4.3. For a rectangular micro-channel with all four sides heated equally, these values become 0.14, 0.05 and  $2/3$ , respectively. Entrance effects in general can be neglected for Graetz numbers less than 10.

Experimental data are available for only a few limited cases, for example for square channels and parallel plates. Overall, the Nusselt numbers are slightly higher in the entrance region when compared to the thermally developing flow case. Such results may often neglect viscous heat dissipation and axial conduction effects. Most results are obtained by performing a numerical analysis from which the viscous dissipation term's variable property effects are included in the Navier-Stokes equations.

**Table 4.3. Constants for circular channels using the expression of Morini (2006).**

Wall Condition	Velocity Profile	Pr	Nu	Nu <sub>H</sub>	K <sub>I</sub>	K <sub>2</sub>	b
(T)	Fully dev.	Any	Avg.	3.66	0.0668	0.04	0.66
(T)	Fully dev.	0.7	Avg.	3.66	0.104	0.016	0.8
(H)	Fully dev.	Any	Local	4.36	0.023	0.0012	1
(H)	Fully dev.	0.7	Local	4.36	0.036	0.0011	1

#### 4.5.4. Temperature Gradient Property Effects

As Mahulikar and Herwig (2006) demonstrated theoretically for incompressible laminar microconvective flows at low Reynolds numbers and high heat fluxes, there is an increase in the radial and axial gradients of the fluid properties, which means that the variation of the fluid thermal properties with temperature has to be taken into account in the evaluation of the convective heat transfer coefficients. The two foremost properties that can influence the convective behavior of a fluid in a microchannel were identified to be the viscosity and the thermal conductivity. With respect to the first property, the viscosity variation significantly distorts the axial velocity profile and this distortion varies along the channel, thereby inducing a radial flow due the necessity to maintain continuity of the flow. Mahulikar and Herwig (2006) in fact demonstrated that the resulting induced radial heat convection can be a significant percentage of the axial heat convection, especially in microchannels. Also, axial conduction is induced to the fluid by the variation of the thermal conductivity along the flow. The effects of the distortion in the axial velocity profile and the induced radial flow due to fluid viscosity variation are in opposition to one another. However, the axial and radial variations in the thermal conductivity in the flow have a superimposing effect on the microconvection process. Consequently, at low Reynolds numbers ( $Re < 10$ ), the average Nusselt number becomes dependent on the fluid average temperature and on the heat flux imposed at the wall, which is contrary to the normal basic premise of laminar convection being heat flux independent.

## 4.6 Mechanisms of Laminar Heat Transfer Augmentation

**Extended Surface Area.** One way to increase laminar heat transfer coefficients is to increase the surface area in contact with the fluid to be heated or cooled. It is most common to develop heat transfer correlations for internal flows in enhanced tubes based on the internal **nominal** surface area, i.e. that of the perimeter of the maximum internal diameter of the tube  $d_i$  (corrugations) or at the base of any internal enhancement (fins or ribs) [**all correlations in this chapter follow this format**]. This heat transfer coefficient is that which can be used directly in calculating the overall heat transfer coefficient at this diameter without use of a surface area ratio. It is *not* common practice to reduce single-phase flow heat transfer data relative to the total internal surface area. On the other hand, if internal fin efficiency becomes important, it is not possible to include this effect in nominal internal area based correlations. However, commonly used fins and ribs are quite small and their fin efficiencies are normally over 0.95 while for copper tubes they approach 0.99. Since the original experimental data would normally have been reduced to a heat transfer correlation without correcting for fin efficiency, this effect is already incorporated for tubes of that same material. Thus, an effect of fin efficiency can normally be safely ignored. On the other hand, twisted tape inserts fit rather loosely inside a tube (thus they have poor thermal contact to the inner tube wall but can be easily installed and removed) and hence the surface area of a twisted tape is not considered to be heat transfer surface area, only that of the plain tube perimeter in which it is installed. Furthermore, any tube surface area blocked by the width of the insert adjacent to the tube wall is still usually considered to be effective heat transfer area.

**Surface Roughness.** The internal roughness of the tube surface is well known to increase the turbulent heat transfer coefficient but usually has little or no effect on laminar heat transfer, except in extreme cases such as very small channel sizes.

**Swirl.** Swirl of the flow is known to augment heat transfer. Large internal helical fins or ribs, corrugations and twisted tapes impart a swirl effect on the fluid. This tends to increase the effective flow length of the fluid through the tube, which increases heat transfer and pressure drop. For twisted tape inserts, the effect of swirl on augmentation plays an important role. With regard to small fins or corrugations, they are often not sufficient to create a swirl effect and hence may not offer any or much in the way of enhancement.

**Laminar Flow Displacement.** The displacement of the laminar flow from the heat transfer wall is a particularly important heat transfer mechanism for augmenting heat transfer. This is for instance done by placing a twisted tape in the path of the flow that forces the flow away from the wall and allows fresh bulk fluid to come into contact with the wall.

## 4.7 Laminar Heat Transfer with Twisted Tape Inserts

A schematic diagram of a twisted tape insert inside a tube is shown in Figure 4.9. The enhancement is defined geometrically by the thickness of the tape  $\delta$  and its twist ratio,  $y$ . The twist ratio is defined as the axial length for a  $180^\circ$  turn of the tape divided by the internal diameter of the tube. ***This is the most common definition used in research literature and that used here.*** It is also common to use the axial length for a complete  $360^\circ$  turn to calculate the twist ratio; hence, one must double-check the definition used before applying a twisted tape prediction method or using experimental results from manufacturer's literature or a scientific publication and then make sure to indicate the definition used in the resulting heat exchanger specification sheet when specifying a twisted tape insert. An excellent overview of laminar flow twisted tape research over the years is available in Manglik and Bergles (1992a). For treatment of turbulent flow and heat transfer with twist tape inserts, refer to Chapter 5 in this book.

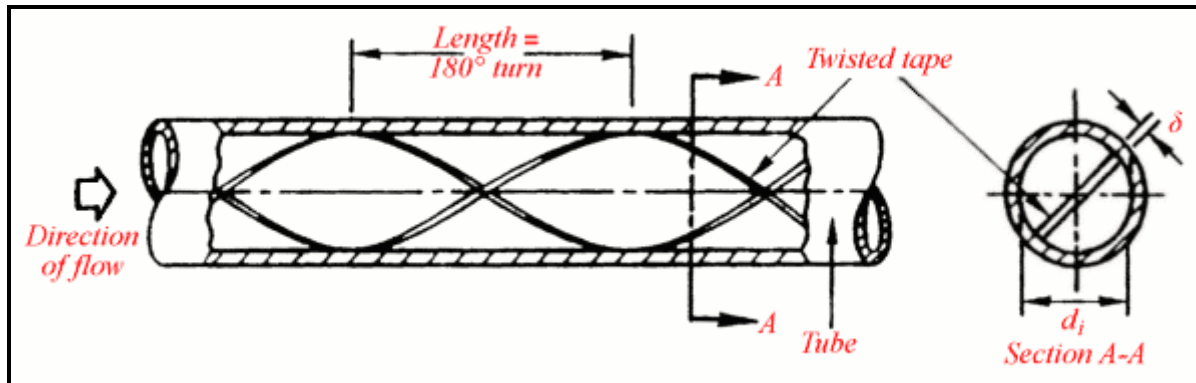


Figure 4.9. Diagram of a twisted tape insert inside a tube.

A twisted tape insert tends to sit loosely within a tube without making “thermal” contact with the tube wall and hence the surface area of the twisted tape itself is not taken into consideration for heat transfer purposes, instead only its effect on the heat transfer coefficient of the tube’s inner surface. The reason that a tight fit is not usually possible is that heat exchanger tubing has tolerances on the tube diameter and wall thickness; hence, when specifying the diameter of the twisted tape, these tolerances must be taken into consideration to make sure the tape will fit into the tube. Furthermore, this means that the tape must be held in place using some type of “hook” at the entrance of the tubesheet to prevent the tape from being pushed downstream by the pressure drop. For cleaning purposes, twisted-tapes can be removed and tend

to bring some of the fouling layer with them; however, the force to remove the tapes that are stuck in the tubes may extend them and require a fresh set of tapes be ready for installation.

Since twisted tapes can be installed in existing heat exchangers (as well as in new heat exchangers), they are often a cost-effective solution for increasing the thermal capacity compared to the installation of a new larger heat exchanger and the associate piping and foundation changes for its installation. On the other hand, the larger pressure drop imposed by the twisted-tape may require the number of tube passes in the heat exchanger to be reduced but normally the thermal performance is still considerably increased. For even higher thermal performance than a twisted-tape insert, one should consider the use of the wire mesh inserts of Cal Gavin Ltd. that have been very successfully applied to enhance many laminar flow services (refer to their manufacturer for details and thermal performance). Below, a summary of the limited number of experimental studies on laminar flow heat transfer with twisted-tape inserts is presented and several methods for predicting their heat transfer and pressure drop characteristics.

Apparently, the first comprehensive study on twisted tape heat transfer in laminar flows was presented in a series of papers by Date and Singham (1972), Date (1973) and Date (1974), in which the uniform heat flux boundary condition ( $H$ ) was investigated numerically and both heat transfer and pressure drop simulations were reported. The flow conditions were idealized for a zero tape thickness but the twist of the tape and heat conduction effects in the tape (as if it were a fin) were included. Shortly after, Hong and Bergles (1976) presented experimental results for water and ethylene glycol in an electrically-heated tube for this boundary condition that demonstrated heat transfer augmentation ratios as high as ten compared to a plain tube, illustrating the very high potential of twisted tape inserts for enhancing laminar flows. They also presented a preliminary heat transfer correlation. DuPlessis (1982) and DuPlessis and Kröger (1983) next made twisted tape measurements for heating and cooling of SAE 20 lubricating oil and presented a method to describe their data. Furthermore, Watanabe, Taira and Mori (1983) experimentally investigated twisted tape inserts for high temperature applications and proposed heat transfer and friction factor correlations.

Marner and Bergles (1978) reported the first heat transfer data for laminar flow of a viscous liquid (ethylene glycol) in tubes with twisted-tape inserts for the uniform wall temperature ( $T$ ) boundary condition, using condensing steam as the heating fluid. They observed heat transfer augmentations up to three times that of a plain tube. Subsequently, Marner and Bergles (1985) extended this experimental study for a 23.0 mm internal diameter, 2.44 m length tube with a twisted tape insert of 22.9 mm diameter, a tape thickness of 1.22 mm and a twist ratio of 5.4. The tests were done with Polybutene 20 and the test conditions were for essentially a constant wall temperature boundary condition when using steam condensation in the annulus of a double-pipe heat exchanger for heating the test fluid but were probably closer to constant heat flux conditions when cooling the test fluid using a counter-current flow of water in the annulus. In isothermal pressure drop tests, they found a Poiseuille number of 54 ( $Po = f Re = 54$ ) compared to  $Po = 16$  for the same tube without the insert, indicating a pressure drop penalty ratio of 3.4 for this particular twisted tape. For viscosity ratio ranges from 7.37 to 33.3 for heating and 0.00464 to 0.0469 for cooling, the twisted tape Nusselt numbers were from 1.5 to 2.25 times those of the plain tube at equivalent Graetz numbers. In contrast to the internally finned tube tested in the same study, they found about the same amount of enhancement for both heating and cooling when using the twisted tape. They explained this as being a sort of “scraping” process of the fluid from the wall of the tube and its replenishment by bulk liquid from the center of the tube. They were able to correlate all their data for both heating and cooling of the test fluid using the following correlation:

$$Nu_{T,tt} = \frac{\alpha_{tt} d_i}{k} = 1.322 Gz^{0.458} \left( \frac{\mu_{bulk}}{\mu_{wall}} \right)^{0.14} \quad [4.7.1]$$

This expression includes the Graetz number, which is defined as:

$$Gz = \left( \frac{\pi}{4} \right) \frac{Re Pr d_i}{L} \quad [4.7.2]$$

Most of the data were predicted to within 20% by this expression for this one twisted tape ratio for their tests covering Reynolds numbers from 15.1 to 575, Prandtl numbers from 1260 to 8130 and Graetz numbers from 868 to 6570 for the above mentioned viscosity ratio range. Entrance length effects are thus included within this correlation as the database was for the mean heat transfer coefficients along the entire tube. From the diabatic pressure drop tests, they recommended different viscosity ratio corrections, mentioned earlier in this chapter in Section 4.3.

Monheit (1987) performed an experimental study on a 21.6 mm internal diameter, 6.7 m length tube with a twisted tape insert of 21.2 mm width before twisting, a tape thickness of 1.0 mm and twist ratios of 2.0, 2.8 and 3.7. The tests were done for cooling of synthetic lubricating oil (Shell turbo-oil 68) in a tube with twisted tape inserts in a double-pipe heat exchanger with water as the cooling fluid, whose experimental boundary condition is probably close to a constant heat flux condition under fully developed flow conditions. Absolute values of the friction factors and Nusselt numbers measured were not however given; all data were presented as ratios with respect to the tape with  $y = 2.8$  at a Reynolds number of 500. In any case, it was found that the  $y = 2.0$  tape outperformed the reference tape by about 20-25% while the  $y = 3.7$  tape performed about 10-15% less than the reference tape. With respect to the pressure drops, the  $y = 2.0$  tape had about 30-40% higher-pressure drops while the  $y = 3.7$  tape had about 16-18% lower ones. In addition to the plain tapes, one twisted tape with punched holes with  $y = 2.8$  and another tape with slit edges with  $y = 7.0$  were tested. No improvement in heat transfer with respect to the  $y = 2.8$  plain tape was found with the punched holes and lower heat transfer performance was found with the larger twist ratio of 7.0. No prediction method was proposed here however.

Manglik and Bergles (1986) numerically examined the special case of a tape insert without twist (that is a straight tape with  $y = \infty$ ) and negligible thickness. The flow is thus in a semi-circular channel. Constant physical properties were assumed. Two numerical cases were examined: (i) uniform axial heat flux and constant circumferential tube wall temperature ( $H$ ) and (ii) constant axial and circular arc section tube wall temperature ( $T$ ). These two conditions they noted essentially form the two extremes of the fin effect of a twisted tape insert, with the second case defining the lower idealized limit. They pointed out that loose fitting tapes used in experiments and industrial practice correspond to a condition in-between these two cases. In particular, for the semi-circular channel they determined the fully developed Nusselt number for case (T) to be  $Nu_T = 4.631$  relative to the value of  $Nu_T = 3.657$  for the circular tube geometry, i.e. 26.6% higher for a straight insert. Following this work, Manglik and Bergles (1987) proposed a new generalized twisted tape heat transfer correlation based on the twist ratio  $y$ .

Saha, Gaitonde and Date (1989) investigated the heat transfer and pressure drop characteristics of laminar flow in a tube with regularly spaced twisted tape segments, looking for ways to reduce pressure drop while maximizing heat transfer. Furthermore, Bandyopadhyay, Gaitonde and Sukhatme (1991) studied the influence of natural convection on heat transfer during laminar flow in tubes with twisted tapes, finding an effect for some conditions.

Manglik and Bergles (1992a) presented a very comprehensive discussion on the influence of twisted tapes on laminar flow and heat transfer, proposing the most general and accurate prediction methods available and those recommended for use here. They proposed the upper bound of laminar flow with twisted tape inserts to be given by

$$Sw = \frac{Re_s}{\sqrt{y}} = \left( \frac{Re}{\sqrt{y}} \right) \left( \frac{\pi}{\pi - (4\delta/d_i)} \right) \left( 1 + \left( \frac{\pi}{2y} \right)^2 \right)^{1/2} \approx 1400 \quad [4.7.3]$$

In this expression,  $Sw$  is the swirl number,  $Re_s$  is the swirl Reynolds number,  $\delta$  is the thickness of the twisted tape and  $y$  is the twist ratio while  $Re$  is the Reynolds number for the tube without the twisted tape present. According to them, the Swirl number represents the force ratio of

$$Sw = \left( \frac{(centrifugal\ force)(convective\ inertia\ force)}{(viscous\ force)^2} \right)^{1/2} \quad [4.7.4]$$

They proposed the following equation to predict the isothermal friction factors for fully developed laminar swirl flow:

$$f_s Re_s = 15.767 \left( \frac{\pi + 2 - (2\delta/d_i)}{\pi - (4\delta/d_i)} \right)^2 \left( 1 + 0.000001 Sw^{2.55} \right)^{1/6} \quad [4.7.5]$$

For a straight insert without twist,  $Sw \rightarrow 0$  as  $y \rightarrow \infty$ , so that the last term in this expression goes to unity, for which their solution then matches that for fully developed laminar flow in a half tube (semi-circular duct). This expression predicted experimental results from three different studies with twist ratios from 3.0 to  $\infty$  to within  $\pm 10\%$ . Presumably, the same viscosity ratio correction can be applied to the isothermal friction factor of the twisted tape as was used for plain straight tubes above. The pressure drop in a tube of length  $L$  with a twisted tape is calculated as:

$$\Delta p = \frac{f_s d_i}{2 \rho U_s^2 L_s} \quad [4.7.6]$$

In this expression, the flow path length of a helical streamline  $L_s$  in a tube with a twisted tape insert compared to the straight length of the tube  $L$  is given by:

$$L_s = L \left[ 1 + \left( \frac{\pi}{2y} \right)^2 \right]^{1/2} \quad [4.7.7]$$

Similarly, the swirl velocity  $U_{sw}$  is given by:

$$U_s = U \left[ 1 + \left( \frac{\pi}{2y} \right)^2 \right]^{1/2} \quad [4.7.8]$$

The actual velocity  $U$  in the tube is that given by the cross-sectional area of the tube minus that occupied by the tape:

$$U = \frac{\dot{m}}{\rho(\pi d_i^2 / 4 - \delta d_i)} \quad [4.7.9]$$

The mean Nusselt number for twisted tape inserts for laminar flow heat transfer with a uniform wall temperature condition ( $T$ ) is given by their expression:

$$Nu_{T,tt} = \frac{\alpha_{tt} d_i}{k} = 4.612 \left\{ \left[ \frac{(1 + 0.0951 Gz^{0.894})^{2.5}}{0.00000006413 (Sw Pr^{0.391})^{3.835}} \right]^{2.0} + 0.0000000000002132 (Re Ra)^{2.23} \right\}^{0.1} \left( \frac{\mu_{bulk}}{\mu_{wall}} \right)^{0.14} \quad [4.7.10]$$

In this expression,  $Re$  is refers to the actual Reynolds number accounting for the blockage of the tape in the tube, that is  $Re = \rho U d_i / \mu$ . The Graetz number is defined as:

$$Gz = \frac{\dot{m} c_p}{k L} \quad [4.7.11]$$

The Rayleigh number includes the buoyancy effects on heat transfer using the coefficient of thermal expansion  $\beta$  and the wall-to-bulk temperature difference and is defined as:

$$Ra = \left( \frac{g \rho^2 d_i^3 \beta |T_{wall} - T_{bulk}|}{\mu^2} \right) Pr \quad [4.7.12]$$

The experimental database for this method covered three different experimental studies including ethylene glycol, water, and Polybutene 20 for twist ratios from 3.0 to  $\infty$ , predicting nearly all the data to be within  $\pm 15\%$ .

## 4.8 Laminar Heat Transfer with Wire Mesh Inserts

Wire mesh inserts developed by Cal Gavin Ltd. have been successfully applied to laminar flows now for several decades in a wide range of applications and are an excellent option for enhancing heat transfer in laminar flows. These inserts tend to yield much higher heat transfer and pressure drop augmentation ratios than twisted tape inserts. However, these are not described here since the design methods are not in the public domain; the reader is referred to Cal Gavin Ltd. for a description of the inserts and thermal design information.

## 4.9 Laminar Heat Transfer in Internally Finned Tubes

Internally finned tubes for application to laminar flows have not been widely investigated in the literature. Marner and Bergles (1985) surveyed the literature at that time, finding only a handful of experimental studies. For example, Watkinson, Milleti and Kubanek (1975) and Soliman and Feingold (1977) carried out tests on specific fin geometries. Choudhury and Patankar (1985) and MacArthur and Patankar (1985) numerically investigated laminar flow and heat transfer inside internally finned tubes and spiral annular passages, respectively. In the first study, they noted significant buoyancy (natural convection) effects in a developing laminar flow, primarily on heat transfer but less so on pressure drop. In the second study, with

fins in the annulus of a double-pipe heat exchanger, they analyzed the effect of the twist (or spiral) of the fins on pressure drop and heat transfer relative to straight fins, finding that for some conditions the Poiseuille number ( $Po = f Re$ ) in spiral fins was doubled while the heat transfer was up to five times higher, both created by the secondary flow effects. This work points to the high heat transfer augmentation effects that may potentially be created by internal fins, either inside tubes or in annuli.

In perhaps the detailed experimental study, Marner and Bergles (1985) tested one internally finned tube with a highly viscous fluid (Polybutene 20). The tests were done under constant wall temperature conditions. Their 25.1 mm internal diameter, finned tube had 16 spiral fins of 0.66 mm thickness and 2.08 mm height with a spiral fin pitch of 88.9 mm. The isothermal friction factors for this tube were 1.7 times those of a comparable diameter plain tube. For heat transfer, the finned tube provided values 3 to 4 times higher than a plain tube when heating the fluid while only a marginal improvement when cooling. During heating, they cited the increased heat transfer surface area of the fins, a beneficial viscosity ratio effect and a swirl effect as being the primary reasons for the higher performance. For cooling this viscous fluid, they instead noted that this fluid apparently tended to “freeze” in the region between the fins, negating the influence of the fins, so that the principal effect on enhancement was only the effective reduction in the tube diameter. Correlations were proposed for the friction factor and heat transfer for this tube, plus viscosity ratio effects of the wall temperature, but these correlations are specific to this one tube and cannot be generalized for use with other internally finned tubes. The interested reader is referred to the original paper for these methods.

In summary, internally finned tubes (and finned annuli) may provide a significant augmentation in heat transfer and pressure drop. However, it seems that they are best used when the fluid is being heated but not when it is being cooled. So far, apparently no general prediction method is available to handle the effects of the fin geometry (number of fins, fin height, fin thickness, fin shape, etc.).

## 4.10 Laminar Heat Transfer in Spirally Fluted Tubes

These spirally fluted tubes (and corrugated tubes) have not seen a significant research effort in the literature. Bergles (1981) presented a detailed survey of heat transfer characteristics of deep spirally fluted tubes. Another review is available in Garimella and Christensen (1992). Spirally fluted tubes for laminar flows were also addressed in the review by Bergles, Webb and Junkhan (1979).

With respect to experimental studies, according to the aforementioned reviews by Bergles, for laminar flows inside a Turbotec spirally fluted tube, heat transfer was increased by up to two times compared to a plain tube when heating the test fluid (Alta-Vis-530) but no improvement was found when cooling the same fluid. Rozalowski and Gater (1975) made tests on a deeply grooved flexible hose in laminar flow with two highly viscous fluids (Zerolene SAE-50 and Alta-Vis-530), finding up to three times heat transfer augmentation during heating, no augmentation when cooling Alta-Vis-530 but up to 100% higher performance when cooling the Zerolene. Even earlier than that, Kalinin and Yarkho (1971) studied deeply deformed tubes with transverse ridges for laminar flow with water, which from limited data showed that three of the seven configurations actually reduced heat transfer rather than augmented it.

With respect to pressure drop in laminar flows, several experimental studies with deep spirally fluted tubes are available. Rozalowski and Gater (1975) found pressure drops to be about four times those of the equivalent diameter plain tube. Kliebe (1978) found isothermal pressure drops from 2 to 4 times higher for the Turbotec tube with Alta-Vis-530. For a large selection of spirally fluted tubes used as the inside tube of an annulus with water as the test fluid, Garimella and Christensen (1992) found pressure drop multipliers to range from 1.1 to 2.0 and also noted that the transition to turbulent flow occurred at a much lower Reynolds number in the range from 310 to 1000.

Based on the wide variety of spirally fluted geometries and shapes, it is not possible apparently to provide a general method for predicting their heat transfer and pressure drop characteristics. Methods have been proposed in some of the above-mentioned experimental papers, but each method is limited to the particular type of flute shape and usually only one tube sample. Thus, no prediction methods are presented here for spirally fluted tubes.

## Chapter 5

# Enhanced Single-Phase Turbulent Tube-side Flows and Heat Transfer

**SUMMARY:** This section presents methods for predicting heat transfer and pressure drop for turbulent flows inside corrugated tubes, internally ribbed or finned tubes, and in tubes with twisted tape inserts. A brief review of prediction methods for turbulent flow heat transfer in plain tubes is also presented for the reader's convenience and the important issues of inlet configuration effects on heat transfer and pressure drop in the transition region between laminar and turbulent flows in plain tubes are addressed.

### 5.1 Introduction

This chapter covers turbulent flow and heat transfer inside plain and enhanced tubes. Only tubular enhancement geometries of particular industrial interest are discussed here. These geometries are corrugated tubes, internally finned or ribbed tubes, and tubes with twisted tape inserts. The commonly used prediction methods for heat transfer and pressure drop for plain tubes are first presented and then the mechanisms of heat transfer augmentation are discussed. Next, design methods for corrugated tubes, internally finned or ribbed tubes, and tubes with twisted tape inserts are presented. The reader is referred to other sources for more detailed reviews of the literature and experimental results, such as the book of Webb (1994).

Tubular enhancements made by Wolverine Tube Inc. include corrugated tubes and tubes with integral internal fins or ribs. Figure 5.1 shows a diagram of a single-start corrugated tube and Figure 5.2 depicts a photograph of a Wolverine Korodense corrugated tube. A corrugated tube is defined geometrically by the corrugation pitch,  $p$ , and the corrugation depth,  $e$ . The axial corrugation pitch is related to the internal diameter  $d_i$ , helix angle  $\beta$  relative to the axis of the tube and the number of starts  $n_s$  by the following geometrical equation:

$$p = \frac{\pi d_i}{n_s \tan \beta} \quad [5.1.1]$$

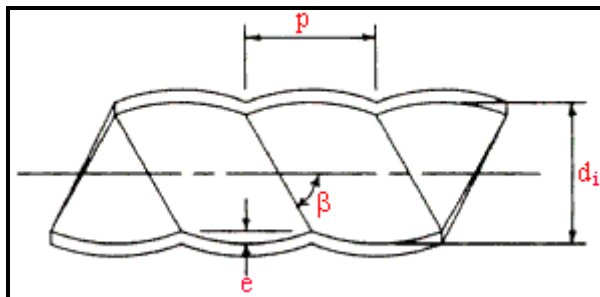


Figure 5.1. Diagram of corrugated tube.



Figure 5.2. Photograph of Wolverine Korodense tube.

The external diameter over the corrugations on the outside of the tube is equal to that of the plain ends of the tube. The internal diameter is taken as the external diameter less twice the tube wall thickness. The internal area ratio of a corrugated tube relative to a plain tube of the same diameter  $d_i$  is slightly larger than one.

Figure 5.3 depicts a schematic diagram for an internally finned or ribbed tube. As it is difficult to geometrically define a difference between a fin and a rib, these two names will be assumed to refer to the same geometry here. Helical internal *fins* or *ribs* (or also referred to as *ridges* in Wolverine Tube literature) are applied to the inside of low finned tubes such as Turbo-Chil and S/T Trufin and to enhanced boiling and condensing tubes, such as the various versions of Turbo-B and Turbo-C. The internal fin (or rib or ridge) geometry is defined by the fin height, the mean fin thickness, the apex angle of the fin, the helix angle of the fin and the axial pitch of one fin to the next. The helix angle is related to the axial fin pitch by applying the expression above using the number of fins in place of the number of starts. The internal area ratio relative to a plain tube of the same diameter  $d_i$  ranges from about 1.3 to 2.0. The internal fins can be of various cross-sectional shapes. Most industrial tubes have fins (or ribs or ridges) with a trapezoidal cross-sectional profile (wider at the base than at the tip of the fin and with rounded corners). Figure 5.4 shows a photograph of a Wolverine Turbo-Chil low finned tube with internal helical fins.

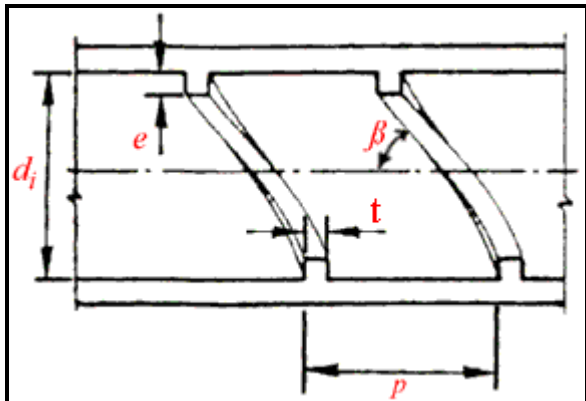


Figure 5.3. Diagram of internally finned or ribbed tube.



Figure 5.4. Photograph of Wolverine Turbo-Chil tube.

## 5.2 Turbulent and Transition Flows and Heat Transfer in Plain Tubes

Before discussing heat transfer enhancement of turbulent, single-phase flows inside tubes, a summary of turbulent and transition flows inside plain tubes and the effects of the tube inlet configuration on heat transfer and transition thresholds are presented below.

The most commonly used correlation for predicting fully developed turbulent flow heat transfer coefficients inside smooth, round tubes is what is known as the Dittus-Boelter (1930) equation:

$$Nu = \frac{\alpha_{pt} d_i}{k} = 0.023 Re^{0.8} Pr^n \quad [5.2.1]$$

where the Nusselt number  $Nu$  is based on the tube diameter  $d_i$  and  $\alpha_{pt}$  is the convective heat transfer coefficient for a plain tube. The tubular Reynolds number  $Re$  is defined as:

$$Re = \frac{\dot{m}d_i}{\mu} \quad [5.2.2]$$

The mass velocity  $\dot{m}$  is in  $\text{kg/m}^2\text{s}$  and is obtained by dividing the mass flow rate in  $\text{kg/s}$  by the cross-sectional area of the tube in  $\text{m}^2$ . The Prandtl number  $Pr$  is obtained from the physical properties of the fluid and is defined as:

$$Pr = \frac{c_p \mu}{k} \quad [5.2.3]$$

The exponent on the Prandtl number for cooling a fluid is  $n = 0.3$  (for  $T_{wall} < T_{bulk}$ ) while for heating a fluid is  $n = 0.4$  (for  $T_{wall} > T_{bulk}$ ), where  $T_{wall}$  is the inside tube wall temperature and  $T_{bulk}$  is the mean fluid temperature. In the above expressions, the fluid properties are as follows:  $c_p$  is the specific heat at constant pressure,  $k$  is the thermal conductivity, and  $\mu$  is the dynamic viscosity. This correlation is generally accurate to about  $\pm 25\%$  as has been confirmed experimentally for the following range of conditions:  $0.7 \leq Pr \leq 160$ ,  $Re \geq 10^4$  and  $L/d_i \geq 10$  where  $L$  is the length from the inlet of the tube. This expression may be used for moderate temperature differences with fluid properties evaluated at the bulk fluid temperature.

Another widely used method from the same time period is that of Sieder and Tate (1936), who recommended the following expression for applications with large property variations from the bulk flow to the wall temperature:

$$Nu = \frac{\alpha_{pt} d_i}{k} = 0.027 Re^{0.8} Pr^{1/3} \left( \frac{\mu_{bulk}}{\mu_{wall}} \right)^{0.14} \quad [5.2.4]$$

for  $0.7 < Pr < 16000$ ,  $Re > 10000$  and  $L/D > 10$ .

For more accurate calculations in fully developed turbulent flow (to within about  $\pm 10\%$ ), it is recommended to use the Petukhov (1970) heat transfer correlation that is valid for  $0.5 < Pr < 2000$  and  $10^4 < Re < 5 \times 10^6$ :

$$Nu = \frac{\alpha_{pt} d_i}{k} = \frac{(f/2)RePr}{1.07 + 12.7(f/2)^{1/2}(Pr^{2/3} - 1)} \left( \frac{\mu_{bulk}}{\mu_{wall}} \right)^{0.14} \quad [5.2.5]$$

where the friction factor  $f$  can be obtained from the Moody diagram or from Petukhov's friction factor correlation for smooth tubes valid for  $3000 < Re < 5 \times 10^6$ :

$$f = (1.58 \ln Re - 3.28)^{-2} \quad [5.2.6]$$

The property ratio  $(\mu_{bulk}/\mu_{wall})^{0.14}$  corrects for property variations for liquid flows being heated or cooled, where  $\mu_{bulk}$  is that at the mean fluid temperature  $T_{bulk}$  and  $\mu_{wall}$  is that at the wall temperature  $T_{wall}$ . No property correction is used for a gas being cooled while the viscosity ratio term is replaced by a

temperature ratio  $[(T_{\text{bulk}}+273)/(T_{\text{wall}}+273)]^{0.25}$  for a gas being heated. Similar corrections should be applied to the friction factor expression above but with the exponent as negative value, where -0.25 is the most often quoted but some texts also recommend a value of -0.14. The other properties are evaluated at the bulk temperature. The pressure drop in a tube of length L is given by the expression:

$$\Delta p = \frac{2f \dot{m}^2 L}{\rho d_i} \quad [5.2.7]$$

Another heat transfer correlation commonly used is that of Gnielinski (1976), which extends the Petukhov correlation down into the transition regime:

$$Nu = \frac{\alpha_{\text{pt}} d_i}{k} = \frac{(f/2)(Re-1000)\Pr}{1+12.7(f/2)^{1/2}(\Pr^{2/3}-1)} \left( \frac{\mu_{\text{bulk}}}{\mu_{\text{wall}}} \right)^{0.14} \quad [5.2.8]$$

where the friction factor  $f$  is obtained from Petukhov's friction factor correlation above or from the Moody diagram. It is accurate to about 10% for the following conditions:  $0.5 < \Pr < 2000$  and  $3000 < Re < 5 \times 10^6$ . Flow is normally considered to be fully developed starting from about 10 to 60 tube diameters from the entrance (see additional discussion below).

Ghajar and coworkers in a series of papers have investigated the **transition region** between laminar and turbulent flow in plain tubes experimentally and also proposed some prediction methods for this regime to bridge between laminar methods and turbulent methods, applicable to forced and mixed convection in the entrance and fully developed regions for three types of inlet configurations: re-entrant (tube extends beyond tubesheet face into head of distributor, square-edged (tube end is flush with tubesheet face) and bell-mouth (a tapered entrance of tube from tubesheet face). Ghajar, Tam and Tam (2004) give a summary of all their heat transfer work and propose an artificial neural network approach for modelling their heat transfer data. Earlier, Ghajar and Tam (1994) proposed an easier to implement method that also captured all the trends with nearly the same accuracy, which is presented below. The local heat transfer coefficient in transition flow is obtained from the transition Nusselt number,  $Nu_{\text{trans}}$ , which is calculated as follows at a distance  $z$  from the entrance:

$$Nu_{\text{trans}} = Nu_{\text{lam}} + \{ \exp[(a-Re)/b] + Nu_{\text{turb}}^c \}^c \quad [5.2.9]$$

where  $Nu_{\text{lam}}$  is the laminar flow Nusselt number for entrance region laminar flows with natural convection effects:

$$Nu_{\text{lam}} = 1.24 \left[ \left( \frac{Re \Pr d_i}{z} \right) + 0.025 (\text{Gr} \Pr)^{0.75} \right]^{1/3} \left( \frac{\mu_{\text{bulk}}}{\mu_{\text{wall}}} \right)^{0.14} \quad [5.2.10]$$

and  $Nu_{\text{turb}}$  is the turbulent flow Nusselt number with developing flow effects:

$$Nu_{\text{turb}} = 0.023 Re^{0.8} \Pr^{0.385} \left( \frac{z}{d_i} \right)^{-0.0054} \left( \frac{\mu_{\text{bulk}}}{\mu_{\text{wall}}} \right)^{0.14} \quad [5.2.11]$$

The Nusselt, Reynolds and Prandtl numbers have their traditional definitions. The Grashof number  $Gr$  is defined as:

$$Gr = g\beta_{th}\rho^2 d_i^3 (T_{wall} - T_{bulk}) / \mu^2 \quad [5.2.12]$$

In this expression the inner tube wall temperature is  $T_{wall}$ , the bulk fluid temperature is  $T_{bulk}$ ,  $\beta_{th}$  is the coefficient of thermal expansion of the fluid at the bulk temperature,  $g$  is the acceleration due to gravity ( $9.81 \text{ m/s}^2$ ) and  $z$  is the distance from the entrance of the tube whose diameter is  $d_i$ . The physical properties ( $k$ ,  $\mu$ ,  $\rho$ ,  $c_p$ ) appearing in the dimensionless numbers (Nu, Re, Pr and Gr) are all evaluated at the bulk fluid temperature ( $T_{bulk}$ ). The values of the empirical constants  $a$ ,  $b$  and  $c$  in [5.2.9] depend on the inlet configuration and are given in Table 5.1. The viscosity ratio accounts for the temperature effect on the process. The range of application of the heat transfer method based on their database of 1290 points (441 points for re-entrant inlet, 416 for square-edged inlet and 433 points for bell-mouth inlet) is as follows:

**Re-entrant:**  $3 \leq z/d_i \leq 192$ ,  $1700 \leq Re \leq 9100$ ,  $5 \leq Pr \leq 51$ ,  $4000 \leq Gr \leq 210000$ ,  $1.2 \leq \mu_{bulk}/\mu_{wall} \leq 2.2$ .

**Square-edged:**  $3 \leq z/d_i \leq 192$ ,  $1600 \leq Re \leq 10700$ ,  $5 \leq Pr \leq 55$ ,  $4000 \leq Gr \leq 250000$ ,  $1.2 \leq \mu_{bulk}/\mu_{wall} \leq 2.6$ .

**Bell-mouth:**  $3 \leq z/d_i \leq 192$ ,  $3300 \leq Re \leq 11100$ ,  $13 \leq Pr \leq 77$ ,  $6000 \leq Gr \leq 110000$ ,  $1.2 \leq \mu_{bulk}/\mu_{wall} \leq 3.1$ .

**Table 5.1. Constants for transition heat transfer and pressure drop correlations.**

Inlet geometry	a	B	c	A	B	C	$m_1$	$m_2$	$m_3$	$m_4$
Re-entrant	1766	276	-0.955	5840	-0.0145	-6.23	-1.10	0.460	-0.133	4.10
Square-edged	2617	207	-0.950	4230	-0.1600	-6.57	-1.13	0.396	-0.160	5.10
Bell-mouth	6628	237	-0.980	5340	-0.0990	-6.32	-2.58	0.420	-0.410	2.46

These methods capture about 70% of their data within an error band of  $\pm 10\%$  and 97% of their data within  $\pm 20\%$ , which is remarkable for transition flows. The individual expressions above for  $Nu_{lam}$  and  $Nu_{turb}$  can be used alone for developing flows in those respective regimes. The lower and upper limits of the transition regime occur at the following conditions according to Ghajar and Tam (1995):

**Re-entrant:**  $Re(\text{lower}) = 2157 - 0.65[192 - (z/d_i)]$  [5.2.13a]  
 $Re(\text{upper}) = 8475 - 9.28[192 - (z/d_i)]$  [5.2.13b]

**Square-edged:**  $Re(\text{lower}) = 2524 - 0.82[192 - (z/d_i)]$  [5.2.14a]  
 $Re(\text{upper}) = 8791 - 7.69[192 - (z/d_i)]$  [5.2.14b]

**Bell-mouth:**  $Re(\text{lower}) = 3787 - 1.80[192 - (z/d_i)]$  [5.2.15a]  
 $Re(\text{upper}) = 10481 - 5.47[192 - (z/d_i)]$  [5.2.15b]

The above equations indicate that the re-entrant inlet configuration causes the earliest transition from laminar flow into the transition regime (at about 2000) while the bell-mouth entrance retards this regime change (at about 3500). The square-edged entrance falls in between (at about 2400), which is close to the often quoted value of 2300 in most textbooks. Figure 5.5 clearly shows the influence of inlet configuration on the beginning and end of the heat transfer transition region. This figure plots the local

average peripheral heat transfer coefficients in terms of the Colburn  $j$  factor ( $St Pr^{0.67}$ ) versus local Reynolds number for all flow regimes at the length-to-diameter ratio of 192, and  $St$  is the Stanton number ( $Nu/(Re Pr)$ ). The filled symbols represent the start and end of the heat transfer transition region for each inlet configuration. Note the large influence of natural convection superimposed on the forced convective laminar flow heat transfer process ( $Nu = 4.364$  for a fully developed laminar flow with a uniform heat flux boundary condition without buoyancy effects), yielding a mixed convection value of about  $Nu = 14.5$ . Expression [5.2.10] includes this buoyancy effect through the Grashof number.

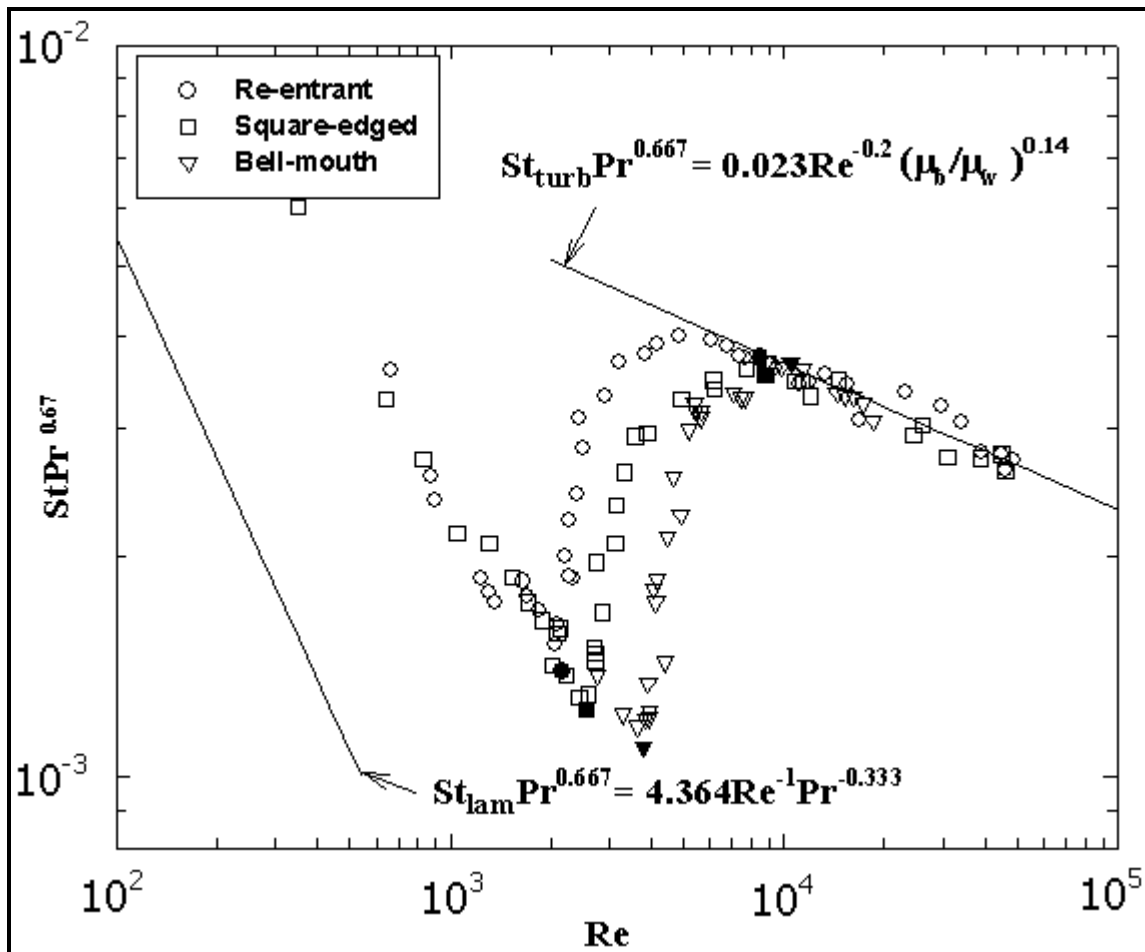


**Figure 5.5. Influence of different inlets on the heat transfer transition region at  $z/D=192$  (filled symbols designate the start and end of the transition region for each inlet) between limits of Dittus-Boelter correlation for fully developed turbulent flow (using  $n = 1/3$ ) and  $Nu = 4.364$  for fully developed laminar flow with a uniform heat flux boundary condition. Note buoyancy effect on the laminar flow data giving the much larger mixed convection heat transfer coefficient. Taken from Ghajar and Tam (1994).**

In a subsequent study, Tam and Ghajar (1998) experimentally investigated the behavior of local heat transfer coefficients in the transition region for a tube with a bell-mouth inlet. This type of inlet is used in some heat exchangers mainly to avoid the presence of eddies which are believed to be one of the causes for erosion in the tube inlet region. For the bell-mouth inlet, the variation of the local heat transfer coefficient with length in the transition and turbulent flow regions is very unusual. For this inlet geometry, the boundary layer along the tube wall is at first laminar and then changes through a transition to the turbulent condition causing a dip in the  $Nu$  vs.  $z/d_i$  curve. In their experiments with a fixed inside

diameter of 15.84 mm (0.624 in.), the length of the dip in the transition region was much longer ( $100 < z/d_i < 175$ ) than in the turbulent region ( $z/d_i < 25$ ). The presence of the dip in the transition region causes a significant influence in both the local and the average heat transfer coefficients. This is particularly important for heat transfer calculations in short tube heat exchangers with a bell-mouth inlet. Figure 5.6 shows the variation of local Nusselt number along the tube length in the transition region for the three inlet configurations at comparable Reynolds numbers.

Ghajar and Madon (1992) and Tam and Ghajar (1997) measured pressure drops in circular plain tubes for fully developed flows in the transition regime for the same three inlet configurations under isothermal and heating conditions, respectively. The widely used expressions for the friction factor  $f$  in laminar and turbulent flows with heat and cooling are, respectively:

$$f_{\text{lam}} = \left( \frac{16}{\text{Re}} \right) \left( \frac{\mu_{\text{bulk}}}{\mu_{\text{wall}}} \right)^m \quad [5.2.16]$$

$$f_{\text{turb}} = \left( \frac{0.0791}{\text{Re}^{0.25}} \right) \left( \frac{\mu_{\text{bulk}}}{\mu_{\text{wall}}} \right)^m \quad [5.2.17]$$

The exponent  $m$  for laminar flows depends on a number of factors while for turbulent flows the most typically quoted value is -0.25. In expressions similar to those above for heat transfer, Tam and Ghajar (1997) give the following expression for the transition friction factor  $f_{\text{trans}}$ :

$$f_{\text{trans}} = \left[ 1 + \left( \frac{\text{Re}}{A} \right)^B \right]^C \left( \frac{\mu_{\text{bulk}}}{\mu_{\text{wall}}} \right)^m \quad [5.2.18]$$

where the exponent  $m$  is obtained from:

$$m = m_1 - m_2 \text{Gr}^{m_3} \text{Pr}^{m_4} \quad [5.2.19]$$

The values of the empirical constants in this expression are listed in Table 5.1. The range of application of the transition friction factor equation based on their database of 83 points (30 points for the re-entrant inlet, 29 points for the square-edged inlet and 24 points for the bell-mouth inlet) is as follows:

**Re-entrant:**  $2700 \leq \text{Re} \leq 5500$ ,  $16 \leq \text{Pr} \leq 35$ ,  $7410 \leq \text{Gr} \leq 158300$ ,  $1.13 \leq \mu_{\text{bulk}}/\mu_{\text{wall}} \leq 2.13$ .

**Square-edged:**  $3500 \leq \text{Re} \leq 6900$ ,  $12 \leq \text{Pr} \leq 29$ ,  $6800 \leq \text{Gr} \leq 104500$ ,  $1.11 \leq \mu_{\text{bulk}}/\mu_{\text{wall}} \leq 1.89$ .

**Bell-mouth:**  $5900 \leq \text{Re} \leq 9600$ ,  $8 \leq \text{Pr} \leq 15$ ,  $11900 \leq \text{Gr} \leq 353000$ ,  $1.05 \leq \mu_{\text{bulk}}/\mu_{\text{wall}} \leq 1.47$ .

These methods captured about 82% of their data within an error band of  $\pm 10\%$  and  $\pm 98\%$  of their data with  $\pm 20\%$ . For laminar flows with heating, they give the following constants for determining the exponent  $m$  in [5.2.16]:  $m_1 = 1.65$ ,  $m_2 = 0.013$ ,  $m_3 = 0.170$  and  $m_4 = 0.840$ , which is applicable over the following range of parameters:  $1100 \leq \text{Re} \leq 7400$ ,  $6 \leq \text{Pr} \leq 36$ ,  $17100 \leq \text{Gr} \leq 95600$  and  $1.25 \leq \mu_{\text{bulk}}/\mu_{\text{wall}} \leq 2.40$ .

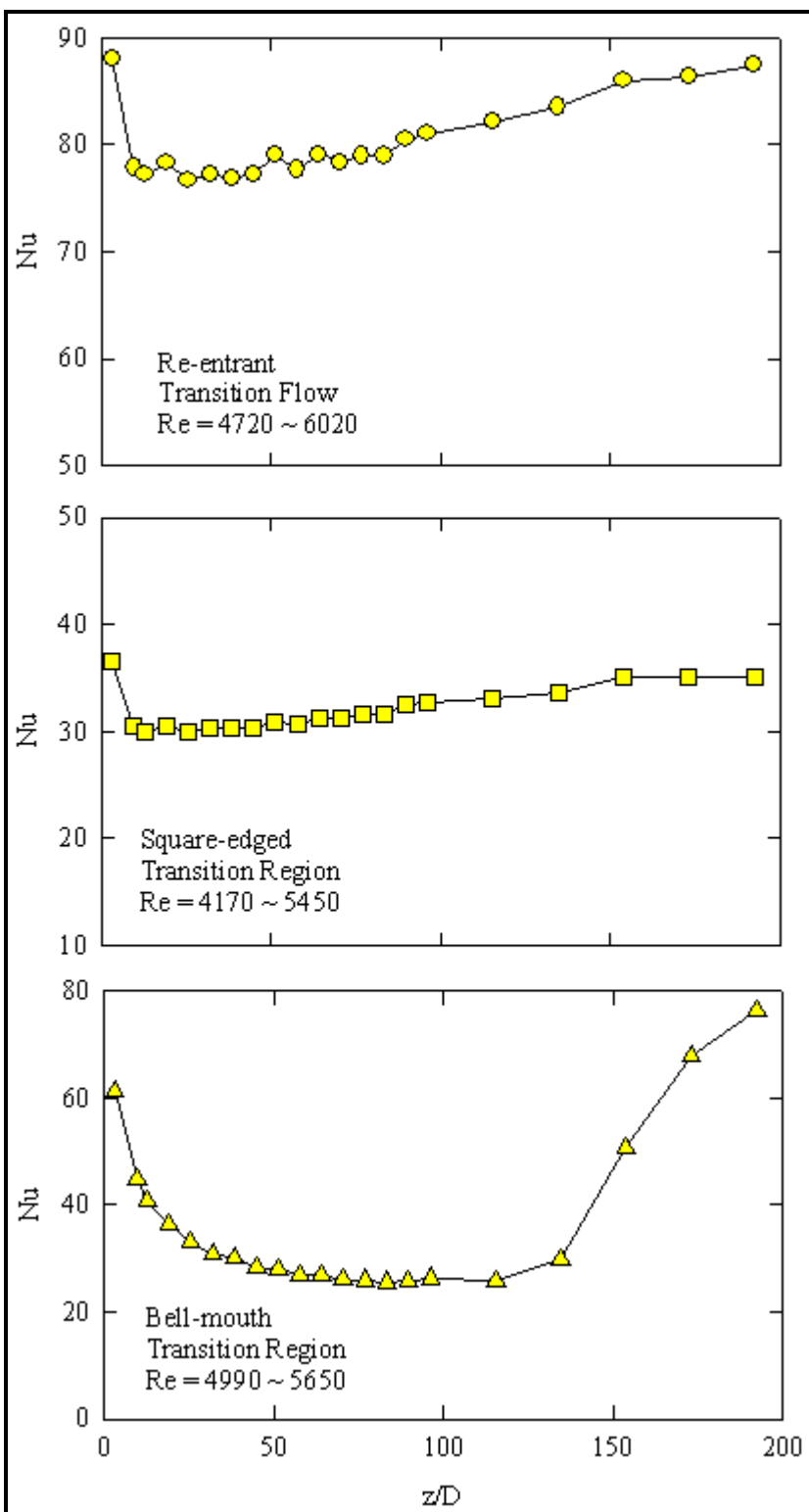


**Figure 5.6.** Variation of local Nusselt number with length for the re-entrant, square-edged, and bell-mouth inlets in the transition region. Taken from Tam and Ghajar (1998).

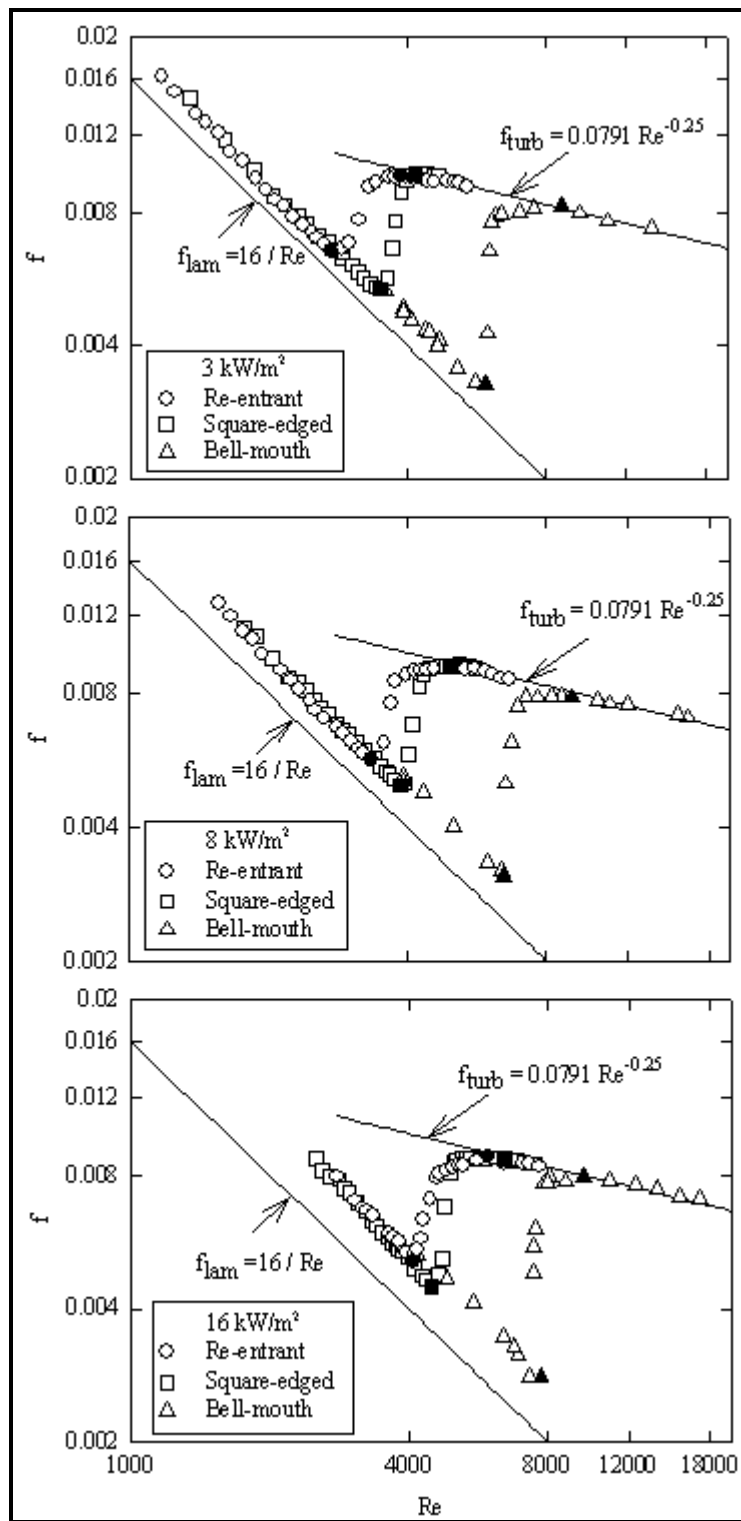


**Figure 5.7.** Fully developed friction factors for three different inlet configurations and heat fluxes (filled symbols designate the start and end of the transition region for each inlet). Taken from Tam and Ghajar (1997).

The fully developed friction factor results for the three different inlet configurations shown in Figure 5.7 clearly establish the influence of heating rate on the beginning and end of the transition region for each inlet configuration (the filled symbols represent the start and end of the transition region). In the laminar and transition regions, heating seems to have a significant influence on the value of the friction factor. However, in the turbulent region, heating did not affect the magnitude of the friction factor. The significant influence of heating on the values of friction factor in the laminar and transition regions is directly due to the effect of secondary flow.

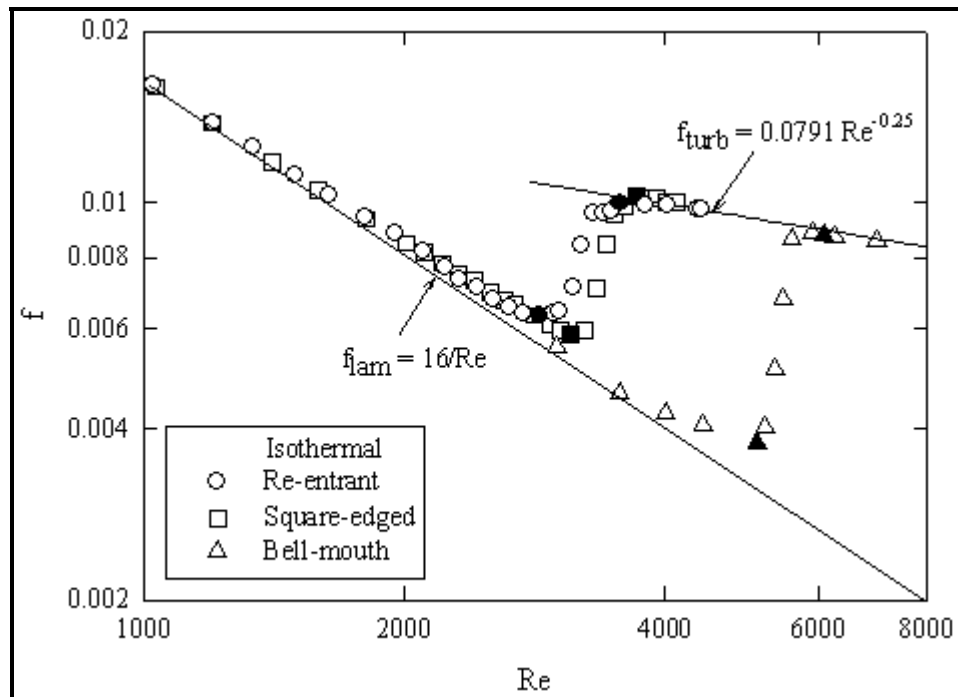


**Figure 5.8. Influence of different inlet configurations on the isothermal fully developed friction factors (filled symbols designate the start and end of the transition region for each inlet). Taken from Tam and Ghajar (1997).**

According to Tam and Ghajar (1997), the isothermal friction factors for the three inlet types showed that the range of the Reynolds number values at which transition flow exists is strongly inlet geometry dependent. Furthermore, heating caused an increase in the laminar and turbulent friction factors and an increase in the lower and upper limits of the isothermal transition regime boundaries. The transition Reynolds number ranges for the isothermal and non-isothermal (three different heating rates) and the three different inlets used in their study are summarized in Table 5.2. Figure 5.8 shows the influence of inlet configuration on the beginning and end of the isothermal fully developed friction factors in the transition region (the filled symbols represent the start and end of the transition region).

**Table 5.2. Transition Reynolds numbers for friction factor.**

Type of Inlet: Heat flux	Re-entrant inlet	Square-edged Inlet	Bell-mouth inlet
0 kW/m <sup>2</sup> (adiabatic)	2870 < Re < 3500	3100 < Re < 3700	5100 < Re < 6100
3 kW/m <sup>2</sup>	3060 < Re < 3890	3500 < Re < 4180	5930 < Re < 8730
8 kW/m <sup>2</sup>	3350 < Re < 4960	3860 < Re < 5200	6480 < Re < 9110
16 kW/m <sup>2</sup>	4090 < Re < 5940	4450 < Re < 6430	7320 < Re < 9560

Note that the fully developed friction factors in the laminar, turbulent and transition regions can be easily obtained from [5.2.16], [5.2.17] and [5.2.18], respectively, by setting the exponent on the viscosity ratio correction to unity (i.e. with  $m = 0$ ).

### Example 5.1: Heat transfer in the transition region

Ethylene glycol-distilled water mixture with a mass fraction of 0.6 and a volumetric flow rate of  $2.6 \times 10^{-4} \text{ m}^3/\text{s}$  (4.12 gpm) flows inside a plain tube with an inside diameter of 0.0158 m (0.622 in.) with a uniform wall heat flux boundary condition. For this flow, determine the Nusselt number at the location  $z/d_i = 90$  if the inlet configuration of the tube is: (a) re-entrant, (b) square-edged, and (c) bell-mouth. At this location, the local Grashof number is  $\text{Gr} = 51770$ . The physical properties of ethylene glycol-distilled water mixture at the location of interest are:  $\text{Pr} = 29.2$ ,  $v = 3.12 \times 10^{-6} \text{ m}^2/\text{s}$  and  $\mu_{\text{bulk}}/\mu_{\text{wall}} = 1.77$ .

**Solution:** For a plain tube with a known diameter and volumetric flow rate, the type of flow regime is determined before making any decision regarding which Nusselt number correlation to use. In this case, the local bulk Reynolds number is calculated with the absolute viscosity evaluated at the fluid bulk temperature:

$$\text{Re} = \frac{(Q/A) d_i}{v} = \frac{[(2.6 \times 10^{-4} \text{ m}^3/\text{s}) / (1.96 \times 10^{-4} \text{ m}^2)](0.0158 \text{ m})}{3.12 \times 10^{-6} \text{ m}^2/\text{s}} = 6713$$

$$\text{where } A = \pi d_i^2 / 4 = 1.96 \times 10^{-4} \text{ m}^2$$

Therefore, the flow regime is in the transition region for all three inlet configurations (thus use Eqs. [5.2.12] to [5.2.14] with  $z/d_i = 90$ ) and therefore Eq. [5.2.9] should be used with the constants  $a$ ,  $b$ ,  $c$  found in Table 5.1. However,  $\text{Nu}_{\text{lam}}$  and  $\text{Nu}_{\text{turb}}$  are the inputs to Eq. [5.2.9] and they need to be evaluated first from Eqs. [5.2.10] and [5.2.11], respectively. It should be mentioned that the correlations for  $\text{Nu}_{\text{lam}}$  and  $\text{Nu}_{\text{turb}}$  have no inlet dependency.

Applying Eq. [5.2.10]:

$$\begin{aligned} \text{Nu}_{\text{lam}} &= 1.24 \left[ \left( \frac{\text{Re} \text{Pr} d_i}{z} \right) + 0.025 (\text{Gr} \text{Pr})^{0.75} \right]^{1/3} \left( \frac{\mu_{\text{bulk}}}{\mu_{\text{wall}}} \right)^{0.14} \\ \text{Nu}_{\text{lam}} &= 1.24 \left[ \left( \frac{(6713)(29.2)}{90} \right) + 0.025 [(51770)(29.2)]^{0.75} \right]^{1/3} (1.77)^{0.14} = 19.9 \end{aligned}$$

Applying Eq. [5.2.11]:

$$\begin{aligned} \text{Nu}_{\text{turb}} &= 0.023 \text{Re}^{0.8} \text{Pr}^{0.385} \left( \frac{z}{d_i} \right)^{-0.0054} \left( \frac{\mu_{\text{bulk}}}{\mu_{\text{wall}}} \right)^{0.14} \\ \text{Nu}_{\text{turb}} &= 0.023 (6713)^{0.8} (29.2)^{0.385} (90)^{-0.0054} (1.77)^{0.14} = 102.7 \end{aligned}$$

Applying Eq. [5.2.9]:

$$\text{Nu}_{\text{trans}} = \text{Nu}_{\text{lam}} + \left\{ \exp[(a - \text{Re})/b] + \text{Nu}_{\text{turb}}^c \right\}^c$$

For re-entrant inlet:

$$Nu_{trans} = 19.9 + \left\{ \exp[(1766 - 6713)/276] + 102.7^{-0.955} \right\}^{-0.955} = 88.2$$

For square-edged inlet:

$$Nu_{trans} = 19.9 + \left\{ \exp[(2617 - 6713)/207] + 102.7^{-0.950} \right\}^{-0.950} = 85.3$$

For bell-mouth inlet:

$$Nu_{trans} = 19.9 + \left\{ \exp[(6628 - 6713)/237] + 102.7^{-0.980} \right\}^{-0.980} = 21.2$$

It is worth mentioning that for the re-entrant and square-edged inlets, the flow behaves normally. For the bell-mouth inlet, the Nusselt number is low in comparison to the other two inlets. This is because of the unusual behavior of the bell-mouth inlet noted earlier, i.e. the boundary layer along the tube wall is at first laminar and then changes through a transition region to the turbulent condition.

### Example 5.2: Non-isothermal fully developed friction factor

A plain tube with a bell-mouth inlet configuration is experiencing an  $8 \text{ kW/m}^2$  uniform wall heat flux boundary condition. The tube has an inside diameter of  $0.0158 \text{ m}$  ( $0.622 \text{ in.}$ ) and a volumetric flow rate of  $1.32 \times 10^{-4} \text{ m}^3/\text{s}$  ( $2.10 \text{ gpm}$ ). The liquid flowing inside the tube is ethylene glycol-distilled water mixture with a mass fraction of 0.34. Determine the fully developed friction factor at a location along the tube where the Grashof number is  $Gr = 60800$ . The physical properties of the ethylene glycol-distilled water mixture at the location of interest are:  $Pr = 11.6$ ,  $v = 1.39 \times 10^{-6} \text{ m}^2/\text{s}$  and  $\mu_{bulk}/\mu_{wall} = 1.14$ . Then recalculate the friction factor if a square-edged inlet is used instead.

**Solution:** For the calculation of the non-isothermal fully developed friction factor, it is necessary to determine the flow regime before making any decision regarding which friction factor correlation should be used. In this case, the local bulk Reynolds number needs to be calculated with the absolute viscosity evaluated at the fluid bulk temperature as follows:

$$Re = \frac{(Q/A) d_i}{v} = \frac{[(1.32 \times 10^{-4} \text{ m}^3/\text{s}) / (1.96 \times 10^{-4} \text{ m}^2)](0.0158 \text{ m})}{1.39 \times 10^{-6} \text{ m}^2/\text{s}} = 7679$$

$$\text{where } A = \pi d_i^2 / 4 = 1.96 \times 10^{-4} \text{ m}^2$$

From Table 5.2 for a bell-mouth inlet and a heat flux of  $8 \text{ kW/m}^2$ , the flow is in the transition region. Therefore, Eq. [5.2.18] with exponent m given by [5.2.19] is applied as follows:

$$f_{trans} = \left[ 1 + \left( \frac{Re}{A} \right)^B \right]^C \left( \frac{\mu_{bulk}}{\mu_{wall}} \right)^m$$

where the constants A, B, C and m are given in Table 5.1. Therefore,

$$f_{trans} = \left[ 1 + \left( \frac{Re}{5340} \right)^{-0.099} \right]^{-6.32} \left( \frac{\mu_{bulk}}{\mu_{wall}} \right)^{-2.58 - 0.42Gr^{-0.41}Pr^{2.46}}$$

$$f_{\text{trans}} = \left[ 1 + \left( \frac{7679}{5340} \right)^{-0.099} \right]^{-6.32} (1.14)^{-2.58 - 0.42 \times 60800^{-0.41} \times 11.6^{2.46}} = 0.0078$$

*Resolving the problem with a square-edged inlet.* For this inlet shape, the Reynolds number of the flow is the same as that of the bell-mouth inlet ( $\text{Re} = 7679$ ). However, it is necessary to check the type of flow regime for this particular inlet with  $8 \text{ kW/m}^2$  of heating. According to Table 5.2, the transition Reynolds number range for this case is  $3860 < \text{Re} < 5200$ , which means that the flow in this case is turbulent and [5.2.17] is the appropriate equation to use:

$$f_{\text{turb}} = \left( \frac{0.0791}{\text{Re}^{0.25}} \right) \left( \frac{\mu_{\text{bulk}}}{\mu_{\text{wall}}} \right)^m = \left( \frac{0.0791}{7679^{0.25}} \right) (1.14)^{-0.25} = 0.0082$$

## 5.3 Mechanisms of Turbulent Heat Transfer Augmentation

**Extended Surface Area.** One way to increase turbulent heat transfer coefficients is to increase the surface area in contact with the fluid to be heated or cooled. Some enhancement correlations incorporate a surface area ratio factor to account for this effect while others do not. It is common practice to develop heat transfer correlations for internal flows in enhanced tubes based on the internal *nominal* surface area, i.e. that of the perimeter of the maximum internal diameter of the tube  $d_i$  (corrugations) or at the base of any internal enhancement (fins or ribs) [*all correlations in this chapter follow this format*]. This heat transfer coefficient is used directly in calculating the overall heat transfer coefficient at this diameter without use of a surface area ratio. It is *not* common practice to reduce single-phase turbulent flow heat transfer data relative to the total internal surface area. If internal fin efficiency becomes important, it is thus difficult to determine the effect from nominal internal area correlations. However, commonly used fins and ribs are quite small in height compared to external fins and their fin efficiencies are normally over 0.95 while for copper tubes they approach 0.99. Since the original experimental data would normally have been reduced to a heat transfer correlation without correcting for fin efficiency, this effect is already incorporated for tubes of that same material. Thus, any effect of fin efficiency can normally be safely ignored. On the other hand, twisted tape inserts normally fit loosely inside a tube (thus they have poor thermal contact to the inner tube wall) and hence the surface area of a twisted tape is not considered to be heat transfer surface area, only that of the plain tube perimeter in which it is installed.

**Surface Roughness.** The internal roughness of the tube surface is well known to increase the turbulent heat transfer coefficient. Normally, a smooth internal surface of a tube is assumed in design, as in all the correlations presented above. However, the Churchill (1983) correlation can be solved for the friction factor of rough tubes with a commercial pipe roughness of  $e$ :

$$\sqrt{\frac{2}{f}} = -2.46 \ln \left[ \frac{e}{d_i} + \left( \frac{7}{\text{Re}} \right)^{0.9} \right] \quad [5.3.1]$$

This form of friction factor correlation has also been modified for predicting heat transfer and pressure drop in enhanced tubes as will be seen later and works in conjunction with [5.2.7].

**Swirl.** Swirl of the flow is also known to augment heat transfer. Internal helical fins or ribs, corrugations and twisted tapes impart a swirl effect on the fluid. This tends to increase the effective flow length of the fluid through the tube, which increases heat transfer and pressure drop. For internal helical fins, ribs and

corrugations however, the effect of swirl tends to decrease or disappear all together at higher helix angles since the fluid flow then simply passes axially over the fins or ribs. For twisted tape inserts, the effect of swirl on augmentation plays an important role.

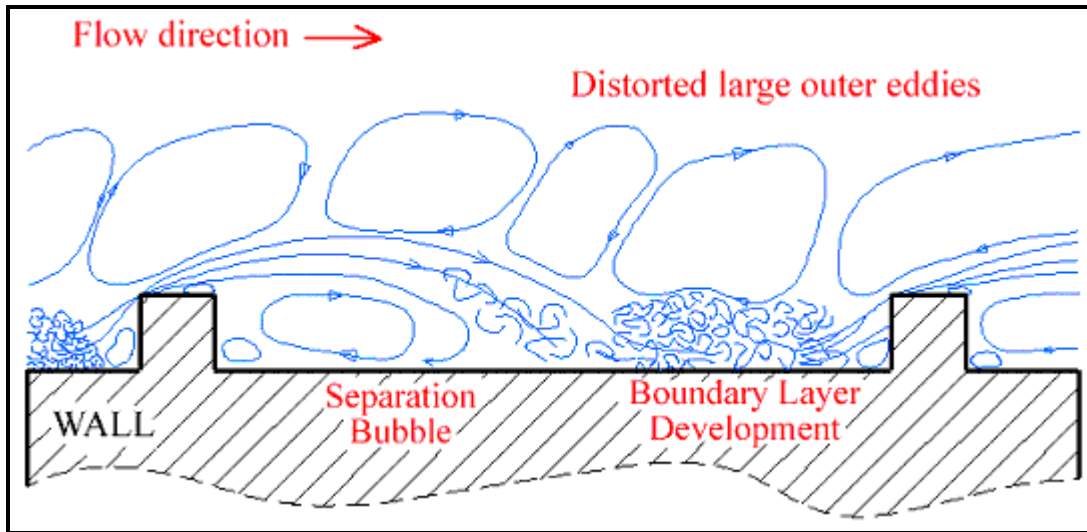


**Figure 5.9. Turbulent flow structure over a two-dimensional rib from Rabas and Arman (1992).**

**Boundary Layer Displacement.** The displacement of the turbulent boundary layer is a particularly important heat transfer mechanism for augmenting heat transfer. Figure 5.9 depicts a diagram that Rabas and Arman (1992) use to illustrate this process. For essentially a two-dimensional flow, it shows the separation of the flow as it passes over a transverse rib (creating a small recirculation zone in front of the rib), the formation of a recirculation zone behind the rib, flow reattachment on the base wall and then flow up and over the next rib. Recirculation eddies are formed above these flow regions. Rabas and Arman commented as follows on a rib's effect on the heat transfer process:

- There are six distinct heat transfer regions, although some are more important than others (the upstream recirculation zone, the rib's upstream, top and downstream faces, the downstream recirculation zone, and finally the boundary layer reattachment/redevelopment zone);
- Two peaks in local heat transfer occur, one at the top of the rib and the other in the downstream recirculation zone just before the reattachment point;
- Heat transfer enhancement increases substantially with increasing Prandtl number, so that for large  $\text{Pr}$  fluids heat transfer is dominated by flow around the rib surfaces;
- The surface-averaged heat transfer performance is directly proportional to the maximum enhancement at the rib;
- The point of the local maximum in the heat transfer coefficient on the base wall between ribs moves upstream towards the back of the rib with increasing Reynolds and Prandtl numbers, and is located on the base wall between the reattachment point and the point of maximum wall shear stress;
- The Prandtl number has the same influence on thermal performance in the downstream recirculation region as at the rib;
- The high heat transfer augmentation in the downstream recirculation region is due to the high turbulence levels near the surface;
- Two more local maximums in heat transfer occur at large Reynolds roughness numbers in the front recirculation zone before the rib and on the rear face of the rib.

Webb, Eckert and Goldstein (1971) have presented an interesting composite diagram of the recirculation and reattachment zones as a function of rib spacing for ribs oriented normal to the flow. Figure 5.10 shows this diagram where the flows are characterized by the axial rib pitch to rib height ( $p/e$ ) ratio. For closely spaced ribs (at bottom of diagram), one large recirculation eddy is trapped between two successive ribs with two small eddies in the corners. As the  $p/e$  ratio increases, the large recirculation eddy elongates until it is broken and a reattachment zone is formed, such that two dominant eddies exist at larger ratios.

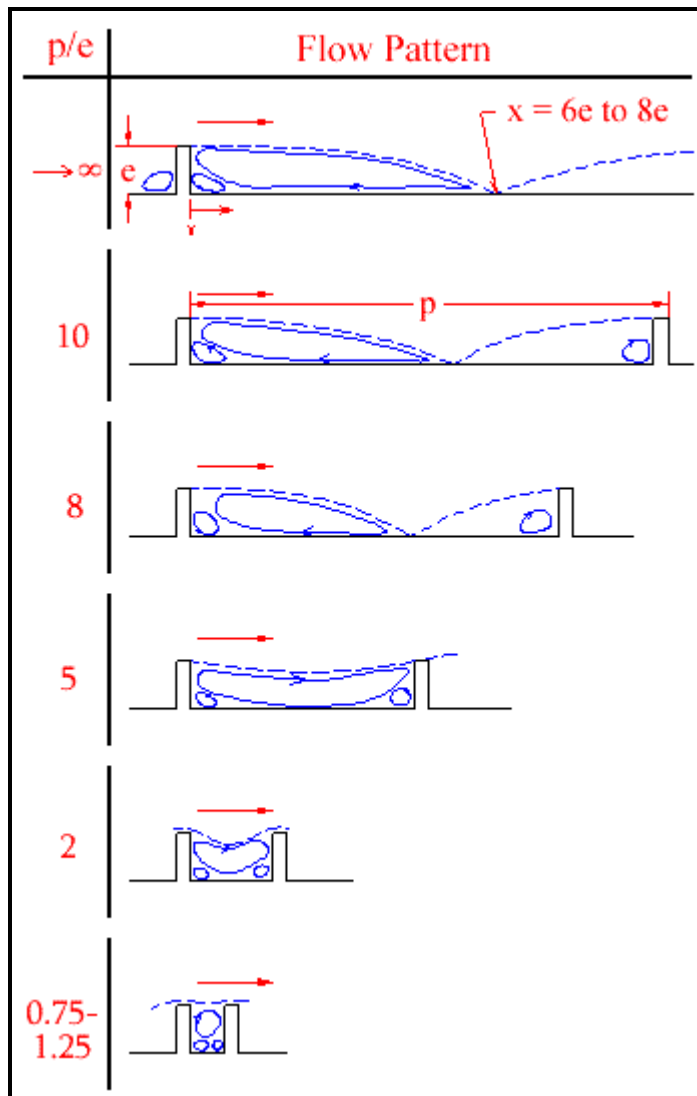


Figure 5.10. Recirculation flow patterns over transverse ribs as a function of rib spacing from Webb, Eckert and Goldstein (1971).

## 5.4 Turbulent Heat Transfer with Twisted Tape Inserts

A schematic diagram of a twisted tape insert inside a tube is shown in Figure 5.11. The enhancement is defined geometrically by the thickness of the tape  $\delta$  and its twist ratio,  $y$ . The twist ratio is defined as the axial length for a  $180^\circ$  turn of the tape divided by the internal diameter of the tube. **This is the most**

common definition used in research literature and that used here. It is also common to use the axial length for a complete  $360^\circ$  turn instead in commercial literature; hence, double-check the definition used before applying a twisted tape prediction method or using experimental results from manufacturer's literature or a scientific publication and then make sure to indicate the definition used in the resulting heat exchanger specification sheet.

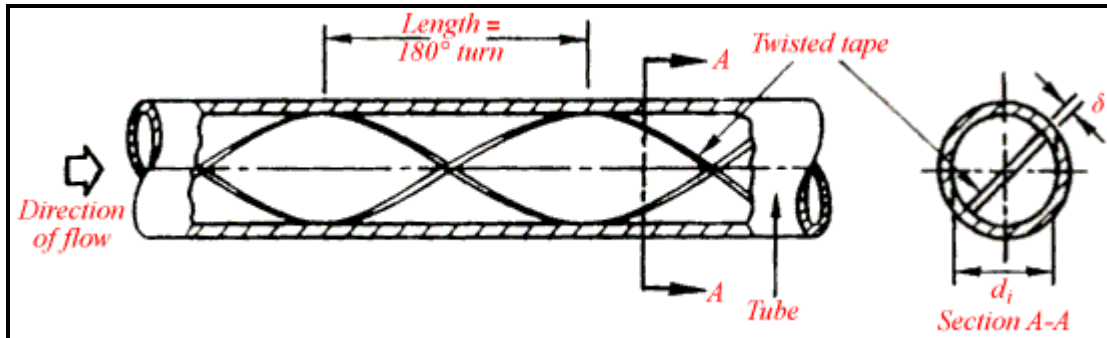


Figure 5.11. Diagram of a twisted tape insert inside a tube.

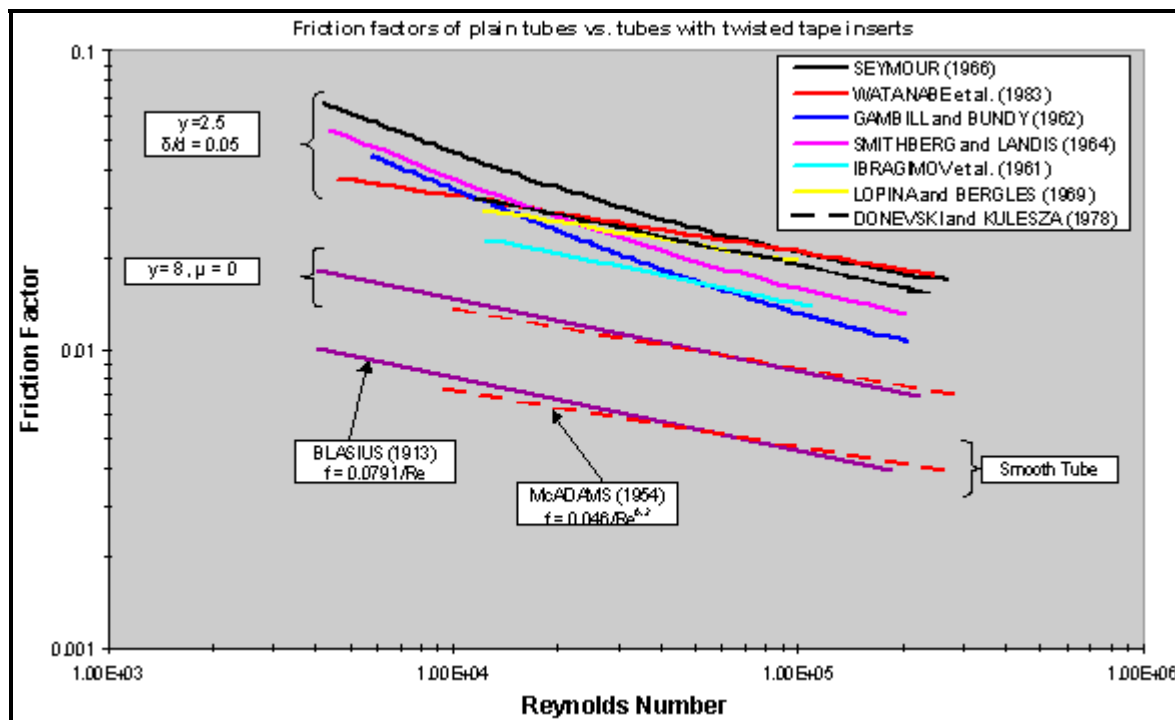


Figure 5.12. Isothermal friction factors in plain tubes with and without tape inserts.

Numerous experimental studies have investigated turbulent flow heat transfer with twisted tape inserts and proposed heat transfer and pressure drop prediction methods. Manglik and Bergles (1992) have presented composite graphs of these prediction methods from selected studies. Figure 5.12 depicts the friction factor correlations for a smooth tube, those of Blasius (1913) and McAdams (1954), that for flow in a half-tube ( $y = \infty$ ,  $\delta = 0$ ) based on its hydraulic diameter, and those from seven studies evaluated for the same choice of twisted tape ( $y = 2.5$ ,  $\delta/d_i = 0.05$ ). First of all, one sees that an important part of the increase in friction factor (based on the internal tube perimeter for all cases) is caused by the flow being

divided into two smaller flow channels. That is, compare the plain tube curves to those for flow in the tube whose cross-section is divided by an infinitesimally thin wall. Secondly, one sees that the effect of the swirl and longer flow path for the tape results in a second important increase in friction factor. The methods presented demonstrate a significant discrepancy in their predictions with one another.

Figure 5.13 and Figure 5.14 depict the Nusselt number predictions from the same studies, evaluated for air and water, respectively. The Nusselt numbers have been divided by the bulk-to-wall viscosity ratio, Prandtl number ratio or temperature ratio to correct for physical property effects for the particular method to remove this effect from the graph. For air, there is reasonable agreement between the prediction methods, except for the method of Ibragimov, Nomofelov and Subbotin (1961). The level of augmentation starts out at about a factor of two at the lower Reynolds numbers and tends to decrease with increasing Reynolds number. For water, the level of augmentation also starts out at about a factor of two at the lower Reynolds numbers and tends to decrease with increasing Reynolds number. There is a larger divergence between the prediction methods for water than for air.

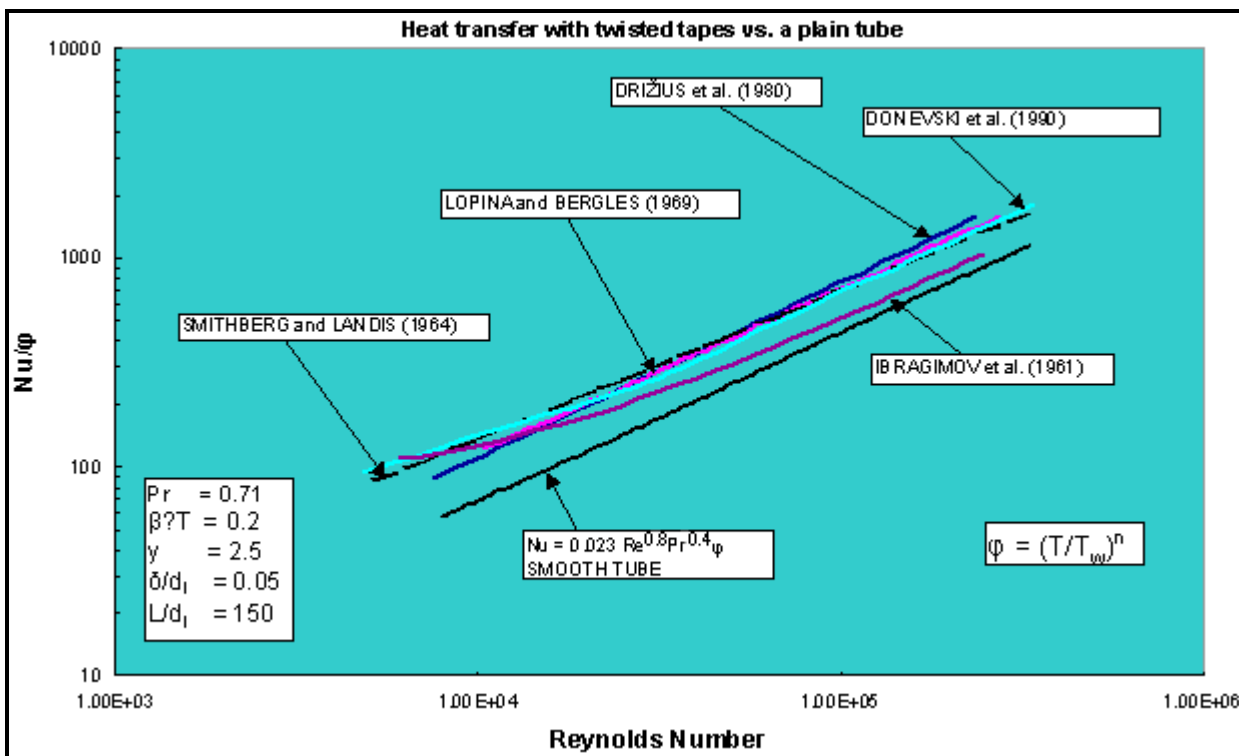
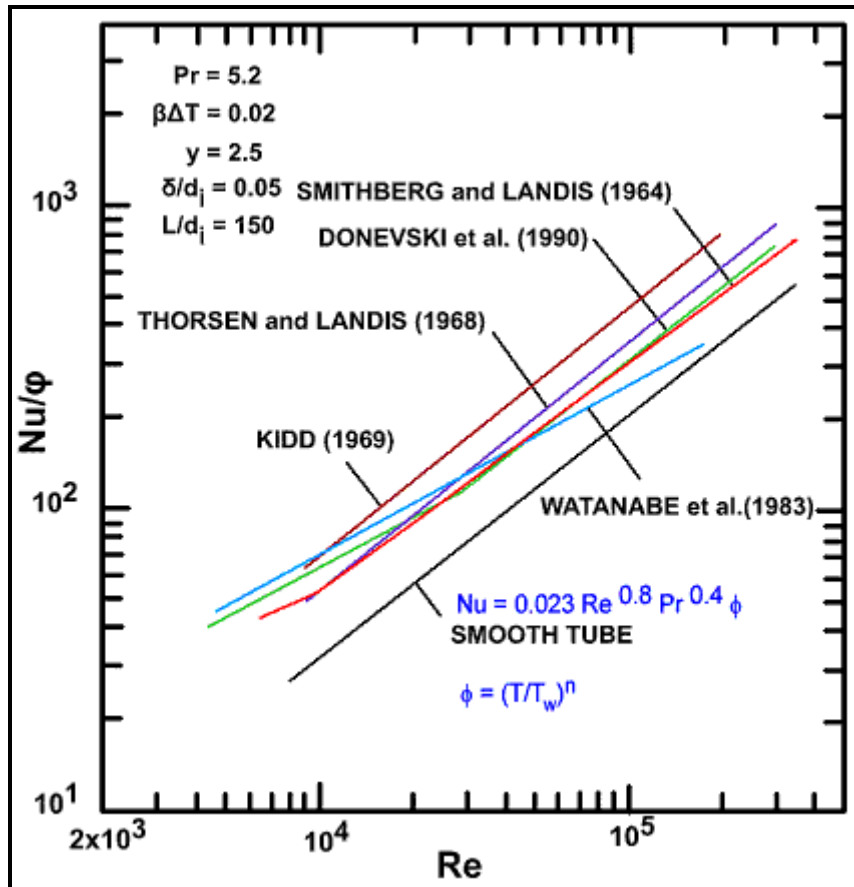


Figure 5.13. Nusselt numbers in plain tubes with and without tape inserts for air.



**Figure 5.14. Nusselt numbers in plain tubes with and without tape inserts for water.**

Manglik and Bergles (1992) proposed the following friction factor correlation for tubes with twisted tape inserts and is the recommended method here for general use:

$$f = \frac{0.0791}{Re^{0.25}} \left[ \frac{\pi}{\pi - 4(\delta/d_i)} \right]^{1.75} \left[ \frac{\pi + 2 - 2(\delta/d_i)}{\pi - 4(\delta/d_i)} \right]^{1.25} \left[ 1 + \frac{2.752}{y^{1.29}} \right] \quad [5.4.1]$$

The value of  $Re$  in this expression is based on the flow in the tube without the insert, i.e. bare tube Reynolds number as in [5.2.2],  $y$  is the twist ratio based on the axial length for a  $180^\circ$  turn,  $\delta$  is the thickness of the tape and  $d_i$  is the internal diameter of the bare tube. This expression described within about  $\pm 5\%$  most of the friction factor data available in the literature covering twist ratios from about 2.5 to 10, which are of most industrial interest. Their corresponding heat transfer correlation for turbulent flows gives the twisted tape Nusselt number as:

$$\frac{Nu_{tt}}{Nu_{y=\infty}} = 1 + \frac{0.769}{y} \quad [5.4.2]$$

where the Nusselt number for the twisted tape  $Nu_{tt}$  is defined as:

$$Nu_{tt} = \frac{\alpha_{tt} d_i}{k} \quad [5.4.3]$$

The Nusselt number for a straight tape without twist ( $y = \infty$ ) is:

$$Nu_{y=\infty} = 0.023 Re^{0.8} Pr^{0.4} \left[ \frac{\pi}{\pi - 4(\delta/d_i)} \right]^{0.8} \left[ \frac{\pi + 2 - 2(\delta/d_i)}{\pi - 4(\delta/d_i)} \right]^{0.2} J_\mu \quad [5.4.4]$$

The physical property correction factor  $J_\mu$  for liquids is given by

$$J_\mu = \left( \frac{\mu_{bulk}}{\mu_{wall}} \right)^n \quad [5.4.5]$$

The exponent  $n$  is equal to 0.18 for liquid heating and 0.30 for liquid cooling. The correction factor for gases is:

$$J_\mu = \left( \frac{T_{bulk}}{T_{wall}} \right)^m \quad [5.4.6]$$

Many publications also refer to  $J_\mu$  as  $\phi$ . The exponent  $m$  is equal to 0.45 for gas heating and 0.15 for gas cooling. The method predicts most of their experimental results to within  $\pm 10\%$  and covers twist ratios from about 2.5 to 10 (based on the 180° definition).

Some other studies of interest on twisted tapes are: Gambill and Bundy (1962), Smithberg and Landis (1964), Seymour (1966), Thorsen and Landis (1968), Kidd (1969), Lopina and Bergles (1969), Drizius, Shkema and Shlanciauskas (1980), Watanabe, Taira and Mori (1983) and Donevski et al. (1990).

## 5.5 Turbulent Heat Transfer in Corrugated Tubes

A significant number of corrugated tube types have been tested over the years. For example, Withers (1980a, 1980b) investigated 14 configurations for water, Li et al. (1982) studied 20 configurations for water, Sethumadhavan and Rao (1986) tested 5 configurations for water-glycerine and Mehta and Rao (1988) looked at 11 configurations for water. Withers (1980a) gave the following design methods for Wolverine Korodense tubes applicable to water in the range  $10^4 < Re < 10^5$  and temperatures below 88°C (190°F). His friction factor correlation was developed by modifying a rough tube correlation to obtain:

$$\sqrt{\frac{2}{f}} = -2.46 \ln \left[ r + \left( \frac{7}{Re} \right)^m \right] \quad [5.5.1]$$

His correlation for the heat transfer coefficient  $\alpha_{ct}$  for Wolverine Korodense tubes is obtained from the following dimensional equation in U.S. units:

$$\alpha_{ct} = \frac{c_p \dot{m} \sqrt{f/2}}{\beta_{ct} \text{Pr} (\text{Re} \sqrt{f/2})^{0.127} + \gamma} \quad [5.5.2]$$

$\text{Re}$  is the plain tube Reynolds number based on the maximum internal diameter of the corrugated tube  $d_i$  and  $\text{Pr}$  is the Prandtl number. The resulting heat transfer coefficient is in  $\text{Btu}/\text{h ft}^2\text{F}$ , the specific heat is in  $\text{Btu/lb}^\circ\text{F}$  and the mass velocity is in  $\text{lb}/\text{h ft}^2$ . For the Korodense type MHT tube, the values of the design constants are:  $m = 0.44$ ,  $r = 0.00595$  and  $\gamma = 2.56$ . This class of Korodense tube has a medium corrugation severity. For the Korodense type LPD tube, the values of the design constants are:  $m = 0.61$ ,  $r = 0.00088$  and  $\gamma = 3.74$ . This class of Korodense tube has a lower corrugation severity and has a pressure drop of about  $\frac{1}{2}$  that of MHT but with lower thermal performance by about 25%. Hence, the user can choose the most appropriate version for his application. The value of his empirical constant  $\beta_{ct}$  is specific to each tube size and tube type. It varies in value from about 5.0 to 7.2 for specific tube part numbers with 6.0 a medium value for all. The actual values for these parameters can be found in the appropriate *Wolverine Engineering Databook II* table on Korodense tubes. The friction factor is placed in equation [5.2.7] to calculate the pressure drop for a corrugated tube of length  $L$ .

### Example 5.3: Heat transfer and pressure drop in a corrugated tube

For a liquid flowing inside a corrugated tube (Korodense type MHT), determine the local heat transfer coefficient and pressure drop at a mass velocity is  $500 \text{ kg/m}^2\text{s}$  assuming the internal diameter is 15.75 mm (0.620 in.) and the tube length is 3 m (9.84 ft). The physical properties of the fluid are:  $\rho = 997 \text{ kg/m}^3$ ;  $\mu_{bulk} = 0.0007 \text{ Ns/m}^2$ ;  $\mu_{wall} = 0.0005 \text{ Ns/m}^2$ ;  $k = 0.6 \text{ W/m K}$ ;  $c_p = 4200 \text{ J/kg K}$ ;  $\text{Pr} = c_p \mu/k = 4.9$ .

**Solution:** For the Korodense type MHT tube, the values of the design constants are:  $m = 0.44$ ,  $r = 0.00595$  and  $\gamma = 2.56$ . The value of the empirical constant  $\beta_{ct}$  is assumed to be 6.0. The Reynolds number  $\text{Re}$  is determined using [5.2.2] as:

$$\text{Re} = \frac{\dot{m} d_i}{\mu} = \frac{500(0.01575)}{0.0007} = 11250$$

The friction factor is obtained from [5.5.1]:

$$\begin{aligned} \sqrt{\frac{2}{f}} &= -2.46 \ln \left[ r + \left( \frac{7}{\text{Re}} \right)^m \right] = -2.46 \ln \left[ 0.00595 + \left( \frac{7}{11250} \right)^{0.44} \right] \\ \sqrt{f/2} &= 0.1309 \end{aligned}$$

Applying the viscosity ratio correction of  $(\mu_{bulk}/\mu_{wall})^{-0.25} = 0.919$ , this value becomes 0.1260. The correlation for the heat transfer coefficient  $\alpha_{ct}$  for Korodense tubes is in U.S. units, so that  $c_p = 4200 \text{ J/kg K} = 1.003 \text{ Btu/lb}^\circ\text{F}$  and the mass velocity is  $367905 \text{ lb/h ft}^2$ . From [5.5.2] and applying the viscosity ratio correction factor:

$$\alpha_{ct} = \frac{c_p \dot{m} \sqrt{f/2}}{\beta_{ct} \text{Pr} (\text{Re} \sqrt{f/2})^{0.127} + \gamma} \left( \frac{\mu_{bulk}}{\mu_{wall}} \right)^{0.14}$$

$$= \frac{1.003(367905)(0.1260)}{6.0(4.9)(11250(0.1260))^{0.127} + 2.56} \left( \frac{0.0007}{0.0005} \right)^{0.14}$$

$$\alpha_{ct} = 637.5 \text{ Btu/h ft}^2 \text{°F} = 3620 \text{ W/m}^2 \text{K}$$

The pressure drop in a tube of length  $L = 3.0$  m is obtained by first determining the friction factor and then applying [5.2.7] to obtain:

$$\Delta p = \frac{2f \dot{m}^2 L}{\rho d_i} = \frac{2(0.03175)(500^2)(3.0)}{(997)(0.01575)} = 3033 \text{ Pa}$$

## 5.6 Turbulent Heat Transfer in Internally Finned or Ribbed Tubes

Withers (1980b) proposed methods for internally helically finned (or ribbed or ridged) Wolverine Turbo-Chil and S/T Trufin tubes that are similar to those he developed for corrugated tubes. In fact, the same friction factor expression [5.5.1] is assumed but uses different values of the empirical constants  $r$  and  $m$ . His correlation for the heat transfer coefficient  $\alpha_{ft}$  for these tubes is obtained from the following dimensional equation that is slightly different than [5.5.2]:

$$\alpha_{ft} = \frac{c_p \dot{m} \sqrt{f/2}}{\beta_{ft} \text{Pr} (\text{Re} \sqrt{f/2})^{0.136} + \gamma} \quad [5.6.1]$$

Here,  $\text{Re}$  is the plain tube Reynolds number based on the maximum internal diameter of the internally finned tube,  $d_i$ , which is the root diameter at the base of internal fins. The resulting heat transfer coefficient is in  $\text{Btu/h ft}^2 \text{°F}$ , the specific heat is in  $\text{Btu/lb°F}$  and the mass velocity is in  $\text{lb/h ft}^2$ . For internally finned tubes, the possible values of  $r$  are 0.0, -0.0004, -0.0022 and -0.0020 depending on the particular tube size and wall thickness. Depending on the particular tube, the values of the correction factor  $\beta_{ft}$  range from about 4.43 to 4.72, the values of  $\gamma$  range from about 3.31 to 5.34, and the values of exponent  $m$  for the friction factor expression range from 0.58 to 0.73. Specific values for these parameters can be found in the *Wolverine Engineering Databook II* table on Turbo-Chil Characteristics for a particular tube.

For Wolverine Turbo-B types of tubes, the internal heat transfer coefficient is correlated relative to the dimensionless Sieder and Tate (1936) turbulent flow heat transfer equation by changing the leading constant, so that:

$$\frac{\alpha_{ft} d_i}{k} = C_{fh} \text{Re}^{0.8} \text{Pr}^{1/3} \left( \frac{\mu_{bulk}}{\mu_{wall}} \right)^{0.14} \quad [5.6.2]$$

where the correlation is based on the maximum internal tube diameter  $d_i$  and  $\alpha_{ft}$  is the heat transfer coefficient. In this expression,  $C_{fh}$  is the empirical leading constant in place of the normal plain tube

value of 0.027. Note that this correlation uses the Prandtl number to the 1/3 power,  $\text{Pr}^{1/3}$ . For the original Turbo-B tube version,  $C_{\text{ft}}$  is equal to 0.060 for 19.05 mm (3/4 in.) tubes and is equal to 0.061 for 25.4 mm (1 in.) versions. The frictional pressure drop is fit by a Blasius type expression:

$$f = \frac{C_{\text{ft}}}{\text{Re}^D} \quad [5.6.3]$$

Here, the values of  $C_{\text{ft}}$  and D are required and depend on the tube type. For instance, for the 19.05 mm (3/4 in.) original Turbo-B version,  $C_{\text{ft}} = 0.198$  and  $D = 0.267$ .  $\text{Re}$  is based on equation [5.2.2] using the maximum internal tube diameter for  $d_i$ .

Arman and Rabas (1992) studied the effect of the specific two-dimensional disruption shape on heat transfer and friction factor using a non-orthogonal, body-fitted numerical code. Figure 5.15 depicts the disruption shapes they considered: semicircular, trapezoidal, sine and arc. They presented graphs showing the local variation in wall shear stress and heat transfer for these geometries and a tabular summary of results. Interestingly, they did not find a large difference in mean heat transfer performance in comparisons at equal e/p ratios, where e is the height of the disruption and p is the axial pitch. The trapezoidal shape gave the best performance but only on the order of 10% better than the others.

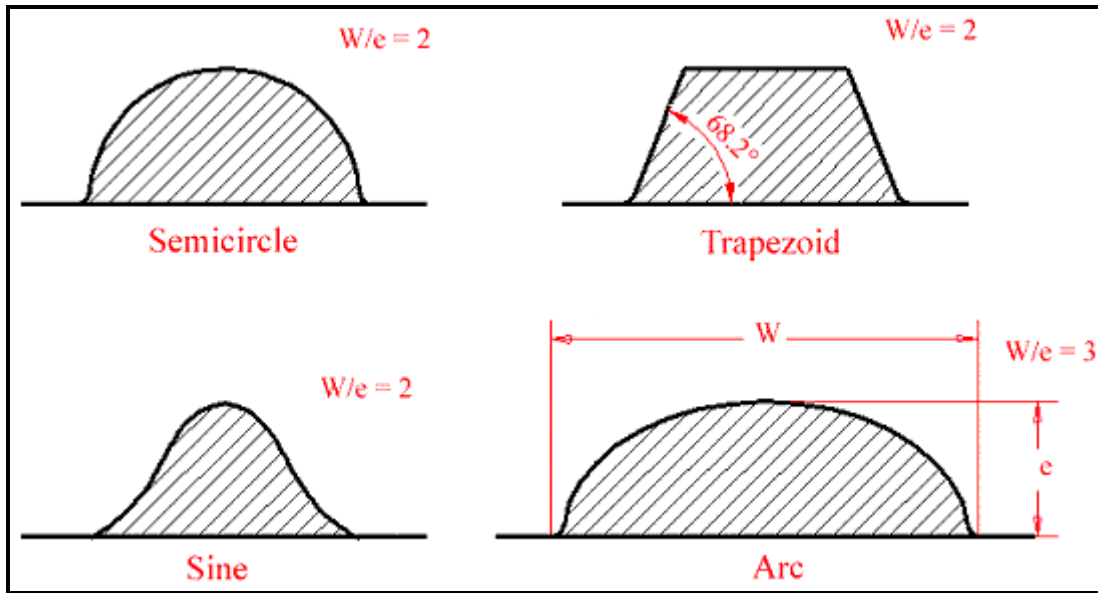


Figure 5.15. Disruption shapes considered by Arman and Rabas (1992).

Nunner (1956) apparently did the first systematic experimental investigation on the effect of disruption shape on heat transfer and friction factor. For four tubes plus one plain tube, the experiments were conducted on three different shapes and two different p/e ratios. The cross-sectional shapes were essentially square ( $p/e = 20$ ), hemispherical ( $p/e = 20$  and  $80$ ) and arc ( $p/e = 80$ ). Figure 5.16 presents curve fits to their Nusselt numbers for these disruption shapes while Figure 5.17 shows the corresponding friction factors for these disruption shapes. The graphs cover both laminar and turbulent flows. For the latter at  $\text{Re} > 2300$ , the square shape has the highest heat transfer performance but also the highest friction factor.

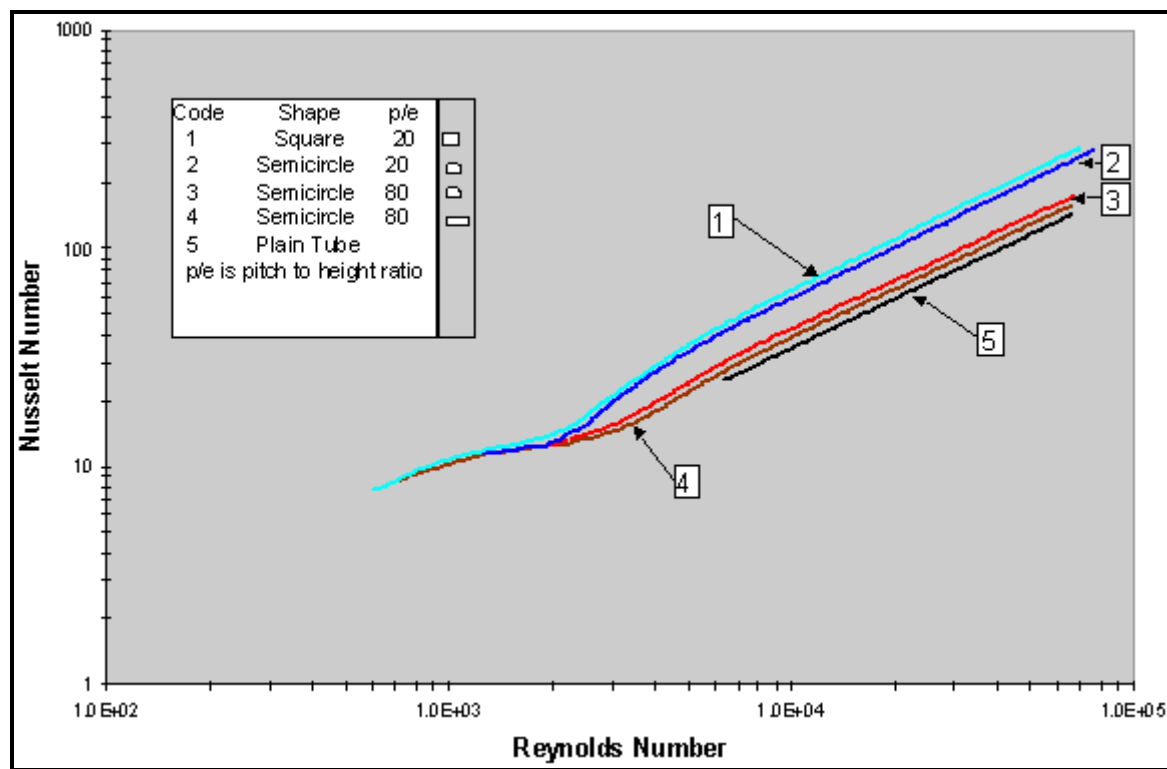


Figure 5.16. Heat performance of disruption shapes from Nunner (1956).

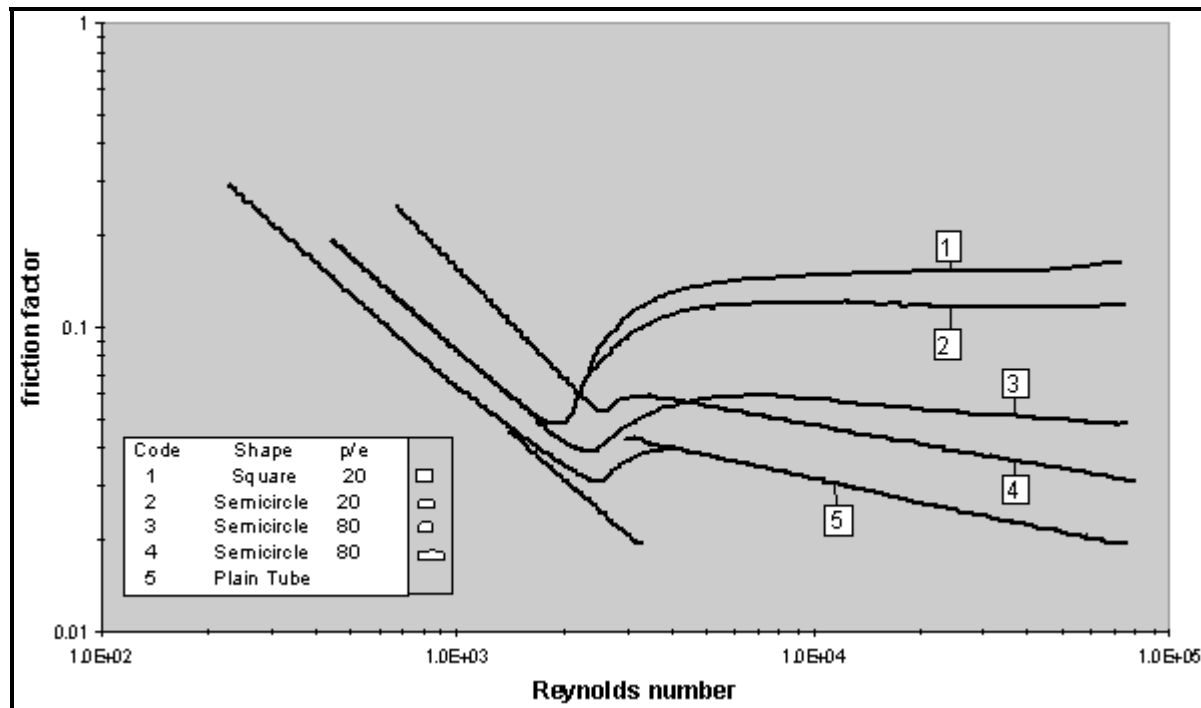


Figure 5.17. Friction factors of disruption shapes from (1956).

Carnavos (1979) proposed heat transfer and friction factor correlations for internally finned tubes in the turbulent flow regime based on experimental tests with 21 tube geometries, including axial fins and helical fins up to 30°. His database covered tests with air, water and an ethylene glycol/water mixture. His heat transfer correlation is:

$$\frac{Nu_{ft}}{Nu_{D-B}} = \frac{\alpha_{ft} d_h / k}{\alpha_{pt} d_i / k} = \left[ \frac{d_i}{d_{im}} \left( 1 - \frac{2e}{d_i} \right) \right]^{-0.2} \left( \frac{d_i d_h}{d_{im}^2} \right)^{0.5} \sec^3 \beta \quad [5.6.4]$$

In this correlation,  $Nu_{D-B}$  is the plain tube Nusselt number given by the Dittus-Boelter equation [5.2.1] where  $Re$  in that expression is based on equation [5.2.2] using the maximum internal tube diameter for  $d_i$ . The hydraulic diameter  $d_h$  is given by:

$$d_h = \frac{4A_{fa}}{A_a} \quad [5.6.5]$$

where  $A_{fa}$  is the actual free flow cross-sectional area in  $m^2$  and  $A_a$  is the actual heat transfer area per unit length in  $m^2/m$ . The meltdown internal diameter  $d_{im}$  in the above expression is that which would exist if the fins were melted down and added to the internal perimeter of the tube. The helix angle of the fins with respect to the axis of the tube is  $\beta$ . His corresponding friction factor expression is:

$$\frac{f_{ft}}{f_{Blasius}} = \frac{d_{im}}{d_i} \sec^{0.75} \beta \quad [5.6.6]$$

This expression gives the finned tube friction factor relative to the Blasius (1913) friction factor equation for a plain, smooth tube:

$$f_{Blasius} = \frac{0.046}{Re^{0.2}} \quad [5.6.7]$$

$Re$  is based on equation [5.2.2] using the maximum internal tube diameter for  $d_i$ . These correlations fit his database to within about ±10%. This expression does not cover helix angles above 30° and it does *not* extrapolate well to higher values. It is applicable to  $10^4 < Re < 10^5$  and  $0.7 < Pr < 30$ . The finned tube friction factor obtained with [5.6.6] can be placed in equation [5.2.7] to calculate the pressure drop for an internally finned tube of length  $L$ .

Ravigururajan and Bergles (1985) have proposed what is here considered to be the most general and accurate method for predicting heat transfer and pressure drop inside internally ribbed tubes (and plain tubes with coiled wire inserts). Their method is also applicable to most internally finned tubes and is hence given in this section and uses the same nomenclature as the methods above. Figure 5.18 depicts the rib geometries and profiles (and wire geometry) that they included in their study where  $e$  is the height of the rib or diameter of the wire,  $p$  is the axial pitch from one rib (or wire) to the next,  $\beta$  is the helix angle of the rib or wire relative to the tube axis,  $\beta_{rib}$  is the profile contact angle of the rib to the internal surface of the tube and  $n_{corners}$  is the number of sharp corners of the rib facing the flow (two for triangular or rectangular cross-section ribs and infinity for smoother profiles). The profile contact angle for a circular sector and circular profiles is taken as 90°. Their experimental database was formed from the results from 17 published studies covering both liquids and gases. Their method is applicable to the following range of parameters:  $0.1 < e/d_i < 0.2$ ,  $0.1 < p/d_i < 7.0$ ,  $0.3 < \beta/90 < 1.0$ ,  $5000 < Re < 250000$  and  $0.66 < Pr < 37.6$ .

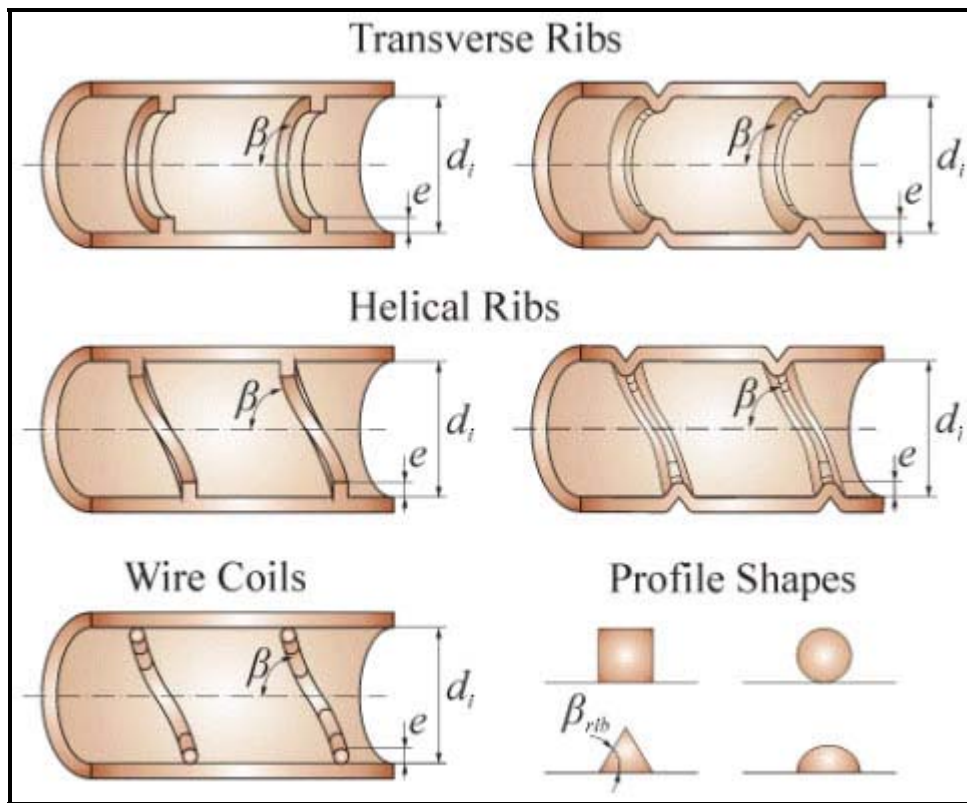


**Figure 5.18. Internal enhancement geometries and profile shapes considered by Ravigururajan and Bergles (1985).**

Their ribbed tube friction factor is correlated as a ratio to the value for a smooth tube of the same internal diameter as:

$$\frac{f_{\text{ft}}}{f} = \left\{ 1 + \left[ 29.1 \text{Re}^{(0.67 - 0.06 p/d_i - 0.49 \beta/90)} \left( \frac{e}{d_i} \right)^{(1.37 - 0.157 p/d_i)} \cdot \left( \frac{p}{d_i} \right)^{(-0.00000166 \text{Re} - 0.33 \beta/90)} \left( \frac{\beta}{90} \right)^{(4.59 + 0.00000411 \text{Re} - 0.15 p/d_i)} \cdot \left( 1 + \frac{2.94}{n_{\text{corners}}} \right) \sin \beta_{\text{rib}} \right]^{15/16} \right\}^{16/15} \quad [5.6.8]$$

Equation [5.2.6] is used to determine the friction factor of the reference tube (smooth, plain internal surface tube) applying the wall-to-bulk property ratios as noted for that expression. The pressure drop is then obtained applying [5.2.7] using the ribbed tube friction factor in place of the plain tube value and using the diameter at the base of the ribs for  $d_i$ .

Their ribbed tube heat transfer correlation is

$$\frac{\alpha_{ft}}{\alpha_{pt}} = \left\{ 1 + \left[ 2.64 \text{Re}^{0.036} \left( \frac{e}{d_i} \right)^{0.212} \left( \frac{p}{d_i} \right)^{-0.21} \left( \frac{\beta}{90} \right)^{0.29} \text{Pr}^{-0.024} \right]^7 \right\}^{1/7} \quad [5.6.9]$$

Equation [5.2.8] is used to determine  $\alpha_{pt}$  with [5.2.6] used to determine the friction factor of the reference tube (smooth, plain internal surface tube) applying the wall-to-bulk property ratios as noted for these expressions. Note that the heat transfer correlation does not contain any shape function and that the enhancement dimensions primarily control the level of augmentation while the flow parameters Re and Pr have small exponents and hence little influence.

Their friction factor correlation predicted 96% of their database to within  $\pm 50\%$  and 77% to within  $\pm 20\%$  while their heat transfer correlation predicted 99% of their database to within  $\pm 50\%$  and 69% to within  $\pm 20\%$ , for all five types of ribs and coiled wires they addressed. As a further note about this method, numerous comparisons to other independent or newer data and even to single-phase microfin data (*unpublished comparisons made by the present author*) show that these independent results are nearly always predicted to within  $\pm 20\%$ , even when extrapolating the method to lower values of  $e/d_i$ ,  $p/d_i$  and  $\beta/90$ . Thus, this method is both accurate and reliable. Furthermore, personal experience has shown that for trapezoidal profile ribs with rounded corners (typical of most commercially available ribbed tubes), the heat transfer correlation works well without modification while the friction factor is close to the mean of the values determined with  $\beta_{ribs} = 2$  and  $\beta_{ribs} = \infty$ .

#### Example 5.4: Heat transfer and pressure drop in a ribbed tube

For a liquid flowing inside a ribbed tube ( $e = 1.4$  mm,  $\beta = 30^\circ$  with 20 rectangular ribs), determine the local heat transfer coefficient and pressure drop at a mass velocity is  $500 \text{ kg/m}^2\text{s}$  assuming the internal diameter at the root of the ribs is  $15.75$  mm (0.620 in.) and the tube length is  $3$  m (9.84 ft). The physical properties of the fluid are:  $\rho = 997 \text{ kg/m}^3$ ;  $\mu_{bulk} = 0.0007 \text{ Ns/m}^2$ ;  $\mu_{wall} = 0.0005 \text{ Ns/m}^2$ ;  $k = 0.6 \text{ W/m K}$ ;  $c_p = 4200 \text{ J/kg K}$ ;  $\text{Pr} = c_p \mu / k = 4.9$ .

**Solution:** Applying [5.1.1] the axial pitch is found to be  $4.285$  mm. The Reynolds number Re is determined using [5.2.2] as:

$$Re = \frac{\dot{m} d_i}{\mu_L} = \frac{500(0.01575)}{0.0007} = 11250$$

The plain and ribbed tube friction factors from [5.2.6] and [5.6.8] are:

$$f = (1.58 \ln 11250 - 3.28)^{-2} \left( \frac{0.0007}{0.0005} \right)^{-0.25} = 0.00700$$

$$\frac{f_{ft}}{f} = \left\{ 1 + \left[ 29.1(11250)^{0.67 - 0.06 \left( \frac{0.004285}{0.01575} \right) - 0.49 \left( \frac{30}{90} \right)} \left( \frac{0.0014}{0.01575} \right)^{1.37 - 0.157 \left( \frac{0.004285}{0.01575} \right)} \right. \right. \right.$$

$$\cdot \left( \frac{0.004285}{0.01575} \right)^{\left( -0.00000166(11250) - 0.33 \left( \frac{30}{90} \right) \right)} \left( \frac{30}{90} \right)^{\left( 4.59 + 0.00000411(11250) - 0.15 \left( \frac{0.004285}{0.01575} \right) \right)} \right. \\ \left. \left. \left. \cdot \left( 1 + \frac{2.94}{2} \right) \sin 90 \right]^{15/16} \right\}^{16/15}$$

$$f_{ft} = 1.233(0.00700) = 0.00863$$

The pressure drop in a tube of length L = 3.0 m is given by [5.2.7] to be:

$$\Delta p = \frac{2f \dot{m}^2 L}{\rho d_i} = \frac{2(0.00863)(500^2)(3.0)}{(997)(0.01575)} = 824 \text{ Pa}$$

Using [5.5.2] and [5.2.8] give:

$$\frac{\alpha_{ft}}{\alpha_{pt}} = \left\{ 1 + \left[ 2.64(11250)^{0.036} \left( \frac{0.0014}{0.01575} \right)^{0.212} \left( \frac{0.004285}{0.01575} \right)^{-0.21} \left( \frac{30}{90} \right)^{0.29} 4.9^{-0.024} \right]^7 \right\}^{1/7}$$

$$\alpha_{pt} = \left( \frac{0.6}{0.01575} \right) \frac{(0.007/2)(11250 - 1000)4.9}{1 + 12.7(0.007/2)^{1/2}(4.9^{2/3} - 1)} \left( \frac{0.0007}{0.0005} \right)^{0.14} = 2905 \text{ W/m}^2\text{K}$$

$$\alpha_{ft} = 2.036(2905)$$

$$\alpha_{ft} = 5915 \text{ W/m}^2\text{K}$$

Hence, for this internal rib design the heat transfer augmentation is 2.036 times the equivalent plain tube while its pressure drop is only 1.233 times larger.

# Chapter 7

## Condensation on External Surfaces

(This chapter was updated in 2007)

**SUMMARY:** The principles of film condensation on external surfaces are presented. Geometries that are addressed are: vertical plates, horizontal tubes, horizontal tube arrays, tube bundles and enhanced surfaces. The effects of vapor shear, interfacial waves, interfacial vapor shear, surface tension and non-condensable gases are addressed. The flow modes of laminar and turbulent films and intertube flow modes between tubes are discussed. Numerous methods are presented for prediction of local condensation heat transfer coefficients for plain surfaces, low finned tubes and now for an enhanced condensing tube.

### 7.1 Modes of Condensation

Condensation is the heat transfer process by which a saturated vapor is converted into a liquid by means of removing the latent heat of condensation. From a thermodynamic standpoint, condensation occurs when the enthalpy of the vapor is reduced to the state of saturated liquid. In practice, the process is dynamic and heat must be transferred in order to achieve condensation. Thus, condensation occurs when a vapor contacts a solid surface or a fluid interface whose temperature is below the saturation temperature of the vapor.

This chapter will deal with condensation on the *outside of surfaces*, such as on plates, horizontal or vertical tubes and tube bundles. The following chapter provides a treatment of *intube condensation*, in which the process takes place inside enclosed channels typically with forced flow conditions.

Four basic mechanisms of condensation are generally recognized: drop-wise, film-wise, direct contact and homogeneous. The first three are categorized as heterogeneous processes. Figure 7.1 illustrates these condensation modes. In *drop-wise condensation*, the drops of liquid form from the vapor at particular nucleation sites on a solid surface, and the drops remain separate during growth until carried away by gravity or vapor shear. In *film-wise condensation*, the drops initially formed quickly coalesce to produce a continuous film of liquid on the surface through which heat must be transferred to condense more liquid. In *direct contact condensation*, the vapor condenses directly on the (liquid) coolant surface, which is sprayed into the vapor space. In *homogeneous condensation*, the liquid phase forms directly from supersaturated vapor, away from any macroscopic surface; it is however generally assumed, in practice, that there are particles of dust or mist particles present in the vapor to serve as nucleation sites.

While drop-wise condensation is alluring because of the very high heat transfer coefficients that result, it is not considered to be suitable for deliberate employment in process equipment. Generally, special materials must be employed (of low thermal conductivity, low surface energy, low wetting or be highly polished) to attain drop-wise condensation. Hence, the process is susceptible to any fouling or oxidation of the surface that may bring the process back into the film-wise mode, with a corresponding reduction in thermal performance. Drop-wise condensation is known to occur unexpectedly in experimental test facilities since the surfaces may be new, polished and very clean, which gives much higher coefficients than for the film-wise conditions under study (some researchers hence deliberately oxidize their test surfaces to avoid the drop-wise mode). For more information on drop-wise condensation, refer for instance to Griffith (1983).

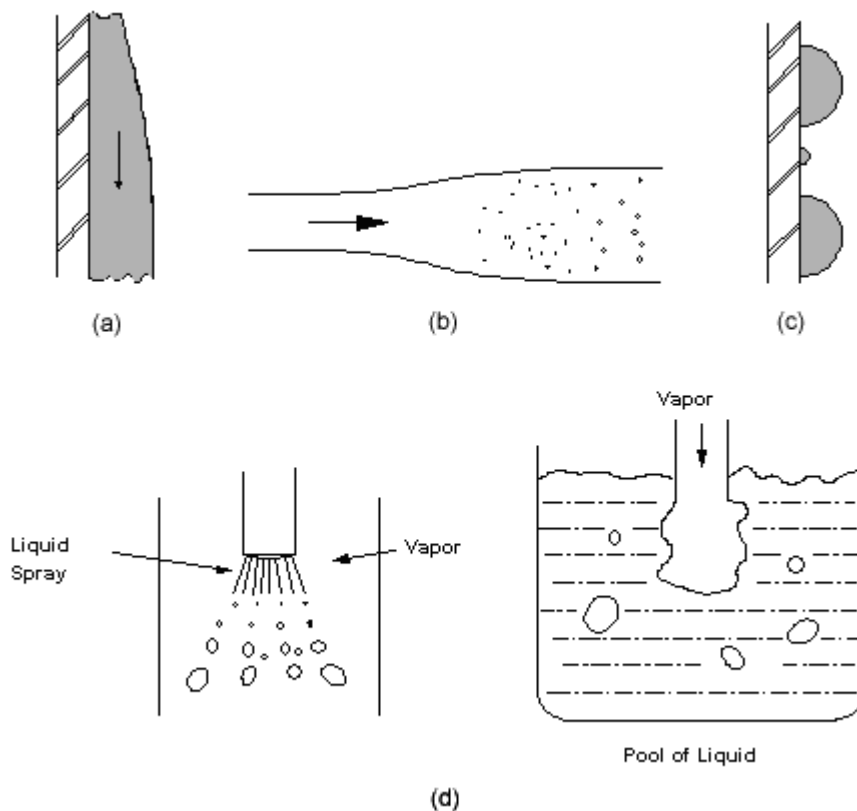


**Figure 7.1. Various modes of condensation.** (a) Filmwise condensation. (b) Homogenous condensation - fog formation. (c) Dropwise condensation. (d) Direct Contact Condensation

Direct contact condensation is a very efficient process, but it results in mixing the condensate with the coolant. Therefore, it is useful only in those cases where the condensate is easily separated, or where there is no desire to reuse the condensate, or where the coolant and condensate are in fact the same substance.

Condensate forming as suspended droplets or mist in a subcooled vapor is called *homogeneous* condensation, of which the most common example in nature is fog. Homogeneous condensation is primarily of concern in fog formation in equipment, i.e. to be avoided, and is not a design mode.

Film-wise condensation is the only of the above processes of particular industrial interest. Thus, all the subsequent treatment of condensation will implicitly mean film-wise condensation, in which the heat transfer surface is covered by a thin film of condensate flowing under the influence of gravity, vapor shear and/or surface tension forces. A review of recent literature is also available in Thome (1998).

## 7.2 Laminar Film Condensation on a Vertical Plate

### 7.2.1 Integral Analysis of Nusselt

Laminar film condensation of a pure single-component saturated vapor was among the first heat transfer problems to be successfully analyzed from a fundamental point of view. The definitive work is by Nusselt (1916) in two papers published two weeks apart in 1916 that has been widely described in numerous books since. The original analysis applies specifically to laminar flow of a condensing film on a vertical

surface. However, it is possible to generalize this approach to a number of other geometric cases, and for this reason it is worthwhile to examine his analysis in some detail here. The Nusselt falling film analysis closely represents experimental results on vertical plates if no ripples or non-condensable gases are present and the film flow is laminar.

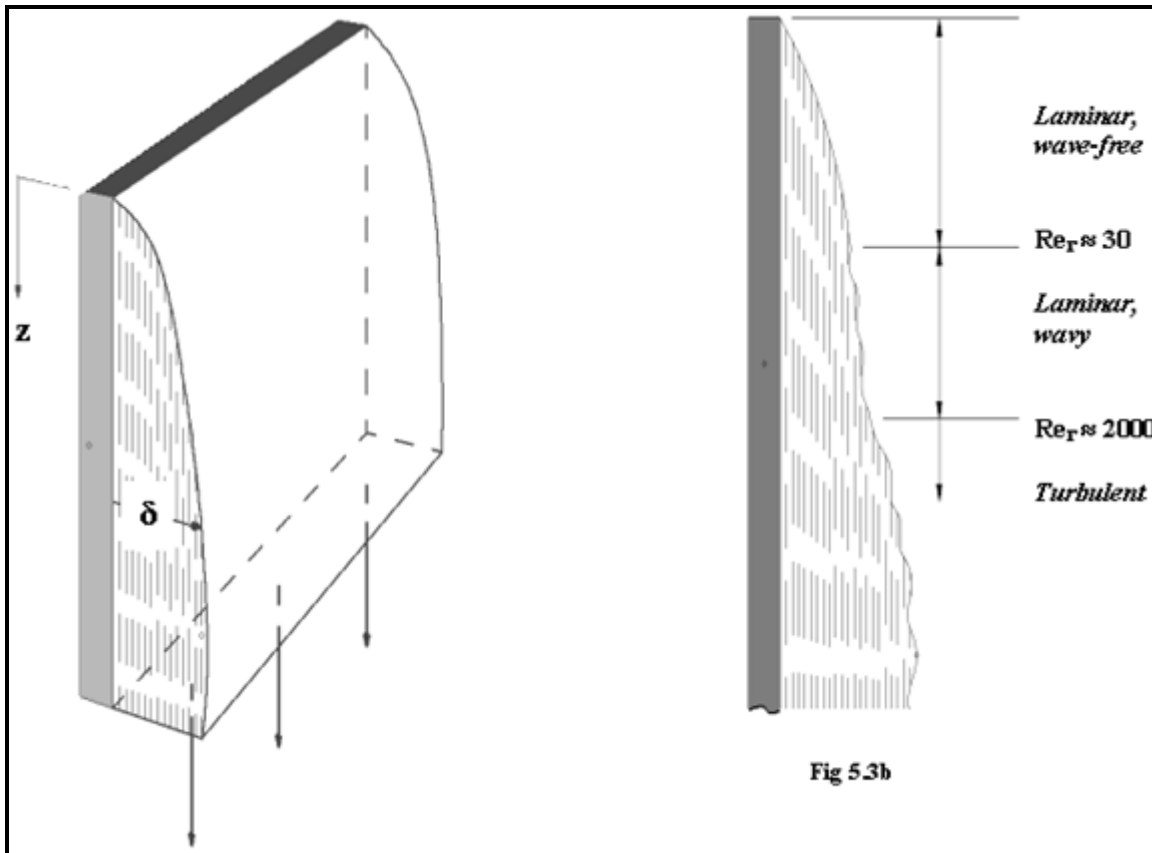


**Figure 7.2. Film condensation on a vertical plate.**

First of all, Figure 7.2 depicts the process of laminar film condensation on a vertical plate from a quiescent vapor. The film of condensate begins at the top and flows downward under the force of gravity, adding additional new condensate as it flows. The flow is laminar and the thermal profile in the liquid film is assumed to be fully developed from the leading edge. Thus, the temperature profile across the film is linear and heat transfer is by one-dimensional heat conduction across the film to the wall. Other assumptions in the Nusselt analysis are as follows:

- The vapor temperature is uniform and is at its saturation temperature;
- Gravity is the only external force acting on the film (momentum is neglected so there is a static force balance);
- The adjoining vapor is stagnant and does not exert drag on the film;
- Fluid properties are constant;
- The sensible cooling of the film is negligible with respect to the latent heat;
- The curvature of the interface is negligible so the saturation temperature of the interface is that of a planar interface determinable from the vapor pressure curve of the fluid.

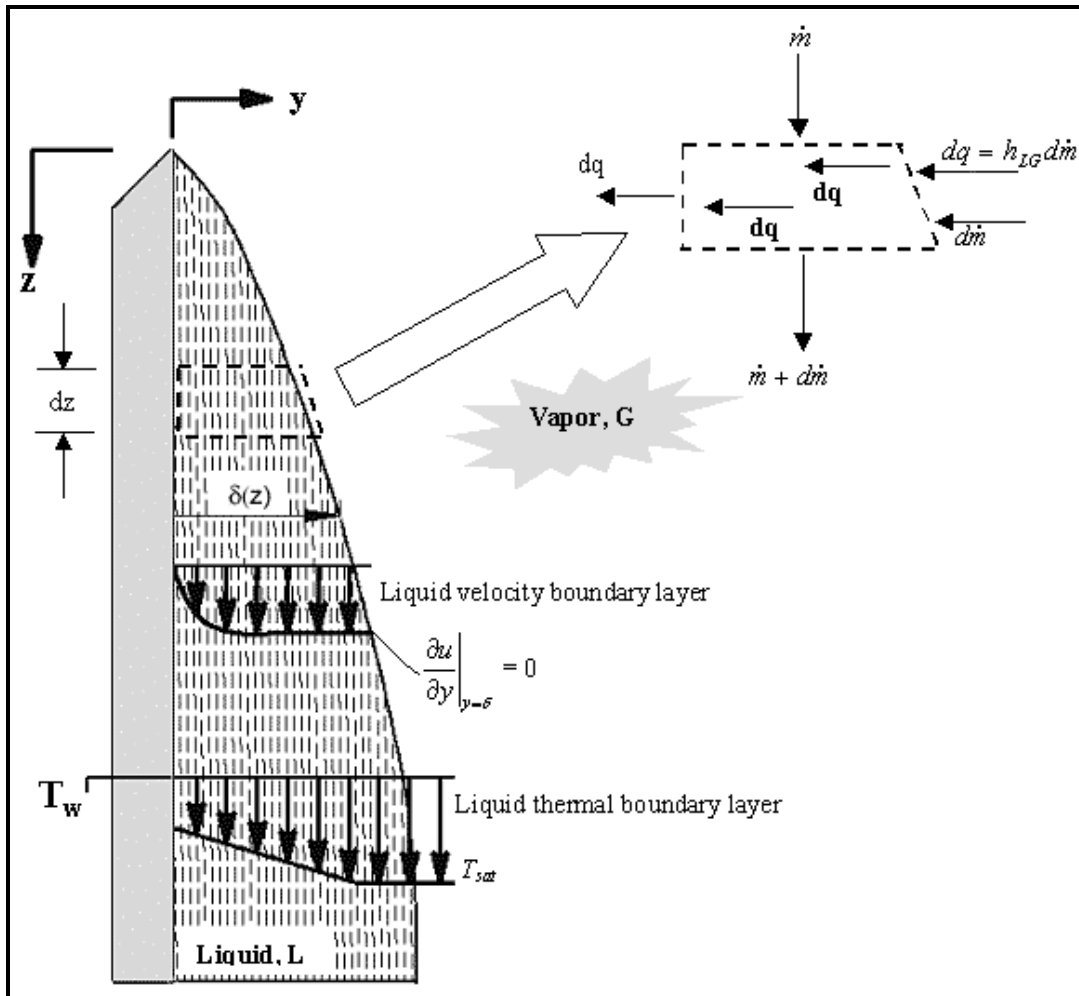


**Figure 7.3. Integral representation of falling laminar film on a vertical plate.**

The integral analysis of the process on a vertical plate is represented in Figure 7.3. At a distance  $z$  from the top, the thickness of the film is  $\delta$ . Ignoring inertia effects, i.e. no acceleration of the flow, a force balance on the liquid element gives

$$(\delta - y)dz(\rho_L - \rho_G)g = \mu_L \left( \frac{du_y}{dy} \right) dz \quad [7.2.1]$$

In this expression gravity acts as a body force on the element of volume  $(\delta-y)(dz)(1)$  where a unit width of the plate is assumed. The viscous force is for the shear on the film at distance  $y$  from the wall over the length  $dz$ . While this expression is for a *vertical* plate, it is applicable to an *inclined* plate as long as the angle of inclination is sufficient for drainage of the condensate. For an inclined plate, the force of gravity  $g$  on the film in the above expression is replaced with  $g \sin \beta$ , where  $\beta$  is the angle of the plate relative to horizontal. Now, rearranging and integrating this expression from the initial boundary condition of  $u_y = 0$  at  $y = 0$ , then the velocity profile at any location  $y$  in the film is obtained to be:

$$u_y = \frac{(\rho_L - \rho_G)g}{\mu_L} \left[ y\delta - \frac{y^2}{2} \right] \quad [7.2.2]$$

Integrating this velocity profile across the film, the mass flow rate of condensate per unit width of the plate  $\Gamma$  is

$$\Gamma = \rho_L \int_0^\delta u_y dy = \frac{\rho_L (\rho_L - \rho_G) g \delta^3}{3 \mu_L} \quad [7.2.3]$$

$\Gamma$  has the dimensions of kg/ms, which represents the flow rate in kg/s per unit width of the plate. Differentiating this expression with respect to  $\delta$ , where  $\delta = 0$  at  $z = 0$ , the rate of increase of the film flow rate with film thickness is

$$\frac{d\Gamma}{d\delta} = \frac{\rho_L (\rho_L - \rho_G) g \delta^2}{\mu_L} \quad [7.2.4]$$

Taking the film surface temperature as  $T_{sat}$  and the wall temperature as  $T_w$ , the heat conducted across the liquid film element of length  $dz$  with a thermal conductivity of  $k_L$  is

$$dq = \frac{k_L}{\delta} (T_{sat} - T_w) dz \quad [7.2.5]$$

Applying an energy balance, this rate of heat transfer by conduction is equal to the rate of latent heat removed from the vapor at the interface, which means  $dq = h_{LG} d\Gamma$ . The rate of condensation on this element ( $d\Gamma$ ) is thus

$$d\Gamma = \frac{k_L}{\delta h_{LG}} (T_{sat} - T_w) dz \quad [7.2.6]$$

Substituting [7.2.6] into [7.2.4], separating variables and then integrating from  $\delta = 0$  at  $z = 0$  gives

$$\mu_L k_L (T_{sat} - T_w) z = \rho_L (\rho_L - \rho_G) g h_{LG} \left( \frac{\delta^4}{4} \right) \quad [7.2.7]$$

Rearranging this expression for the local film thickness, it is

$$\delta = \left[ \frac{4 \mu_L k_L z (T_{sat} - T_w)}{\rho_L (\rho_L - \rho_G) g h_{LG}} \right]^{1/4} \quad [7.2.8]$$

The physical significance of the film thickness is that of the conduction length through a solid of the same thickness, seeing that in laminar film condensation the thermal resistance is only conduction from the interface to the wall. The film thickness is shown by the above expression to be directly proportional to the temperature difference ( $T_{sat} - T_w$ ), such that a larger temperature difference results in a higher condensation rate.

From the thermal conductive resistance across the film, the local condensation heat transfer coefficient  $\alpha_f(z)$  at any point  $z$  from the top of the plate is

$$\alpha_f(z) = \frac{k_L}{\delta} = \left[ \frac{\rho_L(\rho_L - \rho_G)gh_{LG}k_L^3}{4\mu_L z(T_{sat} - T_w)} \right]^{1/4} \quad [7.2.9]$$

Rearranging, the local Nusselt number for film condensation is obtained using  $z$  for the characteristic dimension:

$$Nu(z) = \left[ \frac{\alpha_f(z)z}{k_L} \right] = \left[ \frac{\rho_L(\rho_L - \rho_G)gh_{LG}z^3}{4\mu_L k_L(T_{sat} - T_w)} \right]^{1/4} \quad [7.2.10]$$

Integrating [7.2.9] from  $z = 0$  to  $z$ , the mean heat transfer coefficient for the plate up to point  $z$  is

$$\alpha_f = \frac{1}{z} \int_0^z \alpha_f(z) dz = 0.943 \left[ \frac{\rho_L(\rho_L - \rho_G)gh_{LG}k_L^3}{\mu_L z(T_{sat} - T_w)} \right]^{1/4} \quad [7.2.11]$$

Comparing the above expressions, it is seen that the mean coefficient  $\alpha_f$  on the plate from 0 to  $z$  is  $4/3$  times the value of the local coefficient  $\alpha_f(z)$  at  $z$ . The mean heat transfer coefficient can also be obtained from

$$\alpha_f = \frac{\Gamma(z)h_{LG}}{z(T_{sat} - T_w)} \quad [7.2.12]$$

where  $\Gamma(z)$  is the condensate flow rate per unit width at a distance  $z$  from the top of the plate. Combining [7.2.12] with [7.2.6] to eliminate  $(T_{sat} - T_w)$ , another expression for the thickness of the condensate at point  $z$  from the top is

$$\delta = \frac{k_L \Gamma(z) dz}{\alpha_f z d\Gamma} \quad [7.2.13]$$

Eliminating  $\delta$  by combining [7.2.13] with [7.2.3] yields the differential expression

$$\lambda_L \left[ \frac{\rho_L(\rho_L - \rho_G)g}{3\mu_L} \right]^{1/3} \frac{dz}{z} = \frac{\alpha_f \Gamma^{1/3} d\Gamma}{\Gamma(z)} \quad [7.2.14]$$

Integrating over  $z$  gives the mean heat transfer coefficient as

$$\alpha_f = 0.925 \left[ \frac{\rho_L(\rho_L - \rho_G)gk_L^3}{\mu_L \Gamma(z)} \right]^{1/3} \quad [7.2.15]$$

It is inconvenient to utilize an expression for the condensing heat transfer coefficient in terms of  $(T_{\text{sat}} - T_w)$  as in [7.2.11] since the wall temperature is unknown beforehand in heat exchanger design and results in an iterative solution procedure. For the present situation the heat transfer coefficient can also be expressed in terms of the local film Reynolds number, which at a distance  $z$  below the top of the plate is defined as

$$Re_f = \frac{4\Gamma(z)}{\mu_L} \quad [7.2.16]$$

Substituting [7.2.16] into [7.2.15] and rearranging, the mean heat transfer coefficient up to point  $z$  is

$$\frac{\alpha_f}{k_L} \left[ \frac{\mu_L^2}{\rho_L(\rho_L - \rho_G)g} \right]^{1/3} = 1.47 Re_f^{-1/3} \quad [7.2.17]$$

where the bracketed term to the left of the equal sign together with its exponent is the characteristic length. The local condensing heat transfer coefficient in terms of film Reynolds number is

$$\frac{\alpha_f(z)}{k_L} \left[ \frac{\mu_L^2}{\rho_L(\rho_L - \rho_G)g} \right]^{1/3} = 1.1 Re_f^{-1/3} \quad [7.2.18]$$

The condensing heat transfer coefficient for a laminar film is thus seen to be inversely proportional to the film Reynolds number to the  $1/3$  power. This can be compared, for instance, to fully developed laminar flow inside a tube in which the laminar heat transfer coefficient is independent of the Reynolds number.

Bromley (1952) extended the Nusselt theory to include subcooling of the condensate in the heat balance. Following in this line, Rohsenow (1956) showed that empirically adding a sensible heat term to the latent heat of vaporization gave reasonable results, defining an effective latent heat of evaporation as:

$$h'_{LG} = h_{LG} \left[ 1 + 0.68 \left( \frac{c_{pL} \Delta T_f}{h_{LG}} \right) \right] \quad [7.2.19]$$

where  $\Delta T_f = (T_{\text{sat}} - T_w)$ . The subcooling correction is typically negligible with respect to the latent heat since condensing temperature differences tend to be small.

Regarding other physical properties, Drew (1954) proposed that they be evaluated at an effective film temperature, which he gave as  $[T_w + 0.25(T_{\text{sat}} - T_w)]$ . For small temperature differences, it is sufficiently accurate to calculate the properties at the saturation temperature. The above analysis can also be applied to the outside or inside of a vertical tube, as long as the tube diameter is much larger than  $\delta$  and the effect of vapor shear remains small.

## 7.2.2 Boundary Layer Analysis

Sparrow and Greg (1959) applied boundary layer analysis to the problem of laminar falling film condensation. They removed the assumption of negligible momentum changes in the liquid film but, like Nusselt, they assumed that the shear exerted by the stagnant vapor on the falling film is negligible. Their solution obtains the local film heat transfer coefficient from the heat conducted from the film into the wall

$$\alpha_f(z) = \frac{q}{T_{sat} - T_w} = \frac{k_L}{T_{sat} - T_w} \left( \frac{\partial T}{\partial y} \right)_{y=0} \quad [7.2.20]$$

by evaluating the calculated temperature profile at  $y=0$ . Their analysis gives the local Nusselt number as:

$$Nu(z) = \frac{\alpha_f(z)z}{k_L} = [-\theta'(0)] Ja_L^{1/4} \left[ \frac{g \rho_L (\rho_L - \rho_G) z^3 h_{LG}}{4 \mu_L k_L (T_{sat} - T_w)} \right]^{1/4} \quad [7.2.21]$$

where the Jakob number  $Ja_L$  is defined as

$$Ja_L = \frac{c_{pL}(T_{sat} - T_w)}{h_{LG}} \quad [7.2.22]$$

and  $\theta'$  is the first derivative of the dimensionless temperature at  $\eta = 0$ , defined as

$$\theta(\eta) = \frac{T_{sat} - T}{T_{sat} - T_w} \quad [5.2.23]$$

and the dimensionless variable  $\eta$  is

$$\eta = c_L y z^{-1/4} \quad [5.2.24]$$

The boundary layer solution given by [7.2.21] includes an additional term compared to the Nusselt solution given by [7.2.10], namely  $[\theta'(0) Ja_L^{1/4}]$ . For common fluids with Prandtl numbers near unity, their simulations showed that the momentum effects were negligible as assumed by Nusselt. Furthermore, the error in utilizing [7.2.11] for  $Ja_L \leq 0.1$  and  $1 \leq Pr_L \leq 100$  was less than 3%. On the other hand, for fluid with very low Prandtl numbers, e.g. liquid metals, the heat transfer coefficients are predicted with the boundary layer analysis are much smaller than those given by the Nusselt solution.

## 7.3 Influence of Interfacial Phenomena on Laminar Film Condensation

### 7.3.1. Ripples and Waves

The assumption that the interface of the laminar falling film is smooth is often not true. Observations indicate that the interface becomes unstable and forms ripples or waves as shown in Figure 7.4 and Drew (1954) has pointed to them to explain the positive difference between carefully measured experimental values and those given by Nusselt theory, with up to 50% higher values in some cases. The ripples increase heat transfer by enlarging the interfacial area and by reducing the mean thickness of the film. Based on analysis of experimental observations, Brauer (1956) related the film Reynolds number  $Re_f$  for the onset of waves to the Archimedes number  $Ar_L$ , which is defined as

$$Ar_L = \frac{\rho_L^2 \sigma^{3/2}}{\mu_L^2 g^{1/2} (\rho_L - \rho_G)^{3/2}} \quad [7.3.1]$$

The laminar falling film condensation heat transfer coefficient on vertical plates is enhanced when

$$Re_\Gamma > 9.3 Ar_L^{1/5} \quad [7.3.2]$$

This can be used as a criterion for the onset of ripples or waves; an alternative criterion suggested elsewhere is when  $Re_\Gamma > 30$ . To account for the effect of waves on heat transfer, Kutateladze (1963) suggested multiplying the film Reynolds number in [7.2.18] by an empirical correction of  $[0.8 (Re_\Gamma/4)^{0.11}]$ , such that [7.2.18] becomes

$$\frac{\alpha_f(z)}{k_L} \left[ \frac{\mu_L^2}{\rho_L(\rho_L - \rho_G)g} \right]^{1/3} = 0.756 Re_\Gamma^{-0.22} \quad [7.3.3]$$

Integrating over the film Reynolds number range from 0 to  $Re_\Gamma$

$$\frac{Re_\Gamma}{\alpha_f} = \int_0^{Re_\Gamma} \frac{dRe_\Gamma}{\alpha_f(z)} \quad [7.3.4]$$

using expression [7.2.18] for values up to 30 and [7.3.3] for  $Re_\Gamma > 30$ , the resulting expression is:

$$\frac{\alpha_f}{k_L} \left[ \frac{\mu_L^2}{\rho_L(\rho_L - \rho_G)g} \right]^{1/3} = \frac{Re_\Gamma}{1.08 Re_\Gamma^{1.22} - 5.2} \quad [7.3.5]$$

This expression is that of Butterworth (1983) and is valid up to the onset of turbulence. He noted that most experimental studies give the onset of turbulence at a film Reynolds number of about 1600. Expression [7.3.5] is solved in an iterative fashion up to the point of  $z$  in order to determine the condensate flow rate and film Reynolds number from the heat transferred.

Local expressions for the condensation heat transfer coefficient in terms of the film Reynolds number are helpful during thermal design. For example, a real plate with liquid cooling may have a non-trivial variation in  $(T_{sat}-T_w)$ . Similarly, a non-isothermal plate can be modeled by dividing it into successive isothermal zones, including the variation in local physical properties. Finally, calculation of the local film Reynolds number is an explicit way to determine when the laminar condensation equations are applicable or if the turbulent film flow regime has been reached.

### 7.3.2 Cocurrent Interfacial Vapor Shear

Interfacial shear of cocurrent vapor flow on a laminar falling film tends to thin the film and increase heat transfer. On the other hand, counter-current vapor flow would counteract the body force on the condensate and thicken the film. Nusselt analyzed condensation under the influence of cocurrent

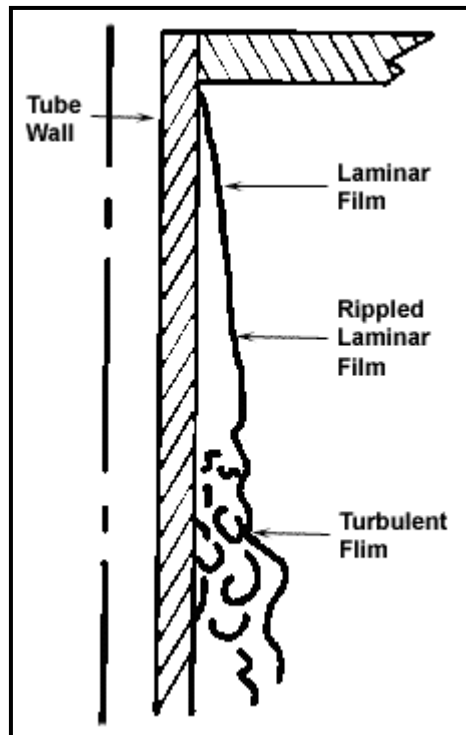


**Figure 7.4. Ripples and waves on a falling film.**

interfacial vapor shear at high vapor velocities for a laminar liquid film and the corresponding equation to [7.2.1] for cocurrent vapor shear conditions is

$$(\delta - y) dz \left( \rho_L g \sin\beta - \left( \frac{dp}{dz} \right) \right) + \tau_i dz = \mu_L \left( \frac{du_y}{dy} \right) dz \quad [7.3.6]$$

The inclination of the plate is included by replacing  $g$  with  $g \sin\beta$  where  $\beta$  is the inclination angle of the surface relative to horizontal. The cocurrent vapor produces an interfacial shear stress  $\tau_i$ . For convenience sake, a fictitious vapor density  $\rho_G^*$  is defined:

$$\left( \frac{dp}{dz} \right) = \rho_G^* g \sin\beta \quad [7.3.7]$$

If the static head of the vapor is taken as the pressure gradient, then  $\rho_G^* = \rho_G$ . Substituting [7.3.7] into [7.3.6] and integrating, the following relationships are obtained:

$$u_y = \frac{(\rho_L - \rho_G^*) g \sin\beta}{\mu_L} \left[ y\delta - \frac{y^2}{2} \right] + \frac{\tau_i y}{\mu_L} \quad [7.3.8]$$

$$\Gamma = \left[ \frac{\rho_L (\rho_L - \rho_G^*) g \sin\beta \delta^3}{3\mu_L} \right] + \frac{\tau_i \rho_L \delta^2}{2\mu_L} \quad [7.3.9]$$

$$\frac{d\Gamma}{d\delta} = \left[ \frac{\rho_L (\rho_L - \rho_G^*) g \sin\beta \delta^2}{\mu_L} \right] + \frac{\tau_i \rho_L \delta}{\mu_L} \quad [7.3.10]$$

Repeating the Nusselt analysis that was used to obtain [7.2.8], the corresponding expression is

$$\frac{4\mu_L k_L z(T_{sat} - T_w)}{g \sin\beta h'_{LG} \rho_L (\rho_L - \rho_G^*)} = \delta^4 + \frac{4}{3} \left[ \frac{\tau_i \delta^3}{(\rho_L - \rho_G^*) g \sin\beta} \right] \quad [7.3.11]$$

Rohsenow, Webber and Ling (1956) defined the three dimensionless variables (film thickness  $\delta^*$ , distance from the leading edge  $z^*$ , and interfacial shear stress  $\tau_i^*$ ) to resolve this expression:

$$\delta^* = \delta \left[ \frac{\rho_L (\rho_L - \rho_G^*) g \sin\beta}{\mu_L^2} \right]^{1/3} \quad [7.3.12]$$

$$z^* = \left( \frac{4k_L z(T_{sat} - T_w)}{h'_{LG} \mu_L \delta} \right) \delta^* \quad [7.3.13]$$

$$\tau_i^* = \left( \frac{\tau_i}{(\rho_L - \rho_G^*) g \sin\beta} \right) \delta^* \quad [7.3.14]$$

and transformed [7.3.11] to

$$z^* = \delta^{*4} + \frac{4}{3} \delta^{*3} \tau_i^* \quad [7.3.15]$$

Integrating, this gives

$$Nu = \frac{\alpha_f}{k_L} \left[ \frac{\mu_L^2}{\rho_L (\rho_L - \rho_G^*) g \sin\beta} \right]^{1/3} = \frac{4}{3} \frac{(\delta_z^*)^3}{z^*} + 2 \frac{\tau_i^* (\delta_z^*)^2}{z^*} \quad [7.3.16]$$

where the corresponding film Reynolds number is

$$\frac{4\Gamma(z)}{\mu_L} = \frac{4}{3} (\delta_z^*)^3 + 2 \tau_i^* (\delta_z^*)^2 \quad [7.3.17]$$

By substituting [7.3.17] into [7.3.16],  $\delta_z^*$  can be eliminated. Figure 7.5 shows this expression evaluated for cocurrent downflow by Rohsenow, Webber and Ling (1956) where the dashed lines depict the onset of turbulence in the film. As an example of the potential effect of vapor shear, at a film Reynolds number of 40 the Nusselt number is increased by about a factor of 1.5 to 6 times for the range of shear stresses simulated!

Butterworth (1981) analyzed an analogous case for the situation where the gravitational forces are negligible with respect to the interfacial shear imposed by the co-current vapor flow and laminar film flow. His dimensionless local condensation heat transfer coefficient for these conditions is:

$$\alpha_f^+(z) = 1.41 Re_{\Gamma}^{-1/2} (\tau_i^+)^{1/2} \quad [7.3.18]$$

where the dimensionless local heat transfer coefficient is

$$\alpha_f^+(z) = \frac{\alpha_f(z)}{k_L} \left[ \frac{\mu_L^2}{\rho_L (\rho_L - \rho_G) g} \right]^{1/3} \quad [7.3.19]$$

and the dimensionless interfacial shear stress is

$$\tau_i^+ = \frac{\rho_L \tau_i}{[\rho_L (\rho_L - \rho_G) \mu_L g]^{2/3}} \quad [7.3.20]$$

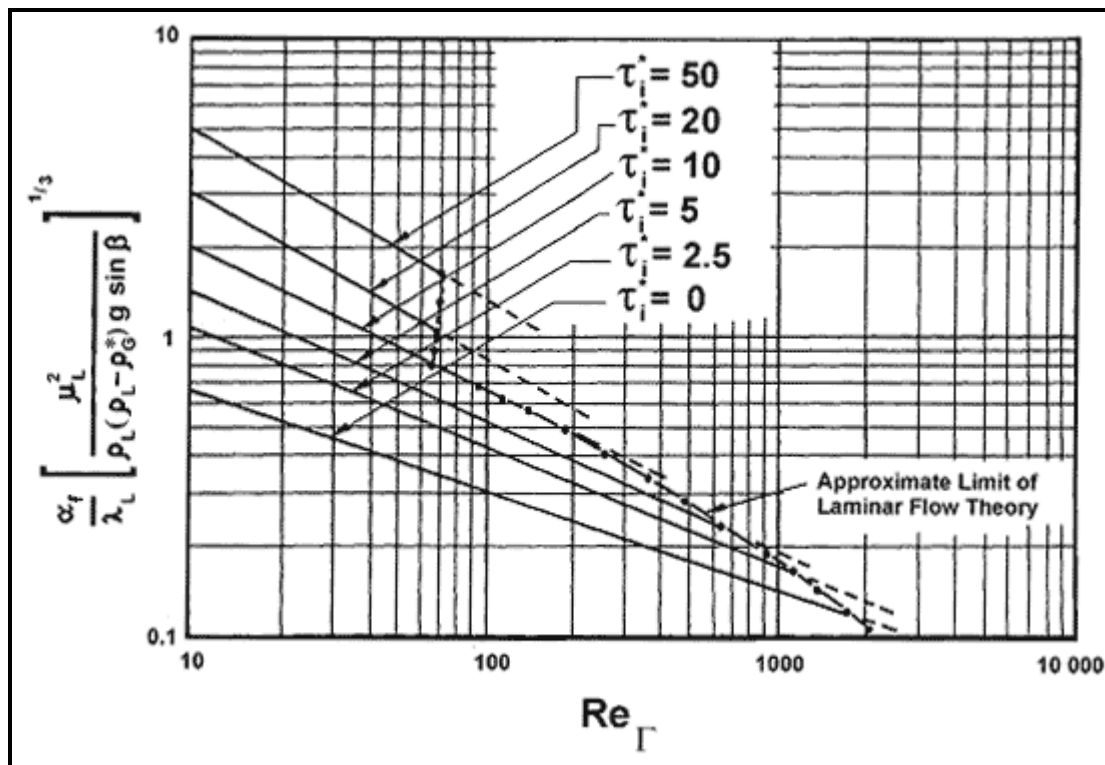


**Figure 7.5.** The influence of co-current vapor shear on the mean laminar falling film condensation heat transfer rate according to Rohsenow et al. (1956) [from Collier and Thome (1994)].

In his reworking of the Rohsenow, Webber and Ling (1956) analysis, low and high vapor shear effects are distinguished by use of a critical liquid film Reynolds number  $Re_{crit}$  for the onset of turbulence. An important effect of the downward interfacial shear created by the vapor is that it reduces the critical Reynolds number at which the film flow becomes turbulent. For  $\tau_i^+ \leq 9.04$ , the critical film Reynolds number is

$$Re_{crit} = 1600 - 226\tau_i^+ + 0.667(\tau_i^+)^3 \quad [7.3.21]$$

For  $\tau_i^+ > 9.04$ ,  $Re_{crit}$  is a fixed value, i.e.

$$Re_{crit} = 50 \quad [7.3.22]$$

The interfacial shear stress  $\tau_i$  is

$$\tau_i = \frac{1}{2} f_i \rho_G u_{LG} \quad [7.3.23]$$

where  $u_{LG}$  is the superficial velocity of the vapor with respect to the velocity of the film. The interfacial friction factor  $f_i$  is assumed to be that for laminar flow on a flat plate:

$$f_i = 0.664 Re_G^{-1/2} \quad [7.3.24]$$

where the local vapor Reynolds number is

$$Re_G = \frac{u_G z}{v_G} \quad [7.3.25]$$

and  $z$  is the distance from the leading edge. Thus, depending on the local value of  $Re_\Gamma$  with respect to  $Re_{crit}$ , the appropriate expression is used to calculate the local heat transfer coefficient. To implement this method, [7.3.18] must be integrated from the leading edge and an energy balance performed to determine the film flow rate and hence the value of  $Re_\Gamma$ .

### 7.3.3 Combined Effects of Gravity and Interfacial Vapor Shear

When both the gravitational and interfacial vapor shear forces are significant, Butterworth (1981) recommends using a simple asymptotic expression to incorporate their respective influences:

$$\alpha = (\alpha_{sh}^2 + \alpha_{grav}^2)^{1/2} \quad [7.3.26]$$

where  $\alpha_{grav}$  is the heat transfer coefficient for gravity-dominated flow from one of the Nusselt expressions, such as [7.3.5], and  $\alpha_{sh}$  is the heat transfer coefficient for shear-dominated flow, such as [7.3.16].

## 7.4 Turbulent Film Condensation on a Vertical Plate without Vapor Shear

The critical film Reynolds number at which a falling film becomes turbulent is still in dispute. Colburn (1934) set the transition at a film Reynolds number of 2000 when comparing his experimental data to the Nusselt theory. Applying an analogy to turbulent liquid flow in pipes, Colburn proposed the following correlation for the local condensing coefficient for turbulent film condensation on a vertical plate

$$\frac{\alpha_f(z)}{k_L} \left[ \frac{\mu_L^2}{\rho_L(\rho_L - \rho_G)g} \right]^{1/3} = 0.056 Re_\Gamma^{0.2} Pr_L^{1/3} \quad [7.4.1]$$

where  $z$  is measured from the top of the isothermal plate. In applying this expression, the Nusselt expression [7.2.9] is used up to a local film Reynolds number of 2000 and then [7.4.1] is used above the value of 2000.

Labuntsov (1957) proposed a similar expression for the local condensation heat transfer coefficient when  $Pr_L \leq 10$ :

$$\frac{\alpha_f(z)}{k_L} \left[ \frac{\mu_L^2}{\rho_L(\rho_L - \rho_G)g} \right]^{1/3} = 0.023 Re_\Gamma^{0.25} Pr_L^{0.5} \quad [7.4.2]$$

There is a notable disagreement between the empirical values in these expressions.

Figure 7.6 depicts the local Nusselt number for condensation on a vertical plate without vapor shear obtained with [7.2.18], [7.3.3] and [7.4.2] for the laminar, wavy laminar and turbulent regimes, respectively. The heat transfer coefficient decreases with increasing film Reynolds number in the laminar regime but increases with increasing Reynolds number in the turbulent regime. The large jump in the heat transfer coefficient when passing from the laminar wavy regime to turbulent film flow is due to the fact that Prandtl number effects were ignored in the Nusselt laminar film theory.

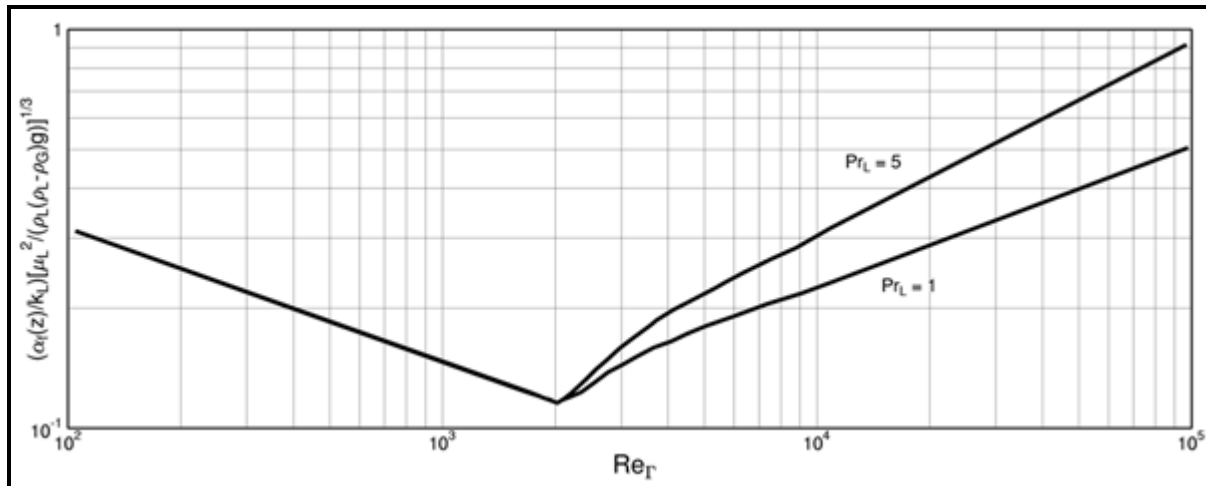


**Figure 7.6. Local Nusselt numbers on a vertical plate.**

Butterworth (1983) obtained the mean heat transfer coefficient over the laminar wave-free, the wavy laminar and the turbulent zones by combining [7.2.18], [7.3.3], and [7.4.2] with the help of [7.3.4]:

$$\frac{\alpha_f}{k_L} \left[ \frac{\mu_L^2}{\rho_L(\rho_L - \rho_G)g} \right]^{1/3} = \frac{Re_\Gamma}{8750 + 58Pr_L^{-0.5}(Re_\Gamma^{0.75} - 253)} \quad [7.4.3]$$

This expression uses a turbulence threshold of 2000 and compares well to experimental data for condensation of steam over the range  $1 < Re_\Gamma < 7200$ .

The film Reynolds number threshold to turbulent film flow remains to this day in dispute. Some publications cite this occurring at a film Reynolds number as low as 1200 while others propose values of 1800 and 2000.

As an alternative to the empirical approaches above, turbulent boundary layer theory has been applied to falling film condensation by Seban (1954), Dukler (1960) and then Lee (1964) using universal velocity profiles to evaluate the eddy diffusivities in the governing boundary layer equations. A comparison of the Nusselt laminar flow theory to the Colburn, Seban and Dukler methods is depicted in Figure 7.7. Mills and Chung (1973) argued that the interface has a damping effect on large turbulent eddies in the film, such that there is a viscous sublayer at both the wall and the interface. Kutateladze (1982) arrived at the same intuitive conclusion and proposed an eddy viscosity variation that goes to zero at the wall and the interface.

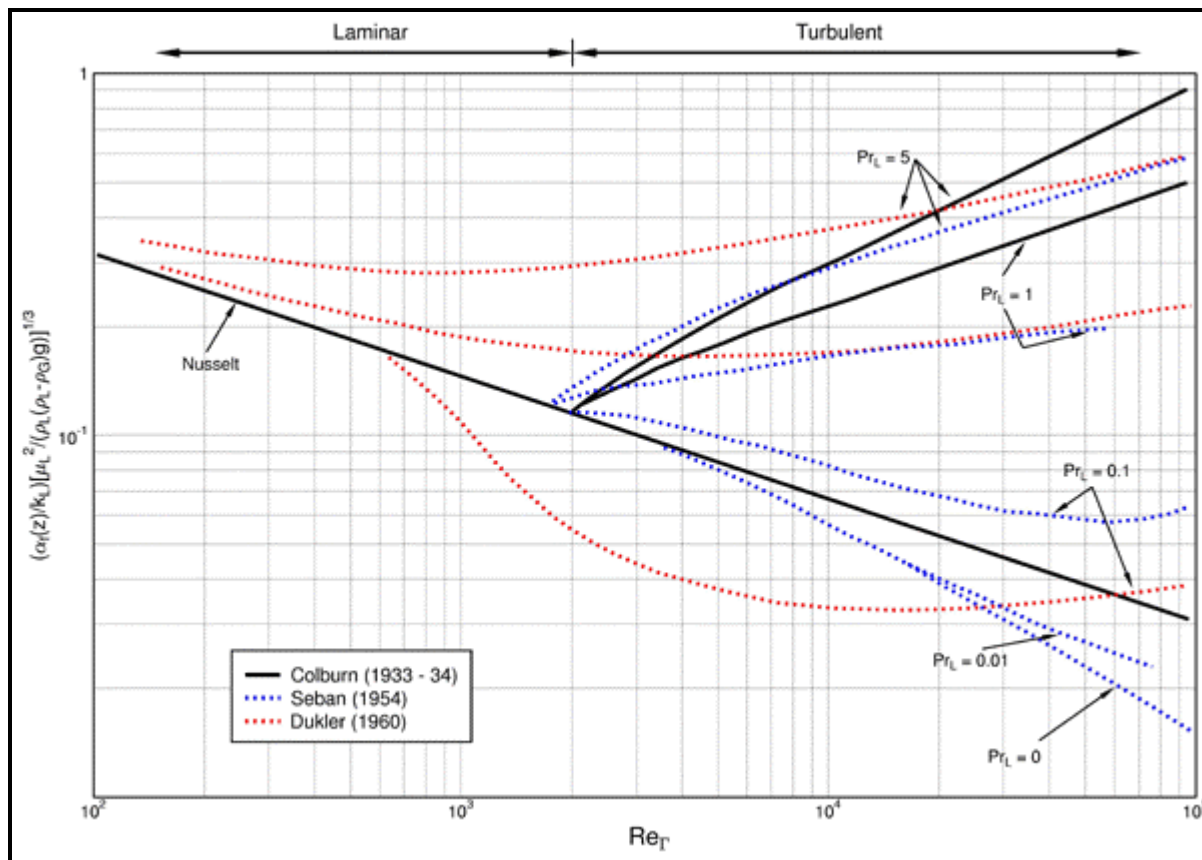


**Figure 7.7.** Mean Nusselt numbers predicted by various methods [from Collier and Thome (1994)].

## 7.5 Laminar Film Condensation on a Horizontal Tube

Applying the Nusselt integral approach to laminar film condensation on a vertical isothermal plate, the similar process on the outside of a single, horizontal isothermal tube can be analyzed. Condensation on the outside of horizontal tube bundles is often used for shell-and-tube heat exchanger applications and the first step is the analysis of a single tube. The flow is nearly always laminar on a single tube because of the short cooling length around the perimeter and is illustrated in Figure 7.8. Taking the same assumptions for the vertical isothermal plate and an integral approach for the flow, an energy balance between the one-dimensional heat conduction across the liquid film of thickness  $\delta$  and the latent heat absorbed by the liquid from the condensing vapor at the interface gives

$$h_{LG} \frac{d\Gamma}{dz} = \frac{k_L [T_{sat}(p_G) - T_w]}{\delta} \quad [7.5.1]$$

Gravitation ( $g \sin\beta$ ) is applied around the circumference of the tube, where  $\beta$  is the angle around the perimeter from the top. Similar to [7.2.2] for a vertical plate, a momentum balance on this element and integration from the initial boundary condition of  $u = 0$  at  $y = 0$  results in the following velocity profile in the film as a function of  $\beta$ :

$$u_y = \frac{(\rho_L - \rho_G)g \sin\beta}{\mu_L} \left[ y\delta - \frac{y^2}{2} \right] \quad [7.5.2]$$

Integrating the velocity profile from the wall to the film interface gives the condensate mass flow rate per unit length of tube,  $\Gamma$  at the angle  $\beta$ :

$$\Gamma = \rho_L \int_0^\delta u_y dy = \frac{\rho_L (\rho_L - \rho_G) g \sin\beta \delta^3}{3\mu_L} \quad [7.5.3]$$

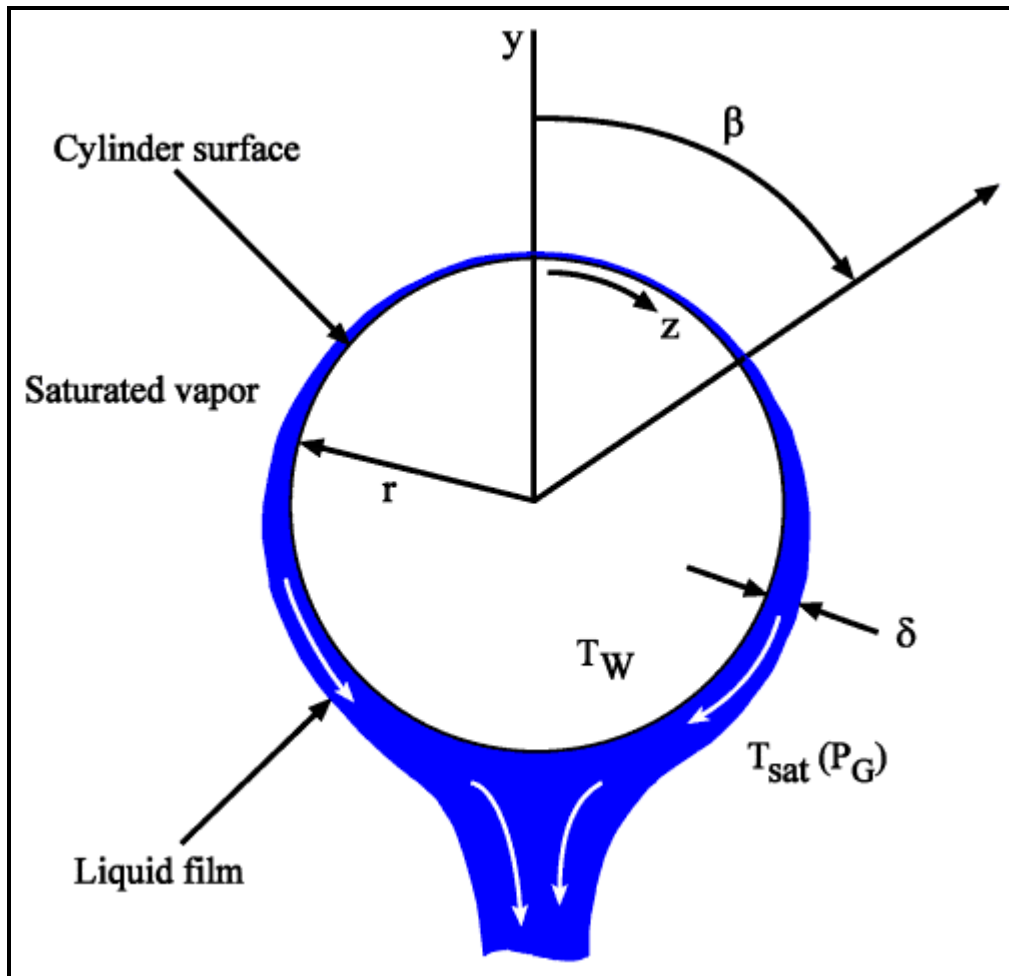


**Figure 7.8. Condensation model for film condensation on a horizontal tube.**

The length from to the top of the tube is  $z$ , which is related to the angle  $\beta$  as  $\beta = z/r$ , where  $r$  is the radius of the tube. Substituting into [7.5.3] and then substituting [7.5.3] into [7.5.1] yields:

$$\Gamma^{1/3} d\Gamma = \frac{r k_L (T_{sat} - T_w)}{h_{LG}} \left[ \frac{(\rho_L - \rho_G) g}{3 \nu_L} \right]^{1/3} \sin^{1/3} \beta d\beta \quad [7.5.4]$$

Integrating from the top of the tube where  $\Gamma = 0$  at  $\beta = 0$  to the bottom where  $\Gamma = \Gamma$  at  $\beta = \pi$  gives the condensate flow rate on one side of the tube per unit axial length of tube

$$\Gamma = 1.924 \left[ \frac{r^3 k_L^3 (T_{sat} - T_w)^3 (\rho_L - \rho_G) g}{h_{LG}^3 v_L} \right]^{1/4} \quad [7.5.5]$$

where  $\Gamma$  is the condensate flow rate for one side of the tube. Here,  $v_L$  is the kinematic viscosity of the liquid. An energy balance on the circumference of the tube gives the mean heat transfer coefficient for the perimeter of the tube as

$$2h_{LG}\Gamma = 2\pi r \alpha_f (T_{sat} - T_w) \quad [7.5.6]$$

Substituting for  $\Gamma$  from [7.5.5], the mean heat transfer coefficient is

$$\alpha_f = 0.728 \left[ \frac{\rho_L (\rho_L - \rho_G) g h'_{LG} k_L^3}{D \mu_L (T_{sat} - T_w)} \right]^{1/4} \quad [7.5.7]$$

where  $D$  is the outside diameter of the tube. The original value of 0.725 was obtained from a numerical solution while the correct analytical value is 0.728. Heat transfer is inversely proportional to the tube diameter to the  $1/4$  power. The mean condensate heat transfer coefficient may also be written in terms of the film Reynolds number as

$$\frac{\alpha_f}{k_L} \left[ \frac{\mu_L^2}{\rho_L (\rho_L - \rho_G) g} \right]^{1/3} = 1.51 \text{Re}_f^{-1/3} \quad [7.5.8]$$

where the film Reynolds number is defined by [7.2.16].  $\Gamma(z)$  is the mass flow rate of condensate draining from the bottom of one side of the tube per unit axial length (i.e. the condensate  $\Gamma$  is given by [7.5.5]). This expression is valid for  $\text{Re}_f$  up to about 1600, which is unlikely to be exceeded on a single tube. The influence of subcooling may be incorporated by introducing [7.2.19]. The mean condensation heat transfer coefficient written in terms of the Nusselt, Rayleigh and Jakob numbers is

$$Nu_D = \frac{\alpha_f D}{k_L} = 0.728 \left( \frac{Ra_L}{Ja_L} \right)^{1/4} \quad [7.5.9]$$

The Nusselt number is written with respect to the tube diameter  $D$ . The Rayleigh number represents the ratio of the buoyancy force acting on the liquid in the film to the viscous force opposing flow while the Jakob number represents the ratio of the liquid sensible heat to the latent heat. The Jakob number  $Ja_L$  is given by [7.2.22] and the Rayleigh number  $Ra_L$  is defined as

$$Ra_L = \frac{g(\rho_L - \rho_G) \text{Pr}_L D^3}{\rho_L v_L^2} \quad [7.5.10]$$

The local heat transfer coefficient around the perimeter of the tube as a function of the angle  $\beta$  is:

$$\alpha_f(\beta) = 0.693 \left[ \frac{\rho_L (\rho_L - \rho_G) g \sin \beta k_L^3}{\Gamma(\beta) \mu_L} \right]^{1/3} \quad [7.5.11]$$

Applying instead a uniform heat flux as the boundary condition around the tube rather than an isothermal temperature, Fujii, Vehara and Kurata (1972) obtained identical expressions to [7.5.7] and [7.5.8] except that the lead constants become 0.70 and 1.47, respectively. The isothermal boundary condition solution is nearly always used for thermal design.

## 7.6 Condensation on Horizontal Tube Bundles

In order to thermally design a shell-side condenser, the previous single tube film condensation analysis must be extended to model the process on horizontal tube bundles, which is the most widespread application of film condensation. Condensation on tube bundles raises several important considerations:

- In what manner does the condensate flow from one tube to the next?
- Is subcooling of the film important?
- Is the influence of vapor shear significant and, if so, how can this be accounted for?
- At which point does the film go through the transition from laminar to turbulent flow?

To date, these have only been partially resolved and the current knowledge will be presented below.

### 7.6.1 Tube Row Effect

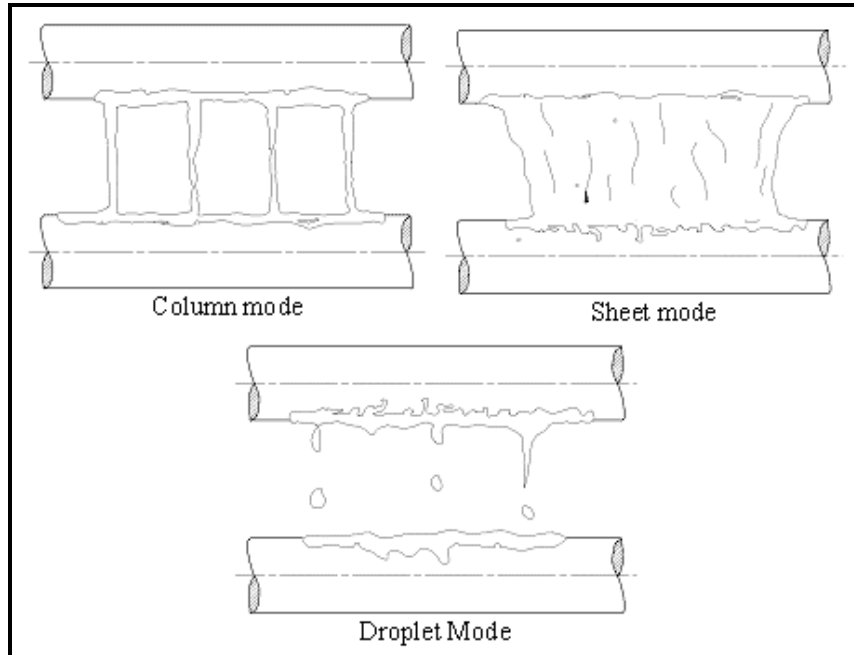


**Figure 7.9. Condensation flow modes on horizontal tube arrays.**

During condensation on a tube bundle, the condensate from the above tubes drains onto the tubes below, increasing the amount of condensate flowing on each tube in addition to the new condensate formed on

that particular tube. This inundation of condensate from tube row to tube row is often referred to as the tube row effect. In fact, it is more complex than just being a factor of how many tubes are located one above the other, as analyzed by Nusselt (1916) in his landmark study in which the original vertical plate Nusselt theory was presented. The tube row effect is not only dependent on how much condensate flows from tube to tube but also in what physical mode the condensate achieves this. The flow regimes formed by the condensate as it flows from one tube to that directly below it in an array of horizontal tubes are depicted schematically in Figure 7.9. The regimes encountered are described as follows for increasing film mass flow rate:

- **Droplet mode.** The liquid flows from tube to tube as individual droplets, often in rapid succession at uniform intervals along the bottom of the upper tube. The droplets range in size depending on the properties of the fluid, primarily density difference, surface tension and liquid viscosity. The droplets essentially form a jet that impinges on the lower tube. The droplets form because a continuous film on the bottom of a tube becomes unstable as a result of the Kelvin-Helmholtz instability, which causes liquid droplets to be formed at characteristic wavelengths such that droplet jets are formed at nearly equal intervals along the bottom of the tube.
- **Column mode.** At higher flow rates, the jets of droplets coalesce to form individual liquid columns that extend from the bottom of the upper tube to the top of the lower tube. The liquid columns hit the top of the lower tube as impinging jets and spread along the tube while flowing on around towards the bottom as shown in Figure 7.10 adapted from Mitrovic (1986), in which the columns are staggered from one tube row to the next. The columns may also be inline, one above the other in each successive tube row.

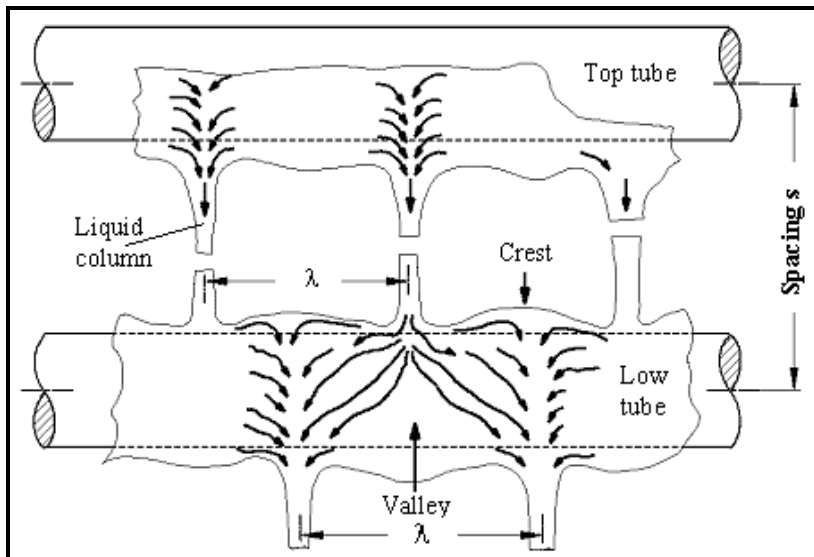


**Figure 7.10. Condensate spreading over the tube for column type of condensate drainage.**

- **Sheet mode.** At even higher flow rates, the columns become unstable and form short patches of liquid sheets that flow from one tube to the next. Eventually, with enough liquid, these unstable sheets join together to form more or less one continuous sheet of liquid falling from the upper tube to the lower one. This occurs only if the intertube spacing is small enough to prevent breakup of the sheet. For staggered tube arrays, if the column sheet is unstable, it may attach to the side of the next lower out-of-line tube without reaching the top of the next inline tube. Waves or ripples are typically noticeable on the flowing sheets.

- **Spray mode.** Under vapor shear conditions with its complex flow field around tubes, the above flow modes may be interrupted and the liquid carried away by the vapor. In this case, there is significant entrainment of liquid droplets into the vapor flowing between the tubes and hence a spray flow is formed. Any liquid flowing from one tube to another does so in a very chaotic manner. For staggered tube arrays, the vertical tube spacing is quite large and these liquid columns and droplet jets are easily influenced by vapor buffeting, especially where the vapor's boundary layer detaches from the sides of the tubes in vortices and in the recirculating flow regions behind the tubes. At high vapor flow rates, a large fraction of the liquid is entrainment as small liquid droplets, resulting in very thin liquid films on the tubes.

For an actual view of these intertube flow modes, which may be thought of as shell-side falling film two-phase flow regimes, Figure 7.11 depicts the three modes (droplet, column and sheet) and their two transitions. The images were taken with a high-speed digital video camera. The columns in this case are inline but staggered columns also occur as mentioned above.

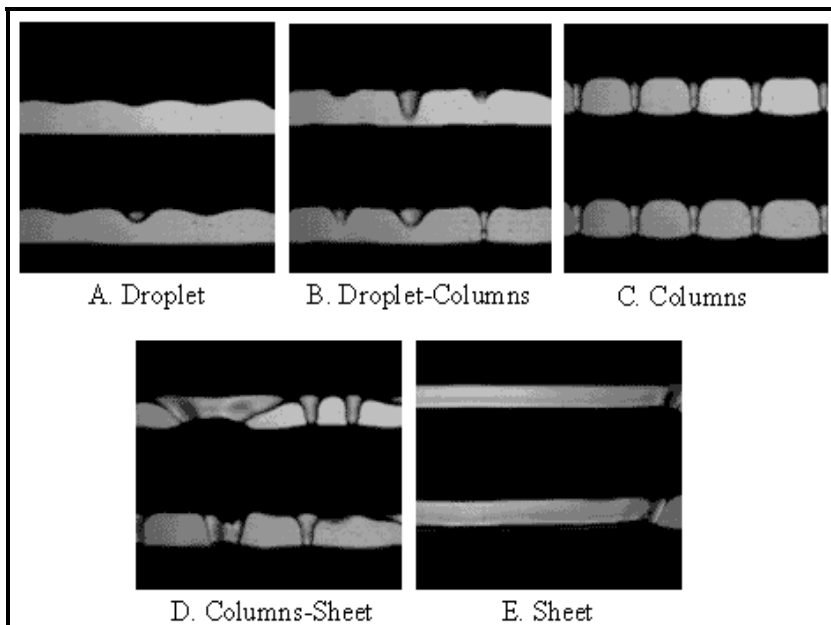


**Figure 7.11.** Video images of three flow modes and their transitions [images courtesy of Laboratory of Heat and Mass Transfer, Swiss Federal Institute of Technology Lausanne].

The Nusselt equation for a single tube may be extended to a vertical array of horizontal tubes, i.e. horizontal tubes situated one above the other, assuming that the sheet mode exists in between all the tubes. Essentially, this is equivalent to assuming that there is an embossed vertical plate of half-tubes with no gap between the tubes with the condensate flowing from one to another. Starting with [7.5.8], the analysis is applied to each individual tube utilizing the summation of the condensate flowing from the above tubes onto the top of the Nth tube, counting the tubes from the top row towards the bottom. Applying an energy balance to the entire surface area of the array of tubes yields

$$2\pi r N \alpha (T_{\text{sat}} - T_w) = 2h_{\text{LG}} [\Gamma_{\text{bottom}}(N)] \quad [7.6.1]$$

where  $\alpha$  is the mean condensation heat transfer coefficient for all the tubes,  $N$  is the number of tubes in the vertical array,  $h_{LG}$  is the latent heat and  $\Gamma_{bottom}(N)$  is the total flow rate of condensate off the bottom tube from one side per unit length of tube. The mean condensation heat transfer coefficient for  $N$  tubes of diameter  $D$  is

$$\frac{\alpha(ND)}{k_L} = 0.728 \left[ \frac{g(\rho_L - \rho_G)(ND)^3 h_{LG}}{k_L v_L (T_{sat} - T_w)} \right]^{1/4} \quad [7.6.2]$$

The mean heat transfer coefficient in terms of the film Reynolds number for the condensate leaving the bottom of the  $N$ th tube is

$$\frac{\alpha}{k_L} \left[ \frac{\mu_L^2}{\rho_L (\rho_L - \rho_G) g} \right]^{1/3} = 1.92 \left( \frac{4\Gamma(N)}{\mu_L} \right)^{-1/3} \quad [7.6.3]$$

where the flow rate of condensate draining from one side of the  $N$ th tube is

$$\Gamma(N) = \frac{N\pi D \alpha (T_{sat} - T_w)}{h_{LG}} \quad [7.6.4]$$

The mean condensation heat transfer coefficient  $\alpha$ , for an entire array of tubes is:

$$\frac{\alpha}{\alpha(N=1)} = N^{-1/4} \quad [7.6.5]$$

where  $\alpha(N=1)$  is the heat transfer coefficient for the top tube row, i.e. the original Nusselt equation for a single tube given by [7.5.7] and [7.5.8]. This method is applicable if the film flow remains *laminar* all the way to the bottom of the  $N$ th row. The heat transfer coefficient on the  $N$ th tube row in the bundle  $\alpha(N)$  is

$$\frac{\alpha(N)}{\alpha(N=1)} = N^{3/4} - (N-1)^{3/4} \quad [7.6.6]$$

Kern (1958) concluded from his practice experience in designing condensers that the above tube row expression was too conservative and that this resulted in condensers that were consistently over-surfaced. To improve his thermal designs, he replaced the exponent of (-1/4) in expression [7.6.5] with a value of (-1/6) so that corresponding equations become

$$\frac{\alpha}{\alpha(N=1)} = N^{-1/6} \quad [7.6.7]$$

$$\frac{\alpha(N)}{\alpha(N=1)} = N^{5/6} - (N-1)^{5/6} \quad [7.6.8]$$

These equations are presently widely used in the thermal design of condensers. Figure 7.12 presents a comparison of experimental data from different sources compiled by Marto (1986) with respect to the

Nusselt and Kern tube row methods. The wide bandwidth of the data compared to the two curves may be some vapor shear effects in the data but is more likely the influence of intertube flow mode types encountered during the experiments, i.e. the modes described above. Experiments have shown that most data are equal to, or higher than, those given by Nusselt's sheet flow analysis. The discrepancy arises because the type of flow has an effect on the analysis. For example, if the flow mode is column-wise, then a portion of the lower tubes will perform without condensate inundation, while the rest of the tube surface will suffer more inundation than in the sheet mode. Hence, the performance will change accordingly. Overall, the column mode is thought to have a positive influence on heat transfer. Therefore, the Nusselt's sheet mode solution is the lower limiting case for the tube row effect. Heat transfer in the other two modes (column and droplet) is expected to be higher.

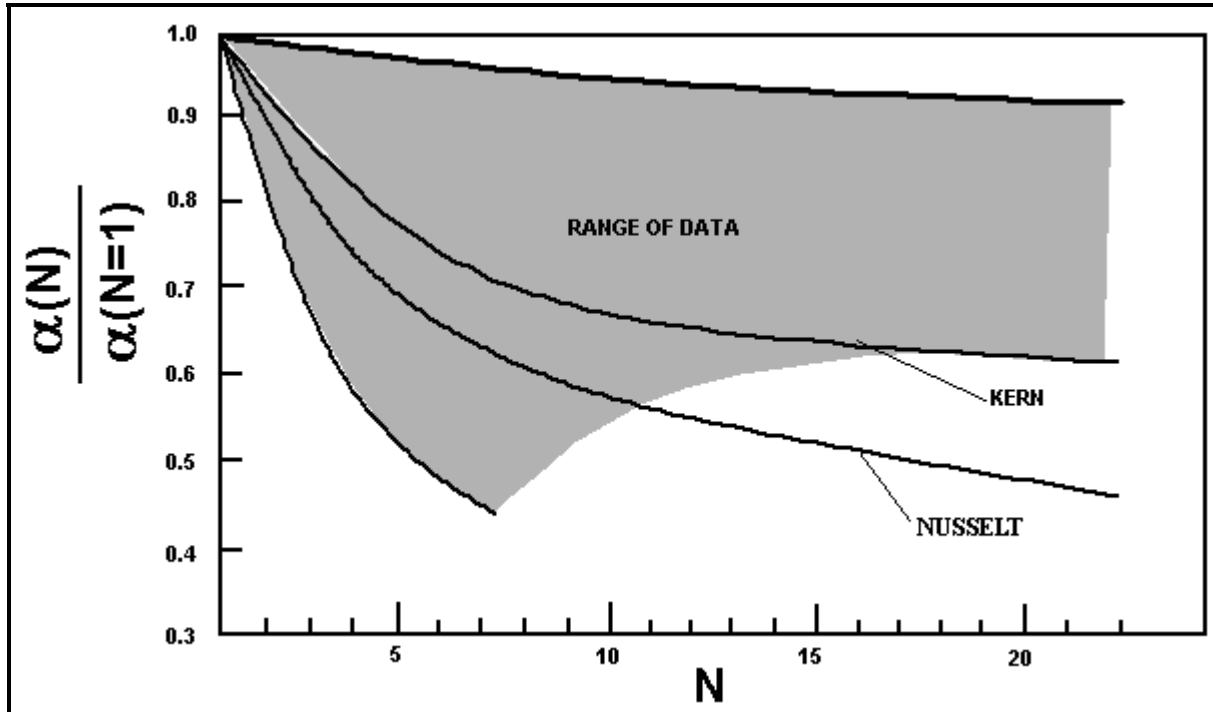


Figure 7.12. Competing tube row methods for condensation on a vertical array of tubes compared to experimental results from Marto (1986).

It is important to understand that these tube row expressions are applied in practice by counting the number of vertical inline tube rows. Hence for an inline or square tube layout, each tube row from the top to the bottom of the bundle is counted in applying these equations. Instead, for staggered tube layouts the condensate is normally assumed to flow to the next inline tube row since it cannot flow onto the top of the out-of-line tube in the next lower row. Thus, the total number of tube rows to use is one-half the actual number, which naturally means that staggered layouts are more advantageous for heat transfer. Since some condensate in a staggered bundle ends up on the sides of the next out-of-line tubes, this assumption is a little optimistic as shown in Figure 7.13 adapted from Marto (1986). Hence, the total number of vertical tube rows in a staggered tube bundle are somewhere between the number of inline rows and the total number of staggered rows, and an average of these two values may be used as a reasonable approximation.

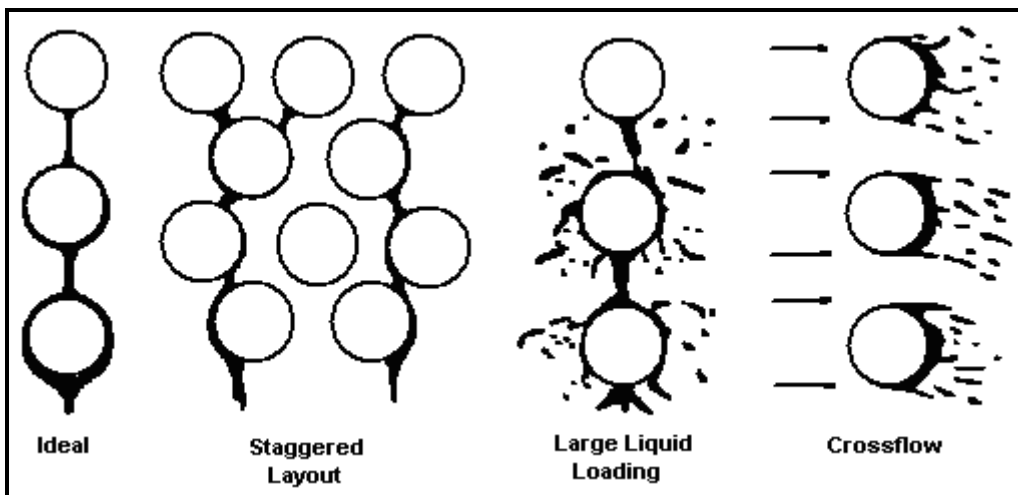


Figure 7.13. Illustration of realistic flow of liquid on tube bundle.

### 7.6.2 Falling Film Flow Regime Transitions on Tube Arrays

At this date, no generalized falling film mode transition map is apparently available for condensation conditions. Honda, Nozo and Takeda (1987) notably, however, has proposed several transition expressions for several refrigerants condensing on low finned tubes. This process is very similar to that of an adiabatic film of liquid falling on a tube array, which has been studied by Hu and Jacobi (1996a) for a variety of fluids, tube diameters, tube pitches and flow rates and with/without cocurrent gas flow and by Mitrovic (1986) as a function of tube spacing, all for plain tubes. More recently by Roques, Dupont and Thome (2002) and Roques and Thome (2001, 2002) have run tests with water, glycol and one water-glycol mixture for one plain tube, then 19 fpi, 26 fpi and 40 fpi low fin tubes, and finally two enhanced tubes (Turbo-Bii and Thermoexcel-E). The 26 fpi tube studied was a [Wolverine Turbo-Chil](#) tube.

Hu and Jacobi (1996a) proposed flow mode transition equations with  $Re_{\Gamma}$  versus  $Ga_L$  (film Reynolds number vs. the Galileo number) for the following principal flow modes: sheet flow, column flow and droplet flow. The mixed mode transition zones of column-sheet and droplet-column were also considered as regimes, bringing the total to five. Hence, they presented four flow transition expressions (valid for passing through the transitions in either direction and hence the symbol  $\Leftrightarrow$ ):

Droplet $\Leftrightarrow$ Droplet-Column:

$$Re_{\Gamma} = 0.148 Ga_L^{0.302} \quad [7.6.9]$$

Droplet-Column $\Leftrightarrow$ Column:

$$Re_{\Gamma} = 0.192 Ga_L^{0.301} \quad [7.6.10]$$

Column $\Leftrightarrow$ Column-Sheet:

$$Re_{\Gamma} = 2.828 Ga_L^{0.233} \quad [7.6.11]$$

Column-Sheet $\Leftrightarrow$ Sheet:

$$Re_f = 2.896 Ga_L^{0.236} \quad [7.6.12]$$

The film Reynolds number  $Re_f$  in their original publication was for flow down *one side* of the tube; hence, the above expressions are evaluated using the film Reynolds number definition given by [7.2.16] with flow down *one side* of the tube to conform to the situation here. The Galileo number  $Ga_L$  is defined as

$$Ga_L = \frac{\rho_L \sigma^3}{\mu_L^4 g} \quad [7.6.13]$$

Figure 7.14 depicts these expressions as a flow transition map, applicable only to plain tubes and air velocities less than 15 m/s.

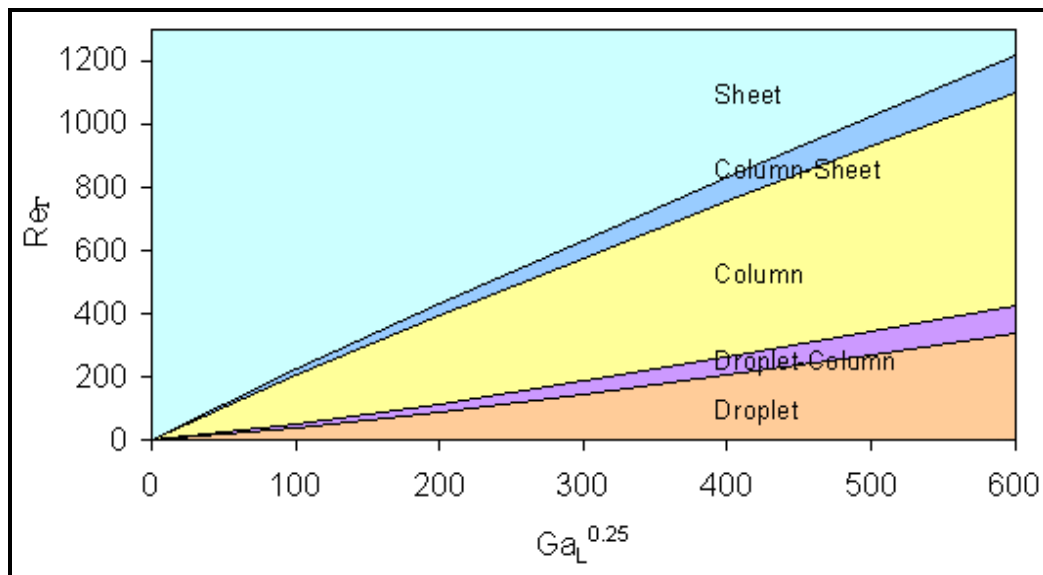


**Figure 7.14. Flow mode map for falling film flow on a vertical array of horizontal tubes.**

Honda, Nuzo and Takeda (1987) have looked at some of the transitions in flow modes on a low finned tube for one refrigerant. More recently, Roques, Dupont and Thome (2002) and Roques and Thome (2001) have reported transition curves similar to those above for plain tubes, low finned tubes (19, 26 and 40 fpi tubes), Thermoexcel-C and Turbo-Bii tubes. They observed that the low finned tubes and the enhanced condensing Thermoexcel-C tube had some significantly different transition thresholds, primarily enlarging the range of conditions at which the column mode exists, which is positive from a heat transfer perspective. These types of studies will eventually lead to condensation design methods in which the tube row effect includes the flow mode effect.

### 7.6.3 Vapor Shear Effects on Tube Bundles

Vapor shear manifests its influence on the condensation process in tube bundles primarily in three ways. First of all, it has an effect of the film flow, tending to increase heat transfer by thinning the film, similar to its effect on vertical plates described earlier. Secondly, the interfacial shear may remove the film from the tube wall, similar to the transition from annular flow to mist flow inside a tube at high vapor core velocities. Thirdly, the vapor shear modifies the intertube flow modes. For instance, the sheet mode is not stable in presence of high velocity vapor and will be broken up into droplets, creating a mist flow. In a

condenser, high vapor velocities may exist near the inlet. Deeper into the bundle, however, the vapor velocity decreases rapidly as the vapor condenses.

McNaught (1982) has estimated the shear-controlled heat transfer coefficient  $\alpha_{sh}$  for the situation where the vapor shear force is dominant and the gravity force on the film is negligible as

$$\alpha_{sh} = 1.26(1/X_{tt})^{0.78}\alpha_L \quad [7.6.14]$$

In this expression the liquid film heat transfer coefficient  $\alpha_L$  is determined assuming that the liquid phase occupies the entire flow channel, i.e. the liquid fraction of the total flow at the minimum cross-sectional area of the bundle, and flows as a turbulent liquid across the bundle. The value of  $\alpha_L$  can be determined from correlations for crossflow heat transfer over tube bundles found in textbooks. The Martinelli parameter  $X_{tt}$  he used is

$$X_{tt} = \left( \frac{1-x}{x} \right)^{0.9} \left( \frac{\rho_G}{\rho_L} \right)^{0.5} \left( \frac{\mu_L}{\mu_G} \right)^{0.1} \quad [7.6.15]$$

where  $x$  is the vapor quality. To find the combined effect of gravity controlled condensation and vapor-shear controlled condensation, the gravity-controlled heat transfer coefficient  $\alpha_{grav}$  is calculated with the Nusselt single tube expression [7.5.7] together with the inundation tube row effect. For staggered and inline layouts, he proposed the following expression

$$\alpha_{grav} = \alpha(N=1) \left[ \frac{\Gamma(N-1) + \Gamma_N}{\Gamma_N} \right]^{-\gamma} \quad [7.6.16]$$

where  $\Gamma(N-1)$  is the total condensate flow rate from one side of the above tubes onto the  $N$ th tube and  $\Gamma_N$  is the condensation rate on one side of the  $N$ th tube itself, whose values may be obtained with [7.6.4]. The heat transfer coefficient for the top tube row is  $\alpha(N=1)$ . The empirical exponent  $\gamma$  is 0.13 for triangular tube layouts and 0.22 for square tube layouts, respecting the larger tube row effect anticipated for the inline tube rows in the square layout, based on a relatively small database. Asymptotic approaches are often used for modeling the combined effects of two different mechanisms on heat transfer on heat transfer and in this case McNaught uses the expression

$$\alpha = (\alpha_{sh}^2 + \alpha_{grav}^2)^{1/2} \quad [7.6.17]$$

where the above two expressions are used to determine the vapor-shear controlled and the gravity-controlled coefficients.

A more detailed method has been proposed by Honda et al. (1989) for condensation on inline and staggered tube bundles of plain tubes using an asymptotic model to the 4<sup>th</sup> power. Refer to that paper, or a summary of it in Collier and Thome (1994), for more information on that method.

#### 7.6.4 Onset of Turbulence and Turbulent Film Heat Transfer

Turbulent flow of the condensate film may be reached in a condenser, which significantly increases heat transfer. Comparatively little has been published on turbulent film condensation on tube bundles

compared to the information available for laminar films. Butterworth (1983) recommends adapting the Labuntsov expression [7.4.2] for turbulent film condensation on a vertical plate to horizontal tubes for predicting local turbulent film condensation on the Nth tube row in horizontal tube bundles:

$$\frac{\alpha(N)}{k_L} \left[ \frac{\mu_L^2}{\rho_L(\rho_L - \rho_G)g} \right]^{1/3} = 0.023 (\text{Re}_\Gamma / 2)^{0.25} \text{Pr}_L^{0.5} \quad [7.6.18]$$

The film Reynolds number is obtained using [7.2.16] with the condensate flow rate on one side of the Nth tube in order to conform to the same definition used for turbulent condensation on a vertical plate. The transition film Reynolds number for the tube bundle is adapted from a vertical plate turbulent transition criterion of 1600 (but also values of 1200, 1800 and 2000 have been proposed) for a film on a plate to one side of a tube. Thus, the film will become turbulent on the tube bundle at  $\text{Re}_\Gamma$  equal to 1600 and thus for values larger than 1600 the above expression should be used.

Similar to the above theory for vertical plates covering laminar and turbulent condensation all in one integrated expression, Honda et al. (1989) achieved the same objective for arrays of horizontal tubes but by a different approach...they assumed an asymptotic model to cover the combined regime effects. For predicting their data for condensation of R-113 (without vapor shear) on a vertical column of inline horizontal tubes, their 4th order asymptotic expression for the condensation heat transfer coefficient on the Nth tube from the top row is:

$$\frac{\alpha(N)}{k_L} \left[ \frac{\mu_L^2}{\rho_L(\rho_L - \rho_G)g} \right]^{1/3} = \left[ (1.2 \text{Re}_\Gamma^{-0.3})^4 + (0.072 \text{Re}_\Gamma^{0.2})^4 \right]^{1/4} \quad [7.6.19]$$

The Reynolds number is defined as above using [7.2.16] for the local condensate flow rate on one side of the tube row. The first term on the right side of the equation is the Nusselt solution for a horizontal tube including the enhancement factor for the surface waves from Kutateladze and Gogonin (1979). The second term on the right is a correlation for turbulent condensation, similar to the expression of Colburn (1934). However, the experimental data of Honda et al. (1989) did not cover the turbulent flow regime so they used the R-12 and R-21 data of Kutateladze and Gogonin (1979) to develop that expression, which does not however explicitly include the effect of the liquid Prandtl number.

Gstöhl and Thome (2006b) have modified the Honda expression slightly to better fit their plain tube R-134a data and to explicitly include the liquid Prandtl number effect, arriving at the following expression:

$$\frac{\alpha(N)}{k_L} \left[ \frac{\mu_L^2}{\rho_L(\rho_L - \rho_G)g} \right]^{1/3} = \left[ (1.2 \text{Re}_\Gamma^{-0.3})^4 + (0.04 \text{Re}_\Gamma^{0.2} \text{Pr}_L^{1/3})^4 \right]^{1/4} \quad [7.6.20]$$

This modified-Honda expression captured their R-134a data very well, predicting 80% of the data to within  $\pm 10\%$ , as long as all the condensate remained on the tube row and was not slung off, giving a minimum in the heat transfer coefficient at about a Reynolds number of 300, as opposed to a much larger transition value for a vertical plate reported earlier. Interestingly, on the lower tubes of their 10 row array run with and without liquid overfeed, Gstöhl and Thome (2006b) observed that a significant amount of condensate was slung off the array by the oscillations of the falling film as it flowed from tube row to tube row. For these conditions, they found experimentally that the heat transfer coefficient was almost constant for Reynolds numbers above 300, which suggests that this liquid slinging process must be accounted for in modeling the process. According to them, the onset of slinging begins when the

maximum deflection angle of the condensate from tube to tube is larger than that of the arc subtended by the next lower tube, such that some of the oscillating condensate misses the lower tube and only a portion of the condensate is deposited on the lower tube. This effect reduces the amount of condensate flowing from tube to tube. Since they measured heat transfer coefficients that rose only slightly with increasing Reynolds numbers above 300, this insinuates that the amount of condensate slung off a tube row is about equal to the new condensate formed on it. The maximum angle of deflection  $\theta_{def}$  for a plain tube row was found empirically to be given in terms of the Reynolds number as follows:

$$\theta_{def} = 0.048 \text{Re}_{\Gamma} \quad [7.6.21]$$

The critical angle  $\theta_{crit}$  is given by the geometry of the tube row, where  $S$  is the vertical tube pitch from tube center to tube center, to be

$$\theta_{crit} = \arcsin\left(\frac{D/2}{S - (D/2)}\right) \quad [7.6.22]$$

In this case, the hypotenuse of the right triangle is  $S - D/2$  (from the bottom point of the upper tube to the center of the lower tube),  $D/2$  is the radius of the tube and  $\theta_{crit}$  is the angle of the tangent line from the bottom of the upper tube that touches the side of the lower tube. Liquid is slung off the tube array when the film Reynolds number is large enough so that  $\theta_{def} > \theta_{crit}$ . Gstöhl and Thome (2006b) also proposed a prediction method for condensation accounting for the influences of the slinging effect and the tube pitch for laminar film condensation, but it is based so far on results for only one fluid (R-134a) and one tube diameter (18.91 mm). It is planned to extend this method to include turbulent films and neighboring tube row effects in the near future while also enlarging the database to additional fluids.

## 7.7 Condensation on Low Finned Tubes and Tube Bundles

Integral low finned tubes have been utilized for enhancing condensation for more than half a century. The geometry of a low finned tube is illustrated in Figure 7.15 and a photograph is shown in Figure 7.16. These tubes have their fins formed by typically three sets of rings of increasing diameter that are forced into the tube wall as the tube is pulled through the ring assemblies. The fins form in the spaces between the rings and hence the term “integral”. The low finned tubes used for condensation typically have a fin tip diameter nearly identical to the diameter of plain ends of the tube such that they are easily inserted through tube sheets into tube bundles. The fins are helical around the tube with a small axial pitch. For condensation, the optimum fin density depends on the particular fluid, primarily the surface tension, and varies from 19 fins/in. (19 fpi or 748 fins/m) up to 42 fpi (1653 fins/m). Fin heights depend on the fin density and the particular tube metal, ranging from about 0.66 to 1.50 mm (0.026 to 0.059 in.). The most typical fin thickness is 0.305 mm (0.012 in.).

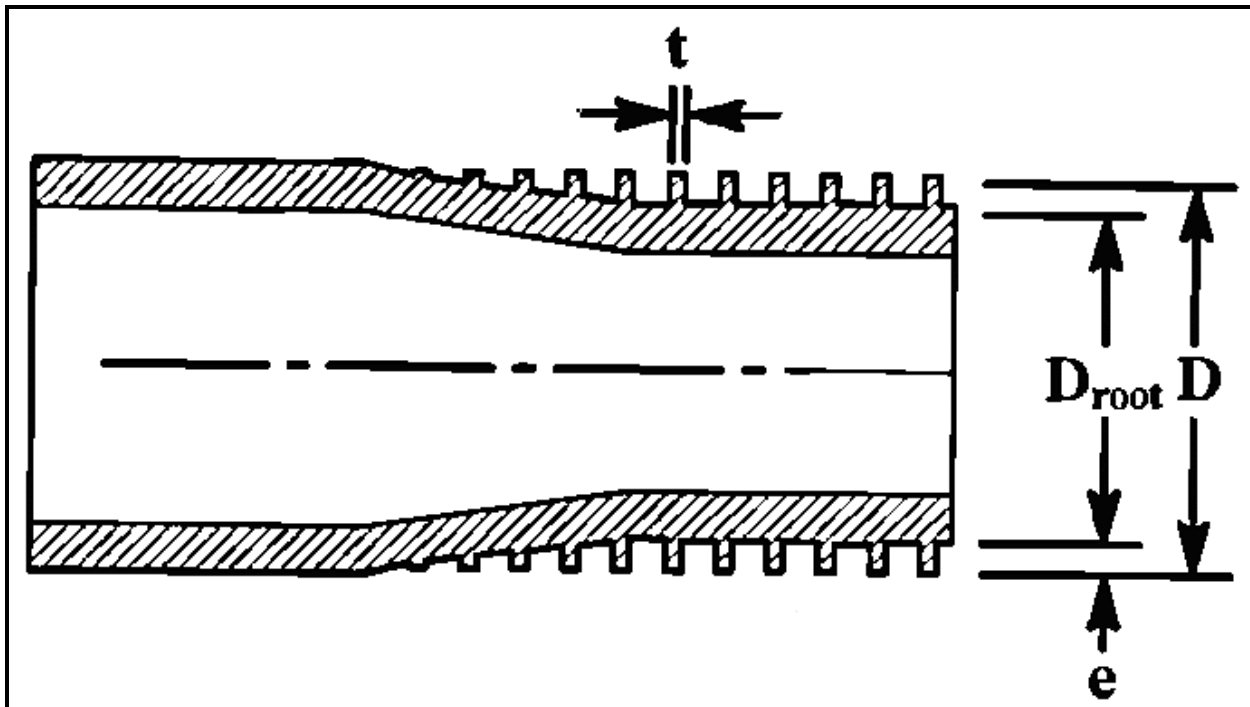


Figure 7.15. Diagram of an integral low finned tube.

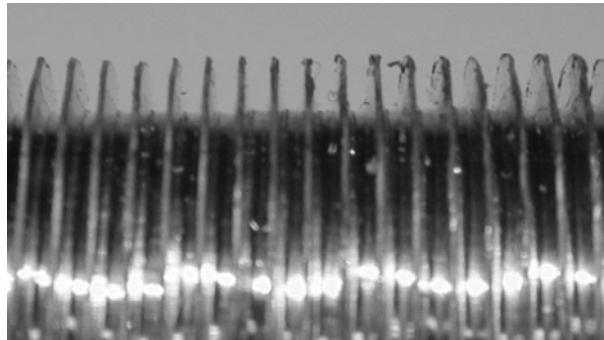


Figure 7.16. Photograph of a low finned tube.

### 7.7.1 Role of Surface Tension on Film Condensation on Low Finned Tubes

The influence of surface tension on two-phase flow and heat transfer is quite complex. Surface tension itself is a cohesive interfacial force created by the difference between the intermolecular forces at the phase transition interface created by the respective molecules, which are closely packed in a liquid and relatively loosely packed in a vapor. Surface tension is what holds a liquid droplet together and tends to form a geometry that minimizes the interfacial surface area, being it a droplet in a vapor or a small film of liquid on a surface. The pressure difference across a liquid-vapor interface of principal radii  $r_1$  and  $r_2$  is given by the Laplace equation, whose general form is

$$\Delta p = \sigma \left( \frac{1}{r_1} + \frac{1}{r_2} \right) \quad [7.7.1]$$

where  $\sigma$  is the surface tension and the pressure difference is

$$\Delta p = p_L - p_G \quad [7.7.2]$$

where  $p_L$  is the local liquid pressure and  $p_G$  is the local vapor pressure and  $r$  is the radius of the interface. For a cylindrical interface, one of the radii goes to infinity and the pressure difference becomes

$$\Delta p = \sigma \left( \frac{1}{r} \right) \quad [7.7.3]$$

Instead, for a spherical surface the two radii are equal and thus

$$\Delta p = \sigma \left( \frac{2}{r} \right) \quad [7.7.4]$$

For a constant vapor pressure at isothermal conditions, if the curvature of the interface is not constant, such as for a liquid film on a fin or a corrugation on the surface of a tube, then the local pressure in the liquid will not be constant. This induces flow of the liquid from the region of small curvature towards that with larger curvature. That is, this will create a surface tension driven flow in the film. On the other hand, if the interface is of uniform radius but is subjected to a temperature gradient, again a pressure gradient will be produced in the liquid and cause liquid to flow from the high temperature region (low surface tension) towards the low temperature region (high surface tension). This latter process is referred to as the *Marangoni effect*. This effect is also created if the fluid is a mixture and a concentration gradient exists in the liquid phase along the interface, which creates a surface tension gradient. Of these two surface tension flows, the pressure difference created by curvature of the interface is typically much stronger in film condensation than that of the Marangoni effect for the small temperature differences involved. Hence, condensate flow from the tip of a fin or corrugation towards its base is primarily from the effect of curvature of the liquid-vapor interface.

For condensate formed on a horizontal low fin tube, the two forces acting on the liquid film in quiescent vapor conditions are gravity and surface tension. Here, surface tension draws the liquid from the fin tip towards its root and dominates the gravity force on the liquid with its downward influence. Instead, in the root area between the fins, the radius of the film around the circumference of the tube is relatively large and uniform; thus, gravity dominates in this direction and governs the drainage of condensate from the tube while surface tension tends to promote retention of the condensate between the fins.

The first to exploit this surface tension induced flow in film condensation was Gregorig (1954) and this has become to be known as the *Gregorig effect*, illustrated in Figure 7.17. He proposed a vertical, longitudinally fluted surface on which the condensate is drawn to the troughs by surface tension forces and then drains downward by gravity forces, enhancing heat transfer relative to a planar surface. His work stimulated numerous developments of enhanced condensation surfaces. For more on this topic, refer to the recent review of Shah, Zhou and Tagavi (1999).

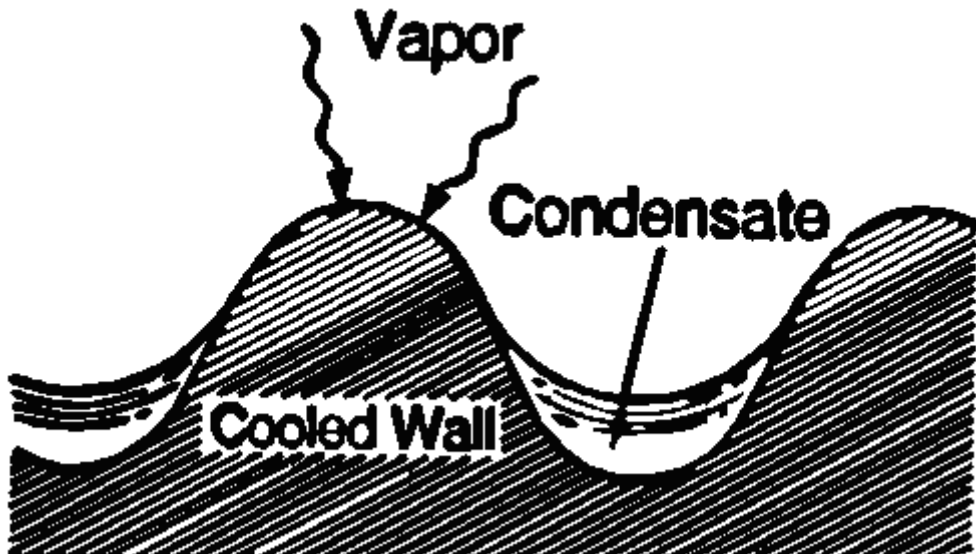


Figure 7.17. Gregorog effect on a liquid film on a fluted surface.

### 7.7.2 Beatty and Katz (1948) Model of Condensation on a Single Horizontal Low Finned Tube

Beatty and Katz (1948) proposed the first model for condensation heat transfer on a horizontal low finned tube. They applied vertical surface Nusselt analysis to condensation on the fin assuming the condensate drains downwards and Nusselt theory for a horizontal tube to condensation on the root area between adjacent fins i.e. a two-zone approach. The condensation heat transfer coefficient is thus an area weighed average of the condensation coefficient on the root area per unit length  $A_{root}$ , referred to as  $\alpha_{root}$ , and the condensation coefficient on the fin area per unit length  $A_{fin}$ , referred to as  $\alpha_{fin}$ . Taking into account the fin efficiency, the condensing coefficient on the low fin tube is

$$\alpha \eta_{surface} = \alpha_{root} \frac{A_{root}}{A_{total}} + \alpha_{fin} \frac{\eta_{fin} A_{fin}}{A_{total}} \quad [7.7.5]$$

where  $\alpha$  is based on the effective external surface area  $A_{eff}$  of the low finned tube. The total surface area per unit length  $A_{total}$  is

$$A_{total} = A_{root} + A_{fin} \quad [7.7.6]$$

where  $A_{fin}$  includes the fin tip area. The surface efficiency  $\eta_{surface}$  is

$$\eta_{surface} = 1 - \frac{A_{fin}}{A_{total}} (1 - \eta_{fin}) \quad [7.7.7]$$

The effective external surface area  $A_{eff}$  is equal to  $\eta_{surface} A_{total}$ . The fin efficiency  $\eta_{fin}$  is normally obtained from the fin efficiency expression for a circumferential fin of uniform thickness with an insulated tip, assuming a uniform heat transfer coefficient over its surface. The fin height is corrected for the latter assumption by adding one-half of the fin tip thickness to the height of the fin when calculating the fin

efficiency. Thus, its value can be estimated from the following expression applying the mean heat transfer coefficient on the fin  $\alpha_{fin}$ , while also introducing the fouling factor R, as follows:

$$\eta_{fin} = \frac{\tanh\left[m\left(e + \frac{t}{2}\right)\right]}{m\left(e + \frac{t}{2}\right)} \quad [7.7.8]$$

$$m = \left[ \frac{2\left(\frac{1}{\alpha_{fin}} + R\right)^{-1}}{k_{fin} t} \right]^{1/2} \quad [7.7.9]$$

Note that the fouling factor R is often neglected in fin efficiency expressions in textbooks. The fouling factor tends to increase the fin efficiency with increasing values of R, very significantly for tubes of low thermal conductivity. Note that the thermal resistances of the condensing coefficient on the fin and the fouling factor are in series in the above expression since the heat first passes through the condensate film and then through the fouling layer into the fin. In the above expressions e is the fin height, t is the mean fin thickness and  $k_{fin}$  is the thermal conductivity of the fin.

For the root area between the fins, the applicable diameter is the root diameter  $D_{root}$  at the base of the fins and this diameter is substituted directly into [7.5.7] for condensation on a horizontal plain tube so that

$$\alpha_{root} = 0.725 \left[ \frac{\rho_L (\rho_L - \rho_G) g k_L^3 h_{LG}}{\mu_L D_{root} (T_{sat} - T_w)} \right]^{1/4} \quad [7.7.10]$$

The equivalent vertical length is then obtained by taking the surface area for one face of the fin and dividing it by the fin tip diameter D, such that the equivalent length of the fin  $L_{fin}$  is

$$L_{fin} = \frac{\pi(D^2 - D_{root}^2)}{4D} \quad [7.7.11]$$

Substituting into [7.2.11], the heat transfer coefficient on the side of the fins is

$$\alpha_{fin} = 0.943 \left[ \frac{\rho_L (\rho_L - \rho_G) g k_L^3 h_{LG}}{\mu_L L_{fin} (T_{sat} - T_w)} \right]^{1/4} \quad [7.7.12]$$

Thus, one first assumes a wall temperature at the root of the fins and then calculates the respective surface areas and heat transfer coefficients. Then the mean coefficient for the entire tube is obtained. The above equations can be incorporated into one single expression as

$$\alpha \eta_{surface} = 0.689 \left[ \frac{\rho_L (\rho_L - \rho_G) g k_L^3 h_{LG}}{\mu_L (T_{sat} - T_w)} \right]^{1/4} \left[ \frac{A_{root}}{A_{total}} D_{root}^{-0.25} + 1.3 \frac{\eta_{fin} A_{fin}}{A_{total}} L_{fin}^{-0.25} \right] \quad [7.7.13]$$

Beatty and Katz replaced the original value of 0.725 in [7.7.10] with an empirical value of 0.689 that fit their experimental data better for four different fluids they tested. Expression [7.2.19] can be used in place of  $h_{LG}$  to include subcooling effects of the condensate. The heat transfer coefficient given by [7.7.13] is defined relative to the effective surface area, i.e.  $A_{eff} = A_{root} + \eta_{fin} A_{fin}$ . The nominal heat transfer coefficient  $\alpha_{nom}$ , based on  $\pi DL$  where  $L$  is the length of the tube, is obtained by multiplying  $\alpha$  by the ratio of  $A_{eff}/\pi DL$ , which allows the low finned tube to be compared to a plain tube on a tube replacement basis. Note that their method does not include the effect of condensate retention (see next section) and also the flow on the fins is actually controlled by surface tension and not gravity. Hence their method is reasonably accurate but is unreliable for fluids with large surface tensions or for large fin densities.

### 7.7.3 Condensate Retention Models for a Horizontal Low Finned Tube

As mentioned above, the Beatty-Katz equation does not account for the condensate retained between the fins on the bottom side of the tube by surface tension forces. The Beatty-Katz approach assumes that all the condensate formed drains off the bottom without any holdup between the fins while a notable perimeter can be affected, typically on the order of 10 to 40% of the circumference. Figure 7.18 depicts the condensate retention half-angle  $\beta$ , which refers to the angle from the bottom of the tube up to the highest point at which condensate is held up to the tip of the fins. Based on a balance of forces, a liquid condensate retention half-angle equation was derived by Honda, Nozu and Mitsumori (1983) as

$$\beta = \cos^{-1} \left\{ 1 - \left( \frac{4\sigma \cos \varphi}{\rho_L g b D} \right) \right\} \quad [7.7.14]$$

where  $D$  is the fin tip diameter and  $b$  is the interfin spacing at the fin tips (e.g. fin pitch minus the fin thickness),  $g$  is the acceleration due to gravity and  $\sigma$  is the surface tension.  $\varphi$  is one-half the apex angle of the fin in radians (typically about 3-7° for standard trapezoidal low fins and 0° for a rectangular fin).

Rudy and Webb (1985) subsequently observed experimentally the retention angle on a variety of low finned tubes and arrived at the following expression for the half-angle of the tube that retains condensate:

$$\beta = \cos^{-1} \left\{ 1 - \left[ \frac{2\sigma \left[ (2e / \cos \varphi) + t_{tip} - t_{root} \right]} {D \rho_L g (s e - A_p)} \right] \right\} \quad [7.7.15]$$

In the above expression, the half-angle  $\beta$  is in radians,  $e$  is the fin height,  $t_{tip}$  is the fin thickness at the tip,  $t_{root}$  is the fin thickness at the root,  $s$  is the fin pitch,  $A_p$  is the cross-sectional area of the fin, and  $\varphi$  is one-half the apex angle of the fin in radians. The expression worked quite well for their measured retention angles. These two expressions give the same retention angle for rectangular fins. For trapezoidal fins, they also give the same result if  $b$  is set to the mean interfin spacing. They are applicable when  $e > b/2$ ; note also that when  $(\sigma \cos \varphi) / (\rho_L g b D) > 0.5$  the interfin space is fully flooded and  $\beta$  should be set to  $\pi$ .

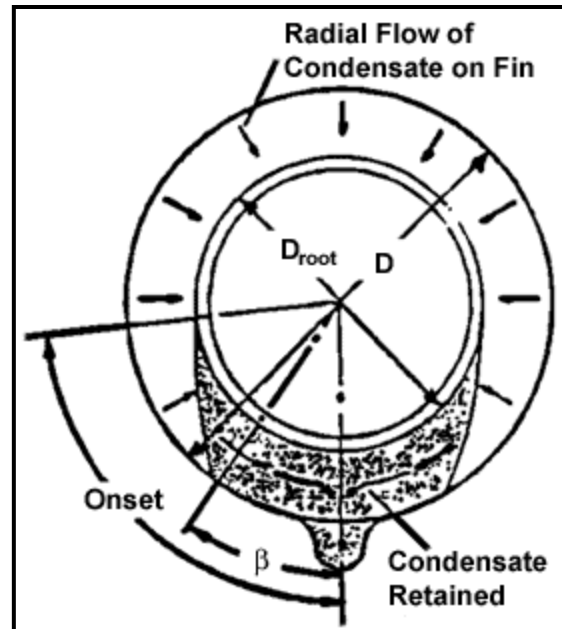


Figure 7.18. Condensate retention angle on a low fin tube.

### 7.7.4 Webb, Rudy and Kedzierski (1985) Model of Condensation on a Single Horizontal Low Finned Tube

Utilizing their condensate retention equation, Webb, Rudy and Kedzierski (1985) improved on the Beatty-Katz model to obtain

$$\alpha\eta_{surface} = (1 - c_b) \left[ \alpha_{root} \frac{A_{root}}{A_{total}} + \eta_{fin} \alpha_{fin} \frac{A_{fin}}{A_{total}} \right] + c_b \alpha_b \quad [7.7.16]$$

Here  $\alpha_{fin}$  is determined from surface tension driven flow on the fins as

$$\alpha_{fin} = 0.943 \left[ \frac{\rho_L k_L^3 h_{LG}}{\mu_L (T_{sat} - T_w)} \right]^{1/4} \left[ \frac{2\sigma}{e^2} \left( \frac{1}{s} + \frac{1}{t} \right) \right]^{1/4} \quad [7.7.17]$$

and  $\alpha_{root}$  is determined based on gravity controlled flow as

$$\alpha_{root} = 1.514 \left[ \frac{\mu_L^2 Re_{root}}{gk_L^3 \rho_L^2} \right]^{-1/3} \quad [7.7.18]$$

where the film Reynolds number of the condensate flowing in the root area is

$$Re_{root} = \frac{4\Gamma_{root}}{\mu_L (s - t_{root})} \quad [7.7.19]$$

$\Gamma_{root}$  is obtained from

$$\Gamma_{root} = \Gamma_{fin} + [\alpha_{root} A_{root} (T_{sat} - T_w) / h_{LG}] \quad [7.7.20]$$

and

$$\Gamma_{fin} = \alpha_{fin} \eta_{fin} A_{fin} (1 - c_b) (T_{sat} - T_w) / h_{LG} \quad [7.7.21]$$

The condensate flooded fraction of the tube perimeter  $c_b$  is equal to  $\beta/\pi$  while the unflooded fraction completely available for film condensation is  $(1-c_b)$ . They also included the heat transfer on the flooded perimeter of the tube  $\alpha_b$ , estimating its value numerically. However, it is simpler to assume laminar, fully developed flow in a rectangular channel of the same width but twice the fin height (to represent the interfin half-channel as a closed channel) and thus allows textbook solutions based on aspect ratio to be applied to calculate the Nusselt number for the laminar flow heat transfer to obtain  $\alpha_b$ .

### 7.7.5 Other Recent Low Finned Tube Condensation Models

More complex theoretical models for condensation on two-dimensional low finned tubes have been developed, such as those of Adamek (1981), Honda and Nozu (1986), and Adamek and Webb (1990). For a more detailed review, refer to Webb (1994) or Shah, Zhou and Tagavi (1999). On the other hand, Rose (1994) proposed a simplified empirical approach that captures most of the features of these analytical models and also predicts a large independent experimental database covering steam, glycol, hydrocarbons

and refrigerants. Furthermore, the method of Rose is able to predict the optimum fin spacing for the fluid in question, which is particularly important when choosing the best available fin density for an application, and the method is still relatively simple to implement. Thus, this method is described below.

Rose (1994) began by defining a condensing enhancement ratio  $\varepsilon_{\Delta T}$  for low finned and smooth tubes operating at the same condensing temperature difference  $\Delta T$  (i.e. the saturation temperature minus the base wall temperature) as:

$$\varepsilon_{\Delta T} = \frac{\alpha \text{ of finned tube}}{\alpha \text{ of smooth tube}} = \frac{(q/\Delta T) \text{ of finned tube}}{(q/\Delta T) \text{ of smooth tube}} = \frac{q \text{ of finned tube}}{q \text{ of smooth tube}} \quad [7.7.22]$$

The enhancement ratio at the same heat flux  $q$  on each tube  $\varepsilon_q$  is instead defined as:

$$\varepsilon_q = \frac{\alpha \text{ of finned tube}}{\alpha \text{ of smooth tube}} = \frac{(q/\Delta T) \text{ of finned tube}}{(q/\Delta T) \text{ of smooth tube}} = \frac{\Delta T \text{ of finned tube}}{\Delta T \text{ of smooth tube}} \quad [7.7.23]$$

In the above expressions, the heat flux  $q$  and heat transfer coefficient  $\alpha$  are based on the same smooth tube surface area, determined with the diameter  $D$  for the smooth tube and the root diameter  $D_{root}$  for the finned tube, respectively. Hence, to convert the low finned tube heat transfer coefficient from its nominal surface area at  $D_{root}$  in this method to its nominal surface area value at the fin tip diameter  $D$ , the former value must be multiplied by the ratio  $D/D_{root}$ . Since  $q$  is typically found to be nearly proportional to  $\Delta T^{4/3}$  for both smooth and low finned tubes according to Rose,  $\varepsilon_{\Delta T}$  and  $\varepsilon_q$  are therefore related as follows:

$$\varepsilon_q = (\varepsilon_{\Delta T})^{4/3} \quad [7.7.24]$$

This means that the enhancement ratio is higher when comparing a low finned tube to a smooth tube at the same heat flux than when making the comparison at the same condensing temperature difference. The general enhancement expression of Rose (1994) for a low finned tube for  $\varepsilon_{\Delta T}$  is:

$$\begin{aligned} \varepsilon_{\Delta T} = & \left( \frac{D}{D_{root}} \right) \left( \frac{t_{tip}}{b + t_{tip}} \right) T_t + \frac{\pi - \beta}{\pi} \left( \frac{1 - F_f}{\cos \varphi} \right) \left( \frac{D^2 - D_{root}^2}{2D_{root}(b + t_{tip})} \right) T_f \\ & + \frac{\pi - \beta}{\pi} (1 - F_s) B_1 \left( \frac{s - t_{root}}{b + t_{tip}} \right) T_s \end{aligned} \quad [7.7.25]$$

In this expression, the first term to the right gives the fin tip enhancement effect, the second term gives that relative to the sides of the fin and the last term gives that regarding the root area between adjacent fins. The thickness of the fin at the tip is  $t_{tip}$ , the thickness of the fin at its root is  $t_{root}$ , the interfin spacing between the flanks of two adjacent fins at their tip is  $b$ , the fin pitch is  $s$ , the condensate retention angle from the *bottom* of the tube is  $\beta$  and one-half of the apex angle of the fin itself is  $\varphi$  (equal to the angle between the flank of the fin and its vertical axis). The term  $(\pi - \beta)/\pi$  in the above expression is equivalent to  $(1 - c_b)$  in the method of Webb, Rudy and Kedzierski (1985) described earlier. Expression [7.7.14] is used by Rose to calculate  $\beta$ . This expression is applicable when  $\beta \leq \pi$ ; at  $\beta = \pi$  only the fin tips contribute to film condensation heat transfer and the other two terms for the fin flanks and interfin root area are neglected when calculating for smaller fin spacings, which produces a sharp inversion in the value of  $\varepsilon_{\Delta T}$  when simulating the effect of interfin spacing with the other geometrical parameters fixed. The other parameters in his method are determined as described below.

In the above expression,  $F_f$  and  $F_s$  are the fractions of the flank areas of the fins and the interfin root area influenced by the liquid retention due to capillary forces at the base of sharp-edged fin roots on the upper part of the tube above the fully flooded zone of the tube perimeter, i.e. the condensate retained as wedges at the roots of the fins in the “unflooded” zone of the tube which reduce heat transfer performance. For trapezoidal fins with sharp-edged fin roots from the analysis of Masuda and Rose (1987), these fractions for the fin flanks and the root area between fins are calculated respectively as:

$$F_f = \left( \frac{1 - \tan(\varphi/2)}{1 + \tan(\varphi/2)} \right) \left( \frac{2\sigma \cos \varphi}{\rho_L g D_{root} e} \right) \left( \frac{\tan((\pi - \beta)/2)}{\pi - \beta} \right) \quad [7.7.26a]$$

$$F_s = \left( \frac{1 - \tan(\varphi/2)}{1 + \tan(\varphi/2)} \right) \left( \frac{4\sigma}{\rho_L g D_{root} (s - t_{root})} \right) \left( \frac{\tan((\pi - \beta)/2)}{\pi - \beta} \right) \quad [7.7.26b]$$

Owing to some approximations in the derivations of these two parameters, they sometimes marginally exceed unity in value and in that case the relevant parameter is reset to unity. For rectangular fins, this expression is simplified with  $\varphi = 0$ . For specially configured fins with a fin root radius such that an inscribed arc touches both the fin flanks and the interfin root surface at the root diameter, no condensate is retained above the angle  $\beta$  and thus  $F_f$  and  $F_s$  are zero according to Masuda and Rose (1987). Refer to Rose (1994) for further details.

Continuing with the description of the Rose (1994) method, the parameters  $T_t$ ,  $T_f$  and  $T_s$  are determined as follows:

$$T_t = \left\{ \frac{D_{root}}{D} + \frac{B_t G_t}{0.728^4} \right\}^{1/4} \quad [7.7.27a]$$

$$T_f = \left\{ \left( \frac{0.943}{0.728} \right)^4 \frac{D_{root}}{e_{eff}} + \frac{B_f G_f}{0.728^4} \right\}^{1/4} \quad [7.7.27b]$$

$$T_s = \left\{ \frac{(\xi(\pi - \beta))^3}{0.728^4} + \frac{B_s G_s}{0.728^4} \right\}^{1/4} \quad [7.7.27c]$$

The effective vertical fin height is used in [7.7.27b], where  $e_{eff} = e(\pi - \beta) / \sin(\pi - \beta)$  when  $(\pi - \beta) \leq \pi/2$  whereas  $e_{eff} = e(\pi - \beta) / (2 - \sin(\pi - \beta))$  when  $\pi \geq (\pi - \beta) \geq \pi/2$ . In [7.7.27c], the function  $\xi(\pi - \beta)$  is determined from the following polynomial fit to the integration of the condensate film thickness in the Nusselt theory to the angle  $(\pi - \beta)$  to simplify the method’s implementation:

$$\begin{aligned} \xi(\pi - \beta) = & 0.874 + 0.001991(\pi - \beta) - 0.02642(\pi - \beta)^2 \\ & + 0.005530(\pi - \beta)^3 - 0.001363(\pi - \beta)^4 \end{aligned} \quad [7.7.28]$$

The parameters  $G_t$ ,  $G_f$  and  $G_s$  are determined as:

$$G_t = \frac{\sigma D_{root}}{(\rho_L - \rho_G) g t_{tip}^3} \quad [7.7.29a]$$

$$G_f = \frac{\sigma D_{\text{root}}}{(\rho_L - \rho_G) g e^3} \quad [7.7.29b]$$

$$G_s = \frac{\sigma D_{\text{root}}}{(\rho_L - \rho_G) g (s - t_{\text{root}})^3} \quad [7.7.29c]$$

The empirical constants found by matching this method to his database yielded  $B_t = B_f = B_s = 0.143$  and  $B_1 = 2.96$ . It predicted his database to a standard deviation of 12.4% and also predicted the trends correctly for fin density (interfin spacing) for three different fluids. To account for the effect of fin efficiency, which is particularly important for tube materials with thermal conductivities lower than copper, Briggs and Rose (2004) have provided a simple iterative method to account for the influences on the fin tip and fin flank heat transfer.

### 7.7.6 Effects of Tube Row and Vapor Shear on Low Finned Tube Arrays

Low finned tubes promote the Helmholtz-Kelvin instability in the condensate flowing off the bottom of the tube such that the column mode is encouraged as shown in Figure 7.19. The low fins also inhibit lateral spreading of the impinging film along the lower tube and the majority of the condensate flows around a low finned tube with minimal lateral spreading. As a consequence, large zones of the finned surface between these columns are unaffected by condensate from the tubes above and hence these zones function as if they were in the top row. Therefore, applying the Nusselt and Kern tube row factors, in [7.6.5] and [7.6.7], to low finned tube bundles is extremely conservative, resulting in significant under-predicting of the bundle's condensing heat transfer coefficient. Some experimental studies found tube row exponents as low as  $-1/25$  but it is more prudent value to use a tube row exponent of  $-1/10$  or  $-1/12$ .

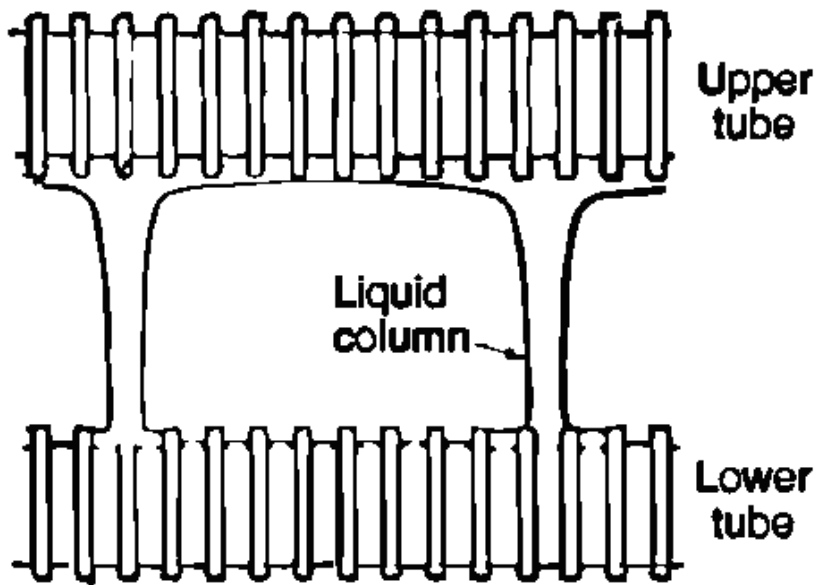
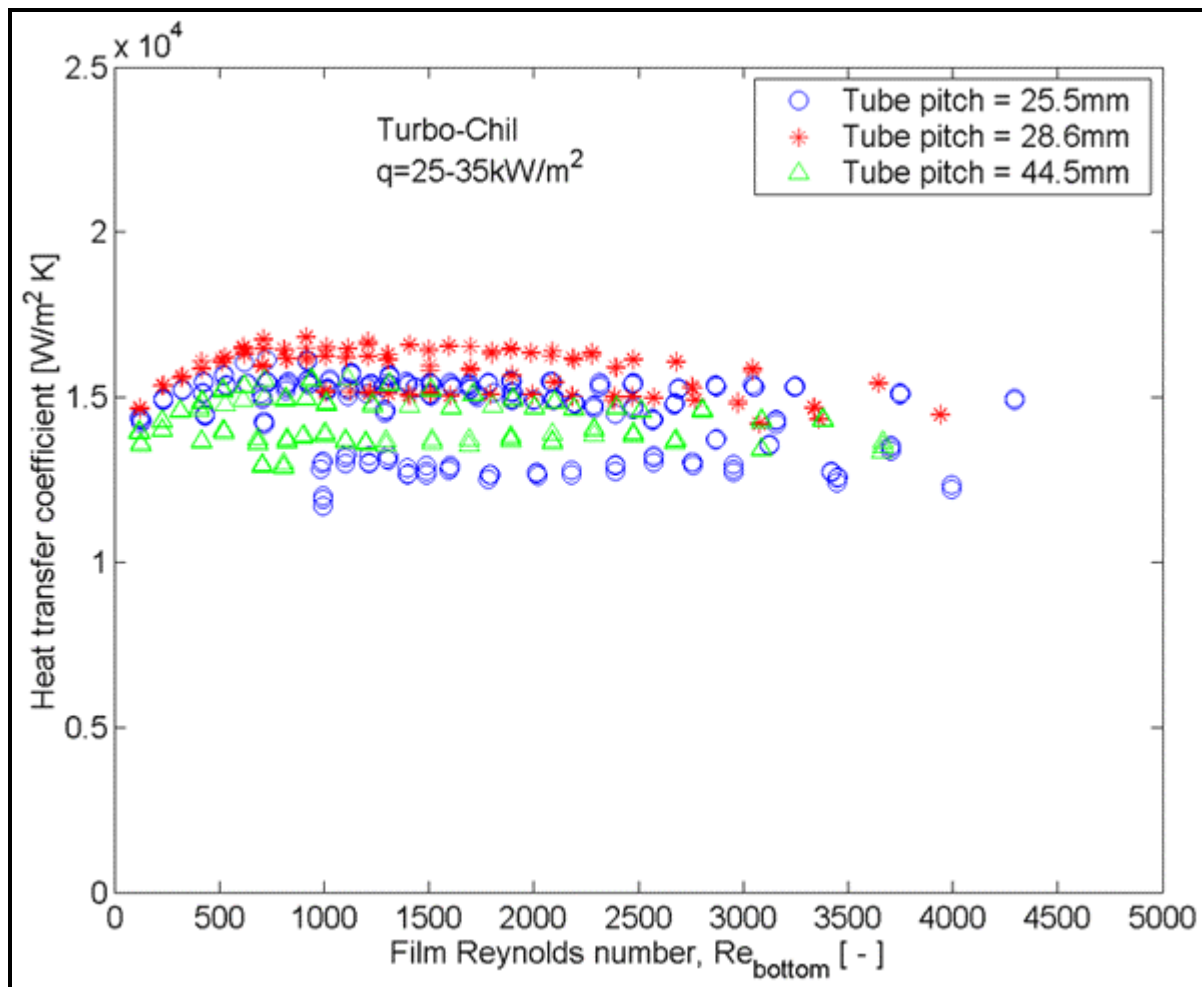


Figure 7.19. Condensate flow as a column jet between low finned tubes.

Furthermore, in the recent study of Gstöhl and Thome (2006a) for R-134a condensing at 30°C on a Wolverine 26 fpi Turbo-Chil tube array of ten tubes, very small tube row effects were found for film Reynolds numbers reaching up to 4250 for vertical tube pitches of 25.5, 28.6 and 44.5 mm for their 18.94 mm fin tip diameter tubes at three levels of nominal heat flux. Their results are shown in Figure 7.20 for

which tube row exponents ranged from  $-1/14$  to  $-1/100$ . Based on all their data, the mean tube row exponent was found to be  $-1/33$ . Thus for thermal design, a prudent value of  $-1/25$  may be the best choice but certainly applying the value  $-1/6$  proposed by Kern (1958) for plain tubes to low finned tubes is too conservative and needlessly penalizes the application of low finned tubes.



**Figure 7.20. Condensation data for Turbo-Chil low finned tube array of Gstöhl and Thome (2006a).**

In order to illustrate the dynamics of the condensate flow on a low finned tube array, Figure 7.21 from Gstöhl and Thome (2006c) shows a time sequence taken during condensation without liquid overfeed at a nominal heat flux of  $40 \text{ kW/m}^2$ . First, three "temporary" columns are formed below the top tube. When they impinge on the second tube, the liquid columns do not spread axially along the tube but instead the condensate is channeled by the fins to flow around the tube. Then the diameters of these columns decrease and they break down. The liquid that impinged on the second tube flows around the tubes and leaves at the bottom at the same axial positions. The three columns formed below the second tube are twisted and exist for about the same period as the "temporary" columns formed below the first tube. If one interprets this in terms of the tube row effect, it is clear that the lower tubes in this array of low finned tubes have only a limited part of their length inundated by condensate from above while most of the length suffers no inundation and this process occurs only intermittently so that for some periods of time there is *no* inundation at all, thus explaining the very small tube row exponent for low finned tubes.

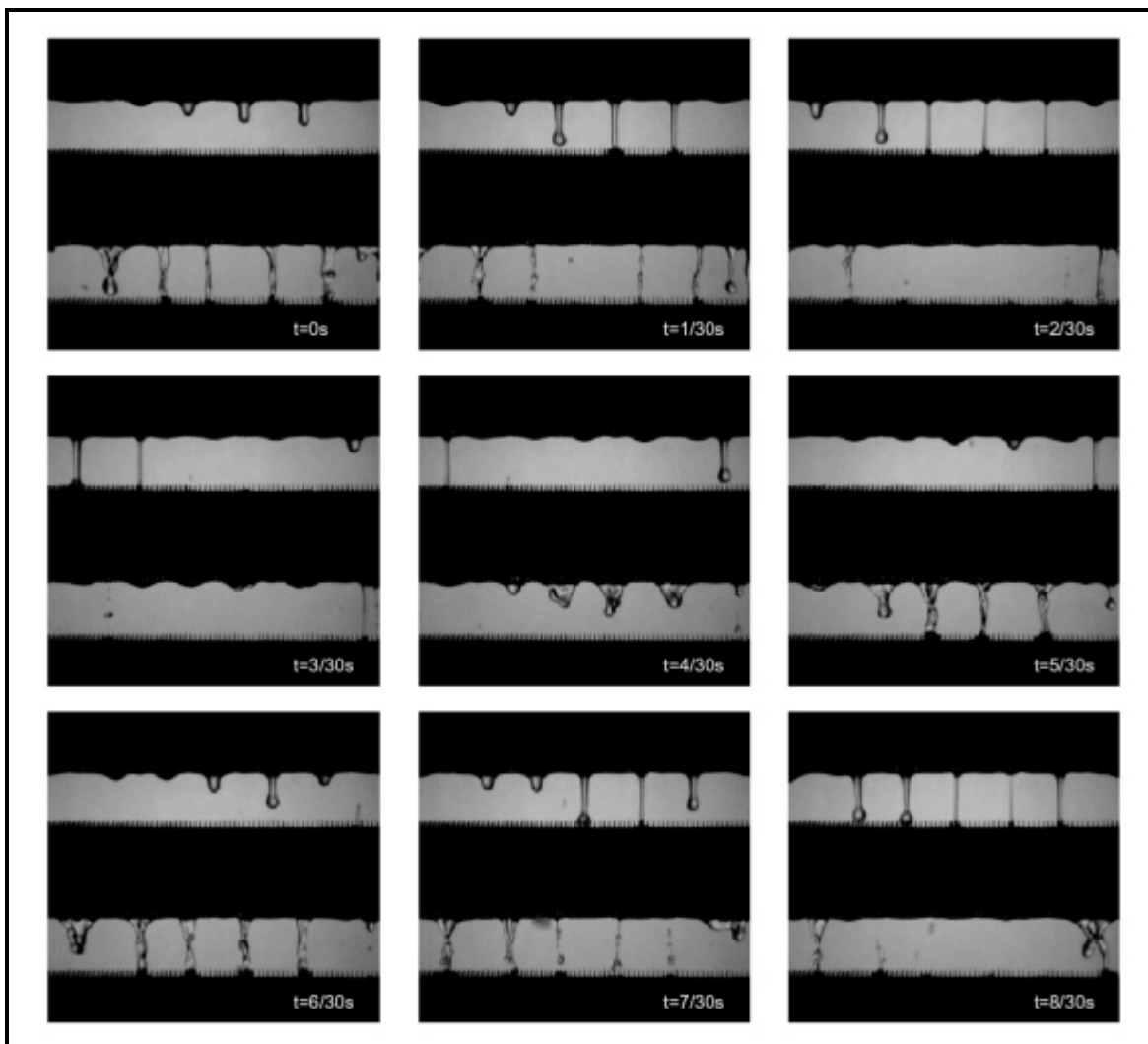


**Figure 7.21. Time sequence of condensate flow on the second tube in an array of low finned tubes at a tube pitch of 28.6 mm for R-134a condensing at a nominal heat flux of 40 kW/m<sup>2</sup> from Gstöhl and Thome (2006c).**

Cavallini et al. (1995) investigated the effect of interfacial vapor shear on condensation on a single low finned tube. According to their experiments, a very large vapor Reynolds number threshold must be surpassed before a significant influence is seen on low finned tube performance. Videos described in Cavallini et al. (1994), with several exemplary photographs, also prove that the vapor shear has little effect on the condensate retention angle, at least up to the point where the condensate is then literally blown off the tube and a mist flow is formed. Thus, low finned tube bundles can be designed using only a single-tube condensation model together with the appropriate tube row equation, as long as the film flow remains in the laminar regime and the vapor Reynolds number remains below 100,000.

Cavallini et al. (1996) proposed an asymptotic method for the combined effect of gravity and vapor shear on a single-tube:

$$\alpha = \left( \alpha_{sv}^2 + \alpha_{fc}^2 \right)^{1/2} \quad [7.7.30]$$

where  $\alpha_{sv}$  is the heat transfer coefficient on the finned tube under stationary vapor conditions and  $\alpha_{fc}$  is the heat transfer coefficient under forced convection (vapor shear controlled) conditions.

$$\alpha_{fc} = C_{fc} \left( \frac{k_L}{D} \right) Re_{eq}^{0.8} Pr_L^{1/3} \quad [7.7.31]$$

and the empirical lead constant is determined from

$$C_{fc} = 0.03 + 0.116(t_{tip}/s) + 0.07(e/s) \quad [7.7.32]$$

$Re_{eq}$  is the equivalent Reynolds number and  $Pr_L$  is the liquid Prandtl number. To extend this method to tube bundles,  $\alpha_{sv}$  could be obtained by applying the tube row correction using an exponent of -1/10 or -1/12 or even to -1/25 based on recent results from the single tube row study by Gstöhl and Thome (2006a) mentioned above.

### 7.7.7 Three-dimensional Enhanced Condensing Tubes

Integral low finned tubes with three-dimensional fins are made by notching of conventional two-dimensional low fins to form saw-toothed fins, or by crosscutting the fins. This greatly reduces condensate retention and enhances heat transfer coefficients on the fins. While several comprehensive experimental studies have been published for these tubes, no general analytical method is available at this time for predicting their performance. Several experimental studies are described below.

Briggs, Yang and Rose (1995) completed a very accurate, comprehensive experimental comparison of 17 commercially available low finned tube geometries, including both 2-d trapezoidal fins and notched 3-d fins, for R-113. One 2-d trapezoidal fin gave the same performance as the best of the 3-d notched fins, but the 3-d fins had not been optimized for use with R-113.

Rewert, Huber and Pate (1996a, 1996b) measured condensing coefficients for R-123 and R-134a in a comparison of a 1024 fpm (26 fpi) low finned tube, a 1575 fpm (40 fpi) low finned tube, a Turbo-CII tube and a Gewa-SC tube (the latter have 3-d enhancements). The Turbo-CII tube significantly outperformed the 40 fpi low finned tube (the better of the two low fin tubes) while the Gewa-SC only provided moderate improvement with respect to the 40 fpi tube. In tests on a five-by-five staggered tube bundle and using liquid overfeed to simulate up to 30 tube rows, they reported data by tube row for these fluids and tubes. Figure 7.22 depicts four graphs of performance. For both fluids, the Turbo-CII shows a faster falloff in tube row performance than the other tubes; since it starts from a much larger top tube row value, its overall condensing performance is still higher than the other tubes, however. The tube row effect of the Gewa-SC tube in the lower left graph is nearly negligible, with the lower tubes performing like the top tube.

Chen and Tuzla (1996) ran extensive tests on a 19 mm (3/4 in.) [Turbo-CII of Wolverine Tube](#) at a saturation temperature of 37.7°C (100°F) for R-22, R-134a, R-410a and several zeotropic refrigerant mixtures. The R-134a performance was slightly above that of R-22 while R-410a outperformed those fluids by about 15%. Performances of the zeotropic mixtures were much lower as they suffered from the mass diffusion resistance in the vapor phase.

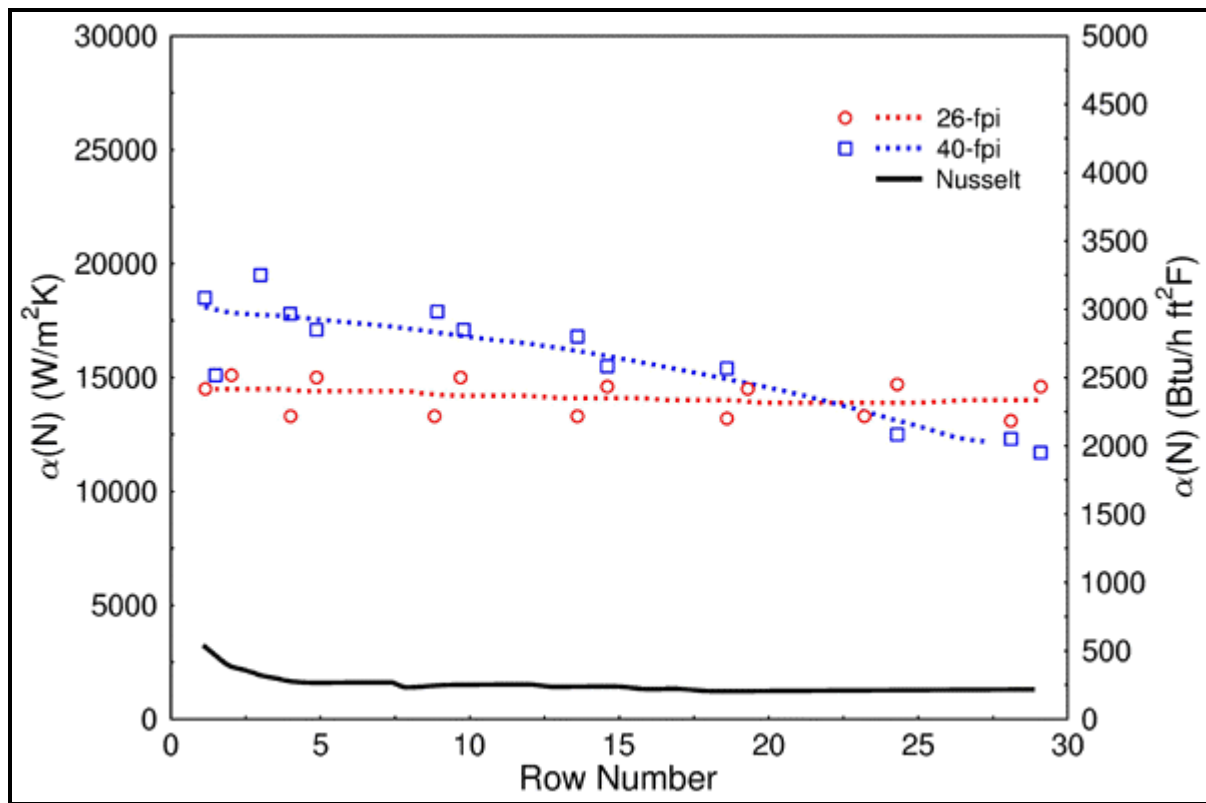


Fig. 7.22 (a): low finned tubes with R-134a.

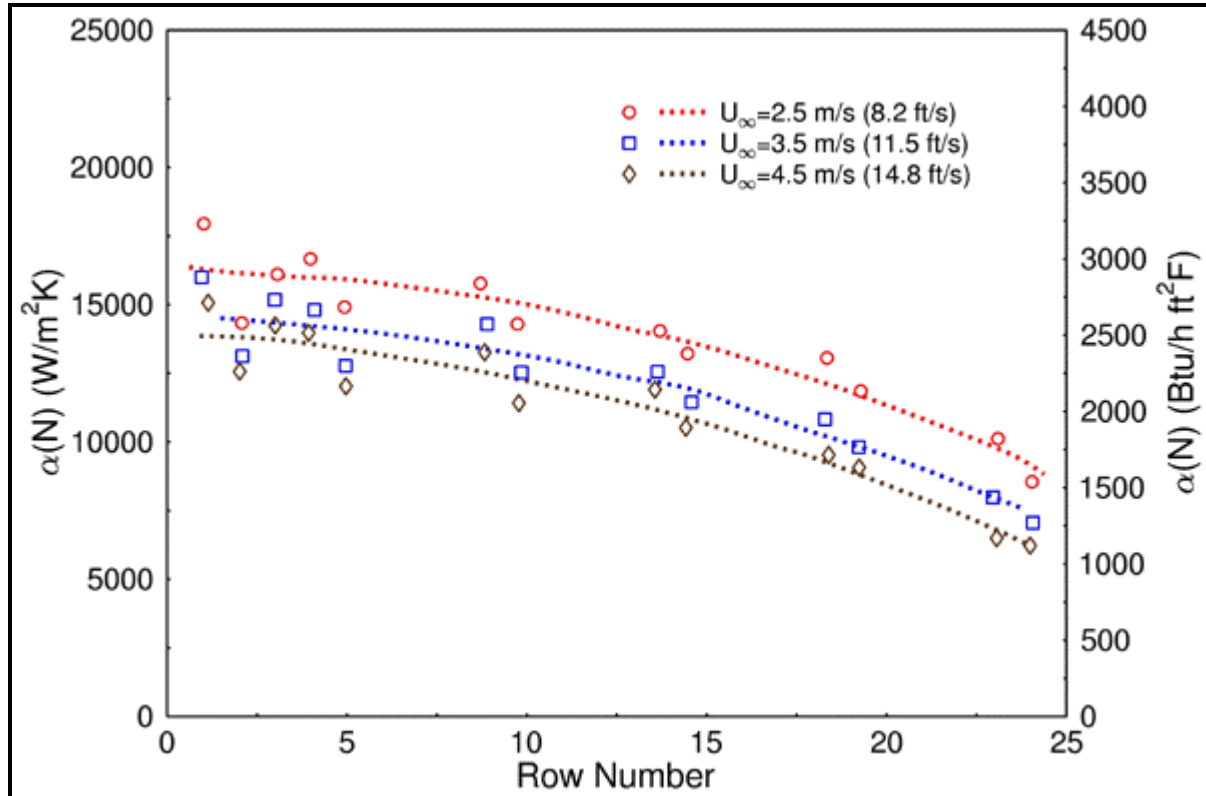


Fig. 7.22 (b): 40-fpi tube with R-123.

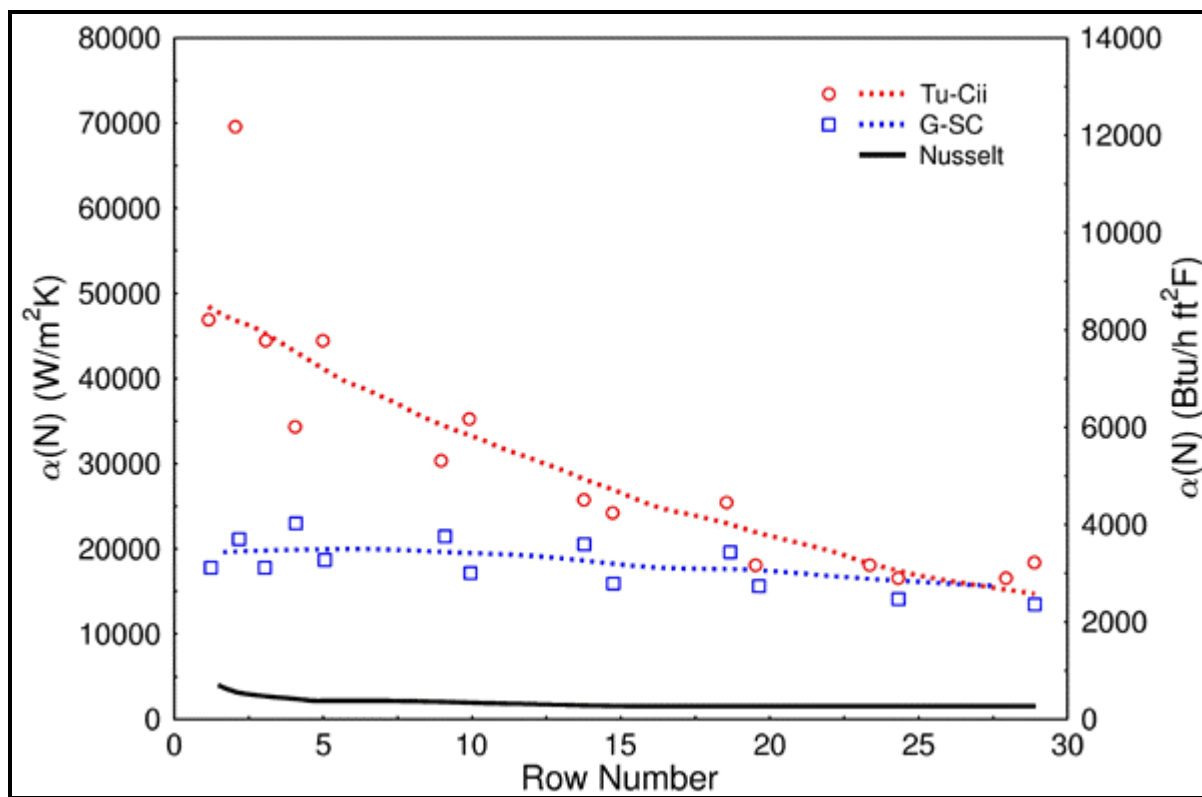


Fig. 7.22 (c): Turbo-Cii and G-SC for R-134a.

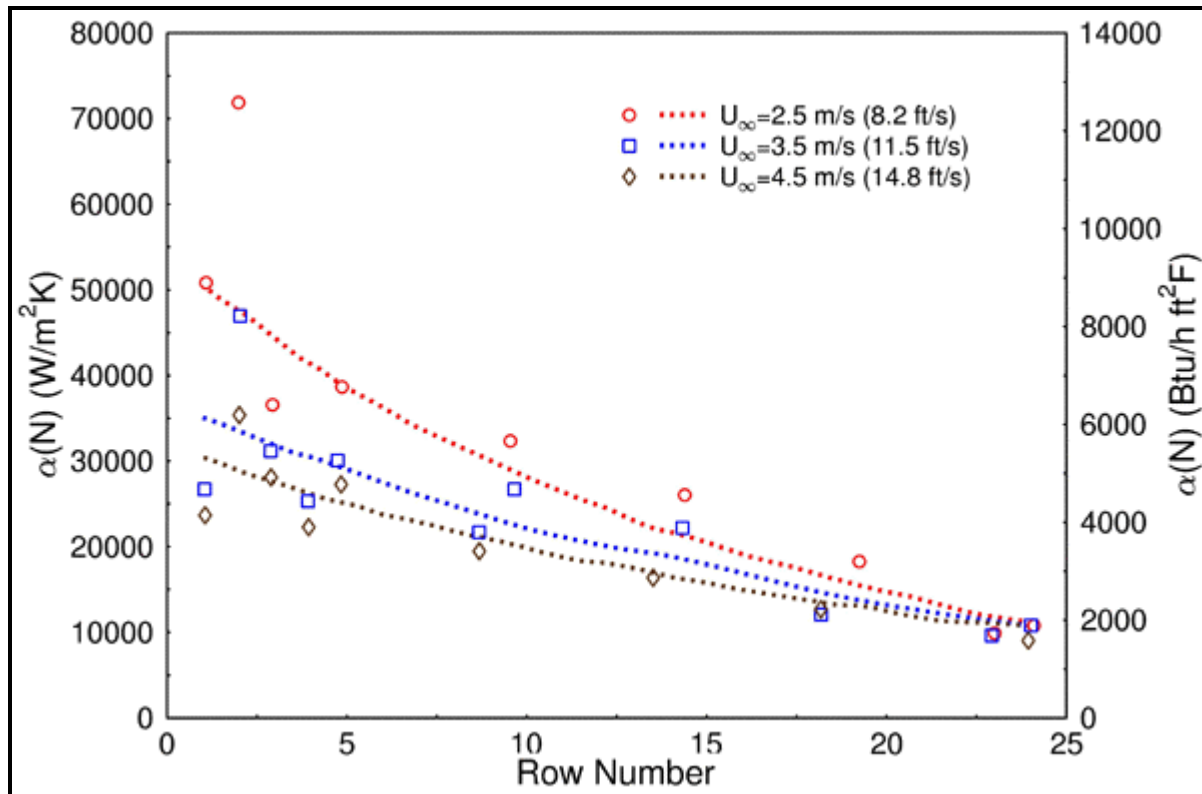
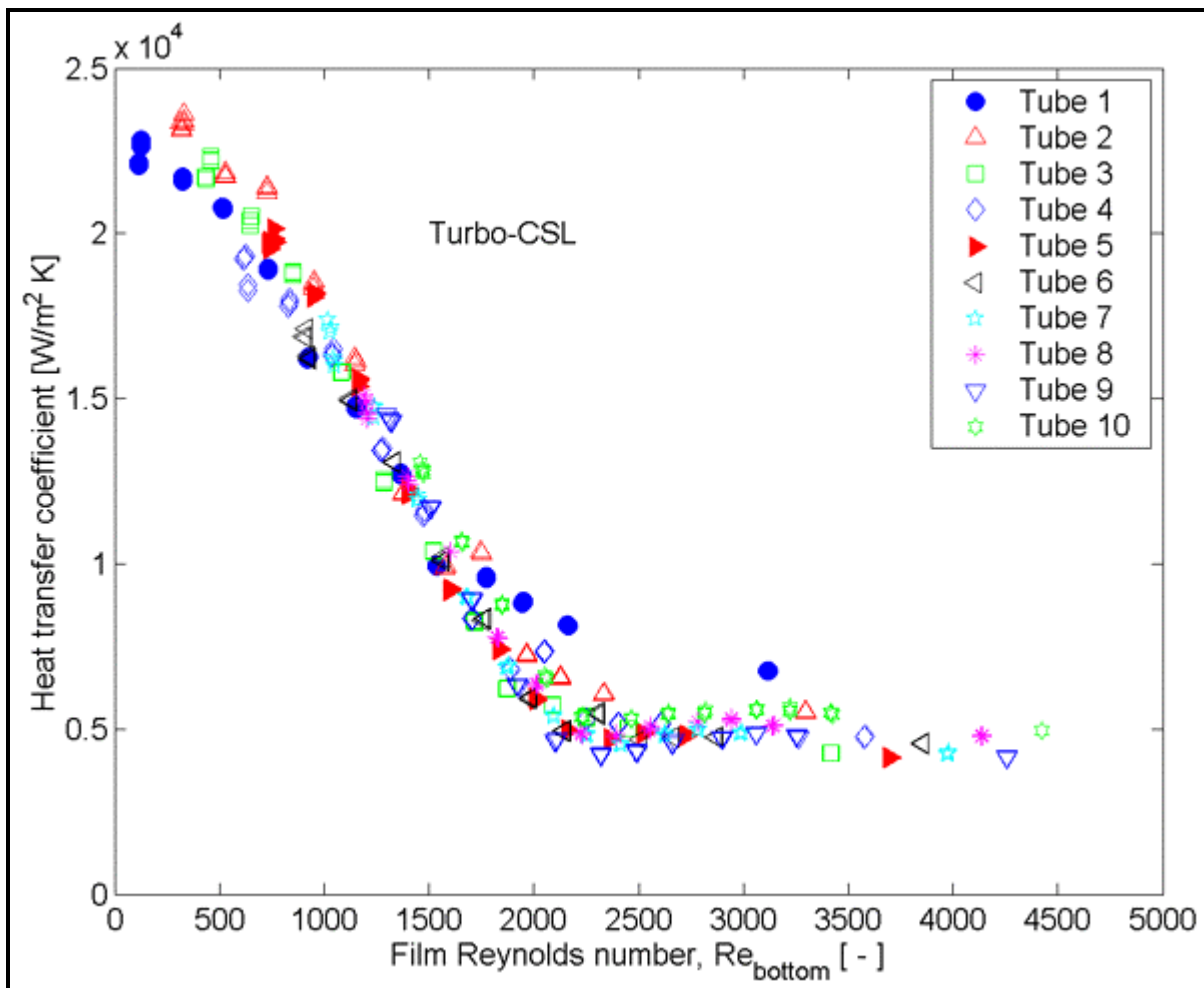


Fig. 7.22 (d): Turbo-Cii for R-123.

**Figure 7.22.** Condensing data of Rewerts, Huber and Pate (1996a, 1996b). (a): low finned tubes with R-134a; (b): 40 fpi tube with R-123; (c): Turbo-Cii and G-SC for R-134a; (d): Turbo-Cii for R-123. [their figs. 4 & 8 and 4 & 5 reprinted by permission of ASHRAE Trans., 1996 copyright by American Society of Heating, Refrigeration and Air-Conditioning Engineers]. [Note: these figures are shown on the two previous pages.]



**Figure 7.23.** Heat transfer measurements with liquid inundation on the Turbo-CSL tube with a tube pitch of 25.5 mm at a nominal heat flux of 40 kW/m<sup>2</sup> from Gstöhl and Thome (2006a).

Gstöhl and Thome (2006a, 2006b, 2006c) performed a study on film condensation of R-134a at a saturation temperature of 30°C for horizontal tube arrays with tube rows numbering from 6 to 10 [Wolverine Turbo-CSL](#) enhanced condensation tubes, obtaining both heat transfer measurements and flow visualizations. The results of one series of tests with liquid overfeed are shown in Figure 7.23 for an array of 10 Turbo-CSL tubes. The heat transfer coefficient is plotted versus the film Reynolds number of the condensate leaving the bottom of each tube. These measurements were performed with a tube pitch of 25.5 mm at a mean nominal heat flux of 40 kW/m<sup>2</sup>. Starting with no liquid overfeed ( $\Gamma=0$  kg/ms), the mass flow rate was increased in 12 steps to a maximum mass flow rate of  $\Gamma=0.135$  kg/ms. The film Reynolds numbers were determined from an energy balance with the assumption that all the liquid condensed on a tube flows onto the tube below. The film Reynolds number is the local value at the midpoint of the tube where the local heat transfer coefficient is determined. Different symbols are used

for the ten tubes to illustrate the evolution of heat transfer performance of every tube as the liquid inundation rate is increased. Without overfeed (lowest film Reynolds number datapoint for each symbol), the heat transfer coefficient decreases from a value of about  $23 \text{ kW/m}^2\text{K}$  on the first tube to a value of about  $13 \text{ kW/m}^2\text{K}$  on the tenth tube in the array. In general, the heat transfer coefficient is high at low film Reynolds numbers and it decreases with increasing film Reynolds number. At a film Reynolds number of about 2200, the heat transfer coefficient reaches a plateau and flattens out. This trend is observed on all ten tubes in the array proving the consistency of the experimental setup with overfeed to simulate a large number of tube rows where only the top tube deviates a little from the others. At low film Reynolds numbers, its heat transfer coefficients are a little below the other tubes and at high film Reynolds numbers its values are higher than the other tubes. This might be explained by the fact that the liquid flow leaving the distribution half tube above the top tube differs from the liquid flow leaving from the bottom of an enhanced tube. The film Reynolds number leaving the tenth tube during the measurement with the highest inundation rate would correspond approximately to the 30th row in a heat exchanger at this heat flux.

During each series of measurements, the nominal row heat flux was held constant, but the experimental setup had five cooling water inlet flows for the 10 tube rows, so that each two rows of tubes constituted two tube passes. Thus, the heat flux varied substantially between the even and odd rows and, as seen in Figure 7.23, the heat transfer coefficients are higher on the upper tubes in the array as the inundation is less. These two effects lead to the following range of heat fluxes for the data at a nominal heat flux of  $40 \text{ kW/m}^2$  with an overfeed rate of  $\Gamma=0.027 \text{ kg/ms}$ , starting at the top tube to the tenth tube: 36, 57, 35, 49, 33, 44, 30, 38, 26 and  $36 \text{ kW/m}^2$ . In fact, about half the scatter of the data points in the figure is due to this difference in heat flux, which is not differentiated in their graph.

Figure 7.24 depicts the heat transfer coefficients measured on a Turbo-CSL tube row as a function of the film Reynolds number for all three tube pitches tested: 25.5, 28.6 and 44.5 mm. For clarity, only the data in the heat flux range from 25 to  $35 \text{ kW/m}^2$  are shown to partly eliminate the effect of heat flux. It can be seen that for all three tube pitches the heat transfer coefficient decreases with increasing film Reynolds number and flattens out at a certain film Reynolds number due to the liquid slinging effect. The larger the tube pitch the earlier this happens, and thus the higher the plateau in the heat transfer coefficient. At the tube pitch of 44.5 mm typical of a staggered tube layout in a condenser, the plateau is reached at  $Re_{bottom}=1100$  and this gives a higher condensing heat transfer performance than that of the Turbo-Chil low finned tube presented earlier in this chapter for similar test conditions which had little tube row effect.

Below, the enhanced tube prediction method for the Turbo-CSL tube proposed by Gstöhl and Thome (2006b) is presented based on their results for one refrigerant (R-134a), at one saturation temperature ( $30^\circ\text{C}$ ), one tube row and the three tube pitches mentioned above. While the method is not general, it can be fit to future data sets for other test conditions, to other tubes and to other fluids to simulate the performance of enhanced tube condensers (albeit without including the effects of nearby tube rows or vapor shear, a topic of current study with the same test facility).

As their first step in correlating the heat transfer behavior of the Turbo-CSL tube, only the measurements without condensate slinging were considered (the data before the plateau). Furthermore, during laminar film condensation, the heat transfer coefficient is dependent on the condensation temperature difference and consequently applying Newton's concept of a heat transfer coefficient defined as the ratio of heat flux to the temperature difference (saturation temperature minus base wall temperature) is debatable in such a case, as pointed out for instance by Rose (2004). In other words, for calculating the heat flux for a given temperature difference, the heat transfer coefficient is multiplied by the temperature difference. When the heat transfer coefficient itself depends on the temperature difference (as is the case here), nothing is gained by separating the correlation for calculating the heat flux into a heat transfer coefficient and a condensation temperature difference.

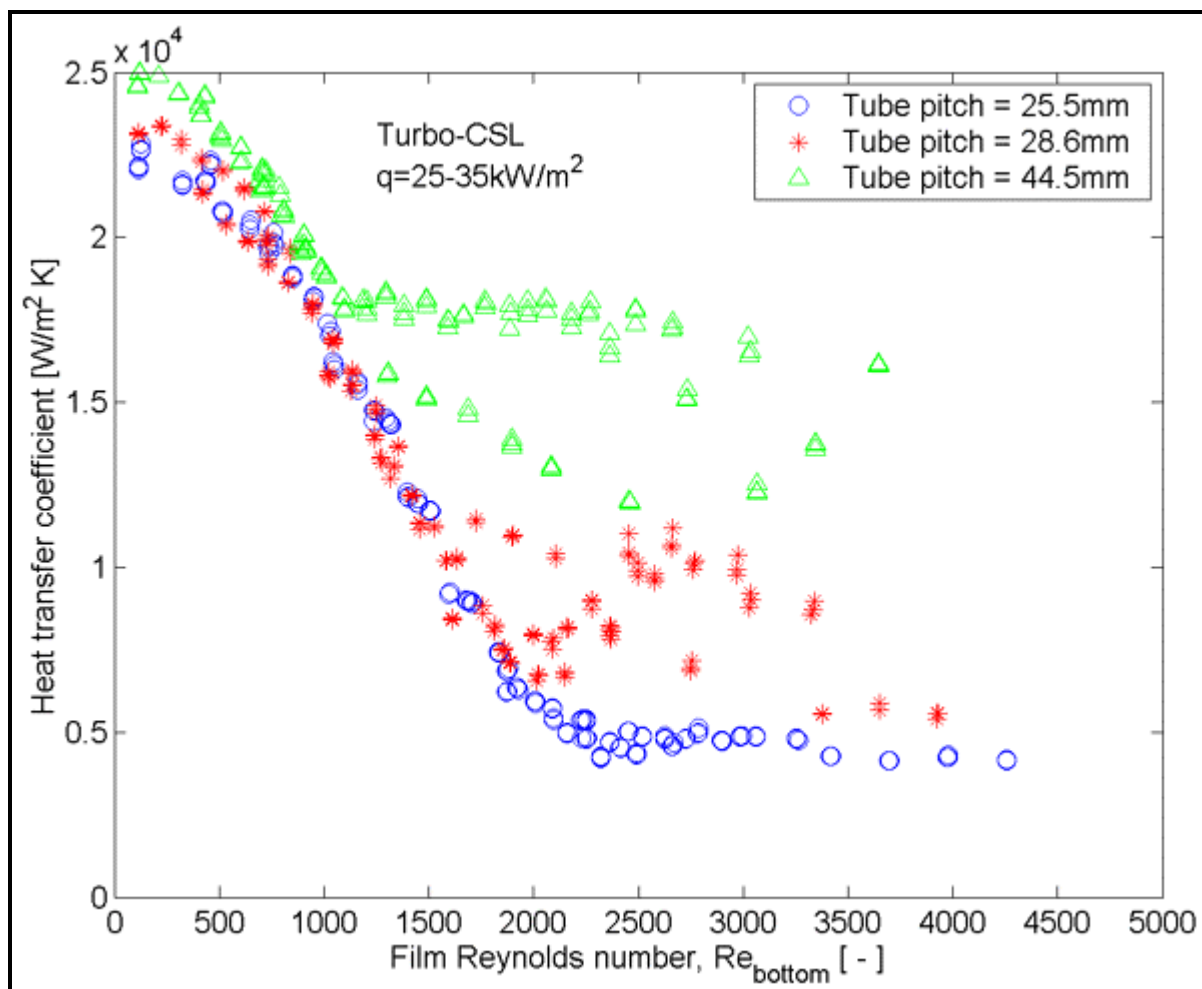


**Figure 7.24. Tube spacing influence of the Turbo-CSL tube at a nominal heat flux of 40 kW/m<sup>2</sup> over a limited heat flux range from Gstöhl and Thome (2006a) illustrating the three plateaus at the three tube pitches created by liquid slinging.**

From a fundamental point of view, it is helpful to look at the local heat flux as a function of the condensation temperature difference since integrating the local heat fluxes in a tube bundle gives its overall heat duty. During the measurements, the heat flux decreases with increasing liquid inundation for the same condensation temperature difference. For the Turbo-CSL tube, the analysis was performed for film Reynolds numbers equal to 0 up to 2000 where the condensate starts to get slung off the tube array. Applying the above logic, the following dimensional equation was proposed by Gstöhl and Thome (2006b) to describe the performance of the Turbo-CSL enhanced tube:

$$q = (a + c \operatorname{Re}_{\text{top},N}) \Delta T^b \quad [7.7.33]$$

The heat flux  $q$  is that for the nominal surface area at the tip of the enhancement while  $\Delta T$  is  $T_{\text{sat}} - T_{\text{wall}}$  where the wall temperature is that at the root of the enhancement, for the  $N$ th tube row. The empirical values of  $a$ ,  $b$  and  $c$  for the Turbo-CSL were found to be 25350 W/m<sup>2</sup>, 0.89 and -9.4 W/m<sup>2</sup>, respectively. The standard deviation gives a measure of how the relative errors are distributed around the mean relative

error. Assuming a Gaussian distribution of relative errors, 68% would be within  $\pm \sigma$  and 95% within  $\pm 2\sigma$ . The mean relative error for the Turbo-CSL tube is -1.0% with a standard deviation of 9.3%.

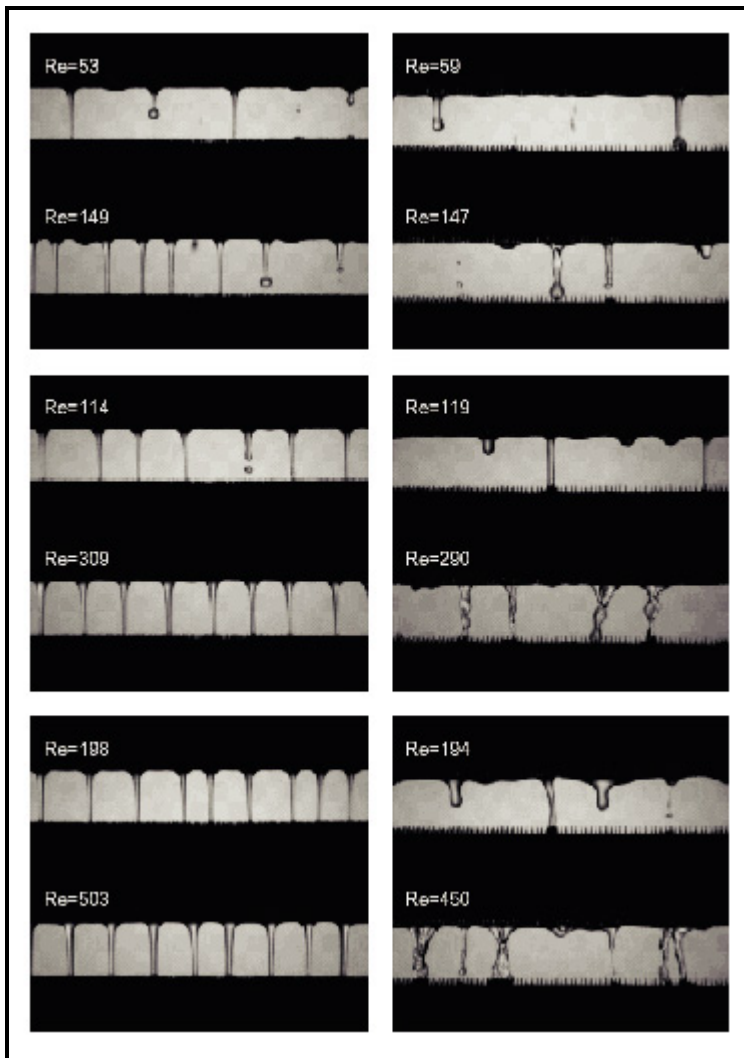


**Figure 7.25. Intertube flow patterns observed on the second tube in the array (without overfeed) at a tube pitch of 28.6 mm for R-134a condensing at a nominal heat flux of 20  $\text{kW}/\text{m}^2$  (top row), 40  $\text{kW}/\text{m}^2$  (middle row), and 60  $\text{kW}/\text{m}^2$  (bottom row): Turbo-CSL (left column) and Turbo-Chil (right column).**

During their visualizations reported in Gstöhl and Thome (2006c), instabilities in the condensate flow between tubes were observed. Figure 7.25 illustrates some images on this process for the Turbo-CSL tube and similar images for the Turbo-Chil low finned tube. For the 3D enhanced tube, the instabilities occurred near the transition to sheet mode or within the sheet mode. At the transition, a continuous sheet was temporarily formed and then when it broke down, some condensate left the array of tubes sideways without contacting the lower tubes. This break down phenomenon was less frequent when the film Reynolds number was increased as the sheet became more continuous. However, the continuous sheet was always unstable, moving a little forward and backward with respect to the vertical axis of the array. For a further increase in film Reynolds number, this unstable movement was amplified and regular

oscillations with frequencies of about 1.5 Hz were observed. At high film Reynolds numbers, the amplitude became so large that a significant fraction of the condensate left the tubes sideways (the amount of which however was not able to be measured experimentally). This phenomenon was regular and it appeared that the amount of liquid leaving the array of tubes on the front was the same as that leaving on the back, indicating that this was not caused by imperfections of the experimental setup. As seen before, heat transfer deteriorates with increasing inundation. When some of the condensate is slung off the array, the tubes below receive less condensate at their top than otherwise expected, which has a beneficial effect on their heat transfer coefficients.

For this reason, a realistic heat transfer model must account for the fraction of condensate leaving the tube row sideways in the sheet mode. In an ideal situation, the condensate flows in a continuous sheet from the bottom of one tube onto the top of the tube below as in Figure 7.26 (left). The actual condensate does not however fall vertically in a stable sheet, but instead, it oscillates back and forth (and front and back), as depicted in Figure 7.26 (middle). With increasing mass flow rate, the amplitude of oscillation increases and the condensate leaves the bottom of the tube at a sufficiently large angle relative to the vertical that some liquid misses the tube below. This maximal angle of deflection varies in time and is denominated  $\theta_{\text{def}}$ . It was assumed that  $\theta_{\text{def}}$  is a function of the film Reynolds number based on their visual observations. The critical angle  $\theta_{\text{crit}}$  is the angle that delineates contact with the next tube row as illustrated in Figure 7.26 (right). As long as  $\theta_{\text{def}} < \theta_{\text{crit}}$ , the condensate sheet oscillates on the top of the lower tube, but all the condensate remains on the tube but when  $\theta_{\text{def}} > \theta_{\text{crit}}$ , a fraction of the condensate misses the lower tube. The critical angle  $\theta_{\text{crit}}$  depends on the geometry of the tube array according to equation [7.6.22].

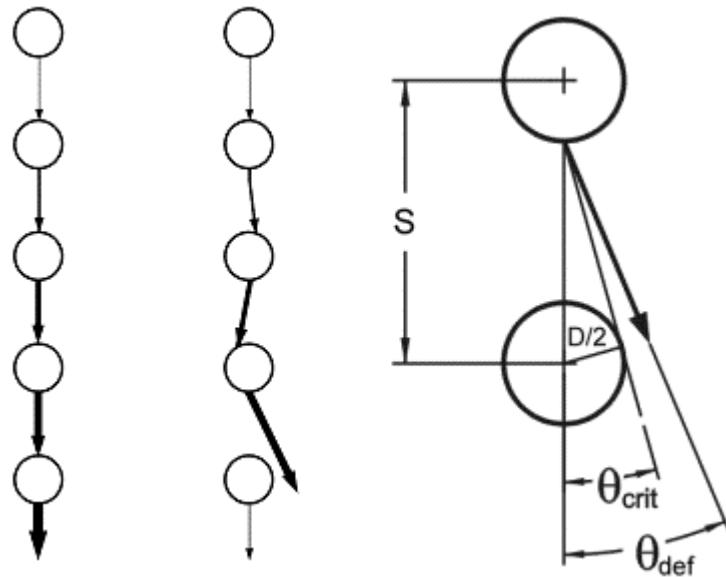


**Figure 7.26. Ideal flow (left), liquid “slinging” (middle) and critical slinging angle (right).**

The fraction of condensate that misses the lower tube is assumed to be proportional to the ratio  $(\theta_{\text{def}} - \theta_{\text{crit}})/\theta_{\text{def}}$ . This means that the film Reynolds number on the top of the nth tube in the array can be expressed as

$$Re_{\text{top}, n} = \frac{\theta_{\text{crit}}}{\theta_{\text{def}}} Re_{\text{bottom}, N-1} \quad [7.7.34]$$

Once the actual amount of condensate that falls on the top of the tube is known, the expression [7.7.33] can be used to determine the heat flux on the particular tube, starting from the top tube row and working down. As long as no condensate leaves ( $\theta_{\text{def}} < \theta_{\text{crit}}$  so that  $Re_{\text{bottom},N-1} = Re_{\text{top},N}$ ), equation [7.7.33] is used to determine the heat flux on the tube and then by an energy balance gives the amount of condensate leaving the bottom of the tube. As soon as part of the condensate starts to leave (when  $\theta_{\text{def}} > \theta_{\text{crit}}$ ), equation [7.7.34] is used to determine the amount of condensate that arrives on the tube below and subsequently [7.7.33] is used to determine the heat flux on the tube. The relationship between the angle  $\theta_{\text{def}}$  and the film Reynolds number was assumed to be a linear function as follows:

$$\theta_{\text{def}} = d Re_{\text{bottom},N-1} + e \quad [7.7.34]$$

The empirical constant  $d$  was found to be 0.00027 radians and  $e$  equal to 0.08 radians for this enhanced tube. Nearly as good a fit was found by setting  $e$  to zero and using  $d = 0.00031$  radians. Thus, the Reynolds number of the condensate coming off the bottom of the upper tube  $Re_{\text{bottom},N-1}$  is used to predict the Reynolds number of the condensate reaching the top of the next tube  $Re_{\text{top},N}$  when  $\theta_{\text{def}} > \theta_{\text{crit}}$ .

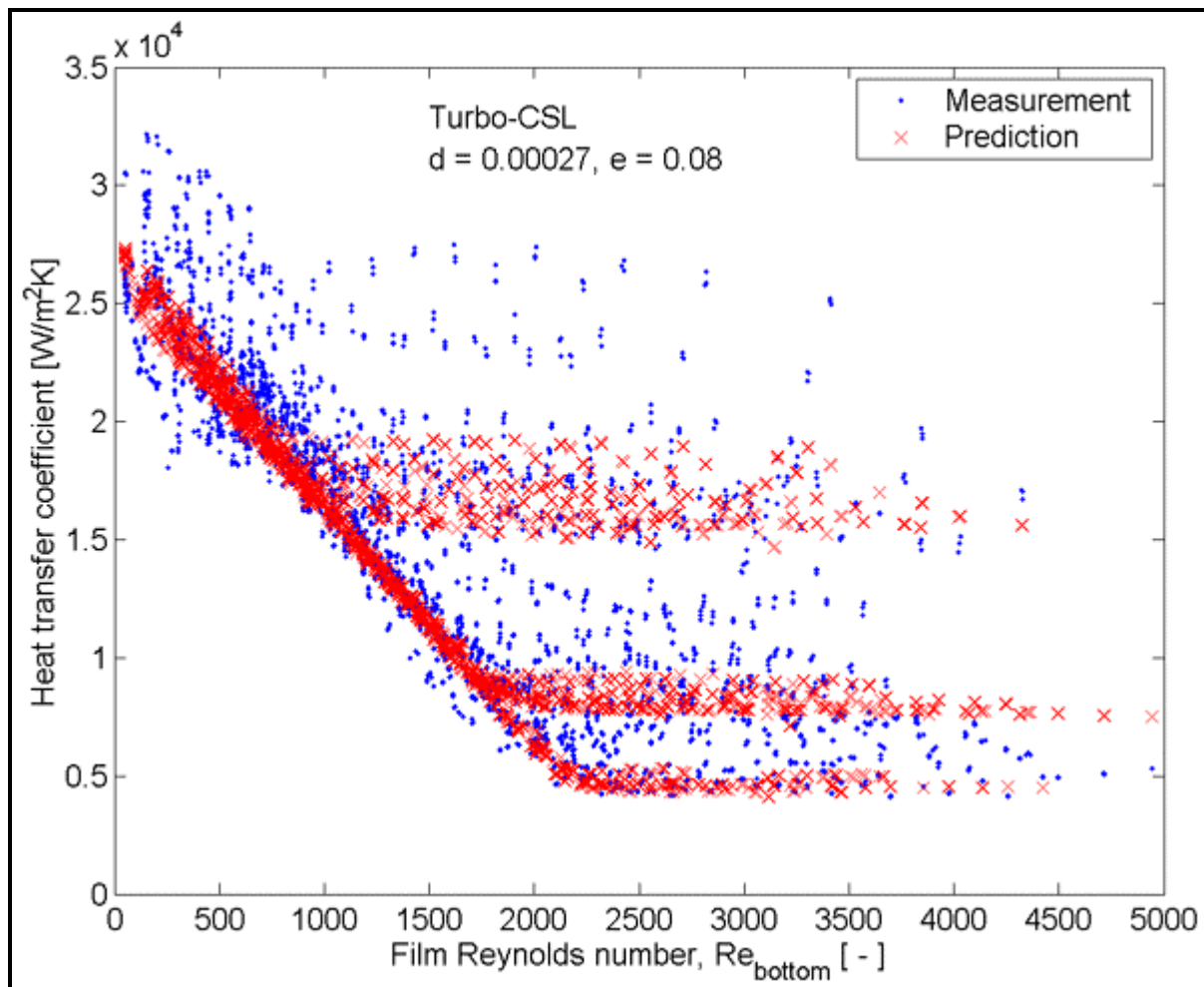


**Figure 7.27. Comparison of predictions to measurements for Turbo-CSL tubes from Gstohl and Thome (2006b), capturing the three slinging levels for the three tube pitches.**

Figure 7.27 shows a comparison of the measured and predicted heat transfer coefficients for all measurements for the Turbo-CSL enhanced tube row data. The predicted heat transfer coefficient flattens out at three different levels corresponding to the three tube pitches (and hence three different values of  $\theta_{crit}$ ). For these points in the plateau, the amount of liquid condensed on the tube must be nearly equal to the amount of liquid that is slung off. The values of  $\theta_{crit}$  for the three tube pitches tested here were 36°, 30° and 16°. The “plateaus” in the predicted heat transfer coefficients for the three different tube pitches can be seen and interpret the associated data quite well. Each level of the plateau corresponds to a certain percentage of condensate leaving the array of tubes sideways. The plateau observed at the smallest tube pitch of 25.5 mm (the lowest plateau) corresponds approximately to 3% of the condensate leaving the array sideways. At the largest tube pitch of 44.5 mm, approximately 10% of the condensate does not fall on the tube below and leaves the array of tubes sideways. The method fit the database including those with the slinging effect to a mean relative error of -3% with a standard deviation of 13%.

## 7.8 Condensation with Non-Condensable Gases

Condensation in the presence of a non-condensable gas occurs in numerous heat exchanger applications. The most common example is dehumidification in an air-conditioning system, in which water vapor is partially condensed out as the humid air passes through the evaporator. Another prime example is shell-side condensation in surface condensers used in central power plants. Here, a small fraction of air that is dissolved in the feedwater and it eventually arrives at the condenser together with the steam, where of course it cannot condense. Hence, it will build up its concentration near the exit region of the condenser if it is not removed with a steam ejector or some other similar device. In chemical processing plants and refineries, non-condensable gases may be present in the process vapor leaving a distillation column that goes to the overhead condenser or be produced in a reactor prior to a feed effluent heater. A non-condensable gas creates a significant mass transfer resistance to heat transfer depending on the circumstances.

Figure 7.28 depicts this process in the presence of air under quiescent conditions. The total pressure of the bulk vapor-air mixture is  $p$  while partial pressures of the vapor ( $G$ ) and non-condensable gas ( $a$ ) are  $p_{G\infty}$  and  $p_{a\infty}$ , respectively. The bulk concentrations of vapor and air are  $W_{G\infty}$  and  $W_{a\infty}$ , respectively (note that  $W_G + W_a = 1$  at any location).  $T_{G\infty}$  is the bulk temperature of the vapor-air mixture and  $T_w$  is the wall temperature where  $T_w$  is less than the dew point temperature of the vapor. As heat is transferred from the vapor-air mixture to the cold wall, a condensate layer is formed on the wall and then condensation proceeds at the interface (denoted by the subscript  $i$ ). The non-condensable gas arriving at the interface does not condense and, assuming it is not absorbed by the condensate (typically only a small fraction is), its local concentration builds up at the interface to  $W_{ai}$ . Since  $W_{Gi} = 1 - W_{ai}$ , then the local concentration of the vapor at the interface is  $W_{Gi}$ . This reduces the partial pressure of the vapor at the interface to  $p_{Gi}$  and the saturation temperature at the interface is  $T_{Gi}$ . Condensation of the vapor at the interface creates a mass diffusion process and its associated mass diffusion layer where the non-condensable gas diffuses away from the interface towards the bulk where its concentration is lower. The vapor arrives at the interface by (i) bulk motion of the vapor towards the interface (where it is removed as condensate) and (ii) by mass diffusion down its concentration gradient from the bulk to the interface.

The thermal resistances encountered by the process are thus *three* rather than *one* for condensation of a pure vapor. First of all, there is the thermal resistance across the condensate film itself, whose value is determined using a pure vapor heat transfer expression for the cold wall (plate or tube) where the film may be laminar, laminar-wavy or turbulent. Then there is either natural convection heat transfer or forced convective heat transfer across the temperature gradient from  $T_{G\infty}$  to  $T_{Gi}$ , depending on whether there is forced flow of the gas-vapor mixture or not. Finally, there exists a mass transfer resistance to the diffusion

of vapor to the interface. Depending on the local circumstances, one or two of these resistances may be negligible with respect to the others.

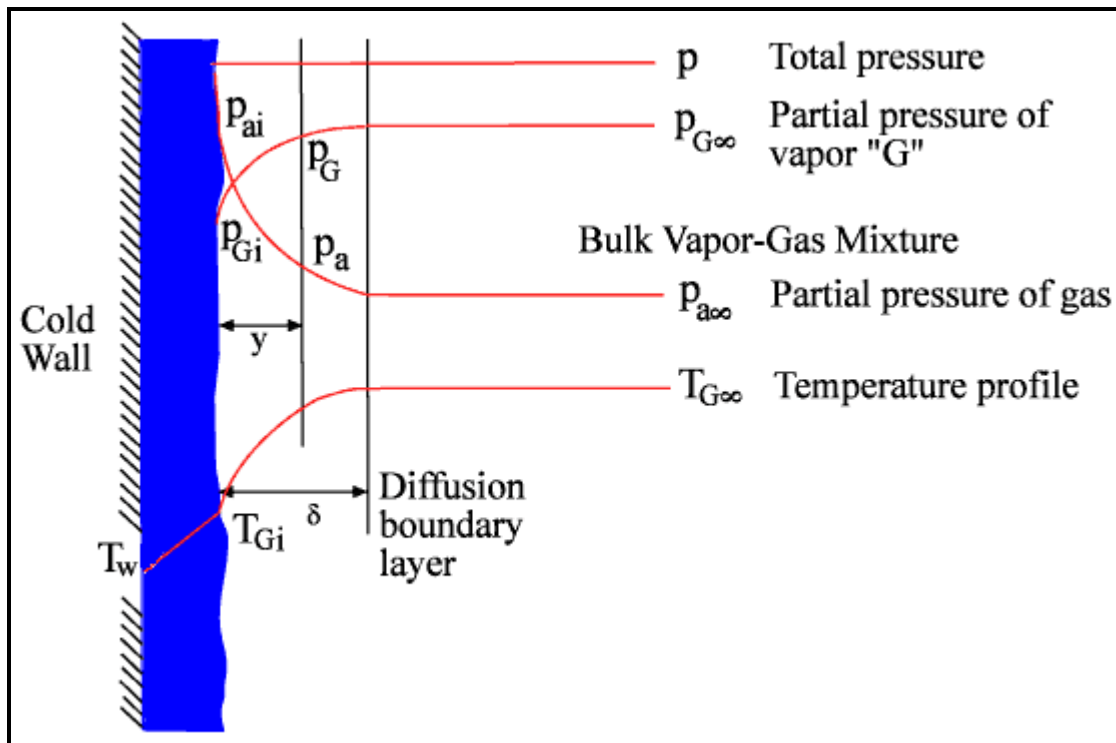


Figure 7.28. Condensation in the presence of a non-condensable gas.

Various boundary layer treatments of condensation with non-condensable gases have been presented in the literature over the years. For example, Minkowycz and Sparrow (1966) analyzed this process for stagnant vapor conditions while Sparrow, Minkowycz and Saddy (1967) studied forced convection conditions. Figure 7.29 depicts the effect of small fractions of air in saturated steam for falling film condensation under stagnant and forced convection conditions. The vertical axis shows the condensing heat flux with air present relative to that of pure steam for otherwise identical conditions, e.g. the ratio is equal to 1.0 for no air present. For quiescent vapor conditions, even a small fraction of air reduces thermal performance significantly. For forced convection conditions, the fall in thermal performance is less but is still of particular magnitude. This comparison shows the importance of attaining high flow rates of the vapor-air mixture to minimize the mass diffusion resistance. A simpler approach by Colburn is described in Collier and Thome (1994).

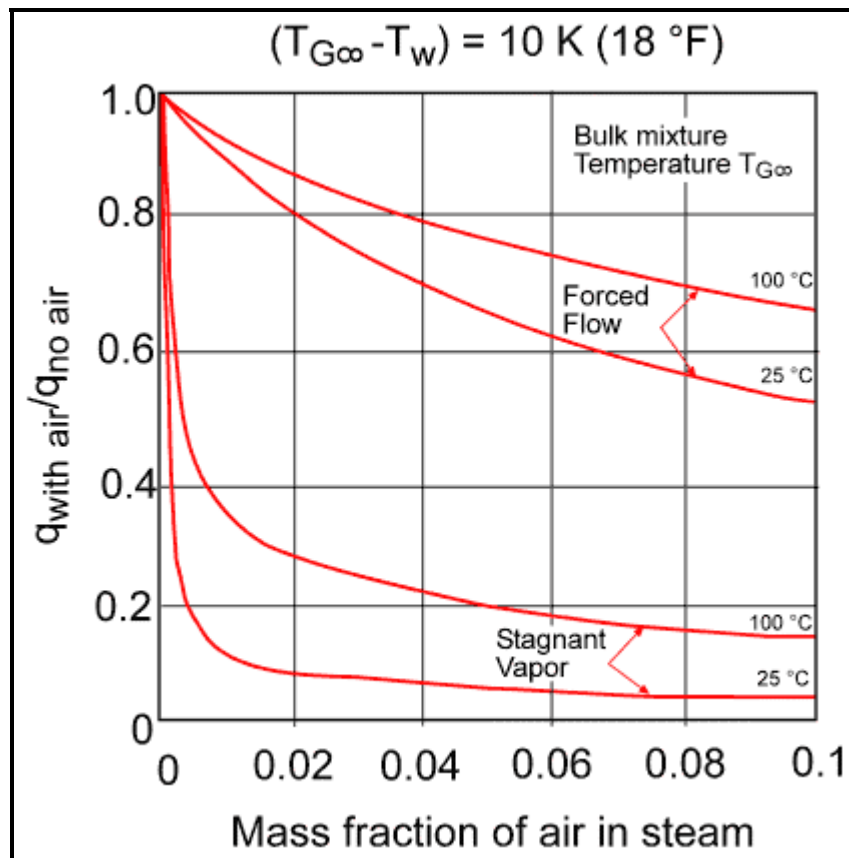


Figure 7.29. Condensation of steam in the presence of air [taken from Collier and Thome (1994)].

**Example Calculation:** Assume R-134a is condensing on the outside of a 25.4 mm diameter, horizontal low finned tube, where the diameter at the fin tips is 25.4 mm, at its saturation temperature of 40°C. The tube wall temperature is 35°C. The tube has the following external dimensions: 1000 fins/meter, fin height of 1.5 mm, fin thickness of 0.3 mm and fin tip diameter of 25.4 mm. The fins can be considered to be rectangular in profile and without fouling. The thermal conductivity of the tube is 390 W/m K. Using the Beatty-Katz method, determine the heat transfer coefficient for the tube based on the effective area, the nominal heat transfer coefficient and the condensate retention angle.

**Solution:** The necessary physical properties at 40°C are:

$$\begin{aligned} \rho_L &= 1147 \text{ kg/m}^3; \rho_G = 50.0 \text{ kg/m}^3; \mu_L = 0.000183 \text{ Ns/m}^2; h_{LG} = 162900 \text{ J/kg}; \lambda_L = 0.0776 \text{ W/mK}; \\ c_{pL} &= 1.508 \text{ kJ/kgK}; \sigma = 0.0061 \text{ N/m}. \end{aligned}$$

Using [7.2.19] to include subcooling of the condensate in the heat balance:

$$h'_{LG} = 162900 \left[ 1 + 0.68 \left( \frac{1508(40 - 35)}{162900} \right) \right] = 162900 [1 + 0.0315] = 168027 \text{ J/kg}$$

$D = 25.4 \text{ mm}$  or  $0.0254\text{m}$  and the root diameter  $D_{\text{root}} = 22.4 \text{ mm} = 25.4 - 2(1.5)$  or  $0.0224 \text{ m}$ . Per meter of tube,  $A_{\text{root}}$  is the surface between the fins, such that for 1000 fins per meter (fpm):

$$A_{\text{root}} = \text{fpm}(s - t_{\text{root}})(\pi D_{\text{root}}) = 1000(0.001 - 0.0003)\pi(0.0224) = 0.04926 \text{ m}^2$$

$A_{\text{fin}}$  is the fin surface area per meter of tube including the tip area:

$$\begin{aligned} A_{\text{fin}} &= A_{\text{sides}} + A_{\text{tip}} = 2 \text{fpm} \pi \left( \frac{D^2 - D_{\text{root}}^2}{4} \right) + \text{fpm} \pi D t_{\text{tip}} \\ &= 2(1000)\pi \left( \frac{(0.0254)^2 - (0.0224)^2}{4} \right) + 1000\pi(0.0254)(0.0003) \\ &= 0.22525 + 0.02394 = 0.24919 \text{ m}^2 \end{aligned}$$

$A_{\text{total}}$  is the total area per unit length of finned tube:

$$A_{\text{total}} = A_{\text{root}} + A_{\text{fin}} = 0.04926 + 0.24919 = 0.29845 \text{ m}^2$$

The equivalent length of the fin is obtained with [7.7.11]:

$$L_{\text{fin}} = \frac{\pi((0.0254)^2 - (0.0224)^2)}{4(0.0254)} = 0.004434 \text{ m}$$

The heat transfer coefficient on the sides of the fin is obtained with [7.7.12]:

$$\alpha_{\text{fin}} = 0.943 \left[ \frac{1147(1147 - 50)(9.81)(0.0776)^3(168027)}{0.000183(0.004434)(40 - 35)} \right]^{1/4} = 3707.3 \text{ W/m}^2\text{K}$$

On the root area, the heat transfer coefficient is obtained with [7.7.10]:

$$\alpha_{\text{root}} = 0.725 \left[ \frac{1147(1147 - 50)(9.81)(0.0776)^3(168027)}{0.000183(0.0224)(40 - 35)} \right]^{1/4} = 1901.2 \text{ W/m}^2\text{K}$$

The parameter  $m$  in the fin efficiency is obtained with [7.7.9]:

$$m = \left[ \frac{2 \left( \frac{1}{3707.3} + 0 \right)^{-1}}{390(0.0003)} \right]^{1/2} = 251.74$$

The fin efficiency  $\eta_{\text{fin}}$  is obtained with [7.7.8]:

$$\eta_{\text{fin}} = \frac{\tanh\left[251.74\left(0.0015 + \frac{0.0003}{2}\right)\right]}{251.74\left(0.0015 + \frac{0.0003}{2}\right)} = 0.946$$

The surface efficiency  $\eta_{\text{surface}}$  is then obtained with [7.7.7]:

$$\eta_{\text{surface}} = 1 - \frac{0.24919}{0.29845}(1 - 0.946) = 0.955$$

The effective heat transfer coefficient for the finned tube is obtained from [7.7.5]:

$$\begin{aligned} \alpha(0.955) &= 1901.2\left(\frac{0.04926}{0.29845}\right) + 3707.3\left(\frac{0.946(0.24919)}{0.29845}\right) = 313.8 + 2928.2 = 3242.0 \\ \alpha &= 3242 / 0.955 = 3395 \text{ W/m}^2\text{K} \end{aligned}$$

The effective surface area is:

$$A_{\text{eff}} = \eta_{\text{surface}} A_{\text{total}} = A_{\text{root}} + \eta_{\text{fin}} A_{\text{fin}} = 0.04926 + 0.946(0.24919) = 0.285 \text{ m}^2$$

The nominal heat transfer coefficient is:

$$\alpha_{\text{nom}} = \alpha\left(\frac{A_{\text{eff}}}{\pi D L}\right) = 3395\left(\frac{0.285}{\pi(0.0254)(1.0)}\right) = 12126 \text{ W/m}^2\text{K}$$

The comparable value for a plain tube of the same diameter was 1850 W/m<sup>2</sup>K. The condensate retention angle is obtained with [7.7.14], where  $\varphi$  is equal to 0 for a rectangular fin, and the intertube fin spacing  $b = 0.001 - 0.0003 = 0.0007 \text{ m}$ , so:

$$\beta = \cos^{-1}\left\{1 - \left(\frac{4(0.0061)\cos(0)}{1147(9.81)(0.0007)(0.0254)}\right)\right\} = 0.499 \text{ radians or } 28.6^\circ$$

Thus about 16% of the circumference of the finned tube retains condensate between the fins.

# Chapter 8

## Condensation Inside Tubes

(Revised in 2006)

**SUMMARY:** The principles of condensation in horizontal tubes are reviewed. The effect of flow regimes and flow stratification are shown to be important in predicting local condensation heat transfer coefficients. In addition to condensation in plain tubes, condensation in microfin tubes and condensation of zeotropic mixtures are also addressed along with condensation of superheated vapor and the subcooling of condensate.

### 8.1 Condensation inside Horizontal Tubes

This chapter covers condensation inside tubes. Presently, only condensation inside *horizontal* tubes is reviewed here. The condensation of both pure vapors and condensable mixtures is covered.

Condensation in horizontal tubes may involve partial or total condensation of the vapor. Depending on the application, the inlet vapor may be superheated, equal to 1.0 or below 1.0. Hence, the condensation process path may first begin with a dry wall desuperheating zone, followed by a wet wall desuperheating zone, then a saturated condensing zone and finally a liquid subcooling zone. The condensing heat transfer coefficient is a strong function of local vapor quality, increasing as the vapor quality increases. The condensing heat transfer coefficient is also a strong function of mass velocity, increasing as the mass velocity increases. Opposed to external condensation, intube condensation is independent of the wall temperature difference ( $T_{sat} - T_w$ ) for most operating conditions, except at low mass flow rates.

#### 8.1.1 Flow Regimes for Condensation in Horizontal Tubes

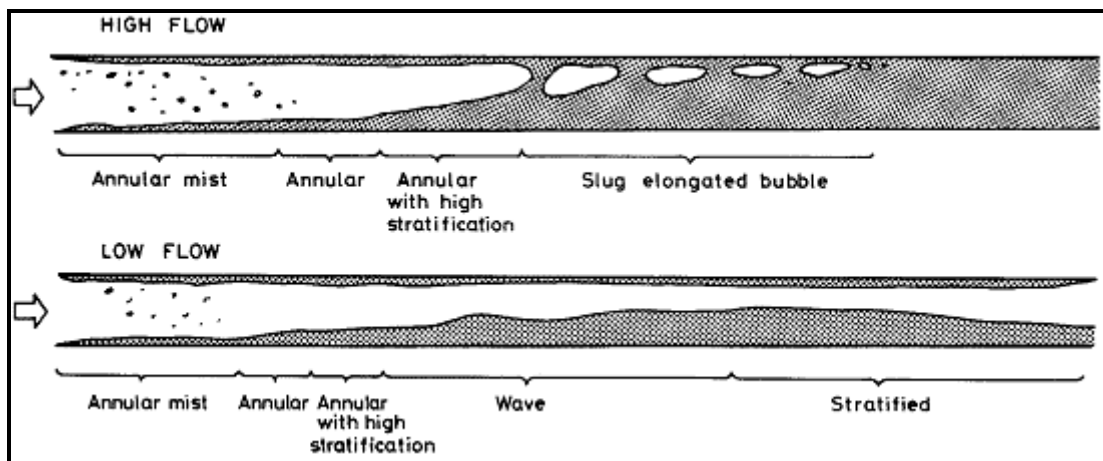


**Figure 8.1. Typical flow patterns encountered for condensation inside horizontal tubes.**

Figure 8.1 from Palen, Breber and Taborek (1979) illustrates the two-phase flow patterns typical of condensation in horizontal tubes. In the top diagram at high mass flow rates, the flow takes on the annular flow regime, where the liquid film is on the perimeter of the wall, the vapor is in the central core and some liquid is entrained in the vapor from the tips of waves on the interface of the film. As condensation

proceeds along the tube, the vapor velocity decreases and thus there is a corresponding decrease in vapor shear on the interface and the liquid film becomes thicker at the bottom of the tube than at the top. New condensate formed adds to the thickness of the liquid film. As the quantity of liquid increases along the tube, slug flow is encountered and still further along all the vapor is finally converted to liquid. At low flow rates depicted in the lower diagram, at the entrance region annular flow is formed but this quickly transforms to intermittent flow with its characteristic large amplitude waves washing the top of the tube or to stratified-wavy flow with smaller amplitude waves. If liquid does not span the cross-section of the tube, vapor may reach the end of the tube without condensing.

There is a great similarity between these flow regimes and those for adiabatic two-phase flows. Here, however, condensate forms all around the tube perimeter even in stratified flows. As illustrated in Figure 8.2, the fully stratified flow regime with all the liquid normally in the lower portion of the tube for adiabatic flow will have a thin layer of condensate around the upper perimeter.

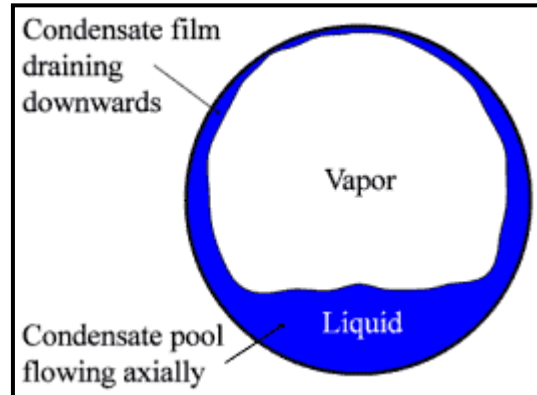


**Figure 8.2. Condensation in fully stratified flow.**

### 8.1.2 Condensation of Pure Vapor in a Horizontal Tube

As illustrated in Figure 8.3, at low flow rates the flow is stratified. There is a film of condensate formed by film-wise condensation that drains from the top of the tube towards the bottom under the force of gravity. The film flow is laminar and primarily downwards when the vapor core velocity is low. If the vapor shear is sufficient and the onset to turbulence has been surpassed, then a turbulent film is formed whose predominant flow direction is axial.

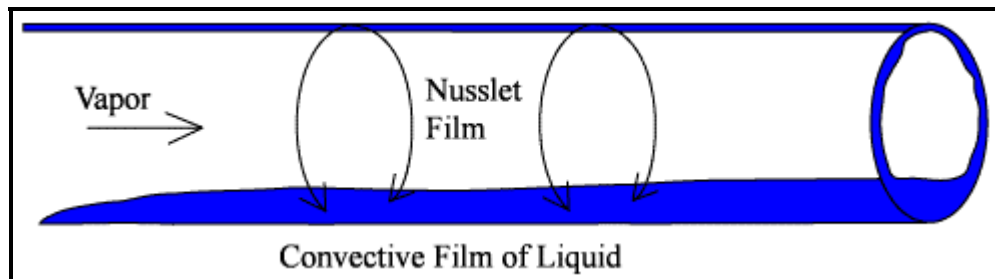


**Figure 8.3. Stratified flow with film condensation around the top internal perimeter of the tube.**

For low vapor shear conditions, the condensation process on the *inside* perimeter around the top and sides of the tube is very similar to that on the *outside* of a horizontal tube. Thus, Nusselt falling film analysis may be applied to the upper zone of the tube, which has been done first by Chaddock (1957) and then by Chato (1962). The cross-sectional area of the stratified liquid layer at the bottom of the tube can be established from the local void fraction  $\varepsilon$ . Then, the stratified liquid angle  $\theta_{\text{strat}}$  is can be determined from geometry. The local heat transfer coefficient at this vapor quality  $x$  is obtained by proration of the respective heat transfer coefficients with respect to the fraction of the perimeter they occupy as

$$\alpha(x) = \frac{\theta_{\text{strat}}}{\pi} \alpha_f + \frac{\pi - \theta_{\text{strat}}}{\pi} \alpha_{\text{strat}} \quad [8.1.1]$$

$\theta_{\text{strat}}$  is the angle from the top of the tube to the stratified layer and is thus equal to  $\pi$  when there is no stratified layer present.  $\theta_{\text{strat}}$  is expressed in radians.  $\alpha_f$  is the mean heat transfer coefficient for the film obtained by integration of [7.5.11] from 0 to  $(\pi - \theta_{\text{strat}})/2$ . The heat transfer coefficient for the stratified flow in the bottom of the tube is  $\alpha_{\text{strat}}$ . Assuming that  $\alpha_{\text{strat}}$  is negligible compared to  $\alpha_f$ , the second term can be neglected while  $\alpha_f$  is determined as:

$$\alpha_f = \Omega \left[ \frac{\rho_L (\rho_L - \rho_G) g k_L^3 h_{LG}}{\mu_L d_i (T_{\text{sat}} - T_w)} \right]^{1/4} \quad [8.1.2]$$

The value of  $\Omega$  is a geometric function of  $\theta_{\text{strat}}$  where  $\Omega = \beta \theta_{\text{strat}} / \pi$  and  $k_L$  is the liquid thermal conductivity. Jaster and Kosky (1976) have shown that the value of  $\Omega$  is related to the vapor void fraction  $\varepsilon$  as  $\Omega = 0.728\varepsilon$ . They used the Zivi (1964) void fraction equation, which is a function of vapor quality  $x$  and the vapor and liquid densities:

$$\varepsilon = \frac{1}{1 + [(1-x)/x](\rho_G / \rho_L)^{2/3}} \quad [8.1.3]$$

At higher flow rates where turbulent annular flow conditions are confronted, numerous correlations have been proposed: Akers, Deans and Crosser (1959), Cavallini and Zecchin (1974), Shah (1979), etc. Akers, Deans and Crosser proposed a modified version of the Dittus-Boelter (1930) single-phase turbulent tube flow correlation, developed with a database for several refrigerants and organic fluids. Their local condensing coefficient is

$$\frac{\alpha(x) d_i}{k_L} = C \text{Re}_e^n \text{Pr}_L^{1/3} \quad [8.1.4]$$

The equivalent Reynolds number for two-phase flow  $\text{Re}_e$  is determined from an equivalent mass velocity, which in turn is obtained by applying a multiplying factor to the total mass velocity:

$$\dot{m}_e = \dot{m} \left[ (1-x) + x \left( \frac{\rho_L}{\rho_G} \right)^{1/2} \right] \quad [8.1.5]$$

The total mass flow rate of liquid plus vapor is used for the total mass velocity. The empirical parameters  $C$  and  $n$  to use in [8.1.4] are:

$$C = 0.0265 \text{ and } n = 0.8 \text{ for } \text{Re}_e > 50,000$$

$$C = 5.03 \text{ and } n = 1/3 \text{ for } \text{Re}_e < 50,000$$

With the Dittus-Boelter correlation as a starting point, Shah (1979) proposed an alternative multiplier (see brackets) acting on the liquid Reynolds number as

$$\frac{\alpha(x) d_i}{k_L} = 0.023 \text{Re}_L^{0.8} \text{Pr}_L^{0.4} \left[ (1-x)^{0.8} + \frac{3.8x^{0.76}(1-x)^{0.04}}{p_r^{0.38}} \right] \quad [8.1.6]$$

He used the reduced pressure  $p_r$  ( $p_r = p_{sat}/p_{crit}$  where  $p_{sat}$  is the saturation pressure and  $p_{crit}$  in the critical pressure of the fluid) rather than the density ratio and a database for condensation of steam, refrigerants and organic fluids.  $Re_L$  is the tubular liquid Reynolds number determined with the total mass flow rate of liquid plus vapor.

Thome (1994b, 1998) recommended using the Shah correlation when mass velocities are greater than 200 kg/m<sup>2</sup>s and that of Akers, Deans and Crosser (1959) when they are lower, based on comparisons to local test data in the literature for R-134a, R-22 and others.

Dobson and Chato (1998) have proposed a vast improvement of the Chato (1962) method that includes both a stratified-wavy flow method with film condensation from the top towards the bottom of the tube and an annular flow correlation. Their annular flow condensation correlation is

$$Nu(x) = 0.023 Re_{Ls}^{0.8} Pr_L^{0.4} \left[ 1 + \frac{2.22}{X_{tt}^{0.89}} \right] \quad [8.1.7]$$

where the local Nusselt number  $Nu(x)$  is based on the tube diameter  $d_i$  as

$$Nu(x) = \frac{\alpha(x) d_i}{k_L} \quad [8.1.8]$$

Their superficial liquid Reynolds number  $Re_{Ls}$  is

$$Re_{Ls} = \frac{\dot{m} d_i (1-x)}{\mu_L} \quad [8.1.9]$$

The Martinelli parameter for turbulent flow in both phases,  $X_{tt}$ , is

$$X_{tt} = \left( \frac{1-x}{x} \right)^{0.9} \left( \frac{\rho_G}{\rho_L} \right)^{0.5} \left( \frac{\mu_L}{\mu_G} \right)^{0.1} \quad [8.1.10]$$

To implement the method for stratified-wavy flow, first the void fraction  $\varepsilon$  is calculated using the Zivi void fraction given by [8.1.3]. Assuming all the liquid is stratified in the bottom of the tube (neglecting condensate formed on the walls), the angle from the top of the tube to the stratified liquid layer in the bottom  $\theta_{strat}$  is then determined

$$1 - \frac{\theta_{strat}}{\pi} \cong \frac{\arccos(2\varepsilon - 1)}{\pi} \quad [8.1.11]$$

The stratified-wavy heat transfer coefficient is obtained by a proration between the film condensation coefficient on the top perimeter of the tube (left term) and the forced convective heat transfer coefficient on the stratified perimeter (right term) as

$$Nu(x) = \frac{0.23 Re_{Go}^{0.12}}{1 + 1.11 X_{tt}^{0.58}} \left[ \frac{Ga_L Pr_L}{Ja_L} \right]^{0.25} + (1 - \theta_{strat}/\pi) Nu_{strat} \quad [8.1.12]$$

Forced convection condensation in the stratified liquid is correlated as

$$Nu_{strat} = 0.0195 Re_{Ls}^{0.8} Pr_L^{0.4} \left( 1.376 + \frac{c_1}{X_{tt}^{c_2}} \right)^{1/2} \quad [8.1.13]$$

The value of 1.376 makes this expression match the Dittus-Boelter correlation when  $x = 0$ . The liquid Galileo number  $Ga_L$  for the tube is

$$Ga_L = \frac{g \rho_L (\rho_L - \rho_G) d_i^3}{\mu_L^2} \quad [8.1.14]$$

while the vapor only Reynolds number  $Re_{Go}$  is

$$Re_{Go} = \frac{\dot{m} d_i}{\mu_G} \quad [8.1.15]$$

The liquid Jakob number  $Ja_L$  defined by [7.5.12],

$$Ja_L = \frac{c_{pL}(T_{sat} - T_w)}{h_{LG}} \quad [8.1.16]$$

and the liquid Froude number  $Fr_L$  is

$$Fr_L = \frac{\dot{m}^2}{\rho_L^2 g d_i} \quad [8.1.17]$$

The empirical constants  $c_1$  and  $c_2$  are obtained as a function of  $Fr_L$  as follows:

For  $0 < Fr_L \leq 0.7$ :

$$c_1 = 4.172 + 5.48 Fr_L - 1.564 Fr_L^2 \quad [8.1.18a]$$

$$c_2 = 1.773 - 0.169 Fr_L \quad [8.1.18b]$$

For  $Fr_L > 0.7$ :

$$c_1 = 7.242 \quad [8.1.19a]$$

$$c_2 = 1.655 \quad [8.1.19b]$$

The Soliman (1982) transition criterion for predicting the transition from annular flow to stratified-wavy flow was used to distinguish which heat transfer regime to apply. His method is based on a Froude transition number  $Fr_{so}$  given as

$$Fr_{so} = 0.025 Re_{Ls}^{1.59} \left( \frac{1 + 1.09 X_{tt}^{0.039}}{X_{tt}} \right)^{1.5} \frac{1}{Ga_L^{0.5}} \quad [8.1.20]$$

for  $Re_{Ls} \leq 1250$  and for  $Re_{Ls} > 1250$  it is

$$Fr_{so} = 1.26 Re_{Ls}^{1.04} \left( \frac{1 + 1.09 X_{tt}^{0.039}}{X_{tt}} \right)^{1.5} \frac{1}{Ga_L^{0.5}} \quad [8.1.21]$$

While Soliman set the transition from annular flow to wavy flow at  $Fr_{so} = 7$ , Dobson and Chato noted that a transition value of 20 fit their heat transfer data better and this is the value they used. Their method is implemented as follows:

- For mass velocities greater than  $500 \text{ kg/m}^2\text{s}$  ( $367,896 \text{ lb/h ft}^2$ ), the annular flow correlation is always utilized;
- For mass velocities less than  $500 \text{ kg/m}^2\text{s}$  ( $367,896 \text{ lb/h ft}^2$ ), the annular flow correlation is used when  $Fr_{so} > 20$ ;
- For mass velocities less than  $500 \text{ kg/m}^2\text{s}$  ( $367,896 \text{ lb/h ft}^2$ ) and for  $Fr_{so} < 20$ , the stratified-wavy correlation is used.

This method does not have a smooth transition in the heat transfer coefficient from annular flow to stratified-wavy flow; instead, it gives a significant step change in value that is not observed experimentally. Other than this inconvenience, their method appears to be the most accurate design method currently available according to Cavallini et al. (1995), who compared it to independent test data. The discontinuity in the heat transfer coefficient may be resolved for now by implementing a simple linear proration based on  $Fr_{so}$  between the corresponding calculated heat transfer coefficients at say  $Fr_{so} = 7$  with the stratified-wavy correlation and at  $Fr_{so} = 20$  with the annular flow correlation.

Tang (1997) has also proposed a simple correlation that is an extension of the Shah (1979) approach and covers reduced pressures from 0.2 to 0.53 and mass velocities from 300 to  $810 \text{ kg/m}^2\text{s}$ . His correlation is applicable to annular flow only and is:

$$\frac{\alpha(x) d_i}{k_L} = 0.023 Re_L^{0.8} Pr_L^{0.4} \left[ 1 + 4.863 \left( \frac{-x \ln p_r}{1-x} \right)^{0.836} \right] \quad [8.1.22]$$

Recent test data for intube condensation for an 8 mm (0.315 in.) tube for a wide range of pressures (0.246 to 3.15 MPa, 35.7 to 456.8 psia) have been reported by Cavallini et al. (2001) for five fluids: R-134a, R-125, R-32, R-410A and R-236ea. They covered mass velocities from 100 to  $750 \text{ kg/m}^2\text{s}$  ( $73,579$  to  $551,844 \text{ lb/h ft}^2$ ) and vapor qualities from 0.15 to 0.85 in quasi-local type of tests.

El Hajal, Thome and Cavallini (2003) proposed a phenomenological condensation model based on local flow patterns and interfacial wave effects for condensation inside plain tubes for a very wide range of

parameters: mass velocities from 16 to 1532 kg/m<sup>2</sup>s (11773 to 1127230 lb/h ft<sup>2</sup>), tube internal diameters from 3.14 to 21.4 mm (0.124 to 0.843 in.), reduced pressures from 0.02 to 0.8, and vapor qualities from 0.03 to 0.97. They used the El Hajal, Thome and Cavallini (2003) flow pattern map for condensation, described in [Chapter 12](#), to predict the local flow patterns in their heat transfer model. So far for heat transfer and flow patterns, the method has been compared with the following twenty fluids: ammonia, R-11, R-12, R-22, R-32, R-113, R-123, R-125, R-134a, R-236ea, R-32/R-125 near azeotrope, R-402A, R-404A, R-407C, R-410A, R-502, propane, n-butane, iso-butane and propylene. They showed not only that the heat transfer model was accurate statistically...85% of the eleven original refrigerants in their database from nine different labs, representing a total of 1850 data points, were predicted within  $\pm 20\%$  but also that it followed the trends within the database well with respect to vapor quality, tube diameter, mass velocity, reduced pressure, void fraction, etc. Below is a detailed description of the model.

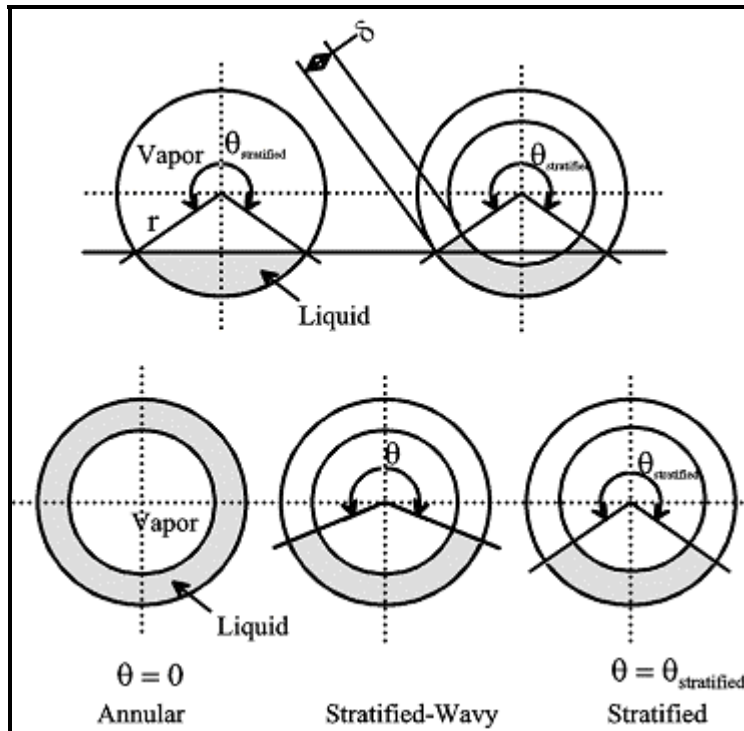


**Figure 8.4. Simplified two-phase flow structures assumed for annular, stratified-wavy and stratified flow regimes.**

**Simplified flow structures for condensation in horizontal tubes.** The same simplified flow structures assumed for evaporation inside horizontal tubes by Kattan, Thome and Favrat (1998c) were applied to condensation, differing only in that the upper perimeter of the tube in a stratified type of condensing flow is wetted by film condensation rather than dry during evaporation. The Thome-El Hajal-Cavallini condensation model assumes three simplified geometries for describing annular flow, stratified-wavy flow and fully stratified-wavy flow as shown in Figure 8.4. For annular flow (bottom left), a uniform liquid film thickness of  $\delta$  is assumed and the effects due to gravity ignored. For fully stratified flow, the stratified geometry (upper left) is converted to an equivalent geometry (upper right) with the same angle of stratification and cross-sectional area occupied by the liquid, but with the liquid distributed as a truncated annular ring of uniform thickness  $\delta$ . In stratified-wavy flow (lower middle diagram), the interfacial waves are small and do not reach the top of the tube and hence the upper perimeter would remain dry if not for the condensate that forms, again assuming that the stratified liquid creates an annular truncated ring. Thus, the angle  $\theta$  varies between its maximum value of  $\theta_{\text{strat}}$  at the threshold to fully

stratified flow and its minimum value of zero at the threshold to annular flow. Importantly, these three simple geometries yield a smooth geometrical transition from one flow structure to another.

**Heat transfer model.** Referring to Figure 8.5, the heat transfer model for stratified types of flow have convective heat transfer applied to the stratified perimeter subtended by  $(2\pi - \theta)$  while film condensation is applied to the upper perimeter subtended by  $\theta$  with the condensate flowing downwards into the stratified liquid below. For annular flow, convective condensation heat transfer occurs around the entire perimeter without any film condensation. It was further found that the annular flow model worked well for intermittent flow regimes and for the limited amount of mist flow data available. Hence, the annular flow heat transfer model is applied to both, maintaining the simplicity of the model, but no bubbly flow heat transfer data were found in the literature and hence no bubbly flow heat transfer model was proposed (which does not fall within common design conditions anyway).

Both of these mechanisms have been included in some previous models, such as that of Dobson and Chato (1998) while applying the Nusselt (1916) film condensation model to the upper perimeter of a horizontal tube with stratified flow was first proposed by Chato (1962). In the Thome-El Hajal-Cavallini model, the above two heat transfer mechanisms are applied to their respective heat transfer surface areas as shown in Figure 8.5. The convective condensation heat transfer coefficient  $\alpha_c$  is applied to the perimeter wetted by the axial flow of liquid film, which refers to the entire perimeter in annular, intermittent and mist flows but only the lower part of the perimeter in stratified-wavy and fully stratified flows. The axial film flow is assumed to be turbulent. The film condensation heat transfer coefficient  $\alpha_f$  is applied to the upper perimeter that would otherwise be dry for stratified-wavy and fully stratified flows. The Nusselt (1916) falling film theory is used to obtain  $\alpha_f$ , which assumes the falling film is laminar (which is essentially always the case for the tube diameters in question here). The effect of vapor shear on this falling film is ignored. Heat transfer coefficients for stratified types of flow are known experimentally to be a function of the wall temperature difference while those for annular flow are not. This effect is thus included here through the Nusselt falling film equation.

The general expression for the local perimeter-averaged condensing heat transfer coefficient  $\alpha(x)$  is thus:

$$\alpha(x) = \frac{\alpha_f \theta + (2\pi - \theta)\alpha_c}{2\pi} \quad [8.1.23]$$

In this expression,  $\theta$  is the falling film angle around the top perimeter. Hence,  $\alpha(x)$  is equal to  $\alpha_c$  for annular, intermittent and mist flows with  $\theta = 0$ . The stratified angle  $\theta_{\text{strat}}$  is calculated from the following implicit geometric equation:

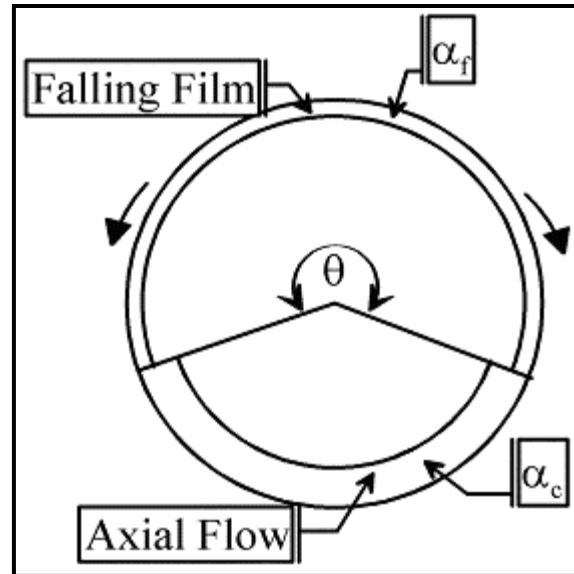


Figure 8.5. Condensation heat transfer model showing the axial convective heat transfer and the falling film heat transfer perimeters around the tube.

$$A_L = \frac{d_i^2}{8} [(2\pi - \theta_{strat}) - \sin(2\pi - \theta_{strat})] \quad [8.1.24]$$

The cross-sectional area occupied by the liquid phase  $A_L$  is

$$A_L = (1 - \varepsilon)A \quad [8.1.25]$$

and the cross-sectional area occupied by the vapor  $A_G$  is

$$A_G = \varepsilon A = 1 - A_L \quad [8.1.26]$$

The total cross-sectional area of the tube is  $A$  and  $\varepsilon$  is the local cross-sectional void fraction, which is determined using the logarithmic mean void fraction using the Steiner (1993) version of the Rouhani drift flux model, see [Chapter 17](#), and the homogeneous model in order to cover the range from low to high reduced pressures. The logarithmic mean void fraction  $\varepsilon$  was defined as:

$$\varepsilon = \frac{\varepsilon_H - \varepsilon_r}{\ln(\varepsilon_H / \varepsilon_r)} \quad [8.1.27]$$

The homogeneous void fraction  $\varepsilon_H$  is:

$$\varepsilon_H = \frac{1}{1 + \left( \frac{1-x}{x} \right) \frac{\rho_G}{\rho_L}} \quad [8.1.28]$$

Steiner (1993) gives the horizontal tube version of the Rouhani void fraction  $\varepsilon_{ra}$  as:

$$\varepsilon_r = \frac{x}{\rho_G} \left( \left[ 1 + 0.12(1-x) \right] \left[ \frac{x}{\rho_G} + \frac{1-x}{\rho_L} \right] + \frac{1.18(1-x)[g\sigma(\rho_L - \rho_G)]^{0.25}}{\dot{m}\rho_L^{0.5}} \right)^{-1} \quad [8.1.29]$$

For annular, intermittent and mist flows,  $\theta = 0$ . For fully stratified flows,  $\theta = \theta_{strat}$ . For stratified-wavy flow, the stratified angle  $\theta$  is obtained by assuming a quadratic interpolation between the maximum value of  $\theta_{strat}$  at the transition from stratified-wavy to fully stratified flow and 0 at the transition from stratified-wavy to annular or intermittent flow, such that:

$$\theta = \theta_{strat} \left[ \frac{(\dot{m}_{wavy} - \dot{m})}{(\dot{m}_{wavy} - \dot{m}_{strat})} \right]^{0.5} \quad [8.1.30]$$

The transition values at the vapor quality in question are determined from their respective transition equations in the condensation flow pattern map of El Hajal, Thome and Cavallini (2003) in [Chapter 12](#). To avoid the iterative calculation in [8.1.24] to solve for  $\theta_{strat}$ , a nearly equivalent explicit expression of Biberg (1999) is evaluated using the value of  $\varepsilon$  from [8.1.27]:

$$\theta_{\text{strat}} = 2\pi - 2 \left\{ \begin{aligned} & \pi(1-\varepsilon) + \left(\frac{3\pi}{2}\right)^{1/3} \left[ 1 - 2(1-\varepsilon) + (1-\varepsilon)^{1/3} - \varepsilon^{1/3} \right] \\ & - \frac{1}{200} (1-\varepsilon) \varepsilon [1 - 2(1-\varepsilon)] \left[ 1 + 4((1-\varepsilon)^2 + \varepsilon^2) \right] \end{aligned} \right\} \quad [8.1.31]$$

The convective condensation heat transfer coefficient  $\alpha_c$  in the annular liquid film is obtained from the following turbulent liquid film correlation:

$$\alpha_c = c \text{Re}_L^n \text{Pr}_L^m \frac{k_L}{\delta} f_i \quad [8.1.32]$$

where the liquid film Reynolds number  $\text{Re}_L$  is based on the mean liquid velocity of the liquid flow through  $A_L$  as:

$$\text{Re}_L = \frac{4\dot{m}(1-x)\delta}{(1-\varepsilon)\mu_L} \quad [8.1.33]$$

and the liquid Prandtl number  $\text{Pr}_L$  is defined as:

$$\text{Pr}_L = \frac{c_p \mu_L}{k_L} \quad [8.1.34]$$

The values of the empirical constants  $c$ ,  $n$  and  $m$  were determined from the heat transfer database whereas  $\delta$  is the thickness of the liquid film. The best value of  $m$  was determined to be  $m = 0.5$ , i.e. the same value found by Labuntsov (1957) for turbulent falling film condensation on a vertical plate, which is larger than the value of 0.4 in the Dittus and Boelter (1930) single-phase tubular flow correlation. The best values of  $c$  and  $n$  were found statistically to be  $c = 0.003$  and  $n = 0.74$  from the annular flow condensation database.

In the above expressions, the liquid film thickness  $\delta$  is obtained by solving the following geometrical expression:

$$A_L = \frac{(2\pi - \theta)}{8} \left[ d_i^2 - (d_i^2 - 2\delta)^2 \right] \quad [8.1.35]$$

where  $d_i$  is the internal diameter of the tube. If the liquid occupies more than one-half of the cross-section of the tube in a stratified-wavy or fully stratified flow at low vapor quality, i.e. when  $\varepsilon < 0.5$ , this expression yields  $\delta > d_i/2$ , which is not geometrically realistic. Hence, whenever  $\delta > d_i/2$  then  $\delta$  is set equal to  $d_i/2$  in their method.

Interfacial surface roughness of the liquid film flow was identified as a new influential parameter on heat transfer in their intube condensation model for the following reasons: (i) the shear of the high speed vapor core is transmitted to the liquid film across the interface and hence increases the magnitude and number of the waves generated at the interface, which in turn increases the available surface area for condensation, tending to increase heat transfer and (ii) the interfacial waves are non-sinusoidal and tend to reduce the mean thickness of the film, again increasing heat transfer. These two aspects are analogous to

the enhancement correction factor of Kutateladze (1963) for interfacial ripples on Nusselt film condensation on a vertical plate. Interfacial roughness and wave formation are also directly relatable to entrainment of liquid droplets into the vapor core, which reduces the thickness of the liquid film and increases heat transfer. Furthermore, interfacial shear tends to create vortices within the liquid film, which also increase heat transfer.

The interfacial roughness is proportional to the interfacial shear  $\tau_i$ , whereas  $\tau_i$  depends on the velocity difference between the two phases,  $(u_G - u_L)$ , and  $u_G$  and  $u_L$  are the mean velocities of the vapor and liquid phases in their respective cross-sectional areas  $A_G$  and  $A_L$  determined with the void fraction:

$$u_L = \frac{\dot{m}(1-x)}{\rho_L(1-\varepsilon)} \quad [8.1.36]$$

$$u_G = \frac{\dot{m}x}{\rho_G\varepsilon} \quad [8.1.37]$$

Usually  $u_G \gg u_L$ , so then  $(u_G - u_L) \approx u_G$ . Normalizing the vapor velocity with that of the liquid gives the slip ratio,  $u_G/u_L$ , typical of void fraction models, and the interfacial shear is thus proportional to  $(u_G/u_L)$ . Consequently, the interfacial roughness  $\Delta\delta$  was assumed to be proportional to  $(u_G/u_L)^p$  where the exponent  $p$  was to be determined. The wavelength of the interfacial waves should be related to the one-dimensional Taylor instability wavelength  $\lambda_T$  for an unsupported liquid film on the top of the tube, the latter which is calculated as:

$$\lambda_T \left[ \frac{(\rho_L - \rho_G)g}{\sigma} \right]^{1/2} = 2\pi\sqrt{3} \quad [8.1.38]$$

Assuming that the interfacial waves have characteristic wavelengths that can be scaled relative to the film thickness, then substituting  $\delta$  for  $\lambda_T$  means that the interfacial roughness  $\Delta\delta$  is described by follow relationship:

$$\Delta\delta \propto \left[ \frac{(\rho_L - \rho_G)g\delta^2}{\sigma} \right]^r \quad [8.1.39]$$

where the term inside the brackets is non-dimensional and  $r$  is an unknown exponent. The interfacial roughness correction factor  $f_i$  in [8.1.32] acts on  $\alpha_c$  to include the effects of vapor shear and interfacial instability on wave formation. Adjusting the values of  $p$  and  $r$  based on the test data to nominal values of  $\frac{1}{2}$  and  $\frac{1}{4}$  but without introducing any additional empirical constants,  $f_i$  is determined for all flow regimes except fully stratified flow as:

$$f_i = 1 + \left( \frac{u_G}{u_L} \right)^{1/2} \left( \frac{(\rho_L - \rho_G)g\delta^2}{\sigma} \right)^{1/4} \quad [8.1.40]$$

The interfacial roughness correction factor  $f_i$  tends to unity as the film becomes very thin (physically, the roughness must be proportional to film thickness) whereas  $f_i$  increases with the slip ratio  $u_G/u_L$  (again physically reasonable). Furthermore,  $f_i$  tends to decrease as  $\sigma$  increases since surface tension acts to

smooth out the waves. For fully stratified flow, interfacial waves are progressively damped out and hence the above expression becomes

$$f_i = 1 + \left( \frac{u_G}{u_L} \right)^{1/2} \left( \frac{(\rho_L - \rho_G)g\delta^2}{\sigma} \right)^{1/4} \left( \frac{\dot{m}}{\dot{m}_{strat}} \right) \text{ for } \dot{m} < \dot{m}_{strat} \quad [8.1.41]$$

This approach produces a smooth variation in  $\alpha(x)$  across the stratified flow transition boundary just like for all the other transition boundaries.

The film condensation heat transfer coefficient  $\alpha_f$  is obtained from the Nusselt (1916) condensation theory for laminar flow of a falling film, see [Chapter 7](#), applied here to the internal perimeter of the tube. Rather than integrating his method from the top of the tube to the stratified liquid layer to obtain  $\alpha_f$ , which would be more theoretically satisfying, it was found sufficient to use the mean value for condensation around the perimeter from top to bottom with its analytical value of 0.728. Hence,  $\alpha_f$  is:

$$\alpha_f = 0.728 \left[ \frac{\rho_L (\rho_L - \rho_G) g h_{LG} k_L^3}{\mu_L d_i (T_{sat} - T_w)} \right]^{\frac{1}{4}} \quad [8.1.42]$$

Alternatively, the heat flux version of the above equation is given by:

$$\alpha_f = 0.655 \left[ \frac{\rho_L (\rho_L - \rho_G) g h_{LG} k_L^3}{\mu_L d_i q} \right]^{\frac{1}{3}} \quad [8.1.43]$$

where the leading constant 0.655 comes from  $0.728^{4/3}$ .

The above heat transfer method cannot be evaluated at  $\epsilon = 1.0$  because of division by zero. Thus, when  $x > 0.99$ ,  $x$  is reset to 0.99. Also, the lower limit of applicability is  $x \geq 0.01$  while the range of the test data was for  $0.97 > x > 0.03$ .

**Implementation.** The Thome-El Hajal-Cavallini flow pattern based intube condensation heat transfer model is implemented as follows:

1. Determine the local vapor void fraction using [8.1.27];
2. Determine the local flow pattern using the flow pattern map and any necessary transition velocities at the same value of  $x$ ;
3. Identify the type of flow pattern (annular, intermittent, mist, stratified-wavy or stratified);
4. If the flow is annular or intermittent or mist, then  $\theta = 0$  and  $\alpha_c$  is determined with [8.1.32] and  $\alpha(x) = \alpha_c$  in [8.1.23] where  $\delta$  is obtained by solving [8.1.35] and  $f_i$  with [8.1.40].
5. If the flow is stratified-wavy,  $\theta_{strat}$  and  $\theta$  are calculated using [8.1.31] and [8.1.30], then  $\alpha_c$  and  $\alpha_f$  are calculated using [8.1.32] and [8.1.42] or [8.1.43], and finally  $\alpha(x)$  is determined using [8.1.23] where  $\delta$  is obtained with [8.1.35] and  $f_i$  with [8.1.40].
6. If the flow is fully stratified,  $\theta_{strat}$  is obtained from [8.1.31] and  $\theta_{strat}$  is set equal to  $\theta$ , then  $\alpha_c$  and  $\alpha_f$  are calculated using [8.1.32] and [8.1.42] or [8.1.43], and  $\alpha(x)$  is determined using [8.1.23] where  $\delta$  is obtained with [8.1.35] and  $f_i$  is determined with [8.1.41].

**Comparison to Refrigerant Database.** The new model was primarily developed using the heat transfer database of Cavallini et al. (1999, 2001) and then the other eight independent studies were used to determine its general applicability. Figure 8.6 shows the new model compared to the Cavallini data and Figure 8.7 depicts a comparison to all 1850 data, except the experimental hydrocarbon data which had unrealistic trends at low mass velocities, where about 85% are predicted within  $\pm 20\%$ .

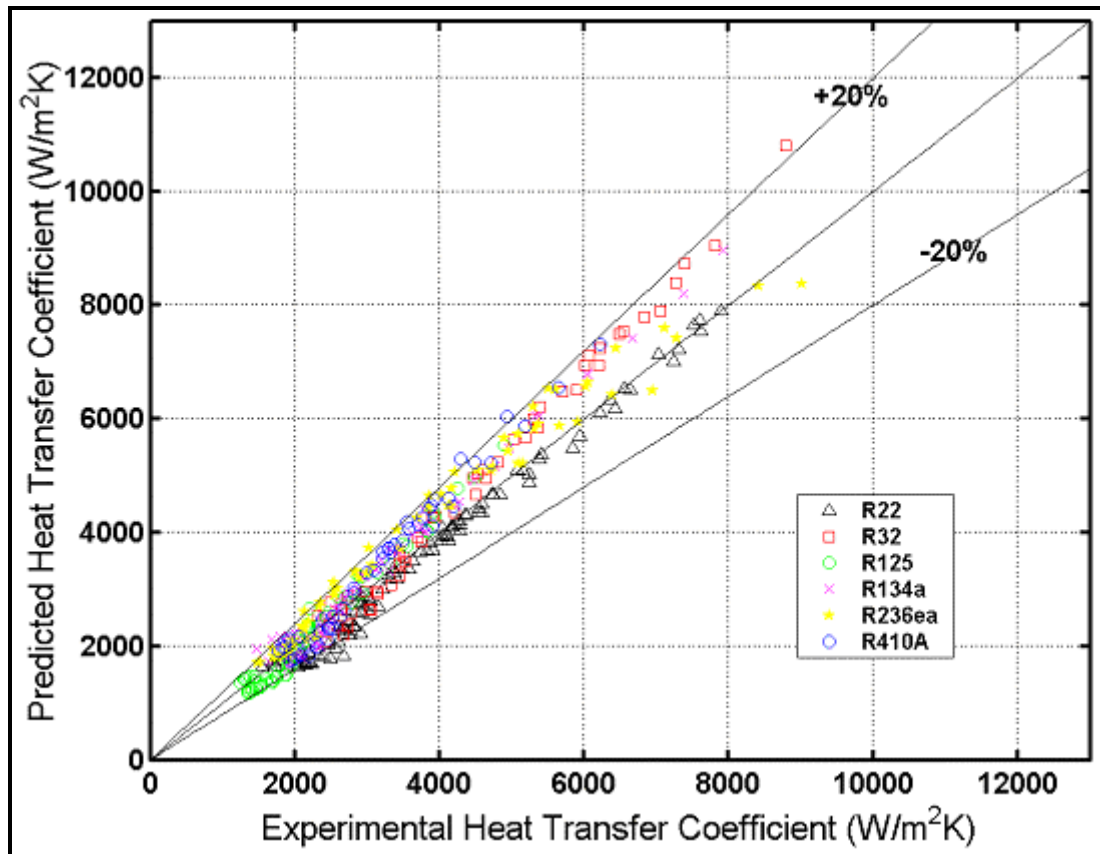


**Figure 8.6. Comparison of the Thome-El Hajal-Cavallini model to the data of Cavallini et al.(1999, 2001) for six refrigerants in an 8.0 mm (0.315 in.) tube.**

**Simulations for R-410A.** The heat transfer model and flow pattern map have been simulated for R-410A condensing at 40°C (104°F) in an 8 mm (0.315 in.) diameter tube. The flow pattern map for three different refrigerants, including R-410A, at these conditions is shown in Figure 8.8. The heat transfer coefficients at  $q = 40 \text{ kW/m}^2$  (12682 Btu/h ft $^2$ ) are shown in Figure 8.9 for a range of mass velocities. At 30 kg/m $^2$ s (22074 lb/h ft $^2$ ), the flow is in the stratified (S) regime from inlet to outlet and the heat transfer coefficient falls off slowly with decreasing vapor quality. At 200 kg/m $^2$ s (147163 lb/h ft $^2$ ), the flow enters in the annular (A) regime and then passes through the intermittent (I) and stratified-wavy (SW) regimes. At 500 kg/m $^2$ s (367906 lb/h ft $^2$ ), the flow enters in the annular (A) regime, converts to intermittent (I) flow and leaves in this same regime. The sharp decline in  $\alpha(x)$  with decreasing  $x$  at high vapor qualities comes from the rapid growth of the annular film thickness  $\delta$ . At 800 kg/m $^2$ s (588650 lb/h ft $^2$ ), the flow enters in the mist flow (MF) regime, goes into the annular (A) regime and leaves in the intermittent (I) regime.

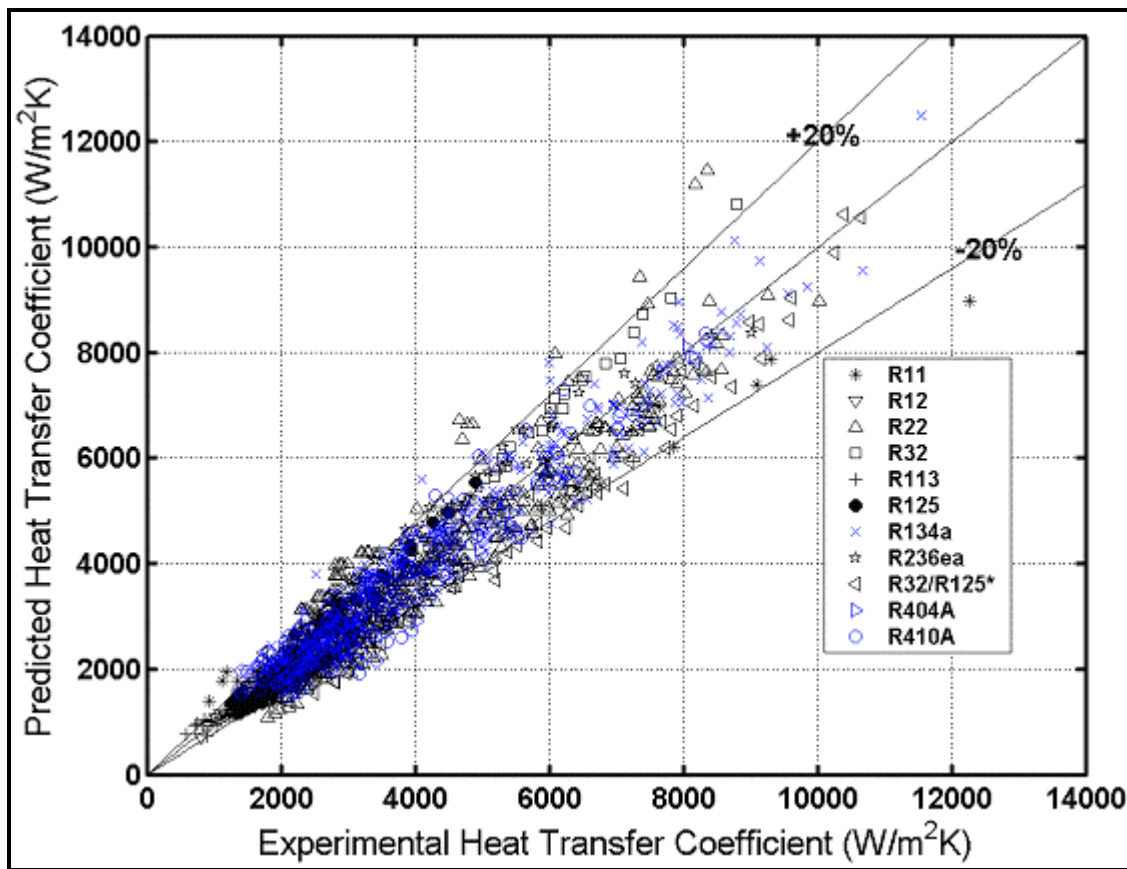
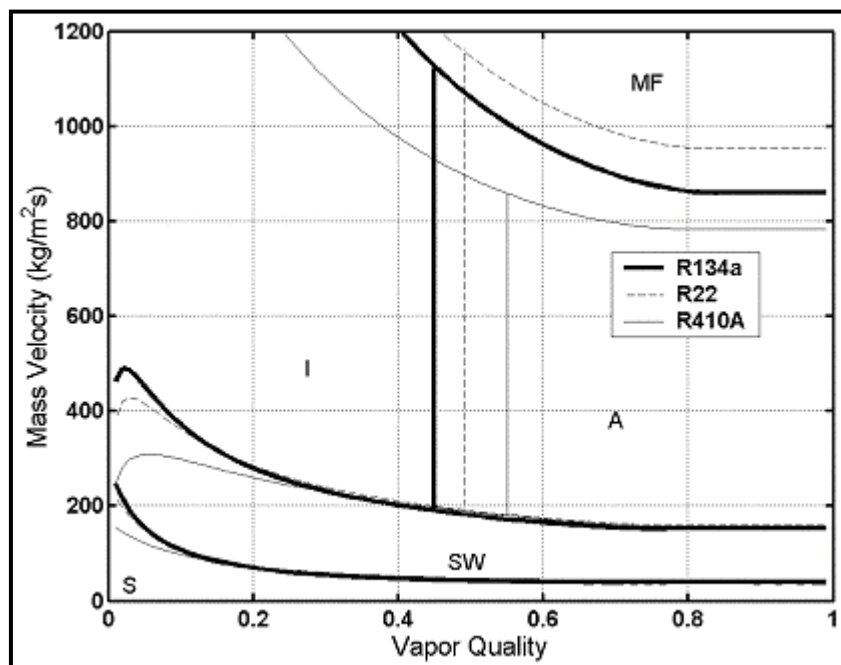
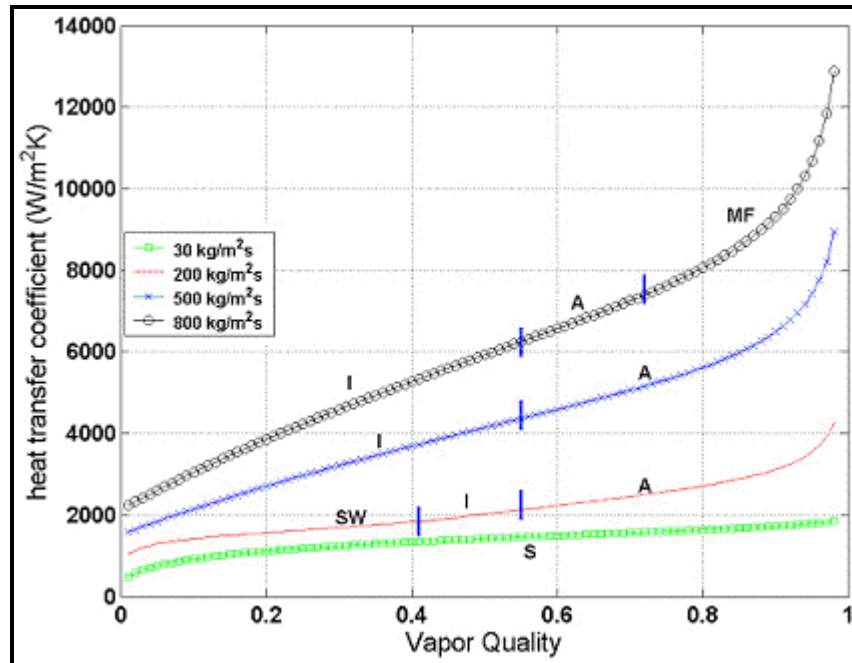


Figure 8.7. Comparison of the Thome-El Hajal-Cavallini model to all their databases for eleven refrigerants.

Figure 8.8. Flow pattern transitions for R-134a, R-22 and R-410A in an 8 mm tube at  $T_{sat} = 40^\circ\text{C}$ , using for simplicity a fixed value of mass velocity of  $300 \text{ kg/m}^2\text{s}$  to evaluate void fractions in preparation of the diagram (in application of the model, the actual mass actual mass velocity is always used for all calculations).





**Figure 8.9. Simulation of heat transfer for R-410A at  $T_{sat} = 40^\circ\text{C}$  in an 8 mm tube at a heat flux of 40 kW/m<sup>2</sup> for 4 mass velocities.**

As can be seen, the new heat transfer model predicts the variation in the local heat transfer coefficients across flow pattern transition boundaries without any discontinuity in the value of  $\alpha(x)$ . This, for example was a problem in the Dobson and Chato (1998) method and also in the recent Cavallini et al. (2002) method going through the transition into their slug flow regime.

Figure 8.10 depicts a similar simulation at heat fluxes of 10 and 40 kW/m<sup>2</sup> at 200 kg/m<sup>2</sup>s (3170 and 12682 Btu/h ft<sup>2</sup> at 147163 lb/h ft<sup>2</sup>), where the lower heat flux is more representative of typical design conditions. Here, the flow enters in the annular regime and converts to intermittent flow and then finally becomes stratified-wavy at about  $x = 0.41$ . In the stratified-wavy regime, the film condensation heat transfer mechanism kicks in around the upper perimeter of the tube and the effect of heat flux is quite evident, where the lower heat flux creates a thinner condensate film and hence a larger heat transfer coefficient.

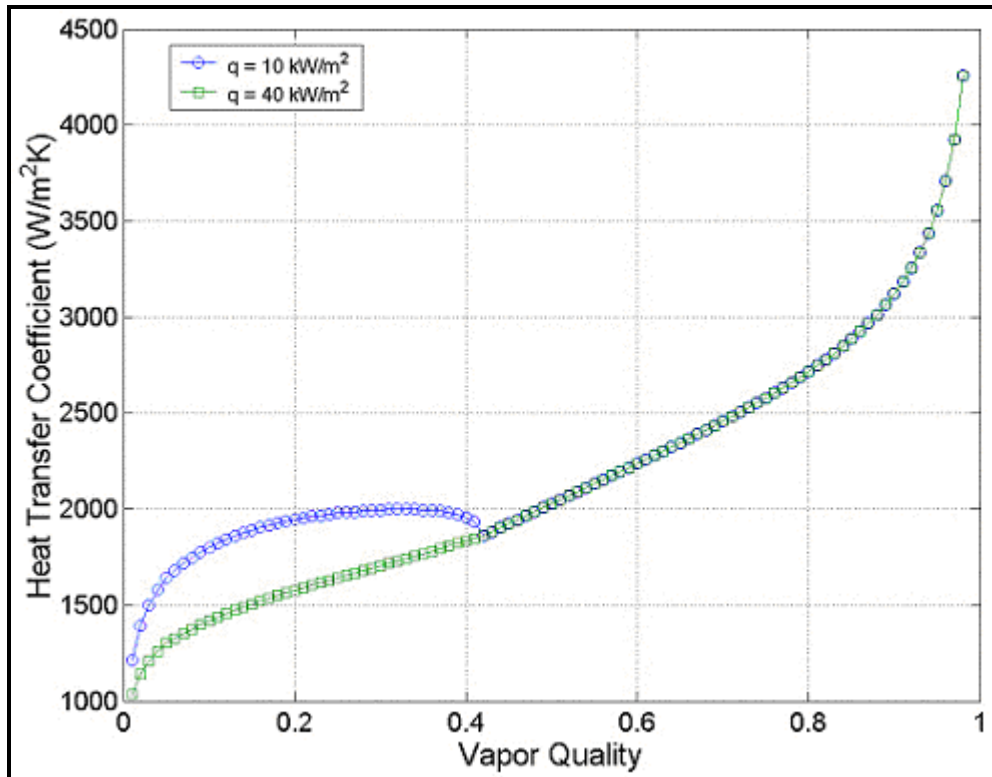
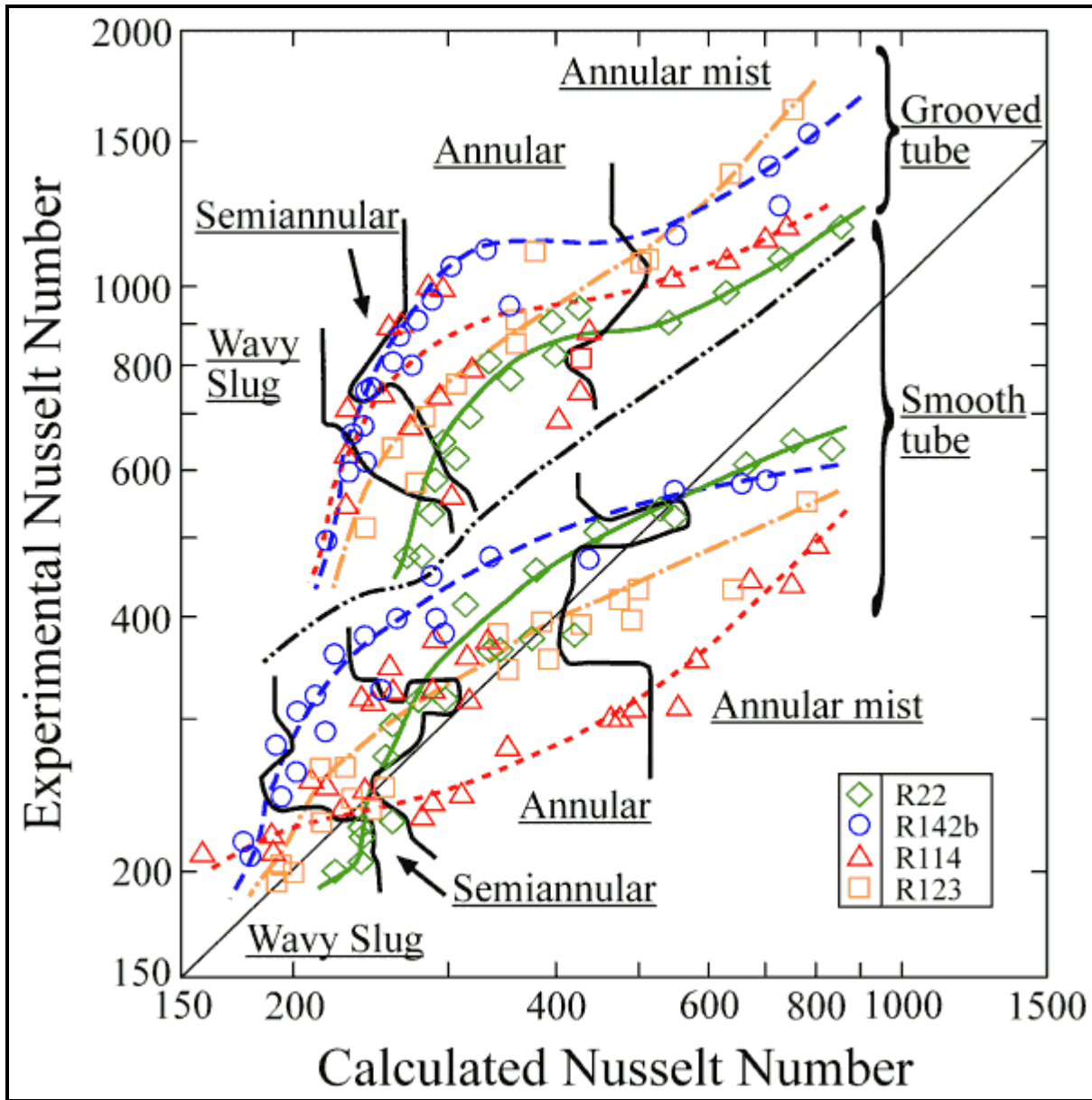


Figure 8.10. Simulation of heat transfer for R-410A at  $T_{sat} = 40^{\circ}\text{C}$  in an 8 mm tube at heat fluxes of 10 and 40  $\text{kW}/\text{m}^2$  for a mass velocity of 200  $\text{kg}/\text{m}^2\text{s}$ .

## 8.2 Condensation in Horizontal Microfin Tubes

Shizuya, Itoh and Hijikata (1995) have done an extensive comparative study between a microfin tube and a plain tube for R-22, R-142b, R-114 and R-123. Their microfin tube had 55 fins with a  $14^{\circ}$  helix angle of 0.19 mm height and an internal area ratio 1.6 times that of an equivalent plain tube. The microfin tube had an internal diameter of 6.26 mm while that of the plain tube was 6.16 mm. Figure 8.11 depicts their comparison, where the flow patterns observed during the tests were also noted. The level of augmentation tends to be larger for wavy-slug flow than for annular flow.



**Figure 8.11. Comparison of microfin tube to plain tube performance by Shizuya, Itoh and Hijikata (1995) for four refrigerants.**

Muzzio, Niro and Arosio (1998) have measured intube-condensing coefficients for a plain tube, a microfin tube with alternating fin heights (VA), a conventional microfin tube (V) and microfin tube with a screw profile (W). Their results for R-22 are shown in Figure 8.12. As is typical of microfin condensation tests, the level of heat transfer augmentation is highest at low mass velocities and tends to fall off towards the value of the area ratio at high mass velocities.

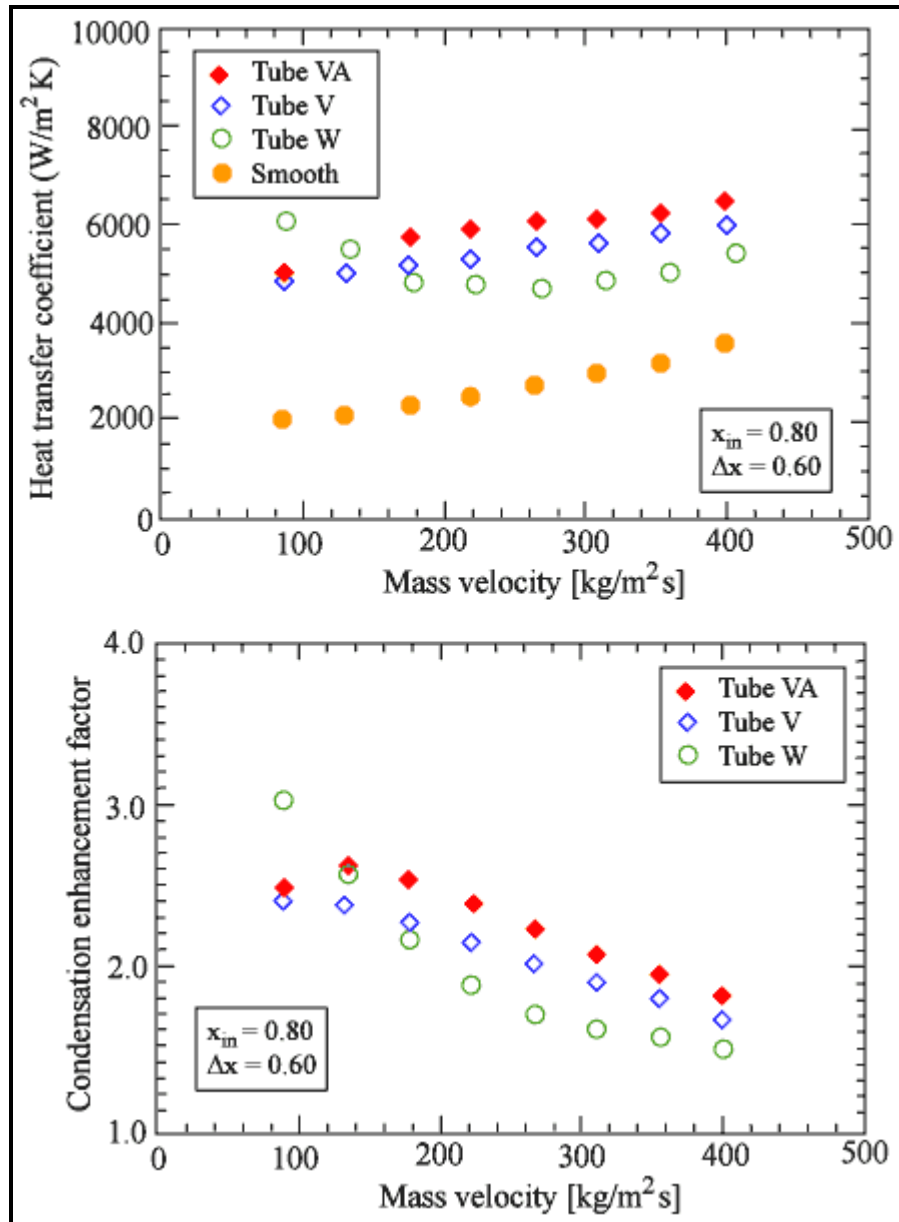


**Figure 8.12. Condensation heat transfer and enhancement factor versus mass velocity at an inlet vapor quality of 0.8 and a vapor quality change of 0.6 obtained by Muzzio, Niro and Arosio (1998).**

Numerous other tests have been done on condensation inside microfin tubes. Some of the following are the more important studies since 1990:

- Koyama, Miyara, Takamatsu and Fujii (1990) measured condensing coefficients for R-22 and R-114.
- Eckels and Pate (1991a) presented a detailed comparison of mean coefficients for R-134a versus R-12.
- Chiang (1993) ran tests with R-22 inside helical and axial microfin tubes, including tests on tubes that had already been mechanically expanded.
- Torikoshi and Ebitsu (1994) ran tests on R-22 and refrigerant mixtures in a microfin tube.

- Du, Xin and Huang (1995) measured condensing coefficients for R-11 in two 2-dimensional axial microfin tubes and three 3-dimensional axial microfin tubes whose fins were cross-cut. In annular flow the cross-cutting provided 34-144% improvement while in stratified flow the improvement was 31-97%.
- Chamra and Webb (1995) also ran comparative tests on 2-d and 3-d microfin geometries for R-22, but found only a marginal improvement of 5-15% from the cross-cutting.
- Uchida, Itoh, Shikazono and Kudoh (1996) also ran similar comparative tests of 2-d and 3-d microfin tube geometries for R-22.
- Dunn (1996) carried out an excellent experimental program on a 9.53 mm (3/8 in.) Wolverine Tube microfin tube Turbo-A for R-22 and R-134a and three azeotropic mixtures. He observed that R-134a had equal or better performance than R-22 while R-410A performed similar to R-22.
- Kedzierski and Goncalves (1997) reported microfin condensation data for R-134a, R-125, R-32 and R-410A. Using a temperature profile approach, they reported true local condensing data rather than quasi-local data typical of other studies.

Methods currently available for simulating local heat transfer coefficients during condensation in microfin tubes are described in Cavallini et al. (1999).

### 8.3 Condensation of Condensable Mixtures in Horizontal Tubes

The Silver-Bell-Ghaly method [Silver (1947) and Bell and Ghaly (1973)] is successfully used to predict condensation of miscible mixtures where all components are condensable but no non-condensable gases are present. When condensing a mixture, the vapor phase must be cooled as the dew point temperature of the mixture falls along the tube, in addition to removing the latent heat. Hence, the process is controlled by condensation and by single-phase cooling of the vapor. This approach assumes two things with respect to cooling of the vapor:

- Mass transfer has no effect on the single-phase heat transfer process in the vapor.
- The vapor occupies the entire tube cross section in determining the vapor phase heat transfer coefficient.

The error in ignoring the first assumption becomes significant for mixtures with large condensing temperature ranges, so their method is reliable for mixtures with small to medium condensing ranges (say smaller than 30 K). The second assumption is conservative since interfacial waves in annular flows augment the vapor phase heat transfer coefficient. The effective condensing heat transfer coefficient  $\alpha_{\text{eff}}$  for condensation of a mixture is calculated by the method as

$$\frac{1}{\alpha_{\text{eff}}} = \frac{1}{\alpha(x)} + \frac{Z_G}{\alpha_G} \quad [8.3.1]$$

To implement this expression, the condensation heat transfer coefficient  $\alpha(x)$  is obtained with an intube correlation for pure fluids in the previous section but inputting the local physical properties of the mixture. The single-phase heat transfer coefficient of the vapor  $\alpha_G$  is calculated with the Dittus-Boelter turbulent flow correlation using the vapor fraction of the flow in calculating the vapor Reynolds number. The parameter  $Z_G$  is the ratio of the sensible cooling of the vapor to the total cooling rate:

$$Z_G = x c_{pG} \frac{dT_{dew}}{dh} \quad [8.3.2]$$

where  $x$  is the local vapor quality,  $c_{pG}$  is the specific heat of the vapor and  $dT_{dew}/dh$  is the slope of the dew point temperature curve with respect to the enthalpy of the mixture as it condenses, i.e. the slope of the condensation curve. This method has been applied to hydrocarbon mixtures and more recently to binary and ternary zeotropic refrigerant blends by Cavallini et al. (1995) and to binary refrigerant mixtures by Smit, Thome and Meyer (2001). For a more complete description of multi-component condensation, refer to Butterworth (1983).

**Table 8.1. Condensation heat transfer database for zeotropic mixtures considered by Del Col, Cavallini and Thome (2005).**

Study	Data Pts.	Mixture (liquid mass fraction)	$d_i$ [mm]	$T_{sat}$ [ $^{\circ}$ C]	$\Delta T_{glide}$ [ $^{\circ}$ C] *	$(T_{sat} - T_w)$ [ $^{\circ}$ C]	Mass Velocity [kg/m <sup>2</sup> s]
<b>Cavallini et al. (1999)</b>	38	R-407C	8.0	38-49	4.9	4.5-13	104-755
<b>Cavallini et al. (2000)</b>	43	R-125/R-236ea (46/54%)	8.0	39-57	21.2	6.5-18	102-753
	31	R-125/R-236ea (63/37%)	8.0	36-55	16.9	5.5-13.5	96-751
	24	R-125/R-236ea (28/72%)	8.0	35-56	21.9	5.7-13.9	98-743
<b>Lee (1994)</b>	27	R-22/R-124 (20/80%)	7.5	19-44	5.5	9.4-19.3	215-305
	26	R-22/R-124 (50/50%)	7.5	22-39	6.7	10.9-19.2	167-369
	24	R-22/R-124 (80/20%)	7.5	22-37	3.6	7.7-15.8	174-358
<b>Kim et al. (1996)</b>	213	R-290/R-600 (25/75%)	8.0	45-54	10.5	2.8-6.9	65-154
	205	R-290/R-600 (50/50%)	8.0	44-55	12.2	3.5-6.9	57-172
	241	R-290/R-600 (75/25%)	8.0	46-54	8.2	3.5-7.3	89-191

(\*) Values of  $\Delta T_{glide}$  are mean values of the range tested in each study.

Del Col, Cavallini and Thome (2005) recently made a detailed study on condensation of mixtures inside plain horizontal tubes covering a multi-laboratory database, shown in Table 8.1. The model by Thome, El Hajal (2003) for local condensation heat transfer coefficient of pure fluids and azeotropic mixtures and the accompanying flow pattern map of El Hajal, Thome and Cavallini (2003) were used as the starting point. It was extended to zeotropic mixtures by modifying the Silver-Bell-Ghaly method already described above. The additional heat transfer resistance created by the mixture was applied to both the convective and the film coefficients, including the effect of interfacial roughness on the vapor heat transfer coefficient  $\alpha_G$  acting on the convective film. A non-equilibrium mixture factor was also introduced to account for non-equilibrium effects on stratified and stratified-wavy flow regimes. The new

method requires much less computational effort than theoretical mass diffusion methods, but still provides accurate predictions of the local heat transfer data and is more accurate than the original Silver-Bell-Ghaly method. Compared against the database shown in Table 8.1 obtained from three independent laboratories, which includes ten different mixtures with temperature glides ranging from 3.5 to 22.8°C (6.3 to 41.0°F) for both refrigerant and hydrocarbon mixtures, the method predicted 98% of the refrigerant heat transfer coefficients measured by Cavallini et al. (1999, 2000) to within  $\pm 20\%$  and 85% of the halogenated plus hydrocarbon refrigerant heat transfer coefficients measured by independent researchers to within  $\pm 20\%$ . This new method is described below.

**Heat transfer database.** The database of condensation heat transfer coefficients available for their study involved four mixture systems representing 10 different zeotropic mixture compositions with a wide range of temperature glides and test conditions. The database covered HCFCs, HFCs and HCs (hydrocarbons). The temperature glide was defined as the difference between the dew point temperature and the bubble point temperature at a fixed pressure and bulk composition. One set of data of Cavallini and coworkers covered R-407C and three mixtures of R-125/R-236ea. The other blends they tested had higher temperature glides from mixing two HFC fluids having far different saturation temperatures, R-125 and R-236ea. R-125 was the “high pressure” fluid whereas R-236ea was the “low pressure” fluid. The data set by Lee (1994) is for the mixture R-22/R-124 at three different mass compositions while the data set of Kim, Chang and Ro (1996) includes heat transfer data on propane/butane mixtures. Figure 8.13 shows some of the test data considered.

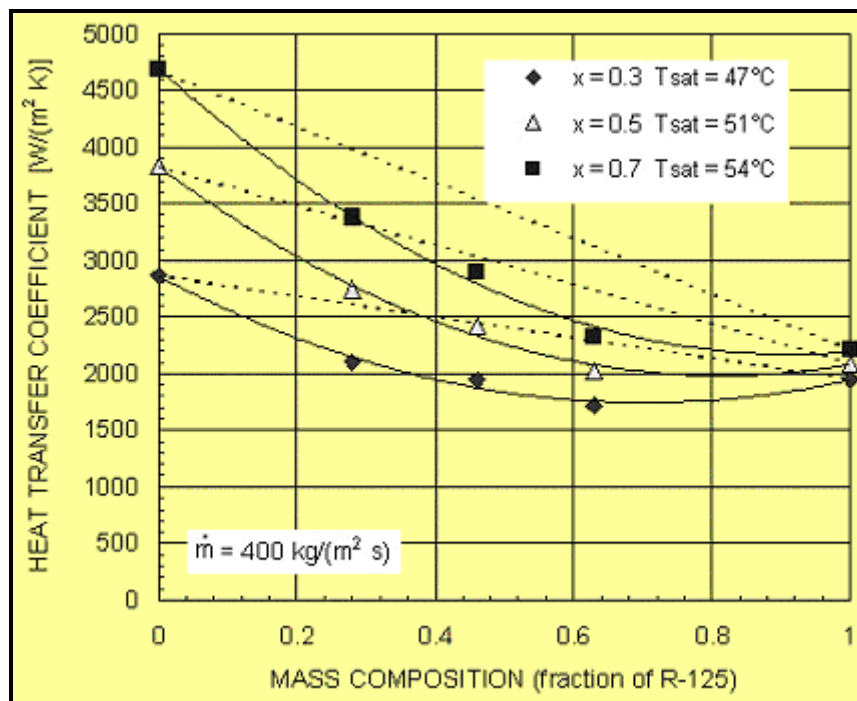


**Figure 8.13. Condensation heat transfer coefficients for R-236fa, R-125 and three of their mixtures from Cavallini et al. (2000) at three different mean vapor qualities at the noted saturation temperatures.**

The term  $1/\alpha(x)$  in [8.3.1] represents the condensate layer resistance and for a mixture it is typically computed using a pure fluid model inputting the liquid mixture properties. The second term in [8.3.1] represents the thermal resistance to cool the vapor flow along the channel to the local, declining saturation

temperature. Primarily, Del Col, Cavallini and Thome (2005) have introduced three improvements to the original Silver-Bell-Ghaly method:

The vapor phase heat transfer coefficient  $\alpha_G$  is corrected for the enhancing effect of the interfacial waves (the waves function essentially like internal ribs in a tube and hence increase the vapor phase heat transfer coefficient above the Dittus-Boelter value);

The interfacial waves are a function of flow pattern as only the perimeter of the tube with axial convection has interfacial waves in the underlying pure fluid model while the upper perimeter with falling film condensation does not and hence the angle  $\theta$  becomes a parameter affecting  $\alpha_G$  in stratified types of flows of mixtures;

Non-equilibrium effects are included, that become more significant in stratified types of flows due to the reduction of mixing.

Similar to the procedure for pure fluids described earlier, the perimeter-averaged local heat transfer coefficient for the mixture  $\alpha_{\text{eff}}$  is obtained from a proration of the film condensation coefficient of the mixture  $\alpha_{\text{fm}}$  and the convective condensation coefficient of the mixture  $\alpha_{\text{cm}}$ , by accounting for the different perimeters pertaining to the two mechanisms:

$$\alpha_{\text{eff}} = \frac{\alpha_{\text{fm}}\theta + (2\pi - \theta)\alpha_{\text{cm}}}{2\pi} \quad [8.3.3]$$

Applying the Thome-El Hajal-Cavallini pure fluid heat transfer model and its flow pattern map to mixtures, the method remains exactly the same as presented earlier in this chapter except for the changes described below. Furthermore, the physical properties of the local mixture composition are used in all calculations. The temperature glide is denoted as  $\Delta T_{\text{glide}}$  and  $\Delta h_m$  refers to the change of enthalpy of the mixture including both the latent heat and the sensible cooling effects on the liquid and vapor phases.  $\theta$  is the falling film angle around the top perimeter of the tube (Figure 8.4) and is computed using [8.1.30]. The convective condensation heat transfer coefficient is obtained from the Bell and Ghaly approach, as follows:

$$\alpha_{\text{cm}} = \left[ \frac{1}{\alpha_c} + R_c \right]^{-1} \quad [8.3.4]$$

$\alpha_c$  is computed from the equations for the pure fluid model. The appropriate Bell and Ghaly resistance  $R_c$  can be calculated as follows:

$$R_c = x c_{pG} \frac{\Delta T_{\text{glide}}}{\Delta h_m} \frac{1}{\alpha_G f_i} \quad [8.3.5]$$

The resistance  $R_c$  is a function of the vapor phase heat transfer coefficient referred to the vapor-liquid interface. Thome, El Hajal and Cavallini (2003) introduced an interfacial roughness factor  $f_i$  to act on the convective coefficient  $\alpha_c$  and to account for the increase in the heat transfer coefficient due to the action of the interfacial shear between the condensate and the vapour, arguing that the vapor shear increases the magnitude and number of the waves generated on the interface, tending to increase heat transfer. The same correction factor acting on  $\alpha_c$  is applied to the vapor heat transfer coefficient in the above

expression, where  $f_i$  is computed from [8.1.40] or [8.1.41]. The vapor heat transfer coefficient  $\alpha_G$  is computed with the Dittus and Boelter (1930) equation:

$$\alpha_G = 0.023 \left( \frac{k_G}{d_i} \right) Re_G^{0.8} Pr_G^{0.33} \quad [8.3.6]$$

using the following expression for the Reynolds number of the vapor phase and  $u_G$  from [8.1.37]:

$$Re_G = \frac{\rho_G u_G d_i}{\mu_G} \quad [8.3.7]$$

Thus, the new approach calculates the vapor heat transfer coefficient from the actual vapor velocity rather assuming the vapor occupies the entire cross-section of the channel.

The Silver-Bell-Ghaly procedure is applied to the film condensation component as in [8.3.4] to [8.3.7] but with  $F_i = 1.0$  since it was assumed in the original pure fluid model that there were no waves on the falling condensation film. The film condensation heat transfer coefficient of the zeotropic mixture in a stratified type of flow is a function of the saturation to wall temperature difference and this effect is incorporated in the expression for  $\alpha_{fm}$  as follows:

$$\alpha_{fm} = F_m \left[ \frac{1}{\alpha_f} + R_c \right]^{-1} \quad [8.3.8]$$

In this expression,  $\alpha_f$  is calculated with mixture properties and  $R_c$  from [8.3.5] with  $F_i = 1.0$ . The non-equilibrium mixture factor  $F_m$  added to this expression accounts for non-equilibrium effects in stratified flow regimes, which was correlated as follows:

$$F_m = \exp \left[ -0.25(1-x) \left( \frac{\dot{m}_{wavy}}{\dot{m}} \right)^{0.5} \left( \frac{\Delta T_{glide}}{T_{sat} - T_w} \right) \right] \quad [8.3.9]$$

Values of  $F_m$  range from 0 and 1, decreasing as the mass velocity and vapor quality decrease. The mass transfer resistance is proportional to the temperature glide and therefore  $F_m$  decreases with increasing  $\Delta T_{glide}$ . The effect of the saturation to wall temperature difference is also included since it drives the mass diffusion process.

Figure 8.14 shows their entire database compared to the new mixture condensation model, plotting the ratio of the predicted values to the experimental values as a function of the temperature glide of the mixture.

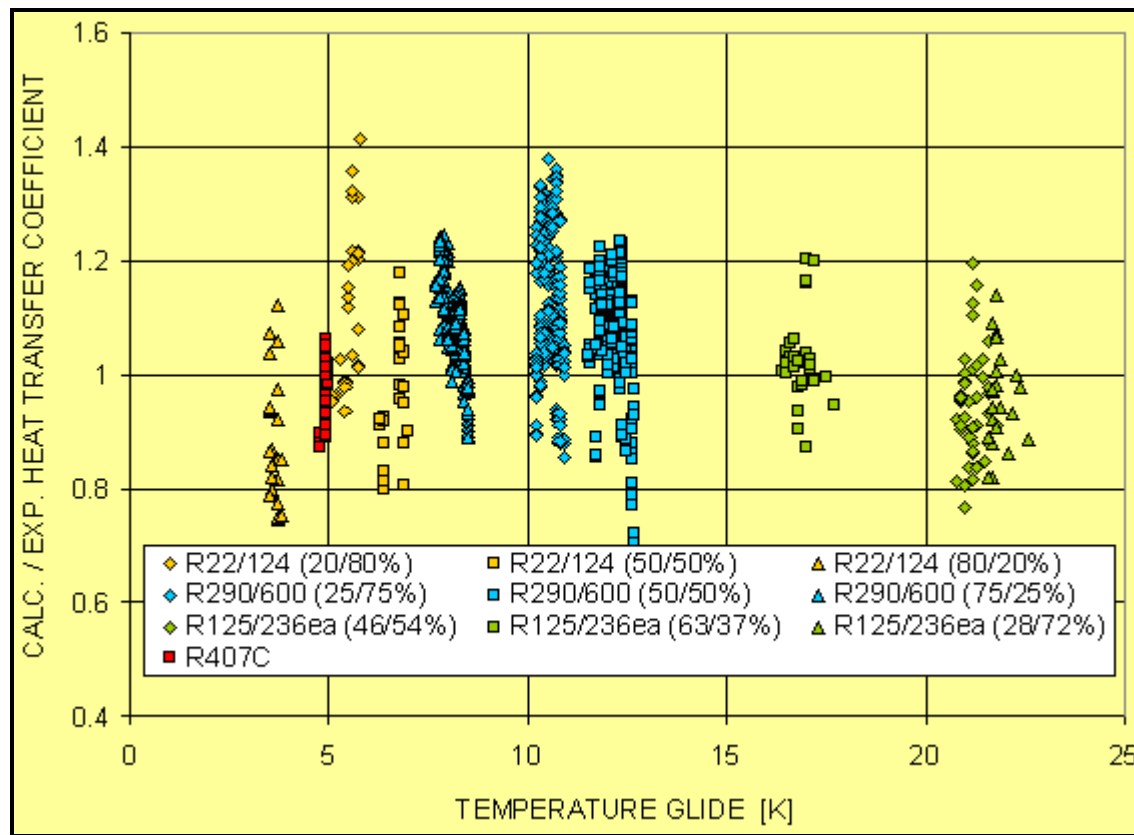


**Figure 8.14. Comparison of the Del Col-Cavallini-Thome mixture condensation model to experimental data plotted versus the temperature glides of the mixtures.**

**Example Calculation:** Propane is condensing inside a horizontal, plain tube whose internal diameter is 15 mm. The refrigerant enters at its saturation temperature of 2°C (5.07 bar) as a saturated vapor and leaves as a saturated liquid. The flow rate of vapor entering is 0.03534 kg/s and the tube wall has a mean internal temperature of -10°C. Determine the following values: the local condensing heat transfer coefficient using the Akers, Shah, and Dobson-Chato methods at a vapor quality of 0.5. Next, assuming a hydrocarbon mixture with the same physical properties as propane but with a linear temperature glide during condensation from 2°C to -3°C, determine the local condensing heat transfer coefficient using the Dobson-Chato method together with the Silver-Bell-Ghaly method at a vapor quality of 0.5. The physical properties of propane at 2°C are:

$$\begin{aligned} \rho_L &= 528 \text{ kg/m}^3; \rho_G = 11.0 \text{ kg/m}^3; \mu_L = 0.0001345 \text{ Ns/m}^2; \mu_G = 0.0000075 \text{ Ns/m}^2; \\ h_{LG} &= 373100 \text{ J/kg}; \lambda_L = 0.108 \text{ W/m K}; c_{pL} = 2470 \text{ J/kg K}; p_{crit} = 4264 \text{ kPa}; \\ Pr_L &= c_{pL}\mu_L/\lambda_L = 3.08; \lambda_G = 0.0159 \text{ W/m K}; c_{pG} = 1880 \text{ J/kg K} \text{ so that } Pr_G = 0.887. \end{aligned}$$

**Solution:** The mass velocity of the total flow of liquid plus vapor is:

$$\dot{m} = \frac{\dot{M}}{\pi D^2 / 4} = \frac{0.03534}{\pi(0.015)^2 / 4} = 200 \text{ kg/m}^2 \text{ s}$$

From [5.8.5], the equivalent Reynolds number of Akers et al. (1959) is:

$$\dot{m}_e = 200 \left[ (1 - 0.5) + 0.5 \left( \frac{528}{11} \right)^{1/2} \right] = 792.8 \text{ kg/m}^2 \text{ s}$$

so that the equivalent Reynolds number is:

$$Re_e = \frac{\dot{m}_e D}{\mu_L} = \frac{792.8(0.015)}{0.0001345} = 88416$$

For  $Re_e > 50,000$ ,  $C = 0.0265$  and  $n = 0.8$ . Applying [8.1.4], the local condensing heat transfer coefficient of Akers is:

$$\frac{\alpha(x)(0.015)}{0.108} = 0.0265(88416)^{0.8}(3.08)^{1/3}$$

$$\alpha(x) = 2516 \text{ W/m}^2\text{K}$$

Turning to the Shah method, the reduced pressure is 0.1189 and the liquid Reynolds number is:

$$Re_L = \frac{\dot{m} D}{\mu_L} = \frac{200(0.015)}{0.0001345} = 22305$$

Using [8.1.6], the local condensing heat transfer coefficient is:

$$\frac{\alpha(x)(0.015)}{0.108} = 0.023(22305)^{0.8}(3.08)^{0.4} \left[ (1 - 0.5)^{0.8} + \frac{3.8(0.5)^{0.76}(1 - 0.5)^{0.04}}{(0.1189)^{0.38}} \right]$$

$$\alpha(x) = 4283 \text{ W/m}^2\text{K}$$

The Dobson and Chato method is implemented as follows. The three dimensionless groups are calculated from [8.1.9], [8.1.10] and [8.1.14]:

$$Re_{Ls} = \frac{200(0.015)(1 - 0.5)}{0.0001345} = 11152$$

$$X_{tt} = \left( \frac{1 - 0.5}{0.5} \right)^{0.9} \left( \frac{11}{528} \right)^{0.5} \left( \frac{0.0001345}{0.0000075} \right)^{0.1} = 0.1926$$

$$Ga_L = \frac{9.81(528)(528 - 11)(0.015)^3}{(0.0001345)^2} = 499600000$$

The transition criterion is obtained from [8.1.20]:

$$Fr_{so} = 0.025(11152)^{1.59} \left( \frac{1 + 1.09(0.1926)^{0.039}}{0.1926} \right)^{1.5} \frac{1}{(499600000)^{0.5}} = 103.7$$

When  $Fr_{so} > 20$ , the annular flow correlation [8.1.7] is used:

$$Nu(x) = 0.023(11152)^{0.8}(3.08)^{0.4} \left[ 1 + \frac{2.22}{(0.1926)^{0.89}} \right] = 662.2$$

From [8.1.8], the local condensing coefficient is obtained:

$$Nu(x) = \frac{\alpha(x)(0.015)}{0.108} = 662.2$$

$$\alpha(x) = 4768 \text{ W/m}^2\text{K}$$

Thus, the methods of Akers, Shah and Dobson-Chato give the respective values of 2516, 4283 and 4768  $\text{W/m}^2 \text{K}$ . The fall in the dew point temperature over the entire condensation range is 5°C ( $= dT_{dew}$ ). The total enthalpy change is that of the latent heat plus sensible heat. The latter can be estimated as the mean of the liquid and vapor specific heats applied to the condensing temperature glide of 5°C. Thus,  $dh = (1/2)(2470+1880)(5) + 373100 = 10875 + 373100 = 383975 \text{ J/kg}$ . Applying [8.3.2] gives:

$$Z_G = 0.5(1880) \frac{5}{383975} = 0.01224$$

The Reynolds number of the vapor fraction is:

$$Re_{Gs} = \frac{200(0.015)(1-0.5)}{0.0000075} = 200000$$

The convection heat transfer coefficient to the vapor is obtained with the Dittus-Boelter single-phase turbulent flow correlation:

$$\frac{\alpha_G(0.015)}{0.0159} = 0.023(200000)^{0.8}(0.887)^{0.4}$$

$$\alpha_G = 404.6 \text{ W/m}^2\text{K}$$

Applying [8.3.1] gives the condensing coefficient of the mixture as:

$$\frac{1}{\alpha_{eff}} = \frac{1}{4768} + \frac{0.01224}{404.6}$$

$$\alpha_{eff} = 4160 \text{ W/m}^2\text{K}$$

The mass transfer effect reduces the condensing heat transfer coefficient by 13% for these conditions.

## 8.4 Condensation of Superheated Vapor

Cooling of superheated vapors involves condensation when the wall temperature is below the saturation temperature of the vapor, or one of its components if a mixture. In order to determine if condensation

occurs, a step-wise calculation of the wall temperature must be performed, using the cooling fluid's heat transfer coefficient and the single-phase heat transfer coefficient of the vapor phase in the thermal resistance analysis. The temperatures of the hot and cold fluids change along the flow path of the superheated vapor and the local values are used to calculate the wall temperature on the vapor-side. If the wall temperature goes below the saturation temperature, then condensation of the superheated vapor will occur in the thermal boundary layer on the tube wall, even though the bulk vapor is superheated. Since condensing heat transfer is much more effective than single-phase heat transfer to a vapor, it is imperative to include this effect in the thermal design of the condenser if this zone is significant with respect to the saturated condensing zone. To estimate the condensing heat transfer coefficient in this desuperheating zone, it is common practice to use the same thermal design equation as in the saturated zone. The saturated zone method should normally be evaluated at a vapor quality of 0.99 and not at 1.0 since some of these methods will "crash" at a vapor quality of 1.0 or go to the single-phase turbulent flow heat transfer coefficient.

The above scenario is based on the assumption that the process reached this operating state from a hot process path, for example if the superheated vapor is flowing through the heat exchanger before the coolant flow is applied. If instead the coolant is applied first to the heat exchanger, then the subsequent flow of the superheated vapor will find a wall temperature below saturation. In this case, the desuperheating zone will be found by using the condensing heat transfer coefficient in the thermal resistance analysis rather than the single-phase heat transfer coefficient of the vapor phase.

## 8.5 Subcooling of Condensate

Methods for predicting heat transfer and pressure drop for single-phase flow of liquids should be used for the subcooling zone of the condenser. In actual fact, the condensate may still contain some bubbles that have not yet condensed (remember this is a dynamic process and not an equilibrium thermodynamic process) but their effect on thermal performance will not be significant. The flow may be either laminar or turbulent. Also, for internally enhanced tubes, an appropriate method for the particular enhancement operating in the single-phase mode should be used. For example, for microfin tubes the methods for predicting heat transfer and pressure drop inside internally ribbed tubes should be used.

## Chapter 9

# Boiling Heat Transfer on External Surfaces

(Revised in 2006)

**SUMMARY:** Boiling on the outside of tubes is surveyed in this chapter. First, nucleate pool boiling is described, which is a two-phase process analogous to single-phase natural convection since the only movement of the pool is due to the boiling process itself. Then, convective boiling on the outside of horizontal tube bundles is discussed. Topics covered include: the pool boiling curve, heat transfer mechanisms for plain and enhanced tubes, nucleate pool boiling correlations for plain tubes, critical heat flux of nucleate boiling, boiling of mixtures, boiling on enhanced tubes, and bundle boiling on plain, low fin and Turbo-B geometry tubes.

## 9.1 Introduction

The basics of boiling on plain tubes, enhanced tubes and tube bundles are addressed here. For other comprehensive reviews and presentations on this subject, refer to Thome (1990) for enhanced boiling and to Collier and Thome (1994) or van Stralen and Cole (1979) for the fundamentals of boiling. Another presentation on boiling heat transfer is a survey presented by Thome (1998) on research in this area in the 1990's.

## 9.2 Enhanced Boiling Surfaces

Numerous enhanced boiling surfaces have been proposed and patented over the years. Figure 9.1 depicts a diagram showing a variety of geometries, most which have never made it to market. The first type of enhanced boiling tube to become successful was the low finned tube. Figure 9.2 depicts a photograph of a Turbo-Chil low finned tube made by Wolverine Tube Inc.

By mechanically deforming low finned tubes, it is possible to create a high density of re-entrant channels and pores on a tube's surface, which increases heat transfer performance significantly. Figure 9.3 shows several diagrams of the Turbo-B tube made by Wolverine Tube Inc. that is widely used in refrigerant flooded evaporators, showing its external enhanced boiling geometry and its internal helical fins for augmenting heat transfer to chilled water. Figure 9.4 shows photographs of some of the various versions of the Turbo-B tubes produced by Wolverine Tube Inc.

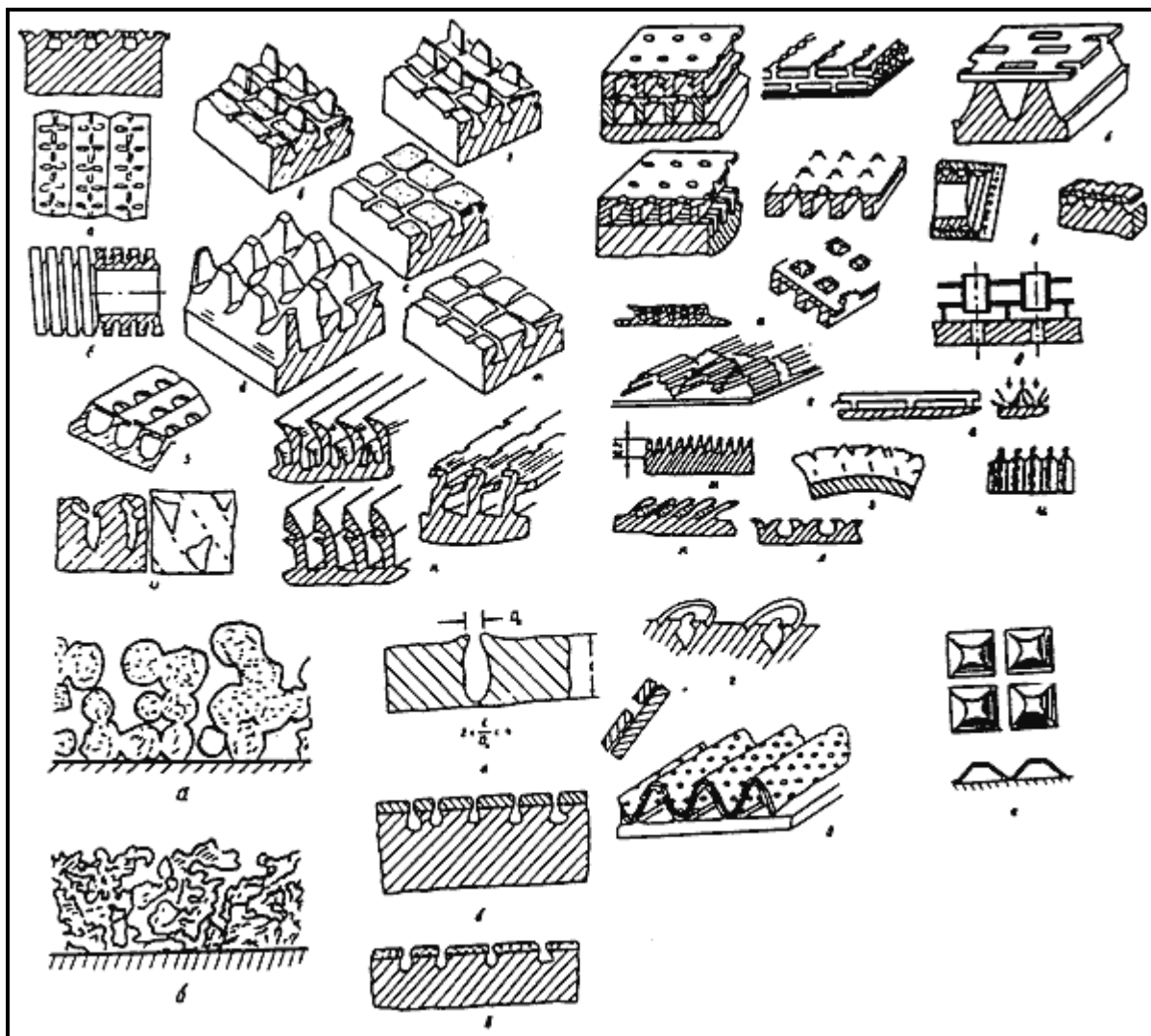


Figure 9.1. Selection of enhanced boiling surfaces.

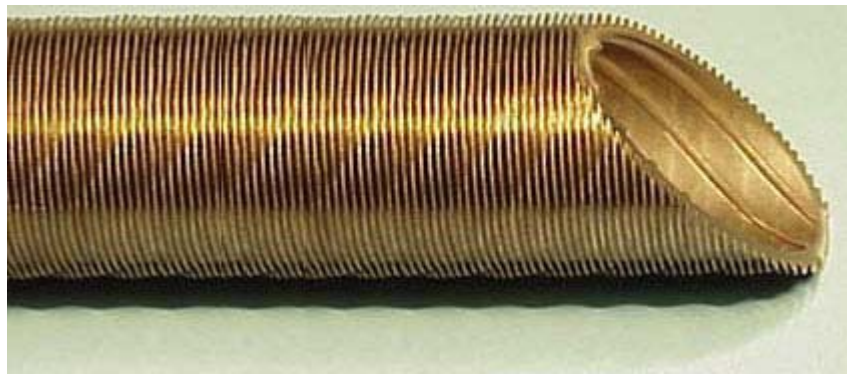


Figure 9.2. Photograph of Turbo-Chil low finned tube.

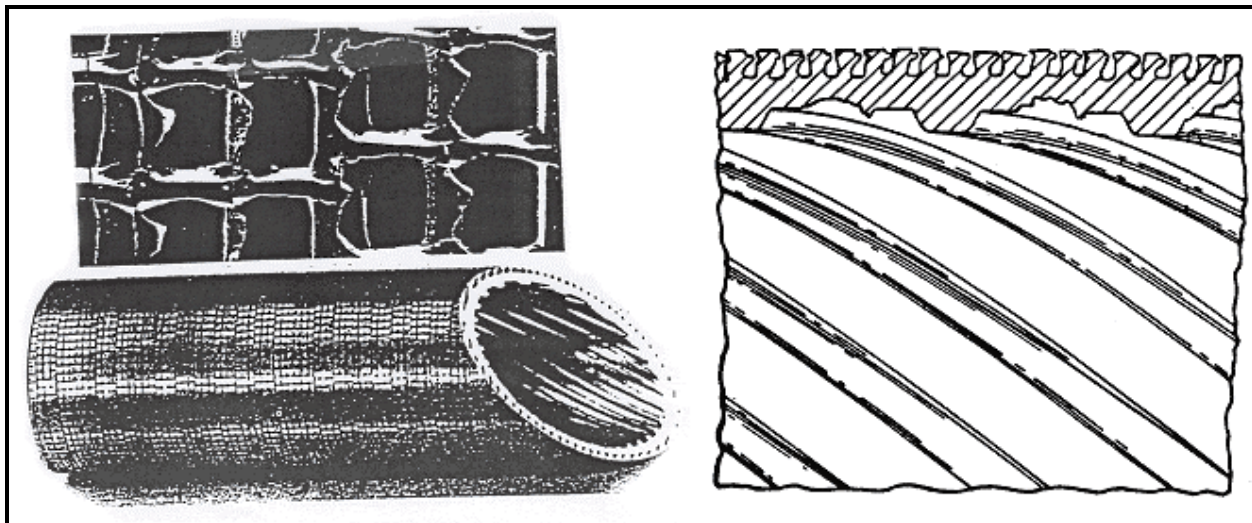


Figure 9.3. Turbo-B enhancement geometry.

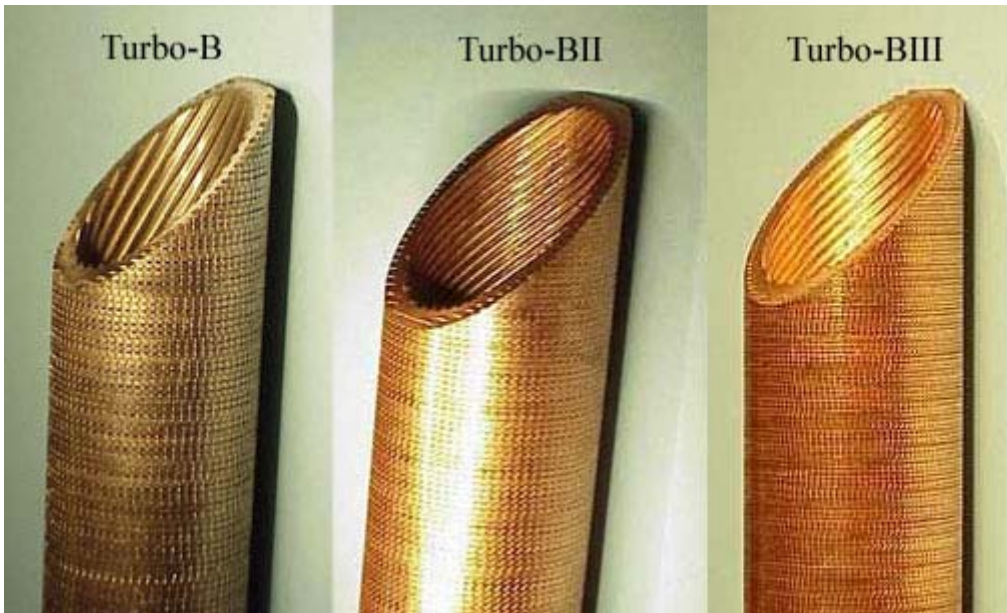


Figure 9.4. Photographs of Turbo-B, Turbo-BII and Turbo-BIII tubes.

### 9.3 Boiling on Plain Tubes

The most important features of pool boiling heat transfer are its characteristic pool boiling curve, the heat transfer mechanisms responsible for removing heat from the heated boiling surface, nucleate pool boiling correlations for predicting heat transfer coefficients and the maximum feasible nucleate pool boiling heat flux. These topics are discussed below.

### 9.3.1 Pool Boiling Heat Transfer

Consider an electrically heated wire (or tube) placed in a large pool of quiescent liquid at or near its saturation temperature. Applying Joule resistance heating and using the wire (or tube) as a resistance thermometer, its surface temperature can be measured as a function of heat flux and plotted as heat flux versus surface temperature as shown in Figure 9.5. This diagram was first presented by Nukiyama (1934) and is often referred to as Nukiyama's curve. It is more common nowadays to plot the wall heat flux  $q$  versus the temperature difference  $\Delta T$  between the wall temperature  $T_{\text{wall}}$  and the saturation temperature  $T_{\text{sat}}$  on logarithmic scales, or to plot the pool boiling heat transfer coefficient  $\alpha_{\text{nb}}$  versus the heat flux. In the curve depicted, four distinct trends of heat transfer regimes can be distinguished:

- Natural convection ( $T_{\text{wall}} < T_{\text{IB}}$ )
- Nucleate boiling ( $T_{\text{IB}} < T_{\text{wall}} < T_{\text{DNB}}$ )
- Transition boiling ( $T_{\text{DNB}} < T_{\text{wall}} < T_{\text{MFB}}$ )
- Film boiling ( $T_{\text{MFB}} < T_{\text{wall}}$ )

that are delineated by the three transition points:

- IB: the point of Incipience of Boiling (IB)
- DNB: the point of Departure from Nucleate Boiling (DNB)
- MFB: the Minimum Film Boiling point.

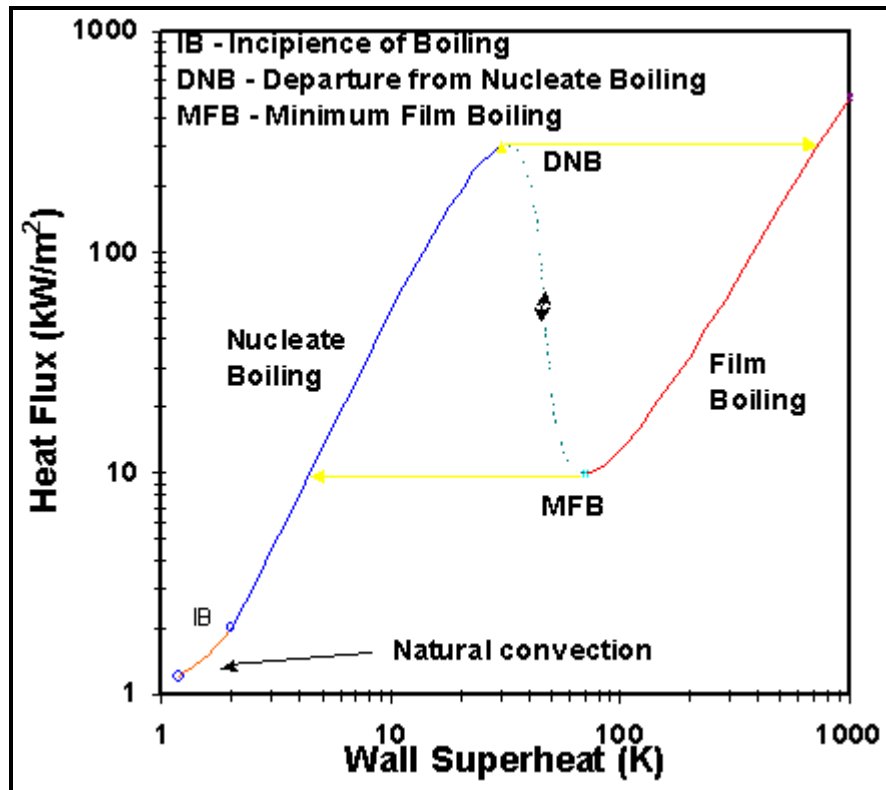


Figure 9.5. Pool boiling curve.

For increasing heat flux, first the natural convection regime is encountered the surface temperature reaches that necessary for boiling nucleation to occur at point IB. Then, the process passes up the *nucleate boiling curve* until arriving at the surface temperature at which departure from nucleate boiling (DNB) occurs, often also referred to as the critical heat flux. At this point, the process jumps to a much higher surface temperature on the *film boiling curve*. Reducing the heat flux, the process follows the film boiling curve until arriving at the surface temperature at which the film boiling process becomes unstable (MFB), a point also sometimes referred to as the Liedenfrost point. At this point, the process jumps to a lower surface temperature and rejoins the nucleate boiling curve. For experiments with a temperature controlled surface temperature rather than for a heat flux controlled process as described above, the process will pass through the *transition boiling curve* between the points DNB and MFB.

A schematic representation of these regimes taken from Collier and Thome (1994) is shown in Figure 9.6. The natural convection part of the curve can be predicted using well-established correlations for single-phase natural convection. In this regime the wall temperature continues to rise as the heat flux is increased until the first bubbles appear, indicating boiling nucleation on the surface (point IB). These bubbles grow from vapor trapped in small cavities in the surface and are the so-called nucleation sites. As the heat flux is increased, more and more nucleation sites become activated. On the nucleate boiling curve, large increases in heat flux are achieved for relatively modest increases in  $\Delta T$  (defined as  $T_{wall} - T_{sat}$ ) until the DNB condition is reached. At DNB, jets of rising vapor are formed that prevents liquid from reaching the heated surface, such that it becomes blanketed by vapor, which greatly degrades heat transfer. On the film boiling region of the curve, the wall is completely covered with a thin film of vapor. Heat is transferred by heat conduction and radiation from the wall through the vapor film. The vapor film is stable in that liquid does not normally wet the heater surface, although some transient wetting may occur, and at the free interface between the film and the liquid pool relatively large bubbles are formed by evaporation at the interface, which then depart from the interface and rise up through the liquid pool.

Heat transfer coefficients on the nucleate pool boiling portion of Nukiyama's curve are much larger than those for simple natural convection to the liquid. The three principal heat transfer mechanisms thought to control the nucleate pool boiling process are illustrated in Figure 9.7 that can be explained as follows:

- **Bubble agitation mechanism.** Intense convection in the liquid adjacent to the heated wall is induced by the lateral pumping motion of growing and departing bubbles, which transforms the natural convection process into a localized forced convection process. Sensible heat is carried away from the surface in the form of superheated liquid.

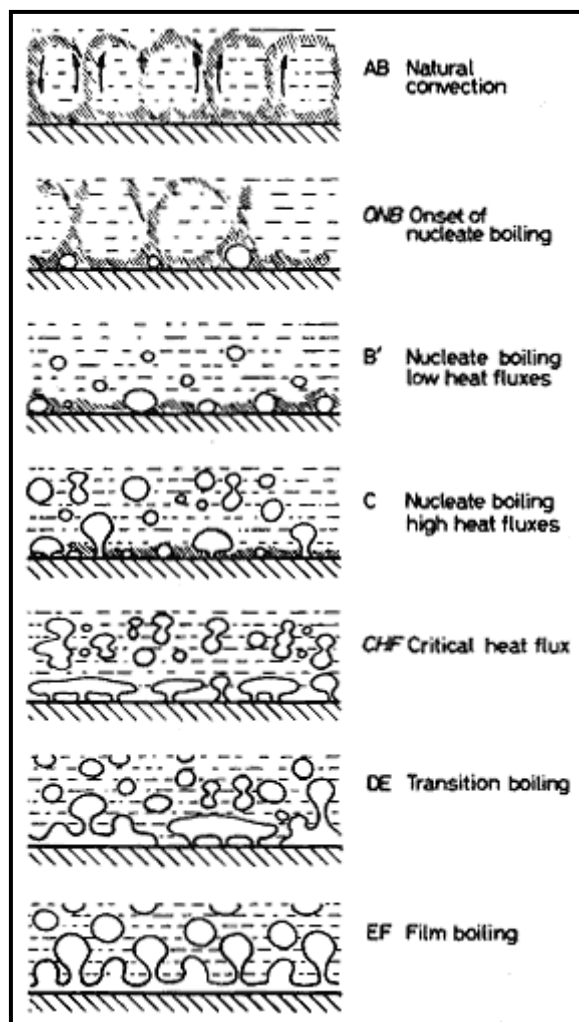
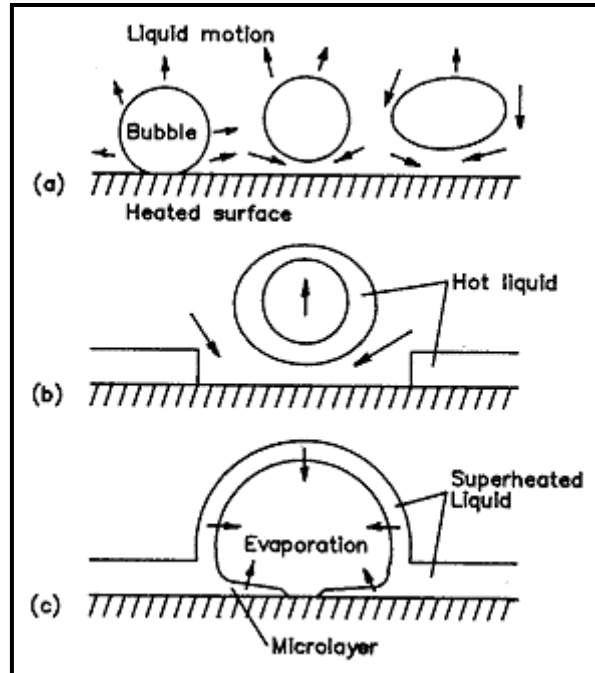


Figure 9.6. Pool boiling processes.

- **Vapor-liquid exchange mechanism.** Transient conduction from the hot wall into the liquid forms a superheated layer on the surface and its removal by departing bubbles gives rise to a cyclic thermal boundary layer stripping phenomenon. Sensible heat is transported away from the surface by this mechanism, whose intensity depends on the rate of layer removal, its mean temperature, the area of influence of departing bubbles and their departure frequency, and finally the density of active boiling sites.
- **Evaporation mechanism.** Vapor bubbles grow in the superheated layer formed on the heated surface. Macro-evaporation occurs over the top of the bubble surrounded by the thermal boundary layer while micro-evaporation occurs underneath the bubble across the thin layer of liquid trapped between a rapidly growing bubble and the surface, the latter which is often referred to as *microlayer evaporation*. Latent heat is transported by this mechanism. Since bubbles rise much faster than liquid natural convection currents and contain a large quantity of energy due to the latent heat absorbed by the bubble, this is a very efficient heat transport mechanism.

The above mechanisms are not exclusive of one another in that each is competing for the same heat. For instance, the evaporation mechanism tries to remove enthalpy from the thermal boundary layer in the form of latent heat while the other two mechanisms try to carry away the same enthalpy as sensible heat. At low heat fluxes with only isolated bubbles on the surface, natural convection occurs on the inactive areas of the surface.



**Figure 9.7. Nucleate boiling mechanisms. (a) bubble agitation, (b) vapor-liquid exchange, (c) evaporation.**

### 9.3.2 Nucleate Pool Boiling Correlations

Experimental results for heat flux  $q$  and wall superheat  $\Delta T$  are typically fit to an exponential equation of one of the following forms:  $q \propto \Delta T^n$ ,  $\alpha_{nb} \propto \Delta T^n$  or  $\alpha_{nb} \propto q^n$ , where  $n$  is on the order of 3, 2 or 0.7, respectively. The nucleate boiling curve is not linear at low heat fluxes nor as it approaches DNB, but these zones are often excluded (or not measured) when fitting a curve to experimental data. Nucleate pool boiling correlations can be formulated in one of the above forms but those presented as  $\alpha_{nb} \propto q^n$  are the easiest to apply. Some nucleate pool boiling correlations are presented below, which are empirical representations of experimental data.

**Rohsenow Correlation.** Rohsenow (1962) proposed one of the first nucleate pool boiling correlations, based on the premise of the bubble agitation mechanism and formulated as a single phase forced convection correlation:

$$Nu = C_1 Re^x Pr^y \quad [9.3.1]$$

The Nusselt number for boiling was defined as follows where the bracketed term is the bubble departure diameter, designated as the characteristic length:

$$Nu = \frac{\alpha_{nb}}{k_L} \left[ \frac{\sigma}{g(\rho_L - \rho_G)} \right]^{1/2} \quad [9.3.2]$$

In this expression,  $\alpha_{nb}$  is the nucleate pool boiling heat transfer coefficient,  $k_L$  is the liquid thermal conductivity,  $\sigma$  is the surface tension,  $g$  is the gravitational acceleration, and  $\rho_L$  and  $\rho_G$  are the densities of the liquid and vapor phases. His Reynolds number was defined in terms of the superficial velocity of the liquid as

$$Re = \frac{q}{h_{LG}\rho_L} \left[ \frac{\sigma}{g(\rho_L - \rho_G)} \right]^{1/2} \frac{\rho_L}{\mu_L} \quad [9.3.3]$$

where  $h_{LG}$  is the latent heat and  $\mu_L$  is the liquid dynamic viscosity. An empirical constant  $C_{sf}$  was introduced to account for the influence of the liquid-surface combination observed in his database as follows:

$$Nu = \frac{1}{C_{sf}} Re^{(1-n)} Pr^{-m} \quad [9.3.4]$$

The Rohsenow correlation is normally presented in the following form:

$$\left[ \frac{c_{pL}\Delta T}{h_{LG}} \right] = C_{sf} \left[ \frac{q}{\mu_L h_{LG}} \left( \frac{\sigma}{g(\rho_L - \rho_G)} \right)^{1/2} \right]^n Pr_L^{m+1} \quad [9.3.5]$$

The specific heat of the liquid is  $c_{pL}$  and  $Pr_L$  is the liquid Prandtl number;  $\alpha_{nb}$  is obtained from the definition of the heat transfer coefficient, that is  $\alpha_{nb} = q/\Delta T$ . The values of the exponents are  $m=0.7$  and  $n=0.33$  (equivalent to  $q \propto \Delta T^3$ ) for all fluids except for water for which Rohsenow recommended setting  $m=0$ . Values of  $C_{sf}$  for various surface-fluid combinations of Rohsenow and additional values proposed by Vachon, Nix and Tangor (1967) are listed in Table 9.1. This method is now mostly of “historical” value, pointing to the importance of the micro-topology of the boiling surface on nucleate boiling heat transfer.

**Mostinski Correlation.** Mostinski (1963) ignored surface effects and applied the principle of corresponding states to nucleate pool boiling heat transfer, correlating data as a function of the reduced pressure of the fluid  $p_r$  and its critical pressure  $p_{crit}$ . His *dimensional* reduced pressure correlation gives  $\alpha_{nb}$  in  $\text{W}/\text{m}^2\text{K}$  as:

$$\alpha_{nb} = 0.00417 q^{0.7} p_{crit}^{0.69} F_p \quad [9.3.6]$$

The correlation must be used with  $q$  in  $\text{W}/\text{m}^2$  and  $p_{crit}$  in  $\text{kN}/\text{m}^2$  (i.e. in  $\text{kPa}$ , not in  $\text{N}/\text{m}^2$ ).  $F_p$  is a non-dimensional pressure correction factor that characterizes pressure effects on nucleate boiling as

$$F_p = 1.8 p_r^{0.17} + 4 p_r^{1.2} + 10 p_r^{10} \quad [9.3.7]$$

This correlation gives reasonable results for a wide range of fluids and reduced pressures.

**Table 9.1. Values of  $C_{sf}$  for Rohsenow correlation.**

Liquid-surface combination	$C_{sf}$
n-Pentane on polished copper	0.0154
n-Pentane on polished nickel	0.0127
Water on polished copper	0.0128
Carbon tetrachloride on polished copper	0.0070
Water on lapped copper	0.0147
n-Pentane on lapped copper	0.0049
n-Pentane on emery polished copper	0.0074
Water on scored copper	0.0068
Water on ground and polished stainless steel	0.0800
Water on PTFE pitted stainless steel	0.0058
Water on chemically etched stainless steel	0.0133
Water on mechanically polished stainless steel	0.0132

**Stephan-Abdelsalam Correlation.** Stephan and Abdelsalam (1980) proposed four specific correlations applying a statistical multiple regression technique to the following fluid classes: water, organics, refrigerants and cryogens. Their organic fluid correlation is the most widely quoted and it is given as:

$$\frac{\alpha_{nb} d_{bub}}{k_L} = 0.0546 \left[ \left( \frac{\rho_G}{\rho_L} \right)^{1/2} \left( \frac{qd_{bub}}{k_L T_{sat}} \right) \right]^{0.67} \left( \frac{h_{LG} d_{bub}^2}{a_L^2} \right)^{0.248} \left( \frac{\rho_L - \rho_G}{\rho_L} \right)^{-4.33} \quad [9.3.8]$$

The expression to the left of the equal sign is a Nusselt number and their bubble departure diameter  $d_{bub}$  is obtained from

$$d_{bub} = 0.0146 \beta \left[ \frac{2\sigma}{g(\rho_L - \rho_G)} \right]^{1/2} \quad [9.3.9]$$

The contact angle  $\beta$  is assigned a fixed value of  $35^\circ$  irrespective of the fluid,  $T_{sat}$  is the saturation temperature of the fluid in K, and  $a_L$  is the liquid thermal diffusivity.

**Cooper Correlation.** Cooper (1984) proposed a new reduced pressure form of pool boiling correlation including the surface roughness of the boiling surface as a variable:

$$\alpha_{nb} = 55 p_r^{0.12 - 0.4343 \ln R_p} (-0.4343 \ln p_r)^{-0.55} M^{-0.5} q^{0.67} \quad [9.3.10]$$

This is a *dimensional* correlation in which  $\alpha_{nb}$  is in  $\text{W}/\text{m}^2\text{K}$ , the heat flux  $q$  is in  $\text{W}/\text{m}^2$ ,  $M$  is the molecular weight of the fluid and  $R_p$  is the surface roughness in  $\mu\text{m}$ . When  $R_p$  is unknown, it is set to  $1.0 \mu\text{m}$ . He recommended multiplying the above heat transfer coefficient by 1.7 for horizontal copper cylinders; however, the correlation seems to be more accurate for boiling of refrigerants on copper tubes without this correction and that is the approach recommended here. The Cooper correlation covers reduced pressures from about 0.001 to 0.9 and molecular weights from 2 to 200.

**Table 9.2. References values of Gorenflo (1993) with  $\alpha_0$  in W/m<sup>2</sup>K at  $p_{ro} = 0.1$ ,  $q_0 = 20,000$  W/m<sup>2</sup> and  $R_{po} = 0.4$   $\mu$ m with  $p_{crit}$  in bar.**

Fluid	$p_{crit}$	M	$\alpha_0$
Methane	<b>46.0</b>	<b>16.04</b>	<b>7000</b>
Ethane	<b>48.8</b>	<b>30.07</b>	<b>4500</b>
Propane	<b>42.4</b>	<b>44.10</b>	<b>4000</b>
n-Butane	<b>38.0</b>	<b>58.12</b>	<b>3600</b>
n-Pentane	<b>33.7</b>	<b>72.15</b>	<b>3400</b>
i-Pentane	<b>33.3</b>	<b>72.15</b>	<b>2500</b>
n-Hexane	<b>29.7</b>	<b>86.18</b>	<b>3300</b>
n-Heptane	<b>27.3</b>	<b>100.2</b>	<b>3200</b>
Benzene	<b>48.9</b>	<b>78.11</b>	<b>2750</b>
Toluene	<b>41.1</b>	<b>92.14</b>	<b>2650</b>
Diphenyl	<b>38.5</b>	<b>154.2</b>	<b>2100</b>
Ethanol	<b>63.8</b>	<b>46.07</b>	<b>4400</b>
n-Propanol	<b>51.7</b>	<b>60.10</b>	<b>3800</b>
i-propanol	<b>47.6</b>	<b>60.10</b>	<b>3000</b>
n-Butanol	<b>49.6</b>	<b>74.12</b>	<b>2600</b>
i-Butanol	<b>43.0</b>	<b>74.12</b>	<b>4500</b>
Acetone	<b>47.0</b>	<b>58.08</b>	<b>3950</b>
R-11	<b>44.0</b>	<b>137.4</b>	<b>2800</b>
R-12	<b>41.6</b>	<b>120.9</b>	<b>4000</b>
R-13	<b>38.6</b>	<b>104.5</b>	<b>3900</b>
R-13B1	<b>39.8</b>	<b>148.9</b>	<b>3500</b>
R-22	<b>49.9</b>	<b>86.47</b>	<b>3900</b>
R-23	<b>48.7</b>	<b>70.02</b>	<b>4400</b>
R-113	<b>34.1</b>	<b>187.4</b>	<b>2650</b>
R-114	<b>32.6</b>	<b>170.9</b>	<b>2800</b>
R-115	<b>31.3</b>	<b>154.5</b>	<b>4200</b>
R-123	<b>36.7</b>	<b>152.9</b>	<b>2600</b>
R-134a	<b>40.6</b>	<b>102.0</b>	<b>4500</b>
R-152a	<b>45.2</b>	<b>66.05</b>	<b>4000</b>
R-226	<b>30.6</b>	<b>186.5</b>	<b>3700</b>
R-227	<b>29.3</b>	<b>170.0</b>	<b>3800</b>
RC318	<b>28.0</b>	<b>200.0</b>	<b>4200</b>
R-502	<b>40.8</b>	<b>111.6</b>	<b>3300</b>
Chloromethane	<b>66.8</b>	<b>50.49</b>	<b>4400</b>
Tetrafluoromethane	<b>37.4</b>	<b>88.00</b>	<b>4750</b>
Hydrogen (on Cu)	<b>12.97</b>	<b>2.02</b>	<b>24000</b>
Neon (on Cu)	<b>26.5</b>	<b>20.18</b>	<b>20000</b>
Nitrogen (on Cu)	<b>34.0</b>	<b>28.02</b>	<b>10000</b>
Nitrogen (on Pt)	<b>34.0</b>	<b>28.02</b>	<b>7000</b>
Argon (on Cu)	<b>49.0</b>	<b>39.95</b>	<b>8200</b>
Argon (on Pt)	<b>49.0</b>	<b>39.95</b>	<b>6700</b>
Oxygen (on Cu)	<b>50.5</b>	<b>32.00</b>	<b>9500</b>
Oxygen (on Pt)	<b>50.5</b>	<b>32.00</b>	<b>7200</b>
Water	<b>220.6</b>	<b>18.02</b>	<b>5600</b>
Ammonia	<b>113.0</b>	<b>17.03</b>	<b>7000</b>
Carbon Dioxide *	<b>73.8</b>	<b>44.01</b>	<b>5100</b>
Sulfur Hexafluoride	<b>37.6</b>	<b>146.1</b>	<b>3700</b>

\* At triple point.

**Gorenflo Correlation.** Gorenflo (1993) proposed a fluid specific reduced pressure correlation and included the effect of surface roughness. His method uses a reference heat transfer coefficient,  $\alpha_o$ , specified for each fluid at the following fixed reference conditions of  $p_{ro}=0.1$ ,  $R_{po}=0.4 \mu\text{m}$  and  $q_o=20,000 \text{ W/m}^2$ . His values of  $\alpha_o$  are listed in Table 9.2 for selected fluids. The nucleate boiling heat transfer coefficient  $\alpha_{nb}$  at other conditions of pressure, heat flux and roughness is then calculated relative to the reference heat transfer coefficient using the following expression:

$$\alpha_{nb} = \alpha_o F_{PF} (q/q_o)^{nf} (R_p/R_{po})^{0.133} \quad [9.3.11]$$

His pressure correction factor  $F_{PF}$  is

$$F_{PF} = 1.2p_r^{0.27} + 2.5p_r + \frac{p_r}{1-p_r} \quad [9.3.12]$$

The effect of reduced pressure on his exponent nf for the heat flux term is given by:

$$nf = 0.9 - 0.3p_r^{0.3} \quad [9.3.13]$$

Its value decreases with increasing reduced pressure, which is typical of experimental data. The surface roughness is  $R_p$  in  $\mu\text{m}$  and is set to  $0.4 \mu\text{m}$  when unknown. The above method is for all fluids except water and helium; for water the corresponding equations are:

$$F_{PF} = 1.73p_r^{0.27} + \left( 6.1 + \frac{0.68}{1-p_r} \right) p_r^2 \quad [9.3.14]$$

and

$$nf = 0.9 - 0.3p_r^{0.15} \quad [9.3.15]$$

This method is applicable over the reduced pressure range from about 0.0005 to 0.95. For fluids not listed, experimental values can be input at the reference conditions, or another correlation can be used to estimate  $\alpha_o$ . For fluids on the list, this method gives accurate results over a very wide range of heat flux and pressure and is probably to most reliable of those presented.

**Example Calculation:** Determine the nucleate pool boiling heat transfer coefficient for n-pentane boiling on a polished copper surface ( $1.0 \mu\text{m}$  roughness) at a pressure of 1.01 bar and a heat flux of  $30 \text{ kW/m}^2$  using the Gorenflo method.

*Solution:* From Table 9.2, we see that  $\alpha_o = 3400 \text{ W/m}^2\text{K}$ ,  $p_{crit} = 33.7 \text{ bar}$  and  $M = 72.15$ . Thus,  $p_r = p_{sat}/p_{crit} = 1.01/33.7 = 0.030$  and thus

$$F_{PF} = 1.73(0.030)^{0.27} + \left( 6.1 + \frac{0.68}{1-0.030} \right) (0.030)^2 = 0.677$$

and

$$nf = 0.9 - 0.3(0.030)^{0.3} = 0.795$$

Substituting these values into his heat transfer correlation:

$$\alpha_{nb} = 3400(0.677)(30000/20000)^{0.795}(1.0/0.4)^{0.133} = 3590 \text{ W/m}^2\text{K}$$

**Ribatski-Siazi Jabardo Correlation.** Surface roughness and material effects have been introduced into a new correlation proposed by Ribatski and Siazi Jabardo (2003) for nucleate pool boiling of halocarbon refrigerants. According to them, the nucleate pool boiling heat transfer coefficient on a horizontal copper tube can be predicted as a function of reduced pressure  $p_r$ , surface roughness  $R_p$ , molecular weight M and heat flux q as:

$$\alpha_{nb} = B \left( q^{0.9-0.3p_r^{0.2}} \right) p_r^{0.45} [-\log(p_r)]^{-0.8} R_p^{0.2} M^{-0.5} \quad [9.3.16]$$

The empirical constant B in this correlation accounts for wall material effects and has the following values: B=100 for copper, B=110 for brass and B=85 for stainless steel. In this dimensional correlation, the heat flux q is input in  $\text{W/m}^2$  and the resulting nucleate boiling heat transfer coefficient  $\alpha_{nb}$  is in  $\text{W/m}^2\text{K}$ .  $R_p$  is the arithmetic mean deviation of the surface profile as per ISO 4287/1:1984 in microns. Averaging 10 measurements from ten different areas on 10 different commercial copper tube samples, they found a mean roughness of 0.6 microns (this is thus the best value to use when its actual value is unknown). This correlation was developed based on pool boiling data for the following conditions:

- Refrigerants: R-11, R-123, R-12, R-134a and R-22;
- Reduced pressure: 0.008 to 0.260;
- Heat flux: 2.3 to 120  $\text{kW/m}^2$  (730 to 38000  $\text{Btu/h ft}^2$ );
- Surface materials: copper, brass and stainless steel;
- Surface roughness: 0.02 to 3.3 microns.

Note that the exponent on the heat flux in their correlation is similar to those in [9.3.13] and [9.3.15] above whereas the exponent of -0.5 on the molecular weight M is the same as in [9.3.10]. This correlation captured most of their heat transfer data within an error band of  $\pm 20\%$  and also worked well for some data from several other studies: R-11, R-113 and R-114 on a 14.2 mm diameter brass tube by Silva (1989) and R-113 on a 12.7 mm diameter stainless steel tube from Jensen (1985).

### 9.3.3 Departure from Nucleate Boiling

The maximum heat flux attainable in the nucleate pool boiling regime of the pool boiling curve illustrated in Figure 9.5 is the DNB point. This heat flux is called  $q_{DNB}$  and is also often referred to as the critical heat flux. The maximum in heat transfer rate occurs at the point of onset of a hydrodynamic instability occurring close to the heater surface, which was first explained by Zuber (1959) to be governed by the Taylor and Helmholtz instabilities. His model has since been refined by Lienhard and Dhir (1973) for an infinite surface.

The *Taylor instability* governs the collapse of an infinite, horizontal planar interface of liquid above a vapor or gas. The Taylor wavelength is that which predominates at the interface during such a collapse. In the present case at the DNB, vapor jets formed above a large, flat horizontal heater surface occur at spacings corresponding to the wavelength of the Taylor instability. The *Helmholtz instability*, instead, describes the point at which a planar liquid interface goes unstable when the velocity of a vapor or gas

flowing parallel to their interface reaches some critical value. Essentially, a small perturbation of the interface creates a low pressure zone on the convex side and a high pressure zone on the concave side. The imbalance of the opposing pressure forces acting on the vapor-liquid interface induces an instability, which is attenuated by interfacial surface tension. According to Zuber, it is the liquid interface of the rising vapor jets that go unstable. The resulting expression for  $q_{DNB}$  from such an analysis is:

$$q_{DNB} = \rho_G h_{LG} \sqrt{\frac{2\pi\sigma}{\rho_G}} \frac{1}{2\pi\sqrt{3}} \sqrt{\frac{g(\rho_L - \rho_G)}{\sigma}} \frac{\pi}{16} \quad [9.3.17]$$

which is equivalent to

$$q_{DNB} = 0.149 \rho_G^{1/2} h_{LG} \sqrt[4]{g(\rho_L - \rho_G)\sigma} \quad [9.3.18]$$

This equation is valid for flat infinite heaters facing upwards. Lienhard and Dhir (1973) observed good agreement as long as the diameters or widths of the heaters were sufficiently large. Kutateladze (1948) had already arrived at nearly the same expression using dimensional analysis:

$$q_{DNB} = C \rho_G^{1/2} h_{LG} \sqrt[4]{g(\rho_L - \rho_G)\sigma} \quad [9.3.19]$$

His empirical factor  $C$  was set to 0.131 based on comparison to experimental data. Zuber's analysis yielded a value of  $C = \pi/24 = 0.1309$ , which is nearly identical to Kutateladze's value. The Lienhard and Dhir solution for an infinite flat surface facing upwards gives  $C = 0.149$ , which is 15% higher. The recommended expression for large surfaces is  $C = 0.1309$  while for tubes this value is corrected by a factor of 0.9. Refer to Collier and Thome (1994) for a description of the methods proposed by Lienhard and Dhir for specific geometries.

**Example Calculation:** Determine the value of the heat flux at the DNB for water at 1.01 bar on a horizontal tube where the required fluid physical properties are:  $\rho_L = 958.25 \text{ kg/m}^3$ ;  $\rho_G = 0.6 \text{ kg/m}^3$ ;  $h_{LG} = 2256120 \text{ J/kg}$ ;  $\sigma = 0.05878 \text{ N/m}$ .

*Solution:* The value of  $q_{DNB}$  is first calculated and then that for the tube applying a correction of 0.9 as follows:

$$q_{DNB,tube} = 0.9 \left( \frac{\pi}{24} \right) (0.6)^{1/2} (2256120)^{1/4} \sqrt{9.81(958.25 - 0.6)(0.05878)}$$

$$q_{DNB,tube} = 998100 \text{ W/m}^2$$

Therefore, the heat flux at DNB for the tube is  $998100 \text{ W/m}^2$  (or  $998.1 \text{ kW/m}^2$ ).

## 9.4 Nucleate Boiling of Mixtures

Nucleate pool boiling of zeotropic mixtures is similar to boiling of pure fluids and azeotropic mixtures, except for two additional complications: mass transfer effects and estimating the mixture physical properties or the mixture critical pressure. Mass transfer occurs in evaporation of *zeotropic* mixtures since they have different compositions in their liquid and vapor phases, but not *azeotropic* mixtures since they have the same composition in each phase. Mass transfer tends to reduce nucleate boiling heat transfer coefficients and, in some cases, may reduce the value of the heat transfer coefficient by up to 90%.

Detailed reviews of mixture boiling are given by Thome and Shock (1984) and by Collier and Thome (1994).

The mass transfer effect on bubble growth can be explained in simple terms as follows. Since the equilibrium composition of the more volatile component is larger in the vapor phase than in the liquid phase, the more volatile component preferentially evaporates at the bubble interface, which in turn reduces its composition there and induces the formation of a diffusion layer in the liquid surrounding the bubble. The partial depletion of the more volatile component at the interface increases that of the less volatile component, which increases the bubble point temperature at the interface. This incremental rise in the local bubble point temperature can be denoted as  $\Delta\theta$ . Hence, to evaporate at the same rate as in a pure fluid, a larger superheat is required for a mixture.

The effect of mass transfer on nucleate pool boiling heat transfer can therefore be explained by introducing the parameter  $\Delta\theta$ , which represents the increase in the bubble point temperature at the surface due to preferential evaporation of the more volatile component. At a given heat flux, the boiling superheat of the mixture is  $\Delta T + \Delta\theta$  while that for an ideal fluid with the same physical properties as the mixture is  $\Delta T_I$ . Thus, the ratio of the mixture boiling heat transfer coefficient  $\alpha_{nb}$  to that of the ideal heat transfer coefficient  $\alpha_{nb,I}$  at the same heat flux is:

$$\frac{\alpha_{nb}}{\alpha_{nb,I}} = \frac{\Delta T_I}{\Delta T_I + \Delta\theta} \quad [9.4.1]$$

The value of  $\Delta T_I$  is the wall superheat that corresponds to  $\alpha_{nb,I}$ , which is determined for instance using the Cooper correlation with the molecular weight and critical pressure of the mixture. Hence, as the value of  $\Delta\theta$  increases, the ratio  $\alpha_{nb}/\alpha_{nb,I}$  decreases, which means that a larger wall superheat is required in a mixture to transfer the same heat flux. As exploited in an early mixture boiling prediction by Thome (1983), the maximum value of  $\Delta\theta$  is the boiling range of the mixture  $\Delta\theta_{bp}$ , which is equal to the difference between the dew point and the bubble point temperatures at the composition of the liquid [ $\Delta\theta_{bp}$  is also referred to as the temperature glide for refrigerant mixtures]. In fact, the actual value of  $\Delta\theta$  varies from zero at the inception of boiling, since no mass transfer occurs until evaporation takes place, up to  $\Delta\theta_{bp}$  at the DNB, where all the liquid is assumed to be converted to vapor. Starting from a mass transfer balance around an evaporating bubble and simplifying with an approximate slope of the bubble point curve, the following expression was obtained to predict heat transfer in the boiling of mixtures

$$\frac{\alpha_{nb}}{\alpha_{nb,I}} = \left\{ 1 + \frac{\alpha_{nb,I}}{q} \Delta\theta_{bp} \left( 1 - \exp \frac{-q}{\rho_L h_{LG} \beta_{mL}} \right) \right\}^{-1} \quad [9.4.2]$$

where  $\beta_{mL}$  is the mass transfer coefficient in the liquid (set to a fixed value of 0.0003 m/s). The value of  $\alpha_{nb,I}$  is determined with one of the pure fluid correlations presented earlier (with the exception of the Gorenflo method that is not adapted to this). This method was proposed in 1985 and later published by Thome (1989). It is applicable to organic, refrigerant, aqueous, hydrocarbon, and cryogenic multi-component mixtures (i.e. with two or more components) for boiling ranges up to 30 K.

**Example Calculation:** Assuming an ideal heat transfer coefficient of 3000 W/m<sup>2</sup>K, determine the mixture boiling coefficient at 50 kW/m<sup>2</sup> for a mixture with a boiling range of 15 K, a liquid density of 700 kg/m<sup>3</sup> and a latent heat of 300000 J/kg.

*Solution:* Substituting values into the above expression,

$$\frac{\alpha_{nb}}{3000} = \left\{ 1 + \frac{3000}{50000} (15) \left( 1 - \exp \frac{-50000}{700(300000)(0.0003)} \right) \right\}^{-1} = 0.670$$

$$\alpha_{nb} = 0.67(3000) = 2009 \text{ W/m}^2\text{K}$$

Thus,  $\alpha_{nb}$  for the mixture is 2009 W/m<sup>2</sup>K, which is 33% lower than that of the equivalent pure fluid.

## 9.5 Boiling on Enhanced Tubes

Boiling heat transfer coefficients on smooth surfaces can be increased by roughening the surface, but this is not normally practical (and perhaps temporal if the surface fouls). To achieve significant enhancement, numerous types of geometries have been proposed and patented. The earliest commercial enhancement was the integral low finned tube, with its continuous helical fins around the circumference of the tube. Tubes with external porous coatings were apparently the next important enhancement to be proposed, yielding augmentations of up to 10-15 times the boiling performances on plain tubes at optimum conditions. In recent years, attention has been nearly entirely focused on mechanically deformed low finned tubes, whose fins can be notched, knurled, bent and/or compressed to form a high density of re-entrant channels and boiling pores, geometries that essentially mechanically emulate a porous coating.

### 9.5.1 Heat Transfer Mechanisms

Compared to a plain tube, enhanced nucleate boiling surfaces have significant performance advantages. For instance, the enhancement ratio at the same wall superheat relative to that of a comparable plain tube range from about 2-4 for low finned tubes but increase up to 15 times for mechanically deformed low finned tubes such as for the Turbo-B tubes of Wolverine Tube Inc. Evaporation and convection occur both on the outside surface of an enhanced boiling surface and inside its re-entrant passageways. Hence, as illustrated in Figure 9.8, there are four possible paths by which heat can leave an enhanced surface:

1. As latent heat in vapor formed within the enhancement passageways (primary importance);
2. As latent heat in bubbles growing on exterior of tube or while they are emerging from re-entrant channels (secondary importance);
3. As sensible heat to liquid “pumped” through the re-entrant passageways (primary importance);
4. As sensible heat to liquid on external of tube (secondary importance).

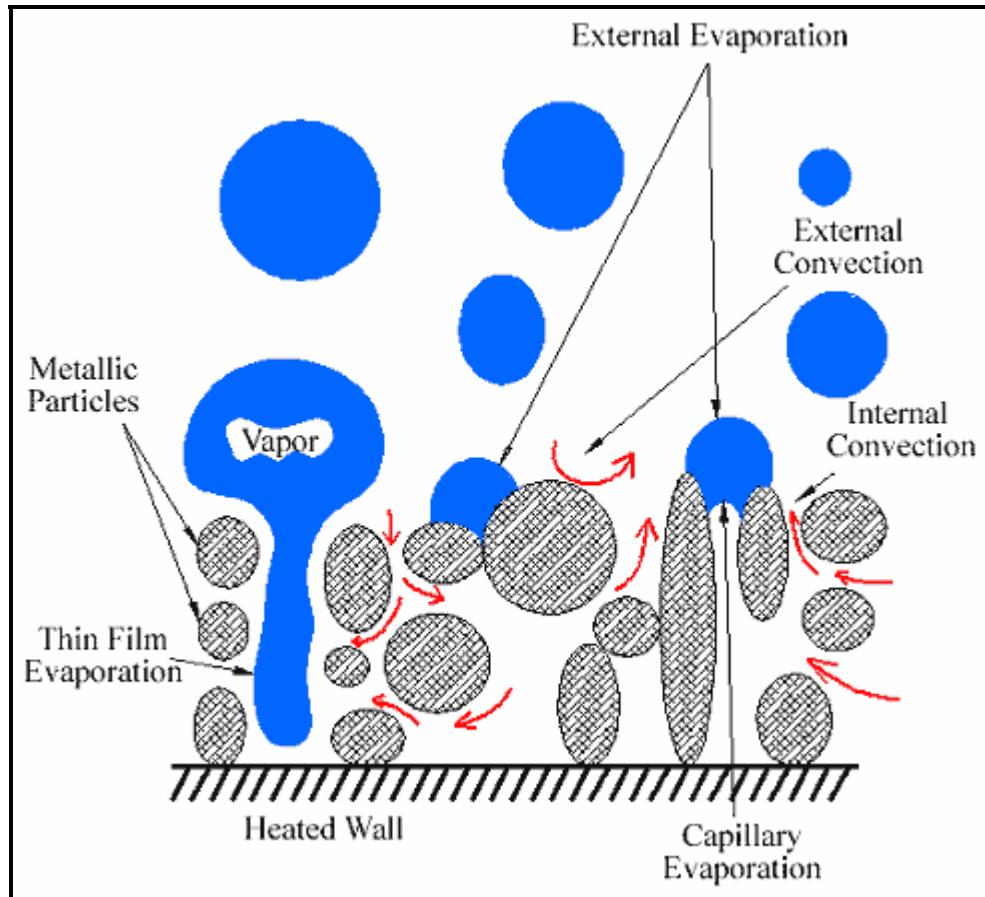


**Figure 9.8. Boiling mechanisms on an enhanced surface tube.**

The principal factors contributing to the high thermal performance of enhanced surfaces have been identified by Thome (1990) as follows:

- **Nucleation superheat.** Enhanced surfaces have re-entrant nucleation cavities (except for low finned tubes) that are able to nucleate at very low wall superheats with respect to plain surfaces, see Figure 9.9.
- **Wetted surface area.** Low finned tubes have from 2 to 4 times the surface area of a plain tube while complex enhancements have area ratios from 4 to 10 times those of plain tubes.
- **Thin film evaporation.** Thin evaporating liquid films form on the extensive inner surfaces of the re-entrant passageways.
- **Capillary evaporation.** In corners, liquid menisci evaporate as heat is conducted into the liquid behind them.

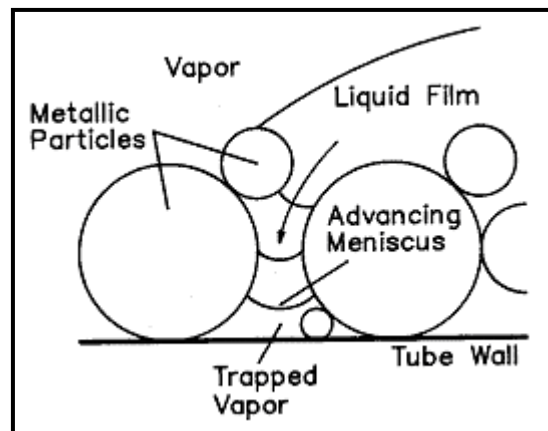


**Figure 9.9. Boiling nucleation on an enhanced surface.**

- **Internal convection.** Liquid is pumped in and then back out of the re-entrant channels by the action of the departing bubbles.
- **External convection.** The high density and departure frequency of the bubbles emerging from the re-entrant channels accentuates the external convection mechanisms, i.e. bubble agitation and thermal boundary layer stripping.

These mechanisms can be compared to those occurring on a plain surface discussed earlier. The thermal effectiveness of these factors depends on the type of enhanced surface geometry and its characteristic dimensions.

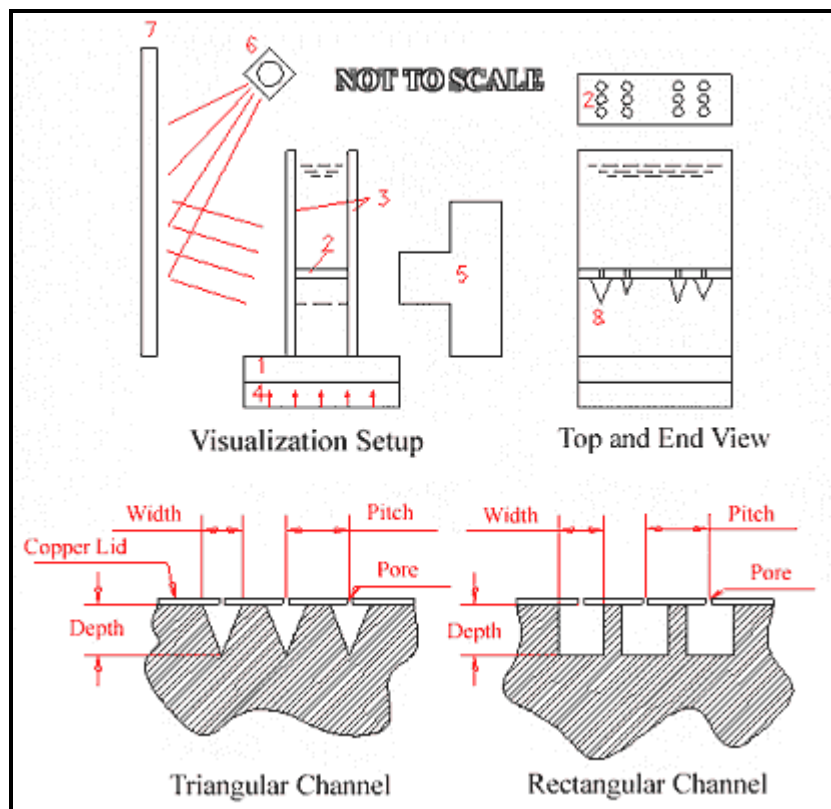


**Figure 9.10.** Setup of Arshad and Thome (1983) for flow visualization in re-entrant channels [1-base block with microgrooves, 2-copper sheet with pores, 3-glass walls, 4-heater, 5-camera, 6-lighting, 7-reflection panel, 8-end view of microgrooves].

The formation of liquid films inside re-entrant channels was originally investigated visually by Nakayama et al. (1979) using side channel walls made of glass. They observed that elongated bubbles formed within the re-entrant channel with thin liquid films covering the walls, particularly in the corners (they had a side view of the process). They noted pulsation of the liquid film upon departure of bubbles from the pores connecting the channels to the exterior.

In a similar study, but with an end (cross-sectional) view of the process in re-entrant channels of circular, triangular and rectangular shape, Arshad and Thome (1983) used a motor driven still camera to observe the formation and dryout of the thin liquid films. Figure 9.10 shows their experimental setup and Figure 9.11 shows some of their photographs of the process. Figure 9.12 illustrates a schematic sequence of nucleation, formation and dryout of a liquid film in a triangular re-entrant channel upon application of a high heating rate. Figure 9.13 illustrates a thin film evaporation model hypothesized by Xin and Chao (1985) for rectangular re-entrant channels with a slit opening. Hence, thin evaporating films were seen to be an important heat transfer mechanism, analogous to the microlayers formed underneath rapidly growing bubbles on plain surfaces, and are active over a large surface area. Refer to Thome (1990) for a comprehensive treatment of this subject.

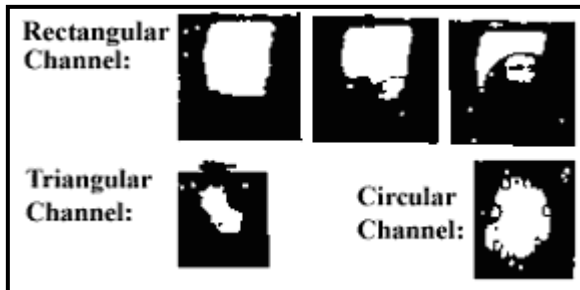


Figure 9.11. Photographs of liquid thin film formation in re-entrant channels.

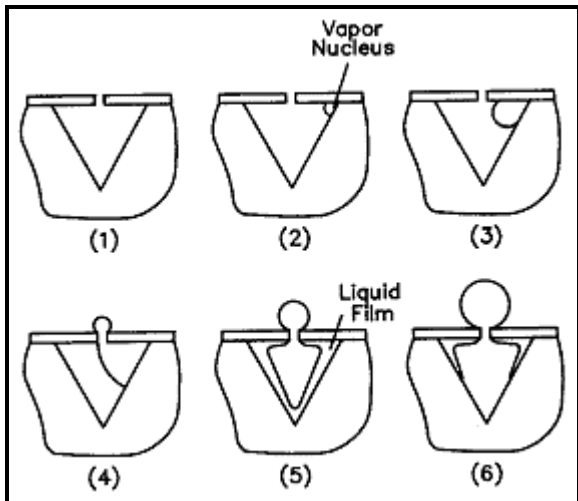


Figure 9.12. Schematic representation of films observed in a triangular re-entrant channel.

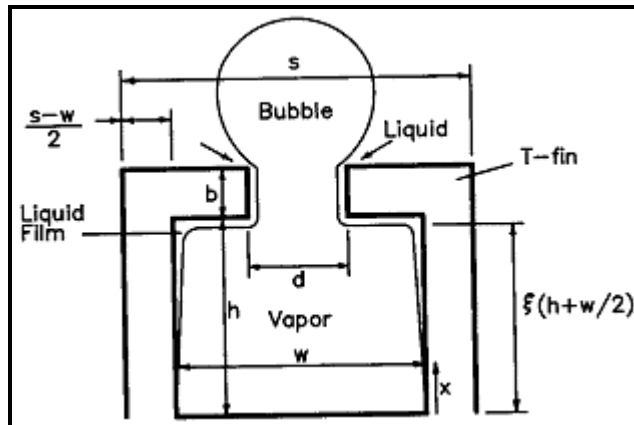


Figure 9.13. Thin film evaporation process in a rectangular re-entrant channel.

### 9.5.2. Enhanced Boiling Results

Experimental results for enhanced boiling surfaces are shown in this section. For an example of relative performance of five refrigerants on a 26 fpi (1024 fins per meter) low finned tube, Figure 9.14 presents the results obtained by Webb and Pais (1992). The boiling performance of R-123 was observed to be similar to that of R-11 while the three higher saturation pressure refrigerants had significantly higher heat transfer coefficients.

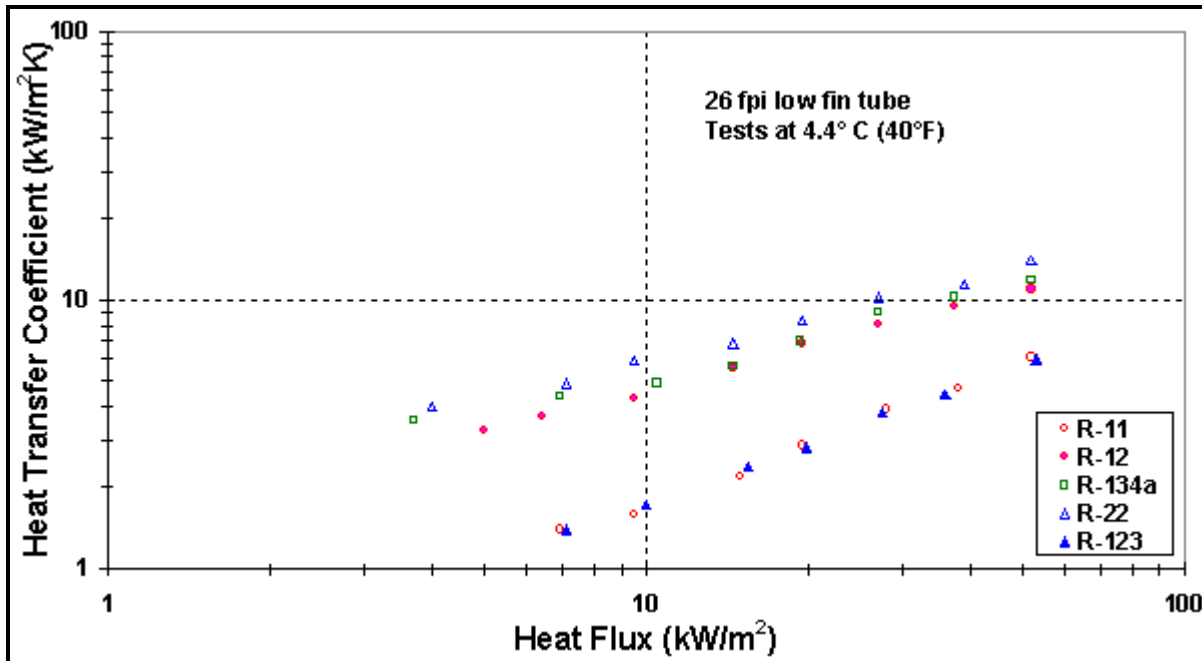


Figure 9.14. Pool boiling of five refrigerants on a low finned by Webb and Pais (1992).

Figure 9.15 shows the nucleate pool boiling results for a low finned tube and a Turbo-B tube compared to a plain tube obtained by Palm (1995) for R-134a at 0.7°C (33.3°F) and R-22 at 0.1°C (32.2°F), albeit plotted in a linear form as in the original publication. The boiling curves illustrate that the most important enhancement factor at a fixed wall superheat is obtained at low superheats.

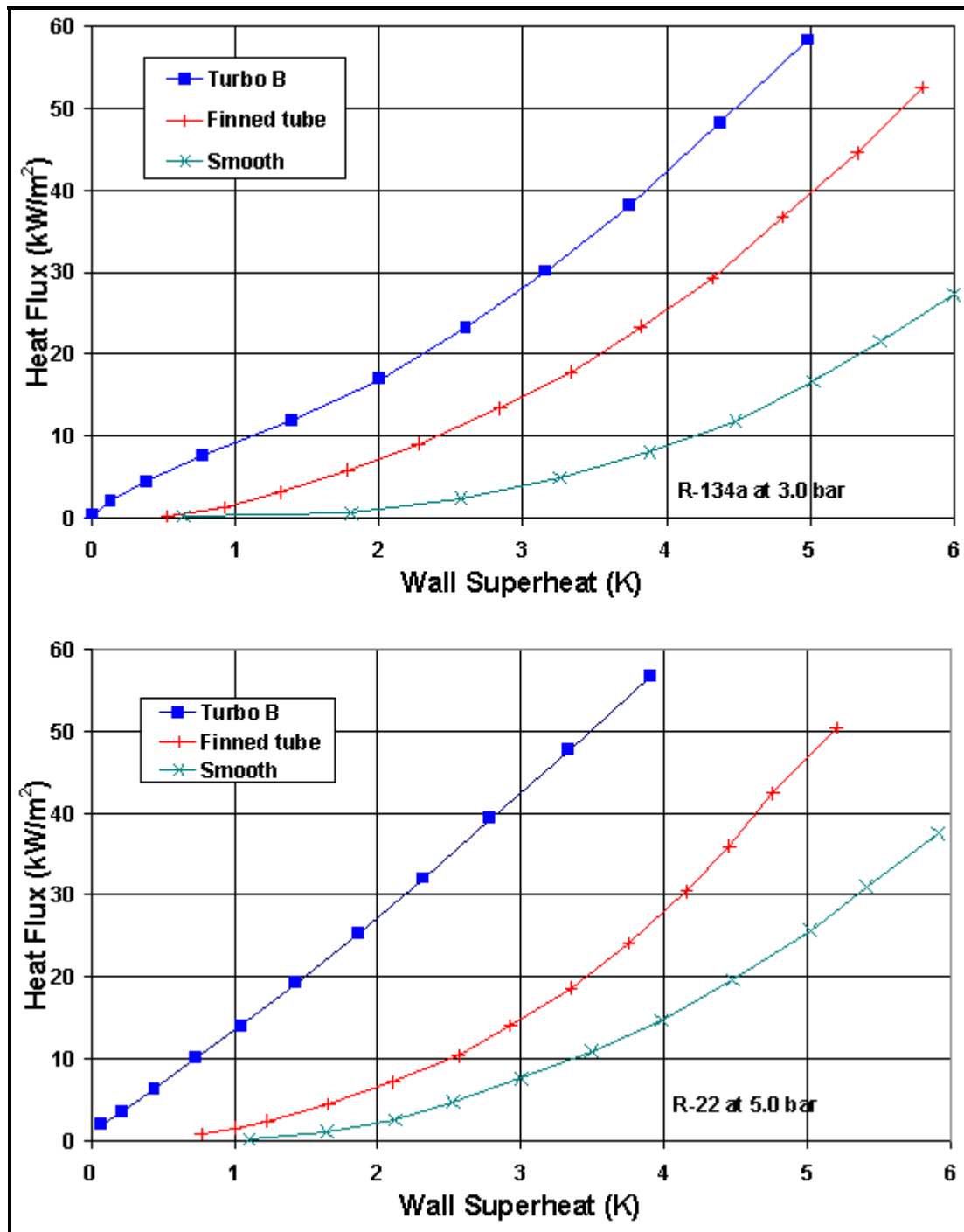
Figure 9.16 shows some pool boiling results for a Turbo-B tube compared to those for a plain tube for R-123 at 4.4°C (40°F) by Webb et al. (1995). Significant boiling enhancement is evident over the entire heat flux range.

Figure 9.17 depicts some other pool boiling for a Turbo-Bii-LP tube for R-123 at 4°C (39°F) taken by Kedzierski (1995) and compared to a low finned tube. They plotted their data on a linear graph as reproduced here. They took a large number of data points with little scatter as can be noted.

Figure 9.18 presents the pool boiling heat transfer coefficients plotted versus heat flux for a Turbo-Bii tube for pure fluids (R-22 and R-134a), a near azeotrope mixture of R-32/R-125 (60/40%) and several zeotropic mixtures by Chen and Tuzla (1996). Note that the mass transfer effect has a very detrimental effect on the boiling performance for the two zeotropic mixtures.

Ribatski and Thome (2006) recently completed a comparative study on four commercially available enhanced tubes (a porous coated tube, two enhanced boiling tubes and an enhanced condensation tube) for R-134a, covering the effect of saturation temperature with tests at 5, 10 and 20°C (41, 50 and 68°F) over heat fluxes from 20 to 70 kW/m<sup>2</sup> (6340 to 22190 Btu/h ft<sup>2</sup>). They also provide an extensive list of about 23 other enhanced pool boiling studies completed since 2000 for those interested. Since it may be beneficial to simplify system construction by using the same enhanced tube in both a refrigeration system's flooded evaporator as in its condenser, pool boiling tests were also done with an enhanced condensing tube to look at this possibility. Their results for two such tubes, one enhanced boiling and one enhanced condensation, are shown in Figure 9.19. The data show that there is some effect of saturation temperature on boiling performance and also that at high heat fluxes the enhanced condensing tube

actually outperforms, by a small margin, the enhanced boiling tube whereas being much less effective at lower heat fluxes.



**Figure 9.15.** Pool boiling of R-22 and R-134a on plain, low finned and Turbo-B tubes by Palm (1995).

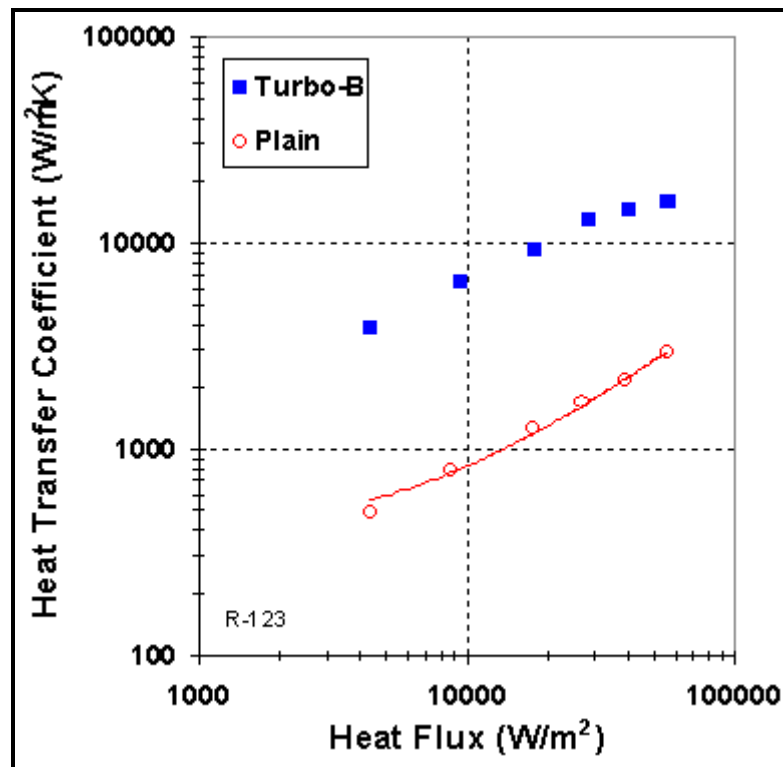


Figure 9.16. Pool boiling on a Turbo-B tube for R-123 by Webb et al. (1995).

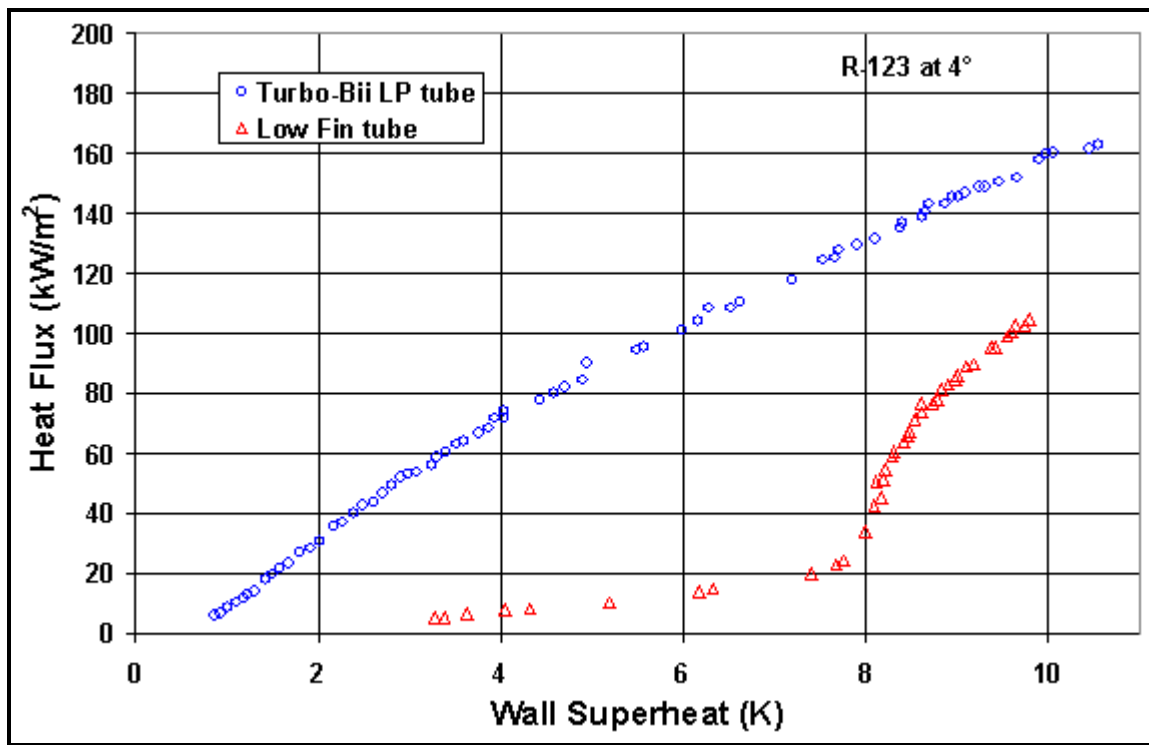
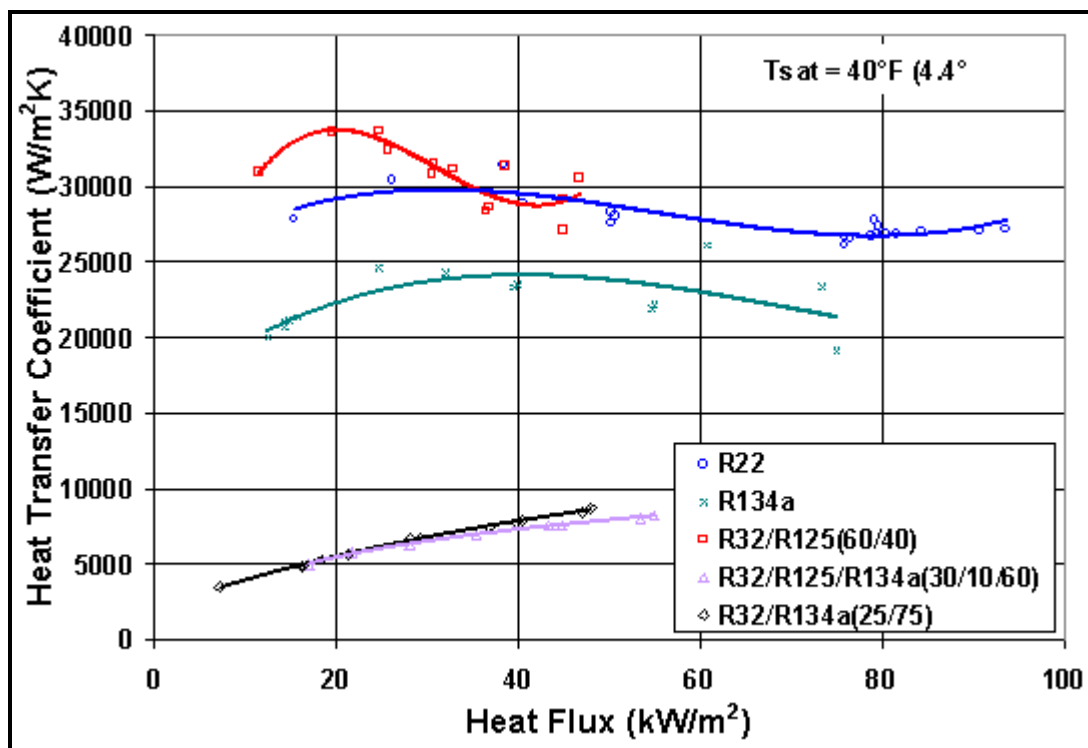


Figure 9.17. Pool boiling on Turbo-Bii-LP tube for R-123 by Kedzierski (1995).



**Figure 9.18.** Pool boiling on Turbo-Bii for pure fluids and mixtures by Chen and Tuzla (1996).

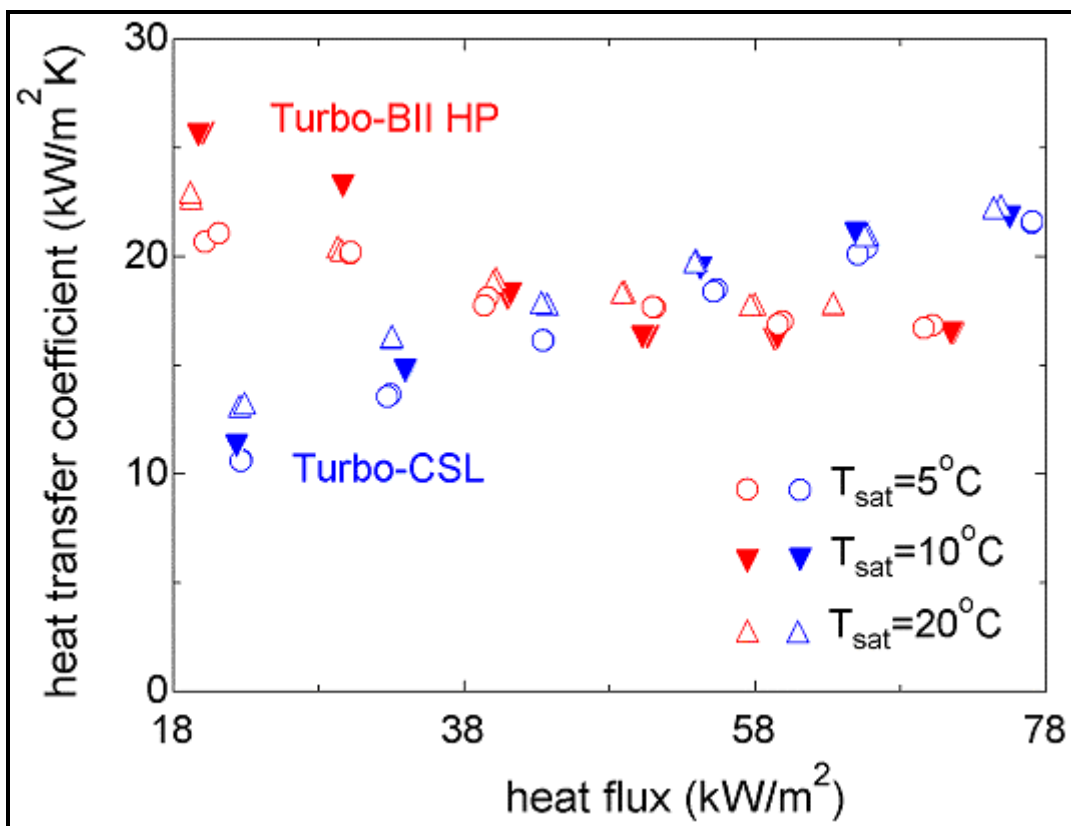


Figure 9.19. Pool boiling results for R-134a on Turbo-BII HP (boiling tube) and Turbo-CSL (condensing tube) at three saturation pressures from Ribatski and Thome (2006).

## 9.6 Bundle Boiling

An important heat transfer process is evaporation on the outside of horizontal tube bundles. This process is generic to refrigerant flooded evaporators, waste heat boilers, fire-tube steam generators, kettle and thermosyphon reboilers, feed effluent heat exchangers, etc. Nearly all the research has focused either on overall bundle boiling data, on mean measurements for selected tubes in the bundle, on bundles immersed in a pool of liquid without measurement of liquid flow rates or on idealized small bundles. Some such exchangers operate in simple vertical upward cross-flow, like flooded evaporators, but others are configured with as single-segmental baffled heat exchangers where the main flow is horizontal crossflow with all the associated problems of leakage streams like in similar single-phase flows. Hence, much still remains to be accomplished on the subject of bundle boiling but fortunately some of what we know about intube evaporation can be applied *qualitatively* to this external flow process. One recent review has been presented by Casciaro and Thome (2001a, 2001b), describing the state-of-the-art with respect to heat transfer, void fractions, flow patterns and maps and two-phase pressure drops with respect to evaporation on tube bundles. Thome (1998) has also summarized the bundle boiling experiments conducted in the 1990's up to that point in time. Jensen (1988) has also presented a detailed state-of-the-art review of boiling on plain tube bundles while Thome (1990) described numerous enhanced tests up to that date.

Figure 9.20 taken from Collier and Thome (1994) depicts a simplified tube bundle layout with uniform heating of the tube for upflow boiling. The flow regimes are shown in schematic form encountered from the bottom to the top, together with the corresponding heat transfer regimes. This is a composite diagram

and not all these flow regimes are necessarily encountered depending on the operating conditions. Here, it is assumed that subcooled liquid enters the bottom from the inlet nozzle and flows upward to the bottom tube row. Hence, the initial heat transfer process is single-phase convection to the subcooled liquid that is followed by subcooled boiling until the liquid reaches its saturation temperature. For example, in a thermosyphon reboiler it is common for the liquid head to impose several degrees of subcooling on the fluid entering. For enhanced tubes, this condition would be particularly acute since they are not effective for single-phase heating nor subcooled boiling. In the lower part of the bundle, bubbly flow then exists up until the transition to bubble jet flow between the tubes. The flow then enters a chugging type of flow regime with large bubbles and liquid slugs populated with numerous small bubbles. Then at some critical condition, the flow transforms into a spray flow with large droplets impinging on the tubes to form thin liquid films. Dryout (not shown) can also occur with very poor heat transfer similar to intube evaporation. With a small amount of oil present in refrigerants, it is also possible to form a frothy flow or foam. It is unlikely that all the liquid is evaporated without carryover and hence normally either a demister pad or a large oversized shell is used to separate the liquid droplets from the outgoing vapor. Figure 9.21 shows a similar diagram from Robinson and Thome (2004a) illustrating this process in a 20-tube test section they used to investigate local flow boiling heat transfer coefficients. The details of the actual process are still not well understood and the above is primarily an intuitive description.

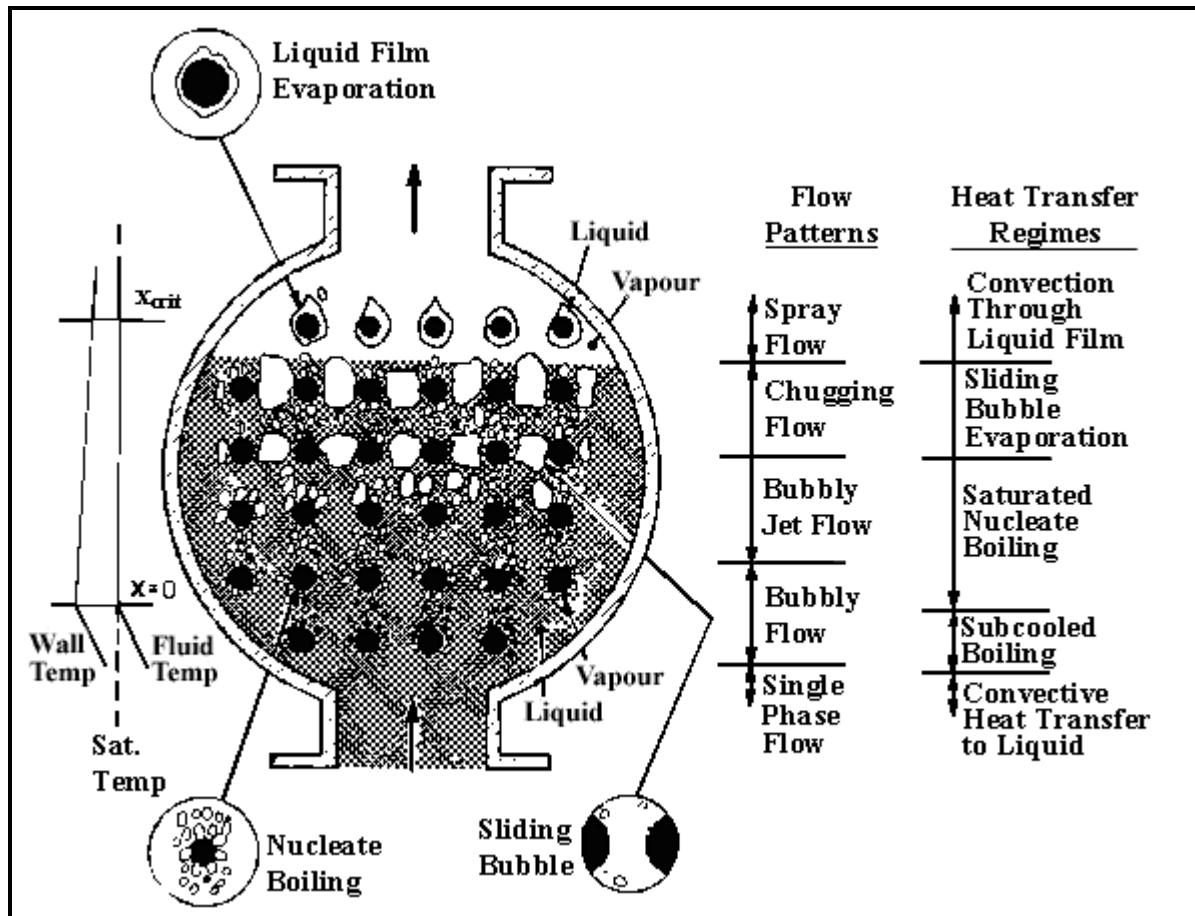
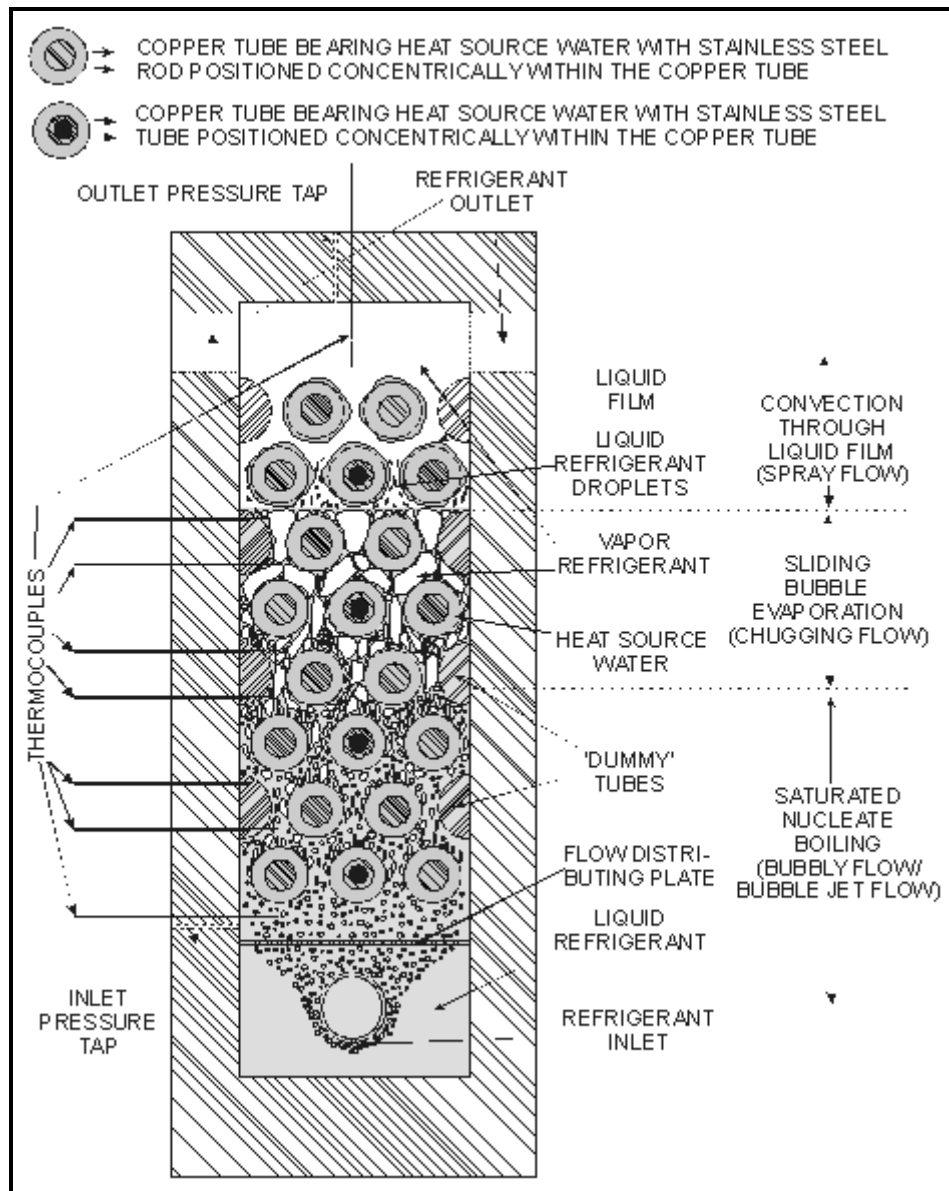


Figure 9.20. Evaporation on a horizontal tube bundle (not to scale).

Older test results in the literature are primarily for overall bundle boiling heat transfer coefficients, which are not very useful since they do not allow local boiling heat transfer models to be developed. Similarly, numerous tests on small tube bundles have been run using electrical cartridge heaters inside the tubes in

which the bundle was immersed in a large pool of liquid; hence local tube-wise heat transfer coefficients were measured but not the liquid flow rate into the bundle. Consequently, the local vapor quality cannot be determined for these test conditions, which renders these data difficult to use for building of bundle boiling models. In recent years, it has become common to run tests with complete control of the process, such that local tube-wise heat transfer coefficients have been obtained as a function of heat flux, vapor quality and mass velocity using electrical-heated or water-heated test sections.



**Figure 9.21. Schematic diagram of boiling in a 20-tube test section.**

For boiling on the 20-tube test bundle illustrated in Figure 9.21, Robinson and Thome (2004a) used hot water heating with a modified-Wilson plot technique for their tests. They also placed dummy tubes inside the heat transfer tubes in order to install two local thermocouples inside the tubes at three locations along the four central tube rows in their bundle, besides measuring the inlet and outlet water temperatures from each tube. Hence, applying an enthalpy profile approach using the temperatures at all these locations, they were able to calculate the local heat flux at 12 locations in the bundle where the local water temperatures

have been simultaneously measured. The local refrigerant-side saturation temperatures were measured using 3 sets of an 8 thermocouple array located at the same axial position along the bundle as the internal water temperature measurements, or can be calculated from differential pressure measurements. Hence, knowing the temperatures of the water and refrigerant at any one of these locations, knowing the heat flux at that point, knowing the water-side heat transfer coefficient from the prior modified-Wilson plot tests, and the tube geometry and wall thermal conductivity, it is possible to determine the local axial flow boiling heat transfer coefficient in the bundle at known conditions of mass velocity, vapor quality and heat flux, similar to intube flow boiling test results. Their test setup hence provides 12 perimeter-averaged local heat coefficients within their tube bundle. The inlet flow conditions to the bundle are changed using a speed controlled pump and a preheater, which allows a wide range of local test conditions to be achieved within the tube bundle.

Figure 9.22 depicts some of the local bundle boiling data for R-134a on a plain tube bundle obtained by Robinson and Thome (2004a) for their tube bundle using 19.05 mm (3/4 in.) tubes on a triangular tube pitch of 22.23 mm (7/8 in.). The effect of heat flux was found to be more dominant than originally expected while the influence of mass velocity was less than expected. The local heat transfer coefficients tend to increase with local vapor quality and are larger than the corresponding nucleate pool boiling heat transfer coefficient. These data are currently being used to develop a local flow boiling heat transfer model that will be reported on in the near future.

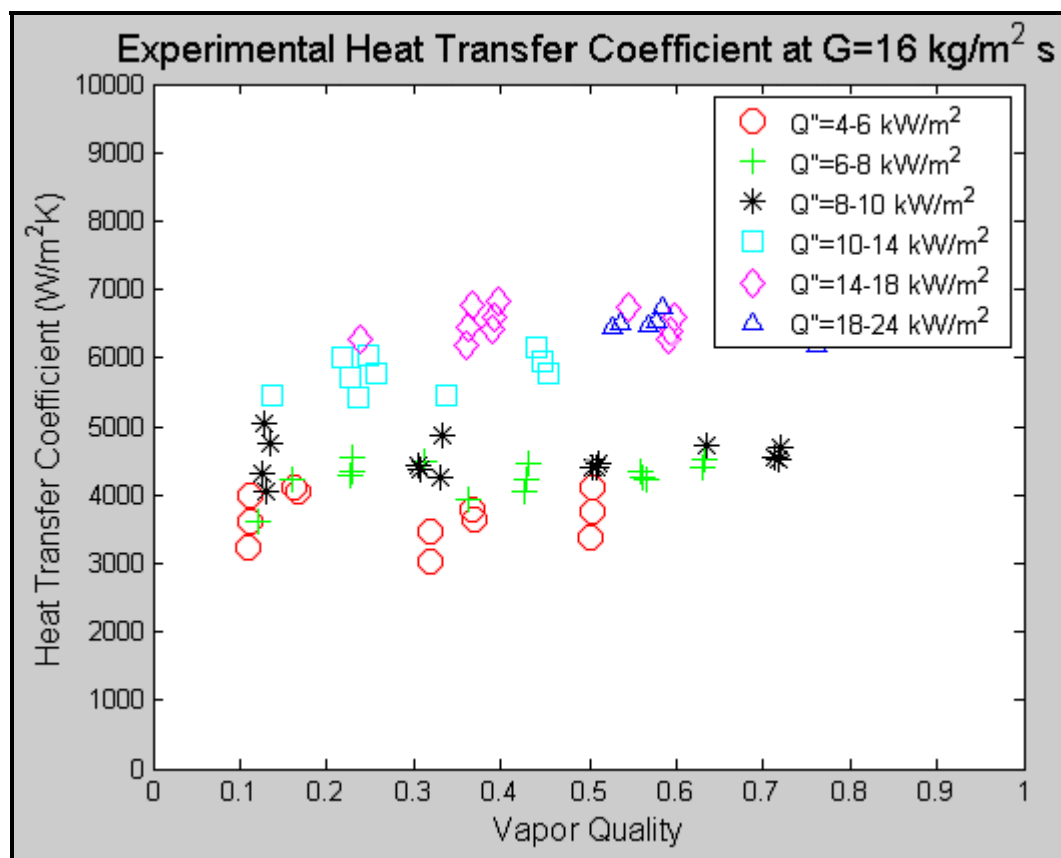


**Figure 9.22. Local bundle boiling data for R-134a on a plain tube bundle of Robinson and Thome (2004a).**

Figure 9.23 shows the local boiling data for R-11 evaporating on an 18.9 fpi (744 fins per meter) low fin tube bundle tested by Gupte and Webb (1995a) at 4.4°C (40°F). They used cartridge heaters to impose a

uniform heat flux in the bundle, a preheater to control the inlet vapor quality and a pump to control the refrigerant flow rate. Also indicated on the graph are the corresponding nucleate pool boiling heat transfer coefficients at the same heat fluxes. Significant convective boiling heat transfer is evident in these data with local bundle boiling coefficients up to nearly three times the nucleate pool boiling values, particularly at low heat flux.

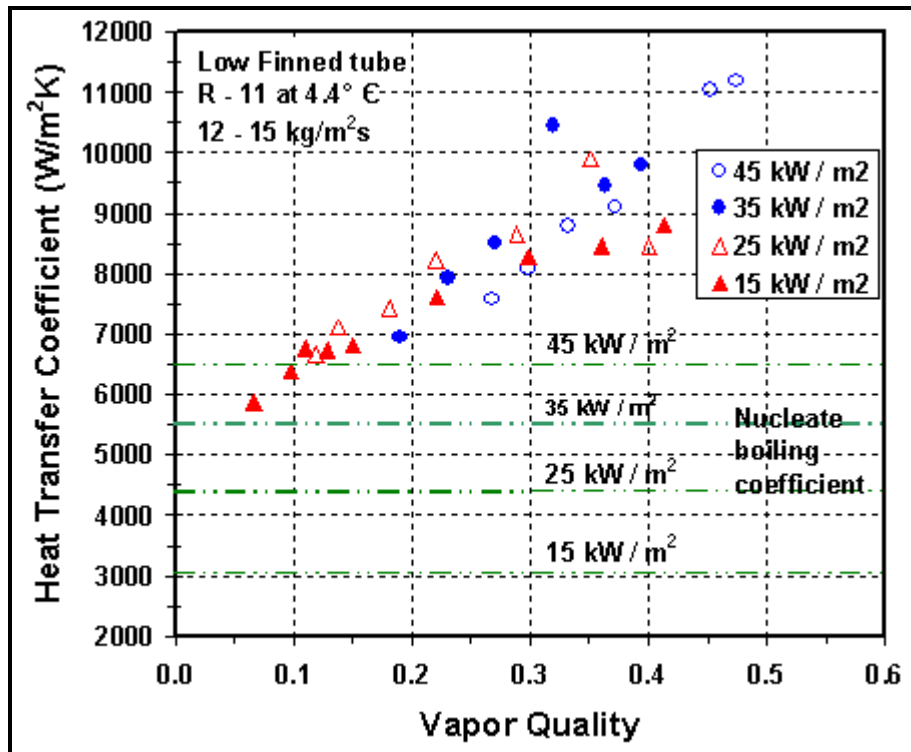


Figure 9.23. Boiling of R-11 on a 18.9 fpi low fin tube bundle by Gupte and Webb (1995a).

Figure 9.24 depicts the corresponding data of Gupte and Webb (1995a) for boiling of R-11 at a higher pressure (26.7°C or 80°F) on the same low fin tube bundle. Here, a noticeable effect of heat flux on the data is evident at the lower vapor qualities since at nucleate pool boiling is much stronger at this higher pressure. At high vapor qualities, the data tend to come together like what happens in intube flow boiling tests, suggesting that the flow is convection dominated at high vapor qualities.

Figure 9.25 shows the bundle boiling data obtained for n-pentane evaporating on 45-tube, 30 fpi low fin tube bundle by Thonon, Roser and Mercier (1997). It was not easy to distinguish the heat fluxes of individual data points on their graph, but it has been reproduced here to illustrate the significant convective effect they also observed for boiling on a low finned tube bundle at a mass velocity typical of normal operating conditions.

Figure 9.26 presents boiling data for R-123 at 4.4°C (40°F) on a Turbo-B tube bundle by Gupte and Webb (1995b) for the same bundle configuration used for their low fin tests described above. Here, they obtained data only at low vapor qualities and found little convective effect on the local boiling heat transfer coefficients, although at the lowest heat flux there appears to be the beginning of such a convective trend.

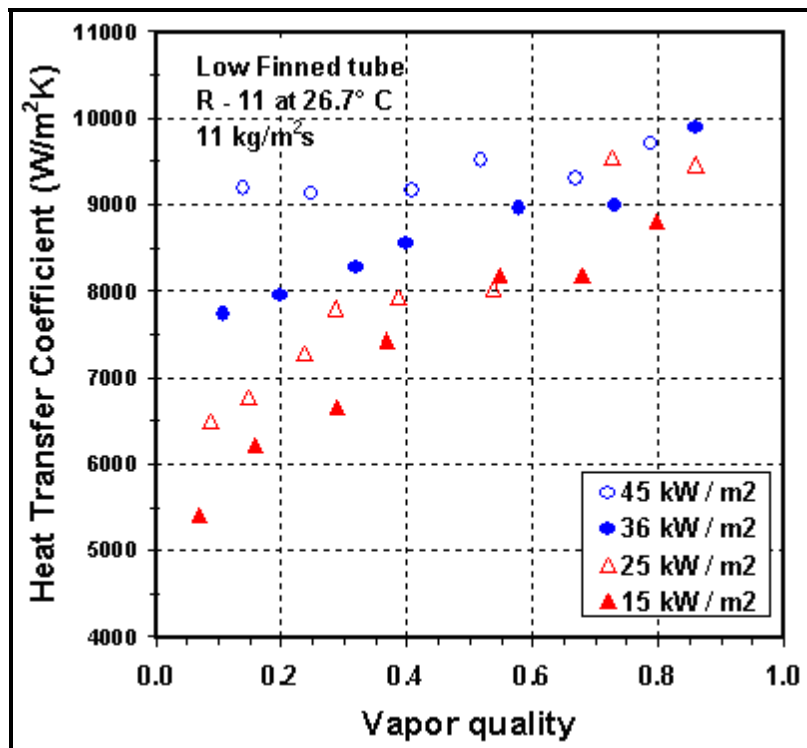


Figure 9.24. Boiling of R-11 on a 18.9 fpi low fin tube bundle by Gupte and Webb (1995a).

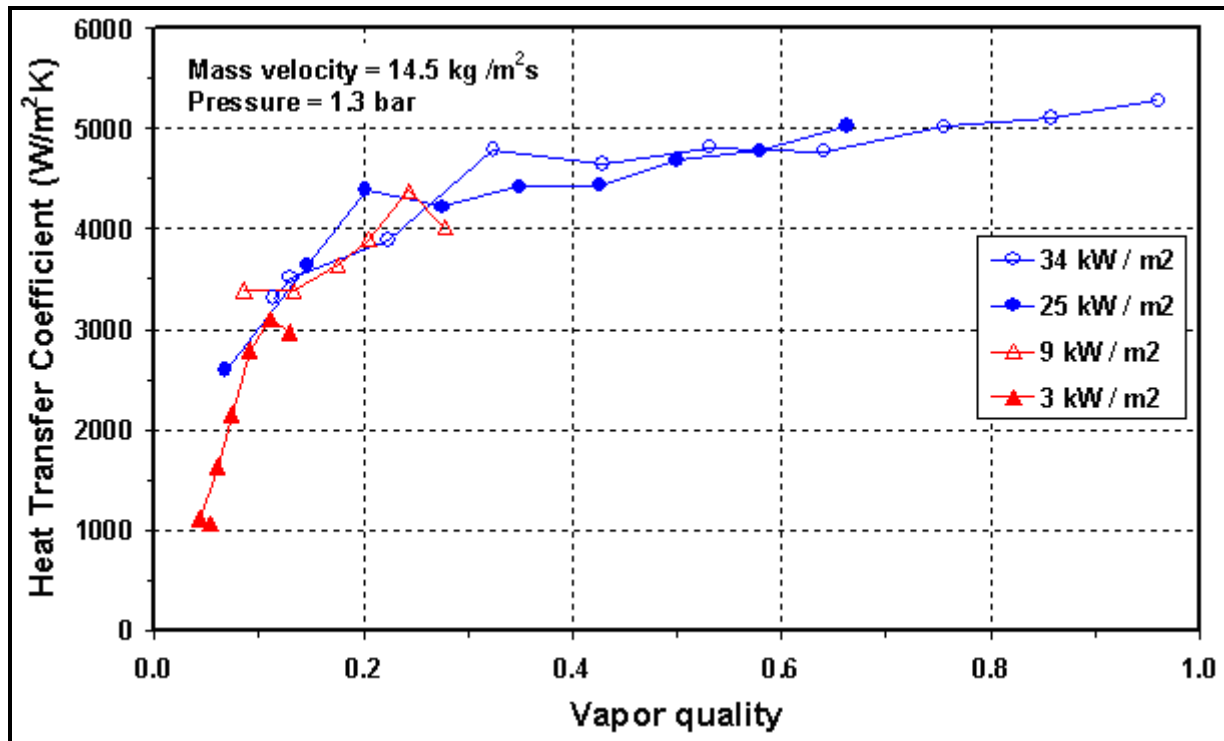


Figure 9.25. Boiling of n-pentane on a 30 fpi low fin tube bundle by Thonon, Roser and Mercier (1997).

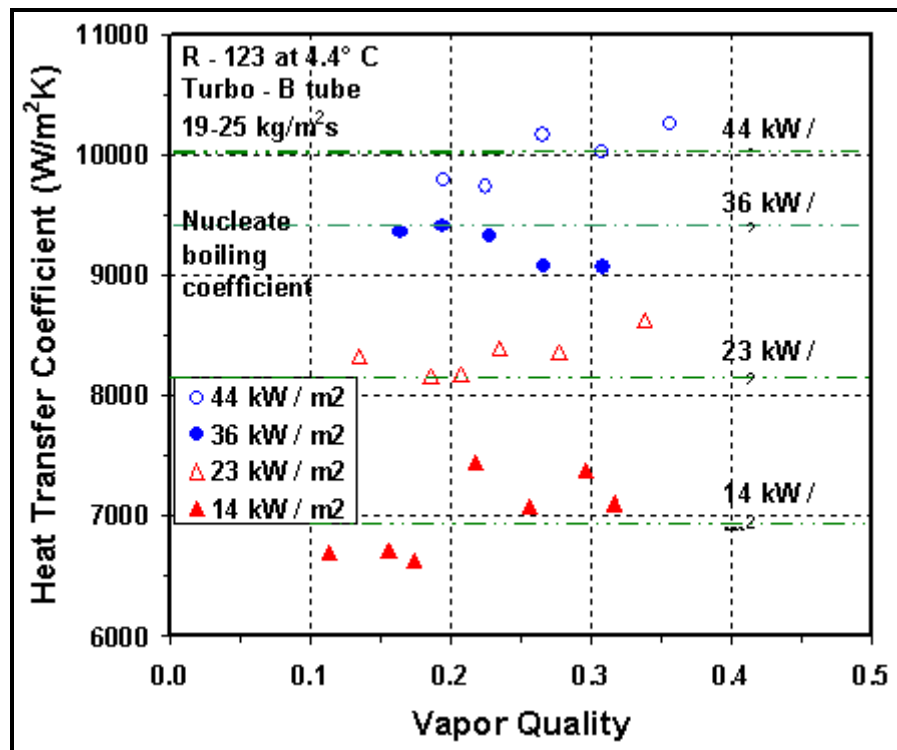


Figure 9.26. Boiling of R-123 on Turbo-B tube bundle by Gupte and Webb (1995b).

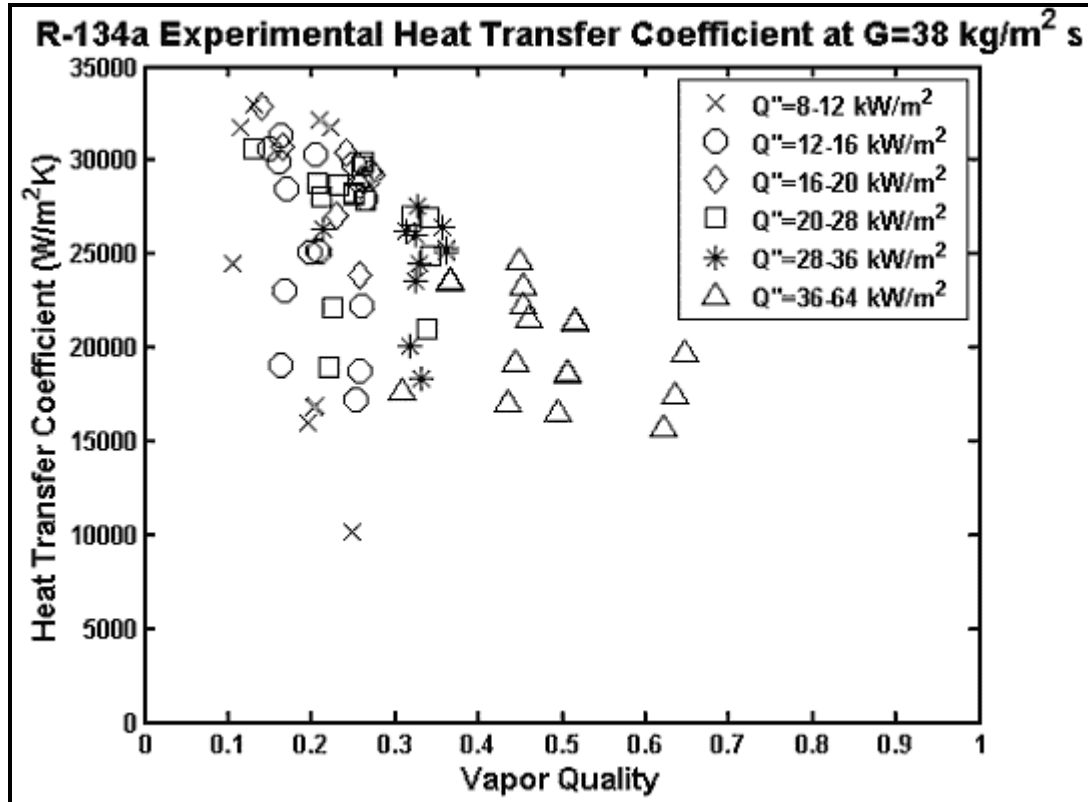


Figure 9.27. Boiling of R-134a on Turbo-Bii tube bundle by Robinson and Thome (2004b).

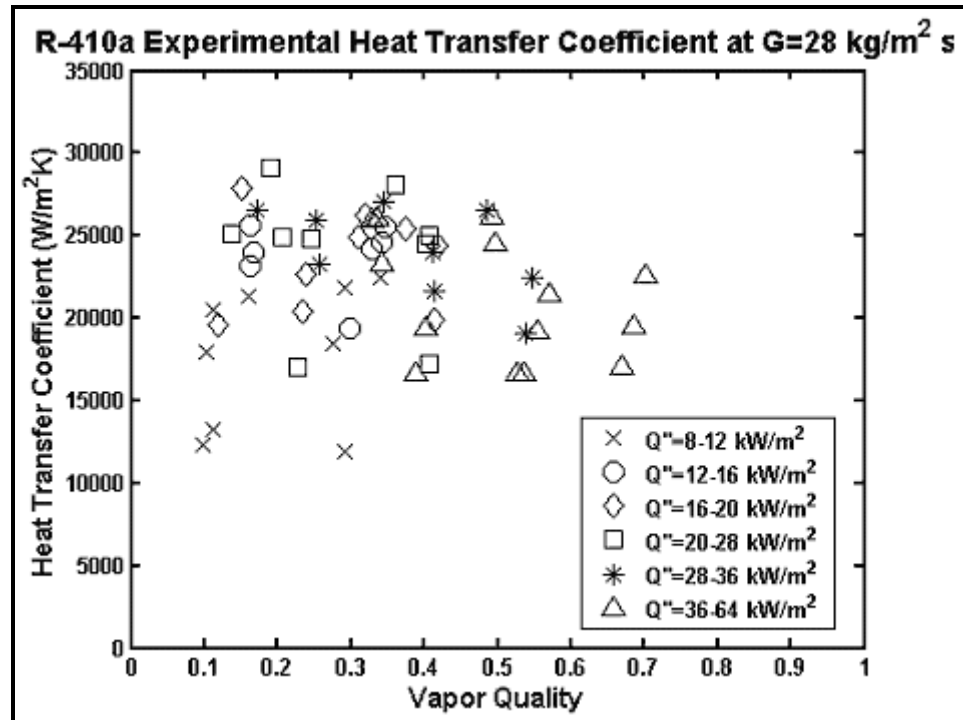


Figure 9.28. Boiling of R-410A on Turbo-Bii tube bundle by Robinson and Thome (2004b).

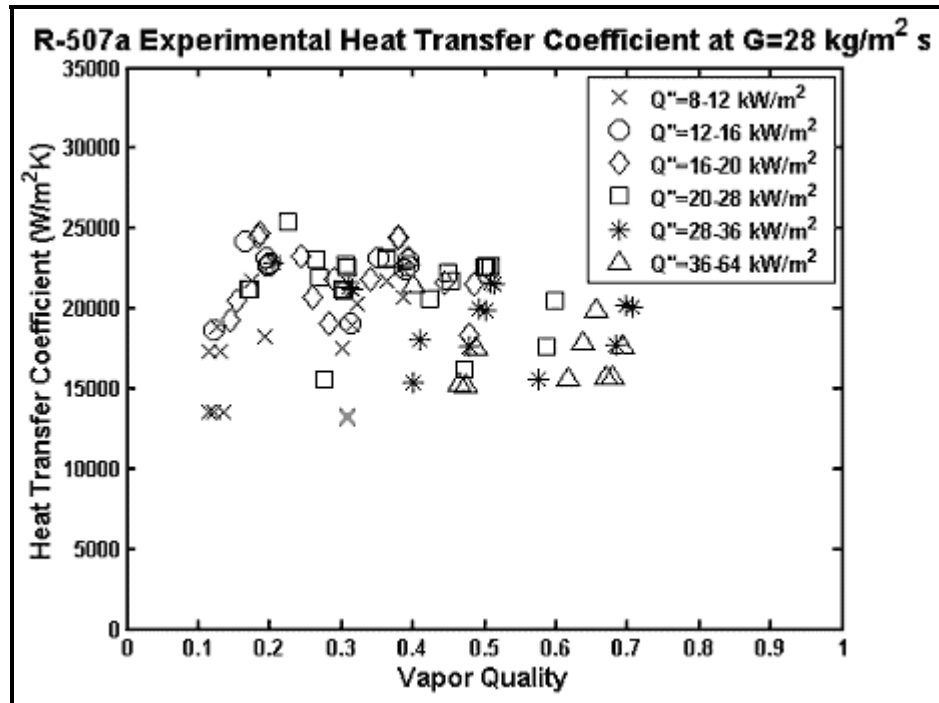


Figure 9.29. Boiling of R-507A on Turbo-Bii tube bundle by Robinson and Thome (2004b).

Most recently, Robinson and Thome (2004b) using the tube bundle layout and experimental technique described above measured local flow boiling heat transfer coefficients for the Turbo-Bii<sub>HP</sub> tube for R-134a, R-410A and R-507a, shown respectively in Figure 9.27, Figure 9.28 and Figure 9.29 (note that heat transfer coefficients range from about 15000 to 35000 W/m<sup>2</sup>K). In these tests they found that convective effects increased local boiling coefficients in the bundle from 10 to 40%, particularly for the low to medium heat fluxes they tested. For comparison, the pool boiling heat transfer coefficient for the Turbo-Bii at  $q = 16 \text{ kW/m}^2$  for R-134a is 20600 W/m<sup>2</sup>K, for R-410A is 23650 W/m<sup>2</sup>K and for R-507A is 21920 W/m<sup>2</sup>K. The tube was not optimized for use with the last two fluids. The heat transfer coefficients are quite large and yield local boiling superheats on the tubes that are only 0.5-1.0°C (0.9-1.8°F), which results for some of the scatter apparent in their data at these challenging test conditions typical of real operating conditions.

Prediction methods for local bundle boiling heat transfer coefficients are much less advanced than for boiling inside of tubes. Most of the bundle boiling methods available were developed from limited databases, typically obtained only in one laboratory for one or two fluids and hence they cannot be considered to be general methods, likely being unreliable when applied to other fluids, pressures and bundle geometries. Bundle boiling methods have been reviewed in Browne and Bansal (1999), Casciaro and Thome (2001a) and Collier and Thome (1994) while Thome (1990) reviewed enhanced bundle boiling in Chapters 10 to 12. Very few correlations specifically for the prediction of local bundle boiling heat transfer coefficients currently exist. Most of these methods use a modified form of the popular Chen (1963) intube boiling correlation, which thus ignores physical differences between internal and external two-phase flows. Any discussion of the local distribution and interaction of the liquid and vapor phases within a tube bundle must begin with the local void fraction. A new preliminary approach based on local void fraction is presented below (based on limited data like other previous methods).

Thome and Robinson (2006) have proposed a set of empirical bundle boiling heat transfer prediction methods for plain tubes, low finned tubes and enhanced boiling tubes. Their methods are based on only one tube diameter/tube pitch combination (19/22.23 mm, 0.74/0.875 in.), all for tests at one saturation temperature of 5°C (41°F) for an equilateral triangular tube layout. The methods presented below, however, have a general format that allows one to utilize the method for other tube layouts and tube pitches. Also, one can use them for other fluids and tube combinations by inputting one's own nucleate boiling curve. Even so, one must remember that these methods cannot be considered as general correlations because the underlying range of experiments (some described above) was quite limited. The void fraction method of Feenstra, Weaver and Judd (2000) described elsewhere in *Databook III* is used for determining  $\varepsilon$  in the methods below.

**Plain Tube Bundle Boiling Prediction Method.** The plain tubes were drawn copper tubes with an untreated surface and were 18.87 mm (0.742 in.) in outside diameter. An asymptotic method was assumed for predicting the local bundle boiling heat transfer coefficient  $\alpha_{\text{bundle}}$  from the nucleate boiling heat transfer coefficient  $\alpha_{\text{nb}}$  and the convective boiling heat transfer coefficient  $\alpha_{\text{cb}}$ :

$$\alpha_{\text{bundle}} = (\alpha_{\text{nb}}^2 + \alpha_{\text{cb}}^2)^{1/2} \quad [9.6.1]$$

The nucleate boiling heat transfer coefficient was predicted using the Cooper (1984) dimensional correlation given by [9.3.10], including its 1.7 multiplier that he recommended be applied to copper tubes with a surface roughness set to  $R_p = 5.7$  microns. Utilizing the Cooper correlation to thus calculate  $\alpha_{\text{nb}}$ , i.e. from its fit to their pool boiling data for R-134a, taking their R-134a experimental local bundle boiling heat transfer coefficients for the values of  $\alpha_{\text{bundle}}$ , the values of  $\alpha_{\text{cb}}$  were backed out of the experimental database applying [9.6.1]. The convective heat transfer coefficients thus obtained were assumed to be for heat transfer through a thin liquid film flowing over the tubes in the bundle, i.e. their version of the

sliding bubble heat transfer mechanism proposed by Cornwell (1989), the latter whose photographs can be seen in Figure 9.27 in Collier and Thome (1994). These convective heat transfer values were empirically fit to the following liquid film convection expression:

$$\alpha_{cb} = 4.032 \text{Re}_{\delta}^{0.236} \text{Pr}_L^{0.4} \left( \frac{k_L}{\delta} \right) \quad [9.6.2]$$

In this expression,  $\text{Pr}_L$  is the liquid Prandtl number,  $k_L$  is the liquid thermal conductivity,  $\delta$  is the liquid film thickness and  $\text{Re}_{\delta}$  is the liquid film Reynolds number, which is defined as:

$$\text{Re}_{\delta} = \frac{4\rho_L u_L \delta}{\mu_L} \quad [9.6.3]$$

The mean liquid velocity in the film  $u_L$  is:

$$u_L = \frac{\dot{m}_{\text{total}}(1-x)}{\rho_L(1-\varepsilon)} \quad [9.6.4]$$

The mass velocity of the flow is calculated using the minimum cross-sectional area of the bundle (like in single-phase cross flows). The liquid film thickness  $\delta$  is determined by fitting a hexagonal grid to the tube layout with one tube at the center of each hexagon (see Figure 9.30). Applying the void fraction to this geometry and its cross-sectional flow area, i.e. the area of the hexagon minus that of the cross-sectional area of the tube, the fraction of the area occupied by the liquid-phase is calculated and this area is applied to the perimeter of the tube to find the mean liquid film thickness. Referring to Figure 9.31, the area encompassed by the hexagon,  $A_{\text{hex}}$  is given by:

$$A_{\text{hex}} = 6 \left( \frac{L_{\text{pp}}}{3} \right) \left( \frac{L_{\text{pn}}}{2} \right) \quad [9.6.5]$$

$L_{\text{pp}}$  is the vertical tube pitch and  $L_{\text{pn}}$  is the horizontal tube pitch. The circumferential flow area  $A_{\text{cfl}}$  to which the void fraction is applicable is:

$$A_{\text{cfl}} = A_{\text{hex}} - \frac{\pi D}{4} \quad [9.6.6]$$

$D$  is the tube outside diameter and the area occupied by saturated liquid  $A_L$  in the hexagon is:

$$A_L = A_{\text{cfl}}(1-\varepsilon) \quad [9.6.7]$$

The diameter of the idealized liquid ring created by the liquid film around the tube  $D_{\delta}$  is:

$$D_{\delta} = \sqrt{\frac{4A_L}{\pi} + D^2} \quad [9.6.8]$$

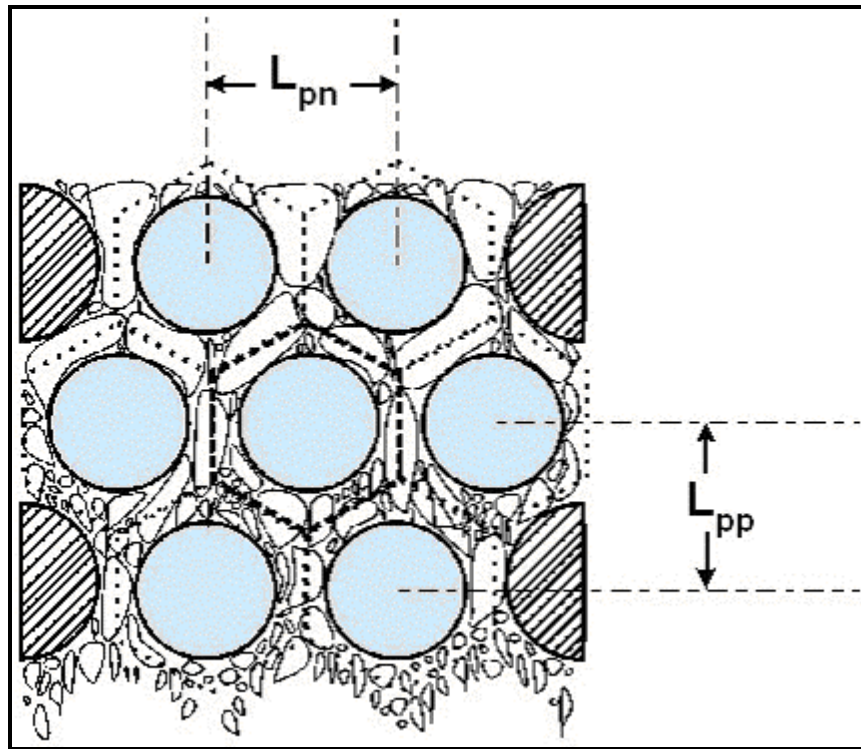


**Figure 9.30.** Idealized hexagonal grid boundary imposed over bundle cross section to identify local void fraction per tube.

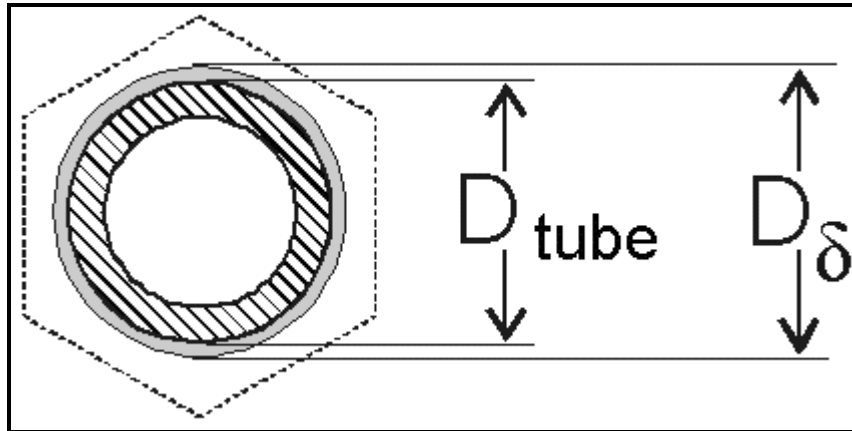


**Figure 9.31.** Idealized local saturated liquid film surrounding circumference of tube.

The liquid film thickness  $\delta$  is thus:

$$\delta = \frac{D_\delta - D}{2} \quad [9.6.9]$$

Though only one tube pitch arrangement was used in the experimental study, the above format is general, allowing future application to other staggered tube layouts, tube diameters and tube pitches similar to the present one.

Figure 9.32 depicts a comparison of the new bundle boiling method to the plain tube bundle boiling database of Robinson and Thome (2004a), capturing a large fraction of the bundle boiling data to within  $\pm 20\%$  as shown. The database covers only boiling of R-134a at a saturation temperature of  $4.4^{\circ}\text{C}$  ( $39.9^{\circ}\text{F}$ ) over the following test conditions: total mass flux from 5 to  $41 \text{ kg/m}^2\text{s}$  ( $3700$  to  $30300 \text{ lb/h ft}^2$ ), heat flux from 2 to  $35 \text{ kW/m}^2$  ( $630$  to  $11100 \text{ Btu/h ft}^2$ ) and vapor qualities from 10 to 87%. The individual values of the predicted smooth tube nucleate and convective boiling contributions varied greatly with different combinations of heat flux and mass flux. On average, the convective boiling contribution was 63% that of the nucleate boiling contribution, which means that the bundle boiling performance was about 63% higher than that of nucleate pool boiling on a single tube.

**Low Finned Tube Bundle Boiling Prediction Method.** The Wolverine Turbo-Chil low fin tube bundle (photo of this tube is shown in Figure 9.2) tested in Robinson and Thome (2004c) had a fin density of 1024 fins/meter (26 fins/inch), a root diameter of 15.88 mm, an inside diameter of 14.45 mm (0.569 in.), a fin height of 1.52 mm (0.060 in.) and a fin thickness of 0.2 mm (0.008 in.). These tubes also had an internal enhancement and were tested with a triangular tube pitch of 22.22 mm (0.875 in.). The above asymptotic method was again assumed for predicting the local bundle boiling heat transfer coefficient  $\alpha_{\text{bundle}}$  for the low finned tube bundle using [9.6.1]. As no reliable method is available for predicting nucleate boiling heat transfer coefficients on low finned tubes, the particular tube's experimentally measured nucleate pool boiling curve was used to determine  $\alpha_{\text{nb}}$ . For R-507A on the present low finned tube, the experimental boiling curve from their study was:

$$\alpha_{\text{nb}} = 93.35q^{0.448} \quad [9.6.10]$$

For R-134a on the same low finned tube, the boiling curve was:

$$\alpha_{\text{nb}} = 90.11q^{0.436} \quad [9.6.11]$$

Note that the heat flux is input in  $\text{W/m}^2$  based on the *nominal* surface area of a plain tube with an outside diameter equal to the fin tip diameter and the heat transfer coefficient is given in  $\text{W/m}^2\text{K}$  based on this same nominal area (not the total area of the low fin tube). The values of  $\alpha_{\text{cb}}$  were again backed out from the measured local bundle boiling heat transfer coefficients for  $\alpha_{\text{bundle}}$  by applying [9.6.1] with the above boiling curves for  $\alpha_{\text{nb}}$ . The convective heat transfer coefficients were assumed to be a function of liquid flow between adjacent fins but not between adjacent tubes, flows which all turned out to be in the laminar regime. They were empirically fit to a Sieder and Tate (1936) type of laminar convection expression where the exponent on the Reynolds number was found from the data to be only 0.0013. Hence, the expression was reduced to that of a fully-developed laminar flow expression, typical of high aspect ratio rectangular channels, as:

$$\frac{\alpha_{\text{cb}} d_h}{k_L} = 13.92 \quad [9.6.12]$$

In this expression,  $d_h$  is the hydraulic diameter for the flow between adjacent fins and is defined as:

$$d_h = \frac{4A_{fa}}{P_L} \quad [9.6.13]$$

For the flow between two adjacent fins,  $P_L$  is the wetted perimeter of the two sides of the fin plus that of the root, so that  $P_L = (s - t_{root}) + 2e$  where  $s$  is the fin pitch,  $t_{root}$  is the fin thickness at its root and  $e$  is the fin height. The cross-sectional area  $A_{fa}$  for free flow area between two fins is  $A_{fa} = (s - t_{root})e$ . The use of this laminar channel flow method between the fins was suggested by the void fraction method used for the plain tube bundle described above since the values of the liquid film thickness calculated for the entire wetted surface area of the low-finned tube were typically larger than half the interfin spacing ( $s - t_{root}$ ) and hence the flow between the fins is not a film flow but rather a channel flow.

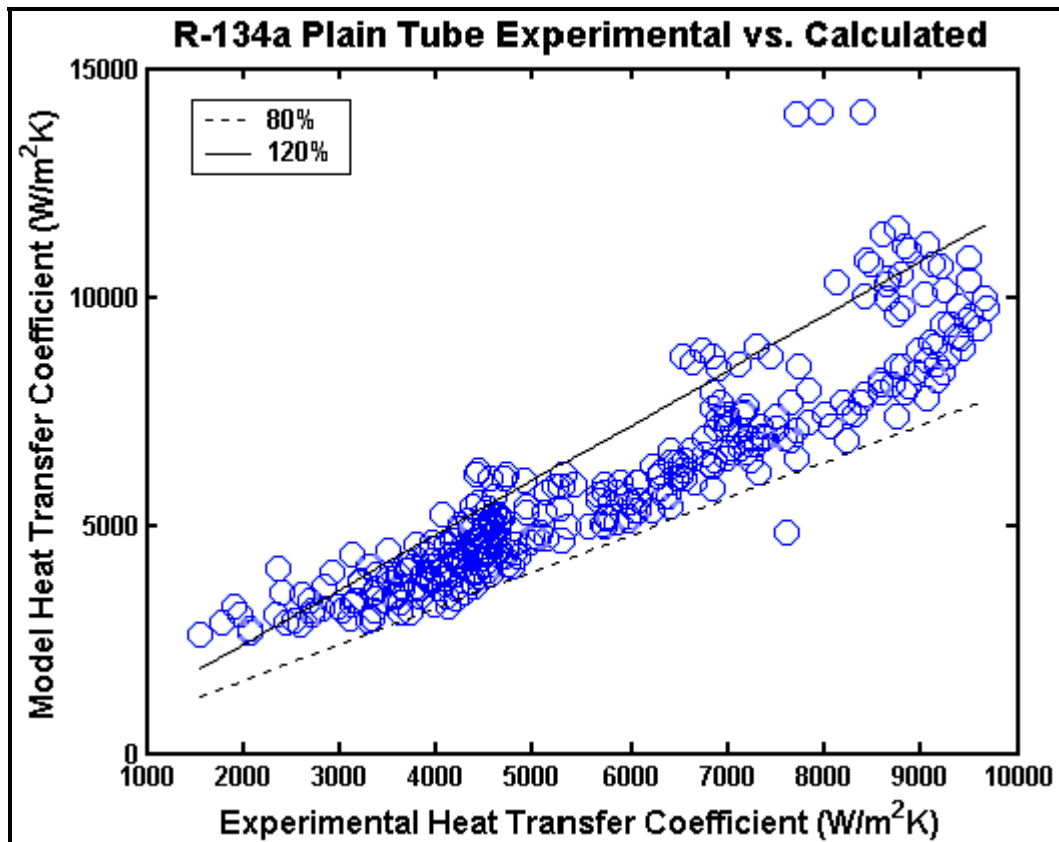


**Figure 9.32. Predicted vs. experimental bundle boiling heat transfer coefficients for plain tube.**

Figure 9.33 shows the comparison of the above prediction method to the finned tube bundle boiling database for R-134a. Similar results were obtained with R-507A on the same bundle. Most of the data were predicted within  $\pm 20\%$ . The database covers only boiling of R-134a and R-507A at a saturation temperature of 4.4 °C (39.9°F) over the following conditions: total mass flux from 3 to 29 kg/m<sup>2</sup>s (2210 to 21400 lb/h ft<sup>2</sup>), heat flux from 2 to 50 kW/m<sup>2</sup> (630 to 15850 Btu/h ft<sup>2</sup>) and vapor qualities from 8 to 82%. The individual values of the finned tube nucleate and convective boiling contributions varied greatly with different heat and mass flux conditions; on average the convective boiling contribution was 68% that of the nucleate boiling contribution.

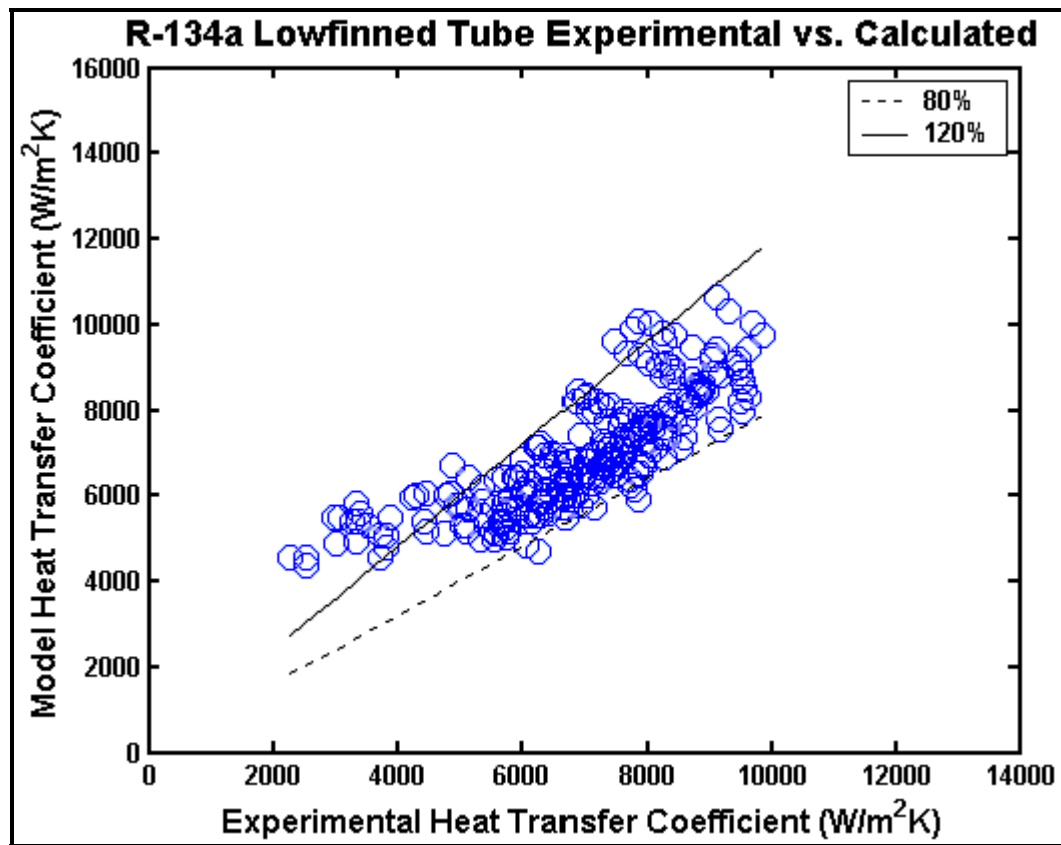


**Figure 9.33.** Predicted vs. experimental bundle boiling heat transfer coefficients for Turbo-Chil low fin tube.

**Turbo-Bii\_HP Bundle Boiling Prediction Method.** The database of Robinson and Thome (2004b) for tests with R-134a, R-507A and R-410A were used to develop this method. The Wolverine Turbo-Bii\_HP tube (shown in Figure 9.4) had a root diameter of 17.48 mm (0.688 in), an outside diameter of 18.69 mm (0.736 in) and an inside diameter of 16.05 mm (0.632 in). They had an internal enhancement and were tested in a bundle with a triangular tube pitch of 22.22 mm (0.875 in.). For predicting the thermal performance of this enhanced boiling tube, another strategy was taken since the convection coefficients  $\alpha_{cb}$  deduced for the plain and low finned tube bundles are insignificant with respect to the Turbo-Bii\_HP bundle performance because of its very high nucleate boiling coefficients, i.e. such  $\alpha_{cb}$  values are on the order of 1 kW/m<sup>2</sup>K whereas those of  $\alpha_{nb}$  are on the order of 20 to 25 kW/m<sup>2</sup>K. The bundle boiling effect (local bundle heat transfer coefficient relative to their corresponding value of  $\alpha_{nb}$ ) was significant as described in Robinson and Thome (2004b). Furthermore, it did not seem justified to multiply  $\alpha_{cb}$  in [9.6.2] by factors up to 5 to account for the “rough” surface of the Turbo-Bii\_HP tube. They thus concluded that the two-phase flow had an enhancing effect on the nucleate boiling process itself, perhaps by increasing the departure frequencies of the bubbles leaving the re-entrant channels, which in turn would augment the thin film evaporation and convection processes inside the re-entrant channels. Hence, a bundle boiling factor approach was taken to predict the local bundle boiling heat transfer coefficients  $\alpha_{bundle}$  for the Turbo-Bii\_HP tube bundle as:

$$\alpha_{bundle} = \alpha_{nb} F_p F_\varepsilon \quad [9.6.14]$$

In the absence of a pool boiling correlation to predict  $\alpha_{nb}$  for this tube, the experimental nucleate boiling curves for the particular fluid boiling on Turbo-Bii\_HP were used to calculate  $\alpha_{nb}$ . The nucleate pool boiling curves from Robinson and Thome (2004b) for the three fluids were:

$$\text{R-134a: } \alpha_{nb} = 30944q^{-0.042} \quad [9.6.15]$$

$$\text{R-507A: } \alpha_{nb} = 37334q^{-0.055} \quad [9.6.16]$$

$$\text{R-410A: } \alpha_{nb} = 43520q^{-0.063} \quad [9.6.17]$$

Here,  $\alpha_{nb}$  was nearly insensitive to heat flux. Their bundle boiling reduced pressure correction factor  $F_p$ , in terms of the reduced pressure  $p_r$ , was:

$$F_p = 1.41 - 2.66p_r \quad [9.6.18]$$

Their bundle boiling void fraction correction factor  $F_\varepsilon$  was correlated as:

$$F_\varepsilon = 1.15 - 2(0.4 - \varepsilon)^2 \quad [9.6.19]$$

In this last expression, the local void fraction is calculated with the tube bundle void fraction method of Feenstra, Weaver and Judd (2000). The void fractions in the tests ranged from 0.16 to 0.85 while the reduced pressures ranged from 0.084 to 0.2. A maximum in the bundle effect for all three fluids occurred at a void fraction of about 0.4, above which the heat transfer performance fell off. The bundle effect was observed experimentally to decrease with increasing reduced pressure and hence the introduction of the factor  $F_p$ . Due to the highly empirical nature of this method and the limited database, it is recommended that caution be used in extrapolating this method outside of its present range of reduced pressures and void fractions.

Figure 9.34 shows their R-134a bundle boiling data compared to the prediction method, with the data segregated by measurement location, dividing them into one set that is for the bottom tube row in the bundle and the other set for upper tube rows (tube rows 3, 5 and 7 counting from the bottom up). As can be seen, the bottom tube row data tend to differ from the other tube rows. Two explanations were offered for this. First of all, the hot water inside the tubes in the bundle entered at the top and hence the water temperature profile became rather flat in the bottom tube row, so those experimental values were more sensitive to the measured slope of the water temperature profile than the others. The bottom row data in fact were grouped by location along the tube, where the left-most data are for the last test location along the bottom tube before the hot water exits the bundle and the right-most are for the first test location along the bottom tube. Secondly, there could have been an “entrance effect” on the bottom tube row since no bubble jet from lower boiling tubes impinges on it. The first case seemed to be the most plausible explanation. Hence, disregarding the data from the last two locations on the bottom tube row, the comparison of the prediction method to the remaining database was quite satisfactory, also for R-410A and R-507A where the same trends were observed, and most of such data were predicted within  $\pm 20\%$ . The database covered R-134a, R-507A, and R-410A at a saturation temperature of 4.4 °C (39.9°F) for: total mass flux from 4 to 38 kg/m²s (2950 to 28040 lb/h ft²), heat flux from 8 to 64 kW/m² (2540 to 20290 Btu/h ft²) and vapor qualities from 8 - 78%.

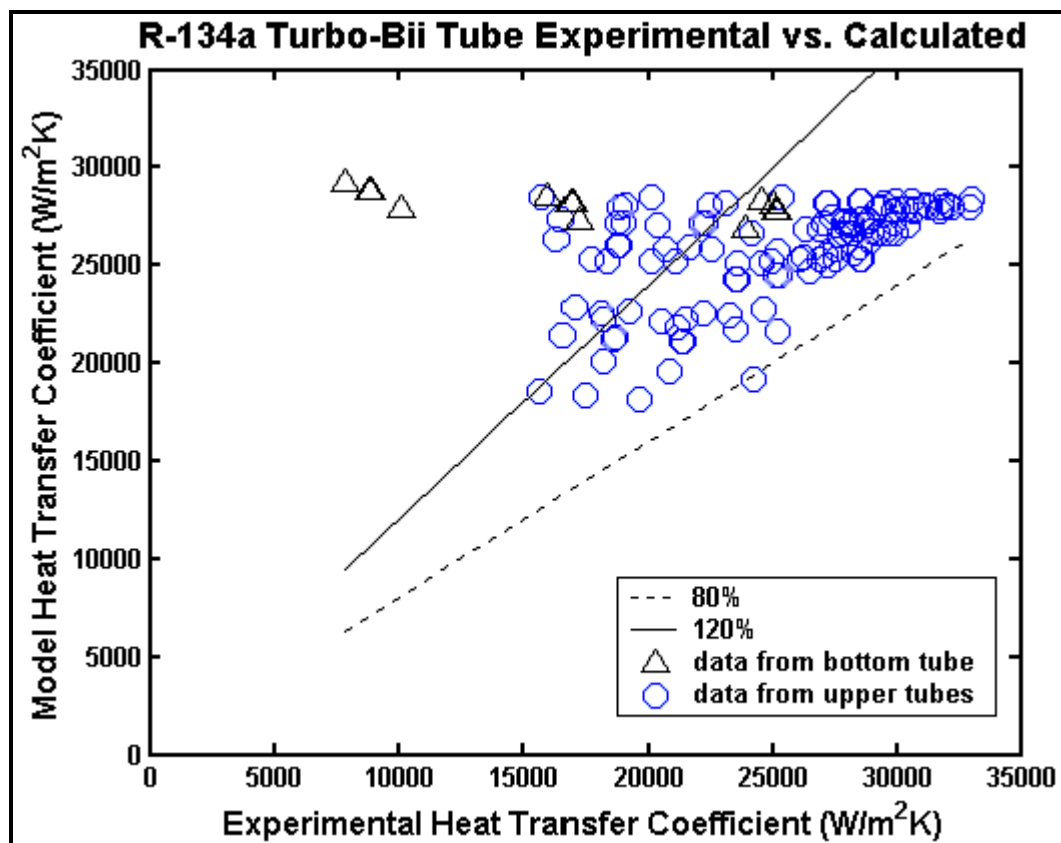


Figure 9.34. Predicted vs. experimental bundle boiling heat transfer coefficients for Turbo-Bii\_HP tube.

## 9.7 Dryout Mechanisms on Bundle Boiling

The upper operating limit of plain and enhanced tube bundles is governed by several possible dryout scenarios. These have been contemplated for those occurring on horizontal kettle reboilers widely used in petro-chemical applications and are in part also applicable to flooded evaporators favored by the refrigeration industry. Figure 9.35 illustrates these. Mechanism (a) is for small tube bundles with few tube rows; here, the maximum heat flux is essentially limited by that for DNB on a single tube, i.e. by expression [9.3.18]. Mechanism (b) refers to a unit with liquid loading onto the bundle from above, where the liquid loaded from above is not able to penetrate to the bottom of a large bundle because of the up flow of the vapor. Mechanism (c) occurs for large tube bundles with too little inflow from beneath, which can create unfavorable circulation of liquid and mal-distribution of liquid in the bundle and hence local dryout. Mechanism (d) refers to another circulation-limited problem in which the bundle is starved for liquid and locally dries out. Mechanism (e) describes the onset of mist flow that can occur at high local vapor qualities where all the liquid is entrained as tiny droplets into the vapor flow.

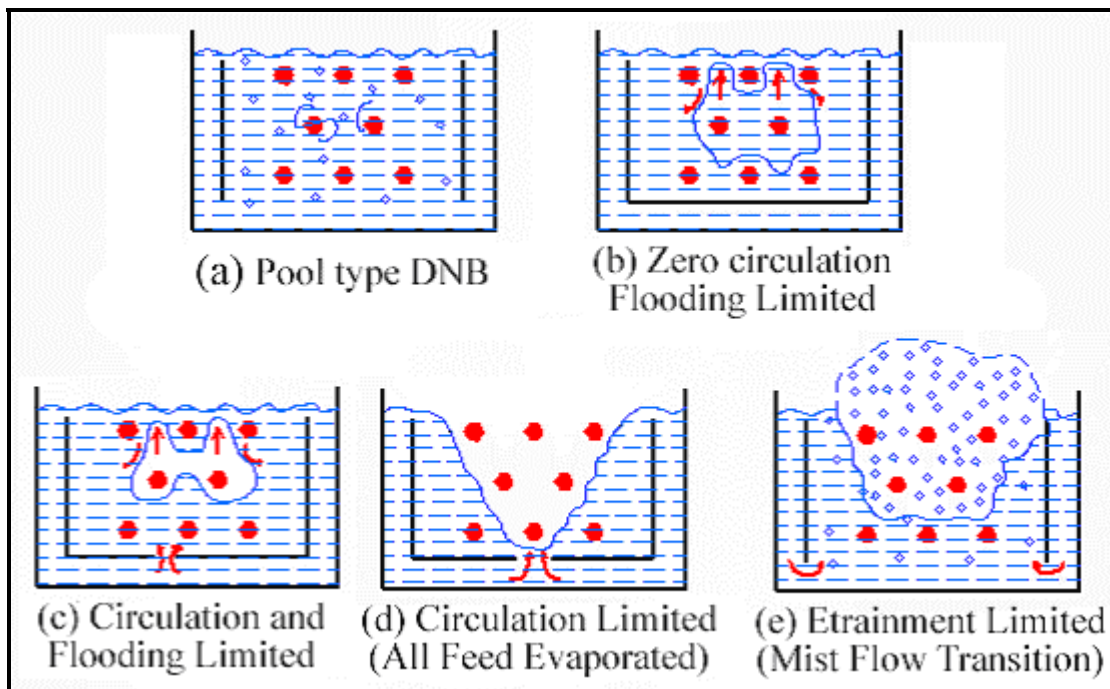


Figure 9.35. Dryout mechanisms on horizontal tube bundles.

## Chapter 10

# Boiling Heat Transfer Inside Plain Tubes

**(This chapter was updated in 2007)**

**SUMMARY:** Evaporation inside plain tubes is described. Methods for evaporation in both vertical and horizontal tubes are covered. Some older design methods are first described and then the newest methods are presented. All these methods provide local predictions for flow boiling heat transfer coefficients for conditions in which the tube perimeter is completely or partially wet, but not for post-dryout heat transfer for mist flow. In addition, evaporation of mixtures is also addressed and a general prediction method is presented. Some of the methods also apply to evaporation in annuli formed by two concentric plain tubes. The recommended method for evaporation in vertical tubes is that of Steiner and Taborek (1992) while for horizontal tubes the method of choice is the updated version by Wojtan, Ursenbacher and Thome (2005a, 2005b) of the model of Kattan, Thome and Favrat (1998a, 1998b, 1998c).

### 10.1 Introduction

The various hydrodynamic conditions encountered when a liquid is evaporated in a confined channel, in this case round tubes, are described in this chapter together with methods to predict their heat transfer coefficients.

First of all, consider a vertical tube heated uniformly along its length (for example, by direct Joule heating of the tube by a DC power supply) at a relatively low heat flux with subcooled liquid entering the tube from the bottom and then completely evaporated over the length of the tube, as shown in Figure 10.1. While the liquid is being heated up to its saturation temperature at the local pressure at that height in the tube, the wall temperature initially is below that necessary for nucleation (zone A). Thus, the heat transfer process in zone A is subcooled, single-phase heat transfer to the liquid, which may be laminar or turbulent. Then, the wall temperature rises above the saturation temperature and boiling nucleation takes place in the superheated thermal boundary layer on the tube wall, such that subcooled flow boiling occurs in zone B with the vapor bubbles condensing as they drift into the subcooled core. The liquid then reaches its saturation temperature and saturated boiling in the form of bubbly flow begins in zone C. Saturated boiling continues through the slug flow regime (zone D), the annular flow regime (zone E) and then the annular flow regime with liquid entrainment in the vapor core (zone F).

At the end of zone F, the annular film is either dried out or sheared from the wall by the vapor, a point that is referred to as the onset of dryout or simply dryout. Above this point, mist flow in the form of entrained droplets occurs with a large increase in wall temperature for this instance of an imposed wall heat flux (zone G). The temperature of the continuous vapor-phase in zone G tends to rise above the saturation temperature and heat transfer is via four mechanisms: single-phase convection to the vapor, heat transfer to the droplets within the vapor, heat transfer to droplets impinging on the wall and thermal radiation from the wall to the droplets. Because of this non-equilibrium effect, droplets continue to exist in the vapor-phase beyond the point of  $x = 1$ , all the way to the beginning of zone H where all the liquid has been evaporated and heat transfer is by single-phase convection to the dry vapor.

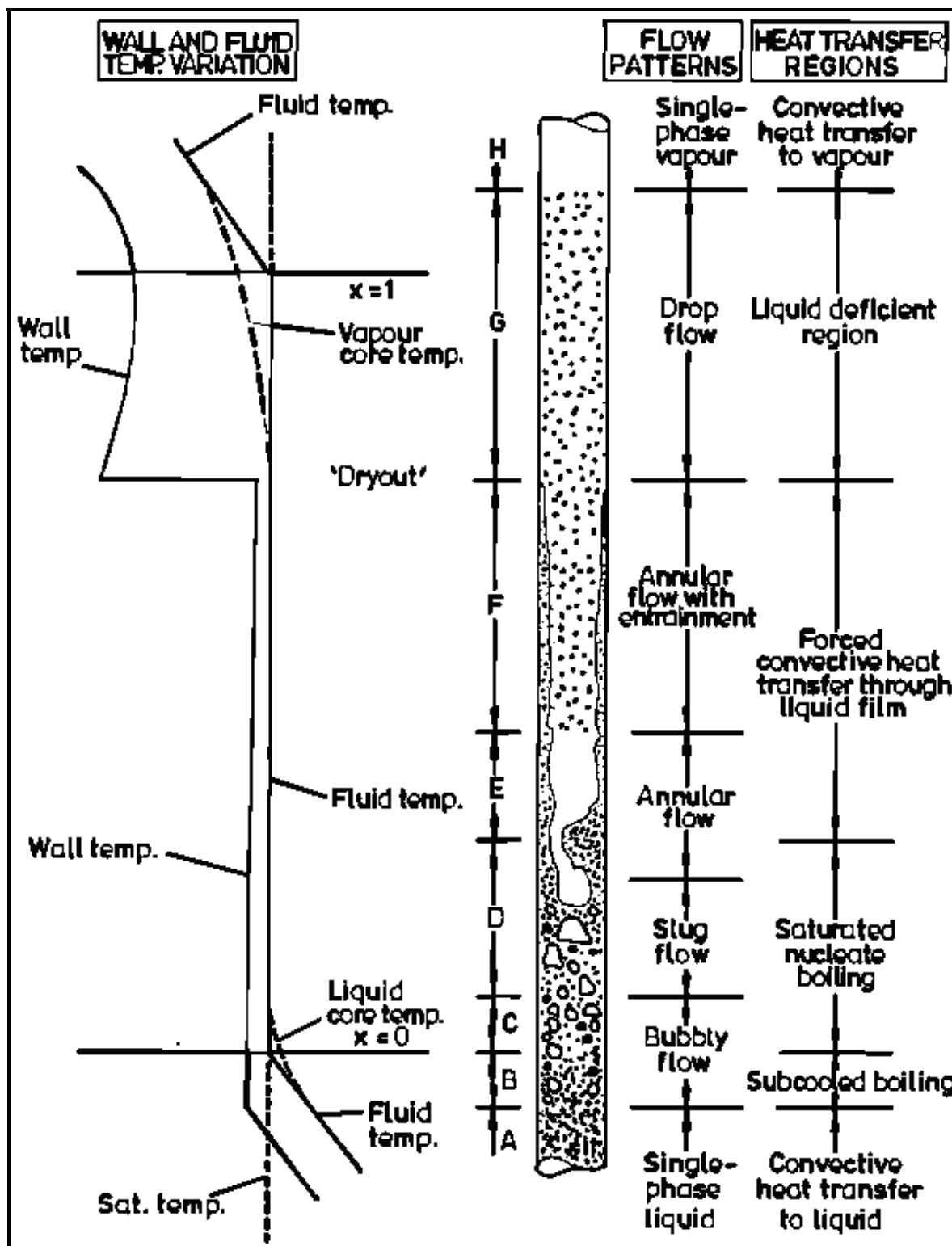


Figure 10.1. Heat transfer regions in convective boiling in a vertical tube from Collier and Thome (1994).

Figure 10.2 shows a “boiling map” for evaporation heat transfer, depicting qualitatively the progressive variation in the local heat transfer coefficient along a heated tube as the fluid evaporates. In essence, the map illustrates the variation in the heat transfer coefficient as a function of quality with increasing heat flux as the parameter, where the heat flux increases from (i) to (vii). At low heat fluxes the liquid deficient region is encountered at the dryout of the annular film. At higher heat fluxes, saturated film boiling is encountered by the process going through the departure from nucleate boiling (DNB), which is also commonly called the critical heat flux. Here, at least ideally, one can image that for film boiling an inverted annular flow occurs with the vapor forming an annular film and the liquid in the central core. As can be seen, at high heat fluxes it is possible to reach DNB under subcooled conditions. The heat transfer coefficients in the film boiling and liquid deficient regions are noticeably smaller than those in the wet wall region.

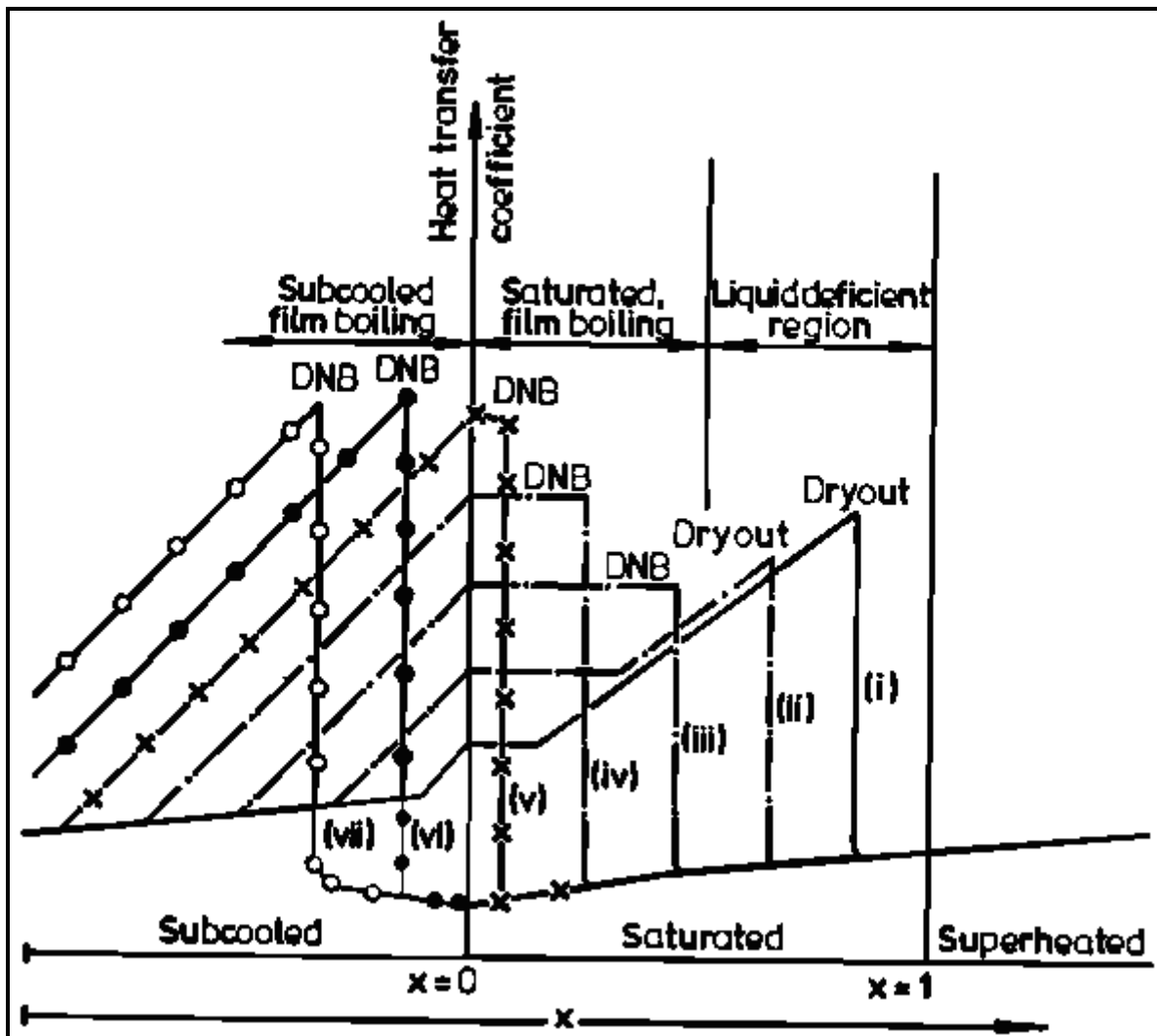


Figure 10.2. Boiling map of Collier and Thome (1994).

## 10.2 Two-Phase Flow Boiling Heat Transfer Coefficient

The local two-phase flow boiling heat transfer coefficient for evaporation inside a tube  $\alpha_{tp}$  is defined as

$$\alpha_{tp} = \frac{q}{(T_{wall} - T_{sat})} \quad [10.2.1]$$

where  $q$  corresponds to the local heat flux from the tube wall into the fluid,  $T_{sat}$  is the local saturation temperature at the local saturation pressure  $p_{sat}$  and  $T_{wall}$  is the local wall temperature at the axial position along the evaporator tube, assumed to be uniform around the perimeter of the tube.

Flow boiling models normally consider two heat transfer mechanisms to be important: nucleate boiling heat transfer ( $\alpha_{nb}$ ) and convective boiling heat transfer ( $\alpha_{cb}$ ). Nucleate boiling under these conditions is similar to nucleate pool boiling except for any effect of the bulk flow on the growth and departure of the bubbles and the bubble induced convection process. The bubbles formed inside a tube may slide along the heated surface due to the axial bulk flow, and hence the microlayer evaporation process underneath the growing bubbles may also be affected. Convective boiling refers to the convective process between the heated wall and the liquid-phase. For instance, for annular flow without nucleate boiling in the liquid film, the convective heat transfer process can be envisioned as single-phase forced convection across the film with evaporation taking place at the liquid-vapor interface of the central core.

Before presenting flow boiling models, it is interesting to see how they can be compared and classified by the manner in which the heat transfer coefficients  $\alpha_{nb}$  and  $\alpha_{cb}$  are combined to obtain  $\alpha_{tp}$  in the following power law format, typical of superposition of two thermal mechanisms upon one another:

$$\alpha_{tp} = [(\alpha_{nb})^n + (\alpha_{cb})^n]^{1/n} \quad [10.2.2]$$

This power law format for  $\alpha_{tp}$  is illustrated in Figure 10.3 for a fluid at a fixed pressure, mass flux, and vapor quality. Assuming that  $\alpha_{cb}$  is not a function of heat flux, which is typical of most flow boiling prediction methods,  $\alpha_{cb}$  is a horizontal line on this plot. Instead,  $\alpha_{nb}$  is typically considered to be a function of heat flux but not mass velocity, and hence gives a nucleate pool boiling type of curve on this plot of heat transfer coefficient versus heat flux. Combining their values together using exponents of 1, 2, 3 and  $\infty$  give the resulting variations in  $\alpha_{tp}$ . Setting  $n = 1$  results in a simple addition of the respective values. Chen (1963, 1966) used this approach but introduced a nucleate boiling suppression factor on  $\alpha_{nb}$  and a two-phase multiplier on  $\alpha_{cb}$ . Kutateladze (1961) proposed an asymptotic method with  $n = 2$ , where the value of  $\alpha_{tp}$  tends to the larger of the two values. Steiner and Taborek (1992) more recently proposed using  $n = 3$ . Setting  $n = \infty$  yields the larger of the two values, which is the approach proposed by Shah (1982).

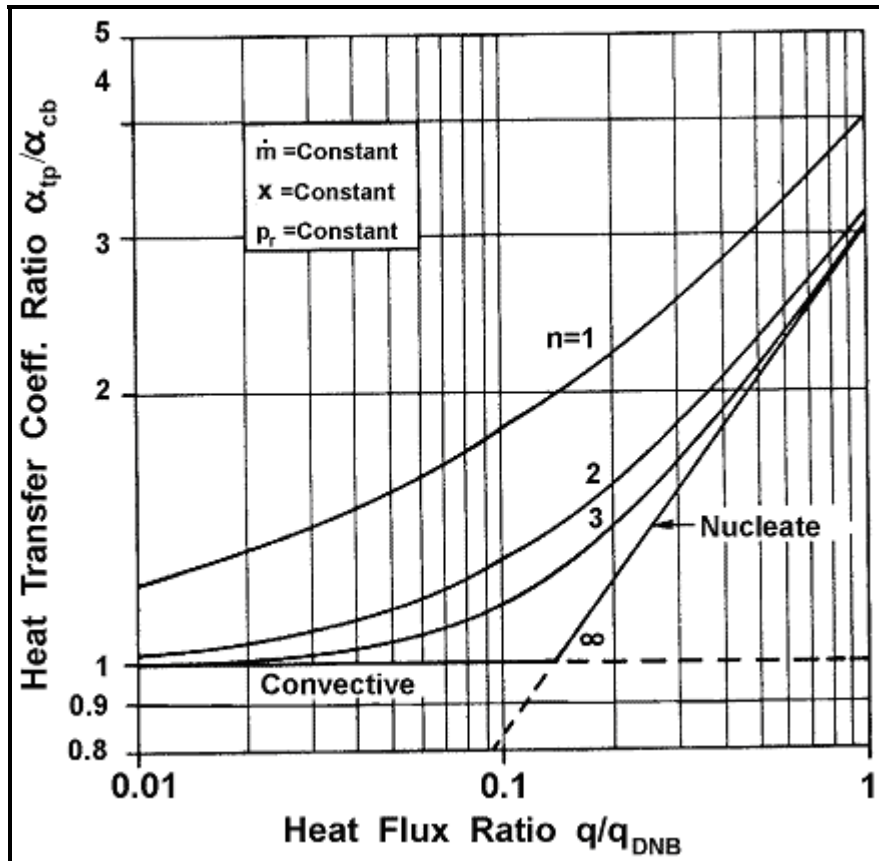


Figure 10.3. Power law representation of flow boiling models of Steiner and Taborek (1992).

### 10.3 Flow Boiling inside Vertical Plain Tubes

Convective evaporation in *vertical* tubes is discussed in this section, which is defined by the regions C, D, E and F in Figure 10.1. This process may either be forced convection, such as in a power boiler or a direct-expansion evaporator, or gravity driven as in a vertical thermosyphon reboiler. At high qualities and mass flow rates, the flow regime is normally annular. At relatively low flow rates at sufficient wall superheats, bubble nucleation at the wall occurs such that nucleate boiling is present within the liquid film. As the flow velocity increases and augments convection in the liquid film, the wall may be cooled below the minimum wall superheat necessary to sustain nucleation and nucleate boiling may thus be suppressed, in which case heat transfer is only by convection through the liquid film and evaporation occurs only at its interface.

Furthermore, at some threshold quality, the liquid film may dry out or become entrained in the high velocity vapor-phase, which results in poor heat transfer. This region is referred to as the post-dryout region, which will not be addressed in this chapter.

In nucleate pool boiling, heat transfer is a strong function of heat flux, by about  $\alpha_{nb} \propto q^{0.7}$ ; instead in forced convective evaporation, heat transfer is less dependent on heat flux while its dependence on the local vapor quality and mass velocity appear as new and important parameters. Thus, both nucleate boiling and convective heat transfer must be taken into account to predict heat transfer data. Nucleate boiling tends to be dominant at low vapor qualities and high heat fluxes while convection tends to

dominate at high vapor qualities and mass velocities and low heat fluxes. For intermediate conditions, both mechanisms are often important.

The principal methods for predicting two-phase flow boiling heat transfer coefficients in vertical tubes are presented below. Generally speaking, the nucleate boiling coefficient  $\alpha_{nb}$  is determined utilizing a nucleate pool boiling correlation from the literature or by proposing a new nucleate boiling term as part of the flow boiling correlation. Similarly, the convective heat transfer coefficient  $\alpha_{cb}$  is typically related to what is sometimes referred to as the liquid only heat transfer coefficient  $\alpha_L$ , which is determined with a single-phase turbulent flow heat transfer correlation, usually that of Dittus-Boelter (1930). Furthermore, these methods normally assume that the liquid fraction flowing in the channel,  $m(1-x)$ , occupies the entire cross-section of the channel in the calculation of  $\alpha_L$ .

### 10.3.1 Chen Correlation

Chen (1963, 1966) proposed the first flow boiling correlation for evaporation in vertical tubes to attain widespread use. He envisioned the local two-phase flow boiling coefficient  $\alpha_{tp}$  to be the sum of the nucleate boiling contribution  $\alpha_{nb}$  and the convective contribution  $\alpha_{cb}$ :

$$\alpha_{tp} = \alpha_{nb} + \alpha_{cb} \quad [10.3.1]$$

He surmised that the steeper temperature gradient in the liquid near the tube wall under forced convection conditions, relative to that in nucleate pool boiling, partially suppressed nucleation of boiling sites and hence reduced the contribution of nucleate boiling. On the other hand, he noted that the vapor formed by the evaporation process increased the liquid velocity and hence the convective heat transfer contribution tends to be increased relative to that of single-phase flow of the liquid. Hence, he formulated the following expression to account for these two effects:

$$\alpha_{tp} = \alpha_{FZ}S + \alpha_L F \quad [10.3.2]$$

where

- the nucleate pool boiling correlation of Forster and Zuber (1955) is used to calculate the nucleate boiling heat transfer coefficient,  $\alpha_{FZ}$ ;
- the nucleate boiling suppression factor acting on  $\alpha_{FZ}$  is  $S$ ;
- the turbulent flow correlation of Dittus-Boelter (1930) for tubular flows is used to calculate the liquid-phase convective heat transfer coefficient,  $\alpha_L$ ;
- and the increase in the liquid-phase convection due to the two-phase flow is given by his two-phase multiplier  $F$ .

The Forster-Zuber correlation gives the nucleate pool boiling coefficient as:

$$\alpha_{FZ} = 0.00122 \left[ \frac{k_L^{0.79} c_{pL}^{0.45} \rho_L^{0.49}}{\sigma^{0.5} \mu_L^{0.29} h_{LG}^{0.24} \rho_G^{0.24}} \right] \Delta T_{sat}^{0.24} \Delta p_{sat}^{0.75} \quad [10.3.3]$$

where the wall superheat  $\Delta T_{sat}$  is the local temperature difference between the inner tube wall ( $T_{wall}$ ) and the local saturation temperature ( $T_{sat}$ ), such that  $\Delta T_{sat} = (T_{wall} - T_{sat})$ . The pressure difference  $\Delta p_{sat}$  is

obtained from the vapor pressures of the fluid at the wall temperature ( $p_{wall}$ ) and at the saturation temperature ( $p_{sat}$ ), such that  $\Delta p_{sat} = (p_{wall} - p_{sat})$ . In this expression,  $\Delta p_{sat}$  is in the units of N/m<sup>2</sup>.

The liquid-phase convective heat transfer coefficient  $\alpha_L$  is given by the Dittus-Boelter (1930) correlation for the fraction of liquid flowing alone in a tube of internal diameter  $d_i$ , i.e. using a mass velocity of  $\dot{m}(1-x)$ , as:

$$\alpha_L = 0.023 \text{Re}_L^{0.8} \text{Pr}_L^{0.4} \left( \frac{k_L}{d_i} \right) \quad [10.3.4]$$

where the liquid Reynolds number  $\text{Re}_L$  is:

$$\text{Re}_L = \frac{\dot{m}(1-x)d_i}{\mu_L} \quad [10.3.5]$$

and  $x$  is the local vapor quality and  $\dot{m}$  is the total mass velocity of the liquid plus vapor in the tube of internal diameter  $d_i$ .  $\text{Pr}_L$  is the liquid Prandtl number defined as:

$$\text{Pr}_L = \frac{c_{pL}\mu_L}{k_L} \quad [10.3.6]$$

The two-phase multiplier  $F$  of Chen is:

$$F = \left( \frac{1}{X_{tt}} + 0.213 \right)^{0.736} \quad [10.3.7]$$

where the Martinelli parameter  $X_{tt}$  is used for the two-phase effect on convection, where  $X_{tt}$  is defined as:

$$X_{tt} = \left( \frac{1-x}{x} \right)^{0.9} \left( \frac{\rho_G}{\rho_L} \right)^{0.5} \left( \frac{\mu_L}{\mu_G} \right)^{0.1} \quad [10.3.8]$$

Note, however, that when  $1/X_{tt} \leq 0.1$ ,  $F$  is set equal to 1.0. The Chen boiling suppression factor  $S$  is

$$S = \frac{1}{1 + 0.00000253 \text{Re}_{tp}^{1.17}} \quad [10.3.9]$$

This in turn is a function of his two-phase Reynolds number:

$$\text{Re}_{tp} = \text{Re}_L F^{1.25} \quad [10.3.10]$$

His fluid database included water in upflow and downflow (pressures from 0.55 to 34.8 bar) and methanol, cyclohexane, n-pentane, n-heptane and benzene, all in upflow at 1 bar. Most of the data were at low vapor qualities but the entire range covers values from 0.01 to 0.71. His correlation is applicable as long as the heated wall remains wet, i.e. up to the onset of dryout. Since the wall superheat  $\Delta T_{sat}$  is

typically not known, an iterative calculation involving  $T_{\text{wall}}$  and  $p_{\text{wall}}$  is required when the heat flux  $q$  is specified.

### 10.3.2 Shah Correlation

The second flow boiling method for evaporation in vertical channels to reach a wide notoriety is that of Shah (1982), who proposed equations to implement his chart calculation method he proposed earlier. While he considered nucleate boiling and convective boiling to be the two important heat transfer mechanisms similar to Chen (1963, 1966), his method instead chooses the *larger* of the two, that is the larger of his nucleate boiling coefficient  $\alpha_{\text{nb}}$  and his convective boiling coefficient  $\alpha_{\text{cb}}$ , for the value of local two-phase flow boiling heat transfer coefficient  $\alpha_{\text{tp}}$ . He proposed a method applicable to both vertical tubes and horizontal tubes. His vertical tube method is presented here, which begins by defining a dimensionless parameter  $N$ , which for vertical tubes at all values of the liquid Froude number  $Fr_L$  is:

$$N = C_0 \quad [10.3.11]$$

and his factor  $C_0$  is determined from the local vapor quality and density ratio as:

$$C_0 = \left( \frac{1-x}{x} \right)^{0.8} \left( \frac{\rho_G}{\rho_L} \right)^{0.5} \quad [10.3.12]$$

while the liquid Froude number is defined as:

$$Fr_L = \frac{\dot{m}^2}{\rho_L^2 g d_i} \quad [10.3.13]$$

To characterize convection, the liquid-phase convective heat transfer coefficient  $\alpha_L$  is determined from the liquid fraction of the flow,  $\dot{m}(1-x)$ , using the Dittus-Boelter (1930) correlation given in [10.3.4]. His convective boiling heat transfer coefficient  $\alpha_{\text{cb}}$  is calculated as:

$$\frac{\alpha_{\text{cb}}}{\alpha_L} = \frac{1.8}{N^{0.8}} \quad [10.3.14]$$

The effect of heat flux on nucleate boiling is characterized by the Boiling number,  $Bo$ , which is defined as:

$$Bo = \frac{q}{\dot{m} h_{LG}} \quad [10.3.15]$$

representing the ratio of the actual heat flux to the maximum heat flux achievable by complete evaporation of the liquid. His parameter  $N$  is then used to determine the appropriate set of equations to use as follows:

When  $N > 1.0$  and  $Bo > 0.0003$ .  $\alpha_{\text{nb}}$  is calculated as below:

$$\frac{\alpha_{nb}}{\alpha_L} = 230 Bo^{0.5} \quad [10.3.16]$$

When  $N > 1.0$  and  $Bo < 0.0003$ ,  $\alpha_{nb}$  is calculated as below:

$$\frac{\alpha_{nb}}{\alpha_L} = 1 + 46 Bo^{0.5} \quad [10.3.17]$$

When  $1.0 > N > 0.1$ ,  $\alpha_{nb}$  is calculated as below:

$$\frac{\alpha_{nb}}{\alpha_L} = F_S Bo^{0.5} \exp(2.74N - 0.1) \quad [10.3.18]$$

When  $N < 0.1$ ,  $\alpha_{nb}$  in the bubble suppression regime is calculated using the equation below:

$$\frac{\alpha_{nb}}{\alpha_L} = F_S Bo^{0.5} \exp(2.74N - 0.15) \quad [10.3.19]$$

In the above equations, Shah's constant  $F_S = 14.7$  when  $Bo > 0.0011$  and  $F_S = 15.43$  when  $Bo < 0.0011$ . The larger value of  $\alpha_{nb}$  or  $\alpha_{cb}$  is then taken for  $\alpha_{tp}$ .

The most notable weakness of his method is that the only physical property in the boiling number  $Bo$  for characterizing nucleate boiling is the latent heat. Furthermore, the latent heat decreases with increasing pressure while  $\alpha_{nb}$  typically increases with pressure.

Shah also applied this method to evaporation in vertical annuli as follows. When the annular gap between the inner and outer tubes is greater than 4 mm, the equivalent diameter to use for  $d_i$  is the difference between the two diameters; when the gap is less than 4 mm, the equivalent diameter to use for  $d_i$  is the hydraulic diameter determined using only the heated perimeter.

### 10.3.3 Gungor-Winterton Correlations

A new form of the Chen flow boiling model was proposed by Gungor and Winterton (1986), who put together a large database of 3,693 points from the literature for water, refrigerants (R-11, R-12, R-22, R-113 and R-114) and ethylene glycol for mostly vertical upflows and some vertical downflows. Their local two-phase flow boiling coefficient  $\alpha_{tp}$  is also the sum of the nucleate boiling contribution  $\alpha_{nb}$  and the convective contribution  $\alpha_{cb}$ , where their basic equation is

$$\alpha_{tp} = E\alpha_L + S\alpha_{nb} \quad [10.3.20]$$

Again,  $\alpha_L$  is calculated from the Dittus-Boelter (1930) correlation given by [10.3.4] using the local liquid fraction of the flow,  $\dot{m}(1-x)$ , while their nucleate pool boiling coefficient is obtained with the Cooper (1984b) nucleate pool boiling equation:

$$\alpha_{nb} = 55 p_r^{0.12} (-0.4343 \ln p_r)^{-0.55} M^{-0.5} q^{0.67} \quad [10.3.21]$$

The above equation is *dimensional* and gives the heat transfer coefficient in W/m<sup>2</sup>K. The heat flux  $q$  must be introduced in W/m<sup>2</sup>. M is the molecular weight and  $p_r$  is the reduced pressure, which is the ratio of the saturation pressure  $p_{sat}$  to the critical pressure  $p_{crit}$ . Their two-phase convection multiplier E is a function of the Martinelli parameter and also the heat flux via the Boiling number:

$$E = 1 + 24000Bo^{1.16} + 1.37 \left( \frac{1}{X_{tt}} \right)^{0.86} \quad [10.3.22]$$

where  $X_{tt}$  and Bo have been defined earlier. Their boiling suppression factor S is

$$S = \left[ 1 + 0.00000115 E^2 Re_L^{1.17} \right]^{-1} \quad [10.3.23]$$

with  $Re_L$  based on  $m(1-x)$ . Compared to their database, this method gave a mean deviation of  $\pm 21.4\%$  compared to  $\pm 57.7\%$  for the Chen (1963, 1966) correlation and  $\pm 21.9\%$  for the Shah (1982) correlation. Hence, as the Shah correlation was not developed using this database, this comparison gives a good independent credibility of its accuracy. Using the same equivalent diameter definitions as Shah above, Gungor and Winterton predicted evaporation in vertical annuli to a mean error of  $\pm 29.4\%$ .

Gungor and Winterton (1987) a year later proposed a newer, simpler version of this correlation based only on convective boiling:

$$\alpha_{tp} = E_{new} \alpha_L \quad [10.3.24]$$

Their new two-phase convection multiplier  $E_{new}$  is:

$$E_{new} = 1 + 3000Bo^{0.86} + 1.12 \left( \frac{x}{1-x} \right)^{0.75} \left( \frac{\rho_L}{\rho_V} \right)^{0.41} \quad [10.3.25]$$

where Bo has been defined earlier and  $\alpha_L$  is calculated as before. The accuracy was similar to their earlier correlation and this version has been recommended in Thome (1997a) as the better of the two compared to flow boiling data for R-134a.

### 10.3.4 Steiner-Taborek Asymptotic Model

**Natural limitations to flow boiling coefficients.** Before presenting a new prediction method, Steiner and Taborek (1992) stated that the following limits should apply to evaporation in vertical tubes:

- For heat fluxes below the threshold for the onset of nucleate boiling ( $q < q_{ONB}$ ), only the convective contribution should be counted and not the nucleate boiling contribution.
- For very large heat fluxes, the nucleate boiling contribution should dominate.
- When  $x = 0$ ,  $\alpha_{tp}$  should be equal to the single-phase liquid convective heat transfer coefficient when  $q < q_{ONB}$  but  $\alpha_{tp}$  should correspond to that plus  $\alpha_{nb}$  when  $q > q_{ONB}$ .
- When  $x = 1.0$ ,  $\alpha_{tp}$  should equal the vapor-phase convective coefficient  $\alpha_{Gt}$  (the forced convection coefficient with the total flow as vapor), assuming no liquid mist still exists in the flow at these conditions.

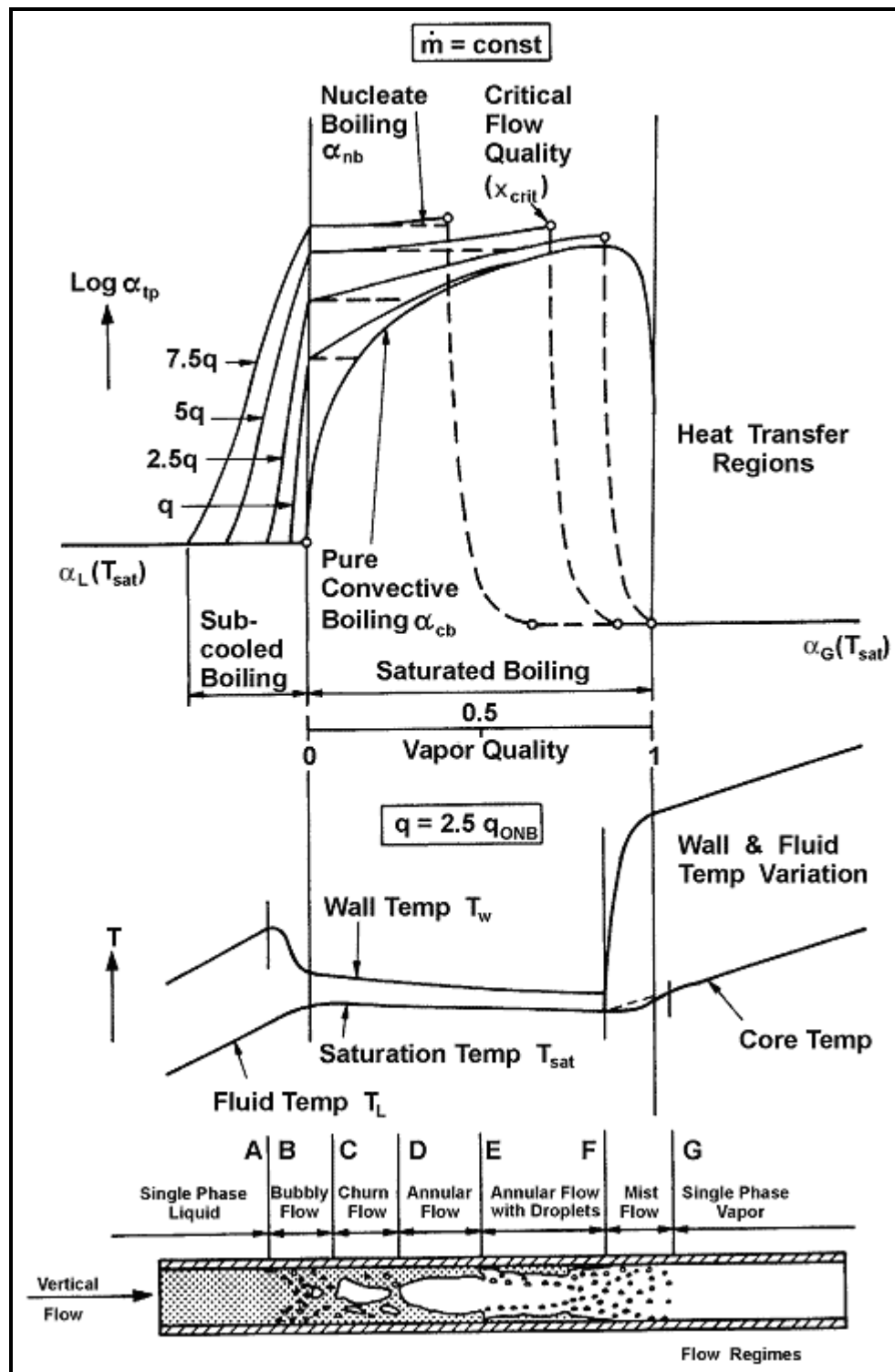


Figure 10.4. Boiling process in vertical tube according to Steiner-Taborek (1992).

Figure 10.4 illustrates the evolution of the heat transfer coefficient for evaporation in vertical tubes according to these limitations, which are further explained as follows:

- **Region A-B.** Before point A, only single-phase convection to the subcooled liquid occurs. Between points A and B, only liquid-phase convection occurs if  $q < q_{ONB}$  while subcooled boiling occurs if  $q > q_{ONB}$ . In subcooled boiling, bubbles grow and collapse near the tube wall, which increases heat transfer.
- **Region B-C-D.** When  $q < q_{ONB}$ , only convective evaporation occurs as indicated by the “pure convective boiling” curve. When  $q > q_{ONB}$ , both nucleate and convective boiling contributions are present and are superimposed. The horizontal dashed lines are the nucleate boiling coefficient at the particular heat flux. The solid curves are the superimposed contribution of nucleate boiling and convective boiling, that is  $\alpha_{tp}$ . The flow pattern passes through the bubbly flow and churn flow regimes as shown in the bottom diagram.
- **Region D-E-F.** When  $q < q_{ONB}$ , the process continues along the “pure convective boiling” curve up to the onset of dryout at high vapor qualities approaching 1.0. When  $q > q_{ONB}$ , the annular flow regime is reached, characterized by a thin turbulent annular liquid layer on the tube wall and a central vapor core, and continues up to the critical vapor quality  $x_{crit}$  reached where the annular film dries out.
- **Region F-G.** At  $x_{crit}$  the liquid film becomes unstable due to interfacial shear and adhesion forces. In the mist flow regime, the heat transfer mechanisms change completely, where heat is now transferred by vapor-phase convection, by evaporation of the entrained liquid droplets within the superheated vapor, by impingement of droplets on the wall and by radiation. (Note: the Steiner-Taborek model does *not* predict the dashed lines of the mist flow regime when  $x > x_{crit}$ ).

**Flow boiling model.** Based on the above premises, Steiner and Taborek (1992) proposed a comprehensive evaporation model for vertical tubes. Their local flow boiling coefficient is obtained from an asymptotic approach using an exponent n equal to 3 as:

$$\alpha_{tp} = \left[ (\alpha_{nb,o} F_{nb})^3 + (\alpha_{Lt} F_{tp})^3 \right]^{1/3} \quad [10.3.26]$$

In this expression, the parameters are as follows:

- $\alpha_{nb,o}$  is the local nucleate pool boiling coefficient at a reference heat flux  $q_0$  at the reduced pressure  $p_r$  equal to 0.1;
- $F_{nb}$  is the nucleate boiling correction factor (but is *not* a boiling suppression factor, which is not required in an asymptotic model);
- $\alpha_{Lt}$  is the local liquid-phase forced convection coefficient based on the *total* flow as liquid (not on the liquid fraction of the flow as in the above methods) and is obtained with the Gnielinski (1976) correlation and not the Dittus-Boelter (1930) correlation;
- $F_{tp}$  is the two-phase multiplier that accounts for enhancement of liquid convection by the higher velocity of a two-phase flow compared to single-phase flow of the liquid in the channel.

The Gnielinski correlation for obtaining  $\alpha_{Lt}$  is:

$$\frac{\alpha_{Lt} d_i}{k_L} = \frac{(f_L / 8)(Re_{Lt} - 1000)Pr_L}{1 + 12.7(f_L / 8)^{1/2}(Pr_L^{2/3} - 1)} \quad [10.3.27]$$

The Fanning friction factor,  $f_L$ , for the liquid is:

$$f_L = [0.7904 \ln(Re_{Lt}) - 1.64]^{-2} \quad [10.3.28]$$

This expression is valid when  $4000 < Re_{Lt} < 5000000$  and  $0.5 < Pr_L < 2000$  for single-phase flows. The total mass velocity of liquid plus vapor is used for evaluating the liquid Reynolds number, so that  $Re_{Lt}$  is:

$$Re_{Lt} = \frac{\dot{m}d_i}{\mu_L} \quad [10.3.29]$$

The two-phase multiplier  $F_{tp}$  is for convective evaporation, which will occur if  $x < x_{crit}$  and  $q > q_{ONB}$  or over the entire range of  $x$  if  $q < q_{ONB}$ . For applications where  $x < x_{crit}$  at the tube exit and  $q > q_{ONB}$ , such as power boilers and thermosyphon reboilers, the following equation is used:

$$F_{tp} = \left[ (1-x)^{1.5} + 1.9x^{0.6} \left( \frac{\rho_L}{\rho_G} \right)^{0.35} \right]^{1.1} \quad [10.3.30]$$

This expression covers  $(\rho_L/\rho_G)$  from 3.75 to 5000 and converges to 1.0 as  $x$  goes to 0.  $x_{crit}$  is often assumed to occur at about 0.5 for these applications.

When  $q < q_{ONB}$ , only pure convective evaporation is present, extending from  $x = 0.0$  to  $x = 1.0$ . At the limiting case at  $x = 1.0$ , the value of  $\alpha_{tp}$  corresponds to  $\alpha_{Gt}$ , which is the forced convection coefficient with the total flow as all vapor. The Gnielinski correlation is also used for obtaining  $\alpha_{Gt}$ :

$$\frac{\alpha_{Gt} d_i}{k_G} = \frac{(f/8)(Re_{Gt} - 1000)Pr_G}{1 + 12.7(f/8)^{1/2}(Pr_G^{2/3} - 1)} \quad [10.3.31]$$

The Fanning friction factor for the vapor,  $f_G$ , is:

$$f_G = [0.7904 \ln(Re_{Gt}) - 1.64]^{-2} \quad [10.3.32]$$

The total mass velocity of liquid plus vapor is used for evaluating the vapor Reynolds number, so that  $Re_{Gt}$  is:

$$Re_{Gt} = \frac{\dot{m}d_i}{\mu_G} \quad [10.3.33]$$

For this case, the following expression is used for  $F_{tp}$ :

$$F_{tp} = \left\{ \left[ (1-x)^{1.5} + 1.9x^{0.6}(1-x)^{0.01} \left( \frac{\rho_L}{\rho_G} \right)^{0.35} \right]^{-2.2} + \left[ \left( \frac{\alpha_G}{\alpha_L} \right) x^{0.01} \left( 1 + 8(1-x)^{0.7} \right) \left( \frac{\rho_L}{\rho_G} \right)^{0.67} \right]^{-2} \right\}^{-0.5} \quad [10.3.34]$$

This expression covers fluids with values of  $(\rho_L/\rho_G)$  from 3.75 to 1017. The terms with exponents of 0.01 make this expression go to its proper limits at  $x = 0$  and  $x = 1$ .

The minimum heat flux for determining the onset of nucleate boiling  $q_{ONB}$  is given by the following expression using the liquid-phase heat transfer coefficient  $\alpha_{Lt}$ :

$$q_{ONB} = \frac{2\sigma T_{sat} \alpha_{Lt}}{r_o \rho_G h_{LG}} \quad [10.3.35]$$

In this expression,  $\sigma$  is the surface tension,  $T_{sat}$  is the saturation temperature in Kelvin,  $r_o$  is the critical nucleation radius for a boiling site in meters and  $h_{LG}$  is the latent heat of vaporization. The recommended value for  $r_o$  is  $0.3 \times 10^{-6}$  m. For  $q > q_{ONB}$ , nucleate boiling is present in the flow boiling process but below this threshold it is not.

The nucleate boiling coefficient  $\alpha_{nb}$  is determined here with a method similar to the nucleate pool boiling method of Gorenflo (1993) but the method below is *not* exactly the same. The *standard* nucleate boiling coefficients for the Steiner-Taborek flow boiling correlation  $\alpha_{nb,o}$  are given in Table 10.1 at the following standard conditions: a reduced pressure of  $p_r = 0.1$ , a mean surface roughness of  $R_{p,o} = 1 \mu\text{m}$  and the heat flux  $q_o$  equal to the value listed for each fluid. The nucleate boiling correction factor  $F_{nb}$  includes the effects of reduced pressure, heat flux, tube diameter, surface roughness and a residual molecular weight correction factor on  $\alpha_{nb,o}$  as follows:

$$F_{nb} = F_{pf} \left( \frac{q}{q_o} \right)^{nf} \left( \frac{d_i}{d_{i,o}} \right)^{-0.4} \left( \frac{R_p}{R_{p,o}} \right)^{0.133} F(M) \quad [10.3.36]$$

The pressure correction factor  $F_{pf}$ , valid for  $p_r < 0.95$ , accounts for the increase in the nucleate boiling coefficient with increasing pressure:

$$F_{pf} = 2.816 p_r^{0.45} + \left\{ 3.4 + \left[ \frac{1.7}{1 - p_r^7} \right] \right\} p_r^{3.7} \quad [10.3.37]$$

The nucleate boiling exponent,  $nf$ , on the normalized heat flux term is:

$$nf = 0.8 - 0.1 \exp(1.75 p_r) \quad [10.3.38]$$

The above expression is for all fluids except cryogens (nitrogen, oxygen, etc.), where it is

$$nf = 0.7 - 0.13 \exp(1.105 p_r) \quad [10.3.39]$$

The standard tube reference diameter  $d_{i,o}$  is 0.01 m, i.e. 10 mm. The standard value of the surface roughness is  $R_{p,o} = 1 \mu\text{m}$  (typical of industrial tubes and the default value if  $R_p$  is unknown) and the surface roughness term covers values of  $R_p$  from 0.1 to 18  $\mu\text{m}$ . The residual molecular weight correction factor is in terms of the liquid molecular weight  $M$  (valid for  $10 < M < 187$ ):

$$F(M) = 0.377 + 0.199 \ln(M) + 0.000028427 M^2 \quad [10.3.40]$$

The maximum value of  $F(M)$  is 2.5, even when the expression gives a larger value. For cryogenic liquids H<sub>2</sub> and He, the values of  $F(M)$  are specifically 0.35 and 0.86, respectively.

Their method is based on an extensive database containing 10,262 data points for water and an additional 2345 data points for four refrigerants (R-11, R-12, R-22 and R-113), seven hydrocarbons (benzene, n-pentane, n-heptane, cyclo-hexane, methanol, ethanol and n-butanol), three cryogens (nitrogen, hydrogen and helium) and ammonia. It is currently regarded as the most accurate vertical tube boiling correlation available for pure fluids. However, it is difficult to extend its use to mixtures since there is no simple way to determine the values of  $\alpha_{nb,0}$  for mixtures.

**Table 10.1. Standard nucleate flow boiling coefficients of Steiner and Taborek (1992) for  $\alpha_{nb,0}$  in W/m<sup>2</sup> K at  $p_r = 0.1$  for  $q_o$  in W/m<sup>2</sup> and  $R_{p,o} = 1 \mu\text{m}$  with  $p_{crit}$  in bar.**

Fluid	$p_{crit}$	M	$q_o$	$\alpha_{nb,0}$
Methane	46.0	16.04	20000	8060
Ethane	48.8	30.07	20000	5210
Propane	42.4	44.10	20000	4000
n-Butane	38.0	58.12	20000	3300
n-Pentane	33.7	72.15	20000	3070
Isopentane	33.3	72.15	20000	2940
n-Hexane	29.7	86.18	20000	2840
n-Heptane	27.3	100.2	20000	2420
Cyclohexane	40.8	84.16	20000	2420
Benzene	48.9	78.11	20000	2730
Toluene	41.1	92.14	20000	2910
Diphenyl	38.5	154.2	20000	2030
Methanol	81.0	32.04	20000	2770
Ethanol	63.8	46.07	20000	3690
n-Propanol	51.7	60.10	20000	3170
Isopropanol	47.6	60.10	20000	2920
n-Butanol	49.6	74.12	20000	2750
Isobutanol	43.0	74.12	20000	2940
Acetone	47.0	58.08	20000	3270
R-11	44.0	137.4	20000	2690
R-12	41.6	120.9	20000	3290
R-13	38.6	104.5	20000	3910
R-13B1	39.8	148.9	20000	3380
R-22	49.9	86.47	20000	3930
R-23	48.7	70.02	20000	4870
R-113	34.1	187.4	20000	2180
R-114	32.6	170.9	20000	2460
R-115	31.3	154.5	20000	2890
R-123	36.7	152.9	20000	2600
R-134a	40.6	102.0	20000	3500
R-152a	45.2	66.05	20000	4000
R-226	30.6	186.5	20000	3700
R-227	29.3	170.0	20000	3800
RC318	28.0	200.0	20000	2710

Fluid	$p_{crit}$	M	$q_o$	$\alpha_{nb,o}$
R-502	40.8	111.6	20000	2900
Chloromethane	66.8	50.49	20000	4790
Tetrachloromethane	45.6	153.8	20000	2320
Tetrafluoromethane	37.4	88.00	20000	4500
Helium I £	2.275	4.0	1000	1990
Hydrogen (para)	12.97	2.02	10000	12220
Neon	26.5	20.18	10000	8920
Nitrogen	34.0	28.02	10000	4380
Argon	49.0	39.95	10000	3870
Oxygen	50.8	32.00	10000	4120
Water	220.6	18.02	150000	25580
Ammonia	113.0	17.03	150000	36640
Carbon Dioxide +	73.8	44.01	150000	18890
Sulfur Hexafluoride	37.6	146.1	150000	12230

£ Physical properties at  $p_r = 0.3$  rather than 0.1;

+ Calculated with properties at  $T_{crit}$ .

## 10.4 Flow Boiling inside Horizontal Plain Tubes

Flow patterns formed during the generation of vapor in horizontal evaporator tubes are shown in Figure 10.5 taken from Collier and Thome (1994). The schematic representation of a horizontal tubular channel heated by a uniform low heat flux and fed with liquid just below the saturation temperature for a relatively low inlet velocity illustrates the sequence of flow patterns that might be observed. Asymmetric distributions of the vapor and liquid phases due to the effects of gravity introduce new complications compared to vertical upflow. Important points to note from a heat transfer standpoint are the possibility of complete drying or intermittent drying of the tube wall around part of the tube perimeter, particularly in slug and wavy flow and for annular flow with partial dryout. For example, in annular flow the film is thicker at the bottom than at the top, meaning the dryout tends to begin at the top and progressively increases around the perimeter of the tube in the direction of flow. In wavy flow, the top of the tube may be intermittently dry if the waves wash the top of the tube or always dry if they do not. These waves leave behind thin films of liquid that may or may not evaporate completely before the arrival of the next wave. The more widely quoted methods for predicting two-phase flow boiling heat transfer coefficients inside plain horizontal tubes are presented below.

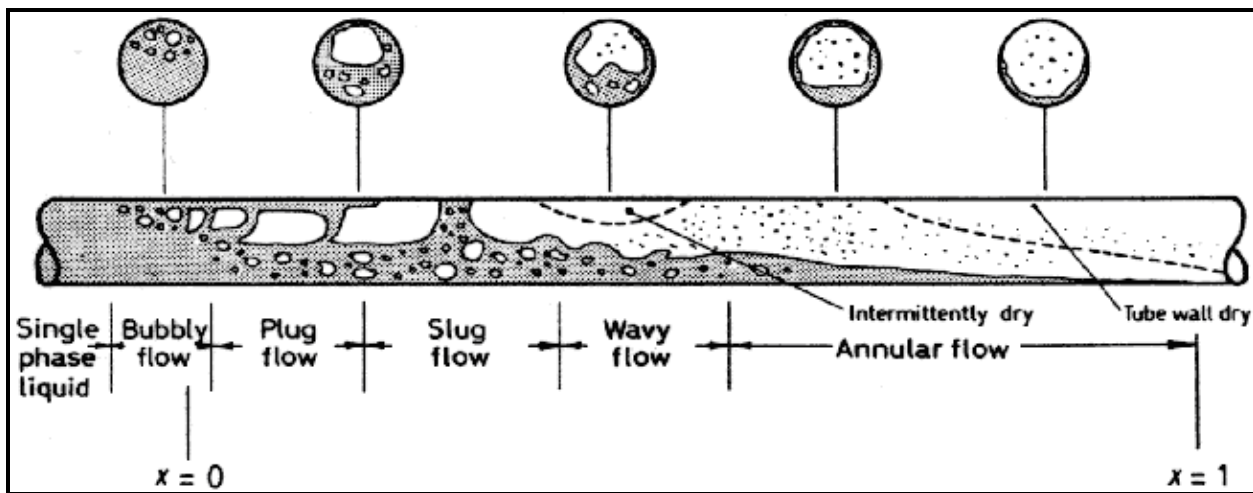


Figure 10.5. Flow patterns during evaporation in a horizontal tube from Collier and Thome (1994).

#### 10.4.1 Vertical Tube Methods Applied to Horizontal Tubes

Many of the methods for predicting local flow boiling heat transfer coefficients in *horizontal* plain tubes are adaptations of *vertical* tube methods to horizontal test data, such as those of Shah (1982), Gungor and Winterton (1986, 1987), Klimenko (1988), Kandlikar (1990) and Wattelet et al. (1994). For instance, Shah (1982) made the following adjustments to his vertical tube method presented earlier. He set a threshold between stratified and non-stratified flow using the liquid Froude number  $Fr_L$ , defined as:

$$Fr_L = \frac{\dot{m}^2}{\rho_L^2 g d_i} \quad [10.4.1]$$

For  $Fr_L < 0.04$ , the flow is stratified and above 0.04 the flow is non-stratified. When  $Fr_L > 0.04$ , his vertical tube method is used without change with  $N = C_o$ . When  $Fr_L < 0.04$ , instead, the value of  $N$  is modified by the liquid Froude number  $Fr_L$  as:

$$N = 0.38 Fr_L^{-0.3} C_o \quad [10.4.2]$$

This correction has the tendency to reduce the two-phase flow boiling heat transfer coefficient at low mass velocities but leaves them unchanged at large mass velocities. It does not however account for the effect of vapor quality on the transition from stratified to non-stratified flow. Gungor and Winterton (1986) followed his example, setting their threshold value a little higher at  $Fr_L < 0.05$ . When  $Fr_L > 0.05$ , their vertical tube method is used without change but when  $Fr_L < 0.05$ , their factor  $E$  is corrected as follows

$$E_2 = Fr_L^{(0.1-2Fr_L)} \quad [10.4.3]$$

Thus, thus new parameter  $E_2$  is applied as a multiplier to  $E$  in their method. Their boiling suppression factor  $S$ , is similarly multiplied by the another correction factor

$$S_2 = (Fr_L)^{1/2} \quad [10.4.4]$$

These two corrections again have the tendency to reduce the two-phase flow boiling heat transfer coefficient at low mass velocities but leaves them unchanged at large mass velocities. Kandlikar (1990) also set his stratification threshold at  $Fr_L = 0.05$ . Noting the difference in the trends in their heat transfer coefficients, Wattelet et al. (1994) classified their data as annular or stratified flow and set their stratification threshold to a much larger value of  $Fr_L = 0.25$ . It is worth emphasizing, however, that the liquid Froude number  $Fr_L$  is not a reliable approach for predicting the onset of stratification, as shown in a direct comparison to experimental flow observations for various refrigerants by Kattan, Thome and Favrat (1995a). This threshold criterion is in fact off by as much as 10 to 16 times in numerous instances! Hence, the above methods do not tend to predict heat transfer in stratified types of flow reliably nor accurately.

Never the less, the methods mentioned above do tend to predict heat transfer reasonably well in the annular flow regime. Their shortcomings can be summarized as follows:

- They only recognize stratified and non-stratified flows but not the different flow patterns occurring in horizontal flow boiling, and they tend to poorly predict the threshold from unstratified to stratified flow;
- Their local boiling coefficients plotted versus local vapor quality at a fixed heat flux  $q$ , that is a plot of  $\alpha_{tp}$  vs.  $x$ , often do not represent the experimental trends nor the slope in  $\alpha_{tp}$  vs.  $x$ ;
- They do not account for the onset of dryout in annular flow at high vapor qualities and hence these methods are incapable of predicting the sharp peak in  $\alpha_{tp}$  vs.  $x$  found in many experimental data sets nor do they predict the subsequent sharp decline in  $\alpha_{tp}$  after the onset of dryout at the top of the tube in annular flows at high vapor qualities. Hence, they often overpredict heat transfer in this region by 100% to 300% or more;
- They attempt to model annular flow by modifying a *tubular* flow correlation (Dittus-Boelter) as opposed to modelling the liquid film using a *film* flow approach.

The foregoing flow boiling correlations therefore do not qualify as general methods, especially for stratified types of flows nor for local conditions with partial dryout on the top perimeter of the tube. In their favor, however, these methods are comprised of a small set of equations and are easy to quickly implement.

#### **10.4.2 Local Flow Pattern Evaporation Model of Kattan-Thome-Favrat**

A more phenomenological approach, incorporating the local two-phase flow structure as a function of the local flow pattern, has been proposed by Kattan, Thome and Favrat (1998a, 1998b, 1998c). Their method is based on their own two-phase flow pattern map for horizontal evaporating flows (described separately in the chapter on two-phase flow patterns). So far, their flow boiling model covers fully stratified flows, stratified-wavy flows, intermittent flows, annular flows and annular flows with partial dryout. Plug and slug flows are classified as intermittent flows, in which the tube wall is assumed to always remain wet by frequent passing of large amplitude waves that leave behind a liquid film on the top of the tube. Intermittent flows have a very complex flow structure and were for simplicity modelled as annular flows with reasonable success. Similarly, annular flow with partial dryout is classified as a form of stratified-wavy flow and is modelled as such. Heat transfer in bubbly and mist flow regimes are not currently addressed in their model.

Figure 10.6 depicts the simplified two-phase flow structures they assumed to represent the fully-stratified, stratified-wavy and annular flow regimes. For fully-stratified flow, the liquid flows in the bottom of the tube with essentially an undisturbed flat horizontal interface with the vapor above; taking the same wetted perimeter as for the flat surface, it is assumed that the equivalent heat transfer process is to a liquid film of thickness  $\delta$  whose cross-sectional area  $A_L$  is equal to that of the stratified area of the liquid. For annular

flow (and intermittent flow), the liquid fraction is assumed to all be in the annular film on the tube wall, again designated by a film thickness  $\delta$ . For stratified-wavy flow (and annular flow with partial dryout), the truncated annular ring varies around the perimeter of the tube from the lower fully-stratified limit up to the annular limit.

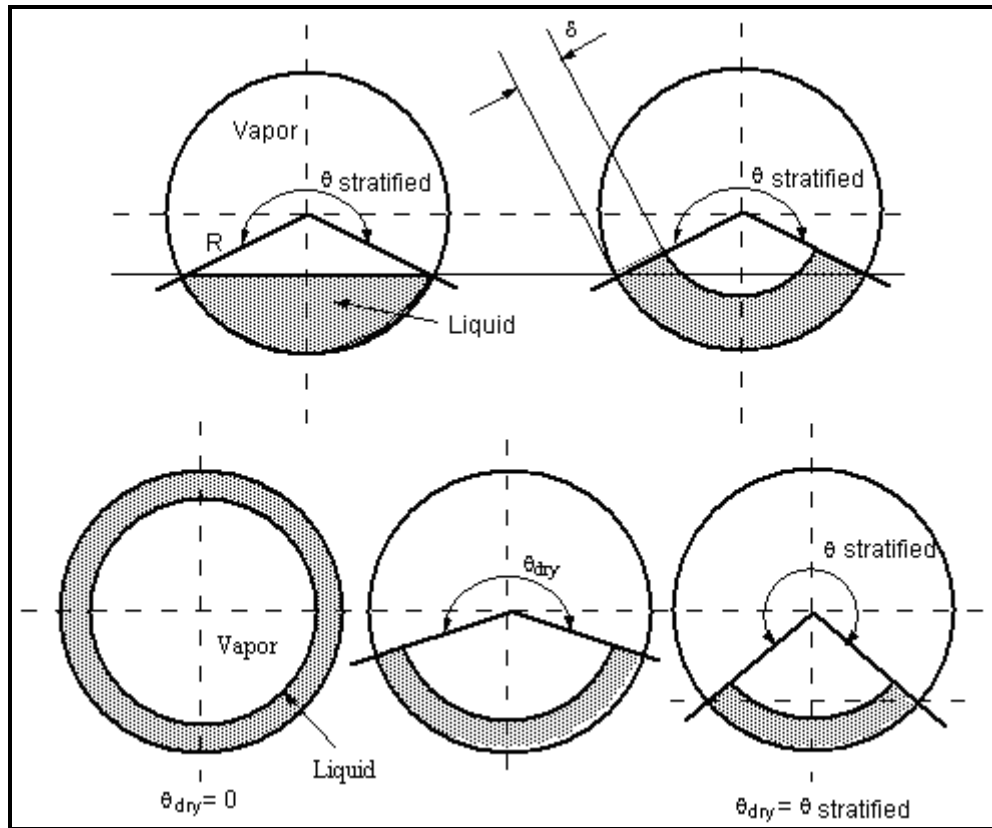


**Figure 10.6. Geometric illustration of liquid and vapor areas, stratified and dry angles, and liquid film thickness in the flow boiling model.**

The general equation for the local flow boiling coefficient  $\alpha_{tp}$  for evaporation in a horizontal, plain tube in the Kattan-Thome-Favrat method for an internal tube diameter of  $d_i$  is:

$$\alpha_{tp} = \frac{d_i \theta_{dry} \alpha_{vapor} + d_i (2\pi - \theta_{dry}) \alpha_{wet}}{2\pi d_i} \quad [10.4.5]$$

The dry perimeter of the tube, if any, is given by the dry angle  $\theta_{dry}$  and the heat transfer coefficient on this surface is  $\alpha_{vapor}$ . On the wetted perimeter, the heat transfer coefficient is  $\alpha_{wet}$ , which is obtained from an asymptotic expression that combines the nucleate boiling  $\alpha_{nb}$  and convective boiling  $\alpha_{cb}$  contributions using an exponent of three as:

$$\alpha_{wet} = (\alpha_{nb}^3 + \alpha_{cb}^3)^{1/3} \quad [10.4.6]$$

The *dimensional* reduced pressure correlation of Cooper (1984b) is used to determine  $\alpha_{nb}$ :

$$\alpha_{nb} = 55 p_r^{0.12} (-\log_{10} p_r)^{-0.55} M^{-0.5} q^{0.67} \quad [10.4.7]$$

The surface roughness in his expression has been set equal to his standard surface roughness factor ( $1.0 \mu\text{m}$ ), such that the surface correction factor equals 1.0 and disappears from the above expression. In applying his correlation,  $\alpha_{nb}$  is in  $\text{W/m}^2\text{K}$ ,  $p_r$  is the reduced pressure,  $M$  is the liquid molecular weight and  $q$  is the heat flux at the tube wall in  $\text{W/m}^2$ . His multiplier of 1.7 for copper tubes is ignored.

Visualizing the annular ring of liquid more realistically as a *film* flow rather than as a *tubular* flow, the convective boiling heat transfer coefficient  $\alpha_{cb}$  is predicted as follows:

$$\alpha_{cb} = 0.0133 \left[ \frac{4\dot{m}(1-x)\delta}{(1-\varepsilon)\mu_L} \right]^{0.69} \left[ \frac{c_{pL}\mu_L}{k_L} \right]^{0.4} \frac{k_L}{\delta} \quad [10.4.8]$$

where 0.0133 and 0.69 are empirical constants determined from their original database for five refrigerants and are generally applicable to other fluids for turbulent annular films. The term in the first bracket is the liquid film Reynolds number  $Re_L$  while the second bracket represents the liquid Prandtl number  $Pr_L$ . The mean liquid velocity in the cross-section of the tube occupied by the liquid is used in this definition of the liquid Reynolds number, which is a function of the vapor quality  $x$ , annular liquid film thickness  $\delta$ , and vapor void fraction  $\varepsilon$ .

Assuming *tubular* flow on the dry perimeter of the tube at the mass velocity of the vapor,  $\dot{m}_x$ , the vapor-phase heat transfer coefficient  $\alpha_{vapor}$  is obtained with the Dittus-Boelter (1930) turbulent flow heat transfer correlation:

$$\alpha_{vapor} = 0.023 \left[ \frac{\dot{m}_x d_i}{\varepsilon \mu_G} \right]^{0.8} \left[ \frac{c_{pG}\mu_G}{k_G} \right]^{0.4} \frac{k_G}{d_i} \quad [10.4.9]$$

The vapor Reynolds number  $Re_G$  in the first bracketed term is based on the mean vapor velocity in the cross-section of the tube occupied by the vapor.

The dry angle  $\theta_{dry}$  around the top of the tube is the angle of the tube wall that is assumed to be constantly dry for stratified types of flows and annular flows with partial dryout. For annular and intermittent flows, the entire tube perimeter is always wet and hence  $\theta_{dry}$  is equal to zero; thus for these latter two flow regimes,  $\alpha_{tp}$  is equal to  $\alpha_{wet}$  (intermittent flow is modelled as annular film flow for heat transfer purposes). In addition,  $k_L$  and  $k_G$  are the liquid and vapor thermal conductivities,  $c_{pL}$  and  $c_{pG}$  are the liquid and vapor specific heats, and  $\mu_L$  and  $\mu_G$  are the liquid and vapor dynamic viscosities. The total mass velocity of the liquid plus vapor through the tube is  $\dot{m}$  and  $x$  is the local vapor quality. Methods for determining  $\theta_{dry}$ ,  $\varepsilon$  and  $\delta$  are described below.

The vapor void fraction  $\varepsilon$  is predicted using the drift flux void fraction model of Rouhani-Axelsson (1970) for vertical tubes that was modified by Steiner (1993) for horizontal tubes:

$$\varepsilon = \frac{x}{\rho_G} \left\{ \left[ 1 + 0.12(1-x) \right] \left( \frac{x}{\rho_G} + \frac{1-x}{\rho_L} \right) + \frac{1.18}{\dot{m}} \left[ \frac{g\sigma(\rho_L - \rho_G)}{\rho_L^2} \right]^{1/4} (1-x) \right\}^{-1} \quad [10.4.10]$$

where  $\dot{m}$  is the total mass velocity of liquid and vapor,  $x$  is the local vapor quality,  $\rho_L$  and  $\rho_G$  are the liquid and vapor densities, and  $\sigma$  is the surface tension (all in SI units). The cross-sectional area of the tube occupied by the liquid-phase  $A_L$  is obtained using the cross-sectional void fraction  $\varepsilon$  as:

$$A_L = A(1 - \varepsilon) \quad [10.4.11]$$

where  $A$  is the total internal cross-sectional area of the tube. For the fully stratified flow regime as illustrated in Figure 10.6, the stratified angle  $\theta_{\text{strat}}$  (in radians) of the liquid layer in the lower part of the tube is:

$$A_L = 0.5r_i^2[(2\pi - \theta_{\text{strat}}) - \sin(2\pi - \theta_{\text{strat}})] \quad [10.4.12]$$

The above equation is an implicit geometrical expression and is solved iteratively to find the value of the stratified angle  $\theta_{\text{strat}}$  using the value of  $A_L$  where  $r_i$  is the internal radius of the tube. The dry angle  $\theta_{\text{dry}}$  varies from its lower limit of  $\theta_{\text{dry}} = 0$  for annular flow with complete wall wetting at the mass velocity  $\dot{m}_{\text{high}}$  to its maximum value of  $\theta_{\text{dry}} = \theta_{\text{strat}}$  for fully stratified flow at the mass velocity  $\dot{m}_{\text{low}}$ . The transition boundary from the intermittent and annular flow regimes to stratified-wavy flow  $\dot{m}_{\text{wavy}}$  is used for  $\dot{m}_{\text{high}}$  while  $\dot{m}_{\text{strat}}$  is used for  $\dot{m}_{\text{low}}$  (refer to the Kattan-Thome-Favrat flow pattern map in the respective chapter). To determine  $\theta_{\text{dry}}$ , a simple linear interpolation between  $\dot{m}_{\text{high}}$  and  $\dot{m}_{\text{low}}$  is assumed when  $x < x_{\text{max}}$  as illustrated in Figures 10.6 and 10.7:

$$\theta_{\text{dry}} = \theta_{\text{strat}} \frac{(\dot{m}_{\text{high}} - \dot{m})}{(\dot{m}_{\text{high}} - \dot{m}_{\text{low}})} \quad [10.4.13]$$

Thus,  $\theta_{\text{dry}}$  changes as the values of  $\dot{m}_{\text{high}}$  and  $\dot{m}_{\text{low}}$  change with  $x$  in the above expression.

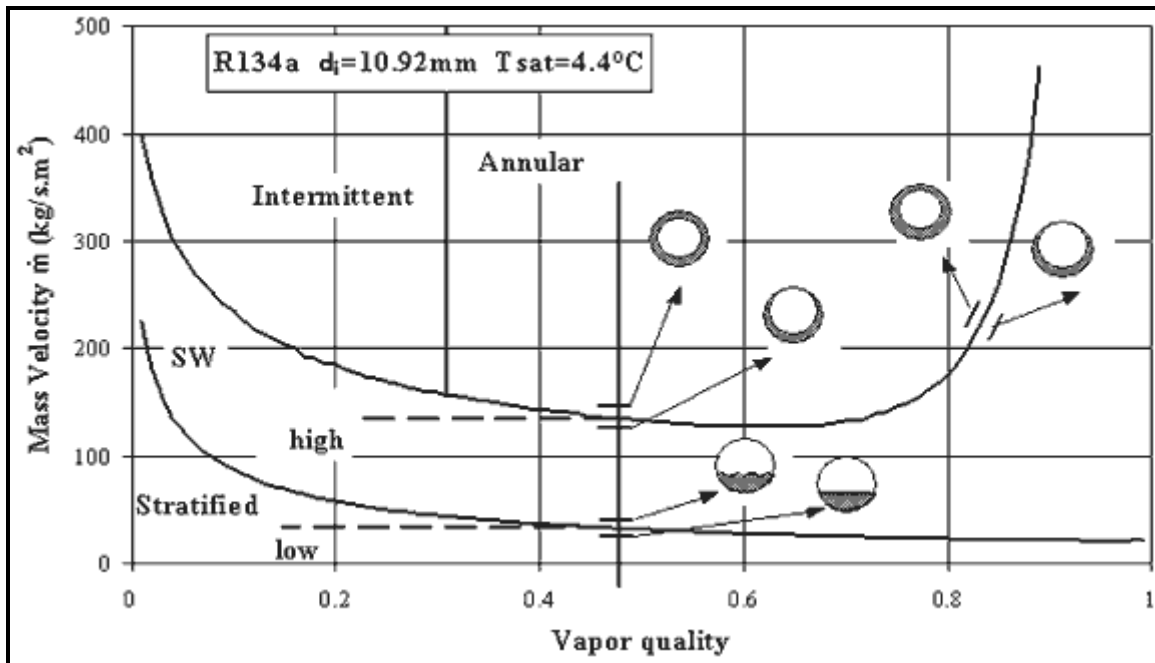


Figure 10.7. Two-phase flow pattern map showing low and high locations when  $x < x_{\text{max}}$ .

The annular liquid film thickness  $\delta$  is determined by equating the cross-sectional area occupied by the liquid phase  $A_L$  for this particular void fraction and dry angle to the area of a truncated annular liquid ring, assuming the thickness  $\delta$  is small compared to the tube radius  $r_i$ :

$$\delta = \frac{A_L}{r_i(2\pi - \theta_{dry})} = \frac{A(1-\varepsilon)}{r_i(2\pi - \theta_{dry})} = \frac{\pi d_i(1-\varepsilon)}{2(2\pi - \theta_{dry})} \quad [10.4.14]$$

When  $x > x_{max}$ , an additional step is required to determine  $\theta_{dry}$  as shown in Figure 10.8. Since  $\dot{m}_{high}$  in this case passes the intersection of the  $\dot{m}_{wavy}$  and  $\dot{m}_{mist}$  curves, when  $x > x_{max}$  there is no  $\dot{m}_{wavy}$  curve for determining  $\dot{m}_{high}$  and thus the dry angle  $\theta_{dry}$  is prorated horizontally:

$$\theta_{dry} = (2\pi - \theta_{max}) \frac{(x - x_{max})}{(1 - x_{max})} + \theta_{max} \quad [10.4.15]$$

assuming that it varies linearly between the values of  $\theta_{max}$  and  $2\pi$ , the latter which is the upper limit at  $x = 1$ , and  $\theta_{max}$  is determined from Equation (10.4.13) with  $x = x_{max}$ .

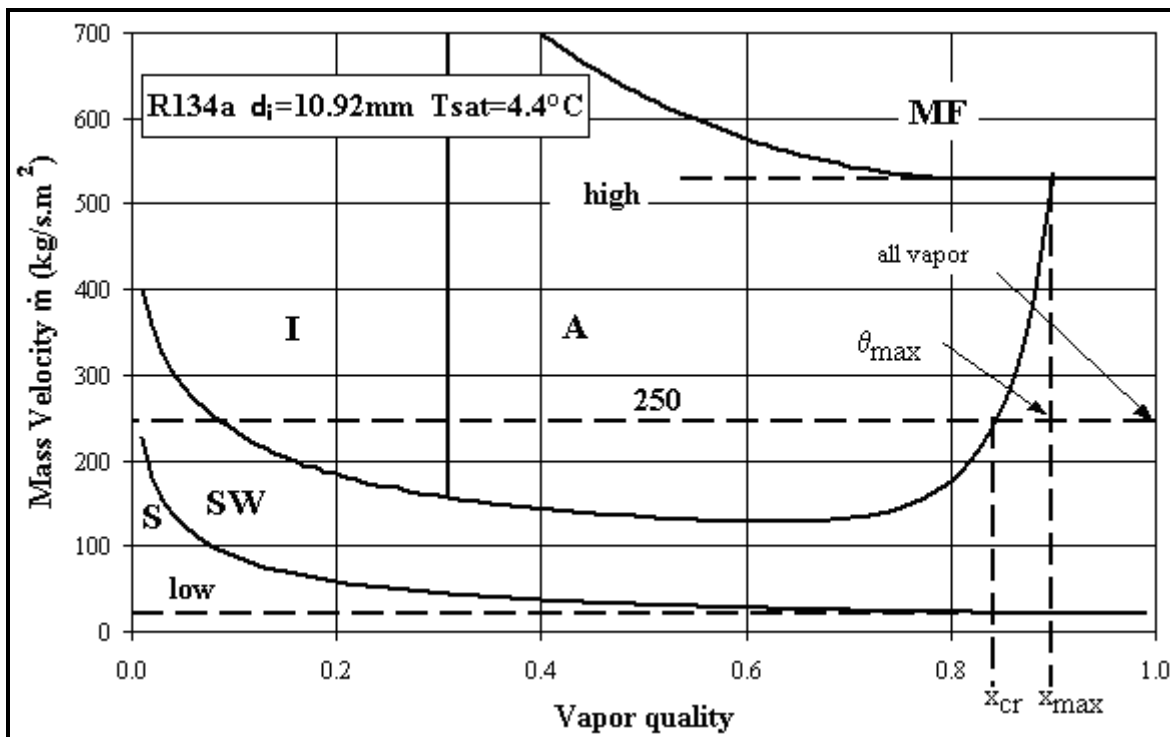


Figure 10.8. Dry angle  $\theta_{dry}$  when  $x > x_{max}$ .

Zürcher, Thome and Favrat (1999) extended application of the Kattan-Thome-Favrat model to evaporation of ammonia for mass velocities as low as  $16.3 \text{ kg/m}^2\text{s}$  ( $11773 \text{ lb/h ft}^2\text{s}$ ), reduced pressures as low as  $0.0085$  and heat fluxes as high as  $71.6 \text{ kW/m}^2$  ( $22700 \text{ Btu/h ft}^2$ ) for stainless and carbon steel tubes. Overall, the Kattan-Thome-Favrat flow boiling model has so far been verified over the following range of conditions:

- $1.12 \leq p_{sat} \leq 8.9 \text{ bar}$  ( $16.2\text{-}129.0 \text{ psia}$ );

- $0.0085 \leq p_r \leq 0.225$ ;
- $16.3 \leq \dot{m} \leq 500 \text{ kg/m}^2\text{s}$  ( $11,773$ - $367,900 \text{ lb/h ft}^2\text{s}$ );
- $0.01 \leq x \leq 1.0$ ;
- $440 \leq q \leq 71,600 \text{ W/m}^2$  ( $140$ - $22700 \text{ Btu/h ft}^2$ );
- $17.03 \leq M \leq 152.9$  (not including values up to about 300 obtained with refrigerant-oil mixtures);
- $74 \leq Re_L \leq 20399$  and  $1,300 \leq Re_G \leq 376,804$ ;
- $1.85 \leq Pr_L \leq 5.47$  (but  $Pr_L$  values up to 134 including tests with refrigerant-oil mixtures);
- $0.00016 \leq \mu_L \leq 0.035 \text{ Ns/m}^2$  (0.16 to 35 cp, including results for refrigerant-oil mixtures);
- $10.9 \leq d_i \leq 16.0 \text{ mm}$  (0.43-0.63 in. but now being compared to a much wider range);
- Fluids: R-134a, R-123, R-502, R-402A, R-404A, R-407C and ammonia;
- Tube metals: copper, carbon steel and stainless steel.

For annular flows, its accuracy is similar to those of the Shah (1982), Jung et al. (1989), and Gungor-Winterton (1986, 1987) correlations, except that these latter methods do not know when annular flow exists nor do they get the correct slope in  $\alpha_{tp}$  vs.  $x$ . When the flow is stratified-wavy, the Kattan-Thome-Favrat model is twice as accurate as the best of these other methods, even though these others have stratified flow threshold criteria and corresponding heat transfer correction factors. For  $x > 0.85$  typical of direct-expansion evaporator applications, the Kattan-Thome-Favrat model is three times more accurate than the best of these other methods, which have standard deviations of  $\pm 80\%$  or more.

Including the update to the wavy flow and stratified flow transition equations in the flow pattern map by Zürcher, Thome and Favrat (1999), Figure 10.9 presents the flow pattern map and heat transfer coefficients predicted by the above Kattan-Thome-Favrat heat transfer model. The simulation is for saturated n-butane at  $60^\circ\text{C}$  ( $140^\circ\text{F}$ ) and 6.4 bar (92.8 psia), a heat flux of  $15 \text{ kW/m}^2$  ( $4756 \text{ Btu/h ft}^2$ ), and an internal tube diameter of 19.86 mm (0.782 in.). The following comments can be made:

- All local heat transfer coefficients are *continuous* from one flow regime to another without any step changes in the values of  $\alpha_{tp}$ ;
- For  $\dot{m} = 20 \text{ kg/m}^2\text{s}$  ( $14716 \text{ lb/h ft}^2\text{s}$ ), *fully stratified flow* occurs at all values of  $x$  and  $\alpha_{tp}$  declines monotonically with increasing  $x$  as the dry angle increases;
- For  $\dot{m} = 60 \text{ kg/m}^2\text{s}$  ( $44150 \text{ lb/h ft}^2\text{s}$ ), *stratified-wavy flow* occurs at all  $x$  with a moderate peak in  $\alpha_{tp}$  vs.  $x$ ;
- For  $\dot{m} = 200 \text{ kg/m}^2\text{s}$  ( $147160 \text{ lb/h ft}^2\text{s}$ ) and  $x \leq 0.4$ , *intermittent flow* occurs with a moderate rise in  $\alpha_{tp}$  vs.  $x$ ;
- For  $\dot{m} = 200 \text{ kg/m}^2\text{s}$  ( $147160 \text{ lb/h ft}^2\text{s}$ ) and  $0.4 < x < 0.93$ , *annular flow* occurs with an increasing rise in  $\alpha_{tp}$  vs.  $x$  as the annular film thins out up to the onset of dryout at  $x = 0.93$ ;
- For  $\dot{m} = 200 \text{ kg/m}^2\text{s}$  ( $14720 \text{ lb/h ft}^2\text{s}$ ) and  $x \geq 0.93$ , *annular flow with partial dryout* (modelled as stratified-wavy flow) occurs with a sharp decline in  $\alpha_{tp}$  vs.  $x$ .

Also, in this model the heat transfer coefficient goes to its natural limit at  $x = 1.0$ , i.e. single-phase turbulent flow of all the flow as vapor. However, for  $x = 0$  the convective boiling heat transfer coefficient  $\alpha_{cb}$  for liquid *film* flow does not go to its natural limit of the *tubular* value. Hence, when  $x = 0$ ,  $\alpha_{cb}$  should be obtained with either the Dittus-Boelter or Gnielinski correlation given earlier.

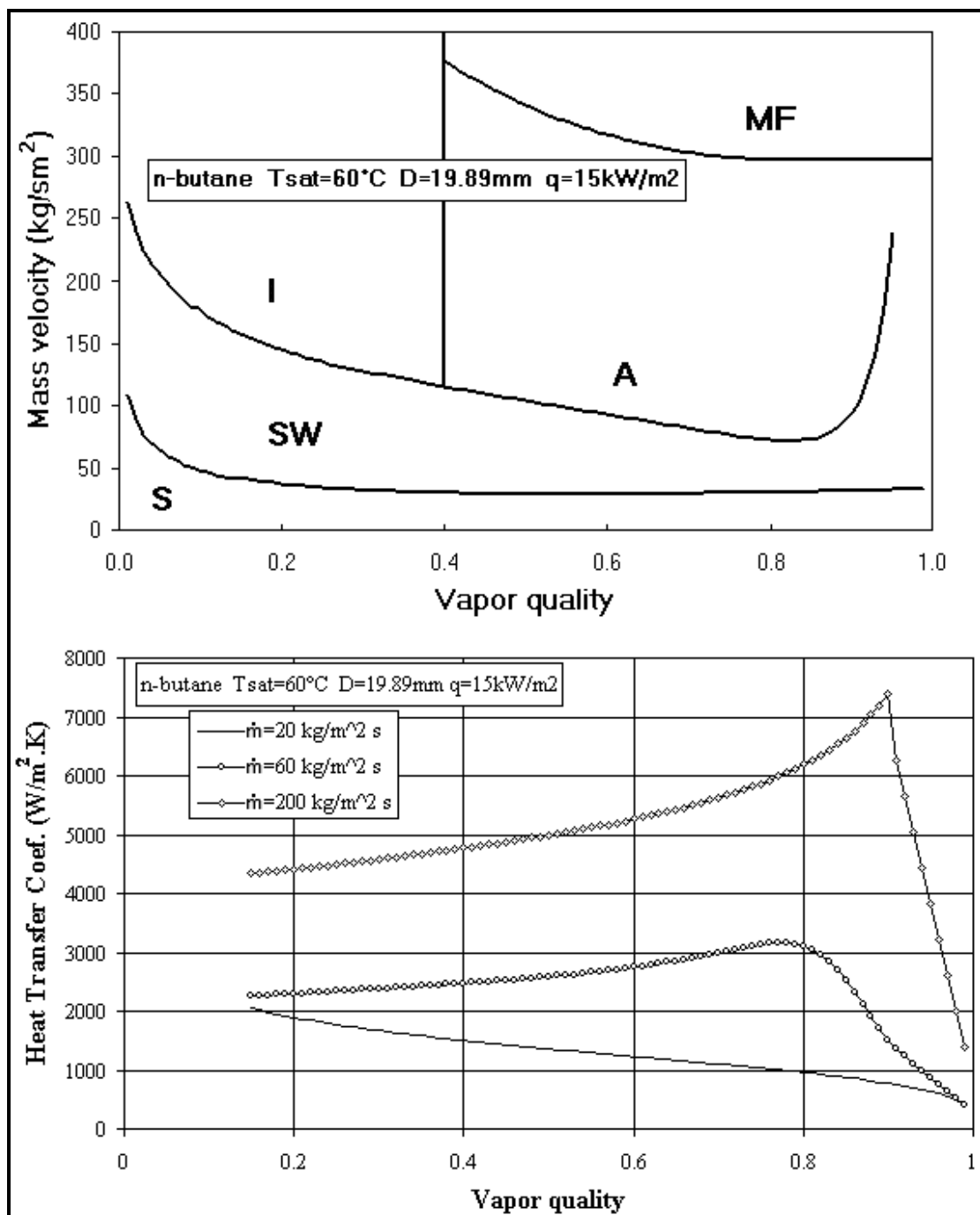


**Figure 10.9. Flow pattern map and heat transfer for pure n-butane at 60°C using Kattan-Thome-Favrat model.**

#### 10.4.3 Evaporation of Mixtures

The Kattan-Thome-Favrat model was formulated as a general model for pure fluids, azeotropic mixtures and multi-component zeotropic mixtures. Multi-component zeotropic mixtures, i.e. mixtures with two or more components, experience a temperature glide during evaporation, such as the three-component mixture R-407C. The effect of liquid-phase mass transfer on the nucleate boiling contribution to flow

boiling was included by introducing the Thome (1989) mixture boiling equation into the Cooper correlation, whose analytical mass transfer resistance factor  $F_c$  for nucleate pool boiling of mixtures is a function of the boiling range  $\Delta T_{bp}$ , i.e. the dew point temperature minus the bubble point temperature of the mixture at its local liquid composition. His factor  $F_c$  is:

$$F_c = \left\{ 1 + \left( \alpha_{id}/q \right) \Delta T_{bp} \left[ 1 - \exp \left( \frac{-q}{\rho_L h_{LG} \beta_L} \right) \right] \right\}^{-1} \quad [10.4.16]$$

In this expression,  $F_c < 1.0$  for zeotropic mixtures since  $\Delta T_{bp} > 0$  but  $F_c = 1.0$  for pure fluids and azeotropes since for these fluids  $\Delta T_{bp} = 0$ . The nucleate boiling heat transfer coefficient for zeotropic mixtures is thus obtained by including  $F_c$  in the Cooper correlation to give:

$$\alpha_{nb} = 55 p_r^{0.12} (-\log_{10} p_r)^{-0.55} M^{-0.5} q^{0.67} F_c \quad [10.4.17]$$

where  $q$  is the total local heat flux and  $p_r$  and  $M$  are those of the liquid mixture. The mass transfer coefficient  $\beta_L$  is a fixed value of 0.0003 m/s based on comparisons to numerous experimental pool boiling studies by Thome and coworkers for hydrocarbon and aqueous mixtures with from two to five components. The ideal heat transfer coefficient  $\alpha_{id}$  is first determined with [10.4.17] with  $F_c$  set equal 1.0. This method is valid for boiling ranges up to about 30 K (54°F) and hence covers many of the zeotropic refrigerant blends and hydrocarbon mixtures of industrial interest.

As an example of its application, Zürcher, Thome and Favrat (1998a) successfully compared the above method to their R-407C flow boiling data. The same approach has also been applied to the vertical tube boiling correlation of Gungor and Winterton (1986).

#### **10.4.4 Instructions for Implementation of Kattan-Thome-Favrat Model**

The Kattan-Thome-Favrat flow boiling model requires more steps than prior methods and the following is a step-by-step procedure for its implementation for a given tube internal diameter, specific design conditions (tube diameter, mass velocity, heat flux, pressure and vapor quality) and fluid physical properties. The steps are as follows:

1. Determine the local flow pattern corresponding to the local design condition using the Kattan-Thome-Favrat flow pattern map (refer to the chapter on flow pattern maps);
2. Calculate the local vapor void fraction  $\varepsilon$ ;
3. Calculate the local liquid cross-sectional area  $A_L$ ;
4. If the flow is annular or intermittent, determine  $\delta$  with  $\theta_{dry}$  set to 0;
5. If the flow is stratified-wavy (note that the flow pattern map classifies annular flow with partial dryout at the top of the tube as being stratified-wavy), iteratively calculate  $\theta_{strat}$ , then the values of  $\dot{m}_{high}$  and  $\dot{m}_{low}$  at  $x$  are used to calculate  $\theta_{dry}$  using the method for  $x \leq x_{max}$  or  $x > x_{max}$ , and then  $\delta$  is determined with this value of  $\theta_{dry}$ ;
6. If the flow is fully stratified, iteratively calculate  $\theta_{strat}$  and then determine  $\delta$  setting  $\theta_{strat}$  equal to  $\theta_{dry}$ ;
7. Determine  $\alpha_{cb}$ ;
8. Calculate  $\alpha_{vapor}$  if part of the wall is dry;
9. If the fluid is a pure, single-component liquid or an azeotropic mixture, directly determine  $\alpha_{nb}$  using the total local heat flux  $q$ ;

10. If the fluid is a zeotropic mixture, determine  $\alpha_{id}$ ,  $F_c$  and then  $\alpha_{nb}$ ;
11. Calculate  $\alpha_{wet}$  using the values of  $\alpha_{nb}$  and  $\alpha_{cb}$ ;
12. Determine the local flow boiling coefficient  $\alpha_{tp}$ .

### 10.4.5 Updated Version of Kattan-Thome-Favrat Model

The Kattan-Thome-Favrat flow boiling model has been updated by improvements to its flow pattern map in Wojtan, Ursenbacher and Thome (2005a) and to its heat transfer model in Wojtan, Ursenbacher and Thome (2005b). For changes to their diabatic two-phase flow pattern map, refer to Chapter 12. The improvements to the flow boiling heat transfer model are described below. Basically, changes to the heat transfer model were made to (i) incorporate the three new subzones of the stratified-wavy region that requires a new approach in the dry angle calculation, (ii) the annular flow zone has been modified by addition of a fixed nucleate boiling suppression factor to better reflect their experimental results, (iii) a mist flow heat transfer model has been added to cover that flow regime for which previously no method had been recommended, and (iv) a dryout region heat transfer method has been added for the region that separates the annular flow and stratified-wavy flow regimes from mist flow. The mist flow and dryout region heat transfer prediction methods of Wojtan, Ursenbacher and Thome (2005a, 2005b) are not described here as they are presented in Chapter 18.

The Kattan-Thome-Favrat model assumed a linear variation of the dry angle in stratified-wavy flow between 0 at  $\dot{m}_{high}$  (that is  $\dot{m}_{wavy}$ ) and  $\theta_{strat}$  at  $\dot{m}_{low}$  (that is  $\dot{m}_{strat}$ ), as shown in expression [14.4.13]. Zürcher, Thome and Favrat (1999) did not make any changes in the heat transfer model in the stratified-wavy region even though that study showed that some experimental data points at low vapor qualities were clearly under predicted by the model of Kattan-Thome-Favrat model (the original model restricted itself to vapor qualities greater than 0.15). However, in an analogous model for condensation in horizontal tubes, Thome, El Hajal and Cavallini (2003) assumed a quadratic interpolation to calculate  $\theta_{dry}$  rather than a linear interpolation:

$$\theta_{dry} = \theta_{strat} \left[ \frac{\dot{m}_{high} - \dot{m}}{\dot{m}_{high} - \dot{m}_{low}} \right]^{0.5} \quad [10.4.18]$$

As noted above, in the Wojtan-Ursenbacher-Thome map and flow boiling model, the stratified-wavy region has been subdivided into three subzones (slug, slug/stratified-wavy and stratified-wavy) and these modifications result in an important change of the dry angle calculation. The following procedures are now utilized to find the dry angle in the three new subzones while still avoiding any jump in the heat transfer coefficient at any transition boundary.

**Slug Regime (Slug).** In this regime, the high frequency slugs are thought to maintain a continuous thin liquid film on the upper tube perimeter, meaning the entire tube perimeter always remains wet. Thus, similar to the intermittent and annular flow regime:

$$\theta_{dry} = 0 \quad [10.4.19]$$

**Stratified-Wavy Regime (SW).** Based on their experimental flow boiling heat transfer data for this region, better agreement has been found using an exponent of 0.61 rather than 1.0 or 0.5 to capture the wetting effect of the side walls of the tube by the waves, such that:

$$\theta_{\text{dry}} = \theta_{\text{strat}} \left[ \frac{\dot{m}_{\text{high}} - \dot{m}}{\dot{m}_{\text{high}} - \dot{m}_{\text{low}}} \right]^{0.61} \quad [10.4.20]$$

**Slug/Stratified-Wavy Regime (Slug+SW):** In the slug/stratified-wavy zone, both low amplitude waves (which do not reach the top of the tube) and liquid slugs that wash the top of the tube and completely wet the tube perimeter are observed. With increasing vapor quality in this region, the slug frequency decreases and the small amplitude waves become dominant, as observed in Wojtan, Ursenbacher and Thome (2004) with their flow visualization/image processing results for cross-sectional void fractions. The slugs disappeared completely approximately at a vapor quality of  $x_{IA}$ . To capture this effect and to avoid a jump in the heat transfer coefficient at the boundaries of this regime, the following interpolation was proposed and applied when  $x < x_{IA}$ :

$$\theta_{\text{dry}} = \theta_{\text{strat}} \left( \frac{x}{x_{IA}} \right) \left[ \frac{\dot{m}_{\text{high}} - \dot{m}}{\dot{m}_{\text{high}} - \dot{m}_{\text{low}}} \right]^{0.61} \quad [10.4.21]$$

All presented modifications assure a smooth transition in the determination of dry angle between respective subzones and also a smooth transition in the heat transfer coefficient from subzone to subzone.

Three more modifications were made in Intermittent, Annular, Stratified and Stratified-Wavy flows (the later subdivided into subzones of Slug, SW+Slug, SW) compared to the original Kattan-Thome-Favrat flow boiling model:

- The liquid film thickness is now calculated as follows instead of using [10.4.14]:

$$\delta = \frac{d_i}{2} - \left[ \left( \frac{d_i}{2} \right)^2 - \frac{2A_L}{2\pi - \theta_{\text{dry}}} \right]^{1/2} \quad [10.4.22]$$

- When the liquid occupies more than one-half of the cross-section of the tube at low vapor quality, this expression would yield a value of  $\delta > d_i/2$ , which is not geometrically realistic. Hence, whenever [10.4.22] gives  $\delta > d_i/2$ ,  $\delta$  is set equal to  $d_i/2$ .
- $\theta_{\text{strat}}$  is calculated non-iteratively using the expression of Biberg (1999) with  $\varepsilon$  from [10.4.10]:

$$\theta_{\text{strat}} = 2\pi - 2 \left\{ \begin{aligned} & \pi(1-\varepsilon) + \left( \frac{3\pi}{2} \right)^{1/3} \left[ 1 - 2(1-\varepsilon) + (1-\varepsilon)^{1/3} - \varepsilon^{1/3} \right] \\ & - \frac{1}{200} (1-\varepsilon) \varepsilon [1 - 2(1-\varepsilon)] [1 + 4((1-\varepsilon)^2 + \varepsilon^2)] \end{aligned} \right\} \quad [10.4.23]$$

A fixed value of a nucleate boiling suppression factor of  $S=0.8$  was introduced to reduce the nucleate boiling contribution based on their database, so that [10.4.6] now becomes:

$$\alpha_{\text{wet}} = [(S\alpha_{\text{nb}})^3 + \alpha_{\text{cb}}^3]^{1/3} \quad [10.4.24]$$

After this modification, the new updated model predicted their experimental points more accurately, particularly for higher heat fluxes. It was also seen that the inception of dryout was better identified and that the new heat transfer model predicted the experimental heat transfer data more accurately for the dryout regime as well as for the mist flow regime.

Figure 10.10 shows a simulation of the Wojtan-Ursenbacher-Thome updated flow pattern map and flow boiling model for R-134a at a saturation temperature of 10°C, a mass velocity of 500 kg/m<sup>2</sup>s and a heat flux of 7500 W/m<sup>2</sup> for a tube of 10 mm internal diameter. The black lines represent the flow pattern transition boundaries, the red line shows the variation in the predicted heat transfer coefficient and the dashed red line shows the process path. The heat transfer coefficient at a vapor quality of 0.5 is 6206 W/m<sup>2</sup>K.

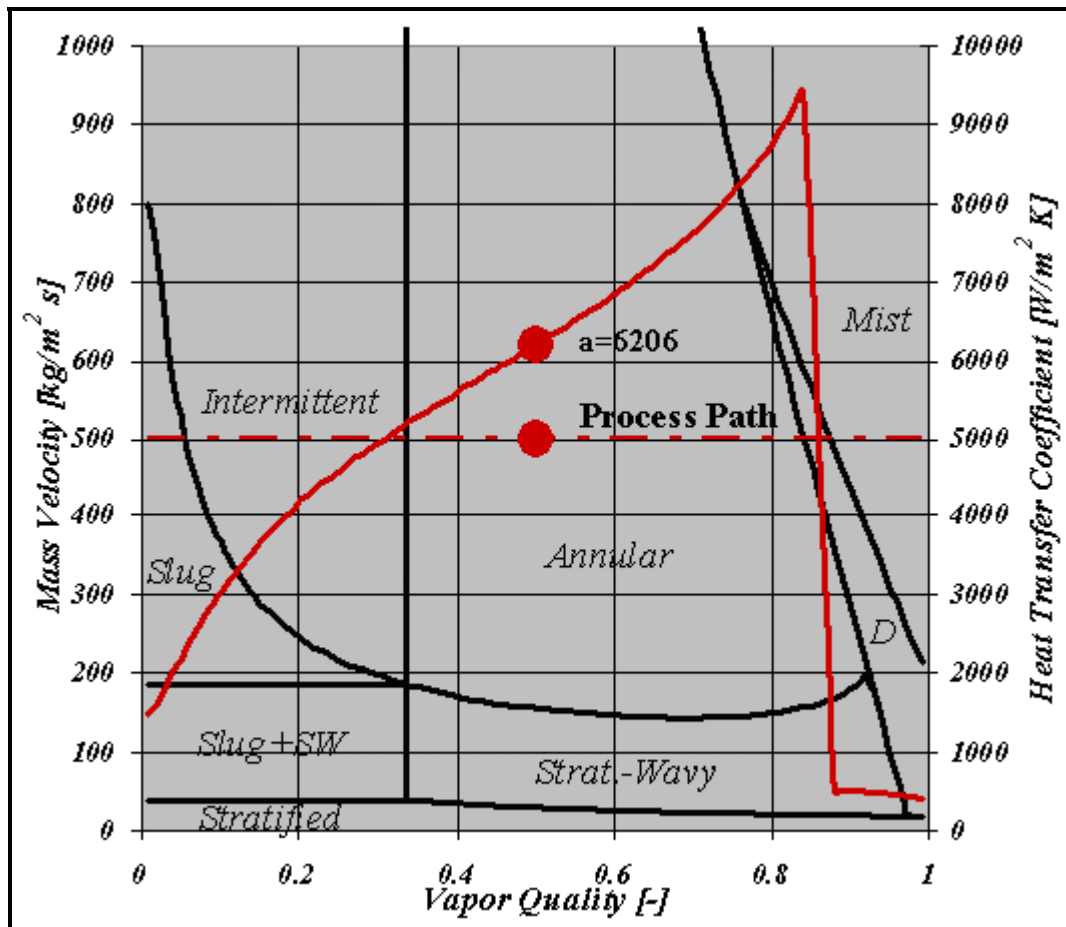


**Figure 10.10. Simulation of Wojtan-Ursenbacher-Thome updated flow pattern map and flow boiling model for R-134a at a saturation temperature of 10°C, a mass velocity of 500 kg/m<sup>2</sup>s and a heat flux of 7500 W/m<sup>2</sup> for a tube of 10 mm internal diameter.**

## 10.5 Heat Transfer Measurements in Horizontal Tubes

Consider the following question. Is it appropriate to measure flow boiling heat transfer data in horizontal tubes using electrical heating (by direct resistance heating of the tube itself or with heated tapes wrapped on the tube)? That is a subject of some debate, where the current preference is to use counter-current hot

water heating. The following comments are pertinent: (i) for annular flow, the values of  $\alpha_{tp}$  will be very similar, (ii) for all types of stratified flow, hot liquid heating induces a nearly uniform temperature boundary condition around the tube perimeter, which is similar to actual operation, while electrical heating creates circumferential heat conduction around the tube from the hot, dry-wall condition at the top to the colder, wet-wall condition at the bottom, yielding an unknown boundary condition, (iii) for annular flow with partial dryout on the top perimeter of the tube, electrical heating is also not advisable because of axial heat conduction along the test section.

In the past, electrical heating had the advantage of providing local heat transfer coefficients while hot water heating normally gave sectional average or what might be called “quasi-local” values for changes in vapor quality from 3-10% or more within the test zone. However, using hot fluid heating and a series of local hot fluid thermocouples to measure the hot fluid’s temperature profile together with wall mounted thermocouples, a technique adopted by Kaul, Kedzierski and Didion (1996) and Zürcher, Thome and Favrat (1999), provides true local flow boiling heat transfer coefficients without resorting to electrical heating nor having to be satisfied with “quasi-local” data. Combining the temperature profile technique with a modified-Wilson plot to obtain the heating fluid’s heat transfer coefficient in the annulus, wall thermocouples are not necessary either. Furthermore, wrapping a wire helically on the outside of the tube increases the water-side coefficient and promotes mixing that minimizes temperature gradients in the hot fluid from the top to the bottom of the annulus that can arise in stratified flow boiling test conditions.

## 10.6 Subcooled Boiling Heat Transfer

Subcooled flow boiling occurs when the local wall temperature during the heating of a subcooled liquid is above the saturation temperature of the fluid and sufficiently high for nucleation to occur. Subcooled boiling is characterized by vapor formation at the heated wall as isolated bubbles or as a bubbly layer along the wall. The bubbles are swept into the subcooled core by the liquid and then condense.

Gungor and Winterton (1986) have adapted their correlation to predict local heat transfer coefficients in the subcooled boiling regime by using separate temperature differences for driving the respective nucleate boiling and convective boiling processes. Thus, the heat flux is calculated as a sum of their two contributions as:

$$q = \alpha_L(T_w - T_L) + S\alpha_{nb}(T_{wall} - T_{sat}) \quad [10.6.1]$$

This predicted their database with a mean error of  $\pm 25\%$ . Analogously, the other methods presented earlier for saturated forced convective evaporation in plain tubes may be adapted to estimate performance in subcooled flow boiling.

## Chapter 11

# Boiling Heat Transfer Inside Enhanced Tubes

**SUMMARY:** In this chapter, evaporation inside enhanced tubes and in tubes with inserts is described. Both evaporation in vertical tubes and horizontal tubes is addressed. The types of enhancements discussed include microfin tubes, twisted tape inserts, corrugated tubes, and internally porous coated tubes. Other enhancements exist but are either not widely used anymore (aluminum star-inserts and internally high finned tubes, for example), are not appropriate for enhancing boiling heat transfer, or do not have very much published about their thermal performance. Several prediction methods are presented for microfin tubes and tubes with twisted tape inserts.

### 11.1 Introduction

In vertical tubes, the most important applications and potential benefits for use of enhancements for evaporation are in the petrochemical industry and hence for vertical thermosyphon reboilers. These units typically evaporate from 10% to 35% of the flow while the inlet is slightly subcooled from the static head with respect to the liquid level in the distillation tower. This application also implies that evaporation of zeotropic multi-component mixtures is of interest, for which little or no data are available in the literature for most enhancements for vertical upflow. Some representative results are presented below for enhanced heat transfer inside vertical tubes.

In horizontal tubes, the most important applications of enhancements are to direct-expansion evaporators in refrigeration, air-conditioning and heat pump units. In the petrochemical industry occasionally a horizontal, tube-side evaporator is used for a service but this is the exception rather than the rule. In direct-expansion evaporators, the fluid enters the tubes after the expansion valve and hence the range of interest is from about 15% to 100% vapor quality, in addition to the superheating zone. Instead, in recirculation type units often favored by ammonia system manufacturers, the fluid enters as a saturated liquid and about 20% to 30% of the fluid is evaporated at the exit. Most of this chapter focuses on microfin tubes, which are of highest industrial interest, while some other enhancement geometries will also be addressed.

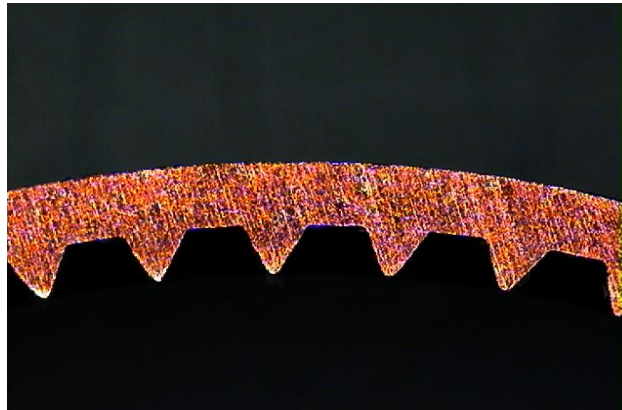
The focus here is on more recent work, primarily that done since 1990. Refer to the book by Thome (1990) for a comprehensive treatment of studies done prior to 1990. Shatto and Peterson (1996) also wrote an extensive review on evaporation in tubes with twisted tapes, covering aspects such as the critical heat flux and dryout.

The standard practice for enhanced boiling inside tubes is to define the internal heat transfer coefficient based on the nominal area at the maximum internal diameter, i.e. at the root of the fins for microfin tubes or that of the plain tube surface for a twisted tape insert. Nearly all test data respect this norm, although not all and hence one must remember to look at this point when comparing data from different sources. For example, some data in the literature are reported based on a nominal diameter at the fin tips or at a mean height of internal fins. However, when calculating the overall heat transfer coefficient for a heat exchanger, that at the maximum internal diameter is required. Hence, the maximum internal diameter will be used here for the nominal diameter and the nominal area corresponding to this diameter will be used for defining heat transfer coefficients and heat fluxes, unless otherwise stated.

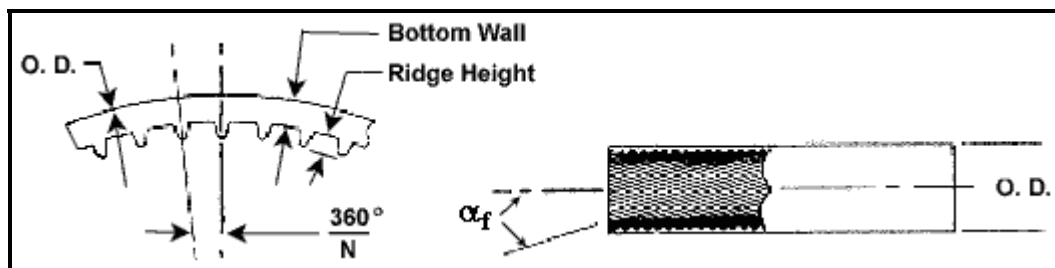
## 11.2 Types of Enhancements and Performance Ratios

The following enhancements are described here for evaporation: microfin tubes, twisted tape inserts, corrugated tubes and tubes with porous coatings. Microfin tubes are also sometimes referred to as inner-grooved tubes. Microfin tubes were originally developed in Japan and widespread use of microfin tubes began in the 1980's. Microfin tubes quickly overtook and replaced the use of star-insert tubes, i.e. tubes with star-shaped aluminum inserts tightly fit into copper tubes, which had been popular up until then. Twisted tape inserts and corrugated tubes have been commercially available for many years, although both have been largely supplanted by microfin tubes. Twisted tape inserts, even with their lower thermal performance and higher two-phase pressure drops, are still a viable alternative as they can be easily retrofit into existing plain-tube equipment without retubing. Corrugated tubes are also still used for a variety of applications.

Figure 11.1 depicts a photograph of the fin profile of a microfin tube. Figure 11.2 shows the characteristic geometry, which is defined by the maximum internal diameter  $d_f$ , number of fins, their helix angle  $\alpha_f$  (or axial pitch), their height  $e_f$ , their thickness, their cross-sectional shape and the internal area ratio. Most microfins have approximately a trapezoidal cross-sectional shape with a rounded top and rounded corners at the root. Other shapes are triangular, rectangular and screw (no root area between fins). The thickness of the fins is not of much importance since the fin efficiencies are close to 1.0 even in alloy tubes since the fins are typically only from 0.2 to 0.3 mm (0.008-0.012 in.) high.



**Figure 11.1. Photograph of fin profile of microfin tube of Wolverine Tube Inc.**



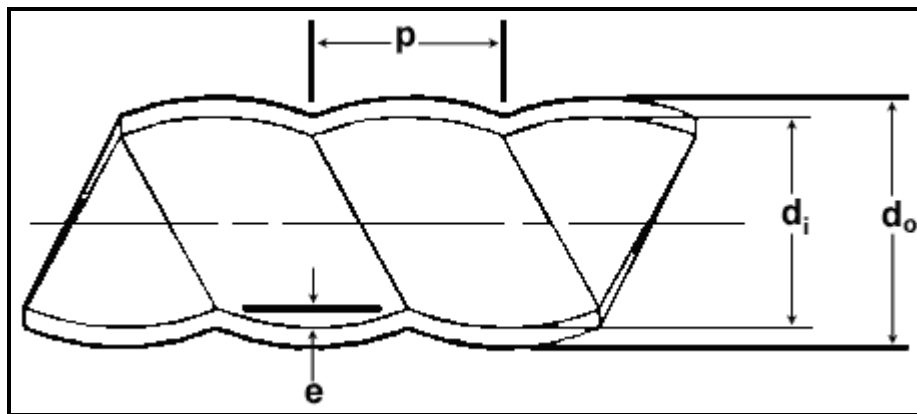
**Figure 11.2. Microfin tube geometry of Wolverine Tube Inc.**

Figure 11.3 depicts a photograph of a twisted tape insert and a diagram of its geometry. The twist ratio is defined as the axial length of tape necessary to make a  $180^\circ$  turn divided by the tube internal diameter. Twist ratios of 3 to 5 are typically used while a twist ratio of infinity represents a straight tape without any twist. As twisted tape inserts fit loosely inside the tubes, the surface area of the tape is not considered to be heat transfer surface area since little heat is conducted into the tape from the tube wall.



**Figure 11.3. Photograph of twisted tape insert and diagram of its geometry.**

Figure 11.4 illustrates a photograph of a corrugated tube and a diagram with its characteristic dimensions. Most corrugated tubes have a single-start of corrugation that is defined by its depth  $e$  and its axial pitch  $p$  (or helix angle). The maximum internal diameter is typically used to define the internal heat transfer coefficient. The internal area ratio is slightly larger than 1.0 but is not often cited in publications.



**Figure 11.4. Photograph and diagram of Korodense corrugated tube of Wolverine Tube Inc.**

Microfin tubes are available primarily in copper. For instance, Wolverine Tube Inc. is a major manufacturer of copper microfin tubes for the air-conditioning and refrigeration industries. Seamless microfin tubes are produced by drawing a plain copper tube over a mandrel to form helical fins. This production method allows microfins to be produced from about 0.1 to 0.4 mm (0.004 to 0.016 in.) in height. The most favorable helix angles for heat transfer and pressure drop range from about 7° to 23°, but 18° seems to be the most popular. Instead, welded microfin tubes are formed from copper strip, whose microfin geometry has been embossed by a rolling operation. This manufacturing method allows a much wider range of microfin geometries to be produced, including 3-dimension fin geometries. In addition, microfin tubes are also becoming available in other materials, such as aluminum, carbon steel, steel alloys, etc.

Corrugated tubes are manufactured in many metals: copper, copper alloys, carbon steels, stainless steels and titanium. The corrugations are defined by the corrugation pitch, corrugation depth and number of corrugations, i.e. the number of starts. Multi-start corrugated tubes with large corrugation depths are typically referred to as fluted tubes.

Twisted tape inserts are available in most metals, diameters and lengths. They are made by twisting metal strip and fit loosely in the tubes to allow for standard tube wall dimensional tolerances.

As an example of enhancement ratios achievable with these geometries, relative to a plain tube of the same diameter at the same mass flux and heat flux, some general qualitative guidelines are as follows:

- **Microfin tubes.** For horizontal applications, heat transfer enhancement ratios are as high as three to four times at low mass velocities while falling off towards their internal area ratio at high mass velocities. Pressure drop ratios most often range from about 1.0 at low mass velocities and up to about a maximum of about 1.5 at high mass velocities. Hence, microfins are very attractive from a heat transfer augmentation to pressure drop penalty point-of-view. For vertical applications, the heat transfer enhancement is less or similar to horizontal expectations, depending on the mass velocity. The small increase in the frictional pressure drop by the microfins in a vertical unit is typically negligible compared to the static head pressure drop in these units and thus plain tube design methods can be used directly.
- **Twisted tape inserts.** Heat transfer augmentation ratios are typically in the range from 1.2 to 1.5 while two-phase pressure drop ratios are often as high as 2.0 since the tape divides the flow channel into two smaller cross-sectional areas with smaller hydraulic diameters. Twisted tapes have seen some applications in both horizontal and vertical units.
- **Corrugated tubes.** Heat transfer ratios are usually between 1.2 to 1.8 with performances matching microfin tubes at high mass velocities but with much larger two-phase pressure drop ratios, which are on the order of 2 times those of a plain tube. Apparently, little experience is available for vertical applications.
- **Porous coated tubes.** These have heat transfer performances similar to those for nucleate pool boiling and are on the order of 5 to 10 times plain tube performance in vertical tubes. For evaporation in horizontal tubes, the porous coating is only effective for annular flows but not for stratified flows where part of the tube perimeter is dry. Not much information is available about two-phase pressure drop penalties, which can be expected to be only marginal in vertical units where the static head dominates while significant in horizontal tubes where the frictional pressure drop is typically dominant.

## 11.3 Flow Boiling in Vertical Microfin Tubes

For microfin tubes, apparently only one test has been done for evaporation in the vertical orientation. Kattan, Thome and Favrat (1995) ran tests for R-134a in a microfin tube with an 11.90 mm (0.469 in.) maximum internal diameter, 18° helix angle, 0.25 mm (0.010 in.) fin height and 60 fins for an internal area ratio of 1.74. Hot water was used as the heating source and the modified-Wilson plot method applied to three zones of a 3 m (10 ft.) long tube to obtain quasi-local heat transfer data. They ran tests for the same test section for vertical upflow and horizontal flow under identical operating conditions to determine the possible benefit of using microfins in vertical thermosyphon reboilers. At low mass velocities and vapor qualities, there was less augmentation in the vertical position than in the horizontal position relative to a plain tube because a vertical plain tube does not suffer from the adverse effect of flow stratification like a horizontal plain tube. On the other hand, at higher mass velocities the level of augmentation was similar and at least as large or larger than the increase in surface area. Figure 11.5 for instance compares their horizontal and vertical flow boiling data for the microfin tube at a mass velocity of  $201.2 \text{ kg/m}^2\text{s}$  ( $148000 \text{ lb/hr ft}^2$ ) at 4.2 bar (60.9 psia), which is a typical flow rate for vertical thermosyphon operation. The performance in the vertical orientation is slightly less than that of the microfin tube compared its horizontal orientation over the range of vapor qualities from 0.23 to 0.5. Heat transfer augmentation is on the order of 2 or more for all the data.

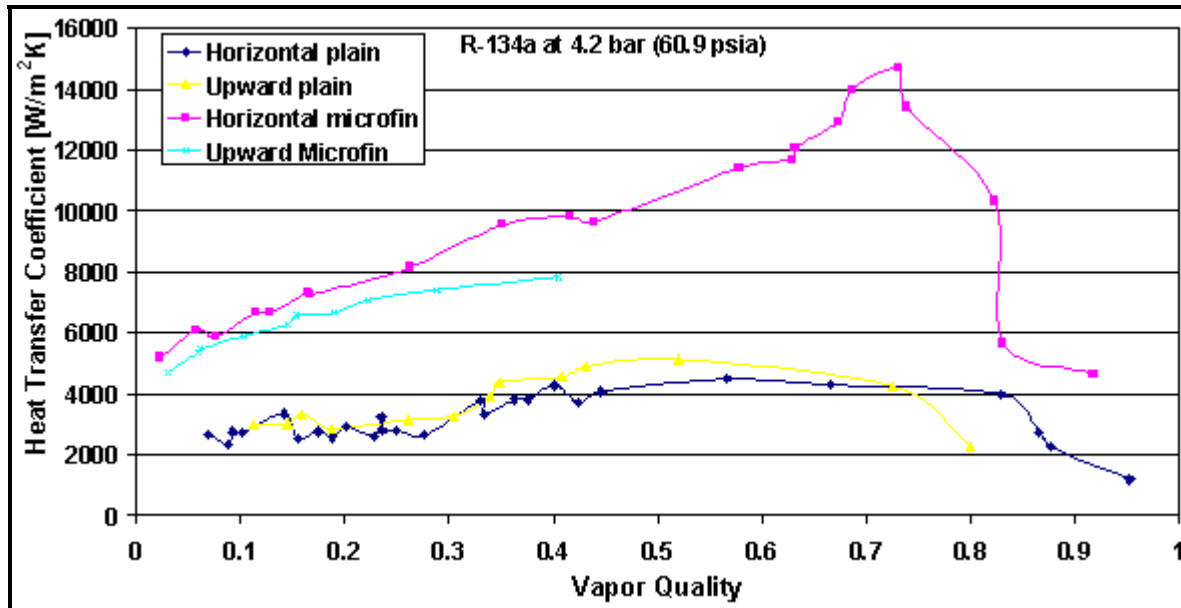


Figure 11.5. Effect of tube orientation on evaporation in a microfin tube from Kattan, Thome and Favrat (1995b) at  $201.2 \text{ kg/m}^2\text{s}$  ( $148000 \text{ lb/hr ft}^2$ ).

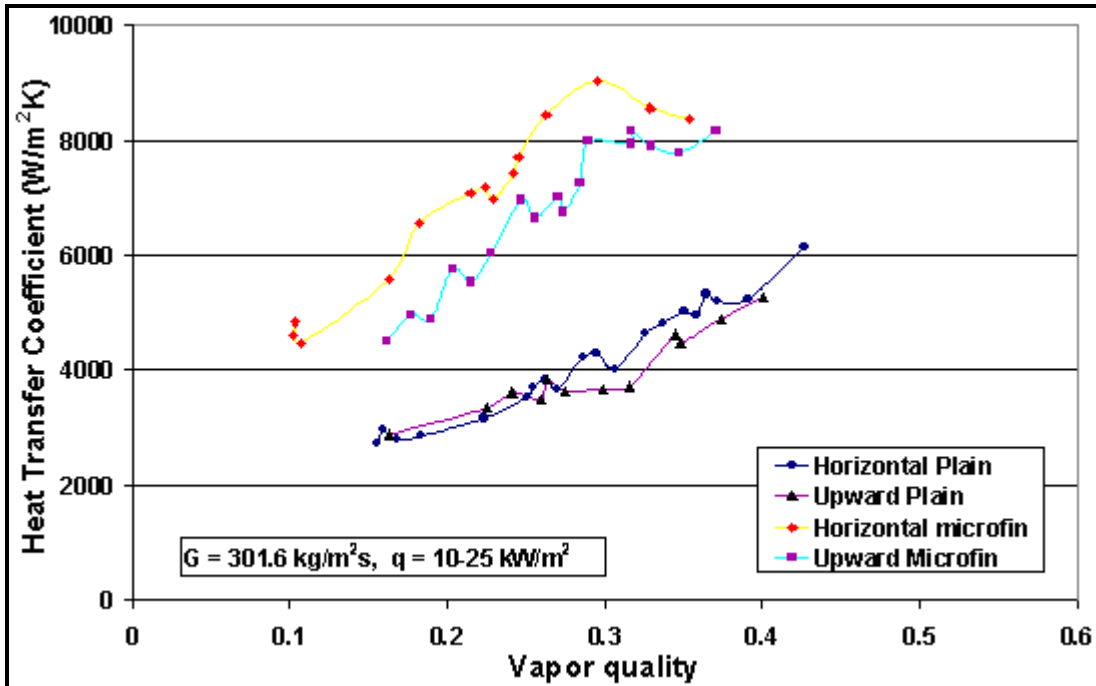


Figure 11.6. Effect of tube orientation on evaporation in a microfin tube from Kattan, Thome and Favrat (1995b) at  $301.6 \text{ kg/m}^2\text{s}$  ( $222000 \text{ lb/hr ft}^2$ ).

Figure 11.6 shows more R-134a data for the same microfin tube at a mass velocity of  $301.6 \text{ kg/m}^2\text{s}$  ( $222000 \text{ lb/hr ft}^2$ ) at the same pressure. Here, the performance in the vertical microfin tube is less than that of the horizontal microfin tube for vapor qualities from 0.16 to 0.37. Heat transfer augmentation is still on the order of 2. Notably, when replacing a vertical plain tube bundle with a vertical microfin tube

bundle, the number of tubes required is less and the microfin tube bundle benefits for the above augmentation ratio in addition to a higher mass velocity, heat flux and exit vapor quality, which further improve the heat transfer performance by perhaps another 50%.

## 11.4 Flow Boiling in Vertical Tubes with Twisted Tape Inserts

Twisted tape inserts have the distinct advantage in that they can be used to increase the thermal capacity of existing evaporators without replacing the tube bundle. Twisted tapes fit loosely within the tubes and hence they enhance heat transfer by the swirl that they impart on the flow but do not provide any additional heat transfer surface area.

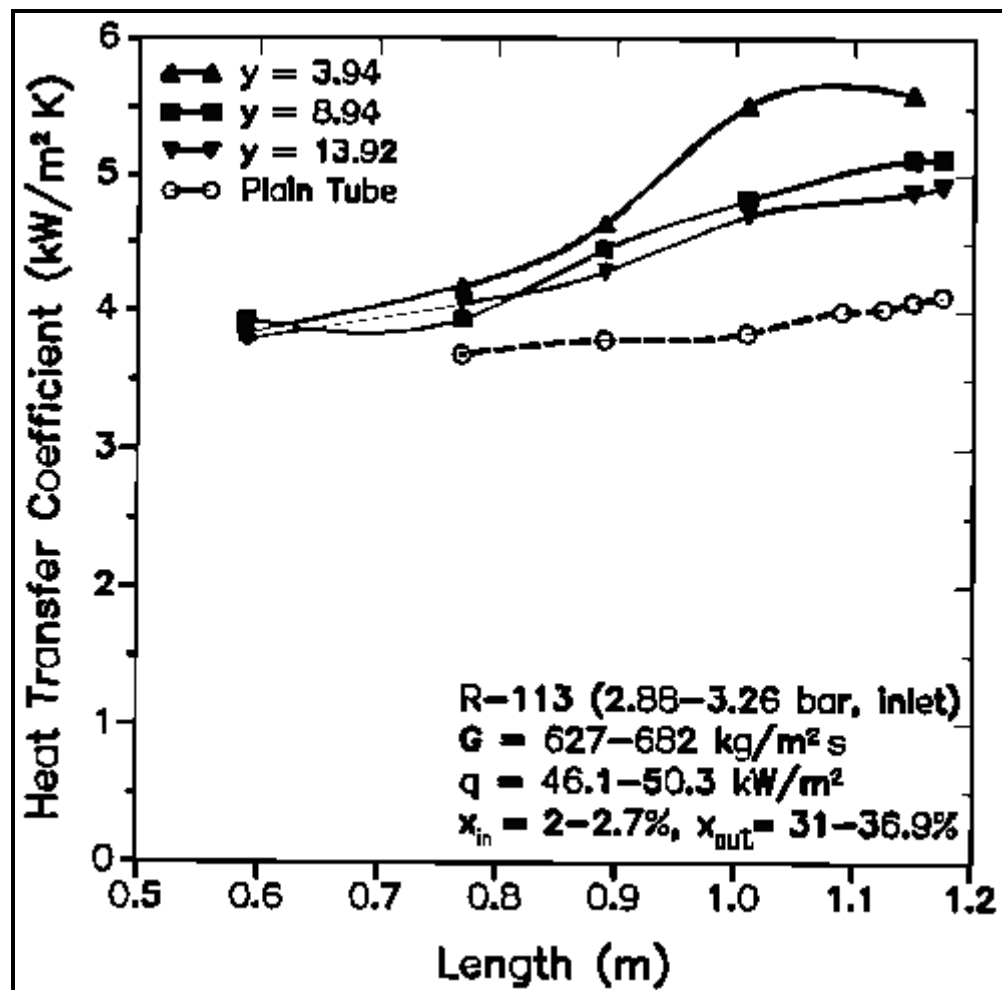


Figure 11.7. Effect of twist ratio on evaporation of R-113 from Jensen and Bensler (1986).

Most experimental tests with twisted tape inserts have been performed for evaporation in horizontal tubes. Jensen and Bensler (1986) studied the effect of twist ratio,  $y$ , defined here as the ratio of the axial length for a 180° twist of the tape to the internal diameter of the tube, on boiling of R-113 in vertical upflow in a tube of 8.10 mm (0.319 in.) internal diameter using electrical heating. Figure 11.7 depicts a comparison between tubes with twisted tapes and one without, plotted as a function of position along the tube rather than vapor quality, where the vapor quality ranged from 0.02-0.027 at the inlet to 0.31-0.37 at the outlet.

The heat transfer coefficients and heat fluxes were calculated based on the internal surface area of the tube after subtracting the heat generated in the tapes themselves. Most of the augmentation is observed at the higher vapor qualities, where it is as much as 40%, while at low vapor qualities it is only on the order of 10%. These test conditions are not necessarily indicative of the augmentation that could be attained in a vertical thermosyphon reboiler, for example, since the mass velocity and heat flux in these tests were quite high compared to typical operating conditions. The swirl effect would be expected to be more effective at lower mass velocities and lower heat flux where the potential for augmenting the convective contribution to the two-phase flow boiling coefficient is most evident.

## 11.5 Flow Boiling in Vertical Tubes with an Internal Porous Coating

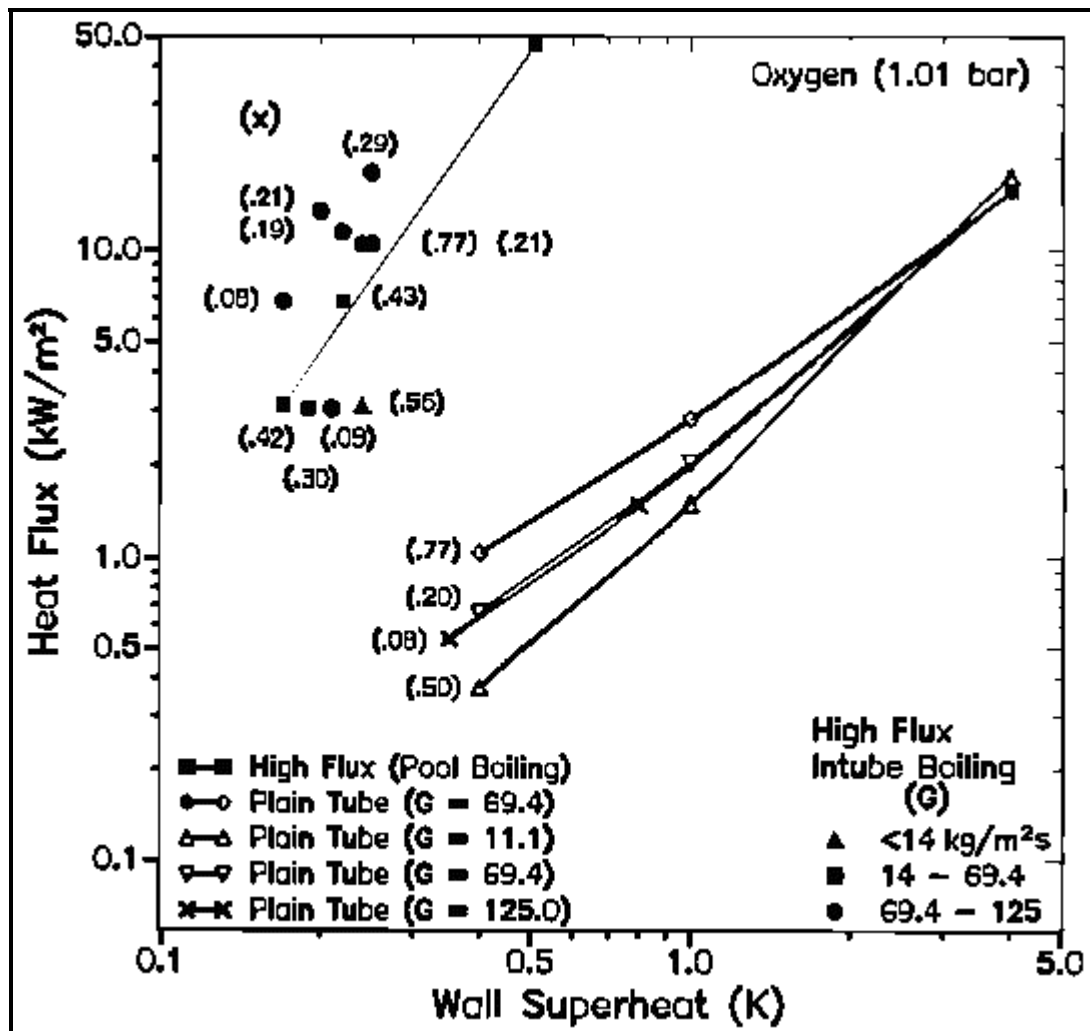


Figure 11.8. Evaporation of oxygen inside vertical High Flux tube relative to plain tube.

Applying a thin porous coating to the inside of vertical evaporator heat transfer tubes is very successful in improving performance. The commercially available enhanced tube High Flux (property and trademark first of Union Carbide and now of UOP) is available with the coating either inside or outside. As an

example of boiling performance, Figure 11.8 depicts intube boiling data for liquid oxygen in a 18.7 mm (0.736 in.) internal diameter High Flux tube, apparently obtained at 1.01 bar (14.7 psia), by Czikk, O'Neill and Gottzmann (1981). The local boiling heat transfer coefficients are plotted as heat flux versus wall superheat as would be typical of nucleate pool boiling since the High Flux heat transfer data are dependent on heat flux but are virtually independent of vapor quality and mass velocity. Comparable plain tube heat transfer coefficients predicted with the Chen (1963) correlation are also shown at similar conditions. In addition, the High Flux pool boiling curve obtained by Antonelli and O'Neill (1981) for liquid oxygen is also shown, which matches the flow boiling data remarkably well. Heat transfer augmentation is on the order of 10-fold. They have noted that single-tube nucleate pool boiling heat transfer data are suitable for predicting the flow boiling performance of the High Flux tube since the nucleate boiling contribution dominates the convective boiling contribution. Hence, their pool boiling curves for the High Flux tube can be used for the design of vertical thermosyphon reboilers for the same fluid.

## 11.6 Flow Boiling of Pure Fluids in Enhanced Horizontal Tubes

Below, a summary of experimental research published since 1990 on intube evaporation of pure refrigerants (and azeotropic refrigerant mixtures) inside horizontal enhanced tubes is presented. Selected studies are shown in Table 11.1 listing the test conditions, type of tube and dimensions as follows:

- $\dot{m}$  ( $\text{kg}/\text{m}^2\text{s}$ ): the mass velocity based on maximum internal diameter at the root of internal fins or corrugations.
- $T_{\text{sat}}$  or  $P_{\text{sat}}$ : the saturation temperature or pressure of the tests.
- *Max ID*: the internal diameter at the root of any internal fins or corrugations.
- *No./Angle/Ht./AR*: the dimensions of the internal fins citing Number of fins/Helix Angle/Fin Height (mm)/Area Ratio (relative to nominal area at Max ID) or the characteristic dimensions of other types of tubes (fluted, twisted tape, helical wires, etc.).
- *Tube Type*: Microfin\* with an asterisk refers crosscut microfins, i.e. notched 3-dimensional microfins.

**Table 11.1. Evaporation Tests on Pure Refrigerants and Azeotropes in Enhanced Tubes**

Reference	Test Conditions			Tube Description (in mm)			
	Name (year)	Fluid	$\dot{m}(\text{kg}/\text{m}^2\text{s})$	$T_{\text{sat}}$ or $p_{\text{sat}}$	Max ID	Type	No./Angle/Ht./AR
Eckels-Pate (1991a)	R-134a	125-400	5, 10, 15°C	8.72	Microfin	60/17°/0.20/1.5	
	"	"	5, 10, 15°C	8.00	Smooth	-	
	R-12	"		8.72	Microfin	60/17°/0.20/1.5	
	"	"		8.00	Smooth	-	
Torikoshi et al. (1992)	R-134a	45-200	5, 15, 30°C	8.7	Smooth	-	
	"	"		8.8	Microfin	60/18°/0.20/1.?	
Hinton et al. (1992)	R-22	176-343 211-421	Not cited Not cited	16.8 13.85	Fluted Smooth	2-start, 0.8/7.1 -	
Eckels et al. (1992)	R-22	150-350	2, 7°C	9.52OD	MicrofinA	?/18°/0.18/1.?	
	"	"	"	"	MicrofinB	?/18°/0.20/1.?	
	"	"	"	"	MicrofinC	?/18°/0.20/1.?	
	"	"	"	"	MicrofinD	?/18°/0.18/1.?	
	"	"	"	"	MicrofinE	?/18°/0.18/1.?	

Reference	Test Conditions			Tube Description (in mm)			
	Name (year)	Fluid	$\dot{m}$ (kg/m <sup>2</sup> s)	T <sub>sat</sub> or p <sub>sat</sub>	Max ID	Type	No./Angle/Ht./AR
	R-22 " "	135-400 " "	2, 7°C " "	7.94OD " "	MicrofinC MicrofinD MicrofinE		?/18°/0.20/1.? ?/18°/0.18/1.? ?/18°/0.18/1.?
Christoffersen et al. (1993)	R-22 R-134a R-22 R-134a R-22 R-134a	204-510 102-510 204-306 102-510 51-510 51-510		5°C " 5°C " 5°C "	7.75 10.92 8.89	Smooth " Smooth " Microfin "	- - - - 60/18°/0.18/1.?
Eckels et al. (1994)	R-134a "	85-375 "		1°C "	8.0 8.92	Smooth Microfin	- 60/17°/0.20/1.5
Torikoshi-Ebisu (1994)	R-22	85-520		5°C	6.40	Microfin	50/18°/0.18/1.?
Thors-Bogart (1994)	R-22 " " " R-22 " "	75-390 " " " 125-430 " "		1.67°C " " " 1.67°C " "	14.86 14.86 14.86 14.10 8.72 8.87 8.87	Smooth Microfin Microfin Corrugat. Plain Microfin Microfin	- 60/27°/0.305/1.? 75/23°/0.305/1.? 1/78°/1.041/1.? - 60/18°/0.203/1.? 72/0°/0.203/1.?
Chamra-Webb (1995)	R-22	151-327		24.4°C	14.66	Microfin	74/15°/0.35/1.? (Crossgrooves)
Kuo et al. (1995)	R-22	100, 200		2, 6, 10°C	6.50	Microfin	60/18°/0.15/1.49
Kido et al. (1995)	R-22 R-22 " " " " " " " " "	86-345 86-345 173 173 86, 173 86, 173“ 173 -		4.9 bar " " " " " " " " "	6.40 6.47 6.50 6.55 6.52 6.54 6.48 6.56	Smooth Microfin " " " " " " " "	- 60/18°/0.15/1.63 70/11°/0.21/2.21 70/17°/0.21/2.24 85/ 9°/0.16/2.07 85/17°/0.16/2.13 85/ 7°/0.21/2.49 100/3°/0.15/2.19
Kattan et al. (1995b)	R-134 R-123	100-300 100-300		2.8-4.2 1.07 bar	11.90 11.90	Microfin Microfin	70/18°/0.25/1.74 70/18°/0.25/1.74
Koyama et al. (1996)	R-134a	307		6.55 bar	8.475	Microfin	60/18°/0.17/1.52
MacBain-Bergles (1996)	R-12	100-400		3.20 bar	12.5	Fluted	3-start/2.7/7.94
Wang et al. (1996), Kuo-Wang (1996a, 1996b)	R-22 R-22	100-300 100-300		6 bar 6 bar	7.92 8.92	Smooth Microfin	- 60/18°/0.20/1.57
Singh et al. (1996)	R-134a	50-150		5.75 bar	11.78	Microfin	60/18°/0.30/1.?
Chamra et al. (1996)	R-22 R-22 " " " " " R-22 "	45-181 45-181 " " " " 45-181 "		2.2°C 2.2°C " " " " 2.2°C "	14.86 14.88 " " " " 14.88	Smooth Microfin " " " " Microfin* Microfin*	- 74/27°/0.35/1.? 78/20°/0.35/1.? 76/17.5°/0.35/1.? 80/15°/0.35/1.? 74/27°/0.35/1.? 78/20°/0.35/1.? 76/17.5°/0.35/1.?

Reference	Test Conditions			Tube Description (in mm)			
	Name (year)	Fluid	m(kg/m²s)	T <sub>sat</sub> or p <sub>sat</sub>	Max ID	Type	No./Angle/Ht./AR
	"	"	"	"	"	"	80/15°/0.35/1.?
Kaul et al. (1996)	R-22	314, 364		4.4°C	8.93	Microfin	?/?/?/1.?
	R-32	"		"	"	"	"
	R-125	"		"	"	"	"
	R-134a	"		"	"	"	"
Nidegger et al.(1997)	R-134a	100-300		4.4°C	11.90	Microfin	70/18°/0.25/1.74
Zürcher et al. (1997b)	Ammo-nia	20-120		4°C	14.00	Smooth	-
	"	"		"	13.46	Microfin	34/18°/0.33/1.33
MacBain et al. (1997)	R-12	100-400		3.20 bar	12.5	Fluted	3-start/2.7/7.94
	R-134a	"		"	"	"	"
Kedzierski-Kim (1997)	R-12	Not cited		Reduced	9.64	Twisted	y=4.15
	R-22	"		Press. from	"	Tape	"
	R-152a	"		0.035-0.2	"	"	"
	R-134a	"		"	"	"	"
	R-290	"		"	"	"	"
	R-290/	"		"	"	"	"
	R-134a	"		"	"	"	"
	R-134a/	"		"	"	"	"
Lan et al. (1997a)	R-113	514-2972		7.9 bar	6.2	Helical	0.81 dia. wire
	"	"		"	"	Wire	"
Lan et al. (1997b)	R-113	305-4361		7.9 bar	6.2	Helical	0.81 dia. wire
Muzzio et al. (1998)	R-22	90-400		5°C	8.92	Smooth	-
	R-22	90-400		5°C	8.92	Microfin	54/18°/0.16-
	"	"		"	8.92	"	0.23/1.51
	"	"		"	8.84	"	60/18°/0.20/1.51
Oh-Bergles (1998)	R-134°	50-200		3.1 bar	8.21	Smooth	-
	"	"		"	8.71	Microfin	60/6°/?/?
	"	"		"	"	"	60/12°/?/?
	"	"		"	"	"	60/18°/?/?
	"	"		"	"	"	60/25°/?/?
	"	"		"	"	"	60/44°/?/?
Kabelac-de Buhr (2001)	Ammo-nia	50-150		-20°, 4°C	10.0	Smooth	-
	50-150			-20°C	11.13	Microfin	21/25°/0.63/1.58
Lallemand et al. (2001)	R-22	150-250		7.7 bar	10.7	Smooth	-
	"	"		"	11.98	Microfin	65/30°/0.25/1.56
	"	"		"	11.98	Microfin	70/20°/0.22-0.25/1.69

A few of the investigations listed in Table 11.1 are described below.

Eckels and Pate (1991a) investigated evaporation in a single microfin tube for refrigerants R-134a and R-12, in a continuation of their earlier study on a plain tube presented in Eckels and Pate (1991b). They reported mean heat transfer coefficients for a vapor quality change of about 75% from inlet to outlet of their test section using counter-current hot water flow. They found slightly smaller microfin enhancement

ratios for R-134a than for R-12. The augmentation ratios were higher at low mass velocities (2.3 to 2.6 times the plain tube coefficients) than at higher mass velocities (1.7 to 1.9 times), compared to the tube's area ratio of 1.5, which was typical of prior studies by others for R-22.

An extensive experimental program by Thors and Bogart (1994) covered two sizes of tubes, 3/8 in. (9.5 mm) and 5/8 in. (15.88 mm), for plain, microfin and corrugated tubes using counter-current hot water heating in 3.66 m (12 ft.) long test sections. Their mean flow boiling coefficients were for an inlet vapor quality of 0.10 and an outlet vapor quality of 0.80 at a saturation temperature of 1.67°C (35°F). Figure 11.9 depicts their results for the 5/8 in. tubes (refer to Table 11.1 for the enhancement dimensions). Heat transfer augmentation for the 75-fin microfin tube was the highest, whose enhancement ratio was nearly four. At very high mass velocities, the corrugated tube's performance nearly matched that of the two microfin tubes, but at a much larger pressure drop penalty. [Refer to the chapter on two-phase pressure drops for their test data with these tubes].

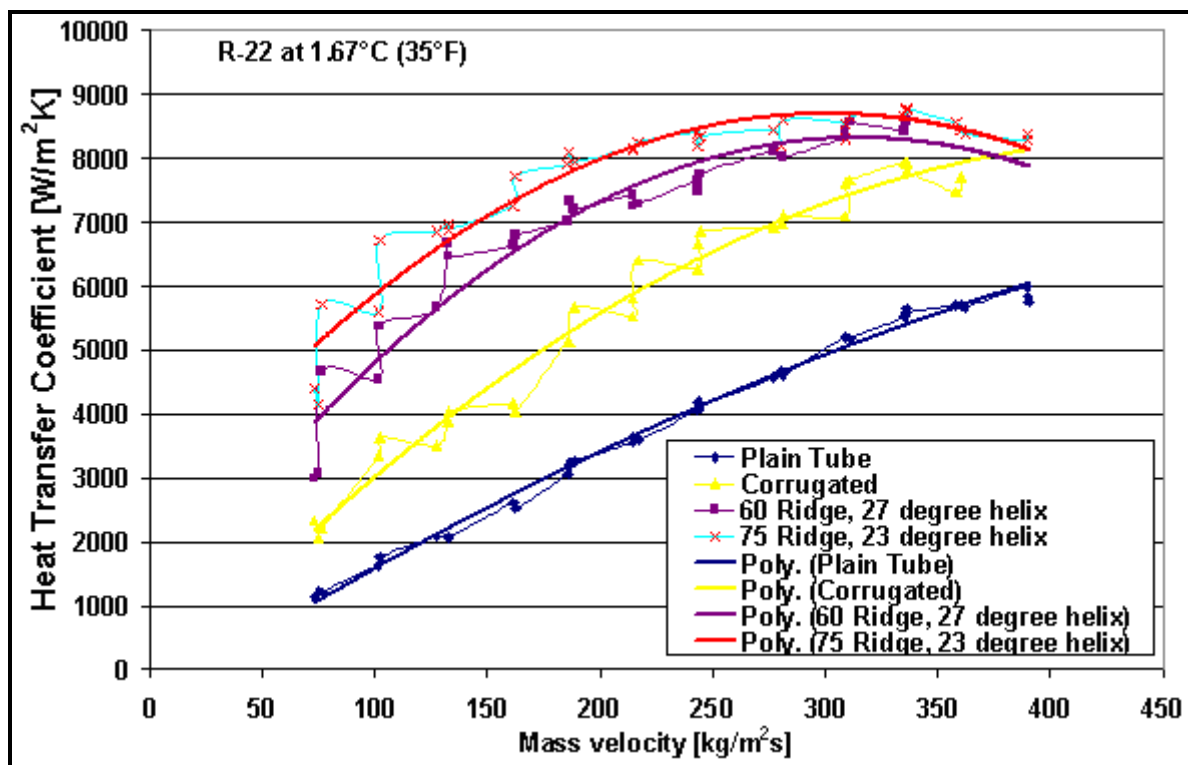


**Figure 11.9. Flow boiling of microfin, corrugated and plain tubes by Thors and Bogart (1994) for R-22.**

Chamra and Webb (1995) measured quasi-local heat transfer coefficients for R-22 using hot water heating. Their microfin tube had fins with a 15° helix angle, which were crosscut to make three-dimensional fins. Interestingly, they measured both flow boiling and condensation heat transfer data at similar test conditions, illustrating that in annular flow the heat transfer processes for evaporation and condensation give similar heat transfer coefficients, except for the additional effect of nucleate boiling. They observed mean augmentation levels up to 3.5 at low mass velocities in the range of 50 kg/m<sup>2</sup>s (36,791 lb/hr ft<sup>2</sup>) that decreased to 1.7 at 200 kg/m<sup>2</sup>s (147,162 lb/hr ft<sup>2</sup>).

A comparative study for local flow boiling coefficients between a microfin tube and a plain tube for R-134a was made by Nidegger, Thome and Favrat (1997) and Zürcher, Thome and Favrat (1997a) at 4.4°C (40°F) using counter-current hot water for heating. The two test sections in series, each 3 m (10 ft) long,

were divided into three subsections of 1 m (3.28 ft) length each, and thus gave quasi-local heat transfer data of each subsection. Augmentation was observed over the entire range of vapor qualities. [Note: some of their data are shown later in a comparison to R-407C in Figure 11.12].

Zürcher, Thome and Favrat (1997b) obtained data for evaporation of ammonia in a stainless steel plain tube and a stainless steel microfin tube, both made in 439-grade steel. The tubes in their test sections were tightly wrapped with a helical wire that was fixed by spot soldering, thus increasing the water-side heat transfer coefficient by about 2 times. Four thermocouples were installed around the circumference of each tube to determine the mean tube wall temperature at two axial locations. They also measured the water temperature profile using thermocouples located along the hot water annulus, determined the local enthalpy gradient on the water-side, then the local heat fluxes to test locations, and thus obtained local boiling heat transfer coefficients rather than quasi-local values. Figure 11.10 depicts their results at four mass velocities. The microfins enhanced local heat transfer coefficients by about 2.2 times at low vapor qualities and up to 7.7 times at high vapor qualities while mean enhancement ratios were 4 to 5 for mass velocities less than  $80 \text{ kg/m}^2\text{s}$  ( $58,865 \text{ lb/hr ft}^2$ ) compared to the tube's area ratio of 1.33. At larger mass velocities, no enhancement was evident. At very low mass velocities, the enhancement ratio began to diminish, most likely because the flow remained stratified in the bottom of the tube.

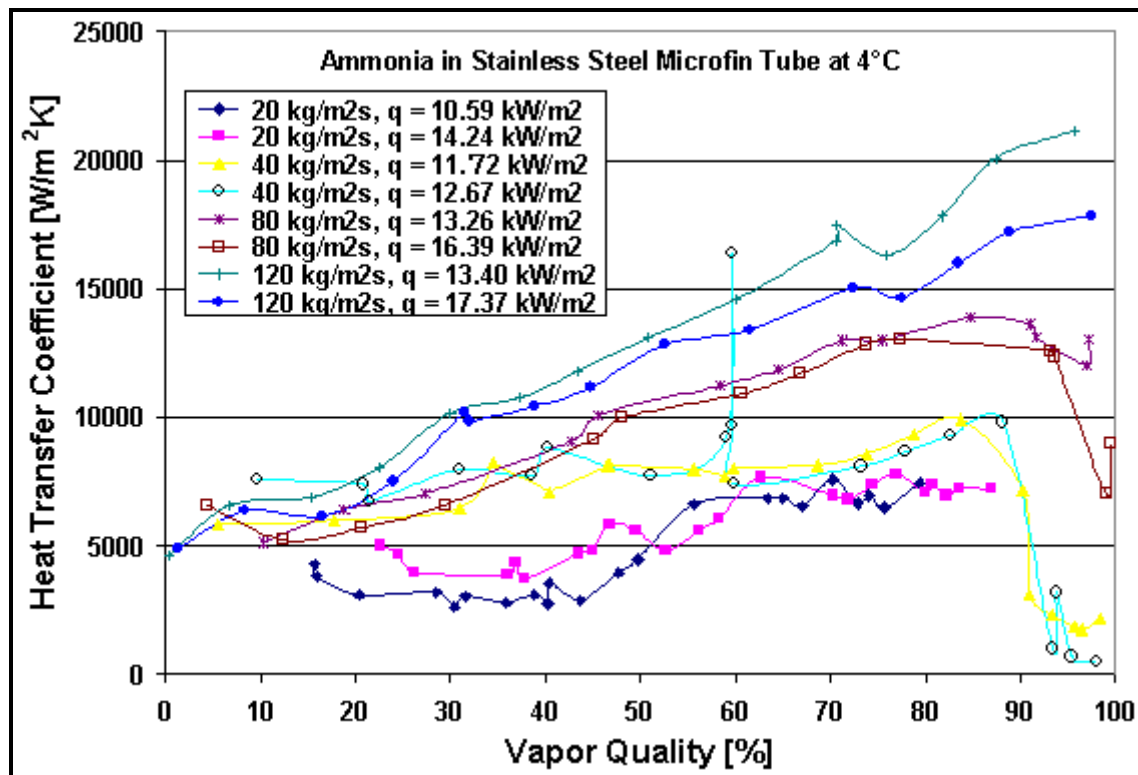


**Figure 11.10. Zürcher, Thome and Favrat [1997b] ammonia flow boiling data for a microfin tube at 4°C (40°F).**

Muzzio, Niro and Arosio (1998) measured heat transfer and pressure drops for four tubes for R-22: a plain tube, a microfin tube with alternating fins of 0.23 mm and 0.16 mm (0.009 and 0.006 in.) height, a second microfin with a conventional microfin geometry, and a third microfin with a screw profile. Quasi-local heat transfer coefficients were measured with a vapor quality change of 30% in their test section. The duo-height microfin tube gave significantly higher heat transfer performance than the other two tubes without much additional pressure drop penalty.

In a comparative study on the effect of microfin helix angle, Oh and Bergles (1998) investigated evaporation of R-134a in similar 60-fin microfin tubes with helix angles of 6°, 12°, 18°, 25° and 44°, although not mentioning the fin height nor the area ratios. They found the optimal helix angle at a vapor quality of 0.5 to depend on mass velocity, with the angles of 6° to 18° giving the best enhancement ratios.

Kabelac and de Buhr (2001) compared flow boiling of ammonia inside a 10.0 mm (0.394 in.) ID plain tube to an 11.13 mm (0.438 in.) ID microfin tube, both made in aluminum. They condensed ammonia on the outside of the tubes and accounted for axial heat conduction from the resulting temperature gradient. Their smooth tube data at 4°C compared well with those of Zürcher, Thome and Favrat (1999) for a slightly larger 14.0 mm (0.551 in.) stainless steel tube and showed that the Kattan, Thome and Favrat (1998a, 1998b, 1998c) plain tube heat transfer model predicted most of their data quite well. They also obtained local boiling coefficients for mass velocities of 50, 100 and 150 kg/m<sup>2</sup>s at -20°C. The enhancement ratios were from about 1.7 to 4.3, compared to the tube's area ratio of 1.58. The data were taken primarily at low vapor qualities, particularly useful for ammonia refrigeration system evaporators operating with liquid recirculation.

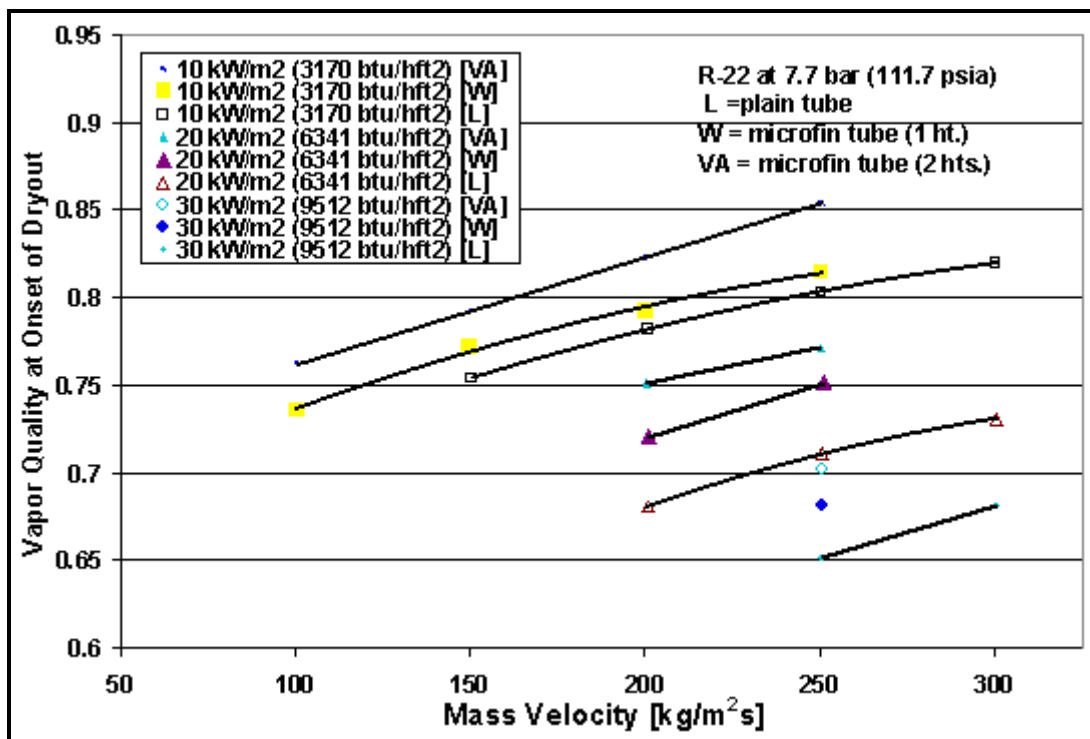


**Figure 11.11. Influence of mass velocity on the onset of dryout for R-22 in a plain tube and two microfin tubes by Lallemand, Branescu and Haberschill (2001).**

An interesting study on evaporation of R-22 (and R-407C) in a 10.7 mm (0.421 in.) plain tube and two 11.98 mm (0.472 in.) microfin tubes at a saturation pressure of 7.7 bar (111.7 psia) was done by Lallemand, Branescu and Haberschill (2001) for vapor qualities from 0.08 to 1.0 but using electrical heating. Their second microfin had microfins of alternating heights of 0.22 and 0.25 mm (0.009 and 0.010 in.), identified as tube VA. Significantly, they measured numerous data at high vapor qualities around the peak in the local heat transfer coefficient vs. vapor quality that occurs in annular flow at the onset of dryout at the top of the tube in horizontal tubes. Figure 11.11 shows their graph for the vapor quality at the onset of dryout plotted versus mass velocity for the three tubes, ranging from 0.65 to 0.85 depending

on the heat flux and mass velocity. The trends in these data match those predicted by the diabatic flow pattern map of Kattan, Thome and Favrat (1998a) for plain tubes with quite similar values for onset of dryout (my personal comparison). The microfins shifted the onset of dryout to slightly higher vapor qualities compared to their plain tube observations, but not significantly so.

## 11.7 Flow Boiling of Zeotropic Mixtures in Enhanced Horizontal Tubes

Before proceeding, some comments on the reduction of test data obtained in evaporation tests on zeotropic mixtures to heat transfer coefficients are in order. For the evaporation of a pure refrigerant, the enthalpy change and local vapor quality can be obtained using only the latent heat of the fluid and its mass flow rate, assuming the pressure drop is small, and the local saturation temperature can be obtained from the local saturation pressure. For a zeotropic mixture, the enthalpy change includes both differential latent heat of evaporation *and* the sensible heat added to the vapor and liquid phases along the bubble point curve of the mixture. Thus, the enthalpy curve of the mixture must be applied and used to calculate the local vapor quality and local bubble point temperature  $T_{\text{bub}}$ , where the local mixture boiling coefficient is defined as  $\alpha = q/(T_{\text{wall}} - T_{\text{bub}})$ . The bubble point temperature rises along the test section as the lighter component preferentially evaporates out of the liquid phase into the vapor phase. Hence, its value must be determined step-wise along the test section channel using an accurate vapor-liquid equilibrium prediction method. Numerous zeotropic refrigerant heat transfer data have unfortunately made it into the literature without use of such an enthalpy curve and thus one must always control this point before using such data.

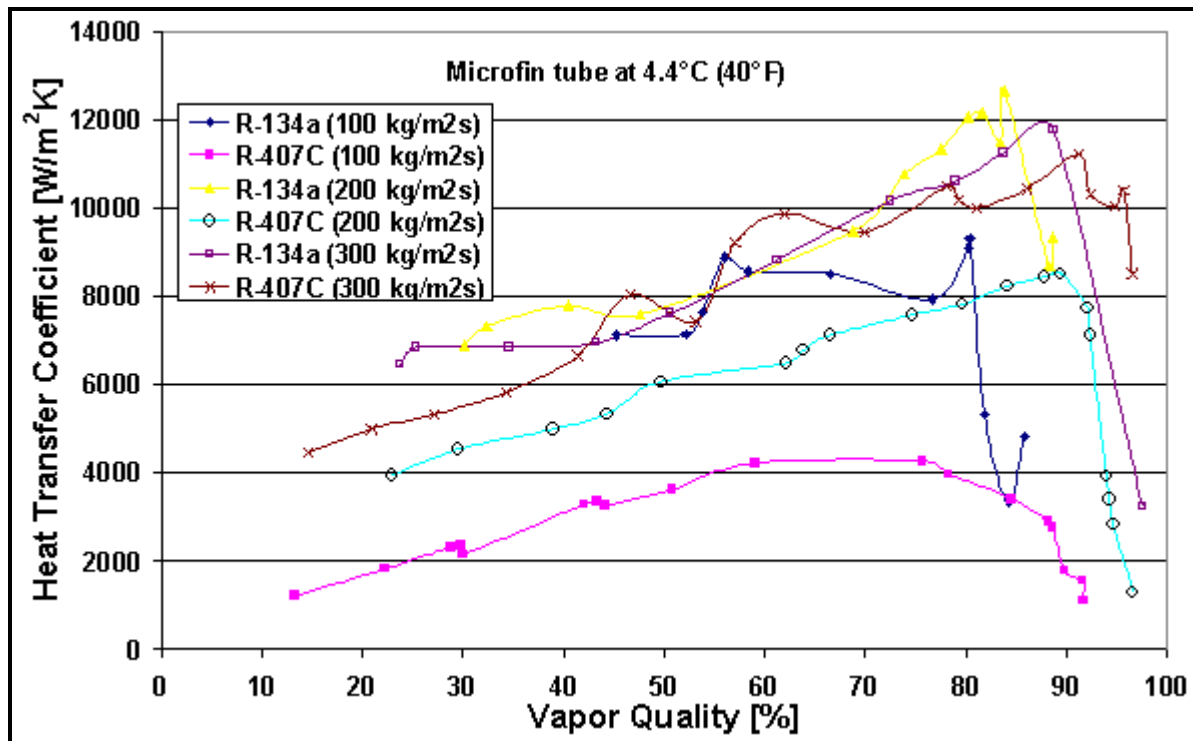


Figure 11.12. Zürcher, Thome and Favrat (1998a, 1998b) data comparing R-407C to R-134a in microfin tube.

Selected studies since 1990 on evaporation of zeotropic refrigerant mixtures inside enhanced tubes are listed in Table 11.2, most of which have used an enthalpy curve to reduce test data. A few of those are described below.

**Table 11.2. Evaporation Tests on Zeotropic Refrigerant Mixtures in Enhanced Tubes**

Reference	Test Conditions			Tube Description (mm)		
Name(year)	Fluid	m(kg/m <sup>2</sup> s)	T <sub>sat</sub> or P <sub>sat</sub>	Max ID	Type	No./Angle/Ht./AR
Christoffersen et al. (1993)	R-32/ R-125	204-510	5°C	7.75	Smooth	-
	"	204-510	5°C	10.92	Smooth	-
	"	51-510	5°C	8.89	Microfin	60/18°/0.18/1.?
Torikoshi-Ebisu (1994)	R-32/ R-134a	130-500	5°C	6.40	Microfin	50/18°/0.18/1.?
	"	"	"	"	"	"
	R-32/ R-125/ R-134a	130-510	"	"	"	"
Wang et al. (1996), Kuo-Wang [1996a, 1996b]	R-407C	100-300	6 bar	7.92	Smooth	-
	R-407C	100-300	6 bar	8.92	Microfin	60/18°/0.20/1.57
Sundaresan et al. (1996)	R-407C	125-375	7°C	8.0	Smooth	-
	"	"	"	8.72	Microfin	60/17°/0.20/1.5
	R-410A	125-375	7°C	8.0	Smooth	-
	"	"	"	8.72	Microfin	60/17°/0.20/1.5
Salehi et al. (1996)	R-404A	50-200	11.0 bar	11.78	Microfin	60/18°/0.25/1.?
Kaul et al. (1996)	R-410B	314, 364	4.4°C	8.93	Microfin	??/?/1.?
	R-407C	314, 364	4.4°C	"	"	"
	R-32/ R-125	314, 364	4.4°C	"	"	"
Kedzierski-Kim (1997)	R-32/ R-134a R-32/ R-152a	Not cited	Reduced Press. 0.035-0.2	9.64	Twisted Tape	y=4.15
Zürcher et al. (1998a, 1998b)	R-407C "	100-300 "	4.4°C "	10.92 11.90	Smooth Microfin	- 70/18°/0.25/1.74
Ebisu-Torikohi (1998)	R-407C	150-300	5.5 bar	6.5	Microfin	Herringbone
Cho-Kim (1998)	R-407C	200, 400	6.5 bar	8.82	Smooth	-
	R-407C	200, 400	6.5 bar	8.53	Microfin	?/18°/?/?
Lallemand et al. (2001)	R-407C	150-250	7.7 bar	10.7	Smooth	-
	"	"	"	11.98	Microfin	65/30°/0.25/1.56
	"	"	"	11.98	Microfin	70/20°/0.22-25/1.69

Flow boiling tests for R-407C evaporating in a plain tube and a microfin tube were performed by Zürcher, Thome and Favrat (1998a, 1998b) using hot water heating. They specifically obtained data at high vapor qualities before and after the peak in  $\alpha_{tp}$  vs. x. Their test data for the microfin tube at an inlet boiling point

temperature of 4°C (40°F) are shown in Figure 11.12, in a comparison of R-407C to R-134a. While their 300 kg/m<sup>2</sup>s (220,743 lb/hr ft<sup>2</sup>) data were similar to R-134a (note: R-134a is a pure fluid and is one of the components in R-407C), the R-407C data were much lower than those of R-134a at the lower two mass velocities. It is not clear why, except for the increased mass transfer resistance at the lower flow rates.

Ebisu and Torikoshi (1998) presented results for R-407C evaporating in a herringbone type of microfin tube. Curiously, their heat transfer coefficients were based on the outside tube diameter rather than the internal diameter. From their circumferential temperature measurements around the perimeter of the tube, they deduced that the herringbone structure created a thicker liquid film at the top and bottom of the tube and thinner films at the two sides. The heat transfer coefficients were 90% higher than for a comparable helically finned microfin tube, but the herringbone geometry had a higher pressure drop. Cho and Kim (1998) reported heat transfer measurements around a U-bend of a microfin tube, whose fin dimensions were not mentioned. The U-bend increased heat transfer in the bend and for a short length after the bend by 4 to 33%.

## 11.8 Flow Boiling Models for Horizontal Microfin Tubes

The first boiling model developed for microfin tubes was that of Thome (1991) that became available in an enhanced heat transfer software program in 1991. A completely general method for microfin geometries was formulated that covered helix angles from 0° to 30°, a number of microfins up to 80, fin heights up to 0.6 mm (0.024 in.) and included the effects of mass velocity and internal surface area ratio. It was originally based on test data for pure refrigerants R-11, R-12, R-113 and R-22 available at that time for numerous microfin tube geometries and tube diameters up to 5/8 in. (15.9 mm). It has since been successfully compared against more recent data for new refrigerants, such as R-134a and R-123, new data for ammonia and zeotropic refrigerant mixtures, such as R-407C.

**Table 11.3. Simulations for R-134a at 200 kg/m<sup>2</sup> s (147000 lb/hr ft<sup>2</sup>) at 3°C (5.4°F)**

Tube	Plain	Microfin #1	Microfin #2	Microfin #3
<b>O.D. (mm)</b>	9.525	9.525	9.525	9.525
<b>I.D. (mm)</b>	8.509	8.509	8.509	8.509
<b>Number of Fins</b>	NA	21	60	75
<b>Fin Height (mm)</b>	NA	0.38	0.20	0.20
<b>Spiral Angle (°)</b>	NA	30	18	18
<b>Area/L (m<sup>2</sup>/m)</b>	0.0267	0.0481	0.0411	0.0438
<b>I.D. Area Ratio</b>	1.0	1.8	1.5	1.6
<b><math>\alpha_{boil}</math> (W/m<sup>2</sup> K)</b>	2741	4951	5649	5917
<b><math>\alpha_{sup}</math>(W/m<sup>2</sup> K)</b>	392	795	663	694
<b><math>\Delta p</math> (kPa)</b>	25.61	55.44	29.22	29.32
<b>EF<sub>boil</sub></b>	1.0	1.806	2.061	2.159
<b>EF<sub>sup</sub></b>	1.0	2.028	1.691	1.770
<b>EF<sub>p</sub></b>	1.0	2.165	1.141	1.145

A parametric study was presented using this method in Thome (1994a) for R-134a for a plain tube, a tube with a twisted tape insert, and three microfin tube geometries. The results are shown in Table 11.3. The microfin tube geometries listed are based on two commercial tubes available at that time (#1 and #2) and a hypothetical tube (#3). All tubes had an external diameter of 9.52 mm (3/8 in.) and a wall thickness of 0.508 mm (0.02 in.), giving an internal diameter of 8.51 mm (0.335 in.). A plain tube and a plain tube with twisted tape, 0.5 mm (0.02 in.) with a twist ratio of four, were also simulated for comparison

purposes. All tubes were assumed to have a length of 6.0 m (19.7 ft.), an inlet vapor quality of 0.15 and 5°C (9°F) of superheating at the outlet. A mass velocity of 200 kg/m<sup>2</sup>s (147,000 lb/hr ft<sup>2</sup>) and a nominal internal heat flux of 8105 W/m<sup>2</sup> (2570 Btu/h ft<sup>2</sup>) were simulated. The boiling zone heat transfer coefficients are mean values from local calculations over the vapor qualities from 0.15 to 1.0 while the superheated coefficients are for single-phase superheating of the vapor. The pressure drops are the total pressure drops for both the evaporating and superheating zones. The enhancement factors (EF) are the respective heat transfer and pressure drops relative to the plain tube. The parametric study shows that the twisted tape is much less effective than the microfin tubes while having a larger pressure drop. The microfin tubes augment heat transfer substantially in both the boiling and superheated zones.

Fujii et al. (1993) next proposed the following microfin correlation:

$$Nu_{mf} = \frac{\alpha_{mf} d_{mean}}{k_L} = Nu_L (4.6/X_{tt}) \quad [11.8.1]$$

where the liquid-phase Nusselt number  $Nu_L$  was correlated as

$$Nu_L = 0.045 Re_L^{0.8} Pr_L^{0.4} \quad [11.8.2]$$

His liquid-phase Reynolds number  $Re_L$  is based on the liquid fraction of the flow:

$$Re_L = \dot{m}(1-x)d_{mean}/\mu_L \quad [11.8.3]$$

The Martinelli parameter for both phases turbulent  $X_{tt}$  is

$$X_{tt} = \left( \frac{1-x}{x} \right)^{0.9} \left( \frac{\rho_G}{\rho_L} \right)^{0.5} \left( \frac{\mu_L}{\mu_G} \right)^{0.1} \quad [11.8.4]$$

In these equations, the maximum internal diameter of the microfin tube was not used. Instead,  $\alpha_{mf}$  refers to the local microfin flow boiling coefficient at  $d_{mean}$ , which is the mean microfin diameter (that at half the fin height). The correlation for  $Nu_L$  was obtained by fitting the Dittus-Boelter correlation to single-phase test data for their one microfin tube, obtaining 0.045 rather than 0.023. Consequently, the method is *not* general but only applicable to that particular microfin tube geometry.

Kido, Taniguchi, Taira and Uehara (1995) measured R-22 heat transfer performances for seven microfin tubes and compared their results to the above method, but found poor agreement. They then proposed another microfin correlation that fit 80% of their data to within ±20% based on their R-22 data. Thus, it must still be compared to other fluids, tube diameters, and microfin geometries to determine if it has general application capabilities. Koyama, Yu, Momoki, Fujii and Honda (1996) ran evaporation tests for R-22, R-134a and R-123 in one microfin tube and proposed a new microfin flow boiling correlation based on these data. However, subcooled liquid test data are required for the particular microfin tube to determine its empirical parameters to correct the Dittus-Boelter correlation, similar to that of Fujii et al. (1993).

Kandlikar and Raykoff (1997) revised an earlier Kandlikar (1991) curvefitting approach for microfin tubes, retaining the fluid specific correction factors from that study, i.e. 1.5 for R-12, 2.2 for R-22, 1.3 for R-113, 1.9 for R-123 and 1.63 for R-134a, similar to the approach in the Kandlikar (1990) plain tube

method. In their approach, each particular microfin geometry requires its own set of three empirical constants to fit the equations to each fluid/tube combination. Subcooled liquid turbulent flow data for each microfin microfin geometry are also required. Hence, this formulation, while interesting, is not amenable to general use.

Thome, Kattan and Favrat (1997) proposed a new microfin flow boiling model, valid for vapor qualities from 0.15 to 0.81, heat fluxes from 2-47 kW/m<sup>2</sup> (630-15000 Btu/h ft<sup>2</sup>) and mass velocities from 100-501 kg/m<sup>2</sup>s (73,581-368,641 lb/hr ft<sup>2</sup>), however only verified for R-134a and R-123 data for one microfin geometry. Compared to their ammonia microfin tube data, Kabelac and de Buhr (2001) on the other hand found it to over predicted their data by 30%. The new microfin model includes some of the Thome (1991) model's concepts adapted to the new annular film flow model of Kattan, Thome and Favrat (1998c) for plain tubes. The new microfin flow boiling model incorporates heat transfer augmentation into their asymptotic flow boiling model, where the local microfin flow boiling heat transfer coefficient  $\alpha_{mf}$  is determined from the following equation

$$\alpha_{mf} = E_{mf} \left[ (\alpha_{nb})^3 + (E_{RB} \alpha_{cb})^3 \right]^{1/3} \quad [11.8.5]$$

$\alpha_{nb}$  is obtained with the Cooper (1984) *dimensional* nucleate pool boiling correlation for pure fluids:

$$\alpha_{nb} = 55 p_r^{0.12} (-\log_{10} p_r)^{-0.55} M^{-0.5} q^{0.67} \quad [11.8.6]$$

in which  $\alpha_{nb}$  is in W/m<sup>2</sup>K,  $p_r$  is the reduced pressure,  $M$  is the molecular weight and  $q$  is the local heat flux in W/m<sup>2</sup> determined from the total internal surface area (not the nominal I.D. area). [Note: this expression only works in SI units]. Since microfins are small, their fin efficiencies are very close to 100% and this is what was assumed. The convective flow boiling contribution to horizontal flow boiling in a microfin tube ( $E_{RB} \alpha_{cb}$ ) is obtained using the turbulent film flow correlation of Kattan, Thome and Favrat (1998c) for plain tubes to calculate  $\alpha_{cb}$ . Their convective boiling heat transfer coefficient for the annular film is:

$$\alpha_{cb} = 0.0133 (Re_L)_{film}^{0.69} Pr_L^{0.4} (k_L/\delta) \quad [11.8.7]$$

where  $k_L$  is the liquid thermal conductivity. The constants 0.0133 and 0.69 are those for the plain tube (not from the present microfin database), which was developed from an experimental database for refrigerants R-123, R-134a, R-502, R-402A and R-404A (since shown to predict R-407C and ammonia flow boiling data without modification). In this expression, the liquid film Reynolds number is determined from the mean velocity of the liquid in the annular film using the local void fraction as:

$$(Re_L)_{film} = \frac{4\dot{m}(1-x)\delta}{(1-\varepsilon)\mu_L} \quad [11.8.8]$$

Here,  $\dot{m}$  is the total mass velocity of liquid and vapor,  $\varepsilon$  is the local void fraction and  $\delta$  is the local thickness of the annular liquid film (ignoring any effect of the microfins) while  $x$  is the local vapor quality and  $\mu_L$  is the liquid dynamic viscosity. The local void fraction is determined using the Rouhani and Axelsson (1970) drift flux model void fraction correlation for plain tubes:

$$\varepsilon = \left( \frac{x}{\rho_L} \right) \left\{ [1 + 0.12(1-x)] \left( \frac{x}{\rho_G} + \frac{1-x}{\rho_L} \right) + \frac{1.18(1-x)[g\sigma(\rho_L - \rho_G)]^{0.25}}{\dot{m}^2 \rho_L^{0.5}} \right\}^{-1} \quad [11.8.9]$$

Here,  $g$  is gravitational acceleration ( $9.81 \text{ m/s}^2$ ) and  $\sigma$  is the surface tension of the fluid (all in SI units). The local annular liquid film thickness is calculated from the cross-sectional area occupied by the liquid phase, assuming uniform thickness of the film around the tube perimeter and ignoring the presence of the microfins, as:

$$\delta = \frac{(1-\varepsilon)d_f}{4} \quad [11.8.10]$$

The maximum internal diameter at the base of the microfin tube is  $d_f$ . The ribbed tube enhancement factor  $E_{RB}$  for single-phase turbulent tube flow correlation of Ravigururajan and Bergles (1985) is introduced to include the enhancement effect of the microfins on the convective boiling coefficient:

$$E_{RB} = \left\{ 1 + \left[ 2.64 Re_{RB}^{0.036} Pr_L^{-0.024} \left( \frac{e_f}{d_f} \right)^{0.212} \left( \frac{p_f}{d_f} \right)^{-0.21} \left( \frac{\alpha_f}{90^\circ} \right)^{0.29} \right]^7 \right\}^{1/7} \quad [11.8.11]$$

where  $e_f$  is the microfin height (in m),  $p_f$  in the axial pitch from fin to fin (in m),  $\alpha_f$  is the helix angle of the microfins (in  $^\circ$ ) and  $Pr_L$  is the liquid Prandtl number.  $Re_{RB}$  is the liquid-phase tubular Reynolds number defined as

$$Re_{RB} = \frac{\dot{m}(1-x)d_f}{\mu_L} \quad [11.8.12]$$

The Grigorig effect enhances film evaporation by drawing the liquid film from the microfin tips towards their roots, similar to film condensation on low finned tubes and corrugated surfaces. Their enhancement factor  $E_{RB}$  is for *tubular* flow, not *film* flow. Thus, an addition enhancement factor for microfin tubes,  $E_{mf}$ , is included to account for these two effects (the only factor specifically based on the microfin test data themselves) and that of mass velocity:

$$E_{mf} = 1.89(\dot{m}/\dot{m}_{ref})^2 - 3.7(\dot{m}/\dot{m}_{ref}) + 3.02 \quad [11.8.13]$$

Here,  $\dot{m}_{ref}$  is a reference value introduced to non-dimensionalize the expression where  $\dot{m}_{ref}$  was set to the maximum value tested, i.e.  $\dot{m}_{ref} = 500 \text{ kg/m}^2\text{s}$  ( $367,900 \text{ lb/hr ft}^2$ ).

Figure 11.13 depicts a comparison of the microfin tube model to R-134a test data at a mass velocity of  $200 \text{ kg/m}^2\text{s}$  ( $147,160 \text{ lb/hr ft}^2$ ). Notably, the slope of the local heat transfer coefficient vs. vapor quality is correctly captured by the void fraction equation in the model. Figure 11.14 shows the predicted local augmentation ratios averaged over a vapor quality from 0.15-0.85 and plotted as a function of mass velocity for R-134a, showing that the model predicts large enhancement at low mass velocities, which then tends towards the microfin's internal area ratio at high mass velocities, typical of nearly all published experimental results.

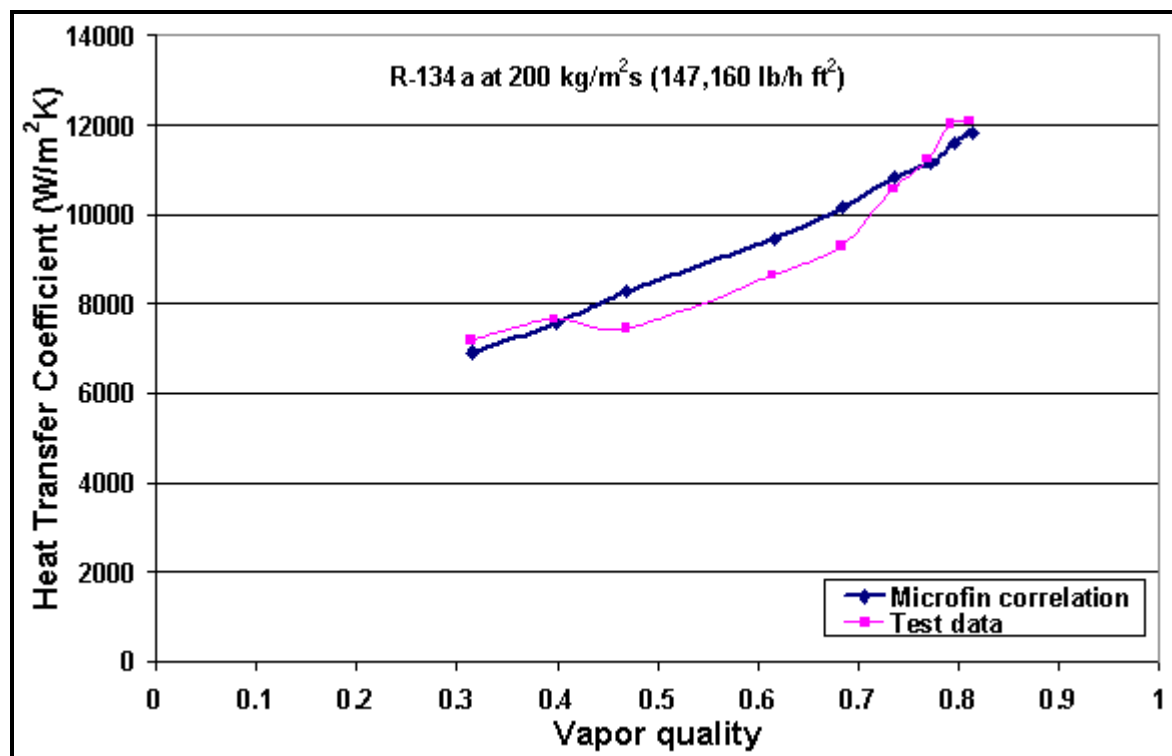


Figure 11.13. Thome, Kattan and Favrat [1997] microfin model compared to R-134a data.

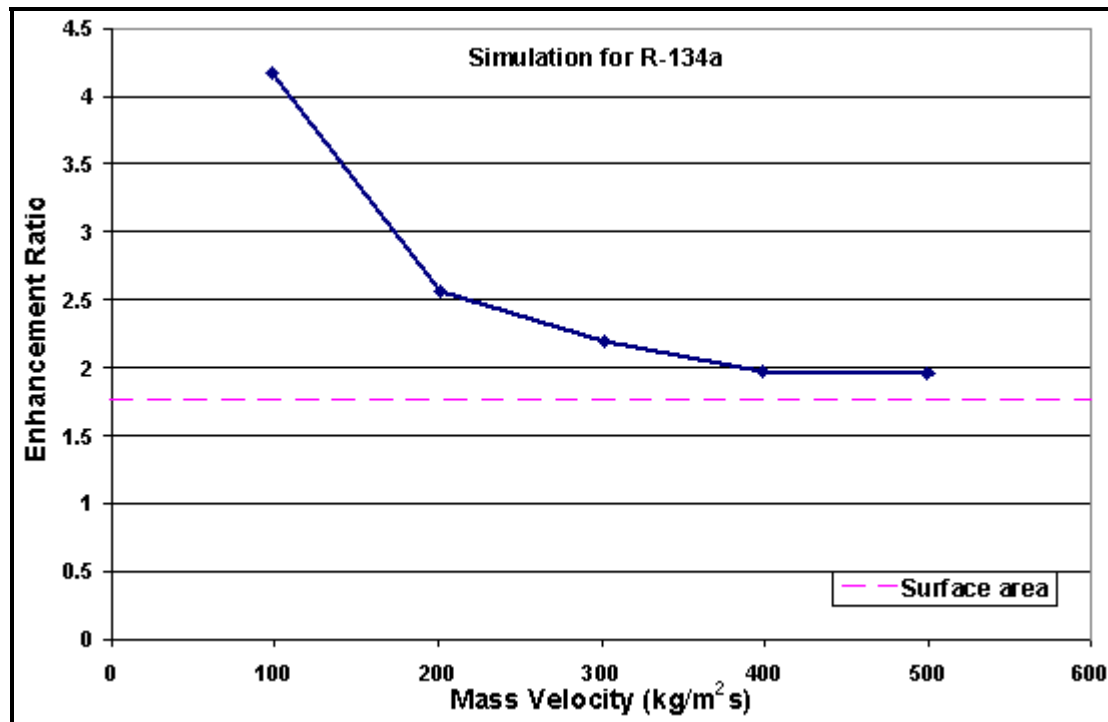


Figure 11.14. Thome, Kattan and Favrat [1997] microfin model showing enhancement ratios as a function of mass velocity.

Since mass velocities in direct-expansion evaporators are normally from about 50 to 500 kg/m<sup>2</sup>s (36,790 to 367,900 lb/hr ft<sup>2</sup>), this expression covers most applications. The value of  $E_{mf}$  varies from as high as 2.36 at 100 kg/m<sup>2</sup>s (73,580 lb/hr ft<sup>2</sup>) to as low as 1.21 at 500 kg/m<sup>2</sup>s (367,900 lb/hr ft<sup>2</sup>). A statistical comparison to 362 local heat transfer coefficients gave a standard deviation, a mean deviation and an average deviation for the R-134a data of 18.5%, 12.8% and 2.0%, respectively, while for R-123 the corresponding values were 12.9%, 11.8% and 6.4%. Additional work is required to compare this method to other microfin geometries and fluids. Presently, it covers vapor qualities up to 0.85, which can be assumed to be the point of onset of dryout. For  $x > 0.85$ , it is recommended that the heat transfer coefficient be prorated between its value at  $x = 0.85$  and its vapor-phase heat transfer coefficient at  $x = 1$ , the latter which is calculated with the Ravikurajan and Bergles (1985) single-phase correlation for ribbed tubes.

In summary, enhancement of microfin flow boiling heat transfer coefficients relative to plain tube values can be attributed to:

- An increase in the convective contribution by the single-phase effect of the microfins;
- A rise in the nucleate boiling contribution by the additional internal surface area;
- Enhancement of annular film evaporation by the Gregorig effect;
- Conversion of stratified-wavy flow (partially wetted tube perimeter) to annular flow (complete wetting) at low mass velocities.

## 11.9 Correlation for Horizontal Tubes with Twisted Tape Insert

For evaporation inside horizontal tubes with twisted tape inserts, Kedzierski and Kim (1998) proposed a correlation based on experimental data for one twisted tape ( $Y = 4.15$ ) with five pure fluids and two azeotropes (1401 data points) where  $Y$  is the twist ratio. The twist ratio  $Y$  is defined as the length along the tube for a 180° turn of the tape divided by the internal tube diameter  $d_i$ . Their correlation for the twisted tape flow boiling heat transfer coefficient  $\alpha_{tt}$  based on the plain tube internal diameter  $d_i$  and reduced pressure  $p_r$  is:

$$\frac{\alpha_{tt} d_i}{k_L} = 1.356 S_w^{c_1} \Pr_L^{c_2} p_r^{c_3} (-\log_{10} p_r)^{c_4} Bo^{c_5} \quad [11.9.1]$$

The Swirl number  $S_w$  is:

$$S_w = \frac{Re_s}{\sqrt{Y}} \quad [11.9.2]$$

The swirl Reynolds number  $Re_s$  is defined as:

$$Re_s = Re_{Lt} \frac{\sqrt{1 + \left(\frac{\pi}{2Y}\right)^2}}{1 - \frac{4t}{\pi d_i}} \quad [11.9.3]$$

where the tape thickness is  $t$ . The Reynolds number  $Re_{Lt}$  for the total flow as liquid is

$$Re_{Lt} = \frac{\rho_L \dot{m} d_i}{\mu_L} \quad [11.9.4]$$

Finally, the Boiling number is defined as

$$Bo = \frac{q}{\dot{m} h_{LG}} \quad [11.9.5]$$

where  $h_{LG}$  is the latent heat,  $q$  is the local heat flux and  $\dot{m}$  is the total mass velocity. The empirical exponents are a function of vapor quality,  $x$ :

$$c_1 = 0.993 - 1.181x + 0.899x^2 \quad [11.9.6]$$

$$c_2 = 1.108 - 2.366x + 1.451x^2 \quad [11.9.7]$$

$$c_3 = -2.383 + 5.255x - 1.791x^2 \quad [11.9.8]$$

$$c_4 = -3.195 + 6.668x \quad [11.9.9]$$

$$c_5 = 1.073 - 2.679x + 1.443x^2 \quad [11.9.10]$$

Hence, they used 15 empirical constants in their correlation. Other than for statistical expediency, it is not clear why the exponent on the liquid Prandtl number should be a function of vapor quality, ranging from a value of  $c_2 = 1.108$  at  $x = 0$  for all liquid flow to only  $c_2 = 0.193$  at  $x = 1$  for all vapor. This method did compared well to the data of Agrawal, Varma and Lal (1986) for R-12 at a twist ratio of 5.58. It is thus okay to use but probably its values should be compared to a good plain tube method to see if the enhancement ratio is reasonable or not.

## Chapter 12

# Two-Phase Flow Patterns

(This chapter was updated in 2007)

**SUMMARY:** For two-phase flows, the respective distribution of the liquid and vapor phases in the flow channel is an important aspect of their description. Their respective distributions take on some commonly observed flow structures, which are defined as two-phase flow patterns that have particular identifying characteristics. Heat transfer coefficients and pressure drops are closely related to the local two-phase flow structure of the fluid, and thus two-phase flow pattern prediction is an important aspect of modeling evaporation and condensation. In fact, recent heat transfer models for predicting intube boiling and condensation are based on the local flow pattern and hence, by necessity, require reliable flow pattern maps to identify what type of flow pattern exists at the local flow conditions. Analogous to predicting the transition from laminar to turbulent flow in single-phase flows, two-phase flow pattern maps are used for predicting the transition from one type of two-phase flow pattern to another.

In this chapter, first the geometric characteristics of flow patterns inside tubes will be described for vertical upward and horizontal flows. Next, several of the widely quoted, older flow pattern maps for vertical and horizontal flows will be presented. Then, a recent flow pattern map and its flow regime transition equations specifically for adiabatic flows and in particular for evaporation and condensation in horizontal tubes will be presented. Finally, flow patterns in two-phase flows over tube bundles will be addressed and a flow pattern map proposed for those flows will be shown.

### 12.1 Flow Patterns in Vertical Tubes

For co-current upflow of gas and liquid in a vertical tube, the liquid and gas phases distribute themselves into several recognizable flow structures. These are referred to as flow patterns and they are depicted in Figure 12.1 and can be described as follows:

- **Bubbly flow.** Numerous bubbles are observable as the gas is dispersed in the form of discrete bubbles in the continuous liquid phase. The bubbles may vary widely in size and shape but they are typically nearly spherical and are much smaller than the diameter of the tube itself.
- **Slug flow.** With increasing gas void fraction, the proximity of the bubbles is very close such that bubbles collide and coalesce to form larger bubbles, which are similar in dimension to the tube diameter. These bubbles have a characteristic shape similar to a bullet with a hemispherical nose with a blunt tail end. They are commonly referred to as Taylor bubbles after the instability of that name. Taylor bubbles are separated from one another by slugs of liquid, which may include small bubbles. Taylor bubbles are surrounded by a thin liquid film between them and the tube wall, which may flow downward due to the force of gravity, even though the net flow of fluid is upward.
- **Churn flow.** Increasing the velocity of the flow, the structure of the flow becomes unstable with the fluid traveling up and down in an oscillatory fashion but with a net upward flow. The instability is the result of the relative parity of the gravity and shear forces acting in opposing directions on the thin film of liquid of Taylor bubbles. This flow pattern is in fact an intermediate regime between the slug flow and annular flow regimes. In small diameter tubes, churn flow may not develop at all and the flow passes directly from slug flow to annular flow. Churn flow is typically a flow regime to be

avoided in two-phase transfer lines, such as those from a reboiler back to a distillation column or in refrigerant piping networks, because the mass of the slugs may have a destructive consequence on the piping system.

- **Annular flow.** Once the interfacial shear of the high velocity gas on the liquid film becomes dominant over gravity, the liquid is expelled from the center of the tube and flows as a thin film on the wall (forming an annular ring of liquid) while the gas flows as a continuous phase up the center of the tube. The interface is disturbed by high frequency waves and ripples. In addition, liquid may be entrained in the gas core as small droplets, so much so that the fraction of liquid entrained may become similar to that in the film. This flow regime is particularly stable and is the desired flow pattern for two-phase pipe flows.
- **Wispy annular flow.** When the flow rate is further increased, the entrained droplets may form transient coherent structures as clouds or wisps of liquid in the central vapor core.
- **Mist flow.** At very high gas flow rates, the annular film is thinned by the shear of the gas core on the interface until it becomes unstable and is destroyed, such that all the liquid in entrained as droplets in the continuous gas phase, analogous to the inverse of the bubbly flow regime. Impinging liquid droplets intermittently wet the tube wall locally. The droplets in the mist are often too small to be seen without special lighting and/or magnification.

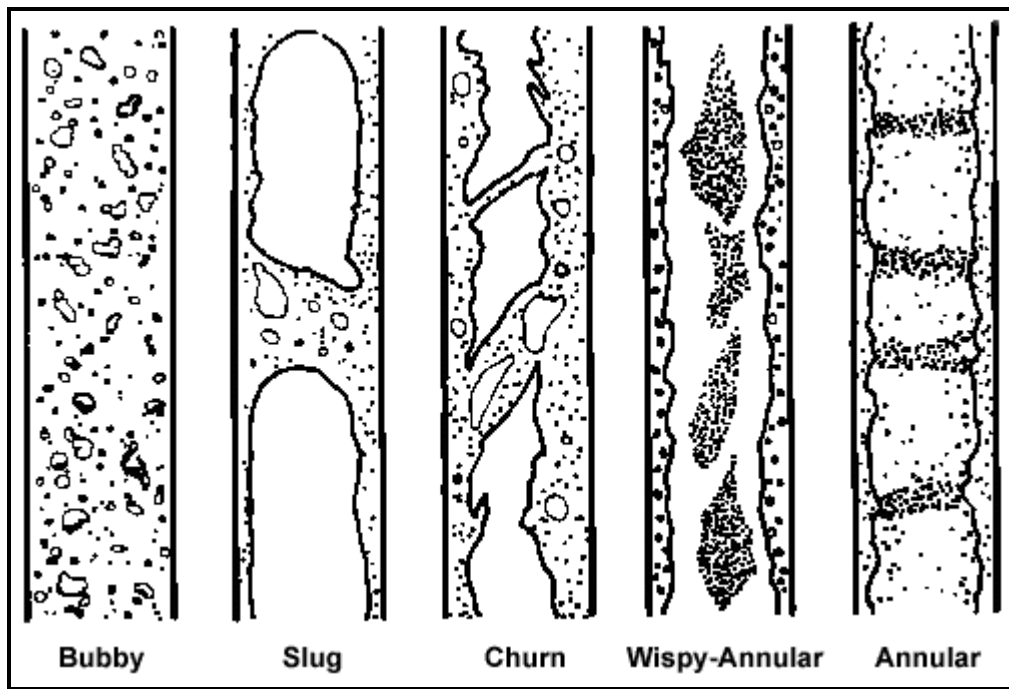


Figure 12.1. Two-phase flow patterns in vertical upflow.

## 12.2 Flow Patterns in Horizontal Tubes

Two-phase flow patterns in horizontal tubes are similar to those in vertical flows but the distribution of the liquid is influenced by gravity that acts to stratify the liquid to the bottom of the tube and the gas to the top. Flow patterns for co-current flow of gas and liquid in a horizontal tube are shown in Figure 12.2 and are categorized as follows:

- **Bubbly flow.** The gas bubbles are dispersed in the liquid with a high concentration of bubbles in the upper half of the tube due to their buoyancy. When shear forces are dominant, the bubbles tend to disperse uniformly in the tube. In horizontal flows, the regime typically only occurs at high mass flow rates.
- **Stratified flow.** At low liquid and gas velocities, complete separation of the two phases occurs. The gas goes to the top and the liquid to the bottom of the tube, separated by an undisturbed horizontal interface. Hence the liquid and gas are fully stratified in this regime.
- **Stratified-wavy flow.** Increasing the gas velocity in a stratified flow, waves are formed on the interface and travel in the direction of flow. The amplitude of the waves is notable and depends on the relative velocity of the two phases; however, their crests do not reach the top of the tube. The waves climb up the sides of the tube, leaving thin films of liquid on the wall after the passage of the wave.
- **Intermittent flow.** Further increasing the gas velocity, these interfacial waves become large enough to wash the top of the tube. This regime is characterized by large amplitude waves intermittently washing the top of the tube with smaller amplitude waves in between. Large amplitude waves often contain entrained bubbles. The top wall is nearly continuously wetted by the large amplitude waves and the thin liquid films left behind. Intermittent flow is also a composite of the plug and slug flow regimes. These subcategories are characterized as follows:
  - **Plug flow.** This flow regime has liquid plugs that are separated by elongated gas bubbles. The diameters of the elongated bubbles are smaller than the tube such that the liquid phase is continuous along the bottom of the tube below the elongated bubbles. Plug flow is also sometimes referred to as *elongated bubble flow*.
  - **Slug flow.** At higher gas velocities, the diameters of elongated bubbles become similar in size to the channel height. The liquid slugs separating such elongated bubbles can also be described as large amplitude waves.
- **Annular flow.** At even larger gas flow rates, the liquid forms a continuous annular film around the perimeter of the tube, similar to that in vertical flow but the liquid film is thicker at the bottom than the top. The interface between the liquid annulus and the vapor core is disturbed by small amplitude waves and droplets may be dispersed in the gas core. At high gas fractions, the top of the tube with its thinner film becomes dry first, so that the annular film covers only part of the tube perimeter and thus this is then classified as stratified-wavy flow.
- **Mist flow.** Similar to vertical flow, at very high gas velocities, all the liquid may be stripped from the wall and entrained as small droplets in the now continuous gas phase.

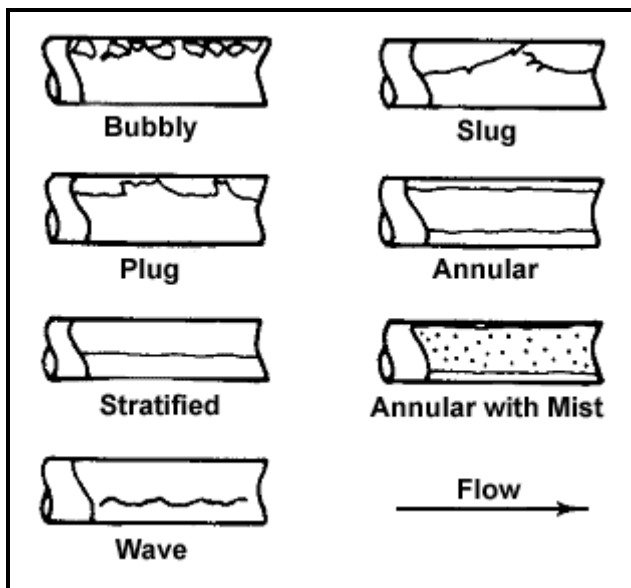


Figure 12.2. Two-phase flow patterns in horizontal flow.

### 12.3 Older Adiabatic Flow Pattern Maps for Vertical and Horizontal Flows in Tubes

For vertical upflow, Figure 12.3 shows the typical order of the flow regimes that would be encountered from inlet to outlet of an evaporator tube. The flow pattern typically begins in the bubbly flow regime at the inlet at the onset of nucleate boiling in the tube. This onset of nucleate boiling may begin in the subcooled zone of the tube, where bubbles nucleate in the superheated thermal boundary layer on the heated tube wall but tend to condense in the subcooled core. The onset of nucleate boiling may also be delayed to local vapor qualities greater than zero in the case of a subcooled inlet and a low heat flux. After bubbly flow the slug flow regime is entered and then the annular flow regime with its characteristic annular film of liquid. This film eventually dries out or the film is entrained by the interfacial vapor shear, taking the flow into the mist flow regime. The entrained liquid droplets may persist in the flow past the point of the vapor quality equal to 1.0.

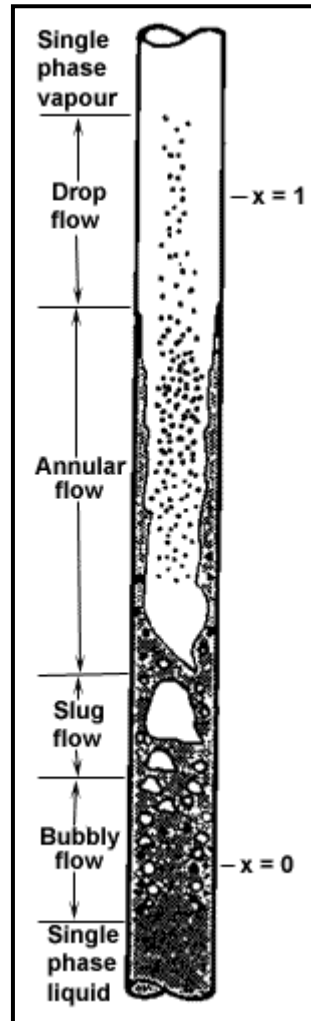
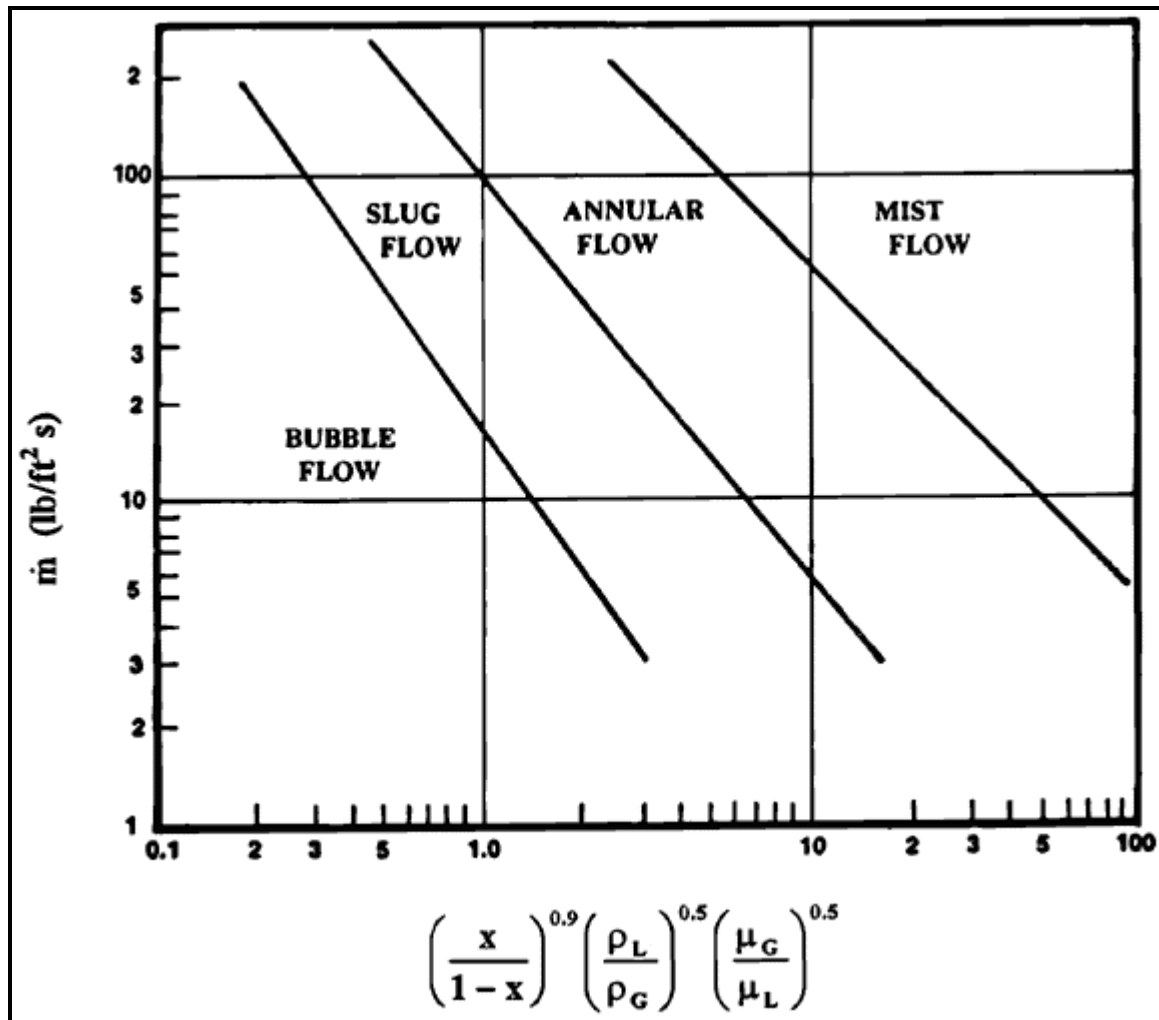


Figure 12.3. Flow regimes in a vertical evaporator tube from Collier and Thome (1994).

To predict the local flow pattern in a tube, a flow pattern map is used. It is a diagram that displays the transition boundaries between the flow patterns and is typically plotted on log-log axes using dimensionless parameters to represent the liquid and gas velocities. Fair (1960) and Hewitt and Roberts (1969) proposed widely quoted flow pattern maps for vertical upflow, illustrated in Figures 12.4 and 12.5, respectively. The most widely quoted flow pattern maps for predicting the transition between two-phase flow regimes for adiabatic flow in horizontal tubes are those of Baker (1954) and Taitel and Dukler (1976), depicted in Figures 12.6 and 12.7. Transition curves on flow pattern maps should be considered as transition zones analogous to that between laminar and turbulent flows. For a more comprehensive and fundamental treatment of two-phase flow transitions, refer to Barnea and Taitel (1986).

To utilize the Fair (1960) map illustrated in Figure 12.4, first one must calculate the value of the x-axis and the mass velocity (here in  $\text{lb}/\text{h ft}^2$ ) for the particular application at hand. The two values are then used to read vertically up and horizontally across the graph to find the point of intersection. The location of this point thus identifies where the flow is in the bubbly flow, slug flow, annular flow or mist flow regime, where the dark lines show the transition thresholds between the regimes.



**Figure 12.4.** Two-phase flow pattern map of Fair (1960) for vertical tubes.

To use the Hewitt and Roberts (1969) map for vertical up flow shown in Figure 12.5, the mass velocities of the liquid  $\dot{m}_L$  and gas (or vapor)  $\dot{m}_G$  must first be calculated using the local vapor quality. Then the values of the x and y coordinates are determined and the intersection of these two values on the map identifies the flow pattern predicted to exist at these flow conditions.

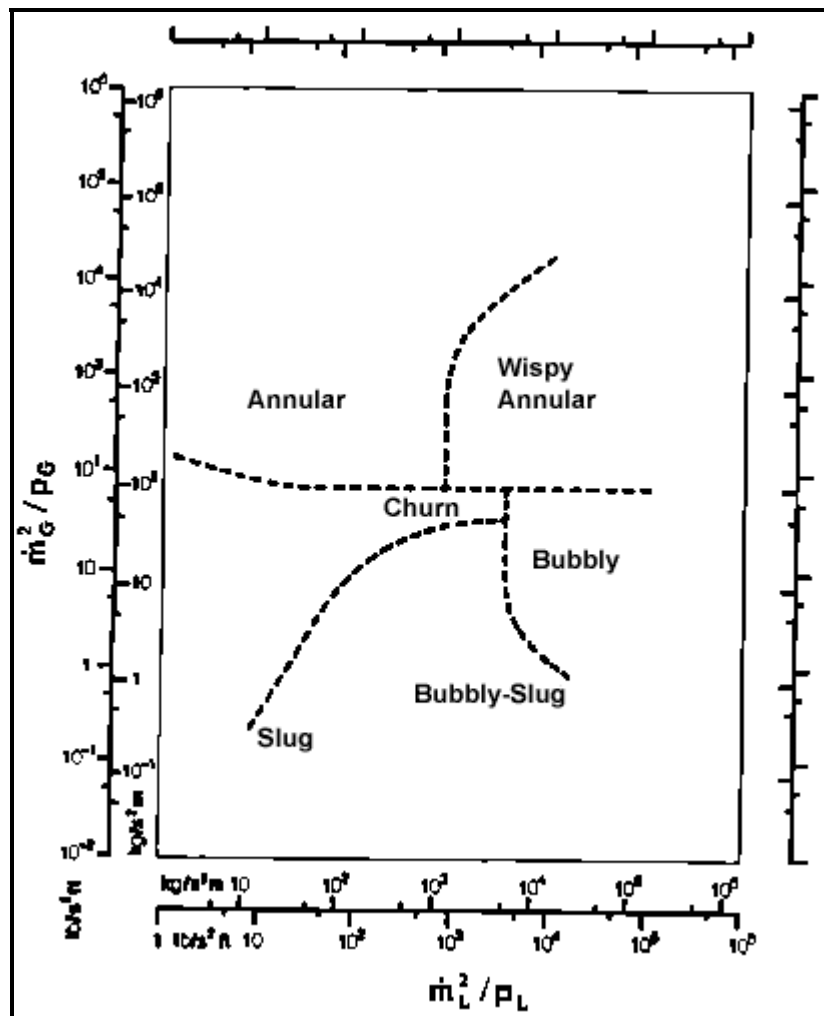


**Figure 12.5.** Two-phase flow pattern map of Hewitt and Roberts (1969) for vertical tubes.

The Baker (1954) map for horizontal two-phase flow in tubes shown in Figure 12.6 is presented in both SI and English units. To utilize the map, first the mass velocities of the liquid and vapor must be determined. Then his parameters  $\lambda$  and  $\psi$  are calculated. The gas-phase parameter  $\lambda$  is:

$$\lambda = \left( \frac{\rho_G}{\rho_{air}} \frac{\rho_L}{\rho_{water}} \right)^{1/2} \quad [12.3.1]$$

and the liquid-phase parameter  $\psi$  is:

$$\psi = \left( \frac{\sigma_{water}}{\sigma} \right) \left[ \left( \frac{\mu_L}{\mu_{water}} \right) \left( \frac{\rho_{water}}{\rho_L} \right)^2 \right]^{1/3} \quad [12.3.2]$$

where  $\rho_G$ ,  $\rho_L$ ,  $\mu_L$  and  $\sigma$  are properties of the fluid and the reference properties are:

- $\rho_{\text{water}} = 1000 \text{ kg/m}^3$ ;
- $\rho_{\text{air}} = 1.23 \text{ kg/m}^3$ ;
- $\mu_{\text{water}} = 0.001 \text{ Ns/m}^2$ ;
- $\sigma_{\text{water}} = 0.072 \text{ N/m}$ .

The values of the x-axis and y-axis are then determined to identify the particular flow regime.

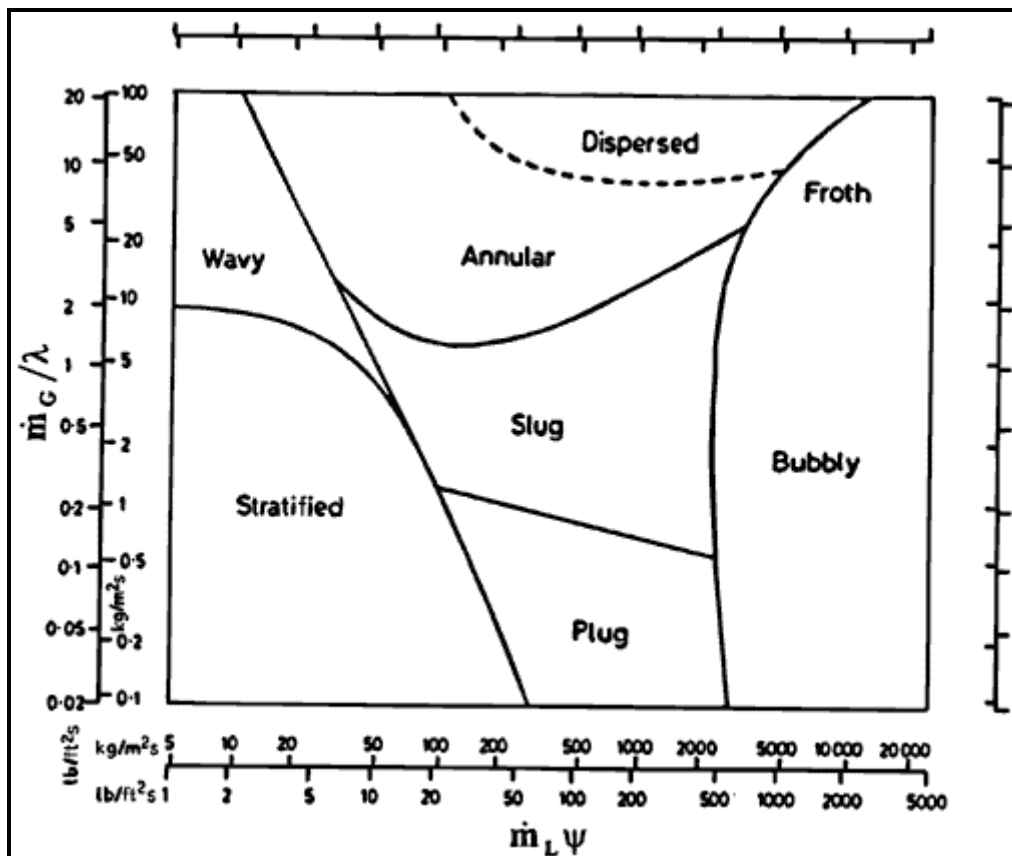


Figure 12.6. Two-phase flow pattern map of Baker (1954) for horizontal tubes.

The Taitel and Dukler (1976) map for horizontal flow in tubes shown in Figure 12.7 is based on their analytical analysis of the flow transition mechanisms together with empirical selection of several parameters. The map uses the Martinelli parameter X, the gas Froude number  $Fr_G$  and the parameters T and K and is composed of three graphs. The Martinelli parameter is:

$$X = \left[ \frac{(dp/dz)_L}{(dp/dz)_G} \right]^{1/2} \quad [12.3.3]$$

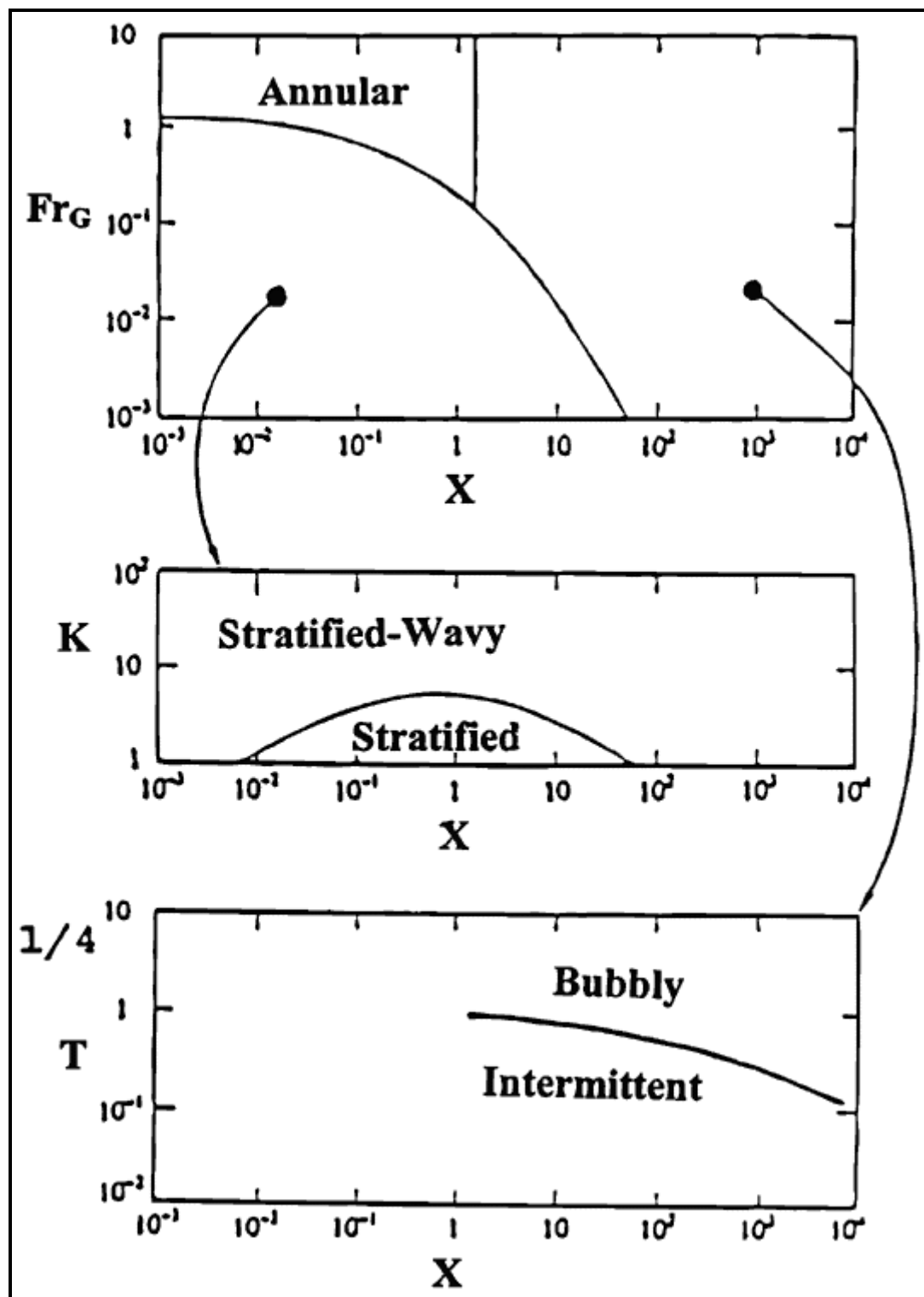


Figure 12.7. Two-phase flow pattern map of Taitel and Dukler (1976) for horizontal tubes.

The gas-phase Froude number is:

$$Fr_G = \frac{\dot{m}_G}{[\rho_G(\rho_L - \rho_G)d_i g]^{1/2}} \quad [12.3.4]$$

Their parameter T is:

$$T = \left[ \frac{|(dp/dz)_L|}{g(\rho_L - \rho_G)} \right]^{1/2} \quad [12.3.5]$$

where g is the acceleration due to gravity ( $g = 9.81 \text{ m/s}^2$ ). Their parameter K is:

$$K = Fr_G \text{Re}_L^{1/2} \quad [12.3.6]$$

where the liquid-phase and vapor-phase Reynolds numbers are:

$$\text{Re}_L = \frac{\dot{m}_L d_i}{\mu_L} \quad [12.3.7]$$

$$\text{Re}_G = \frac{\dot{m}_G d_i}{\mu_G} \quad [12.3.8]$$

The pressure gradient of the flow for phase k (where k is either L or G) is:

$$(dp/dz)_k = -\frac{2f_k \dot{m}_k^2}{\rho_k d_i} \quad [12.3.9]$$

For  $\text{Re}_k < 2000$ , the laminar flow friction factor equation is used:

$$f_k = \frac{16}{\text{Re}_k} \quad [12.3.10]$$

For  $\text{Re}_k > 2000$ , the turbulent flow friction factor equation is used (even for the transition regime from 2000 to 10,000):

$$f_k = \frac{0.079}{\text{Re}_k^{1/4}} \quad [12.3.11]$$

To implement the map, one first determines the Martinelli parameter X and  $Fr_G$ . Using these two parameters on the top graph, if their coordinates fall in the annular flow regime, then the flow pattern is annular. If the coordinates of  $Fr_G$  and X fall in the lower left zone of the top graph, then K is calculated. Using K and X in the middle graph, the flow regime is identified as either stratified-wavy or as fully stratified. If the coordinates of  $Fr_G$  and X fall in the right zone on the top graph, then T is calculated. Using T and X in the bottom graph, the flow regime is identified as either bubbly flow or intermittent (plug or slug) flow.

These flow pattern maps were all developed for adiabatic two-phase flows but are often extrapolated for use with the diabatic processes of evaporation or condensation. As with any extrapolation, this may or may not produce reliable results. For a description of flow pattern transition theory, a good review was presented by Taitel (1990).

## 12.4 Flow Pattern Map for Evaporation in Horizontal Tubes

For evaporation in horizontal tubes, Figure 12.8 from Collier and Thome (1994) depicts the typical flow regimes, including cross-sectional views of the flow structure. For condensation, the flow regimes are similar with the exception that the top tube wall is not dry in stratified types of flow but instead is coated with a thin condensing film of condensate.

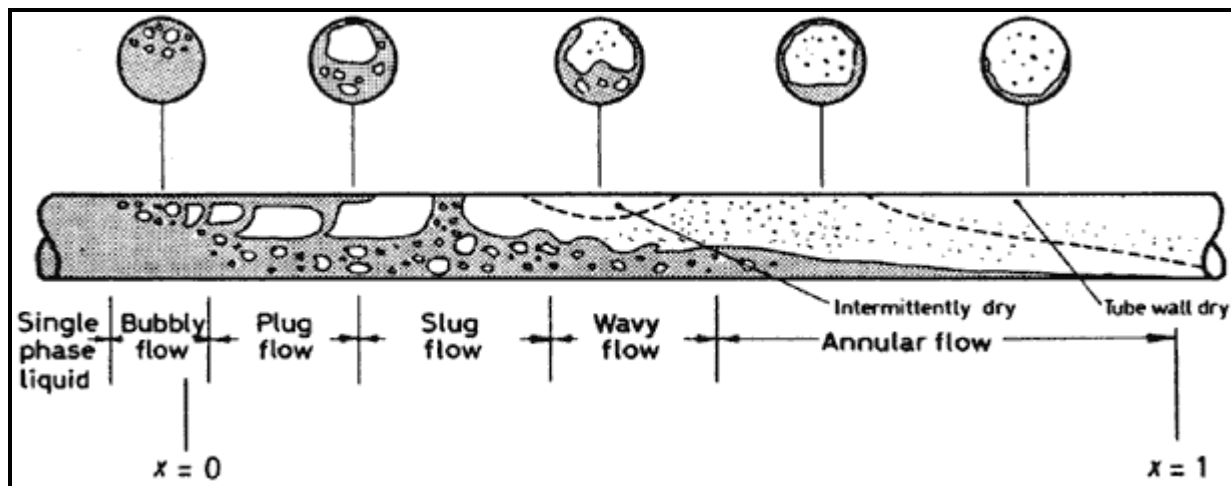


Figure 12.8. Flow patterns during evaporation in a horizontal tube from Collier and Thome (1994).

**Kattan-Thome-Favrat map.** For small diameter tubes typical of heat exchangers, Kattan, Thome and Favrat (1998a, 1998b, 1998c) proposed a modification of the Steiner (1993) map, which itself is a modified Taitel-Dukler map, and included a method for predicting the onset of dryout at the top of the tube in evaporating annular flows. This flow pattern map will be presented here as it is used in Chapter 10 for predicting local flow boiling coefficients based on the local flow pattern. The flow regime transition boundaries of the Kattan-Thome-Favrat flow pattern map are depicted in Figure 12.9 (bubbly flow is at very high mass velocities and is not shown). This map provides the transition boundaries on a linear-linear graph with mass velocity plotted versus gas or vapor fraction for the particular fluid and flow channel, which is much easier to use than the log-log format of other maps.

The transition boundary curve between *annular* and *intermittent* flows to *stratified-wavy* flow is:

$$\dot{m}_{\text{wavy}} = \left\{ \frac{16 A_{Gd}^3 g d_i \rho_L \rho_G}{x^2 \pi^2 (1 - (2h_{Ld} - 1)^2)^{0.5}} \left[ \frac{\pi^2}{25 h_{Ld}^2} (1-x)^{-F_1(q)} \left( \frac{We}{Fr} \right)_L^{-F_2(q)} + 1 \right] \right\}^{0.5} + 50 \quad [12.4.1]$$

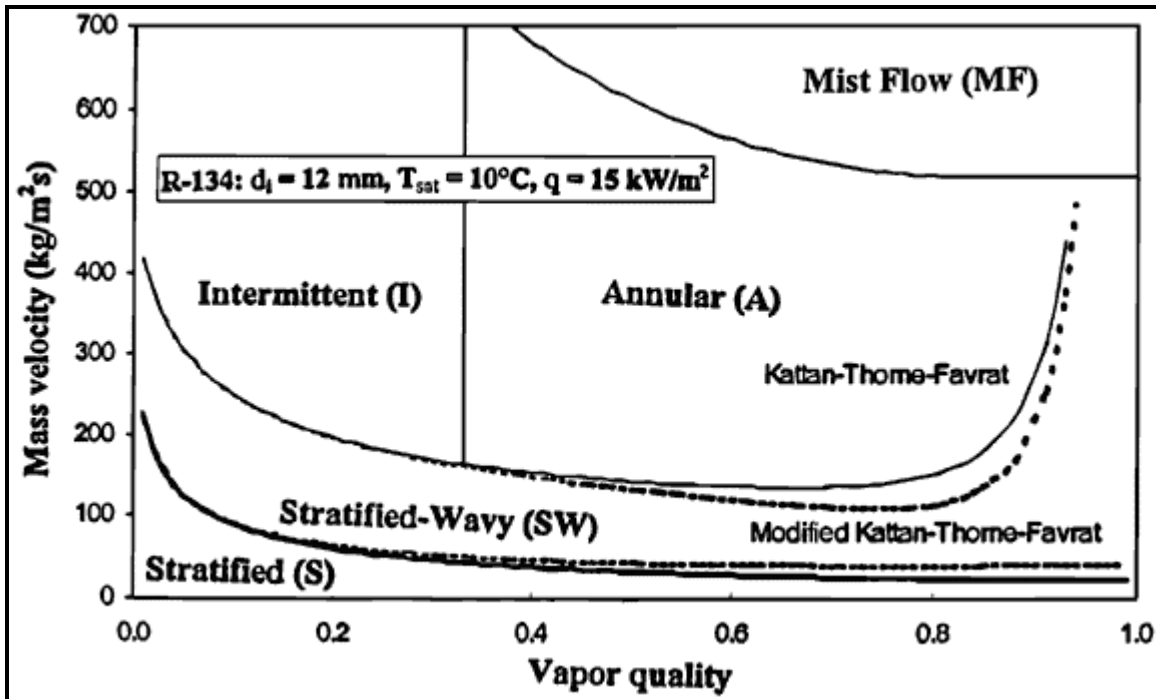


Figure 12.9. Kattan-Thome-Favrat flow pattern map illustrating flow regime transition boundaries.

The high vapor quality portion of this curve depends on the ratio of the Froude number ( $Fr_L$ ) to the Weber number ( $We_L$ ), where  $Fr_L$  is the ratio of the inertia to the surface tension forces while  $We_L$  is the ratio of inertia to gravity forces. The mass velocity threshold for the transition from *annular flow* to *mist flow* is:

$$\dot{m}_{mist} = \left\{ \frac{7680 A_{Gd}^2 g d_i \rho_L \rho_G}{x^2 \pi^2 \xi_{Ph}} \left( \frac{Fr}{We} \right)_L \right\}^{0.5} \quad [12.4.2]$$

Evaluating the above expression for the minimum mass velocity of the mist flow transition gives the value of  $x_{min}$ , which for  $x > x_{min}$ :

$$\dot{m}_{mist} = \dot{m}_{min} \quad [12.4.3]$$

The transition between *stratified-wavy flow* and *fully stratified flow* is given by the expression

$$\dot{m}_{strat} = \left\{ \frac{(226.3)^2 A_{Ld} A_{Gd}^2 \rho_G (\rho_L - \rho_G) \mu_L g}{x^2 (1-x) \pi^3} \right\}^{1/3} \quad [12.4.4]$$

The transition threshold into *bubbly flow* is

$$\dot{m}_{bubbly} = \left\{ \frac{256 A_{Gd} A_{Ld}^2 d_i^{1.25} \rho_L (\rho_L - \rho_G) g}{0.3164 (1-x)^{1.75} \pi^2 P_{id} \mu_L^{0.25}} \right\}^{1/1.75} \quad [12.4.5]$$

In the above equations, the ratio of We to Fr is

$$\left(\frac{We}{Fr}\right)_L = \frac{g d_i^2 \rho_L}{\sigma} \quad [12.4.6]$$

and the friction factor is

$$\xi_{Ph} = \left[ 1.138 + 2 \log \left( \frac{\pi}{1.5 A_{Ld}} \right) \right]^{-2} \quad [12.4.7]$$

The non-dimensional empirical exponents  $F_1(q)$  and  $F_2(q)$  in the  $\dot{m}_{wavy}$  boundary equation include the effect of heat flux on the onset of dryout of the annular film, i.e. the transition of annular flow into annular flow with partial dryout, the latter which is classified as stratified-wavy flow by the map. They are:

$$F_1(q) = 646.0 \left( \frac{q}{q_{DNB}} \right)^2 + 64.8 \left( \frac{q}{q_{DNB}} \right) \quad [12.4.8a]$$

$$F_2(q) = 18.8 \left( \frac{q}{q_{DNB}} \right) + 1.023 \quad [12.4.8b]$$

The Kutateladze (1948) correlation for the heat flux of departure from nucleate boiling,  $q_{DNB}$  is used to normalize the local heat flux:

$$q_{DNB} = 0.131 \rho_G^{1/2} h_{LG} [g(\rho_L - \rho_G)\sigma]^{1/4} \quad [12.4.9]$$

The vertical boundary between *intermittent flow* and *annular flow* is assumed to occur at a fixed value of the Martinelli parameter,  $X_{tt}$ , equal to 0.34, where  $X_{tt}$  is defined as:

$$X_{tt} = \left( \frac{1-x}{x} \right)^{0.875} \left( \frac{\rho_G}{\rho_L} \right)^{0.5} \left( \frac{\mu_L}{\mu_G} \right)^{0.125} \quad [12.4.10]$$

Solving for  $x$ , the threshold line of the intermittent-to-annular flow transition at  $x_{IA}$  is:

$$x_{IA} = \left\{ \left[ 0.2914 \left( \frac{\rho_G}{\rho_L} \right)^{-1/1.75} \left( \frac{\mu_L}{\mu_G} \right)^{-1/7} \right] + 1 \right\}^{-1} \quad [12.4.11]$$

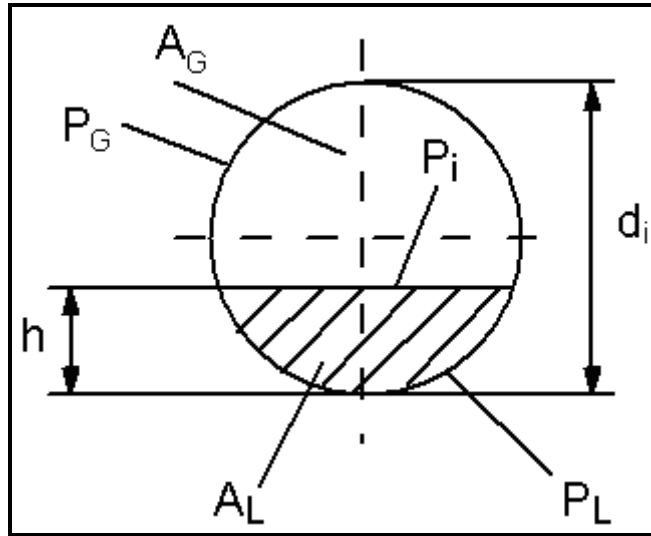


**Figure 12.10. Cross-sectional and peripheral fractions in a circular tube.**

Figure 12.10 defines the geometrical dimensions of the flow where  $P_L$  is the wetted perimeter of the tube,  $P_G$  is the dry perimeter in contact with only vapor,  $h$  is the height of the completely stratified liquid layer, and  $P_i$  is the length of the phase interface. Similarly  $A_L$  and  $A_G$  are the corresponding cross-sectional areas. Normalizing with the tube internal diameter  $d_i$ , six dimensionless variables are obtained:

$$h_{Ld} = \frac{h}{d_i}, \quad P_{Ld} = \frac{P_L}{d_i}, \quad P_{Gd} = \frac{P_G}{d_i}, \quad P_{id} = \frac{P_i}{d_i}, \quad A_{Ld} = \frac{A_L}{d_i^2}, \quad A_{Gd} = \frac{A_G}{d_i^2} \quad [12.4.12]$$

For  $h_{Ld} \leq 0.5$ :

$$\begin{aligned} P_{Ld} &= \left( 8(h_{Ld})^{0.5} - 2(h_{Ld}(1-h_{Ld}))^{0.5} \right) / 3, \quad P_{Gd} = \pi - P_{Ld} \\ A_{Ld} &= \left( 12(h_{Ld}(1-h_{Ld}))^{0.5} + 8(h_{Ld})^{0.5} \right) h_{Ld} / 15, \quad A_{Gd} = \frac{\pi}{4} - A_{Ld} \end{aligned} \quad [12.4.13]$$

For  $h_{Ld} > 0.5$ :

$$\begin{aligned} P_{Gd} &= \left( 8(1-h_{Ld})^{0.5} - 2(h_{Ld}(1-h_{Ld}))^{0.5} \right) / 3, \quad P_{Ld} = \pi - P_{Gd} \\ A_{Gd} &= \left( 12(h_{Ld}(1-h_{Ld}))^{0.5} + 8(1-h_{Ld})^{0.5} \right) (1-h_{Ld}) / 15, \quad A_{Ld} = \frac{\pi}{4} - A_{Gd} \end{aligned} \quad [12.4.14]$$

For  $0 \leq h_{Ld} \leq 1$ :

$$P_{id} = 2(h_{Ld}(1-h_{Ld}))^{0.5} \quad [12.4.15]$$

Since  $h$  is unknown, an iterative method utilizing the following equation is necessary to calculate the reference liquid level  $h_{Ld}$ :

$$X_{tt}^2 = \left[ \left( \frac{P_{Gd} + P_{id}}{\pi} \right)^{1/4} \left( \frac{\pi^2}{64 A_{Gd}^2} \right) \left( \frac{P_{Gd} + P_{id}}{A_{Gd}} + \frac{P_{id}}{A_{Ld}} \right) \right] \left( \frac{\pi}{P_{Ld}} \right)^{1/4} \left( \frac{64 A_{Ld}^3}{\pi^2 P_{Ld}} \right) \quad [12.4.16]$$

Once the reference liquid level  $h_{Ld}$  is known, the dimensionless variables are calculated from equations [12.4.13] to [12.4.15] and the transition curves for the new flow pattern map are determined with equations [12.4.1] to [12.4.11].

This map was developed from a database for five refrigerants: two single-component fluids (R-134a and R-123), two near-azeotropic mixtures (R-402A and R-404A) and one azeotropic mixture (R-502). The test conditions covered the following range of variables: mass flow rates from 100 to 500 kg/m<sup>2</sup>s, vapor qualities from 4-100%, heat fluxes from 440 to 36500 W/m<sup>2</sup>, saturation pressures from 0.112 to 0.888 MPa, Weber numbers from 1.1 to 234.5, and liquid Froude numbers from 0.037 to 1.36. The Kattan-Thome-Favrat flow pattern map correctly identified 96.2% of these flow pattern data.

Zürcher, Thome and Favrat (1997c) obtained additional two-phase flow pattern observations for the zeotropic refrigerant mixture R-407C at an inlet saturation pressure of 0.645 MPa and the map accurately identified these new flow pattern data. Zürcher, Thome and Favrat (1999) also obtained two-phase flow pattern data for ammonia with a 14 mm bore sight glass for mass velocities from 20 to 140 kg/m<sup>2</sup>s, vapor qualities from 1-99% and heat fluxes from 5000 to 58000 W/m<sup>2</sup>, all taken at a saturation temperature of 4°C and saturation pressure of 0.497 MPa. Thus, the mass velocity range in the database was extended from 100 kg/m<sup>2</sup>s down to 20 kg/m<sup>2</sup>s. In particular, it was observed that the transition curve  $\dot{m}_{strat}$  was too low and Eq. [12.4.4], was empirically corrected by adding +20x as follows:

$$\dot{m}_{strat} = \left\{ \frac{(226.3)^2 A_{Ld} A_{Gd}^2 \rho_G (\rho_L - \rho_G) \mu_L g}{x^2 (1-x) \pi^3} \right\}^{1/3} + 20x \quad [12.4.17]$$

where  $\dot{m}_{strat}$  is in kg/m<sup>2</sup>s. The transition from stratified-wavy flow to annular flow at high vapor qualities was instead observed to be too high and hence an additional empirical term with an exponential factor modifying the boundary at high vapor qualities was added to Equation [12.4.1] to take this into account as:

$$\dot{m}_{wavy(new)} = \dot{m}_{wavy} - 75e^{-\left(\frac{(x^2-0.97)^2}{x(1-x)}\right)} \quad [12.4.18]$$

where the mass velocity is in kg/m<sup>2</sup>s. The movement of these boundaries has an effect on the dry angle calculation  $\theta_{dry}$  in the Kattan, Thome and Favrat (1998c) flow boiling heat transfer model and shifts the onset of dryout to slightly higher vapor qualities, which is in agreement with the ammonia heat transfer test data.

In addition, Zürcher, Thome and Favrat (1999) found that the onset of dryout effect in the Kattan-Thome-Favrat map was too strong compared to their new, more extensive observations for ammonia. They recommended reducing that the influence by one-half, so the value of q in expressions [12.4.8a] and [12.4.8b] should be replaced with q/2.

To utilize this map, the following parameters are required: vapor quality ( $x$ ), mass velocity ( $\dot{m}$ ), tube internal diameter ( $d_i$ ), heat flux ( $q$ ), liquid density ( $\rho_L$ ), vapor density ( $\rho_G$ ), liquid dynamic viscosity ( $\mu_L$ ), vapor dynamic viscosity ( $\mu_G$ ), surface tension ( $\sigma$ ), and latent heat of vaporization ( $h_{LG}$ ), all in SI units. The local flow pattern is identified by the following procedure:

1. Solve Eq. [12.4.16] iteratively with Eqs. [12.4.10], [12.4.13], [12.4.14] and [12.4.15];
2. Evaluate Eq. [12.4.12];
3. Evaluate Eqs. [12.4.6], [12.4.7], [12.4.8a], [12.4.8b] and [12.4.9];
4. Evaluate Eqs. [12.4.1], [12.4.2] or [12.4.3], [12.4.4], [12.4.5] and [12.4.11];
5. Compare these values to the given values of  $x$  and  $\dot{m}$  to identify the flow pattern.

Note that Eq. [12.4.18] should be used in place of Eq. [12.4.1] and Eq. [12.4.17] should be used in place of Eq. [12.4.11] to utilize the most updated version. The map is thus specific to the fluid properties, flow conditions (heat flux) and tube internal diameter input into the equations. The map can be programmed into any computer language, evaluating the transition curves in incremental steps of 0.01 in vapor quality to obtain a tabular set of threshold boundary points, which can then be displayed as a complete map with  $\dot{m}$  vs.  $x$  as coordinates.

**Zürcher-Favrat-Thome map.** Following the above work, based on extensive flow pattern observations for ammonia at 5°C in a 14.0 mm horizontal sight glass tube at the exit of the same diameter of evaporator tube, Zürcher, Favrat and Thome (2002) proposed a new version of the transition boundary curve between *annular and intermittent flows to stratified-wavy flow*, i.e. for equation [12.4.1], based on an indepth analysis of the dissipation effects in a two-phase flow. The interested reader is referred to their paper for the details.

**Thome-El Hajal map.** For practicality and for consistency between the flow map and the heat transfer model, an easier to implement version of the Kattan-Thome-Favrat map was proposed by Thome and El Hajal (2003). In the previously presented flow pattern map, dimensionless variables  $A_{Ld}$ ,  $A_{Gd}$ ,  $h_{Ld}$  and  $P_{id}$  were calculated in an iterative way using the stratified flow void fraction model illustrated in Fig.12.10. On the other hand, the flow boiling heat transfer model of Kattan, Thome and Favrat (1998c) uses the Steiner (1993) version of the Rouhani-Axelson drift flux model for horizontal tubes for the cross-sectional void fraction  $\varepsilon$  (see Chapter 17):

$$\varepsilon = \frac{x}{\rho_G} \left[ (1 + 0.12(1-x)) \left( \frac{x}{\rho_G} + \frac{1-x}{\rho_L} \right) + \frac{1.18(1-x)[g\sigma(\rho_L - \rho_G)]^{0.25}}{\dot{m}\rho_L^{0.5}} \right]^{-1} \quad [12.4.19]$$

This drift flux void fraction model is easy to apply and gives the void fraction as an explicit function of total mass velocity, whereas the iterative method of Taitel and Dukler used previously does not. Hence, it makes sense to use the same void fraction model in both the flow pattern map and the flow boiling heat transfer model. For this, the Rouhani-Axelson model is a good choice as the general method, at least for refrigerants, which has been proven experimentally by 238 void fraction measurements for R-22 and R-410A made by Ursenbacher, Wojtan and Thome (2004) for stratified-wavy and intermittent types of flow. Using this void fraction model, the values  $A_{Ld}$  and  $A_{Gd}$  are now directly determinable by first calculating the void fraction using the above expression:

$$A_{Ld} = \frac{A(1-\varepsilon)}{d_i^2} \quad [12.4.20]$$

$$A_{Gd} = \frac{A\varepsilon}{d_i^2} \quad [12.4.21]$$

The dimensionless liquid height  $h_{Ld}$  and the dimensionless length of the liquid interface  $P_{id}$  can be expressed as a function of the stratified angle  $\theta_{strat}$  (stratified angle around upper perimeter of the tube to stratified liquid level):

$$h_{Ld} = 0.5 \left[ 1 - \cos \left( \frac{2\pi - \theta_{strat}}{2} \right) \right] \quad [12.4.22]$$

$$P_{id} = \sin \left( \frac{2\pi - \theta_{strat}}{2} \right) \quad [12.4.23]$$

To avoid completely any iteration, the geometrical expression for the stratified angle  $\theta_{strat}$  is calculated from an approximate expression by Biberg (1999), evaluated in terms of void fraction, as follows:

$$\theta_{strat} = 2\pi - 2 \begin{Bmatrix} \pi(1-\varepsilon) + \left(\frac{3\pi}{2}\right)^{1/3} \left[ 1 - 2(1-\varepsilon) + (1-\varepsilon)^{1/3} - \varepsilon^{1/3} \right] \\ - \frac{1}{200} (1-\varepsilon) \varepsilon [1 - 2(1-\varepsilon)] [1 + 4((1-\varepsilon)^2 + \varepsilon^2)] \end{Bmatrix} \quad [12.4.24]$$

As the void fraction is a function of mass velocity, it influences the position of the transition curves that involve  $\varepsilon$  in the Thome-El Hajal map. The effect of mass velocity on flow regime transitions is shown in Figure 12.11, where the influence is only significant at low mass velocities. The strongest effect of mass velocity is observed on the SW-I/A transition curve for vapor qualities below 0.1 and at very low mass velocities, where the transition curve goes up with increasing mass velocity. This divergence becomes less significant as the vapor quality increases and at higher mass velocities. The boundary curve A-M also moves up marginally with increasing mass velocity. In implementing the method for design purposes, the actual mass velocity is used to calculate the transition curves while for expediency in calculating the flow pattern maps below, a fixed value of mass velocity was used for evaluating the entire map.

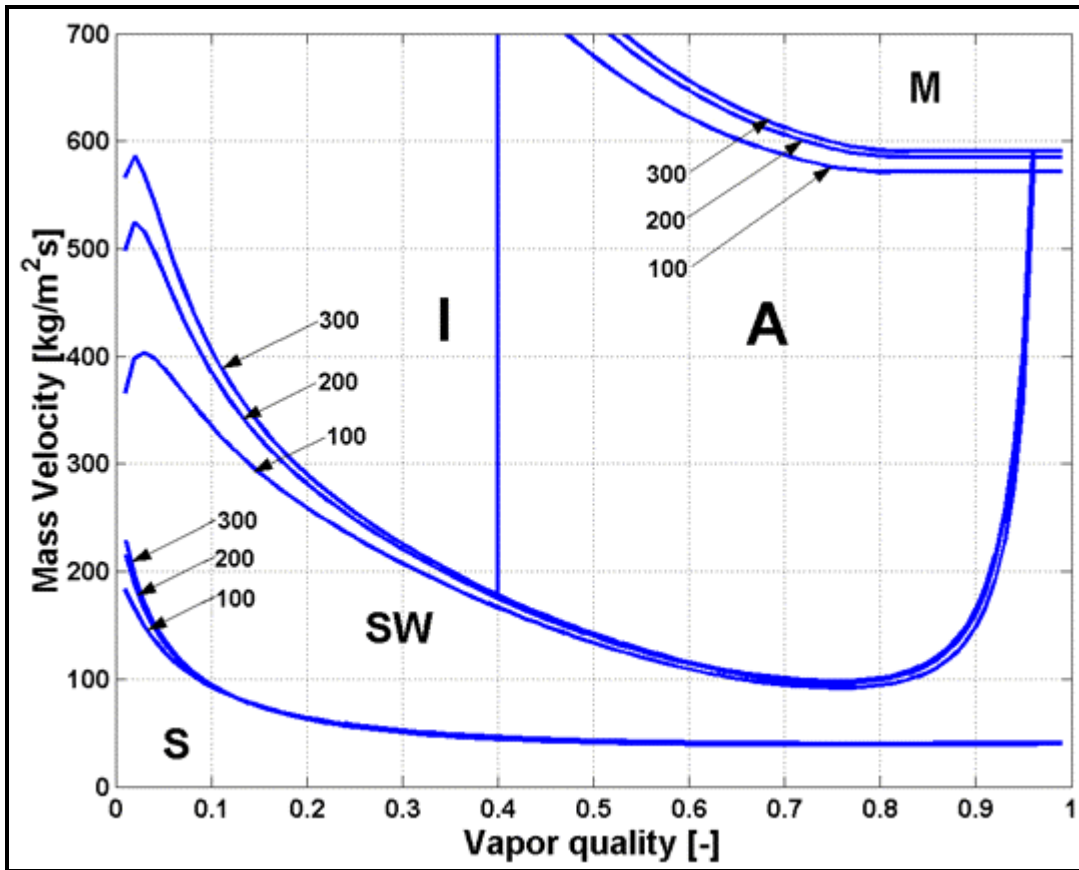


**Figure 12.11. Flow pattern map of Thome-El Hajal for R-410A at 5°C in a 13.84 mm internal diameter tube with its equations evaluated at mass velocities of 100, 200 and 300  $\text{kg}/\text{m}^2\text{s}$  at a heat flux of 17.5  $\text{kW}/\text{m}^2$ .**

Some high quality photographs of two-phase flow patterns in horizontal tubes are available from Barbieri, Sáiz-Jabardo and Bandarra Filho (2005) taken in the test facility described in Barbieri and Sáiz-Jabardo (2006). They are for 500  $\text{kg}/\text{m}^2\text{s}$  for R-134a in a sight glass tube at the exit of an evaporator tube (note some external condensation on the outside of the tube in some of the photographs). Figure 12.12 shows some high quality photographs of stratified types of flow. Figure 12.13 shows the sequence of events in the intermittent flow regime, characterized by a cyclic variation between low amplitude waves (top photograph) and large amplitude waves (bottom photograph). Figure 12.14 presents some images of annular flow.

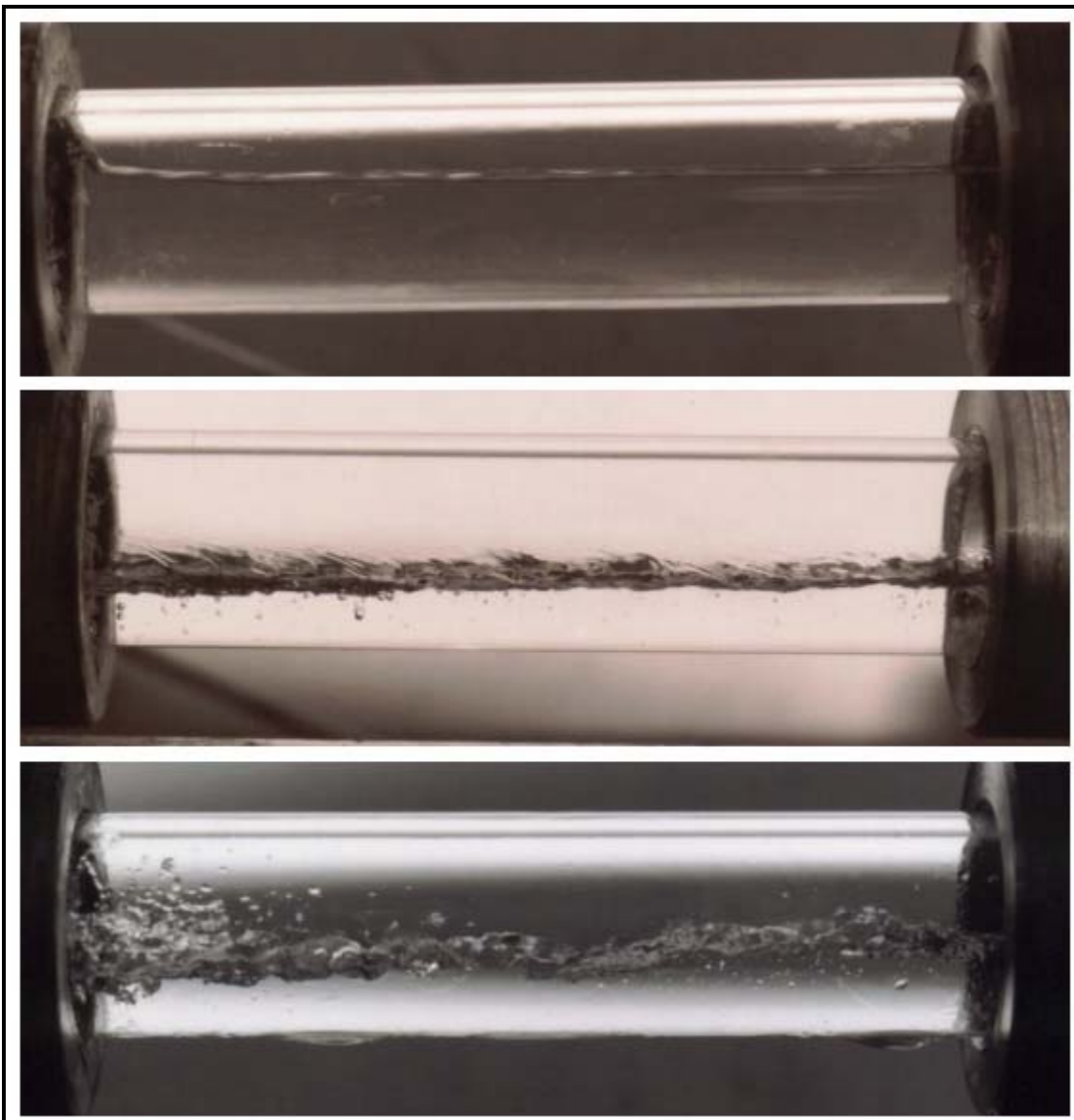


**Figure 12.12. Stratified flow regime photographs of Barbieri, Sáiz-Jabardo and Bandarra Filho (2005). Top: stratified flow; middle and bottom: stratified-wavy flow. Tube diameter: 15.8 mm.**

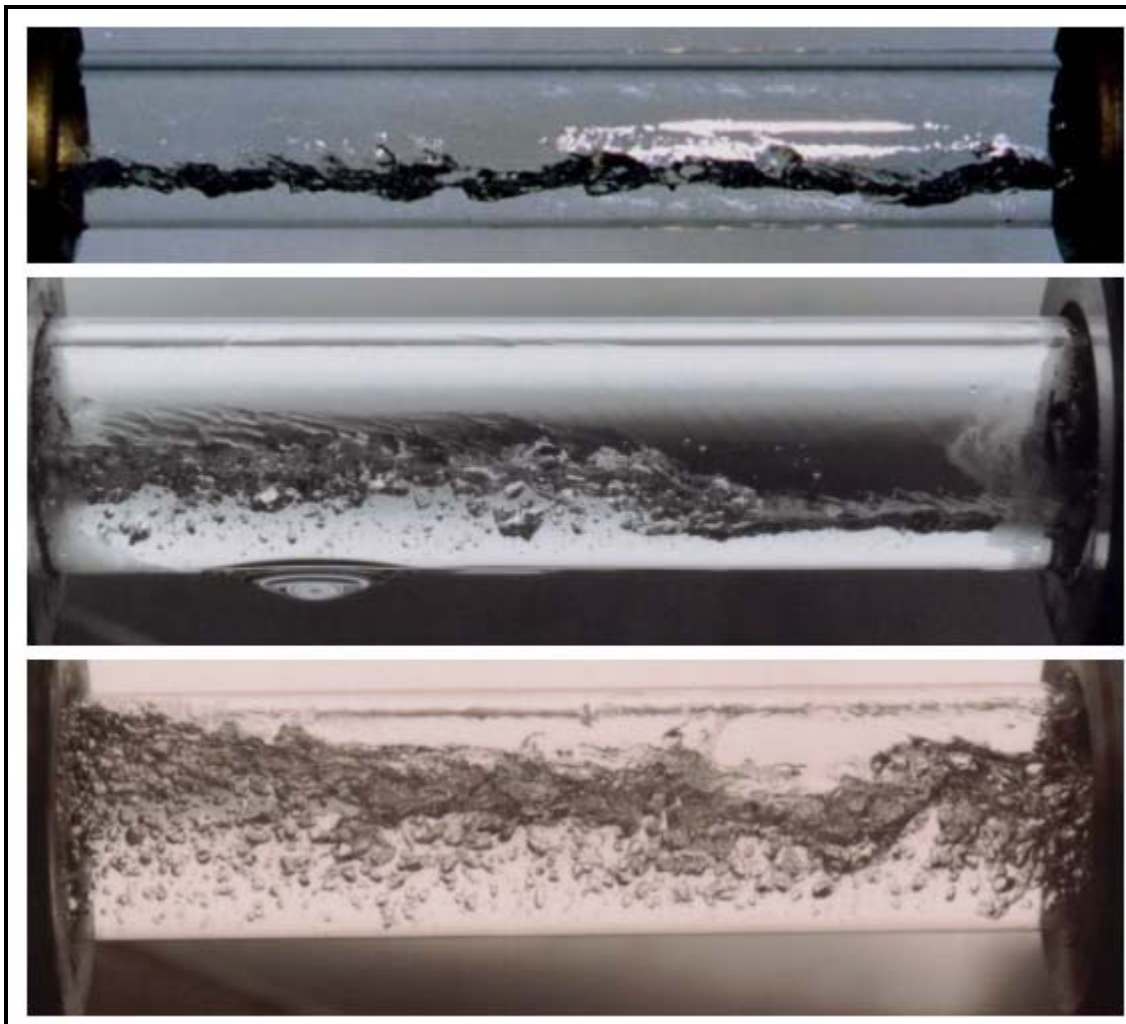


**Figure 12.13.** Intermittent flow regime photographs of Barbieri, Sáiz-Jabardo and Bandarra Filho (2005) with a sequence of interfacial waves in a 9.52 mm tube (top) followed by climbing waves in a 15.8 mm tube (middle) and then a large amplitude wave reaching the top of the channel in a 15.8 mm tube (bottom).

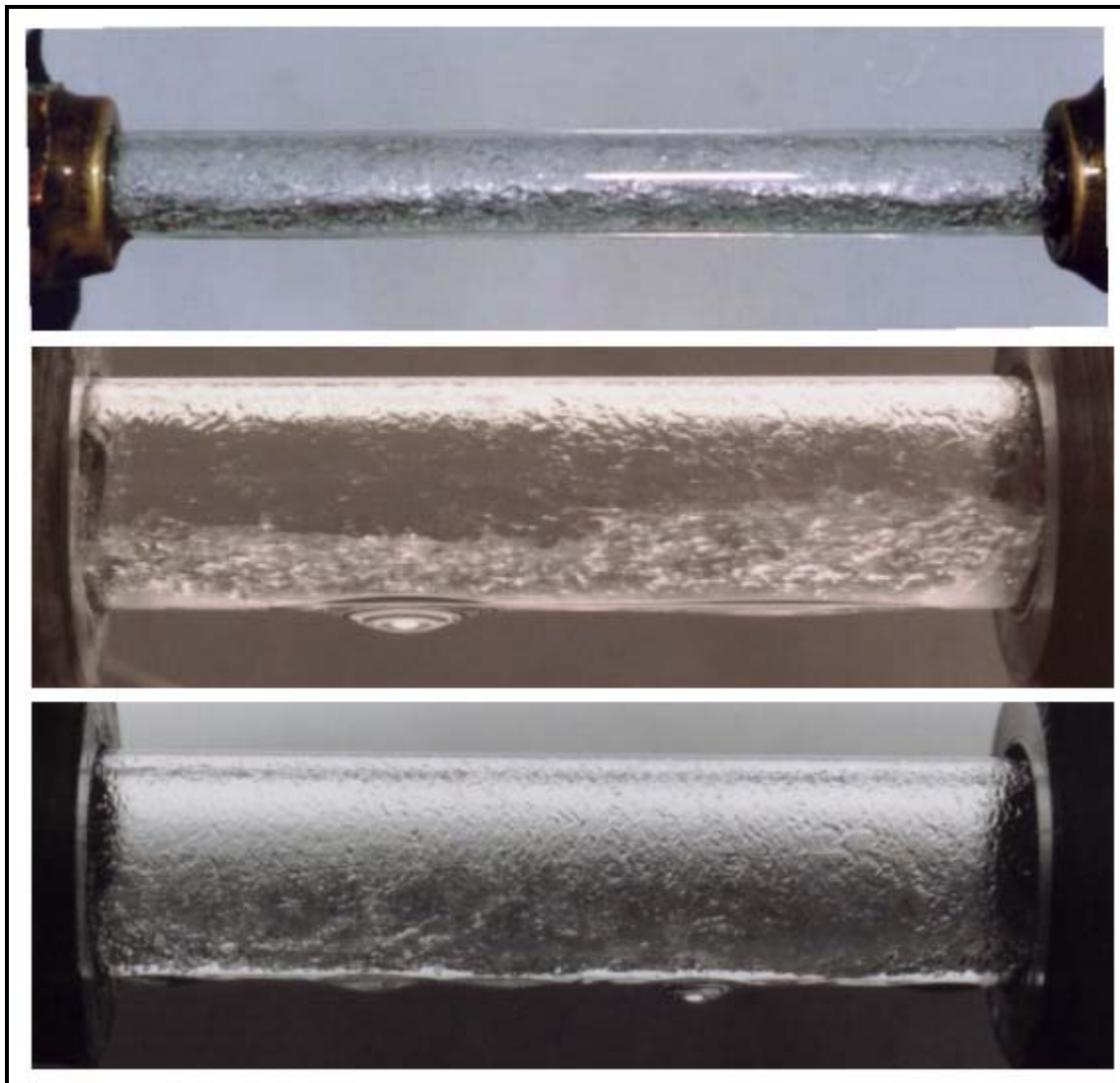


**Figure 12.14. Annular flow regime photographs of Barbieri, Sáiz-Jabardo and Bandarra Filho (2005) showing three images of the interfacial waves on an annular liquid film. Top: 9.52 mm tube; middle: 15.8 mm tube; bottom: 15.8 mm tube.**

**Wojtan-Ursenbacher-Thome map.** The flow pattern map of Kattan, Thome and Favrat (1998a) was developed primarily for vapor qualities higher than 0.15 and also without benefit of a dedicated experimental campaign on the effect of heat flux on the initiation and completion of dryout at high vapor qualities. In light of the dynamic void fraction measurements made by Wojtan, Ursenbacher and Thome (2004) and their video observations for mass velocities between 70-200 kg/m<sup>2</sup>s in a 13.84 mm horizontal sight glass tube, the following conclusions were reached:

1. Fully stratified flow was not detected at any of the mass velocities tested;
2. In the vapor quality range  $0 < x < x_{IA}$ , an alternating flow structure of liquid slugs and stratified-wavy interfaces was observed (where  $x_{IA}$  is the vertical line separating intermittent and annular flows);
3. The transition from slug/stratified-wavy flows to fully stratified-wavy flows without any slugs appeared approximately to occur at  $x_{IA}$ ;

4. Only slug flow was observed for the zone identified by the Thome-El Hajal map to be in the stratified-wavy region for  $\dot{m} > \dot{m}_{wavy}(x_{IA})$ .

Based on these observations, the stratified-wavy flow region of the Thome-El Hajal version of the flow map was modified by Wojtan, Ursenbacher and Thome (2005a) as follows:

1. A new transition line was added at  $\dot{m}_{strat} = \dot{m}_{strat}(x_{IA})$  at  $x < x_{IA}$  (this creates a new horizontal transition line to the left of  $x_{IA}$  and modifies the boundary of the stratified (S) regime);
2. The stratified-wavy region has been divided into three subzones:
  - For  $\dot{m} > \dot{m}_{wavy}(x_{IA})$ , this becomes the Slug zone.
  - For  $\dot{m}_{strat} < \dot{m} < \dot{m}_{wavy}(x_{IA})$  and  $0 < x < x_{IA}$ , this becomes the Slug/Stratified-Wavy zone.
  - For  $1 > x \geq x_{IA}$ , this remains as the Stratified-Wavy zone.

Figure 12.15 depicts the new flow pattern map calculated for R-22 with the above modifications applied to the Thome-El Hajal version of Kattan-Thome-Favrat flow pattern map to better describe the actual character of the flow. The dash lines correspond to the new dryout and mist flow transition curves described below.

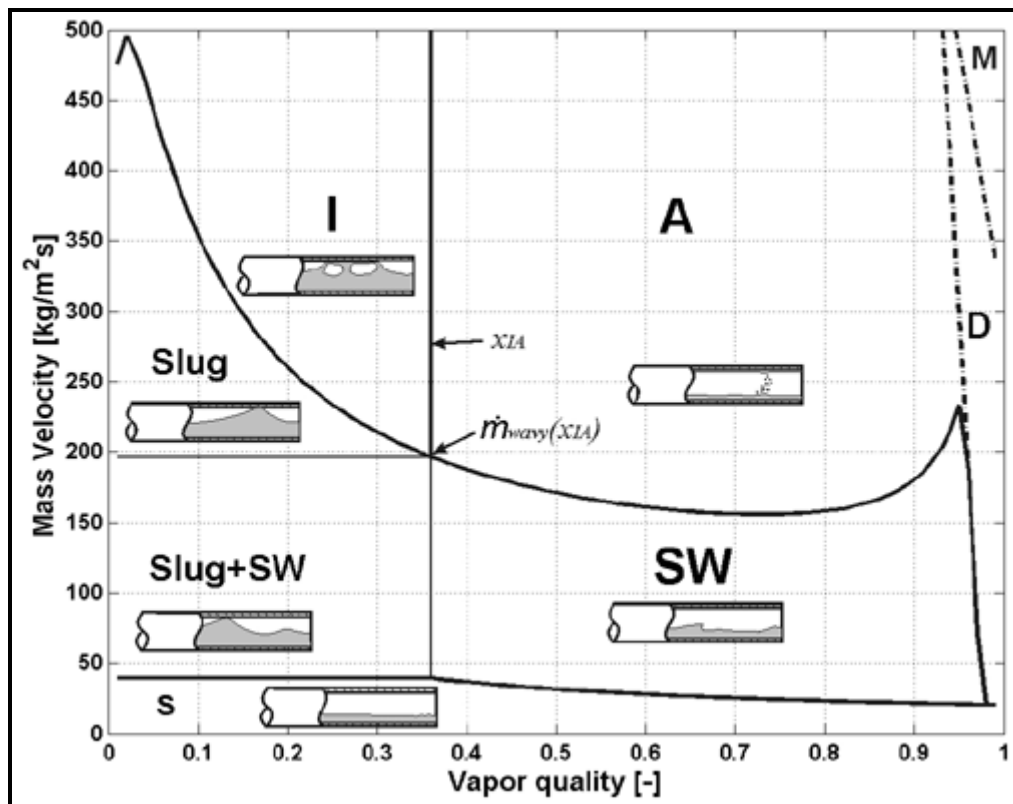


**Figure 12.15. New flow pattern map simulated for R-22 at 5°C in a 13.84 mm channel using 100 kg/m²s and 2.1 kW/m² to calculate the transition curves.**

As depicted in Figure 12.16, dryout occurs at the top of a horizontal tube first at  $x_{di}$  (cross section A-A), where the annular liquid film is thinner, and then dryout proceeds around the perimeter of the tube along its length (cross section B-B) until reaching the bottom (cross section C-C) where the liquid film disappears at  $x_{de}$ . Thus, dryout in a horizontal tube takes place over a range of vapor qualities, beginning

as an annular flow and ending when the fully developed mist flow regime is reached. This flow regime between  $x_{di}$  and  $x_{de}$  is called dryout.

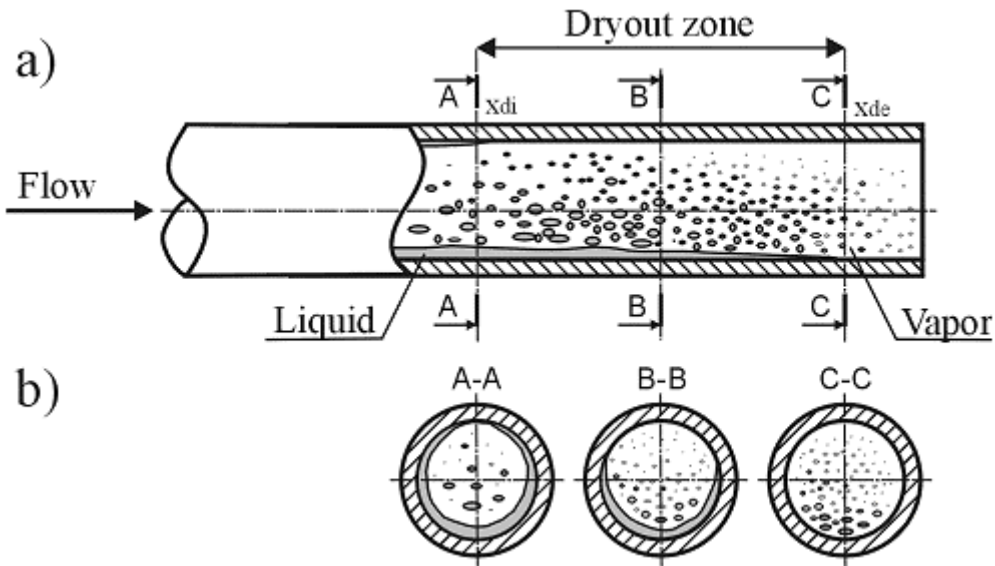


**Figure 12.16. Dryout in a horizontal tube. (a) Dryout zone during evaporation in a horizontal tube beginning at  $x_{di}$  at top of tube and ending at  $x_{de}$  at bottom of tube; (b) Cross sections: A-A onset of dryout in annular flow; B-B dryout; C-C end of dryout and beginning of mist flow.**

Since it is difficult to determine the onset and completion of dryout only from visual observations in a sight glass tube, a large number of experimental flow boiling heat transfer points were measured by Wojtan, Ursenbacher and Thome (2005a) for R-22 and R-410A at mass velocities from 70 to 700 kg/m<sup>2</sup>s and heat fluxes from 2.0 to 57.5 kW/m<sup>2</sup>. The tube internal diameters tested were 13.84 mm for R-22 and R-410A as well as 8.00 mm for R-410A. These flow boiling heat transfer data were used to identify the locations of  $x_{di}$  and  $x_{de}$ . As illustrated in Figure 12.17, the sharp change in the heat transfer coefficient with increasing vapor quality indicates the inception of dryout whereas the end of this decrease of heat transfer coefficient marks the end of dryout and the beginning of mist flow. The observations in the sight glass confirmed that the onsets of dryout and mist flow appeared at the same vapor quality as detected by the heat transfer measurements.

Analyzing experimental results and observations in the sight glass, it is obvious that usually there is no step-wise transition from annular flow to mist flow. The first attempt to model the annular-dryout transition during evaporation in horizontal tubes was made by Lavin and Young (1965). They proposed a new transition between the annular and dryout zones based on the Weber number for R-22 and R-12. Lavin and Young observed the dryout process, but with the apparatus used, they could not obtain the heat transfer coefficient within the dryout regime nor study the conditions under which the dryout regime ends and a stable mist flow was established.

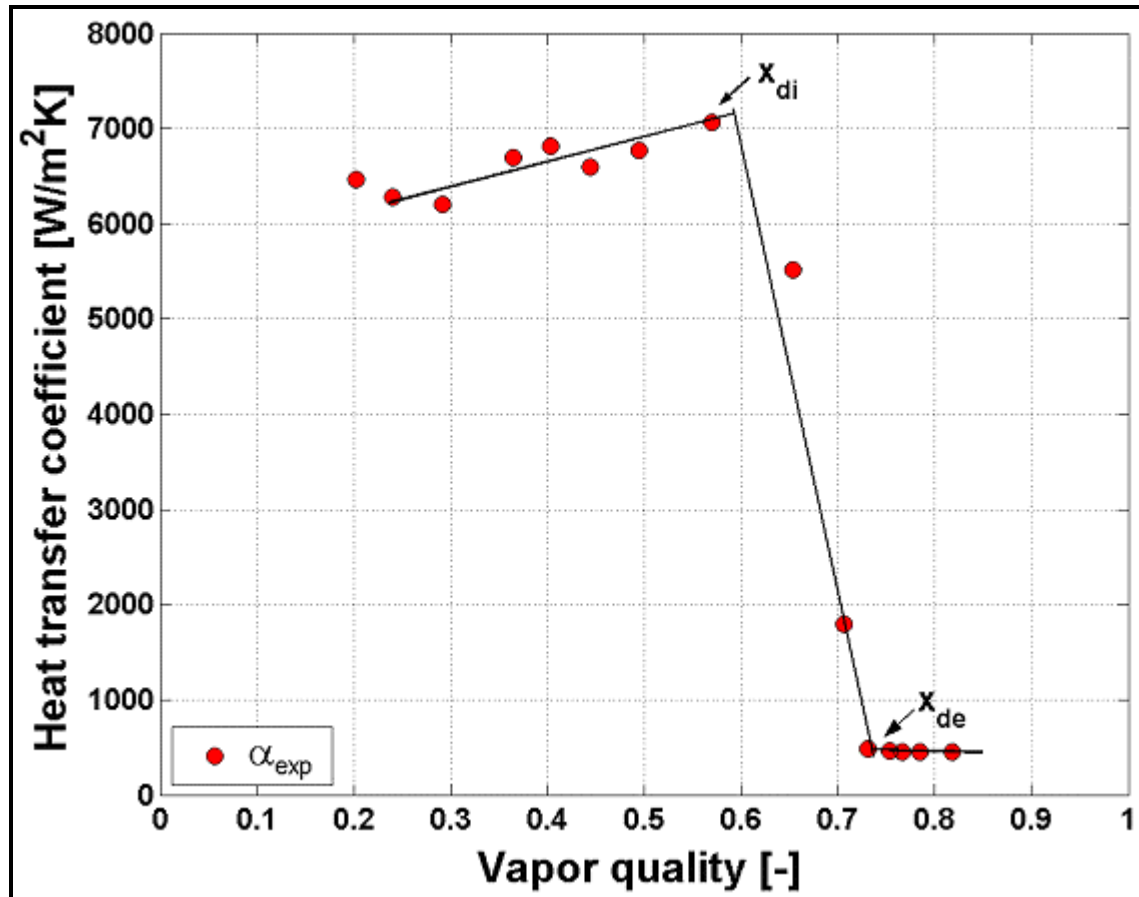


**Figure 12.17. Experimental heat transfer coefficients in the 13.84 mm test section for R-22 at 5°C with an initial heat flux of 57.5 kW/m<sup>2</sup> at 600 kg/m<sup>2</sup>s.**

Since dryout occurs over an interval of vapor quality, Mori et al. (2000) defined the inception of dryout to be  $x_{di}$  and the completion of dryout to be  $x_{de}$  and then used three characteristic regimes that they named  $S1$ ,  $S2$  and  $S3$  to predict their values. The best agreement of the Wojtan, Ursenbacher and Thome (2005a) values of  $x_{di}$  and  $x_{de}$  identified from their heat transfer data were given by their regime  $S2$ , whose corresponding transition expressions by Mori et al. (2000) are:

$$x_{di} = 0.58 e^{[0.52 - 0.000021 We_G^{0.96} Fr_G^{-0.02} (\rho_G / \rho_L)^{-0.08}]} \quad [12.4.25]$$

$$x_{de} = 0.61 e^{[0.57 - 0.0000265 We_G^{0.94} Fr_G^{-0.02} (\rho_G / \rho_L)^{-0.08}]} \quad [12.4.26]$$

The approach of Mori et al. was modified by Wojtan, Ursenbacher and Thome (2005a) to include the heat flux effect observed from their results for R-22 and R-410A evaporating at 5°C in 8.00 and 13.84 mm diameter test sections for heat fluxes up to 57.5 kW/m<sup>2</sup>, using the dimensionless heat flux ratio ( $q/q_{DNB}$ ) and new empirical factors. Thus, the new limits for the beginning and end of the dryout regime are calculated with their following transition equations:

$$x_{di} = 0.58 e^{[0.52 - 0.235 We_G^{0.17} Fr_G^{0.37} (\rho_G / \rho_L)^{0.25} (q/q_{DNB})^{0.7}]} \quad [12.4.27]$$

$$x_{de} = 0.61 e^{[0.57 - 0.0058 We_G^{0.38} Fr_G^{0.15} (\rho_G/\rho_L)^{-0.09} (q/q_{DNB})^{0.27}]} \quad [12.4.28]$$

where  $q_{DNB}$  is calculated with the expression [12.4.9] of Kutateladze (1948). After inversion of these two equations to solve for the mass velocity in terms of vapor quality, the annular-to-dryout boundary (A-D) and the dryout-to-mist flow boundary (D-M) transition equations for  $x_{di}$  and  $x_{de}$  become respectively:

$$\dot{m}_{dryout} = \left[ \frac{1}{0.235} \left( \ln \left( \frac{0.58}{x} \right) + 0.52 \right) \left( \frac{d_i}{\rho_G \sigma} \right)^{-0.17} \left( \frac{1}{gd_i \rho_G (\rho_L - \rho_v)} \right)^{-0.37} \left( \frac{\rho_G}{\rho_L} \right)^{-0.25} \left( \frac{q}{q_{DNB}} \right)^{-0.7} \right]^{0.926} \quad [12.4.29]$$

$$\dot{m}_{mist} = \left[ \frac{1}{0.0058} \left( \ln \left( \frac{0.61}{x} \right) + 0.57 \right) \left( \frac{d_i}{\rho_G \sigma} \right)^{-0.38} \left( \frac{1}{gd_i \rho_G (\rho_L - \rho_v)} \right)^{-0.15} \left( \frac{\rho_G}{\rho_L} \right)^{0.09} \left( \frac{q}{q_{DNB}} \right)^{-0.27} \right]^{0.943} \quad [12.4.30]$$

Including the above modifications also to the stratified-wavy region and integrating the new A-D and D-M transition curves into their map, the implementation procedure for the Wojtan-Ursenbacher-Thome map is as follows:

1. The geometric parameters  $\epsilon$ ,  $A_{Ld}$ ,  $A_{Gd}$ ,  $h_{Ld}$ ,  $P_{id}$  and  $\theta_{strat}$  are calculated using the expressions [12.4.19] to [12.4.24], respectively.
2. As the effect of heat flux at high vapor quality is captured by the A-D and D-M transition curves, the SW-I/A transition is first calculated from the following adiabatic version of expression [12.4.1]:

$$\dot{m}_{wavy} = \left\{ \frac{16 A_{Gd}^3 g d_i \rho_L \rho_G}{x^2 \pi^2 [1 - (2h_{Ld} - 1)^2]^{0.5}} \left[ \frac{\pi^2}{25 h_{Ld}^2} \left( \frac{We_L}{Fr_L} \right)^{-1} + 1 \right] \right\}^{0.5} + 50 \quad [12.4.31]$$

3. The stratified-wavy region is then subdivided into three zones as follows:
  - i.  $\dot{m} > \dot{m}_{wavy}(x_{IA})$  gives the slug flow zone;
  - ii.  $\dot{m}_{strat} < \dot{m} < \dot{m}_{wavy}(x_{IA})$  and  $0 < x < x_{IA}$  give the Slug/Stratified-Wavy zone;
  - iii.  $1 > x \geq x_{IA}$  gives the Stratified-Wavy zone.
4. The S-SW transition is calculated from the original boundary expression [12.4.4] but now  $\dot{m}_{strat} = \dot{m}_{strat}(x_{IA})$  when  $x < x_{IA}$ , the latter which gives the flat horizontal part of the boundary for  $0 \leq x \leq x_{IA}$ .
5. The I-A transition is calculated from the original boundary given by [12.4.11] and extended down to its intersection with  $\dot{m}_{strat}$ .
6. The A-D boundary is calculated from [12.4.29] where its value takes precedent over the value from step 2 above when its value is smaller than  $\dot{m}_{wavy}$ .

7. The D-M boundary is calculated from [12.4.30] but since the A-D and D-M lines are not parallel these boundaries can intersect, so that when  $x_{de} < x_{di}$  then  $x_{de}$  is set equal to the value of  $x_{di}$  and no D region exists (at high mass velocities and low heat fluxes where this occurs, the high vapor shear will tend to make the annular film to be of uniform thickness and hence it seems reasonable that the entire perimeter becomes dry simultaneously at  $x_{di}$ ).
8. The following logic is applied to define the transitions in the high vapor quality range for the onset of dryout in the map, referred to as  $\dot{m}_{dryout}$ , implemented in the following order:
  - If  $\dot{m}_{strat}(x) \geq \dot{m}_{dryout}(x)$ , then  $\dot{m}_{dryout} = \dot{m}_{strat}(x)$ ;
  - If  $\dot{m}_{wavy}(x) \geq \dot{m}_{dryout}(x)$ , then  $\dot{m}_{dryout} = \dot{m}_{dryout}(x)$  and the  $\dot{m}_{wavy}$  curve ceases to exist, which means that the rightmost boundary of the  $\dot{m}_{wavy}$  curve is its intersection with the  $\dot{m}_{dryout}$  curve;
  - If  $\dot{m}_{dryout}(x) \geq \dot{m}_{mist}(x)$ , which is possible at low heat fluxes and high mass velocities, then  $\dot{m}_{dryout} = \dot{m}_{dryout}(x)$  and the dryout regime disappears at this mass velocity.

Figure 12.18 shows the flow pattern maps calculated for R-22 for four heat fluxes, where the movements of the A-D and D-M boundaries are quite evident. Compared to the Kattan-Thome-Favrat map, the new regimes slug (Slug), slug/stratified-wavy (Slug+SW) and dryout (D) are now encountered. Notably, it is observed that the dryout and mist flow regions become smaller as the heat flux decreases.

This map was developed from a database for R-22 and R-410A at 5°C but its prior versions covered eight other refrigerants (R-134a, R-123, R-402A, R-404A, R-502, R-407C, R-507A and ammonia) for tube diameters from 8 to 14 mm. The test conditions in all these experiments covered the following range of variables: mass flow rates from 16 to 700 kg/m<sup>2</sup>s, vapor qualities from 1-99% and heat fluxes from 440 to 57500 W/m<sup>2</sup>. It is believed that the map is appropriate for refrigerants (and fluids with similar physical properties such as light hydrocarbons) at low to medium pressures but not for CO<sub>2</sub> (too high of operating pressures for the map) nor for air-water or steam-water systems (their surface tension and density ratio are too high with respect to the refrigerant database).

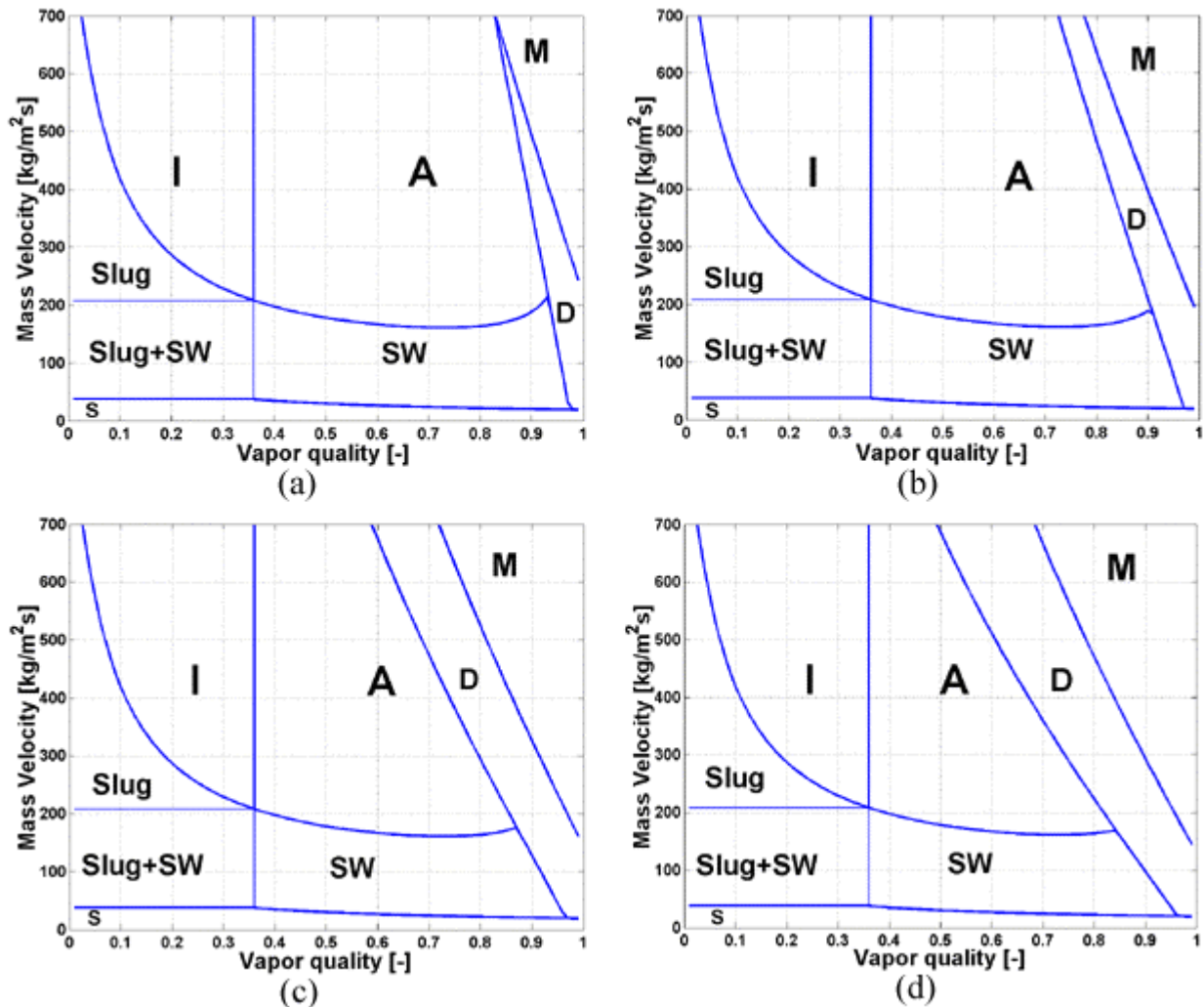


Figure 12.18. Flow pattern maps for R-22 at  $5^\circ\text{C}$  in a  $13.84\text{ mm}$  tube evaluated at  $300\text{ kg/m}^2\text{s}$  for four heat fluxes: a)  $7.5\text{ kW/m}^2$ , b)  $17.5\text{ kW/m}^2$ , c)  $37.5\text{ kW/m}^2$ , d)  $57.5\text{ kW/m}^2$ .

#### 12.4.1 Example flow pattern maps for selected fluids for evaporation in horizontal tubes

Figure 12.19 displays various flow pattern maps calculated with the most recent version of the Thome and coworkers flow pattern maps described above for the hydrocarbon fluids n-butane and propane. The conditions of the calculations are listed in the maps where the flow regimes shown are: Mist Flow (MF), Intermittent (I), Annular (A), Stratified-Wavy (SW) and Stratified (S). The bubbly flow regime is not depicted as it occurs at much larger mass velocities than those shown.

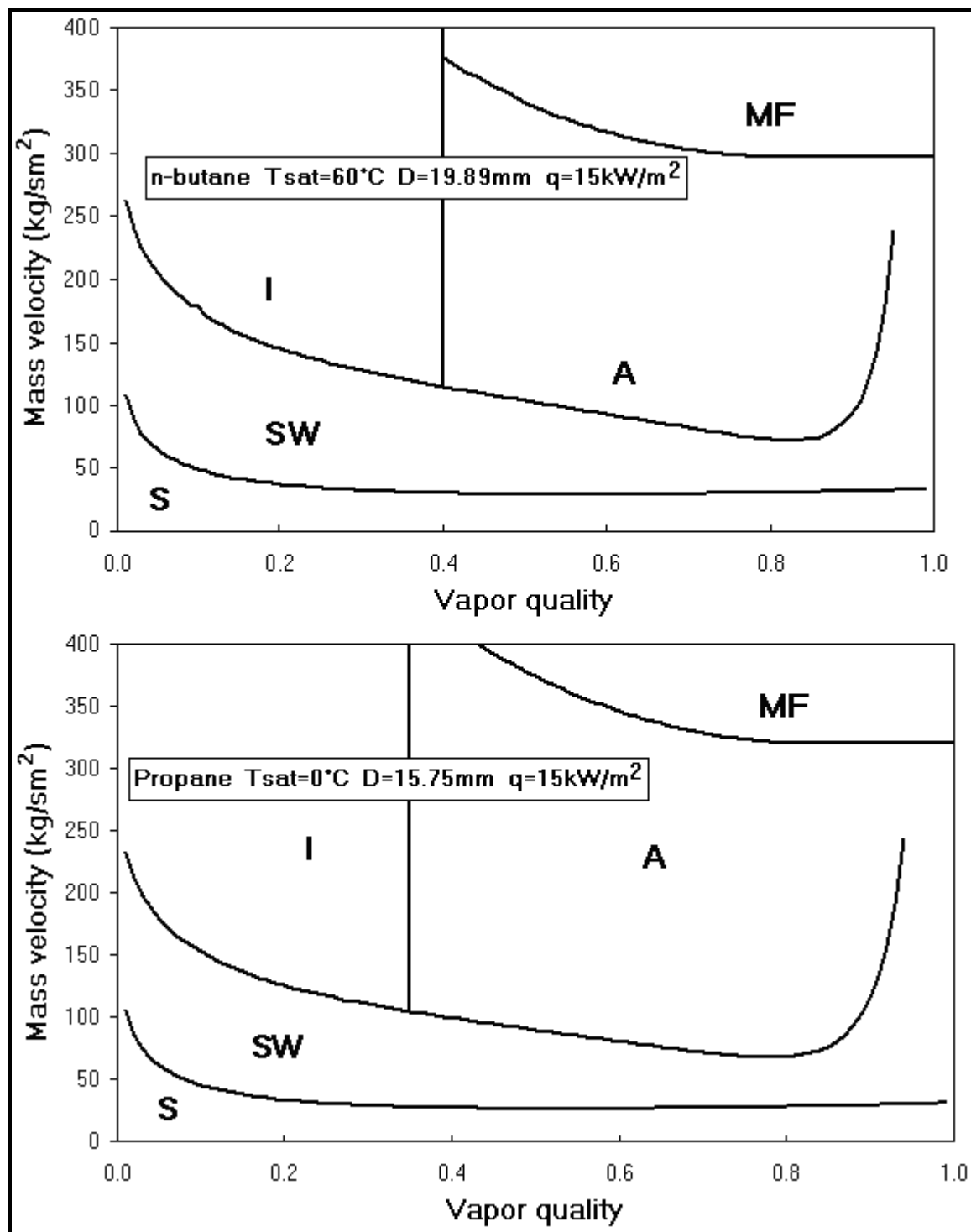


Figure 12.19. Flow pattern map for n-butane and propane evaporating in a horizontal tube.

## 12.5 Flow Pattern Map for Condensation in Horizontal Tubes

Flow patterns that occur during condensation inside horizontal tubes are similar to those for evaporation described in the previous section with the following exceptions:

1. Dry saturated vapor is entering the tube and hence the process begins without any entrainment of liquid while for evaporating flows the liquid bridging across the flow channel in churn and intermittent flow can result in significant entrainment when these flow structures break up.
2. During evaporation, the annular film eventually dries out while for condensation no dryout occurs. In fact, for condensation at high vapor qualities the flow is annular and there is no passage from stratified-wavy flow into annular flow while for evaporation the flow reverts to stratified-wavy flow at the onset of dryout at the top of the tube.
3. During condensation, the condensate formed coats the tube perimeter with a liquid film. In what would otherwise be a mist flow for adiabatic or evaporating flows, in condensation the flow regime will look like annular flow since the entrainment of liquid into the vapor core will leave bare surface available for rapid formation of a new liquid layer via condensation.
4. During condensation in stratified flow regimes, the top of the tube is wetted by the condensate film while in adiabatic and evaporating flows the top perimeter is dry.

Hence, the three principal flow patterns encountered during condensation inside horizontal tubes are:

- Annular flow (often referred to as the shear-controlled regime in condensation heat transfer literature);
- Stratified-wavy flow (characterized by waves on the interface of the stratified liquid flowing along the bottom of the tube with film condensation on the top perimeter);
- Stratified flow (no interfacial waves on the stratified liquid flowing along the bottom of the tube with film condensation on the top perimeter that drains into the stratified liquid).

The latter are sometimes referred to as the gravity-controlled regime in condensation heat transfer literature. These flow regimes can tentatively be predicted using the Kattan-Thome-Favrat flow pattern maps for intube evaporation as proposed by El Hajal, Thome and Cavallini (2003). First, the mist flow transition is eliminated because flow in this zone may be considered to be annular flow since a condensate film is always formed, even if the liquid is then entrained. Secondly, the stratified-wavy transition curve is modified by first eliminating the transition from annular flow to stratified-wavy flow at high vapor qualities by solving for the minimum in the stratified-wavy flow transition curve and then extending this curve as a straight line from that point to the end of the stratified transition curve for  $m_{strat}$  at a vapor quality of  $x = 1.0$ . Figure 12.20 illustrates this flow pattern map for condensation of R-134a at 40°C in a horizontal tube of 8.0 mm internal diameter.

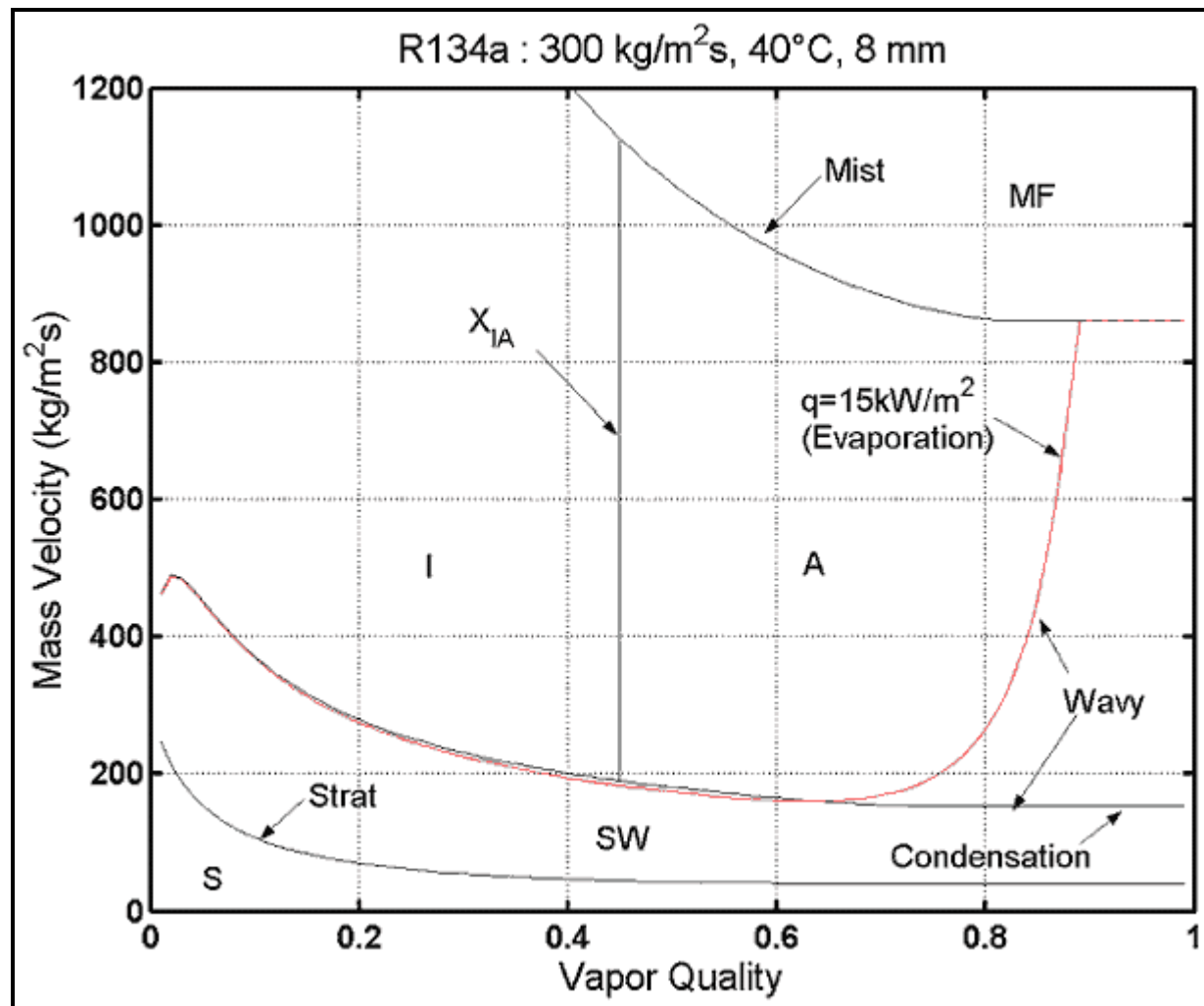


**Figure 12.20.** Flow pattern map for intube condensation of R-134a at 40°C in a horizontal tube of 8.0 mm internal diameter by El Hajal, Thome and Cavallini (2003).

Soliman (1982) also proposed a method for prediction of the transition from annular flow to stratified-wavy flow during condensation inside horizontal tubes. Refer to Chapter 8 for a description of his method that was used by Dobson and Chato (1998) in their intube condensation heat transfer model.

## 12.6 Flow Patterns in Horizontal Enhanced Tubes

Not many systematic flow pattern studies on two-phase flows in internally enhanced tubes have been undertaken, although it is thought that an enhancement can have a significant effect of the location of flow pattern transitions and can also change what a flow pattern looks like. For instance, it is thought that an internally microfinned tube will decrease the annular to stratified-wavy flow threshold to lower mass velocities, hence increasing heat transfer at lower mass velocities by achieving complete wetting of the tube perimeter. For instance, visual observations of Cavallini et al. (2002) have confirmed this hypothesis, whose comparative videos can be seen in Chapter 1.

Some videos illustrating two-phase flows inside a plain glass tube with a twisted tape insert by Moreno Quiben and Thome can also be seen in Chapter 1, where a swirl effect is seen to be imparted on the flow.

Again, it is believed that the annular-stratified wavy transition threshold  $\dot{m}_{\text{wavy}}$  is displaced to lower mass velocities, but this was not systematically documented, however.

Within annular flow itself, microfins create more turbulence in the liquid film as shown in Figure 12.21 with photographs provided by Sáiz-Jabardo (2005) using the test facility described in Bandarra Filho and Sáiz-Jabardo (2006). It appears from the photographs that the microfin tube also increases liquid entrainment in the central vapor core (the photographs are for a smooth sight glass tube at the exit of the evaporator tubes so the direct effect of the microfins cannot be seen).

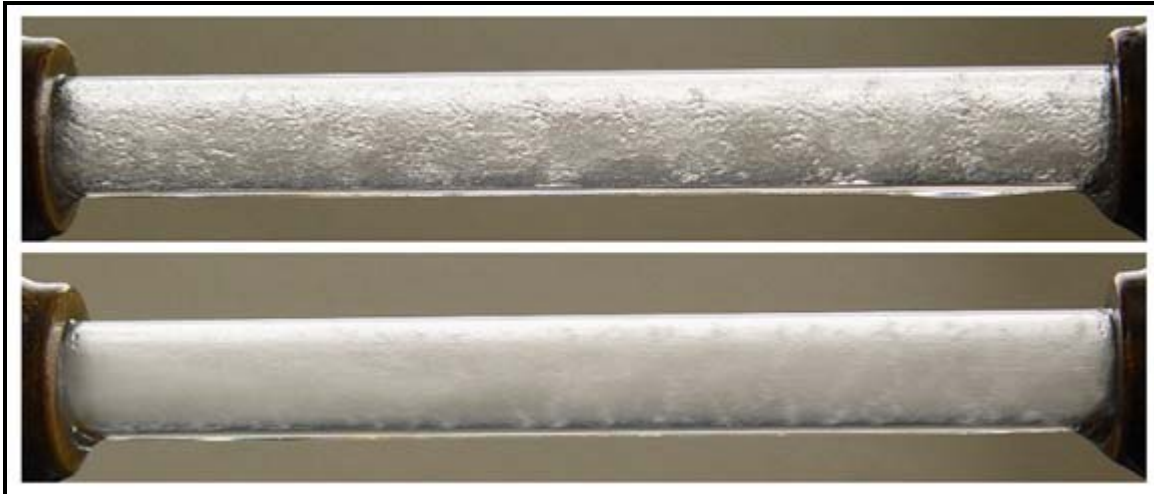


**Figure 12.21. Annular flow patterns for R-134a at 5°C and 500 kg/m<sup>2</sup>s from Bandarra Filho and Sáiz-Jabardo (2006) at the exit of an evaporator tube. Top photo: smooth tube; bottom photo: microfin tube. Tube diameter: 9.52 mm.**

Bukasa, Liebenberg and Meyer (2004), Olivier et al. (2004), Liebenberg, Thome and Meyer (2005) and Olivier et al. (2007) have investigated flow patterns in a plain tube, a helical microfin tube (Wolverine Tube), a herringbone microfin tube (Wolverine Tube) and a tube with helical wire inserts. Meyer and Liebenberg (2006) have also summarized this work in a state-of-the-art review paper. While finding that the intermittent-to-annular flow transition equation [12.4.11] for  $x_{IA}$  worked well for their smooth bore tube, they found that an internal enhancement delayed the transition to lower vapor qualities for the microfin tubes during the condensation of R-22, R-134a and R-407C, as depicted in Figure 12.22. They observed the flow patterns directly at the exit of their condensation test sections in that study while also using a power-spectral analysis of the absolute pressure signal to identify the transitions in previous studies. In their most recent tests, helical wires with axial pitches of 5.0, 7.7 and 11.0 mm were tested. While the wire insert displaced the  $x_{IA}$  transition to lower vapor qualities, they on the other hand found little effect of the wire pitch itself on the location of the  $x_{IA}$  transition boundary. In these tests with wires, the internal tube diameter was 8.1 mm and the wire diameter was 0.5 mm.

Based on their results, Meyer, Liebenberg and coworkers proposed the following expression for the transition  $x_{IA}$  for the intermittent-to-annular flow transition line for tubes with such helical wire inserts:

$$x_{IA} = \left\{ \left[ 0.484 \left( \frac{\rho_G}{\rho_L} \right)^{-5/9} \left( \frac{\mu_L}{\mu_G} \right)^{-1/9} \right] + 1 \right\}^{-1} \quad [12.6.1]$$

Similar transition lines for the helical microfin and herringbone microfin tubes were also proposed, with values of 0.678 and 0.790 in place of 0.484, respectively, in their earlier studies mentioned above.

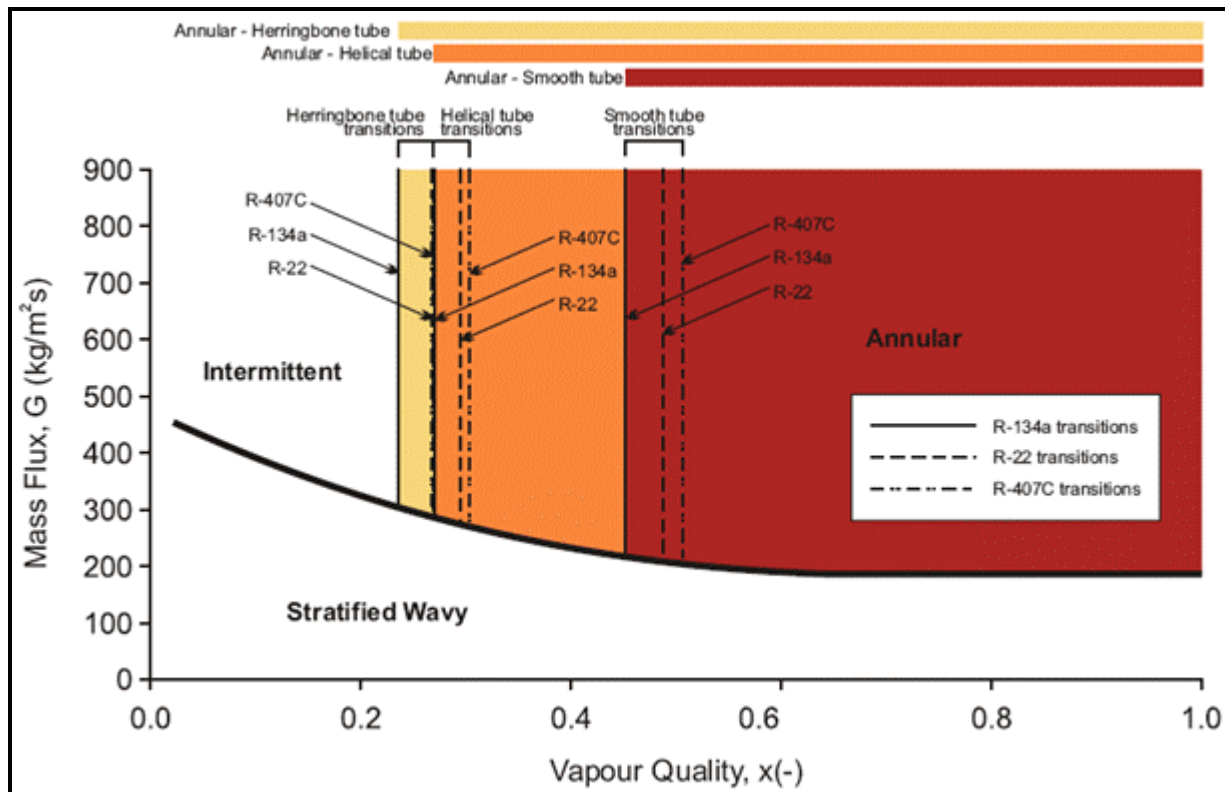


**Figure 12.22.** Flow pattern map of Kattan, Thome and Favrat (1998a) modified by Meyer and coworkers to illustrate their new intermittent-annular flow transitions observed for a smooth tube and two microfin tubes for three refrigerants.

## 12.7 Flow Patterns and Map for Two-Phase Flows over Horizontal Tube Bundles

Shell-side two-phase flow patterns (crossflow over tube arrays) and flow pattern maps have received much less attention than for intube flow. Some investigations only qualitatively described the flow patterns observed, such as Leong and Cornwell (1979), Cornwell, Duffin and Schuller (1980), Diehl (1958), Diehl and Unruh (1958) and Nakajima (1978). Other studies have attempted to quantify the observations through the development of flow pattern maps, for example those of Grant and Murray (1972, 1974), Grant (1973), Grant and Chisholm (1979), Kondo and Nakajima (1980) and Chisholm (1985). Not much work has been done on two-phase flow patterns for shell-side flows since the mid-1980's.

The two-phase flow pattern in shell-side flows is important to thermal performance as it has an effect on the two-phase friction multiplier, and hence on the two-phase frictional pressure drop. The flow pattern must also have an effect on bundle boiling heat transfer coefficients and on condensation heat transfer, but no research has confirmed this relationship so far. In any case, the knowledge of flow patterns and prediction of their transitions from one to another is key to making "thought experiments" in which the

two-phase flow structure in new systems can be predicted. Such predictions are helpful in establishing what the operating characteristics of the system will be, and thus avoid potential operating problems.

Leong and Cornwell (1979) and Cornwell, Duffin and Schuller (1980) have made visual observations of two-phase flows in a kettle reboiler slice during evaporation. They reported that two main flow patterns are dominant. In the lower zone of their 241-tube inline tube bundle, the flow was predominantly bubbly. In the upper zone where the vapor quality is larger, a distinct change in the appearance of the flow occurred, where it took on a "frothy" character. This transition was estimated to occur at a void fraction of about 60%. On the other hand, for a staggered tube bundle with two-phase upflow, Nakajima (1978) observed only bubbly and slug flows for tests at very low mass velocities and low qualities. For downflow at much higher mass velocities for a staggered tube bundle, Diehl (1957) observed only annular and spray flows. Diehl and Unruh (1958) described spray flow as one with a high-entrained liquid fraction while they defined annular flow as a flow with a low entrainment. In a more comprehensive study, Grant and Chisholm (1979) studied vertical upflow and downflow over a wide range of mass velocities and qualities in a staggered tube array, observing bubbly, intermittent (slug), and spray flows. The Diehl and Diehl-Unruh annular flow observations are probably the same as the spray flow category of Grant and Chisholm.

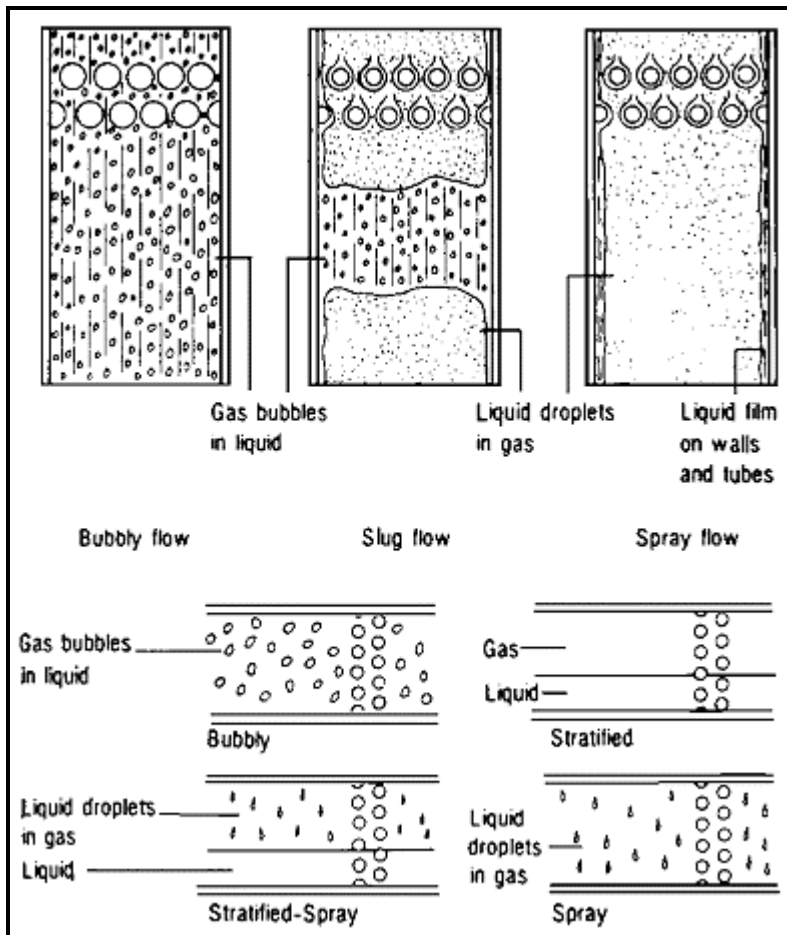


**Figure 12.23. Flow patterns in tube bundles from Chisholm (1983). Upper diagram is for vertical flow and lower diagram is for horizontal flow.**

For horizontal two-phase flows across tube bundles, Diehl and Unruh (1958) investigated both staggered and inline tube arrays. They observed spray, annular, slug, and stratified flows, noting that slug flow was only observed to occur in a large pitch-to-diameter ratio inline tube bundle. Grant and Chisholm (1979) and Grant (1973), on the other hand, did not observe slug flow in their horizontal flows but they did see bubbly, stratified, stratified-spray, and spray flows.

Figure 12.23 depicts and defines the names of the most prevalent flow patterns reported in the above investigations and Figure 12.24 shows the map proposed by Grant and Chisholm. Bubbly and spray flows are common to both vertical and horizontal flows while slug or intermittent flow and stratified flow generally only occur in horizontal flows. These idealized flow patterns will be affected by the leakage streams in a bundle in a heat exchanger shell, for example by flow separation around the baffles, leakage between tubes and tube holes in baffles, and any other bypass stream.

Chisholm (1985) more recently has presented the following transition thresholds in terms of vapor quality for horizontal flows:

$$\text{Stratified flow: } \frac{1-x_S}{x_S} = \left( \frac{R-1}{B_S} \right)^{2/(2-m)} \quad [12.7.1]$$

$$\text{Bubbly flow: } \frac{1-x_B}{x_B} = \left( \frac{R-1}{B_B} \right)^{2/(2-m)} \quad [12.7.2]$$

$$\text{Spray flow: } \frac{1-x_F}{x_F} = \left( \frac{R-1}{B_F} \right)^{2/(2-m)} \quad [12.7.3]$$

In these equations,  $x_S$ ,  $x_B$ , and  $x_F$  are the transition qualities for the stratified, bubbly, and spray transition points, respectively. The other parameters are defined as:

$$B_S = \frac{(2^{2-m} - 2)}{(Y+1)}; \quad B_B = \left( \frac{\rho_L}{\rho_G} \right)^{1/2}; \quad B_F = \left( \frac{\mu_L}{\mu_G} \right)^{m/2} \quad [12.7.4]$$

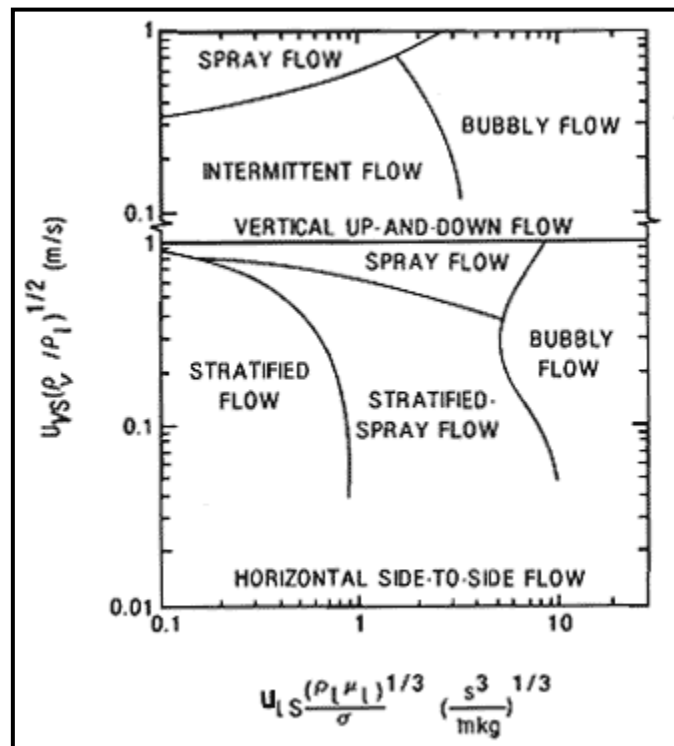


Figure 12.24. Shell-side Flow Pattern Maps of Grant and Chisholm (1979).

$$R = 1.3 + 0.59 Fr_L N^2 \left( \frac{\mu_L}{\mu_G} \right)^m \quad [12.7.5]$$

$$Y = \left( \frac{dp}{dz} \right)_G / \left( \frac{dp}{dz} \right)_L = \left( \frac{\rho_L}{\rho_G} \right) \left( \frac{\mu_L}{\mu_G} \right)^{-m} \quad [12.7.6]$$

and  $m$  is the exponent in a Blasius-type single-phase friction factor equation. The quantity  $Fr_L$ , is the Froude number for the total flow as liquid with the velocity based on the minimum cross-sectional area in the tube bundle normal to the flow direction. The reliability of general use of these methods for prediction of flow pattern transitions is not able to be qualified here.

## CONCLUSIONS

Flow patterns have an important influence on prediction of the void fraction, flow boiling and convective condensation heat transfer coefficients, and two-phase pressure drops. The prediction of flow pattern transitions and their integration into a flow pattern map for general use is thus of particular importance to the understanding of two-phase flow phenomena and design of two-phase equipment.

For vertical tubes, the flow pattern maps of Fair (1960) and Hewitt and Roberts (1969) are those most widely recommended for use. For horizontal tubes, the methods of Taitel and Dukler (1976) and Baker (1954) are widely used. The more recent flow pattern map of Kattan, Thome and Favrat (1998a) and its more subsequent improvements, which was developed specifically for small diameter tubes typical of shell-and-tube heat exchangers for both adiabatic and evaporating flows, is that recommended here for heat exchanger design. Another version of their map has also been proposed by El Hajal, Thome and Cavallini (2003) for intube condensation.

Shell side flow patterns and flow patterns maps have received very little attention compared to intube studies. Qualitative and quantitative attempts have been made to obtain flow pattern maps, but to date no method has been shown to be of general application. The flow pattern map of Grant and Chisholm (1979) has been presented here but its use must be taken as a best estimate only at this point.

**Example Calculation:** A two-phase fluid is flowing upwards in a vertical pipe of internal diameter of 1.0 in. The fluid properties are as follows: liquid density = 60 lb/ft<sup>3</sup>; vapor density = 2 lb/ft<sup>3</sup>; liquid viscosity = 0.4 cp; vapor viscosity = 0.01 cp. If the vapor quality is 0.2 and the total flow rate of liquid and vapor is 3600 lb/h, using the Fair flow pattern map, what is the local flow pattern expected to be?

**Solution:** The mass flow rate of 3600 lb/h is equivalent to 1.0 lb/s. The internal diameter is 1 in. = 1/12 ft. The mass velocity is then obtained by dividing the mass flow rate by the internal cross-sectional area of the tube, such that the mass velocity = 183.3 lb/s ft<sup>2</sup>. The parameter on the x-axis of the Fair map is:

$$\left( \frac{x}{1-x} \right)^{0.9} \left( \frac{\rho_L}{\rho_G} \right)^{0.5} \left( \frac{\mu_G}{\mu_L} \right)^{0.1} = \left( \frac{0.2}{1-0.2} \right)^{0.9} \left( \frac{60}{2} \right)^{0.5} \left( \frac{0.01}{0.4} \right)^{0.1} = 1.09$$

Thus, using the values of 183.3 and 1.09 on the map, the flow regime is identified to be *annular* flow.

# Chapter 13

## Two-Phase Pressure Drops

**(Revised in 2006)**

**Summary:** Accurate prediction of two-phase pressure drops in direct-expansion and flooded evaporators, in tube-side and shell-side condensers, and in two-phase transfer lines is of paramount importance to the design and optimization of refrigeration, air-conditioning and heat pump systems. Taking direct-expansion evaporators as an example, the optimal use of the two-phase pressure drop to obtain the maximum flow boiling heat transfer performance is one of the primary design goals. In these evaporators, typically a two-phase pressure drop equivalent to a loss of 1.4°C (2.5°F) in saturation temperature from inlet to outlet is set as the design limit. Yet, pressure drops predicted using leading methods differ by up to 100%. Putting this into perspective, if an evaporator is inaccurately designed with a two-phase pressure drop only one-half the real value, then the system efficiency will suffer accordingly from the larger than expected fall in saturation temperature and pressure through the evaporator. On the other hand, if the predicted pressure drop is too large by a factor of two, then fewer tubes of longer length could have been utilized to obtain a more compact unit. Hence, accurate prediction of two-phase pressure drops is a key aspect in the first law and second law optimization of these systems.

In this chapter, methods for predicting two-phase pressure drops for flows inside tubes (horizontal and vertical) and for flows over tube bundles (horizontal) will be presented. In addition, two-phase pressure drop data for microfin tubes and corrugated tubes will be presented and a prediction method for microfin tubes described.

### 13.1 Homogeneous Flow Model Applied to Intube Flow

A homogeneous fluid is a convenient concept for modeling of two-phase pressure drops; it is a pseudo-fluid that obeys the conventional design equations for single-phase fluids and is characterized by suitably averaged properties of the liquid and vapor phase. The homogeneous design approach is presented below.

The total pressure drop of a fluid is due to the variation of kinetic and potential energy of the fluid and that due to friction on the walls of the flow channel. Thus, the total pressure drop  $\Delta p_{\text{total}}$  is the sum of the static pressure drop (elevation head)  $\Delta p_{\text{static}}$ , the momentum pressure drop (acceleration)  $\Delta p_{\text{mom}}$ , and the frictional pressure drop  $\Delta p_{\text{frict}}$ :

$$\Delta p_{\text{total}} = \Delta p_{\text{static}} + \Delta p_{\text{mom}} + \Delta p_{\text{frict}} \quad [13.1.1]$$

The static pressure drop for a homogeneous two-phase fluid is:

$$\Delta p_{\text{static}} = \rho_H g H \sin \theta \quad [13.1.2]$$

where  $H$  is the vertical height,  $\theta$  is the angle with respect to the horizontal, and the homogeneous density  $\rho_H$  is

$$\rho_H = \rho_L (1 - \varepsilon_H) + \rho_G \varepsilon_H \quad [13.1.3]$$

and  $\rho_L$  and  $\rho_G$  are the liquid and gas (or vapor) densities, respectively. The homogeneous void fraction  $\varepsilon_H$  is determined from the quality  $x$  as

$$\varepsilon_H = \frac{1}{1 + \left( \frac{u_G}{u_L} \frac{(1-x)\rho_G}{x\rho_L} \right)} \quad [13.1.4]$$

where  $u_G/u_L$  is the velocity ratio, or slip ratio ( $S$ ), and is equal to 1.0 for a homogeneous flow. The momentum pressure gradient per unit length of the tube is:

$$\left( \frac{dp}{dz} \right)_{mom} = \frac{d(\dot{m}_{total}/\rho_H)}{dz} \quad [13.1.5]$$

The most problematic term is the frictional pressure drop, which can be expressed as a function of the *two-phase friction factor*  $f_{tp}$ , and for a steady flow in a channel with a constant cross-sectional area is:

$$\Delta p_{frict} = \frac{2f_{tp} L \dot{m}_{total}^2}{d_i \rho_{tp}} \quad [13.1.6]$$

The friction factor may be expressed in terms of the Reynolds number by the Blasius equation:

$$f_{tp} = \frac{0.079}{Re^{0.25}} \quad [13.1.7]$$

where the Reynolds number is

$$Re = \frac{\dot{m}_{total} d_i}{\mu_{tp}} \quad [13.1.8]$$

The viscosity for calculating the Reynolds number can be chosen as the viscosity of the liquid phase or as a quality averaged viscosity  $\mu_{tp}$ :

$$\mu_{tp} = x \mu_G + (1-x) \mu_L \quad [13.1.9]$$

This correlation is suitable for mass velocities greater than 2000 kg/m<sup>2</sup>s (1,471,584 lb/h ft<sup>2</sup>) in the case of the frictional pressure drop calculations and for mass velocities less than 2000 kg/m<sup>2</sup>s (1,471,584 lb/h ft<sup>2</sup>) and  $(\rho_L/\rho_G) < 10$  for gravitational pressure drop calculations. Generally speaking this correlation should be used at high-reduced pressures and very high mass velocities.

**Example Calculation:** Using the homogeneous flow pressure drop method, calculate the two-phase pressure drop for up-flow in a vertical tube of 10 mm internal diameter that is 2 m long. The flow is adiabatic, the mass flow rate is 0.02 kg/s and the vapor quality is 0.05. The fluid is R-123 at a saturation temperature of 3°C and saturation pressure of 0.37 bar, whose physical properties are: liquid density = 1518 kg/m<sup>3</sup>, vapor density = 2.60 kg/m<sup>3</sup>, liquid dynamic viscosity = 0.0005856 kg/m s, vapor dynamic viscosity = 0.0000126 kg/m s.

**Solution:** The homogeneous void fraction  $\varepsilon_H$  is determined from the quality  $x$  using Eq. 13.1.4 where  $u_G/u_L = 1$ :

$$\varepsilon_H = \frac{1}{1 + \left( \left( \frac{u_G}{u_L} \right) \frac{(1-x)}{x} \frac{\rho_G}{\rho_L} \right)} = \frac{1}{1 + \left( (1) \frac{(1-0.05)}{0.05} \frac{2.60}{1518} \right)} = 0.9685$$

The homogeneous density  $\rho_H$  is obtained using Eq. 13.1.3:

$$\rho_H = \rho_L (1 - \varepsilon_H) + \rho_G \varepsilon_H = 1518(1 - 0.9685) + 2.60(0.9685) = 50.3 \text{ kg/m}^3$$

The static pressure drop for a homogeneous two-phase fluid with  $H = 2 \text{ m}$  and  $\theta = 90^\circ$  is obtained using Eq. 13.1.2:

$$\Delta p_{\text{static}} = \rho_H g H \sin \theta = 50.3(9.81)(2) \sin 90^\circ = 987 \text{ N/m}^2$$

The momentum pressure drop is  $\Delta p_{\text{mom}} = 0$  since the vapor quality is constant from inlet to outlet. The viscosity for calculating the Reynolds number choosing the quality averaged viscosity  $\mu_{tp}$  is obtained with Eq. 13.1.9:

$$\mu_{tp} = x \mu_G + (1-x) \mu_L = 0.05(0.0000126) + (1-0.05)(0.0005856) = 0.000557 \text{ kg/m s}$$

The mass velocity is calculated by dividing the mass flow rate by the cross-sectional area of the tube and is  $254.6 \text{ kg/m}^2\text{s}$ . The Reynolds number is then obtained with Eq. 13.1.8:

$$Re = \frac{\dot{m}_{\text{total}} d_i}{\mu_{tp}} = \frac{254.6(0.01)}{0.000557} = 4571$$

The friction factor is obtained from Eq. 13.1.7:

$$f_{tp} = \frac{0.079}{Re^{0.25}} = \frac{0.079}{4571^{0.25}} = 0.00961$$

The frictional pressure drop is then obtained with Eq. 13.1.6:

$$\Delta p_{\text{frict}} = \frac{2f_{tp} L \dot{m}_{\text{total}}^2}{d_i \rho_{tp}} = \frac{2(0.00961)(2)(254.6^2)}{0.01(50.3)} = 4953 \text{ N/m}^2$$

Thus, the total pressure drop is obtained with Eq. 13.1.1:

$$\Delta p_{\text{total}} = \Delta p_{\text{static}} + \Delta p_{\text{mom}} + \Delta p_{\text{frict}} = 987 + 0 + 4953 = 5940 \text{ N/m}^2 = 5.94 \text{ kPa (0.86 psi)}$$

## 13.2 Separated Flow Models for Flows inside Plain Tubes

The two-phase pressure drops for flows inside tubes are the sum of three contributions: the static pressure drop  $\Delta p_{\text{static}}$ , the momentum pressure drop  $\Delta p_{\text{mom}}$  and the frictional pressure drop  $\Delta p_{\text{frict}}$  as:

$$\Delta p_{\text{total}} = \Delta p_{\text{static}} + \Delta p_{\text{mom}} + \Delta p_{\text{frict}} \quad [13.2.1]$$

The static pressure drop is given by

$$\Delta p_{\text{static}} = \rho_{\text{tp}} g H \sin \theta \quad [13.2.2]$$

For a horizontal tube, there is no change in static head, i.e.  $H = 0$  so  $\Delta p_{\text{static}} = 0$  while  $\sin \theta$  is equal to 1.0 for a vertical tube. The momentum pressure drop reflects the change in kinetic energy of the flow and is for the present case given by:

$$\Delta p_{\text{mom}} = \dot{m}_{\text{total}}^2 \left\{ \left[ \frac{(1-x)^2}{\rho_L(1-\varepsilon)} + \frac{x^2}{\rho_G \varepsilon} \right]_{\text{out}} - \left[ \frac{(1-x)^2}{\rho_L(1-\varepsilon)} + \frac{x^2}{\rho_G \varepsilon} \right]_{\text{in}} \right\} \quad [13.2.3]$$

where  $\dot{m}_{\text{total}}$  is the total mass velocity of liquid plus vapor and  $x$  is the vapor quality.

The separated flow model considers the two phases to be artificially separated into two streams, each flowing in its own pipe. The areas of the two pipes are proportional to the void fraction  $\varepsilon$ . Numerous methods are available for predicting the void fraction. It is recommended here to use the Steiner (1993) version of the drift flux model of Rouhani and Axelsson (1970):

$$\varepsilon = \frac{x}{\rho_G} \left[ \left( 1 + 0.12(1-x) \right) \left( \frac{x}{\rho_G} + \frac{1-x}{\rho_L} \right) + \frac{1.18(1-x)[g\sigma(\rho_L - \rho_G)]^{0.25}}{\dot{m}_{\text{total}}^2 \rho_L^{0.5}} \right]^{-1} \quad [13.2.4a]$$

For vertical flows, the Rouhani and Axelsson (1970) expression can be used when  $\varepsilon > 0.1$ :

$$\varepsilon = \frac{x}{\rho_G} \left[ \left[ 1 + 0.2(1-x) \left( \frac{gd_i \rho_L^2}{\dot{m}_{\text{total}}^2} \right)^{1/4} \right] \left( \frac{x}{\rho_G} + \frac{1-x}{\rho_L} \right) + \frac{1.18(1-x)[g\sigma(\rho_L - \rho_G)]^{0.25}}{\dot{m}_{\text{total}}^2 \rho_L^{0.5}} \right]^{-1} \quad [13.2.4b]$$

The two-phase density is obtained from:

$$\rho_{\text{tp}} = \rho_L(1-\varepsilon) + \rho_G \varepsilon \quad [13.2.4c]$$

The momentum pressure drop is calculable by input of the inlet and outlet vapor qualities. When measuring two-phase pressure drops for evaporation in horizontal tubes, for instance, the frictional pressure drop is obtainable by subtracting the momentum pressure drop from the measured total pressure drop since the static pressure drop is nil.

For an evaporating flow, the kinetic energy of the outgoing flow is larger than that of the incoming flow since the density of the vapor phase is less than that of the liquid. Hence, the momentum pressure drop results in a lower pressure at the exit than at the inlet. Instead, for a condensing flow the kinetic energy of the outgoing flow is smaller than that of the incoming flow. Hence, the momentum pressure drop results in an increase in pressure at the exit than at the inlet, i.e. a pressure recovery. For condensing flows, it is common to ignore the momentum recovery as only some of it may actually be realized in the flow and ignoring it provides some conservatism in the design.

The frictional pressure drop in two-phase flows is typically predicted using separated flow models. The first of these analyses was performed by Lockhart and Martinelli (1949) and then followed by many others. The basic equations for the separated flow model are not dependent on the particular flow configuration adopted. It is assumed that the velocities of each phase are constant, in any given cross-section, within the zone occupied by the phase. Some common methods for *intube* flow will be given below.

### 13.2.1 Friedel correlation

The correlation method of Friedel (1979) utilizes a two-phase multiplier:

$$\Delta p_{\text{frict}} = \Delta p_L \Phi_{\text{fr}}^2 \quad [13.2.5]$$

where  $\Delta p_L$  is calculated for the liquid-phase flow as

$$\Delta p_L = 4f_L(L/d_i)\dot{m}_{\text{total}}^2(1/2\rho_L) \quad [13.2.6]$$

The liquid friction factor  $f_L$  and liquid Reynolds number are obtained from

$$f = \frac{0.079}{Re^{0.25}} \quad [13.2.7]$$

$$Re = \frac{\dot{m}_{\text{total}}d_i}{\mu} \quad [13.2.8]$$

using the liquid dynamic viscosity  $\mu_L$ . His two-phase multiplier is

$$\Phi_{\text{fr}}^2 = E + \frac{3.24FH}{Fr_H^{0.045}We_L^{0.035}} \quad [13.2.9]$$

The dimensionless factors  $Fr_H$ ,  $E$ ,  $F$  and  $H$  are as follows:

$$Fr_H = \frac{\dot{m}_{\text{total}}^2}{gd_i\rho_H} \quad [13.2.10]$$

$$E = (1-x)^2 + x^2 \frac{\rho_L f_G}{\rho_G f_L} \quad [13.2.11]$$

$$F = x^{0.78}(1-x)^{0.224} \quad [13.2.12]$$

$$H = \left(\frac{\rho_L}{\rho_G}\right)^{0.91} \left(\frac{\mu_G}{\mu_L}\right)^{0.19} \left(1 - \frac{\mu_G}{\mu_L}\right)^{0.7} \quad [13.2.13]$$

The liquid Weber  $We_L$  is defined as:

$$We_L = \frac{\dot{m}_{\text{total}}^2 d_i}{\sigma \rho_H} \quad [13.2.14]$$

using the following alternative definition of the homogeneous density  $\rho_H$  based on vapor quality:

$$\rho_H = \left( \frac{x}{\rho_G} + \frac{1-x}{\rho_L} \right)^{-1} \quad [13.2.15]$$

This method is typically recommended when the ratio of  $(\mu_L/\mu_G)$  is less than 1000 is applicable to vapor qualities from  $0 \leq x \leq 1$ .

### 13.2.2 Lockhart and Martinelli correlation

The method of Lockhart and Martinelli (1949) is the original method that predicted the two-phase frictional pressure drop based on a two-phase multiplier for the liquid-phase, or the vapor-phase, respectively, as:

$$\Delta p_{\text{frict}} = \Phi_{Ltt}^2 \Delta p_L \quad [13.2.16]$$

$$\Delta p_{\text{frict}} = \Phi_{Gtt}^2 \Delta p_G \quad [13.2.17]$$

where Eq. 13.2.6 is used for  $\Delta p_L$  with  $(1-x)^2$  applied to the mass velocity term and  $\Delta p_G$  is obtained from

$$\Delta p_G = 4f_G(L/d_i)\dot{m}_{\text{total}}^2 x^2 (1/2\rho_G) \quad [13.2.18]$$

The single-phase friction factors of the liquid  $f_L$  and the vapor  $f_G$ , are calculated using Eq. 13.2.7 with their respective physical properties. Their corresponding two-phase multipliers are

$$\Phi_{Ltt}^2 = 1 + \frac{C}{X_{tt}} + \frac{1}{X_{tt}^2}, \text{ for } Re_L > 4000 \quad [13.2.19]$$

$$\Phi_{Gtt}^2 = 1 + CX_{tt} + X_{tt}^2, \text{ for } Re_L < 4000 \quad [13.2.20]$$

where  $X_{tt}$  is the Martinelli parameter for both phases in the turbulent regimes defined as

$$X_{tt} = \left( \frac{1-x}{x} \right)^{0.9} \left( \frac{\rho_G}{\rho_L} \right)^{0.5} \left( \frac{\mu_L}{\mu_G} \right)^{0.1} \quad [13.2.21]$$

The value of  $C$  in Eqs. 13.2.19 and 13.2.20 depends on the regimes of the liquid and vapor. The appropriate values to use are listed in Table 13.1. The correlation of Lockhart and Martinelli is applicable to the vapor quality range of  $0 < x \leq 1$ .

**Table 13.1. Values of C**

Liquid	Gas	C
Turbulent	Turbulent	20
Laminar	Turbulent	12
Turbulent	Laminar	10
Laminar	Laminar	5

### 13.2.3 Grönnerud correlation

The method of Grönnerud (1972) was developed specifically for refrigerants and is as follows:

$$\Delta p_{\text{frict}} = \Phi_{\text{gd}} \Delta p_L \quad [13.2.22]$$

and his two-phase multiplier is

$$\Phi_{\text{gd}} = 1 + \left( \frac{dp}{dz} \right)_{\text{Fr}} \left[ \frac{\left( \frac{\rho_L}{\rho_G} \right)}{\left( \frac{\mu_L}{\mu_G} \right)^{0.25}} - 1 \right] \quad [13.2.23]$$

where Eq. 13.2.6 is used for  $\Delta p_L$ . His frictional pressure gradient depends on the Froude number and is

$$\left( \frac{dp}{dz} \right)_{\text{Fr}} = f_{\text{Fr}} \left[ x + 4(x^{1.8} - x^{10} f_{\text{Fr}}^{0.5}) \right] \quad [13.2.24]$$

When applying this expression, if the liquid Froude number  $Fr_L \geq 1$ , then the friction factor  $f_{\text{Fr}} = 1.0$ , or if  $Fr_L < 1$ , then:

$$f_{\text{Fr}} = Fr_L^{0.3} + 0.0055 \left( \ln \frac{1}{Fr_L} \right)^2 \quad [13.2.25]$$

where

$$Fr_L = \frac{\dot{m}_{\text{total}}^2}{gd_1 \rho_L^2} \quad [13.2.26]$$

The correlation of Grönnerud is applicable to vapor qualities from  $0 \leq x < 1$ .

### 13.2.4 Chisholm correlation

Chisholm (1973) proposed an extensive empirical method applicable to a wide range of operating conditions. His two-phase frictional pressure drop gradient is given as

$$\left(\frac{dp}{dz}\right)_{\text{frict}} = \left(\frac{dp}{dz}\right)_L \Phi_{\text{Ch}}^2 \quad [13.2.27]$$

The frictional pressure gradients for the liquid and vapor phases are:

$$\left(\frac{dp}{dz}\right)_L = f_L \frac{2\dot{m}_{\text{total}}^2}{d_i \rho_L} \quad [13.2.28]$$

$$\left(\frac{dp}{dz}\right)_G = f_G \frac{2\dot{m}_{\text{total}}^2}{d_i \rho_G} \quad [13.2.29]$$

The friction factors are obtained with Eq. 13.2.7 using Eq. 13.2.8 and the respective dynamic viscosities of the liquid and the vapor for turbulent flows while for laminar flows ( $\text{Re} < 2000$ )

$$f = 16 / \text{Re} \quad [13.2.30]$$

The flow is considered here to be fully turbulent at  $\text{Re} \geq 2000$  to avoid an undefined interval in his method. The parameter Y is obtained from the ratio of the frictional pressure gradients:

$$Y^2 = \frac{\left(\frac{dp}{dz}\right)_G}{\left(\frac{dp}{dz}\right)_L} \quad [13.2.31]$$

His two-phase multiplier is then determined as:

$$\Phi_{\text{Ch}}^2 = 1 + (Y^2 - 1) \left[ B x^{(2-n)/2} (1-x)^{(2-n)/2} + x^{2-n} \right] \quad [13.2.32]$$

where n is the exponent from the friction factor expression of Blasius ( $n = 0.25$ ). For  $0 < Y < 9.5$ , Chisholm's parameter B is calculated as:

$$\begin{aligned} B &= \frac{55}{\dot{m}_{\text{total}}^{1/2}} && \text{for } \dot{m}_{\text{total}} \geq 1900 \text{ kg/m}^2\text{s} \\ B &= \frac{2400}{\dot{m}_{\text{total}}} && \text{for } 500 < \dot{m}_{\text{total}} < 1900 \text{ kg/m}^2\text{s} \\ B &= 4.8 && \text{for } \dot{m}_{\text{total}} < 500 \text{ kg/m}^2\text{s} \end{aligned} \quad [13.2.33]$$

For  $9.5 < Y < 28$ , then B is calculated as:

$$\begin{aligned} B &= \frac{520}{Y \dot{m}_{\text{total}}^{1/2}} && \text{for } \dot{m}_{\text{total}} \leq 600 \text{ kg/m}^2\text{s} \\ B &= \frac{21}{Y} && \text{for } \dot{m}_{\text{total}} > 600 \text{ kg/m}^2\text{s} \end{aligned} \quad [13.2.34]$$

For  $Y > 28$ , then B is calculated as:

$$B = \frac{15000}{Y^2 \dot{m}_{\text{total}}^{1/2}} \quad [13.2.35]$$

In the above expressions, to convert  $\text{kg/m}^2\text{s}$  to  $\text{lb/h ft}^2$ , multiply by 735.8. The correlation of Chisholm is applicable to vapor qualities from  $0 \leq x \leq 1$ .

### 13.2.5 Bankoff correlation

This method of Bankoff (1960) is an extension of the homogeneous model. His two-phase frictional pressure gradient is

$$\left( \frac{dp}{dz} \right)_{\text{frict}} = \left( \frac{dp}{dz} \right)_L \Phi_{\text{bf}}^{\frac{7}{4}} \quad [13.2.36]$$

The liquid-phase friction pressure gradient is calculated with Eq. [13.2.28] and his two-phase multiplier is

$$\Phi_{\text{bf}} = \frac{1}{1-x} \left[ 1 - \gamma \left( 1 - \frac{\rho_G}{\rho_L} \right) \right]^{\frac{3}{7}} \left[ 1 + x \left( \frac{\rho_L}{\rho_G} - 1 \right) \right] \quad [13.2.37]$$

where

$$\gamma = \frac{0.71 + 2.35 \left( \frac{\rho_G}{\rho_L} \right)}{1 + \left( \frac{1-x}{x} \right) \left( \frac{\rho_G}{\rho_L} \right)} \quad [13.2.38]$$

This method is applicable to vapor qualities from  $0 < x < 1$ .

### 13.2.6 Chawla correlation

Chawla (1967) suggested the following method based on the vapor pressure gradient:

$$\left( \frac{dp}{dz} \right)_{\text{frict}} = \left( \frac{dp}{dz} \right)_G \Phi_{\text{Chawla}} \quad [13.2.39]$$

The vapor-phase frictional pressure gradient is determined from Eq. 13.2.29 and the two-phase multiplier is

$$\Phi_{\text{Chawla}} = x^{1.75} \left[ 1 + S \left( \frac{1-x}{x} \frac{\rho_G}{\rho_L} \right) \right]^{2.375} \quad [13.2.40]$$

and his slip ratio S is:

$$S = \frac{u_G}{u_L} = \frac{1}{9.1 \left[ \frac{1-x}{x} (Re_G Fr_H)^{-0.167} \left( \frac{\rho_L}{\rho_G} \right)^{-0.9} \left( \frac{\mu_L}{\mu_G} \right)^{-0.5} \right]} \quad [13.2.41]$$

where  $Fr_H$  is determined with Eq. 13.2.10 and  $Re_G$  is determined with Eq. 13.2.8 using the vapor viscosity. His method is for vapor qualities from  $0 < x < 1$ .

### 13.2.7 Müller-Steinhagen and Heck correlation

Müller-Steinhagen and Heck (1986) proposed a two-phase frictional pressure gradient correlation that is in essence an empirical interpolation between all liquid flow and all vapor flow:

$$\left( \frac{dp}{dz} \right)_{frict} = G(1-x)^{1/3} + Bx^3 \quad [13.2.42]$$

where the factor G is

$$G = A + 2(B - A)x \quad [13.2.43]$$

The factors A and B are the frictional pressure gradients for all the flow liquid  $(dp/dz)_L$  and all the flow vapor  $(dp/dz)_G$ , obtained respectively from Eqs. 13.2.28 and 13.2.29. Tribbe and Müller-Steinhagen (2000) have shown that this method gave the best results in a comparison of competing methods to a large database that covered air-oil, air-water, water-steam and several refrigerants, applicable for  $0 \leq x \leq 1$ .

### 13.2.8 Comparison of above methods to more recent databases

Whalley (1980) made an extensive comparison between various published correlations, and the HTFS database (which consisted of over 25,000 data points). The recommendations he made are as follows:

- $(\mu_L/\mu_G) < 1000$  and mass velocities less than  $2000 \text{ kg/m}^2\text{s}$  ( $1,471,584 \text{ lb/h ft}^2$ ), the Friedel (1979) correlation should be used.
- $(\mu_L/\mu_G) > 1000$  and mass velocities greater than  $100 \text{ kg/m}^2\text{s}$  ( $73,579 \text{ lb/h ft}^2$ ), the Chisholm (1973) correlation should be used.
- $(\mu_L/\mu_G) > 1000$  and mass velocities less than  $100 \text{ kg/m}^2\text{s}$  ( $73,579 \text{ lb/h ft}^2$ ), the Lockhart and Martinelli (1949) correlation should be used.
- For most fluids,  $(\mu_L/\mu_G) < 1000$  and the Friedel correlation will be the preferred method for intube flow according to Whalley.

More recently, Tribbe and Müller-Steinhagen (2000) compared some of the leading two-phase frictional pressure drop correlations to a large database including the following combinations: air-oil, air-water, water-steam and several refrigerants. They found that statistically the method of Müller-Steinhagen and Heck (1986) gave the best and most reliable results. In another recent comparison, Ould Didi, Kattan and Thome (2002) compared the two-phase frictional pressure drop correlations described in the previous section to experimental pressure drops obtained in 10.92 and 12.00 mm (0.430 and 0.472 in.) internal diameter tubes of 3.013 m (9.885 ft) length for R-134a, R-123, R-402A, R-404A and R-502 over mass velocities from 100 to 500  $\text{kg/m}^2\text{s}$  ( $73,579$  to  $367,896 \text{ lb/h ft}^2$ ) and vapor qualities from 0.04 to 0.99. Overall, they found the Grönnerud (1972) and the Müller-Steinhagen and Heck (1986) methods to be

equally best with the Friedel (1979) method the 3<sup>rd</sup> best. As an example, Figure 13.1 depicts a comparison of five of the above methods to some R-134a two-phase frictional pressure drop data.

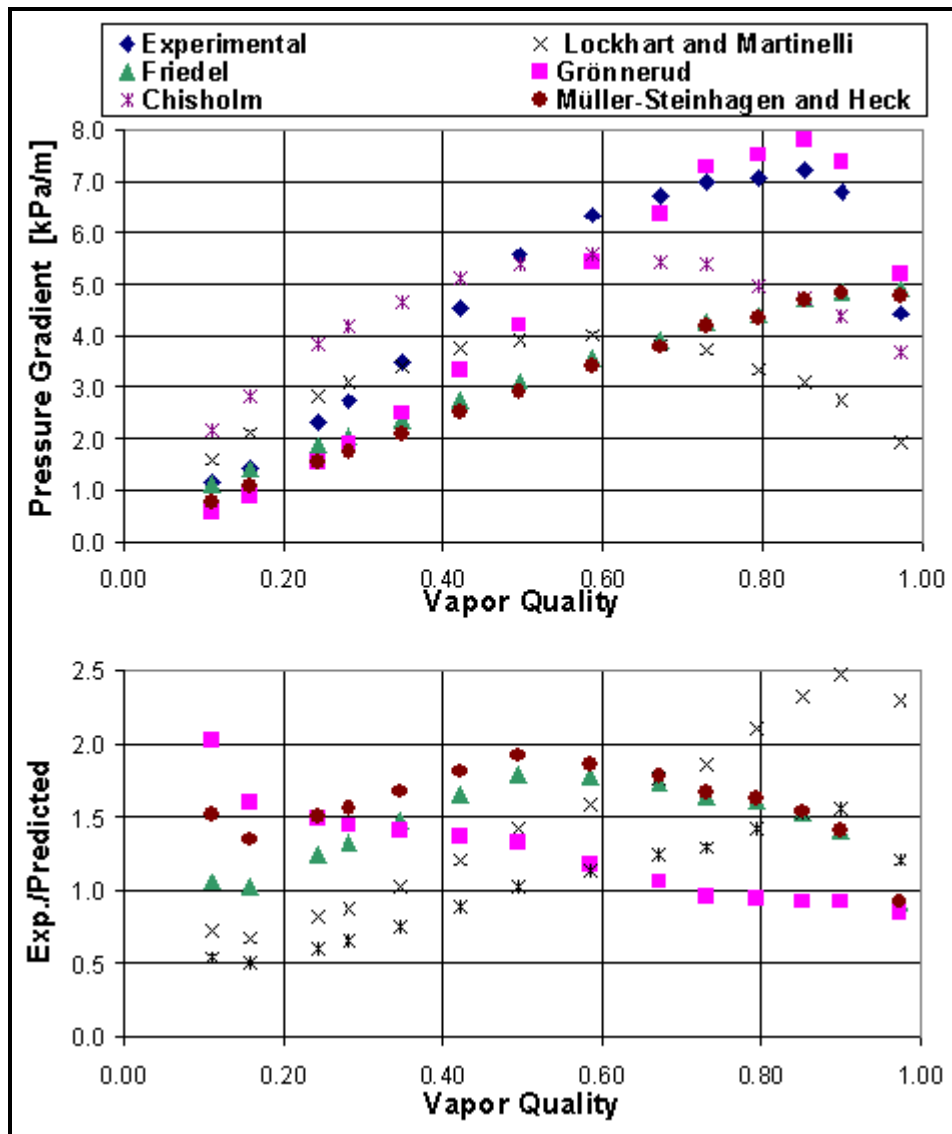


**Figure 13.1. Five methods compared to R-134a evaporating in a 12.0 mm (0.472 in.) horizontal tube at 4.4 °C (40 °F) and 300 kg/m<sup>2</sup>s (220740 lb/h ft<sup>2</sup>).**

In addition, Ould Didi, Kattan and Thome (2002) classified their data by flow pattern using the Kattan, Thome and Favrat (1998a) flow pattern map and thus obtained pressure drop databases for Annular flow, Intermittent flow and Stratified-Wavy flow. They found that the best method for annular flow was that of Müller-Steinhagen and Heck (1986), the best for Intermittent flow was that of Grönnerud (1972), and the best for Stratified-Wavy flow was that of Grönnerud (1972).

Two-phase friction pressure drop data of Moreno Quibén and Thome (2006a, 2006b) are compared in Figure 13.2 to two leading methods described above for R-22, R-410A and R-134a in 8.0 mm and 13.8 mm (0.315 and 0.543 in.) horizontal tubes, involving 1745 data points. Only about 40% of the data are captured within  $\pm 20\%$  by the Grönnerud (1972) correlation whereas that of Müller-Steinhagen and Heck (1986) was the best of existing methods, but still not satisfactory with only 50% captured within  $\pm 20\%$ .

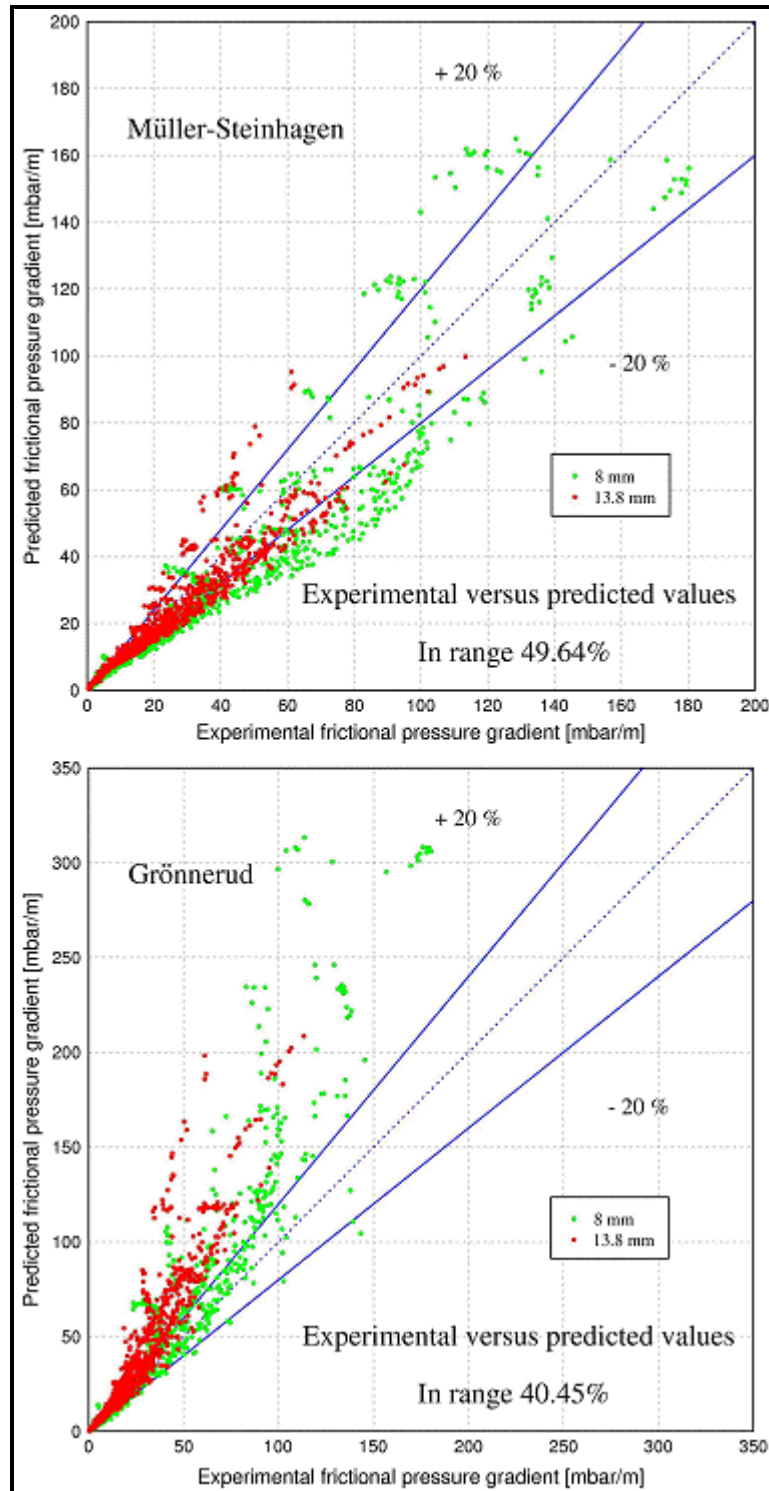


**Figure 13.2.** Two-phase friction pressure drop data of Moreno Quibén and Thome (2006a, 2006b) compared to two leading methods for R-22, R-410A and R-134a in 8.0 and 13.8 mm (0.315 and 0.543 in.) horizontal tubes.

In summary, even these “best” methods still have very large standard, mean and average deviations. Hence, the disagreement between measured pressure drops and predicted pressure drops using these methods can still easily be  $\pm 50\%$  and sometimes more.

### 13.2.9 New flow pattern based two-phase pressure drop model

In an attempt to better capture the experimental trends and to improve the accuracy and reliability in the prediction of two-phase frictional pressure drops, Moreno Quibén and Thome (2006a, 2006b) proposed a new phenomenological two-phase frictional pressure drop model for horizontal tubes based on local flow patterns and interfacial wave effects for horizontal plain tubes. The complete description of the work is available in Moreno Quibén (2005). Their experimental study covered the following range of parameters: mass velocities from 70 to 700 kg/m<sup>2</sup>s (51500 to 515000 lb/h ft<sup>2</sup>), tube internal diameters of 8.0 mm and 13.8 mm (0.315 and 0.543 in.) and vapor qualities from 0.01 to 0.99, all at one saturation temperature of 5°C (41°F) for primarily R-22 and R-410A with a limited amount of data also for R-134a. Their two-phase frictional pressure drop database was obtained from both adiabatic and diabatic tests, the latter with heat fluxes from 6 to 57.5 kW/m<sup>2</sup> (1900 to 18230 Btu/h ft<sup>2</sup>). They used the latest version of the Thome flow pattern map for adiabatic and evaporating flows in horizontal plain tubes proposed in Wojtan, Ursenbacher and Thome (2005a), to be described in an updated version of Chapter 12 in *Databook III*, to predict the local flow patterns in their pressure drop model. Below is a detailed description of their new flow pattern based frictional pressure drop model.

**Simplified flow structures assumed for horizontal tubes.** The same simplified flow structures assumed for evaporation inside horizontal tubes by Kattan, Thome and Favrat (1998c) and for condensation inside horizontal tubes by Thome, El Hajal and Cavallini (2003) were applied to the frictional pressure drop model, differing only in that the upper perimeter of the tube in a stratified type of condensing flow is wetted by film condensation rather than dry during evaporation (presently, the pressure drop data are for adiabatic and evaporating flows so the upper perimeter is assumed to be dry in stratified types of flow). The Moreno Quibén-Thome pressure drop model assumes three simplified geometries for describing annular flow, stratified-wavy flow and fully stratified-wavy flow as shown in Figure 13.3. For annular flow (bottom left), a uniform liquid film thickness of  $\delta$  is assumed and the effects due to gravity are ignored. For fully stratified flow, the stratified geometry (upper left) is converted to an equivalent geometry (upper right) with the same angle of stratification and cross-sectional area occupied by the liquid, but with the liquid distributed as a truncated annular ring of uniform thickness  $\delta$  as shown in the lower right diagram. In stratified-wavy flow (lower middle diagram), the interfacial waves are small and do not reach the top of the tube and hence the upper perimeter remains dry, and again it is assumed that the stratified-wavy liquid creates an annular truncated ring. Thus, the dry angle  $\theta_{dry}$  varies between its maximum value of  $\theta_{strat}$  at the threshold to fully stratified flow and its minimum value of zero at the threshold to annular flow.

Importantly, the three simple geometries shown above yield a smooth geometrical transition from one flow structure to another. A mist flow model with all the perimeter dry is used for that regime and transitions between these structures and the limits of all liquid flow at  $x = 0$  and all vapor flow at  $x = 1$  are applied to those boundaries. Figure 13.4 shows an example flow pattern map with the regimes considered by the present model, calculated using the Wojtan, Ursenbacher and Thome (2005a) map for the conditions noted. Below are the frictional pressure gradient prediction methods for individual flow regimes.

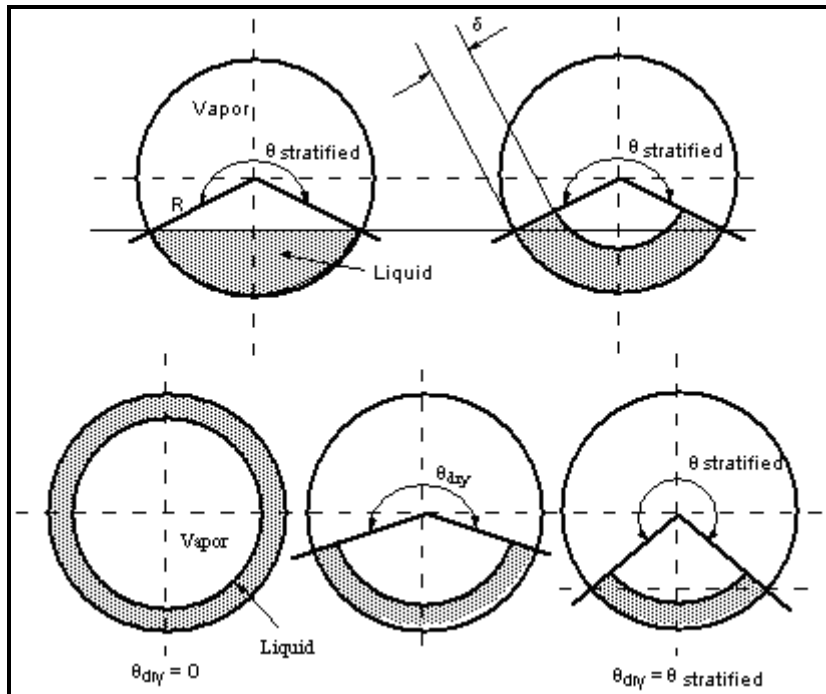


Figure 13.3. Simplified two-phase flow structures for pressure drop model. Lower left: annular flow structure, lower right: fully stratified flow structure equivalent to upper two figures, lower middle: stratified-wavy flow structure.

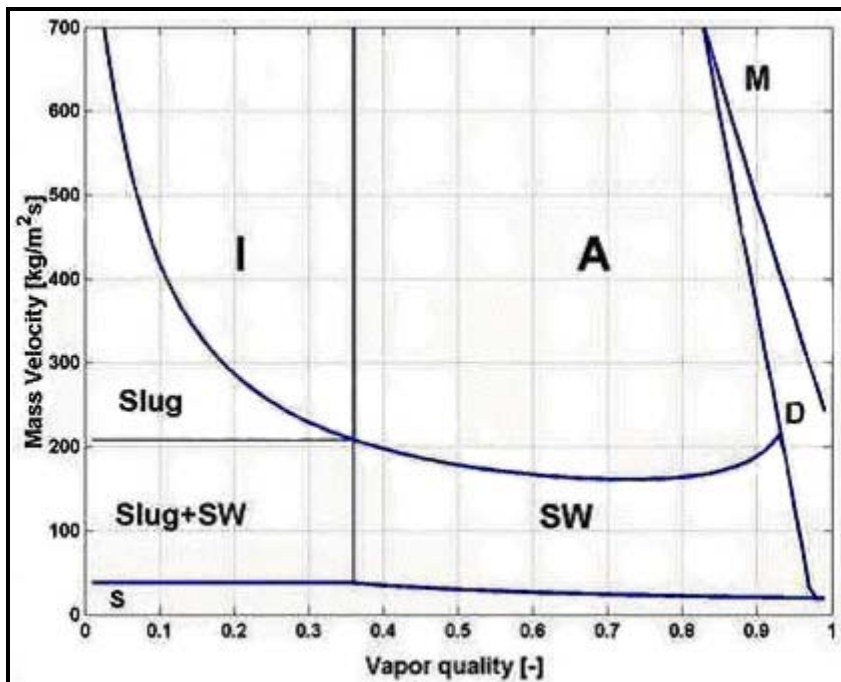


Figure 13.4. Flow pattern map for R-22 at  $T_{sat} = 5 \text{ }^{\circ}\text{C}$  ( $41 \text{ }^{\circ}\text{F}$ ) in the 13.84 mm (0.545 in.) test section with the void fractions evaluated using the mass velocity set to  $300 \text{ kg/m}^2\text{s}$  ( $220740 \text{ lb/h ft}^2$ ) and  $q = 7.5 \text{ kW/m}^2$  ( $2378 \text{ Btu/h ft}^2$ ).

**Annular flow (A).** The two-phase frictional pressure gradient in their model for annular flow is calculated with the following expression:

$$\left( \frac{dp}{dz} \right)_{\text{annular}} = 2(f_i)_{\text{annular}} \frac{\rho_G u_G^2}{d_i} \quad [13.2.44]$$

Their interfacial film friction factor expression for annular flow is:

$$(f_i)_{\text{annular}} = 0.67 \left[ \frac{\delta}{d_i} \right]^{1.2} \left[ \frac{(\rho_L - \rho_G)g\delta^2}{\sigma} \right]^{-0.4} \left[ \frac{\mu_G}{\mu_L} \right]^{0.08} \text{We}_L^{-0.034} \quad [13.2.45]$$

To the right of the equal sign in this expression, the first term scales the interfacial friction factor to the ratio of the film thickness to the tube diameter whilst the second term comes from a manipulation of the Helmholtz instability equation using  $\delta$  as the scaling factor for the most dangerous wavelength for the formation of interfacial waves. This term is the same one used to implement the interfacial wave effect in the convective condensation heat transfer model by Thome, El Hajal and Thome (2003). The other two terms were used to bring in the viscosity ratio and surface tension effects. The empirical constant and exponents were obtained from analysis of only their annular flow pressure drop database. The liquid film thickness  $\delta$  for a truncated annular ring as shown in Figure 13.3 is calculated from geometry to be:

$$\delta = \frac{d_i}{2} - \left[ \left( \frac{d_i}{2} \right)^2 - \frac{(1-\varepsilon)\pi d_i^2}{2(2\pi - \theta_{\text{dry}})} \right]^{1/2} \quad [13.2.46]$$

For annular flow  $\theta_{\text{dry}} = 0$  and the cross-sectional void fraction  $\varepsilon$  is calculated using equation [13.2.4a] above. In implementing the calculation for  $\delta$ , whenever  $\varepsilon < 0.5$ ,  $\delta$  is set equal to  $d_i/2$  (the radius of the channel). The true average velocities of the two phases are calculated as:

$$u_G = \frac{\dot{m}_{\text{total}} x}{\rho_G \varepsilon} \quad [13.2.47a]$$

$$u_L = \frac{\dot{m}_{\text{total}} (1-x)}{\rho_L (1-\varepsilon)} \quad [13.2.47b]$$

In their method, the liquid Weber number is defined using the true average velocity of the liquid phase as:

$$\text{We}_L = \frac{\rho_L u_L^2 d_i}{\sigma} \quad [13.2.48]$$

It should be noted that the above expressions can produce a maximum in the pressure gradient before reaching the transition to the dryout regime. This is because the annular film becomes very thin at high void fractions and hence its interfacial roughness diminishes accordingly, reducing friction like in the Moody diagram for roughened pipes.

**Slug + intermittent flow (Slug + I).** These two flow regimes were treated together since their experimental trends were noted to be similar. Rather than trying to capture their complex flow structures,

which would require methods to predict slug frequencies, slug and bubble lengths, etc., this regime was predicted using a proration between all liquid flow at  $x = 0$  and annular flow at the intermittent-to-annular flow transition at  $x_{IA}$  using the void fraction  $\varepsilon$  as:

$$\left(\frac{dp}{dz}\right)_{\text{slug+int errmittent}} = \left(\frac{dp}{dz}\right)_L \left(1 - \frac{\varepsilon}{\varepsilon_{IA}}\right)^{0.25} + \left(\frac{dp}{dz}\right)_{\text{annular}} \left(\frac{\varepsilon}{\varepsilon_{IA}}\right)^{0.25} \quad [13.2.49]$$

The all liquid flow pressure gradient  $(dp/dz)_L$  is calculated using expressions [13.2.6] to [13.2.8] with all the flow liquid and using liquid properties. In the above expression,  $(dp/dz)_{\text{annular}}$  is the annular flow frictional pressure gradient from [13.2.44] using the actual vapor quality  $x$  of the slug or intermittent flow (not  $x_{IA}$ ) in its evaluation with  $\theta_{\text{dry}} = 0$  and also the actual value of  $x$  is used to calculate  $\varepsilon$ . At the limit of  $x = 0$ , this expression correctly reduces to that of an all liquid turbulent flow (or laminar flow but no such data were in their database) while at  $x = x_{IA}$  it goes to the annular flow prediction without a jump in value at the transition. The value of  $\varepsilon_{IA}$  is obtained by evaluating [13.2.4a] with  $x$  set equal to  $x_{IA}$ . The proration exponent of 0.25 was determined statistically to be the best value to use for all such prorations in their method.

**Stratified-wavy flow (SW).** For this regime, the frictional pressure gradient is calculated from:

$$\left(\frac{dp}{dz}\right)_{\text{stratified-wavy}} = 2(f_i)_{\text{stratified-wavy}} \frac{\rho_G u_G^2}{d_i} \quad [13.2.50]$$

The friction factor for stratified-wavy flow is obtained by a proration around the perimeter of the tube. The vapor phase friction factor is applied to the dry perimeter while that of annular flow is applied to the wetted perimeter as in the lower middle diagram in Figure 13.3, so that:

$$(f_i)_{\text{stratified-wavy}} = \theta_{\text{dry}}^* f_G + (1 - \theta_{\text{dry}}^*) (f_i)_{\text{annular}} \quad [13.2.51]$$

The friction factor for the lower wetted fraction of the perimeter of the tube  $(f_i)_{\text{annular}}$  is calculated using [13.2.45] with the actual vapor quality in the calculation and using [13.2.46] to obtain the film thickness  $\delta$ . The friction factor for the upper dry fraction of the perimeter of the tube  $f_G$  is calculated using [13.2.7] with vapor properties but here with the Reynolds number defined with respect to the true average vapor velocity in the cross-section of the tube occupied by the vapor:

$$Re_G = \frac{\dot{m}_{\text{total}} x d_i}{\mu_G \varepsilon} \quad [13.2.52]$$

The upper dry fraction of the tube perimeter is obtained from its geometric definition:

$$\theta_{\text{dry}}^* = \frac{\theta_{\text{dry}}}{2\pi} \quad [13.2.53]$$

The dry angle in a stratified-wavy flow is calculated based on the mass velocity of the flow using the following expression from Wojtan, Ursenbacher and Thome (2005b) and the transition boundary values of this flow regime from their flow pattern map:

$$\theta_{\text{dry}} = \left[ \frac{\dot{m}_{\text{wavy}} - \dot{m}_{\text{total}}}{\dot{m}_{\text{wavy}} - \dot{m}_{\text{strat}}} \right]^{0.61} \theta_{\text{strat}} \quad [13.2.54]$$

Note that the wavy flow transition mass velocity is used in this calculation even when the upper boundary of the stratified-wavy flow regime on the flow pattern map becomes that of the dryout region; this is because if the dryout boundary were used, the value of  $\theta_{\text{dry}}$  would incorrectly go to zero with increasing vapor quality. The stratified angle can be calculated explicitly from the following expression of Biberg (1999) from the value of the void fraction determined using [13.2.4a], avoiding use of its exact but iterative geometrical expression:

$$\theta_{\text{strat}} = 2\pi - 2 \left\{ \pi(1-\varepsilon) + \left( \frac{3\pi}{2} \right)^{1/3} \left[ 1 - 2(1-\varepsilon) + (1-\varepsilon)^{1/3} - \varepsilon^{1/3} \right] \right\} - \frac{1}{200}(1-\varepsilon)\varepsilon [1 - 2(1-\varepsilon)] [1 + 4((1-\varepsilon)^2 + \varepsilon^2)] \quad [13.2.55]$$

Notice that this expression goes to the correct limits of  $\varepsilon = 0$  at  $x = 0$  and  $\varepsilon = 1$  at  $x = 1$ .

**Slug + stratified-wavy flow (Slug + SW).** Referring to the flow pattern map shown in Figure 13.4, it is seen that this flow regime is bounded by slug flow at the top, fully stratified flow at the bottom, stratified-wavy flow at the right and all liquid flow at the left. Hence, these transition boundaries were taken into account when they proposed the frictional pressure drop method for this regime without any jumps in its values at these boundaries. Furthermore, in this regime Wojtan, Ursenbacher and Thome (2003) observed a cyclic behaviour of the flow, alternating between low amplitude waves that did not reach the top of the tube and slug flow with its large amplitude waves washing the top of the tube perimeter. The following expression was found by Moreno Quibén and Thome to reflect these observations and limits:

$$\left( \frac{dp}{dz} \right)_{\text{slug+SW}} = \left( \frac{dp}{dz} \right)_L \left( 1 - \frac{\varepsilon}{\varepsilon_{IA}} \right)^{0.25} + \left( \frac{dp}{dz} \right)_{\text{stratified-wavy}} \left( \frac{\varepsilon}{\varepsilon_{IA}} \right)^{0.25} \quad [13.2.56]$$

The values of  $(dp/dz)_L$  and  $\varepsilon_{IA}$  are evaluated as explained already above while  $(dp/dz)_{\text{stratified-wavy}}$  is the stratified-wavy flow frictional pressure gradient from [13.2.50] using the actual vapor quality of flow in its calculation and that of  $\varepsilon$ . Referring again to Figure 13.4,  $\theta_{\text{dry}}$  is obtained from [13.2.54] by using the horizontal upper and lower transition boundaries of this regime, whose respective mass velocity values are those at  $x_{IA}$ . The value of  $\delta$  is obtained using [13.2.46]. It should be pointed that when  $\varepsilon < 0.5$ , the liquid occupies more than one-half of the cross-section of the tube. Hence, the convention used in their method is that whenever  $\varepsilon < 0.5$ ,  $\delta$  is set equal to  $d_i/2$ . This convention still brings their method to the correct pressure gradient for all liquid flow at  $x = 0$  because of the proration.

**Mist flow (M).** The mist flow regime is characterized by all the liquid entrained in the continuous vapor phase as minute droplets. The droplets travel at nearly the same velocity as the vapor and hence the homogeneous model given by [13.1.4] is used to determine the homogeneous void fraction  $\varepsilon_H$ . For homogeneous flows as explained earlier, the flow is assumed to be one fluid possessing mean fluid properties. The frictional pressure gradient of a mist flow is obtained from manipulation of [13.1.6] to be:

$$\left( \frac{dp}{dz} \right)_{\text{mist}} = \frac{2(f_i)_{\text{mist}} \dot{m}_{\text{total}}^2}{d_i \rho_H} \quad [13.2.57]$$

The expressions [13.1.7], [13.1.8] and [13.1.9] presented in Section 13.1 are then used to calculate the mist flow friction factor. At the limit of  $x = 1$  where  $\epsilon = 1$ , this expression goes to the limit of an all vapor flow frictional pressure gradient. While this may at first appear to be a satisfactory bound, in reality the entrained droplets in a mist flow are typically not yet all evaporated and the pressure drops measured at  $x = 1$  are usually still larger than would otherwise be expected. This aspect has not yet been taken into account in the Moreno Quibén-Thome flow pattern based pressure drop model.

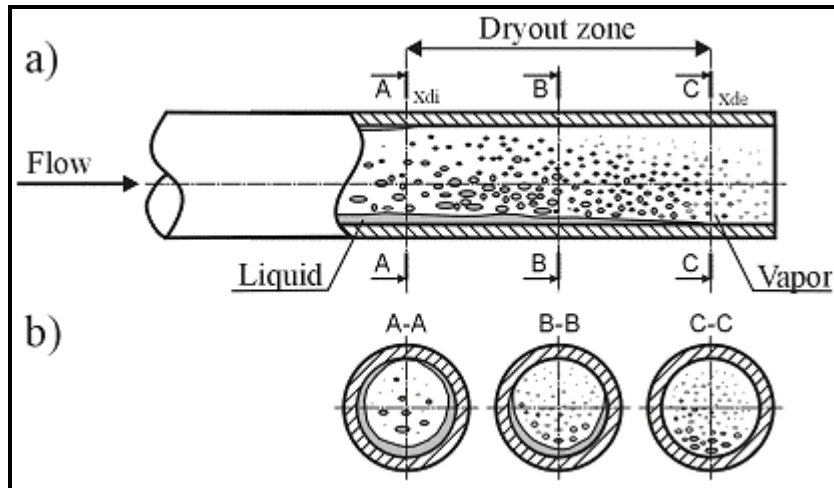


**Figure 13.5. Schematic diagram of transition from annular flow to mist flow through the dryout regime: (a) side view, (b) cross-sectional view.**

**Dryout flow (D).** Figure 13.5 depicts a schematic diagram of the transition from annular flow to mist flow at low to medium mass velocities, passing through the dryout regime. Since the annular film is thinner at the top than the bottom of the tube, the upper film becomes entrained as droplets in the vapor core first, leaving the lower perimeter still wet. Referring to Figure 13.4, this regime is bounded at the left by the annular and stratified-wavy flow regimes and at the right by the mist flow regime. At high mass velocities, the left and right transition lines of the dryout regime meet and form one line, and hence the dryout regime at that point disappears. This disappearance seems to reflect the actual process because at high mass velocities the thickness of the annular film at the top and bottom of the tube become identical as gravity effects have become negligible and hence entrainment should then happen simultaneously around the entire perimeter. For such situations, the frictional pressure drop gradient *jumps* from the annular flow value to the mist flow value, again probably reflecting the actual process (no data at these conditions were obtained in their experimental study to verify this, however). When the dryout regime does exist, the following linear interpolation was used to capture the variation in frictional pressure gradient across this regime without introducing any jump in the value:

$$\left( \frac{dp}{dz} \right)_{\text{dryout}} = \left( \frac{dp}{dz} \right)_{x=x_{di}} - \frac{x - x_{di}}{x_{de} - x_{di}} \left[ \left( \frac{dp}{dz} \right)_{x=x_{di}} - \left( \frac{dp}{dz} \right)_{x=x_{de}} \right] \quad [13.2.58]$$

In this expression,  $x_{di}$  is the inception quality of dryout at the top of the tube and  $x_{de}$  is the dryout completion quality at the bottom of the tube. The value of frictional pressure gradient at  $x=x_{di}$  is obtained using either [13.2.44] or [13.2.50] for annular and stratified-wavy flows, respectively, evaluated for  $x$  set equal to  $x_{di}$ . The value of mist flow frictional pressure gradient at  $x=x_{de}$  is calculated using [13.2.57] with

$x$  set equal to  $x_{de}$ . Wojtan, Ursenbacher and Thome (2005a) gave the following prediction methods for  $x_{di}$  and  $x_{de}$ :

$$x_{di} = 0.58 \exp \left[ 0.52 - 0.000021 We_G^{0.96} Fr_G^{-0.02} \left( \frac{\rho_G}{\rho_L} \right)^{-0.08} \right] \quad [13.2.59]$$

$$x_{de} = 0.61 \exp \left[ 0.57 - 0.0000265 We_G^{0.94} Fr_G^{-0.02} \left( \frac{\rho_G}{\rho_L} \right)^{-0.08} \right] \quad [13.2.60]$$

In these expressions, the Weber and Froude numbers are defined as:

$$We_G = \frac{\dot{m}_{total}^2 d_i}{\rho_G \sigma} \quad [13.2.61]$$

$$Fr_G = \frac{\dot{m}_{total}^2}{\rho_G (\rho_L - \rho_G) g d_i} \quad [13.2.62]$$

At high mass velocities, the transition line of  $x_{de}$  intersects with that of  $x_{di}$  and above this intersection the value of  $x_{di}$  is tentatively used as the direct transition between annular and mist flow. At very low mass velocities, the lower bound of this flow regime is fully stratified flow, the latter which extends from  $x = 0$  all the way to  $x = 1.0$ . Implementing the expression for  $x_{de}$  one will also find that when decreasing the mass velocity one reaches a value of  $x_{de} = 1.0$ , which is the maximum possible value of  $x_{de}$  even when [13.2.60] yields values larger than 1.0.

**Stratified flow (S).** Although no fully stratified two-phase pressure drop data were obtained in the study of Moreno Quibén and Thome (2006a, 2006b), a logical extension of their above model to stratified flows without imposing any jumps at the stratified flow transition boundary was proposed. If  $x_{IA} \leq x \leq x_{di}$ , then the friction factor for stratified flow is calculated as:

$$(f_i)_{stratified} = \theta_{strat}^* f_G + (1 - \theta_{strat}^*) (f_i)_{annular} \quad [13.2.63]$$

Similar to the method for stratified-wavy flow, the single-phase vapor friction factor is calculated with [13.2.7] in the same manner as noted above and the friction factor for the lower wetted fraction of the perimeter of the tube  $(f_i)_{annular}$  is calculated using [13.2.45] with the actual vapor quality in the calculation and using [13.2.46] to obtain the film thickness  $\delta$  while the value of  $\theta_{dry}$  becomes that of  $\theta_{strat}$ , such that:

$$\theta_{strat}^* = \frac{\theta_{strat}}{2\pi} \quad [13.2.64]$$

The frictional pressure gradient for stratified flow then is obtainable from:

$$\left( \frac{dp}{dz} \right)_{stratified(x \geq x_{IA})} = 2(f_i)_{stratified} \frac{\rho_G u_G^2}{d_i} \quad [13.2.65]$$

If  $0 \leq x < x_{IA}$ , then the frictional pressure gradient for stratified flow is given by the following proration between all liquid flow and [13.2.65] evaluated with the actual vapor quality:

$$\left( \frac{dp}{dz} \right)_{\text{stratified } (x < x_{IA})} = \left( \frac{dp}{dz} \right)_L \left( 1 - \frac{\varepsilon}{\varepsilon_{IA}} \right)^{0.25} + \left( \frac{dp}{dz} \right)_{\text{stratified } (x \geq x_{IA})} \left( \frac{\varepsilon}{\varepsilon_{IA}} \right)^{0.25} \quad [13.2.66]$$

As can be observed in Figure 13.4, the stratified regime extends all the way to  $x = 1.0$  and the lower bound of the transition line for  $x_{di}$  stops at the stratified flow boundary. For the small range where the vapor quality in a stratified flow is larger than  $x_{di}$ , the frictional pressure gradient could experience a jump at the stratified flow to dryout boundary when changing the mass velocity. Since this is not significant in practice, this minor jump has been ignored in their method. The problem can be resolved with a small modification to the flow pattern map by allowing the  $x_{di}$  transition line to go all the way to zero mass velocity, at which point  $x_{di} = 0.976$ . Then the expression [13.2.58] would be applicable to this small area and the limit of all vapor flow at  $x = 1$  would still be respected.

**Bubbly flow (B).** A prediction method for bubbly flows was not addressed in their pressure drop model as they had no test data in this regime. Bubbly flows tend to occur in horizontal tubes at very high mass velocities beyond the range of industrial interest.

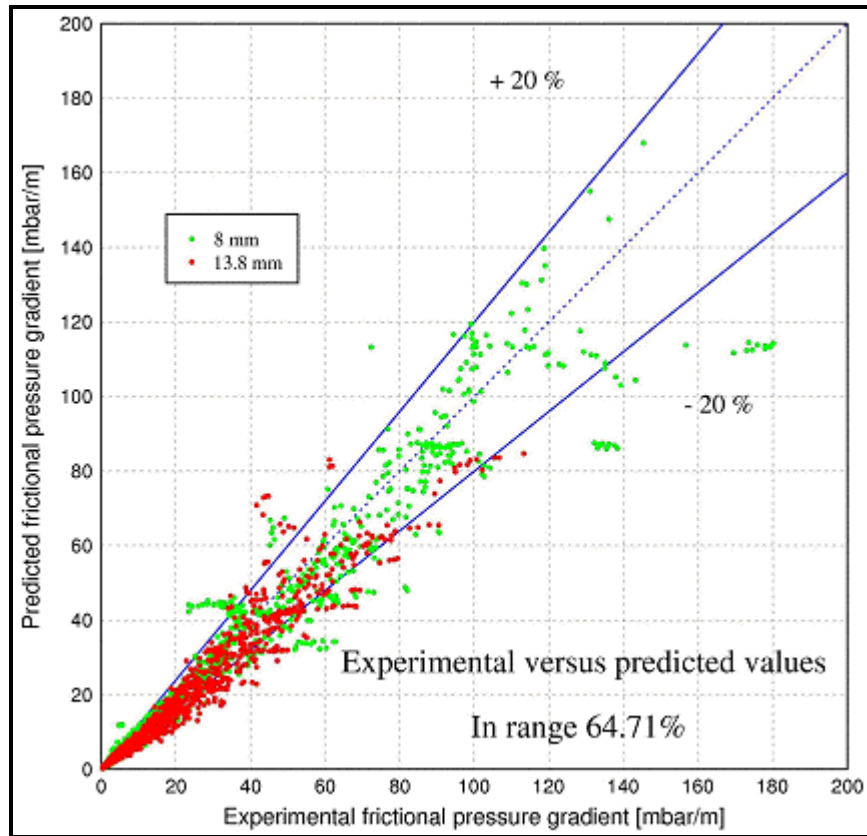


**Figure 13.6.** Two-phase frictional pressure drop data of Moreno Quibén and Thome (2006a, 2006b) compared to their new flow pattern based method for R-22, R-410A and R-134a in 8.0 and 13.8 mm (0.315 and 0.543 in.) horizontal tubes.

**Comparison of the new flow regime model to their database.** Figure 13.6 shows the two-phase frictional pressure drop data of Moreno Quibén and Thome (2006a, 2006b) compared to their new flow pattern based method for R-22, R-410A and R-134a in 8.0 mm and 13.8 mm (0.315 and 0.543 in.) horizontal tubes. A statistical comparison of their new flow pattern based model versus the best three of the older models is shown in Table 13.2. As can be seen, the new flow pattern based model is able to predict more than 4 of every 5 data points within  $\pm 30\%$  while also getting about 2 out of 3 within  $\pm 20\%$ , which are both considerable improvements on the older competing methods. As can be noted, the simpler to implement method of Müller-Steinhagen and Heck (1986) comes in second best here and in fact captures about 3 of every 4 data points within  $\pm 30\%$ ; it tends to not work well at high vapor qualities (typical of direct-expansion evaporator design conditions) and for stratified-wavy flows.

**Table 13.2. Statistical comparison of data to four methods.**

Data predicted within	$\pm 30\%$	$\pm 20\%$
<b>Friedel (1979)</b>	67.3%	51.8%
<b>Grönnerud (1972)</b>	46.2%	40.5%
<b>Müller-Steinhagen and Heck (1986)</b>	75.8%	49.6%
<b>Moreno-Quibén and Thome (2006b)</b>	82.3%	64.7%

Composite simulations of (i) the flow pattern map of Wojtan, Ursenbacher and Thome (2005a), (ii) the flow pattern based two-phase frictional pressure drop model of Moreno-Quibén and Thome (2006b), and (iii) the flow pattern based flow boiling model of Wojtan, Ursenbacher and Thome (2005b) for R-410A at 5°C (41°F) at two heat flux levels at a mass velocity of 300 kg/m<sup>2</sup>s (220740 lb/h ft<sup>2</sup>) are shown in Figure 13.7. Comparing the upper graph to the lower one, one can appreciate the effect of heat flux on the location of the boundaries of the dryout regime. Furthermore, one can note that the peak in the two-phase frictional pressure drop gradient does not necessarily coincide with the peak in the local flow boiling heat transfer coefficient, which was also noticed in their experimental results. The explanation for this is that the peak in the frictional pressure drop in an annular flow occurs either within the annular flow regime as the liquid film becomes very thin and reduces the interfacial surface roughness or when the onset of dryout at  $x_{di}$  occurs, which ever is reached first, whereas the heat transfer coefficient continues to increase until  $x_{de}$  is reached. Regarding the flow pattern based model, most of the points predicted with errors larger than 20-30% are those near flow pattern transition boundaries, particularly those at which a large change in trend occurs, such as at  $x_{di}$  and  $x_{de}$ . In this latter case, a map error of 2-3% in predicting the values of  $x_{di}$  and  $x_{de}$  or in the measurement of the vapor quality can lead to large errors because of the sharp change in slope of the pressure gradient in the dryout zone.

From a point of view of a recommendation, the new flow pattern based model is the most complete of those present in the literature, also capturing the trends in experimental data better than the older methods, but on the other hand it is more complex to implement and still requires more verification (and thus possible improvements) versus a broader range of fluids, pressures and tube sizes. So far, the individual phases have always been considered to be turbulent while in the future the database and model need to be expanded to cover laminar and transition regimes as well.

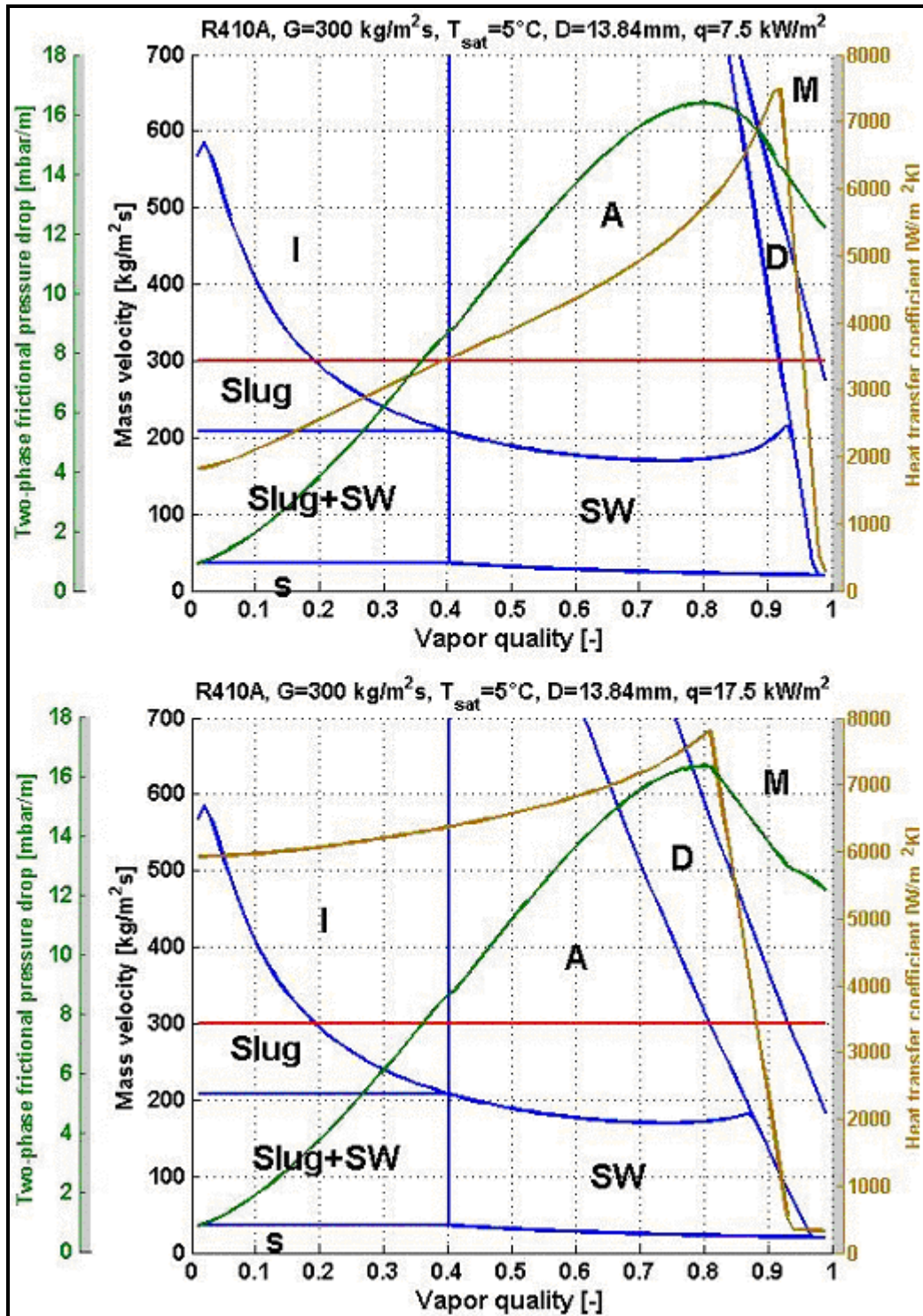


Figure 13.7. Composite simulations of (i) the flow pattern map of Wojtan, Ursenbacher and Thome (2005a), (ii) the flow pattern based two-phase frictional pressure drop model of Moreno-Quibén and Thome (2006b), and (iii) the flow pattern based flow boiling model of Wojtan, Ursenbacher and Thome (2005b) for R-410A at  $5^\circ\text{C}$  ( $41^\circ\text{F}$ ) at two heat fluxes levels and a mass velocity of  $300 \text{ kg/m}^2\text{s}$  ( $220740 \text{ lb/h ft}^2$ ).

### 13.2.10 Two-phase pressure drops in flattened plain tubes

Thome and Moreno Quibén (2004) completed an extensive experimental study on two-phase pressure drops inside horizontal flattened plain tubes. The tube samples they tested are shown in Figure 13.8 and the dimensions of the flattened tube geometries are shown in Figure 13.9 with internal heights of 2 and 3 mm (0.079 and 0.118 in.). The 13.8 mm (0.543 in.) flattened tubes had equivalent diameters of 8.60 and 7.17 mm (0.339 and 0.282 in.) and hydraulic diameters of 4.40 and 3.24 mm (0.173 and 0.128 in.), respectively, while the 8.0 mm (0.315 in.) flattened tubes had equivalent diameters of 6.25 and 5.30 mm (0.246 and 0.209 in.) and hydraulic diameters of 3.55 and 2.80 mm (0.140 and 0.110 in.), respectively. The hydraulic diameter is the traditional single-phase flow definition while an equivalent diameter is that of a round tube whose cross-sectional area is equal to that of the flattened tube. The latter definition seems to be more appropriate for two-phase flows since it keeps the mass velocities and velocity ratio of the two phases the same as in the flattened tube while a hydraulic diameter definition does not. In fact, they found that applying the equivalent diameter approach in their frictional prediction method yielded better results. The flattened tube samples were provided by [Wolverine Tube, Inc.](#) and were made by an extrusion process to obtain a more accurate and uniform shape than possible from simply flattening a tube in a press. The flattened tubes were tested with their flat sides oriented horizontally.



**Figure 13.8. Photograph of round and flattened tubes.**

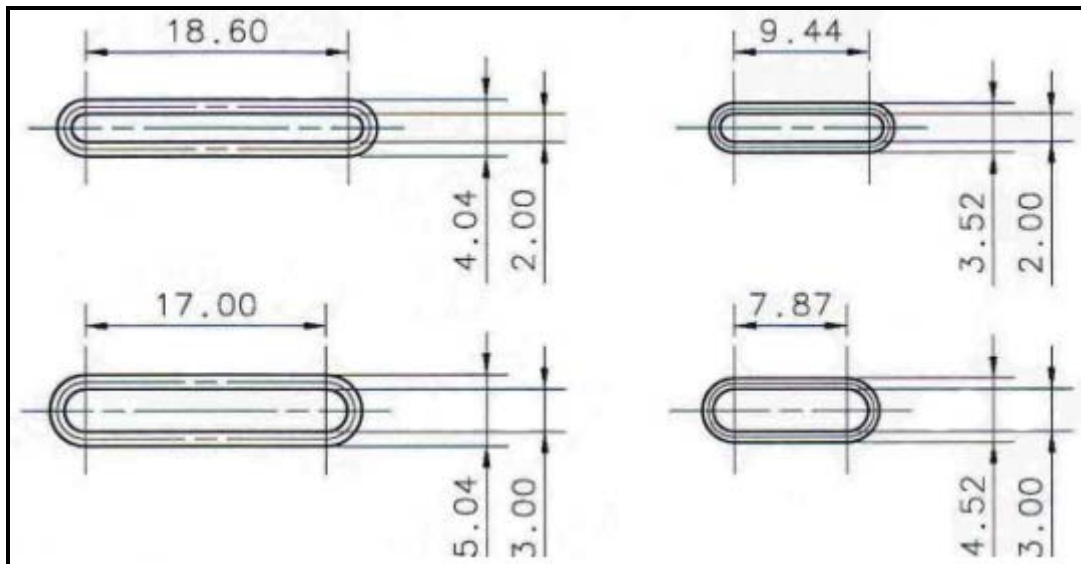


**Figure 13.9. Dimensions of the flattened tubes studied.**

Figure 13.10 depicts some of their two-phase pressure drop data measured for the larger size tube samples for R-22 and R-410A. As can be noticed, the pressure drop penalty of the flattened tubes at the same mass velocity as the round tube can be as high as seven! Thus, careful thermal design to find a balance between heat transfer and pressure drop is required for applying flattened tubes to reduce refrigerant charge in such evaporators.

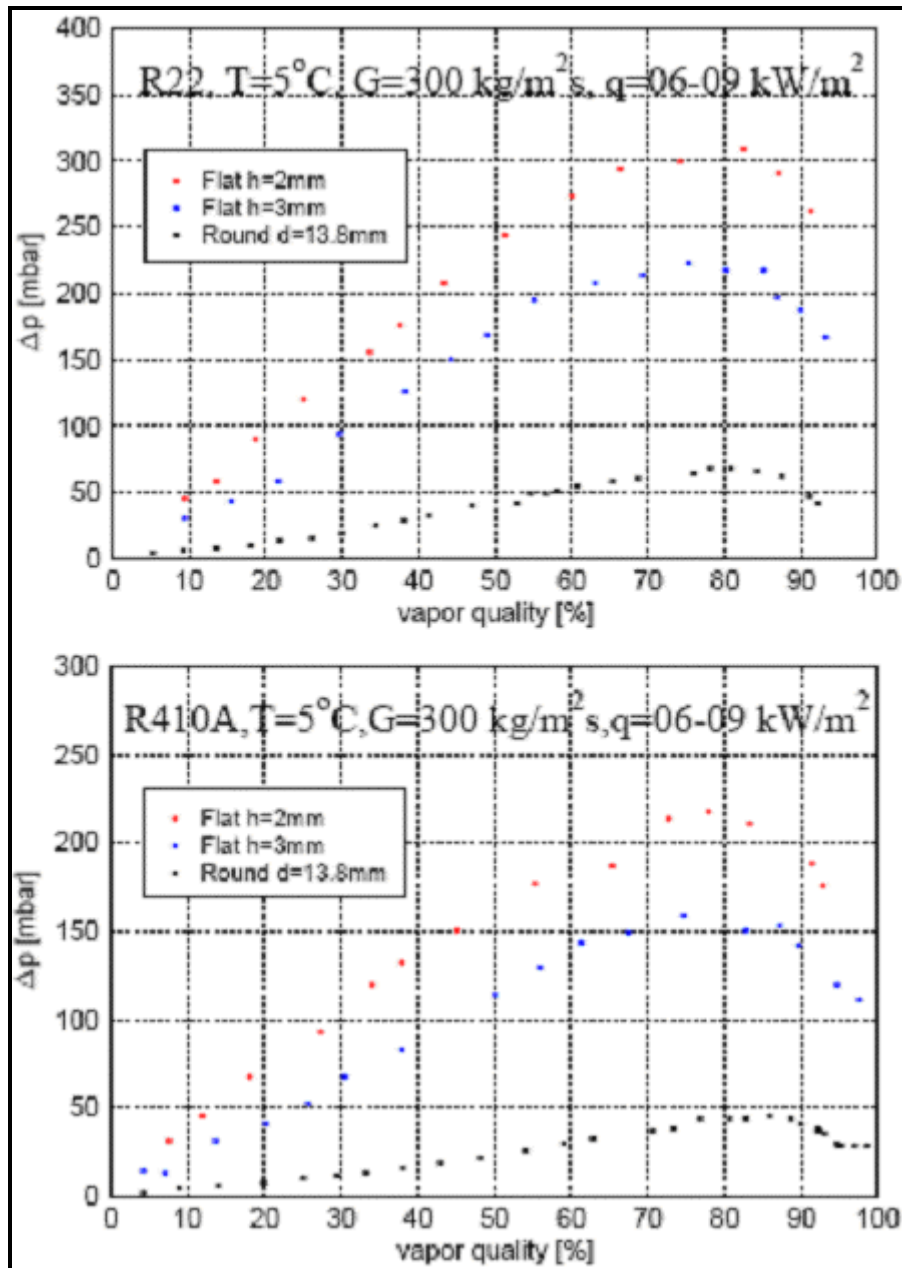


**Figure 13.10. Flattened tube pressure drop data for round 13.8 mm (0.543 in.) tube and flattened versions with heights of 2 and 3 mm (0.079 and 0.118 in.). Top: Results for R-22; bottom: Results for R-410A.**

To predict the two-phase frictional pressure drops in flattened tubes, Thome and Moreno Quibén (2004) modified the method of Grönnerud (1972) presented above. The modified expression became:

$$\Delta p_{\text{frict}} = \Phi_{\text{gd}} \Delta p_L F_{\text{round}} F_{\text{flat}} \quad [13.2.67]$$

His two-phase multiplier given by [13.2.23] and the calculation of  $\Delta p_L$  remain the same as in the original method except that the equivalent diameter is used in place of  $d_i$ . The mass velocity is based on the actual cross-sectional area of the flattened tube. To correct the Grönnerud method to better predict their round tube data over the entire range of vapor qualities, they applied the correction factor  $F_{\text{round}}$  as:

$$F_{\text{round}} = 1.21 - 0.63x \quad [13.2.68]$$

To then correct the method to fit the flattened tube data, one further correction factor  $F_{\text{flat}}$  was applied:

$$F_{\text{flat}} = 3.2 - 1.42x \quad [13.2.69]$$

Figure 13.11 shows a comparison of the predicted values to those measured. The flattened tube method captured most of their 359 data points within  $\pm 30\%$  error and also followed the trends in the experimental data. Their tests covered R-22 and R-410A at 5°C (41°F) over nearly the entire vapor quality range for mass velocities from 150 to 500 kg/m<sup>2</sup>s (110400 to 367900 lb/h ft<sup>2</sup>).

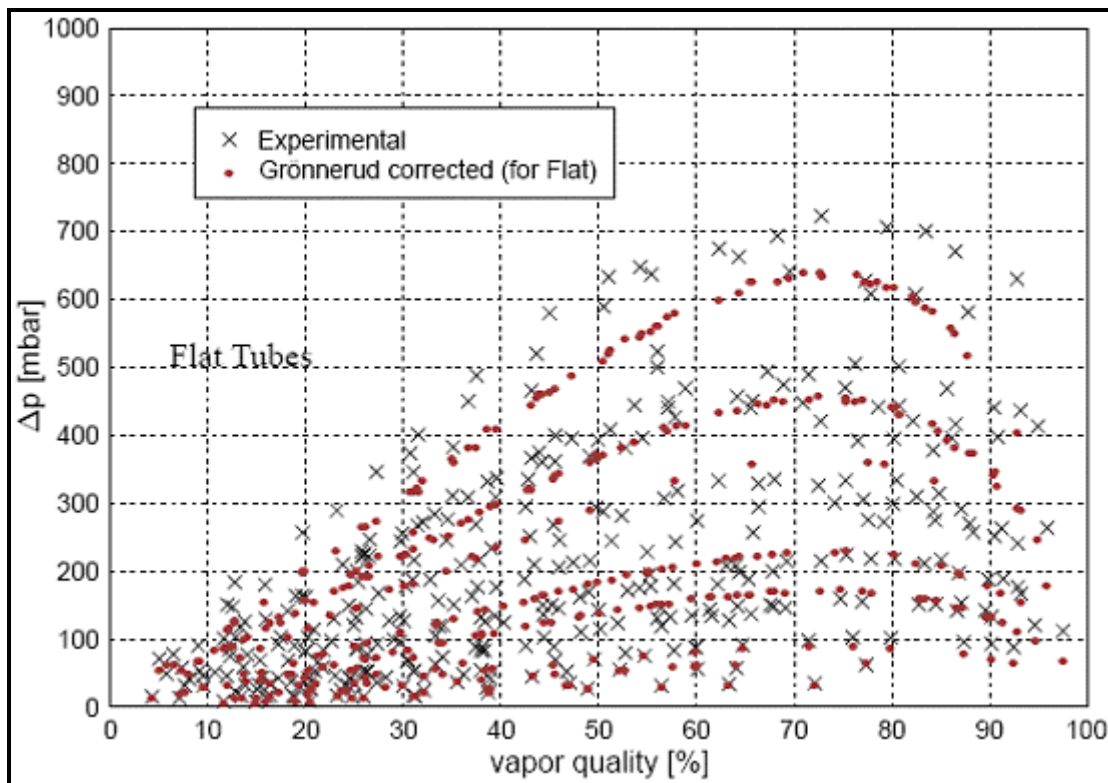
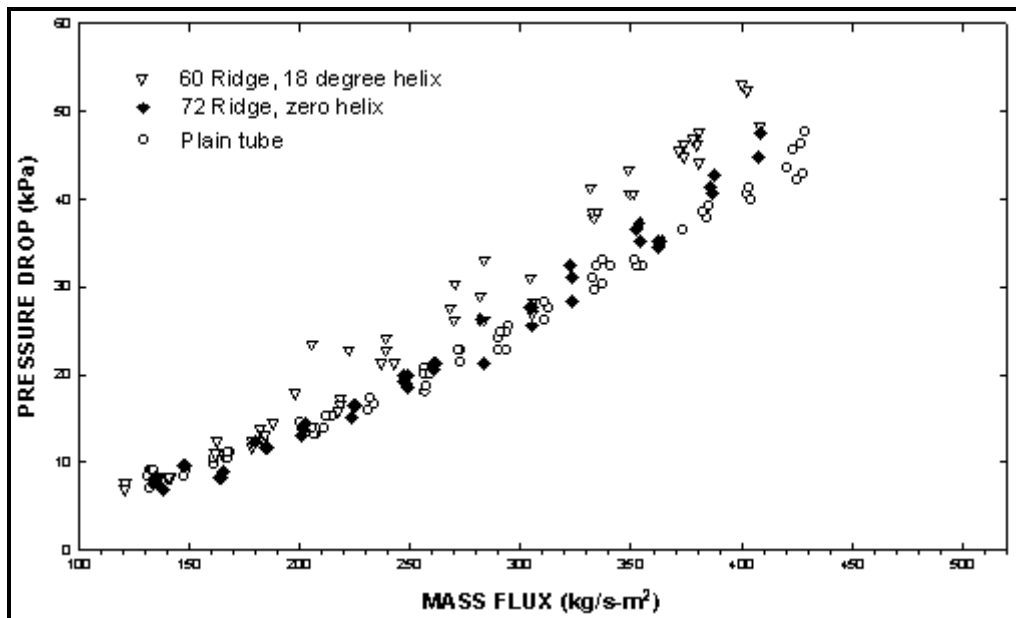


Figure 13.11. Comparison of predictions to measurements for flattened tube data.

### 13.3 Two-Phase Pressure Drops in Microfin Tubes

Thors and Bogart (1994) measured two-phase pressure drops for a 3.66 m (12 ft) long horizontal test sections of 9.53 mm (3/8 in.) and 15.9 mm (5/8 in.) diameter tubes for several microfin tubes in

comparison to plain bore tubes for R-22 at a saturation temperature of 1.67°C (35°F) for evaporation from an inlet vapor quality of 10% to an outlet vapor quality of 80%. Figure 13.12 depicts their comparison of two-phase pressure drops for the smaller tubes: plain tube of 8.72 mm (0.343 in.) internal diameter, microfin tube of 8.87 mm (0.349 in.) internal diameter with 60 fins of 18° helix angle and 0.203 mm height (0.008 in.) and microfin tube of 8.87 mm (0.349 in.) internal diameter with 72 fins of 0° helix angle and 0.203 mm height (0.008 in.). As can be noted, the pressure drops for the longitudinal micron fin tube are identical to those of the plain tube, i.e. no pressure drop penalty, while those of the 18° microfin tube are only marginally higher at the higher mass velocities (by about 10-20%).



**Figure 13.12. Thors and Bogart (1994) comparison of two-phase pressure drops for R-22 in 9.53 mm (3/8 in.) tubes.**

Similarly, in Figure 13.13 their comparable results for the large tube size are shown. The tests were run for the following tubes: plain tube of 14.86 mm (0.585 in.) internal diameter, microfin tube of 14.86 mm (0.585 in.) internal diameter with 60 fins of 27° helix angle and 0.305 mm height (0.012 in.), microfin tube of 14.86 mm (0.585 in.) internal diameter with 75 fins of 23° helix angle and 0.305 mm height (0.012 in.) and corrugated tube of 14.10 mm (0.555 in.) internal diameter with one start giving a helix angle of 78° and corrugation depth of 1.041 mm (0.041 in.). Here, the microfin tubes have the same pressure drop as the plain tube at low mass velocities while they are up to 50% higher at the highest mass velocity. The corrugated tube also begins at the low mass velocity with the same pressure drop as the other tubes but then its pressure drop increases rapidly up to 200% higher than that of the plain tube and up to 100% higher than the microfin tubes.

In similar tests, Muzzio, Niro and Arosio (1998) presented a comparison of two-phase pressure drops for a variety of microfin tubes, arriving at similar conclusions to those above, i.e. microfin tubes have two-phase pressure drops similar or slightly higher than those of plain bore tubes. Numerous other studies on two-phase pressure drops for microfin tubes are in the literature, such as those of Schlager, Pate and Bergles (1990) for R-22, Chamra, Webb and Randlett (1996) for R-22, Nidegger, Thome and Favrat (1997) for R-134a and Zürcher, Thome and Favrat (1998b) for R-407C.

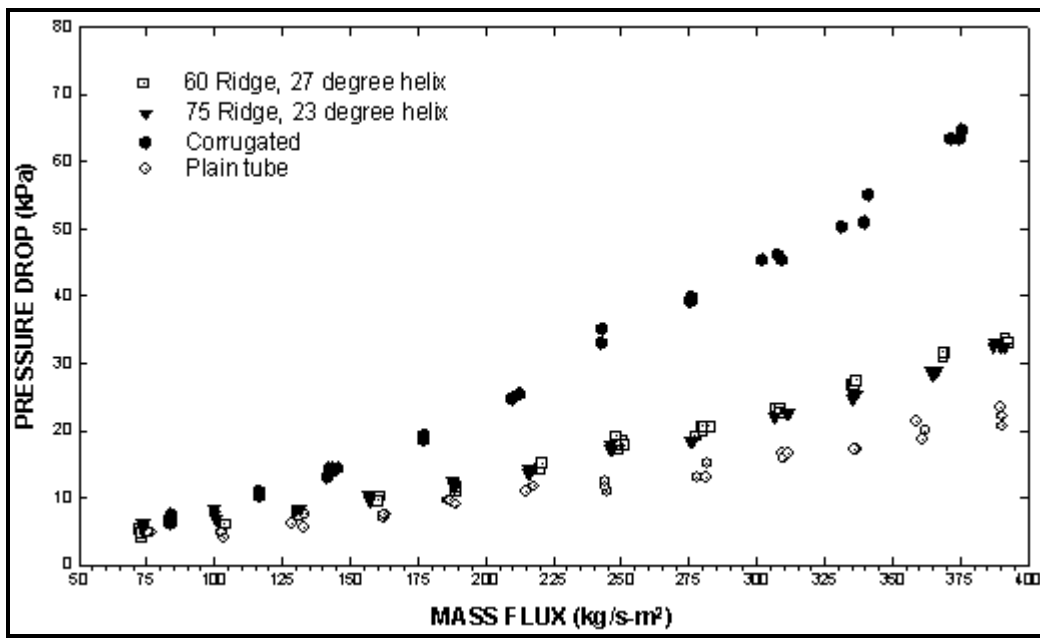


**Figure 13.13.** Thors and Bogart (1994) comparison of two-phase pressure drops for R-22 in 15.88 (5/8 in.) tubes.

Yashar et al. (2001) made comprehensive measurements for void fractions during evaporation and condensation in microfin tubes using the quick closing valve technique, which had an uncertainty of about 10%, which is quite large considering that two-phase pressure drops are particularly sensitive to the local void fraction. They correlated their data with the following method applicable to plain tubes and microfin tubes under evaporating and condensing conditions based on tests with R-134a and R-410a:

$$\varepsilon = \left( 1 + \frac{1}{Ft} + X_{tt} \right)^{-0.321} \quad [13.3.1]$$

where the Froude rate  $Ft$  is given as

$$Ft = \left( \frac{\dot{m}_{\text{total}}^2 X^3}{(1-x) \rho_G^2 g d_i} \right)^{0.5} \quad [13.3.2]$$

The tube diameter  $d_i$  is that of the plain tube or that at the root of the fins of microfin tubes. The Martinelli parameter  $X_{tt}$  is given by Eq. 13.2.21. This method combines the effects of two important parameters: the Martinelli parameter, which is essentially a ratio of viscous drag effects to the vapor kinetic energy and the Froude rate, which is a ratio of the vapor kinetic energy to gravitational drag effects. This method, however, sometimes erroneously predicts void fractions larger than the homogeneous void fraction.

## 13.4 Two-Phase Pressure Drops in Corrugated Tubes

For two-phase flows in corrugated tubes, the two-phase pressure drops are typically much larger than those of plain tubes and microfin tubes. For example, Figure 13.13 depicted some experimental results of Bogart and Thors (1994) for R-22 compared to a plain tube and two microfin tubes. Withers and Habdas (1974) have presented an earlier experimental study on a corrugated tube for R-12. No general method is

available for predicting two-phase pressure drops in corrugated tubes. There are numerous tube diameters, corrugation depths and corrugation pitches among the tubes commercially available and there has apparently not been a systematic study to develop such a method.

## 13.5 Two-Phase Pressure Drops for Twisted Tape Inserts in Plain Tubes

A twisted tape insert is a metal strip that is twisted into a helix before its insertion into a plain tube. In order to install the twisted tape, its diameter must be slightly less than that of the tube, accounting for the normal manufacturing tolerance of tube wall thickness and roundness. Hence, twisted tapes are in rather poor contact with the tube wall. In fact, a large two-phase pressure drop may drive the insert out of the tube if it is not firmly fixed at the entrance.

For two-phase flows in tubes with twisted tape inserts, the two-phase pressure drops are typically much larger than those of plain tubes and microfin tubes and similar to those of corrugated tubes. No general method is available for predicting two-phase pressure drops in tubes with twisted tape inserts. As a rough approximation, the hydraulic diameter of one of the two flow channels inside the tube, which is bisected by the tape, can be used in one of the plain tube two-phase frictional pressure drop correlations, assuming one-half of the flow goes through this channel. This typically results in two-phase pressure drops twice as large as in the same tube without the tape.

## 13.6 Two-Phase Pressure Drops in Shell-side Flows

### 13.6.1 Plain tube bundles

The following approach is probably the best currently available. The total pressure drop  $\Delta p_{\text{total}}$  of a two-phase fluid flowing in cross-flow over a tube bundle is the sum of the static pressure drop (elevation head)  $\Delta p_{\text{static}}$ , the momentum pressure drop (acceleration)  $\Delta p_{\text{mom}}$ , and the frictional pressure drop  $\Delta p_{\text{frict}}$ :

$$\Delta p_{\text{total}} = \Delta p_{\text{static}} + \Delta p_{\text{mom}} + \Delta p_{\text{frict}} \quad [13.6.1]$$

For shell-side flows, there is little known about the void fraction and since the bubbles formed would seem to have a velocity similar to that to the liquid-phase in this well-mixed type of flow, the static pressure drop is recommended to be determined using the homogeneous void fraction as:

$$\Delta p_{\text{static}} = \rho_H g H \sin \theta \quad [13.6.2]$$

where  $H$  is the vertical height and the homogeneous density  $\rho_H$  is

$$\rho_H = \rho_L (1 - \varepsilon_H) + \rho_G \varepsilon_H \quad [13.6.3]$$

The liquid and gas (or vapor) densities are  $\rho_L$  and  $\rho_G$ , respectively. The homogeneous void fraction  $\varepsilon_H$  is

$$\varepsilon_H = \frac{1}{1 + \left( \frac{u_G}{u_L} \frac{(1-x)}{x} \frac{\rho_G}{\rho_L} \right)} \quad [13.6.4]$$

where  $u_G/u_L$  is the velocity ratio, or slip ratio ( $S$ ), and is equal to 1.0 for a homogeneous flow. The momentum pressure drop is also calculated with the homogeneous void fraction as:

$$\Delta p_{\text{mom}} = \dot{m}_{\text{total}}^2 \left\{ \left[ \frac{(1-x)^2}{\rho_L(1-\varepsilon_H)} + \frac{x^2}{\rho_G \varepsilon_H} \right]_{\text{out}} - \left[ \frac{(1-x)^2}{\rho_L(1-\varepsilon_H)} + \frac{x^2}{\rho_G \varepsilon_H} \right]_{\text{in}} \right\} \quad [13.6.5]$$

The momentum pressure drop results in a decrease in the pressure of the fluid when  $x_{\text{out}} > x_{\text{in}}$  (evaporation) but a decrease in pressure when  $x_{\text{out}} < x_{\text{in}}$  (condensation). Hence, in condensation a pressure recovery occurs; however, it is common to ignore the momentum recovery in condenser design and use it as a design safety factor.

For prediction of two-phase frictional pressure drops, the method of Ishihara, Palen and Taborek (1980) is recommended. Their correlation as it applies to crossflow over a tube bundle is as follows:

$$\Delta p_{\text{frict}} = \Phi_{Ltt}^2 \Delta p_L \quad [13.6.6]$$

or

$$\Delta p_{\text{frict}} = \Phi_{Gtt}^2 \Delta p_G \quad [13.6.7]$$

where

$$\Delta p_L = 4f_L N \dot{m}_{\text{max}}^2 (1-x)^2 (1/2\rho_L) \quad [13.6.8]$$

$$\Delta p_G = 4f_G N \dot{m}_{\text{max}}^2 x^2 (1/2\rho_G) \quad [13.6.9]$$

$N$  is the number of rows crossed and  $f_L$  and  $f_G$  are single-phase friction factors for tube bundles, which can be taken from ideal tube bank correlations for the particular tube layout and Reynolds number (refer to an appropriate textbook or handbook). The maximum mass velocity of all the flow across the minimum bundle cross-section is used in the above expression, i.e. as is common for single-phase flows over tube bundles. For evaluation of these expressions, the liquid Reynolds number is calculated using the liquid fraction of the flow and the vapor Reynolds number using the vapor fraction of the flow; furthermore, [13.6.6] is used when  $Re_L > 2000$  while [13.6.7] is utilized when  $Re_L \leq 2000$ . Their database covered values of  $X_{tt} > 0.2$  and seems to work well when above this value. The liquid and vapor two-phase multipliers that go with these two expressions are

$$\Phi_{Ltt}^2 = 1 + \frac{C}{X_{tt}} + \frac{1}{X_{tt}^2}, \quad C = 8 \quad [13.6.10]$$

$$\Phi_{Gtt}^2 = 1 + CX_{tt} + X_{tt}^2, \quad C = 8 \quad [13.6.11]$$

The Martinelli parameter  $X_{tt}$  is that for both phases in turbulent, given by Eq. 3.2.21.

For flooded evaporators, the static head ( $\Delta p_{\text{static}}$ ) typically dominates at low mass velocities. Hence, the influence of the void fraction is particularly significant on the value of  $\Delta p_{\text{total}}$ , especially at low vapor

quality. For other types of heat exchangers, such as TEAM E-shells with their segmental baffles, the prediction method is much more complex since the flow in the windows is longitudinal to the tubes. Modeling of two-phase flows in such configurations is beyond the scope of the present review.

The above method has been simulated for complete evaporation (100% evaporation from inlet to outlet) of R-134a at a saturation temperature of 4.4 °C (40°F) and a mass velocity of 16 kg/m<sup>2</sup>s (11,773 lb/h ft<sup>2</sup>) by Casciaro and Thome (2001b). Their results are shown in Figure 13.14. The total pressure drop is plotted as a function of vapor quality from inlet to outlet in a tube bundle, which was composed of 8 vertical staggered tube rows with a triangular pitch of 22.22 mm (0.875 in) for a tube external diameter of 19.05 mm (0.75 in.). The combined contributions of the momentum pressure drop (M.P.D.) and the frictional pressure drop (F.P.D.) are about 20% while the static head (S.P.D.) is the dominant one.

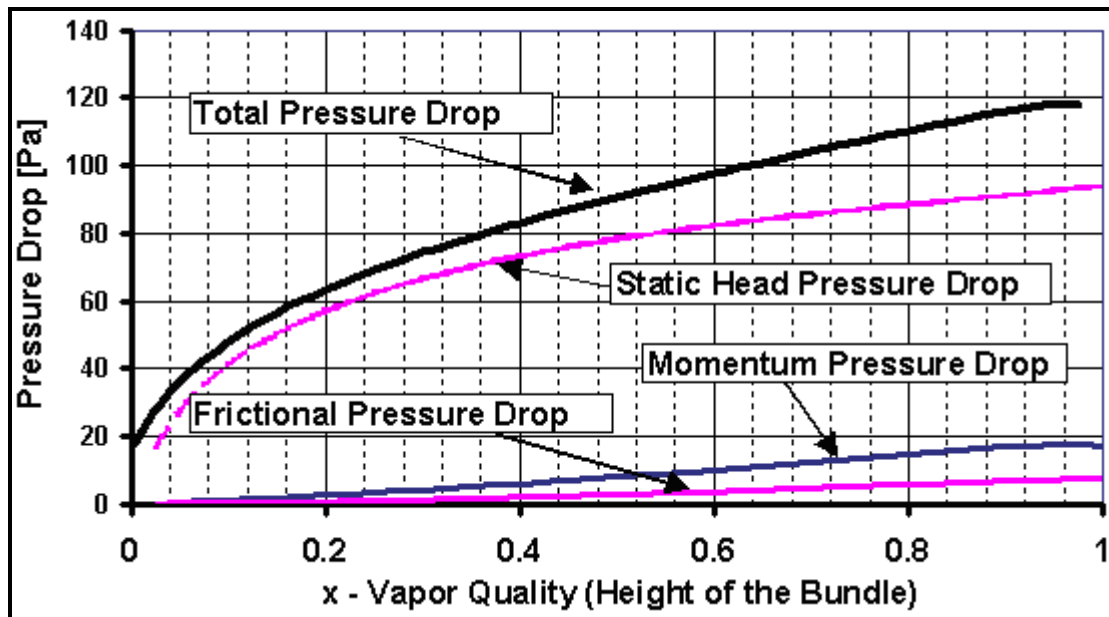


**Figure 13.14. Pressure drop contributions in an evaporating shell-side flow at a constant mass velocity for R-134a [diagram from Casciaro and Thome (2001b) and reproduced from Int. J. HVAC&R Research].**

For the same conditions as above, total pressure drops have been calculated for several mass velocities and are shown in Figure 13.15. In the range from 4 to 16 kg/m<sup>2</sup>s (2,943 – 11,773 lb/h ft<sup>2</sup>), there is not a big increase in the total pressure drop inside the tube bundle as the static pressure drop dominates. At higher mass velocities, the frictional pressure drop contribution becomes important.

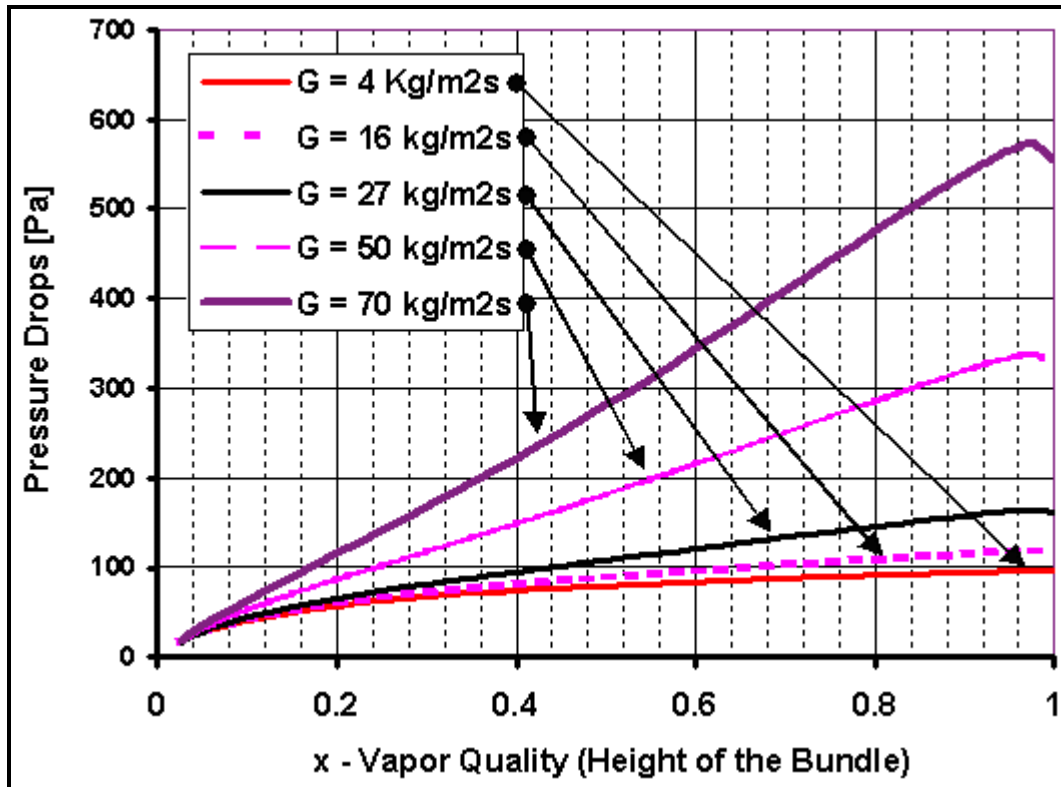


Figure 13.15. Total pressure drops as a function of shell-side mass velocity for R-134a [diagram from Casciaro and Thome (2001b) and reproduced from Int. J. HVAC&R Research].

### 13.6.2 Low finned tube and enhanced tube bundles

For prediction of two-phase pressure drops across a low finned tube bundle, the same method as recommended above is used except for the single-phase friction factors and the mass velocity. The mass velocity is calculated using the equivalent cross-flow area taking into account the area blocked by the fins. The single-phase frictional pressure drops are then calculated using the plain tube factors based on this mass velocity.

The Ishihara, Palen and Taborek (1980) method described above for *plain* tube bundles, in following the Martinelli approach, omits an explicit dependency of void fraction on the frictional pressure drop, which is likely to have an effect on the transport of momentum between and within the two phases since through the void fraction the ratio of the vapor to liquid velocity ratio is introduced. Furthermore, their database covered only conditions for  $X_{tt} > 0.2$ , which is above those typical in a flooded evaporator. Consequently, Consolini, Robinson and Thome (2006) have recently proposed a new tentative design method for *plain*, *low finned* and *enhanced* tube bundles. It covers the bundle, tube and test conditions described in Table 13.3, with liquid Reynolds numbers for R-134a ranging from about 240 to 3300, defined as:

$$Re_L = \frac{\dot{m}_{max} D}{\mu_L} \quad [13.6.12]$$

For the vapor, the equivalent maximum Reynolds number reached about 70000. This means the liquid flow changes from laminar to transition flow within the database while the vapor flow will most likely

always be turbulent. The Reynolds numbers for R-410A and R-507A are approximately similar to those for R-134a. These liquid Reynolds numbers are much lower than those in the database of Ishihara, Palen and Taborek (1980), being representative of those confronted in flooded evaporator designs.

**Table 13.3. Test conditions for method of Consolini, Robinson and Thome (2006).**

<b>Tube Type</b>	Plain	Outside Diameter = 18.87 mm (0.743 in.)
	Low-Finned	Fin Tip Diameter = 18.92 mm (0.745 in.)
		Root Diameter = 15.88 mm (0.625 in.)
		Fin Height = 1.52 mm (0.060 in.)
		Fin Density = 1024 fins/m (26 fpi)
	Turbo-BII HP	Outside Diameter = 18.69 mm (0.736 in.)
		Root Diameter = 17.48 mm (0.688 in.)
<b>Tube Pitch</b>	22.22 mm (0.875 in.)	
<b>Tube Layout</b>	Equilateral Triangle	
<b>Mass Velocity</b>	3 to 42 kg/m <sup>2</sup> s (2210-30920 lb/h ft <sup>2</sup> )	
<b>Inlet Vapor Quality</b>	0.08 to 0.50	
<b>Exit Vapor Quality</b>	0.17 to 0.99	
<b>Saturation Pressure</b>	R-134a: ~ 3.4 bar (49.8 psia)	
	R-410A: ~ 9.2 bar (133.4 psia)	
	R-507A: ~ 7.2 bar (104.4 psia)	

In general, the two-phase frictional pressure drop is not the dominant component of the total pressure drop when the flow mass velocity is very low, but its importance increases with increasing mass velocity. Based on their analysis, Consolini, Robinson and Thome (2006) recommended using the Feenstra, Weaver and Judd (2000) void fraction method for tube bundles for calculating the static and momentum pressure drops, i.e. use  $\varepsilon$  from the Feenstra-Weaver-Judd method in [13.6.2], [3.6.3] and [13.6.5] instead of  $\varepsilon_H$ . This was the method they used to extract their frictional pressure drop and momentum pressure drop values from the measured total bundle pressure drops during boiling of the three refrigerants at the test conditions in Table 13.3. A description of the Feenstra, Weaver and Judd (2006) void fraction method is available in [Chapter 17](#) in *Databook III*.

Consolini, Robinson and Thome (2006) proposed the following new two-phase frictional pressure drop method for low mass velocities:

$$\Delta p_{\text{frict}} = 4\lambda f N \dot{m}_{\max}^2 (1/2\rho) \quad [13.6.13]$$

In this expression,  $f$  refers to the fluid friction factor obtained using the appropriate single-phase tube bundle correlation, evaluated with the fluid Reynolds number defined as:

$$Re = \frac{\dot{m}_{\max} D}{\mu} \quad [13.6.14]$$

where the fluid density and viscosity are given by:

$$\rho = \rho_L(1 - \varepsilon) + \rho_G \varepsilon \quad [13.6.15]$$

$$\mu = \mu_L(1-\varepsilon) + \mu_G\varepsilon \quad [13.6.16]$$

The local void fraction  $\varepsilon$  in the bundle is calculated with the Feenstra-Weaver-Judd method. In an approach that is somewhat similar to that proposed by Müller-Steinhagen and Heck (1986) for intube two-phase flow, the value of their two-phase friction factor multiplier  $\lambda$  is obtained from the expression:

$$\lambda = \Lambda + (1 - \Lambda)(2x - 1)^2 \quad [13.6.17]$$

The value of  $\lambda$  goes to unity when the vapor quality goes to 0 and 1, i.e. the correct limits of all liquid and all vapor flow, respectively. Their experimental frictional pressure drops suggested a strong influence of the mass velocity on  $\lambda$ . Their correction factor  $\Lambda$  was thus obtained from:

$$\Lambda = \left( \frac{\dot{m}_{\max}}{400} \right)^{-1.5} \quad [13.6.18]$$

The local maximum mass velocity is input in kg/m<sup>2</sup>s to non-dimensionalize  $\Lambda$ . This expression and method are valid over the conditions cited in Table 13.3. In their work, they utilized the single-phase friction factor correlations of Žukauskas and Ulinskas (1983).

To implement their frictional pressure drop method, one must: (i) evaluate the void fraction using the Feenstra-Weaver-Judd method, (ii) calculate the fluid density and viscosity using [13.6.15] and [13.6.16], (iii) calculate the fluid Reynolds number using [13.6.14]; (iv) use an appropriate tube cross-flow friction factor correlation for single-phase flow over tube bundles to calculate  $f$ , (v) obtain  $\Lambda$  and  $\lambda$  from [13.6.18] and [13.6.17], and (vi) calculate the two-phase frictional pressure drop from [13.6.13]. In the calculation of the maximum mass velocity in this method, the outside diameter of the plain tube or the diameter over the enhancement of an enhanced boiling tube is used. For the low finned tube bundle, the cross-sectional blockage diameter of the finned tube is used (which equals  $D_{root} + 2te_f/s$  where  $D_{root}$  is the root diameter,  $t$  is the mean fin thickness,  $e_f$  is the fin height and  $s$  is the fin pitch).

Figure 13.16 depicts the predictions using their new two-phase frictional pressure drop method compared with their experimental database (showing pressure drop data from center of bundle, but similar results near the two ends) showing the ratio of the predicted total pressure drops divided by the corresponding experimental values. In predicting the total pressure drops, the static and momentum pressure drops were evaluated using the Feenstra, Weaver and Judd (2000) void fraction model, while the frictional contributions were obtained by their new method. This was implemented as a tube row by tube row stepwise calculation and then summing the incremental pressure drops. Most of the total pressure drops were predicted to within  $\pm 20\%$  of their measured values; instead, extrapolating the Ishihara, Palen and Taborek (1980) frictional pressure drop method down to these low mass velocities, most of the data were under predicted by 50% or more. However, even though the Consolini-Robinson-Thome method was proposed in a general format and hence can be applied to other tube layouts, tube diameters, tube pitches, tube types, etc., it should still be considered as a preliminary method since it was developed only for one tube layout and tube pitch for a limited range of test conditions.

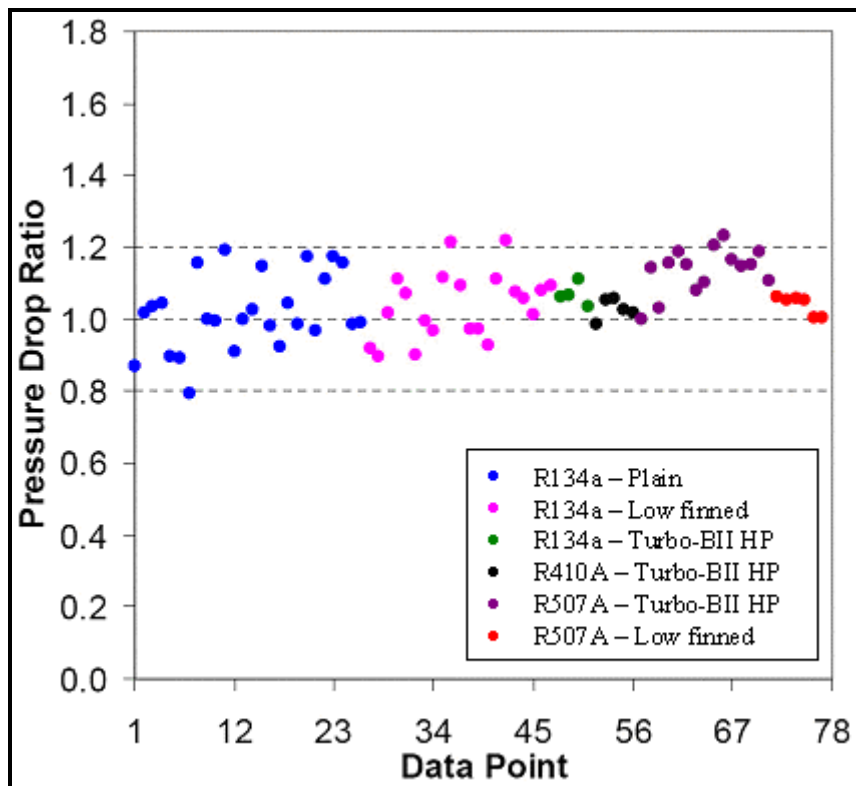


**Figure 13.16. Comparison of total bundle pressure drops measured to predictions at central location along their test bundle.**

## Chapter 14

# Falling Film Evaporation

(This chapter was updated in 2009.)

**Summary:** Horizontal, shell-side falling film evaporators have a significant potential to replace flooded evaporators in large refrigeration systems and also to be used in place of vertical tube-side falling evaporators in the petrochemical industry. The main advantages for the first application are higher heat transfer performance and reduced refrigerant charge. For petrochemical applications, shell-side falling film evaporation on horizontal tube bundles is advantageous because enhanced boiling tubes, such as the Turbo-Bii or Turbo-Biii, can be utilized and hence a much more compact design is obtained compared to vertical plain tube units. Additionally, such a unit can also take advantage of multiple tube passes for the heating fluid, further improving heat transfer performance and compactness.

In this chapter, the state-of-the-art of evaporation on horizontal single tubes and horizontal tube bundles is reviewed. Emphasis is placed on recent work on enhanced tubes. The effects of lubricating oils on thermal performance are also described and some test results presented. Numerous experimental tests have been made for plain, low fin and enhanced geometry tubes in the past decade, primarily for fluids such as water, refrigerants and ammonia. Based on these test data, enhanced tubes have demonstrated significant heat transfer augmentation for falling film evaporation on horizontal bundles with respect to plain tube units. In fact, some enhanced tubes demonstrate higher performance functioning with evaporating falling films than for their original pool boiling performance. Heat transfer design methods for horizontal units are presented and discussed as well as methods for predicting the film flow mode transitions between vertical tube rows (droplet, column and sheet) in horizontal bundles. No comprehensive design method is yet available, however. The relative benefits of horizontal falling film units compared to vertical intube units, and to a lesser extent to flooded evaporators, are addressed. Some remarks on liquid distributors and minimum overfeed rates are also presented.

### 14.1 INTRODUCTION TO FALLING FILM EVAPORATION

Falling film evaporation is a process controlled by two different heat transfer processes. First of all, thin film evaporation is a heat transfer mechanism controlled by conduction and/or convection across the film where phase change is at the interface and whose magnitude is directly related to the thickness of the film and whether or not the film is laminar or turbulent. If the heat flux is above that required for onset of nucleation (nearly always the case for enhanced boiling tubes), nucleate boiling is also present, where bubbles grow in the thin film at the heated wall (or in the re-entrant channels of an enhanced structured surface) and migrate to the interface. The film normally flows downward under the force of gravity. Therefore, except for the nucleate boiling mechanism, this process is quite similar to *falling film condensation* and in fact many analogies can be drawn between these two processes. For instance, falling film evaporation can occur in a laminar film flowing down the outside of a horizontal tube, similar to the Nusselt (1916) theory for laminar film condensation. In both cases, heat transfer is mainly dictated by film thickness. Furthermore, this film may develop surface waves or become turbulent, depending on the local film Reynolds number. On the contrary, a falling evaporating film often also has nucleate boiling occurring in it, which further increases the heat transfer coefficient. Furthermore, the formation of dry patches on the tube of an evaporating film may occur, which is very detrimental to heat transfer since heat transfer is then only to the vapor-phase on those parts of the surface.

Figure 14.1 shows a schematic illustration of falling film evaporation on a single horizontal tube, with nucleate boiling occurring in the falling film. Hence, both thin falling film evaporation and nucleate

boiling play a role in the heat transfer process. In a falling film evaporator, an array of horizontal tubes arranged in a matrix is used with the liquid falling from tube to tube.

Vertical falling film evaporators have been used for many years in the petrochemical industry. As evidence, Kern (1950) included the design method of Bays and McAdams (1937) for vertical intube units in his widely used book. In the chemical industry, vertical falling film evaporators are utilized to evaporate fluids under vacuum conditions where the liquid static head from the distillation column would otherwise create too much subcooling for efficient operation as a vertical or horizontal thermosyphon reboiler. They are also used to evaporate temperature sensitive fluids and to remove volatiles from mixtures. The falling liquid film is placed on the tube-side of these vertical, plain tube exchangers so that uniform liquid distribution to the tubes on the top tubesheet can be achieved by placing liquid distributor caps on each tube hole. The flow rate of liquid is controlled so as to inundate the tubes with liquid but rather to form a uniformly distributed falling liquid film inside each tube. Hence, it is very important to install these units with a strict tolerance to the vertical plumb line since a small inclination would result in dryout at the lower end of the tubes on the *higher* side.

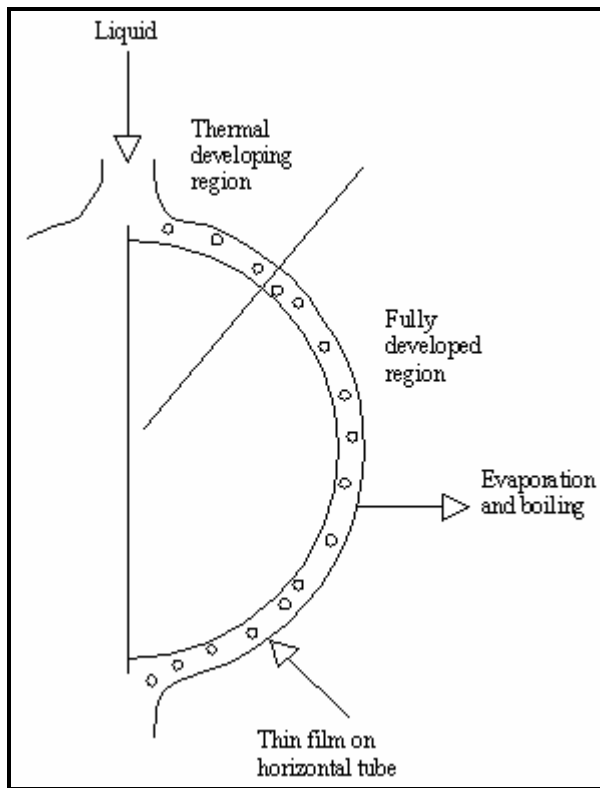


**Figure 14.1. Falling film evaporation on a heated horizontal tube with nucleate boiling.**

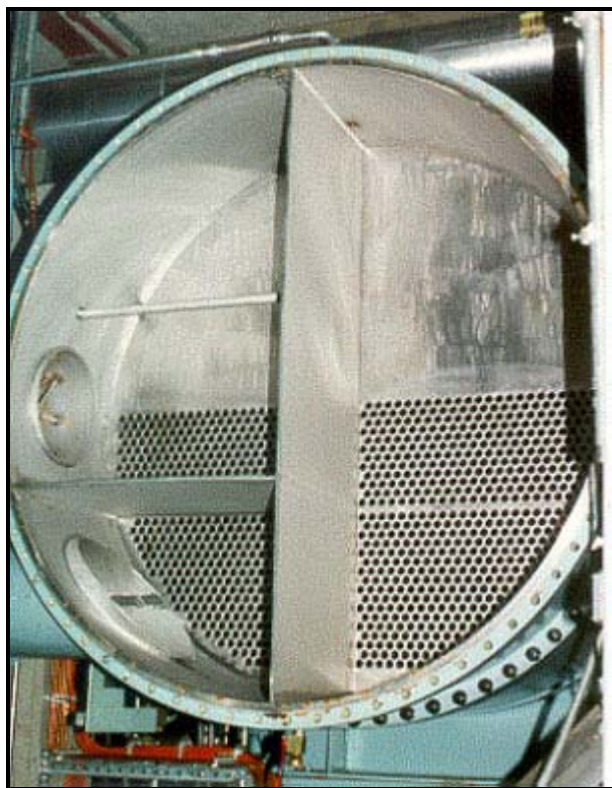


**Figure 14.2. Ammonia falling film evaporator at EPFL (view of head and tube sheet).**

Falling film evaporation has also been used on the shell-side of large heat pump systems. For example, an ammonia-cycle heat pump system at the Swiss Federal Institute of Technology in Lausanne (EPFL) takes thermal energy from Lake Geneva for central heating of the campus buildings, utilizing two 2 m diameter and 10 m long, horizontal shell-and-tube units that function with a significant amount of immiscible lubricating oil in the working fluid (refer to Figure 14.2). The desalination industry also exploits falling film evaporators, typically utilizing plain, horizontal tube bundles. This allows for closer temperature approaches and very significant energy savings. In large tonnage air-separation plants, massive vertical coiled-tube-in-shell units with shell-side falling film evaporation are used to take advantage of the close

temperature approaches that can be attained to save on energy consumption. Here the tubes are nearly horizontal in their spiral within the coil. Falling film evaporators have also been tested in Ocean Thermal Energy Conversion (OTEC) pilot plants, again to achieve a closer temperature approach between the evaporating fluid and the heating fluid, and hence attain higher cycle thermal efficiency. Falling film evaporation has also been exploited in absorbers and vapor generators of absorption heat pump systems. Falling film evaporators are also sometimes referred to as spray-film evaporators.

With respect to large refrigeration systems, one major U.S. refrigeration company brought out a complete new line of refrigeration units operating with R-134a at the beginning of 1998 based on enhanced tube falling film evaporators, achieving significant performance improvements compared to traditional enhanced tube flooded evaporators. A company in Texas has experience in using an inhouse enhanced tube for ammonia falling film evaporators since about 1992.

One of the significant advantages of falling film operation is the large reduction in liquid charge in the evaporator. Furthermore, higher heat transfer performance can also be attained. Also, for falling film evaporators applied to refrigeration units, the bottom tube rows can be purposely flooded to evaporate the access liquid reaching the bottom of the bundle and thus minimize the liquid that must be pumped back to the inlet. Horizontal falling film evaporators are to some extent similar to kettle-type steam generators in that the liquid is fed to the bundle overhead, using sprinklers or trays. The difference is that to achieve a falling film, the liquid holdup in the shell is reduced to a minimum and the liquid flow rate is limited to that required to wet the entire bundle without the formation of dry patches, rather than flooding the shell in a pool of liquid. The unevaporated liquid can be removed from the bottom of the bundle by placing a nozzle at the bottom of the shell as shown in Figure 14.3.

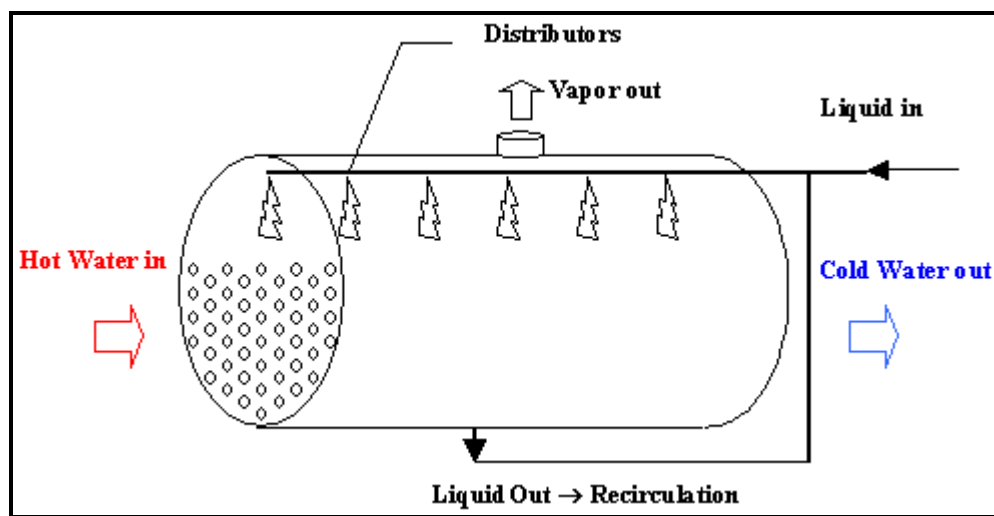


Figure 14.3. A horizontal shell-and-tube falling film evaporator.

## 14.2 AN ASSESSMENT OF ADVANTAGES/DISADVANTAGES

Before looking at the scientific details of falling film evaporation, let's first consider their overall attributes. Comparing horizontal falling film evaporators to flooded evaporators, the former have the following *potential benefits*:

- Reduction in working fluid to about 1/3 that of a comparable flooded unit;
- Higher heat transfer performance;

- More uniformity in the overall U within the bundle;
- Closer temperature approach in some cases;
- More compact evaporator design;
- Improved oil removal (oil holds up in a flooded bundle but drains to the bottom of a falling film unit).

Comparing horizontal falling film evaporators to flooded evaporators, the former also have ***potential disadvantages***:

- Less design experience with falling film units;
- Uniformity of liquid distribution onto the top tube row;
- Less tolerance for undercharging of refrigerant to the unit.

For petrochemical applications, the ***potential advantages*** of using horizontal falling film units as opposed to vertical units can be summarized as follows:

- Heat transfer coefficients on plain horizontal tubes are higher than those for vertical tubes since the heated flow length is much shorter;
- External enhancements are available for tubes in copper, copper-nickel, carbon and stainless steels, etc. for up to a 10-fold increase in boiling coefficients;
- The temperature approach between the evaporating fluid and the heating fluid can be reduced to an absolute minimum for maximum thermal efficiency;
- A horizontal bundle can have multiple tube passes of the heating fluid to significantly increase its heat transfer coefficient compared to a single shell pass in vertical units;
- Longer, smaller diameter horizontal shell-and-tube units can be designed rather than short, large diameter shells often required in vertical units to avoid dryout and flooding in the tubes;
- Two-pass floating head (or even U-tube) designs can be specified in the horizontal units, which are much more convenient to maintain and cheaper than one-pass floating heads in vertical units;
- The reduced flow length of the liquid film minimizes the liquid holdup and residence time of temperature sensitive fluids;
- A horizontal orientation reduces the height of the liquid nozzle inlet with respect to grade and hence may reduce the amount of piping and the required elevation of the distillation column with respect to the top of the exchanger.

The principal disadvantage of horizontal units is for corrosive applications where alloy tubes are needed, which would mean placing the corrosive fluid on the shell-side. However, on the shell-side an enhanced surface may be applicable, which would greatly reduce the size of the unit with the potential of being more economical. In some materials, including carbon steel and copper-nickel alloys, doubly-enhanced tubes with internal helical ribs are available for augmenting the heating fluid side of horizontal falling film evaporators while little experience is available in using internal helically ribbed tubes for falling film evaporation in vertical units.

## 14.3 THERMAL DESIGN CONSIDERATIONS

Before looking at the state-of-the-art of falling film heat transfer, let's first consider what special aspects must be taken into account when designing a horizontal falling film evaporator. Indeed, much less experience and know how is generally available for designing horizontal falling film evaporators and thus ***new challenges*** face thermal designers, such as:

- Choice of the most appropriate enhanced tube for the fluid to be handled. Note that conventional low finned tubes should *not* be used since they tend to inhibit longitudinal spreading of the liquid film along the tube. On the other hand, enhanced pool boiling tubes and also enhanced falling film condensation tubes perform very well in the falling film evaporation mode.
- Choice of the optimum tube bundle layout (number of tubes and their length, bundle width and height, tube pitch and layout and number of tube passes). Optimizing the bundle size depends significantly on all these factors.
- Selection and proper placement of the spray nozzles or sprinklers or distribution trays to achieve uniform liquid distribution on the top row of tubes in the bundle. These systems are not readily available and most likely the designer will have to come up with his own solution.
- Minimum liquid overfeed necessary for proper operation of the unit. This involves avoiding the formation of dry patches (very low thermal performance) while at the same time limiting the flow rate of the liquid on the top of the bundle. Normally, the intertube flow mode between tubes should be sheet mode or staggered column mode, with the second one requiring a lower flow rate to achieve. The minimum liquid feed rate is hence that which still gives the staggered column mode on the lowest tube row.
- Vapor escape from the bundle. The tube layout should include a consideration of how to best facilitate the escape of vapor from the bundle.
- Local modeling of the heat transfer coefficients and mass transfer effects (important if the fluid is a zeotropic mixture) plus the influence of viscous components on performance, such as a lubricating oil in a refrigeration system;
- Proper oil separation in the liquid pool beneath the bundle in refrigeration evaporators to avoid oil builds up in the unit.

These points would also be relevant if designing a horizontal falling film evaporator in place of a horizontal flooded evaporator, a kettle reboiler, or a horizontal thermosyphon reboiler for petrochemical applications. In summary, there are numerous aspects to be considered and not all of them well understood, and some of them can only be resolved with experimental tests on prototype units.

There are also various ***thermal mechanisms*** and ***flow phenomena*** specific to falling film evaporation on horizontal tube bundles that must be kept in mind during thermal design:

- prediction of liquid film flow mode transitions between tubes;
- vapor shear effects on the liquid film flow in a tube bundle;
- crossflow effects of vapor flow on film flow modes between tubes;
- nucleate boiling in the film and its onset;
- prediction of heat transfer coefficients by tube row and intertube flow regime;
- prediction of the onset of dry patch formation;
- critical heat flux for nucleate boiling in thin films;
- effect of enhancement geometry on the above processes;
- effect of lubricating oil on the above processes.

All of these have an important influence on proper operation of these units and their thermal optimization, and essentially all require further study (in particular for fluids other than water and refrigerants).

## 14.4 INTERTUBE FALLING FILM MODES

Before discussing the research work on falling film evaporation heat transfer, it is instructive to first review the literature on the prediction of intertube falling film modes for plain and enhanced tubes. Figure

14.4 shows photographs of the five flow modes. The intertube flow modes are classified from observations as follows:

- A. **Droplet mode.** The flow is in droplet mode when there is only a flow of liquid in the form of distinct droplets between the tubes.
- B. **Droplet-Columns mode.** This intermediate mode is present when at least one stable column exists between the tubes in addition to falling droplets. A column is a continuous liquid link between tubes. A column can move horizontally along the tubes but has to be continuous to define this mode.
- C. **Column mode.** This mode is simply when there is only liquid flow in columns between the tubes. At lower flow rates in this mode the columns tend to be *inline* while at higher flow rates they are *staggered* from one tube to the next.
- D. **Column-Sheet mode.** In this intermediate mode, both columns and a liquid sheet are simultaneously flowing between the tubes at different locations along the tubes. It is reached when at least one small sheet is visible. This small sheet is formed by the merging of two nearby columns and typically has a triangular profile.
- E. **Sheet mode.** This mode is when the fluid flows uniformly between the tubes as a continuous film or sheet.

The flow progresses from mode A to mode E as the mass flow rate is increased. There is normally some hysteresis in these transitions when observing them for increasing and decreasing flow rates. For practical purposes, it is probably best to ignore this secondary effect on thermal design.

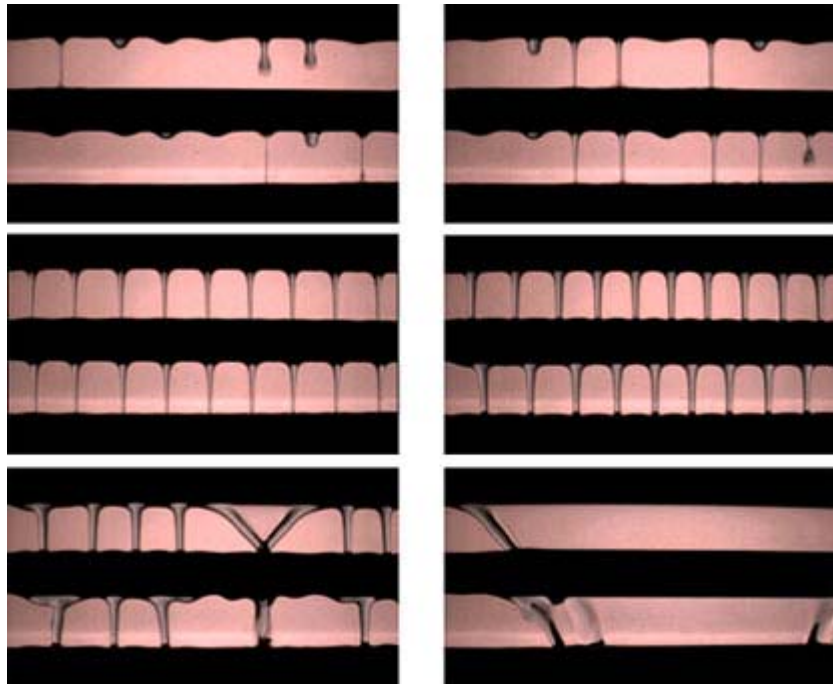


**Figure 14.4. Photographs of flow modes on plain tubes (from left to right, top to bottom): droplet, droplet-column, column (inline), column (staggered), column-sheet, and sheet.**

Despite numerous observations of condensation and falling film evaporation on rows of tubes, apparently no generalized flow mode map is currently available, although Honda et al. (1987) have made some transition expressions for individual fluids condensing on low finned tubes. These processes however are similar to adiabatic falling films of liquid fed onto the top of a tube array, which has been studied extensively by Hu and Jacobi (1996a) for a variety of fluids, tube diameters, tube pitches and flow rates and with/without cocurrent gas flow. Based on their observations, they proposed a flow mode map with coordinates of film Reynolds number versus modified Galileo number,  $Re_{\Gamma}$  vs.  $Ga_L$ . The mixed mode zones of column-sheet and droplet-column are transition zones between the three dominant modes of sheet, column and droplet in which both modes are present. Their four flow transition expressions, between these five zones, are given below (valid for passing through the transitions in either direction and hence the symbol  $\Leftrightarrow$ ):

$$\text{Droplet} \Leftrightarrow \text{Droplet-Column: } Re_{\Gamma} = 0.074 Ga_L^{0.302} \quad [14.4.1]$$

$$\text{Droplet-Column} \Leftrightarrow \text{Column: } Re_{\Gamma} = 0.096 Ga_L^{0.301} \quad [14.4.2]$$

$$\text{Column} \Leftrightarrow \text{Column-Sheet: } Re_{\Gamma} = 1.414 Ga_L^{0.233} \quad [14.4.3]$$

$$\text{Column-Sheet} \Leftrightarrow \text{Sheet: } Re_{\Gamma} = 1.448 Ga_L^{0.236} \quad [14.4.4]$$

The modified Galileo number  $Ga_L$  is defined as

$$Ga_L = \frac{\rho_L \sigma^3}{\mu_L^4 g} \quad [14.4.5]$$

The film Reynolds number  $Re_{\Gamma}$  is defined in these transition equations as

$$Re_{\Gamma} = \frac{4\Gamma_L}{\mu_L} \quad [14.4.6]$$

where  $\Gamma_L$  is the flow rate of liquid on one side of the tube per unit length of tube in kg/ms, so that the total flow rate on both sides of the tube is  $2\Gamma_L$ . This definition is consistent with  $Re_{\Gamma}$  for a vertical plate where the flow rate in the film is  $\Gamma_L$ . Their map is applicable to plain tubes for air velocities less than 15 m/s. The modified Galileo number is sometimes referred to as the “film number” and is in fact the inverse of the Kapitza number,  $Ka$ , which is defined as

$$Ka = \frac{g\mu_L^4}{\rho_L \sigma^3} \quad [14.4.7]$$

Figure 14.5 of Roques, Dupont and Thome (2002) shows their flow mode transition map for an array of smooth 19.05 mm tubes obtained with observations for water, glycol and a 50%/50% water/glycol mixture. Their transition curves were quite similar to those reported earlier by Hu and Jacobi (1996a).

Figure 14.6 of Roques, Dupont and Thome (2002) gives their comparison of the transition boundaries obtained for the Turbo-Bii tube versus a plain, smooth tube of the same size. The primary difference is an enlargement of the zone in which column mode exists; that is, the column to column-sheet transition

occurs at higher film Reynolds numbers while the column to droplet-column transition occurs at lower  $Re_f$ . In practice, this means that an evaporating falling film will tend to stay in the advantageous column mode down to lower overfeed rates on Turbo-Bii tubes than on an array of plain tubes.

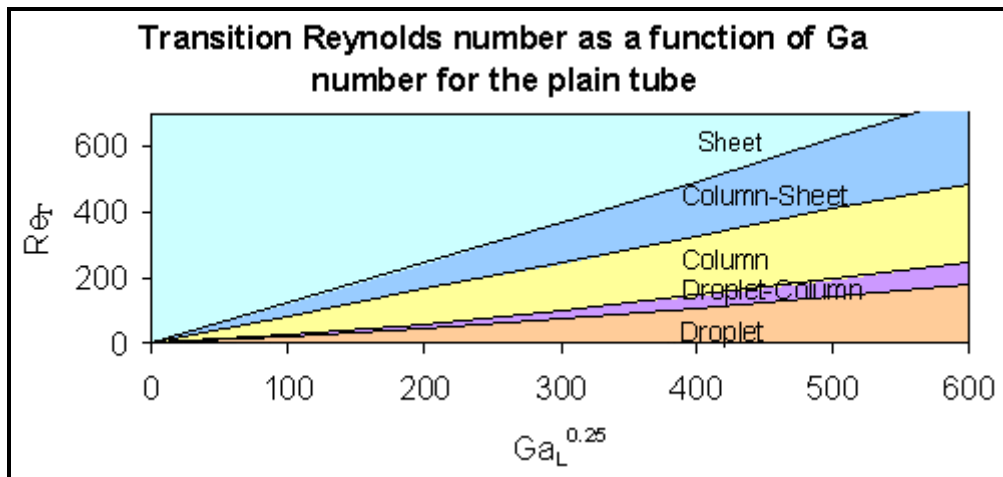


Figure 14.5. Flow mode transition map for plain tubes.

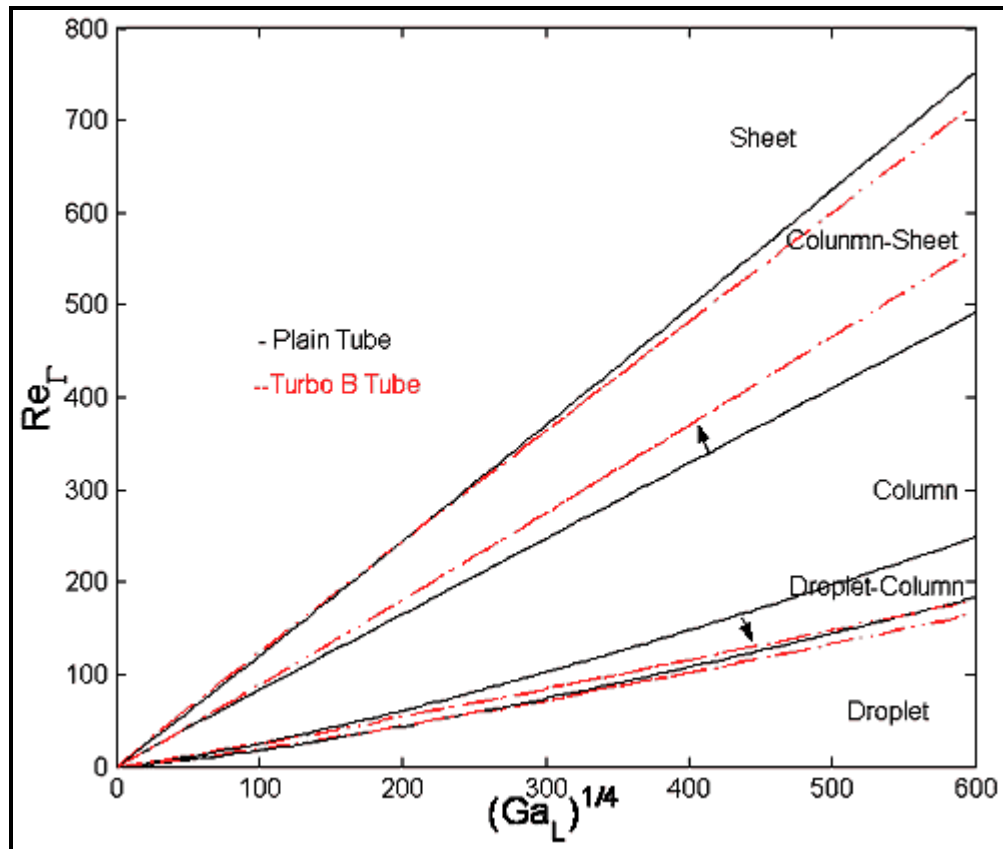
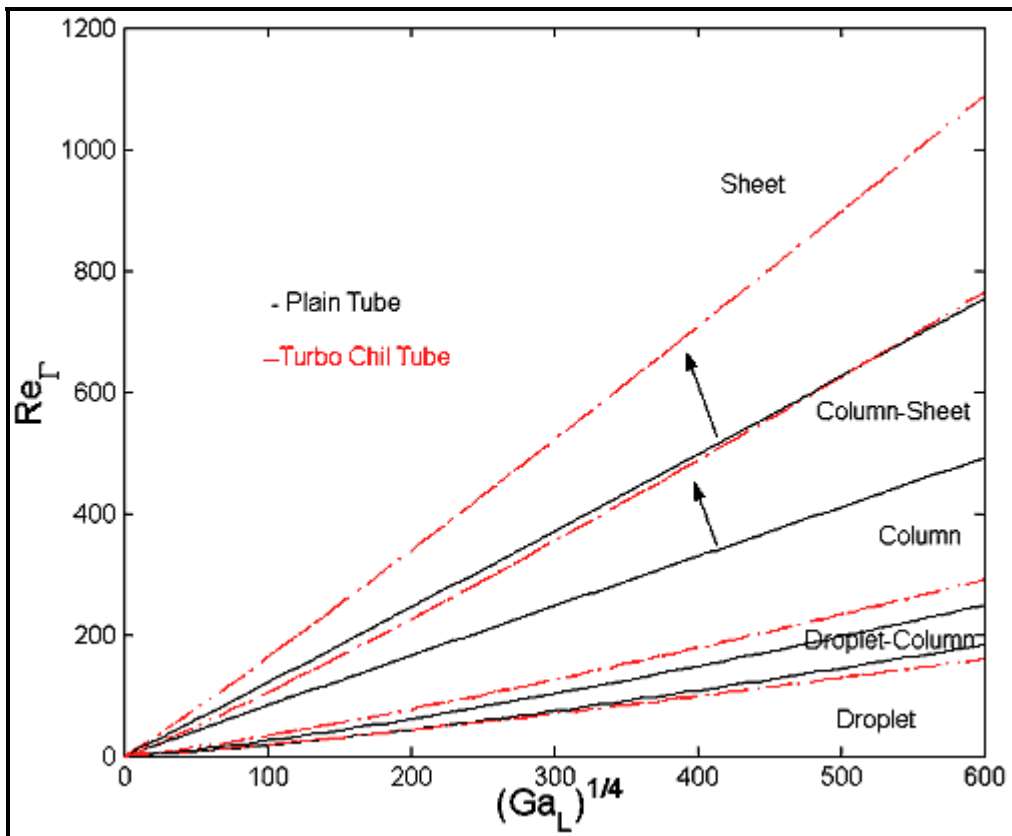


Figure 14.6. Flow mode transition map for the Wolverine Turbo-Bii enhanced boiling tube.

Figure 14.7 of Roques, Dupont and Thome (2002) shows a similar flow mode transition map for the 26 fpi Wolverine Turbo-Chil low finned tube versus a plain, smooth tube of the same size (note that low finned tubes are *not* recommended for falling film evaporation, however). Again, the primary difference is an enlargement of the zone in which column mode exists; that is, the column to column-sheet transition occurs at much higher film Reynolds numbers while the column to droplet-column transition occurs at somewhat lower  $Re_f$ . Roques and Thome (2002) have also presented transition expressions for 19 fpi and 40 fpi low finned tubes.



**Figure 14.7. Flow mode transition map for the Wolverine Turbo-Chil low fin tube.**

Since enhanced condensation tubes have been found experimentally to have significant performances when used for falling film evaporation, Figure 14.8 of Roques (2004) presents a flow mode transition map for the Wolverine Turbo-CSL tube. The primary difference relative to the plain tube array is an enlargement of the zone in which column mode exists; that is, the column to column-sheet transition occurs at much higher film Reynolds numbers while the column to droplet-column transition occurs at much lower  $Re_f$ .

The transition flow measurements and observations of Roques, Dupont and Thome (2002) have been correlated with the following expression

$$Re_f = a Ga_L^b \quad [14.4.8]$$

The values of the coefficients  $a$  and  $b$  are listed in Table 14.1 for various tubes taken from the Thome and coworkers tests. The values can be compared to those of Hu and Jacobi (1996a) for plain tubes, which

give rather similar transition values considering the difficult in determining exactly where the transition occurs because of the subjectivity of visual observations.

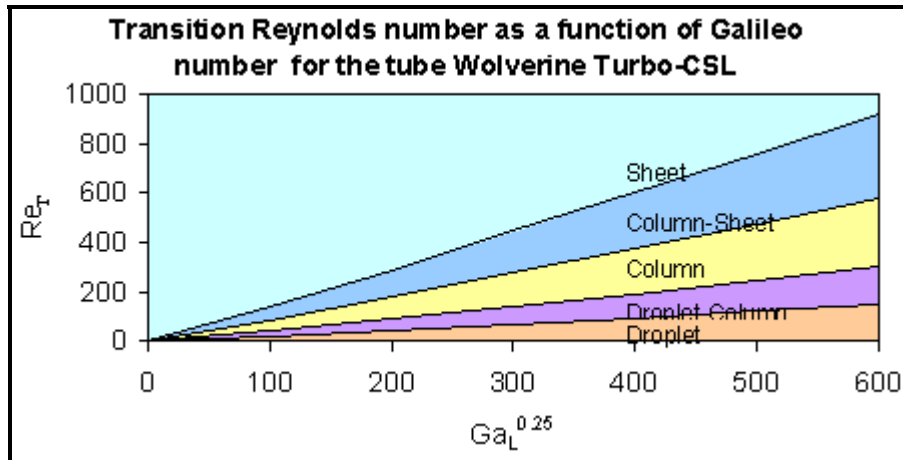


**Figure 14.8. Flow mode transition map for the Wolverine Turbo-CSL enhanced condensing tube.**

Earlier, Honda, Nozu and Takeda (1987) presented the transition expressions for their observations on a 27 fpi low finned tube of 15.9 mm (5/8 in.) diameter for R-113, methanol and n-propanol. Note that low finned tubes are not appropriate for falling film evaporators and this information is only given for comparison purposes to plain and other enhanced tubes. They gave transitions from droplet to column mode (ignoring the intermediate mode of droplet-column) and from column to column-sheet as follows:

$$\text{Droplet} \Leftrightarrow \text{Column} \text{ (for n-propanol)}: \quad Re_T = 0.244 Ga_L^{0.25} \quad [14.4.9]$$

$$\text{Droplet} \Leftrightarrow \text{Column} \text{ (for R-113)}: \quad Re_T = 0.52 Ga_L^{0.25} \quad [14.4.10]$$

$$\text{Column} \Leftrightarrow \text{Column-Sheet} \text{ (all 3 liquids)}: \quad Re_T = 1.28 Ga_L^{0.25} \quad [14.4.11]$$

$$\text{Column-Sheet} \Leftrightarrow \text{Sheet} \text{ (all 3 liquids)}: \quad Re_T = (1.48 \text{ to } 1.88) Ga_L^{0.236} \quad [14.4.12]$$

The last two expressions predict transitions similar to those found by Roques, Dupont and Thome (2002) for their 26 fpi low finned tube.

Hu and Jacobi (1998) have studied the horizontal distance between droplets and between columns in those respective flow modes, looking at the effect of intertube spacing of the tubes. More recently, Wei and Jacobi (2002) have investigated the effects of vapor-shear, tube diameter, tube spacing and bundle depth of the flow mode transitions. They observed that upflow of gas counter-current to the liquid flow tends to destabilize the sheet and column modes. Tube spacing effects become important to mode transition thresholds, especially for  $(S-D)/Ca < 6$  where  $S$  is the vertical tube pitch,  $D$  is the tube diameter and  $Ca$  is the capillary constant

$$Ca = \left( \frac{\sigma}{g\rho_L} \right)^{1/2} \quad [14.4.13]$$

Regarding tube row effects, they observed that the flow generally became less stable farther down into the bundle from the top. This tended to eliminate the hysteresis effect on the transitions but also raised some of the transition film Reynolds numbers to higher values.

**Table 14.1. Coefficients for flow mode transitions for a selection of tubes.**

Tube	Transition	a	b
<b>Plain</b>	Droplet to/from Droplet-Columns	0.0417	0.3278
	Droplet-Columns to/from Columns	0.0683	0.3204
	Columns to/from Columns-Sheet	0.8553	0.2483
	Columns-Sheet to/from Sheet	1.068	0.2563
<b>Low Fin (19fpi)</b>	Droplet to/from Droplet-Columns	0.0827	0.3048
	Droplet-Columns to/from Columns	0.1217	0.3041
	Columns to/from Columns-Sheet	0.8573	0.2589
	Columns-Sheet to/from Sheet	1.3557	0.2532
<b>Low Fin (26fpi)</b>	Droplet to/from Droplet-Columns	0.0743	0.3000
	Droplet-Columns to/from Columns	0.1263	0.3025
	Columns to/from Columns-Sheet	0.6172	0.2783
	Columns-Sheet to/from Sheet	1.2015	0.2661
<b>Low Fin (40fpi)</b>	Droplet to/from Droplet-Columns	0.0622	0.3087
	Droplet-Columns to/from Columns	0.1148	0.2947
	Columns to/from Columns-Sheet	0.7198	0.2553
	Columns-Sheet to/from Sheet	0.9414	0.2662
<b>Turbo-BII HP</b>	Droplet to/from Droplet-Columns	0.0754	0.3007
	Droplet-Columns to/from Columns	0.1594	0.2748
	Columns to/from Columns-Sheet	0.7591	0.2482
	Columns-Sheet to/from Sheet	1.3487	0.2453
<b>Thermo-excel-E</b>	Droplet to/from Droplet-Columns	0.0975	0.2514
	Droplet-Columns to/from Columns	0.2293	0.2451
	Columns to/from Columns-Sheet	0.8146	0.2602
	Columns-Sheet to/from Sheet	1.5859	0.2561
<b>Turbo-CSL</b>	Droplet to/from Droplet-Columns	0.0690	0.3010
	Droplet-Columns to/from Columns	0.2380	0.2799
	Columns to/from Columns-Sheet	0.6686	0.2642
	Columns-Sheet to/from Sheet	1.1310	0.2620

## 14.5 HIGHLIGHTS OF HEAT TRANSFER STUDIES PRIOR TO 1994

No comprehensive review on falling film evaporation has appeared in recent years nor has any review provided a complete summary of the various design methods that have been proposed. In view of this fact, first the important publications prior to 1994 will be surveyed, where most of the research was on plain tubes and for fluids such as water or since retired refrigerants like R-11. After this, a more comprehensive review of publications since 1994 will be given. At the same time, a selection of the best design methods for horizontal units will also be presented, which at present are limited to pure fluids and thus require eventual extension to mixtures. Regarding prior reviews, Chyu and Bergles (1987) presented a well-written discussion on the effects of film flow rate, liquid feed height, and wall superheat on evaporation of falling films on plain tubes. Cerza (1992) summarized the nucleate boiling mechanisms occurring in thin falling films, paying particular attention to nucleation and rewetting of dry patches. Also, Thome (1999) presented an earlier version of the present review.

In a landmark paper of those presented before 1994, Chun and Seban (1971) reported falling film heat transfer coefficients for water on a vertical plain tube, in both laminar flow and turbulent flow regimes. In the laminar regime, they noted that heat is transferred by conduction across the falling liquid film according to the expression

$$h_{LG} \frac{d\Gamma_L}{dz} = k_L \frac{T_w - T_{sat}}{\delta} \quad [14.5.1]$$

This is the same assumption assumed by Nusselt (1916) in his classic theory on falling film condensation. The mass flow rate per unit width of the wall  $\Gamma_L$  in the above expression is modeled to be

$$\Gamma_L = \frac{g\rho_L^2 \delta^3}{3\mu_L} \quad [14.5.2]$$

Also relevant, Kapitza [cf. Dukler (1960)] predicted the formation of capillary waves on the interface of a falling laminar film when the film Reynolds number exceeded some critical value of the Kapitza number,  $K_a$ . Other criteria for the onset of interfacial waves on falling condensing films are presented in Chapter 7.

For film flow with interfacial waves, Chun and Seban (1971) estimated that the reduction in the average film thickness by the ripples was responsible for the increase in heat transfer they observed experimentally. They then presented the following empirical equations for predicting laminar and turbulent heat transfer in evaporating films on vertical tubes without nucleate boiling, respectively, in the fully developed region:

$$\alpha_{\Gamma, lam} = 0.821 \left( \frac{\mu_L^2}{g\rho_L^2 k_L^3} \right)^{-0.333} Re_\Gamma^{-0.22} \quad [14.5.3]$$

$$\alpha_{\Gamma, turb} = 0.00381 \left( \frac{\mu_L^2}{g\rho_L^2 k_L^3} \right)^{-0.333} Re_\Gamma^{0.4} \left( \frac{v_L}{a_L} \right)^{0.65} \quad [14.5.4]$$

where the film Reynolds number is

$$Re_F = \frac{4\Gamma_L}{\mu_L} \quad [14.5.5]$$

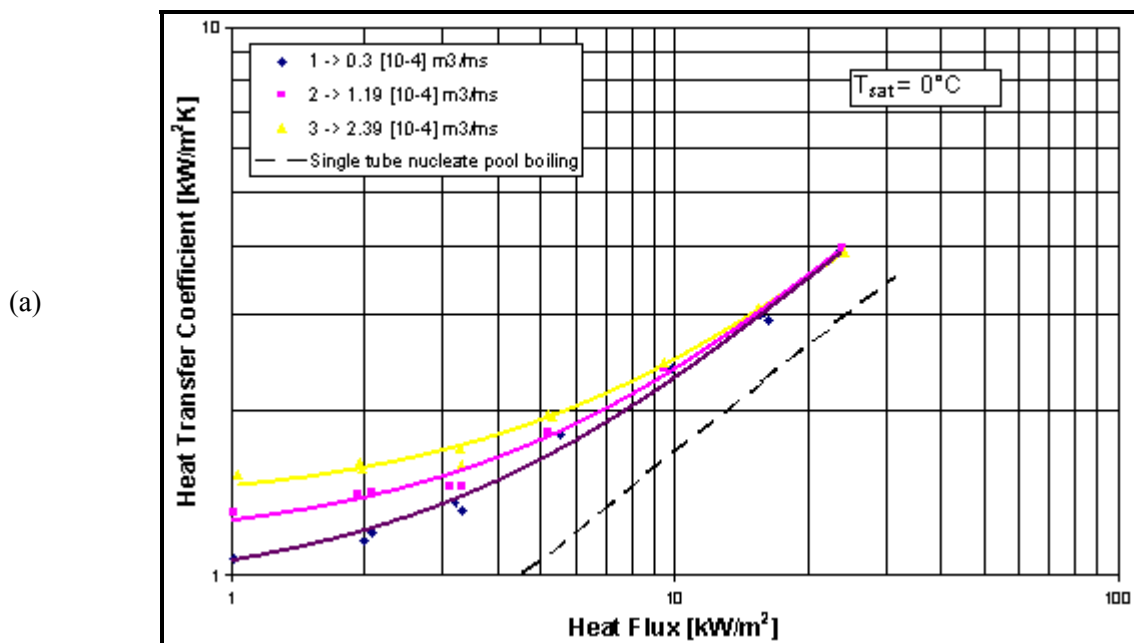
Chun and Seban (1971) further suggested that the Weber number is a good parameter for predicting the transition from laminar to turbulent flow in falling films, defined as

$$We = \left( \frac{\rho_L u_L^2}{\sigma} \right)^{1/2} \quad [14.5.6]$$

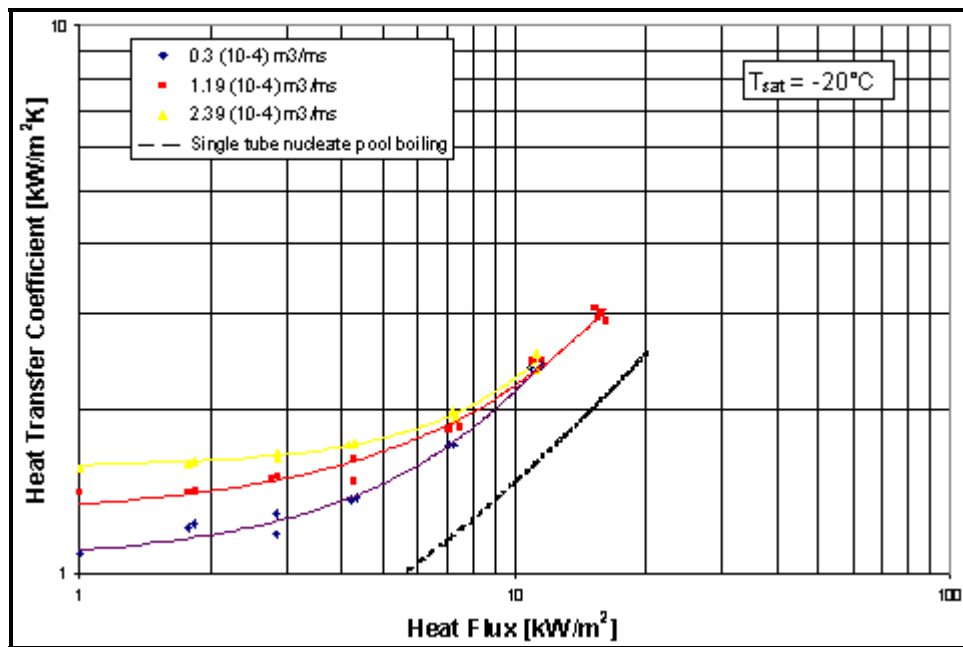
They proposed a transition criterion with  $We = 1$ . Fletcher et al. (1974) later experimentally studied falling film evaporation also for water, but on a horizontal plain tube using a liquid distributor system along its axis.

In one of the most comprehensive falling film evaporation studies to date on horizontal, plain tube bundles, Danilova et al. (1976) tested R-12, R-22 and R-113 on simulated bundles up to 40 rows deep. They tested 330 mm long, electrically heated stainless steel tubes of 18 mm O.D. with a 0.3 mm wall and nominal surface roughness of 1 micron. Their tubes were arranged in a tube bundle, utilizing the top tube for liquid distribution onto the lower tubes. Staggered tube bundles from one to three rows wide and six tube rows deep were tested with vertical tube pitch to tube diameter ratios of 1.1, 1.3, 1.5 and 2.2. Rather than reporting film mass flow rate per unit length of one side of the tube in  $\text{kg}/(\text{m s})$ , i.e.  $\Gamma_L$ , they have reported their data as volumetric flow rates per unit length of tube in  $\text{m}^3/(\text{m s})$ . Figure 14.9 shows some of their results for R-22 in which three distinct heat transfer zones are evident:

1. In the film evaporation zone, the heat transfer coefficient is controlled by the liquid volumetric flow rate and is almost independent of heat flux  $q$  and saturation temperature  $T_{sat}$ ;
2. In the developed boiling zone, the heat transfer coefficient is controlled by  $q$  and  $T_{sat}$  but is nearly independent of liquid volumetric flow rate;
3. In the transition zone between the above two regimes, the heat transfer coefficient is affected by all three factors.



(b)



(c)

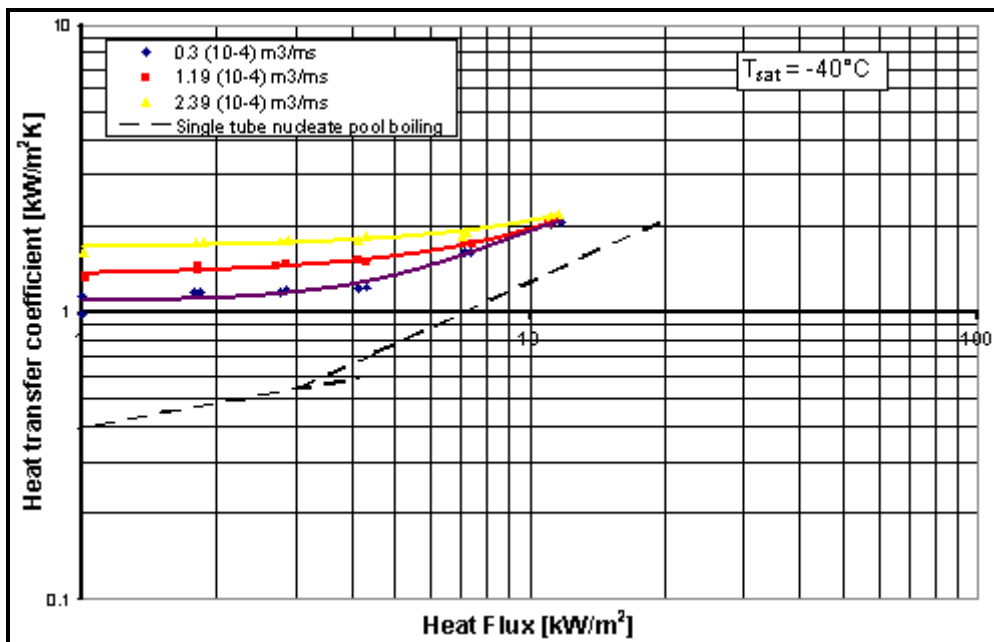


**Figure 14.9.** Average heat transfer coefficients for R-22 for a selection of film flow rates compared to nucleate pool boiling from Danilova et al. (1976). Legend:  $T_{sat}$  for (a)  $0^{\circ}\text{C}$ , (b)  $-20^{\circ}\text{C}$  and (c)  $-40^{\circ}\text{C}$  while volumetric flow rates per unit length were (1)  $0.3 \times 10^{-4}$  m<sup>3</sup>/(m s), (2)  $1.19 \times 10^{-4}$  m<sup>3</sup>/(m s) and (3)  $2.39 \times 10^{-4}$  m<sup>3</sup>/(m s). The dashed lines depict single-tube nucleate pool boiling curves.

Based on these test results, they proposed an empirical correlation for film vaporization as a function of liquid film Reynolds number, liquid Prandtl number and the ratio of vertical tube pitch to tube diameter (S/D) and a second one for nucleate boiling. For film evaporation, all their data were correlated as a film Nusselt number:

$$Nu_{\Gamma} = 0.03 Re_{\Gamma}^{0.22} Re_{*\Gamma}^{0.04} Pr_L^{0.32} \left( \frac{S}{D} \right) \quad [14.5.7]$$

For nucleate boiling, the corresponding nucleate boiling Nusselt number is:

$$Nu_{nb} = 0.00132 Re_{nb}^{0.63} K_p^{0.72} Pr_L^{0.48} \quad [14.5.8]$$

Equation [14.5.5] is used for the film Reynolds number and  $Pr_L$  is the liquid Prandtl number. The dimensionless numbers they used are defined below:

$$Nu_{\Gamma} = \frac{\alpha_{\Gamma}}{k_L} \left( \frac{\mu_L^2}{g\rho_L^2} \right)^{0.333} \quad [14.5.9]$$

$$Nu_{nb} = \frac{\alpha_{\Gamma}}{k_L} \left( \frac{\sigma}{g(\rho_L - \rho_G)} \right)^{0.5} \quad [14.5.10]$$

$$Re_{*\Gamma} = \frac{q\rho_L}{h_{LG}\rho_G\mu_L} \left( \frac{\mu_L^2}{g\rho_L^2} \right)^{0.333} \quad [14.5.11]$$

$$Re_{nb} = \frac{q\rho_L}{h_{LG}\rho_G\mu_L} \left( \frac{\sigma}{g(\rho_L - \rho_G)} \right)^{0.5} \quad [14.5.12]$$

$$K_p = \frac{p_{sat}}{\sigma} \left( \frac{\sigma}{g(\rho_L - \rho_G)} \right)^{0.5} \quad [14.5.13]$$

Choosing the larger of these two values as the correct one, the maximum experimental deviation of their test points from these equations did not exceed  $\pm 15\%$ .

Lorenz and Yung (1978, 1979) developed a combined model for film evaporation and nucleate boiling in liquid films flowing over a single, horizontal plain tube of circumferential length  $L$ , where  $L$  was set equal to the entire perimeter, i.e.  $L = \pi D$ . They considered three heating modes: that of a subcooled film over length  $L_{dev}$ , evaporation of a saturated film over the remaining length and nucleate boiling in the film over the entire perimeter. The mean heat transfer coefficient  $\alpha_{mean}$  on the tube perimeter is the sum of these three individual contributions:

$$\alpha_{mean} = \alpha_{nb} + \alpha_{\Gamma,dev} \left( \frac{L_{dev}}{L} \right) + \alpha_{\Gamma} \left( 1 - \frac{L_{dev}}{L} \right) \quad [14.5.14]$$

where  $\alpha_{nb}$  is the nucleate boiling coefficient over the entire length  $L$ ,  $\alpha_{\Gamma,dev}$  is the convective film heat transfer in the thermally developing region of length  $L_{dev}$ , and  $\alpha_{\Gamma}$  is the convective film coefficient in the fully developed region given by either Equation [14.5.3] or [14.5.4] of Chun and Seban (1971) for vertical tubes. The developing region convective film heat transfer coefficient is for the initial subcooled zone

where the film is heated up to the saturation temperature of the liquid, and was derived based on simple heat conduction across the liquid film, such that

$$\alpha_{\Gamma,\text{dev}} = 0.375 c_{pL} \left( \frac{\Gamma_L}{L_{\text{dev}}} \right) \quad [14.5.15]$$

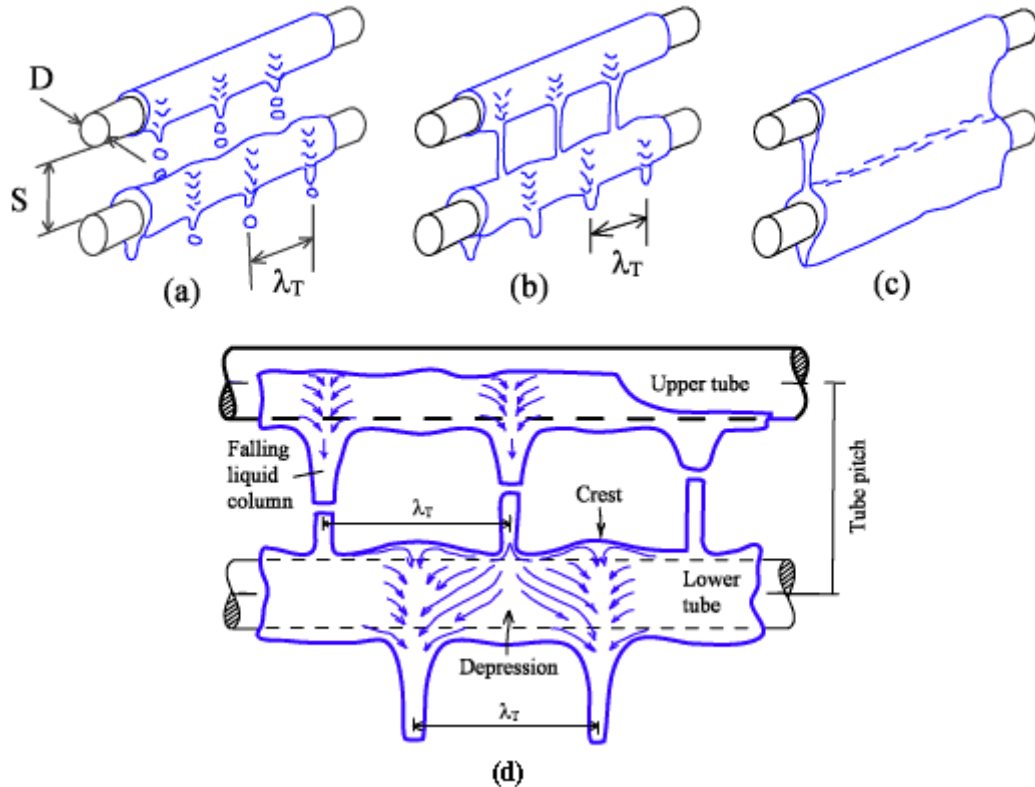


**Figure 14.10. Liquid falling film in (a) droplet mode, (b) in stable column mode, (c) in sheet mode and (d) the Taylor instability of vapor/liquid interface beneath a horizontal tube in staggered column mode.**

Continuing this work, Yung et al. (1980) investigated the effects of vapor/liquid interactions on the mode of liquid film flow off the bottom of horizontal tubes plus that of liquid entrainment caused by vapor crossflow in plain horizontal tube bundles. Notably, they presented a criterion for the transition from the liquid droplet mode to the column flow mode from one tube row to the next, similar to process occurring during intertube drainage of condensation on vertical tube rows, which is illustrated in Figure 14.10. They observed that the Taylor instability wave most likely to occur on the liquid interface underneath the tube has a wavelength  $\lambda_T$ :

$$\lambda_T = 2\pi \left( \frac{n\sigma}{g\rho_L} \right)^{1/2} \quad [14.5.16]$$

The constant  $n$  in this expression is equal to 3 if the liquid film is relatively thick (thick film Taylor wavelength) or is equal to 2 if the liquid film is relatively thin (thin film Taylor wavelength). The value of 2 gave good agreement to their observations. For predicting the transition to column flow mode in Figure

14.10(b) from droplet mode in Figure 14.10(a), they predicted that this occurred at film flow rate per unit length of tube equal to:

$$\Gamma_{L,trans} = \left( \frac{0.81\pi\rho_L d_p^3}{6\lambda_T} \right) \left( \frac{2\pi\sigma}{\rho_L \lambda_T^3} \right)^{1/2} \quad [14.5.17]$$

The primary droplet diameter  $d_p$  is given by the following equation where the best constant found to match their observations was 3.0:

$$d_p = 3 \left( \frac{\sigma}{g\rho_L} \right)^{1/2} \quad [14.5.18]$$

Consequently, there was now a second method for predicting local heat transfer coefficients on horizontal tubes and a criterion for predicting one of the intertube film flow mode transitions.

To account for the effect of liquid feed height above a horizontal tube on falling film evaporation, Owens (1978) proposed several correlations based on his data and that of another two studies for evaporating falling films without nucleate boiling. For laminar films, he proposed:

$$Nu_{\Gamma,lam} = 2.2 \left( \frac{H}{D} \right)^{0.1} Re_{\Gamma}^{1/3} \quad [14.5.19]$$

For turbulent films, he proposed:

$$Nu_{\Gamma,turb} = 0.185 \left( \frac{H}{D} \right)^{0.1} Re_{\Gamma}^{1/2} \quad [14.5.20]$$

where  $H$  is the liquid feed height above the top of the tube and  $D$  is the tube diameter. The transition between these two flow regimes was predicted to occur when:

$$Re_{\Gamma,trans} = 1680 Pr_L^{0.5} \quad [14.5.21]$$

where the film Reynolds number  $Re_{\Gamma}$  as defined in Equation [14.5.5]. This criterion is surprisingly a function of the liquid Prandtl number.

Nakayama et al. (1982) made a comparative experimental study, measuring falling film heat transfer coefficients for a vertical plate with a Hitachi Thermoexcel-E type of enhanced pool boiling surface, a vertical surface with vertically cut grooves and a vertical surface with horizontally cut grooves, all tested with R-11. The Thermoexcel-E type of surface promoted nucleate boiling on the plate, giving the best heat transfer performance, whose heat transfer coefficients in the falling film mode were larger than those for the pool boiling conditions. The horizontal grooves on the third plate promoted liquid holdup on the plate, i.e. thicker films, and hence yielded lower thermal performance than the plate with vertical grooves.

Chyu et al. (1982) measured falling film heat transfer coefficients for water on a horizontal plain tube, a UOP High Flux porous coated tube and a Wieland Gewa-T tube. The High Flux tube has a thin porous metallic coating to promote nucleate boiling while the Gewa-T geometry has characteristic T-shaped fins.

Both greatly outperformed the plain tube. Chyu and Bergles (1985a, 1987) later presented a method for predicting falling film coefficients on a plain, horizontal tube by zone. As illustrated in Figure 14.11, the perimeter of the tube was divided up into the following regions: stagnation flow at the top, an impingement flow region near the top, a thermally developing flow region, and finally a fully developed flow region around the rest of the tube. Their method is not presented here because it involves a numerical solution. In addition, Chyu and Bergles (1985b, 1989) reported falling film coefficients for water for four tubes: a Wieland Gewa-T tube, a Hitachi Thermoexcel-E tube, a UOP High Flux tube and a plain tube. The optimum type of geometry was found to depend on whether there was nucleate boiling in the film (favoring the High Flux and Thermoexcel-E geometries) or only film evaporation (which favored the Gewa-T's fins for thinning the liquid film).

The influence of intertube spacing and flow rate on falling film heat transfer on horizontal plain tube bundles for subcooled liquid without evaporation was investigated by Mitrovic (1986) for iso-propanol and water. Figure 14.10 depicts the flow pattern modes between two adjacent horizontal tubes in a vertical row that they observed: discrete droplet flow, liquid column flow and laminar or turbulent sheet flow. Figure 14.10(d) shows the flow structure for stationary liquid columns with flow from the top to bottom tube. A crest in the liquid film is also formed between the columns at the top of the tube when the columns are staggered as shown. Mitrovic measured the distance between the columns from still photographs, obtaining a value of 22 mm for water at 25°C and 13.5 mm for iso-propanol at 21.5°C, noting that these values fell between the critical wavelength  $\lambda_{\text{crit}}$  and the most dangerous wavelength  $\lambda_d$  calculated according to the following equations of Lienhard and Wong (1964):

$$\lambda_{\text{crit}} = 2\pi \left( \frac{g(\rho_L - \rho_G)}{\sigma} + \frac{2}{D^2} \right)^{-1/2} \quad [14.5.22]$$

$$\lambda_d = \sqrt{3} \lambda_{\text{crit}} \quad [14.5.23]$$

Similar values of wavelengths between liquid columns were also reported by Yung et al. (1980). For subcooled, non-evaporating liquid flows, Mitrovic proposed the following correlation for heat transfer where the Nusselt number of the liquid film  $Nu_\Gamma$  is defined as in Equation [14.5.9] while the film Reynolds number is defined in the standard way by Equation [14.5.5] rather than using Mitrovic's definition of  $\Gamma_L/\mu_L$ :

$$Nu_\Gamma = 0.0175 \left( \frac{Re_\Gamma}{4} \right)^{0.349} Pr_L^{0.5} \Omega \quad [14.5.24]$$

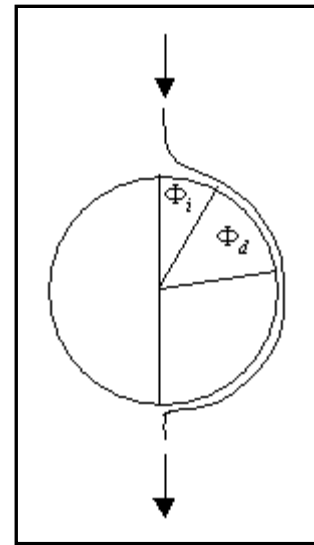


**Figure 14.11. Model of Chyu and Bergles (1985a) for falling film evaporation on a horizontal tube.**

His tube spacing correction factor  $\Omega$  is based on the vertical tube pitch to tube diameter ratio (S/D) as:

$$\Omega = \frac{(S/D)^{0.158}}{1 + \exp\left[-0.008\left(\frac{Re_{\Gamma}}{4}\right)^{1.32}\right]} \quad [14.5.25]$$

Parken et al. (1990) measured local coefficients for both the nucleate boiling and film evaporation regimes around horizontal, plain brass tubes of 2.54 mm and 5.08 mm diameter as a function of angle. Non-boiling subcooled heat transfer coefficients tended to decrease sharply from the top of the tube to an angle of about 90° and then either continue to fall off more gradually or level off for the rest of the perimeter towards the bottom of the tube. Some data even showed a slight secondary maximum at 180° from the top, i.e. right at the bottom. Instead, the variation in local heat transfer around the tube was more complex for evaporating flows with some local nucleate boiling in the film and was not necessarily symmetric on both sides of the horizontal tubes. Rather than presenting general correlations, they presented separate methods for each size of tube.

Cerza (1992) surveyed previous studies with particular attention to the mechanisms of nucleate boiling in thin falling films. He identified the following *influential parameters* on the heat transfer process:

- Waves or ripples on the film interface;
- Heat flux (for onset of nucleation and nucleate boiling);
- Thermal entrance length for heating the film to the saturation temperature;
- Thermally fully developed length;
- Fluid-surface wettability (dry patch formation);
- Nucleate site distribution.

Rifert et al. (1992) reported falling film coefficients for a plain tube and horizontal tubes with longitudinally grooves in a vertical tube row of six tubes for water. This gave about 1.4 to 1.9 heat transfer augmentation factors for the grooves.

## 14.6 HEAT TRANSFER STUDIES SINCE 1994

These more recent heat transfer studies are described below, more or less in chronological order. These investigations have covered a very broad range of geometries for horizontal falling film evaporation: plain tubes, enhanced tubes, oil effects, intertube flow mode effects on subcooled films, tube layout effects, tube diameter effects, types of sprayers, etc.

Fujita and Tsutsui (1994) obtained R-11 falling film heat transfer coefficients at a pressure of 0.2 MPa for a vertical array of plain, horizontal tubes of 25 mm diameter with a 50 mm vertical tube pitch. They observed the following intertube flow modes of the falling films from tube to tube: discrete droplets, droplets, columns, disturbed columns and sheets. Using various combinations of feeder and dummy tubes over their vertical array of horizontal tubes, the random axial movement of the falling droplets made one dummy tube sufficient to provide a uniform liquid distribution on the lower tubes.

Although the Lorenz and Yung (1978, 1979) correlation presented earlier predicted their data reasonably well, Fujita and Tsutsui (1994) proposed the new more detailed multi-zone model, depicted in Figure 14.12, with a stagnation region, impingement flow region, thermal developing region and a fully developed region. Since the impingement zone is only a small fraction of the tube perimeter, they ignored

it for simplicity. They assumed that the thermal boundary layer grows from the stagnation point at the top of the tube around its perimeter. In the thermally developing zone ( $0 < \phi < \phi_d$ ), the liquid film absorbs the sensible heat conducted into it with negligible evaporation, and this zone ends when the growing thermal boundary layer reaches the liquid film interface. In the fully developed zone ( $\phi_d < \phi$ ), the process is first characterized by simultaneous superheating of the film and partial evaporation of the film at its interface as the temperature profile in the film gradually changes from its 3<sup>rd</sup> order polynomial profile at the beginning of the zone to a linear profile (i.e. one-dimensional conduction). Then, for all larger angles up to  $\phi = \pi$ , all the heat conducted into the film from the wall is assumed to evaporate at the film interface. They also proposed an empirical correlation that reasonably predicted their test data.

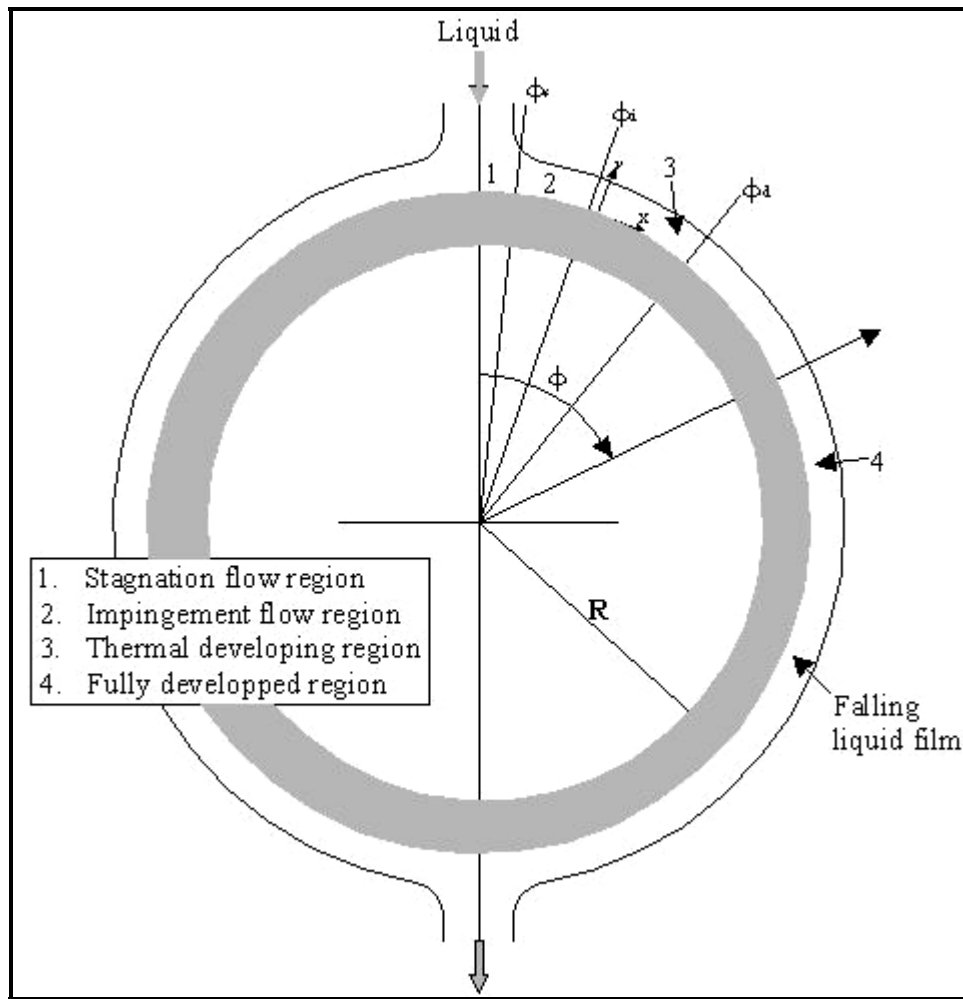


**Figure 14.12. Three zone model of Fujita and Tsutsui (1994).**

In a review on falling film evaporation on vertical surfaces, but also pertinent to horizontal tubes, Gross (1994) discussed the problem of dry patch formation. He concluded that formation of a dry patch was an instability problem, influenced by the following forces on the film:

- **Liquid inertia forces.** The static pressure head within the liquid film at its stagnation point at the top edge of a dry patch favors rewetting of the dry patch;
- **Surface tension forces.** The surface tension forces at the interface of the film have a tendency to enlarge the size of a dry patch;

- **Marangoni effect.** The surface tension gradient created by the temperature profile within the film, particularly near the boundary of a dry patch, acts to transport liquid away from the edge and hence to enlarge the dry patch;
- **Vapor inertia forces.** The acceleration of the vapor-phase adjacent to the evaporating film acts to increase or decrease the dry patch size depending on the direction of the vapor;
- **Interfacial shear forces.** These forces create two competing effects on a dry patch size, one trying to spread the liquid and rewet its top edge and the other trying to elongate its lower edge.

However, no method to predict the onset of dry patch formation was provided.

Chen et al. (1994) obtained falling film heat transfer coefficients for tests with R-11 on the outside of two vertical tubes: a plain tube and a Wolverine enhanced pool boiling Turbo-B tube. They did not measure local values but instead mean heat transfer coefficients for their 1.8 m (5.9 ft) long test sections. Figure 14.13 depicts their test data. The falling film performance of the Turbo-B tube was similar to its pool boiling performance. In addition, the enhanced surface was observed to be particularly beneficial in retarding dry patch formation compared to the plain tube (apparently by capillary forces at the pores), thus allowing higher heat fluxes to be reached before complete dryout of the film. Hence, an enhanced boiling tube can potentially achieve a higher maximum vaporization fraction operating under falling film conditions compared to a plain tube, in addition to augmenting heat transfer.

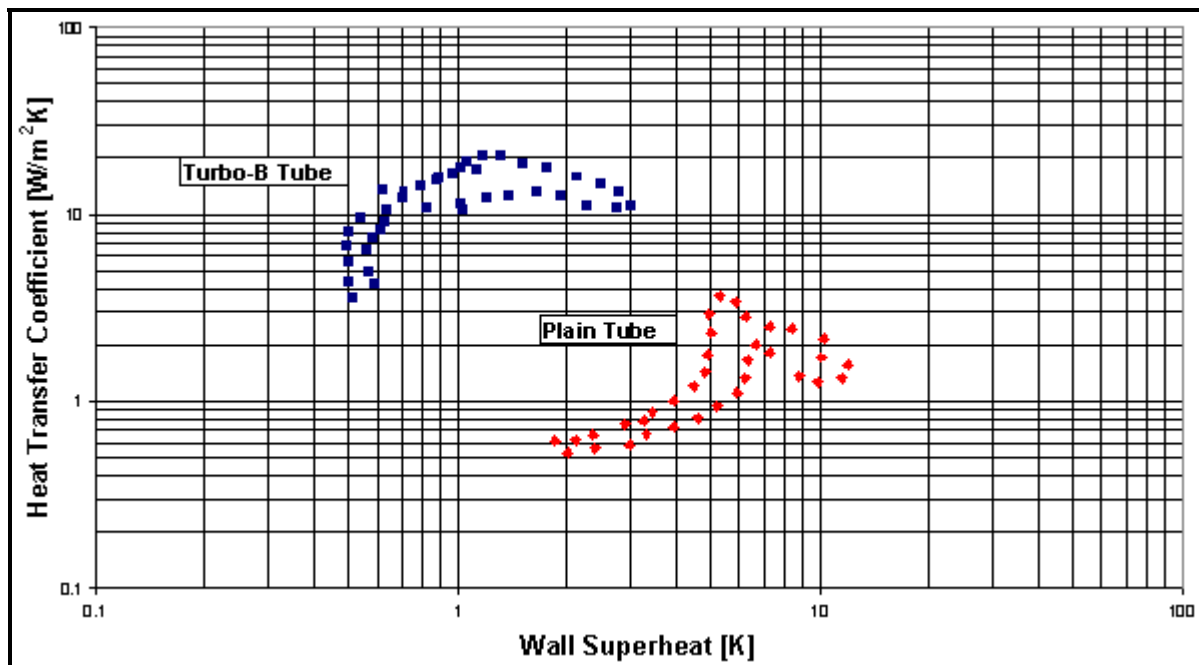


Figure 14.13. Falling film test results for R-11 of Chen et al. (1994).

Fluid spray distribution rates and axial flow rate uniformity were studied by Zeng et al. (1994) on horizontal tube bundles to investigate geometry effects on 3 by 1 tube arrays, i.e. 3 tubes wide and only one row deep. All tubes were 19.05 mm in diameter. A plain tube array, a low finned tube array and a grooved tube array were tested. The low fin tubes had 1575 fpm (40 fpi) with fins 0.97 mm high and 0.33 mm thick. The grooved tubes had 60 longitudinal grooves around the perimeter with a 0.64 mm depth and a 0.4 mm pitch. They observed that the plain tube bundles attained more uniform liquid distribution than the low fin bundles because the fins prevented the liquid film from spreading along the axis of the tube; the grooved tube bundle functioned similar to the plain tube bundle. Consequently, significant non-

uniformity in the local flow rates occurred on the low fin tube bundle but quite uniform distribution was achieved for the other tubes.

Moeykens and Pate (1994) measured heat transfer coefficients for falling film evaporation of R-134a at a saturation temperature of 2°C on two different single, plain horizontal tubes. They were copper tubes of 12.7 mm and 19.05 mm diameter, respectively. They investigated the use of a wide-angle, low-pressure-drop (0.02 Mpa, 3 psi) nozzle compared to a high-pressure-drop (0.86 MPa, 125 psi) nozzle, noting the following trends:

- **Tube diameter effect:** the 12.7 mm tube gave 5-10% better performance than the 19.05 mm tube;
- **Liquid overfeed effect:** heat transfer was not affected by the refrigerant flow rate, if it was sufficient to avoid dry patch formation, since nucleate boiling dominated at their test conditions;
- **Nozzle type:** the high-pressure-drop nozzle yielded better heat transfer because of its impinging jet spray on the top of the tube while the low pressure nozzle provided a wider angle of spray;
- **Relative performance:** the falling film coefficients were higher than the corresponding pool boiling coefficients measured on the same tubes.

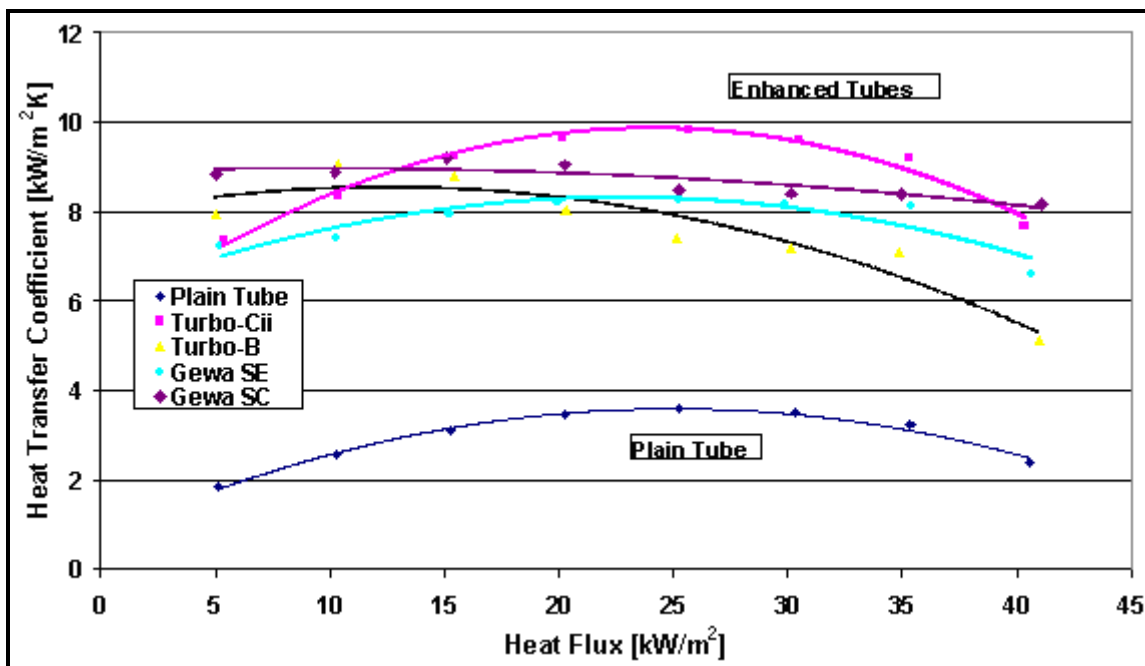


Figure 14.14. Falling film coefficients for R-134a on single enhanced tubes from Moeykens et al. (1995a).

Moeykens et al. (1995a) continued the above study, extending it to R-134a and R-134a/oil mixtures in single-tube tests at 2°C and tested four types of tubes: an enhanced pool boiling tube (Turbo-B), three enhanced condensation tubes (Turbo-Cii, Gewa-SC and Gewa-SE), two low fin tubes (1575 fpm/40 fpi, 1024 fpm/26 fpi) plus a plain tube, all about 19 mm in diameter. Note that first types of tubes have three-dimensional types of enhancement geometries while the low fins are considered as two-dimensional enhancements. Figure 14.14 shows a comparison of the 3-d enhanced tubes to the plain tube for pure R-134a, where the enhanced *condensing* tubes outperformed the Turbo-B, almost certainly because they were more effective in promoting the formation of thin liquid films similar to what they were designed to do for falling film *condensation*. The falloff in the heat transfer coefficients at high heat fluxes occurred because of dry patch formation on the tubes. The low fin tubes (not shown in Figure 14.14) gave

performances in the range of about 6000-7500 W/m<sup>2</sup>K, less than the enhanced geometry tubes. Adding small mass fractions of polyol-ester lubricating oils to R-134a, viscosity grades of 32cs and 68cs, the heat transfer increased when foaming occurred. Overall, the best performing falling film tube was the Wolverine Turbo-Cii.

Moeykens et al. (1995b), in the next phase of their study, tested small tube bundles comprised of 20 tubes. These tests were run with pure R-134a with liquid overfeed ratios from 1.4 to 7.9 at 2°C. The overfeed ratio is defined as  $\Gamma_{\text{feed}}/\Gamma_{\text{evap}}$ , where  $\Gamma_{\text{feed}}$  is the flow rate of liquid applied to the top of the array and  $\Gamma_{\text{evap}}$  is the flow that has been evaporated when reaching the bottom of the array. Both square and triangular tube layouts were utilized for the same types of tubes as above, with the exception of the 1024 fpm (26 fpi) low fin tube. The refrigerant was sprayed onto the top of the bundle using low pressure drop, wide-angle, solid-cone nozzles. Bubbles were visible in the thick liquid layer at the bottom of the tubes, indicating nucleate boiling was occurring in the films on all the tubes. The enhanced condensation tube Turbo-Cii again gave by far the best performance. In fact, the Turbo-Cii tube bundle operating in the falling film mode nearly doubled the pool boiling performance of the Turbo-B bundle.

Moeykens and Pate (1995) also investigated the influence of nozzle height and orifice size for spray evaporation of R-134a at 2°C on one 1575 fpm (40 fpi) low fin tube bundle with 20 tubes in a triangular tube layout. The vertical tube pitch was 19.1 mm, the horizontal tube pitch was 22.2 mm, and the tube diameter over the fins was 18.70 mm. Five different nozzle orifice diameters from 4.0-5.6 mm were tested in either circular or square spray patterns. The 0.0172 MPa (2.5 psi) pressure drop nozzles were located from 41.3 to 66.7 mm above the top tube row. The falling film coefficients at the optimal film-feed rate were higher than those obtained for pool boiling on the same tube bundle. Regarding the objective of obtaining uniform liquid spray over the top tube row, the advantage of a square nozzle spray pattern compared to a circular spray pattern became insignificant with increasing overlap of the sprays from adjacent nozzles. This small bundle was prone to local dryout on the bottom tube rows because the low fins inhibited longitudinal spreading of the liquid film along the tubes.

Moeykens and Pate (1996) continued these tests, investigating staggered tube bundles with four types of tubes: plain, 1575 fpm (40 fpi) low fin, Wieland Gewa-SC and Wolverine Turbo-B. Oil effects were checked using 340 SUS polyol-ester oil with 1.0 and 2.5 wt.% oil in the liquid feed of R-134a onto the top of the tubes. The tube bundles had the same geometry as their prior low finned tube bundle. R-22 with 300 SUS alkyl benzene oil was also tested on the plain tube and Turbo-B tube bundles. The results for two types of the tubes are compared in Figure 14.15, where the heat transfer coefficient is the mean for the bundle from individual measurements on the central vertical tube row of 4 tubes. These oils promoted foaming, which was thought to retard the formation of dry patches and hence was beneficial for heat transfer at higher heat fluxes. The oil improved plain tube and Turbo-B tube heat transfer but with the benefit decreased for the Turbo-B with increasing heat flux.

Moeykens et al. (1996) next extended their falling film fluid database to R-123 and R-123/oil mixtures for staggered and inline tube bundles. Plain, Turbo-Cii and Turbo-B tubes were tested at a saturation pressure of 0.0357 MPa. A 303 SUS naphthenic mineral oil was used with R-123. Curiously, foaming was only observed on the plain tube bundles. For R-123, the Turbo-B tube provided better performance than the Turbo-Cii and its falling film performance was about 2-2.6 times that of its pool boiling performance in R-123! The oil improved Turbo-Cii performance by up to 90% at some test conditions but degraded it at others, depending on the liquid feed flow rate. High performance was observed without foaming on the enhanced tubes and, consequently, it may be that foaming does not increase resistance to dry patch formation as suggested in their earlier study.

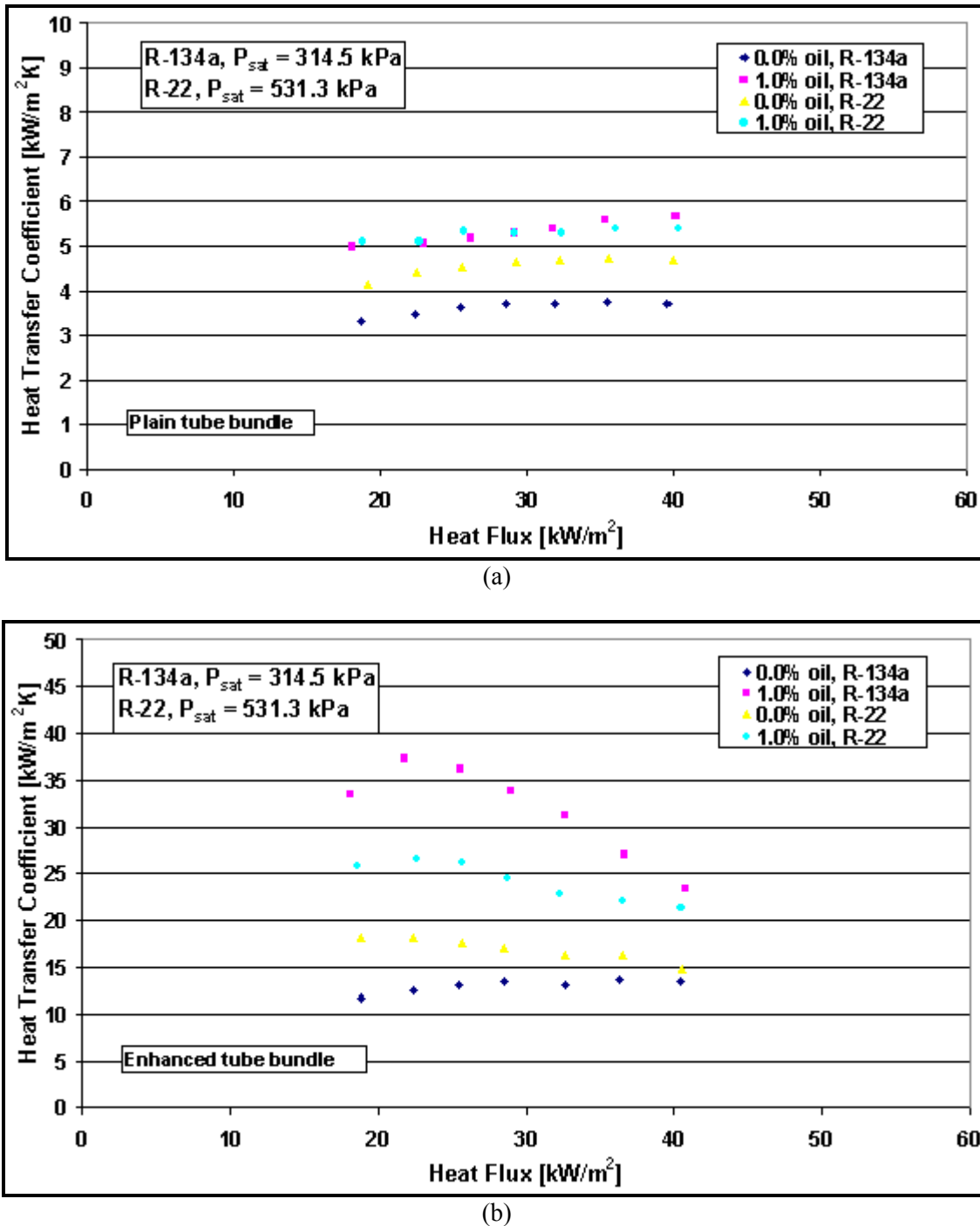


Figure 14.15. R-22 and R-134a tests with and without oil on triangular pitch tube bundles of Moeykens and Pate (1996): (a) plain tube, (b) Turbo-B tube.

Regarding other effects of oil on the falling film evaporation process, oil may have an effect on the falling film modes from tube to tube due to the higher surface tension and viscosity of the oil, e.g. this may convert the intertube film flow from column mode to sheet mode. Another mechanism that may well be important is liquid retention (in a further analogy between enhanced falling film evaporation and condensation), which may be the reason that the Turbo-B outperformed the Turbo-Cii for R-123 while the opposite was observed for R-134a. The Turbo-Cii, being an enhanced condensation surface, retains

liquid between adjacent fins on the lower portion of the tube; hence minimizing the liquid retention angle and the film thickness are important, both values which would tend to increase in value with the larger surface tension of R-123 compared to R-134a. On the contrary, the Turbo-B tube promotes thin film evaporation inside its reentrant channels and is thus much less susceptible to liquid retention since its pore openings act as self-regulating orifices for controlling the liquid flow rate into the reentrant channels.

The mass transfer resistance created by the oil in evaporation of the liquid film is detrimental to heat transfer, having a larger influence on the Turbo-B tube (like in pool boiling) since it has the higher pure fluid performance. Since the oil is non-volatile, its tends to build up its concentration at the evaporating interface, which in turn increases the local bubble point temperature of the refrigerant-oil mixture at the interface. For nucleate pool boiling, this effect has been explained in Thome (1996) for refrigerant-oil mixtures with the expression

$$\frac{\alpha}{\alpha_i} = \frac{(T_w - T_{bub})}{(T_w - T_{bub}) + dT_{bub}} \quad [14.6.1]$$

where  $\alpha$  is the actual heat transfer coefficient,  $\alpha_i$  is the ideal coefficient of the pure refrigerant,  $(T_w - T_{bub})$  is the wall superheat for the pure refrigerant without oil at the specified heat flux, and  $dT_{bub}$  is the rise in the bubble point temperature from its bulk value to the interfacial value at the vapor-liquid interface as a result of the depletion of refrigerant in the liquid boundary layer adjacent to the interface where the oil cannot evaporate. The effect is to reduce the superheat available for the evaporation process. This mass transfer resistance effect increases with heat flux, from no effect at zero heat flux up to a significant impact at high heat flux where the evaporation rate of the refrigerant reaches its highest level and thus increases  $dT_{bub}$  across the diffusion boundary layer. Consequently, the mass transfer effect tends to decrease the ratio ( $\alpha/\alpha_i$ ) with increasing heat flux while on the other hand the oil may impact on the value of  $\alpha_i$  by a direct influence on the heat transfer mechanisms themselves.

Hu and Jacobi (1996a) investigated adiabatic falling film modes on vertical tube rows, i.e. droplet, column, sheet and their combinations, in an experimental program with four plain tubes in a vertical tube row, where the top tube acted as the liquid distributor. The fluid from the feed tube flowed over the second tube and then onto the third tube which acted as the test tube, and then onto the bottom 'dummy' tube, and finally into an open liquid catching tube. Air flow from top to bottom was applied at velocities up to 15 m/s by placing the test set up in a wind tunnel. Water, ethylene glycol, water/glycol, oil and alcohol were tested. The flow patterns and heat were categorized into droplet, droplet-jet, in-line jet, staggered jet, jet-sheet and sheet modes, where some are transition modes from one regime to another. Empirical correlations for the transition boundaries were determined (presented earlier in this chapter). In Part 2 of their study, Hu and Jacobi (1996b) measured falling film heat transfer coefficients to subcooled liquid (without evaporation) for test conditions similar to the above tests. They presented empirical correlations for predicting heat transfer coefficients for film Reynolds numbers up to about 1900 for a wide range of fluid properties, including the ratio of vertical intertube spacing (S-D) to tube diameter D. The following expressions were proposed:

$$\text{Sheet mode: } Nu_{\Gamma,\text{sub}} = 2.194 Re_{\Gamma}^{0.28} Pr_L^{0.14} Ar_L^{-0.20} \left( \frac{S-D}{D} \right)^{0.07} \quad [14.6.2]$$

$$\text{Column mode: } Nu_{\Gamma,\text{sub}} = 1.378 Re_{\Gamma}^{0.42} Pr_L^{0.26} Ar_L^{-0.23} \left( \frac{S-D}{D} \right)^{0.08} \quad [14.6.3]$$

Droplet mode:  $Nu_{\Gamma,sub} = 0.113 Re_{\Gamma}^{0.85} Pr_L^{0.85} Ar_L^{-0.27} \left( \frac{S-D}{D} \right)^{0.04}$  [14.6.4]

The Archimedes number  $Ar_L$ , based on tube diameter, is defined as:

$$Ar_L = \frac{D^3 g}{v_L^2} \quad [14.6.5]$$

The Nusselt number  $Nu_{\Gamma,sub}$  is the same as that defined in Equation [14.5.9] and the film Reynolds number is the same as that defined in Equations [14.4.6] and [14.5.6] based on the liquid flow rate on one side of the tube.

Falling film coefficients for ammonia were measured by Zeng et al. (1995) using commercial spray nozzles for distribution of the liquid overfeed. They tested a single, horizontal plain, stainless steel tube of 19.1 mm diameter at saturation temperatures from -23.3°C to 10°C. Their results are shown in Figure 14.16 compared to a correlation of Parken et al. (1990). In another study, Chyu et al. (1995) did a geometrical analysis on nozzle layouts. Figure 14.17 shows their comparison of the same type of nozzles arranged in a triangular array compared to a square array. There is less overlap of the spray areas using the triangular layout and hence a more uniform liquid distribution is achieved.

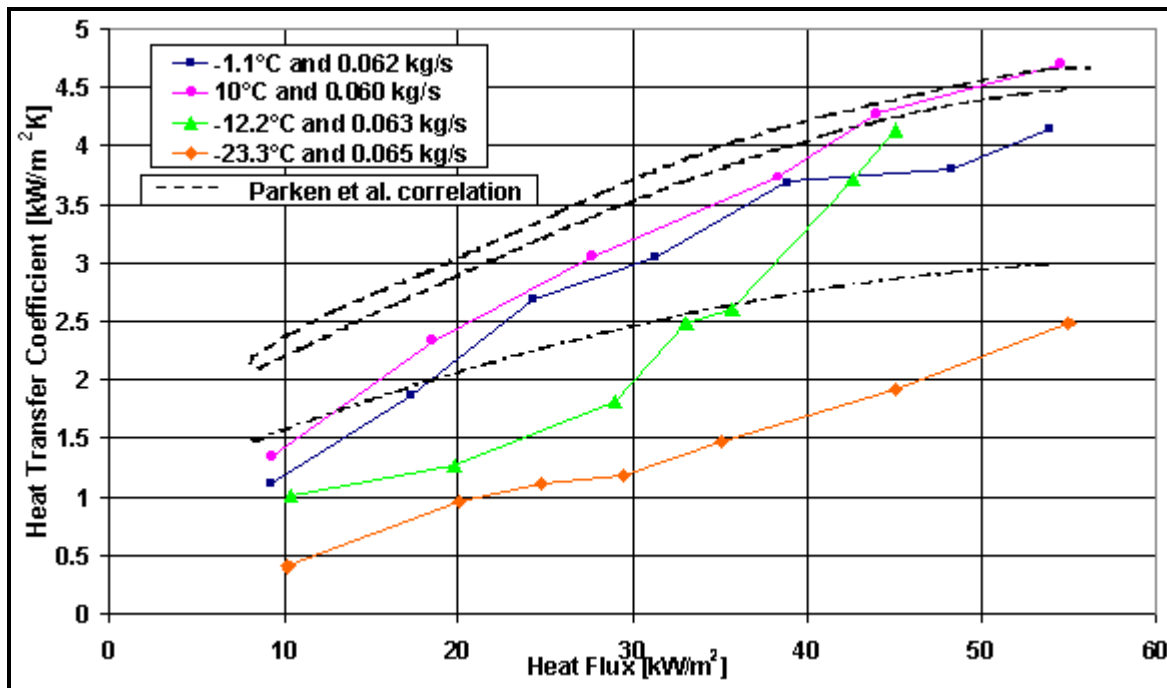
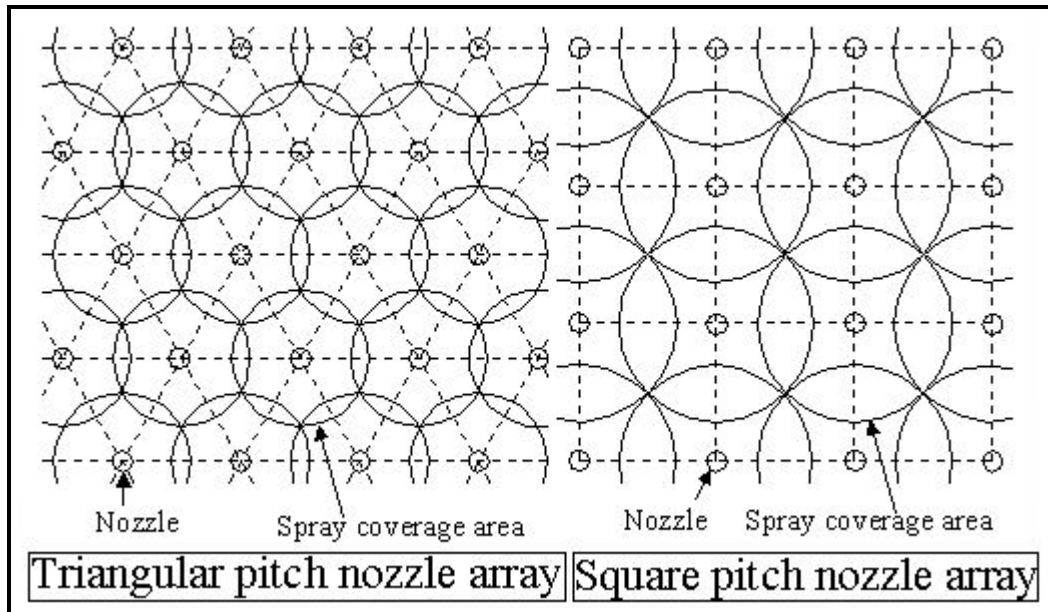


Figure 14.16. Ammonia falling film results on a single, plain tube from Zeng et al. (1995).

Zeng et al. (1997) extended their earlier single-tube tests for pure ammonia to a 3-tube by 3-tube square layout with a 1.25 pitch ratio for a horizontal plain tube bundle made with 19.1 mm stainless steel tubes. Saturation temperatures ranged from -23°C to 10°C. They also boiled ammonia on the same small tube bundle to get some bundle boiling performance data as a comparison to falling film performance. Their bundle in the flooded evaporator mode performed only slightly better than predicted for a single tube since the bundle is small with little convection effect, while in falling film mode the performance was

better by a factor of 1.5 to 2 times. These test data covered the range where the influences of both evaporation and nucleate boiling were significant.



**Figure 14.17. Nozzle spray area layouts. (left) triangular pitch nozzle array, (right) square pitch nozzle array of Chyu et al. (1995).**

Zeng et al. (1998) extended their single-tube tests to falling film evaporation of ammonia to a carbon steel low fin tube and a corrugated tube. Their 1575 fpm (40fpi) low finned tube had a fin tip diameter of 19.85 mm and fin height of 1.0 mm but its surface area per unit length was not cited. The Wolverine corrugated tube was 19.05 mm in outside diameter over the corrugations with a corrugation pitch of 7.94 mm, but the corrugation depth was not cited. A large number of single-tube tests were run at the previously tested saturation temperatures from -23.3°C to 10°C. The low fin tube increased performance by up to 2.8 times with respect to their prior plain tube tests at high heat fluxes where nucleate boiling occurred in the film but offered little augmentation at low heat fluxes. The corrugated tube performed similar to that of the plain tube, i.e. minimal augmentation.

## 14.7 RECENT STUDIES SINCE 2004

Extensive experimental tests on pool boiling and falling film evaporation on plain and enhanced tubes have been undertaken by Thome and co-workers over the past years. The tests have primarily used R-134a as the test fluid but more recently also the refrigerant R-236fa has been added to diversify the fluid properties in their database. The experimental program included testing of plain tubes and enhanced boiling tubes in nucleate pool boiling mode, falling film mode on a single-tube row with up to 10 horizontal tubes one above one another and falling film mode on a three-row bundle with up to 30 tubes in the bundle. This experimental work was then the starting point for improving prediction methods for falling film evaporation. This work is summarized below, with special attention on the plain tube and Wolverine enhanced tube results.

Figure 14.18 depicts some falling film test results for a single-row of 10 horizontal plain tubes placed one over the other with a tube pitch of 22.3 mm with tube diameter of 18.91 mm (odd tube data only here). The outside nominal heat flux is 35.6 kW/m<sup>2</sup>. Using hot water heating with five tube passes for ten tubes,

the hot water enters the even tube rows, turns around and passes through the odd tube rows. This configuration creates a nearly uniform evaporation rate after each pair of tubes, such that the falling liquid film remains uniformly distributed along the tube array (*note*: using a one-pass design would create a high heat flux at one end and a low heat flux at the other of the array, creating a very non-uniform liquid distribution down the tube row and initiation of early dryout at the high heat flux end, while instead their setup avoids this pitfall). Thus, any effect of any maldistribution is smallest at the midpoint of their 0.5 m long tubes, and that is where the local heat transfer coefficients of all the tubes were measured. Quite noticeable in their data, there are two distinct trends:

- There is a more or less horizontal plateau in the data for all the tubes at a film Reynolds number greater than 500. The scatter in the data within the plateau is due first to the experimental errors in their measurements and secondly to the range of heat fluxes of about  $\pm 10\%$  from the nominal value cited. The plateau is at a much higher heat transfer performance than pool boiling heat transfer measured at the same heat flux on one of the plain tubes (up to about 80%), indicating a substantial enhancement effect of the falling film on the nucleate boiling process in the film.
- The falloff in the heat transfer coefficient at film Reynolds less than 500 was observed visually to be due to the formation of dry patches on the tubes. As the size and residence time of the dry patches increased, the time-averaged local heat transfer coefficient decreased towards an all dry state. Thus, the onset of dryout is an important operating criterion to divide the all wet from the partially-wet operating conditions and thermal performance.

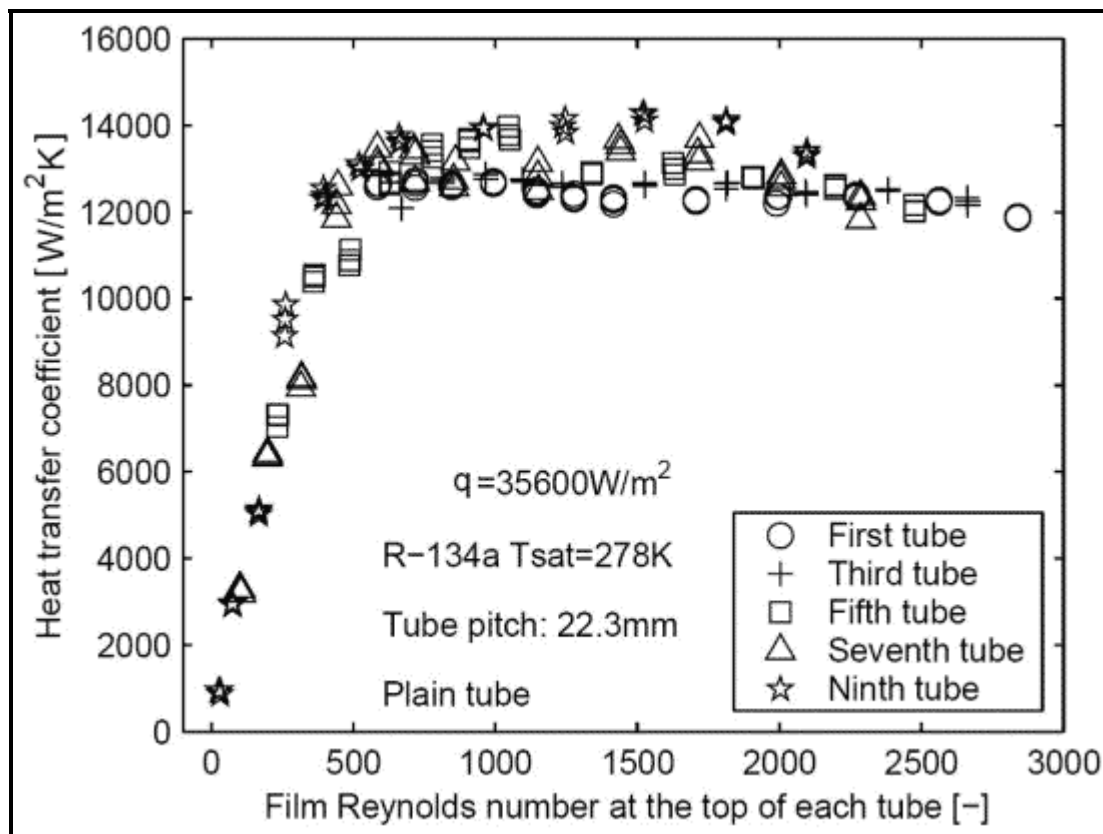


**Figure 14.18. Falling film on a single-row of ten plain tubes from Roques and Thome (2007a) showing odd tube results.**

Figure 14.19 depicts some falling film test results for a single-row of 10 horizontal, Wolverine Turbo-BII tubes placed one over the other with a tube pitch of 22.3 mm with tube diameter of 18.84 mm (odd row tubes only here). The nominal heat flux is  $37.2 \text{ kW/m}^2$ . The same setup for the heating water was also used here. Again, there is a plateau in the heat transfer coefficients above a film Reynolds number of about 500 and a falloff below where the formation of dry patches becomes more extensive. Hence, the optimal design conditions are to maintain the film Reynolds number at the top of each tube above 500 to insure high thermal performance while the tubes below this threshold can instead be immersed in a liquid pool in an actual falling film evaporator to function like flooded evaporator tubes. Notably, the tubes above this threshold will have a nearly uniform thermal performance and hence create a nearly uniform overall heat transfer coefficient. The heat transfer coefficients on the Turbo-BII array in the all wet plateau are a little more than twice those of the plain tube array. Furthermore, the Turbo-BII falling film heat transfer coefficients tended to be on average about 10-15% higher than their corresponding pool boiling values.

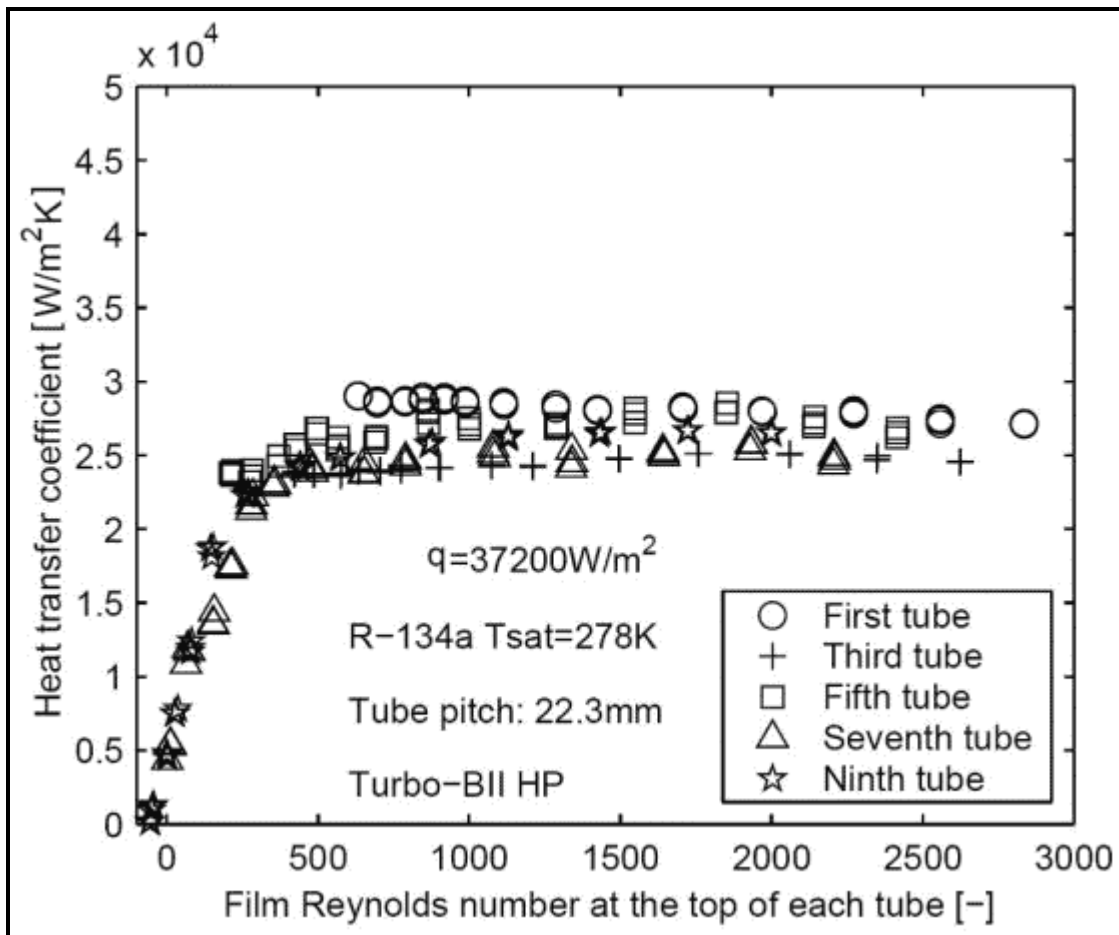


**Figure 14.19. Falling film on a single-row of ten Wolverine Turbo-BII tubes from Roques and Thome (2007a) showing odd row results.**

Figure 14.20 depicts some falling film test results for a single-row of 10 horizontal, UOP High Flux tubes placed one over the other with a tube pitch of 25.5 mm with tube diameter of 18.87 mm (odd tube row data only here). The nominal heat flux is  $49.7 \text{ kW/m}^2$ . The same setup for the heating water was also used here. Again, there is a plateau in the heat transfer coefficients above a film Reynolds number of about 500-600 and a falloff below where the formation of dry patches becomes more extensive. The larger

dispersion of the data in the plateau is primarily due to the propagation of errors in these measurements, which are larger due to the very high heat transfer coefficients from 45000 to 67000 W/m<sup>2</sup>K. The High Flux falling film heat transfer coefficients tended to be on average about the same as their corresponding pool boiling values.

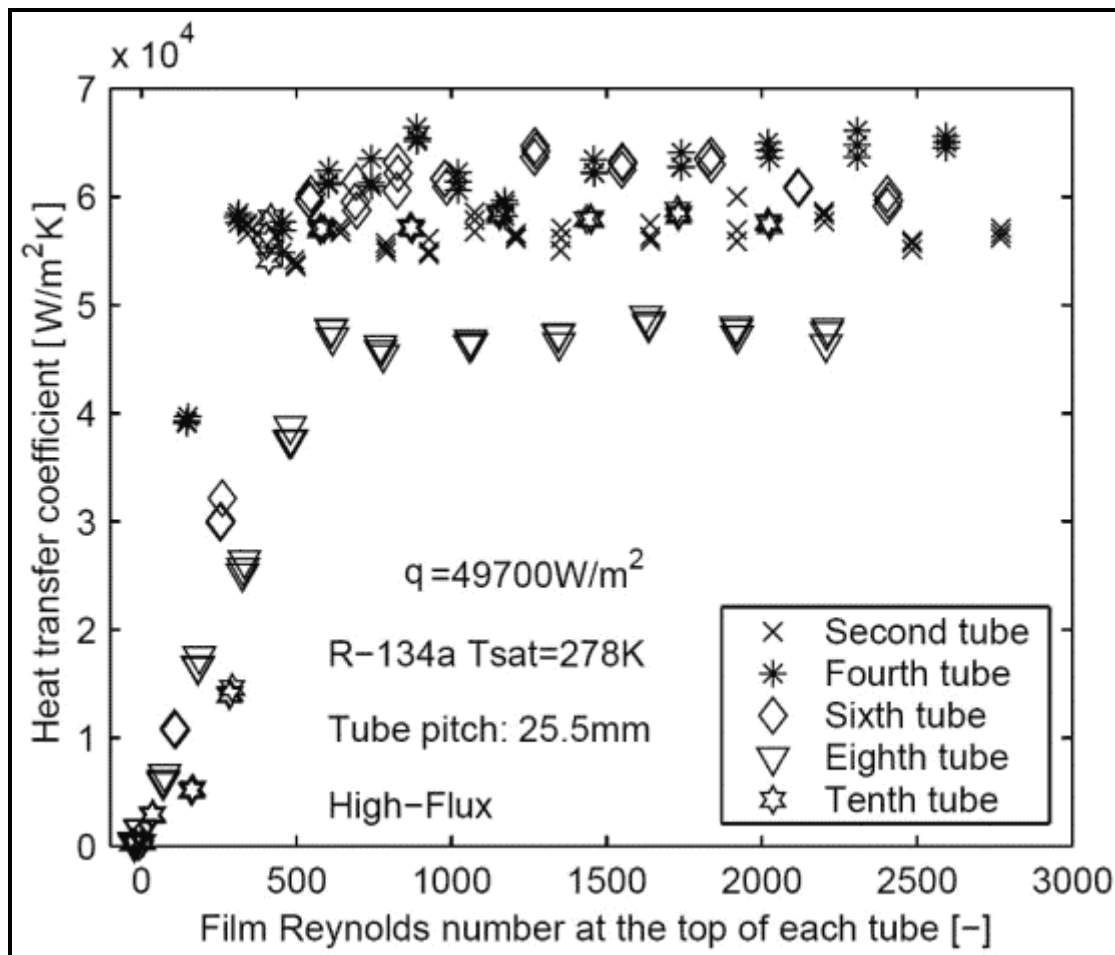


**Figure 14.20. Falling film on a single-row of ten High Flux tubes from Roques and Thome (2007a) showing even row results.**

It is thus interesting to see that the general trend in the data, a plateau of heat transfer coefficients insensitive to the film Reynolds number above the dryout threshold and a rather linear falloff below the threshold, holds for a plain tube, a mechanically enhanced surface tube and a porous coated enhanced tube. Similar data were obtained at other test conditions and also for another enhanced boiling tube. These can be found in Roques and Thome (2007a) and even more details in the thesis of Roques (2004) available for free online.

The more recent results of Habert and Thome (2010a, 2010b) for the new Turbo-EDE2 enhanced boiling tube of Wolverine are shown in Figure 14.21. On the left, results for R-134a are depicted at three nominal heat fluxes, notably with the highest performance at the lowest heat flux where local heat transfer coefficients in the “plateau” averaged about 78000 W/m<sup>2</sup>K! The mechanism responsible for reducing the performance at higher heat fluxes (but still with heat transfer coefficients from 38000 to 50000 W/m<sup>2</sup>K) was not identified. Results for a second fluid, R-236fa, gave similar trends but lower performance as this tube was optimized for use with R-134a but not with R-236fa. Once again, the general trends were the

same as those in the earlier tests described above. More details on these tests can be found in Habert (2009).

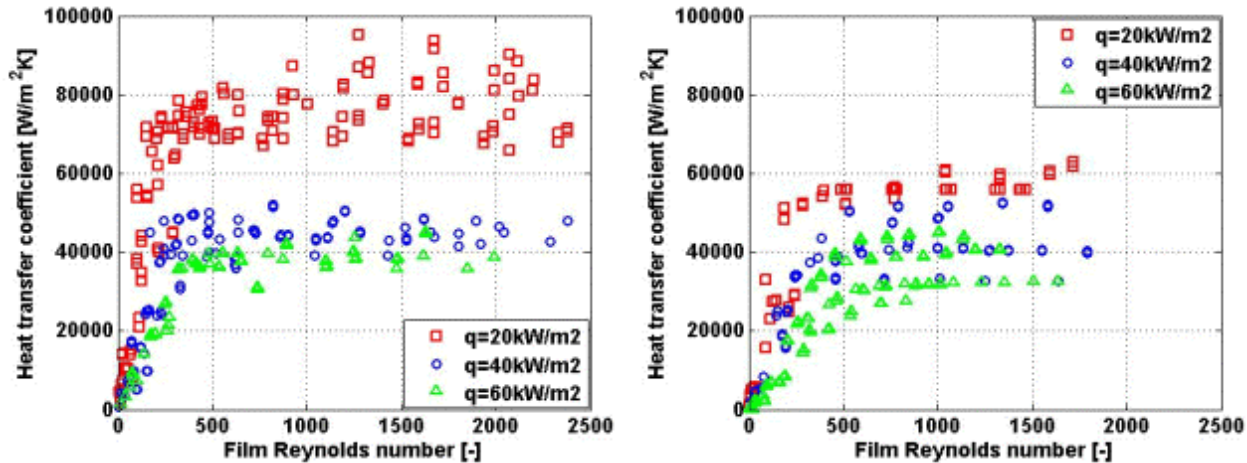


Figure 14.21. Falling film results on a single-row of ten Wolverine Turbo-EDE2 tubes from Habert and Thome (2010a) for R-134a (left) and R-236fa (right) at 5°C saturation temperature.

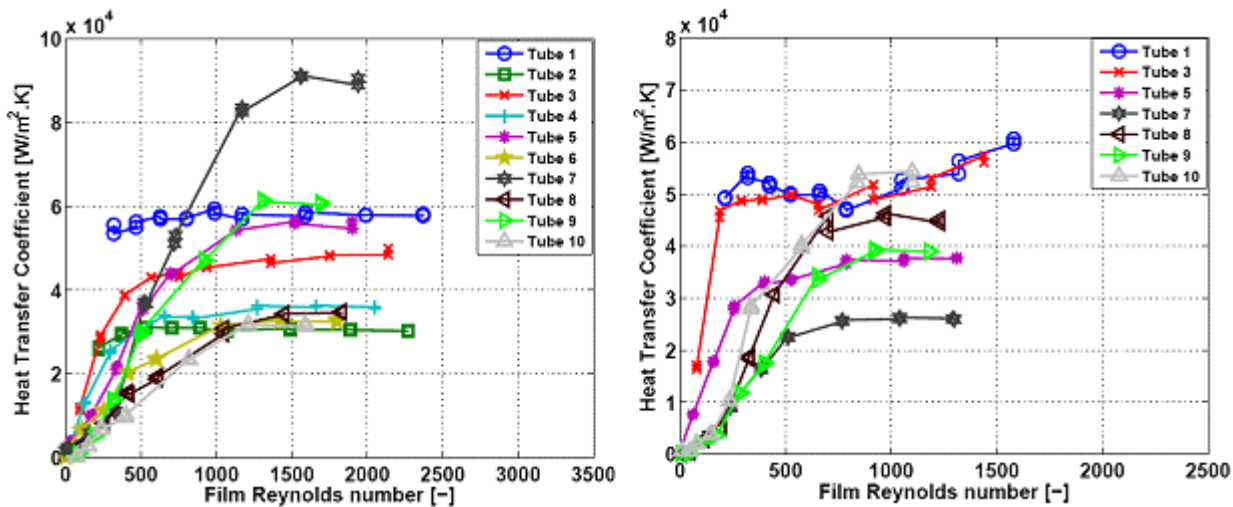


Figure 14.22. Falling film results on a single-row of ten Wolverine Turbo-EDE2 tubes from Habert and Thome (2010a) for R-134a (left) and R-236fa (right) at 5°C saturation temperature and heat flux of 40 kW/m<sup>2</sup>.

Figure 14.22 depicts some bundle falling film heat transfer coefficients that were measured for a 30-tube bundle of Wolverine Turbo-EDE2 tubes that were 0.5 meters long. The same procedure as described above was used to determine the local heat transfer coefficients at the midpoint of each tube in the central row of three rows. The tubes had a 22.30 mm vertical pitch and a 22.30 mm horizontal pitch in a staggered arrangement. Referring to the single-row tests results presented above, the bundle results are approximately in the same range, but exhibit a bundle effect that can increase or decrease the local heat transfer performance. While the bundle results still illustrate a plateau and a drop off in performance at lower film Reynolds numbers, the distinction is now less clear. The reason for this is believed to be due to the non-ideal liquid distribution within the bundle (all tubes were wetted and in nucleate boiling conditions). The liquid may preferentially flow around one side of a tube and not the other side; for

instance, creating a local partially wet condition due to flow maldistribution rather than dry patch formation. Thus, a lower tube may have a higher heat transfer coefficient than the tube above it.

For the prediction of falling film heat transfer coefficients (all data with nucleate boiling present in the film), Roques (2004) and Roques and Thome (2007b) proposed a simple correlation for plain and enhanced tubes to predict the falling film heat transfer coefficient on a single-row (array with up to 10 tubes) when the tubes are all wet (no dryout patches):

$$\alpha_{\text{array}} = \alpha_{\text{wet}} = \alpha_{\text{nb}} K_{\text{ff}} \quad [14.7.1]$$

Their multiplier  $K_{\text{ff}}$  represents the effect of falling film on the nucleate pool boiling heat transfer coefficient on the same tube at the same operating conditions. Based on their R-134a data,  $K_{\text{ff}}$  was correlated as a function of the tube pitch and heat flux as:

$$K_{\text{ff}} = \left( 1 + b_1 \frac{L_{\text{pn}}}{L_{\text{pn,ref}}} \right) \left( b_2 + b_3 \left( \frac{q}{q_{\text{DNB}}} \right) + b_4 \left( \frac{q}{q_{\text{DNB}}} \right)^2 \right) \quad [14.7.2]$$

The heat flux  $q$  is for the particular tube in the array, giving the heat transfer coefficient for that tube, with  $\alpha_{\text{nb}}$  evaluated at this value of  $q$ . In this empirically fit equation, the tube pitch normal to direction of flow  $L_{\text{pn}}$  (i.e. the vertical tube pitch) is non-dimensionalized with the minimum tube pitch tested,  $L_{\text{pn,ref}} = 22.25$  mm, and the heat flux  $q$  is non-dimensionalized using the departure from nucleate boiling heat flux  $q_{\text{DNB}}$  from Kutateladze's correlation (1948) that was discussed in Chapter 9:

$$q_{\text{DNB}} = 0.131 \rho_G^{1/2} h_{\text{LG}} \sqrt[4]{g(\rho_L - \rho_G)\sigma} \quad [14.7.3]$$

The method takes the nucleate pool boiling curve of the tube/fluid combination as an input. It can be calculated for a plain tube (see methods in Chapter 9) or taken from an experimental pool boiling curve, which is a necessity for enhanced boiling tubes since no general method is available to predict them. The tube pitches center-to-center in the vertical tube array of horizontal tubes tested were: 22.25 mm, 23.9 mm and 25.5 mm (which represent vertical spacing between the tubes of about 3.4, 5.0 and 6.6 mm in respect to the nominal outside tube diameters). They performed their experiments within a heat flux range from about 20 to 60 kW/m<sup>2</sup> and extrapolating to lower heat fluxes that might be typical of actual design is not advised. For R-134a at 5°C in particular,  $q_{\text{DNB}}$  is 361.3 kW/m<sup>2</sup>.

**Table 14.2. Empirical constants for the falling film coefficient prediction.**

Tube:	Plain Tube	Turbo-BII HP	High Flux
<b>b<sub>1</sub></b>	-0.335	-0.361	-0.0104
<b>b<sub>2</sub></b>	2.059	2.891	0.540
<b>b<sub>3</sub></b>	2.370	-16.314	5.723
<b>b<sub>4</sub></b>	-7.793	59.906	-4.714

The values of the empirical constants are given in Table 14.2 for some of the tubes they tested. The constant  $b_1$  accounts for the tube pitch influence and its value is nearly the same for the plain and Turbo-BII HP tubes. This value is negative, indicating that the value of the falling film coefficient decreases as the tube pitch increases. The decrease in heat transfer is approximately 8% from the smallest to the largest

pitch, indicating that the velocity of the liquid impinging on the top of each tube has a negative impact on heat transfer, perhaps by having an adverse effect locally on the nucleate boiling process; however, the 8% found here is only a minor impact. For the High Flux tube of UOP, this influence is only 1% from the minimum tube pitch to the maximum one and hence negligible. In actual falling film evaporators, the tube pitch will normally be close to the smallest pitch they tested.

The heat flux has a weak influence on the falling film factor  $K_{ff}$  of the plain tube, which has a mean value of 1.4. This means that the performance in falling film evaporation conditions is thus on average 40% higher than in pool boiling. Zeng, Chyu and Ayub (1996) for their bundle with ammonia found a falling film enhancement of about 1.5 to 2 for a plain tube while Danilova, Burkin and Dyundin (1976) found respectively values of 1.5, 1.4 and 1.33 for R-22 at a heat flux of 16 kW/m<sup>2</sup> and saturation temperatures of 273, 253 and 233 K. For the Turbo-BII HP, the falling film factor ranged from 1.3 at 20 kW/m<sup>2</sup> to 1.15 at 50 kW/m<sup>2</sup>. For the High Flux tube, the falling film factor increased nearly linearly with the heat flux from 1.0 to 1.5, which is the opposite of its nucleate pool boiling heat transfer coefficient that decreased by a factor of 1.4 in this heat flux range. The falling film heat transfer coefficient of the High Flux tube consequently only increased slightly with heat flux.

More recently, Ribatski and Thome (2007) developed a predictive method for plain tubes with R-134a to characterize both the *all wet* and *partially-wet* conditions. They defined an objective criterion to characterize the onset of dryout based on  $K_{ff}$ . The onset of dryout (i.e. formation of dry patches) was defined by a drastic decrease of the heat transfer coefficient with decreasing film flow rate and a decrease in the average heat flux. This criterion was used to segregate the experimental data as either being under all wet or partially-wet conditions. In their method, for partial wetting of the tube caused by the dry patches, the heat transfer area was divided into all wet and all dry regions respectively governed by nucleate boiling heat transfer and natural convection heat transfer to the vapor. The local external heat flux and heat transfer coefficient were determined by:

$$\begin{cases} q = q_{wet}F + q_{dry}(1-F) \\ \alpha_{array} = \alpha_{wet}F + \alpha_{dry}(1-F) \end{cases} \quad [14.7.4]$$

In these expressions F represents the apparent wet area fraction defined as the ratio between the wet area and the total area of the tube's nominal outside surface. Based on a regression analysis of the all wet data in the plateau, a simple correlation of  $\alpha_{wet}$  was obtained, following a Cooper-type expression for pool boiling:

$$\alpha_{wet} = 376 p_r^{0.22} q_{wet}^{0.38} \quad [14.7.5]$$

The values of  $\alpha_{dry}$  were calculated using a correlation for free convection assuming a quiescent vapor condition within the falling film evaporator. Notably, the  $\alpha_{dry}$  is much smaller than  $\alpha_{wet}$  so its value can be neglected for all practical purposes. Using the partially-wet database and the above expressions, values of F were backed out and correlated as function of the film Reynolds number:

$$F = a Re_{top}^b \quad [14.7.6]$$

The empirical values are:  $a = 0.0024$  and  $b = 0.91$ . Their prediction method captured the heat flux effect on the heat transfer coefficient and the onset of dryout.

Habert and Thome (2010a, 2010b) and Habert (2009) analyzed their new data and the previous data of Roques (2004) to formulate an improved method for predicting the onset of dryout (to divide the all wet regime from the partially-wet regime) and an updated method for predicting the heat transfer coefficients in each regime. To begin with, the falling film evaporation prediction process is composed of five steps:

1. Prediction of the *film Reynolds number at onset of dryout* to define the transition between all-wet and partially-wet tube surface operation;
2. Prediction (or measurement) of the nucleate pool boiling curve to obtain the *nucleate pool heat transfer coefficient* for the particular tube/fluid combination at the design saturation temperature;
3. Prediction of the *local heat transfer coefficient for the all-wet region on a single-row* with respect to the nucleate pool boiling performance;
4. Prediction of the *local heat transfer coefficient for the partially-wet region on a single-row*, characterized by a rapid decrease of the heat transfer coefficient with increasing dry area fraction;
5. Prediction of the *local bundle heat transfer coefficient* by accounting for the bundle effect with respect to the single-row performance.

Their method focuses primarily on the all-wet data as they are the most important for actual falling film evaporator applications since partially-wet operation will have quite poor thermal performance. Inclusion of the partially-wet design method is primarily important such that one can simulate a bundle's performance also at "off-design" operating conditions.

**Prediction of Film Reynolds Number at Onset of Dryout.** Based on the results from Habert (2009) and the previous results of Roques (2004), the characteristic film Reynolds numbers for onset of dryout were found to be primarily a function of heat flux for the two fluids tested (R134a and R-236fa) for plain and enhanced tubes. The onset of film breakdown Reynolds number increased with increasing heat flux for all tested surfaces, following a similar trend for both fluids. A single form of prediction was thus used for these tube/fluid combinations. The parameters that significantly vary between the two fluids and that could affect the onset of dryout are the local heat flux  $q$ , the dynamic liquid viscosity  $\mu_L$ , the latent heat of vaporization  $h_{LG}$  and the tube diameter  $D$ . A parameter analysis in Habert and Thome (2010b) led to the following dimensionless expression for the film Reynolds number at the onset of dryout at the top of the tube:

$$Re_{onset} = 65.8 \left( \frac{qD}{\mu_L h_{LG}} \right)^{0.63} \quad [14.7.7]$$

This new expression proposed for the onset of film breakdown takes into account fluid properties and heat flux effects and gives a good agreement based on a large database. For the plain and enhanced tubes tested by Habert (2009) and the previous study of Roques (2004), the expression was found to predict 81.6% of the data within  $\pm 30\%$  for the 10 tube/fluid combinations out of 11 total (including the plain tube, the High Flux tube, the Turbo-BII HP tube and the Turbo-EDE2 tube) under single-tube row conditions. Extrapolating this expression to tube bundles, the location of the onset of dryout in a tube bundle can be determined from a row by row energy balance starting at the top of the bundle. Thus, the rate of overfeed required to avoid the onset of dryout can be calculated or the number of tubes adjusted.

**Prediction of Heat Transfer on a Single-Tube Row for All-Wet Condition.** The heat transfer method proposed by Habert and Thome (2010b) is an updated combination of the methods of Roques and Thome (2007b) and Ribatski and Thome [11]. Their new method gives good agreement when applied to the new database of Habert and Thome (2010a) and the previous database of Roques (2004) applying the appropriate empirical constants. Their new method obtained a good prediction of the local heat transfer

coefficient for all wet conditions with the pool boiling correlation (or boiling curve fit to the experimental pool boiling data) for each given tube/fluid combination, using two empirical constants to obtain the falling film multiplier  $K_{ff}$ :

$$\alpha_{array} = \alpha_{wet} = K_{ff} \alpha_{nb} \quad [14.7.8]$$

$$K_{ff} = c \left( \frac{q}{q_{DNB}} \right)^d \quad [14.7.9]$$

The value of  $\alpha_{nb}$  is determined at the heat flux  $q$  on the particular tube in the array and  $q_{DNB}$  is determined using Kutateladze's correlation (1948) described earlier. The values of  $c$  and  $d$  for a selection of tubes they tested are given in Table 14.3. It was not possible to collapse all the data onto just one set of constants  $c$  and  $d$  to reflect how the particular surface interacts with the falling bubbly film. The method is applicable to a range of heat fluxes from about 20 to 60 kW/m<sup>2</sup> and does not necessarily extrapolate well at all to lower heat fluxes. The method is also applicable up to film Reynolds numbers of about 2500.

**Table 14.3. Coefficients for  $K_{ff}$  for the new database.**

Tube	R-134a		R-236fa	
	c	d	c	d
<b>Plain</b>	1.6951	-0.324	3.8124	-0.172
<b>Turbo-BII HP</b>	1.1453	0.037	-	-
<b>High Flux</b>	2.0508	0.234	-	-
<b>Turbo-EDE2</b>	0.8497	-0.306	1.5650	0.135

**Prediction of Heat Transfer on a Single-Tube Row for Partially-Wet Conditions.** The heat transfer coefficient for the dry region  $\alpha_{dry}$ , that is for the natural convection, has a negligible contribution to the calculation of  $\alpha$  for the entire surface of a partially-wet tube. Since  $\alpha_{dry} \ll \alpha_{wet}$ , the heat transfer coefficient can be simply expressed using a linear expression:

$$\alpha_{array} = F \alpha_{wet} \quad [14.7.10]$$

In this expression,  $F$  represents the fraction of the tube surface covered by liquid. Their new method for prediction of  $F$  is a simple linear relationship with respect to  $Re_{onset}$ , taking into account both the heat flux and fluid property effects:

$$F = \begin{cases} Re_{top}/Re_{onset} & \text{for } Re_{top} < Re_{onset} \\ 1 & \text{for } Re_{top} \geq Re_{onset} \end{cases} \quad [14.7.11]$$

For the all wet condition, when  $Re_{top} \geq Re_{onset}$ ,  $F = 1.0$ ; otherwise  $F < 1.0$  and decreases the heat transfer coefficient. This method is simple to use and is based on  $Re_{onset}$  calculated at each heat flux. No additional empirical constant is needed to obtain the value of  $F$ . Hence, in their new method only two fluid/tube specific empirical constants are required, much fewer than before but still not a general expression applicable without experimental single-row test data available.

Table 14.4 shows their method's accuracy versus a selection of tubes, citing the percent of the predicted values within  $\pm 30\%$  of the corresponding measured values (the uncertainty of the experimental value is

also shown for comparison). As the prediction method will in practice be primarily applied to all wet data, the prediction accuracies of the local heat transfer coefficients for partially-wet and all wet conditions are segregated in Table 14.5 within a  $\pm 20\%$  interval. As can be seen, the method works quite well for the all wet data, where the larger discrepancies come from the very highly performing tubes for which the experimental uncertainties are larger than the  $\pm 20\%$  interval.

**Table 14.4. Accuracy of the prediction method for all data (all wet plus partially-wet).**

Tube	R-134a		R-236fa	
	all	uncertainty	all	uncertainty
Plain	$89.9 \pm 30\%$	10 – 20%	$82.1 \pm 30\%$	15 – 25%
Turbo-EDE2	$77.6 \pm 30\%$	25 – 35%	$81.2 \pm 30\%$	25 – 30%
Turbo-BII HP	$90.7 \pm 30\%$	10 – 20%	-	-
High Flux	$72.2 \pm 30\%$	25 – 35%	-	-

**Table 14.5. Accuracy of the prediction method for data segregated into partially-wet and all-wet data.**

Tube	R-134a	R-236fa	partially-wet	all-wet
	partially-wet	all-wet		
Plain	$61.2 \pm 20\%$	$94.6 \pm 20\%$	$28.9 \pm 20\%$	$87.1 \pm 20\%$
Turbo-EDE2	$35.6 \pm 20\%$	$75.5 \pm 20\%$	$34.2 \pm 20\%$	$80.6 \pm 20\%$
Turbo-BII HP	$36.1 \pm 20\%$	$95.8 \pm 20\%$	-	-
High Flux	$81.5 \pm 20\%$	$30.3 \pm 20\%$	-	-

Direct comparison of the present method with other authors' data in the literature was not appropriate as those data are tube length averaged data (not local data), which may include local areas of dryout along part of the tube in the average, making it impossible to correctly analyze such data.

**Prediction of Heat Transfer on a Tube Bundle.** The falling film evaporation bundle results in Habert and Thome (2010a) were rather scattered because of: (i) a large error propagation on the measurements of such high heat transfer coefficients and (ii) the liquid maldistribution within the tube bundle that induced prematurely tripping the onset of dryout for some tubes by creating a bypass around some tubes but not others. Due to this, the prediction method proposed in Habert and Thome (2010b) was restricted to only their data for the top three tubes, as they are less affected by any non-ideal liquid distribution and performed relatively well. The typical bundle effect they observed on these three tubes is shown schematically in Figure 14.23: with decreasing film Reynolds number for a film flowing from the top of a bundle towards the bottom, the heat transfer coefficient begins at a plateau corresponding to approximately the single-row array plateau value, then increases to a peak, then falls off again to the single-plateau value, and then falls off rapidly below the onset of dryout threshold. As it was not possible to identify the mechanism creating the peak, an empirical factor B was defined that satisfactorily predicts the results from their database as follows:

$$\alpha_{\text{bundle}} = B \alpha_{\text{array}} \quad [14.7.12]$$

$$B = 1 + e \cdot \exp(-f(\text{Re}_{\text{top}} - \text{Re}_{\text{peak}})^2) \quad [14.7.13]$$

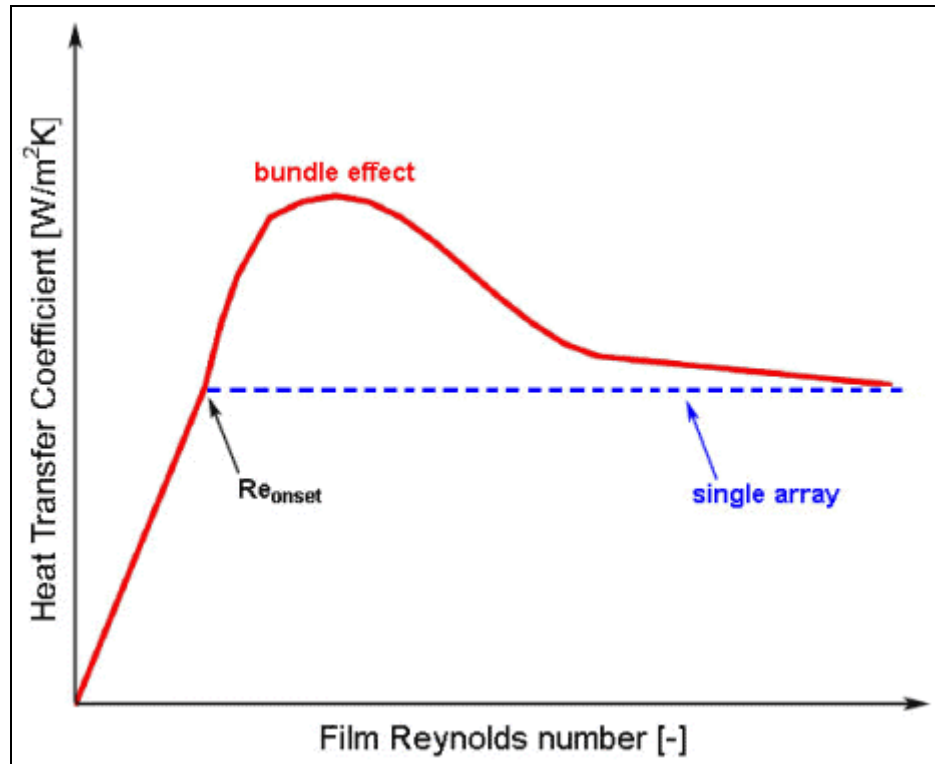


**Figure 14.23. Heat transfer trends observed for falling film evaporation on the first three rows of the tube bundle of Habert and Thome (2010b).**

This approach was applied with limited success to the plain tube results for all the database excluding the R-236fa results at 60kW/m<sup>2</sup>, in which almost all the tubes were partially-wet or nearly completely dry. Table 14.6 shows the values of e, f and Re<sub>peak</sub> for the plain tube. The method predicts both partially-wet and wet data reasonably well. The bundle factor satisfactorily predicts the peak and the subsequent decrease in heat transfer coefficient. Predicting the partially-wet data becomes less precise when increasing the heat flux, due to an increase in bubble generation causing premature local dryout. The single array prediction method (B = 1) was used for the R-134a data at 60 kW/m<sup>2</sup>, giving good prediction of the wet data. This suggests that the bundle effect tends to disappear with increasing heat flux. Future tests with more extensive data and flow visualization are required for refinement of the method and the physics of the flow.

**Table 14.6. Empirical constants e and f and the value of Re<sub>peak</sub> for the plain tube bundle prediction.**

	R-134a			R-236fa		
	e	f	Re <sub>peak</sub>	e	f	Re <sub>peak</sub>
Heat Flux						
20kW/m <sup>2</sup>	0.6	9 10 <sup>-7</sup>	800	0.8	4 10 <sup>-7</sup>	600
40kW/m <sup>2</sup>	0.2	9 10 <sup>-7</sup>	1000	0.3	4 10 <sup>-7</sup>	800

Due to the higher propagation of error on the very large heat transfer coefficients for the Turbo-EDE2 tubes, only tubes 1 and 2 could be correlated as they are the less disturbed by the non-uniformity of the liquid flow experienced on the lower tubes. For these tubes, the range of film Reynolds numbers tested was not wide enough to characterize the onset of dryout. For these all wet data, the heat transfer

performance had little influence from the film Reynolds number (similar to this tube's single-row data), and thus the bundle factor B becomes simply a non-unity constant. Table 14.7 gives the values of the bundle factor B at different heat flux conditions with their respective precision (% of data points within the indicated error interval). Interestingly, B = 1.1 for three of the four cases. Furthermore, it is interesting to note that with B = 0.6, this effectively degrades the bundle performance with respect to the single-array results by 40% while with B = 1.1 it increases performance by 10%. Their bundle method presented here is taken as a preliminary method that requires more experimental tests that includes flow visualization to investigate the flow maldistribution problem that leaves some tubes unexpectedly partially dry.

**Table 14.7. Empirical constant B for the Turbo-EDE2 bundle.**

	R-134a		R-236fa	
Heat Flux	B	Precision	B	Precision
<b>40 kW/m<sup>2</sup></b>	1.1	94.5% in $\pm 5\%$	1.1	88.9% in $\pm 20\%$
<b>60 kW/m<sup>2</sup></b>	0.6	87.5% in $\pm 10\%$	1.1	73.5% in $\pm 20\%$

Summarizing, most existing falling film evaporation prediction methods, including those above, have a quite limited range of application because they require empirical parameters obtained from experimental tests to finalize the prediction method. Furthermore, most have been developed using data for only one or two fluid/surface combination(s) at one test pressure, making their application to other situations only a qualitative guess. On the other hand, there is no general method yet for predicting falling film evaporation heat transfer coefficients and the methods noted above are applicable to R-134a for several types of tubes at the typical operation saturation temperature of 5°C.

## 14.8 SUMMARY

Falling film heat transfer under evaporating conditions is controlled by two heat transfer mechanisms: (i) the evaporating film coefficient for heat conduction and/or convection of heat through the film to the interface, and (ii) the nucleate boiling heat transfer coefficient if present in the film. Film evaporation creates vapor at the interface of the liquid film while nucleate boiling evaporates liquid within the film itself. The evaporating film coefficient can be for a thermally developing flow at the top of the horizontal tube or for a fully developed flow. The film flow can be either laminar or turbulent with or without interfacial ripples. Nucleate boiling is only present if the heat flux threshold for onset of nucleate boiling has been surpassed. Intense nucleate boiling in the film can also cause premature formation of dry patches on the surface.

Experimental heat transfer data for numerous horizontal single-tube and small horizontal tube bundles have measured for numerous fluids, such as water, iso-propanol, ethylene glycol, and refrigerants R-12, R-22, R-113, R-123 (plus oil), R-134a (plus oil), and R-717 (ammonia). These studies covered plain tubes, low finned tubes, enhanced boiling tubes and enhanced condensation tubes. Most tests were for single-tubes but some were also performed for small tube bundles.

For refrigerant R-134a and R-123 applications, the principal interest is in enhanced tube performance. Some enhanced condensation surfaces performed very well, such as the Turbo-Cii, while some enhanced boiling tubes performed better under falling film conditions with nucleate boiling in the film compared to their original pool boiling curves. The influence of oil was to increase heat transfer significantly in most cases, even for the enhanced tubes; however this positive effect tended to diminish with increasing heat flux.

The influences of film feed rate, heat flux, enhancement geometry effects, staggered or inline tube layouts, tube pitch, tube diameter, nozzle type and height above the bundle, saturation temperature, oil concentration, etc. have been investigated for heat transfer and film flow modes between tube rows. All of these are important factors in the heat transfer process and require further study before useful design guidelines can be proposed.

Numerous design methods have been proposed for falling film evaporation, with and without nucleate boiling in the film, for plain tubes. In addition, methods for identifying flow modes between vertical tube rows on plain tube and enhanced tube bundles have been developed. Heat transfer correlations for subcooled falling liquid films (i.e. without evaporation) flow down a vertical array of horizontal tubes have been proposed. A selection of these methods has been presented here. These methods so far can only predict a few of the influences of the above mentioned parameters on thermal performance and few of these proposed methods have been validated against independent data sets and none against sizable databases.

## Chapter 15

# Thermodynamics of Refrigerant Mixtures and Refrigerant-Oil Mixtures

**SUMMARY:** The principles of phase equilibrium of zeotropic mixtures are presented in an abbreviated form, including the phase diagram and preparation of enthalpy profiles for describing their evaporation (or condensation) over a temperature glide. Next the thermodynamic description of refrigerant-oil mixtures is presented, including methods to predict the local oil mass fraction, the local bubble point temperature rise caused by the oil, enthalpy changes for their evaporation (or condensation) and the effect of oil on log mean temperature differences. This chapter focuses on the thermodynamics of mixtures during their evaporation but these methods are equally applicable to condensation.

### 15.1 Introduction

A basic working knowledge of phase equilibria is required to understand the evaporation (and condensation) of zeotropic mixtures and also is an important prerequisite for the design of evaporators that properly take into account the effect of oil on thermal performance. The objective of this chapter is to provide this necessary background. Topics covered include the phase equilibrium diagram, the dew point temperature, the bubble point temperature, the boiling range or temperature glide, the phase equilibria of refrigerant-oil mixtures, enthalpy curves for mixtures and a few other concepts important to the subject. For a more detailed introduction to phase equilibria, the reader is referred to Chapter 12 in Collier and Thome (1994, 1996). Instead, for a comprehensive treatment of prediction of phase equilibria, numerous chemical engineering textbooks are available, such as that by Prausnitz (1969), or can be found in the chapter by Smith, Block and Hickman (1963) appearing in the Chemical Engineer's Handbook (available in more recent editions).

A zeotropic mixture refers to a mixture whose components have different mass fractions in the liquid phase than in the vapor phase at equilibrium conditions. An example of such a mixture is R-407C, which has three components. In contrast, an azeotropic mixture refers to a mixture whose components have the same compositions in both phases. A well-known example is refrigerant R-502, which is a binary refrigerant mixture at the azeotropic composition of its two components. An azeotropic fluid functions just like a pure fluid and hence pure fluid design methods can be applied. Instead, a zeotropic mixture evaporates (or condenses) over a temperature range and hence this must be taken into account in thermal design methods.

A refrigerant-oil mixture functions as an azeotropic mixture in which the refrigerant (either a pure refrigerant such as R-134a or a zeotropic mixture such as R-407C) is combined with a miscible, lubricating oil. The oil for our purposes here can be considered to be one component in such a mixture, even though normally lubricating oil is a multi-component mixture including various additives, long-chain molecules, etc. In this chapter, only refrigerant-oil mixtures that are completely miscible will be considered. These mixtures act as zeotropic mixtures and the refrigerant and oil are miscible in the liquid phase. Some refrigerant-oil mixtures are not miscible, which means they do not mix together in equilibrium conditions, such as is also true for water and oil. Immiscible refrigerant-oil mixtures are not addressed here. One must be careful, however, as some refrigerant-oil mixtures are miscible only within a certain range of temperature or up to a certain oil mass fraction, so that part of the refrigerant cycle or test facility fluid loop may pass outside the miscible range.

## 15.2 Simple Principles of Phase Equilibrium

This section presents a very brief description of the thermodynamics of zeotropic mixtures. For a more extensive treatment, refer to a chemical engineering handbook or textbook. The following discussion is for a binary mixture, i.e. a mixture with two different fluids for its components. These ideas can be extended to ternary mixtures and multi-component mixtures in general.

### 15.2.1 Phase Equilibrium Diagram

Phase equilibriums of binary mixtures are represented on phase diagrams. Figure 15.1 depicts a phase diagram for a binary mixture system at constant pressure. Temperature is plotted along the vertical axis while vapor and liquid compositions are plotted along the horizontal axis, in this case shown in mole fractions. The dew point line represents the dew point temperatures of all the possible mixture compositions, where  $T_{\text{dew}}$  is defined as the temperature at which a superheated vapor mixture will first begin to condense upon cooling. The bubble point line represents the bubble point temperatures of all the possible mixture compositions, where  $T_{\text{bub}}$  is defined as the temperature at which a subcooled mixture will first begin to evaporate upon heating. The composition of one of the components, in this case the component with the lowest boiling point, is depicted on the lower axis, where the equilibrium vapor composition Y is that which corresponds to the liquid composition X at the same temperature.

In Figure 15.1 the saturation temperature of one pure component is on the left vertical axis while that of the other component is on the right vertical axis. The boiling point temperatures for evaporation of the mixtures correspond to the bubble point line. The condensing temperatures for condensation of the mixtures correspond to the dew point line. The temperature difference between the dew point temperature and the bubble point temperature for a specific liquid composition is defined as the *boiling range* (BR =  $T_{\text{dew}} - T_{\text{bub}}$ ). For evaporation of a mixture, the parameter BR is used in modeling the effect of mass transfer. The boiling range is also referred to as the *temperature glide* in literature referring to zeotropic refrigerant mixtures.

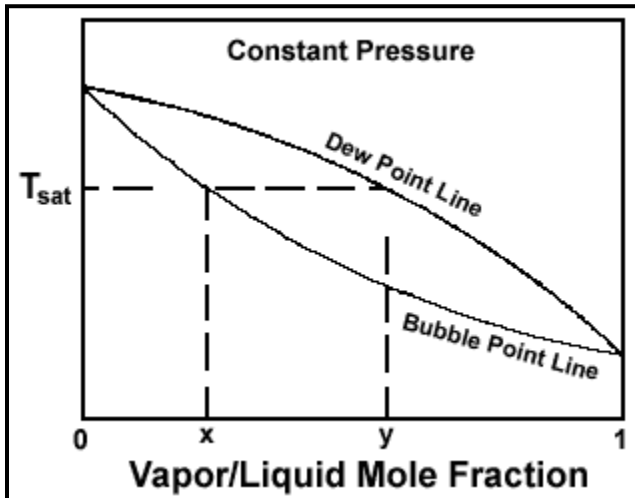


Figure 15.1. Phase equilibrium diagram at constant pressure for a binary mixture.

### 15.2.2 Definition of Mixture Compositions and Components

On a phase diagram, the compositions can be depicted in units of mass fraction, mole fraction or volume fraction. Refrigerant-oil mixtures are usually referred to in ASHRAE publications in terms of *weight fraction* or weight percent, where the first of these is a colloquial term for *mass fraction*. The mass fraction of a component is defined as its mass in kg (or lb.) divided by the total mass of the mixture in kg (or lb.), respectively, in a particular phase (liquid or vapor). For instance, if a liquid refrigerant-oil mixture weighs 10.0 kg (11.0 lb.) and the oil in this mixture is measured to weigh 0.5 kg (1.1 lb.), then the mass fraction of the oil in the mixture is 0.05 and its mass percent is 5.0%. The mass fraction of the refrigerant is thus 0.95 (i.e. 1.0-0.05) and its mass percent is 95.0%.

Referring again to the phase diagram in Figure 15.1, the more volatile component (also referred to as the lighter component) is defined as the fluid that has the lower boiling point temperature at the pressure of the diagram. This is the fluid with its saturation temperature on the right vertical axis in Figure 15.1. This fluid is more volatile in the sense that this component is always above its normal boiling point. For a refrigerant-oil mixture, the refrigerant will always be the more volatile component since the boiling point temperatures of lubricating oils are in the range from 300 °C to 510 °C (570-950°F), and are thus much larger than those of refrigerants. Hence, the oil will be the less volatile component (also referred to as the heavier component).

For the present situation, a refrigerant-oil mixture can be considered as a zeotropic binary mixture, which is a mixture with two components that does not form an azeotrope. One component is the pure refrigerant, be it R-134a, R-22, or any other single-component refrigerant (R-123, R-125, ammonia, etc.) and the second component is the oil. Even though lubricating oils are multi-component blends of oil plus additives, for the present purposes it is more than adequate to consider them here as a single component fluid.

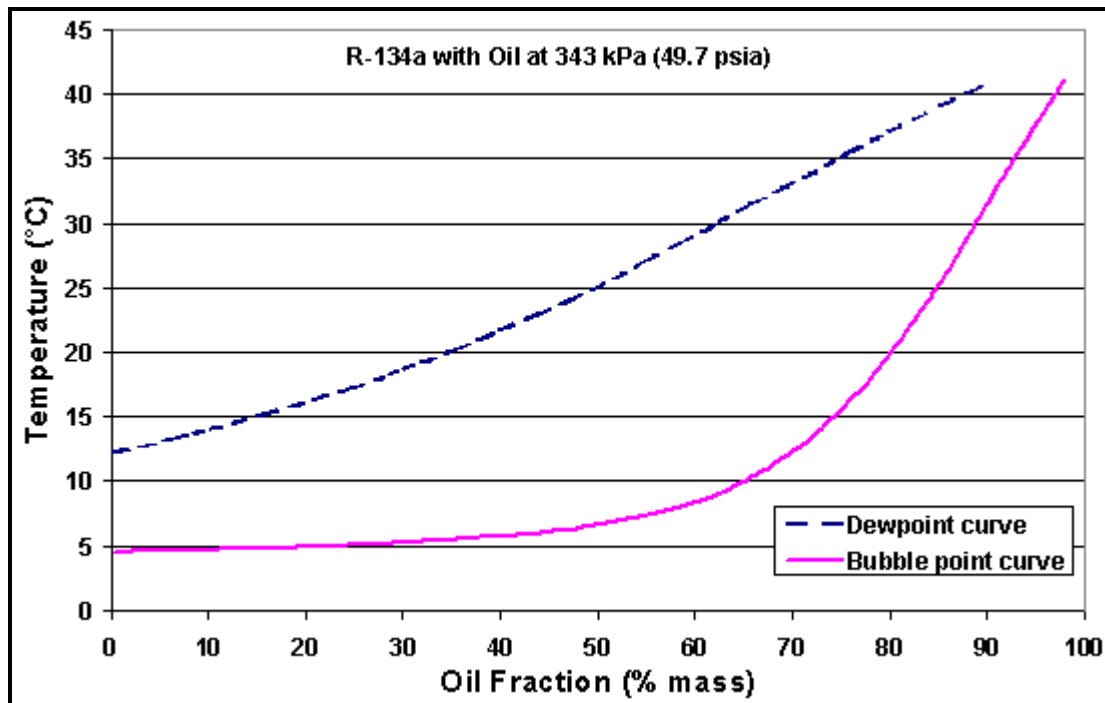


**Figure 15.2. Phase equilibrium diagram for a binary mixture of R-134a and oil at a pressure of 3.43 bar (49.7 psia).**

Figure 15.2 depicts an approximate phase diagram for R-134a mixed with Mobil Arctic EAL 68 lubricating oil at 3.43 bar (49.7 psia). In this case, the horizontal axis shows the oil composition in mass %. At the left axis of the diagram, the saturation temperature of pure R-134a is 4.44°C (40°F). Near the right axis, the dew and bubble point temperatures rise rapidly towards the saturation temperature of the pure oil (not shown), which is in the neighborhood of 350°C (662°F). The bubble point curve is nearly horizontal with a slightly upward slope from left to right at low oil compositions. It then begins to rise more rapidly at intermediate compositions and then rises rapidly when above 70 mass % oil. The actual location of the dew point curve is not known for refrigerant-oil mixtures; it was drawn assuming negligible amounts of oil enter the vapor phase at liquid oil compositions below 70 mass %, i.e. the part of the dew point line on the left y-axis at 0.0 mass % oil. Above this value its composition is represented

here by a simple extrapolation towards the pure oil value. The method for predicting the bubble point curve shown here is given later in this Chapter.

### 15.2.3 Piston-and-Cylinder Analogy for a Binary Mixture

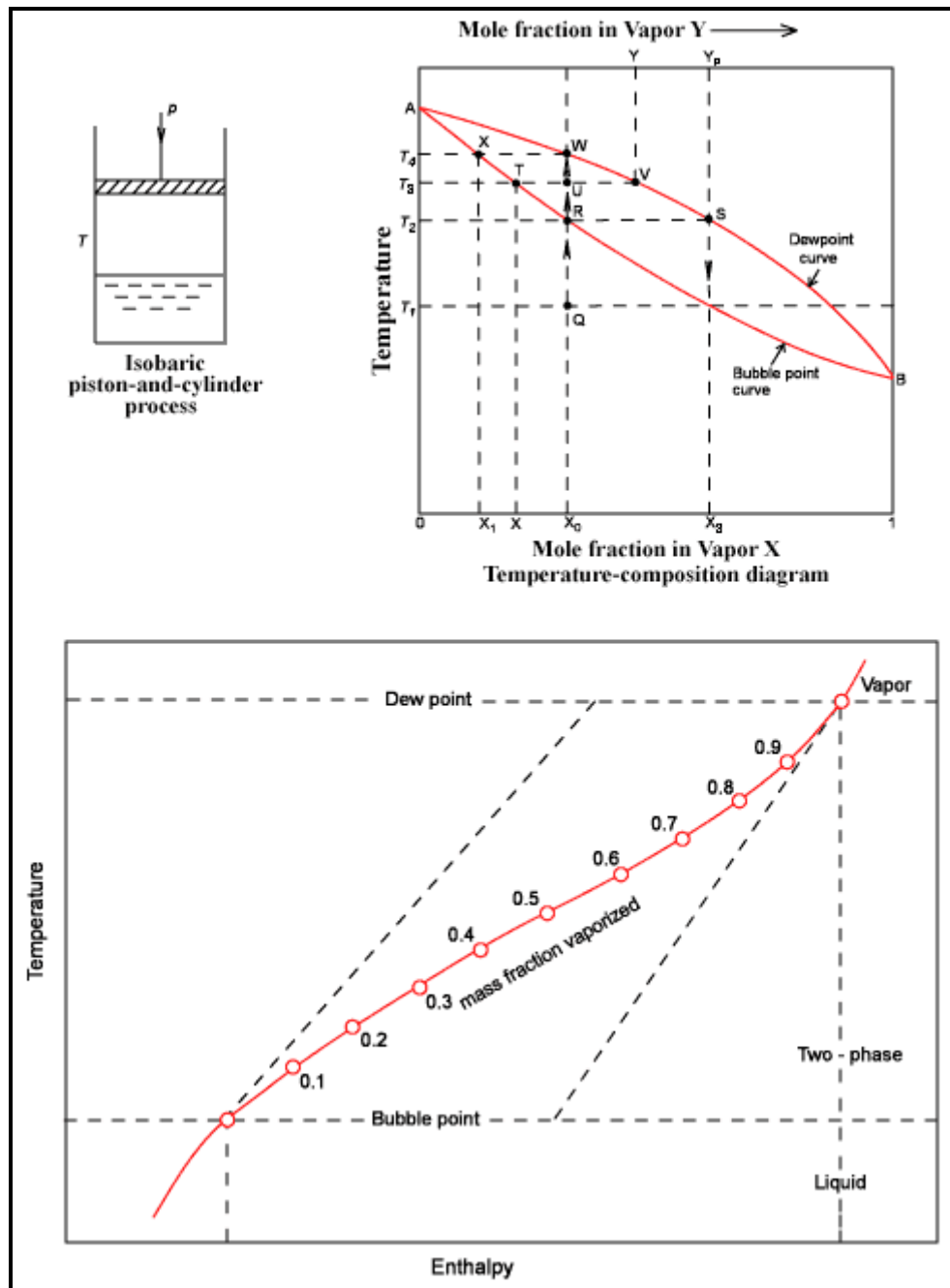


**Figure 15.3. Isobaric process path and enthalpy curve of a binary mixture.**

To better illustrate these concepts, consider now a situation excerpted from Collier and Thome (1994, 1996). Figure 15.3 shows a piston-and-cylinder setup that contains a binary liquid mixture whose mole fraction of the more volatile component is  $X_0$  and which is held at a fixed pressure of  $p$  and temperature of  $T_1$ . What happens to the liquid mixture as it evaporates is conveniently depicted on the temperature-

composition phase diagram at the right, where the mole fraction of the more volatile component is plotted along the horizontal axis and the temperature of the mixture on the vertical axis. Denoting the initial conditions in the vessel by point Q, the piston-and-cylinder is now heated under constant pressure maintaining an isothermal temperature throughout the vessel. When the temperature  $T_2$  is reached, liquid will begin to evaporate at point R. The vapor formed at temperature  $T_2$  has a composition  $Y_o$  as shown by point S. This vapor is richer in the more volatile component than the liquid. If this procedure is repeated for the complete range of initial liquid compositions, then a series of points R, T and X will be found. The locus of the curve formed by points AXTRB is known as the bubble point curve and the curve formed by points AWVSB is the dew point curve.

If the vessel is heated above point R, the composition of the liquid will change because of the loss of some of its more volatile component to the vapor. The boiling point temperature will rise to some new temperature  $T_3$  and the compositions in both the liquid and vapor phases will change, both becoming richer in the less volatile component represented by points T and V, respectively. Since no material is lost, the relative volumes occupied by the two phases also change during this process; the volume occupied by the liquid decreases while that of the vapor increases. On still further heating to temperature  $T_4$ , all the liquid is evaporated and the vapor in the vessel at point W has the same composition as the original liquid  $X_o$ . The last drop of liquid in the vessel disappears at the temperature  $T_4$  with a composition of  $X_1$ , indicated by point X on the phase diagram, and is very rich in the less volatile component.

During this experiment the amount of heat added to the system could be noted. In addition, there is a clear analogy between this isobaric evaporation process in the piston-and cylinder chamber and evaporation of a refrigerant-oil mixture inside an evaporator tube. Similar to evaporation of the liquid mixture in the vessel, a refrigerant-oil mixture will evaporate along its bubble point curve. However, since essentially none of the oil enters the vapor phase because of the extremely low vapor pressure of the oil relative to the refrigerant (on the order of one millionth that of the refrigerant), the situation is simplified. Thus, as one moves along an evaporator tube from the inlet towards the outlet, the local oil mass percent in the remaining liquid increases, the vapor phase composition remains pure refrigerant, and the local boiling point temperature  $T_{bub}$  increases. The amount of heat necessary to evaporate the refrigerant-oil mixture is therefore equal to the sensible heating of the liquid and vapor phases caused by the increase in the bubble point temperature along the tube plus the latent heat for vaporizing the refrigerant from the liquid to the vapor phase. These points will be discussed in more detail in the following sections.

#### **15.2.4 Oil "Contamination" Approach**

Until recently, a small fraction of lubricating oil in a refrigerant charge has been treated by refrigeration and air-conditioning system manufacturers as a contaminant in an otherwise pure refrigerant. Thus, pure refrigerant saturation temperatures and properties have been utilized for determining heat transfer coefficients while the oil composition has been considered an independent "contamination" parameter. In practice, this means that during flow boiling experiments with oil to determine local heat transfer coefficients, the local wall temperature difference ( $T_w - T_{sat}$ ) has been determined using  $T_{sat}$  from the vapor pressure curve of the pure refrigerant and the measured pressure, where  $T_w$  is the inner tube wall temperature.

This oil "contamination" approach has hindered a better understanding of the problem and created a roadblock to development of accurate generalized design methods. The reason for this is that the "contamination" approach is not thermodynamically correct. That is, it ignores the influence of the oil on the boiling point temperature, specific heat, latent heat, viscosity, density, etc. This in turn alters energy balances, local boiling temperature superheats, local vapor qualities and so on in the data reduction process to calculate heat transfer coefficients and two-phase pressure drops. To put this approach in

perspective, it is analogous to assuming that a zeotropic refrigerant mixture, such as R-407C, may be modeled using the vapor pressure curve of only one of its three components, say R-134a. Clearly that is not correct thermodynamically. Thus, the "contamination" approach will not lead to a resolution of the long-standing problem of how to model the influence of oil on flow boiling of refrigerants.

### 15.2.5 Thermodynamic Approach to Modeling Refrigerant-Oil Mixtures

The thermodynamically correct approach is to treat the refrigerant-oil mixture as the real mixture that it in fact is. This will be referred to as the Thermodynamic Approach. It requires methods to determine the boiling point temperature and enthalpy changes during evaporation (or condensation). Methods for doing this are now available from Thome (1995) and are presented in the next section. The additional complexity is not that great since the oil remains very predominately in the liquid phase (the vapor pressures of lubricating oils are on the order of one-millionth that of refrigerants) and hence its composition in the vapor phase is negligible and happily does *not* have to be predicted. Consequently, dealing with a refrigerant-oil mixture is in this context easier than modeling zeotropic refrigerant mixtures, whose vapor-phase compositions change as the azeotrope evaporates along an evaporator tube.

## 15.3 Thermodynamics of Refrigerant-Oil Mixtures

### 15.3.1. Definition of Boiling Heat Transfer Coefficient

To include oil effects correctly in measuring and modeling flow boiling coefficients, the local bubble point temperature and the temperature-enthalpy-vapor quality ( $T-h-x$ ) relationship have to be calculated. They are then used in determining the local temperature differences and energy balances, and hence the local vapor quality, analogous to how these concepts are applied to zeotropic refrigerant mixtures. Adding miscible oil to a refrigerant increases the bubble point temperature at which the fluid evaporates.

The boiling heat transfer coefficient  $\alpha$  is defined as

$$\alpha = \frac{q}{T_w - T_{bub}} \quad [15.3.1]$$

where  $q$  is the heat flux through the wall to the evaporating fluid,  $T_w$  is the wall temperature and  $T_{bub}$  is the bubble point temperature of the fluid. Since the value of  $T_{bub}$  for a refrigerant-oil mixture is higher than  $T_{sat}$  for the pure refrigerant, reducing raw test data in this correct manner (rather than reducing it using  $T_{sat}$  as has been incorrectly but widely done in the past) results in an increase in the heat transfer coefficient. On the other hand, use of  $T_{bub}$  rather than  $T_{sat}$  for the pure refrigerant in an incremental log mean temperature difference (LMTD) calculation for an evaporator will decrease the value of the LMTD, which partially compensates for the larger boiling coefficient when using  $T_{bub}$  in the definition of  $\alpha$ . In any case, it should be remembered that the difference between using  $T_{bub}$  or  $T_{sat}$  typically only becomes significant when reducing test data at vapor qualities greater than about 80%. Thome (1995) presented a detailed discussion of the thermodynamic effects on boiling points and enthalpy caused by oil and these are discussed below.

### 15.3.2. Bubble Point Temperatures

Takaishi and Oguchi (1987) proposed the following empirical method to predict bubble point temperatures for a specific lubricating oil mixed with R-22 based on their measurements:

$$\ln(p_{\text{sat}}) = [A/T_{\text{bub}}] + B \quad [15.3.2]$$

where  $p_{\text{sat}}$  is the saturation pressure in MPa and  $T_{\text{bub}}$  is the bubble point temperature in K. Rearranging [15.3.2] in order to calculate the bubble point temperature for a given saturation pressure and oil mass fraction, it becomes:

$$T_{\text{bub}} = A / [\ln(p_{\text{sat}}) + B] \quad [15.3.3]$$

The amount of oil in the liquid-phase is given by  $w$ , i.e. in mass *fraction*, not mass *percent*. A and B are given by the following empirical expressions:

$$A = a_0 + a_1 w + a_2 w^3 + a_3 w^5 + a_4 w^7 \quad [15.3.4]$$

$$B = b_0 + b_1 w + b_2 w^3 + b_3 w^5 + b_4 w^7 \quad [15.3.5]$$

where the values of the empirical constants are:

$a_0 = -2394.5$	$b_0 = 8.0736$
$a_1 = 182.52$	$b_1 = -0.72212$
$a_2 = -724.21$	$b_2 = 2.3914$
$a_3 = 3868.0$	$b_3 = -13.779$
$a_4 = -5268.9$	$b_4 = 17.066$

Evaluating [15.3.3] at a saturation pressure of 0.55 MPa (79.8 psia), Table 15.1 depicts the effect of oil mass fraction on the bubble point temperature for R-22 mixed with various mass fractions of oil. The right column shows the difference between the bubble point temperatures of the mixtures and the saturation temperature of pure R-22 ( $T_{R-22}$ ) at this pressure.

**Table 15.1. Bubble point temperatures of R22/oil mixtures at 0.55 MPa (79.8 psia).**

w (mass fraction)	$T_{\text{bub}}$ (°C)	$T_{\text{bub}} - T_{R-22}$ (°C)	w (mass fraction)	$T_{\text{bub}}$ (°C)	$T_{\text{bub}} - T_{R-22}$ (°C)
0.00	2.99	0.00	0.09	3.17	0.18
0.01	3.01	0.02	0.10	3.19	0.20
0.02	3.03	0.04	0.20	3.44	0.45
0.03	3.04	0.05	0.30	3.79	0.80
0.04	3.06	0.07	0.40	4.31	1.32
0.05	3.09	0.10	0.50	5.25	2.26
0.06	3.11	0.12	0.60	7.22	4.23
0.07	3.13	0.14	0.70	11.53	8.54
0.08	3.15	0.16	0.80	[19.95]	[16.96]

[] - Extrapolated value.

Thome (1995) generalized the above method for application to refrigerants other than R-22 and also temperatures outside the original experimental range. This was accomplished by replacing the original values of  $a_0$  and  $b_0$  that are specifically for R-22 with new ones for the desired refrigerant, such as R-134a. Since the vapor pressure of oil is very small compared to that of the refrigerant, it was demonstrated that the effect of the specific type of oil on the empirical constants  $a_1$  to  $a_4$  and  $b_1$  to  $b_4$  is negligible for oil

fractions below 0.50 of oil (50% mass). Rather than using fixed values of  $a_o$  and  $b_o$  for a particular pure refrigerant, an accurate equation of state for the pure refrigerant vapor pressure curve is used to determine the values of  $a_o$  and  $b_o$  at the specified saturation pressure instead of the simple Antoine expression, i.e. [15.3.2]. Using these new values of  $a_o$  and  $b_o$ , [15.3.2] and [15.3.3] are now accurate for predicting saturation temperatures and bubble point temperatures over narrow temperature ranges for essentially any miscible mixture of commonly used refrigerants and oil. Thome (1997b) [also see Zürcher, Thome and Favrat (1998b)] has also applied this method to zeotropic refrigerant blends mixed with miscible oils (in particular R-407C/oil mixtures) and showed that it accurately matched experimental measurements over a wide range of oil mass fractions.

The procedure to use the expression [15.3.3] for any refrigerant is thus:

- Determine the pure refrigerant saturation temperature and pressure just above and just below the design pressure with an accurate equation-of-state of the user's choice;
- Use these two sets of values for  $T_{bub}$  and  $p_{sat}$  to solve for  $a_o$  and  $b_o$  in [15.3.3] with  $w$  set to zero. The solution is straightforward with two equations and two unknowns.
- These new values of  $a_o$  and  $b_o$  replace those of  $a_o = -2394.5$  and  $b_o = 8.0736$  for R-22, respectively. All the other values of  $a_1$  to  $a_4$  and  $b_1$  to  $b_4$  remain the same since they only refer to the effect of the oil on  $T_{bub}$ .
- Equations [15.3.3], [15.3.4] and [15.3.5] are then evaluated for the desired oil mass fraction,  $w$ , to obtain  $T_{bub}$  for the desired value of  $p_{sat}$  and  $w$ ; instead,  $p_{sat}$  can be obtained for specified values of  $T_{bub}$  and  $w$  using [15.3.2], [15.3.4] and [15.3.5].

### 15.3.3 Local Oil Mass Fractions

Preparation of a T-h-x (temperature-enthalpy-vapor quality) curve and determination of local thermodynamic and transport properties of refrigerant-oil mixtures require knowledge of the local oil mass fraction in the liquid at locations along the evaporator tube. From a thermodynamic viewpoint, the ideal evaporation process is infinitesimally slow such that thermodynamic equilibrium exists and consequently the liquid phase has a uniform oil mass fraction and temperature at any cross-sectional location along the tube. Enthalpy curves are prepared assuming that thermodynamic equilibrium exists throughout the process, exactly the same as assumed for evaporating a pure fluid.

The liquid-phase mass fraction of the oil circulating in a refrigeration system is a function of its location in the system. Thus, to unequivocally define this mass fraction, a point is chosen where all the circulating fluid is in the liquid-phase, which occurs in the refrigerant line between the exit of the condenser and the entrance into the expansion valve or expansion device. The oil mass fraction at this location is defined as  $w_{inlet}$ . When the local vapor quality  $x$  is 0.0, the local oil mass fraction  $w$  is equal to  $w_{inlet}$ . If all the refrigerant could be evaporated out of the liquid-phase, then the local vapor quality  $x$  would be equal to  $(1-w_{inlet})$  at that point since all of the refrigerant would be in the vapor-phase and all the oil in the liquid-phase;  $w$  would be equal to 1.0 at this point since only oil remains in the liquid-phase. Hence, the maximum exit vapor quality is equal to  $(1-w_{inlet})$ . This is an important limiting point to remember in designing a system with say 3 (% mass) oil, since the exit vapor quality from the evaporator has to be less than 0.97. Also, for refrigerant-oil flow boiling experiments the maximum outlet vapor quality must be less than  $(1-w_{inlet})$ .

From a design viewpoint, the local oil mass fraction as a function of vapor quality is required. The expression that relates the local oil mass fraction,  $w$ , to the local vapor quality,  $x$ , and the inlet oil mass fraction  $w_{inlet}$  is obtained from a conservation of mass and is a simple expression:

$$w = w_{\text{inlet}} / (1 - x) \quad [15.3.6]$$

As an illustration, assume that 100 g of refrigerant-oil mixture enters the expansion valve with an inlet oil mass fraction,  $w_{\text{inlet}}$ , equal to 0.05 (thus, there are 5 g of oil and 95 g of refrigerant):

1. Before the expansion valve the local vapor quality is 0.0 and  $w = w_{\text{inlet}} = 0.05$  as indicated by [15.3.6];
2. For a local vapor quality equal to 0.20 immediately after the expansion valve,  $w$  is 0.0625 [i.e.  $0.05/(1-0.20)$ ];
3. For a local vapor quality of 0.90,  $w$  is 0.50 or 50 mass % oil, i.e.  $[0.05/(1-0.90)]$ ;
4. If the entire refrigerant was evaporated from the liquid mixture, the local vapor quality would be  $(1 - w_{\text{inlet}})$  or 0.95 and [15.3.6] appropriately predicts that  $w$  for this situation is 1.0 [i.e.  $0.05/(1-0.95)$ ].

### 15.3.4 Enthalpy Curves

The change in enthalpy  $dh$  of a mixture during evaporation is referred to as the enthalpy curve. The change in  $dh$  with respect to  $h_L$  for completely saturated liquid, i.e. with respect to  $h$  at  $x = 0$ , as the bubble point temperature rises is comprised of three contributions:

- The latent heat to the fraction of liquid vaporized,  $x$ ;
- The sensible heat to the fraction of fluid in the liquid phase ( $1-x$ );
- The sensible heat to the fraction of fluid in the vapor phase  $x$ .

In mathematical terms for a refrigerant-oil mixture this is:

$$dh = h_{LG}x + (1-x)dT_{\text{bub}}c_{pL} + xdT_{\text{bub}}c_{pG} \quad [15.3.7]$$

where  $x$  is the local vapor quality,  $h_{LG}$  is the latent heat of vaporization of the pure refrigerant since no oil enters the vapor-phase,  $c_{pL}$  is the specific heat of the liquid-phase refrigerant-oil mixture and  $c_{pG}$  is the specific heat of the pure refrigerant vapor. The values of  $h_{LG}$  and  $c_{pG}$  are obtained from equations for the pure refrigerant at the local saturation temperature while  $c_{pL}$  is a function of the local oil composition and bubble point temperature. Equation [15.3.7] reduces to only the latent heat for a pure refrigerant without oil.

A heat release curve is not actually implemented as a curve. Instead, it is prepared as a table of values at set intervals of temperature or vapor quality that gives the amount of heat absorbed by the fluid per unit mass (i.e.  $dh$  is in J/kg or Btu/lb) relative to its inlet state together with the bubble point temperature and vapor qualities that correspond to these points.

At a standard evaporation temperature of 4.44°C (40°F) in a refrigeration system, for pure R-134a this corresponds to a saturation pressure of 3.43 bar (49.7 psia) absolute. For a mixture with 3 (% mass) oil in R-134a at this saturation pressure, Table 15.2 lists the enthalpy curve in tabular form at this pressure covering the vapor quality range from 0.15 to 0.95 utilizing the method of Thome (1995). The oil is Mobil Arctic EAL 68 whose density is 971 kg/m<sup>3</sup> (60.7 lb/ft<sup>3</sup>) at 15.56°C (60°F) {Note: the oil's density is utilized to predict its liquid specific heat, cf. Thome (1995) and thus that of the refrigerant-oil mixture}. The first column in Table 15.2 shows the local vapor quality intervals along the evaporator tube. The next two columns list  $T_{\text{bub}}$  and  $w$ . The total heat absorbed relative to the inlet condition is shown in the 4<sup>th</sup> column (in kJ/kg). The contributions of the heat absorbed as latent heat  $dh_{\text{latent}}$  and as sensible heating of the liquid and vapor  $dh_{\text{sensible}}$  are given in the last two columns (in kJ/kg), respectively. As can be seen, the rise in the bubble point temperature and oil mass fraction in the liquid is most rapid at high vapor

qualities. The contribution of sensible heat is important at high vapor qualities since its effect is directly dependent on the rise in  $T_{bub}$ .

**Table 15.2. An enthalpy curve for R-134a/3 (% mass) oil mixture at 3.43 bar.**

x	$T_{bub}$ (°C)	w	$dh_{total}$ (kJ/kg)	$dh_{latent}$ (kJ/kg)	$dh_{sensible}$ (kJ/kg)
0.150	4.509	3.53	0.00	0.00	0.00
0.230	4.516	3.90	15.64	15.63	0.01
0.310	4.525	4.35	31.28	31.26	0.02
0.390	4.536	4.92	46.92	46.29	0.03
0.470	4.550	5.66	62.56	62.51	0.05
0.550	4.570	6.67	78.20	78.13	0.07
0.630	4.598	8.11	93.85	93.75	0.10
0.710	4.643	10.34	109.52	109.37	0.15
0.790	4.729	14.29	125.23	124.99	0.24
0.870	4.954	23.08	141.05	140.59	0.46
0.950	8.289	60.00	159.76	156.07	3.69

Table 15.2 also illustrates the influence of oil on  $T_{bub}$  with respect to the pure refrigerant (R-134a) saturation temperature  $T_{sat}$  of 4.44°C (40°F). For  $x < 0.50$ , the increase in boiling point tends to be 0.1°C (0.2°F) or less, for  $0.50 < x < 0.80$ , the rise increases up to about 0.3°C (0.54°F), and for  $x > 0.80$  the elevation of the boiling point can become very significant (3.845°C or 6.921°F at  $x = 0.95$  in Table 15.2!). The temperature difference between  $T_{bub}$  and  $T_{sat}$  depends on the local vapor quality and the inlet oil mass fraction.

For refrigerant-oil mixtures, it is preferable to use set intervals of vapor quality for determining the points on a heat release curve rather than set intervals of temperature. If an evaporator is to be designed with an inlet vapor quality after the expansion valve of 0.20 and an outlet vapor quality of 0.90, then the heat absorbed and bubble point temperatures might be determined at vapor qualities of 0.20, 0.30, 0.40, 0.50, 0.60, 0.70, 0.80 and 0.90. The heat absorbed at  $x = 0.20$  would be zero and would serve as the datum for the other values. In practice, the number of intervals to use is up to the designer and should be sufficient to accurately represent the heat release curve and also the variation in the two-phase heat transfer coefficient as a function of vapor quality. Normally eight to ten intervals are recommended, but more can be used as desired.

For refrigerant-oil mixtures, the following procedure is used for preparation of a heat release curve at a fixed, isobaric pressure:

1. Select the desired pressure  $p_{sat}$  and inlet oil mass fraction before the expansion valve,  $w_{inlet}$ .
2. Determine two sets of pure refrigerant saturation temperature and pressure just above and just below  $p_{sat}$  with an accurate equation-of-state;
3. Use these two sets of values for  $T_{bub}$  and  $p_{sat}$  to solve for  $a_o$  and  $b_o$  with  $w$  set to zero from the two equations and two unknowns.
4. The new values of  $a_o$  and  $b_o$  are used in place of  $a_o = -2394.5$  and  $b_o = 8.0736$ , respectively. All the other values of  $a_1$  to  $a_4$  and  $b_1$  to  $b_4$  remain the same.

5. Choose the inlet vapor quality, the exit vapor quality (always less than the value of  $1-w_{inlet}$ ), and the number of design intervals desired (for example, if the evaporator is divided into ten heat transfer zones, then 11 points are needed in the heat release curve).
6. Calculate the local oil fractions corresponding to the local vapor qualities using [15.3.6] (for example, determine  $w$  for each of the eleven vapor quality points above).
7. Calculate the local bubble point temperatures corresponding to the local vapor qualities and local oil mass fractions at each point.
8. Calculate the values of  $h_{LG}$  and  $c_{PG}$  at these bubble point temperatures using methods for pure refrigerants. Determine the liquid specific heat of the refrigerant-oil mixture  $c_{pL}$  for each point based on the local values of  $w$  and  $T_{bub}$  using [15.4.1] and [15.4.2].
9. Determine the heat absorbed by the refrigerant-oil fluid in each interval,  $dh$ , and then add these up to obtain the total heat absorbed per unit mass of fluid from inlet to outlet.

The heat release curve preparation is now complete and the following values required for thermal design of the evaporator are known at each local vapor quality  $x$ :  $w$ ,  $T_{bub}$  and  $dh$ .

## 15.4 Liquid Specific Heats of Oils and Refrigerant-Oil Mixtures

### 15.4.1 Liquid Specific Heat of Lubricating Oils

Liquid specific heats of lubricating oils are often not available from their manufacturers; hence a general correlating equation is required for their estimation. Based on a literature search, Thome (1995) recommended the following equation cited by Liley and Gambill (1973) for predicting liquid specific heats of petroleum oils, specified to be accurate to within 5%:

$$(c_{pL})_{oil} = 4.186 \{ [0.388 + 0.00045(1.8T + 32)] / s^{1/2} \} \quad [15.4.1]$$

where the liquid specific heat  $(c_{pL})_{oil}$  is in units of  $\text{kJ/kg}^\circ\text{C}$ , the temperature of the oil,  $T$ , must be in  $^\circ\text{C}$  (valid for  $-18 < T < 204^\circ\text{C}$ ) and  $s$  is the liquid specific gravity at  $15.56^\circ\text{C}$  ( $60^\circ\text{F}$ ) and is valid for  $0.75 < s < 0.96$ . Literature furnished by manufacturers of lubricating oils usually provides the density or specific gravity of the oil at a temperature of  $60^\circ\text{F}$  ( $15.56^\circ\text{C}$ ). Thus, application of [15.4.1] for general use for lubricating oils presents no problem. In preparation of a heat release curve, the temperature,  $T$ , in [15.4.1] is the bubble point temperature  $T_{bub}$  for the local vapor quality in question.

The above correlation compares well with tabular values for engine lubricating oil in Incropera and DeWitt (1981), giving maximum deviations of -2% and +7%. This equation has also been double-checked against numerous heavy hydrocarbons and viscous commercial heat transfer fluids with good results over the temperature range of interest for lubricating oils. Thus it should be sufficiently accurate since liquid sensible heat normally only contributes a small fraction of the total heat absorbed by an evaporating refrigerant-oil mixture.

Some lubricating oils have a specific gravity as high as 1.05, i.e. not very far outside the range cited by Liley and Gambill, and use of [15.4.1] is still recommended in the absence of values from the

manufacturer. As an example calculation, consider an oil at 4.44°C (40°F) with a specific gravity of 0.890 at 15.56°C (60°F). Equation [15.4.1] predicts the liquid specific heat to be 1.80 kJ/kg°C (0.43 Btu/lb°F). In comparison, the values for R-134a and R-22 at 4.44°C (40°F) are 1.354 and 1.187 kJ/kg°C, respectively (0.323 and 0.283 Btu/lb°F).

### 15.4.2 Liquid Specific Heat of Refrigerant-Oil Mixtures

For preparation of a heat release curve, the liquid specific heat of the refrigerant-oil mixture is required at each local vapor quality as a function of oil fraction,  $w$ , and bubble point temperature,  $T_{bub}$ . In the absence of experimental data, the only practical approach for predicting specific heats of liquid mixtures is to weigh the single-component values by their mass fractions, according to Liley and Gambill (1973). Thus, heats of mixing are ignored, unless specific information is available, and ideal mixing is assumed. Sophisticated methods in the literature involving corresponding states cannot be applied because the molecular weight of the oil and its critical properties are not known.

Working in the units of kJ/kgK (Btu/lb°F), a linear mixing law based on mass fractions of liquid phase is used. For liquid specific heats the mixture expression is

$$c_{pL} = w(c_{pL})_{oil} + (1-w)(c_{pL})_{ref} \quad [15.4.2]$$

The above equation is evaluated with the refrigerant and oil properties at the local bubble point temperature of the mixture. For example for 30 mass % oil ( $w = 0.30$ ), if the specific heat at 4.44°C for the oil is 1.80 kJ/kgK while that of R-22 is 1.187 kJ/kgK, then the liquid specific heat of the mixture is 1.371 kJ/kgK [= 0.3 (1.80) + (1.0-0.3)(1.187)].

## 15.5 Example of Application of Thermodynamic Approach

Using the new Thermodynamic Approach, Table 15.3 shows a temperature-enthalpy curve in tabular form calculated for R-134a mixed with 5 mass % oil. The oil is Mobil Arctic EAL 68 whose properties are: specific gravity of 0.971 at 15°C, viscosities of 62.5 and 8.1 mm<sup>2</sup>/s at 40°C and 100°C, respectively, and assumed molecular weight of 590) at the isobar of 2.93 bar (where  $T_{sat} = 0.0^\circ\text{C}$  for pure R-134a at this pressure). Column one gives the local vapor qualities used in the calculation while columns 2 and 3 list the calculated bubble point temperatures and local oil mass fractions,  $w$ . The total heat absorbed by the fluid  $dh_{total}$  (in kJ/kg of flowing fluid) is given in column 4 while the next two columns show the individual contributions of latent heat  $dh_{latent}$  and sensible heat  $dh_{sensible}$ .

As can be observed, the bubble point temperature at first increases slowly relative to  $T_{sat}$  of pure R-134a and then rises rapidly at vapor qualities above 0.80. For  $x < 0.90$ , the contribution of sensible heat is less than 1% of the total but its influence rises rapidly afterwards; thus for test data for  $x > 0.90$ , the reported vapor qualities become ever too high. For example, if 181.41 kJ/kg of heat is added to the refrigerant-oil mixture, its local vapor quality should be 0.902 according to Table 15.3; using only the latent heat and neglecting sensible heat the vapor quality would be calculated to be 0.9114, i.e. 0.0112 too high. Thus, the error in reported vapor qualities is not very significant except at vapor qualities approaching 1.0. It should be pointed out however that many data reported in the literature incorrectly use a vapor quality based on the local mass of refrigerant vapor divided by the total mass of refrigerant, i.e. ignoring the presence of the oil, while instead the thermodynamic vapor quality  $x$  is the local mass of vapor divided the total mass of refrigerant and oil. For the highest vapor quality shown in the table,  $x = 0.93$ , the bubble point temperature is predicted to be 8.015°C (14.4°F) above the pure refrigerant value.

**Table 15.3. R134a-oil temperature-enthalpy curve at 2.93 bar (42.5 psia) for 5 mass % oil at inlet.**

x	T <sub>bub</sub> (°C)	w (%)	dh <sub>total</sub> (kJ/kg)	dh <sub>latent</sub> (kJ/kg)	dh <sub>sensible</sub> (kJ/kg)	5°C %Error	2°C %Error
0.000	0.076	5.00	0.00	0.00	0.00	-1.5	-3.8
0.093	0.084	5.51	18.53	18.52	0.01	-1.7	-4.2
0.186	0.094	6.14	37.06	37.04	0.02	-1.9	-4.7
0.279	0.106	6.93	55.60	55.56	0.04	-2.1	-5.3
0.372	0.123	7.96	74.14	74.08	0.06	-2.5	-6.2
0.465	0.146	9.35	92.68	92.59	0.06	-2.9	-7.3
0.558	0.180	11.31	111.23	111.10	0.13	-3.6	-9.0
0.651	0.236	14.33	129.80	129.63	0.16	-4.7	-11.8
0.744	0.346	19.53	148.42	148.11	0.31	-6.9	-17.3
0.837	0.663	30.67	167.22	166.59	0.63	-13.3	-33.2
0.846	0.729	32.47	169.14	168.44	0.70	-14.6	-36.5
0.856	0.819	34.72	171.08	170.29	0.79	-16.4	-41.0
0.865	0.922	37.04	173.03	172.14	0.89	-19.4	-46.1
0.874	1.056	39.68	175.00	173.98	1.02	-21.1	-52.8
0.883	1.240	42.74	177.02	175.82	1.20	-24.8	-62.0
0.893	1.541	46.73	179.15	177.66	1.49	-30.8	-
0.902	1.974	51.02	181.41	179.50	1.91	-39.5	-
0.911	2.726	56.18	183.93	181.33	2.63	-54.5	-
0.921	4.435	63.29	187.43	183.15	4.28	-	-
0.930	8.015	71.43	192.70	184.95	7.75	-	-

(% errors determined assuming a heat flux of 10,000 W/m<sup>2</sup>).

In the last two columns in Table 15.3, the effect of erroneously using T<sub>sat</sub> in place of T<sub>bub</sub> in converting "raw" data to experimental heat transfer coefficients is shown for wall superheats of 5°C (9°F) and 2°C (3.6°F). It is evident that existing published data using T<sub>sat</sub> are always too low compared to their more correct values. For instance, at a vapor quality of 0.837 and a wall superheat of 5°C (9°F), published values would be 13.3% lower than the thermodynamically correct values.

For a plain tube the effect of the oil on flow boiling heat transfer becomes significant (> 5%) at a local oil mass fraction greater than 15% while for a micro fin tube it becomes significant at w > 6.5%. At high vapor qualities and oil mass fractions, the effect becomes very significant, substantially changing the trends reported in the literature. Published test data reduced with the "oil contamination" method that fall in these ranges should be used with caution or better yet, the heat transfer coefficients should be recalculated.

## 15.6 Illustration of Physical Properties of Refrigerant-Oil Mixtures

Thome (1993) put together a comprehensive set of prediction methods that may be the best currently available (but would really benefit from further research). Table 15.4 shows the calculated physical properties that correspond to the enthalpy curve in Table 15.3 at several vapor qualities using his methods. Note that since the vapor pressures of oils are about one-ten millionth those of refrigerants, no oil enters the vapor-phase and hence vapor properties are determined for the pure refrigerant at a saturation temperature corresponding to the local bubble point temperature. For the present conditions, the physical properties that demonstrate a significant change from inlet to outlet (> 5%) are: liquid density

(-17.2%), liquid viscosity (+9003%), liquid specific heat (+23.6%), liquid thermal conductivity (+11.7%), critical pressure (-58.1%), critical temperature (+103%) and liquid Prandtl number (+10,021%). Also shown is the ratio of the liquid Reynolds number relative to that for the inlet at  $x = 0.0$ , which decreases drastically as the liquid viscosity rises. Thus, the variation in local physical properties can potentially have a significant effect on the local heat transfer coefficients, both for nucleate pool boiling and for flow boiling.

**Table 15.4. R134a-oil properties at 2.93 bar for 5 mass % oil at inlet over a range of vapor qualities.**

Local Vapor Quality	0.000	0.279	0.558	0.744	0.930
Oil Mass Fraction %	5.00	6.93	11.31	19.53	71.43
Liquid Molecular Weight	126.4	135.9	157.2	197.3	450.6
Bubble Point Temp. (°C)	0.076	0.106	0.180	0.346	8.015
Heat Absorbed (kJ/kg)	0.00	55.6	37.1	148.4	192.6
Liquid Density (kg/m <sup>3</sup> )	1276	1270	1256	1230	1057
Vapor Density (kg/m <sup>3</sup> )	14.5	14.5	14.5	14.6	16.8
Liquid Viscosity (cp)	0.398	0.458	0.628	1.137	35.83
Vapor Viscosity (cp)	0.011	0.011	0.011	0.011	0.011
Liquid Sp. Heat (kJ/kg K)	136.3	1.372	1.391	1.428	1.684
Vapor Sp. Heat (kJ/kg K)	0.889	0.889	0.889	0.889	0.906
Liquid Th. Cond. (W/m K)	0.094	0.095	0.095	0.096	0.105
Vapor Th. Cond. (W/m K)	0.012	0.012	0.012	0.012	0.013
Surface Tension (dyne/cm)	11.7	11.7	11.7	11.8	17.2
Latent Heat (kJ/kg)	199.1	191.1	1.991	198.9	195.5
Critical Pressure (bar)	38.9	38.2	36.7	33.9	16.3
Critical Temperature (K)	405.7	417.9	445.5	497.4	824.7
Liquid Prandtl Number	5.75	6.64	9.20	16.9	576.2
Relative Liquid Re Number	1.000	0.869	0.634	0.350	0.011

## 15.7 Online Measurement of Refrigerant-Oil Mass Fractions

The Thermodynamic Approach allows the local bubble point temperature, local oil mass fraction, local heat transfer coefficient, change in enthalpy and (potentially) local physical properties to be calculated for an evaporator from knowledge of  $w_{inlet}$  for any refrigerant and lubricating oil mixture, as long as they are miscible and the local oil mass fraction is below 70% oil. To implement the Thermodynamic Approach, an accurate method is required for measurement of the oil composition. For this purpose, a new online measurement system was developed and described in Bayini, Thome and Favrat (1995).

### 15.7.1 Previous Test Methods

Over the years, oil mass fractions circulating in test facilities and equipment qualification facilities have been inferred from: (i) measuring the masses of refrigerant and oil charged into the system, (ii) measuring the separate oil and refrigerant flow rates leaving an oil separator, or (iii) by withdrawing liquid samples during tests. The 1<sup>st</sup> approach is often not able to be implemented. The 2<sup>nd</sup> method is not necessarily accurate since an oil separator actually acts as a liquid-vapor separator and thus some refrigerant remains in the oil leaving the separator as liquid but gets counted as if it were oil. The 3<sup>rd</sup> method uses ASHRAE Standard 41.4-1994 to determine oil compositions for liquid samples withdrawn from the flow circuit. Each sample is weighed together with its bottle and then the refrigerant is allowed to slowly evaporate off through a valve. To be accurate, the sample must also be evacuated with a vacuum pump and heated up to

150°C (302°F) to drive off the refrigerant, then weighed again with a top loading balance accurate to 0.01 g or better. The oil composition can then be calculated from the initial and final weights. While this method is appropriate as a standard, it is not very convenient for practice. Shortcuts to the standard method, i.e. dispensing with the heating and/or evacuation procedures, result in overstating the oil concentration by as much as 1.5 mass % oil or more. Consequently, it is felt that an online method is imperative in order to measure the oil compositions conveniently and accurately over the range of test conditions to be encountered.

Various methods for determining oil compositions online have been proposed and several have been tested. Baustian, Pate and Bergles (1988a, 1988b, 1988c) have used a Coriolis density meter, an acoustic velocity sensor and a viscosity meter, respectively, to measure oil concentrations with accuracies in the range of 1-2 mass % oil. The Coriolis meter used in their tests had a density measurement accuracy of 10 kg/m<sup>3</sup> (0.6 lb/ft<sup>3</sup>) and the effect of compressibility on the subcooled liquid passing through the meter was not accounted for; however, newer more accurate Coriolis meters are now available and may suit industrial use. Meyer and Saiz Jabardo (1994) built an ultrasonic acoustic velocity device and accurately calibrated it for measuring concentrations for R-12 and R-134a with various oils (95% confidence level accuracy of 0.23-0.26 mass % oil). Suzuki, Fujisawa, Nakarazawa and Matsuoka (1993) instead have used a light absorption method for measuring oil concentrations online.

### **15.7.2 Online Density Flowmeter**

A very high accuracy, commercially available density flowmeter was used Bayini, Thome and Favrat (1995) as the measuring device, a model available from Schlumberger (Liquid Density Transducer type 7847 in stainless steel). This method will be described in some detail here. The meter is a vibrating tube type, where the tube is a 25.4 mm diameter, stainless steel corrugated tube about 1.0 meter long. The meter has a calibrated accuracy of 0.1 kg/m<sup>3</sup> (0.006 lb/ft<sup>3</sup>) over a wide range of density and temperature, including compensating equations to account for nonlinear temperature effects on the instrument's operation. A digital display gives the density and temperature and a digital signal for the density, which was read into our data acquisition system. It operates with subcooled refrigerant-oil flowing through the meter, such that measurements are continuous and no bypass circuit is required.

The density flowmeter is used to measure the density of subcooled liquid, either pure refrigerant or refrigerant-oil mixture, after it leaves the flow loop's condenser. To avoid cavitation in the vibrating corrugated tube (apparently caused by its high vibration frequency), a minimum of 8°C (14.4°F) of subcooling was required at its outlet. A further consideration is the sensitivity of the density flowmeter. The density difference between pure R-134a and the oil is approximately 300 kg/m<sup>3</sup> at the test conditions. Thus, in order to determine oil concentrations accurate to 0.1 mass % oil, one must measure density to an accuracy of  $\pm 0.30 \text{ kg/m}^3$  ( $\pm 0.019 \text{ lb/ft}^3$ ) including temperature and liquid compressibility effects.

### **15.7.3 Oil Concentration Calibration Correlation**

Measured liquid densities are not only a function of temperature and oil concentration but also liquid compressibility. For example, the density of compressed R-134a increases by about 0.3-0.4 kg/m<sup>3</sup> (0.019-0.025 lb/ft<sup>3</sup>) for each increase of 1 bar (14.5 psi) with respect to the saturation pressure at the measured temperature. The calibration should thus take the liquid compressibility into account, which for mixtures in the range from 0-6 mass % oil can reasonably be assumed to match that of the pure refrigerant. Compressed liquid densities for R-134a were reported for instance by Hou et al. (1992) over a wide range of temperature and pressure. They fit the Tait equation to their data with separate empirical parameters for each isotherm they tested. Refer to Bayini, Thome and Favrat (1995) for further details on this and the calibration procedure.

Their calibration correlation had an average error of 0.09 mass % oil for all 246 data points measured for the oil concentrations of 0.0, 0.5, 1.0, 2.0, 3.0, 4.0, 5.0 and 6.0 mass %, a maximum error of 0.69 mass % oil and a 95% confidence limit of 0.21 mass % oil.

### 15.7.4 Industrial Application of a Density Flowmeter

As a shortcut "industrial" method, the saturation density of the refrigerant-oil mixture can be determined using a linear mixing law of the specific volume. The refrigerant-oil saturation density  $\rho$  is defined by this ideal mixing law as:

$$\rho = \rho_{\text{oil}} / [1 + (1 - w)(\rho_{\text{oil}} / \rho_{\text{ref}} - 1)] \quad [15.6.1]$$

Solving this expression to obtain the oil mass fraction  $w$  (in mass fraction, not mass %) gives

$$w = [(\rho_{\text{oil}} / \rho)(\rho_{\text{ref}} - \rho)] / (\rho_{\text{ref}} - \rho_{\text{oil}}) \quad [15.6.2]$$

The refrigerant saturation density  $\rho_{\text{ref}}$  in this equation is calculated from an accurate equation for the refrigerant (such as ASHRAE methods). The lubricating oil density  $\rho_{\text{oil}}$  can either be measured as a function of temperature or obtained from data supplied by the manufacturer. Otherwise, using a method adapted from Thome (1992), it can be estimated from the following equation for lubricating oils:

$$\rho_{\text{oil}} = \rho_{\text{man}} [(T_{\text{crit}} - T) / (T_{\text{crit}} - (T_{\text{man}} + 273.15))]^{0.29} \quad [15.6.3]$$

where  $\rho_{\text{man}}$  is the oil density ( $\text{kg/m}^3$ ) at the temperature provided by the manufacturer  $T_{\text{man}}$  (normally  $15^\circ\text{C}$ ),  $T_{\text{crit}}$  is the critical temperature of the oil (assume equal to 760 K for all oils as an approximation), and  $T$  is the measured temperature (K). Subtracting the density difference due to compressibility from the measured density  $\rho$  and using the pure refrigerant and oil densities determined as discussed, the oil composition is determined with [15.6.2]. This simplified method has been successfully compared to R-134a/oil density test data of Bayini, Thome and Favrat (1995) with a mean error of  $\pm 0.22$  mass % oil. Because of nonlinear variations in density with composition, the accuracy varies from about  $\pm 0.1$  mass % mean error for the 0.5 mass % mixture up to about  $\pm 0.5$  mass % mean error for the 6.0 mass % mixture, which is more than satisfactory for most applications.

To get the best results, the meter should be calibrated against the pure refrigerant first, i.e. measure the pure refrigerant's density with the meter, correct this value for liquid compressibility and then compare it against the calculated saturated refrigerant density.

**Example Calculation:** Assume a density meter is used to measure oil mass fraction of a slightly subcooled mixture of R-134a and oil at the conditions of  $0^\circ\text{C}$  and 2.93 bar. R-134a has a density of  $1276 \text{ kg/m}^3$  at this temperature while the oil has a density of  $900 \text{ kg/m}^3$  at the  $15^\circ\text{C}$  according to the manufacturer. If the density measured is  $1270 \text{ kg/m}^3$ , what is the oil mass fraction?

**Solution:** The density of the oil at  $0^\circ\text{C}$  (273.15 K) is obtained with [15.6.3]:

$$\begin{aligned} \rho_{\text{oil}} &= \rho_{\text{man}} [(T_{\text{crit}} - T) / (T_{\text{crit}} - (T_{\text{man}} + 273.15))]^{0.29} \\ \rho_{\text{oil}} &= 900 [(760 - 273.15) / (760 - (15 + 273.15))]^{0.29} = 908.2 \text{ kg/m}^3 \end{aligned}$$

The oil mass fraction w (in mass fraction) is obtained with [15.6.2]:

$$w = [(\rho_{\text{oil}}/\rho)(\rho_{\text{ref}} - \rho)]/(\rho_{\text{ref}} - \rho_{\text{oil}})$$

$$w = [(908.2/1270)(1276 - 1270)]/(1276 - 908.2) = 0.0117$$

Thus, the oil mass fraction is 0.0117 or 1.17 % oil.

## Chapter 16

# Effects of Oil on Thermal Performance of Heat Exchangers

**SUMMARY:** Miscible lubricating oils in refrigeration system working fluids can have a dramatic effect on boiling heat transfer performance and two-phase pressure drops in direct-expansion evaporators and flooded evaporators, representing one of the old unresolved problems of refrigeration heat transfer. This survey presents a summary of recent experimental work of the influence of oil on nucleate pool boiling, bundle boiling and flow boiling heat transfer coefficients and two-phase pressure drops for plain and enhanced tubes. Some methods for predicting the effect of oil on intube evaporation and intube pressure drops are also described. The influence of oil on condensation tends to be less than for evaporation and less information is available. This chapter addresses the influence of oil on boiling heat transfer only, but not on condensation heat transfer.

The general trends for evaporation of refrigerant-oil mixtures inside plain tubes are that (i) oil increases the local boiling heat transfer coefficient at low to intermediate vapor qualities on the order of 10-30% and (ii) this is followed by a sharp reduction by up to -90% at high vapor qualities with respect to pure refrigerant performance. The general trend for microfin tubes is (i) little (5-10%) or no enhancing effect of the oil on heat transfer at low and medium vapor qualities but sometimes a detrimental influence of as much as -30% and (ii) then a substantial reduction up to -90% at high vapor qualities.

Presently, there is no model that can explain why oil has an enhancing effect in plain tubes at the low and medium vapor qualities. Instead, at high vapor qualities, the large increase in local liquid viscosity explains the sharp reduction in heat transfer coefficients at high vapor qualities. Using the flow boiling model and flow pattern map of Kattan, Thome and Favrat (1998a, 1998b, 1998c), where the refrigerant-oil viscosity,  $\mu_{ref\text{-}oil}$ , is used in place of the pure refrigerant value,  $\mu_{ref}$ , heat transfer to refrigerant-oil mixtures has been successfully predicted. No method is currently available for predicting the oil effect for microfin tubes and hence only the plain tube approach can be extrapolated to microfin tubes at present. Oil also increases two-phase pressure drops sharply at high local vapor qualities for evaporation in plain and microfin tubes. Using an oil-to-refrigerant viscosity correction factor, local two-phase pressure drops are adequately predicted for foaming and non-foaming refrigerant-oil mixtures evaporating inside plain tubes. No such method is available for microfin tubes so for now the plain tube method is extrapolated to applications to microfin tubes.

For evaporation on a single plain tube or a single low finned tube, oil normally tends to increase the boiling heat transfer coefficient up to some limiting % mass composition and then reduce it, although some tests show no augmentation effect of oil but only a detrimental effect. For evaporation on single enhanced boiling tubes, oil always tends to reduce the boiling coefficient with increasing % mass of oil composition. Effects of oil on tube bundle boiling are not yet well understood.

### 16.1 Introduction

Evaporation inside tubes and on the outside of tube bundles is an important heat transfer process in direct-expansion and flooded evaporators widely used for refrigeration, air-conditioning and heat pump systems. Plain tubes may be used but tubes with internal microfins (such as **Turbo-A** and **Turbo-D**) or external boiling enhancements (such as the various versions of **Turbo-B**) are now widely and routinely used in these services. Plain tubes are used in some applications, primarily for air-heated coils where the limiting

thermal resistance is on the airside of the tube; however, for these units microfin tubes are often used to achieve a more compact, economical design.

Lubricating oil from the compressor's bearings typically enters the refrigerant as a mist in a vapor compression cycle, dissolves into the liquid refrigerant in the condenser, and then circulates around the flow circuit to the evaporator. The oil may leave the evaporator as a liquid mist in the refrigerant vapor but may also build up in the evaporator tubes in the high vapor quality zone, held in place by the oil's high surface tension and viscosity. The amount of oil may seem to be negligible in these systems, often ranging from only 0.5-1.0 (% mass) of the total refrigerant charge but up to 3-5 (% mass) in severe cases. Yet, even a small oil mass fraction may have a very detrimental effect on evaporator thermal capacity in one or more of the following manners:

- decreasing the evaporating heat transfer coefficient;
- increasing the two-phase pressure drop;
- elevating the boiling point temperature;
- preventing all the refrigerant from evaporating;
- reducing the log mean temperature difference.

Considering lubricating oils in general, their normal boiling points are about 300°C (572°F) or above; hence it is very high relative to that of a refrigeration system evaporator. In addition, the vapor pressure of oil at 20°C (68°F) is only about 1 millionth that of the refrigerant, so its partial pressure in the vapor-phase is extremely negligible. Thus, the oil is essentially non-volatile at normal operating conditions, which means that the oil remains in its liquid-phase, either dissolved in the liquid refrigerant (if miscible) or is in the form of entrained droplets at the exit of the evaporator. Consequently, for a certain mass of oil in the refrigerant charge, the oil mass fraction in the liquid-phase will tend to increase along the evaporation flow path through a direct-expansion evaporator as more and more liquid refrigerant is evaporated. Thus, the highest oil mass fraction in the liquid-phase will be at the outlet of the evaporator.

As an example, let us assume that refrigerant with 1.0 (% mass) oil in the total flow of subcooled liquid leaves the condenser for the expansion device, i.e. 1 g of oil for every 100 g of liquid refrigerant and oil. For a local vapor quality of 0.25 at the exit of the expansion device (valve or capillary tube), the local oil mass fraction in the remaining liquid will be 1.33 (% mass), i.e. 1 g of oil per 75 g of the remaining liquid (74 g of liquid refrigerant + 1 g of oil) at that location. Near the exit of the evaporator at a local vapor quality of 0.95, the local oil mass fraction in the remaining liquid will be 20 (% mass), i.e. 1 g of oil in every 5 g of liquid. At the outlet of the evaporator, the local vapor quality when oil is present cannot in fact reach 1.0 since the oil cannot be evaporated at this temperature. For a nominal 1.0 (% mass) oil circulating in the unit, the highest local vapor quality that can be attained is less than 0.99 since 0.01 represents the oil in the liquid and some refrigerant will remain as liquid too. Since the local oil mass fraction increases with local vapor quality, it can thus be expected to have its dominant effect on thermal performance (heat transfer, two-phase pressure drop and local boiling point temperature) at the high quality end of a direct-expansion evaporator.

The evaporation of refrigerant/lubricating oil mixtures is thus a thermodynamic problem as well as a heat transfer problem, analogous to evaporation of zeotropic refrigerant mixtures (e.g. R-407C). However, a refrigerant-oil mixture has a temperature glide on the order of 300°C (572°F) since the oil increases the local bubble point temperature with increasing oil mass fraction, i.e. the local saturation temperature at which evaporation of a mixture takes place. Furthermore, to be thermodynamically correct and to respect the definition of the boiling heat transfer coefficient, the local bubble point temperature should be used to calculate the boiling wall superheat between the tube wall and the refrigerant-oil mixture, not the saturation temperature of the pure refrigerant, and also to determine the log-mean temperature difference.

In addition, the physical properties of the liquid-phase tend to be significantly affected by the oil, especially the liquid dynamic viscosity. Lubricating oils have dynamic viscosities on the order of 1000 times that of a liquid refrigerant at normal evaporation temperatures. Therefore, a nominal 1.0 (% mass) oil mixture will substantially increase the local liquid viscosity at the point in the evaporator where the local vapor quality reaches 0.95 and thus the oil's local mass fraction in the liquid is 20 (% mass). Hence, locally the liquid viscosity may go as high as  $0.035 \text{ Ns/m}^2$  (35 cp) compared to  $0.0002\text{-}0.00035 \text{ Ns/m}^2$  (0.2-0.35 cp) for pure refrigerants such as R-134a or R-22, i.e. an increase of 100-175 times! Other key physical properties are also affected, but to a much lesser extent.

The thermodynamics of refrigerant-oil mixtures are discussed in detail in Chapter 15. Refer to Chapter 15 for more information on this topic.

The first part of this review is on the influence of oil on evaporation of refrigerant-oil mixtures inside tubes. The second part will cover oil effects on evaporation outside of tubes. Other previous reviews on this subject have been presented by Schlager, Pate and Bergles (1987) and by Thome (1990, 1994b, 1995, 1996). The present review will cover the most important recent work on this topic.

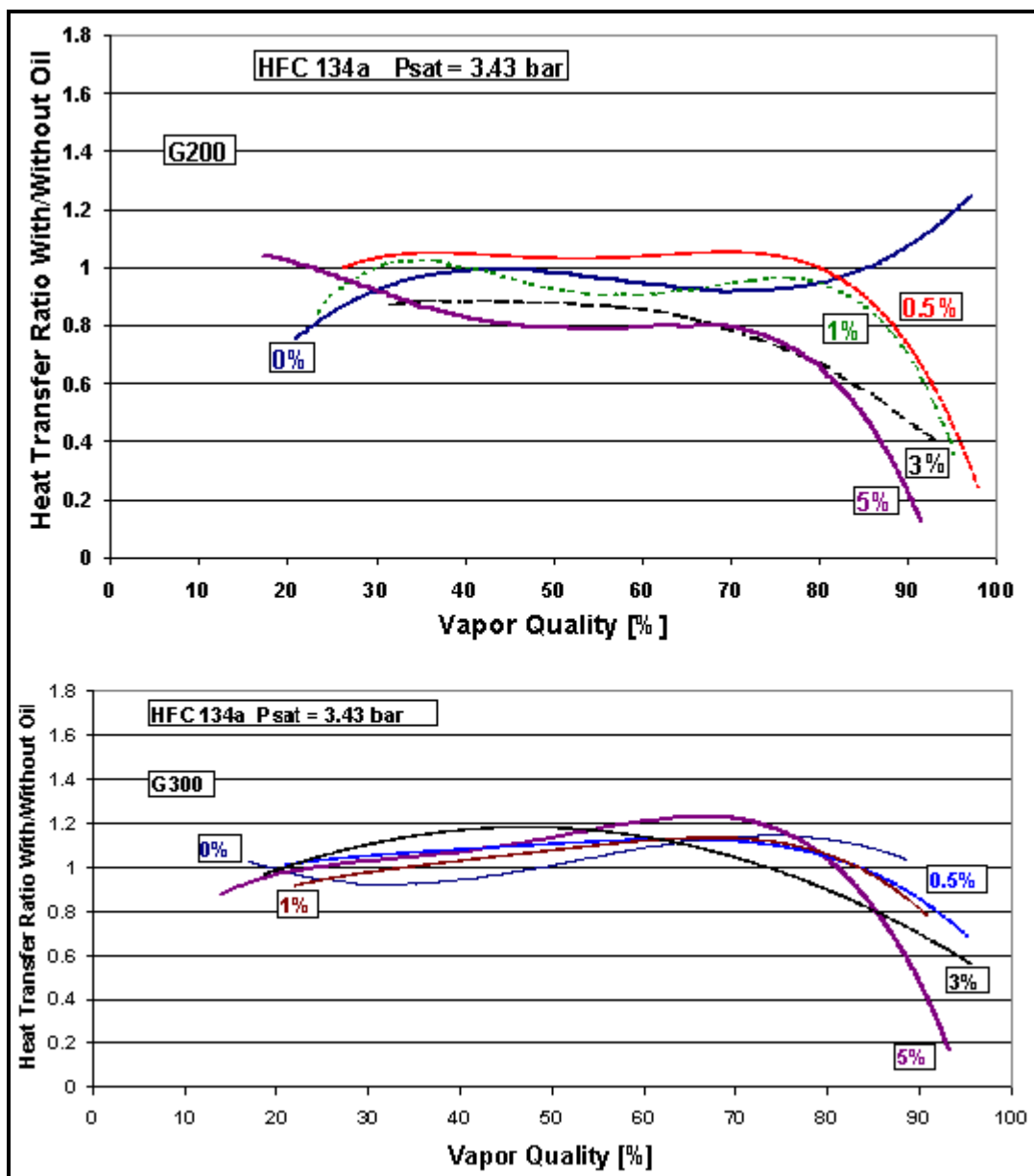
## 16.2 Summary of Oil Effects on Evaporation inside Tubes

Figure 16.1 from Zürcher, Thome and Favrat (1997a) depicts some local flow boiling data for R-134a/oil mixtures evaporating inside a plain horizontal tube of 10.92 mm (0.430 in.) internal diameter at 3.43 bar (49.7 psia), where the local measured heat transfer coefficients with and without oil have been normalized using calculated values for pure R-134a obtained with the new intube flow boiling model of Kattan, Thome and Favrat (1998a, 1998b, 1998c). The test conditions are two fixed mass velocities of 100 and  $300 \text{ kg/m}^2\text{s}$  and nominal inlet oil mass fractions of 0, 0.5, 1.0, 3.0 and 5.0. These results demonstrate most of the trends typically observed in local flow boiling data for refrigerant-oil mixtures inside plain tubes:

- At low mass velocities and intermediate vapor qualities, the oil enhances heat transfer by 10% to 60% depending on the inlet oil mass fraction and flow conditions in the study;
- At higher mass velocity and intermediate vapor qualities, the oil may still enhance heat transfer but by a smaller amount (0 to 20%);
- At vapor qualities above about 0.70 for all mass velocities, oil has a very adverse influence on heat transfer, reducing heat transfer coefficients by up to 90%.

Therefore, the effect of oil on evaporation heat transfer may be very positive, insignificant or very negative, depending on the local operating conditions at that point in the evaporator. A direct-expansion evaporator, in any case, must operate in the high vapor quality region where oil effects on heat transfer are particularly adverse.

Referring again to Figure 16.1, the two mass velocities shown are  $200 \text{ kg/m}^2\text{s}$  ( $147,158 \text{ lb/h ft}^2$ ) and  $300 \text{ kg/m}^2\text{s}$  ( $220,738 \text{ lb/h ft}^2$ ) over the wide vapor quality range from 0.18 to 0.93. At these diverse conditions, the Kattan-Thome-Favrat flow-boiling model is seen to predict all the pure R-134a data (0% curves) to within -8% and +21%. For accurate thermal design of direct-expansion evaporators, the influence of oil on the local heat transfer coefficient must be taken into account, especially at high vapor qualities where the local coefficient becomes very low and is hence the controlling thermal resistance in the overall heat transfer coefficient. In fact, the local flow-boiling coefficient with oil at high vapor qualities may even be as low as the airside heat transfer coefficient and hence appropriate design measures should be taken if possible.



**Figure 16.1.** Heat transfer ratios for evaporation of R-134a/oil mixtures in a plain tube from Zürcher, Thome and Favrat (1997a) at two mass velocities at 3.43 bar (49.7 psia) [reprinted from *HVAC&R Research*, ASHRAE, Atlanta, Georgia].

For evaporation in microfin tubes, Figure 16.2 from Zürcher, Thome and Favrat (1998a) illustrates the typical effects of oil in the same format as in Figure 16.1 but for R-407C/oil mixtures. The microfin tube had an internal diameter of 11.90 mm (0.469 in.) at the root on the internal fins, 70 helical fins of 0.254 mm (0.010 in.) height and 18° helix angle, and an internal area ratio of 1.74. The local heat transfer coefficients with oil were normalized using the experimental data for pure R-407C. The test conditions were at two fixed mass velocities of 200 and 300 kg/m<sup>2</sup>s (147,158 and 220,738 lb/h ft<sup>2</sup>) and nominal inlet oil mass fractions of 0, 0.5, 1.0, 3.0 and 5.0. All these data were reduced experimentally utilizing the Thermodynamic Approach described in Chapter 15. The typical trends observed in local microfin flow boiling data for refrigerant-oil mixtures are:

- At low mass velocities not shown and intermediate vapor qualities, the oil can either have a very detrimental effect or nearly no effect on heat transfer (from about -30% to -1%);
- At higher mass velocity and intermediate vapor qualities, the oil may either degrade heat transfer or slightly increase it (from about -20% to +10%);
- At high vapor qualities for all mass velocities, the oil has a very detrimental influence on local heat transfer, resulting in lowering heat transfer coefficients by up to 90%.

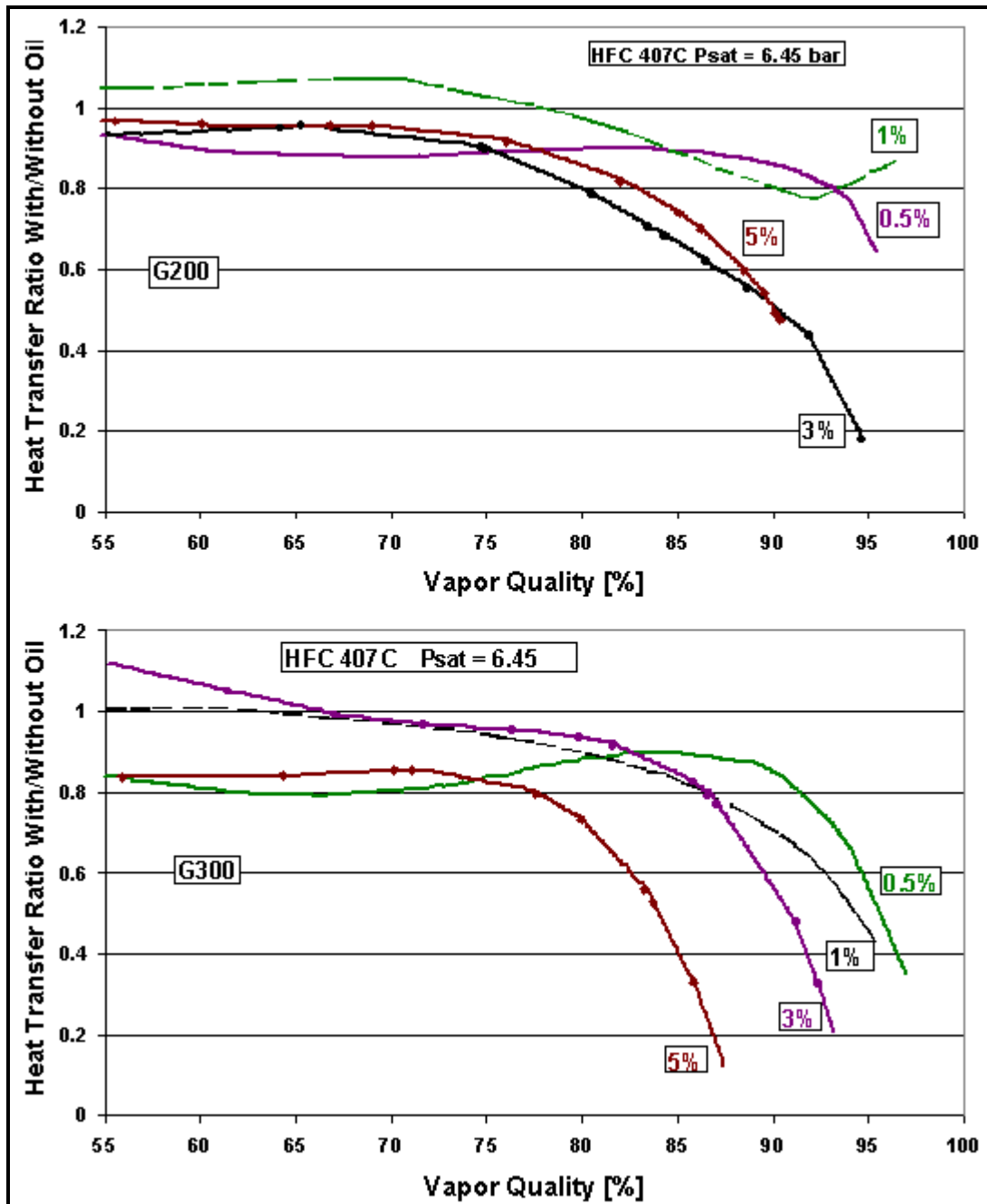


**Figure 16.2.** Heat transfer ratios for evaporation of R-407C/oil mixtures in a microfin tube from Zürcher, Thome and Favrat (1998a) at two mass velocities at 6.45 bar (93.5 psia) [reprinted from *HVAC&R Research*, ASHRAE, Atlanta, Georgia].

Hence, the effect of oil on evaporation heat transfer can either be slightly positive, insignificant or very negative, depending on the local operating conditions at that point in an evaporator. The overall effect of oil on the thermal capacity of an evaporator requires a thermal rating of the unit to be performed.

Twelve thermal effects of miscible lubricating oils on evaporation of refrigerants inside plain and microfin tubes have been identified, based on the results shown above and those in the literature. They are as follows:

- **Bubble point temperatures of refrigerant-oil mixtures.** Oil has a much higher boiling point than common refrigerants. Hence adding oil to a refrigerant increases its bubble point temperature relative to the saturation temperature of the pure refrigerant. This becomes increasingly important at local oil mass fractions greater than 10-20% oil mass that occur at high vapor qualities in an evaporator.
- **Oil effects on thermodynamic and transport properties.** Lubricating oils have much larger molecular weights than common refrigerants. For refrigerant-oil mixtures, this significantly affects the liquid density, where often the density difference between the oil and refrigerant is as much as 300-400 kg/m<sup>3</sup> (19-25 lb/ft<sup>3</sup>), the liquid viscosity, the liquid specific heat, the critical pressure and the surface tension. Since the oil is essentially non-volatile at refrigeration operating conditions, the oil only affects liquid-phase properties but not vapor-phase properties.
- **Oil effects on enthalpy.** Adding oil to a refrigerant has primarily two effects. First, it increases the bubble point temperature (as noted above) as the mixture evaporates along the heat transfer tube. Secondly, it changes the liquid specific heat, which becomes a function of oil mass fraction. The combined influence of these two effects is that the change in enthalpy during evaporation of a refrigerant-oil mixture includes both sensible and latent heat while isobaric evaporation of a pure refrigerant only involves latent heat.
- **Oil viscosity effects on convection.** The rapid rise in local liquid viscosity with local oil mass fraction as the local vapor quality approaches 1.0 has a detrimental effect on the liquid only heat transfer coefficient,  $\alpha_L$ , typically used as the starting basis in modeling flow boiling heat transfer ( $\alpha_L$  in turbulent flow is inversely proportional to  $\mu_L$ ).
- **Oil holdup effects.** The actual local oil mass fraction may be much larger than expected at some flow conditions in the high vapor quality zone of the evaporator because the vapor shear may not be strong enough to effectively drag the viscous refrigerant-oil liquid film along the tube, and may prevent adequate oil return to the compressor. This occurs in both plain and microfin tubes.
- **Foaming.** Some oils promote the formation of foam when evaporated with particular refrigerants. The consequences of foam on the heat transfer process are poorly understood at present. The foam can be postulated to influence the onset of dry out in evaporating annular flows and shift its location to lower than expected vapor qualities (by thinning the annular liquid film) and it may have the positive affect of wetting the top of the tube under otherwise stratified flow conditions (by virtue of the height of the foam above the normal liquid level). Significant increases in local evaporating heat transfer coefficients by the oil at intermediate vapor qualities are often ascribed by researchers to foaming. However, for R-134a/oil results at 100 kg/m<sup>2</sup>s (73,579 lb/ h ft<sup>2</sup>) in the stratified-wavy flow regime in the previously mentioned study, there was significant augmentation by the oil even though no foaming was observed). Consequently, the influence of foaming is not well understood.
- **Wetting effects.** The larger surface tension of oil and its surfactant effect tends to increase the wetted fraction of the tube perimeter in stratified flows in horizontal tubes, which occur at low mass

velocities, and hence could be the mechanism responsible for an oil's heat transfer augmentation effect at low to medium vapor qualities in plain tubes mentioned above.

- **Influence on flow pattern transitions.** The oil's effects on physical properties have the potential to modify the threshold of transition between different flow patterns, such as annular flow and stratified-wavy flow. Manwell and Bergles (1990), for instance, have reported two-phase flow patterns for R-12/oil mixtures and discussed their observations. Videos were also obtained for the tests described earlier in Figure 16.1 and Figure 16.2.
- **Mass transfer effect of oil on heat transfer.** Oil builds up at evaporating interfaces just like the heavier component(s) in zeotropic refrigerant blends, creating a mass fraction gradient and thus increasing the bubble point temperature at the vapor-liquid interface. This in turn reduces the superheat across the evaporating film, which drives the evaporation process, and consequently adversely affects the rate of heat transfer.
- **Viscous transition to laminar film flow.** As oil becomes increasingly concentrated in the liquid phase during evaporation in the annular flow regime, i.e. in the liquid film, the film is prevented from drying out at the top of the tube at high vapor quality because the bubble point temperature of the film rises towards that of the heated wall. For refrigerant-oil mixtures, the less profound peaks in plots of heat transfer coefficient versus local vapor quality ( $\alpha$  vs.  $x$  at constant mass flux) observed experimentally may represent a transition in the liquid annular film from a *turbulent* convection regime to the less thermally effective *laminar* convection regime. In fact, such slow flowing laminar films have been observed and reported in the literature.
- **Nucleate boiling augmentation.** Oil may increase the nucleate boiling contribution to flow boiling over the low and intermediate vapor quality range {as discussed for nucleate pool boiling of refrigerant-oil mixtures in Thome (1995)}. Even so, this does not seem likely to be particularly significant in flow boiling conditions where the nucleate boiling contribution is typically of secondary importance to the convective contribution.
- **Solubility effects.** Some refrigerant-oil combinations are soluble (and miscible) over the entire mass fraction range while others are only soluble for oil mass fractions less than 5-10 (% mass) depending on the temperature. Consequently, at high vapor qualities where the liquid can reach 30-60% oil mass, the local mixture may no longer be in the soluble range {for instance, refer to Hewitt and McMullan (1995)}.

The complex trends observed experimentally for evaporation inside plain and microfin tubes with oil in the refrigerant charge are a composite of these effects, and their impact on heat transfer depends on local flow conditions (oil mass fraction, mass velocity, vapor quality, heat flux, flow pattern, plain or enhanced surface, foaming if any, etc.).

### 16.3 Experimental Studies on Intube Flow Boiling

Some flow boiling studies still investigate the effect of oil on *mean* evaporating coefficients obtained over a wide change of vapor quality from inlet to outlet of the test section rather than on *local* coefficients. This is typical of industrial experimental facilities and some university test rigs too. Also, most experimental studies reported in the literature have used the pure refrigerant saturation temperature  $T_{\text{sat}}$  rather than  $T_{\text{bub}}$  to calculate the heat transfer coefficient (i.e. the oil contamination approach described in Chapter 15), and since  $T_{\text{bub}} > T_{\text{sat}}$ , such heat transfer coefficients are smaller than the thermodynamically

correct values, especially for vapor qualities greater than 0.8. For  $x < 0.8$ , the influence of oil on  $T_{bub}$  is relatively small, especially for mean data. This difference becomes significant at high oil mass fractions and also for microfin tubes, which have small boiling wall superheats. It should be pointed out that the only studies in the technical literature that have apparently correctly reduced their raw test measurements to refrigerant/oil boiling heat transfer coefficients utilizing bubble point temperatures and enthalpy curves (i.e. the Thermodynamic Approach described in Chapter 15) are those by Thome and coworkers. Hence, experimental heat transfer coefficients from other studies may include some combination of the real oil effects and those attributable to the improper use of  $T_{sat}$  of the pure refrigerant rather than  $T_{bub}$  of the mixture. Therefore, only the recent experimental work of Thome and coworkers will be discussed here (all though the qualitative trends in other studies are similar to these).

Nidegger, Thome and Favrat (1997) ran local R-134a/oil evaporation tests for a *microfin* tube with an internal diameter of 11.90 mm (0.470 in.), seventy 18° helical fins of 0.254 mm (0.010 in.) and internal area ratio of 1.74 at nominal oil mass fractions of 0, 0.5, 1.0, 3.0 and 5.0 (% mass). They measured the actual oil mass fractions circulating in their loop with an accurate online density flowmeter {cf. Bayini, Thome and Favrat (1995) in Chapter 15}. They used counter-current hot water in a double-pipe test section to obtain their data using the modified-Wilson plot approach. Hence, mean heat transfer coefficients were measured for subsections of 1.0 m (3.37 ft) length in their 3.0 m (10.1 ft) long test section, which gave *quasi-local* heat transfer test data for a change in vapor quality of about 0.045 to 0.12 in a subsection. The Thermodynamic Approach for refrigerant/oil mixtures was used to reduce their raw data to heat transfer coefficients, determining the bubble point temperatures of the local refrigerant-oil mixture at the inlet and outlet of their test zones and the corresponding enthalpy curves. Mobil Arctic Grade EAL 68 ester oil was used, which has a kinematical viscosity of 62.5 mm<sup>2</sup>/s at 40°C (104°F) and was completely miscible over all test conditions.

Figure 16.3 shows their data at a mass velocity of 200 kg/m<sup>2</sup>s (147,158 lb/ h ft<sup>2</sup>) plotted in two different ways, first in the traditional way as a function of the nominal inlet oil mass fraction in the subcooled liquid and then in a more appropriate way as a function of the local oil mass fraction corresponding to the local vapor quality. Adding oil to R-134a always reduced heat transfer at vapor qualities before the peak in  $\alpha$  vs.  $x$ , but after the peak a few data were higher than the pure R-134a values, apparently because a small amount of oil retarded the onset of dry out (or eliminated it since the refrigerant-oil mixture cannot dry out). At high local oil mass fractions, the heat transfer coefficients were well below those for pure R-134a. They reported that no foaming occurred in any of their R-134a/oil tests.

Zürcher, Thome and Favrat (1997a) ran *plain* tube tests with R-134a/oil at the same test conditions, i.e. constant inlet saturation pressure of 3.40 bar (49.3psia) corresponding to  $T_{sat} = 4.4^\circ\text{C}$  (40°F) for pure R-134a. Figure 16.4 depicts their test data for a plain tube of 10.92 mm (0.430 in.) internal diameter. The oil mass fractions of 0.5% and 1.0% tended to increase boiling performance at low to intermediate vapor qualities while 3.0% and 5.0% oil tended to decrease it. At high vapor qualities, the 0.5% oil mixture had a performance similar to pure R-134a until after the peak in  $\alpha$  vs.  $x$ . The mixtures with higher levels of oil suffered very severe performance degradations at high vapor quality, falling by as much as -90% relative to the pure R-134a data and noticeably shifted the peak in  $\alpha$  vs.  $x$  towards lower vapor qualities and to lower amplitudes.

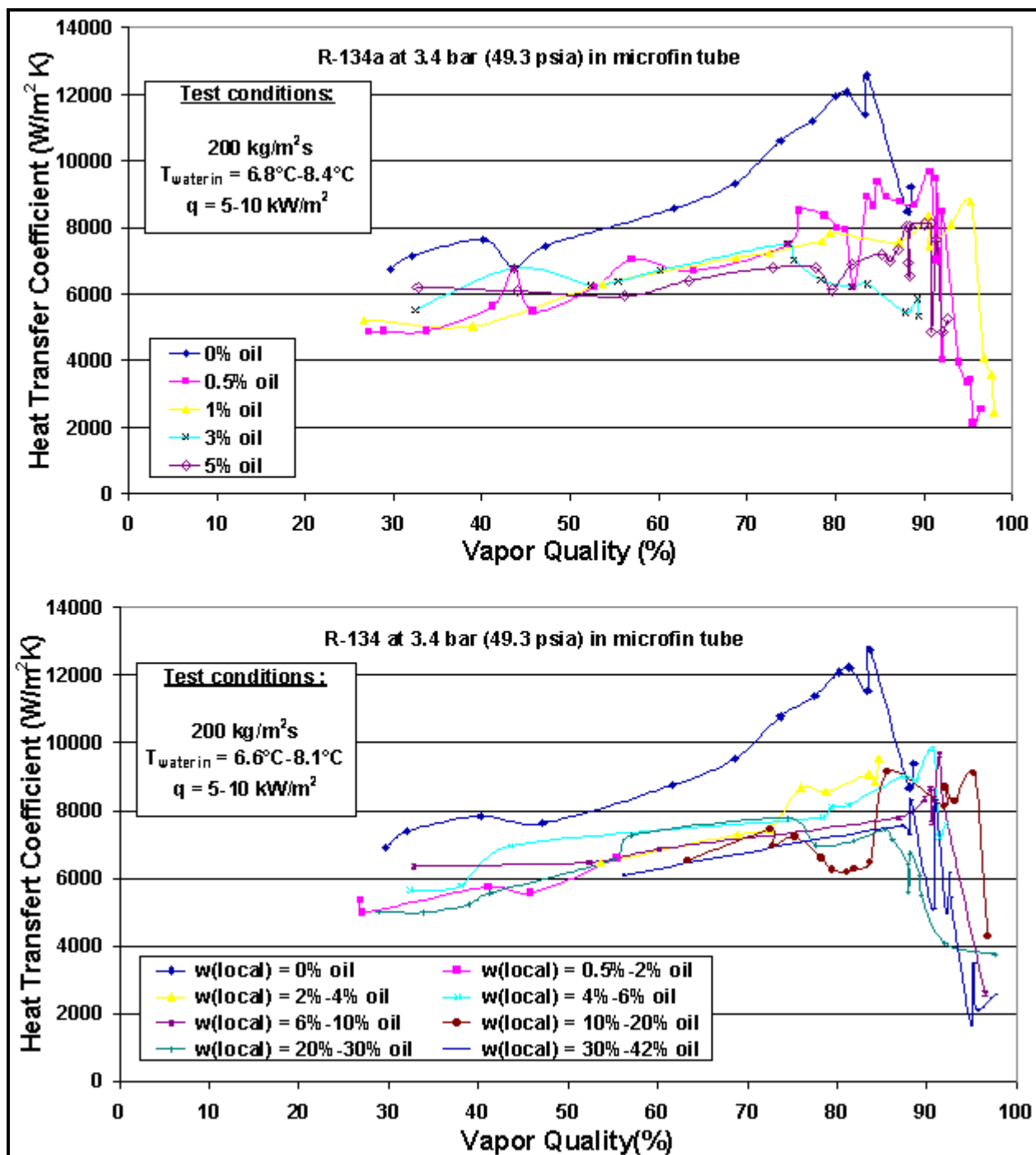


Figure 16.3. Nidegger, Thome and Favrat (1997) flow boiling data for R-134a/oil mixtures in a microfin tube. Top: Plotted as inlet oil mass fraction. Bottom: Plotted as local oil mass fraction [reprinted from *HVAC&R Research*, ASHRAE, Atlanta, Georgia].

Zürcher, Thome and Favrat (1998a) ran local R-407C/oil evaporation tests for a *microfin* tube test section for nominal inlet oil mass fractions of 0, 0.5, 1.0, 3.0 and 5.0 (% mass) at 6.45 bar. The microfin tube was the same tested previously with R-134a/oil mixtures and described above. They reduced their data using the Thermodynamic Approach for refrigerant/oil mixtures and oil mass fractions were measured online. They observed that their inlet and outlet temperature measurements for the test fluid compared well with

their calculated values of bubble point temperatures of the temperature glides for both R-407C and R-407C/oil mixtures as a function of vapor quality. [They also presented a complete set of thermodynamic equations for describing R-407C mixtures valid from -5°C to +50°C (23°F to 122°F) for reducing test data and for thermal design of R-407C evaporators and condensers]. The same Mobil Arctic Grade EAL 68 ester oil as in the prior R-134a tests was used (always completely miscible according to the oil manufacturer). Their data were quasi-local data obtained with modified-Wilson plot tests. Figure 16.2 presented earlier shows their data as normalized values relative to pure R-407C. Adding oil to R-407C always reduced heat transfer at all vapor qualities except for a minor increase of 6-8% over part of the range for 3.0 % oil mass that probably is not significant. This combination of refrigerant and oil caused a lot of foaming to occur, which seemed to intensify with increasing oil mass fraction, mass velocity and local vapor quality.

Zürcher, Thome and Favrat (1998b) ran the analogous *plain* tube tests with R-407C/oil at similar test conditions, i.e. constant inlet saturation pressure of 6.45 bar (93.5 psia) corresponding to a saturation temperature of 4.4°C (40°F) for pure R-407C at a vapor quality of 0.0. Figure 16.5 depicts their 10.92 mm (0.430 in.) bore, plain tube test data at 300 kg/m<sup>2</sup>s (220,738 lb/h ft<sup>2</sup>) that have been normalized by the Kattan, Thome and Favrat (1998c) flow boiling model. At high vapor qualities, the heat transfer coefficients of the refrigerant-oil mixtures suffered very severe degradations with increasing oil mass fraction, falling by as much as -90%. Note that the Kattan-Thome-Favrat flow boiling model, including the mass transfer effect of the mixture, predicts their pure R-407C data (0% curve) to within a maximum error of ±20% and a mean error of less than 10%.

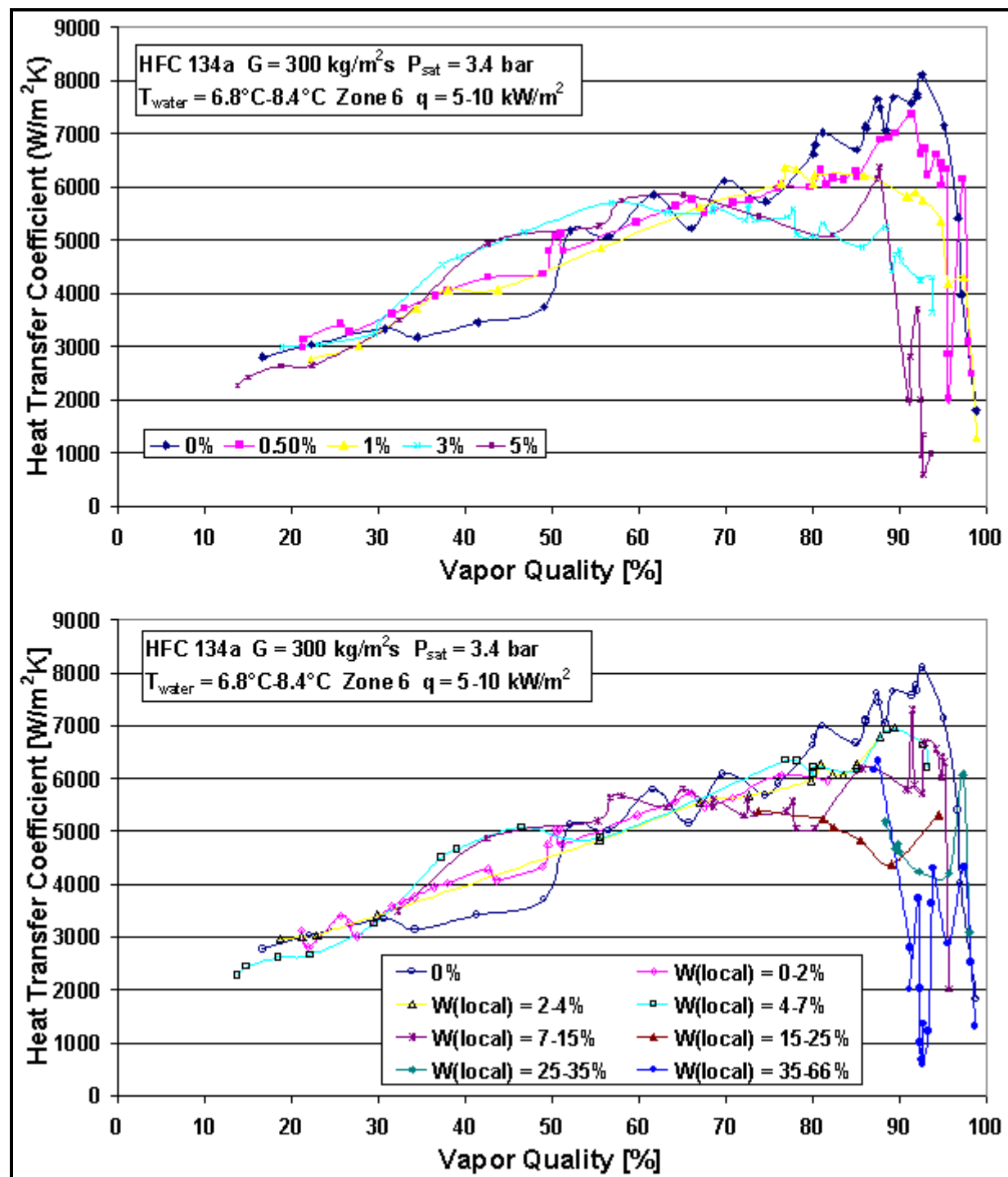
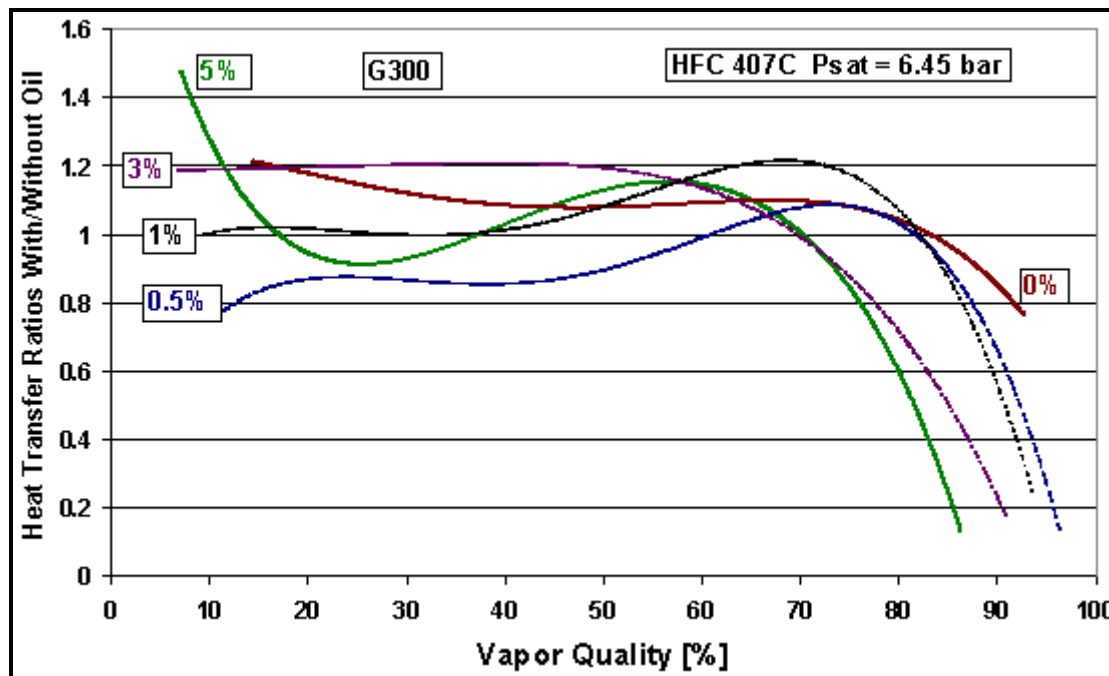


Figure 16.4. Zürcher, Thome and Favrat (1997a) flow boiling data for R-134a/oil mixtures in a plain tube. Top: Plotted as inlet oil mass fraction. Bottom: Plotted as local oil mass fraction [reprinted from *HVCA&R Research*, ASHRAE, Atlanta, Georgia].



**Figure 16.5.** Zürcher, Thome and Favrat (1998a) flow boiling data for R-407C/oil mixtures in a plain tube plotted as normalized coefficients at 6.45 bar (93.5 psia) [reprinted from HVAC&R Research, ASHRAE, Atlanta, Georgia].

The phenomenon of oil build up in plain and microfin tubes during evaporation was quantified in Zürcher, Thome and Favrat (1998a) for the first time. Figure 16.6 depicts their oil mass fractions measured online for subcooled refrigerant-oil liquid flowing into their preheater compared to the 5 (% mass oil) mixture charged into the flow boiling loop. At local vapor qualities below about 0.72 (which corresponds to a local oil mass fraction of 18%), no oil held up in the two 3-meter long microfin tube test sections connected in series, as indicated by the online value which matches that charged into the loop. In sharp contrast, at high outlet vapor qualities, oil did build up, becoming more severe with decreasing mass velocity. The oil does not actually remain stationary within the microfin tube but the flow of the very viscous refrigerant-oil mixture at high vapor qualities is extremely slow, as observed in a tubular sight glass located directly at the exit of the microfin tube. The flow of the annular film has in fact become laminar and the local oil mass fraction builds up beyond that estimated from equilibrium flow conditions. As a consequence, the local oil mass fraction at high vapor qualities in microfin tubes is higher than that calculated, which means that the actual local bubble point temperature is higher than that estimated assuming no local build up of oil. *In similar tests with the plain tube test section, the same oil build up phenomenon manifested itself, beginning at only slightly higher vapor qualities.*

The amount of oil build up and its vapor quality threshold is directly dependent on the nominal oil composition circulating in the loop. The above example is perhaps a worst-case scenario, i.e. 5% oil, while oil compositions of 0.5 to 1% (more typical of industrial practice) will only reach that point at close to complete evaporation. For example, extrapolating the above threshold for oil build up at a vapor quality of 0.72 for 5% oil to a 1% oil mixture at that same mass velocity, the threshold to oil build up in the evaporator would occur at a vapor quality of 0.944 while for a 0.5% oil mixture it would occur at 0.972. Hence, while oil build up is a possible problem for proper operation, the actual conditions will have a large influence on its onset and the magnitude of its effect.

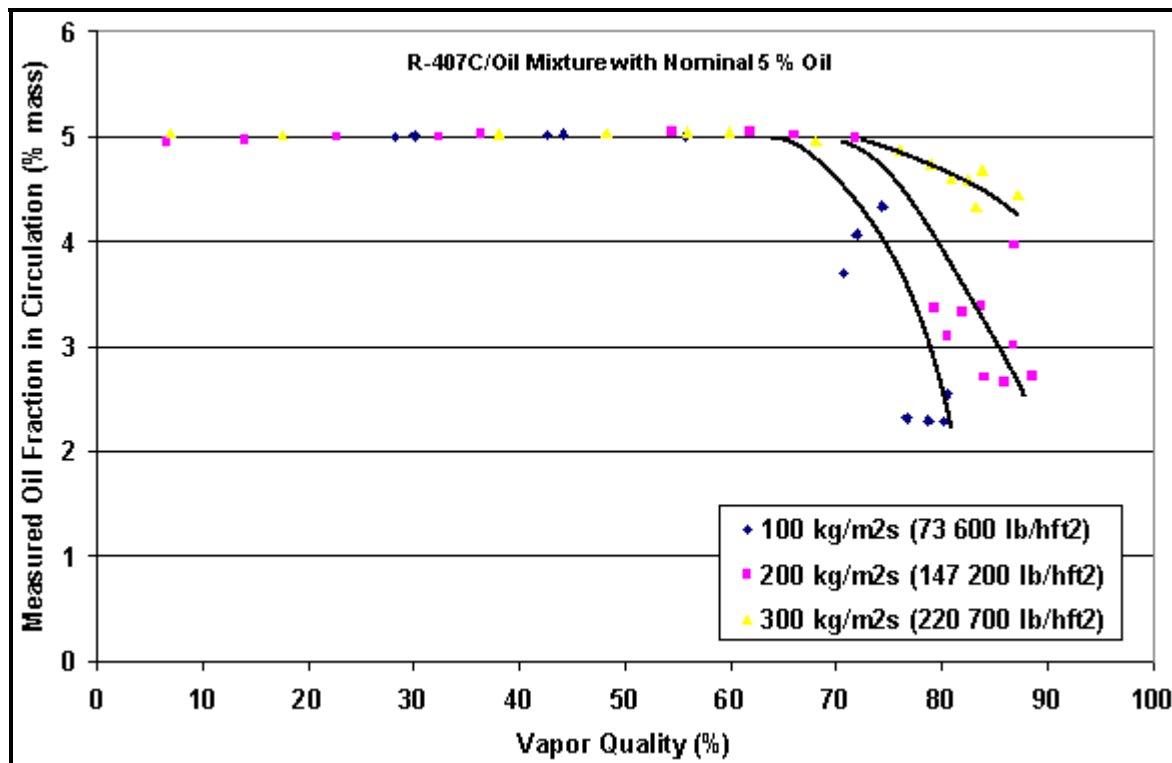


Figure 16.6. Online oil mass fraction measurements illustrating the effect of mass flow rate on oil holdup in their microfin tube test section with R-407C for a nominal mass fraction of 5 (% mass) oil [reprinted from *HVAC&R Research*, ASHRAE, Atlanta, Georgia].

## 16.4 Modeling Oil Effects on Flow Boiling Heat Transfer in Plain Tubes

Zürcher, Thome and Favrat (1998b) showed that the sharp reduction in heat transfer coefficients at high vapor quality caused by oil can be accurately predicted with the Kattan, Thome and Favrat (1998a, 1998c) flow boiling model and flow pattern map, if the pure refrigerant's liquid viscosity  $\mu_{ref}$  is replaced with that of the local refrigerant-oil viscosity  $\mu_{ref-oil}$ . For the mass velocities of 200 and 300 kg/m<sup>2</sup>s (147,158 and 220,738 lb/h ft<sup>2</sup>) for R-134a/oil and R-407C/oil at  $x > 0.70$ , i.e. where there is the most severe effect, they predicted these data to a standard deviation of 22.3%, which is only slightly higher than for the same refrigerants without oil in this range of vapor quality, i.e. about 17%.

To incorporate this viscosity effect, the local liquid dynamic viscosity of the refrigerant-oil mixture  $\mu_{ref-oil}$  is calculated using the Arrhenius mixing law, which after rearranging into a convenient form is:

$$\mu_{ref-oil} = (\mu_{ref})^{(1-w)} (\mu_{oil})^w \quad [16.4.1]$$

where  $w$  is the local oil mass fraction in the liquid, which in terms of the local vapor quality  $x$  and the inlet oil mass fraction  $w_{inlet}$  is:

$$w = w_{inlet} / (1-x) \quad [16.4.2]$$

where  $\mu_{ref}$  is the liquid dynamic viscosity of the pure refrigerant and  $\mu_{oil}$  is the liquid dynamic viscosity of the pure oil, all evaluated at the local bubble point temperature of the mixture. Their data cover local liquid viscosities up to about  $0.0035 \text{ Ns/m}^2$  (35 cp), which is up to 150 times the values of pure R-134a and R-407C.

Figure 16.7 shows their simulation applying this method to R-134a with Mobil EAL 68 oil for several inlet oil compositions. The resulting curves capture the shifts of the peak in  $\alpha$  vs.  $x$  to lower vapor qualities together with their smaller amplitude peaks.

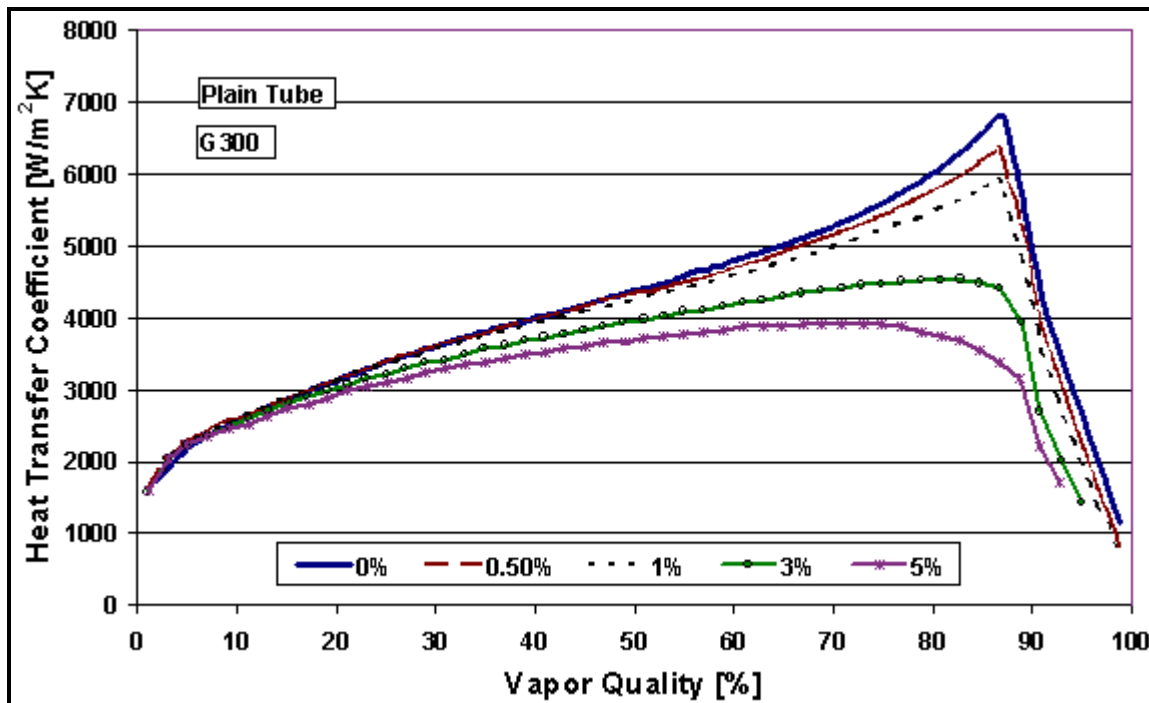


**Figure 16.7. Predicted variation in R-134a/oil flow boiling coefficients in a plain tube at  $q = 10 \text{ kW/m}^2$  (3170 Btu/h ft $^2$ ) at 3.43 bar (49.7 psia) [reprinted from HVAC&R Research, ASHRAE, Atlanta, Georgia].**

As another approach, Thome (1997b) proposed a multiplier be applied to pure refrigerant heat transfer coefficients, either predicted or measured, to obtain the flow-boiling coefficient with oil,  $\alpha_{ref-oil}$ . The multiplier  $[\mu_{ref}/\mu_{oil}]^{0.26w}$  for plain tubes is applied to the pure refrigerant heat transfer coefficient  $\alpha_{ref}$  as:

$$\alpha_{ref-oil}/\alpha_{ref} = [\mu_{ref}/\mu_{oil}]^{0.26w} \quad [16.4.3]$$

where  $w$  is the local oil mass fraction. This approach and that above are only reliable if the mass flow rate is at or above about  $200 \text{ kg/m}^2\text{s}$  ( $147,158 \text{ lb/h ft}^2$ ) and  $0.05 \geq w_{inlet}$ .

## 16.5 Modeling Oil Effects on Flow Boiling Heat Transfer in Microfin Tubes

No prediction method for refrigerant-oil effects on microfin tubes has yet been proposed. In the absence of other alternatives, the multiplier  $[\mu_{\text{ref}}/\mu_{\text{oil}}]^{0.26w}$  for plain tubes can be applied as a correction to local pure refrigerant microfin experimental data as an interim approach.

## 16.6 Modeling Oil Effects on Two-Phase Pressure Drops for Plain Tubes

Numerous test measurements of two-phase pressure drops for evaporation of refrigerant-oil mixtures are available for plain and microfin tubes, both for quasi-local pressure drops over a narrow change in vapor quality and mean pressure drops over a wide change in vapor quality. Space limitations do not allow all this experimental work to be reviewed here. Similar to evaporation, quasi-local two-phase pressure drop data are more valuable than mean data since the higher mass fraction of oil in the liquid-phase at high vapor qualities results in a significant increase in two-phase frictional pressure drop while only a minor effect of oil occurs at lower vapor qualities.

As an example, Figure 16.8 depicts the plain tube pressure drop data for R-134a and R-407C mixed with Mobil Arctic EAL 68 oil obtained by Nidegger, Thome and Favrat (1997) and Zürcher, Thome and Favrat (1998b), respectively, during their boiling tests described earlier. Their quasi-local refrigerant-oil measurements were normalized by the corresponding pure refrigerant values, and polynomial curve fits are shown in the graphs at a mass velocity of 300 kg/m<sup>2</sup>s (220,738 lb/h ft<sup>2</sup>) for vapor qualities greater than 55%. The influence of oil increases with its local oil mass fraction in the liquid-phase, where the local refrigerant-oil liquid viscosity can be calculated by Equation (7).

Friedel (1979) is just one of many two-phase frictional pressure drop correlations available in the literature for plain tubes and has been recommended for general use in Collier and Thome (1994, 1996). The frictional two-phase pressure drop gradient ( $dp/dz$ )<sub>frict</sub> is defined as

$$(dp/dz)_{\text{frict}} = 2f_L \dot{m}_{\text{total}}^2 (\rho_L d_i) \phi_{Lo}^2 \quad [16.4.4]$$

where  $\rho_L$  is the density of the liquid-phase,  $f_L$  is the Fanning friction factor for turbulent flow for all flow as liquid,  $\dot{m}_{\text{total}}$  is the total mass velocity,  $d_i$  is the tube internal diameter, and  $\phi_{Lo}^2$  is the two-phase friction multiplier. The influence of the oil on liquid viscosity is the dominant oil related factor on the two-phase pressure drop. Adding an empirical correction parameter  $n$  to the Arrhenius mixing law for liquid viscosities, i.e. Eq. [16.4.1], and rearranging, the following factor was obtained by Zürcher, Thome and Favrat (1998b):

$$f_{\text{oil}} = [\mu_{\text{ref-oil}}/\mu_{\text{ref}}]^n = [\mu_{\text{oil}}/\mu_{\text{ref}}]^{nw} \quad [16.4.5]$$

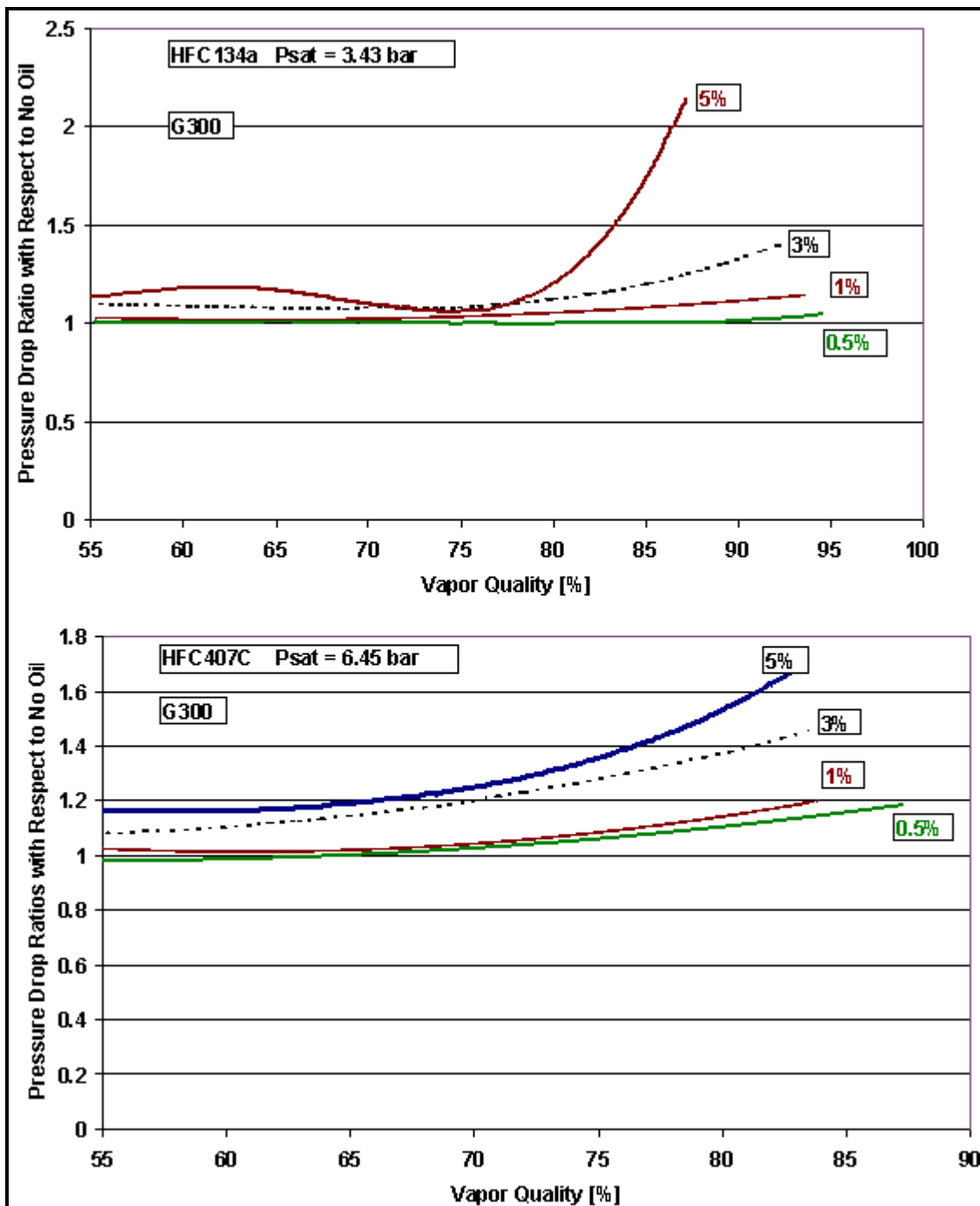


Figure 16.8. Two-phase pressure drop ratios for evaporation of refrigerant-oil mixtures in a 10.92 mm (0.430 in.) diameter tube at 300 kg/m<sup>2</sup>s (220,738 lb/h ft<sup>2</sup>). Top: R-134a; Bottom: R-407C [reprinted from HVAC&R Research, ASHRAE, Atlanta, Georgia].

where  $w$  is the local oil fraction in the liquid-phase determined with Eq. [16.4.2]. Thus the two-phase friction multiplier for refrigerant-oil mixtures becomes:

$$(\phi_{Lo}^2)_{ref-oil} = (\phi_{Lo}^2)_{ref} f_{oil} = (\phi_{Lo}^2)_{ref} [\mu_{oil}/\mu_{ref}]^{nw} \quad [16.4.7]$$

where  $n = 0.18355$  without foaming (R-134a/oil mixtures) and

$$n = w(3.583w_{inlet} + 0.0616) \quad [16.4.7]$$

with foaming (R-407C/oil mixtures). Overall standard deviations at mass velocities of 200 and 300 kg/m<sup>2</sup>s (147,158 and 220,738 lb/h ft<sup>2</sup>) with inlet oil fractions from 0.005 to 0.05 and  $w$  from 0.01-0.4 were 9.2% and 7.3% for R-134a/oil and R-407C/oil mixtures, respectively. Thus, the effect of oil can easily be included in local two-phase pressure drop calculations.

## 16.7 Modeling Oil Effects on Two-Phase Pressure Drops for Microfin Tubes

For microfin tubes, in the absence of a specific method, the above approach for plain tubes can be utilized to estimate the influence of oil on microfin tubes.

## 16.8 Nucleate Pool Boiling of Refrigerant-Oil Mixtures

In refrigeration systems with flooded evaporators, operational oil mass fractions are normally in the range from 0.5% to 3.0% oil, depending on the type of compressor and whether or not an oil separator is used and its effectiveness. This range in values refers to the oil mass in the subcooled liquid prior to the expansion device; the local oil mass fraction in the liquid rises rapidly in the evaporator as the refrigerant evaporates into the vapor-phase. At the exit of an evaporator, the local mass fraction in the liquid can reach 50% oil or more.

In recent years it has become common for academic tests to include oil effects as part of nucleate pool boiling studies for refrigerants on enhanced boiling surfaces, which has been reviewed in Thome (1996). The present review will present the highlights and conclusions drawn from them.

Before proceeding, the bubble point temperature  $T_{bub}$  and the definition of mixture heat transfer coefficients need to be discussed. The effect of oil on bubble point temperatures in mixture pool boiling tests is not severe since 1-5% oil has only a minimal effect on  $T_{bub}$  compared to the pure refrigerant saturation temperature, e.g. about 0.1-0.2°C (0.2-0.4°F). Yet, for an enhanced boiling surface, this represents about 10-20% of the measured boiling superheat. Therefore, it is very important as pointed out in Thome (1994b) to use the bubble point temperature  $T_{bub}$  of the mixture to determine the boiling heat transfer coefficient  $\alpha$  from its definition, i.e.

$$\alpha = q / (T_w - T_{bub}) \quad [16.9.1]$$

and not the saturation temperature  $T_{sat}$  of the pure refrigerant with the expression

$$\alpha = q / (T_w - T_{sat}) \quad [16.9.2]$$

where  $T_w$  is the heated wall temperature. The bubble point temperature can be calculated either with the generalized method presented in Chapter 15 or measured as the bulk liquid temperature during the tests. Only experimental studies that have correctly reduced their boiling data using the bubble point temperature of the refrigerant-oil mixture are described below to avoid showing incorrect trends in the data.

Memory, Bertsch and Marto (1993) ran nucleate pool boiling tests for pure refrigerant R-124 and its mixtures with an alkyl benzene oil. These single tube tests studied boiling on plain and enhanced tubes at a saturation temperature of 2.2°C (36°F). Figure 16.9 depicts the effect of oil mass fraction on these tubes boiling heat transfer coefficients at  $q = 25,000 \text{ W/m}^2$  (7926 Btu/h ft<sup>2</sup>), normalized by their corresponding values for pure R-124. For the plain tube, boiling performance increased up to 22% at 6% oil while for a small amount of oil (0.5%) no change occurred relative to the pure R-124 value. For the plain tube this is quite a common trend where the maximum occurs for an oil mass fraction in the range from 3-6% and the maximum increase in performance is typically from 20-40%.

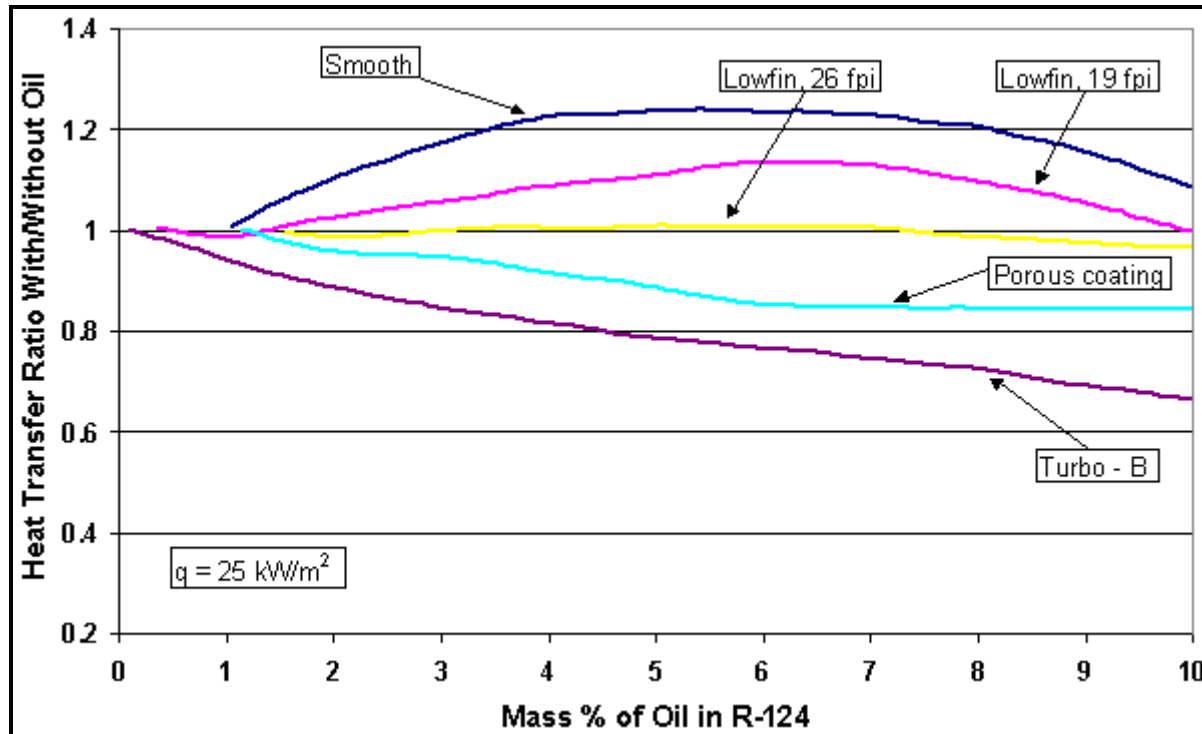


Figure 16.9. Boiling of R-124 with oil on plain and enhanced tubes by Memory, Bertsch and Marto (1993).

For the 19-fpi, low-finned tube they tested, a similar trend to the plain tube was observed. On the other hand, their 26 fpi low-finned tube had essentially no oil effect over the entire oil mass fraction range tested. For the High Flux tube instead, the boiling coefficients dropped off monotonically to an 18% reduction at 10% oil. Similarly, the Turbo-B tube was adversely affected, its performance decreasing by 35% for 10% oil. While it would be extremely unusual operating conditions for a refrigeration system to be operating with 10% oil in its charge, at local evaporating conditions within the tube bundle this local oil fraction is easily reached but only near the top of the bundle. The level of improvement or degradation caused by the oil is a function of heat flux, where the plain and low finned tube coefficients tend to improve with increasing heat flux while the two enhanced boiling tubes declined further. Even so, the two enhanced boiling tubes still significantly outperformed the two low finned tubes.

Memory, Sugiyama and Marto (1995) continued the above tests with equivalent tests for R-114/oil mixtures at 2.2°C (36°F) using the same tubes for oil mass fractions from 0-10%. They tested a completely miscible mineral oil (York-C), which caused foaming during their tests. They observed that a small amount of oil (3%) increased the boiling coefficient compared to pure R-114 for the two low finned

tubes they tested. In contrast, oil decreased performance for their plain tube and for all reentrant types of enhanced boiling tubes (High Flux, Turbo-B, Gewa-YX, Gewa-T and Thermoexcel-HE).

Webb and McQuade (1993) investigated the effect of oil on boiling of R-123 and R-11 using a mineral oil. Opposed to the above study, their plain tube displayed a monotonic degradation in performance with increasing oil mass fraction relative to pure R-123 at a heat flux of  $30 \text{ kW/m}^2$ , i.e. no maximum as in the above study. For 5% oil in fact, the plain tube's performance decreased by 15%. In comparison, the Gewa SE enhanced boiling tube experienced more degradation than the plain tube, falling by 24% at 5% oil. Similar to the R-124 tests, the Turbo-B tube had a large degradation with its boiling performance dropping by 28% relative to its pure refrigerant value.

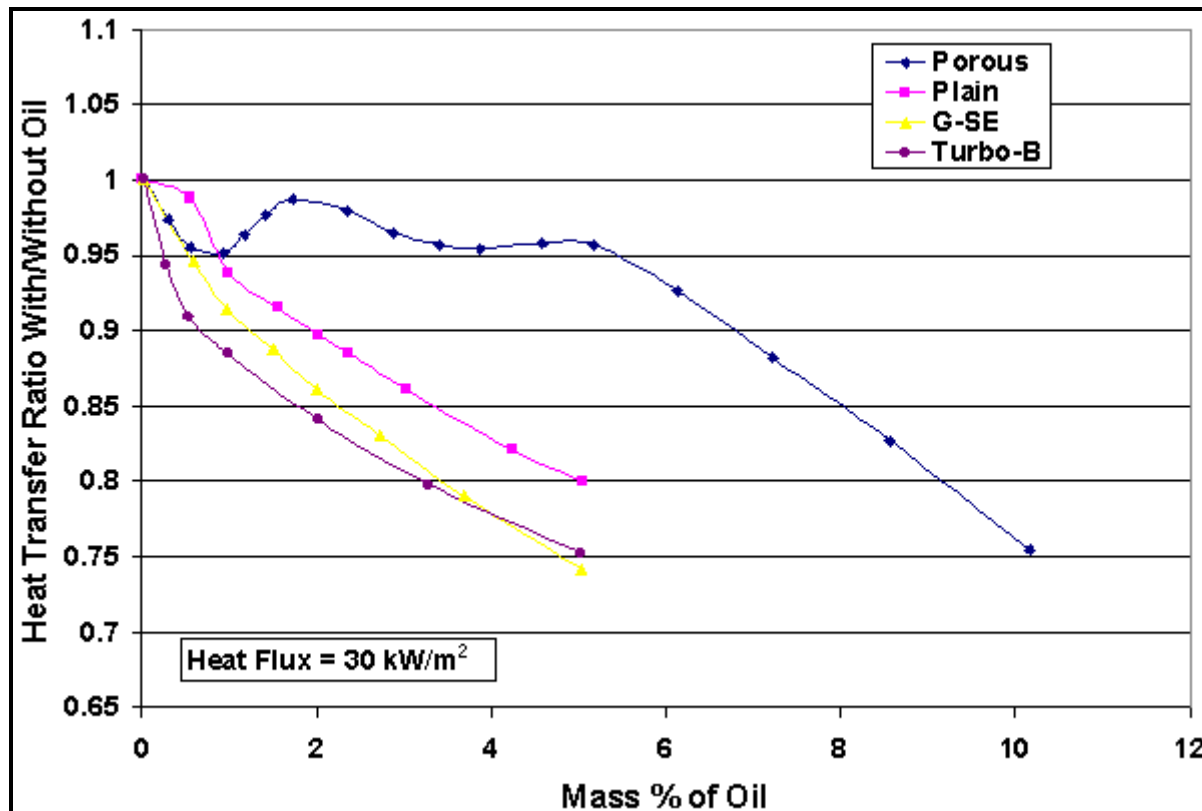
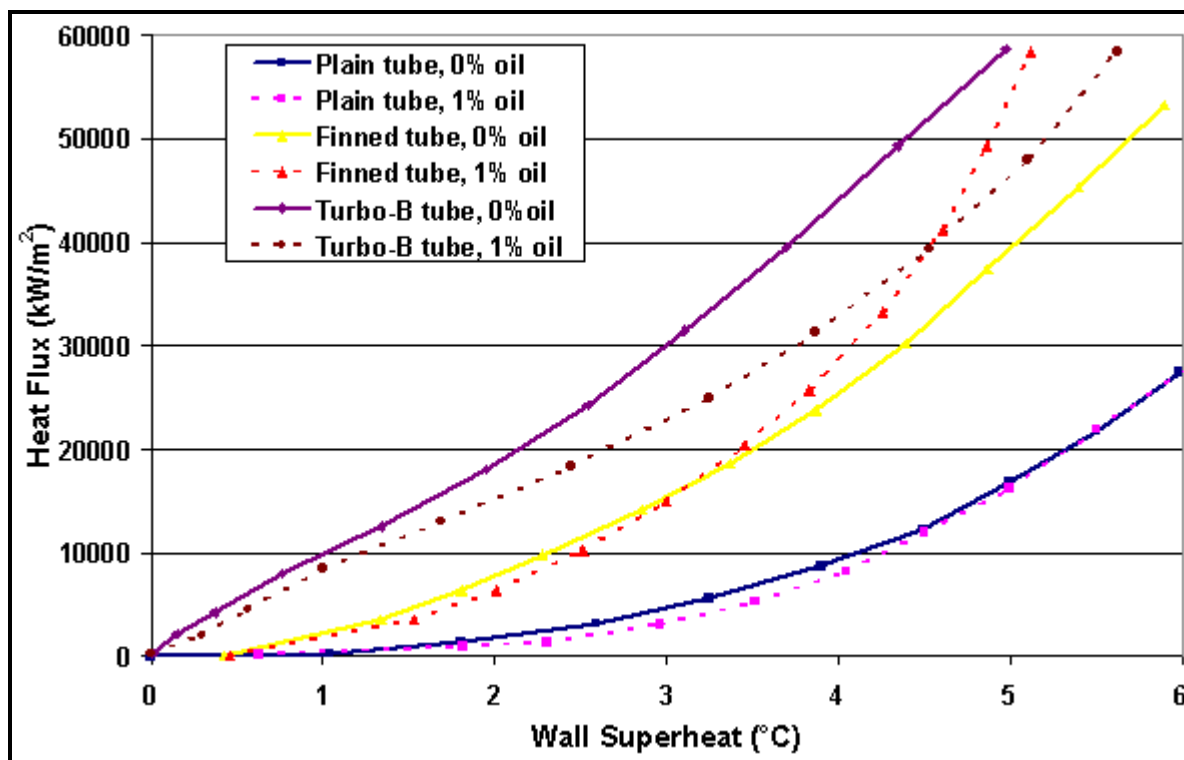


Figure 16.10. Webb, Chien, McQuade and Imadojemu (1995) R-123/oil results normalized by their pure fluid coefficients.

Webb, Chien, McQuade and Imadojemu (1995) ran further tests for R-123/oil mixtures on plain, High Flux, Gewa-SE, and Turbo-B tubes over the range of 0-10% oil. The tests were run at a temperature of  $4.4^\circ\text{C}$  ( $40^\circ\text{F}$ ) and they correctly used the measured value of  $T_{\text{bub}}$  in the liquid pool to reduce their data. They tested a mineral oil identified as GA-155 supplied by the Mobil Research and Development Company. They observed foaming for oil mass fractions of 2% or larger. Figure 16.10 depicts their test results normalized by the pure refrigerant heat transfer coefficients at a heat flux of  $30 \text{ kW/m}^2$  ( $9512 \text{ Btu/h ft}^2$ ). Surprisingly, the High Flux tube had little degradation in performance for oil mass fractions less than 5%, which is contrary to what Marto and coworkers found for R-114/oil and R-124/oil mixtures on this tube. The other results for R-123/oil were similar to those of Marto and coworkers with performance dropping off monotonically with increasing oil.

Palm (1995) did tests with R-134a and oil for plain and enhanced tubes. Figure 16.11 depicts his results, which give similar trends to those illustrated above.



**Figure 16.11. Palm (1995) R-134a/oil pool boiling results.**

Chen and Tuzla (1996) obtained Turbo-BII pool boiling coefficients at 4.4°C (40°F) for R-22, R-134a and three refrigerant blends with 1% and 5% oil mass fractions. They used hot water heating in accurately run tests. Figure 16.12 shows their results with 5% oil. R-22 was tested with a petroleum based York-C oil while the others were tested with an ester type Mobil EAL Arctic 46 lubricant. With 1% oil, the Turbo-BII boiling performance for R-22, R-134a and the azeotropic blend fell by 10-30% while about 25-40% with 5% oil. The Turbo-BII tube did not suffer a fall in performance from the oil for the two-zeotropic blends. Hence, while their non-oil boiling performance penalty in an evaporator with respect to R-22 is substantial, but it is less so once oil effects are included.

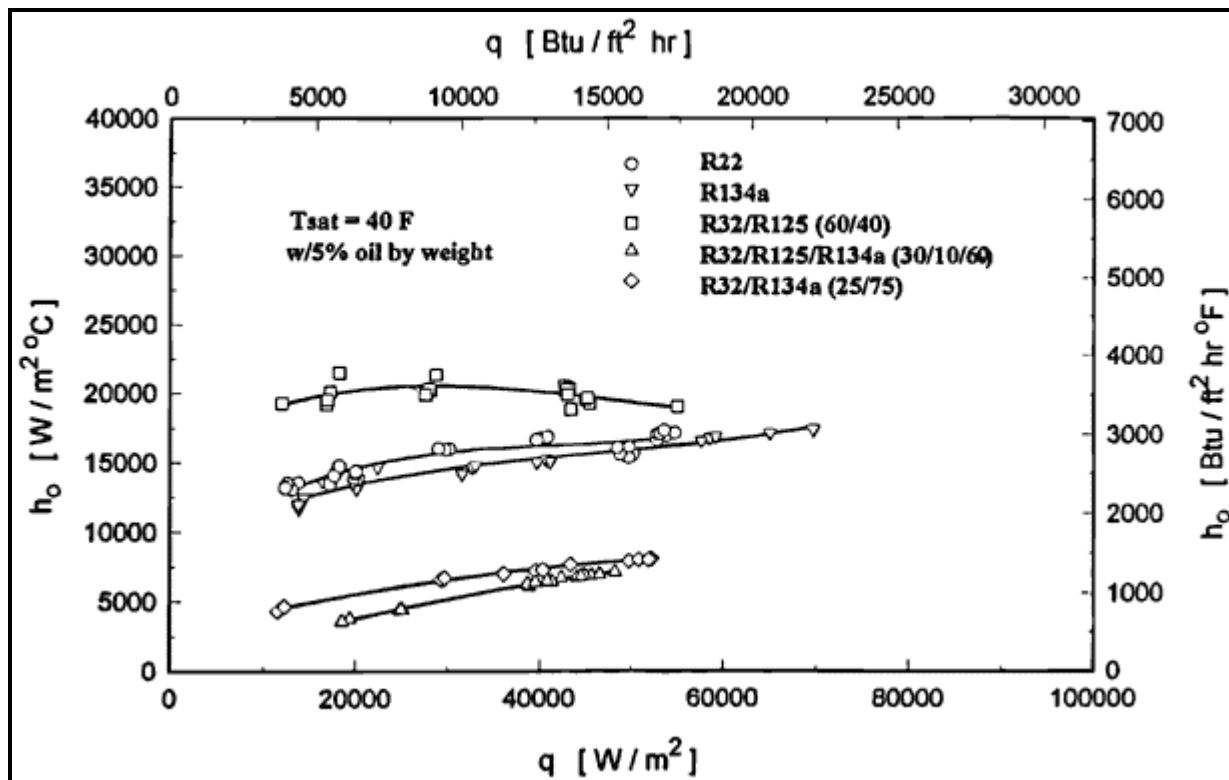


**Figure 16.12.** Chen and Tuzla (1996) boiling data for Turbo-BII tube with 5 % oil [their fig. 16 reprinted by permission of EPRI].

Gorenflo and Koster (1997) compared the oil effects measured in four independent refrigerant-oil studies, depicted in Figure 16.13. In the top graph, Moller, Spindler and Hahne (1993) found that oil increased boiling performance in R-134a by up to 20% depending on heat flux and oil mass fraction. In the lower graphs from tests by Marto and coworkers, the oil either increased or decreased performance depending on the type of tube. For a tube bundle, the effect of oil was to enhance performance for plain and low finned tubes more than in the comparable single-tube tests while for the enhanced tubes (High Flux and Turbo-B) single-tube and bundle results were similar.

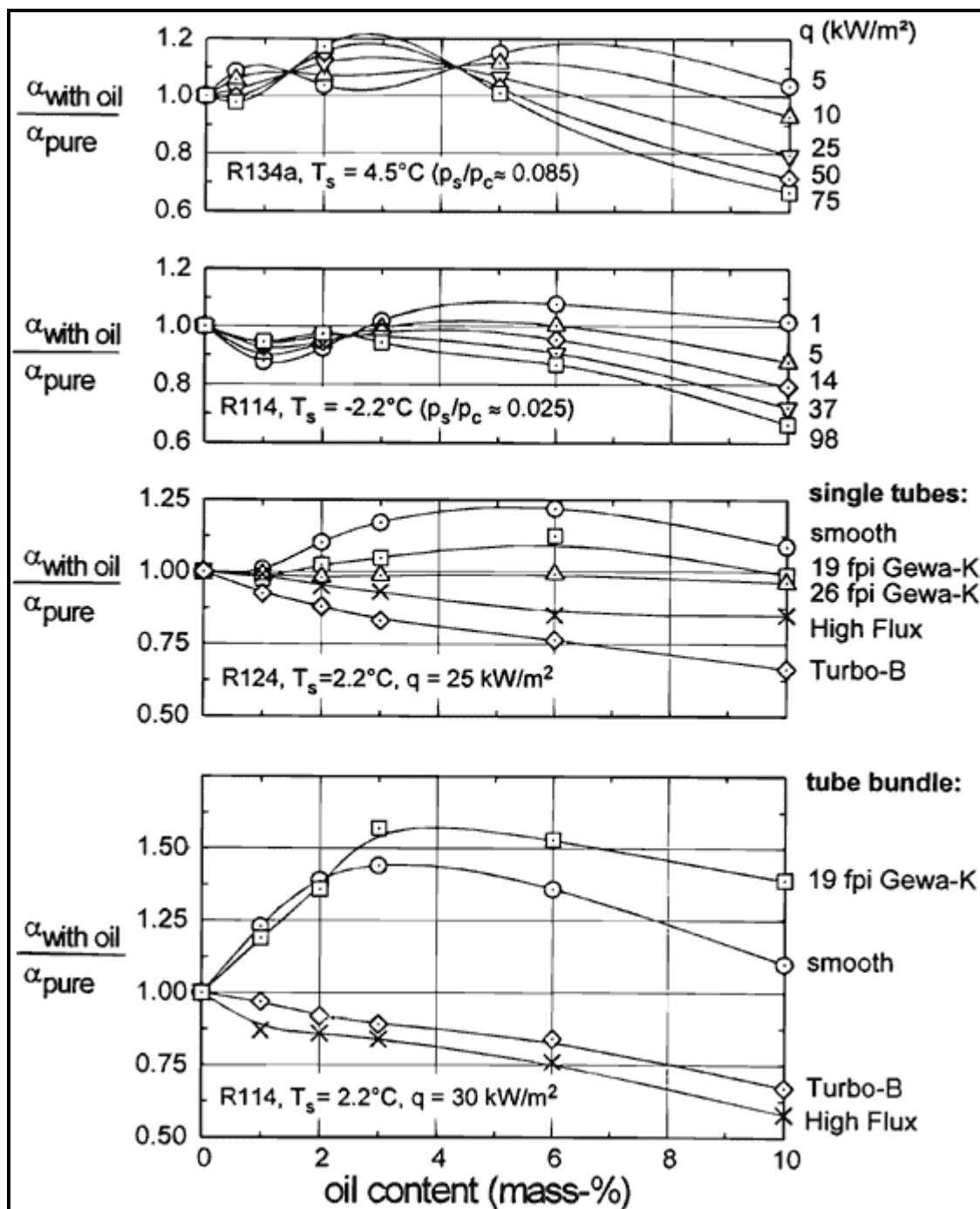


Figure 16.13. Relative influence of oil on boiling from Gorenflo and Koster (1997). *Top:* R-134a/polyester oil on a stainless steel tube from Moller, Spindler and Hahne (1993); *Second:* R-114/oil on a copper tube from Warriarachchi, Marto and Reilly (1986); *Third:* R-124/alkylbenzene oil on single tubes from Memory, Bertsch and Marto (1993); *Bottom:* R-114/mineral oil on small bundles from Memory, Akcasayar, Eraydin and Marto (1995) [their fig. 4 reprinted by permission of D. Gorenflo].

For boiling in mixtures, it is common to describe the degradation in heat transfer caused by mass transfer effects with an expression proposed by Stephan and Körner (1969) that can be adapted for refrigerant-oil mixtures as:

$$\frac{\alpha}{\alpha_I} = \frac{(T_w - T_{bub})}{(T_w - T_{bub}) + dT_{bub}} \quad [16.9.3]$$

where the ideal boiling heat transfer coefficient  $\alpha_I$  is for an equivalent pure fluid with physical properties identical to the mixture and the mixture heat transfer coefficient  $\alpha$  is defined as in expression [16.9.1]. The rise in the local bubble point temperature at the interface of a growing bubble,  $dT_{bub}$ , due to the congregation of oil (which gets transported to the interface but cannot evaporate), decreases the ratio of  $\alpha/\alpha_I$ , such that  $\alpha$  of the mixture is less than or equal to  $\alpha_I$ . The larger degradation in  $\alpha/\alpha_I$  typically observed for enhanced boiling tubes compared to plain and low finned tubes is expected, as pointed out in Thome (1987), since  $(T_w - T_{bub})$  for an enhanced tube is much less than that of a plain or low finned tube. This increases the relative importance of  $dT_{bub}$  in [16.9.3]. For instance, if  $dT_{bub} = 0.5^\circ\text{C}$  ( $0.9^\circ\text{F}$ ) and  $(T_w - T_{bub}) = 10^\circ\text{C}$  ( $18^\circ\text{F}$ ) for a plain tube, the relative degradation in the mixture coefficient is only 4.8%; for an enhanced boiling tube with  $(T_w - T_{bub}) = 1.0^\circ\text{C}$  ( $1.8^\circ\text{F}$ ), the degradation is 33.3%!

In addition to the mass diffusion effect noted above, two other aspects play a role in boiling of refrigerant-oil mixtures: (i) a change in physical properties and (ii) a modification of the underlying heat transfer mechanisms. Both of them may be important. First of all, lubricating oils have critical pressures much lower than refrigerants so adding oil to a refrigerant substantially decreases the critical pressure of the mixture. Other properties affected significantly by the oil are liquid viscosity, surface tension and contact angle. Secondly, oil may promote foaming at the boiling surface that in turn influences bubble growth and departure. This foaming action may modify the underlying heat transfer mechanisms for plain and low finned tubes and the thin film evaporation process occurring inside reentrant channels of an enhanced tube. More fundamental study of these mechanisms is required in order to understand their consequences before generalized predictive methods can be developed.

In summary, oil effects on the nucleate pool boiling heat transfer coefficient are numerous and quite complex. For plain tubes, oil can either cause a slow monotonic decrease in  $\alpha$  with increasing oil mass fraction relative to the pure refrigerant coefficient or first increase and then decrease with increasing oil to create a local maximum in  $\alpha$ . No concrete explanation with conclusive experimental proof is available explain why oil sometimes increases plain tube boiling performance by 30-40% but in other cases has no effect or monotonically degrades performance. The same comments are applicable to low finned tubes. For enhanced boiling tubes, even a small amount of oil usually decreases the boiling performance in nucleate pool boiling tests. A better understanding of the influence of oil is required for enhanced tubes. Also, test results tend to depict a complicated influence of heat flux on the oil effect for all types of tubes. Not surprisingly, there are not any prediction methods for the influence of oil on nucleate pool boiling performances of plain, low fin and enhanced tubes to be recommended at this time.

## 16.9 Bundle Boiling of Refrigerant-Oil Mixtures

For evaporation of a refrigerant-oil mixture on a horizontal tube bundle, the local oil mass fraction increases from bottom to top in the bundle as the local vapor quality rises since no oil evaporates into the vapor-phase and consequently it builds up in the liquid-phase. Hence, the local oil mass fraction may reach levels, under exceptional conditions, as high as 20% to 50% near the top of the tube bundle. Therefore, using single-tube nucleate pool boiling test data for say 1% oil typical of industrial practice to size an enhanced tube flooded-evaporator does not realistically account for the oil's influence on local performance near the top of the bundle. Unfortunately, single-tube boiling tests rarely go beyond oil mass fractions of 5%, although some tests up to 10% have been published. Hence, caution is required in using single-tube tests with 1% oil for thermal design. The best approach would be to use test data for a range

of oil mass fractions and apply these to the mass fraction profile that occurs up through the bundle as the refrigerant evaporates out of the mixture.

Not many boiling tests on tube bundles that have correctly reduced their data using the Thermodynamic Approach described in Chapter 15 are available. Results reduced using the saturation temperatures of the pure refrigerant are not thermodynamically correct and do not abide by the definition of the heat transfer coefficient for a mixture given by expression [16.9.1]. There is, however, the excellent study by Memory, Akacasayer, Eraydin and Marto (1995) on R-114/oil mixtures on plain and enhanced tube bundles.

The Thermodynamic Approach presented in Chapter 15 for prediction of bubble point temperatures of refrigerant-oil mixtures and preparation of temperature-enthalpy-vapor quality (T-h-x) curves for thermal design should also be used to determine the LMTD, either global or incremental, for a flooded-evaporator with oil in the evaporating refrigerant. Current design practice in the refrigeration industry ignores these aspects of oil on flooded-evaporator design and hence do not account for oil effects in a proper manner.

## 16.10 Comments of Practical Importance

From an overall perspective, it is particularly important to think of oil in a refrigerant charge not as an *impurity* but as a *component in a binary mixture*. Hence, the theory and methodologies available for dealing with heat transfer and flow of mixtures can be brought to focus on the problem.

Running fundamental tests, coil and bundle tests and equipment validation tests with disregard to the quantity of oil still remains common practice; however, it is only by accounting for the oil as a binary component in a mixture that we can arrive at a better understanding of this complex problem. Disregarding the mass fraction of oil circulating in the flow loop and not applying an enthalpy curve of the mixture to reduce test data on an evaporator is not correct. Thus, it is very easy to arrive at results that do not respect the correct energy balance and consequently to arrive at wrong conclusions.

As noted in Chapter 15, it is clear that the oil can have a significant effect on the temperature profile of the evaporating fluid. A local oil mass fraction of 0.50 at high vapor qualities, which means that one-half of the local liquid is oil, is within the normal operating range of many units. For example, a circulating mass fraction of 0.02 of oil at a local vapor quality of 0.96 achieves this local mass fraction and hence results in a rise in the local boiling point temperature by 2.3°C (4.1°F) for R-22. Similarly, an oil mass fraction of 0.01 at a vapor quality of 0.98 produces the same result. Hence, it is easy to mistake a temperature measurement at the exit of an evaporator as having achieved 2.3°C (4.1°F) of superheat when in fact not all the refrigerant has been evaporated and naturally none of the oil. What is actually being measured is the local bubble point temperature. Thus, the wrong conclusions about performance will be reached unless the enthalpy approach is applied. Since obtaining test results is expensive, it makes sense to implement the enthalpy approach to get better, more accurate information from such tests.

---

**Example Calculation:** Assume that 3% oil (mass) is circulating in a refrigeration system with a direct-expansion evaporator. The viscosity of the pure refrigerant is 0.4 cp while that of the oil is 400 cp at the operating temperature of the evaporator. At a local vapor quality of 0.95, what will be the local reduction in the boiling heat transfer coefficient?

**Solution:** The local oil mass fraction w for  $w_{inlet} = 0.03$  and  $x = 0.95$  is obtained using [16.4.2]:

$$w = w_{inlet} / (1 - x) = 0.03 / (1 - 0.95) = 0.60$$

The ratio of  $\alpha_{\text{ref-oil}}/\alpha_{\text{ref}}$  for this situation is obtained with [16.4.3]:

$$\alpha_{\text{ref-oil}}/\alpha_{\text{ref}} = [\mu_{\text{ref}}/\mu_{\text{oil}}]^{0.26w} = [0.4/400]^{0.26(0.60)} = 0.340$$

Hence, the boiling heat transfer coefficient with oil will only be 0.34 that of the pure refrigerant without oil or a reduction of 66%.

# **III. Fundamentals of Void Fraction in Two-Phase Flows**

## **(Chapter 17 in Databook III)**

**Prof. John R. Thome**

**Laboratory of Heat and Mass Transfer**

**Faculty of Engineering Science**

**Swiss Federal Institute of Technology Lausanne**

**CH-1015 Lausanne, Switzerland**

# Objectives of Lecture:

- Describe geometrical definitions of void fraction.
- Describe some measurement techniques.
- Present homogeneous void fraction model.
- Describe one-dimensional models.
- Discuss radial void fraction distributions.
- Discuss empirical and drift flux type of models.
- Describe effect of flow pattern on void fraction.
- Describe LTCM dynamic void fraction measurement technique.

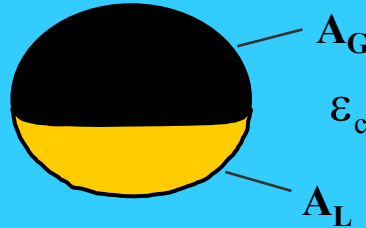
# Geometrical Void Fraction Definitions: Section 17.1

## 1 - Local void fraction

$$r \rightarrow + \quad P_k(r, t) = \begin{cases} 1 & \text{if point } r \text{ is in phase G} \\ 0 & \text{if point } r \text{ is in phase L} \end{cases}$$

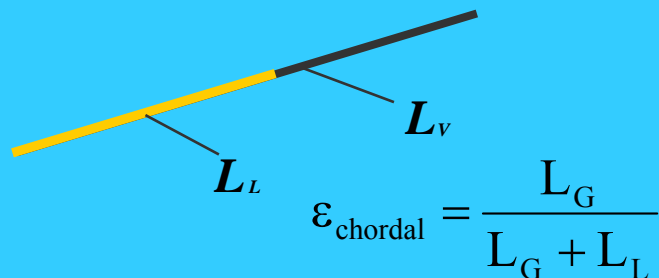
$$\varepsilon_{\text{local}}(r, t) = \frac{1}{t} \int_t P_k(r, t) dt$$

## 3 - Cross-sectional void fraction



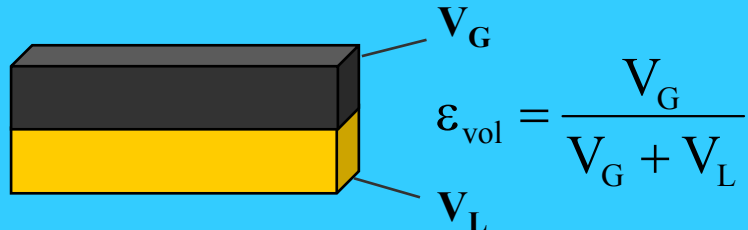
$$\varepsilon_{\text{c-s}} = \frac{A_G}{A_G + A_L}$$

## 2 - Chordal void fraction



$$\varepsilon_{\text{chordal}} = \frac{L_G}{L_G + L_L}$$

## 4 - Volumetric void fraction



$$\varepsilon_{\text{vol}} = \frac{V_G}{V_G + V_L}$$

Figure 17.1

# Geometrical Void Fraction Definitions

- *Point-wise void fraction definition:*  $\varepsilon_{\text{local}} = 0 \text{ or } 1$

$$\varepsilon_{\text{local}}(r, t) = \frac{1}{t} \int_t P_k(r, t) dt \quad \text{Time-averaged at a point}$$

- *Chordal void fraction definition:*

$$\varepsilon_{\text{chordal}} = \frac{L_G}{L}$$

- *Cross-sectional void fraction definition:*

$$\varepsilon_{\text{c-s}} = \frac{A_G}{A}$$

- *Volumetric void fraction definition:*

$$\varepsilon_{\text{vol}} = \frac{V_G}{V}$$

# Void Fraction: Meaning and Methods

For those new to the idea of a void fraction of a two-phase flow, it is important to distinguish the difference between **void fraction** of the vapor phase and the **thermodynamic vapor quality**. To illustrate the difference, consider a closed bottle half full of liquid and the remaining volume occupied by its vapor. The vapor quality is the ratio of the mass of vapor in the bottle to the total mass of liquid plus vapor. If the density ratio of liquid to vapor is 5/1, then the vapor quality is 1/6. Instead, the volumetric void fraction is obtained by applying the expression for  $\epsilon_{vol}$  and in this case would be equal to 1/2.

The most widely utilized void fraction definition is the **cross-sectional average void fraction**, which is based on the relative cross-sectional areas occupied by the respective phases. In this chapter, the cross-sectional void fraction of the gas or vapor phase  $\epsilon_{c-s}$  will henceforth be referred to simply as  $\epsilon$ . Cross-sectional void fractions are usually predicted by one of the following types of methods:

- Homogeneous model (which assumes the two phases travel at the same velocity);
- One-dimensional models (which account for differing velocities of the two phases);
- Drift flux models including radial variations in local void fraction and flow velocity;
- Models based on the physics of specific flow regimes;
- Empirical and semi-empirical methods.

# Homogeneous Void Fraction Model: Section 17.2.1

- *Cross-sectional void fraction definition:*  $\varepsilon = \frac{A_G}{A}$
- *Mean vapor and liquid velocities in their respective areas:*

$$u_G = \frac{\dot{Q}_G}{A\varepsilon} = \frac{\dot{m}}{\rho_G} \left( \frac{x}{\varepsilon} \right)$$

$$u_L = \frac{\dot{Q}_L}{A(1-\varepsilon)} = \frac{\dot{m}}{\rho_L} \left( \frac{1-x}{1-\varepsilon} \right)$$

- *In homogeneous flow,*

$$u_G = u_L \text{ so that:}$$

$$\varepsilon = \frac{x/\rho_G}{\left(\frac{1-x}{\rho_L}\right) + \left(\frac{x}{\rho_G}\right)}$$

Volumetric flow rate  
Vapor Quality

Liquid density                          Vapor density

*Rearranging gives [17.2.4]:*

$$\varepsilon_H = \frac{1}{1 + \left(\frac{1-x}{x}\right) \frac{\rho_G}{\rho_L}}$$

# Definition of Velocity Ratio in Separated 2-Phase Flows: Section 17.2.2

- Velocity ratio  $S$  is often called slip ratio.
- When  $u_G$  does not equal  $u_L$ ,  $S = \frac{u_G}{u_L}$  [17.2.6]  
we can write their ratio as:
- Introducing  $S$  into the prior equations for  $u_G$  and  $u_L$  , we get:

$$\varepsilon = \frac{1}{1 + \left( \frac{1-x}{x} \right) \frac{\rho_G}{\rho_L} S}$$

- $S > 1$  for most flows except some gravity driven *down* flows when  $S < 1$ . When  $S > 1$ , the void fraction is smaller than the homogeneous void fraction (which is maximum value).

# Relationship between Cross-Sectional and Volumetric Void Fractions

Utilizing the definition of the velocity ratio and the respective definitions above, a relationship between the **cross-sectional void fraction** and the **volumetric void fraction** (the latter obtained by the *quick-closing valve measurement technique*) can be derived.

Returning to the nomenclature used in Section 17.1:

$$\varepsilon_{\text{vol}} = \frac{\varepsilon_{\text{c-s}}}{\frac{1}{S}(1 - \varepsilon_{\text{c-s}}) + \varepsilon_{\text{c-s}}} \quad [17.2.7]$$

Thus, it can be seen that  $\varepsilon_{\text{vol}}$  is only equal to  $\varepsilon_{\text{c-s}}$  for the special case of homogeneous flow. For all other cases the **velocity ratio must be known** in order to convert volumetric void fractions to cross-sectional void fractions.

# Momentum Flux Void Fraction Model: Section 17.3.1

- Momentum flux of a fluid is:

$$\text{momentum flux} = \dot{m}^2 v_H$$

- Where specific volume of a homogeneous fluid is  $v_H$ :

$$v_H = v_G x + v_L (1 - x)$$

- For separated flows, the momentum flux is:

$$\text{momentum flux} = \dot{m}^2 \left[ \frac{x^2 v_G}{\varepsilon} + \frac{(1-x)^2 v_L}{1-\varepsilon} \right]$$

- Differentiating with respect to  $\varepsilon$  and setting the momentum flux to zero, velocity ratio is:

$$S = \left( \frac{\rho_L}{\rho_G} \right)^{1/2}$$

# Zivi Kinetic Energy Model 1 for Annular Flow: 17.3.2

- This model is based on the premise that the total kinetic energy of the two phases will seek to be a minimum. The kinetic energy of each phase  $\mathbf{KE}_k$  is given by

- $$\mathbf{KE}_k = \frac{1}{2} \rho_k u_k^2 Q_k \quad [17.3.5]$$

where the volumetric flow rate is in  $\text{m}^3/\text{s}$  and  $\mathbf{u}_k$  is the mean velocity in each phase  $k$  in  $\text{m}/\text{s}$ . Starting with the definition of the volumetric flow rate for each phase as

$$\dot{Q}_G = \frac{\dot{m}x A}{\rho_G}$$

$$\dot{Q}_L = \frac{\dot{m}(1-x)A}{\rho_L}$$

# Zivi Kinetic Energy Model 1, cont.

- The total kinetic energy of the flow **KE** is then

$$\text{KE} = \sum_{k=1}^2 \text{KE}_k = \text{KE}_G + \text{KE}_L = \frac{1}{2} \rho_G \frac{\dot{m}^2 x^2}{\varepsilon^2 \rho_G^2} \frac{\dot{m}x A}{\rho_G} + \frac{1}{2} \rho_L \frac{\dot{m}^2 (1-x)^2}{(1-\varepsilon)^2 \rho_L^2} \frac{\dot{m}(1-x)A}{\rho_L}$$

$$\text{or } \text{KE} = \frac{A \dot{m}^3}{2} \left[ \frac{x^3}{\varepsilon^2 \rho_G^2} + \frac{(1-x)^3}{(1-\varepsilon)^2 \rho_L^2} \right] = \frac{A \dot{m}^3}{2} y$$

$$\text{where the parameter } y \text{ is: } y = \frac{x^3}{\varepsilon^2 \rho_G^2} + \frac{(1-x)^3}{(1-\varepsilon)^2 \rho_L^2}$$

Differentiating parameter **y** with respect to  $\varepsilon$  in the above expression to find the minimum kinetic energy flow gives

$$\frac{dy}{d\varepsilon} = \frac{-2x^3}{\varepsilon^3 \rho_G^2} + \frac{2(1-x)^3}{(1-\varepsilon)^3 \rho_L^2} = 0 \quad [17.3.11]$$

# Zivi Kinetic Energy Model 1, cont.

- The minimum is found when  $\frac{\varepsilon}{1-\varepsilon} = \frac{x}{1-x} \left( \frac{\rho_L}{\rho_G} \right)^{2/3}$  [17.3.12]

$$\text{The velocity ratio } S \text{ is thus: } S = \frac{u_G}{u_L} = \left( \frac{\rho_L}{\rho_G} \right)^{1/3} \quad [17.3.13]$$

- The velocity ratio is therefore only dependent on the density ratio and the Zivi void fraction expression is

$$\varepsilon = \frac{1}{1 + \frac{1-x}{x} \left( \frac{\rho_G}{\rho_L} \right)^{2/3}} \quad [17.3.14]$$

# Zivi Kinetic Energy Model 2, with Entrainment

- If the fraction of the liquid entrained as droplets in vapor phase is  $e$ , summing the kinetic energies of the vapor, liquid in the annular film, and liquid entrained in the vapor (assuming the droplets travel at the same velocity as the vapor), Zivi's 2nd method is

$$\varepsilon = \frac{1}{1 + e\left(\frac{1-\chi}{\chi}\right)\left(\frac{\rho_G}{\rho_L}\right) + (1-e)\left(\frac{1-\chi}{\chi}\right)\left(\frac{\rho_G}{\rho_L}\right)^{2/3} \left[ \frac{1 + e\left(\frac{1-\chi}{\chi}\right)\left(\frac{\rho_G}{\rho_L}\right)}{1 + e\left(\frac{1-\chi}{\chi}\right)} \right]^{1/3}}$$

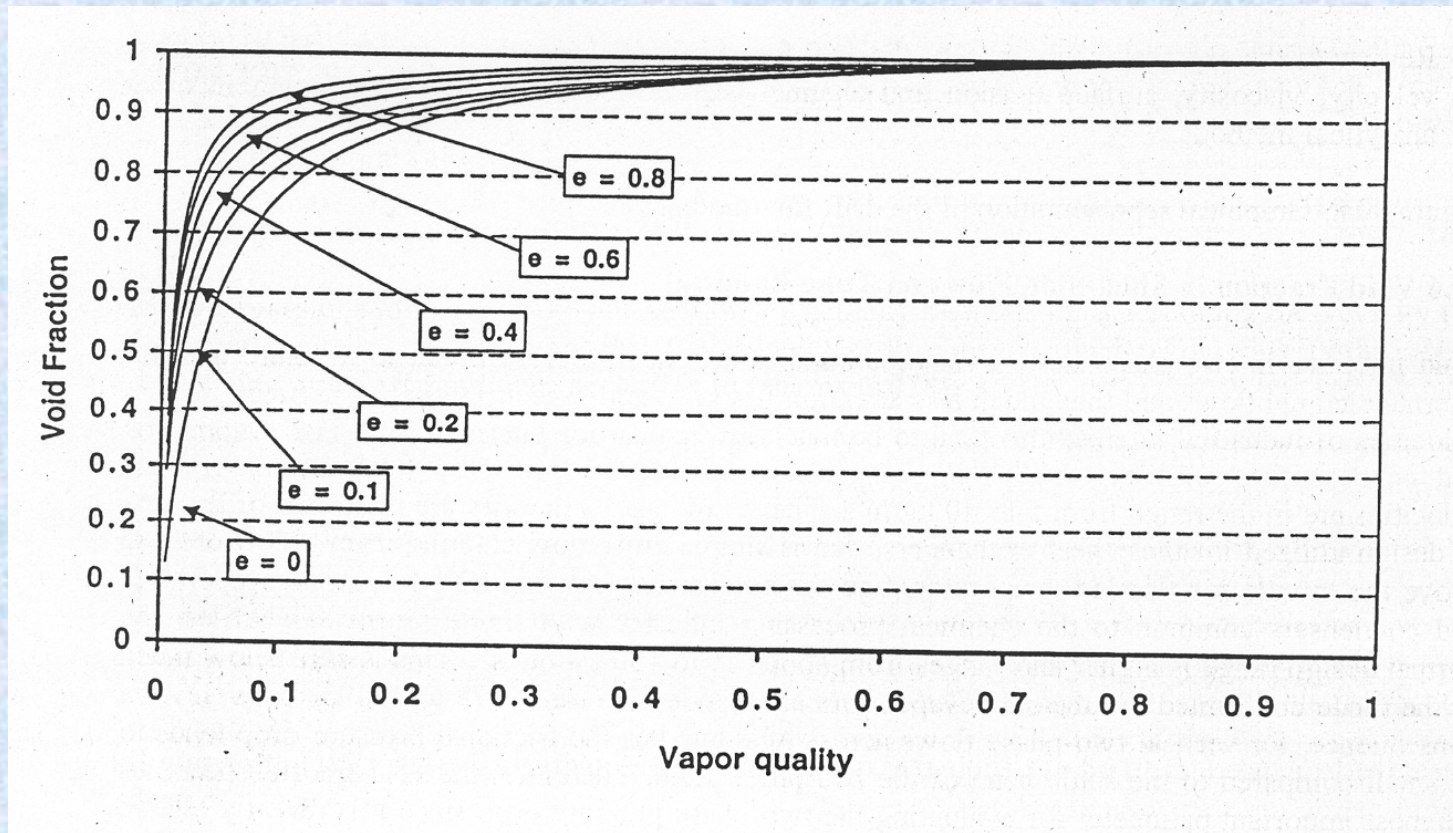
[17.3.15]

Actual value of  $e$  is *unknown* and feasible limits are:

- For  $e = 0$ , the above expression reduces to the prior expression of Zivi for the void fraction, namely [17.3.14];
- For  $e = 1$ , the expression reduces to the homogeneous void fraction equation, namely [17.2.4].

# Zivi Kinetic Energy Model 2, cont.

Figure 17.2. Influence of entrained liquid fraction on void fraction for ammonia using Zivi (1964) equation [figure taken from Zürcher (2000)].



**Example 17.2:** Determine the void fraction for the following vapor qualities (0.01, 0.05, 0.1, 0.25, 0.50, 0.75, 0.95) using the following methods: homogeneous flow, momentum flux model and both of Zivi's expressions. The liquid density is 1200 kg m<sup>-3</sup> and the gas density is 20 kg m<sup>-3</sup>. Assume the liquid entrainment is equal to 0.4.

**Solution:** the density ratio of  $\rho_G/\rho_L$  is equal to 0.0167.

Quality, x	0.01	0.05	0.10	0.25	0.50	0.75	0.95
(1-x)/x	99	19	9	3	1	0.3333	0.0526
$\varepsilon = \varepsilon_H$ Homogeneous [17.2.4]	0.377	0.759	0.870	0.952	0.984	0.994	0.999
$\varepsilon$ [17.3.4] Momentum flux	0.0726	0.290	0.463	0.721	0.886	0.959	0.993
$\varepsilon$ [17.3.14] Zivi #1	0.134	0.446	0.630	0.836	0.939	0.979	0.997
$\varepsilon$ [17.3.15] Zivi #2	0.251	0.665	0.784	0.900	0.960	0.985	0.998

# Smith (1969) Separated Flow Model: Section 17.4.1

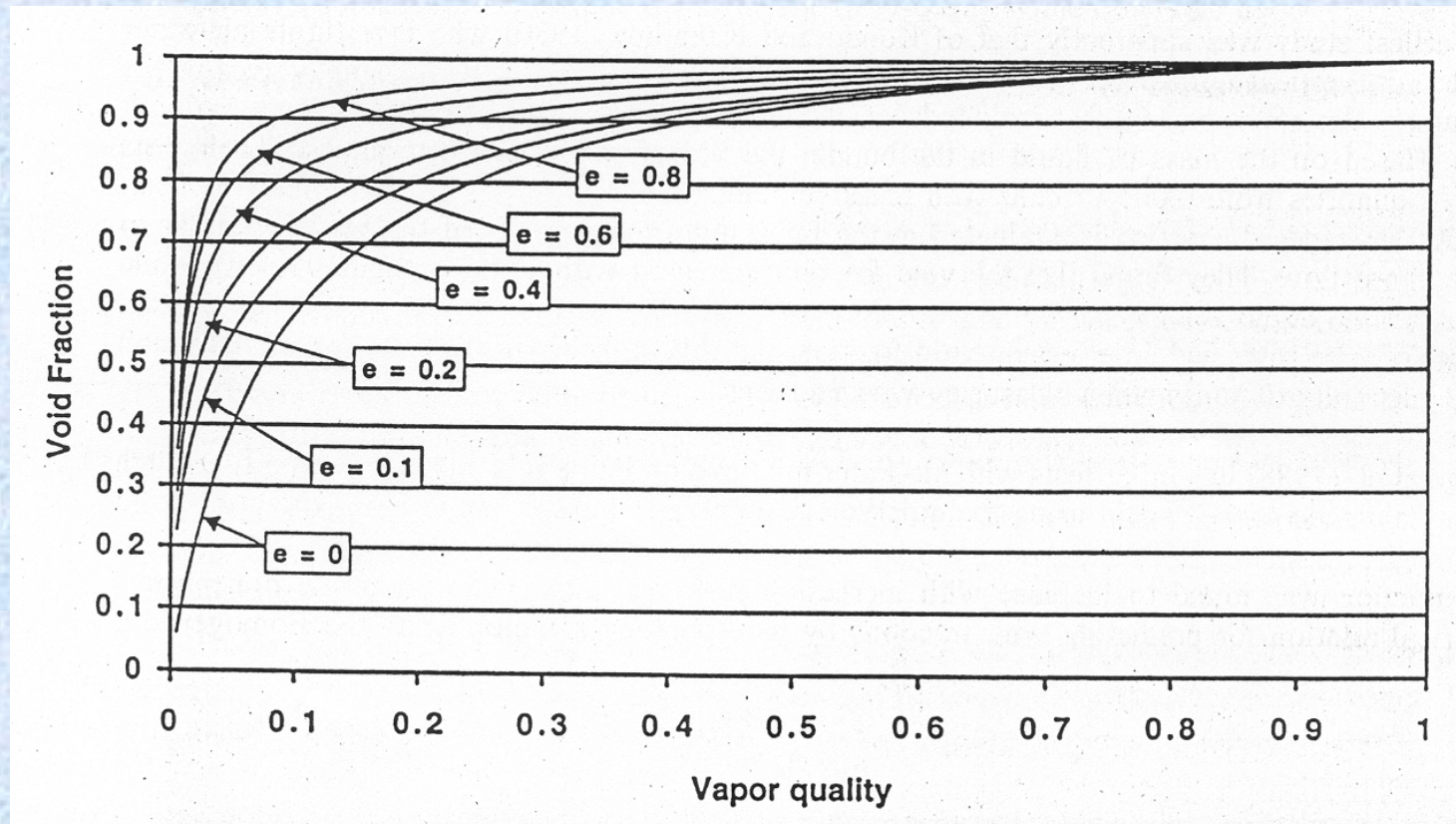
Smith (1969) assumed a separated flow consisting of a liquid phase and a gas phase with a fraction  $e$  of the liquid entrained in the gas as droplets *and that the momentum fluxes in the two phases were equal*, arriving at the following velocity ratio:

$$S = e + (1 - e) \left[ \frac{\left( \frac{\rho_L}{\rho_G} \right) + e \left[ \frac{1-x}{x} \right]}{1 + e \left[ \frac{1-x}{x} \right]} \right]^{1/2} \quad [17.4.1]$$

For  $e = 0.4$ , this gives:  $\varepsilon = \frac{1}{1 + 0.79 \left( \frac{1-x}{x} \right)^{0.78} \left( \frac{\rho_G}{\rho_L} \right)^{0.58}} \quad [17.4.2]$

# Smith (1969) Void Fraction Model

Figure 17.3. Influence of entrained liquid on void fraction by Smith (1969) equation with ammonia [figure taken from Zürcher (2000)].



# Chisholm (1972) Annular Flow Method: 17.4.2

This expression results from simple annular flow theory and application of the homogeneous theory to the fluid density, producing approximately equal *frictional pressure gradients* in each phase. It is also notable because it goes to the correct thermodynamic limits. Thus,  $S \Rightarrow 1$  as  $x \Rightarrow 0$ , i.e. at very low void fraction the vapor velocity of the very small bubbles should tend towards the liquid velocity since their buoyancy will be negligible. Also,  $S \Rightarrow (\rho_L/\rho_G)^{1/2}$  as  $x \Rightarrow 1$ , i.e. [17.3.4].

$$S = \frac{u_G}{u_L} = \left( \frac{\rho_L}{\rho_H} \right)^{1/2} = \left[ 1 - x \left( 1 - \frac{\rho_L}{\rho_G} \right) \right]^{1/2} \quad [17.4.3]$$

**Example 17.3:** For the same conditions as in Example 17.2, determine the void fraction for the following vapor qualities (0.01, 0.05, 0.1, 0.25, 0.50, 0.75, 0.95) using the methods of Smith and Chisholm. Assume the liquid entrainment is equal to 0.4. Also, determine the velocity ratio using the Chisholm equation.

**Solution:** the density ratio of  $\rho_G/\rho_L$  is equal to 0.0167.

Quality, $x$	0.01	0.05	0.10	0.25	0.50	0.75	0.95
$\varepsilon$ [17.4.2] Smith	0.274	0.578	0.710	0.852	0.932	0.970	0.993
$S$ [17.4.3]	1.26	1.99	2.63	3.97	5.52	6.73	7.55
$\varepsilon$ (Chisholm)	0.325	0.614	0.717	0.834	0.916	0.964	0.993

# Drift Flux Void Fraction Model: Section 17.4.3

The drift flux model was developed principally by Zuber and Findlay (1965), although Wallis (1969) and Ishii (1977) in particular and others have added to its development.

Its original derivation was presented in Zuber and Findlay (1965) and a comprehensive treatment of the basic theory supporting the drift flux model can be found in Wallis (1969).

Below, methods for determining void fraction based on the drift flux model are presented first for vertical channels and then a method is given for horizontal tubes.

Also, the general approach to include the effects of radial void fraction and velocity profiles within the drift flux model is presented.

# Drift Flux Void Fraction Model: cont.

The drift flux  $U_{GL}$  represents the volumetric rate at which vapor is passing forwards or backwards through a unit plane normal to the channel axis that is itself traveling with the flow at a velocity  $U$  where  $U = U_G + U_L$  and thus  $U$  remains a local parameter, where superficial velocity of the vapor  $U_G$  and the superficial velocity of the liquid  $U_L$  are defined as:

$$U_G = u_G \varepsilon \quad [17.4.4a]$$

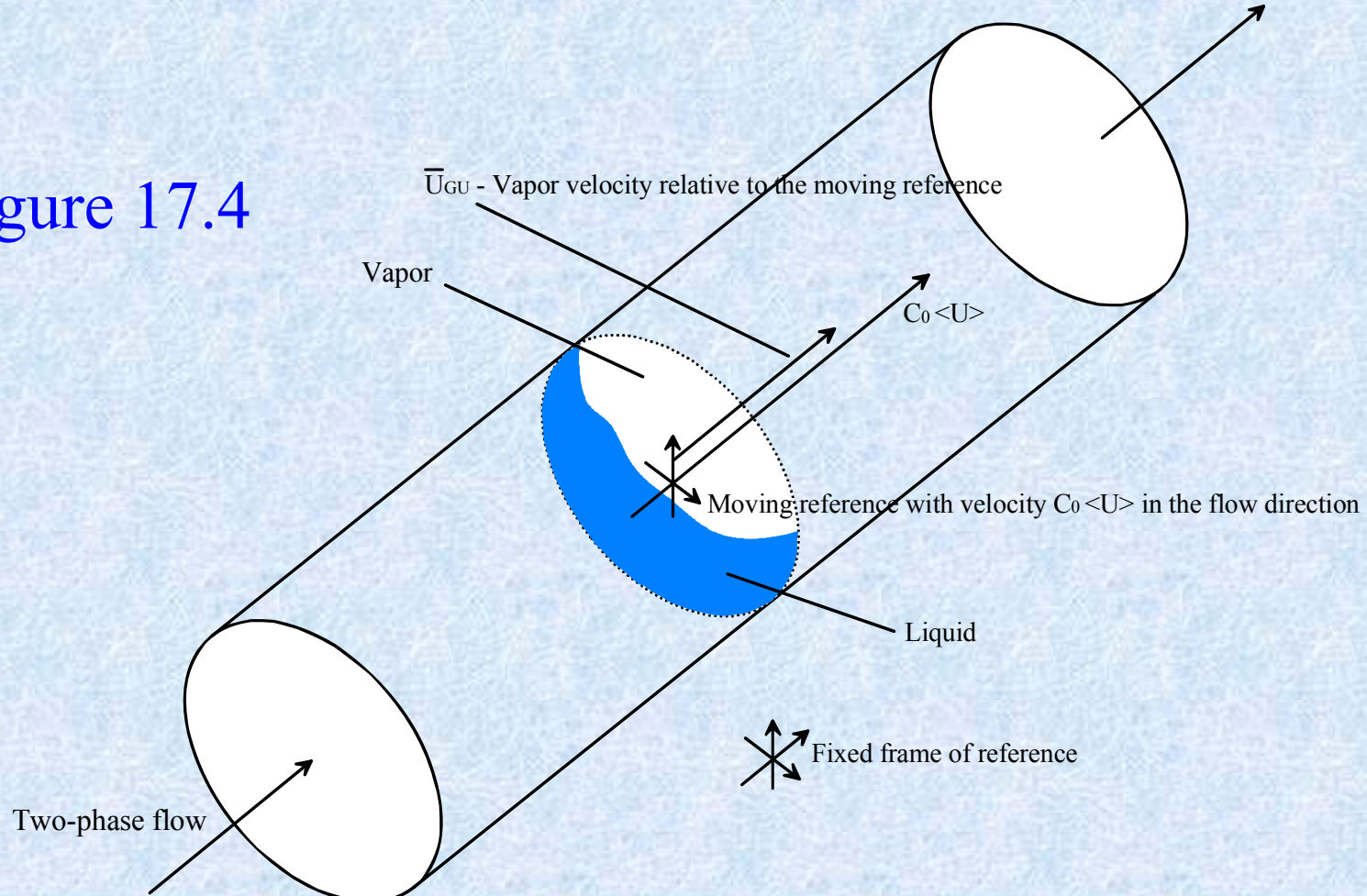
$$\cdot U_L = u_L (1 - \varepsilon) \quad [17.4.4b]$$

Here,  $u_G$  and  $u_L$  refer to the actual local velocities of the vapor and liquid and  $\varepsilon$  is the local void fraction, as defined by [17.1.1] but dropping the subscript local here.

The physical significance of the drift velocity is illustrated in Figure 17.4. These expressions are true for one-dimension flow or at any local point in the flow. Based on these three quantities, the drift velocities can now be defined as  $U_{GU} = u_G - U$  and  $U_{LU} = u_L - U$ .

# Drift Flux Void Fraction Model: cont.

Figure 17.4



# Drift Flux Void Fraction Model: cont.

Now proceeding as a one-dimensional flow and taking these parameters as local values in their respective profiles across the channel and denoting the cross-sectional average properties of the flow with  $\langle \cdot \rangle$ , which represents the average of a quantity F over the cross-sectional area of the duct as  $\langle F \rangle = (\int_A F dA)/A$ . The mean velocity of the vapor  $\langle u_G \rangle$  is thus given by the above expressions to be  $\langle u_G \rangle = \langle U \rangle + \langle U_{GU} \rangle = \langle U_G/\varepsilon \rangle$ . In addition,  $\langle U_G \rangle = \langle u_G \varepsilon \rangle$  and also

$$\langle U_G \rangle = \frac{\dot{Q}_G}{A} \quad [17.4.5a]$$

$$\langle U_L \rangle = \frac{\dot{Q}_L}{A} \quad [17.4.5b]$$

The weighed mean velocity  $\bar{u}_G$  is instead given by  $\bar{u}_G = \langle u_G \varepsilon \rangle / \langle \varepsilon \rangle$ . The definition of the drift velocity of the vapor phase  $U_{GU}$  yields the following expression for  $\bar{u}_G$ :

$$\bar{u}_G = \frac{\langle U_G \rangle}{\langle \varepsilon \rangle} = \frac{\langle \varepsilon U \rangle}{\langle \varepsilon \rangle} + \frac{\langle \varepsilon U_{GU} \rangle}{\langle \varepsilon \rangle} \quad [17.4.6]$$

where  $\langle \varepsilon \rangle$  is the cross-sectional average of the local void fraction.

# Drift Flux Void Fraction Model: cont.

The drift flux is the product of the local void fraction with the local drift velocity

$$U_{GL} = \varepsilon U_{GU} \quad [17.4.7a]$$

Using the fact that  $U_{GU} = u_G - U$  combined with the expression for  $u_G$  in [17.4.4a], rearranging and substituting for  $U_{GU}$  in [17.4.7a], the drift flux  $U_{GL}$  is also given by the expression:

$$U_{GL} = (1 - \varepsilon)U_G - \varepsilon U_L \quad [17.4.7b]$$

A distribution parameter  $C_o$  can now be defined as

$$C_o = \frac{\langle \varepsilon U \rangle}{\langle \varepsilon \rangle \langle U \rangle} \quad [17.4.7c]$$

This ratio accounts for the mathematical difference in averaging  $\varepsilon$  and  $U$  as a product rather than separately. A weighed mean drift velocity  $\bar{U}_{GU}$  can also be defined as

$$\bar{U}_{GU} = \frac{\langle U_{GL} \rangle}{\langle \varepsilon \rangle} \quad [17.4.7d]$$

# Drift Flux Void Fraction Model: cont.

Then the following expression is obtained

$$\bar{u}_G = \frac{\langle U_G \rangle}{\langle \varepsilon \rangle} = C_o \langle U \rangle + \bar{U}_{GU} \quad [17.4.8]$$

Now dividing through by  $\langle U \rangle$  gives

$$\frac{\bar{u}_G}{\langle U \rangle} = \frac{\langle \beta \rangle}{\langle \varepsilon \rangle} = C_o + \frac{\bar{U}_{GU}}{\langle U \rangle} \quad [17.4.9]$$

or

$$\langle \varepsilon \rangle = \frac{\langle \beta \rangle}{C_o + \frac{\bar{U}_{GU}}{\langle U \rangle}} \quad [17.4.10]$$

where  $\langle \beta \rangle$  is the volumetric quality defined as

$$\langle \beta \rangle = \frac{\langle U_G \rangle}{\langle U \rangle} = \frac{\langle U_G \rangle}{\langle U_G \rangle + \langle U_L \rangle} = \frac{\dot{Q}_G}{\dot{Q}_G + \dot{Q}_L} \quad [17.4.11]$$

where the volumetric flow rates of each phase are from [17.3.6] and [17.3.7].

# Drift Flux Void Fraction Model: cont.

For the case where there is no relative motion between the two phases, that is when  $\bar{U}_{GU} = 0$ , then

$$\langle \varepsilon \rangle = \frac{\langle \beta \rangle}{C_o} \quad [17.4.12]$$

Thus, it is evident that  $C_o$  is an empirical factor that corrects one-dimensional homogeneous flow theory to separated flows to account for the fact that the void concentration and velocity profiles across the channel can vary independently of one another. It follows then for homogeneous flow that

$$\langle \varepsilon \rangle = \langle \beta \rangle \quad [17.4.13]$$

The above expression [17.4.11] demonstrates that  $\langle \beta \rangle$  is the ratio of the volumetric vapor (or gas) flow rate to the total volumetric flow rate. Rearranging that expression in terms of the specific volumes,  $v_G$  and  $v_L$ , gives:

$$\langle \beta \rangle = \frac{x v_G}{x v_G + (1 - x) v_L} \quad [17.4.14a]$$

# Drift Flux Void Fraction Model: cont.

The two-phase density  $\rho$  can be expressed as the inverse of the two-phase specific volume  $v$  as:

$$v = xv_G + (1-x)v_L \Rightarrow \rho = \frac{1}{v} = \frac{1}{\frac{x}{\rho_G} + \frac{1-x}{\rho_L}} \quad [17.4.14b]$$

Furthermore, the mass velocity can be written as follows:

$$\dot{m} = \rho \langle U \rangle \quad [17.4.14c]$$

# Drift Flux Void Fraction Model: cont.

Now, using these three expressions, [17.4.10] for  $\langle \varepsilon \rangle$  can be rewritten as:

$$\langle \varepsilon \rangle = \frac{\frac{x}{\rho_G}}{\frac{x}{\rho_G} + \frac{1-x}{\rho_L}} \left[ C_o + \frac{\bar{U}_{GU}}{\dot{m} \left( \frac{x}{\rho_G} + \frac{1-x}{\rho_L} \right)} \right]^{-1} \quad [17.4.14d]$$

Rearranging, the general drift flux void fraction equation becomes

$$\langle \varepsilon \rangle = \frac{x}{\rho_G} \left[ C_o \left( \frac{x}{\rho_G} + \frac{1-x}{\rho_L} \right) + \frac{\bar{U}_{GU}}{\dot{m}} \right]^{-1} \quad [17.4.14e]$$

The above expression shows that void fraction is a function of mass velocity, while the previously presented analytical theories did not capture this effect.

**Further note:** elsewhere in this book, i.e. other than here in Section 17.4 on drift flux models, the cross-sectional average of the local void fraction  $\langle \varepsilon \rangle$  is written simply as  $\varepsilon$ .

# Drift Flux Void Fraction Model: cont.

The drift flux model can be used with or without reference to the particular flow regime as shown by Ishii (1977). The drift flux model, however, is only valuable when the drift velocity is significantly larger than the total volumetric flux, say when  $\bar{U}_{GU}$  is larger than  $0.05\langle U \rangle$ . Also, note that the above drift flux equation [17.4.14e] reduces to the homogeneous void fraction when  $C_o = 1$  and either  $\bar{U}_{GU} = 0$  or the mass velocity becomes very large. Several of its applications are discussed below.

At elevated pressures, Zuber et al. (1967) have shown that using

$$C_o = 1.13 \quad [17.4.15]$$

$$\bar{U}_{GU} = 1.41 \left[ \frac{\sigma g (\rho_L - \rho_G)}{\rho_L^2} \right]^{1/4} \quad [17.4.16]$$

in [17.4.14e] gives a good representation of their data for R-22 and similar data for water-steam, regardless of the flow regime, and includes surface tension into the method.

# Drift Flux Void Fraction Model: cont.

For the bubbly flow regime with one-dimensional vertical upflow of small, isolated bubbles without coalescence, **Wallis (1969)** has suggested the following equations to use in the drift flux model:

$$C_o = 1.0 \quad [17.4.17]$$

$$\bar{U}_{GU} = 1.53 \left[ \frac{\sigma g (\rho_L - \rho_G)}{\rho_L^2} \right]^{1/4} \quad [17.4.18]$$

It is notable that this expression of  $\bar{U}_{GU}$  can be interpreted to represent the buoyancy effect of the bubbles on the vapor rise velocity, increasing the vapor velocity with respect to a homogeneous flow. Also for the bubbly vertical upflow regime, **Zuber et al. (1967)** recommended using [17.4.16] where the value of  $C_o$  is dependent on the reduced pressure  $p_r$  and channel internal diameter  $d_i$ , depending on channel size and shape as follows:

- For tubes with  $d_i > 50$  mm:  $C_o = 1 - 0.5p_r$  (except for  $p_r < 0.5$  where  $C_o = 1.2$ );
- For tubes with  $d_i < 50$  mm:  $C_o = 1.2$  for  $p_r < 0.5$ ;
- For tubes with  $d_i < 50$  mm:  $C_o = 1.2 - 0.4(p_r - 0.5)$  for  $p_r > 0.5$ ;
- For rectangular channels:  $C_o = 1.4 - 0.4p_r$ .

# Drift Flux Void Fraction Model: cont.

For slug flows, Zuber et al. (1967) recommended using

$$C_o = 1.2 \quad [17.4.19]$$

$$\bar{U}_{GU} = 0.35 \left[ \frac{g(\rho_L - \rho_G)d_i}{\rho_L} \right]^{1/2} \quad [17.4.20]$$

For annular flow, Ishii et al. (1976) proposed using

$$C_o = 1.0 \quad [17.4.21]$$

$$\bar{U}_{GU} = 23 \left( \frac{\mu_L U_L}{\rho_G d_i} \right) \left( \frac{\rho_L - \rho_G}{\rho_L} \right) \quad [17.4.22]$$

The latter expression introduces the effect of liquid dynamic viscosity on void fraction. Ishii (1977) has also given some additional recommendations.

For vertical downflow, the sign of  $\bar{U}_{GU}$  in [17.4.14e] is changed.

# Drift Flux Void Fraction Model: Non-Uniform Distributions

**Effect of Non-Uniform Flow Distributions.** The definition of  $C_o$  given by [17.4.7c] may be rewritten for integration of the void fraction profile and the velocity profile as

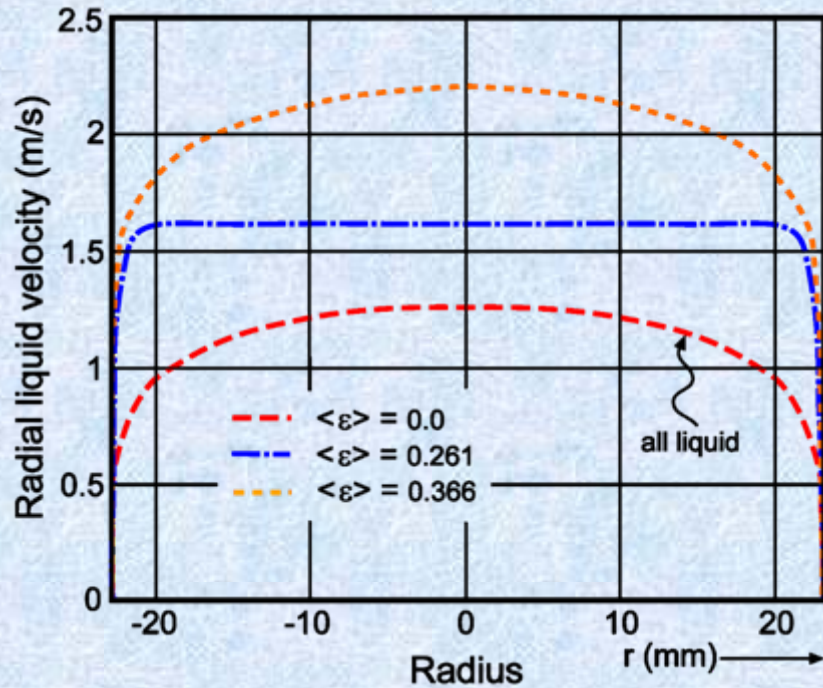
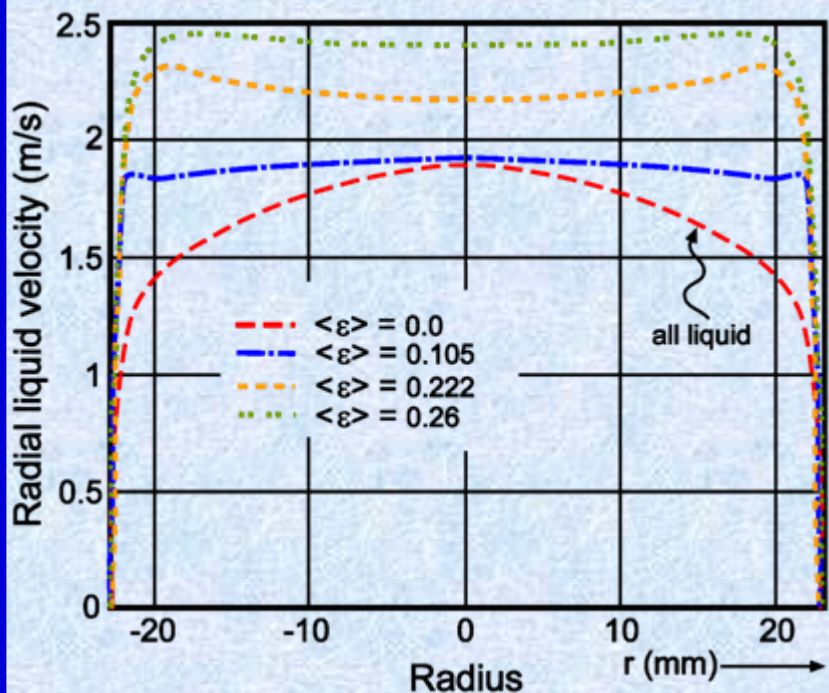
$$C_o = \frac{\frac{1}{A} \int_A \varepsilon U dA}{\left[ \frac{1}{A} \int_A \varepsilon dA \right] \left[ \frac{1}{A} \int_A U dA \right]} \quad [17.4.23]$$

Its value is thus seen to depend on the distribution of the local void fraction and local phase velocities across the flow channel.

As an example, Figures 17.5 and 17.6 depict some experimentally measured values of radial liquid velocity and void fraction profiles for flow of air and water inside a 50 mm bore vertical tube obtained by Malnes (1966). In Figure 17.5, the typical velocity profile for all liquid flow is shown for  $\langle \varepsilon \rangle = 0$  at two different flow rates.

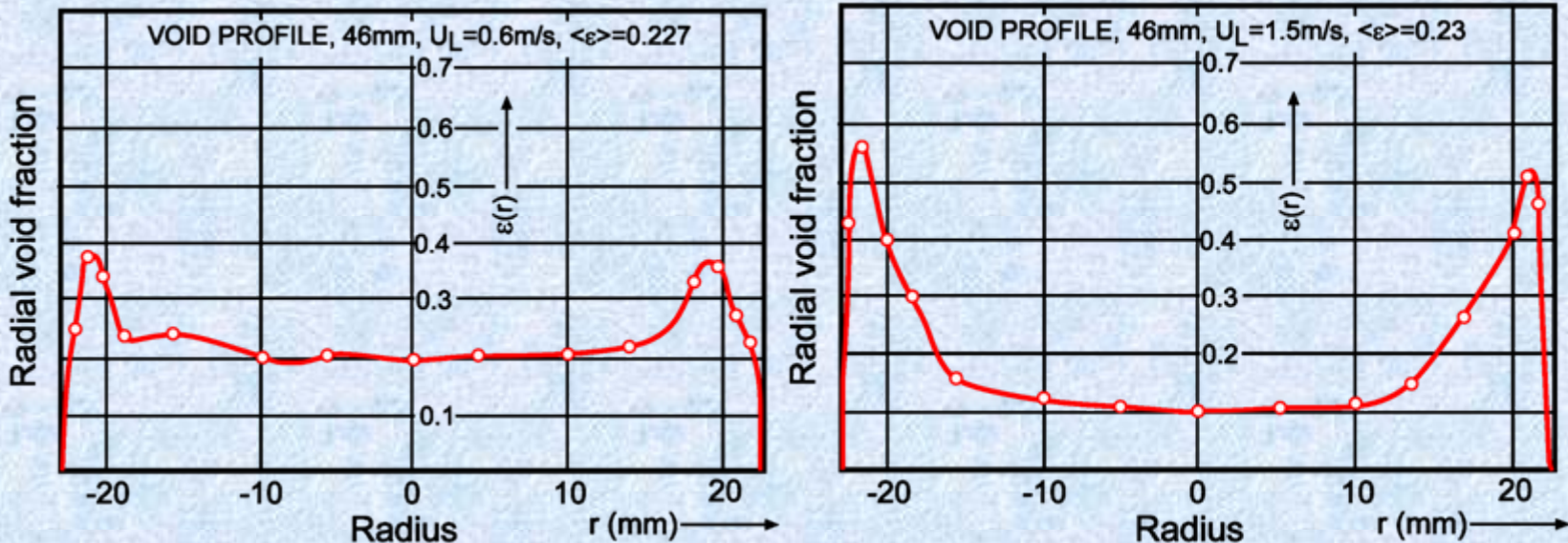
# Radial Velocity Profiles for Upflow

Figure 17.5. Radial liquid velocity profiles for air-water flow measured by Malnes (1966).



# Radial Void Fraction Profiles for Upflow

Figure 17.6. Radial void fraction profiles for air-water flow measured by Malnes (1966).



# Drift Flux Void Fraction Model: Non-Uniform Distrib., cont.

Assuming an axially symmetric flow through a vertical circular pipe of internal radius  $r_i$  and assuming that the flow distributions are given by the following radial functions,

$$\frac{U}{U_c} = 1 - \left( \frac{r}{r_i} \right)^m \quad [17.4.24]$$

$$\frac{\varepsilon - \varepsilon_w}{\varepsilon_c - \varepsilon_w} = 1 - \left( \frac{r}{r_i} \right)^n \quad [17.4.25]$$

where the subscripts **c** and **w** refer to the values at the centerline and the wall, Zuber and Findlay (1965) integrated [17.4.23] to obtain the following expression for the distribution parameter  $C_o$

$$C_o = 1 + \frac{2}{m+n+2} \left[ 1 - \frac{\varepsilon_w}{\langle \varepsilon \rangle} \right] \quad [17.4.26]$$

when expressed in terms of  $\varepsilon_w$  or

$$C_o = \frac{m+2}{m+n+2} \left[ 1 + \frac{\varepsilon_c}{\langle \varepsilon \rangle} \left( \frac{n}{m+2} \right) \right] \quad [17.4.27]$$

when expressed in terms of  $\varepsilon_c$ .

# Drift Flux Void Fraction Model: Non-Uniform Distrib., cont.

They noted that if the void fraction is uniform across the channel, i.e. if  $\varepsilon_w = \varepsilon_c = \langle \varepsilon \rangle$ , then it follows that  $C_o = 1$ .

If  $\varepsilon_c > \varepsilon_w$ , then  $C_o > 1$ .

On the other hand, if  $\varepsilon_c < \varepsilon_w$ , then  $C_o < 1$ .

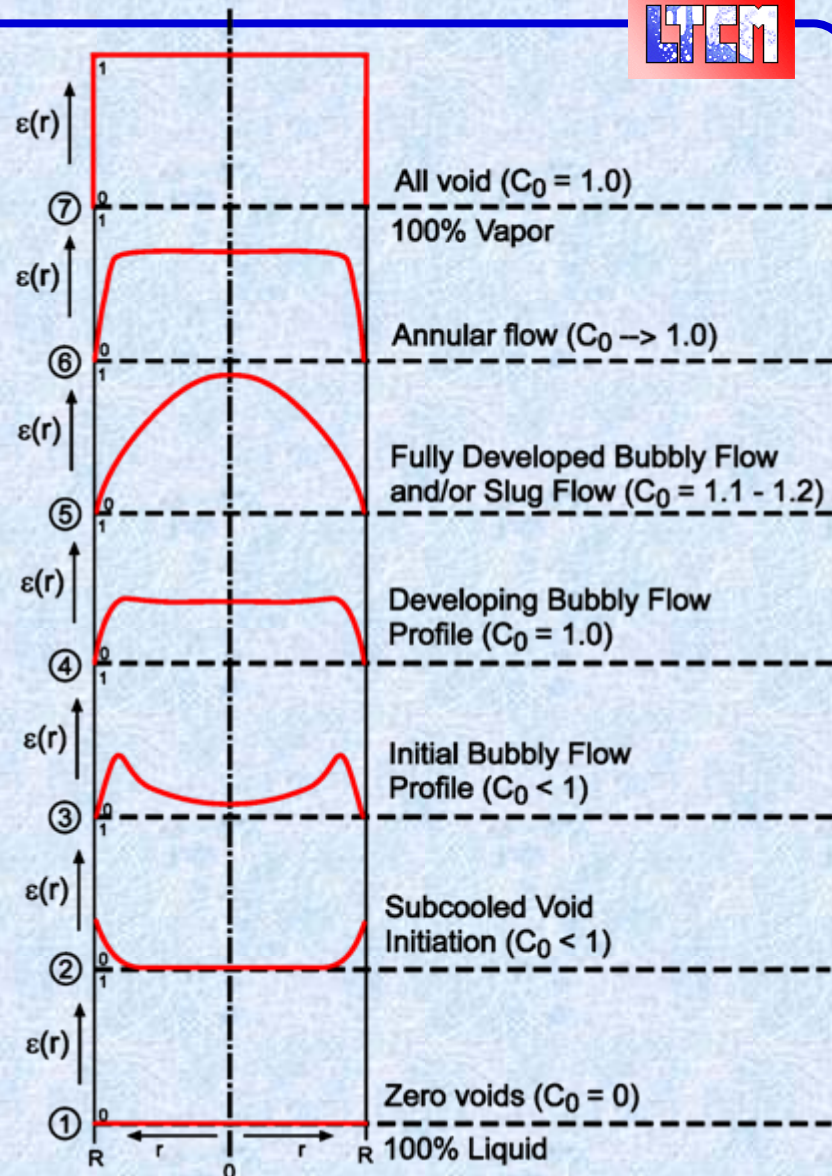
Furthermore, if  $m$  is assumed to be equal to  $n$  and the flow is adiabatic ( $\varepsilon_w = 0$ ), then [17.4.26] reduces to

$$C_o = \frac{n+2}{n+1} \quad [17.4.28]$$

# Void Fraction Profiles by Flow Pattern

Lahey (1974) presented an interesting picture of the variation in radial void fraction and values of  $C_o$  for different types of flow patterns in vertical upflow.

Figure 17.7. Diabatic void fraction profiles for selected flow regimes as presented by Lahey (1974).



# Rouhani-Axelsson Drift Flux Void Fraction Model

Rouhani and Axelsson (1970) correlated the drift velocity for vertical channels as

$$\overline{U}_{GU} = 1.18 \left[ \frac{g\sigma(\rho_L - \rho_G)}{\rho_L^2} \right]^{1/4} \quad [17.4.29]$$

where

- $C_o = 1.1$  for mass velocities greater than  $200 \text{ kg m}^{-2} \text{s}^{-1}$ ;
- $C_o = 1.54$  for mass velocities less than  $200 \text{ kg m}^{-2} \text{s}^{-1}$ .

Instead, the following correlation of Rouhani (1969) can be used for  $C_o$  over a wide range of mass velocities:

$$C_o = 1 + 0.2(1-x) \left( \frac{gd_i \rho_L^2}{\dot{m}^2} \right)^{1/4} \quad [17.4.30]$$

This expression is valid for void fractions larger than 0.1. By combining these expressions with [17.4.14e], it is possible to obtain an explicit value for  $\langle \varepsilon \rangle$ .

**Example 17.4:** Determine the local void fractions using the Rouhani-Axelsson expression [17.4.30] for the following qualities (0.1, 0.50, 0.95) for a fluid flowing at a rate of 0.1 kg/s in a vertical tube of 22 mm internal diameter. The fluid has the following physical properties: liquid density is  $1200 \text{ kg m}^{-3}$ , gas density is  $20 \text{ kg m}^{-3}$  and surface tension is  $0.012 \text{ N m}^{-1}$ .

**Solution:** The mass flux for this situation is  $263.1 \text{ kg m}^{-2} \text{ s}^{-1}$  while the gravitational acceleration  $g = 9.81 \text{ m s}^{-2}$ .

Quality, $x$	0.10	0.50	0.95
$C_o$ [17.4.30]	1.262	1.146	1.015
$\bar{U}_{GU}$ [17.4.29]	0.10525	0.05847	0.00585
$\langle \varepsilon \rangle$ [17.4.14e]	0.653	0.852	0.984

# Steiner version of Rouhani-Axelsson Model

Horizontal tubes. All the above methods are for vertical tubes. For horizontal tubes, Steiner (1993) reports that the following method of Rouhani (1969) is in good agreement with experimental data, whose modified form was chosen in order to go to the correct limit of  $\langle \varepsilon \rangle = 1$  at  $x = 1$ :

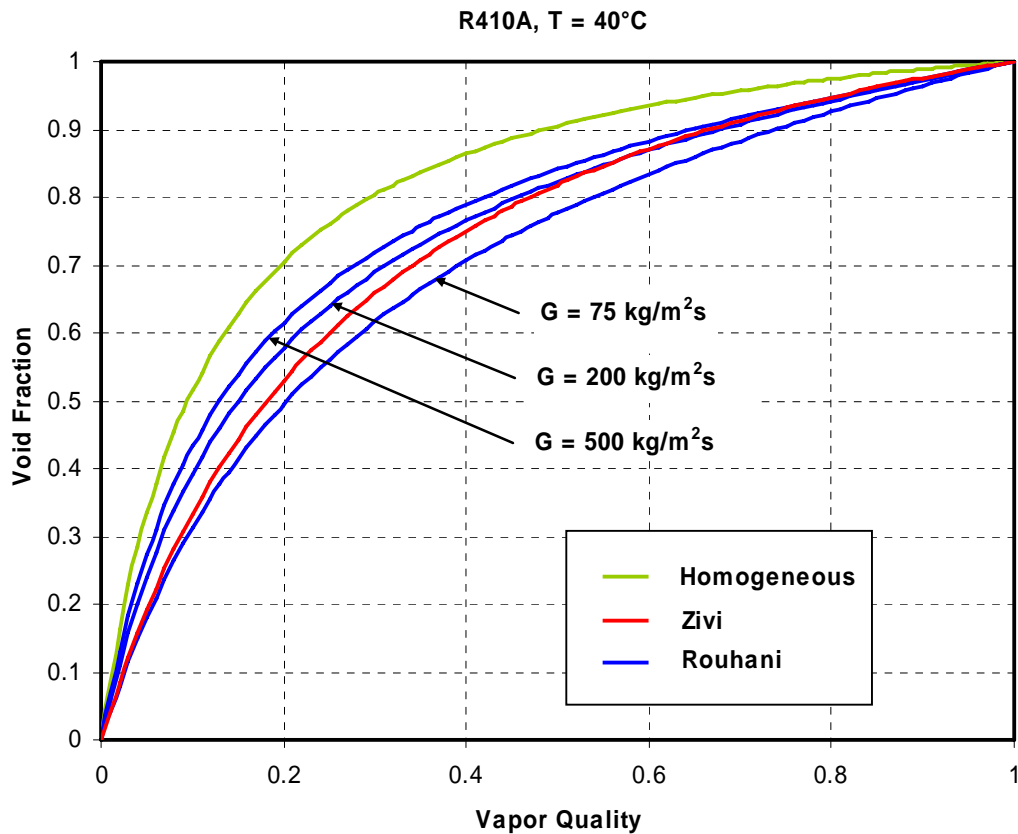
$$C_o = 1 + c_o(1 - x) \quad [17.4.31]$$

where  $c_o = 0.12$  and the term  $(1-x)$  has been added to the other expression to give:

$$\overline{U}_{GU} = 1.18(1 - x) \left[ \frac{g\sigma(\rho_L - \rho_G)}{\rho_L^2} \right]^{1/4} \quad [17.4.32]$$

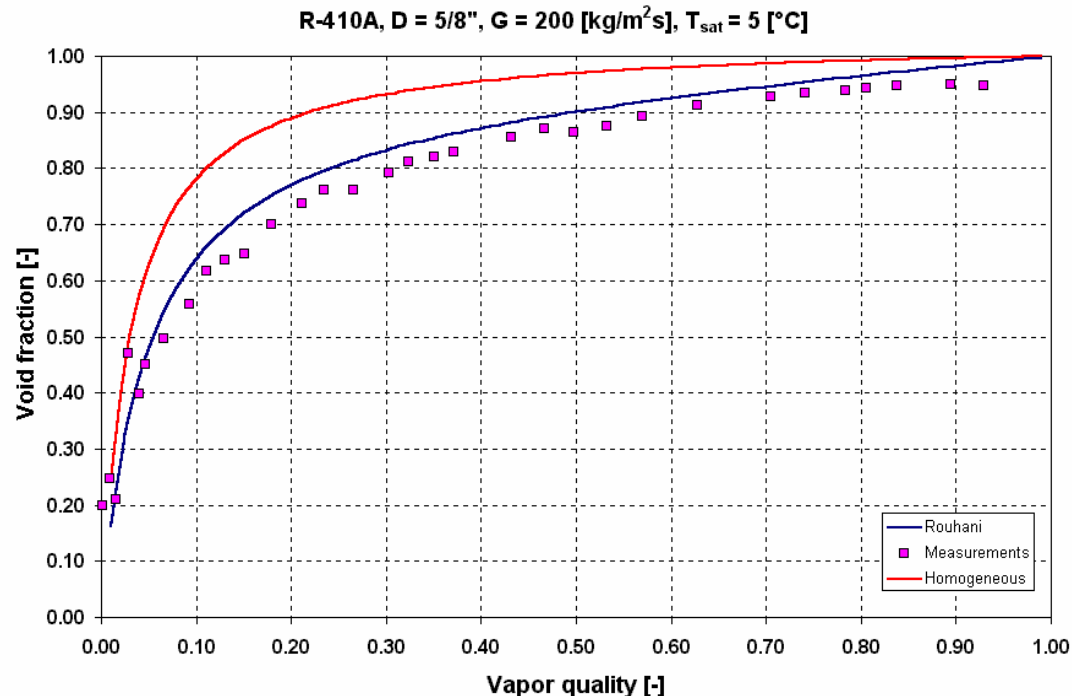
# Comparison of Three Competing Methods

Fig.17.8. Comparison of three methods for R-410A in 8 mm tube showing effect of mass velocity in Steiner/Rouhani-Axelsson equation.



# Comparison of Steiner's Rouhani Method to Data

Wojtan, Ursenbacher and Thome (2003) have measured 238 time-averaged cross-sectional void fractions in an 13.6 mm horizontal glass tube using a new optical measurement technique, processing about 227,000 images. Figure 17.9 shows a comparison using [17.4.31] and [17.4.32] and the homogeneous model.



# Comparison of Void Fraction Methods: Section 17.5

**Butterworth (1975).** Many void fraction methods have a standard form of:

$$\varepsilon = \left[ 1 + n_B \left( \frac{1-x}{x} \right)^{n_1} \left( \frac{\rho_G}{\rho_L} \right)^{n_2} \left( \frac{\mu_L}{\mu_G} \right)^{n_3} \right]^{-1} \quad [17.5.1]$$

which allows for a comparison to be made and also inconsistencies to be noted, e.g. if the densities and viscosities in both phases are equal, i.e.  $\rho_L = \rho_G$  and  $\mu_L = \mu_G$ , then the void fraction should be equal to the quality  $x$ .

This means that  $n_3$  and  $n_1$  should be equal to 1.0 in all void fraction equations in order to be valid at the limit when the critical point is approached. The exponent on the density ratio is always less than that of the homogeneous model. Importantly, some methods include the influence of viscosity while others do not.

# Comparison of Void Fraction Methods: Section 17.5, cont.

Which is the best general approach? The drift flux model appears to be the preferred choice for the following reasons:

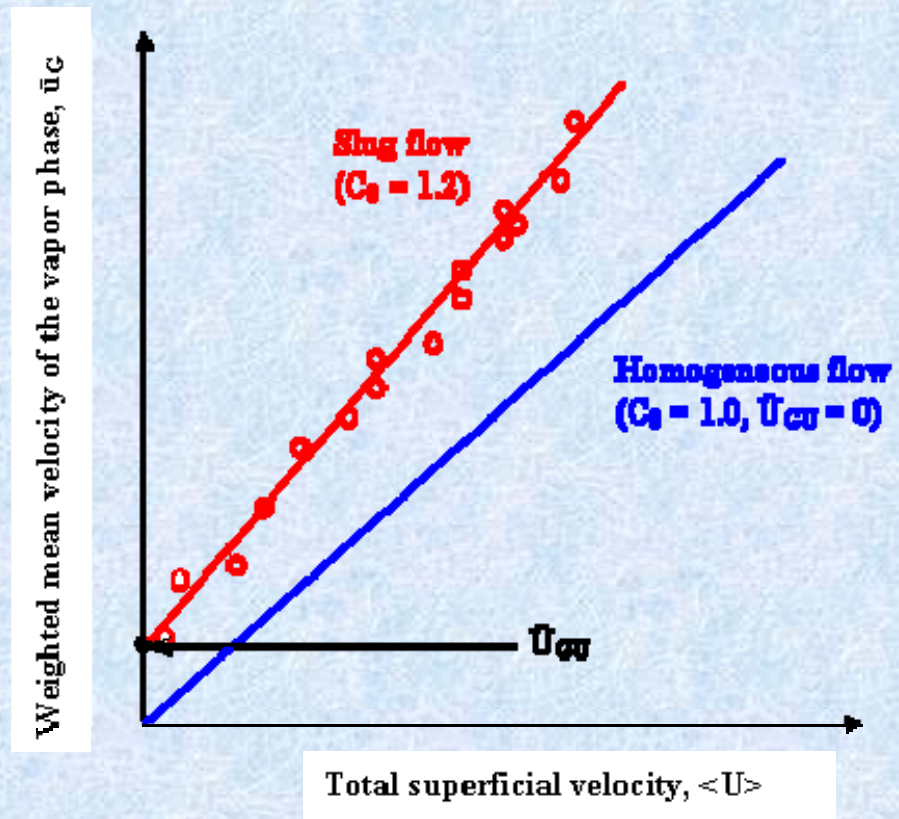
1. Plotting measured flow data in the format of  $\bar{u}_G$  versus  $\langle U \rangle$  yields linear representations of the data for a particular type of flow pattern. This was known empirically to be the case, and then Zuber and Findley arrived at the reason for this linear relationship analytically with [17.4.8]. Hence, analysis of experimental data can yield values of  $C_o$  (the slope) and  $\bar{U}_{GU}$  (the y-intercept) for different types of flow patterns using [17.4.8].
2. Various profiles can be assumed for integrating [17.4.23] and hence appropriate values of  $C_o$  can be derived for different flow patterns and specific operating conditions (e.g. high reduced pressures).
3. As a general approach, the drift flux model provides a unified approach. It is capable of being applied to all directions of flow (upward, downward, horizontal and inclined) and potentially to all the types of flow patterns.
4. Reviewing of the expressions for  $\bar{U}_{GU}$ , the drift flux model includes the important effects of mass velocity, viscosity, surface tension and channel size.

# Comparison of Void Fraction Methods: Section 17.5, cont.

Plotting measured flow data in the format of  $\bar{u}_G$  versus  $\langle U \rangle$ , as shown in Figure 17.10, yields linear (or nearly linear) representations of the data for a particular type of flow pattern. This was known empirically to be the case, and then Zuber and Findley arrived at the reason for this linear relationship analytically with [17.4.8].

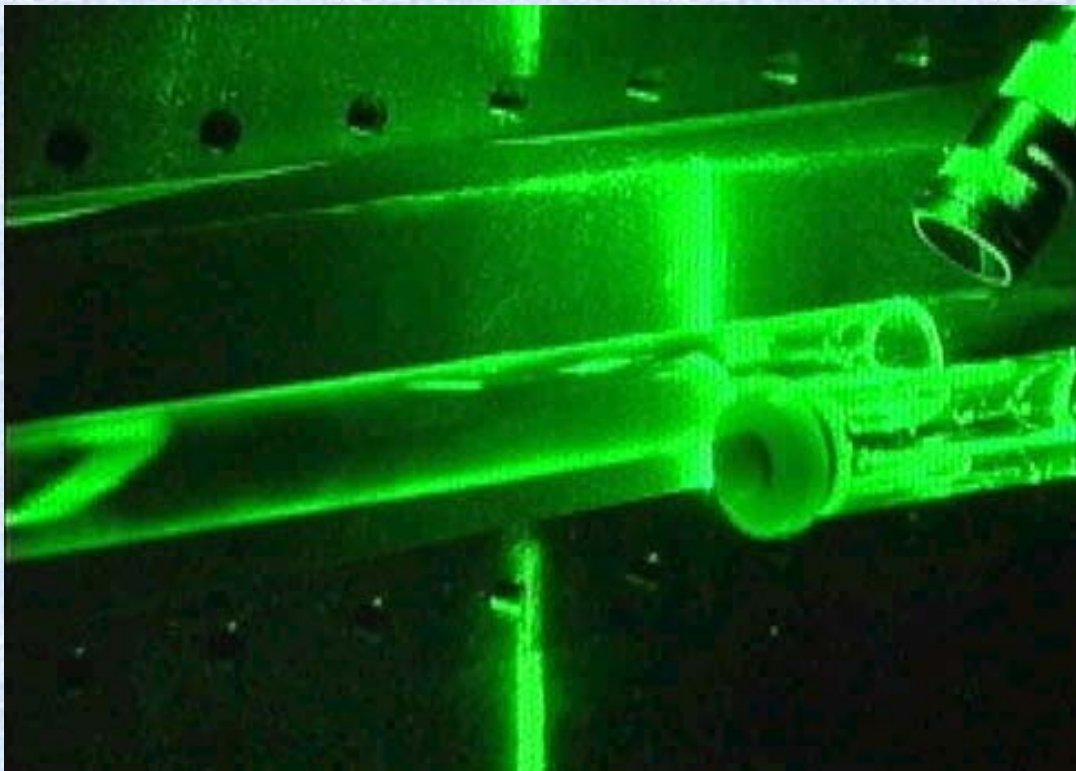
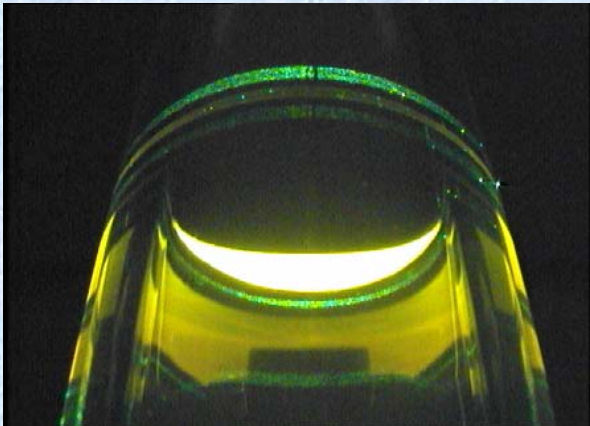
Hence, analysis of experimental data can yield values of  $C_o$  (the slope) and  $\bar{U}_{GU}$  (the y-intercept) for different types of flow patterns using [17.4.8]. Note that homogeneous flow gives the diagonal straight line dividing adiabatic upflow from adiabatic downflow.

$$\bar{u}_G = \frac{\langle U_G \rangle}{\langle \varepsilon \rangle} = C_o \langle U \rangle + \bar{U}_{GU}$$



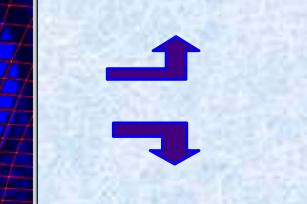
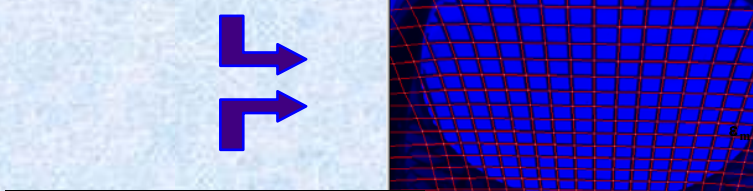
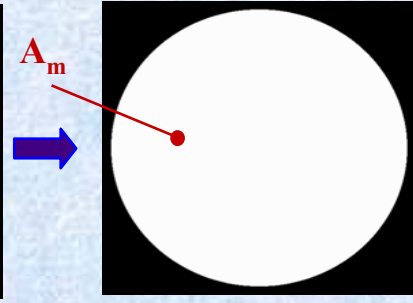
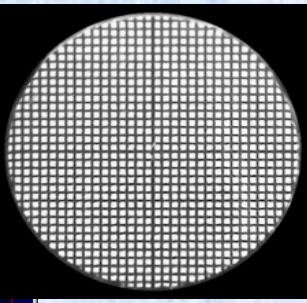
# Dynamic Flow Visualization and Image Processing of Two-Phase Flows – New Experimental Technique of LTCM

## Image Acquisition with Laser

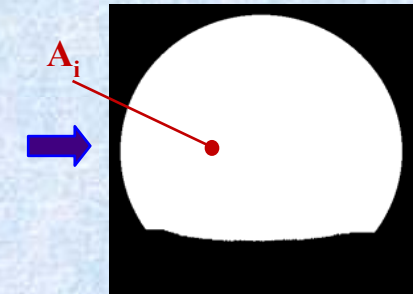
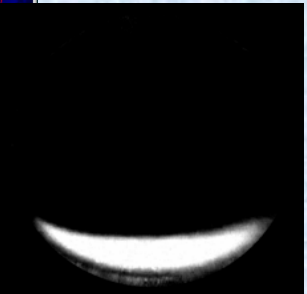
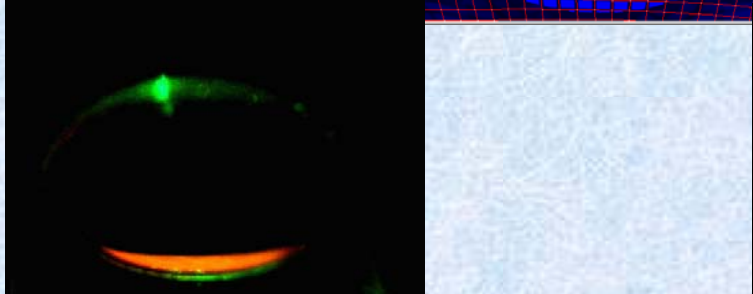


# Dynamic Flow Visualization and Image Processing of Two-Phase Flows – New Experimental Technique of LTCM

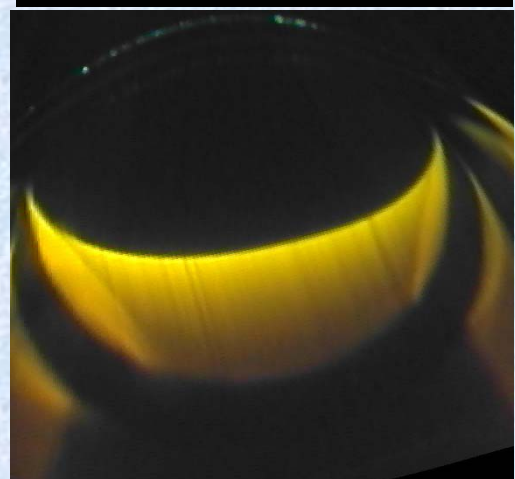
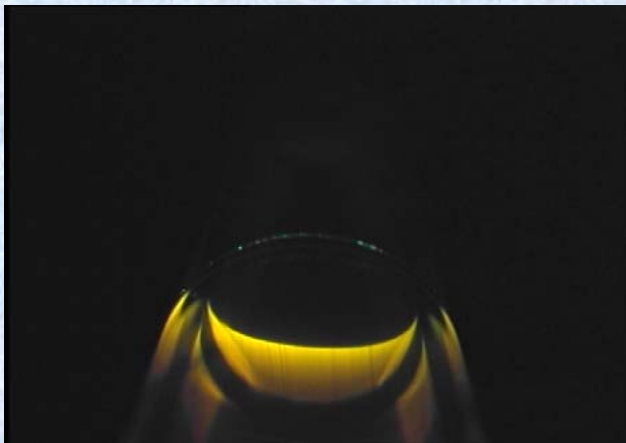
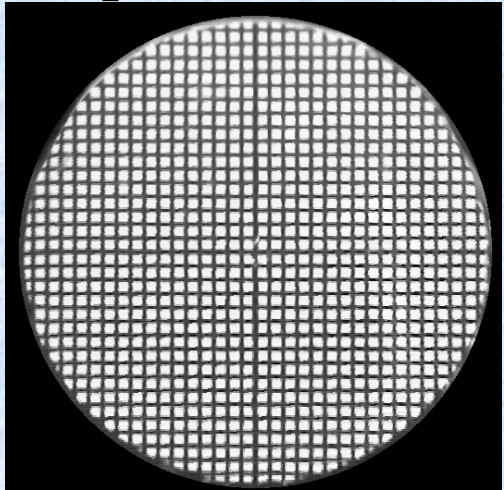
## Image Processing Technique to Measure Flow Phenomena



$$\varepsilon_m = \frac{A_i}{A_m}$$



# Dynamic Flow Visualization and Image Processing Applied to Two-Phase Flows – New Experimental Technique of LTCM



# Comments on Quick-Closing Valve Void Fraction Measurements:

It is the *cross-sectional* void fraction, not the *volumetric* void fraction, that is required for prediction of *flow boiling coefficients*, *flow pattern transitions* and *two-phase pressure drops*. Cross-sectional void fractions *cannot* be determined using the quick-closing valve method since that gives volumetric void fractions, except for homogeneous flow. The relationship between the cross-sectional void fraction  $\varepsilon$  and the volumetric void fraction  $\varepsilon_{\text{Vol}}$  is

$$\varepsilon_{\text{Vol}} = \frac{\varepsilon}{\frac{1}{S}(1 - \varepsilon) + \varepsilon}$$

*Cross-sectional void fraction*

$S$  is the velocity or “slip” ratio between the two phases. Since typically  $S > 1$ , incorrectly using the volumetric void fraction  $\varepsilon_{\text{Vol}}$  in place of the cross-sectional void fraction  $\varepsilon$  overpredicts the latter’s value, and in some cases gives void fractions *larger* than the homogeneous void fraction (for which  $S = 1$ )!!! For example, if  $\varepsilon = 0.20$  and  $S = 1.5$ , then  $\varepsilon_{\text{Vol}} = 0.273$ , or a 36% increase in value!

Hence, the assumption that the quick-closing valve technique can yield a cross-sectional void fraction database (*done in recent published studies*) is quickly shown to be fundamentally *incorrect* and gives unreasonable values.

# Void Fraction Methods for Tube Bundles:

- Void fractions in two-phase flows over tube bundles are much more difficult to measure than for internal channel flows.
- Mass velocities of industrial interest tend to be lower than for internal flows.
- For evaporation and condensation in refrigeration systems:  $5 \text{ to } 40 \text{ kg m}^{-2} \text{ s}^{-1}$ .
- In partial evaporators and condensers common to the chemical processing industry with single segmental baffles, design range is from  $25 \text{ to } 150 \text{ kg m}^{-2} \text{ s}^{-1}$ .
- For vertical two-phase flows across tube bundles the frictional pressure drop tends to be small compared to the static head of the two-phase fluid at low G's.
- The void fraction thus becomes the most important parameter for evaluating the two-phase pressure drop via the local two-phase density of shell-side flows.
- Even though shell-side void fractions have been studied less than internal channel flows, they are still important for obtaining accurate thermal designs.
- In flooded type evaporators with close temperature approaches in refrigeration and heat pumps, the effect of the two-phase pressure drop on the saturation temperature may be significant in evaluating the log mean temperature difference.

# Void Fraction Methods for Tube Bundles, Vertical Flows:

- The earliest study was apparently that of **Kondo and Nakajima (1980)** who investigated air-water mixtures in vertical upflow for staggered tube layouts.
- They utilized quick-closing valves at the inlet and outlet of the bundle that included not only the tube bundle but also the entrance and exit zones. Based on the mass of liquid in the bundle, the void fraction was determined.
- Their tests covered qualities from 0.005 to 0.90 with mass velocities of 10 to 60 kg m<sup>-2</sup> s<sup>-1</sup>, where the mass velocity as standard practice is evaluated at the minimum cross section of the bundle similar to single-phase flow.
- They found that the void fraction increased with superficial gas velocity while the superficial liquid velocity had almost no affect on void fraction.
- The number of tube rows had an effect on void fraction, probably resulting from inclusion of their inlet and exit zones when measuring void fractions.
- The quick-closing valve technique yields volumetric void fractions, which are only equal to cross-sectional void fractions when  $S = 1$ ; when  $S > 1$ , the volumetric void fraction is larger than the cross-sectional void fraction.

# Void Fraction Methods for Tube Bundles, Vertical Flows:

Shrage et al. (1988) made similar tests with air-water mixtures on inline tube bundles with a tube pitch to diameter ratio of 1.3, again using the quick-closing valve technique, ran tests for qualities up to 0.65, pressures up to 0.3 MPa and mass velocities from 54 to 683 kg m<sup>-2</sup> s<sup>-1</sup>. At a fixed quality  $x$ , the void fraction was found to increase with increasing mass velocity. They offered a dimensional empirical relation for predicting void fractions by incorporating a multiplier to the homogeneous void fraction, referred to as  $\varepsilon_H$ . A non-dimensional version was obtained using further refrigerant R-113 data and it is as follows:

$$\frac{\varepsilon_{\text{vol}}}{\varepsilon_H} = 1 + 0.123 \left( \frac{\ln x}{\text{Fr}_L^{0.191}} \right) \quad [17.6.1]$$

where the liquid Froude number was defined as

$$\text{Fr}_L = \frac{\dot{m}}{\rho_L (g d_o)^{1/2}} \quad [17.6.2]$$

# Void Fraction Methods for Tube Bundles, Vertical Flows:

Ishihara et al. (1980) presented the following method for predicting the local void fraction in tube bundles based on the two-phase friction multiplier of the liquid:

$$\varepsilon = 1 - \frac{1}{\phi_L} \quad [17.6.3]$$

Their liquid two-phase friction multiplier  $\phi_L$  is given by

$$\phi_L = 1 + \frac{8}{X_{tt}} + \frac{1}{X_{tt}^2} \quad [17.6.4]$$

$X_{tt}$  is the Martinelli parameter for both phases in turbulent flow across the bundle, which reduces to the simplified form

$$X_{tt} = \left( \frac{1-x}{x} \right) \left( \frac{\rho_G}{\rho_L} \right)^{0.57} \left( \frac{\mu_L}{\mu_G} \right)^{0.11} \quad [17.6.5]$$

# Void Fraction Methods for Tube Bundles, Vertical Flows:

Fair and Klip (1983) offered a method for upflow on horizontal reboilers:

$$(1 - \varepsilon)^2 = \frac{1}{\phi_L} \quad [17.6.6]$$

Their liquid two-phase friction multiplier  $\phi_L$  is given by

$$\phi_L = 1 + \frac{20}{X_{tt}} + \frac{1}{X_{tt}^2} \quad [17.6.7]$$

where  $X_{tt}$  is for both fluids turbulent is the same as in Ishihara et al.  
above.

# Void Fraction Methods for Tube Bundles, Vertical Flows:

Feenstra, Weaver and Judd (2000) developed a completely empirical expression to predict the velocity ratio  $S$ , where the expression for  $S$  obeys the correct limits at vapor qualities of 0 and 1.

From dimensional analysis, the following parameters influenced  $S$ : two-phase density, liquid-vapor density difference, pitch flow velocity of the fluid, dynamic viscosity of the liquid, surface tension, gravitational acceleration, the gap between neighboring tubes, tube diameter, tube pitch and the frictional pressure gradient.

The two-phase density and density difference were included as they are always key parameters in void fraction models.

The tube pitch  $L_{tp}$  and tube diameter  $D$  were included for their influence on the frictional pressure drop.

Furthermore, the surface tension  $\sigma$  was selected since it affects the bubble size and shape and the liquid dynamic viscosity  $\mu_L$  was included because of its affect on bubble rise velocities.

# Void Fraction Methods for Tube Bundles, Vertical Flows:

Feenstra et al. proposed the following void fraction prediction method:

$$\varepsilon = \frac{1}{1 + S \left( \frac{(1-x)}{x} \frac{\rho_G}{\rho_L} \right)} \quad [17.6.8]$$

where the velocity (or slip) ratio **S** is calculated as:

$$S = 1 + 25.7 \left( \text{Ri Cap} \right)^{0.5} \left( L_{tp}/D \right)^{-1} \quad [17.6.9]$$

In this expression,  $L_{tp}/D$  is the tube pitch ratio and the Richardson number **Ri** is defined as:

$$\text{Ri} = \frac{(\rho_L - \rho_G)^2 g (L_{tp} - D)}{\dot{m}^2} \quad [17.6.10]$$

The Richardson number represents a ratio between the buoyancy force and the inertia force. The mass velocity, as in all these methods for tube bundles, is based on the minimum cross-sectional flow area like in single-phase flows.

# Void Fraction Methods for Tube Bundles, Vertical Flows:

**Feenstra et al., cont.**: The characteristic dimension is the gap between the tubes, which is equal to the tube pitch less the tube diameter,  $L_{tp} - D$ . The Capillary number **Cap** is:

$$\text{Cap} = \frac{\mu_L u_G}{\sigma} \quad [17.6.11]$$

It represents the ratio between the viscous force and the surface tension force. The mean vapor phase velocity **u<sub>G</sub>** is determined as

$$u_G = \frac{x\dot{m}}{\varepsilon\rho_G} \quad [17.6.12]$$

Hence, an iterative procedure is required to determine the void fraction using this method.

# Void Fraction Methods for Tube Bundles, Vertical Flows:

Feenstra et al., cont.:

This method was successfully compared to air-water, R-11, R-113 and water-steam void fraction data obtained from different sources, including the data of Schrage, Hsu and Jensen (1988).

It was developed from triangular and square tube pitch data with tube pitch to tube diameter ratios from 1.3 to 1.75 for arrays with from 28 to 121 tubes and tube diameters from 6.35 to 19.05 mm.

Their method was also found to be the best for predicting static pressure drops at low mass flow rates for an 8-tube row high bundle under evaporating conditions (where the accelerational and frictional pressure drops were relatively small) by Consolini, Robinson and Thome (2006).

Hence, the Feenstra-Weaver-Judd method is thought to be the most accurate and reliable available for predicting void fractions in vertical two-phase flows on tube bundles.

# Void Fraction Methods for Tube Bundles, Vertical Flows:

**Example 17.5:** Determine the void fraction and velocity ratio using the Feenstra-Weaver-Judd method at  $x = 0.2$  for R-134a at a saturation temperature of  $4^\circ\text{C}$  (3.377 bar) for a mass velocity of  $30 \text{ kg/m}^2\text{s}$ , a tube diameter of  $19.05 \text{ mm}$  ( $3/4$  in.) and tube pitch of  $23.8125 \text{ mm}$  ( $15/16$  in.). The properties required are:  $\rho_L = 1281 \text{ kg/m}^3$ ;  $\rho_G = 16.56 \text{ kg/m}^3$ ;  $\sigma = 0.011 \text{ N/m}$ ;  $\mu_L = 0.0002576 \text{ Ns/m}^2$ .

**Solution:** Begin by assuming a value for the void fraction, where here the value of 0.5 is taken as the starting point in the iterative procedure. First, the mean vapor velocity is determined to be:

$$u_G = \frac{0.2(30)}{0.5(16.56)} = 0.725 \text{ m/s}$$

Next the Capillary number is determined:

$$\text{Cap} = \frac{0.0002576(0.725)}{0.011} = 0.0170$$

The Richardson number  $Ri$  is determined next:

$$Ri = \frac{(1281 - 16.56)^2 (9.81)(0.0238125 - 0.01905)}{30^2} = 83.0$$

# Void Fraction Methods for Tube Bundles, Vertical Flows:

Example 17.5, cont.:

The void fraction is then:

$$\varepsilon = \frac{1}{1 + 25.4 \left( \frac{(1 - 0.2)}{0.2} \frac{16.56}{1281} \right)} = 0.432$$

The second iteration begins using this value to determine the new mean vapor velocity and so on until the calculation converges. After 6 iterations,  $\varepsilon$  becomes 0.409 (with an error of less than 0.001).

# Void Fraction Methods for Tube Bundles, Horizontal Flows:

Grant and Chisholm (1979), using air-water mixtures, tested a baffled heat exchanger with 4 crossflow zones and 3 window areas (note: a window refers to where the flow goes through the baffle cut and is hence longitudinal to the tubes rather than across the tubes). They studied stratified flows and measured the liquid levels in the first and fourth baffle compartments, noting that the void fraction was less in the first baffle compartment with respect to the fourth compartment for all mass velocities tested. They proposed:

$$1 - \varepsilon = \frac{1}{1 + \left( \frac{x}{1-x} \right) \left( \frac{\rho_L}{\rho_G} \right) \left( \frac{1}{K_2} \right)} \quad [17.6.13]$$

The empirical factor  $K_2$  is a velocity ratio evaluated as

$$K_2 = \left( \frac{\mu_L}{\mu_G} \right)^{\frac{m}{2-m}} \left( \frac{\rho_L}{\rho_G} \right)^{\frac{1-m}{2-m}} \quad [17.6.14]$$

where  $m$  is obtained by fitting the method to experimental data. They noted that this method worked well at low qualities but overestimated the measured void fractions at higher qualities.

# Void Fraction Exercises:

**17.1:** Determine the void fraction for the following vapor qualities (0.01, 0.1 and 0.25) using the following methods: homogeneous flow, momentum flux model and both of Zivi's expressions. The liquid density is  $1200 \text{ kg/m}^3$  and the gas density is  $200 \text{ kg/m}^3$ . Assume the liquid entrainment is equal to 0.4.

**17.2:** Determine the void fraction for a vapor quality of 0.1 using the second of Zivi's expressions using the properties above. Assume liquid entrainments equal to 0.0, 0.2, 0.4, 0.6, 0.8 and 1.0.

**17.3:** Determine the local void fractions using the Rouhani expressions [17.4.31] and [17.4.32] for the following qualities (0.1, 0.50, 0.95) for a fluid flowing at rates of 0.05 and 0.2 kg/s in a horizontal tube of 22 mm internal diameter for the same conditions as in Example 17.4. Compare and comment. The surface tension is 0.012 N/m.

**17.4:** Determine the local void fraction using the drift flux model assuming bubbly flow for the following qualities (0.01, 0.05, 0.1) for a fluid flowing at a rate of 0.5 kg/s in a vertical tube of 40 mm internal diameter. The fluid has the following physical properties: liquid density is  $1200 \text{ kg/m}^3$ , gas density is  $20 \text{ kg/m}^3$  and surface tension is 0.012 N/m.

# Void Fraction Exercises:

**17.5:** Determine the local void fraction using the drift flux model assuming slug flow for the following qualities (0.05, 0.1) for the same conditions as in Problem 17.4.

**17.6:** Determine the local void fraction using the drift flux model assuming annular flow at a quality of 0.5 for a fluid flowing at a rate of 0.5 kg/s in a vertical tube of 40 mm internal diameter. The fluid has the following physical properties: liquid density is  $1000 \text{ kg/m}^3$ , gas density is  $50 \text{ kg/m}^3$ , surface tension is  $0.05 \text{ N/m}$  and the liquid dynamic viscosity is  $0.0006 \text{ Ns/m}^2$ .

**17.7:** Determine the local void fractions using the method of Ishihara et al. for the following qualities (0.05, 0.1, 0.50) at a mass velocity of  $100 \text{ kg/m}^2\text{s}$  flowing across a tube bundle with tubes of 25.4 mm outside diameter. The fluid has the following physical properties: liquid density is  $1200 \text{ kg/m}^3$ , gas density is  $20 \text{ kg/m}^3$ , surface tension is  $0.012 \text{ N/m}$  and the liquid and vapor dynamic viscosities are  $0.0003 \text{ Ns/m}^2$  and  $0.00001 \text{ Ns/m}^2$

# Void Fraction Exercises:

**17.8:** Determine the local void fractions using the method of Fair and Klip for the same conditions as in Problem 17.7.

**17.9:** Derive expression [17.3.13] from [17.3.12].

**17.10:** Derive Zivi's second void fraction expression with entrained liquid in the gas phase, i.e. expression [17.3.15].

**17.11:** Derive expressions [17.4.26] and [17.4.27].

**17.12:** Prove expression [17.2.7].

## Chapter 18

# Post Dryout Heat Transfer

**Summary:** The heat transfer process and prediction methods for describing heat transfer in the post dryout regime are presented in this chapter. First, the processes leading to the transition to the post dryout regime are described and then non-equilibrium effects. This is followed by a presentation of the leading correlations for predicting heat transfer coefficients in the post dryout regime in first vertical channels and then horizontal channels. Finally, a general method for predicting the critical heat flux in uniformly vertical tubes is presented.

### 18.1 Introduction

The regime of post dryout heat transfer is encountered when the heated wall becomes dry before complete evaporation. For instance, this regime is reached when an evaporating annular film dries out and the remaining liquid is entrained as droplets, such that the vapor quality  $x$  is large but less than 1.0. It also refers to heat transfer downstream from the point at which the critical heat flux has been reached, thus even when  $x$  is small or close to 0.0, or in fact when the remaining liquid in the flow is still subcooled. Post dryout heat transfer is sometimes referred to as the liquid deficient regime or as mist flow heat transfer, but these last two terms are too restrictive since they do not describe the process when it occurs at low vapor quality.

In general, the post dryout heat transfer regime is reached from the wet wall regime by passing through one of three different transitions in the evaporation process:

- *Critical heat flux.* The heat flux at the wall or the imposed wall superheat is so high that a continuous vapor film is formed on the wall, somewhat analogous to surpassing the peak nucleate heat flux in pool boiling (this is determined using a method to calculate the value of  $q_{\text{crit}}$ );
- *Dryout of the liquid film.* The liquid within an annular film may completely evaporate, leaving the entrained liquid droplets in the vapor to still be evaporated (this is determined using a method to calculate the vapor quality at which dryout occurs);
- *Entrainment of the liquid film.* At some point, the vapor shear stress on the liquid film is strong enough to completely remove the film from the channel wall, such that all the liquid is entrained in the vapor phase as droplets (this is a hydrodynamic problem and can be estimated using an appropriate two-phase flow pattern map).

In the post dryout heat transfer regime, also often referred to as mist flow, the wall is not necessarily always dry. Entrained liquid droplets can impinge on the wall and momentarily wet it locally before either evaporating or “bouncing off” back into the vapor phase. Furthermore, only a portion of the heated periphery of the flow channel may be dry, particularly in horizontal flows and in channels with a wide variation in the peripheral heat flux (such as those heated radiantly by combustion). In particular, a progressive dryout in horizontal tubes tends to occur along the tube instead of occurring “simultaneously” around the entire perimeter as typically imagined in vertical tubes. Since the annular film is thinner at the top of the tube compared to the bottom in horizontal tubes, dryout tends to occur first at the top and then progress around the perimeter towards the bottom, creating a dryout zone along the tube.

Typically heat transfer coefficients in the post dryout regime are significantly lower than those encountered in the wet wall regime, as small as  $1/10^{\text{th}}$  to  $1/30^{\text{th}}$  those of the annular regime that typically

precedes it. This not only affects heat exchanger surface area calculations (e.g. most refrigeration heat exchanger design softwares do not utilize a mist flow threshold criteria and unwittingly continue modeling heat transfer as an annular flow rather than a mist flow) but perhaps the integrity of the heat exchanger itself, if the wall temperature becomes too high. The post dryout heat transfer regime may be encountered in fossil fuel boilers of electric power plants, on nuclear power plant fuel rod assemblies during a hypothetical loss of coolant, in fired heaters of petrochemical plants, and in direct-expansion evaporators and air-conditioning coils. It may also, unexpectedly, occur in liquid-liquid heat exchangers if there is a large temperature difference between the two fluids and the resulting wall temperature is significantly higher than the saturation temperature of the cold fluid.

## 18.2 Departure from Thermodynamic Equilibrium

During wet wall evaporation, the wall temperature remains close to the local saturation temperature corresponding to the local pressure. In contrast, in the post dryout regime, the local wall temperature may become significantly higher than the saturation temperature and hence departure from equilibrium occurs. The two limiting cases are illustrated in Figure 18.1.

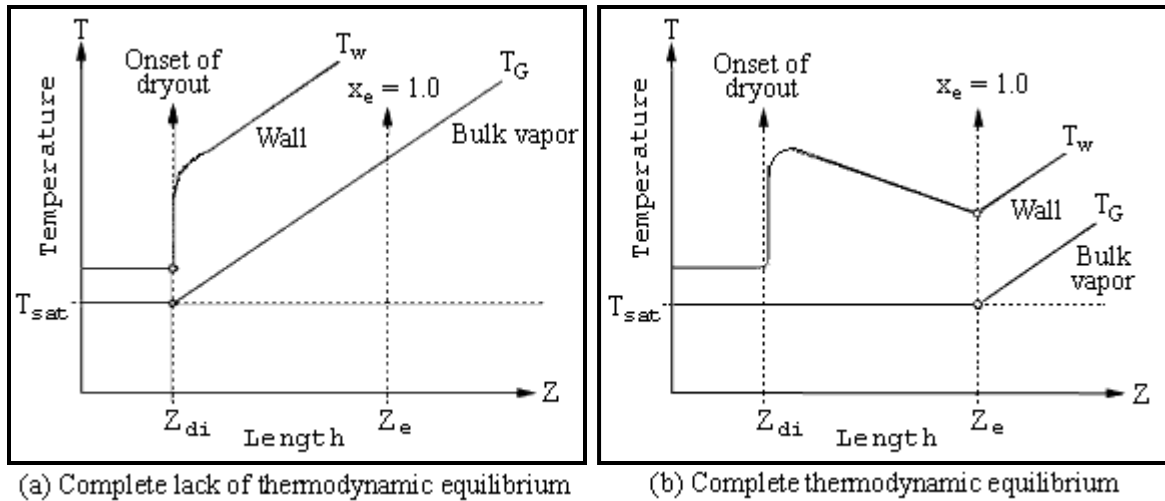


**Figure 18.1. Thermodynamic states in the post dryout regime.**

The first case represents complete departure from equilibrium, where heat is transferred only to the continuous vapor phase that is in contact with the heated wall, which results in superheating of the vapor. If the rate of heat transfer from the superheated vapor phase to the entrained droplets is so slow that their presence may be ignored, at the location  $z$  the vapor temperature  $T_G(z)$  downstream of the dryout point may be calculated on the basis that all the heat added to the fluid superheats the vapor. In this case, the wall temperature  $T_w(z)$  rises like that of a single-phase flow and its value can be calculated using a single-phase heat transfer correlation together with the imposed heat flux, giving the profile illustrated in Figure 18.1a.

The other limiting case is complete thermodynamic equilibrium as shown in Figure 18.1b. In this case, the rate of heat transfer from the vapor phase to the entrained droplets is assumed to be so effective that the vapor temperature  $T_G(z)$  remains at the saturation temperature until all the droplets have been completely evaporated. The downstream wall temperature  $T_w(z)$  may vary nonlinearly and a maximum may be reached, in part because of the cooling effect of impingement of liquid droplets on the heated wall.

The post dryout heat transfer process tends towards the case of thermal non-equilibrium, as shown in Figure 18.1a, at low pressures and low mass flow rates. At the other extreme, the process tends towards thermal equilibrium, as depicted in Figure 18.1b, at high reduced pressures and very high mass flow rates. A typical thermodynamic path of the process is illustrated in Figure 18.2 where the local temperature is lower than the maximum occurring during complete non-equilibrium, but is still significantly above the local saturation temperature of the complete equilibrium case. Hence, in post dryout heat transfer the local bulk temperature of the vapor is unknown *a priori* and thus becomes an added complication in describing and modeling the process.

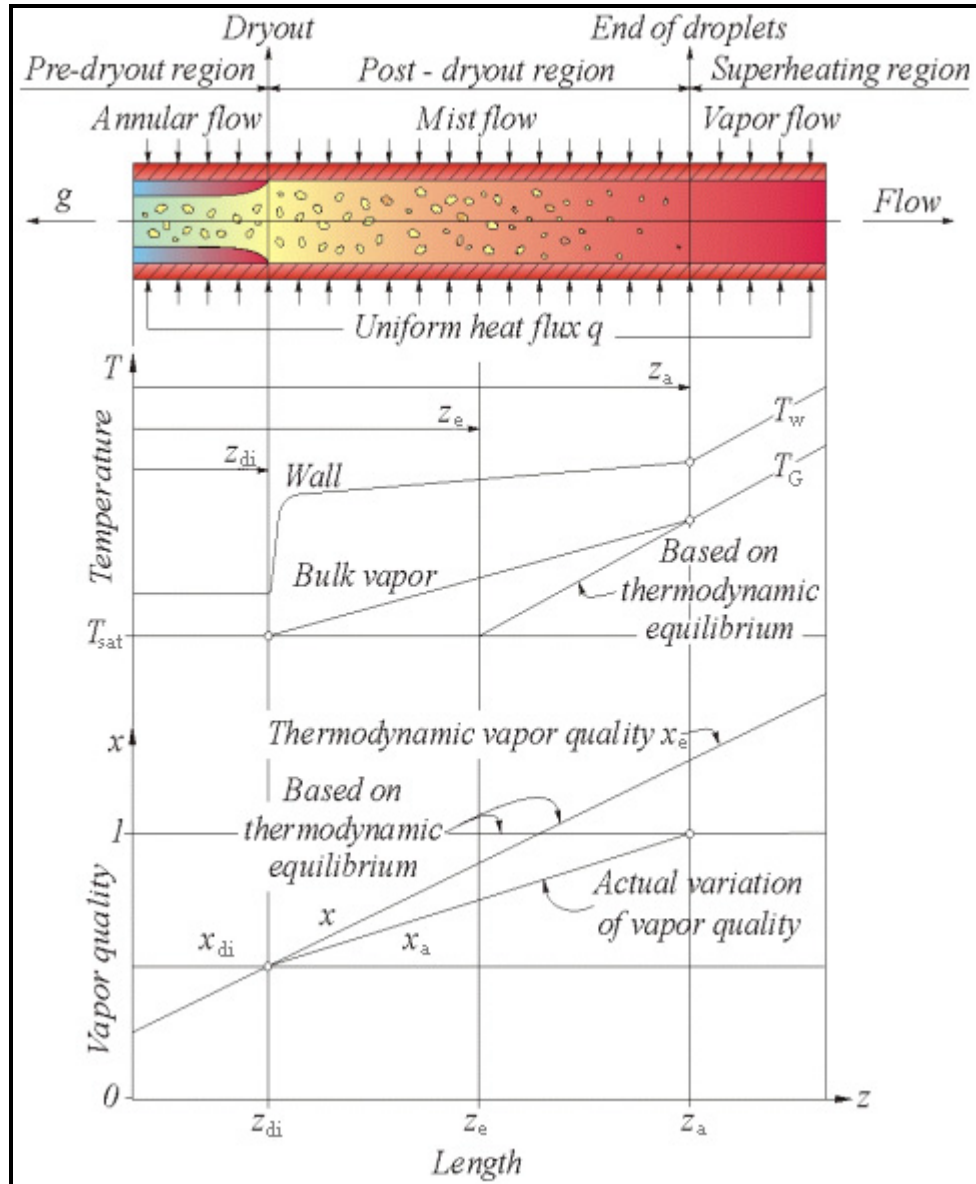


**Figure 18.2. Departure from thermodynamic equilibrium in the post dryout regime in a vertical tube.**

Another complicating aspect of post dryout heat transfer is that of the local vapor quality. Thermodynamic equilibrium of the two-phases as in Figure 18.1b means that all the heat absorbed by the

fluid is utilized to evaporate the liquid and hence the local equilibrium vapor quality at location  $z$  is  $x_e(z)$ . On the other hand, if all the heat is used to superheat the vapor after the onset of dryout as in Figure 18.1a, the vapor quality remains fixed at that at the dryout point,  $x_{di}(z)$ . In reality, the actual local vapor quality  $x_a(z)$  is less than that estimated from complete thermodynamic equilibrium and hence it follows that  $x_{di}(z) < x_a(z) < x_e(z)$ .

Consider Figure 18.2 which depicts post dryout in a *vertical* tube of internal diameter  $d_i$  heated uniformly with a heat flux of  $q$ . Dryout occurs at a length  $z_{di}$  from the inlet, and it is assumed that thermodynamic equilibrium exists at the dryout point. If complete equilibrium is maintained after dryout, all the liquid will be evaporated when the point  $z_e$  is reached. However, in the actual situation, only a fraction ( $\kappa$ ) of the surface heat flux is used to evaporate the remaining liquid in the post dryout region, while the remainder is used to superheat the bulk vapor. The liquid is thus completely evaporated only when a downstream distance of  $z_a$  is reached.

Now, assume that  $q$ , the total heat flux from the tube wall to the fluid at location  $z$ , can be subdivided into two components: the heat flux associated with droplet evaporation  $q_L(z)$  at location  $z$  and the heat flux associated with vapor superheating  $q_G(z)$  at location  $z$ . Thus,

$$q = q_L(z) + q_G(z) \quad [18.2.1]$$

Furthermore, let

$$\kappa = q_L(z) / q(z) \quad [18.2.2]$$

For simplicity,  $\kappa$  is considered independent of the length along the tube  $z$ , although this is not the case in general. Hence, the profiles of the actual bulk vapor temperature and actual vapor quality are linear as shown in Figure 18.2. The variation in the thermodynamic vapor quality with tube length for  $z < z_e$  is given by an energy balance

$$x(z) - x_{di} = \frac{4q}{d_i \dot{m} h_{LG}} (z - z_{di}) \quad [18.2.3]$$

where  $h_{LG}$  is the latent heat of vaporization and  $\dot{m}$  is the total mass velocity. The location of point  $z_e$  is given by

$$z_e = \left[ \frac{d_i \dot{m} h_{LG}}{4q} (1 - x_{di}) \right] + z_{di} \quad [18.2.4]$$

The actual vapor quality  $x_a(z)$  variation with length for  $z < z_a$  is given by

$$x_a(z) - x_{di} = \frac{4\kappa q}{d_i \dot{m} h_{LG}} (z - z_{di}) \quad [18.2.5]$$

and  $z_a$  is given by

$$z_a = \left[ \frac{d_i m h_{LG} (1 - x_{di})}{4 \kappa q} \right] + z_{di} \quad [18.2.6]$$

By combining [18.2.3] and [18.2.6], the resulting expression for  $\kappa$  is

$$\kappa = \left[ \frac{x_a(z) - x_{di}}{x(z) - x_{di}} \right] = \left[ \frac{z_a - z_{di}}{z_e - z_{di}} \right] \quad [18.2.7]$$

Similarly, the actual bulk vapor temperature  $T_{G,a}(z)$  is obtained:

$$T_G(z) = T_{sat} + \left[ \frac{4(1-\kappa)q(z - z_{di})}{\dot{m}c_{pG}d_i} \right] \quad [18.2.8]$$

for  $z < z_a$  while for  $z_a > z$  it is:

$$T_G(z) = T_{sat} + \left[ \frac{4q(z - z_e)}{\dot{m}c_{pG}d_i} \right] \quad [18.2.9]$$

The two limiting cases illustrated in Figure 18.1 are clearly recognized by setting  $\kappa = 0$  and  $\kappa = 1$ , respectively, in the above expressions. In reality,  $\kappa$  is not independent of tube length and must be predicted from the actual process conditions.

From a practical standpoint, as shown in Figure 18.2, liquid may remain entrained as small droplets in the vapor well beyond the location of  $x_e(z)$ . This fine mist gives rise to thermodynamic non-equilibrium and affects the thermal efficiency of a vapor compression or power cycle. For processes requiring dry saturated vapor or dry superheated vapor, such as a compressor or steam turbine, wet vapor can represent an operational liability.

## 18.3 Heat Transfer Regimes and Mechanisms

Two principal types of evaporation processes are encountered in the post dryout heat transfer regime. The first of these is the *dispersed flow regime*, in which the vapor phase becomes the continuous phase and all the liquid is entrained as dispersed droplets as illustrated in Figure 18.2. The second process is that of *inverted annular flow*, in which the vapor forms an annular film on the tube wall and the liquid is in the central core as shown in Figure 18.3 (where  $q_w$  is the wall heat flux,  $q_r$  is the radiant heat flux from the wall to the liquid and  $q_G$  is the heat flux across the vapor film to the interface while  $\lambda$  is the wavelength between bubble departures from the interface). The dispersed flow regime typically occurs after dryout or entrainment of an annular film flow. The inverted annular flow regime is encountered when the critical heat flux is surpassed for a flow at low vapor quality or even for subcooled liquid. In this case, the wall is too hot to be rewetted by the liquid and a continuous but highly disturbed vapor film is formed between the wall and the continuous liquid core.

For horizontal and inclined tubes, where dryout does not occur uniformly on the tube perimeter, only the upper part of the tube wall may be in the post dryout heat transfer regime while the lower part remains wet. This may also occur in vertical or inclined tubes that are heated non-uniformly, e.g. in the radiant

section of a fired heater or fossil fuel steam generator, where only one side of the tube is exposed to the flame.

Before discussing methods for predicting post dryout heat transfer coefficients in the next sections, it is instructive to first look at possible modes of heat transfer under these conditions:

- *Wall-to-vapor heat transfer.* Heat is transferred by convection from the wall to the continuous vapor phase in the dispersed flow regime (similar to single-phase flow in a channel) while in inverted annular flow heat is transferred by conduction (or convection) across the vapor film to the interface of the liquid core;
- *Wall-to-droplet heat transfer.* Heat is transferred to the droplets that impinge on the hot wall, which may be completely evaporated or only partially so before becoming re-entrained. The impinging droplets are evaporated either by transient, thin film evaporation or by nucleate boiling within the film if sites become active when a large droplet impacts on the wall;
- *Vapor-to-droplet heat transfer.* Heat is transferred by convection from the bulk-superheated vapor to the saturated liquid in the droplets. The saturation temperature is a function of the radius of the droplet (analogous to a bubble nucleus) and makes complete evaporation difficult to attain as the radius becomes small and smaller. Heat is also transferred by convection to any droplets passing through the thermal boundary layer on the wall that do not actually contact the wall;
- *Radiation heat transfer from the wall-to-droplets/vapor/upstream wall.* This mechanism only becomes important at large superheats. The vapor is almost transparent to thermal radiation while the droplets tend to absorb, transmit and reflect radiation and thus evaporate. The downstream wall also exchanges radiant energy with a hotter or cooler upstream wall. The net radiation flux depends on the view factor, the emissive properties of the surface and the respective temperatures.

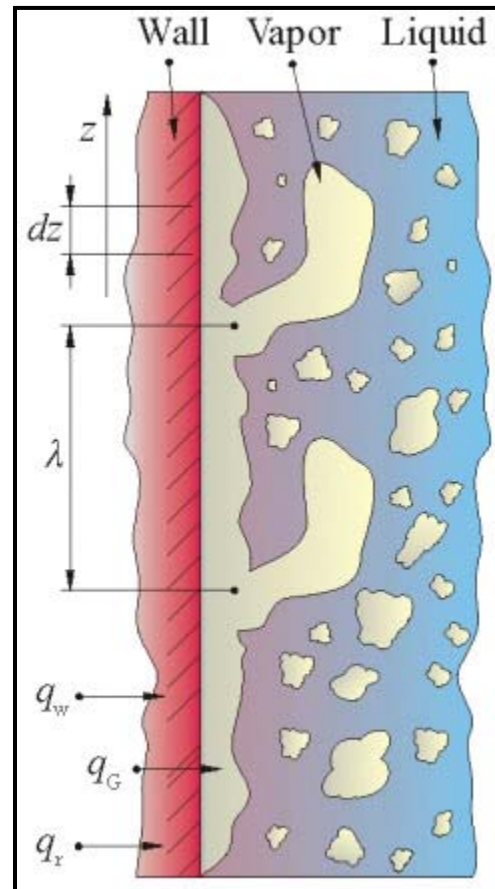


**Figure 18.3. Inverted annular flow regime.**

## 18.4 Heat Transfer in Inverted Annular Flow

This regime is illustrated in Figure 18.3 and is also sometimes referred to as forced convection film boiling. Dougall and Rohsenow (1963) made observations of film boiling inside a vertical tube and they noted that at low vapor quality and low flow rates the flow structure consisted of a central liquid core and a thin annular film of vapor on the heated wall. The interface between the two phases was not smooth but noticeably disturbed by waves traveling at a velocity similar to that of the liquid core. Because of the density difference between the two phases, the vapor was assumed to be traveling at a much higher velocity than the liquid core. Depending on the imposed conditions on vertical upward flow, the liquid core was observed to flow upward, remain more or less stationary, or even flow downward. Entrained vapor bubbles were also observed in the liquid core.

Inverted annular flow heat transfer is particularly amicable to analytical analysis because the problem of bubble nucleation at the heated wall is not present. In fact, the heat transfer through the vapor film can be treated as an analogy to film-wise condensation. Solutions are available for a variety of heated surface geometries for internal and external flows for both laminar and turbulent conditions with and without interfacial stress. The simplest situation is that of a laminar vapor film with a linear temperature profile. For a vertical flat surface, the analysis is similar to the Nusselt solution for falling film condensation on a vertical flat plate, and the local heat transfer coefficient  $\alpha_{\text{invert}}$  at a distance  $z$  from the point of onset of film boiling is

$$\alpha_{\text{invert}} = C \left[ \frac{k_g^3 \rho_g (\rho_L - \rho_g) g h_{LG}}{z \mu_g \Delta T} \right]^{1/4} \quad [18.4.1]$$

In this expression, the wall superheat is  $\Delta T = (T_w - T_{\text{sat}})$ . The value of the constant  $C$  depends on the boundary conditions. For zero interfacial stress  $C = 0.707$  while for zero interfacial velocity  $C = 0.5$ .

Wallis and Collier (1968) also analyzed inverted annular flow with a turbulent vapor film. They arrived at the following expression in which the heat transfer coefficient is inversely dependent on the distance  $z$ :

$$\frac{\alpha_{\text{invert}} z}{k_g} = 0.056 Re_G^{0.2} [\Pr_G \text{Gr}_G]^{1/3} \quad [18.4.2]$$

$\Pr_G$  is the vapor Prandtl number while  $\text{Gr}_G$  is the vapor Grashof number, defined as

$$\text{Gr}_G = \frac{z^3 g \rho_g (\rho_L - \rho_g)}{\mu_g^2} \quad [18.4.3]$$

The vapor Reynolds number  $Re_G$  is that of the vapor fraction flowing alone in the tube, i.e. the vapor flow is assumed to occupy the total cross-section of the tube, which is also sometimes referred to as the vapor only Reynolds number and given the symbol  $Re_{Go}$ . This expression is similar to the empirical expressions for turbulent, falling film condensation. More complex analytical approaches attempt to capture important aspects of the flow structure at the interface, such as waves, periodic disturbances, instabilities, subcooling of the vapor core, etc.

**Example 18.1:** Determine the local heat transfer coefficient for inverted annular flow at distances of 0.01, 0.1, 0.5 and 1.0 m from the lower edge of a vertical plate heated to a uniform temperature of 150°C. The fluid has the following physical properties at its saturation temperature of 100°C: liquid density is 1200 kg/m<sup>3</sup>, vapor density is 20 kg/m<sup>3</sup>, vapor thermal conductivity is 0.01 W/mK, latent heat of vaporization is 200 kJ/kg and vapor viscosity is 0.000011 Ns/m<sup>2</sup>.

**Solution:** Substituting the values into [18.4.1] and assuming no interfacial stress (so  $C = 0.707$ ) gives:

$$\alpha_{\text{invert}} = 0.707 \left[ \frac{(0.01)^3 (20)(1200 - 20)(9.81)(200000)}{z(0.000011)(150 - 100)} \right]^{1/4} = \frac{67.72}{z^{1/4}}$$

Thus, the local heat transfer coefficients at 0.01, 0.1, 0.5 and 1.0 m are 214.2, 120.4, 80.5 and 67.7 W/m<sup>2</sup>K, respectively. Thus, the local heat transfer coefficient decreases as z increases and the local heat flux, i.e.  $q = \alpha_{\text{invert}} \Delta T$ , ranges from 10710 to 3386 W/m<sup>2</sup>.

## 18.5 Heat Transfer in Mist Flow in Vertical Channels

Numerous empirical methods for predicting heat transfer in the mist flow regime, i.e. the dispersed liquid regime, have been proposed, in vertical tubes. Most can be classified as simple modifications of single-phase heat transfer correlations such as that of Dittus-Boelter (1930). Only a representative sample of these will be presented here and more complete treatments can be found in Groeneveld (1973), Mayinger and Langer (1978) and Collier (1982). The equilibrium vapor quality is used in most of the following methods and will be referred to as x.

### 18.5.1. Dougall and Rohsenow Method

For single-phase turbulent flow, it is usual to use the Dittus and Boelter (1930) correlation

$$\text{Nu} = a \text{Re}^b \text{Pr}^c \quad [18.5.1]$$

where a = 0.023, b = 0.8 and c = 0.4. The mean velocity of the fluid can be interpreted as the homogeneous velocity of the two-phases  $u_H$ :

$$u_H = \frac{\dot{m}}{\rho_H} = \dot{m} \left( \frac{x}{\rho_G} + \frac{1-x}{\rho_L} \right) \quad [18.5.2]$$

The definition of the homogeneous vapor Reynolds number is thus

$$\text{Re}_{GH} = \frac{\dot{m}d_i}{\mu_G} \left[ x + \frac{\rho_G}{\rho_L} (1-x) \right] \quad [18.5.3]$$

Hence, assuming homogeneous flow, the mist flow heat transfer coefficient is:

$$\text{Nu}_G = \frac{\alpha d_i}{k_G} = 0.023 \text{Re}_{GH}^{0.8} \text{Pr}_G^{0.4} \quad [18.5.4]$$

This was first proposed by Dougall and Rohsenow (1963). The vapor quality to use in the expression is the equilibrium vapor quality  $x_e$  and all properties are evaluated at the saturation temperature. A similar result can be obtained making the same modification to the well-known Gnielinski (1976) correlation that covers the transition and turbulent flow regimes such that

$$\text{Nu}_G = \frac{(f/2)(\text{Re}_{GH}-1000)\text{Pr}_G}{1+12.7(f/2)^{1/2}(\text{Pr}_G^{2/3}-1)} \quad [18.5.5]$$

where the friction factor f is obtained from

$$f = (1.58 \ln Re_{GH} - 3.28)^{-2} \quad [18.5.6]$$

and  $Re_{GH}$  is defined as in [18.5.3] above.

The limitations of this type of approach are:

- All other heat transfer mechanisms in mist flow, except for wall-to-vapor heat transfer, are ignored;
- The non-equilibrium effects of superheating the vapor driving the convection process is neglected;
- The heat transfer coefficient is predicted to rise in the mist flow regime with increasing vapor quality, which is not typically observed experimentally.

Hence, this very simplified approach should only be used as a first approximation.

### 18.5.2 Groeneveld Method

In the above homogeneous approach, the definition of the Reynolds number is not actually consistent with homogeneous flow theory because some gas phase properties are used in conjunction with the homogeneous density when only homogeneous properties should be used. In view of this fact, Groeneveld (1973) added another multiplying factor  $Y$  defined as

$$Y = 1 - 0.1 \left[ \left( \frac{\rho_L}{\rho_G} - 1 \right) (1 - x) \right]^{0.4} \quad [18.5.7]$$

to correct for this. The new expression for the Nusselt number is then

$$Nu_G = a \left\{ \frac{\dot{m} d_i}{\mu_G} \left[ x + \frac{\rho_G}{\rho_L} (1 - x) \right] \right\}^b Pr_G^c Y^d \quad [18.5.8]$$

The empirical constants giving the best fit to his database are as follows:  $a=0.00327$ ,  $b=0.901$ ,  $c=1.32$  and  $d=-1.50$ . The most significant change is to the exponent on the Prandtl number. The database covers the following range of conditions:

- $2.5 \text{ mm} < d_i < 25 \text{ mm}$ ,
- $34 \text{ bar} < p < 215 \text{ bar}$ ,
- $700 \text{ kg/m}^2\text{s} < \dot{m} < 5300 \text{ kg/m}^2\text{s}$ ,
- $< x < 0.9$ ,
- $120 \text{ kW/m}^2 < q < 2100 \text{ kW/m}^2$ .

This correlation is applicable to vertical and horizontal tubes and to vertical annuli. The large values of the pressure, heat flux and mass velocity in the database are typical of power boilers but they are beyond those of most other industrial applications.

**Example 18.2:** Compare the local heat transfer coefficients for mist flow obtained with Dougall and Rohsenow method and the Groeneveld correlation at a vapor quality of 0.85 for a tube of 22 mm diameter and a flow rate of 0.3 kg/s. The fluid has the following physical properties: liquid density is  $900 \text{ kg/m}^3$ ,

vapor density is  $70 \text{ kg/m}^3$ , vapor thermal conductivity is  $0.02 \text{ W/mK}$ , vapor specific heat of  $2.5 \text{ kJ/kgK}$  and vapor viscosity is  $0.000015 \text{ Ns/m}^2$ .

**Solution:** First of all, the mass velocity is determined to be  $789.2 \text{ kg/m}^2\text{s}$ . Then, the vapor Prandtl number is calculated:

$$\text{Pr}_G = \frac{\mu_G c_{pG}}{k_G} = \frac{(0.000015)(2500)}{0.02} = 1.875$$

The vapor Reynolds number is then obtained with [18.5.3]:

$$\text{Re}_{GH} = \left( \frac{789.2(0.022)}{0.000015} \right) \left( 0.85 + \frac{70}{900} (1 - 0.85) \right) = 997373$$

The Dougall and Rohsenow method is evaluated by substituting the values in [18.5.4]:

$$\begin{aligned} \frac{\alpha(0.022)}{0.02} &= 0.023(997373)^{0.8}(1.875)^{0.4} \\ \alpha &= 1693 \text{ W/m}^2\text{K} \end{aligned}$$

The Groeneveld correlation is evaluated by first determining the factor Y with [18.5.7]:

$$Y = 1 - 0.1 \left[ \left( \frac{900}{70} - 1 \right) (1 - 0.85) \right]^{0.4} = 0.8741$$

The Nusselt number is obtained then with [18.5.8]:

$$\begin{aligned} \text{Nu}_G &= \frac{\alpha(0.022)}{0.02} = 0.00327 \left\{ \left( \frac{789.2(0.022)}{0.000015} \right) \left[ 0.85 + \frac{70}{900} (1 - 0.85) \right] \right\}^{0.901} (1.875)^{1.32} (0.8741)^{-1.50} \\ \alpha &= 2119 \text{ W/m}^2\text{K} \end{aligned}$$

Thus, the Groeneveld correlation gives a heat transfer coefficient 25% larger than the Dougall and Rohsenow method.

### 18.5.3 Groeneveld and Delorme Method

Groeneveld and Delorme (1976) subsequently proposed a new correlation that empirically accounts for the non-equilibrium effects. The new correlation has the same form as Groeneveld's earlier expression but with one additional empirical group. Notably, the actual non-equilibrium temperature  $T_{G,a}$  and actual vapor quality  $x_a$  are utilized rather than the saturation temperature and equilibrium vapor quality. The new expression is

$$\frac{\alpha d_i}{k_{G,f}} = \frac{qd_i}{(T_w - T_{G,a})k_{G,f}} = a \left[ \left( \frac{md_i}{\mu_{G,f}} \right) \left( x_a + \frac{\rho_G}{\rho_L} (1 - x_a) \right) \right]^b \text{Pr}_{G,f}^c \left( e + f \frac{d_i}{L} \right)^g \quad [18.5.9]$$

Although the above expression may be used with its numerous empirical constants (refer to their publication), Groeneveld and Delorme found that using the following simpler expression also predicted their data quite well:

$$\frac{\alpha d_i}{k_{G,f}} = \frac{qd_i}{(T_w - T_{G,a})k_{G,f}} = 0.008348 \left[ \left( \frac{\dot{m}d_i}{\mu_{G,f}} \right) \left( x_a + \frac{\rho_G}{\rho_L} (1 - x_a) \right) \right]^{0.8774} Pr_{G,f}^{0.6112} \quad [18.5.10]$$

The subscript  $G,f$  in these expressions indicates that the vapor properties should be evaluated at the film temperature defined as

$$T_{G,f} = (T_w + T_{G,a})/2 \quad [18.5.11]$$

To determine the values of  $T_{G,a}$  and  $x_a$ , an energy balance is used where  $h_{G,a}$  is the actual vapor enthalpy and  $h_{L,sat}$  is the enthalpy of the saturated liquid while  $x_e$  is the equilibrium vapor quality and  $h_{LG}$  is the latent heat of evaporation. The actual vapor quality is obtained from

$$x_a = \frac{h_{LG} x_e}{h_{G,a} - h_{L,sat}} \quad [18.5.12]$$

The change in enthalpy is computed from the expression

$$h_{G,a} - h_{L,sat} = h_{LG} + \int_{T_{sat}}^{T_{G,a}} c_{pG} dT_G \quad [18.5.13]$$

The approximate homogeneous Reynolds number  $Re_{GH,e}$  is used, based on the equilibrium vapor quality, as follows:

$$Re_{GH,e} = \left( \frac{\dot{m}d_i}{\mu_G} \right) \left( x_e + \frac{\rho_G}{\rho_L} (1 - x_e) \right) \quad [18.5.14]$$

For values of  $x_e$  greater than unity (i.e. when the enthalpy added to the fluid places its equilibrium state in the superheated vapor region),  $x_e$  is set equal to 1.0 in the above expression. The difference between the actual vapor enthalpy  $h_{G,a}$  and the equilibrium vapor enthalpy  $h_{G,e}$  is given by

$$\frac{h_{G,a} - h_{G,e}}{h_{LG}} = \exp(-\tan \psi) \quad [18.5.15]$$

The correlating parameter  $\psi$  is obtained with the following expression

$$\psi = a_1 Pr_G^{a_2} Re_{GH,e}^{a_3} \left( \frac{qd_i c_{pG,e}}{k_G h_{LG}} \right)^{a_4} \sum_{i=0}^2 b_i x_e^i \quad [18.5.16]$$

which is valid for  $0 \leq \psi \leq \pi/2$ . Furthermore, when  $\psi < 0$ , its value is set to 0.0; when  $\psi > \pi/2$ , it is set to  $\pi/2$ . The empirical values determined from a database of 1400 points for only water are as follows:

$$a_1 = 0.13864, a_2 = 0.2031, a_3 = 0.20006, a_4 = -0.09232 \\ b_0 = 1.3072, b_1 = -1.0833, b_2 = 0.8455$$

For  $0 \leq x_e \leq 1$ , the equilibrium vapor enthalpy  $h_{G,e}$  is that of the saturated vapor, i.e.

$$h_{G,e} = h_{G,sat} \quad [18.5.17]$$

For  $x_e > 1$ , the equilibrium vapor enthalpy  $h_{G,e}$  is calculated as

$$h_{G,e} = h_{G,sat} + (x_e - 1)h_{LG} \quad [18.5.18]$$

This prediction method is implemented as follows to find the values of  $\alpha$ ,  $T_{G,a}$  and  $x_a$  when given those of  $m$ ,  $x_e$  and  $q$ :

1. Estimate an initial value of  $T_{G,f}$  to evaluate the fluid properties,
2. Use [18.5.14] and [18.5.16] to determine  $Re_{GH,e}$  and  $\psi$ ,
3. Utilize either [18.5.17] or [18.5.18] together with [18.5.15] to obtain  $h_{G,a}$ ,
4. Input the value of  $h_{G,a}$  into [18.5.12] to obtain  $x_a$ ,
5. Solve [18.5.13] iteratively to find  $T_{G,a}$ ,
6. Input the resulting values in [18.5.10] to determine the wall temperature  $T_w$  and then the heat transfer coefficient  $\alpha$ ,
7. A new film temperature  $T_{G,f}$  may now be calculated with [18.5.11] and the whole procedure is repeated until the iteration reaches a stable result.

This method is more accurate than the simpler method of Groeneveld (1973) and has a similar range of application. The method does, however, ignore the effects of wall-to-droplet, vapor-to-droplet and radiation heat transfer, but importantly it does include the effect of departure from equilibrium.

#### **18.5.4 Ganic and Rohsenow Method**

Ganic and Rohsenow (1977) proposed a more complete model for heat transfer in the mist flow regime. The total heat flux was assumed to be the sum of three contributions: wall-to-vapor convection  $q_G$ , wall-to-droplet evaporation  $q_L$  and radiation  $q_r$ . Thus, the total heat flux is the sum of these contributions so that

$$q = q_G + q_L + q_r \quad [18.5.19]$$

They predict the wall-to-vapor convection contribution using a modification of the McAdams turbulent flow correlation as follows

$$q_G = 0.0023 \left( \frac{k_G}{d_i} \right) \left( \frac{m \times d_i}{\epsilon \mu_G} \right)^{0.8} Pr_G^{0.4} (T_w - T_{sat}) \quad [18.5.20]$$

The Reynolds number includes the void fraction  $\varepsilon$  to determine the mean velocity of the vapor phase while the physical properties are evaluated at the saturation temperature. The total radiation contribution is the sum of the radiation from the wall-to-droplets and from the wall-to-vapor:

$$q_r = F_{WL}\sigma_{SB}(T_w^4 - T_{sat}^4) + F_{WG}\sigma_{SB}(T_w^4 - T_{sat}^4) \quad [18.5.21]$$

$F_{WL}$  and  $F_{WG}$  are the respective view factors,  $\sigma_{SB}$  is the Stephan-Boltzmann constant ( $\sigma_{SB} = 5.67 \times 10^{-8} \text{ W/m}^2\text{K}^4$ ) and blackbody radiation is assumed. For a transparent vapor,  $F_{WG}$  equals 0. Based on their subsequent simulations, the radiant heat flux is negligible except at very large wall temperatures.

The interesting aspect of this model is that a detailed analysis of the wall-to-droplet heat transfer mechanisms was attempted, although non-equilibrium effects were ignored. They proposed the following expression for the heat flux due to this impinging droplet mechanism:

$$q_L = u_d(1-\varepsilon)\rho_L h_{LG} f_{cd} \exp\left[1 - \left(\frac{T_w}{T_{sat}}\right)^2\right] \quad [18.5.22]$$

where the droplet deposition velocity  $u_d$  is calculated from

$$u_d = 0.15 \frac{\dot{m}_x}{\rho_L \varepsilon} \sqrt{\frac{f_G}{2}} \quad [18.5.23]$$

In the above expressions  $f_{cd}$  is the cumulative deposition factor and  $f_G$  is the single-phase friction factor calculated at the effective vapor Reynolds number, i.e.  $(\dot{m}_x d_i)/(\varepsilon \mu_G)$ . A complex method was presented for determination of  $f_{cd}$  as a function of droplet size and can be found in the original reference. Because of the larger quantity of liquid at lower vapor qualities, there is a higher propensity for the liquid to contact the hot tube wall at these conditions. Hence the importance of  $q_L$  to heat transfer is more significant at low to medium vapor qualities than at high vapor qualities, where non-equilibrium effects become important.

## 18.6 Critical Heat Flux in Vertical Channels

The critical heat flux in tubes and channels has been investigated extensively and the reader is referred to Chapters 8 and 9 in Collier and Thome (1994) for an extensive review of prediction methods and parameters influencing the process. Presently, the critical heat flux occurring in uniformly heated vertical tubes is addressed and the widely quoted, general method of Katto and Ohno (1984) is presented below. This method is the result of progressive improvements over the years and is applicable to a wide range of conditions for which the critical heat flux is reached in the saturated zone of a vertical tube for saturated or subcooled liquid inlet conditions. In their method, the critical heat flux  $q_{crit}$  is determined from the following expression that corrects for the level of inlet subcooling as follows:

$$q_{crit} = q_{crit,i} \left[ 1 + K_i \left( \frac{\Delta h_{L,inlet}}{h_{LG}} \right) \right] \quad [18.6.1]$$

where  $q_{crit,i}$  is a reference critical heat flux at saturated liquid inlet conditions obtained from one of five different correlations to be given below,  $K_i$  is an inlet subcooling factor and  $h_{L,inlet}$  is the change of enthalpy of the liquid from its subcooled inlet temperature to its saturation temperature. Their method uses the following three dimensionless groups:

$$Z = z/d_i \quad [18.6.2]$$

$$R = \rho_G / \rho_L \quad [18.6.3]$$

$$W = \frac{\sigma \rho_L}{\dot{m}^2 Z} \quad [18.6.4]$$

Depending on the operating conditions, there are five methods to choose from to determine the reference critical heat flux  $q_{crit,i}$  as follows:

$$\frac{q_{crit,1}}{\dot{m}h_{LG}} = \frac{CW^{0.043}}{Z} \quad [18.6.5]$$

$$\frac{q_{crit,2}}{\dot{m}h_{LG}} = \frac{0.1 R^{0.133} W^{0.333}}{1 + 0.0031 Z} \quad [18.6.6]$$

$$\frac{q_{crit,3}}{\dot{m}h_{LG}} = \frac{0.098 R^{0.133} W^{0.433} Z^{0.27}}{1 + 0.0031 Z} \quad [18.6.7]$$

$$\frac{q_{crit,4}}{\dot{m}h_{LG}} = \frac{0.0384 R^{0.6} W^{0.173}}{1 + 0.28 W^{0.233} Z} \quad [18.6.8]$$

$$\frac{q_{crit,5}}{\dot{m}h_{LG}} = \frac{0.234 R^{0.513} W^{0.433} Z^{0.27}}{1 + 0.0013 Z} \quad [18.6.9]$$

The value of  $K_i$  in [18.6.1] also depends on the particular conditions and is determined with one of the following three expressions:

$$K_1 = \frac{0.261}{CW^{0.043}} \quad [18.6.10]$$

$$K_2 = \frac{0.833[0.0124 + (1/Z)]}{R^{0.133} W^{0.333}} \quad [18.6.11]$$

$$K_2 = \frac{1.12[1.52W^{0.233} + (1/Z)]}{R^{0.6} W^{0.173}} \quad [18.6.12]$$

The value of C is given by:

$$C = 0.25 \text{ for } Z < 50$$

$$C = 0.25 + 0.0009(Z - 50) \text{ for } 50 \leq Z \leq 150$$

$C = 0.34$  for  $Z > 50$ .

The appropriate choice of expressions to use for  $q_{crit,i}$  and  $K_i$  is determined as follows:

For  $R < 0.15$ :

if $q_{crit,1} < q_{crit,2}$ ,	then $q_{crit,i} = q_{crit,1}$ ;
if $q_{crit,1} > q_{crit,2}$ and $q_{crit,2} < q_{crit,3}$ ,	then $q_{crit,i} = q_{crit,2}$ ;
if $q_{crit,1} > q_{crit,2}$ and $q_{crit,2} > q_{crit,3}$ ,	then $q_{crit,i} = q_{crit,3}$ ;
if $K_1 > K_2$ ,	then $K_i = K_1$ ;
if $K_1 < K_2$ ,	then $K_i = K_2$ .

For  $R > 0.15$ :

if $q_{crit,1} < q_{crit,5}$ ,	then $q_{crit,i} = q_{crit,1}$ ;
if $q_{crit,1} > q_{crit,5}$ and $q_{crit,5} > q_{crit,4}$ ,	then $q_{crit,i} = q_{crit,5}$ ;
if $q_{crit,1} > q_{crit,5}$ and $q_{crit,5} < q_{crit,4}$ ,	then $q_{crit,i} = q_{crit,4}$ ;
if $K_1 > K_2$ ,	then $K_i = K_1$ ;
if $K_1 < K_2$ and $K_2 < K_3$ ,	then $K_i = K_2$ ;
if $K_1 < K_2$ and $K_2 > K_3$ ,	then $K_i = K_3$ .

Their critical heat flux database covers the following conditions:

$$\begin{aligned}0.01 < z < 8.8 \text{ m} \\ 0.001 < d_i < 0.038 \text{ m} \\ 5 < Z < 880 \\ 0.0003 < R < 0.41 \\ 3 \times 10^{-9} < W < 0.02 \\ 0.4 < \Delta h_{LG} < 39.9 \text{ kJ/kg}\end{aligned}$$

Furthermore, mass velocities in their database ranged from about  $11\text{-}8800 \text{ kg/m}^2\text{s}$  while the test fluids were refrigerants (R-12, R-22, R-115) and liquid helium. The critical heat flux condition is normally reached at or near the exit of the tube. The exit vapor quality  $x_{exit}$  corresponding to  $q_{crit}$  can be obtained from an energy balance along the tube from its inlet, so that:

$$x_{exit} = \frac{4q_{crit}}{\dot{m}h_{LG}} \left( \frac{z}{d_i} \right) - \frac{\Delta h_{L,inlet}}{h_{LG}} \quad [18.6.13]$$

## 18.7 Heat Transfer with Progressive Dryout in Horizontal Tubes

The process of evaporation in **horizontal tubes** during the transition from annular flow to mist flow is depicted in Figure 18.4. Dryout occurs first at the top of the tube where the liquid film is thinner, denoted as vapor quality  $x_{di}$  (section A-A), and then progresses downward around the perimeter (section B-B) until reaching the bottom (section C-C) at the vapor quality  $x_{de}$ . The process of dryout thus takes place over a vapor quality range and ends at the bottom of the tube when the fully developed mist flow regime

is reached. This regime between  $x_{di}$  and  $x_{de}$  will be called dryout (in contrast, dryout in a vertical tube is typically assumed to occur simultaneously around the entire perimeter of the tube at one particular vapor quality). The mist flow heat transfer methods described above, when applied to horizontal tubes, do *not* account for this progressive transition from annular to mist flow and hence cannot predict the heat transfer coefficient in the dryout regime.

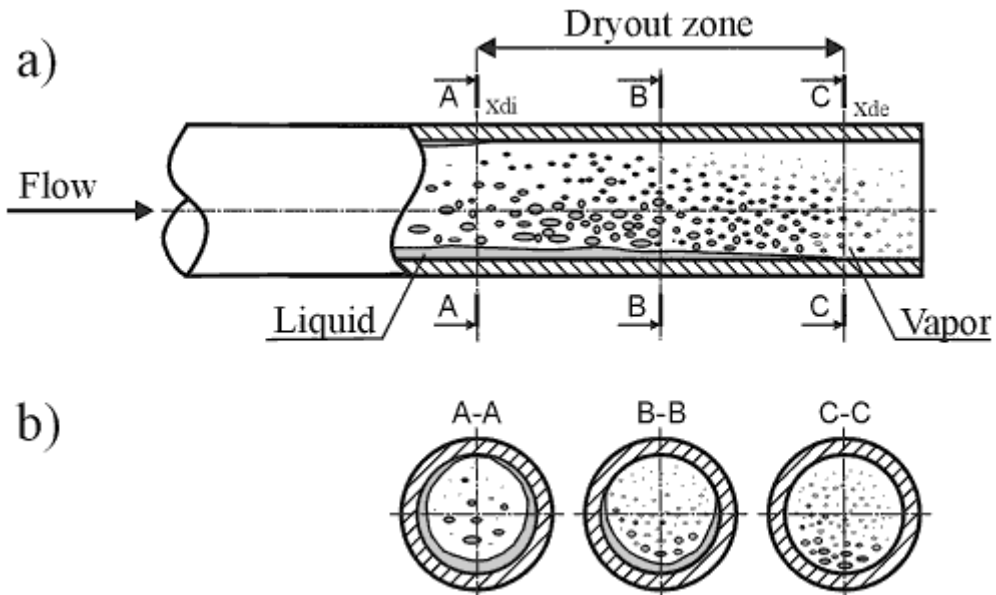


**Figure 18.4. (a) Dryout zone during evaporation in a horizontal tube; (b) Cross sectional views: A-A onset of dryout in annular flow at top of tube; B-B partial dryout around tube perimeter; C-C end of dryout at bottom of tube and beginning of mist flow.**

The onset of dryout at the top of a horizontal tube is accompanied by a drastic drop in the heat transfer coefficient relative to that prior to dryout (annular flow typically). The heat transfer coefficient falls rapidly in the dryout zone as a smaller and smaller fraction of the tube perimeter is wetted by what is left of the annular liquid film and then becomes nearly constant in value when the mist flow regime is reached, as seen in Figure 18.5 of Mori et al. (2000) while noting that the lines AB, BC and CD represent a fit to the data points, not a prediction method. The point of intersection B indicates the inception point of dryout at the top of the horizontal tube, where locally the heat transfer begins to fall as the annular film dries out. The point of intersection C indicates the location where dryout is complete around the tube perimeter, and thus also where the deterioration of heat transfer ends. The dryout qualities at inception and ending of this process at these respective points are denoted  $x_{di}$  and  $x_{de}$ . The distinction of these two points is caused by the shift of the dryout position from the top to the bottom around and along the tube perimeter with increasing quality. The heat transfer process from point A to B is that of annular flow boiling while that from C to D is mist flow heat transfer. From B to C, a transition zone exists that will be called **dryout heat transfer** here to distinguish it from **mist flow heat transfer**.

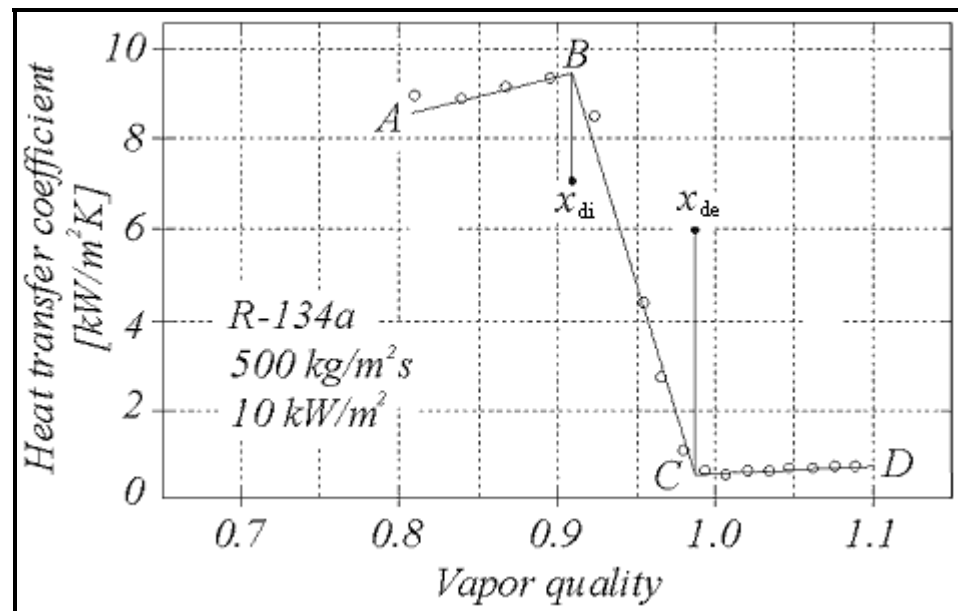
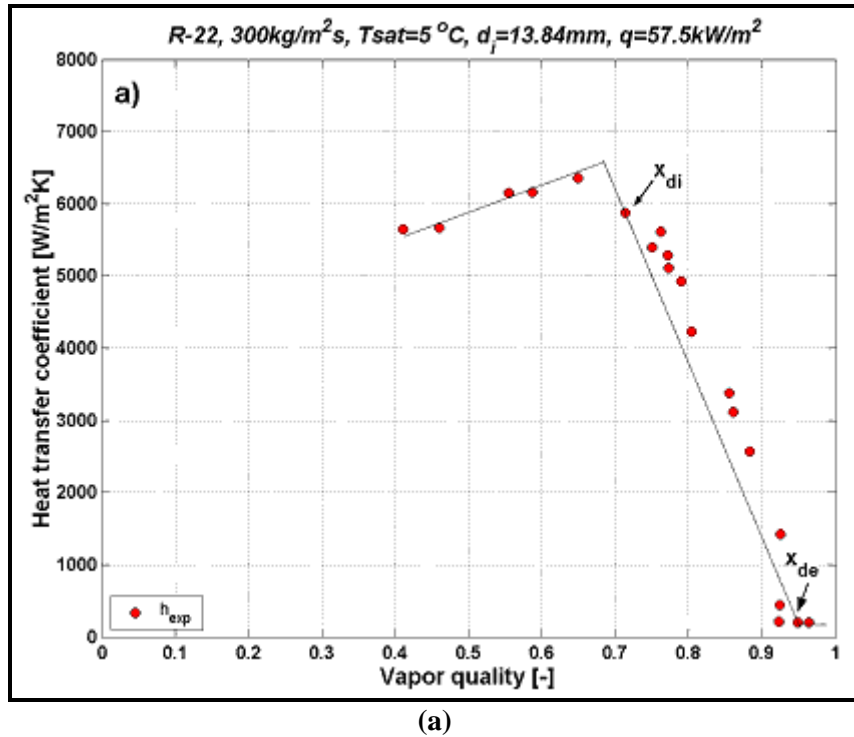
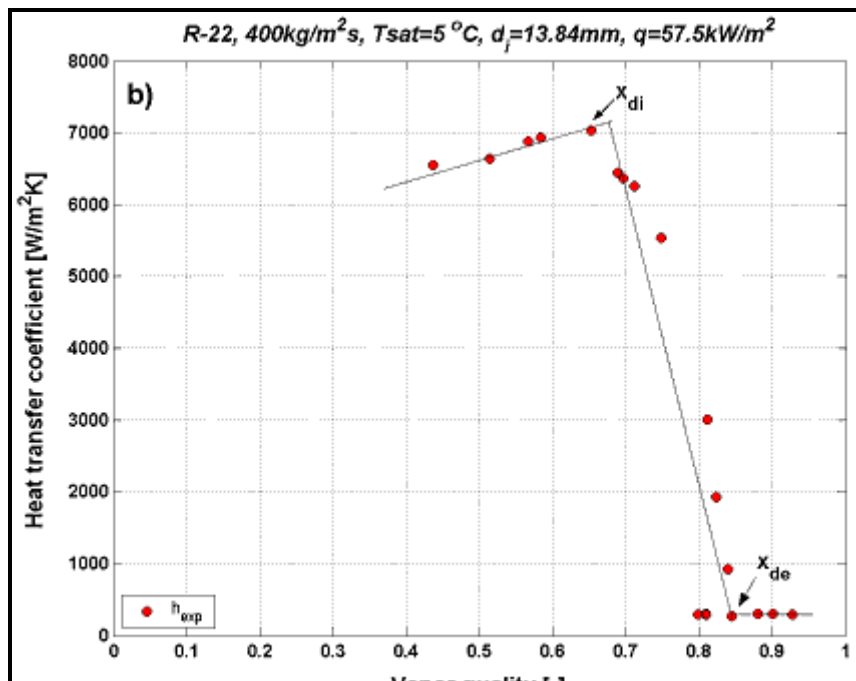


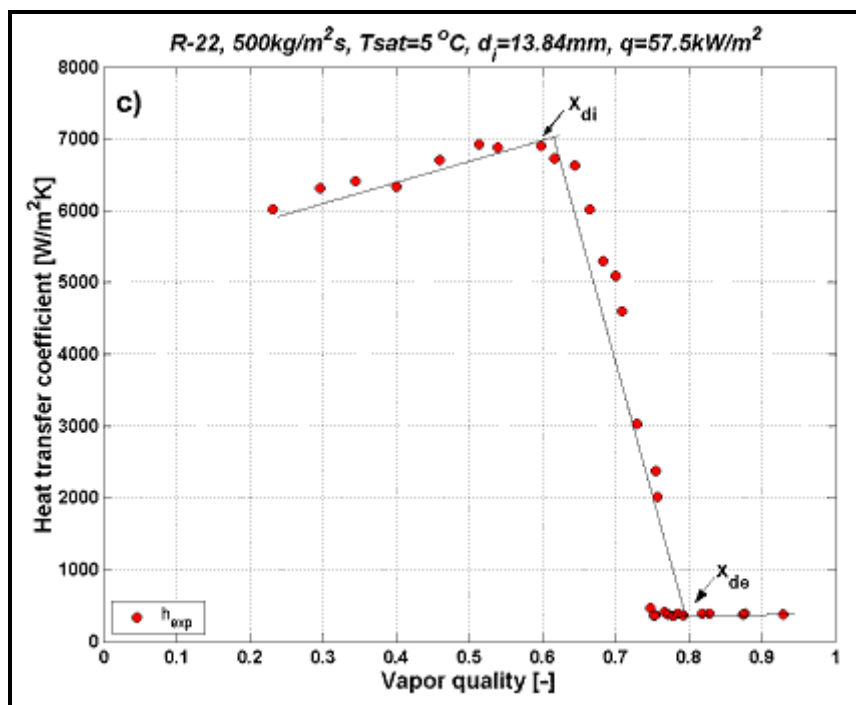
Figure 18.5. Variation in local heat transfer coefficient during dryout from Mori et al. (2000).



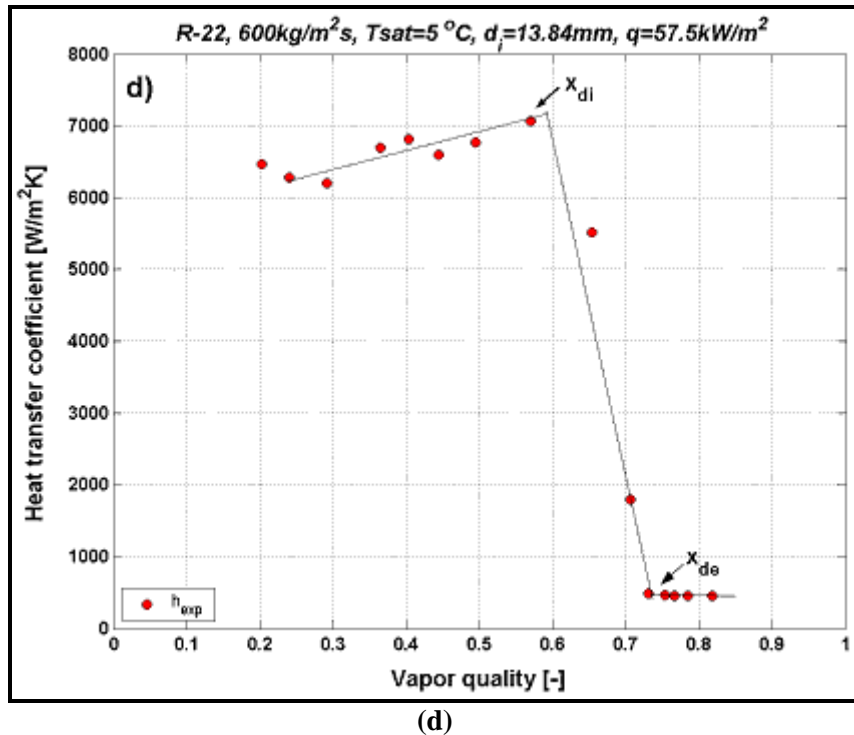
(a)



(b)



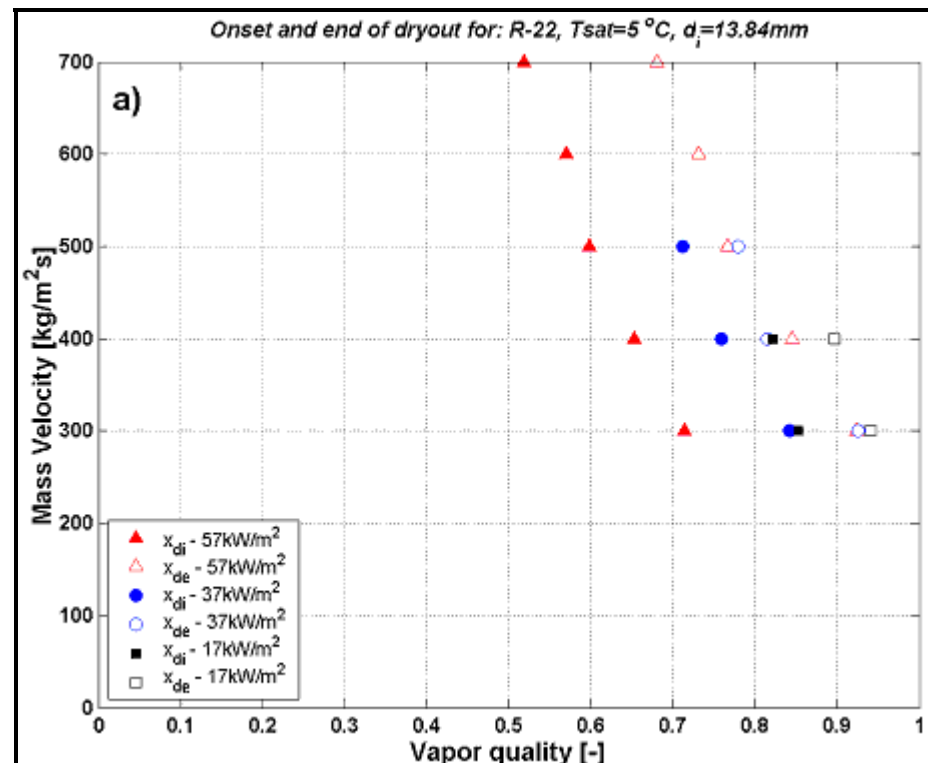
(c)



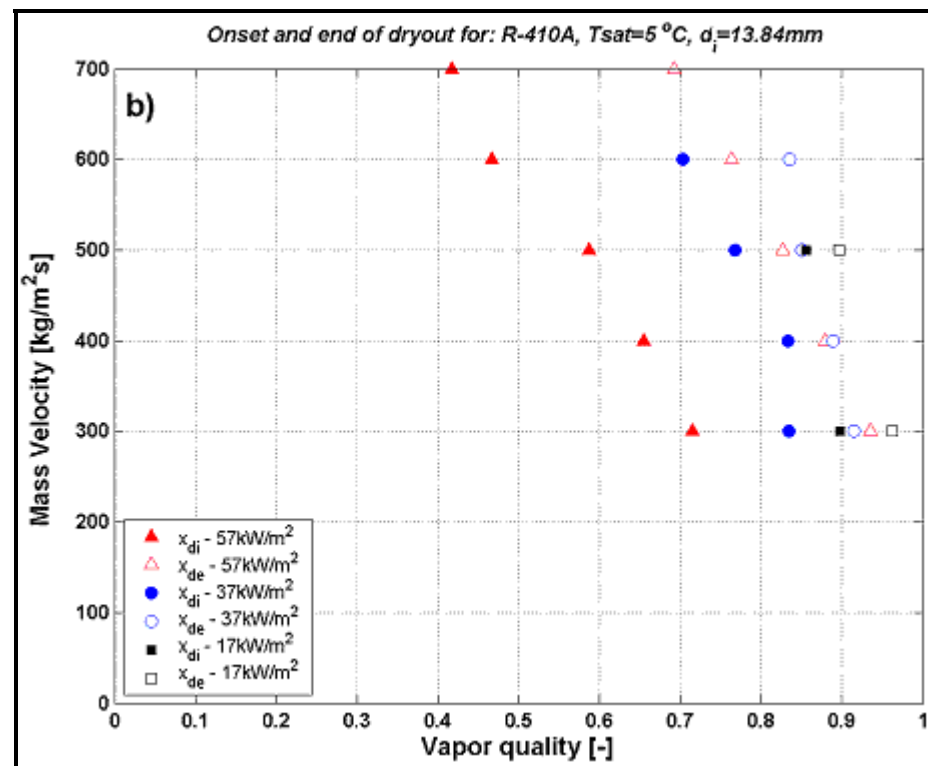
(d)

**Figure 18.6. Heat transfer for R-22 with an initial heat flux  $q = 57.5 \text{ kW/m}^2$  before the onset of dryout at four mass velocities: a) 300  $\text{kg/m}^2\text{s}$ , b) 400  $\text{kg/m}^2\text{s}$ , c) 500  $\text{kg/m}^2\text{s}$ ; d) 600  $\text{kg/m}^2\text{s}$ .**

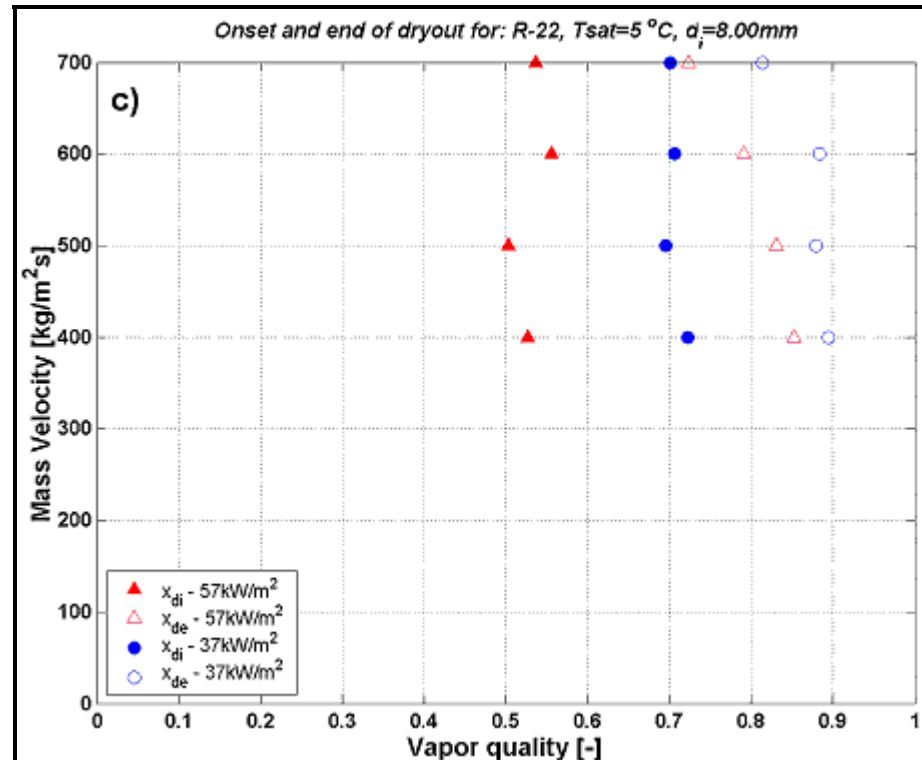
Figure 18.6 shows similar results for the transition from annular flow to mist flow in tests done by Wojtan, Ursenbacher and Thome (2005a) for evaporation of R-22 in a horizontal 13.84 mm internal diameter, plain copper tube at 5°C using hot water heating (again with the lines through the data indicating trends, not prediction methods). The exact vapor quality at the onset of dryout  $x_{di}$  is not known because of the finite number of tests run and hence its expected point of occurrence is indicated. The end of dryout is also indicated by  $x_{de}$ . Some hysteretic effect was also noted when going back into the dryout zone from mist flow but this complication was for now ignored. They did systematic tests for onset heat fluxes ranging from 7.5 to 57.5  $\text{kW/m}^2$  for R-22 and R-410A in 8.00 and 13.84 mm internal diameter tubes in order to develop a database on the effect of heat flux on the dryout process. Analyzing all their series of test results, the dryout inception vapor qualities  $x_{di}$  and dryout ending vapor qualities  $x_{de}$  were found from their R-22 and R-410A data and are presented in Figure 18.7 for two tube diameters as a function of heat flux. Comparing the dryout inception points for both fluids, it can be seen that  $x_{di}$  occurs earlier for R-410A than for R-22. This can be explained by the influence of surface tension, which is 30% lower for R-410A than R-22. That is, as the surface tension decreases, the vapor shear meets less resistance to entrain the liquid film into the high velocity vapor core and thus the inception of dryout is therefore encountered at a lower vapor quality for R-410A compared to that for R-22.



(a)



(b)



(c)

**Figure 18.7.** The dryout inception  $x_{di}$  and the dryout completion  $x_{de}$  for: (a) R-22,  $d_i = 13.84$  mm; (b) R-410A,  $d_i = 13.84$  mm; (c) R-22,  $d_i = 8.00$  mm from Wojtan, Ursenbacher and Thome (2005a).

Mori et al. (2000) classified their dryout results into three characteristic regimes (S1, S2 and S3) based on the experimental trends they observed and presented prediction methods for their values of  $x_{di}$  and  $x_{de}$ . The Wojtan, Ursenbacher and Thome (2005a) experimental data agreed best, qualitatively speaking, with the dryout regime S2 prediction method where the inception  $x_{di}$  and dryout completion  $x_{de}$  expressions are as follows:

$$x_{di} = 0.58 \exp \left[ 0.52 - 0.000021 We_G^{0.96} Fr_G^{-0.02} \left( \frac{\rho_G}{\rho_L} \right)^{-0.08} \right] \quad [18.7.1]$$

$$x_{de} = 0.61 \exp \left[ 0.57 - 0.0000265 We_G^{0.94} Fr_G^{-0.02} \left( \frac{\rho_G}{\rho_L} \right)^{-0.08} \right] \quad [18.7.2]$$

In these expressions, the Weber and Froude numbers are defined as:

$$We_G = \frac{\dot{m}^2 d_i}{\rho_G \sigma} \quad [18.7.3]$$

$$Fr_G = \frac{\dot{m}^2}{\rho_G (\rho_L - \rho_G) g d_i} \quad [18.7.4]$$

The above approach has been extended by Wojtan, Ursenbacher and Thome (2005a) to include the strong influence of heat flux they observed. This was incorporated by introducing a non-dimensional heat flux term in the above expressions and then finding new empirical constants using their heat flux dependent database. Thus, the new criteria for the beginning and ending of dryout are calculated from their following equations, where  $q$  is the heat flux just prior to the onset of dryout:

$$x_{di} = 0.58 \exp \left[ 0.52 - 0.235 We_G^{0.17} Fr_G^{0.37} \left( \frac{\rho_G}{\rho_L} \right)^{0.25} \left( \frac{q}{q_{DNB}} \right)^{0.70} \right] \quad [18.7.5]$$

$$x_{de} = 0.61 \exp \left[ 0.57 - 0.0058 We_G^{0.38} Fr_G^{0.15} \left( \frac{\rho_G}{\rho_L} \right)^{-0.09} \left( \frac{q}{q_{DNB}} \right)^{0.27} \right] \quad [18.7.6]$$

Applying these expressions, an additional rule is that  $x_{de} = x_{di}$  when [18.7.6] gives a smaller value than that given by [18.7.5], i.e. no cross over of these transition lines is allowed. Also, the maximum value in applying the method is  $x_{de} = 0.99$ , i.e.  $x_{de} = 0.99$  whenever  $x > 0.99$ . The definitions of  $We_G$  and  $Fr_G$  remain the same as above and the heat flux at departure from nucleate boiling  $q_{DNB}$  is that of Kutateladze (1948):

$$q_{DNB} = 0.131 \rho_G^{0.5} h_{LG} (g(\rho_L - \rho_G)\sigma)^{0.25} \quad [18.7.7]$$

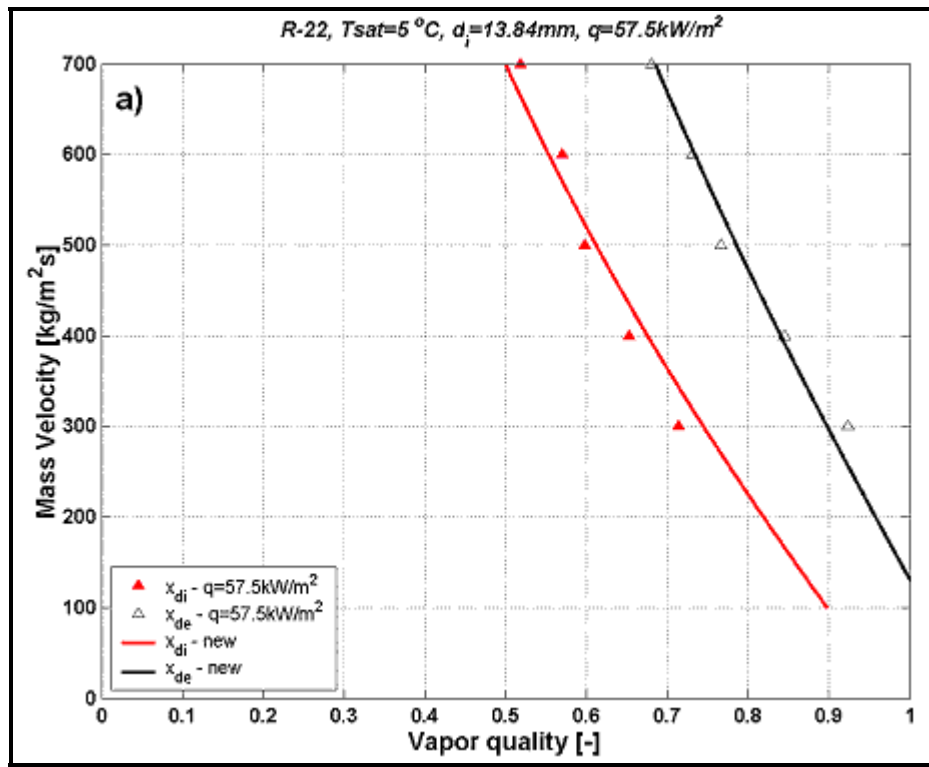
Important from an application point-of-view, besides determining the respective values of  $x_{di}$  and  $x_{de}$ , the above expressions can be inverted to obtain the transition mass velocities for the initiation and ending of the dryout zone, respectively, as a function of vapor quality:

$$\dot{m}_{dryout} = \left[ \frac{1}{0.235} \left( \ln \left( \frac{0.58}{x} \right) + 0.52 \right) \left( \frac{d_i}{\rho_G \sigma} \right)^{-0.17} \left( \frac{1}{gd_i \rho_G (\rho_L - \rho_G)} \right)^{-0.37} \left( \frac{\rho_G}{\rho_L} \right)^{-0.25} \left( \frac{q}{q_{DNB}} \right)^{-0.70} \right]^{0.926} \quad [18.7.8]$$

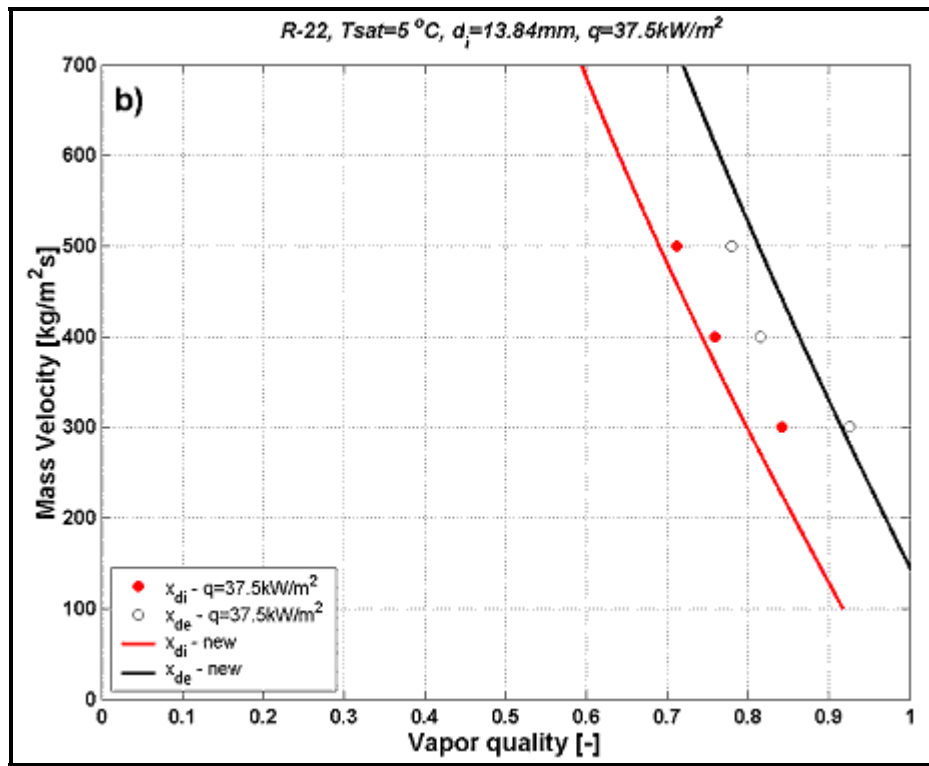
$$\dot{m}_{mist} = \left[ \frac{1}{0.0058} \left( \ln \left( \frac{0.61}{x} \right) + 0.57 \right) \left( \frac{d_i}{\rho_G \sigma} \right)^{-0.38} \left( \frac{1}{gd_i \rho_G (\rho_L - \rho_G)} \right)^{-0.15} \left( \frac{\rho_G}{\rho_L} \right)^{0.09} \left( \frac{q}{q_{DNB}} \right)^{-0.27} \right]^{0.943} \quad [18.7.9]$$

Figure 18.8 illustrates the new transition curves calculated from the new expressions compared to the values of  $x_{di}$  and  $x_{de}$  obtained during their evaporation tests with R-22 in a 13.84 mm internal diameter test section. As can be seen, very good agreement has been found for all three initial heat fluxes. Similar results were obtained for the evaporation tests with R-410A and for their 8.0 mm tube. It should be noted that the above dryout criteria were developed from tests with hot water heated tubes; many tests in the literature use direct Joule heating of the tube and hence the dry fraction of the perimeter experiences an uncharacteristically large rise in wall temperature which tends to propagate around and up the tube,

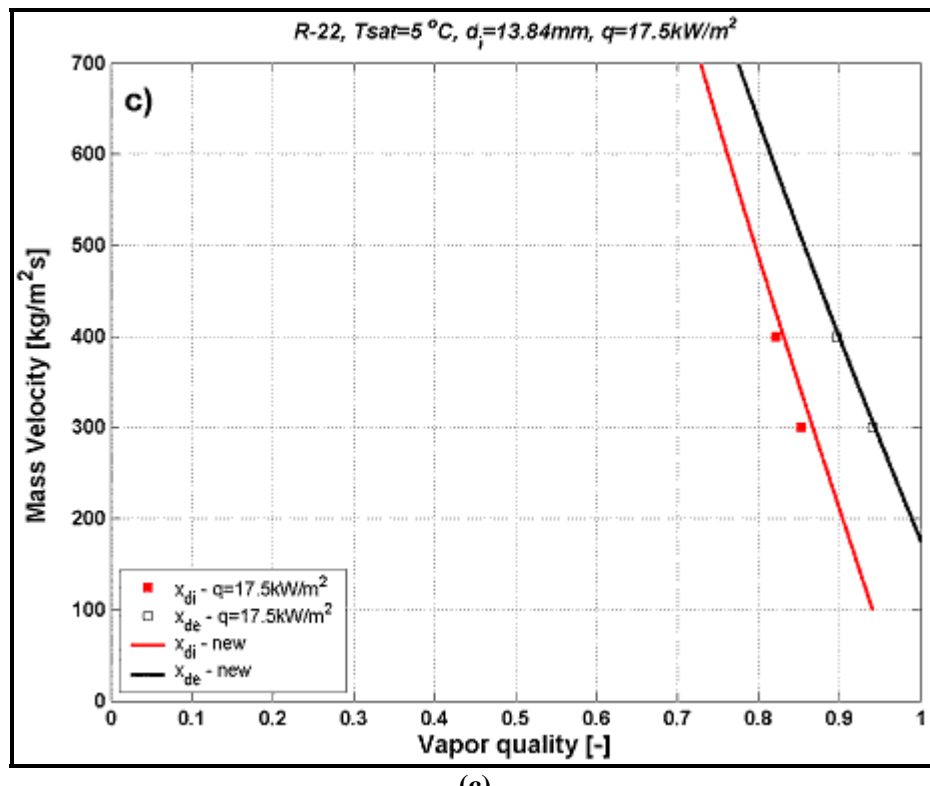
rendering such results less useful for development of thermal design methods in and near the dryout regime.



(a)



(b)



(c)

**Figure 18.8. New annular-to-dryout and dryout-to-mist flow transition expressions compared experimental results of R-22 in the 13.84 mm test section at three initial heat fluxes: (a) 57.5 kW/m<sup>2</sup>, (b) 37.5 kW/m<sup>2</sup>, (c) 17.5 kW/m<sup>2</sup>.**

Defining mist flow heat transfer coefficients as those results when  $x > x_{de}$ , Wojtan, Ursenbacher and Thome (2005b) noted that the mist flow heat transfer coefficients increased with increasing mass velocity but did not show any significant influence from the initial heat flux that was responsible for the onset of dryout. Furthermore, the measured vapor temperatures in the mist flow regime also corresponded to those calculated at the exit saturation pressure, which means that no vapor superheating or departure from equilibrium was observed at the current mist flow test conditions. Since using hot water heating precludes a significant increase in the wall temperature compared to those with imposed heat fluxes (electrically heated test sections), a notable departure from equilibrium is not expected. The flow pattern oriented, flow boiling model of Kattan, Thome and Favrat (1998a, 1998b, 1998c), presented elsewhere in Chapter 10, does not cover either the new dryout or the mist flow heat transfer regimes. Thus, the new methods proposed by Wojtan, Ursenbacher and Thome (2005b) to cover both the mist flow regime and the dryout regime are presented below.

Since vapor and liquid phases were observed to be in thermal equilibrium during evaporation in mist flow during the above Wojtan-Ursenbacher-Thome tests, the measured heat transfer coefficients were compared to the thermal equilibrium correlations of Dougall and Rohsenow (1963) and Groeneveld (1973) presented earlier. The Dougall-Rohsenow method was found to significantly over predict their R-22 and R-410A data while that of Groeneveld gave more reasonable results, over predicting by an average of 13.6%, which is quite good when considering that their method was extrapolated beyond its original range to much lower heat fluxes, pressures and mass velocities (as documented earlier, the database Groeneveld used to determine his empirical factors covered high mass velocities, saturation pressures and

heat fluxes, mostly for water). Based on the new R-22 and R-410A mist heat transfer data, the correlation of Groeneveld was re-optimized for the prediction of the mist flow heat transfer coefficients at design conditions typical of direct-expansion evaporators for refrigerants. Hence, for tube diameters from 8.00 to 13.84 mm and mass velocities from 300-700 kg/m<sup>2</sup>s, Wojtan, Ursenbacher and Thome (2005b) made a modified Groeneveld correlation where equation [18.5.8] has been changed as below to calculate the mist heat transfer coefficient when  $x \geq x_{de}$ :

$$Nu_G = \frac{\alpha d_i}{k_G} = 0.0117 \left\{ \frac{\dot{m}d_i}{\mu_G} \left[ x + \frac{\rho_G}{\rho_L} (1-x) \right] \right\}^{0.79} Pr_G^{1.06} Y^{-1.83} \quad [18.7.10]$$

The definition of Y remains the same as before in [18.5.7]. Compared to the original version, the values of exponents and leading constant were changed and the new exponent on the Reynolds number (0.79) becomes nearly that of a single phase flow (0.80). Figure 18.9 shows the comparison of the mist flow heat transfer results measured in the 13.84 mm test section with the new method for both refrigerants. The agreement of the experimental and predicted points was improved and statistical analysis gave an average deviation, mean deviation and standard deviation for all 71 experimental points of only -0.04%, 6.31% and 8.32% using the new modified version, respectively. The new method predicts 93% of experimental results obtained for the two refrigerants at five different mass velocities and two different initial heat fluxes within  $\pm 15\%$  error.

As has been shown earlier, the heat transfer coefficient falls sharply in the dryout region until it reaches mist flow. For the dryout region in the range  $x_{di} > x > x_{de}$ , the dryout heat transfer coefficient  $\alpha_{dryout}$  at a particular vapor quality x is calculated from the following linear interpolation:

$$\alpha_{dryout} = \alpha_{tp}(x_{di}) - \frac{x - x_{di}}{x_{de} - x_{di}} [\alpha_{tp}(x_{di}) - \alpha_{mist}(x_{de})] \quad [18.7.11]$$

In this expression,  $\alpha_{tp}(x_{di})$  is the two-phase flow heat transfer coefficient prior to dryout inception at  $x_{di}$  evaluated at its local pre-dryout heat flux and  $\alpha_{mist}(x_{de})$  is the mist flow heat transfer coefficient calculated from [18.7.10] at the dryout completion quality  $x_{de}$ . The Kattan-Thome-Favrat method for calculating  $\alpha_{tp}$  at  $x_{di}$  is described in Chapter 10. This interpolation approach works fairly well (considering the sharp fall in the dryout heat transfer coefficient with vapor quality that unavoidably creates sizable errors in  $\alpha_{dryout}$  with only small errors in x) and smoothly links the heat transfer coefficients in the annular and mist flow regimes. This simple linear interpolation method has a tendency to under predict heat transfer coefficients in the dryout region. Furthermore, it should be noted that the dryout regime and its heat transfer coefficients are particularly sensitive to the predicted values of  $x_{di}$  and  $x_{de}$  and that the above methods are derived only for a limited range of test conditions (R-22 and R-410A at 5°C). The Kattan-Thome-Favrat flow pattern based flow boiling heat transfer model has thus now been extended to all flow patterns except bubbly flow, which occurs at very high mass velocities outside of normal engineering practice.

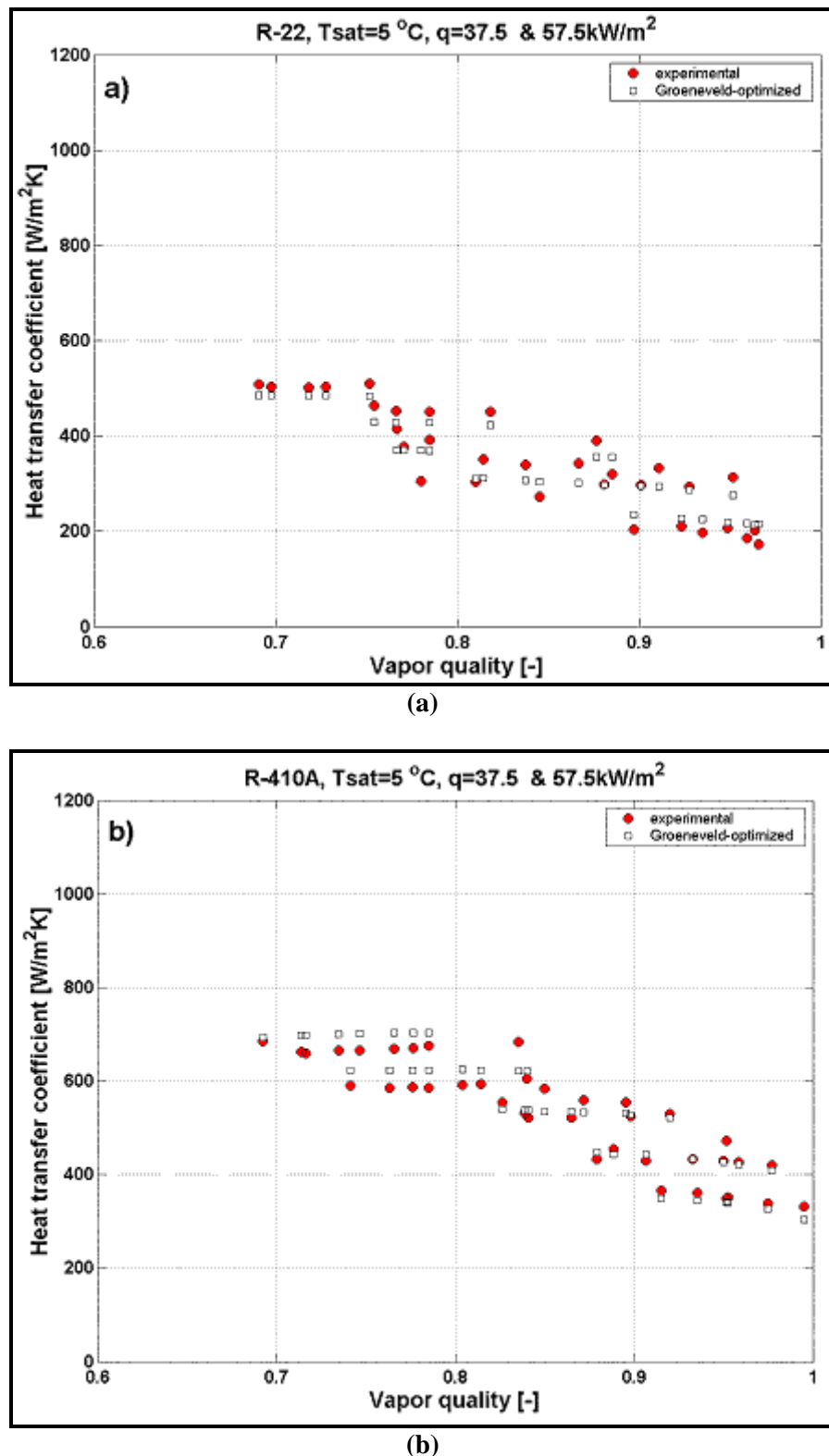


**Figure 18.9. Comparison of the mist flow heat transfer results measured in the 13.84 mm test section with the new version of Groeneveld correlation for: (a) R-22, (b) R-410A.**

**Example 18.3:** Determine the vapor qualities at the initiation and ending of dryout in an 8.0 mm tube evaporating R-134a at 4°C (3.377 bar) for a mass velocity of 300 kg/m<sup>2</sup>s where the local heat flux prior to the initiation of dryout is 15 kW/m<sup>2</sup>.

**Solution:** The properties required are:

$$\rho_L = 1281 \text{ kg/m}^3; \rho_G = 16.56 \text{ kg/m}^3; h_{LG} = 195500 \text{ J/kg}; \sigma = 0.011 \text{ N/m.}$$

Weber and Froude numbers are determined from [18.7.3] and [18.7.4]:

$$We_G = \frac{\dot{m}^2 d_i}{\rho_G \sigma} = \frac{300^2 (0.008)}{16.56 (0.011)} = 3952.6$$

$$Fr_G = \frac{\dot{m}^2}{\rho_G (\rho_L - \rho_G) g d_i} = \frac{300^2}{16.56 (1281 - 16.56) (9.81) (0.008)} = 54.77$$

The heat flux at the departure from nucleate boiling is obtained from [18.7.7]:

$$q_{DNB} = 0.131 \rho_G^{0.5} h_{LG} (g(\rho_L - \rho_G)\sigma)^{0.25}$$

$$= 0.131 (16.56)^{0.5} (195500) (9.81 (1281 - 16.56) 0.011)^{0.25} = 356195 \text{ W/m}^2$$

The vapor qualities at the beginning and ending of dryout are calculated from [18.7.5] and [18.7.6]:

$$x_{di} = 0.58 \exp \left[ 0.52 - 0.235 We_G^{0.17} Fr_G^{0.37} \left( \frac{\rho_G}{\rho_L} \right)^{0.25} \left( \frac{q}{q_{DNB}} \right)^{0.70} \right]$$

$$= 0.58 \exp \left[ 0.52 - 0.235 (3952.6)^{0.17} (54.77)^{0.37} \left( \frac{16.56}{1281} \right)^{0.25} \left( \frac{15000}{356195} \right)^{0.70} \right]$$

$$= 0.835$$

$$x_{de} = 0.61 \exp \left[ 0.57 - 0.0058 We_G^{0.38} Fr_G^{0.15} \left( \frac{\rho_G}{\rho_L} \right)^{-0.09} \left( \frac{q}{q_{DNB}} \right)^{0.27} \right]$$

$$= 0.61 \exp \left[ 0.57 - 0.0058 (3952.6)^{0.38} (54.77)^{0.15} \left( \frac{16.56}{1281} \right)^{-0.09} \left( \frac{15000}{356195} \right)^{0.27} \right]$$

$$= 0.924$$

Thus, the annular flow heat transfer coefficient will begin to fall off sharply at  $x_{di} = 0.835$  and will reach the mist flow heat transfer coefficient at  $x_{de} = 0.924$ ; therefore, the dryout zone extends over a vapor quality change of about 0.09. If the inlet vapor quality to the direct-expansion evaporator after the expansion valve is assumed to be 0.28, then about 1/8<sup>th</sup> of the heat transfer occurs in the dryout regime and about 1/9<sup>th</sup> in the mist flow regime, both of which have a significant effect on the size of the resulting unit.

## 18.8 Droplet Heat Transfer

Besides convective heat transfer from the wall to the vapor, radiation from the wall to the droplets and radiation from the wall to the vapor and transient conduction from the wall to impinging droplets, the fourth heat transfer mechanism is evaporation of the entrained droplets by the superheated vapor. In this section, a simple analysis of heat transfer from the superheated vapor to an entrained liquid droplet will be presented.

For the simplified situation considered below by Ganic and Rohsenow (1977), heat transfer to a droplet is simulated utilizing methods developed for particulate flows. For a single particle, or, in this case, an isolated droplet, the droplet heat transfer coefficient  $\alpha_D$  is estimated with the expression

$$Nu_D = 2 + 0.6 Re_D^{1/2} Pr_G^{1/3} \quad [18.8.1]$$

The Nusselt number  $Nu_D$  in the above equation is defined based on the droplet diameter  $D$ . Similarly, the droplet Reynolds number  $Re_D$  is defined using the droplet diameter and the difference between the vapor velocity  $u_G$  and the droplet velocity  $u_D$ . These two dimensionless groups are given as

$$Nu_D = \frac{\alpha_D D}{k_G} \quad [18.8.2]$$

$$Re_D = \frac{\rho_G D(u_G - u_D)}{\mu_G} \quad [18.8.3]$$

The convective heat transfer coefficient from the vapor to the droplet is  $\alpha_D$  and Prandtl number  $Pr_G$  is based on vapor properties as

$$Pr_G = \frac{\mu_G c_{pG}}{k_G} \quad [18.8.4]$$

In equation [18.8.1], the “2” on the right hand side is for pure conduction to the droplet while the second term accounts for convection to the droplet. The heat transfer to a droplet is driven by the temperature difference between the superheated vapor temperature  $T_{G,a}$  and the droplet temperature  $T_D$ , the latter which is assumed to be the saturation temperature. The rate of heat transfer is given by

$$Q = \pi D^2 \alpha_D (T_G - T_D) \quad [18.8.5]$$

One of the unknowns in the above analysis is the velocity difference,  $(u_G - u_D)$ . This difference may be obtained from a force balance on the droplet for vertical flow. If it is assumed that the droplet is spherical and not accelerating, then the hydrodynamic drag lifting the droplet is equal to the gravity force acting downward on it. The drag force  $F_{drag}$  is estimated from the drag coefficient as

$$C_{drag} = \frac{\left( \frac{F_{drag}}{\pi D^2 / 4} \right)}{\rho_G (u_G - u_D)^2 / 2} \quad [18.8.6]$$

and the drag coefficient  $C_{\text{drag}}$  is calculated from

$$C_{\text{drag}} = \frac{24}{Re_D} + 0.44 \quad [18.8.7]$$

The first term on the right hand side is the laminar flow term while the second is the turbulent term, such that the expression gives a reasonable representation of the drag over the whole range of Reynolds numbers. The gravity force acting on the droplet is

$$F_{\text{drag}} = \frac{\pi D^3}{6} (\rho_L - \rho_G) g \quad [18.8.8]$$

and is thus a function of the droplet size. The initial droplet size is another important unknown. Whalley et al. (1982) suggest using the following equation

$$\frac{D}{d_i} = 1.9 Re_G^{0.1} We_G^{-0.6} \left( \frac{\rho_G}{\rho_L} \right)^{0.6} \quad [18.8.9]$$

In this expression the vapor phase Reynolds number  $Re_G$  for a tube with a diameter  $d_i$  is used:

$$Re_G = \frac{\dot{m} x d_i}{\mu_G} \quad [18.8.10]$$

The vapor Weber number  $We_G$  of the tube is defined by Whalley et al. as:

$$We_G = \frac{\dot{m}^2 x^2 d_i}{\rho_G \sigma} \quad [18.8.11]$$

As the liquid droplets evaporate and the vapor superheats, the value of  $u_G$  increases along the tube. Hence, the increased shear on the droplet interface may make the surface of the droplet become unstable. This instability is expected to occur when the droplet Weber number reaches a value of about 7.5 according to their analysis, where the droplet Weber number  $We_D$  is defined as

$$We_D = \frac{\rho_G (u_G - u_D)^2 D}{\sigma} \quad [18.8.12]$$

At breakup of a droplet, it can be assumed that two new identical droplets are formed with a combined volume equal to that of the original droplet.

The rate of evaporation of a droplet  $Q$  is given by

$$\frac{dm}{dt} = \frac{Q}{h_{LG}} \quad [18.8.13]$$

where  $m$  is the mass of the droplet. The mass of the droplet can be calculated from its diameter  $D$  and thus

$$m = \frac{1}{6} \pi D^3 \rho_L \quad [18.8.14]$$

The rate of change of mass in the droplet is therefore given by

$$\frac{dm}{dt} = \frac{1}{2} \pi D^2 \rho_L \frac{dD}{dt} \quad [18.8.15]$$

and it follows that

$$\frac{dD}{dt} = \frac{dm}{dt} \frac{2}{\pi D^2 \rho_L} \quad [18.8.16]$$

The rate of change of the droplet diameter during its evaporation is thus

$$\frac{dD}{dt} = \frac{(2Q/h_{LG})}{\pi D^2 \rho_L} \quad [18.8.17]$$

Utilizing a step-wise calculation approach for various droplet sizes up to their complete evaporation, the lifetimes of droplets can be estimated.

It can also be noted that as a droplet becomes small, the value of the droplet Reynolds number  $Re_D$  becomes small in [18.8.3]. Thus, the heat transfer is dominated by conduction from the vapor to the droplet interface and the heat transfer coefficient is inversely proportional to the droplet diameter  $D$ , i.e.  $\alpha_D \propto 1/D$  in [18.8.1]. On the other hand, when the turbulence mode is dominant, the heat transfer coefficient is still inversely proportional to the droplet diameter but to the  $1/2$  power, i.e.  $\alpha_D \propto 1/D^{1/2}$ .

There are some aspects not addressed above. For instance, the non-equilibrium temperature of the vapor  $T_{G,a}$  is another important unknown. The method presented earlier by Groeneveld and Delorme (1976) can be used to estimate its value. Just as important, the number of droplets and their size at any cross-section of the tube must be known in order to perform an energy balance along the heated flow channel. Consequently, modeling heat transfer in mist flow quickly becomes very complex. At the same time, the fundamental parameters that need to be measured experimentally to verify these methods are difficult to obtain without disturbing the flow itself.

Methods to numerically model the thermal hydrodynamics of mist flow have progressed rapidly in recent years. This is illustrated, for example, by the work of Andreani and Yadigaroglu (1997), who have developed a 3-dimensional Eulerian-Lagrangian model of dispersed flow boiling that includes a mechanistic description of the droplet spectrum evolution.

**Homework Problems:**

**18.1:** Determine the local mist flow heat transfer coefficient as a function of vapor quality at 0.5, 0.6, 0.7, 0.8 and 0.9 for a tube of 14 mm diameter and a flow rate of 0.1 kg/s. The fluid has the following physical properties: liquid density is  $1147 \text{ kg/m}^3$ , vapor density is  $50 \text{ kg/m}^3$ , vapor thermal conductivity is  $0.011 \text{ W/mK}$ , vapor specific heat of  $1.7 \text{ kJ/kgK}$  and vapor viscosity is  $0.000012 \text{ Ns/m}^2$ . Use the Dougall and Rohsenow method.

**18.2:** Repeat Problem 18.1 for an 8.0 mm diameter tube with a flow rate of  $0.032653 \text{ kg/s}$ .

**18.3:** Determine the local mist flow heat transfer coefficient for steam as a function of vapor quality at 0.5, 0.6, 0.7, 0.8 and 0.9 for a tube of 20 mm diameter and a flow rate of  $0.3 \text{ kg/s}$ . The steam /water system is at a saturation pressure of 40 bar with the following physical properties: liquid density is  $1147 \text{ kg/m}^3$ , vapor density is  $50 \text{ kg/m}^3$ , vapor thermal conductivity is  $0.011 \text{ W/mK}$ , vapor specific heat of  $1.7 \text{ kJ/kgK}$  and vapor viscosity is  $0.000012 \text{ Ns/m}^2$ . Use the Groeneveld method.

**18.4:** Repeat Example 18.3 for heat fluxes of 5, 10 and  $20 \text{ kW/m}^2$  and comment on the trends observed.

## Appendix A

**Nomenclature:**

A	empirical constant [-]
A	cross-sectional area of tube [ $m^2$ ]
$A_a$	actual heat transfer area per unit length [ $m^2/m$ ]
$A_{clf}$	circumferential flow area [ $m^2$ ]
$A_{fa}$	actual free flow cross-sectional area [ $m^2/m$ ]
$A_{eff}$	effective surface area of finned tube per unit length [ $m^2/m$ ]
$A_{fin}$	surface area of fins per unit length [ $m^2/m$ ]
$A_{fo}$	external heat transfer area of low finned tube per unit length [ $m^2/m$ ]
$A_G$	cross sectional area occupied by vapor [ $m^2$ ]
$A_{Gd}$	dimensionless cross sectional area occupied by vapor [-]
$A_{hex}$	hexagonal area [ $m^2$ ]
$A_L$	cross-sectional area occupied by liquid-phase [ $m^2$ ]
$A_{Ld}$	dimensionless cross sectional area occupied
$A_o$	external heat transfer area of tube bundle [ $m^2$ ]
$A_p$	cross-sectional area of fin [ $m^2$ ]
$Ar_L$	Archimedes number [-]
$A_{root}$	root area between fins on tube per unit length [ $m^2/m$ ]
$A_{total}$	total surface area of finned tube per unit length [ $m^2/m$ ]
a	empirical constant [-]
a	one-half of long side of rectangular channel [m]
$a_0-a_4$	empirical constants [-]
$a_1-a_4$	empirical constants [-]
$a_L$	thermal diffusivity of the liquid [ $m^2/s$ ]
B	empirical constant [-]
B	empirical factor [-]
$B_B$	Chisholm parameter for bubbly flow transition [-]
$B_c$	baffle cut [%]
$B_F$	Chisholm parameter for spray flow transition [-]
$B_f$	empirical constant of Rose [-]
Bo	boiling number [-]
BR	boiling range (or temperature glide) [K]
Br	Brinkman number [-]
$B_S$	Chisholm parameter for stratified flow transition [-]
$B_s$	empirical constant of Rose [-]
$B_t$	empirical constant of Rose [-]
$B_1$	empirical constant of Rose [-]
b	empirical constant [-]
b	empirical exponent [-]
b	interfin spacing at the fin tips [m]
b	one-half of short side of rectangular channel [m]
$b_0-b_4$	empirical constants [-]
$b_1-b_4$	empirical constants [-]
C	constant in DNB equation [-]
C	constant in Katto and Ohno correlation
C	empirical constant [-]

$C_o$	Shah factor [-]
$C_o$	distribution parameter [-]
$C_1$	constant in Rohsenow correlation [-]
$C_1$	constant in tube number expression [-]
$C_{bh}$	constant in bundle bypass expression [-]
$C_{bp}$	constant in bundle bypass expression [-]
$C_{drag}$	drag coefficient [-]
$C_{ft}$	empirical friction factor constant for finned tube [-]
$C_{fth}$	empirical heat transfer constant for finned tube [-]
$C_{sf}$	empirical surface factor in Rohsenow correlation [-]
$Ca$	capillary number [m]
$Cap$	capillary number [-]
$c$	empirical exponent [-]
$c_b$	fraction of tube perimeter retaining condensate [-]
$c_L$	similarity factor [ $m^{-3/4}$ ]
$c_o$	constant [-]
$c_p$	specific heat [J/kg K]; specific heat at constant pressure [J/kg K]
$c_{pG}$	vapor specific heat [J/kg K]
$(c_p)_G$	vapor specific heat [J/kg K]
$c_{pL}$	liquid specific heat [J/kg K]
$(c_p)_L$	liquid specific heat [J/kg K]
$c_1, c_2$	empirical parameters [-]
$c_1-c_5$	empirical constants [-]
$D$	droplet diameter [m]
$D$	exponent [-]
$D$	external tube diameter [m]
$D$	tube diameter [m]
$D$	fin tip diameter [m]
$D$	tube or cylinder diameter [m]
$D_b$	diameter of baffle [m]
$D_{ctl}$	centerline tube limit diameter of tube bundle [m]
$D_\delta$	diameter of liquid ring on tube [m]
$D_{fo}$	diameter over fins [m]
$D_{fr}$	root diameter of low finned tube [m]
$D_{otl}$	outer tube limit diameter of tube bundle [m]
$D_{req}$	equivalent projected tube diameter of low finned tube [m]
$D_{root}$	root diameter of finned tube [m]
$D_s$	internal diameter of heat exchanger shell [m]
$D_t$	outside tube diameter [m]
$d$	empirical constant [-]
$d_{bub}$	bubble departure diameter [m]
$d_f$	internal tube diameter at base of microfins [m]
$d_h$	hydraulic diameter [m]
$d_i$	internal tube diameter [m]
$d_{im}$	melt down internal tube diameter [m]
$d_{i,o}$	reference internal tube diameter ( $= 0.01$ m) [m]
$d_{mean}$	internal tube diameter at mean height of microfins [m]
$d_p$	droplet detachment diameter [m]
$dT_{bub}$	rise in bubble point temperature [K]
$E$	convection enhancement factor [-]
$E_2$	stratified flow correction factor [-]

$E_c$	Eckert number [-]
$E_{mf}$	microfin factor [-]
$E_{new}$	new convection enhancement factor [-]
$E_{RB}$	microfin convection factor [-]
$e$	empirical constant [-]
$e$	fin or rib or obstruction height [m]
$e$	surface roughness [m]
$e$	corrugation depth [m]
$e$	fraction of liquid entrained as droplets [-]
$e_{eff}$	effective fin height of Rose method [m]
$e_f$	fin height [m]
$F$	two-phase multiplier [-]
$F$	apparent wet fraction of tube [-]
$F_{aspect}$	aspect ratio correction factor [-]
$F_i$	interfacial correction factor [-]
$F(M)$	residual correction factor [-]
$F_1(q)$	dimensionless exponent as function of $q$ [-]
$F_2(q)$	dimensionless exponent as function of $q$ [-]
$F_C$	area fraction occupied by tubes between baffle tips [-]
$F_e$	bundle boiling void fraction correction factor [-]
$F_c$	mixture correction factor [-]
$F_{drag}$	drag force [N]
$F_{flat}$	correction factor for flattened tubes [-]
$F_m$	non-equilibrium mixture factor [-]
$F_{nb}$	nucleate boiling correction factor [-]
$F_p$	pressure correction factor [-]
$F_{PF}$	pressure correction factor of Gorenflo [-]
$Fr_G$	Froude number of vapor phase [-]
$Fr_L$	liquid Froude number [-]
$Fr_{so}$	Soliman liquid Froude number [-]
$F_{pf}$	pressure correction factor [-]
$F_{round}$	correction factor to Grönnerud correlation [-]
$F_S$	Shah factor [-]
$F_s$	fraction of fin flank area covered by condensate wedge [-]
$F_{sbp}$	ratio of bypass area to cross flow area [-]
$F_t$	fraction of interfin root area covered by condensate wedge [-]
$F_w$	area fraction occupied by baffle window [-]
$F_{WL}$	radiative view factor from wall to liquid droplets [-]
$F_{WG}$	radiative view factor from wall to vapor [-]
$F_{tp}$	two-phase convective multiplier [-]
$f$	empirical constant [-]
$f$	Fanning friction factor [-]
$f$	friction factor [-]
$f_{app}$	apparent friction factor [-]
$f_{Blasius}$	Blasius friction factor [-]
$f_{cd}$	cumulative deposition factor [-]
$f_{ft}$	finned tube friction factor [-]
$f_G$	vapor-phase friction factor [-]
$f_i$	interfacial friction factor [-]
$f_l$	tube bank friction factor [-]

$f_{l,plain}$	plain tube bank friction factor [-]
$f_k$	friction factor of phase k (where k is either G or L) [-]
$f_L$	Fanning friction factor of liquid [-]
$f_{lam}$	friction factor for laminar flow [-]
$f_{oil}$	mixture factor on pressure drop [-]
$f_s$	swirl friction factor [-]
$fpm$	fins per meter [ $m^{-1}$ ]
$f_{trans}$	friction factor for transition flow [-]
$f_{turb}$	friction factor for turbulent flow [-]
$G$	total mass velocity [ $kg/m^2s$ ]
$G_f$	Rose low finned tube parameter for fin flanks [-]
$G_s$	Rose low finned tube parameter for interfin root area [-]
$G_t$	Rose low finned tube parameter for fin tips [-]
$Gal$	Galileo number of liquid [-]
$Gr_G$	Grashof number of vapor [-]
$Gz$	Graetz number [-]
$g$	acceleration due to gravity [9.81 m/s <sup>2</sup> ]
$g$	empirical exponent [-]
$H$	height of channel [m]
$H$	height of nozzle above top tube row [m]
$h$	liquid height inside channel [m]
$h$	height of flattened tube [m]
$h$	enthalpy [J/kg]
$h_{G,a}$	actual vapor enthalpy [J/kg]
$h_{G,e}$	equilibrium vapor enthalpy [J/kg]
$h_{G,sat}$	enthalpy of saturated vapor [J/kg]
$h_{L,sat}$	enthalpy of saturated liquid [J/kg]
$h_L$	enthalpy of saturated liquid [J/kg]
$h_{Ld}$	dimensionless liquid height inside channel [m]
$h_{LG}$	latent heat of vaporization [J/kg]
$\dot{h}_{LG}$	latent heat of vaporization corrected from subcooling [J/kg]
$h_{latent}$	latent heat absorbed by fluid [J/kg]
$h_{LV}$	latent heat of vaporization [J/kg]
$h_{sensible}$	sensible heat absorbed by fluid [J/kg]
$h_{total}$	total heat absorbed by fluid [J/kg]
$dh$	change in enthalpy [J/kg]
$\Delta h_{L,inlet}$	inlet subcooling enthalpy change [J/kg]
$Ja_L$	Jakob number of liquid [-]
$J_B$	bundle bypass correction factor [-]
$J_C$	baffle cut correction factor [-]
$J_f$	laminar flow correction factor for low finned tubes [-]
$J_g$	superficial velocity (m/s)
$j$	Colburn j-factor [-]
$j_I$	ideal heat transfer factor [-]
$J_L$	baffle leakage correction factor [-]
$J_R$	laminar flow correction factor [-]
$(J_R)_{20}$	laminar flow correction factor at $Re = 20$ [-]
$J_S$	unequal baffle spacing correction factor [-]
$J_\mu$	wall viscosity correction factor [-]
$K$	Taitel and Dukler parameter [-]

---

K	factor in hydrodynamic developing flow [-]
$K_{ff}$	falling film heat transfer multiplier relative to pool boiling [-]
$K_{fluid}$	thermal conductivity of fluid [W/m K]
$K_i$	inlet subcooling factor at conditions $i = 1$ to 3 [-]
$K_p$	boiling factor of Danilova [-]
Ka	Kapitza number [-]
$KE_G$	kinetic energy of vapor phase [J]
$KE_k$	kinetic energy of phase k [J]
$KE_L$	kinetic energy of liquid phase [J]
k	thermal conductivity [W/m K]
$k_G$	thermal conductivity of vapor [W/m K]
$k_L$	liquid thermal conductivity [W/m K]
$k_{wall}$	thermal conductivity of wall material [W/m K]
L	length [m]
L	length of tube [m]
$L_{bb}$	diametral clearance between $D_s$ and $D_{otl}$ [m]
$L_{bi}$	inlet baffle spacing [m]
$L_{bc}$	central baffle spacing [m]
$L_{bch}$	height of baffle cut [m]
$L_{bo}$	outlet baffle spacing [m]
$L_{dev}$	developing length [m]
$L_{fin}$	equivalent vertical height of fin [m]
$L_{fh}$	fin height [m]
$L_{fs}$	average fin thickness assuming rectangular profile [m]
$L_G$	chordal length through vapor phase [m]
$L_L$	chordal length through liquid phase [m]
$L_p$	width of pass partition lane [m]
$L_{pl}$	width of bypass lane between tubes [m]
$L_{pn}$	tube pitch normal to direction of flow [m]
$L_{pp}$	tube pitch parallel to direction of flow [m]
$L_S$	swirl flow streamline length [m]
$L_{sb}$	diametral clearance between $D_s$ and $D_b$ [m]
$L_{ta}$	effective tube length [m]
$L_{tb}$	tube-to-baffle hole diametral clearance [m]
$L_{tp}$	tube pitch from tube center to tube center [m]
$L_{tp,eff}$	effective tube pitch from tube center to tube center [m]
$L_x$	length of outside of a rectangular channel [m]
$L_y$	length of outside of a rectangular channel [m]
M	mass flow rate [kg/s]
M	molecular weight [kg/kmol]
$M_N$	additional term from integration $[(kg/ms)^{4/3}]$
m	Blasius exponent [-]
m	exponent [-]
m	exponent on velocity profile [-]
m	fin efficiency parameter [ $m^{-1}$ ]
m	mass of droplet [kg]
$\dot{m}$	mass velocity of fluid $[kg/m^2 s]$
$\dot{m}$	mass velocity of fluid at maximum cross-section of bundle $[kg/m^2 s]$
$\dot{m}$	total mass velocity of liquid and vapor $[kg/m^2 s]$
$\dot{m}_{bubbly}$	bubbly flow transition mass velocity $[kg/m^2 s]$

---

$\dot{m}_e$	equivalent mass velocity [ $\text{kg}/\text{m}^2 \text{s}$ ]
$\dot{m}_{\text{dryout}}$	mass velocity at onset of dryout [ $\text{kg}/\text{m}^2 \text{s}$ ]
$\dot{m}_G$	mass velocity of vapor [ $\text{kg}/\text{m}^2 \text{s}$ ]
$\dot{m}_{\text{high}}$	mass velocity at transition from annular to stratified-wavy flow [ $\text{kg}/\text{m}^2 \text{s}$ ]
$\dot{m}_L$	mass velocity of liquid [ $\text{kg}/\text{m}^2 \text{s}$ ]
$\dot{m}_{\text{low}}$	mass velocity at transition from stratified-wavy to stratified flow [ $\text{kg}/\text{m}^2 \text{s}$ ]
$\dot{m}_{\text{min}}$	minimum value of mist flow transition mass velocity [ $\text{kg}/\text{m}^2 \text{s}$ ]
$\dot{m}_{\text{mist}}$	mass velocity at transition from mist flow [ $\text{kg}/\text{m}^2 \text{s}$ ]
$\dot{m}_{\text{ref}}$	reference mass velocity [= 500 $\text{kg}/\text{m}^2 \text{s}$ ]
$\dot{m}_{\text{strat}}$	mass velocity at transition from stratified-wavy to stratified flow [ $\text{kg}/\text{m}^2 \text{s}$ ]
$\dot{m}_{\text{total}}$	total mass velocity of liquid plus vapor [ $\text{kg}/\text{m}^2 \text{s}$ ]
$\dot{m}_w$	window mass velocity of fluid [ $\text{kg}/\text{m}^2 \text{s}$ ]
$\dot{m}_{\text{wavy}}$	mass velocity at transition from annular to stratified-wavy flow [ $\text{kg}/\text{m}^2 \text{s}$ ]
$\dot{m}_{\text{wavy(new)}}$	new wavy flow transition mass velocity [ $\text{kg}/\text{m}^2 \text{s}$ ]
N	number of tubes passed in crossflow [-]
N	Shah parameter [-]
N	tube row number from top [-]
$N_b$	number of baffles [-]
$N_c$	total number of tube rows crossed by flow in entire heat exchanger [-]
$N_f$	number of fins per unit length of tube [fins/m]
$N_{ss}$	number of sealing strip pairs [-]
$N_{\text{tcc}}$	number of tube rows crossed between baffle tips in one baffle compartment [-]
$N_{\text{tew}}$	number of tube rows crossed in one baffle window [-]
$N_{\text{tt}}$	number of tubes [-]
$N_{\text{tw}}$	number of tubes in the window [-]
Nu	Nusselt number [-]
$\text{Nu}_D$	Nusselt number based on droplet diameter [-]
$\text{Nu}_D$	mean Nusselt number based on tube diameter [-]
$\text{Nu}_{D-B}$	Dittus-Boelter Nusselt number [-]
$\text{Nu}_{ft}$	internally finned tube Nusselt number [-]
$\text{Nu}_G$	Nusselt number of vapor [-]
$\text{Nu}_H$	mean or fully developed Nusselt number at uniform heat flux condition [-]
$\text{Nu}_{H,\text{visc}}$	fully developed Nusselt number at uniform heat flux condition [-]
$\text{Nu}_{HA}$	Nusselt number for 2 <sup>nd</sup> type of uniform heat flux condition [-]
$\text{Nu}_{H,z}$	local Nusselt number at uniform heat flux condition [-]
$\text{Nu}_L$	liquid Nusselt number [-]
$\text{Nu}_{mf}$	microfin Nusselt number [-]
$\text{Nu}_{nb}$	nucleate boiling Nusselt number [-]
$\text{Nu}_{\Gamma}$	liquid film Nusselt number [-]
$\text{Nu}_{\Gamma,\text{lam}}$	laminar liquid film Nusselt number [-]
$\text{Nu}_{\Gamma,\text{sub}}$	subcooled liquid film Nusselt number [-]
$\text{Nu}_{\Gamma,\text{turb}}$	turbulent liquid film Nusselt number [-]
$\text{Nu}_{\text{strat}}$	local Nusselt number for stratified flow [-]
$\text{Nu}_T$	mean or fully developed Nusselt number at uniform wall temperature condition [-]
$\text{Nu}_{T,\text{tt}}$	Nusselt number for twisted tape insert at uniform wall temperature condition [-]
$\text{Nu}_{T,z}$	local Nusselt number at uniform wall temperature condition [-]
$\text{Nu}_{tt}$	twisted tape Nusselt number [-]
$\text{Nu}_{y=\infty}$	twisted tape Nusselt number without twist [-]

$\text{Nu}(x)$	local Nusselt number [-]
$\text{Nu}(z)$	local film Nusselt number [-]
$n$	empirical exponent [-]
$n$	exponent [-]
$n$	exponent on void fraction profile [-]
$n$	factor equal to 3 [-]
$n$	power law exponent [-]
$n_1$	exponent [-]
$n_2$	exponent [-]
$n_3$	exponent [-]
$n_B$	void fraction factor [-]
$n_{\text{corners}}$	number of sharp corners facing flow of rib or fin [-]
$n_f$	exponent on heat flux [-]
$n_f$	nucleate boiling exponent [-]
$n_s$	number of starts or fins [-]
$P$	perimeter of channel [m]
$P_G$	dry perimeter in contact with vapor [m]
$P_{Gd}$	dimensionless dry perimeter in contact with vapor [m]
$P_i$	perimeter of liquid-vapor interface [m]
$P_{id}$	dimensionless perimeter of liquid-vapor interface [m]
$P_k$	phase [-]
$P_L$	wetted perimeter [m]
$P_{Ld}$	dimensionless wetted perimeter [m]
$Po$	Poiseuille number [-]
$Pr$	Prandtl number [-]
$Pr_G$	Prandtl number of vapor [-]
$Pr_L$	liquid Prandtl number [-]
$p$	axial pitch [m]
$p$	exponent
$p$	pressure [ $\text{N/m}^2$ ]
$p$	pitch of corrugation [m]
$p_{\text{crit}}$	critical pressure [ $\text{N/m}^2$ ]
$p_f$	axial fin pitch [m]
$p_G$	vapor pressure [ $\text{N/m}^2$ ]
$p_r$	reduced pressure ( $p_r = p_{\text{sat}}/p_{\text{crit}}$ ) [-]
$p_{ro}$	reference reduced pressure of Gorenflo [-]
$p_{\text{sat}}$	saturation pressure [ $\text{N/m}^2$ ]
$p_{\text{wall}}$	saturation pressure at wall temperature [ $\text{N/m}^2$ ]
$\Delta p$	pressure drop [Pa]
$\Delta p_{\text{bl}}$	ideal bundle pressure drop for one baffle compartment [ $\text{N/m}^2$ ]
$\Delta p_c$	central baffle compartment pressure drop [ $\text{N/m}^2$ ]
$\Delta p_e$	end zone pressure drop [ $\text{N/m}^2$ ]
$\Delta p_{\text{total}}$	bundle pressure drop [ $\text{N/m}^2$ ]
$\Delta p_w$	window zone pressure drop [ $\text{N/m}^2$ ]
$(dp/dz)_G$	frictional pressure gradient of the vapor [Pa/m]
$(dp/dz)_L$	frictional pressure gradient of the liquid [Pa/m]
$(dp/dz)_{\text{frict}}$	frictional pressure gradient [Pa/m]
$Q$	heat transfer rate [W]
$Q$	volumetric flow rate [ $\text{m}^3/\text{s}$ ]
$\dot{Q}_G$	vapor volumetric flow rate [ $\text{m}^3/\text{s}$ ]

$\dot{Q}_k$	volumetric flow rate of phase k [ $m^3/s$ ]
$\dot{Q}_L$	liquid volumetric flow rate [ $m^3/s$ ]
$q$	heat flux [ $W/m^2$ ]
$q_o$	reference heat flux [ $W/m^2$ ]
$q_{crit}$	critical heat flux [ $W/m^2$ ]
$q_{crit,i}$	reference critical heat flux at conditions i = 1 to 5 [ $W/m^2$ ]
$q_{DNB}$	heat flux at departure from nucleate boiling (critical heat flux) [ $W/m^2$ ]
$q_{DNB,tube}$	heat flux at DNB of tube [ $W/m^2$ ]
$q_{dry}$	heat flux on dry fraction of tube [ $W/m^2$ ]
$q_G$	heat flux resulting from wall-to-droplet evaporation [ $W/m^2$ ]
$q_L$	heat flux resulting from droplet evaporation [ $W/m^2$ ]
$q_{ONB}$	heat flux at onset of nucleate boiling [ $W/m^2$ ]
$q_r$	radiation heat flux [ $W/m^2$ ]
$q_{wet}$	heat flux on wet fraction of tube [ $W/m^2$ ]
R	density ratio in Katto and Ohno correlation [-]
R	fouling factor on fin [ $m K/W$ ]
R	Chisholm parameter [-]
R	radius of tube [m]
$R_c$	mixture resistance [ $m^2K/W$ ]
$R_b$	bypass pressure drop correction factor [-]
$R_L$	leakage pressure drop correction factor [-]
$R_p$	root mean surface roughness [ $\mu m$ ]
$R_{po}$	reference root mean surface roughness of Gorenflo [ $\mu m$ ]
$R_{p,o}$	standard surface roughness (= 1.0 $\mu m$ ) [ $\mu m$ ]
$R_S$	baffle end zones pressure drop correction factor [-]
$R_\mu$	viscosity pressure drop correction factor [-]
Ra	Rayleigh number [-]
$R_{aL}$	Rayleigh number [-]
Re	Reynolds number [-]
$Re_{crit}$	critical film Reynolds number [-]
$Re_D$	droplet Reynolds number [-]
$Re_\delta$	Reynolds number of liquid film on tube bundle [-]
$Re_e$	equivalent liquid Reynolds number [-]
$Re_{eq}$	equivalent liquid Reynolds number [-]
$Re_G$	local vapor Reynolds number [-]
$Re_{GH}$	homogeneous Reynolds number [-]
$Re_{Go}$	local vapor only Reynolds number [-]
$Re_{Gs}$	superficial vapor Reynolds number, also $Re_{SG}$ [-]
$Re_{Gt}$	Reynolds number with total flow as vapor [-]
$Re_L$	liquid Reynolds number for all flow as liquid [-]
$Re_{L_f}$	liquid film Reynolds number for liquid fraction of flow [-]
$Re_{LS}$	superficial liquid Reynolds number, also $Re_{SL}$ [-]
$Re_{Lt}$	Reynolds number with total flow as liquid [-]
$(Re_L)_{film}$	Reynolds number with total flow as liquid [-]
$Re_{RB}$	Reynolds number [-]
$Re_{root}$	film Reynolds number of the condensate flowing in the root area [-]
$Re_\Gamma$	film Reynolds number [-]
$Re_\Gamma$	liquid Reynolds number of film [-]
$Re^{*}_\Gamma$	modified liquid Reynolds number of film [-]

$Re_{\Gamma, \text{trans}}$	transition liquid film Reynolds number [-]
$Re_{\text{nb}}$	nucleate boiling Reynolds number [-]
$Re_{\text{onset}}$	falling film Reynolds number at top of tube at onset of dryout [-]
$Re_{\text{peak}}$	falling film Reynolds number at top of tube at peak performance [-]
$Re_{\text{s}}$	swirl Reynolds number [-]
$Re_{\text{SG}}$	vapor superficial Reynolds number [-]
$Re_{\text{SL}}$	liquid superficial Reynolds number [-]
$Re_{\text{top}}$	falling film Reynolds number at top of tube [-]
$Re_{\text{tp}}$	two-phase Reynolds number [-]
$Ri$	Richardson number [-]
$R_{\text{wall}}$	wall thermal resistance [K/W]
$r$	constant [-]
$r$	external radius of tube [m]
$r$	radius from centreline [m]
$r_i$	internal tube radius [m]
$r_{lm}$	leakage area parameter [-]
$r_o$	critical nucleation radius [m]
$r_s$	leakage area parameter [-]
$r_{ss}$	sealing strip parameter [-]
$S$	nucleation suppression factor
$S$	velocity ratio [-]
$S$	vertical pitch between centerline of tubes [m]
$S_2$	stratified flow correction factor [-]
$S_b$	bypass area [m]
$S_m$	cross-sectional flow area at centerline [m]
$S_{sb}$	shell-to-baffle leakage area [m]
$S_{tb}$	tube-to-baffle leakage area [m]
$S_w$	net flow area in window [m]
$S_{wg}$	gross flow area in window without tubes [m]
$S_{wt}$	area in window occupied by tubes [m]
$St_{\text{lam}}$	Stanton number for laminar flow [-]
$St_{\text{turb}}$	Stanton number for turbulent flow [-]
$Sw$	swirl number [-]
$s$	fin pitch [m]
$s$	specific gravity [-]
$T$	temperature [K or °C]
$\Delta T$	wall-to-fluid temperature difference [K]
$\Delta T$	wall superheat [K]
$\Delta T_{\text{bp}}$	boiling range or temperature glide of mixture [K]
$\Delta T_{\text{bulk}}$	bulk temperature difference from inlet to outlet [K]
$\Delta T_{\text{glide}}$	temperature glide of a zeotropic mixture [K]
$T_{\text{bub}}$	bubble point temperature [K]
$T_{\text{bub}}$	bubble point temperature of mixture [K]
$T_{\text{bulk}}$	mean bulk temperature of fluid [K]
$T_{\text{crit}}$	critical temperature of mixture [K]
$T_{\text{dew}}$	dew point temperature of condensable mixture [K]
$T_D$	droplet temperature [K]
$T_{\text{DNB}}$	wall temperature at point DNB [K]
$T_f$	Rose low finned tube parameter for fin flanks [-]
$\Delta T_f$	temperature difference across film ( $= T_{\text{sat}} - T_w$ ) [K]
$T_G$	vapor temperature [K]

---

$T_{G,a}$	actual bulk vapor temperature [K]
$T_{G\infty}$	bulk temperature of gas-vapor mixture [K]
$T_{Gi}$	interfacial temperature of gas-vapor mixture [K]
$\Delta T_I$	ideal wall superheat for boiling of a mixture [K]
$T_{IB}$	wall temperature at point IB [K]
$T_L$	local subcooled temperature of liquid [K]
$T_{MFB}$	wall temperature at point MFB [K]
$T_{man}$	manufacturers reference temperature [°C]
$\Delta T_q$	bulk temperature change due to wall heat flux from inlet to outlet [K]
$\Delta T_{ref}$	reference temperature rise [K]
$T_s$	Rose low finned tube parameter for interfin root area [-]
$T_{sat}$	saturation temperature [K]
$T_{sat}$	saturation temperature of pure refrigerant [K]
$\Delta T_{sat}$	wall superheat ( $= T_{wall} - T_{sat}$ ) [K]
$T_t$	Rose low finned tube parameter for fin tips [-]
$\Delta T_{visc}$	bulk temperature rise due to viscous heat dissipation from inlet to outlet [K]
$T_w$	wall temperature [K]
$T_{wall}$	wall temperature [°C]
$T_{wall}$	wall temperature [K]
$T, t$	time [s]
$t$	fin thickness [m]
$t$	mean thickness of fin [m]
$t$	twisted tape thickness [m]
$t_{root}$	thickness at root of fin [m]
$t_{tip}$	thickness at tip of fin [m]
$t_{wall}$	wall thickness of channel [m]
$U$	flow velocity [m/s]
$U$	overall heat transfer coefficient [W/m <sup>2</sup> K]
$\langle U \rangle$	cross-sectional averaged drift velocity [m/s]
$U_G$	superficial velocity of vapor [m/s]
$\langle U_G \rangle$	cross-sectional averaged vapor drift velocity [m/s]
$U_{GL}$	drift flux [m/s]
$\langle U_{GL} \rangle$	cross-sectional average vapor drift flux velocity relative to $U_L$ [m/s]
$U_{GU}$	vapor phase drift velocity [m/s]
$\bar{U}_{GU}$	weighted mean drift velocity [m/s]
$U_L$	superficial velocity of liquid [m/s]
$U_{LU}$	liquid phase drift velocity [m/s]
$U_S$	swirl fluid velocity [m/s]
$u$	velocity in x-direction [m/s]
$u_D$	droplet velocity [m/s]
$u_d$	droplet deposition velocity [m/s]
$u_G$	vapor velocity [m/s]
$\bar{u}_G$	weighted mean velocity of vapor [m/s]
$\langle u_G \rangle$	cross-sectional average of vapor velocity [m/s]
$u_{Gs}$	modified Baker parameter based on superficial vapor velocity [m/s]
$u_H$	homogeneous velocity [m/s]
$u_i$	suction velocity at interface [m/s]
$u_k$	velocity of phase k [m/s]
$u_L$	liquid velocity [m/s]
$u_{LG}$	superficial velocity of vapor with respect to liquid [m/s]
$u_{Ls}$	modified Baker parameter based on superficial liquid velocity [m/s]

---

---

$u_y$	velocity in y-direction [m/s]
$u_\infty$	free stream velocity in z-direction [m/s]
$V_G$	volume of vapor phase [ $\text{m}^3$ ]
$V_L$	volume of liquid phase [ $\text{m}^3$ ]
$v$	velocity in y-direction [m/s]
$v$	specific volume [ $\text{m}^3/\text{kg}$ ]
$v_G$	specific volume of vapor [ $\text{m}^3/\text{kg}$ ]
$v_H$	homogeneous specific volume [ $\text{m}^3/\text{kg}$ ]
$v_i$	velocity of interface in z-direction [m/s]
$v_L$	specific volume of liquid [ $\text{m}^3/\text{kg}$ ]
$W$	ratio in Katto and Ohno correlation [-]
$We$	Weber number [-]
$We_D$	droplet Weber number [-]
$We_G$	vapor Weber number [-]
$We_L$	Weber number of liquid [-]
$w$	local oil mass fraction [kg/kg]
$w_{\text{inlet}}$	inlet oil mass fraction [kg/kg]
$X$	mass fraction of mixture in liquid phase [kg/kg]
$X_{tt}$	Martinelli parameter with both phases turbulent [-]
$x$	exponent in Rohsenow correlation [-]
$x$	vapor quality [-]
$x_a$	actual local vapor quality [-]
$x_B$	vapor quality at transition to bubbly flow [-]
$x_{\text{crit}}$	vapor quality at location of critical heat flux [-]
$x_{\text{di}}$	vapor quality at onset of dryout [-]
$x_{\text{de}}$	vapor quality at end of dryout zone [-]
$x_e$	local equilibrium vapor quality [-]
$x_{\text{exit}}$	exit vapor quality at the critical heat flux [-]
$x_F$	vapor quality at transition to spray flow [-]
$x_{IA}$	vapor quality at transition from intermittent to annular flow [-]
$x_{\max}$	vapor quality at the intersection of annular flow and mist flow transition curves [-]
$x_{\min}$	vapor quality at minimum of mist flow transition equation [-]
$x_S$	vapor quality at transition to stratified flow [-]
$Y$	Greoneveld multiplying factor [-]
$Y$	ratio of vapor to liquid frictional pressure gradient [-]
$Y$	mass fraction of mixture in vapor phase [kg/kg]
$Y$	twist ratio [-]
$y$	exponent in Rohsenow correlation [-]
$y$	length [m]
$y$	twist ratio for 180° turn [-]
$y$	parameter [-]
$Z$	heated length of tube to diameter ratio [-]
$Z_G$	ratio of sensible cooling duty for vapor to total condensing duty [-]
$z$	distance along y-axis [m]
$z$	distance from entrance [m]
$z$	length from top [m]
$z$	length around perimeter of tube from top [m]
$z^*$	dimensionless length from top [m]
$z^*$	Graetz length parameter [-]
$z_a$	length from inlet where liquid is actually completely evaporated [m]
$z_{\text{di}}$	length from inlet where dryout occurs [m]

---

$z_e$	length from inlet where liquid is completely evaporated under equilibrium conditions [m]
$z_{eh}$	hydrodynamic entrance length of developing flow [m]
$z_{et}$	thermal entrance length of developing flow [m]

### Greek symbols:

$\alpha$	heat transfer coefficient [ $\text{W}/\text{m}^2\text{K}$ ]
$\alpha$	mean film heat transfer coefficient on tube array [ $\text{W}/\text{m}^2\text{K}$ ]
$\alpha$	local perimeter averaged heat transfer coefficient inside a tube [ $\text{W}/\text{m}^2\text{K}$ ]
$\alpha(N)$	heat transfer coefficient on Nth tube [ $\text{W}/\text{m}^2\text{K}$ ]
$\alpha(N=1)$	heat transfer coefficient on top tube [ $\text{W}/\text{m}^2\text{K}$ ]
$\alpha(x)$	local perimeter averaged heat transfer coefficient inside a tube at vapor quality $x$ [ $\text{W}/\text{m}^2\text{K}$ ]
$\alpha_{\text{array}}$	falling film heat transfer coefficient on single-row tube array [ $\text{W}/\text{m}^2\text{K}$ ]
$\alpha_b$	heat transfer coefficient on bottom of finned tube retaining condensate [ $\text{W}/\text{m}^2\text{K}$ ]
$\alpha_{\text{bundle}}$	local bundle boiling heat transfer coefficient [ $\text{W}/\text{m}^2\text{K}$ ]
$\alpha_{\text{bundle}}$	local bundle boiling heat transfer coefficient for falling film evaporation [ $\text{W}/\text{m}^2\text{K}$ ]
$\alpha_c$	convective condensation heat transfer coefficient [ $\text{W}/\text{m}^2\text{K}$ ]
$\alpha_{cb}$	convective boiling heat transfer coefficient [ $\text{W}/\text{m}^2\text{K}$ ]
$\alpha_{ct}$	corrugated tube turbulent heat transfer coefficient [ $\text{W}/\text{m}^2\text{K}$ ]
$\alpha_D$	convective heat transfer coefficient from vapor-to-droplet [ $\text{W}/\text{m}^2\text{K}$ ]
$\alpha_{\text{dry}}$	falling film heat transfer coefficient on dry fraction of tube [ $\text{W}/\text{m}^2\text{K}$ ]
$\alpha_{\text{dryout}}$	heat transfer coefficient in dryout zone [ $\text{W}/\text{m}^2\text{K}$ ]
$\alpha_{\text{eff}}$	effective condensing coefficient for condensable mixture [ $\text{W}/\text{m}^2\text{K}$ ]
$\alpha_f$	mean film heat transfer coefficient [ $\text{W}/\text{m}^2\text{K}$ ]
$\alpha_f$	local film condensing coefficient around non-stratified top perimeter of tube [ $\text{W}/\text{m}^2\text{K}$ ]
$\alpha_f$	helix angle of microfins [degrees]
$\alpha_f(z)$	local film heat transfer coefficient [ $\text{W}/\text{m}^2\text{K}$ ]
$\alpha_f^+(z)$	dimensionless local film heat transfer coefficient [ $\text{W}/\text{m}^2\text{K}$ ]
$\alpha_f(\beta)$	local film heat transfer coefficient at angle $\beta$ from top of tube [ $\text{W}/\text{m}^2\text{K}$ ]
$\alpha_f(x)$	local condensing coefficient at vapor quality $x$ [ $\text{W}/\text{m}^2\text{K}$ ]
$\alpha_{\text{fin}}$	heat transfer coefficient on fin [ $\text{W}/\text{m}^2\text{K}$ ]
$\alpha_{ft}$	finned tube turbulent heat transfer coefficient [ $\text{W}/\text{m}^2\text{K}$ ]
$\alpha_{FZ}$	Forester-Zuber nucleate boiling heat transfer coefficient [ $\text{W}/\text{m}^2\text{K}$ ]
$\alpha_G$	turbulent heat transfer coefficient of vapor [ $\text{W}/\text{m}^2\text{K}$ ]
$\alpha_{\text{Gt}}$	forced convection heat transfer coefficient with total flow as vapor [ $\text{W}/\text{m}^2\text{K}$ ]
$\alpha_{\text{grav}}$	gravity-dominated film heat transfer coefficient [ $\text{W}/\text{m}^2\text{K}$ ]
$\alpha_I$	ideal heat transfer coefficient [ $\text{W}/\text{m}^2\text{K}$ ]
$\alpha_I$	ideal boiling heat transfer coefficient [ $\text{W}/\text{m}^2\text{K}$ ]
$\alpha_I$	ideal tube bank heat transfer coefficient [ $\text{W}/\text{m}^2\text{K}$ ]
$\alpha_{\text{id}}$	ideal heat transfer coefficient [ $\text{W}/\text{m}^2\text{K}$ ]
$\alpha_{\text{invert}}$	heat transfer coefficient in inverted annular flow regime [ $\text{W}/\text{m}^2\text{K}$ ]
$\alpha_L$	liquid only heat transfer coefficient [ $\text{W}/\text{m}^2\text{K}$ ]
$\alpha_{\text{Lt}}$	forced convection heat transfer coefficient with total flow as liquid [ $\text{W}/\text{m}^2\text{K}$ ]
$\alpha_{\text{mean}}$	mean heat transfer coefficient [ $\text{W}/\text{m}^2\text{K}$ ]
$\alpha_{\text{mf}}$	microfin convective boiling heat transfer coefficient [ $\text{W}/\text{m}^2\text{K}$ ]
$\alpha_{\text{mist}}$	mist flow heat transfer coefficient [ $\text{W}/\text{m}^2\text{K}$ ]
$\alpha_{\text{nb}}$	nucleate boiling heat transfer coefficient [ $\text{W}/\text{m}^2\text{K}$ ]

$\alpha_{\text{nom}}$	nominal heat transfer coefficient [W/m <sup>2</sup> K]
$\alpha_{\text{nb}}$	nucleate boiling heat transfer coefficient [W/m <sup>2</sup> K]
$\alpha_{\text{nb,I}}$	ideal nucleate pool boiling heat transfer coefficient of mixture [W/m <sup>2</sup> K]
$\alpha_{\text{nb,o}}$	standard nucleate boiling heat transfer coefficient [W/m <sup>2</sup> K]
$\alpha_o$	reference nucleate pool boiling heat transfer coefficient [W/m <sup>2</sup> K]
$\alpha_{\text{pt}}$	plain tube turbulent heat transfer coefficient [W/m <sup>2</sup> K]
$\alpha_{\Gamma}$	falling film heat transfer coefficient [W/m <sup>2</sup> K]
$\alpha_{\Gamma,\text{dev}}$	developing region falling film heat transfer coefficient [W/m <sup>2</sup> K]
$\alpha_{\Gamma,\text{lam}}$	laminar falling film heat transfer coefficient [W/m <sup>2</sup> K]
$\alpha_{\Gamma,\text{lturb}}$	turbulent falling film heat transfer coefficient [W/m <sup>2</sup> K]
$\alpha_{\text{ref-oil}}$	flow boiling heat transfer coefficient of refrigerant-oil mixture [W/m <sup>2</sup> K]
$\alpha_{\text{sh}}$	shear-dominated film heat transfer coefficient [W/m <sup>2</sup> K]
$\alpha_{\text{ss}}$	shell-side single-phase heat transfer coefficient [W/m <sup>2</sup> K]
$\alpha_{\text{strat}}$	mean film heat transfer coefficient around bottom of tube in stratified flow [W/m <sup>2</sup> K]
$\alpha_{\text{tp}}$	two-phase flow boiling heat transfer coefficient [W/m <sup>2</sup> K]
$\alpha_{\text{tt}}$	twisted tape turbulent heat transfer coefficient [W/m <sup>2</sup> K]
$\alpha_{\text{tt}}$	twisted tape two-phase flow boiling heat transfer coefficient [W/m <sup>2</sup> K]
$\alpha_{\text{vapor}}$	vapor phase heat transfer coefficient [W/m <sup>2</sup> K]
$\alpha_{\text{wet}}$	wetted wall heat transfer coefficient [W/m <sup>2</sup> K]
$\alpha_{\text{wet}}$	falling film heat transfer coefficient on wetted fraction of tube [W/m <sup>2</sup> K]
$\beta$	angle of surface with respect to the horizontal [rad]
$\beta$	angle around perimeter of tube with respect to top [rad]
$\beta$	coefficient of thermal expansion [K <sup>-1</sup> ]
$\beta$	condensate retention angle from bottom of tube [rad]
$\beta$	contact angle [deg]
$\beta$	helix angle of corrugation or fin [°]
$\beta$	value used for calculation of $\Omega$ [-]
$\beta$	volumetric quality [-]
$<\beta>$	cross-sectional averaged volumetric quality [-]
$\beta_L$	liquid mass transfer coefficient [= 0.0003 m/s]
$\beta_{\text{ct}}$	constant for corrugated tube [-]
$\beta_{\text{ft}}$	constant for finned tubes [-]
$\beta_{\text{mL}}$	mass transfer coefficient in liquid [0.0003 m/s]
$\beta_{\text{rib}}$	profile contact angle [°]
$\Delta\delta$	interfacial roughness [m]
$\delta$	liquid film thickness [m]
$\delta$	thickness of twisted tape [m]
$\delta^*$	non-dimensional liquid film thickness [m]
$\varepsilon$	void fraction of vapor [-]
$<\varepsilon>$	cross-sectional averaged void fraction of vapor [-]
$\varepsilon_c$	void fraction of vapor at centreline of channel [-]
$\varepsilon_{\text{c-s}}$	cross-sectional void fraction of vapor [-]
$\varepsilon_{\text{chordal}}$	chordal void fraction of vapor across channel [-]
$\varepsilon_H$	homogeneous void fraction [-]
$\varepsilon_{\text{IA}}$	void fraction evaluated at $x_{\text{IA}}$ [-]
$\varepsilon_{\text{local}}$	local void fraction of vapor at a point or small volume [-]
$\varepsilon_r$	void fraction of Rouhani drift flux model [-]
$\varepsilon_q$	Rose low finned tube enhancement ratio at same q [-]

$\varepsilon_{\Delta T}$	Rose low finned tube enhancement ratio at same $\Delta T$ [-]
$\varepsilon_{vol}$	volumetric void fraction of vapor [-]
$\varepsilon_w$	void fraction of vapor at wall [-]
$\phi$	angle from top of tube [rad]
$\phi_d$	angle at end of developing region [rad]
$\phi_f$	angle at end of stagnation flow region [rad]
$\phi_i$	angle at end of impingement region [rad]
$\phi_L$	liquid two-phase friction multiplier [-]
$\Gamma$	condensate flow rate per unit width of wall [kg/ms]
$\Gamma_{evap}$	liquid flow that has been evaporated when reaching the bottom of the array [kg/m s]
$\Gamma_{feed}$	liquid flow rate of liquid applied to the top of the array [kg/m s]
$\Gamma_L$	liquid flow rate per unit length on plate or one side of tube [kg/m s]
$\Gamma(\beta)$	condensate flow rate per unit width at angle $\beta$ from top [kg/ms]
$\Gamma(N)$	condensate flow rate (on one side) per unit length off bottom of tube N [kg/ms]
$\Gamma_{bottom}(N)$	condensate flow rate (from one side) per unit length off bottom of tube N [kg/ms]
$\Gamma_{top}(N)$	condensate flow rate (from one side) per unit length onto top of tube N [kg/ms]
$\Gamma(z)$	condensate flow rate per unit width at distance z from top [kg/ms]
$\gamma$	constant for finned tubes [-]
$\eta$	similarity variable [-]
$\eta_{fin}$	fin efficiency [-]
$\eta_{surface}$	surface efficiency [-]
$\varphi$	bulk-to-wall property correction ratio [-]
$\varphi$	one-half of apex angle of a trapezoidal fin [rad]
$\kappa$	ratio of droplet heat flux to total heat flux [-]
$\kappa$	ratio of the temperature rises due to viscous heating and wall heat flux [-]
$\kappa_{lim}$	limit of ratio of temperature rise [-]
$\Lambda$	correction factor [-]
$\lambda$	Baker gas-phase parameter [-]
$\lambda$	wavelength between bubble departures from interface [m]
$\lambda$	friction factor multiplier [-]
$\lambda_{crit}$	critical wavelength [m]
$\lambda_d$	dangerous wavelength [m]
$\lambda_T$	Taylor wavelength [m]
$\mu$	dynamic viscosity [ $Ns/m^2$ ]
$\mu_{bulk}$	dynamic viscosity at bulk temperature [ $Ns/m^2$ ]
$\mu_G$	vapor dynamic viscosity [ $Ns/m^2$ ]
$\mu_L$	liquid dynamic viscosity [ $Ns/m^2$ ]
$\mu_{oil}$	dynamic viscosity of pure oil [ $Ns/m^2$ ]
$\mu_{ref}$	dynamic viscosity of pure refrigerant [ $Ns/m^2$ ]
$\mu_{ref-oil}$	dynamic viscosity of local refrigerant-oil mixture [ $Ns/m^2$ ]
$\mu_{wall}$	dynamic viscosity at wall [ $Ns/m^2$ ]
$\mu_{water}$	dynamic viscosity of water [ $Ns/m^2$ ]
$\nu$	kinematic viscosity [ $m^2/s$ ]
$\nu_L$	liquid kinematic viscosity [ $m^2/s$ ]
$\xi(\pi-\beta)$	function in Rose low finned tube method [-]
$\theta$	similarity variable [-]
$\theta_{crit}$	critical angle of deflection for tube array [radians]
$\theta_{ctl}$	centerline angle around top perimeter of tube [degrees]

$\theta_{\text{def}}$	maximum angle of deflection of condensate flowing from tube to tube [radians]
$\theta_{\text{dry}}$	dry angle around top perimeter of tube [radians]
$\theta_{\text{dry}}^*$	dimensionless dry angle [-]
$\theta_{\text{ds}}$	baffle cut angle on shell diameter [degrees]
$\theta_{\text{max}}$	dry angle at $x_{\text{max}}$ [radians]
$\theta_{\text{strat}}$	stratified angle around upper perimeter of the tube to stratified liquid level [radians]
$\theta_{\text{strat}}^*$	dimensionless stratified angle [-]
$\Delta\theta$	bubble point temperature rise at interface relative to bulk [K]
$\Delta\theta_{\text{bp}}$	boiling range or temperature glide of a mixture [K]
$\rho$	density [ $\text{kg}/\text{m}^3$ ]
$\rho$	liquid density of refrigerant-oil mixture [ $\text{kg}/\text{m}^3$ ]
$\rho_{\text{air}}$	density of air [ $\text{kg}/\text{m}^3$ ]
$\rho_G$	vapor density [ $\text{kg}/\text{m}^3$ ]
$\rho_G^*$	fictitious vapor density [ $\text{kg}/\text{m}^3$ ]
$\rho_H$	homogeneous density of fluid [ $\text{kg}/\text{m}^3$ ]
$\rho_k$	density of phase k [ $\text{kg}/\text{m}^3$ ]
$\rho_L$	liquid density [ $\text{kg}/\text{m}^3$ ]
$\rho_{\text{man}}$	liquid density of oil according to manufacturer [ $\text{kg}/\text{m}^3$ ]
$\rho_{\text{oil}}$	liquid density of oil [ $\text{kg}/\text{m}^3$ ]
$\rho_{\text{ref}}$	liquid density of refrigerant [ $\text{kg}/\text{m}^3$ ]
$\rho_v$	vapor density [ $\text{kg}/\text{m}^3$ ]
$\rho_{\text{water}}$	density of water [ $\text{kg}/\text{m}^3$ ]
$\sigma_{\text{SB}}$	Stephan-Bolzmann constant [ $\text{W}/\text{m}^2\text{K}^4$ ]
$\sigma$	surface tension [ $\text{N}/\text{m}$ ]
$\sigma$	parameter for aspect ratios of rectangular channels [-]
$\sigma_{\text{water}}$	surface tension of water [ $\text{N}/\text{m}^2$ ]
$\tau_i$	interfacial shear stress [ $\text{N}/\text{m}^2$ ]
$\tau_i^*$	dimensionless interfacial shear stress [ $\text{N}/\text{m}^2$ ]
$\tau_i^+$	dimensionless interfacial shear stress [ $\text{N}/\text{m}^2$ ]
$\Omega$	geometrical function [-]
$\Omega$	intertube spacing factor [-]
$\xi_{\text{Ph}}$	friction factor [-]
$\chi$	dimensionless factor in hydrodynamic developing flow [-]
$\psi$	correlating parameter of Groeneveld and Delorme [-]
$\psi$	similarity variable [-]

### Subscripts :

1,2...	subscripts of empirical constants
D	droplet
G	vapor
H	homogeneous
k	phase
L	liquid
a	actual
b	bottom of tube
c	centerline

e equilibrium  
f evaluated at film temperature  
fin fin  
top top of tube  
w wall

## Appendix C

[Microheat](#) is a program used to help engineers in designing advanced heat exchanger tubes.

[Wolverine Products Catalog](#) is a website that provides a list of products and theirs descriptions that [Wolverine Tube, Inc.](#) sells.

### [National Institute of Standards and Technology \(NIST\)](#)

NIST's motto: "Working with industry to develop and apply technology, measurements and standards." NIST was founded in 1901. It is a non-regulatory federal agency within the U. S. Commerce Department's Technology Administration. NIST's mission is to develop and promote measurement, standards, and technology to enhance productivity, facilitate trade, and improve the quality of life.

## References

- Adamek, T.A. (1981).** Bestimmung der Kondensationgroß auf Feinewellten Oberflächen zur ausle-gun  
Optimaler Wandprofile, *Wärme-und Stoffübertragung*, Vol. 15, pp. 255-270.
- Adamek, T.A. and Webb, R.L. (1990).** Prediction of Film Condensation on Horizontal Integral Fin  
Tubes, *Int. J. Heat Mass Transfer*, Vol. 33, pp. 1721-1735.
- Agostini, B. (2002).** Etude Expérimentale de l'Ebullition de Fluide Réfrigérant en Convection Forcée  
dans des Mini-Canaux, Ph.D. Thesis, Université Joseph Fourier, Grenoble, France.
- Agostini, B., Revellin, B. and Thome, J.R. (2008).** Elongated Bubbles in Microchannels. Part I:  
Experimental Study and Modeling of Elongated Bubble Velocity, *Int. J. Multiphase Flow*, Vol.  
34, pp. 590-601.
- Agostini, B. and Thome, J.R. (2005).** Comparison of an Extented Database for Flow Boiling Heat  
Transfer Coefficients in Multi-Microchannels Elements with the Three-Zone Model, *ECI Heat  
Transfer and Fluid Flow in Microscale*, Castelvecchio Pascoli, Italy, Sept. 25-30.
- Agostini, B., Thome, J.R., Fabbri, M., Calmi, D., Kloter, U. and Michel, B. (2008a).** High Heat Flux  
Flow Boiling in Silicon Multi-Microchannels: Part I – Heat Transfer Characteristics of R-236fa,  
*Int. J. Heat Mass Transfer*, Vol. 41, pp. 5400-5414.
- Agostini, B., Thome, J.R., Fabbri, M., Calmi, D., Kloter, U. and Michel, B. (2008b).** High Heat Flux  
Flow Boiling in Silicon Multi-Microchannels: Part II – Heat Transfer Characteristics of R-245fa,  
*Int. J. Heat Mass Transfer*, Vol. 41, pp. 5415-5425.
- Agostini, B., Revellin, R., Thome, J.R., Fabbri, M., Michel, B., Kloter, U. and Calmi, D. (2008c).**  
High Heat Flux Flow Boiling in Silicon Multi-Microchannels: Part III – Saturated Critical Heat  
Flux of R236fa and Two-Phase Pressure Drop, *Int. J. Heat Mass Transfer*, Vol. 41, pp. 5426-  
5442.
- Agostini, B., Thome, J.R., Fabbri, M. and Michel, B. (2008d).** High Heat Flux Two-Phase Cooling in  
Silicon Multi-Microchannels, *IEEE Trans. on Components and Packaging Technologies*, Vol. 31,  
pp. 691-701.
- Agrawal, K.N., Varma, H.K. and Lal, S. (1986).** Heat Transfer during Forced Convection Boiling of  
R12 under Swirl Flow, *J. Heat Transfer*, Vol. 108, pp. 567-573.
- Akbar, M.K., Plummer, D.A. and Ghiaasiaan, S.M. (2003).** On Gas-Liquid Two-Phase Flow Regimes  
in Microchannels, *Int. J. Multiphase Flow*, Vol. 29, pp. 855-865.
- Akers, W.W., Deans, H.A. and Crosser, O.K. (1959).** Condensation Heat Transfer within Horizontal  
Tubes, *Chem. Eng. Prog. Symp. Ser.*, Vol. 55, pp. 171-176.
- Ali, M.I., Sadatomi, M. And Kawaji, M. (1993).** Two-Phase Flow in Narrow Channels between Two  
Flat Plates, *Canadian J. Chemical Engineering*, Vol. 71, pp. 657-666.
- Andreani, M. and Yadigaroglu, G. (1997).** A 3-D Eulerian-Lagrangian Model of Dispersed Flow  
Boiling Including a Mechanistic Description of the Droplet Spectrum Evolution, Parts 1 and 2,  
*Int. J. Heat Mass Transfer*, Vol. 40, pp. 1753-1793.
- Antonelli, R. and O'Neill, P.S. (1981).** Design and Application Consideration for Heat Exchanger with  
Enhanced Boiling Surfaces, Paper read at International Conference on Advances in Heat  
Exchangers, Dubrovnic, September.
- Arman, B. and Rabas, T.J. (1992).** Disruption Shape Effects on the Performance of Enhanced Tubes  
with the Separation and Reattachment Mechanism, *Enhanced Heat Transfer*, HTD Vol. 202,  
ASME, pp. 67-76.
- Armand, A.A. and Treschev, G.G. (1946).** *Izv. Vses. Teplotek. Inst.*, Vol. 1, pp. 16-23.
- Arnold, C.R. and Hewitt, G.F. (1967).** Further Developments in the Photography of Two Phase Gas-  
Liquid Flow, *The Journal of Photographic Science*, Vol. 15, pp. 97-114.
- Arshad, J. and Thome, J.R. (1983).** Enhanced Boiling Surfaces: Heat Transfer Mechanism and Mixture  
Boiling, *Proc. ASME-JSME Thermal Engineering Joint Conference*, Vol. 1, pp. 191-197.

- Badie, S., Lawrence, C.J. and Hewitt, G.F. (2001).** Axial Viewing Studies of Horizontal Gas-Liquid Flows with Low Liquid Loading, *Int. J. Multiphase Flow*, Vol. 27, pp. 1259-1269.
- Baker, O. (1954).** Design of pipelines for simultaneous flow of oil and gas, *Oil and Gas J.*, July, pp. 26.
- Bandarra Filho, E.P. and Sáiz-Jabardo, J.M. (2006).** Convective Boiling Performance of Refrigerant R-134a in Herringbone and Microfin Copper Tubes, *Int. J. Refrigeration*, Vol. 29, pp. 81-91.
- Bandyopadhyay, P.S., Gaitonde, U.N. and Sukhatme, S.P. (1991).** Influence of Free Convection on Heat Transfer during Laminar Flow in Tubes with Twisted Tapes, *Experimental Thermal and Fluid Science*, Vol. 4, pp. 577-586.
- Bankoff, S.G. (1960).** A Variable Density Single-Fluid Model for Two-Phase Flow with Particular Reference to Steam-Water, *J. Heat Transfer*, Vol. II, Series B, pp. 265-272.
- Bao, Z.Y., Fletcher, D.F. and Haynes, B.S. (2000).** Flow Boiling Heat Transfer of Freon R11 and HFCFC123 in Narrow Passages, *Int. J. Heat Mass Transfer*, Vol. 43, pp. 3347-3358.
- Baird, J.R., Bao, Z.Y., Fletcher, D.F. and Haynes, B.S. (2000).** Local Flow Boiling Heat Transfer Coefficients in Narrow Conduits, *Boiling 2000: Phenomena and Engineering Applications*, ed. A. Bar-Cohen, Anchorage Alaska, April 30 – May 5, Vol. 2, pp. 447-466.
- Barbieri, P.E.L. and Sáiz-Jabardo, J.M. (2006).** The Effect of the Diameter in Convective Boiling of Refrigerant R-134a, *Proc. 13th International Heat Transfer Conference*, Sydney, August 14-18.
- Barbieri, P.E.L., Sáiz-Jabardo, J.M., Bandarra Filho, E.P. (2005).** Nucleate and Convective Boiling of Refrigerants, Invited Lecture by Sáiz-Jabardo at LTCM-EPFL, Lausanne, Switzerland.
- Barnea, D. and Taitel, Y. (1986).** Flow pattern transition in two-phase gas-liquid flows, *Encyclopedia of Fluid Mechanics*, Vol. 3, Gulf Publishing, pp. 403-474.
- Baustian, J.J., Pate, M.B. and Bergles, A.E. (1988a).** Measuring the Concentration of a Flowing Oil-Refrigerant Mixture with a Vibrating U-Tube Densitometer, *ASHRAE Trans.*, Vol. 94, Part 2, pp. 571-587.
- Baustian, J.J., Pate, M.B. and Bergles, A.E. (1988b).** Measuring the Concentration of a Flowing Oil-Refrigerant Mixture with an Acoustic Velocity Sensor, *ASHRAE Trans.*, Vol. 94, Part 2, pp. 602-615.
- Baustian, J.J., Pate, M.B. and Bergles, A.E. (1988c).** Measuring the Concentration of a Flowing Oil-Refrigerant Mixture with a Bypass Viscometer, *ASHRAE Trans.*, Vol. 94, Part 2, pp. 588-601.
- Bayini, A., Thome, J.R. and Favrat, D. (1995).** Online Measurement of Oil Concentrations of R-134a/Oil Mixtures with a Density Flowmeter, *HVAC&R Research*, ASHRAE, 1(3), pp. 232-241.
- Bays, G.S. and McAdams, W.H. (1937).** *Ind. Eng. Chem.*, Vol. 29, pp. 1240-1246.
- Beatty, K.O. and Katz, D.L. (1948).** Condensation of Vapors on Outside of Finned Tubes, *Chem. Eng. Prog.*, Vol. 44, No. 1, pp. 55-70.
- Bell, K.J. (1960).** Exchangers Design Based on the Delaware Research Program, *Petroleum Engineering*, Vol. 32, No. 11, pp. C26-36 and C40a-C40c.
- Bell, K.J. (1963).** Final Report of the Cooperative Research Program on Shell-and-Tube Heat Exchangers, *Univ. of Delaware Eng. Exp. Sta. Bull.*, No. 5.
- Bell, K.J. (1986).** Delaware Method for Shell Side Design, *Heat Exchanger Sourcebook*, Edited by J.W. Palen, Hemisphere, New York, Chapter 6, pp. 129-166.
- Bell, K.J. and Ghaly, M.A. (1973).** An Approximate Generalized Design Method for Multi-Component Partial Condensers, *AIChE Symp. Ser.*, Vol. 69, pp. 72-79.
- Bergles, A.E. (1981).** Survey of Heat Transfer Characteristics of Deep Spirally Fluted Tubing, *Advances in Enhanced Heat Transfer-1981*, Eds. R.L. Webb, T.C. Carnavos, E.F. Park, Jr. and K.M. Hostetler, ASME HTD Vol. 18, pp. 21-33.
- Bergles, A.E. and Joshi, S.D. (1983).** Augmentation Techniques for Low Reynolds Number In-Tube Flow, *Low Reynolds Number Flow Heat Exchangers*, Eds. S. Kakac, R.K. Shah and A.E. Bergles, Hemisphere, Washington D.C., pp. 695-720.
- Bergles, A.E. and Kandlikar, S.G. (2005).** On the Nature of Critical Heat Flux in Microchannels, *J. Heat Transfer*, Vol. 127, pp. 101-107.

- Bergles, A.E., Lienhard V, J.H., Kendall, G.E, Griffith, P. (2003).** Boiling and Evaporation in Small Diameter Channels, *Heat Transfer Engineering*, Vol. 24, No. 1, pp. 18-40.
- Bergles, A.E., Webb, R.L. and Junkhan, G.H. (1979).** Energy Conservation via Heat Transfer Enhancement, *Energy*, Vol. 4, pp. 193-200.
- Biberg, D. (1999).** An explicit approximation for the wetted angle in two-phase stratified pipe flow, *Canadian J. Chemical Engineering*, Vol. 77, pp. 1221-1224.
- Blasius, H. (1913).** Das Ahnlichkeitgesetz bei Reibungsvorgangen in Flüssigkeiten, *Forschg. Arb. Ing.-Wes.*, No. 131, Berlin.
- Bowers, M.B. and Mudawar, I. (1994).** High Flux Boiling in Low Flow Rate, Low Pressure Drop Mini-Channel and Micro-Channel Heat Sinks, *Int. J. Heat Mass Transfer*, Vol. 37, pp. 321-332.
- Brauer, H. (1956).** Stromung und Wärmeübergang bei Reiselfilmen, *VDI Forschung*, Vol. 22, pp. 1-40.
- Brauner, N. and Moalem-Maron, D. (1992).** Identification of the Range of "Small Diameter" Conduits, Regarding Two-Phase Flow Pattern Transition, *Int. Comm. Heat Mass Transfer*, Vol. 19, pp. 29-39.
- Bredesen, A., Hafner, A., Pettersen, J., Neksa, P. And Aflekt, K. (1997).** Heat Transfer and Pressure Drop for In-Tube Evaporation of CO<sub>2</sub>, *Proceedings of the International Conference on Heat Transfer Issues in Natural Refrigerants*, University of Maryland, pp. 1-15.
- Bretherton, E.P. (1961).** The Motion of Long Bubbles in Tubes, *J. Fluid Mechanics*, Vol. 10, pp. 166-188.
- Briggs, A. and Rose, J.W. (1994).** Effect of Fin Efficiency on a Model for Condensation Heat Transfer on a Horizontal, Integral-Fin Tube, *Int. J. Heat Mass Transfer*, Vol. 37 (Supplement 1), pp. 457-463.
- Briggs, A., Yang, X.X. and Rose, J.W. (1995).** An Evaluation of Various Enhanced Tubes for Shell-Side Condensation of Refrigerant, *Heat Transfer in Condensation*, Eurotherm Seminar 47, Paris, Oct. 4-5, pp. 62-70.
- Bromley, L.A. (1952).** Effect of Heat Capacity of Condensate, *Ind. Eng. Chem.*, Vol. 44, pg. 2966.
- Browne, M.W. and Bansal, P.K. (1999).** Heat Transfer Characteristics of Boiling Phenomenon in Flooded Refrigerant Evaporators, *Applied Thermal Engineering*, Vol. 19, pp. 595-624.
- Brunschwiler, T., Michel, B., Rothuizen, H., Kloster, U., Wunderle, B., Oppermann, H. and Reichl, H. (2008).** Interlayer Cooling Potential in Vertically Integrated Packages, *Microsyst Tecrol*, DOI 10.1007/s00542-008-0690-4, Springer-Verlag.
- Buchholz, M. (2005).** Lokale Mechanismen des Wärmeübergangs beim Behältersieden in allen Bereichen der Siedekennlinie, *Dissertation*, TU Berlin, Germany.
- Buchholz, M., Lüttich, T., Auracher, H. and Marquardt, W. (2004).** Experimental Investigation of Local Processes in Pool Boiling along the Entire Boiling Curve, *Int. J. Heat and Fluid Flow*, Vol. 25, pp. 243-261.
- Bukasa, J.P., Liebenberg, L. and Meyer, J.P. (2004).** Heat Transfer Performance during Condensation inside Spiraled Micro-Fin Tubes, *J. Heat Transfer*, Vol. 126, pp. 321-328.
- Burnside, B.M., Bruce, T., Martin,, A.J., McNeil, D.A., Miller, K.M. and Wilkinson, D.A. (1999).** Velocity and Heat Transfer Measurements in a Kettle Reboiler, *Two-Phase Flow Modelling and Experimentation 1999*, Eds. G.P. Celata, P. di Marco and R.K. Shah, Edizioni ETS, Pisa, Vol. 3, pp. 1719-1726.
- Butterworth, D. (1975).** A Comparison of Some Void Fraction Relationships for Co-Current Gas-Liquid Flow, *Int. J. Multiphase Flow*, Vol. 1, pp. 845-850.
- Butterworth, D. (1981).** Simplified Methods for Condensation on a Vertical Surface with Vapour Shear, UKAEA Rept. AERE-R9683.
- Butterworth, D. (1983).** Film Condensation of Pure Vapor, *Heat Exchanger Design Handbook*, Chapter 2.6.2, Hemisphere, Washington.
- Carnavos, T.C. (1979).** Heat Transfer Performance of Internally Finned Tubes in Turbulent Flow, *Advances in Enhanced Heat Transfer*, ASME, pp. 61-67.

- Casciaro, S. and Thome, J.R. (2001a).** Thermal Performance of Flooded Evaporators, Part 1: Review of Boiling Heat Transfer Studies, *ASHRAE Trans.*, Vol. 107, Pt. 1, paper AT-01-16-1.
- Casciaro, S. and Thome, J.R. (2001b).** Thermal Performance of Flooded Evaporators, Part 1: Review of Void Fraction, Two-Phase Pressure Drop, and Flow Pattern Studies, *ASHRAE Trans.*, Vol. 107, Pt. 1, paper AT-01-16-2.
- Cavallini, A., Bella, B., Longo, G.A. and Rossetto, L. (1995).** Experimental Heat Transfer Coefficients during Condensation of Halogenated Refrigerants on Enhanced Tubes, *J. Enhanced Heat Transfer*, Vol. 2, No. 1-2, pp. 115-125.
- Cavallini A., Censi G., Del Col D., Doretti L., Longo G.A., Rossetto L. and Zilio C. (2000).** Analysis and Prediction of Condensation Heat Transfer of the Zeotropic Mixture R-125/236ea, *Proc. of the ASME Heat Transfer Division*, HTD-Vol. 366-4, pp.103-110.
- Cavallini, A., Censi, G., Del Gol, D., Doretti, L., Longo, G.A. and Rossetto, L. (2001).** Experimental Investigation on Condensation Heat Transfer and Pressure Drop of New HFC Refrigerants (R134a, R125, R32, R410A, R236ea), *Int. J. Refrig.*, Vol. 24, pp. 73-87.
- Cavallini, A., Censi, G., Del Col, D., Doretti, L., Longo, G.A. and Rossetto, L. (2002).** In-tube Condensation of Halogenated Refrigerants, *ASHRAE Trans.*, Vol. 108, Pt. 1, paper 4507.
- Cavallini, A., Del Gol, D., Doretti, L., Longo, G.A. and Rossetto, L. (1999).** Condensation Heat Transfer with Refrigerants, *Two-Phase Modelling and Experimentation 1999*, Edizioni ETS, pp. 71-88.
- Cavallini A., Del Col, D., Doretti, L., Longo, G.A. and Rossetto, L. (1999).** Condensation of R-22 and R-407C inside a Horizontal Tube, *Proc. of 20<sup>th</sup> International Congress of Refrigeration*, IIR/IIF, Sydney.
- Cavallini, A., Doretti, L., Klammsteiner, N., Longo, G.A. and Rossetto, L. (1995).** Condensation of New Refrigerants inside Smooth and Enhanced Tubes, *Proc. 19<sup>th</sup> International Congress of Refrigeration*, The Hague, Vol. Iva, pp. 105-114.
- Cavallini, A., Doretti, L., Longo, G.A. and Rossetto, L. (1994).** Flow Patterns during Condensation of Pure Refrigerants on Enhanced Tubes under High Vapour Velocity, *Proc. 1994 International Refrigeration Conference at Purdue*, July 19-22, pp. 311-316.
- Cavallini, A., Doretti, L., Longo, G.A. and Rossetto, L. (1996).** A New Model for Forced-Convection Condensation on Integral-Fin Tubes, *J. Heat Transfer*, Vol. 118, pp. 689-693.
- Cavallini, A., Doretti, L., Matkovic, M. and Rossetto, L. (2006).** Update on Condensation Heat Transfer and Pressure Drop inside Microchannels, *Heat Transfer Engineering*, Vol. 27, No. 4, pp. 74-87.
- Cavallini, A. and Zecchin, R. (1974).** A Dimensionless Correlation for Heat Transfer in Forced Convective Condensation, *Proc. 5<sup>th</sup> International Heat Transfer Conference*, Tokyo, Vol. 3, pp. 309-313.
- Celata, G.P. (2004).** *Heat Transfer and Fluid Flow in Microchannels*, Begel Press, New York.
- Celata, G.P., Cumo, M., Katto, Y. and Mariani, A. (1999).** Prediction of the Critical Heat Flux in Water Subcooled Flow Boiling Using a New Mechanistic Approach, *Int. J. Heat Mass Transfer*, Vol. 42, pp. 1457-146.
- Celata, G.P., Cumo, M., Marconi, V., McPhail, S.J. and Zummo, G. (2006).** Microtube Liquid Single-Phase Heat Transfer in Laminar Flow, *Int. J. Heat Mass Transfer*, Vol. 49, pp. 3538-3546.
- Celata, G.P., Cumo, M., Marconi, V., McPhail, S.J. and Zummo, G. (2006b).** Microtube Liquid Single-Phase Heat Transfer in Laminar Flow, *Int. J. Heat Mass Transfer*, Vol. 49, pp. 3538-3546.
- Celata, G.P., Cumo, M. and Mariani, A. (1999).** Visual Investigation of High Heat Flux Burnout in Subcooled Flow Boiling of Water, *International Symposium on Applied Optical Measurements*, Munich, 23-24 September, pp. 79-93.
- Celata, G.P., Cumo, M., Mariani, A. and Zummo, G. (2000).** Burnout in Subcooled Flow Boiling of Water. A Visual Experimental Study, *International Journal of Thermal Sciences*, Vol. 39, nos. 9-10-11, pp. 896-908.

- Celata, G.P., Cumo, M., McPhail, S.J. and Zummo, G. (2006a).** Characterization of Fluid Dynamic Behaviour and Channel Wall Effects in Microtubes, *Int. J. Heat and Fluid Flow*, Vol. 27, pp. 135-143.
- Celata, G.P., Lorenzini, M., McPhail, S.J., Morini, G.L. and Zummo, G. (2008).** Experimental Analysis of Liquid Forced Convection in Rough Microtubes, *Proc. of 5th Eurotherm European Thermal Sciences Conference*, Eindhoven, May 19-22.
- Censi G., Doretti L., Rossetto L., Zilio C. (2003).** Flow Pattern Visualisation during Condensation of R134a inside Horizontal Microfin and Smooth Tubes, 21<sup>st</sup> IIR Int. Congress of Refrigeration, Washington DC, USA August 17-22.
- Cerza, M. (1992).** Nucleate Boiling in Thin Falling Liquid Films, Pool and External Flow Boiling Conference, Santa Barbara, pp. 459-466.
- Chaddock, J.B. (1957).** Film Condensation of Vapors in Horizontal Tubes, *Refrig. Engng.*, Vol. 65, pp. 36-41 and 90-95.
- Chamra, L.M. and Webb, R.L. (1995).** Condensation and Evaporation in Micro-Fin Tubes at Equal Saturation Temperatures, *J. Enhanced Heat Transfer*, Vol. 2, No. 3, pp. 219-229.
- Chamra, L.M., Webb, R.L. and Randlett, M.R. (1996).** Advanced Micro-Fin Tubes for Evaporation, *Int. J. Heat Mass Transfer*, Vol. 39, No. 9, pp. 1827-1838.
- Chato, J.C. (1962).** Laminar Condensation inside Horizontal and Inclined Tubes, *ASHRAE J.*, Vol. 4, pp. 52-60.
- Chawla, J. M (1967).** Wärmeubergang und Druckabfall in Waagerechten Rohren beider Strömung von verdampfenden Kältemitteln, *Kältetechnik-Limatisirung*, Vol. 8, pp. 246-252.
- Chen, J.C. (1963).** A Correlation for Boiling Heat Transfer of Saturated Fluids in Convective Flow, ASME Paper 63-HT-34, 6<sup>th</sup> National Heat Transfer Conference, Boston, Aug. 11-14.
- Chen, J.C. (1966).** A Correlation for Boiling Heat Transfer of Saturated Fluids in Convective Flow, *Ind. Eng. Chem. Process Des. Dev.*, Vol. 5, No. 3, pp. 322-329.
- Chen, J.C. and Tuzla, K. (1996).** Heat Transfer Characteristics of Alternate Refrigerants, Vol. 3: Condenser and Evaporator Outside Tube, EPRI TR-106016-V3, Lehigh University, January.
- Chen, J.C., Tuzla, K., Wang, Q. and Starner, K. (1994).** Falling Film Evaporation of Refrigerants, *Proc. 10<sup>th</sup> International Heat Transfer Conference*, Brighton, Vol. 6, pp. 169-173.
- Chen, L., Tian, Y.S. and Karayiannis, T.G. (2006).** The Effect of Tube Diameter on Vertical Two-Phase Flow Regimes in Small Tubes, *Int. J. Heat Mass Transfer*, Vol. 49, pp. 4220-4230.
- Chen, Y., Yang, K.-S., Chang, Y.-J. and Wang, C.-C. (2001).** Two-Phase Pressure Drop of Air-Water and R-410A in Small Horizontal Tubes, *Int. J. Multiphase Flow*, Vol. 27, pp. 1293-1299.
- Cheng, L. and Mewes, D. (2006).** Review of Two-Phase Flow and Flow Boiling of Mixtures in Small and Mini Channels, *Int. J. Multiphase Flow*, Vol. 32, pp. 183-207.
- Cheng, L., Ribatski, G., Moreno Quiben, J. and Thome, J.R. (2008a).** New Prediction Methods for CO<sub>2</sub> Evaporation inside Tubes: Part I – A Two-Phase Flow Pattern Map and a Flow Pattern Based Phenomenological Model for Two-Phase Flow Frictional Pressure Drops, *Int. J. Heat Mass Transfer*, Vol. 51, pp. 111-124.
- Cheng, L., Ribatski, G. and Thome, J.R. (2008).** Two-Phase Flow Patterns and Flow Pattern Maps: Fundamentals and Applications, *ASME Appl. Mech. Reviews*, Vol. 31, pp. 050802.
- Cheng, L., Ribatski, G. and Thome, J.R. (2008b).** New Prediction Methods for CO<sub>2</sub> Evaporation inside Tubes: Part II – An Updated General Flow Boiling Heat Transfer Model Based on Flow Patterns, *Int. J. Heat Mass Transfer*, Vol. 51, pp. 125-135.
- Cheng, L., Ribatski, G., Wojtan, L. and Thome, J.R. (2006).** New Flow Boiling Heat Transfer Model and Flow Pattern Map for Carbon Dioxide Evaporating inside Tubes, *Int. J. Heat Mass Transfer*, Vol. 49, pp. 4082-4094.
- Cheng, L., Ribatski, G., Wojtan, L. and Thome, J.R. (2007).** Erratum to: “New Flow Boiling Heat Transfer Model and Flow Pattern Map for Carbon Dioxide Evaporating inside Tubes” [*Int. J. Heat Mass Transfer*, Vol. 49, pp 4082-4094], *Int. J. Heat Mass Transfer*, Vol. 50, pp. 391.

- Cheng, P. and Wu, H.Y. (2006).** Mesoscale and Microscale Phase-Change Heat Transfer, *Advances in Heat Transfer*, Elsevier, Vol. 39, pp. 461-563.
- Chiang, R. (1993).** Heat Transfer and Pressure Drop during Evaporation and Condensation of Refrigerant-22 in a 7.5 mm and 10 mm Axial and Helical Grooved Tubes, *AIChE Symp. Ser.*, Vol. 89, No. 295, pp. 205-210.
- Chisholm, D. (1967).** A Theoretical Basis for the Lockhart-Martinelli Correlation for Two-Phase Flow, *Int. J. Heat Mass Transfer*, Vol. 10, pp. 1767-1778.
- Chisholm, D. (1972).** An Equation for Velocity Ratio in Two-Phase Flow, NEL Report 535.
- Chisholm, D. (1973).** Pressure Gradients Due to Friction during the Flow of Evaporating Two-Phase Mixtures in Smooth Tubes and Channels, *Int. J. Heat Mass Transfer*, Vol. 16, pp. 347-358.
- Chisholm, D. (1983).** Two-Phase Flow in Pipelines and Heat Exchangers, Longman, New York.
- Chisholm, D. (1985).** Two-phase flow in heat exchangers and pipelines, *Heat Trans. Engineering*, Vol. 6, pp. 48-57.
- Cho, K. and Kim, B.G. (1998).** Heat Transfer Characteristics in the U-bend of a Microfin Tube Evaporator using R-407C, *ASHRAE Trans.*, Vol. 104, Part 2, Paper TO-98-19-3.
- Choudhury, D. and Patankar, S.V. (1985).** Analysis of Developing Laminar Flow and Heat Transfer in Tubes with Radial Internal Fins, *Advances in Enhanced Heat Transfer – 1985*, ASME HTD Vol. 43, eds. S.M. Shenkman, J.E. O'Brian, I.S. Habib and J.A. Kohler, pp. 57-71.
- Christoffersen, B.R., Chato, J.C., Wattelet, J.P. and de Souza, A.L. (1993).** Heat Transfer and Flow Characteristics of R-22, R-32/R-125 and R-134a in Smooth and Micro-Fin Tubes, ACRC Report TR-47, University of Illinois at Urbana-Champaign.
- Chun, K.R. and Seban, R.A. (1971).** Heat Transfer to Evaporating Liquid Films, *J. Heat Transfer*, Vol. 93, November, pp. 391-396.
- Chung-Chiang, L. (1994).** Investigation of Condensation Heat Transfer of R124/22 Nonazeotropic Refrigerant Mixtures in Horizontal Tubes, Ph.D. Thesis, National Chiao Tung University, Taiwan.
- Chung, P.M.Y. and Kawaji, M. (2004).** The Effect of Channel Diameter on Diabatic Two-Phase Flow Characteristics in Microchannels, *Int. J. Multiphase Flow*, Vol. 30, pp. 735-761.
- Churchill, S.W. (1983).** The Development of Theoretically Based Correlations for Heat and Mass Transfer, *Latin American Journal of Heat and Mass Transfer*, Vol. 7, pp. 207-229.
- Chyu, M.-C. and Bergles, A.E. (1985a).** Falling Film Evaporation on a Horizontal Tube, *Multiphase Flow and Heat Transfer*, ASME HTD Vol. 47, pp. 39-48.
- Chyu, M.-C. and Bergles, A.E. (1985b).** Enhancement of Horizontal Tube Spray Film Evaporators by Structured Surfaces, *Advances in Enhanced Heat Transfer-1985*, ASME HTD Vol. 43, pp. 39-47.
- Chyu, M.-C. and Bergles, A.E. (1987).** An Analytical and Experimental Study of Falling-Film Evaporation on a Horizontal Tube, *J. Heat Transfer*, Vol. 109, No. 4, pp. 983-990.
- Chyu, M.-C. and Bergles, A.E. (1989).** Horizontal Tube Falling-Film Evaporation with Structured Surfaces, *J. Heat Transfer*, Vol. 111, pp. 518-524.
- Chyu, M.-C., Bergles, A.E., and Mayinger, F. (1982).** Enhancement of Horizontal Tube Spray Film Evaporators, *Proc. 7<sup>th</sup> International Heat Transfer Conf.*, Munich, Vol. 6, pp. 275-280.
- Chyu, M.-C., Zeng, X., Ayub, Z.H. (1995).** Nozzle-Sprayed Flow Rate Distribution on a Horizontal Tube Bundle, *ASHRAE Trans.*, Vol. 101, Part 2, Paper 3919.
- Cicchitti, A., Lombardi, C., Silvestri, M., Soldaini, G. and Zavattarelli, R. (1960).** Two-Phase Cooling Experiments – Pressure Drop, Heat Transfer and Burnout Measurements, *Energia Nucleare*, Vol. 7, pp. 407-425.
- Cognata, T., Hollingsworth, K. and Witte, L. (2006).** High-Speed Visualization of Two-Phase Flow in a Micro-Scale Pin-Fin Heat Exchanger, *Heat Transfer Engineering*, Vol. 28, No. 9.
- Colburn, A.P. (1934).** Notes on the Calculation of Condensation where a Portion of the Condensate Layer is in Turbulent Motion, *Trans. AIChE*, Vol. 30, pp. 187-193.
- Coleman, J.W. and Garimella, S. (1999).** Characterization of Two-Phase Flow Patterns in Small Diameter Round and Rectangular Tubes, *Int. J. Heat Mass Transfer*, Vol. 42, pp. 2869-2881.

- Coleman, J.W. and Garimella, S. (2000).** Two-Phase Flow Regime Transitions in Microchannel Tubes: the Effect of Hydraulic Diameter, *Proceedings of the ASME Heat Transfer Division*, Vol. 4, pp. 71-83.
- Coleman, J.W. and Garimella, S. (2003).** Two-Phase Flow Regimes in Round, Square and Rectangular Tubes during Condensation of Refrigerant R134a, *Int. J. Refrig.*, Vol. 26, pp. 117-128.
- Colgan, E.G., Furman, B., Gaynes, M., Graham, W.S., LaBianca, N.C., Magerlein, J.H., Polastre, R.J., Rothwell, M.B., Bezama, R.J., Choudhary, R., Marston, K.C., Toy, H., Zitz, J.A. and Schmidt, R.R. (2007).** A Practical Implementation of Silicon Microchannel Coolers for High Power Chips, *IEEE Trans. of Components and Packaging Technologies*, Vol. 30, No. 2, pp. 218-225.
- Collier, J.G. (1982).** Heat Transfer in the Postburnout Region and during Quenching and Reflooding, in *Handbook of Multiphase Flows*, G. Hetsroni, ed., Hemisphere, New York, Section 6.5, pp. 6-142 to 6-188.
- Collier, J.G. and Thome, J.R. (1994).** *Convective Boiling and Condensation*, 3<sup>rd</sup> Edition, Oxford University Press, Oxford.
- Collier, J. G. and Thome, J. R. (1996).** *Convective Boiling and Condensation*, 3rd Edition, Oxford University Press, Oxford (paperback edition).
- Consolini, L. (2008).** Convective Boiling Heat Transfer in a Single Micro-Channel, Ph.D. thesis, Ecole Polytechnique Fédérale de Lausanne, Lausanne, Switzerland, available for free downloading at <http://library.epfl.ch/en/theses/?nr=4024>.
- Consolini, L., Robinson, D. and Thome, J.R. (2006).** Void Fraction and Two-Phase Pressure Drops for Evaporating Flow over Horizontal Tube Bundles, *Heat Transfer Engineering*, Vol. 27, No. 3, pp. 5-21.
- Cooper, M.G. (1984).** Heat Flow Rates in Saturated Nucleate Pool Boiling – A Wide Ranging Examination using Reduced Properties, *Advances in Heat Transfer*, Eds. Hartnett and Irvine, Academic Press, Princeton, Vol. 16, pp. 157-239.
- Cooper, M.K. (1984a).** Saturated Nucleate Pool Boiling: A Simple Correlation, 1st U.K. National Heat Transfer Conference, Vol. 2, pp. 785-793.
- Cooper, M.K. (1984b).** *Advances in Heat Transfer*, Academic Press, Orlando, Vol. 16, pp. 157-139.
- Cornwell, K. (1989).** The Influence of Bubbly Flow on Boiling from a Tube in a Bundle, *Advances in Pool Boiling Heat Transfer*, Eurotherm No. 8, Paderborn, Germany, May 11-12, pp. 177-184.
- Cornwell, K., Duffin, N.W. and Schuller, R.B. (1980).** An Experimental Study of the Effects of Fluid Flow on Boiling within a Kettle Reboiler Tube Bundle, ASME Paper No. 80-HT-45.
- Cornwell, K. and Kew, P.A. (1992).** Boiling in Small Channels. *Proceedings of CEC Conference on Energy Efficiency in Process Technology*, P. Pilavachi (editor), Athens, Elsevier, pp. 624–638.
- Cubaud, T. and Ho, C.M. (2004).** Transport of Bubbles in Square Microchannels, *Phys. Fluids*, Vol. 16, No. 12, pp. 4575-4585.
- Czikk, A.M., O'Neill, P.S. and Gottzmann, C.F. (1981).** Nucleate Boiling from Porous Metal Films: Effect of Primary Variables, *Advances in Enhanced Heat Transfer*, ASME, New York, HTD Vol. 18, pp. 109-122.
- Damianides, C.A. and Westwater, J.M. (1988).** Two-Phase Flow Patterns in a Compact Heat Exchanger and in Small Tubes, *Proceedings 2nd U.K. National Conference on Heat Transfer*, Glasgow, Scotland, Vol. 2, pp. 1257–1268.
- Danilova, G.N., Burkin, V.G. and Dyundin, V.A. (1976).** Heat Transfer in Spray-Type Refrigerator Evaporators, *Heat Transfer-Soviet Research*, Vol. 8, No. 6, pp. 105-113.
- Date, A.W. (1973).** Flow in Tubes Containing Twisted Tapes, *Heating and Ventilating Engineering*, Vol. 47, pp. 240-249.
- Date, A.W. (1974).** Prediction of Fully-Developed Flow in a Tube Containing a Twisted-Tape, *Int. J. Heat Mass Transfer*, Vol. 17, pp. 845-859.

- Date, A.W. and Singham, J.R. (1972).** Numerical Prediction of Friction and Heat-Transfer Characteristics of Fully Developed Laminar Flow in Tubes Containing Twisted Tapes, ASME Paper No. 72-HT-17.
- Del Col, D., Cavallini, A. and Thome, J.R. (2005).** Condensation of Zeotropic Mixtures in Horizontal Tubes: New Simplified Heat Transfer Model Based on Flow Regimes, *J. Heat Transfer*, Vol. 127, pp. 221-230.
- Diehl, J.E. (1957).** Calculate Condenser Pressure Drop, *Hydrocarbon Processing*, Vol. 36, No. 10, pp. 147-153.
- Diehl, J.E. and Unruh, C.H. (1958).** Two-phase Pressure Drop in Horizontal Crossflow through Tube Banks, ASME Paper No. 58-HT-20.
- Dittus, E.J. and Boelter, L.M.K. (1930).** *Publications on Engineering*, Univ. California, Berkeley, Vol. 2, pp. 443.
- Dobson, M.K. and Chato, J.C. (1998).** Condensation in Smooth Horizontal Tubes, *J. Heat Transfer*, Vol. 120, No. 1, pp. 193-213.
- Donevski, B., Plocek, M., Kulesz, J. and Sasic, M. (1990).** Analysis of Tubeside Laminar and Turbulent Flow Heat Transfer with Twisted Tape Inserts, *Heat Transfer Enhancement and Energy Conservation*, Hemisphere Publishing Corp., New York, pp. 175-185.
- Dougall, R.S. and Rohsenow, W.M. (1963).** Film Boiling on the Inside of Vertical Tubes with Upward Flow of the Fluid at Low Vapor Qualities, Mech. Engng. Dept., Engineering Project Laboratory, MIT Report No. 9079-26, September.
- Drew, T.B. (1954).** See McAdams, W.H., *Heat Transmission*, 3<sup>rd</sup> Edition, McGraw-Hill, New York.
- Drizius, M.R.M., Shkema, R.K. and Shlanciauskas, A.A. (1980).** Heat Transfer in a Twisted Stream of Water in a Tube, *International Chemical Engineering*, Vol. 20, pp. 486-489.
- Du, D., Xin, M.D. and Huang, S.M. (1995).** Experiment for Condensing Heat Transfer Performance in Horizontal Three Dimensional Inner Microfin Tubes, *Two-Phase Flow Modelling and Experimentation 1995*, Rome, Vol. 1, pp. 235-241.
- Dukler, A.E. (1960).** Fluid Mechanics and Heat Transfer in Vertical Falling Film Systems, *Chem. Eng. Prog. Symp. Ser.*, Vol. 56, No. 30, pp. 1-10.
- Dukler, A.E., Wicks, M. and Cleveland, R.G. (1964).** Pressure Drop and Hold-Up in Two-Phase Flow Part A- A Comparison of Existing Correlation, Part B - An Approach Through Similarity Analysis, *AICHE Journal*, Vol. 10, pp. 38-51.
- Dunn, B. (1996).** Heat Transfer Characteristics of Alternate Refrigerants Volume 2: Condensation inside Tube, EPRI TR-106016-V2 Report, University of Illinois at Urbana-Champaign, January.
- DuPlessis, J.P. (1982).** Laminar Flow and Heat Transfer in a Smooth Tube with a Twisted-Tape Insert, Ph.D. thesis, University of Stellenbosch, Stellenbosch, South Africa.
- DuPlessis, J.P. and Kröger, D.G. (1983).** Heat Transfer Correlation for Laminar Flow in a Smooth Tube with a Twisted-Tape Insert, Report TW83-9, University of Stellenbosch, Stellenbosch, South Africa.
- Dupont, V., Thome, J.R. and Jacobi, A. (2004).** Heat Transfer Model for Evaporation in Microchannels, Part II: Comparison with the Database, *Int. J. Heat Mass Transfer*, Vol. 47, pp. 3387-3401.
- Ebisu, T. and Torikoshi, K. (1998).** Experimental Study on Evaporation and Condensation Heat Transfer Enhancement for R-407C Using Herringbone Heat Transfer Tube, *ASHRAE Trans.*, Vol. 104, Part 2, Paper TO-98-16-2.
- Eckels, S.J., Doerr, T.M. and Pate, M.B. (1994).** In-Tube Heat Transfer and Pressure Drop of R-134a and Ester Lubricant Mixtures in a Smooth Tube and a Micro-Fin Tube: Part I-Evaporation, *ASHRAE Trans.*, Vol. 100, Part 2, pp. 265-282.
- Eckels, S.J. and Pate, M.B. (1991a).** Evaporation and Condensation of HFC-134a and CFC-12 in a Smooth Tube and a Micro-Fin tube, *ASHRAE Trans.*, Vol. 97, Part 2, pp. 71-81.
- Eckels, S.J. and Pate, M.B. (1991b).** An Experimental Comparison of Evaporation and Condensation Heat Transfer Coefficients for HFC-134a and CFC-12, *Int. J. Refrig.*, Vol. 14, No. 3, pp. 70-77.

- Eckels, S.J., Pate, M.B. and Bemisderfer, C.H. (1992).** Evaporation Heat Transfer Coefficients for R-22 in Micro-Fin Tubes of Different Configurations, *Enhanced Heat Transfer*, ASME HTD Vol. 202, pp. 117-125.
- El Hajal, J., Thome, J.R. and Cavallini, A. (2003).** Condensation in Horizontal Tubes, Part 1: Two-Phase Flow Pattern Map, *Int. J. Heat Mass Transfer*, Vol. 46, pp. 3349-3363.
- Fair, J.R. (1960).** What You Need to Know to Design Thermosyphon Reboilers, *Petroleum Refiner*, Vol. 39, No. 2, pp. 105.
- Fair, J.R. and Klip, A. (1983).** Thermal Design of Reboilers, *Chem. Engng. Prog.*, Vol. 79, No. 8, pp. 86-96.
- Feeenstra, P.A., Weaver, D.S. and Judd, R.L. (2000).** An Improved Void Fraction Model for Two-Phase Cross-Flow in Horizontal Tube Bundles, *Int. J. of Multiphase Flow*, Vol. 26, pp. 1851-1883.
- Fletcher, L.S., Sernas, V. and Galowin, L.S. (1974).** Evaporation from Thin Water Films on Horizontal Tubes, *Industrial Engineering Chemistry-Process Design and Development*, Vol. 13, No. 3, pp. 265-269.
- Forster, H.K. and Zuber, N. (1955).** Dynamics of Vapor Bubble Growth and Boiling Heat Transfer, *AICHE J.*, Vol. 1, pp. 531-535.
- Friedel, L. (1979).** Improved Friction Pressure Drop Correlations for Horizontal and Vertical Two-Phase Pipe Flow, European Two-Phase Flow Group Meeting, Ispra, Italy, June, Paper E2.
- Fritz, W. (1935).** Berechnung des Maximal Volume von Dampfblasen, *Phy. Z.*, Vol. 36, pp. 379-388.
- Fujii, T., Koyama, S., Inoue, N., Kuwahara, K. and Hirakuni, M. (1993).** An Experimental Study of Evaporation Heat Transfer of Refrigerant HCFC22 inside an Internally Grooved Horizontal Tube, *Trans. of JSME*, Vol. 59, No. 562, pp. 2035-2042.
- Fujii, T., Vehara, H., and Kurata, C. (1972).** Laminar Filmwise Condensation of Flowing Vapor on a Horizontal Cylinder, *Int. J. Heat Mass Transfer*, Vol. 15, pp. 235-246.
- Fujita, Y. and Tsutsui, M. (1996).** Experimental and Analytical Study of Evaporation Heat Transfer in Falling Films on Horizontal Tubes, *Proc. 10<sup>th</sup> International Heat Transfer Conference*, Brighton, Vol. 6, pp. 175-180.
- Gambill, W.R. and Lienhard, J.H. (1989).** An Upper Bound for the Critical Boiling Heat Flux, *J. Heat Transfer*, Vol. 111, pp. 815-818.
- Ganic, E.N. and Rohsenow, W.M. (1977).** Dispersed Flow Heat Transfer, *Int. J. Heat Mass Transfer*, Vol. 20, pp. 855-866.
- Gao, L. and Honda, T. (2005).** Effects of Lubricant Oil on Boiling Heat Transfer of CO<sub>2</sub> inside a Horizontal Smooth Tube, *42nd National Heat Transfer Symposium of Japan*, pp. 269-270.
- Gao, L. and Honda, T. (2005).** An Experimental Study on Flow Boiling Heat Transfer of Carbon Dioxide and Oil Mixtures inside a Horizontal Smooth Tube, *IIR 2005 Vicenza Conference-Thermophysical Properties and Transfer Processes of Refrigerants*, Vicenza, Italy, pp. 237-243.
- Garimella, S. and Christensen, R.N. (1992).** Experimental Investigation of Pressure Drop Characteristics of Annuli with Spirally Fluted Inner Tubes, *Enhanced Heat Transfer*, Eds. M.B. Pate and M.K. Jensen, ASME HTD Vol. 202, pp. 107-116.
- Garimella, S., Killion, J.D. and Coleman, J.W. (2002).** An Experimental Validated Model for Two-Phase Pressure Drop in the Intermittent Flow Regime for Circular Channel, *J. of Fluid Engineering*, Vol. 124, pp. 205-214.
- Gasche, J.L. (2006).** Carbon Dioxide Evaporation in a Single Micro-Channel, *J. Brazilian Soc. Mech. Sci. Eng.*, Vol. 28, No. 1, pp. 69-83.
- Ginoux, J.J. (1978).** *Two-Phase Flows and Heat Transfer with Applications to Nuclear Reactor Design Problems*, Hemisphere, Washington.
- Gambill, W.R. and Bundy, R.D. (1962).** An Evaluation of the Present Status of Swirl Flow Heat Transfer, ASME Paper 62-HT-42, ASME, New York.
- Ghajar, A. J. and Tang, C.C. (2007).** Heat Transfer Measurements, Flow Pattern Maps and Flow Visualization for Non-Boiling Two-Phase Flow in Horizontal and Slightly Inclined Pipe, *Heat Transfer Engineering*, Vol. 28, No. 6 (in press).

- Ghajar, A.J. and Madon, K.F. (1992).** Pressure Drop Measurements in the Transition Region for a Circular Tube with Three Different Inlet Configurations, *Experimental Thermal and Fluid Science*, Vol. 5, pp. 129-135.
- Ghajar, A.J. and Tam, L.M. (1994).** Heat Transfer Measurements and Correlations in the Transition Region for a Circular Tube with Three Different Inlet Configurations, *Experimental Thermal and Fluid Science*, Vol. 8, pp. 79-90.
- Ghajar, A.J. and Tam, L.M. (1995).** Flow Regime Map for a Horizontal Pipe with Uniform Wall Heat Flux and Three Inlet Configurations, *Experimental Thermal and Fluid Science*, Vol. 10, pp. 287-297.
- Ghajar, A.J., Tam, L.M. and Tam, S.C. (2004).** Improved Heat Transfer Correlation in the Transition Region for a Circular Tube with Three Inlet Configurations Using Artificial Neural Networks, *Heat Transfer Engineering*, Vol. 25, No. 2, pp. 30-40.
- Gnielinski, V. (1976).** *Int. Chem. Eng.*, Vol. 6, pp. 359-368.
- Gnielinski, V. (1995).** Ein Neues Berechnungsverfahren fur die Wärmeübertragung im Übergangsbereich zwischen Laminaren und Turbulenter Rohstromung, *Forschung im Ingenieurwesen-Engineering Research*, Vol. 61, pp. 240-248.
- Gorenflo, D. (1993).** Pool Boiling, VDI-Heat Atlas, VDI-Verlag, Düsseldorf (English version).
- Gorenflo, D. and Koster, R. (1997).** Pool Boiling Heat Transfer from Horizontal Tubes to Mixtures, Convective Flow Boiling and Pool Boiling Conference, Irsee, Germany, May 18-23.
- Gorenflo, D. and Kotthoff, S. (2006).** Review on Pool Boiling Heat Transfer of Carbon Dioxide, *Int. J. Refrigeration*, Vol. 28, pp. 1169-1185.
- Grant, I.D.R. (1973).** Two-Phase Flow and Pressure Drop on the Shell-Side of Shell-and-Tube Heat Exchangers, *Heat and Fluid Flow in Steam and Gas Turbine Plants*, Pub. No. 3, Inst. Mech. Engr., London, pp. 244-251.
- Grant, I.D.R. and Chisholm, D. (1979).** Two-Phase Flow on the Shell-Side of a Segmentally Baffled Shell-and-Tube Heat Exchanger, *J. Heat Transfer*, Vol. 101, pp. 38-42.
- Grant, I.D.R. and Murray (1972).** Pressure Drop on the Shell-Side of a Segmentally Baffled Shell-and-Tube Heat Exchanger with Vertical Two-Phase Flow, NEL Report, No. 500.
- Grant, I.D.R. and Murray (1974).** Pressure Drop on the Shell-Side of a Segmentally Baffled Shell-and-Tube Heat Exchanger with Horizontal Two-Phase Flow, NEL Report, No. 560.
- Gregorig, R. (1954).** Film Condensation on Finely Rippled Surface with Consideration of Surface Tension, *Z. Agnew. Math. Phys.*, Vol. 5, pp. 36-49.
- Griffith, P. (1983).** Dropwise Condensation, *Heat Exchanger Design Handbook*, Vol. 2, Chapter 2.6.5, Hemisphere, Washington.
- Groeneveld, D.C. (1973).** Post-Dryout Heat Transfer at Reactor Operating Conditions, Report AECL-4513 (ANS topical meeting on Water Reactor Safety, Salt Lake City).
- Groeneveld, D.C. and Delorme, G.G.J. (1976).** Prediction of the Thermal Non-Equilibrium in the Post-Dryout Regime, *Nuclear Engineering and Design*, Vol. 36, pp. 17-26.
- Grönnerud, R. (1972).** Investigation in Liquid Holdup, Flow Resistance and Heat Transfer in Circular Type Evaporators, Part IV: Two-Phase Resistance in Boiling Refrigerants, *Bulletin de l'Inst. du Froid*, Annexe 1972-1.
- Gross, U. (1994).** Falling Film Evaporation Inside a Closed Thermosyphon, *Proc. 10<sup>th</sup> International Heat Transfer Conference*, Brighton, Vol. 7, pp. 443-448.
- Gstöhl, D. and Thome, J.R. (2006a).** Film Condensation of R-134a on Tube Arrays with Plain and Enhanced Surfaces: Part I – Experimental Heat Transfer Coefficients, *J. Heat Transfer*, Vol. 128, pp. 21-32.
- Gstöhl, D. and Thome, J.R. (2006b).** Film Condensation of R-134a on Tube Arrays with Plain and Enhanced Surfaces: Part II – Prediction Methods, *J. Heat Transfer*, Vol. 128, pp. 33-43.
- Gstöhl, D. and Thome, J.R. (2006c).** Visualization of R-134a Flowing on Tube Arrays with Plain and Enhanced Surfaces under Adiabatic and Condensing Conditions, *Heat Transfer Engineering*, Vol. 27(10), pp. 44-62.

- Gungor, K.E. and Winterton, R.H.S. (1986).** A General Correlation for Flow Boiling in Tubes and Annuli, *Int. J. Heat Mass Transfer*, Vol. 29, pp. 351-358.
- Gungor, K.E. and Winterton, R.H.S. (1987).** Simplified General Correlation for Saturated Flow Boiling and Comparisons of Correlations with Data, *Chem. Eng. Res. Des.*, Vol.65, pp. 148-156.
- Gupte, N. and Webb, R.L. (1995a).** Shell-Side Boiling in Flooded Refrigerant Evaporators Part I: Integral Finned Tubes, *HVAC&R Research*, ASHRAE, Vol. 1, Part 1, pp. 35-47.
- Gupte, N. and Webb, R.L. (1995b).** Shell-Side Boiling in Flooded Refrigerant Evaporators Part II: Enhanced Tubes, *HVAC&R Research*, ASHRAE, Vol. 1, Part 1, pp. 48-60.
- Habert, M. (2009).** Falling Film Evaporation on a Tube Bundle with Plain and Enhanced Tubes, Ph.D. thesis, Ecole Polytechnique Fédérale de Lausanne, Department of Mechanical Engineering, available for free at <http://library.epfl.ch/theses/?display=detail&nre=4341>.
- Habert, M. and Thome, J.R. (2010a).** Falling Film Evaporation on Tube Bundle with Plain and Enhanced Tubes, Part I: Experimental Results, *Experimental Heat Transfer*, Vol. 23.
- Habert, M. and Thome, J.R. (2010b).** Falling Film Evaporation on Tube Bundle with Plain and Enhanced Tubes, Part II: New Prediction Methods, *Experimental Heat Transfer*, Vol. 23.
- Hausen, H.Z. (1943).** *VDI Beith. Verfahrenstechn.*, Vol. 4, pp. 91.
- Herwig, H. and Hausner, O. (2003).** Critical View on “New Results in Micro-Fluid Mechanics”: an Example, *Int. J. Heat Mass Transfer*, Vol. 46, pp. 935-937.
- Hetsroni, G. (2005).** Flow and Heat Transfer in Micro-Channels, *5<sup>th</sup> International Symposium on Multiphase Flow, Heat Mass Transfer and Energy Conversion*, Xi'an, China, July 3-6, pp. 26-38.
- Hetsroni, G., Mosyak, A., Pogrebnyak, E. and Yarin, L.P. (2005).** Heat Transfer in Micro-Channels: Comparison of Experiments with Theory and Numerical Results, *Int. J. Heat Mass Transfer*, Vol. 48, pp. 5580-5601.
- Hetsroni, G., Mosyak, A., Segal, Z. and Pogrebnyak, E. (2003).** Two-Phase Flow Patterns in Parallel Microchannels, *Int. J. Multiphase Flow*, Vol. 29, pp. 341-360.
- Hetsroni, G., Mosyak, A., Segal, Z. and Ziskind, G. (2002).** A Uniform Temperature Heat Sink for Cooling of Electronic Devices, *Int. J. Heat Mass Transfer*, Vol. 45, pp. 3275-3286.
- Hewitt, G.F. and Jayanti, S. (1992).** Prediction of Film Inversion in 2-Phase Flow in Coiled Tubes, *J. Fluid Mechanics*, Vol. 236, pp. 497-511.
- Hewitt, G.F., Martin, C.J. and Wilkes, N.S. (1985).** Experimental and Modeling Studies of Annular Flow in the Region between Flow Reversal and the Pressure Drop Minimum, *Physico Chemical Hydrodynamics*, Vol. 6, pp. 69-86.
- Hewitt, G.F. and Roberts, D.N. (1969).** Studies of Two-Phase Flow Patterns by Simultaneous X-ray and Flash Photography, AERE-M 2159, HMSO.
- Hewitt, G. F. and Whalley, P. B. (1980).** Advanced Optical Instrumentation Methods, *Int. J. Multiphase Flow*, Vol. 6, No. 12, pp. 136-156.
- Hewitt, G.F., Whalley, P.B. and Terry, J.W. (1979).** Photographic Studies of Two Phase using a Parallel Light Technique, UKAEA Harwell Report No. AERE-R9389, Harwell, United Kingdom.
- Hewitt, N.J. and McMullan, J.T. (1995).** Refrigerant-Oil Solubility and Its Effect on System Performance, *Proc. 19<sup>th</sup> International Congress of Refrigeration*, The Hague, Vol. IVa, pp. 290-296.
- Hihara, E. (2000).** Heat Transfer Characteristics of CO<sub>2</sub>, *Workshop Proceedings - Selected Issues on CO<sub>2</sub> as working Fluid in Compression Systems*, Trondheim, Norway, pp. 77-84.
- Hinton, D.L., Conklin, J.C. and Vineyard, E.A. (1992).** Evaporation Characteristics of R22 Flowing inside a Corrugated Tube, *Enhanced Heat Transfer*, ASME HTD Vol. 202, pp. 127-132.
- Honda, H., Uchima, B., Nozu, S., Nakata, H. and Fujii, T. (1989).** Condensation of Downward Flowing R-113 Vapor on Bundles of Horizontal Smooth Tubes, *Heat Transfer-Japanese Research*, Vol. 18, No. 6, pp. 31-52.
- Honda, H. and Nozu, S. (1986).** A Prediction Method for Heat Transfer during Film Condensation on Horizontal Low Integral-Fin Tubes, *J. Heat Transfer*, Vol. 108, pp. 218-225.

- Honda, H., Nozu, S. and Takeda, Y. (1987).** Flow Characteristics of Condensation on a Vertical Column of Horizontal Tubes, *Proc. 1987 ASME-JSME Thermal Engineering Joint Conference*, Honolulu, Vol. 1, pp. 517-524.
- Honda, Nozu, S. and Mitsumori, K. (1983).** Augmentation of Condensation on Horizontal Finned Tubes by Attaching a Porous Drainage Plate, *Proc. ASME-JSME Thermal Engng. Joint Conference*, Vol. 3, pp. 289-296.
- Hong, S.W. and Bergles, A.E. (1976).** Augmentation of Laminar Flow Heat Transfer in Tubes by Means of Twisted-Tape Inserts, *J. Heat Transfer*, Vol. 98, pp. 251-256.
- Hou, H., Holste, J.C., Gammon, B.E. and Marsh, K.N. (1992).** Experimental Densities for Compressed R134a, *Int. J. Refrig.*, Vol. 15, No. 6, pp. 365-371.
- Huo, Y., Tian, Y.S., Wadekar, V.V., Karayiannis, T.G. (2001).** Review of Aspects of Two-Phase Flow and Boiling Heat Transfer in Small Diameter Tubes, *Proc. 3rd Int. Conf. on Compact Heat Exchangers and Enhancement Technology for the Process Industries*, Davos, Switzerland, 335-346.
- Hu, X. and Jacobi, A.M. (1996a).** The Intertube Falling Film: Part 1-Flow Characteristics, Mode Transitions, and Hysteresis, *J. Heat Transfer*, Vol. 118, August, pp. 616-625.
- Hu, X. and Jacobi, A.M. (1996b).** The Intertube Falling Film: Part 2-Mode Effects on Sensible Heat Transfer to a Falling Liquid Film, *J. Heat Transfer*, Vol. 118, August, pp. 626-633.
- Hu, X. and Jacobi, A.M. (1998).** Departure-Site Spacing for Liquid Droplets and Jets Falling between Horizontal Circular Tubes, *Experimental Thermal and Fluid Science*, Vol. 16, pp. 322-331.
- Hughmark, G.A. (1962).** Hold-up in Gas Liquid Flow, *Chemical Engineering Progress*, Vol. 58, No. 4, pp. 62-65.
- Ibragimov, M.H., Nomofelov, E.V. and Subbotin, V.I. (1961).** Heat Transfer and Hydraulic Resistance with Swirl-Type Motion of Liquid in Pipes, *Teploenergetika*, Vol. 8, No. 7, pp. 57-60 (in Russian).
- Incropera, F.P. and DeWitt, D.P. (1981).** *Fundamentals of Heat Transfer*, Wiley, New York, 780.
- Ishii, M. (1975).** *Thermo-Fluid Dynamic Theory of Two-Phase Flow*, Chapters 9 and 10, Eyrolles, Paris, Scientific and Medical Publication of France, New York.
- Ishii, M., Chawla, T.C. and Zuber, N. (1976).** Constitutive Equation for Vapor Drift Velocity in Two-Phase Annular Flow, *AICHE J.*, Vol. 22, No. 2, pp. 283-289.
- Ishii, M. (1977).** One Dimensional Drift-Flux Model and Constitutive Equations for Relative Motion between Phases in Various Two-Phase Flow Regimes, Argonne National Laboratory, Report ANL-77-47, October, Argonne, IL.
- Ishihara, K., Palen, J. W. and Taborek, J. (1980).** Critical Review of Correlations for Predicting Two-Phase Pressure Drop across Tube Banks, *Heat Transfer Engineering*, Vol. 1, pp. 23-32.
- Jacobi, A. and Thome, J.R. (2002).** Heat Transfer Model for Evaporation of Elongated Bubble Flows in Microchannels, *J. Heat Transfer*, Vol. 124, pp. 1131-1136.
- Jassim, E.W., Newell, T.A. and Chato, J.C. (2006).** Two-Phase Flow Visualization in Chevron and Bumpy Style Flat Plate Heat Exchangers, *Heat Transfer Engineering*, Vol. 27, pp. 20-27.
- Jassim, E.W., Newell, T.A., Chato, J.C. (2007).** Probabilistic Determination of Two-Phase Flow Regimes in Horizontal Tubes Utilizing an Automated Image Recognition Technique, *Experiments in Fluids*, in review.
- Jassim, E.W. (2000).** Investigation of Adiabatic Refrigerant Pressure Drop and Flow Visualization in Flat Plate Evaporators, M.S. Thesis, Department of Mechanical and Industrial Engineering at the University of Illinois at Urbana-Champaign, Urbana, IL, USA.
- Jassim, E.W. (2006).** Probabilistic Flow Regime Map Modeling of Two-Phase Flow, Ph.D. thesis, Department of Mechanical Science Engineering, University of Illinois at Urbana-Champaign, Urbana, IL, USA.
- Jaster, H. and Kosky, P.G. (1976).** Condensation Heat Transfer in a Mixed Flow Regime, *Int. J. Heat Mass Transfer*, Vol. 19, pp. 95-99.

- Jensen, M.K. (1988).** Boiling on the Shellside of Horizontal Tube Bundles, *Two-Phase Flow Heat Exchangers*, Kluwer, Dordrecht, The Netherlands, pp. 707-746.
- Jensen, M.K. (1985).** Physical Properties, Data Tables and Experimental Boiling Data, Personal Communication, cf. Ribatski and Saiz Jabardo (2003).
- Jensen, M.K. and Bensler, H.P. (1986).** Saturated Forced-Convection Boiling Heat Transfer with Twisted-Tape Inserts, *J. Heat Transfer*, Vol. 108, pp. 93-99.
- Jensen, M.K. and Memmel, G.J. (1986).** Evaluation of Bubble Departure Diameter Correlations, *Proceedings 8th Int. Heat Transfer Conf.*, San Francisco, Vol. 4, pp. 1907-1912.
- Jeong, S., Cho, E., and Kim, H. (2005).** Evaporative Heat Transfer and Pressure Drop in a Microchannel Tube, *Proceedings of the 3rd International Conference on Microchannels and Minichannels*, Toronto, Canada, Part B, pp. 103-108.
- Jiang, L., Koo, J.M., Zhang, L., Wang, E., Im, S., Yao, S., Zeng, S., Bari, A., Santiago, J.G., Kenny, T.W. and Goodson, K.E. (2002).** Progress on Two-Phase Convection in Microchannel Heat Sinks, *Proceedings of Fourth Pacific Rim Thermal Science and Energy Workshop (PARTSEE-4)*, May 31-June 2, Kyoto, pp. 124-129.
- Jung, D. S., McLinden M., Radermacher R., Didion D. (1989).** A Study of Flow Boiling Heat Transfer with Refrigerant Mixtures, *Int. J. Heat Mass Transfer*, Vol. 32, No. 9, pp. 1751-1764.
- Kabelac, S. and de Buhr, H.J. (2001).** Flow Boiling of Ammonia in a Plain and a Low Finned Horizontal Tube, *Int. J. Refrig.*, Vol. 24, pp. 41-50.
- Kalinin, E.K. and Yarkho, C.A. (1971).** Study of Intensification of Heat Transfer to Liquids and Gases in Channels, *Journal of Engineering Physics*, Vol. 20, pp. 592-599.
- Kandlikar, S.G. (1990).** A General Correlation of Saturated Two-Phase Flow Boiling Heat Transfer inside Horizontal and Vertical Tubes, *J. Heat Transfer*, Vol. 112, pp. 219-228.
- Kandlikar, S.G. (1991).** A Model for Predicting the Two-Phase Flow Boiling Heat Transfer Boiling Heat Transfer Coefficient in Augmented Tubes and Compact Evaporator Geometries, *J. Heat Transfer*, Vol. 113, pp. 966-972.
- Kandlikar, S.G. (2001).** Two-Phase Flow Patterns, Pressure Drop and Heat Transfer during Boiling in Minichannel and Microchannel Flow Passages of Compact Heat Exchangers, *Compact Heat Exchangers and Enhancement Technology for the Process Industries – 2001*, Begell House, New York, 319-334.
- Kandlikar, S.G. and Balasubramanian, P. (2004).** An Extension of the Flow Boiling Correlation to Transition, Laminar, and Deep Laminar Flows in Minichannels and Microchannels, *Heat Transfer Engineering*, Vol. 25, pp. 86-93.
- Kandlikar, S.G. and Garimella, S. (2005).** *Heat Transfer and Fluid Flow in Minichannels and Microchannels*, Elsevier Science, USA.
- Kandlikar, S.G., and Grande, W.J. (2003).** Evolution of Microchannel Flow Passages – Thermohydraulic Performance and Fabrication Technology, *Heat Transfer Engineering*, 24(1), pp. 3-17.
- Kandlikar, S.G., Joshi, S. and Tian, S. (2001).** Effect of Channel Roughness on Heat Transfer and Fluid Flow Characteristics at Low Reynolds Numbers in Small Diameter Tubes, *Proc. of 35th National Heat Transfer Conference*, Anaheim, Paper 12134.
- Kandlikar, S.G. and Raykoff, T. (1997).** Predicting Flow Boiling Heat Transfer of Refrigerants in Microfin Tubes, *J. Enhanced Heat Transfer*, Vol. 4, No. 4, pp. 257-268.
- Kasza, K.E., Didascalou, T. and Wambsganss, M.W. (1997).** Microscale Flow Visualization of Nucleate Boiling in Small Channels: Mechanisms Influencing Heat Transfer, *Proceedings of International Conference on Compact Heat Exchangers for Process Industries*, R.K. Shah (editor), Begell House, New York, pp. 343-352.
- Kattan, N., Thome, J.R. and Favrat, D. (1995a).** R-502 and Two Near Azeotropic Alternatives Part II: Two-Phase Flow Patterns, *ASHRAE Trans.*, Vol. 101, Part 1, paper CH-95-14-3.
- Kattan, N., Thome, J.R. and Favrat, D. (1995b).** Int. Congress of Refrigeration, *The Hague*, Vol. 4.

- Kattan, N., Thome, J.R. and Favrat, D. (1998a).** Flow Boiling in Horizontal Tubes. Part 1: Development of a Diabatic Two-Phase Flow Pattern Map, *J. Heat Transfer*, Vol. 120, No. 1, pp. 140-147.
- Kattan, N., Thome, J.R. and Favrat, D. (1998b).** Flow Boiling in Horizontal Tubes. Part 2: New Heat Transfer Data for Five Refrigerants, *J. Heat Transfer*, Vol. 120, No. 1, pp. 148-155.
- Kattan, N., Thome, J.R. and Favrat, D. (1998c).** Flow Boiling in Horizontal Tubes. Part 3: Development of a New Heat Transfer Model Based on Flow Patterns, *J. Heat Transfer*, Vol. 120, No. 1, pp. 156-165.
- Katto, Y. and Ohno, H. (1984).** An Improved Version of the Generalized Correlation of Critical Heat Flux for the Forced Convective Boiling in Uniformly Heated Vertical Channels, *Int. J. Heat Mass Transfer*, Vol. 27, pp. 1641-1648.
- Katto, Y. and Shimizu, M. (1979).** Upper Limit of the CHF in the Forced Convective Boiling on a Heated Disc with a Small Impinging Jet, *J. Heat Transfer*, Vol. 101, pp. 265-269.
- Kaul, M.P., Kedzierski, M.A. and Didion, D. (1996).** Horizontal Flow Boiling of Alternative Refrigerants within a Fluid Heated Micro-Fin Tube, in *Process, Enhanced, and Multiphase Heat Transfer, Afestschirft for A.E. Bergles*, Begell House, New York, pp. 167-173.
- Kawaji, M. (2007).** Personal communication.
- Kawaji, M. and Chung, M.Y. (2003).** Unique Characteristics of Adiabatic Gas-Liquid Flows in Microchannels: Diameter and Shape Effects on Flow Patterns, Void Fraction and Pressure Drop, *Proceedings of the 1<sup>st</sup> International Conference on Microchannels and Minichannels*, April 24-25, Rochester, NY, pp. 115-128.
- Kawahara, A., Sadatomi, M., Okayama, K., Kawaji, M., and Chung, P.M.Y. (2005).** Effects of Channel Diameter and Liquid Properties on Void Fraction in Adiabatic Two-Phase Flow through Microchannels, *Heat Transfer Engineering*, Vol. 26, No. 3, pp. 13-19.
- Kedzierski, M.A. (1995).** Calorimetric and Visual Measurements of R123 Pool Boiling on Four Enhanced Surfaces, National Institute of Standards and Technology, Gaithersburg, MD, Report NISTIR 5732.
- Kedzierski, M.A. and Goncalves, J.M. (1997).** Horizontal Convective Condensation of Alternative Refrigerants within a Micro-Fin Tube, National Institute of Standards and Technology, Gaithersburg, MD, Report NISTIR 6095.
- Kedzierski, M.A. and Kim, M.S. (1997).** Convective Boiling and Condensation Heat Transfer with a Twisted-Tape Insert for R12, R22, R152a, R134a, R290, R32/R134a, R32/R152a, R290/R134a, R134a/R600a, *Thermal Science & Engineering*, Vol. 6, No. 1, pp. 113-122.
- Kedzierski, M.A. and Kim, M.S. (1998).** Convective Boiling and Condensation Heat Transfer with a Twisted-Tape Insert for R12, R22, R152a, R134a, R290, R32/R134a, R32/R152a, R290/R134a, R134a/R600a, National Institute of Standards and Technology, Gaithersburg, MD, Report NISTIR 5905.
- Kern, D.Q. (1950).** *Process Heat Transfer*, McGraw-Hill, New York.
- Kern, D.Q. (1958).** Mathematical Development of Loading in Horizontal Condensers, *AIChE J.*, Vol. 4, No. 2, pp. 157-160.
- Kew, P. and Cornwell, K. (1997).** Correlations for Prediction of Boiling Heat Transfer in Small Diameter Channels, *Applied Thermal Engineering*, Vol. 17, No. 8-10, pp. 705-715.
- Khodabandeh, R. (2003).** Influence of Channel Diameter on Boiling Heat Transfer in a Closed Advanced Two-Phase Thermosiphon Loop, *Proc. 5<sup>th</sup> International Boiling Conference*, Montego Bay, Jamaica, May 4-8.
- Kidd, G.J. (1969).** Heat Transfer and Pressure Drop for Nitrogen Flowing in Tubes Containing Twisted Tapes, *AIChE Journal*, Vol. 15, pp. 581-585.
- Kido, O., Taniguchi, M., Taira, T. and Uehara, H. (1995).** Evaporation Heat Transfer of HCFC22 inside an Internally Grooved Horizontal Tube, *ASME/JSME Thermal Engineering Joint Conference*, Maui, March 19-24, Vol. 2, pp. 323-330.

- Kim M. S., Chang Y. S. and Ro S. T. (1996).** Performance and Heat Transfer of Hydrocarbon Refrigerants and Their Mixtures in a Heat Pump System, *Proc. of IIR Meeting of Comm. B1, B2, E1, E2*, Aarhus, pp. 477-486.
- Kliebe, D. (1978).** Waermedurchgangsuntersuchungen am Ringspalt zwischen einem Turbotec – Rohr und einem Glattrohr, Diplom-Arbeit, Fachhochschule Giessen, Germany.
- Klimenko, V.V. (1988).** A Generalized Correlation for Two-Phase Forced Flow Heat Transfer, *Int. J. Heat Mass Transfer*, Vol. 31, No. 3, pp. 541-552.
- Knudsen, H.K. and Jensen, R.H. (1997).** Heat Transfer Coefficient for Boiling Carbon Dioxide, *Workshop Proceedings - CO<sub>2</sub> Technologies in Refrigeration, Heat Pumps and Air Conditioning Systems*, Trondheim, Norway, pp. 319-328.
- Kondo, M. and Nakajima, K.I. (1980).** Experimental Investigation of Air-Water Two-Phase Upflow Across Horizontal Tube Bundles (Part I: Flow Pattern and Void Fraction), *Bulletin of the JSME*, Vol. 23, No. 177, pp. 385-393.
- Koyama, S., Kuwahara, K., Shinmura, E. and Ikeda, S. (2001).** Experimental Study on Flow Boiling of Carbon Dioxide in a Horizontal Small Diameter Tube, IIR Commission B1 Meeting, Paderborn, Germany, pp. 526-533.
- Koyama, S., Miyara, A., Takamatsu, H. and Fujii, T. (1990).** Condensation Heat Transfer of Binary Refrigerant Mixtures of R22 and R114 inside a Horizontal Tube with Internal Spiral Grooves, *Int. J. Refrig.*, Vol. 13, No. 7, pp. 256-263.
- Koyama, S., Yu, J., Momoki, S., Fujii, T. and Honda, H. (1996).** Forced Convective Flow Boiling Heat Transfer of Pure Refrigerants inside a Horizontal Microfin Tube, *Convective Flow Boiling*, Eds. J.C. Chen et al., Taylor & Francis, pp. 137-142.
- Kuo, C.S. and Wang, C.C. (1996a).** Horizontal Flow Boiling of R22 and R407C in a 9.52 mm Micro-Fin Tube, *Applied Thermal Engineering*, Vol. 16, Nos. 8/9, pp. 719-731.
- Kuo, C.S. and Wang, C.C. (1996b).** In-tube Evaporation HFC-22 in a 9.52 mm Micro-Fin/Smooth Tube, *Int. J. Heat Mass Transfer*, Vol. 39, No. 12, pp. 2559-2569.
- Kuo, C.S., Wang, C.C., Cheng, W.Y. and D.C. Lu, D.C. (1995).** Evaporation of R-22 in a 7-mm Microfin Tube, *ASHRAE Trans.*, Vol. 101, Part 2, pp. 1055-1061.
- Kutateladze, S.S. (1948).** On the Transition to Film Boiling under Natural Convection, *Kotloturbostroenie*, No. 3, pp. 10 and 152-158.
- Kutateladze, S.S. (1961).** Boiling Heat Transfer, *Int. J. Heat Mass Transfer*, Vol. 4, pp. 3-45.
- Kutateladze, S.S. (1963).** *Fundamentals of Heat Transfer*, Academic Press, New York.
- Kutateladze, S.S. (1982).** Semi-Empirical Theory of Film Condensation of Pure Vapors, *Int. J. Heat Mass Transfer*, Vol. 25, pp. 653-660.
- Kutateladze, S.S. and Gogonin, I.I. (1979).** Heat Transfer in Film Condensation of Slowly Moving Vapor, *Int. J. Heat Mass Transfer*, Vol. 22, pp. 1593-1599.
- Kutateladze, S.S. and Gogonin, I.I. (1979a).** Growth Rate and Detachment Diameter of a Vapor Bubble in Free Convection Boiling of a Saturated Liquid, *High Temperature*, Vol. 17, pp. 667-671.
- Labuntsov, D.A. (1957).** Heat Transfer in Film Condensation of Steam on a Vertical Surface and Horizontal Tubes, *Teploenergetika*, Vol. 4, No. 7, pp. 72-80.
- Lahey, R.T., Jr. (1974).** Two-Phase Flow in Boiling Water Nuclear Reactors, *NEDO* 13388.
- Lallemand, M., Branescu, C. and P. Haberschill, P. (2001).** Local Heat Transfer Coefficients during Boiling of R22 and R407C in Horizontal Smooth and Microfin Tubes, *Int. J. Refrig.*, Vol. 24, pp. 57-72 [in French].
- Lan, J., Disimile, P.J. and Weisman, J. (1997a).** Two-Phase Flow Patterns and Boiling Heat Transfer in Tubes Containing Helical Wire Inserts - Part I - Flow Patterns and Boiling Heat Transfer Coefficients, *J. Enhanced Heat Transfer*, Vol. 4, No. 4, pp. 269-282.
- Lan, J., Disimile, P.J. and Weisman, J. (1997b).** Two-Phase Flow Patterns and Boiling Heat Transfer in Tubes Containing Helical Wire Inserts - Part II - Critical Heat Flux Studies, *J. Enhanced Heat Transfer*, Vol. 4, No. 4, pp. 283-296.

- Lavin, J.G. and Young, E.H. (1965).** Heat Transfer to Evaporating Refrigerants in Two-Phase Flow, *AICHE J.*, Vol. 11, no. 6, pp. 1124-1132.
- Lazarek, G.M. and Black, S.H. (1982).** Evaporating Heat Transfer, Pressure Drop and Critical Heat Flux in a Small Vertical Tube with R-113, *Int. J. Heat Mass Transfer*, Vol. 25, pp. 945-960.
- Lee, H.J. and Lee, S.Y. (2001).** Pressure Drop Correlations for Two-Phase Flow within Horizontal Rectangular Channels with Small Heights, *Int. J. Multiphase Flow*, Vol. 27, pp. 783-796.
- Lee, J. (1964).** Turbulent Film Condensation, *AICHE J.*, Vol. 10, pp. 540-544.
- Lee, J. and Mudawar, I. (2005).** Two-Phase Flow in High Heat Flux Microchannel Heat Sink for Refrigeration Cooling Applications, *Int. J. Heat Mass Transfer*, Vol. 48, pp. 928-940.
- Leong, L.S. and Cornwell, K. (1979).** Heat Transfer Coefficients in a Reboiler Tube Bundle, *The Chemical Engineer*, No. 343, pp. 219-221.
- Levi, S. (1967).** Forced Convection Subcooled Boiling Prediction of Vapor Volumetric Fraction, *Int. J. Heat Mass Transfer*, Vol. 10, pp. 951-965.
- Liebenberg, L., Thome, J.R. and Meyer, J.P. (2005).** Flow Visualization and Flow Pattern Identification with Power Spectral Density Distributions of Pressure Traces during Refrigerant Condensation in Smooth and Micro-Fin Tubes, *J. Heat Transfer*, Vol. 127, pp. 209-220.
- Li, H.M., Ye, K.S., Tan, Y.K. and Den, S.J. (1982).** Investigation of Tube-Side Flow Visualization, Friction Factors and Heat Transfer Characteristics of Helical-Ridging Tubes, *Proc. 7<sup>th</sup> International Heat Transfer Conference*, Munich, Vol. 3, pp. 75-80.
- Li, J.M. and Wang, B.X. (2003).** Size Effect on Two-Phase Regime for Condensation in Micro/Mini Tubes, *Heat Transfer-Asian Research*, Vol. 32, pp. 65-71.
- Li, J., Peterson, G.P. and Cheng, P. (2004).** Three-Dimensional Analysis of Heat Transfer in a Micro-Heat Sink with Single Phase Flow, *Int. J. Heat Mass Transfer*, Vol. 47, pp. 4215-4231.
- Lienhard, J.H. and Dhir, V.K. (1973).** Extended Hydrodynamic Theory of the Peak and Minimum Pool Boiling Heat Fluxes, NASA CR-2270, July.
- Lienhard IV, J.H. and Lienhard V, J.H. (2006).** A *Heat Transfer Textbook*, 3<sup>rd</sup> Edition, available at <http://web.mit.edu/lienhard/www/ahttproject.pdf>.
- Lienhard, J.H. and Wong, P.T.Y. (1964).** The Dominant Useable Wavelength and Minimum Heat Flux during Film Boiling on a Horizontal Cylinder, *J. Heat Transfer*, Vol. 86, pp. 220-226.
- Liley, P.E. and Gambill, W.R. (1973).** Physical and Chemical Data, in *Chemical Engineering Handbook*, 5th ed. (Perry and Chilton), McGraw-Hill, New York, Chapter 3, pg. 3-226 to 3-250.
- Lin, S., Kew, P.A. and Cornwell, K. (1998).** Two-Phase Flow Regimes and Heat Transfer in Small Tubes and Channels, *Proceedings of 11th International Heat Transfer Conference*, Kyongju, Korea, Vol. 2, pp. 45-50.
- Lin, S., Kew, P.A. and Cornwell, K. (2001).** Two-Phase Heat Transfer to a Refrigerant in a 1 mm Diameter Tube, *Int. J. Refrig.*, Vol. 24, pp. 51-56.
- Lockhart, R. W. and Martinelli, R. C. (1949).** Proposed Correlation Data for Isothermal Two-Phase Two-Component Flow in Pipes, *Chem. Eng. Progr.*, Vol. 45, pp. 39-45.
- Lopina, R.F. and Bergles, A.E. (1969).** Heat Transfer and Pressure Drop in a Tape Generated Swirl Flow of Single-Phase Water, *J. Heat Transfer*, Vol. 91, pp. 434-442.
- Lorenz, J.J. and Yung, D. (1978).** Combined Boiling and Evaporation of Liquid Films on Horizontal Tubes, Proc. of 5<sup>th</sup> OTEC Conference, Vol. 3, pp. 46-70.
- Lorenz, J.J. and Yung, D. (1979).** A Note on Boiling and Evaporation of Liquid Films on Horizontal Tubes, *J. Heat Transfer*, Vol. 101, pp. 178-180.
- MacArthur, J.W. and Patankar, S.V. (1985).** Effects of Swirling Laminar Flow on Heat Transfer Augmentation in Annular Passages with Twisted Radial Fins, *Advances in Enhanced Heat Transfer – 1985*, ASME HTD Vol. 43, eds. S.M. Shenkman, J.E. O'Brian, I.S. Habib and J.A. Kohler, pp. 73-80.
- MacBain, S.M. and Bergles, A.E. (1996).** Heat Transfer and Pressure Drop Characteristics of Forced Convective Evaporation in Deep Spirally Fluted Tubing, *Convective Flow Boiling*, Eds. J.C. Chen et al., Taylor & Francis, pp. 143-148.

- MacBain, S.M., Bergles, A.E. and Raina, S. (1997).** Heat Transfer and Pressure Drop Characteristics of Flow Boiling in a Horizontal Deep Spirally Fluted Tube, *HVAC&R Research*, Vol. 3, No. 1, pp. 65-80.
- Mahulikar, S.P. and Herwig, H. (2006).** Physical Effects in Laminar Microconvection due to Variations in Incompressible Fluid Properties, *Physics of Fluids*, Vol. 18, no. 073601.
- Malnes, D. (1966).** Slip Ratios and Friction Factors in the Bubble Flow Regime in Vertical Tubes, *KR*, pp. 110.
- Manglik, R.M. and Bergles, A.E. (1986).** An Analysis of Laminar Flow Heat Transfer in Uniform Temperature Circular Tubes with Tape Inserts, Heat Transfer Laboratory Report HTL-39, ISU-ERI-Ames-86290, Iowa State University, Ames, Iowa.
- Manglik, R.M. and Bergles, A.E. (1987).** A Correlation for Laminar Flow Enhanced Heat Transfer in Uniform Wall Temperature Circular Tubes with Twisted-Tape Inserts, *Advances in Enhanced Heat Transfer*, Eds. M.K. Jensen and V.P. Carey, AMSE HTD Vol. 68, pp. 19-25.
- Manglik, R.M. and Bergles, A.E. (1992a).** Heat Transfer and Pressure Drop Correlations for Twisted-Tape Inserts in Isothermal Tubes: Part 1 – Laminar Flows, *Enhanced Heat Transfer*, Eds. M.B. Pate and M.K. Jensen, AMSE HTD Vol. 202, pp. 89-98.
- Manglik, R.M. and Bergles, A.E. (1992).** Heat Transfer and Pressure Drop Correlations for Twisted-Tape Inserts in Isothermal Tubes: Part II – Transition and Turbulent Flows, *Enhanced Heat Transfer*, HTD Vol. 202, ASME, pp. 99-106.
- Manwell, S.P. and Bergles, A.E. (1990).** Gas-Liquid Flow Patterns in Refrigerant-Oil Mixtures, *ASHRAE Trans.*, Vol. 96, Part 2, Paper SL-90-1-4.
- Maranzana, G., Perry, I. and Maillet, D. (2004).** Mini- and Micro-Channels: Influence of Axial Conduction in the Walls, *Int. J. Heat Mass Transfer*, Vol. 47, pp. 3993-4004.
- Marner, W.J. and Bergles, A.E. (1978).** Augmentation of Tubeside Laminar Flow Heat Transfer by Means of Twisted-Tape Inserts, Static-Mixer Inserts, and Internally Finned Tubes, *Heat Transfer 1978, Proc. 6<sup>th</sup> International Heat Transfer Conference*, San Francisco, Hemisphere, Washington, D.C. Vol. 2, pp. 583-588.
- Marner, W.J. and Bergles, A.E. (1985).** Augmentation of Highly Viscous Laminar Tubeside Heat Transfer by Means of a Twisted Tape Insert and Internally Finned Tube, *Advances in Enhanced Heat Transfer – 1985*, ASME HTD Vol. 43, pp. 19-28.
- Martin-Callizo, C., Ali, R. and Palm, B. (2007).** New Experimental Results on Flow Boiling of R-134a in a Vertical Microchannel, *UK Heat Transfer 2007 Proceedings*, Edinburgh, Sept. 10-11, Session 2, Paper 1.
- Marto, P.J. (1986).** Recent Progress in Enhancing Film Condensation Heat Transfer on Horizontal Tubes, *Heat Transfer Engineering*, Vol. 7, pp. 53-63.
- Masuda, H. and Rose, J.W. (1987).** Static Configuration of Liquid Films on Horizontal Tubes with Low Radial Fins, *Proc. Royal Society of London*, Vol. A420, pp. 125-139.
- Mayinger, F. and Langer, H. (1978).** Post-Dryout Heat Transfer, *Proc. 6<sup>th</sup> International Heat Transfer Conference*, Toronto, Vol. 6, pp. 181-198.
- McAdams, W.M. (1954).** *Heat Transmission*, 3<sup>rd</sup> Edition, McGraw-Hill, New York.
- McAdams, W.H., Woods, W.K. and Bryan, R.L. (1942).** Vaporization inside Horizontal Tubes – II – Benzene-Oil Mixtures, *Trans. ASME*, Vol. 64, pp. 193.
- McNaught, J.M. (1982).** Two-Phase Forced Convection Heat-Transfer during Condensation on Horizontal Tube Bundles, *Proc. 7<sup>th</sup> International Heat Transfer Conference*, Munich, Vol. 5, pp. 125-131.
- Médéric, B., Lavieille, P. and Miscevic, M. (2005).** Void Fraction Invariance Property of Complete Condensation Flow inside a Capillary Glass Tube, *Int. J. Multiphase Flow*, Vol. 31, pp. 1049-1058.
- Mehendale, S.S., Jacobi, A.M. (2000).** Evaporative Heat Transfer in Mesoscale Heat Exchangers, *ASHRAE Trans.*, Vol. 106, Part 1, pp. 446-452.

- Mehta, M.H. and Rao, R. (1988).** Analysis and Correlation of Turbulent Flow Heat Transfer and Friction Coefficients in Spirally Corrugated Tubes for Steam Condenser Application, *Proc. of the 1988 National Heat Transfer Conference*, HTD-Vol. 96, ASME, Vol. 3, pp. 307-312.
- Memory, S.B., Akacasayer, N., Eraydin, H. and Marto, P.J. (1995).** Nucleate Pool Boiling of R-114 and R-114-Oil Mixtures from Smooth and Enhanced Surface II. Tube Bundles, *Int. J. Heat Mass Transfer*, Vol. 38, pp. 1363-1376.
- Memory, S.B., Bertsch, G. and Marto, P.J. (1993).** Pool Boiling of HCFC-124-Oil Mixtures from Smooth and Enhanced Surfaces, *Heat Transfer with Alternative Refrigerants*, ASME HTD-Vol. 243, pp. 9-18.
- Memory, S.B., Sugiyama, D.C. and Marto, P.J. (1995).** Nucleate Pool Boiling of R-114 and R-114-Oil Mixtures from Smooth and Enhanced Surface I. Single Tubes, *Int. J. Heat Mass Transfer*, Vol. 38, pp. 1347-1361.
- Mertz, R., Wein, A. and Groll, M. (1996).** Experimental Investigation of Flow Boiling Heat Transfer in Narrow Channels, *Calore e Tecnologia*, Vol. 14, pp. 47-54.
- Meyer, J.J. and Saiz Jabardo, J.M. (1994).** An Ultrasonic Device for Measuring the Oil Concentration in Flowing Liquid Refrigerant, *Int. J. Refrig.*, Vol. 17, No. 7, pp. 481-486.
- Meyer, J.P. and Liebenberg, L. (2006).** In Search of Objective Heat Transfer and Pressure Drop Models, *Proc. 13th International Heat Transfer Conference*, Sydney, August 14-18.
- Mills, A.F. and Chung, D.K. (1973).** Heat Transfer across Turbulent Falling Films, *Int. J. Heat Mass Transfer*, Vol. 16, pp. 694-696.
- Minkowycz, W.J. and Sparrow, E.M. (1966).** Condensation Heat Transfer in the Presence of Non-Condensables, Interfacial Resistance, Superheating, Variable Properties and Diffusion, *Int. J. Heat Mass Transfer*, Vol. 9, pp. 1125-1144.
- Mishima, K. and Hibiki, T. (1996).** Some Characteristics of Air-Water Two-Phase Flow in Small Diameter Vertical Tubes, *Int. J. Multiphase Flow*, Vol. 22, pp. 703-712.
- Mitrovic, J. (1986).** Influence of Tube Spacing and Flow Rate on Heat Transfer from a Horizontal Tube to a Falling Liquid Film, *Proc. 8<sup>th</sup> International Heat Transfer Conference*, San Francisco, Vol. 4, pp. 1949-1956.
- Moeykens, S.A., Huebsch, W.W. and Pate, M.B. (1995a).** Heat Transfer of R-134a in Single-Tube Spray Evaporation including Lubricant Effects and Enhanced Surface Results, *ASHRAE Trans.*, Vol. 101, Part 1, pp. 111-123.
- Moeykens, S.A., Newton, B.J. and Pate, M.B. (1995b).** Effects of Surface Enhancement, Film-Feed Supply Rate, and Bundle Geometry on Spray Evaporation Heat Transfer Performance, *ASHRAE Trans.*, Vol. 101, Part 2, pp. 408-419.
- Moeykens, S.A. and Pate, M.B. (1994).** Spray Evaporation Heat Transfer of R-134a on Plain Tubes, *ASHRAE Trans.*, Vol. 100, Part 2, pp. 173-184.
- Moeykens, S.A. and Pate, M.B. (1995).** The Effects of Nozzle Height and Orifice Size on Spray Evaporation Heat Transfer Performance for a Low-Finned, Triangular-Pitch Tube Bundle with R-134a, *ASHRAE Trans.*, Vol. 101, Part 2, pp. 420-433.
- Moeykens, S.A. and Pate, M.B. (1996).** Effect of Lubricant on Spray Evaporation Heat Transfer Performance of R-134a and R-22 in Tube Bundles, *ASHRAE Trans.*, Vol. 102, Part 1, pp. 410-426.
- Moeykens, S.A., Kelly, J.E. and Pate, M.B. (1996).** Spray Evaporation Heat Transfer Performance of R-123 in Tube Bundles, *ASHRAE Trans.*, Vol. 102, Part 2, pp. 259-272.
- Moller, C., Spindler, K. and Hahne, E. (1993).** Wärmeübergangsmesungen beim Sieden von R134a/Ol Gemischen am Rohr und Draht, *DKV-Tagungsbericht*, Vol. 20, paper 21.
- Monheit, M. (1987).** Experimental Evaluation of the Convective Characteristics of Tubes with Twisted Tape Inserts, *Advances in Enhanced Heat Transfer*, Eds. M.K. Jensen and V.P. Carey, AMSE HTD Vol. 68, pp. 11-18.

- Moreno Quibén, J. (2005).** Experimental and Analytical Study of Two-Phase Pressure Drops during Evaporation in Horizontal Tubes, Ph.D. Thesis no. 3337, Swiss Federal Institute of Technology Lausanne, available for free at <http://library.epfl.ch/theses/?display=detail&nr=3337>.
- Moreno Quibén, J. and Thome, J.R. (2003).** Two-Phase Pressure Drops in Horizontal Tubes: New Results for R-410A and R-134a Compared to R-22, 21<sup>st</sup> IIR International Congress of Refrigeration, Washington, D.C., Aug. 17-22, Paper ICR045.
- Moreno Quibén, J. and Thome, J.R. (2007a).** Flow Pattern Based Two-Phase Frictional Pressure Drop Model for Horizontal Tubes, Part I: Diabatic and Adiabatic Experimental Study, *Int. J. Heat and Fluid Flow*, Vol. 28, pp. 1049-1059.
- Moreno Quibén, J. and Thome, J.R. (2007b).** Flow Pattern Based Two-Phase Frictional Pressure Drop Model for Horizontal Tubes, Part II: New Phenomenological Model, *Int. J. Heat and Fluid Flow*, Vol. 28, pp. 1060-1072.
- Mori, S., Sakakibara, M. and Tanimoto, A. (1974).** Steady Heat Transfer to Laminar Flow in a Circular Tube with Conduction in the Tube Wall, *Heat Transfer-Japanese Research*, Vol. 3(2), pp. 37-46.
- Mori, H., Yoshida, S., Ohishi, K., Kokimoto, Y. (2000).** Dryout Quality and Post-dryout Heat Transfer Coefficient in Horizontal Evaporator Tubes, *Proc of 3<sup>rd</sup> European Thermal Sciences Conference*, pp. 839-844.
- Morini, G.L. (2004).** Single-Phase Convective Heat Transfer in Microchannels: A Review of Experimental Results, *Int. J. of Thermal Sciences*, Vol. 43, pp. 631-651.
- Morini, G.L. (2005).** The Viscous Heating in Liquid Flows in Microchannels, *Int. J. Heat and Mass Transfer*, Vol.48, pp. 3637-3647.
- Morini, G.L. (2006).** Scaling Effects for Liquid Flows in Microchannels, *Heat Transfer Engineering*, Vol. 27(4), pp. 64-73.
- Morini, G.L. and Spiga, M. (2007).** The Role of the Viscous Dissipation in Heated Microchannels, *J. Heat Transfer*, Vol.129, pp. 308-318.
- Morini, G.L. (2008).** Single-Phase Convective Heat Transfer in Laminar and Transitional Regime in Microchannels, ECI International Conference on Heat Transfer and Fluid Flow in Microscale, Whistler, September 21-26.
- Moriyama, K. and Inoue, A. (1996).** Thickness of the Liquid Film Formed by a Growing Bubble in a Narrow Gap between Two Horizontal Plates, *J. Heat Transfer*, Vol. 118, pp. 132-139.
- Mostinski, I.L. (1963).** Application of the Rule of Corresponding States for Calculation of Heat Transfer and Critical Heat Flux, *Teploenergetika*, Vol. 4, pp. 66.
- Müller-Steinhagen, H. and Heck, K. (1986).** A simple Friction Pressure Drop Correlation for Two-Phase Flow in Pipes, *Chem. Eng. Processing*, Vol. 20, pp 297-308.
- Muwanga, R. and Hassan, I. (2007).** A Flow Boiling Heat Transfer Investigation of FC-72 in a Microtube Using Liquid Crystal Thermography, *J. Heat Transfer*, Vol. 129, pp. 977-987.
- Muzychka, Y.S. and Yovanovich, M.M. (2004).** Laminar Forced Convection Heat Transfer in the Combined Entry Region of Non-Circular Ducts, *J. Heat Transfer*, Vol. 126, pp. 54-61.
- Muzzio, A., Niro, A. and Arosio, S. (1998).** Heat Transfer and Pressure Drop during Evaporation and Condensation of R22 inside 9.52-mm O.D. Microfin Tubes of Different Geometries, *J. Enhanced Heat Transfer*, Vol. 5, No. 1, pp. 39-52.
- Nakajima, K. (1978).** Boiling heat transfer outside horizontal multitube bundles, *Heat Transfer-Jap. Res.*, Vol. 7(1), pp. 1-24.
- Nakayama, W., Daikoku, T., Kuwara, H. and Nakajima, T. (1979).** Dynamic Model of Enhanced Boiling Heat Transfer on Porous Surfaces, *Advances in Enhanced Heat Transfer*, ASME, New York, pp. 31-43.
- Nakayama, W., Daikoku, T. and Nakajima, T. (1982).** Enhancement of Boiling and Evaporation on Structured Surfaces with Gravity Driven Film Flow of R-11, *Proc. 7<sup>th</sup> International Heat Transfer Conference*, Vol. 4, pp. 409-414.
- Nakayama, A. and Kano, M. (1983).** Effect of Bubble Frequency on Bubble Departure Diameter in Nucleate Pool Boiling, *Heat Transfer-Japanese Research*, Vol. 12, No. 3, pp. 32-47.

- Nidegger, E., Thome, J.R. and Favrat, D. (1997).** Flow Boiling and Pressure Drop Measurements for R-134a/Oil Mixtures Part 1: Evaporation in a Microfin Tube, *HVAC&R Research*, Vol. 3, No. 1, pp. 38-53.
- Nishikawa, K. et al. (1976).** *Jap. Soc. Mech. Engrs.*, 42-361, 2879.
- Nukiyama, S. (1934).** The Maximum and Minimum Values of Heat Q Transmitted from Metal to Boiling Water under Atmospheric Pressure, *J. Jap. Soc. Mech. Eng.*, Vol. 37, pp. 367-374 (in Japanese) (trans. in *Int. J. Heat Mass Transfer*, Vol. 9, pp. 1419-1433 (1966)).
- Nunner, W. (1956).** Heat Transfer and Pressure Drop in Rough Tubes, *VDI-Forschungsheft 455*, Series B, Vol. 22, A.E.R.E. Library Translation 786.
- Nusselt, W. (1916).** Die Oberflächenkondensation des Wasserdampfes, *Zeitschr. Ver. Deutch. Ing.*, Vol. 60, pp. 541-546 and pp. 569-575.
- Oh, S.Y. and Bergles, A.E. (1998).** Experimental Study on the Effects of the Spiral Angle on Evaporative Heat Transfer Enhancement in Microfin Tubes, *ASHRAE Trans.*, Vol. 104, Part 2, Paper TO-98-19-1.
- Olivier, J.A., Liebenberg, L., Kedzierski, M.A. and Meyer, J.P. (2004).** Pressure Drop during Refrigerant Condensation inside Horizontal Smooth, Helical Micro-Fin and Herringbone Micro-Fin Tubes, *J. Heat Transfer*, Vol. 126, pp. 687-696.
- Olivier, J.A., Liebenberg, L., Thome, J.R. and Meyer, J.P. (2007).** Heat Transfer, Pressure Drop, and Flow Pattern Recognition during Condensation inside Smooth, Helical Micro-Fin and Herringbone Tubes, *Int. J. Refrigeration*, Vol. 30, pp. 609-623.
- Onbasioglu, S.U. (2004).** Modelling of Two-Phase Fluid Flow in Small Circular and Rectangular Channels, *Proc. of 2<sup>nd</sup> Int. Conference on Microchannels and Minichannels*, Rochester, June 17-19, pp. 367-372.
- Ornatski, A.P. and Vinyarsk, L.S. (1965).** Heat Transfer Crisis in a Forced Flow of Underheated [Subcooled] Water in Small-Bore Tubes, *High Temperature*, Vol. 3, No. 3, pp. 400-406.
- Ould Didi, M. B., Kattan, N. and Thome, J. R. (2002).** Prediction of Two-Phase Pressure Gradients of Refrigerants in Horizontal Tubes, *Int. J. Refrigeration*, Vol. 25, No. 7, pp. 935-947.
- Owens, W.L. (1978).** Correlation of Thin Film Evaporation Heat Transfer Coefficients for Horizontal Tubes, ASME Paper 78-WA/HI-67.
- Owhaib, W., Martin-Callizo, C. and Palm, B. (2004).** Evaporative Heat Transfer in Vertical Circular Microchannels, *Applied Thermal Engineering*, Vol. 24, pp. 1241-1253.
- Owhaib, W. and Palm, B. (2003).** Flow Boiling Heat Transfer in a Vertical Circular Microchannel Tube, *Eurotherm Seminar No.72*, Valencia, Spain, 31 March-2 April.
- Palen, J.W., Breber, G. and Taborek, K. (1979).** Prediction of Flow Regimes in Horizontal Tube-Side Condensation, *Heat Transfer Engineering*, Vol. 1, No. 2, pp. 47-57.
- Palm, B.E. (1995).** Pool Boiling of R22 and R134a on Enhanced Surfaces, *Proc. 19<sup>th</sup> International Congress of Refrigeration*, The Hague, Vol. 4a, pp. 465-471.
- Palm, B. (2003).** Mini-and Microchannel Research in Sweden, *Proc. of First ASME Int. Conf. on Microchannels and Minichannels*, Rochester, New-York, pp. 25-31.
- Parken, W.H., Fletcher, L.S., Sernas, V. and Han, J.C. (1990).** Heat Transfer Through Falling Film Evaporation and Boiling on Horizontal Tubes, *J. Heat Transfer*, Vol. 112, pp. 744-750.
- Park, J.E. (2008).** Ph.D. thesis, Ecole Polytechnique Fédérale de Lausanne, Lausanne, Switzerland, downloadable for free at: <http://library.epfl.ch/theses/?nr=4223>.
- Peterson, R.B. (1999).** Numerical Modeling of Conduction Effects in Microscale Counterflow Heat Exchangers, *Nanoscale and Microscale Thermophysical Engineering*, Vol. 3(1), pp. 17-30.
- Pettersen J. (2004a).** Two-Phase Flow Patterns in Microchannel Vaporization of CO<sub>2</sub> at Near-Critical Pressure, *Heat Transfer Engineering*, Vol. 25, pp. 52-60.
- Pettersen, J. (2004b).** Flow Vaporization of CO<sub>2</sub> in Microchannel Tubes, *Experimental Thermal and Fluid Science*, Vol. 28, pp. 111-121.
- Petukhov, B.S. (1970).** Heat Transfer and Friction in Turbulent Pipe Flow with Variable Physical Properties, *Advances in Heat Transfer*, Academic Press, New York, Vol. 6, pp. 503-564.

- Plesset, M. S. and Zwick, S. A. (1954).** The Growth of Vapour Bubble in Superheated Liquid, *J. Appl. Phys*, Vol. 25, pp. 493-500.
- Poiseuille, J.M. (1840).** Recherches expérimentales sur le mouvement des liquides dans les tubes de très petits diamètres, *Comptes Rendus Hebdomadaires de l'Académie des Sciences*, Vol. 11, pp. 961-967, 1041-1048.
- Prausnitz, J.M. (1969).** *Molecular Thermodynamics of Fluid-Phase Equilibria*, Prentice-Hall, Englewood Cliffs, NJ.
- Pribyl, D.J., Bar-Cohen, A. and Bergles, A.E. (2003).** An Investigation of Critical Heat Flux and Two-Phase Flow Regimes for Upward Steam and Water Flow, *Proc. of the 5<sup>th</sup> International Conference in Boiling Heat Transfer*, Jamaica, May 4-8.
- Qi, S.L., Zhang, P., Wang, R.Z. and Xu, L.X. (2007a).** Flow Boiling of Liquid Nitrogen in Micro-Tubes: Part I – The Onset of Nucleate Boiling, Two-Phase Flow Instability and Two-Phase Pressure Drop, *Int. J. Heat Mass Transfer*, Vol. 50, pp. 4999-5016.
- Qi, S.L., Zhang, P., Wang, R.Z. and Xu, L.X. (2007b).** Flow Boiling of Liquid Nitrogen in Micro-Tubes: Part II – Heat Transfer Characteristics and Critical Heat Flux, *Int. J. Heat Mass Transfer*, Vol. 50, pp. 5017-5030.
- Qu, I. and Mudawar, W. (2004).** Measurement and Correlation of Critical Heat Flux in Two-Phase Micro-Channel Heat Sinks, *Int. J. of Heat and Mass Transfer*, Vol. 47, pp. 2045-2059.
- Rabas, T.J. and Arman, B. (1992).** The Influence of the Prandtl Number on the Thermal Performance of Tubes with the Separation and Reattachment Mechanism, *Enhanced Heat Transfer*, HTD Vol. 202, ASME, pp. 77-87.
- Ravigururajan, T.S. and Bergles, A.E. (1985).** General Correlations for Pressure Drop and Heat Transfer for Single-Phase Turbulent Flow in Internally Ribbed Tubes, *Augmentation of Heat Transfer in Energy Systems*, ASME HTD Vol. 52, pp. 9-20.
- Revellin, R. (2005).** Experimental Two-Phase Fluid Flow in Microchannels, Ecole Polytechnique Fédérale de Lausanne (Lausanne, Switzerland), Ph.D. thesis no. 3437, available free online at <http://library.epfl.ch/theses/?nr=3437>.
- Revellin, R., Agostini, B. and J.R. ThomeThome, J.R. (2008).** Elongated Bubbles in Microchannels Part II: Experimental Study and Modeling of Bubble Collisions, *Int. J. Multiphase Flow*, Vol. 34, pp. 602-613.
- Revellin, R., Agostini, B., Ursenbacher, T. and Thome, J.R. (2008b).** Experimental Investigation of Elongated Bubble Velocity and Length for Flow of R-134a in a 0.5 mm Microchannel, *Experimental Thermal and Fluid Science*, Vol. 32, pp. 870-881.
- Revellin, R., Dupont, V., Ursenbacher, T., Thome, J.R. and Zun, I. (2006).** Characterization of Two-Phase Flows in Microchannels: Optical Measurement Technique and Flow Parameter Results for R-134a in a 0.5 mm Channel, *Int. J. Multiphase Flow*, Vol. 32, pp. 755-774.
- Revellin, R., Moreno Quiben, J., Bonjour, J. and Thome, J.R. (2008a).** Effect of Local Hot Spots on the Maximum Heat Transfer during Flow Boiling in a Microchannel, *IEEE Trans. on Components and Packaging Technologies*, Vol. 31, pp. 407-416.
- Revellin, R. and Thome, J.R. (2007).** Experimental Investigation of R-134a and R-245fa Two-Phase Flows in Microchannels for Different Flow Conditions, *Int. J. Heat and Fluid Flow*, Vol. 28, No. 1, pp. 63-71.
- Revellin, R. and Thome, J.R. (2007a).** A New Type of Diabatic Flow Pattern Map for Boiling Heat Transfer in Microchannels, *J. of Micromechanics and Microengineering*, Vol. 17, pp. 788-796.
- Revellin, R. and Thome, J.R. (2007b).** Adiabatic Two-Phase Frictional Pressure Drops in Microchannels, *Experimental Thermal and Fluid Science*, Vol. 31, Issue 7, pp. 673-685.
- Revellin, R. and Thome, J.R. (2008).** A Theoretical Model for the Prediction of the Critical Heat Flux in Heated Microchannels, *Int. J. Heat Mass Transfer*, Vol. 51, pp. 1216-1225.
- Rewert, L.E., Huber, J.B. and Pate, M.B. (1996a).** The Effect of R-123 Condensate Inundation and Vapor Shear on Enhanced Tube Geometries, *ASHRAE Trans.*, Vol. 102, Part 2, pp. 273-284.

- Rewert, L.E., Huber, J.B. and Pate, M.B. (1996b).** The Effect of R-134a Condensate Inundation on Enhanced Tube Geometries, *ASHRAE Trans.*, Vol. 102, Part 2, pp. 285-296.
- Ribatski, G. and Saiz Jabardo, J.M. (2003).** Experimental Study of Nucleate Boiling of Halocarbon Refrigerants on Cylindrical Surfaces, *Int. J. Heat Mass Transfer*, Vol. 46, pp. 4439-4451.
- Ribatski, G. and Thome, J.R. (2006).** Nucleate Boiling Heat Transfer of R134A on Enhanced Tubes, *Applied Thermal Engineering*, Vol. 26(10), pp. 1018-1031.
- Ribatski, G. and Thome, J.R. (2007).** Experimental Study on the Onset of Local Dryout in an Evaporating Falling Film on Horizontal Plain Tubes, *Experimental Thermal and Fluid Science*, Vol. 31, pp. 483-493.
- Ribatski, G., Wojtan, L. and Thome, J.R. (2006).** An Analysis of Experimental Data and Prediction Methods for Flow Boiling Heat Transfer and Two-Phase Frictional Pressure Drop in Micro-Scale Channels, *Experimental Thermal and Fluid Science*, Vol. 31, pp. 1-19.
- Rifert, V.G., Putilin, Ju.V. and Podberezny, V.L. (1992).** Evaporation Heat Transfer in Liquid Films Flowing Down the Horizontal Smooth and Longitudinally-Profiled Tubes, *Heat Transfer: 3<sup>rd</sup> UK National Conference incorporating 1<sup>st</sup> European Conference of Thermal Sciences*, Taylor&Francis, Vol. 2, pp. 1283-1289.
- Robinson, D. and Thome, J.R. (2004a).** Local Bundle Boiling Heat Transfer Coefficients on a Plain Tube Bundle, *HVAC&R Research*, ASHRAE, Vol. 10, No. 1, pp. 33-51.
- Robinson, D. and Thome, J.R. (2004b).** Boiling of R-134a, R-410A and R-507A on an Enhanced Tube Bundle, *HVAC&R Research*, ASHRAE, Vol. 10, No. 4, pp. 441-457.
- Robinson, D. and Thome, J.R. (2004c).** Local Bundle Boiling Heat Transfer Coefficients on a Low Finned Tube Bundle, *HVAC&R Research*, Vol. 10, pp. 331-344.
- Rohsenow, W.M. (1956).** Heat Transfer and Temperature Distribution in Laminar Film Condensation, *Trans. ASME*, Vol. 79, pp. 1645-1648.
- Rohsenow, W.M. (1962).** A Method of Correlating Heat Transfer Data for Surface Boiling of Liquids, *Trans. ASME (later J. Heat Transfer)*, Vol. 74, pp. 969-975.
- Rohsenow, W.M., Webber, J.H. and Ling, A.T. (1956).** Effect of Vapor Velocity on Laminar and Turbulent Film Condensation, *Trans. ASME*, Vol. 78, pp. 1637-1643.
- Roques, J.F. (2004).** Falling Film Evaporation on a Single Tube and on a Tube Bundle, Ph.D. thesis 2987, Swiss Federal Institute of Technology Lausanne (EPFL), CH-1015 Lausanne, Switzerland, available free at <http://library.epfl.ch/theses/?nr=2987>.
- Roques, J.F., Dupont, V. and Thome, J.R. (2002).** Falling Film Transitions on Plain and Enhanced Tubes, *J. Heat Transfer*, Vol. 124, June, pp. 491-499.
- Roques, J.F. and Thome, J.R. (2001).** Flow Patterns and Phenomena for Falling Films on Plain and Enhanced Tube Arrays, *Proc. of Int. Conference on Compact Heat Exchangers for the Process Industries*, Davos, Switzerland, July 1-6.
- Roques, J.F. and Thome, J.R. (2002).** Falling Film Transitions between Droplets, Column and Sheet Flow Modes on a Vertical Array of Horizontal 19 fpi and 40 fpi Low Finned Tubes, *Proc. 1<sup>st</sup> Int. Conf. On Heat Transfer, Fluid Mechanics and Thermodynamics*, HEFAT 2002, Skukuza, South Africa, Vol. 1, pp. 523-528.
- Roques, J.F. and Thome, J.R. (2007a).** Falling Films on Horizontal Tubes with R-134a, Part I: Boiling Heat Transfer Results for Four Types of Tubes, *Heat Transfer Engineering*, Vol. 28, No. 5, pp. 398-414.
- Roques, J.F. and Thome, J.R. (2007b).** Falling Films on Horizontal Tubes with R-134a, Part II: Flow Visualization, Onset of Dryout and Heat Transfer Predictions, *Heat Transfer Engineering*, Vol. 28, No. 5, pp. 415-434.
- Rose, J.W. (1994).** An Approximate Equation for the Vapour-Side Heat-Transfer Coefficient for Condensation on Low-Finned Tubes, *Int. J. Heat Mass Transfer*, Vol. 37, pp. 865-875.
- Rose, J.W. (2004).** Heat-Transfer Coefficients, Wilson Plots and Accuracy of Thermal Measurements, *Exp. Thermal Fluid Science*, Vol. 28, pp. 77-86.
- Rouhani, Z. (1969).** AB Atomenergi, Sweden, Internal Report, AE-RTV 841.

- Rouhani, Z. and Axelsson, E. (1970).** Calculation of Volume Void Fraction in the Subcooled and Quality Region, *Int. J. Heat Mass Transfer*, Vol. 13, pp. 383-393.
- Rozalowski, G.R. and Gater, R.A. (1975).** Pressure Loss and Heat Transfer Characteristics for High Viscous Fluid Flow in Convoluted Tubing, ASME Paper No. 75-HT-40.
- Rudy, T.M. and Webb, R.L. (1985).** An Analytical Model to Predict Condensate Retention on Horizontal Integral-Fin Tubes, *J. Heat Transfer*, Vol. 107, pp. 361-368.
- Saha, S.K., Gaitonde, U.N. and Date, A.W. (1989).** Heat Transfer and Pressure Drop Characteristics of Laminar Flow in a Circular Tube Fitted with Regularly Spaced Twisted-Tape Elements, *Experimental Thermal and Fluid Science*, Vol. 2, pp. 310-322.
- Salehi, M., Ohadi, M.M. and Dessiatoun, S. (1998).** The Applicability of the EHD Technique for Convective Boiling of Refrigerant Blends - Experiments with R-404A, *ASHRAE Trans.*, Vol. 102, Part 1, pp. 839-844.
- Schlager, L.M., Bergles, A.E. and Pate, M.B. (1987).** A Survey of Refrigerant Heat Transfer and Pressure Drop Emphasizing Oil Effects and In-Tube Augmentation, *ASHRAE Trans.*, Vol. 93, Part 1, pp. 392-416.
- Schlager, L.M., Pate, M.B., and Bergles, A.E. (1990).** Evaporation and Condensation Heat Transfer and Pressure Drop in Horizontal, 12.7-mm Microfin Tubes with Refrigerant 22, *J. Heat Transfer*, Vol. 112, pp. 1041-1047.
- Schrage, D.S., Hsu, J.-T. and Jensen, M.K. (1988).** Two-Phase Pressure Drop in Vertical Crossflow across a Horizontal Tube Bundle, *AICHE J.*, Vol. 34, No. 1, pp. 107-115.
- Schrage, R.W. (1953).** A Theoretical Study of Interphase Mass Transfer, *Columbia University Press*, New York, Chap. II.
- Seban, R. (1954).** Remarks on Film Condensation with Turbulent Flow, *Trans. ASME*, Vol. 76, pp. 299-303.
- Seider, E.N. and Tate, C.E. (1936).** Heat Transfer and Pressure Drop of Liquids in Tubes, *Industrial and Engineering Chemistry*, Vol. 28, pp. 1429-1435.
- Serizawa, A. (2004).** Multiphase Flow in Microchannels, *Second International Symposium on Multiphase, Non-Newtonian and Reacting Flows'04*, Hangzhou, China, September 10-12.
- Serizawa, A. and Feng, Z.P. (2001).** Two-Phase Flow in Microchannels, International Conference of Multiphase Flows, New Orleans, Keynote Lecture.
- Serizawa, A., Feng, Z. and Kawara, Z. (2002).** Two-Phase Flow in Microchannels, *Exp. Thermal Fluid Sci.*, Vol. 26, pp. 703-714.
- Serizawa, A., Kunugi, T., Kawara, Z. and Takahashi, O. (2002).** Two-Phase Flow in Micro-Channels, *Proceedings of Fourth Pacific Rim Thermal Science and Energy Workshop (PARTSEE-4)*, May 31-June 2, Kyoto, pp. 136-141.
- Sethumadhavan, R. and Rao, R. (1986).** Turbulent Flow Friction and Heat Transfer Characteristics of Single- and Multi-Start Spirally Enhanced Tubes, *J. Heat Transfer*, Vol. 108, pp. 55-61.
- Seymour, E.V. (1966).** Fluid Flow Through Tubes Containing Twisted Tapes, *The Engineer*, Vol. 222, pp. 634-642.
- Shah, M.M. (1979).** A General Correlation for Heat Transfer during Film Condensation inside of Pipes, *Int. J. Heat Mass Transfer*, Vol. 22, pp. 547-556.
- Shah, M. M. (1982).** Chart Correlation for Saturated Boiling Heat Transfer: Equations and Further Study, *ASHRAE Trans.*, Vol. 88, Part 1, pp. 185-196.
- Shah, M.M. (1987).** Improved General Correlation of Critical Heat Flux during Upflow in Uniformly Heated Vertical Tubes, *Int. J. Heat Fluid Flow*, Vol. 8, pp. 326-335.
- Shah, R.K. and London, A.L. (1978).** *Laminar Flow Forced Convection in Ducts*, Academic Press, New York. Supplement 1 to the series *Advances in Heat Transfer*.
- Shah, R.K. and Sekulić, D.P. (2003).** *Fundamentals of Heat Exchanger Design*, John Wiley, New York.
- Shah, R.K., Zhou, S.Q. and Tagavi, K.A. (1999).** The Role of Surface Tension in Film Condensation in Extended Surface Passages, *Enhanced Heat Transfer*, Vol. 6, pp. 179-216.

- Shatto, D.P. and Peterson, G.P. (1996).** A Review of Flow Boiling Heat Transfer with Twisted Tape Inserts, *J. Enhanced Heat Transfer*, Vol. 3, No. 4, pp. 233-257.
- Shemer, L., Gulitski, A. and Barnea, D. (2007).** Movement of Two Consecutive Taylor Bubbles in Vertical Pipes, *Multiphase Science and Technology*, Vol. 19, pp. 99-120.
- Sheng, C.H. and Palm, B. (2001).** The Visualization of Boiling in Small-Diameter Tubes, *Heat Transport and Transport Phenomena in Microsystems*, Banff, Canada.
- Shiferaw, D., Karayiannis, T.G. and Kenning, D.B.R. (2006).** A Comparison with the Three-Zone Model for Flow Boiling Heat Transfer in Small Diameter Tubes, *13<sup>th</sup> International Heat Transfer Conference*, Sydney, Aug. 14-18.
- Shiferaw, D., Huo, X., Karayiannis, T.G. and Kenning, D.R.B. (2007).** Examination of Heat Transfer Correlations and a Model for Flow Boiling of R134a in Small Diameter Tubes, *Int. J. Heat Mass Transfer*, Vol. 50, pp. 5177-5193.
- Shinmura, E., Take, K. and Koyama, S. (2006).** Development of High-Performance CO<sub>2</sub> Evaporator, *JSME Automotive Air-Conditioning Symposium*, pp. 217-227.
- Shizuya, M., Itoh, M. and Hijakata, K. (1995).** Condensation of Nonazeotropic Binary Refrigerant Mixtures including R22 as a More Volatile Component inside a Horizontal Tube, *J. Heat Transfer*, Vol. 117, No. 5, pp. 538-543.
- Sieder, E.N. and Tate, G.E. (1936).** *Ind. Eng. Chem.*, Vol. 28, pp. 1429.
- Silva, C.L. (1989).** Experimental Investigation of the Nucleate Boiling of Refrigerant-Oil Mixtures, Ph.D. thesis, Escola Politécnica, University of São Paulo, Brazil.
- Silver, L. (1947).** Gas Cooling with Aqueous Condensation, *Trans. Inst. Chem. Eng.*, Vol. 25, pp. 30-42.
- Simões-Moreira, J.R. (1994).** Adiabatic Evaporation Waves, Ph.D. Thesis, Rensselaer Polytechnic Institute, Troy, New York.
- Simões-Moreira, J.R., and Shepherd, J.E. (1999).** Evaporation Waves in Superheated Dodecane, *J. Fluid Mechanics*, Vol. 382, pp. 63-68.
- Singh, A., Ohadi, M.M. and Dessiatoun, S. (1996).** Flow Boiling Heat Transfer Coefficients of R-134a in a Microfin Tube, *J. Heat Transfer*, Vol. 118, pp. 497-499.
- Smit, F.J., Thome, J.R. and Meyer, J. (2001).** Heat Transfer Coefficients during Condensation of the Zeotropic Refrigerant Mixture R-22/R-142b, *J. Heat Transfer*, Vol. 124, pp. 1137-1146.
- Smith, B.D., Block, B., and Hickman, C.D. (1963).** Distillation, *Chemical Engineers' Handbook*, McGraw-Hill, New York, pg. 13-4 to 13-14.
- Smith, S.L. (1969).** Void Fractions in Two-Phase Flow. A Correlation Based on an Equal Velocity Head Model, *Proc. Inst. Mech. Engng.*, Vol. 184, No. 36, pp. 647-664.
- Smithberg, E. and Landis, F. (1964).** Friction and Forced Convection Heat Transfer Characteristics in Tubes with Twisted Tape Swirl Generators, *J. Heat Transfer*, Vol. 86, pp. 39-49.
- Soliman, H.M. (1982).** On the Annular-to-Wavy Flow Pattern Transition during Condensation inside Horizontal Tubes, *The Canadian Journal of Chemical Engineering*, Vol. 60, pp. 475-481.
- Soliman, H.M. and Feingold, A. (1977).** Heat Transfer, Pressure Drop, and Performance Evaluation of a Quintuplex Internally Finned Tube, ASME Paper No. 77-HT-46.
- Sparrow, E.M. and Gregg, J.L. (1959).** A Boundary-Layer Treatment of Laminar Film Condensation, *J. Heat Transfer*, Series C, Vol. 81, pp. 13.
- Sparrow, E.M., Minkowycz, W.J. and Saddy, M. (1967).** Forced Convection Condensation in the Presence of Non-Condensables and Interfacial Resistance, *Int. J. Heat Mass Transfer*, Vol. 10, pp. 1829-1845.
- Steiner, D. (1993).** *VDI-Wärmeatlas (VDI Heat Atlas)*, Verein Deutscher Ingenieure, VDI-Gesellschaft Verfahrenstechnik und Chemieingenieurwesen (GCV), Düsseldorf, Chapter Hbb.
- Steiner, D. and Taborek, J. (1992).** Flow Boiling Heat Transfer in Vertical Tubes Correlated by an Asymptotic Model, *Heat Transfer Engng.*, Vol. 13, No. 2, pp. 43-69.
- Stephan, K. and Abdelsalam, M. (1980).** Heat Transfer Correlations for Natural Convection Boiling, *Int. J. Heat Mass Transfer*, Vol. 23, pp. 73-87.

- Stephan, K. and Körner, M. (1969).** Calculation of Heat Transfer in Evaporating Binary Liquid Mixtures, *Chemie-Ingenieur Technik*, Vol. 41, No. 7, pp. 409-417.
- Sundaresan, S.G., Pate, M.B., Doerr, T.M. and Ray, D.T. (1996).** A Comparison of the Effects of POE and Mineral Oil Lubricants on the In-Tube Evaporation of R-22, R-407C and R-410A, *Proc. 1996 International Refrigeration Conference at Purdue*, West Lafayette, IN, July 23-26, pp. 187-192.
- Suo, M. and Griffith, P. (1964).** Two-Phase Flow in Capillary Tubes. *J. Basic Engineering*, Vol. 9, pp. 576-582.
- Suzuki, S., Fujisawa, Y., Nakarazawa, S. and Matsuoka, M. (1993).** Measuring Method of Oil Circulating Ratio using Light Absorption, *ASHRAE Trans.*, Vol. 99, Part 1, pp. 413-421.
- Taborek, J. (1983).** Shell-and-Tube Heat Exchangers: Single-Phase Flow, *Heat Exchanger Design Handbook*, Chapter 3.3, Hemisphere, New York.
- Taitel, Y. (1990).** Flow pattern transition in two-phase flow, *Proc. 9<sup>th</sup> International Heat Transfer Conference*, Jerusalem, Vol. 1, pp. 237-254.
- Taitel, Y. and Dukler, A.E. (1976).** A model for predicting flow regime transitions in horizontal and near horizontal gas-liquid flow, *AICHE J.*, Vol. 22, pp. 47-55.
- Takaishi, Y. and Oguchi, K. (1987).** Measurements of Vapor Pressures of R22/Oil Solutions, *18<sup>th</sup> International Congress of Refrigeration*, Vienna, B, pp. 217-222.
- Talvy, C.A., Shemer, L. and Barnea, D. (2000).** On the Interaction between Two Consecutive Elongated Bubbles in a Vertical Pipe, *Int. J. Multiphase Flow*, Vol. 26, pp. 1905-1923
- Tam, L.M. and Ghajar, A.J. (1997).** Effect of Inlet Geometry and Heating on the Fully Developed Friction Factor in the Transition Region of a Horizontal Tube, *Experimental Thermal and Fluid Science*, Vol. 15, pp. 52-64.
- Tam, L.M. and Ghajar, A.J. (1998).** The Unusual Behavior of Local Heat Transfer Coefficient in a Circular Tube with a Bell-Mouth Inlet, *Experimental Thermal and Fluid Science*, Vol. 16, pp. 187-194.
- Tanaka, S., Daiguji, H., Takemura, F. and Hihara, E. (2001).** Boiling Heat Transfer of Carbon Dioxide in Horizontal Tubes, *38th National Heat Transfer Symposium of Japan*, pp. 899-900.
- Tandon, T.N., Varma, H.K. and Gupta, C.P. (1985).** A Void Fraction Model for Annular Two-Phase Flow, *Int. J. Heat Mass Transfer*, Vol. 28, pp. 191-198.
- Tang (1997).** Empirical Study of New Refrigerant Flow Condensation inside Horizontal Smooth and Micro-Fin Tubes, Ph.D. Thesis, University of Maryland.
- Thom, J.R.S. (1964).** Prediction of Pressure Drop during Forced Circulation Boiling of Water, *Int. J. Heat Mass Transfer*, Vol. 7, pp. 709-724.
- Thome, J.R. (1983).** Prediction of Binary Mixture Boiling Heat Transfer Coefficients Using Only Phase Equilibrium Data, *Int. J. Heat Mass Transfer*, Vol. 26, pp. 965-974.
- Thome, J.R. (1987).** Enhanced Boiling of Mixtures, *Chem. Eng. Science*, Vol. 42, pp. 1909-1917.
- Thome, J.R. (1989).** Prediction of the Mixture Effect on Boiling in Vertical Thermosyphon Reboilers, *Heat Transfer Engineering*, Vol. 12, No. 2, pp. 29-38; originally presented at the HTFS Meeting at Heriot-Watt University in 1985.
- Thome, J.R. (1990).** *Enhanced Boiling Heat Transfer*, Hemisphere (Taylor & Francis), Washington.
- Thome, J.R. (1991).** *Enhanced Heat Transfer Software Program*, John Thome Inc., Ionia, MI, USA. [licensed and available through HTRI].
- Thome, J.R. (1992).** Thermodynamic and Transport Properties of Lubricating Oils, Swiss Federal Institute of Technology, Lausanne, LENI Report (December 21).
- Thome, J.R. (1993).** Thermodynamic and Transport Properties of Refrigerant and Lubricating Oil Mixtures, Swiss Federal Institute of Technology, Lausanne, LENI Report (Jan. 28).
- Thome, J.R. (1994a).** High Performance Augmentations for Refrigeration System Evaporators and Condensers, *J. Enhanced Heat Transfer*, Vol. 1, No. 3, pp. 275-286.
- Thome, J.R. (1994b).** Two-Phase Heat Transfer to New Refrigerants, Special Keynote Lecture, *Proc. of 10<sup>th</sup> International Heat Transfer Conference*, Brighton, Vol. 1, pp. 19-41.

- Thome, J.R. (1995).** Comprehensive Thermodynamic Approach to Modelling Refrigerant-Oil Mixtures, *HVAC&R Research*, ASHRAE, 1(2), pp. 110-126.
- Thome, J.R. (1996).** Boiling of New Refrigerants: A State-of-the-Art Review, *Int. J. Refrig.*, Vol. 19, No. 7, pp. 435-457.
- Thome, J.R. (1997a).** Boiling of New Refrigerants: A State-of-the-Art Review, *Int. J. Refrig.*, Vol. 19, No. 7, pp. 435-457.
- Thome, J.R. (1997b).** Heat Transfer and Pressure Drop in the Dryout Region of Intube Evaporation with Refrigerant/Lubricant Mixtures, ASHRAE Final Report of Project 800-RP, February.
- Thome, J.R. (1998).** Condensation, Boiling and Evaporation of Fluorocarbon and Other Refrigerants: A State-of-the-Art Review, ARI Technical Report, Air-Conditioning and Refrigeration Institute, Arlington, VA 22203-1627.
- Thome, J.R. (1999).** Falling Film Evaporation: State-of-the-Art Review of Recent Work, *Journal of Enhanced Heat Transfer*, Vol. 6, No. 2, pp. 263-277.
- Thome, J.R. (2003).** Evaporation in Microchannels: Experiments and Theory, 5<sup>th</sup> Int. Boiling Conference, Jamaica, May, Invited Keynote Lecture.
- Thome, J.R. (2006).** Fundamentals of Boiling and Two-Phase Flows in Microchannels, 13<sup>th</sup> International Heat Transfer Conference, Sydney, Australia, Aug. 13-18.
- Thome, J.R., Dupont, V. and Jacobi, A. (2004).** Heat Transfer Model for Evaporation in Microchannels, Part I: Presentation of the Model, *Int. J. Heat Mass Transfer*, Vol. 47, pp.3375-3385.
- Thome, J.R. and El Hajal, J. (2003).** Two-Phase Flow Pattern Map for Evaporation in Horizontal Tubes: Latest Version, *Heat Transfer Engineering*, Vol. 24, No. 6, pp. 3-10.
- Thome, J.R., El Hajal, J. (2004).** Flow Boiling Heat Transfer to Carbon Dioxide: General Prediction Method. *Int. J. Refrig.*, Vol. 27(3), pp. 294-301.
- Thome, J.R., El Hajal, J., Cavallini, A. (2003).** Condensation in Horizontal Tubes, Part 2: New Heat Transfer Model Based on Flow Regimes. *Int. J. Heat Mass Transfer*, Vol. 46, pp. 3365-3387.
- Thome, J.R., Groll, M., Mertz, R. (2003).** Section 2.13.4 Microscale Heat Transfer: Boiling and Evaporation in Chapter 2.13 Heat Transfer and Fluid Flow in Microchannels, *Heat Exchanger Design Update*, Begell House, New York, 2.13.4.1-27.
- Thome, J.R., Kattan, N. and Favrat, D. (1997).** Evaporation in Microfin Tubes: a Generalized Prediction Model, Convective Flow and Pool Boiling Conference, Irsee, Germany, May 18-23, Paper VII-4.
- Thome, J.R. and Moreno Quibén, J. (2004).** Refrigeration Evaporation Characteristics inside Flat Passages, ARTI Final Report ARTI-21CR/605-20040-01, Arlington, VA, USA, December.
- Thome, J.R., Revellin, R., Agostini, B. and Park, J.E. (2007).** Recent Advances in Thermal Modeling of Micro-Evaporators for Cooling of Microprocessors, 2007 ASME International Mechanical Engineering Congress and Exhibition, Seattle, Nov. 11-15, Invited paper IMECE2007-42900.
- Thome, J.R. and Ribatski, G. (2005).** State-of-the Art of Flow Boiling and Two-Phase Flow of CO<sub>2</sub> in Macro- and Micro-Channels, *Int. J. Refrigeration*, Vol. 28, pp. 1149-1168.
- Thome, J.R. and Robinson, D.M. (2006).** Prediction of Local Bundle Boiling Heat Transfer Coefficients: Pure Refrigerant Boiling on Plain, Low Fin and Turbo-BII HP Tube Bundles, *Heat Transfer Engineering*, Vol. 27(10), pp. 20-29.
- Thome, J.R. and Shock, R.A.W. (1984).** Boiling of Multicomponent Liquid Mixtures, *Advances in Heat Transfer*, Eds. Hartnett and Irvine, Academic Press, Princeton, Vol. 16, pp. 59-156.
- Thonon, B., Roser, R. and Mercier, P. (1997).** Pool Boiling of Propane and Pentane on a Bundle of Low-Finned Tubes, Convective Boiling Conference, Kloster Irsee, Germany, May 18-23.
- Thors, P. and Bogart, J.E. (1994).** In-Tube Evaporation of HCFC-22 with Enhanced Tubes, *J. Enhanced Heat Transfer*, Vol. 1, No. 4, pp. 365-377.
- Thorsen, R.S. and Landis, F. (1968).** Friction and Heat Transfer Characteristics in Turbulent Swirl Flow Subjected to Large Transverse Temperature Gradients, *J. Heat Transfer*, Vol. 90, pp. 87-98.

- Tien, C.L. and Lienhard, J.H. (1976).** *Solutions Manual to Accompany Statistical Thermodynamics*, revised printing, Hemisphere, Washington, pp. 13.
- Tien, C.L. and Lienhard, J.H. (1979).** *Statistical Thermodynamics*, revised printing, Hemisphere, Washington, pp. 55.
- Tinker, T. (1951).** Shell Side Characteristics of Shell and Tube Heat Exchangers, *General Discussion on Heat Transfer*, Institution of Mechanical Engineers, London, pp. 97-116.
- Tiselj, I., Hetsroni, G., Mavko, B., Mosyak, A., Pogrebnyak, E. and Segal, Z. (2004).** Effect of Axial Heat Conduction on Heat Transfer in Micro-Channels, *Int. J. Heat Mass Transfer*, Vol. 47, pp. 2551-2565.
- Torikoshi, K. and Ebisu, T. (1994).** In-Tube Heat Transfer Characteristics of Refrigerant Mixtures of HFC-32/134a and HFC-32/125/134a, *Proc. 1994 International Refrigeration Conference at Purdue*, July 19-22, West Lafayette, IN, pp. 293-298.
- Torikoshi, K., Kawabata, K. and Ebisu, T. (1992).** Heat Transfer and Pressure Drop Characteristics of HFC-134a in a Horizontal Heat Transfer Tube, *Proc. 1992 International Refrigeration Conf. at Purdue*, West Lafayette, Vol. 1, pp. 167-176.
- Tran, T.N., Wambsganss, M.W. and France, D.M. (1996).** Small Circular and Rectangular Channel Boiling with Two Refrigerants, *Int. J. Multiphase Flow*, Vol. 22, pp. 485-498.
- Tran, T.N., Chyu, M.-C., Wambsganss, M.W. and France, D.M. (2000).** Two-Phase Pressure Drop of Refrigerants during Flow Boiling in Small Channels: An Experimental Investigation and Correlation Development, *Int. J. Multiphase Flow*, Vol. 26, pp. 1739-1754.
- Tribbe, C. and Müller-Steinhagen, H. M. (2000).** An Evaluation of the Performance of Phenomenological Models for Predicting Pressure Gradient during Gas-Liquid Flow in Horizontal Pipelines, *Int. J. of Multiphase Flow*, Vol. 26, pp. 1019-1036.
- Triplett, K.A., Ghiaasiaan, S.M., Abdel-Khalik, S.I. and Sadowski, D.L. (1999a).** Gas-Liquid Two-Phase Flow in Microchannels Part I: Two-Phase Flow Patterns, *Int. J. Multiphase Flow*, Vol. 25, pp. 377-394.
- Triplett, K.A., Ghiaasiaan, S.M., Abdel-Khalik, S.I., LeMouel, A. and McCord, B.N. (1999b).** Gas-Liquid Two-Phase Flow in Microchannels Part II: Void Fraction and Pressure Drop, *Int. J. Multiphase Flow*, Vol. 25, pp. 395-410.
- Uchida, M., Itoh, M., Shikazono, N. and Kudoh, M. (1996).** Experimental Study on the Heat Transfer Performance of a Zeotropic Refrigerant Mixture in Horizontal Tubes, *Proc. 1996 International Refrigeration Conference at Purdue*, July 23-26, West Lafayette, IN, pp. 133-138.
- Ullmann, A. and Brauner, N. (2007).** The Prediction of Flow Patterns in Minichannels, *Multiphase Science and Technology*, Vol. 19, Issue 1, pp. 49-73.
- Ursenbacher, T., Wojtan, L., Thome, J.R. (2004).** Dynamic Void Fractions in Stratified Types of Flow, Part I: New Optical Measurement Technique and Dry Angle Measurements, *Int. J. Multiphase Flow*, Vol. 30, pp. 107-124.
- Vachon, R.I., Nix, G.H. and Tangor, G.E. (1967).** Evaluation of Constants for the Rohsenow Pool Boiling Correlation, U.S. National Heat Transfer Conference, Paper 67-HT-33.
- VDI-Wärmeatlas (1997).** Springer-Verlag Berlin Heidelberg.
- Walklate, P.J. and Martin, C.J. (1983).** The Measurement of Liquid Phase Velocity Profiles in Vertical Two-Phase Flows, IUTAM Symposium on Measuring Techniques in Gas-Liquid Two-Phase Flows, Nancy, France, July 5-8.
- Wallis, G.B. (1969).** *One Dimensional Two-Phase Flow*, McGraw-Hill, New York.
- Wang, C.C., Kuo, S.S., Chang, Y.J. and Lu, D.C. (1996).** Two-Phase Flow Heat Transfer and Friction Characteristics of R-22 and R-407C, *ASHRAE Trans.*, Vol. 102, Part 1, pp. 830-838.
- Wang, H.S. and Rose, J.W. (2005).** A Theory of Film Condensation in Horizontal Noncircular Section Microchannels, *J. of Heat Transfer*, Vol. 127, pp. 1096-1105.
- Van Stralen, S. and Cole, R. (1979).** *Boiling Phenomena*, Hemisphere, Washington.

- Warriarachchi, A.S., Marto, P.J. and Reilly, J.T. (1986).** The Effect of Oil Contamination on Nucleate Pool-Boiling of R-114 from a Porous Coated Surface, *ASHRAE Trans.*, Vol. 92, Part 2, pp. 525-538.
- Warrier, G.R., Dhir, V.K. and Momoda, L.A. (2002).** Heat Transfer and Pressure Drop in Narrow Rectangular Channels, *Exp. Thermal Fluid Sci.*, Vol. 26, pp. 53-64.
- Watanabe, K., Taira, T. and Mori, Y. (1983).** Heat Transfer Augmentation in Tubular Flow by Twisted Tapes at High Temperatures and Optimum Performance, *Heat Transfer-Japanese Research*, Vol. 12, No. 3, pp. 1-31.
- Watkinson, A.P., Milleti, D.L. and Kubanek (1975).** Heat Transfer and Pressure Drop of Internally Finned Tubes in Laminar Oil Flow, ASME Paper No. 75-HT-41.
- Wattelet, J.P., Chato, J.C., Souza, A.L. and Christoffersen, B.R. (1994).** Evaporation Characteristics of R-12, R-134a and MP-39 at Low Fluxes, *ASHRAE Trans.*, Vol. 100, Part 1, paper NO-94-2-1.
- Webb, R.L. (1994).** *Principles of Enhanced Heat Transfer*, Wiley, New York.
- Webb, R.L., Chien, L.H., McQuade, W.F. and Imadojema, H.E. (1995).** Pool Boiling of Oil-Refrigerant Mixtures on Enhanced Tubes, *Proc. ASME/JSME Thermal Engineering Joint Conference*, Maui, Vol. 2, pp. 247-255.
- Webb, R.L., Eckert, E.R.G. and Goldstein, R.J. (1971).** Heat Transfer and Friction in Tubes with Repeated-Rib Roughness, *Int. J. Heat Mass Transfer*, Vol. 14, pp. 601-617.
- Webb, R.L. and McQuade, W.F. (1993).** Pool Boiling of R-11 and R-123 Oil-Refrigerant Mixtures on Plain and Enhanced Tube Geometries, *ASHRAE Trans.*, Vol. 99, Part 1, pp. 1225-1236.
- Webb, R.L. and Paek, J.W. (2003).** Letter to editors: comments by R. L. Webb and J.W. Paek, *Int. J. Heat Mass Transfer*, vol. 46, pp. 1111-1113.
- Webb, R.L. and Pais, C (1992).** Nucleate Boiling Data for Five Refrigerants on Plain, Integral Fin, and Enhanced Tube Geometries, *Int. J. Heat Mass Transfer*, Vol. 35, No. 8 pp. 1893-1904.
- Webb, R.L., Rudy, T.M. and Kedzierski, M.A. (1985).** Prediction of Condensation on Horizontal Integral-Fin Tubes, *J. Heat Transfer*, Vol. 107, pp. 369-376.
- Wei, Y.H. and Jacobi, A.M. (2002).** Vapor-Shear, Geometric and Bundle-Depth Effects on the Intertube Falling-Film Modes, *Proc. 1<sup>st</sup> International Conference on Heat Transfer, Fluid Mechanics and Thermodynamics*, HEFAT 2002, Skukuza, South Africa, Vol. 1, pp. 40-46.
- Wei, X. and Joshi, Y. (2004).** Stacked Microchannel Heat Sinks for Liquid Cooling of Microelectronic Components, *Journal of Electronic Packaging*, Vol. 126, pp. 60-66.
- Whalley, P. (1980).** See Hewitt, G. F. (1983). Multiphase Flow and Pressure Drop, *Heat Exchanger Design Handbook*, Hemisphere, Washington, D. C., Vol. 2, pp. 2.3.2-11.
- Whalley, P.B., Azzopardi, B.J., Hewitt, G.F. and Owen, R.G. (1982).** A Physical Model of Two-Phase Flow with Thermodynamic and Hydrodynamic Non-Equilibrium, *Proc. of 7<sup>th</sup> International Heat Transfer Conf.*, Munich, Vol. 5, pp. 181-188.
- White, F.M. (1991).** *Viscous Fluid Flow*, 2<sup>nd</sup> Edition, McGraw-Hill, Singapore.
- Wibulswas, P. (1966).** Laminar-Flow Heat-Transfer in Non-Circular Ducts, Ph.D. Thesis, University of London, London.
- Withers, J.G. (1980a).** Tube-Side Heat Transfer and Pressure Drop for Tubes Having Helical Internal Ridging with Turbulent/Transitional Flow of Single-Phase Fluid, Part 1, Single-Helix Ridging, *Heat Transfer Engineering*, Vol. 2, No. 1, pp. 48-58.
- Withers, J.G. (1980b).** Tube-Side Heat Transfer and Pressure Drop for Tubes Having Helical Internal Ridging with Turbulent/Transitional Flow of Single-Phase Fluid, Part 2, Multiple-Helix Ridging, *Heat Transfer Engineering*, Vol. 2, No. 2, pp. 43-50.
- Withers, J. G. and Habdas, E. P. (1974).** Heat Transfer Characteristics of Helical-Corrugated Tubes for In-Tube Boiling of Refrigerant R-12, *AICHE Symp. Ser.*, Vol. 70, No. 138, pp. 98-106.
- Wojtan, L., Revellin, R. and Thome, J.R. (2007).** Investigation of Critical Heat Flux in Single, Uniformly Heated Microchannels, *Experimental Thermal and Fluid Science*, Vol. 30, pp. 765-774.

- Wojtan, L., Ursenbacher, T., Thome, J.R. (2004).** Dynamic Void Fractions in Stratified Types of Flow, Part II: Measurements for R-22 and R-410a. *Int. J. Multiphase Flow*, Vol. 30, pp. 125-137.
- Wojtan, L., Ursenbacher, T. and Thome, J.R. (2005a).** Investigation of Flow Boiling in Horizontal Tubes: Part I – A New Diabatic Two-Phase Flow Pattern Map, *Int. J. Heat Mass Transfer*, Vol. 48, pp.2955-2969.
- Wojtan, L., Ursenbacher, T. and Thome, J.R. (2005b).** Investigation of Flow Boiling in Horizontal Tubes: Part II – Development of a New Heat Transfer Model for Stratified-Wavy, Dryout and Mist Flow Regimes, *Int. J. Heat Mass Transfer*, Vol. 48, pp. 2970-2985.
- Xin, M. and Chao, Y. (1985).** Analysis and Experiment of Boiling Heat Transfer on T-shaped finned surfaces, Paper read at 23<sup>rd</sup> National Heat Transfer Conference, Denver, August 4-7; refer to Thome (1990) for description of paper on pp. 172-169.
- Xu, J., Gan, Y., Zhang, D. and Li, X. (2005).** Microscale Boiling Heat Transfer in a Micro-Timescale at High Heat Fluxes, *J. of Micromechanics and Microengineering*, Vol. 15, pp. 362-376.
- Xu, G.P., Tou, K.W. and Tso, C.P. (1998).** Two-Phase Void Fraction and Pressure Drop in Horizontal Crossflow Across a Tube Bundle, *J. Fluids Engineering*, Vol. 120, pp. 140-145.
- Yang, C.Y. and Shieh, C.C. (2001).** Flow Pattern of Air-Water and Two-Phase R134a in Small Circular Tubes, *Int. J. Multiphase Flow*, Vol. 27, pp. 1163-1177.
- Yan, Y.Y. and Lin, T.F. (1998).** Evaporation Heat Transfer and Pressure Drop of Refrigerant R-134a in a Small Pipe, *Int. J. Heat and Mass Transfer*, Vol. 41, pp. 4183-4194.
- Yan, Y.Y. and Lin, T.F. (2003).** Letter to Editors, Comments by R. L. Webb and J.W. Park and Reply by Y-Y Yan and T-F Lin, *Int. J. Heat Mass Transfer*, Vol. 46, pp. 1111-1113.
- Yashar, D.A., Wilson, M.J., Kopke, H.R., Graham, D.M., Chato, J.C. and Newell, T.A. (2001).** An Investigation of Refrigerant Void Fraction in Horizontal, Microfin Tubes, *HVAC&R Research*, Vol. 7, No. 1, pp. 67-82.
- Yen, T.-H., Shoji, M., Takemura, F., Suzuki, Y., and Kasagi, N. (2005).** Visualization of Convective Boiling Heat Transfer in Single Micro-Conduits with Different Shapes of Cross Sections, *Proc. 3rd Int. Conf. Microchannels and Minichannels (ICMM2005)*, Toronto, June 13-15, CD-ROM Paper No. ICMM2005-75228.
- Yen, T.-H., Shoji, M., Takemura, F., Suzuki, Y. and Kasagi, N. (2006).** Visualization of Convective Boiling Heat Transfer in Single Microchannels with Different Shaped Cross-sections, *Int. J. Heat Mass Transfer*, Vol. 49, pp. 3884-3894.
- Yoon, S.H., Cho, E.S., Kim, M.S. and Kim, Y. (2003).** Studies on the Evaporative Heat Transfer and Pressure Drop of Carbon Dioxide near the Critical Point, *21<sup>st</sup> IIR International Congress of Refrigeration*, Washington DC, USA.
- Yoon, S.H., Cho, E.S., Hwang, Y.W., Kim, M.S., Min, K. and Kim, Y. (2004).** Characteristics of Evaporative Heat Transfer and Pressure Drop of Carbon Dioxide and Correlation Development, *Int. J. Refrigeration*, Vol. 27, pp. 111-119.
- Yung, D., Lorenz, J.J. and Ganic, E.N. (1980).** Vapor/Liquid Interaction and Entrainment in Falling Film Evaporators, *J. Heat Transfer*, Vol. 102, No. 1, pp. 20-25.
- Yun, R., Choi, C. and Kim, Y. (2002).** Convective Boiling Heat Transfer of Carbon Dioxide in Horizontal Small Diameter Tubes, IIR/IIF-Commission B1, B2, E1 and E2, Guangzhou, China, pp.293-303.
- Yun, R. and Kim, Y. (2003a).** Two-Phase Pressure Drop of CO<sub>2</sub> in Mini Tubes and Microchannels, *Proc. First International Conference on Microchannels and Minichannels*, Rochester, NY, pp. 507-511.
- Yun, R. and Kim, Y. (2003b).** Critical Quality Prediction for Saturated Flow Boiling of CO<sub>2</sub> in Horizontal Small Diameter Tubes, *Int. J. Heat Mass Transfer*, Vol. 46, pp. 2527-2535.
- Yun, R. and Kim, Y. (2004).** Flow Regimes for Horizontal Two-Phase Flow of CO<sub>2</sub> in a Heated Narrow Rectangular Channel, *International Journal of Multiphase*, Vol. 30, pp. 1259-70.
- Yun, R., Kim, Y., and Kim, M.S. (2003).** Two-Phase Flow Patterns of CO<sub>2</sub> in a Narrow Rectangular Channel, *21<sup>st</sup> IIR International Congress of Refrigeration*, Washington DC, USA.

- Yun, R., Kim, Y. and Kim, M.S. (2005a).** Convective Boiling Heat Transfer Characteristics of CO<sub>2</sub> in Microchannels, *Int. J. Heat Mass Transfer*, Vol. 48, pp. 235-242.
- Yun, R., Kim, Y., and Kim, M.S. (2005b).** Flow Boiling Heat Transfer of Carbon Dioxide in Horizontal Mini Tubes, *Int. J. Heat Fluid Flow*, Vol. 26, pp. 801-809.
- Yun, R., Kim, Y., Kim, M.S. and Choi, Y. (2003).** Boiling Heat Transfer and Dryout Phenomenon of CO<sub>2</sub> in a Horizontal Smooth Tube, *Int. J. Heat Mass Transfer*, Vol. 46, pp. 2353-2361.
- Zeng, X., Chyu, M.-C. and Ayub, Z.H. (1994).** Characteristic Study of Sprayed Fluid Flow in a Tube Bundle, *ASHRAE Trans.*, Vol. 100, Part 1, pp. 63-72.
- Zeng, X., Chyu, M.-C. and Ayub, Z.H. (1995).** Evaporation Heat Transfer Performance of Nozzle-Sprayed Ammonia on a Horizontal Tube, *ASHRAE Trans.*, Vol. 101, Part 1, pp. 136-149.
- Zeng, X., Chyu, M.-C. and Ayub, Z.H. (1997).** Performance of Nozzle-Sprayed Ammonia Evaporator with Square-Pitch Plain-Tube Bundle, *ASHRAE Trans.*, Vol. 103, Part 2, Paper 4059.
- Zeng, X., Chyu, M.-C. and Ayub, Z.H. (1998).** Ammonia Spray Evaporation Heat Transfer Performance of Single Low-Fin and Corrugated Tubes, *ASHRAE Trans.*, Vol. 104, Part 1, Paper SF-98-15-2 (4109).
- Zhang, M. and Webb, R.L. (2001).** Correlation of Two-Phase Friction for Refrigerants in Small-Diameter Tubes, *Experimental Thermal Fluid Science*, Vol. 25, pp. 131-139.
- Zhang, W., Hibiki, T. and Mishima, K. (2004).** Correlation for Flow Boiling Heat Transfer in Mini-Channels, *Int. J. Heat Mass Transfer*, Vol. 47, pp. 5749-5763.
- Zhang, W., Hibiki, T., Mishima, K. And Mi, Y. (2006).** Correlation for Critical Heat Flux for Flow Boiling of Water in Mini-Channels, *Int. J. Heat Mass Transfer*, Vol. 49, pp. 1058-1072.
- Zhao, Y., Molki, M., Ohadi, M.M. and Dessiatoun, S.V. (2000).** Flow Boiling of CO<sub>2</sub> in Microchannels, *ASHRAE Transactions*, Vol. 106, Part I, pp. 437-445.
- Zivi, S.M. (1964).** Estimation of Steady-State Steam Void-Fraction by Means of the Principle of Minimum Entropy Generation, *J. Heat Transfer*, Vol. 86, pp. 247-252.
- Zuber, N. (1959).** Hydrodynamic Aspects of Boiling Heat Transfer, AEC Report AECU-4439, Physics and Mathematics.
- Zuber, N. and Findlay, J. (1965).** Average Volumetric Concentration in Two-Phase Flow Systems, *J. Heat Transfer*, Vol. 87, pp. 453.
- Zuber, N., Staub, F.W., Bijwaard, G. and Kroeger, P.G. (1967).** Steady State and Transient Void Fraction in Two-Phase Flow Systems, GEAP Report 5417.
- Žukauskas, A., and Ulinskas, R. (1983).** Banks of Plain and Finned Tubes, in *Heat Exchanger Design Handbook*, ed. E.U. Schlünder, Hemisphere Publishing Corp., Washington, D.C.
- Zun, I. (2007).** Numerical Modeling of Two-Phase Flows in Microchannels, 2<sup>nd</sup> Microscale Heat Transfer Shortcourse, Lausanne, June 4-8.
- Zun, I. and Polutnik, E. (2001).** Bubble to Slug Flow Transition: Experimental and Numerical Experience in Bubble Tracking Studies, 4<sup>th</sup> International Conference on Multiphase Flow, New Orleans, May 27 - June 1.
- Zürcher, O. (2000).** Contribution to the Heat Transfer Analysis of Substitute and Natural Refrigerants Evaporating in a Horizontal Plain Tube, Ph.D. thesis, Swiss Federal Institute of Technology Lausanne (EPFL), Switzerland.
- Zürcher, O., Favrat, D. and Thome, J.R. (2002).** Development of a Diabatic Two-Phase Flow Pattern Map for Horizontal Flow Boiling, *Int. J. Heat Mass Transfer*, Vol. 45, pp. 291-303.
- Zürcher, O., Thome, J.R. and Favrat, D. (1997a).** Flow Boiling and Pressure Drop Measurements for R-134a/Oil Mixtures Part 2: Evaporation in a Plain Tube, *HVAC&R Research*, Vol. 3, No. 1, pp. 54-64.
- Zürcher, O., Thome, J.R. and Favrat, D. (1997b).** Flow Boiling of Ammonia in Smooth and Enhanced Horizontal Tubes, *Compression Systems with Natural Working Fluids*, IEA Annex 22 Workshop, Gatlinburg, TN, USA, October 2-3.

- Zürcher, O., Thome, J.R. and Favrat, D. (1997c).** Prediction of Two-Phase Flow Patterns for Evaporation of Refrigerant R-407C inside Horizontal Tubes, Convective Flow and Pool Boiling Conference, Irsee, Germany, May 18-23, paper IX-1.
- Zürcher, O., Thome, J.R. and Favrat, D. (1998a).** Intube Flow Boiling of R-407C and R-407C/Oil Mixtures Part I: Microfin Tube, *HVAC&R Research*, Vol. 4, No. 4, pp. 347-372.
- Zürcher, O., Thome, J.R. and Favrat, D. (1998b).** Intube Flow Boiling of R-407C and R-407C/Oil Mixtures Part II: Plain Tube Results and Predictions, *HVAC&R Research*, Vol. 4, No. 4, pp. 373-399.
- Zürcher, O., Thome, J.R. and Favrat, D. (1999).** Evaporation of Ammonia in a Smooth Horizontal Tube: Heat Transfer Measurements and Predictions, *J. Heat Transfer*, Vol. 121, February, pp. 89-101.